The Physics of Compressible Turbulent Mixing

Editors
M. Legrand &
M. Vandenboomgaerde

The Physics of Compressible Turbulent Mixing

FOREWORD

The 10th International Workshop on the Physics of compressible Turbulent Mixing (IWPCTM) was held from the 17th to the 21st of July, 2006, in the Ecole Nationale Supérieure de Techniques Avancées in Paris, France.

The first Workshop was held in Princeton, NJ (USA) in 1988, followed by Pleasanton, CA (USA) in 1989, Royaumont (France) in 1991, Cambridge (UK) in 1993, Stony Brook, NY (USA) in 1995, Marseille (France) in 1997, St Petersburg (Russia) in 1999, Pasadena, CA (USA) in 2001 and Cambridge (UK) in 2004. The name IWPCTM was adopted in 1991.

These workshops are mainly devoted to the problems of hydrodynamic instabilities of different density fluid interfaces submitted either to a constant or varying acceleration (Rayleigh-Taylor Instability, RTI) or to an impulsive acceleration generated by a shock wave (Richtmyer-Meshkov Instability, RMI). These instabilities are studied at all stages, that is from the development of the initial small perturbation (linear phase) to the end of the process (turbulent mixing phase).

The total number of participants registered was 143. During the Workshop, 65 oral presentations have been given, and 62 posters have been exposed and discussed, and among these 127 papers, 83 are published in the present proceedings. Papers are classified by sender's name, in alphabetical order, for technical reasons.

The scientific committee meeting held on Thursday July 20th, 2006, decided that the 11th International Workshop on the Physics of Compressible Turbulent Mixing will be held in USA and will be chaired by Guy Dimonte (Los Alamos National Laboratory).

First of all, I would like to express my friendly thanks to my colleague Marc Vandenboomgaerde for doing so much in organizing the workshop.

My sincere gratitude goes to the Commissariat à l'Energie Atomique / Direction des Applications Militaires for contributing financial support essential to the operation of the workshop.

I would like especially to thank the Atomic Weapon Establishment (AWE, UK), the European Community on Flow, Turbulence and Combustion (ERCOFTAC, Europe), the Los Alamos National Laboratory (LANL, USA), the Lawrence Livermore Laboratory (LLNL, USA) and the Universitat Politecnica de Catalunya (UPC, Spain) for their rapid decision to support the organization of the 10th International Workshop on the Physics of Compressible Turbulent Mixing, financially.

I wish to thank all the members of the Local Organizing Committee and Mr M. Grangeon and Mr Ph. Mirveaux for their help in the organization of the workshop. I would like to thank the members of the Paper Selection Committee as well for their hard work.

Finally, I would like to express my gratefulness to the IWPCTM10 participants who contributed to making this workshop a real success.

Thank you.

February 2007
Michel Legrand

The 10th IWPCTM was held from the 17th to the 21st of July 2006 in the Ecole Nationale Supérieure de Techniques Avancées (ENSTA) in Paris (France).

S CIENTIFIC C OMMITTEE

M. Andrews (Texas A&M University)
G. Ben-Dor (Ben-Gurion University of the Neguev, Beer-Sheeva)
D. Besnard (CEA)
S. Dalziel (University of Cambridge)
G. Dimonte (LANL)
S. Gauthier (CEA)
J. Glimm (Stony Brook)
B. Goodwin (LLNL)
J.-F. Haas (CEA)
R. Holmes (LANL)
L. Houas (IUSTI)
J. Jacobs (University of Arizona)
Yu. Kucherenko (Russian Federal Nuclear Center-VNIITF)
M. Legrand (CEA)
D. Meiron (Caltech)
E. Meshkov (Russian Federal Nuclear Center-VNIIEF)
P. Miller (LLNL)
V. Neuvazhaev (Russian Federal Nuclear Center-VNIITF)
J. Redondo (Universitat Politecnica de Catalunya, Barcelona)
V. Rozanov (Lebedev Physical Institute, Moscow)
O. Schilling (LLNL)
D. Sharp (LANL)
D. Shvarts (Nuclear Research Center, Beer-Sheeva)
E. Son (Moscow Physical and Technical Institute)
H. Takabe (University of Osaka)
K. Takayama (Tohoku University, Sendai)
R. Williams (AWE)
D. Youngs (AWE)
S. Zaytsev (ENIN, Moscow)

PAPER SELECTION COMMITTEE

- S. Bouquet (CEA)
- C. Cherfils-Clérouin (CEA)
- B. Desjardins (CEA)
- J.-F. Haas (CEA)
- L. Houas (IUSTI)
- J. Redondo (Universitat Politecnica de Catalunya, Barcelona)
- D. Souffland (CEA)

LOCAL ORGANIZING COMMITTEE

- D. Besnard (CEA)
- S. Bouquet (CEA)
- M. Brusy (CEA)
- J.-F. Haas (CEA)
- N. James (CEA)
- M. Legrand (CEA) Chairman
- J. Redondo (Universitat Politecnica de Catalunya, Barcelona)
- M. Vandenboomgaerde (CEA)

FINANCIAL SUPPORT ORGANIZATIONS

We gratefully acknowledge the following organizations for their financial support of the accomplishment of the 10th IWPCTM:

- Atomic Weapon Establishment
- Commissariat à l'Energie Atomique / Direction des Applications Militaires
- European Community on Flow, Turbulence and Combustion
- Lawrence Livermore Laboratory
- Los Alamos National Laboratory
- Universitat Politecnica de Catalunya

Papers are classified by sender's name, in alphabetical order, for technical reasons.

Contents

e-mail: `almarcha@irphe.univ-mrs.fr`

Use of boundary integral methods for classical and ablative Rayleigh-Taylor instabilities

Christophe ALMARCHA[1], Paul CLAVIN[1], Laurent DUCHEMIN[1] and Christophe JOSSERAND[2]

[1] *Institut de Recherche sur les Phénomenes Hors Equilibre, UMR 6594, CNRS-universités d'Aix Marseille I & II*
49, rue Joliot-Curie, BP 146, technopôle de Château-Gombert, 13384 Marseille cedex 13, FRANCE
[2] *Laboratoire de Modélisation en Mécanique, Université Pierre et Marie Curie UMR CNRS 7607*
tour 55/65, 4 place Jussieu 75005 PARIS FRANCE
josseran@lmm.jussieu.fr

Abstract: The instability of ablation fronts strongly accelerated towards the dense medium under the conditions of inertial confinement fusion (ICF) is addressed in the limit of an infinitely large density ratio, or in the limit of a strong dependance of conductivity on temperature. An analysis [1] shows that flows on both sides of the ablation front are irrotational to first order, reducing the nonlinear analysis to a two-potential flows problem. Vorticity appears at the following orders in the perturbation analysis. This result gives the possibility of using boundary integral methods and opens new perspectives in the nonlinear theory of ablative RT instability in ICF. Examples of 2D simulations with several initial conditions are presented. We also investigate the occurrence of a finite time singularity in the slope of the ablation front.

These accurate boundary integral methods are also used to investigate long time numerical simulations of the inviscid Rayleigh-Taylor instability with Atwood number equal one [2]. In this case, They allow us to attain the spike asymptotic behavior predicted by theoretical analysis [3]. In particular we observe that the spike's curvature evolves like t^3 while the overshoot in acceleration shows a good agreement with the suggested $1/t^5$ law. Moreover, consistent results for the prefactor coefficients of the asymptotic laws are obtained. Eventually we exhibit the self-similar behavior of the interface profile near the spike.

1 INTRODUCTION

Inertial confinement fusion aims at imploding a spherical shell of deuterium tritium thanks to high power laser radiation, in order to rise the conditions of high density and temperature required for ignition of nuclear reactions. To do so, the conservation of spherical geometry is crucial but a hydrodynamic instability comparable to Rayleigh-Taylor instability develops and breaks the symmetry. In compression stage, an equivalent centripetal gravity destabilizes a thin layer of density gradient (ablation front) followed by a thermal wave created by laser energy deposition. Although some linear models developed last decades accurately describe the first stages of destabilization ([9] [10] [11]), a non-linear simple model for larger amplitudes is still required. Such a model has already been developed for pure Rayleigh-Taylor instability and we present here an extension to ICF configuration, in the limit of strong density jump at ablation front or in the limit of a strong dependence of conductivity on temperature. This model is particularly interesting due to the related potential behavior of the flow. It allows to use Boundary integral methods which are simple to use and much powerful when precision is required. In chapter 1, the power of the method is demonstrated through the study of late time development of Rayleigh-Taylor instability. Chapter 2 deals with a model for the non linear development of this instability in ICF, with the appearance in simulations of a singularity on the shape of the front.

2 ACCURACY OF THE METHOD IN PURE RAYLEIGH-TAYLOR INSTABILITY

2.1 Necessity of an accurate numerical method

The pure Rayleigh-Taylor problem has been studied for decades. A single-mode simplified assumption has been used by Layzer [7] to study the long-time asymptotic bubble behavior. The results obtained have been confirmed by many numerical simulations. Such a simplified hypothesis cannot be used when focusing on the spike asymptotic behavior. This is a reason why models of spikes have been recently developed [3]. The main

hypothesis they use is a free fall approximation for the spike with quasi steady assumption of the potential flow. Under such conditions, an evolution of the spike curvature like t^3 has been predicted with an overshoot in $1/t^5$ towards gravity acceleration.

To confirm predictions of these models, an accurate method was necessary. The choice of a boundary integral method was quite natural because of the potential hypothesis for the flow and the necessity to reach the high amplitudes of the interface required to see the asymptotic behavior. Thanks to potential flow assumption, dimensions of the problem to be solved are reduced by one. Indeed, knowing the velocity on the surface of a closed domain is enough to determine the flow everywhere inside. 2D simulations were performed using cauchy theorem, following the early work [4].

2.2 Boundary integral method principle

We investigate physical problems which are periodics in the horizontal direction. Using the conformal map e^z (figure 2.1)we transform the fluid domain into a closed domain where we can apply the following Cauchy theorem. Considering the complex potentiel $\beta = \phi + i\psi$ giving the complex velocity $\frac{\partial \beta}{\partial z} = u - iv$, we write Cauchy theorem for a point z_0 outside the closed boundary :

$$\oint \frac{\beta(z)}{z - z_0} dz = 0 \qquad (2.1)$$
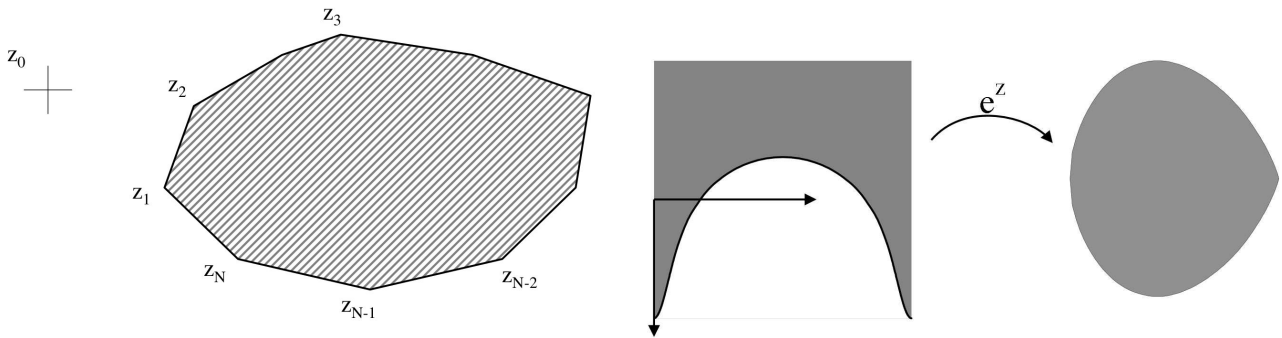
Fig. 2.1. closed domain of the flow and conformal mapping

When considering the domain in figure 2.1 delimited by N nodes, we can write the cauchy theorem N times for a point z_0 reaching each point of the contour. The potential is considered continuous and linear between each point of the surface. It gives us a system of N equations envolving the real and imaginary parts of the complex potential at each point. Knowing the real part of the complex potential we deduce the imaginary part. Then, the normal velocity at the interface is the derivative along the boundary of the imaginary part of complex potential and the tangential velocity at the interface is the derivative along the boundary of the real part of complex potential. This way, the knowledge of the potential function on the boundary provides us with the flow everywhere inside the domain through solving a system. This can be done by a standard triangular decomposition or with an iterative method.

2.3 Application to Rayleigh-Taylor instability with A=1

We choose a configuration with vertical coordinate ξ pointing the same direction as gravity g, with ξ_f the vertical coordinate of the interface. The fluid location is at $\xi < \xi_f$ The non dimensional equations to solve are:

the kinematic condition at the interface that says that the normal velocity of the flow equals the velocity of the interface: $n.\nabla\phi = U_n^f$

the potential hypothesis:$\Delta\phi = 0$ for $\xi < \xi_f$

the assumption of no perturbation at infinity: $\phi_{\xi \to -\infty} = 0$

the Bernoulli equation: $[\frac{\partial\phi}{\partial\tau} + \frac{(\nabla\phi)^2}{2}]_{\xi=\xi_f} = \xi_f$ that updates in time the value of the potential function on interface

It remains to know the new values of velocities when knowing the new value of potential after iteration in time with Bernoulli equation. This is done with boundary integral method. But as mentioned before, this method applies to a closed contour. The interface in Rayleigh-Taylor problem is 2π periodic. So we transform a period into a closed domain thanks to a conformal mapping (figure 2.1) that transforms the coordinate z into e^z, with the main advantage that the precision is then extended around the spike.

With all the equations and methods required we perform the simulation of Rayleigh-Taylor instability with Atwood number A=1. The iteration in time is performed with a fourth-order Runge-Kutta algorithm.

Several results are reported below. Simulations Started with a small amplitude sine-mode. The asymptotic bubble speed is close to the classical Layzer result as expected ($\sqrt{\frac{g}{3k}}$). The spike asymptotic acceleration reaches gravity, confirming the assumption of [3]. The predicted asymptotic spike curvature going like t^3 was also confirmed, with the t^-5 overshoot in acceleration (see 2.2). See [2] for more details.
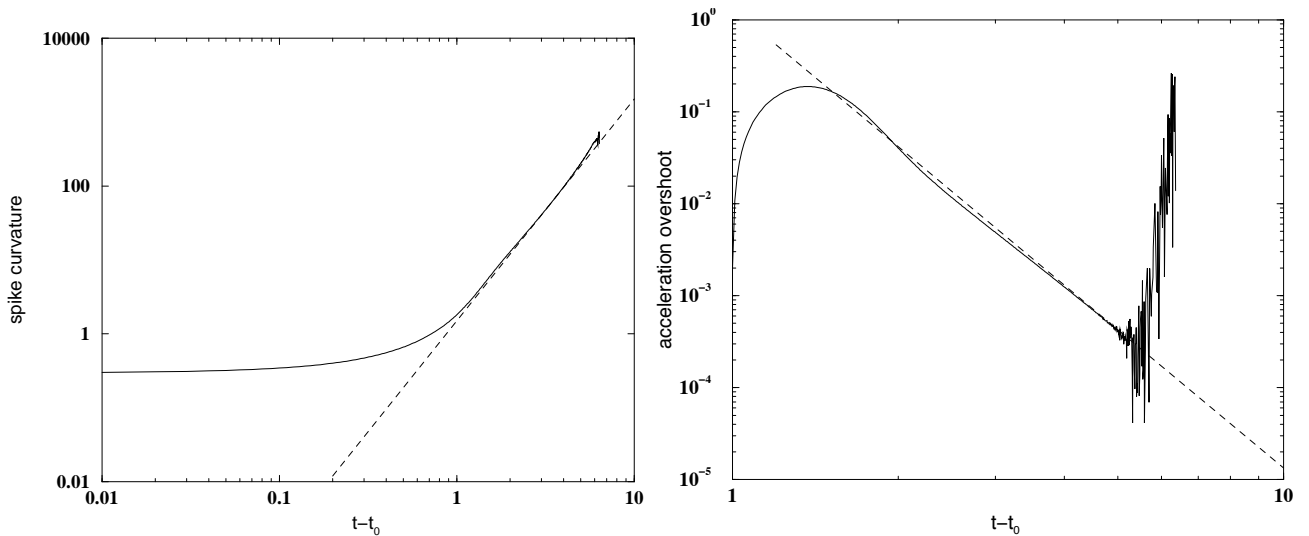
Fig. 2.2. curvature evolution and overshoot in acceleration (from [2])

3   SIMPLIFICATIONS IN ICF: A DOUBLE POTENTIAL MODEL

When considering sketches of density and temperature along the radius of the shell in Inertial Confinement Fusion, a jump of density is clearly visible on a small distance: this is the ablation front. Its behavior is comparable to Rayleigh-Taylor instability, especially for disturbances with a wavelength larger then the ablation width. The flow upstream the front can be considered as potential but the flow downstream does have a rotational part due to deflection of streamlines through the interface. However, in the limit of an infinite density jump at ablation front (Sharp Boundary Model with infinite jump in density), the rotational part, which is of order of the inverse of the density jump, can be neglected [1]. The temperature, which is uniform upstream, satisfies a laplacian equation downstream and follows exactly the flow. The system of equations obtained is decribed below (ϕ_- and ϕ_+ are the reduced potential on each side of the front and ξ is the reduced coordinate):

On the cold side, (subscript "-"): $\Delta\phi_- = 0$ and $\lim_{\xi\to-\infty}\phi_- = 0$

On the hot side, (subscript "+"): $\Delta\phi_+ = 0$ and $\phi_+ \overset{\xi\to\infty}{\sim} \xi$

$\phi_+ |_{\underline{\xi}=\underline{\xi}_f} = 0$ (the flow dowstream is normal to the front)

$\underline{n}.\underline{\nabla}\phi_- |_{\underline{\xi}=\underline{\xi}_f} = U_n^f$ (kinematic condition)

$[\frac{\partial\phi_-}{\partial\tau} + \frac{|\underline{\nabla}\phi_-|^2}{2} + \frac{|underline\nabla\phi_+|^2}{2}]_{\underline{\xi}=\underline{\xi}_f} = \xi_f$, (Bernoulli revisited)

Such a system of equations can also be derived in another limit. Indeed, in such Sharp Boundary Model an arbitrary constant (jump density at the front) has been introduced. Similar equations have also been obtained in a self-consistent model from the basic equations in the limit of a strong sensitivity of the thermal conduction to temperature variations ($\lambda \sim T^\nu$ with $\nu \to \infty$). Taking the infinitesimal parameter $\epsilon = (\frac{Fr^{-1}}{\nu})^{\frac{1}{\nu-1}}$ in the

limit of large ν, the same system of equations is obtained [5]. Under these considerations, an adaptation of the numerical study of Rayleigh-Taylor instability can be easily found for ICF problem.

3.1 numerical simulations of ICF problem and occurrence of a finite-time singularity

The resolution is pretty similar to the one for Rayleigh-Taylor instability. The potential flow on the hot side being solved thanks to a boundary integral method too, the velocities on both sides of the front are calculated. Iteration in time is then made in new Bernoulli equation thanks to a fourth order Runge-Kutta algorithm. If necessary, redistribution of points on surface is made thanks to a spline interpolation method.
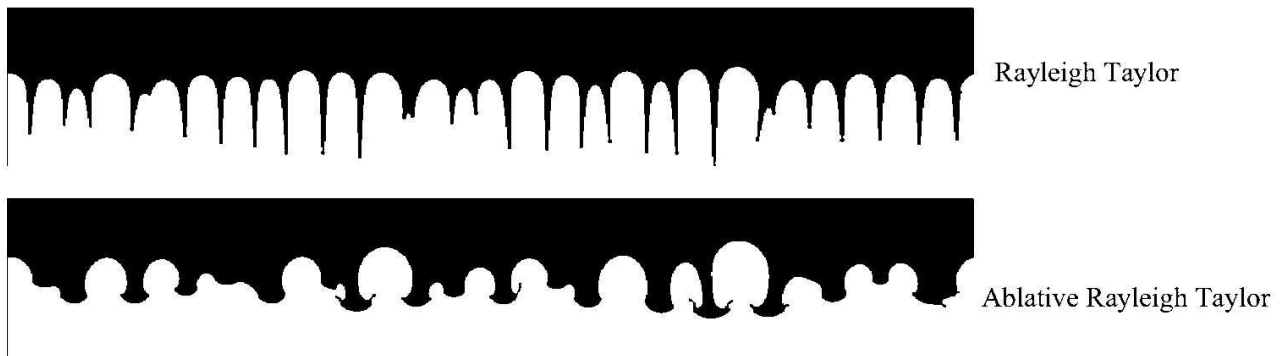
Fig. 3.3. Bubble competition. comparison of late time simulations in pure Rayleigh-Taylor configuration and ICF configuration
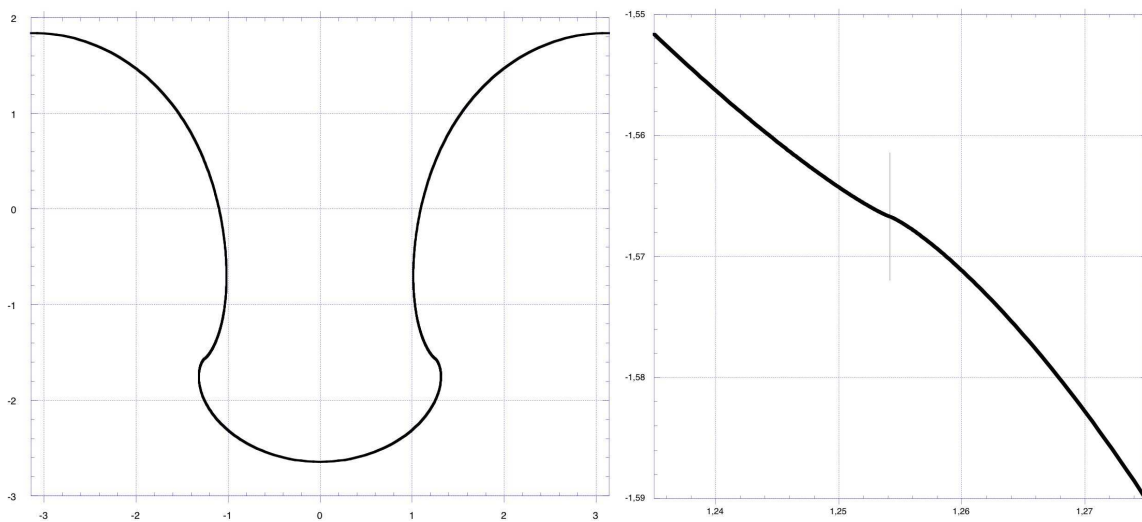
Fig. 3.4. shape of the front (and zoom near inflection point) close to singularity time

The simulations shown in figure 3.3 were performed with 1000 points equally distributed along a period of the interface. This cannot allow to describe with enough precision the diverse derivatives of the front. When focusing on the curvature in a simulation of one period, a singularity develops and diverges in finite time, as shown in figures 3.4 and 3.5. It appears exactly at an inflexion point, around which curvature rises a positive maximum and a negative minimum, with diverging values. These extrema are located closer and closer to the inflexion point as time reaches singularity time. Thanks to a redistribution of points around the singularity in order to get better accuracy, an asymptotic behavior has been identified on 3 orders of magnitude in $t' - t$, t' being the singularity time. the asymptotic behavior of maximum curvature C_{max}, minimum curvature C_{min}, and the distance between them δ_s , respectively called "Maximum", "minimum" and "length" on figure 3.5),
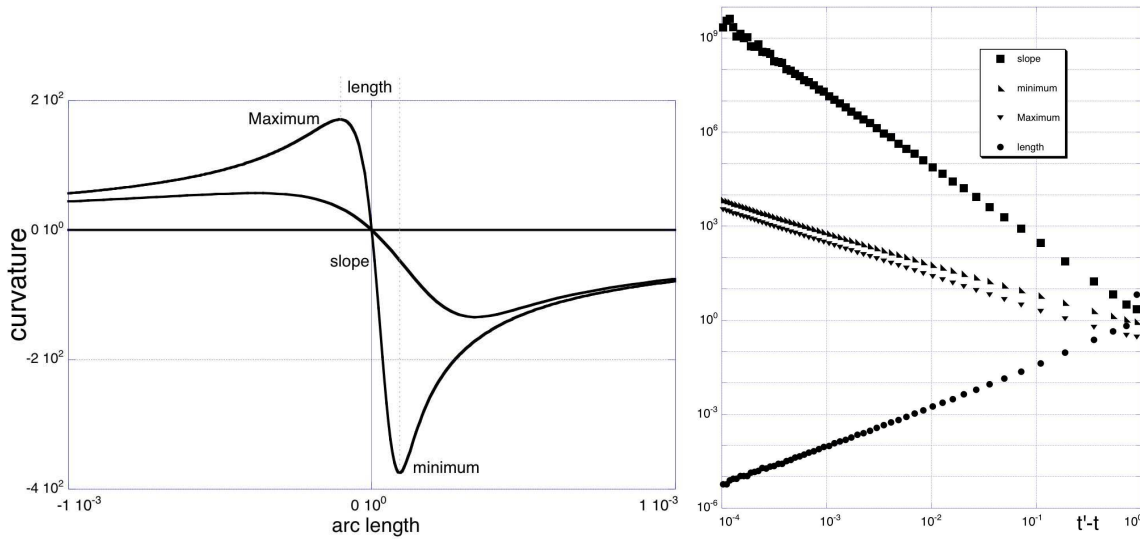
Fig. 3.5. sketches of curvature along the arc length around the inflexion point (left) and asymptotic behavior of curvature characteristics close to singularity time (right)

are found to scale like:

$$C_{max} \sim (t' - t)^{-1} \tag{3.1}$$

$$C_{min} \sim (t' - t)^{-1} \tag{3.2}$$

$$\delta_s \sim (t' - t)^{4/3} \tag{3.3}$$

$$\frac{dC}{ds}_{max} \sim (t' - t)^{-7/3} \tag{3.4}$$

Such singular behavior is close to the one occurring in Kelvin-Helmholtz instability, although equations are quite different [6]. Moreover, when rescaling curvature by $(t' - t)^1$ and lengths by $(t' - t)^{-4/3}$, a self-similar behavior can be observed. This singularity is actually under study but It seems to disappear when a small surface tension-like effect is introduced in equations. Such a term may appear at the following order in the non-linear system, due to the finite thickness effect of the curved front (see [8]).

4 SUMMARY

Boundary integral methods have been successfully used in order to simulate late time asymptotic evolution of two-dimensional bubble and the spike in classical Rayleigh-Taylor instability, and to simulate non-linear stages of ablative Rayleigh-Taylor instability. Two different models provide us with the same system of equations. Thanks to it, fronts in ICF are easily studied until the sudden formation of a singularity in front curvature, which disappears when introducing terms at the following order.

REFERENCES

[1] Clavin, P. and Almarcha, C. 2005, Ablative Rayleigh-Taylor instability in the limit of an infinitely large density ratio. *C. R. Mécanique* **33**, pp. 379-388.

[2] Duchemin, L., Josserand, C. and Clavin, P. 2005, Asymptotic behavior of the Rayleigh-Taylor instability, *Phys. Rev. Lett.* **94**, 224501

[3] Clavin, P. and Williams, F. 2005, Asymptotic spike evolution in Rayleigh-Taylor instability, *J. Fluid. Mech.* **525**, pp 105-113

[4] Vinje, T and Brevig, P. 1980, Breaking Waves on Finite Water Depths: A Numerical Study, *Norwegian Institute of Technology*

[5] Almarcha, C., Clavin, P., Duchemin, L., Sanz, J. 2005, Ablative Rayleigh-Taylor instability with strong temperature dependance of the thermal conductivity. *J. Fluid. Mech.* to be published

[6] Moore, D.W. 1979, The spontanous appearance of a singularity in the shape of evolving vortex sheet. *Proc.Roy.Soc.* , pp 105-119

[7] Layzer, D. 1955, On the instability of superimposed fluids in a gravitational fiel. *Astrophys. J.***122** , pp 1-12

[8] Pelc, P. and Clavin, P. 1982, Influence of hydrodynamics and diffusion upon the stability limits of laminar premixed flames. *J. Fluid. Mech.***124** , pp 219-237

[9] Betti, R., Goncharov, V., McCrory, R. L. and Verdon, C.P. 1995, Self consistent cutoff wave numbers of the Rayleigh-Taylor instability. *Phys. Plasmas***2** , pp 3844-3851

[10] Sanz, J. 1994, Self-consistent analytical model of the Rayleigh-Taylor instability in inertial confinement fusion. *Phys. Rev. Lett.***73** , pp 2700-2707

[11] Sanz, J., Masse, L. and Clavin, P. 2006, The Darrieus-Landau and Rayleigh-Taylor instabilities in inertial confinement fusion revisited. *Phys. plasma***13** , 102702

e-mail: `a.j.aspden@damtp.cam.ac.uk`

Monotone Integrated Large Eddy Simulation of Buoyant Turbulent Jets With Off-Source Heating

A. J. ASPDEN[1], N. NIKIFORAKIS[1] and S. B. DALZIEL[1]

[1] *Department of Applied Mathematics and Theoretical Physics, University of Cambridge, CB3 0WA, UK*

Abstract: Monotone Integrated Large Eddy Simulation (MILES) is becoming increasingly popular for simulating turbulent mixing, particularly in Rayleigh-Taylor and Richtmeyer-Meshkov flows. It is a form of LES designed to capture inherently the correct flow of energy through the inertial range and the decay at the grid-scale cut-off. The method does not use an explicit turbulence model and hence makes no assumptions about the structure of the flow. This paper addresses the applicability of the MILES approach for simulating turbulent mixing in the context of buoyant turbulent jets. It is well documented that different values for the coefficient in Taylor's entrainment model have to be used to capture correctly the observed spread rates in turbulent jets and plumes. In a buoyant turbulent jet there is a transition from a jet-like region near the source, to a plume-like region in the far field, and various models have been proposed to interpolate the entrainment coefficient between these two regions. Similarly, in a buoyant atmospheric plume the latent heat release due to condensation of water vapour provides a secondary source of buoyancy away from the origin of the plume, resulting in a change in entrainment behaviour. Bhat and Narasimha (1996) reproduced analogous off-source heating in the laboratory by using electrodes to heat an acidic jet in a deionised ambient. A series of numerical experiments have been conducted to simulate the above flows with the aims of assessing the MILES approach in this context, and increasing the understanding of the entrainment mechanism and the assumptions made in constructing an appropriate analytical model.

1   INTRODUCTION

The principle aim of this paper is to use numerical simulation to investigate the entrainment of fluid into turbulent jets, and the response due to volumetric heating. Entrainment is conventionally modelled using Taylor's entrainment hypothesis, introduced in Morton, Taylor and Turner [7], and states that the rate at which ambient fluid is entrained into the jet at each streamwise station is proportional to a characteristic velocity within the jet, usually taken to be the centreline velocity at that streamwise station. This entrainment hypothesis has been applied successfully in many applications, see Turner [10] for a review. The constant of proportionality, the entrainment coefficient, is found to take different values in jets and plumes, and can vary more substantially in non-canonical situations.

This study is motivated by cloud formation by condensation in atmospheric plumes, where the introduction of buoyancy due to an associated latent heat release significantly modifies the entrainment behaviour. Based on the entrainment hypothesis, the acceleration of the fluid due to the enhanced buoyancy should lead to an increase in entrainment. However, photographs of cumulus clouds (see Scorer [9], for example) depict tall vertically-sided clouds, which suggests a decrease in entrainment results, and field observations (see Paluch [8], for example) indicate that it is reduced almost to zero. By considering the effects of turbulent momentum flux, J. C. R. Hunt [6] proposed that any positive forcing, such as buoyancy, should lead to an increase in entrainment, but a increase in relative turbulent intensity could lead to a decrease in entrainment.

To study the problem Bhat, Narasimha and Arakeri [4] pioneered a laboratory analogue of the problem. An acidic aqueous jet was injected into a deionised ambient, and electrodes were used to selectively heat the conducting jet fluid. Bhat and Narasimha [3] (henceforth referred to as BN) report a dramatic change in structure of the jet, along with a drastic reduction in the spread rate and mass flux. It was concluded that a constant entrainment coefficient was not valid for this flow. Furthermore, a decrease in the relative turbulent intensity was observed, and so it was concluded that Hunt's proposal was not verified by these results. More recently, the experiments have been repeated with more detailed diagnostics by Agrawal and Prasad [1] (henceforth referred to as AP), including measurements of the temperature field. An increase in relative turbulent intensity was reported, supporting the argument of Hunt [6].
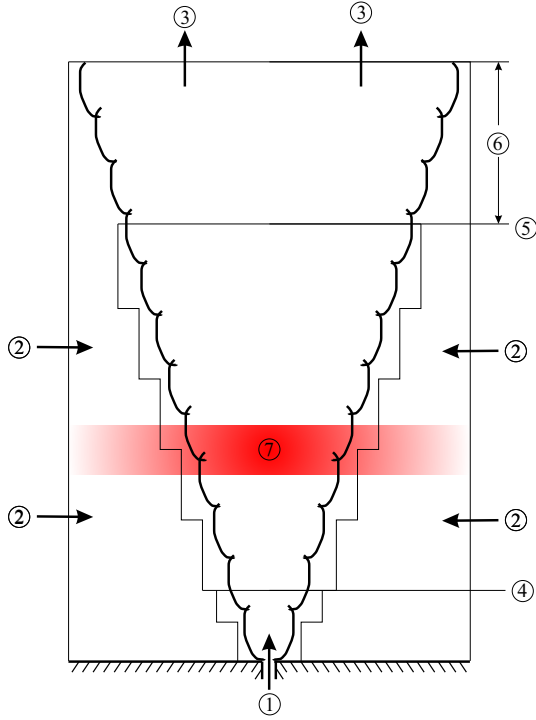
(1) Source of momentum.

(2) Transmissive boundary conditions allow for the entrainment of ambient fluid without inducing a large recirculation.

(3) Transmissive upper boundary condition allows fluid to pass out of the domain.

(4) Two levels of AMR are used below here to resolve the nozzle.

(5) One level of AMR is used below here to resolve the similarity region.

(6) A buffer zone is specified at the top of the domain to reduce the impact of the imperfect upper boundary condition.

(7) The heat injection zone (HIZ), where heating is applied proportional to the tracer concentration.

Fig. 2.1. Schematic of the computational configuration for spatially evolving turbulent heated jets.

Closer inspection of the analysis reveals two important factors that have to be addressed before the argument can be applied to this problem. Firstly, it is assumed that the mean momentum flux remains constant, which cannot be true in this case. Secondly, self-similarity is assumed to relate the centreline relative turbulent intensity to the turbulent momentum flux. Consider the jet width (b), mean and turbulent velocities ($\bar{u}_z$ and $\overline{u_z'^2}$), mean mass flux (Q), mean and turbulent momentum fluxes ($\bar{M}$ and M'), and forcing term (F) through two planes at heights z_1 and z_2. Then following Hunt [6] it is possible to relate the change in mass flux through the expression

$$\frac{Q_2}{Q_1} = \frac{b_2}{b_1}\sqrt{\lambda}, \qquad \text{where} \qquad \lambda = 1 + \left(\frac{1}{\bar{M}_1}\int_{z_1}^{z_2} F \, \mathrm{d}z\right) - \left(\frac{M_2' - M_1'}{\bar{M}_1}\right). \tag{1.1}$$

From this, Hunt deduced that any positive forcing F would lead to an increase in entrainment, whereas an increase in the relative turbulent intensity will result in a decrease in entrainment. Dropping the assumptions of constant mean momentum flux and self-similarity, a decrease in entrainment may be expected from positive values of $\bar{M}^{-1}\mathrm{d}M'/\mathrm{d}z$ instead of an increase in $\overline{u_z'^2}/\bar{u}_z^2$.

In this paper, numerical simulations are conducted following the laboratory experiments of turbulent jets with off-source heating. The data are then used to investigate the reappraisal of Hunt's theory presented above, and to examine the behaviour observed in the experiments.

2   SIMULATIONS

Due to the broad range of time and length scales involved in turbulent jets, a fully-resolved direct numerical simulation is prohibitively expensive, and so different a approach is required to circumvent this issue. One such approach, introduced by Boris *et al.*, is to take a finite-volume approach with a carefully constructed scheme so that the inviscid cascade of energy from large to small scales is well captured and dissipated at the grid scale cut-off by the inherent truncation error. Since the cell-averaging can be considered an implicit filter, and the truncation error an implicit sub-grid scale model, this approach forms a natural form of large eddy simulation, which has come to be known as Monotone Integrated Large Eddy Simulation, or more generally as Implicit Large Eddy Simulation. A more extensive discussion of the approach can be found in Grinstein and Fureby [5], for example. In high Reynolds number turbulent jets, the specific details of viscous dissipation are

Unheated jet	Type I $\alpha_c = 0.5$	Type I $\alpha_c = 2$	Type I $\alpha_c = 4$	Type II $\alpha_c = 2$
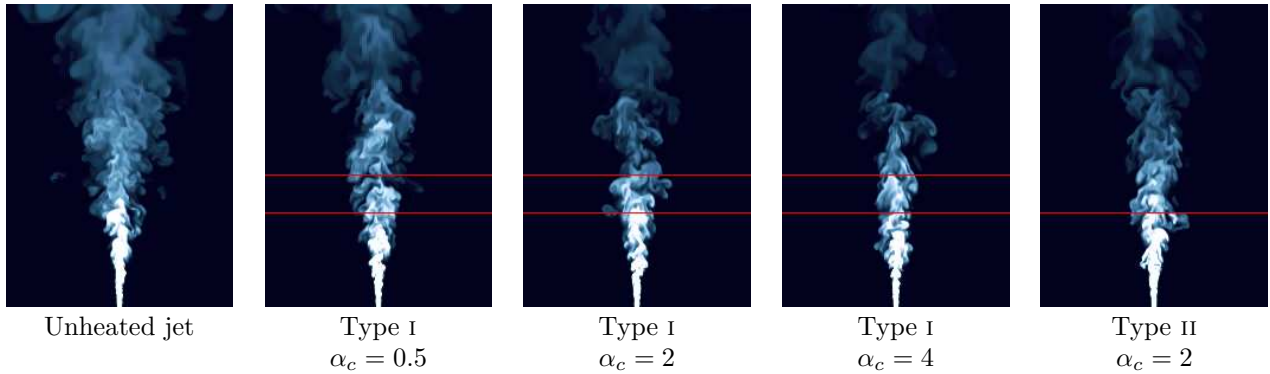
Fig. 3.2. Heated Jets: Instantaneous plots of tracer concentration through vertical slices through the axis of the different heated jets. Left to right are pure jet, low heating ($\alpha_c = 0.5$), intermediate heating ($\alpha_c = 2$), high heating ($\alpha_c = 4$), and type II heating.

not important and dominated by the Reynolds stresses. Therefore, the MILES approach is particularly suited to free shear flows.

The numerical code used in the present study is IAMR, which was written at the Center for Computational Sciences and Engineering at the Lawrence Berkeley National Laboratory. It uses a second-order projection method to solve the Navier-Stokes equations, is capable of Adaptive Mesh Refinement (AMR) and is parallelised. A fractional-step scheme is used, specifically a two-step predictor-corrector method. The equations are solved along with any relevant source terms for updated scalar quantities and an intermediate velocity field. This velocity field may not be divergence free, and so a projection step is taken to enforce the constraint. The details of the AMR method and the development of the algorithm can be found in Almgren *et al.* [2], and the references therein. The buoyancy due to heating was captured using the Boussinesq approximation, and so the equations of motion used are

$$\nabla \cdot \mathbf{u} = 0 \tag{2.1}$$

$$\left(\frac{\partial}{\partial t} + \mathbf{u} \cdot \nabla\right) \begin{pmatrix} \mathbf{u} \\ T \\ c \end{pmatrix} = \begin{pmatrix} -\nabla P + \alpha_T T \mathbf{e}_z \\ Q \\ 0 \end{pmatrix}, \tag{2.2}$$

where $\mathbf{u}$ is the three-dimensional velocity, P is the pressure, α_T is coefficient of thermal expansion, T is the temperature, c is a tracer used for the heat injection Q, which is injected proportional to the tracer concentration by setting $Q = \alpha_c c$ in the heat injection zone (HIZ), and zero elsewhere, where α_c is the heating rate.

Figure 2.1 shows a schematic of the computational set-up. The domain size was $48d \times 48d \times 64d$, where d is the jet nozzle diameter. Two levels of AMR were used to move the boundaries away from the region of interest without prohibitively increasing the computational expense. The first level of AMR was restricted to a vertical extent of $45d$ so that there was a large buffer zone at the top of the domain to reduce the effect of the imperfect upper boundary condition. The second level of AMR was used to resolve the nozzle. The base grid had a resolution of $96 \times 96 \times 128$ and each level of AMR had a refinement factor of 2. This configuration was found to be adequate to establish a region within the domain in which the mean and turbulent statistics were comparable with a self-similar turbulent jet. Two different types of heated simulations were run. Firstly, the HIZ was placed between $20d$ and $28d$, and will be referred to as type I heating. Secondly, heat was injected at all heights above $20d$, and will be referred to as type II heating. Three different heating rates were used for the type I heating ($\alpha_c = 0.5$, 2, and 4), and one heating rate used for type II ($\alpha_c = 2$).

3   RESULTS

3.1   Comparison with laboratory experiments

Figure 3.2 shows vertical slices through the axis for each of the simulations. On the left is the unheated jet, where the natural spread rate can be see. The middle three plots depict the type I heating, increasing in heating rate left to right. The right-hand plot shows the type II heating. The horizontal lines define the heat injection
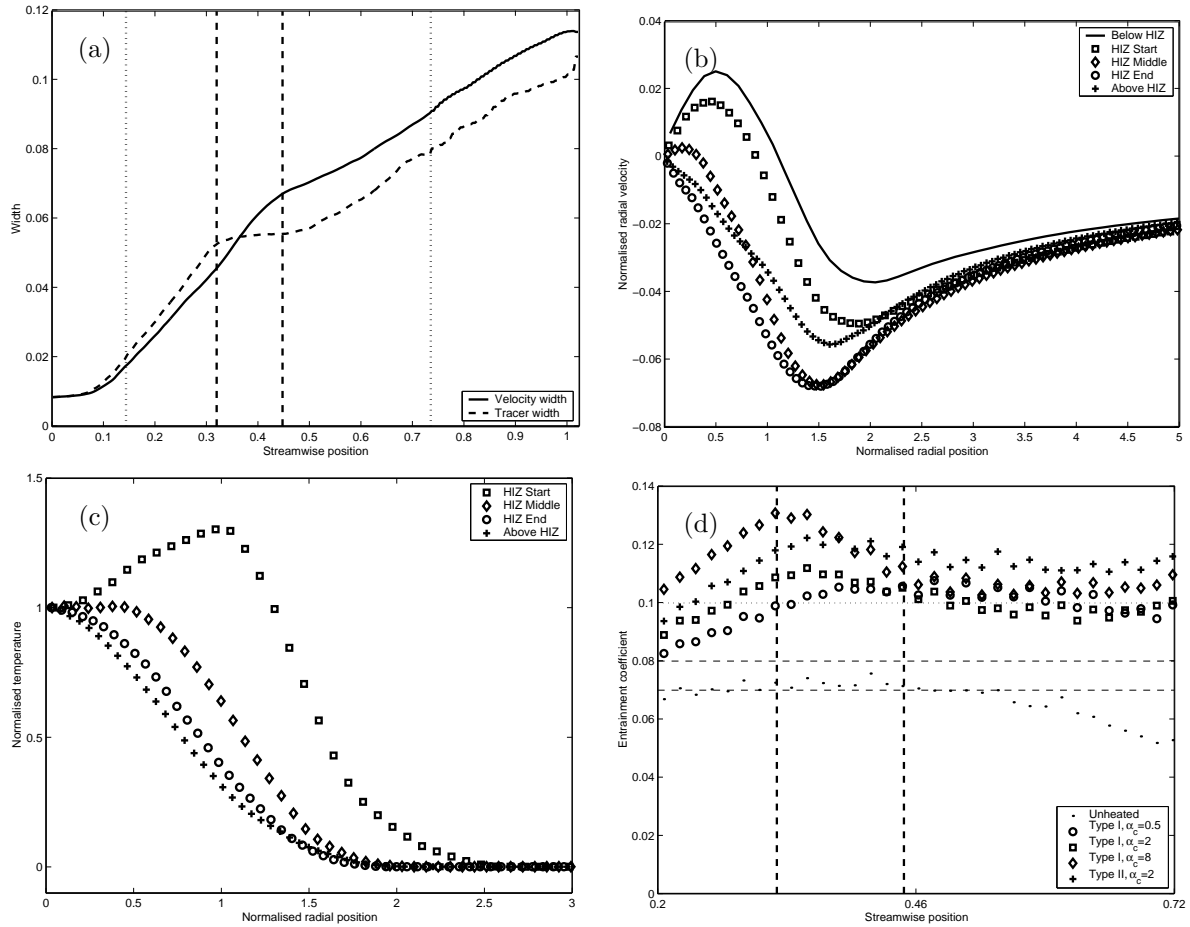
Fig. 3.3. (a) Streamwise evolution of the widths of the mean velocity and tracer profiles. Type I, $\alpha_c = 2$. Vertical dashed lines denote the HIZ, vertical dotted lines denote coarse-fine boundaries. (b) Radial profiles of normalised mean radial velocity at different heights. Type I, $\alpha_c = 2$. (c) Radial profiles of normalised mean temperature profiles at different heights. Type I, $\alpha_c = 2$. (d) Streamwise evolution of the entrainment coefficient for the different cases. Horizontal dashed lines denotes the range of values reported in jet experiments, and the dotted line shows a lower bound for plumes, the upper bound is around 0.16.

zones. The decrease in spread rate is very clear, and at the highest heating rate, the jet radius can actually decrease. This is consistent with the experimental results of both BN an AP.

The visual thinning is reflected by the tracer width shown in figure 3.3(a), where the velocity width is also shown, both are for the type I, $\alpha_c = 2$, case. These widths are defined as the distance from the axis where the mean is e^{-1} times the centreline mean value. In stark contrast to the thinning of the tracer width, the velocity width spread rate increases at the beginning of the HIZ, and only decreases at the top of the HIZ. Similar results are observed in the other heating cases and is also the same as that observed in the laboratory experiments of BN and AP.

The cause of the visual thinning is the change in behaviour of the mean radial velocity, shown in figure 3.3. The profile below the HIZ, characteristic of an unheated jet, has an outflow near the axis and the entrainment inflow outside the jet. Upon heating, the profile changes to inflow at all radial positions, as was found to be the case in the laboratory experiments of AP. The heat injection accelerates the jet fluid upwards, and to satisfy continuity fluid is drawn inwards, primarily laterally, which carries the tracer towards the axis resulting in a reduced visual spread rate.

Radial profiles of the normalised mean temperature are shown in figure 3.3(c). As reported by AP, at the beginning of the HIZ, the peak temperature lies away from the axis. This off-axis peak results from a competition between the tracer concentration and residence time in the HIZ. The fluid near the axis has a high tracer concentration and so experiences strong heating, but it is also travelling more quickly than fluid at larger
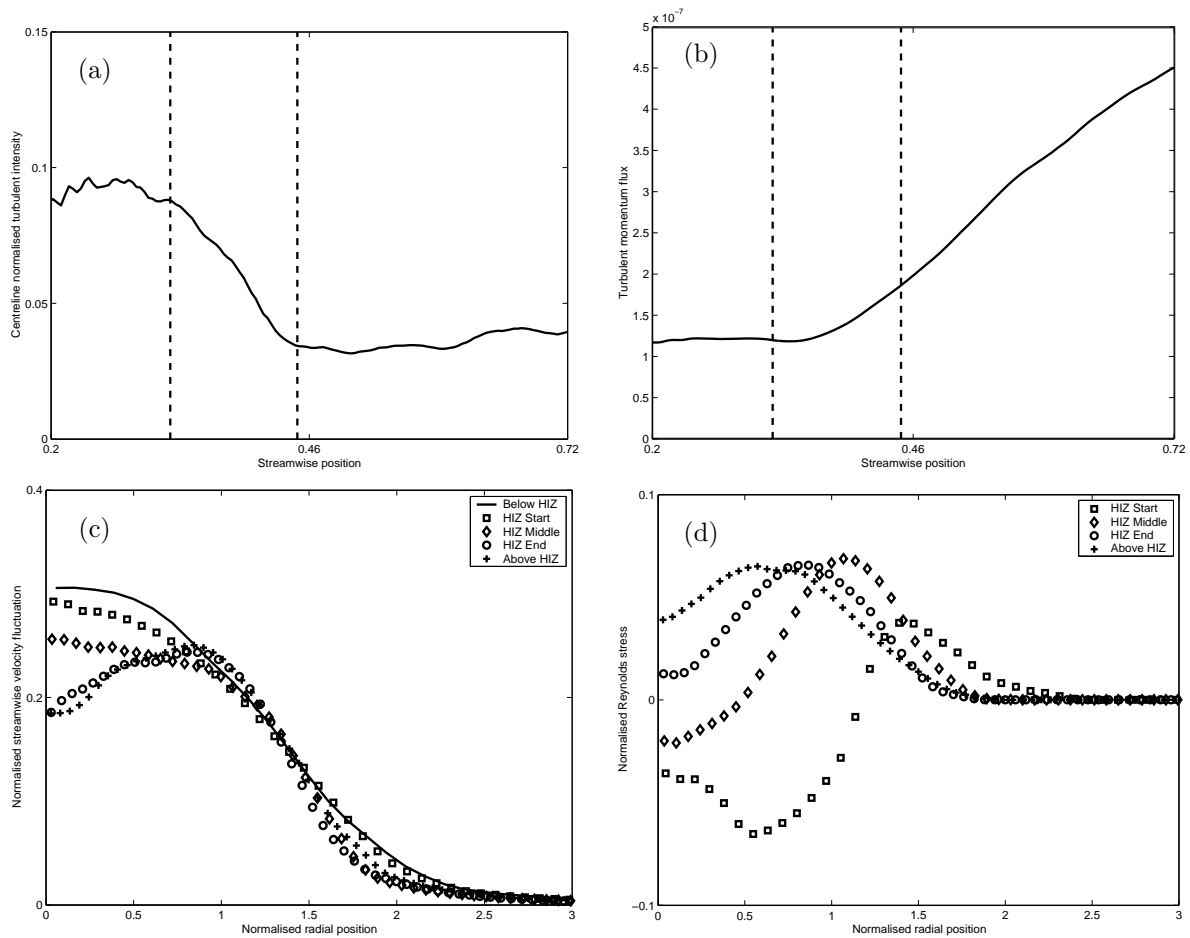
Fig. 3.4. (a) Streamwise evolution of the centreline relative turbulent intensity. Type I, $\alpha_c = 2$. (b) Streamwise evolution of the turbulent momentum flux. Type I, $\alpha_c = 2$. (c) Radial profiles of the mean streamwise turbulent intensity at different heights. Type I, $\alpha_c = 2$. (d) Radial profiles of the velocity-temperature correlation at different heights.

radial positions and so experiences this heating for less time. Conversely, fluid near the jet edge has a lower tracer concentration so only undergoes gentle heating, but is travelling much more slowly and so is heated for longer. This results in the observed off-axis temperature peak. This peak decays with height and the profile becomes more Gaussian. This explains why the velocity width spread rate increases near the bottom of the HIZ, but decreases above it. Where the temperature peak is off the axis, the fluid is accelerated over a wide area and so the velocity width grows more rapidly, and then when the off-axis temperature peak has diminished the inward radial velocity leads to a decrease in the growth of the velocity width. Since there is no generation of tracer, the tracer width decreases as it is swept towards the axis by the inward radial velocity.

3.2 Entrainment behaviour

The streamwise evolution of the entrainment coefficient is shown in figure 3.3(d). It is clear that, in general, heating leads to a higher value of entrainment coefficient than in the unheated jet, even at heights below the HIZ. This is because heating brings about a global response, not just a change in lateral entrainment. This response is also more pronounced with higher heating rates. However, upon entering the HIZ, there is a significant decrease in the entrainment coefficient, which indicates that local changes also occur.

Figures 3.4(a) and (b) compare the terms in the readdressed theory of Hunt [6], specifically the evolution of the centreline relative turbulent intensity and the evolution of the turbulent momentum flux ($\alpha_c = 2$). Consistent with BN, but inconsistent with AP, a decrease is observed in the relative turbulent intensity upon heating, which does not support the original proposal of Hunt. However, when the turbulent momentum flux

is considered, support is found for a link between the change in turbulent behaviour and the observed decrease in the entrainment coefficient. It should be noted that it is not simply the change in normalisation that is important, but also a significant change in self-similar structure. Figure 3.4(c) shows radial profiles of the normalised streamwise turbulence intensity. It is clear that upon heating, the centreline value decreases, but there is an increase away from the axis, even though the mean streamwise velocity used to normalise the profile increases. When coupled with the change in normalisation, the change in self-similar structure leads to an increase in turbulent momentum flux, despite a decrease in the centreline relative turbulent intensity. This suggests that the original experimental data support the essence of Hunt's proposal, with the modifications highlighted above. Similar results are obtained for the other heating rates.

Figure 3.4(d) shows normalised radial profiles of the streamwise velocity-temperature correlation, which appears as a source term in the transport equation for the turbulent intensity. At the bottom of the HIZ, there is a significant negative region near the axis, and a positive region near to the jet edge - it is this term that is responsible for the change in self-similar structure observed.

4 SUMMARY

Simulations have been run using an implicit turbulence model to investigate the response of a turbulent jet to volumetric heating. The data were found to be consistent with laboratory experiments. The analysis of Hunt [6], which related changes in turbulent momentum flux to entrainment behaviour, was revisited and the simulation data was used to support the new argument. Details of the turbulence showed a change in self-similar structure that proved to be significant in confirming the differences with the new analysis and also suggested that the original experimental data also support the argument. This study is a successful application of the MILES approach that has given insight into a complicated problem.

5 ACKNOWLEDGEMENTS

REFERENCES

[1] A. Agrawal and A. K. Prasad. Evolution of a turbulent jet subjected to volumetric heating. *Journal of Fluid Mechanics*, 511:95–123, July 2004.

[2] A. S. Almgren, J. B. Bell, P. Colella, L. H. Howell, and M. L. Welcome. A Conservative Adaptive Projection Method for the Variable Density Incompressible Navier-Stokes Equations. *Journal of Computational Physics*, 142(1):1–46, 1998.

[3] G. S. Bhat and R. Narasimha. A volumetrically heated jet: large-eddy structure and entrainment characteristics. *Journal of Fluid Mechanics*, 325:303–330, 1996.

[4] G. S. Bhat, R. Narasimha, and V. H. Arakeri. A new method of producing local enhancement of buoyancy in liquid flows. *Experiments in Fluids*, 7:99–102, 1989.

[5] F. F. Grinstein and C. Fureby. Recent Progress on MILES for High Reynolds Number Flows. *Journal of Fluids Engineering*, 124:848–861, December 2002.

[6] J. C. R. Hunt. Atmospheric jets and plumes. In P. A. Davies and M. J. Valente, editors, *Recent Research Advances in the Fluid Mechanics of Turbulent Jets and Plumes, Proc. NATO Advanced Study Institute, Viano di Castello, Portugal*, pages 309–334. Kluwer Academic, Netherlands, 1994.

[7] B. R. Morton, G. Taylor, and J. S. Turner. Turbulent Gravitational Convection from Maintained and Instantaneous Sources. *Royal Society of London Proceedings Series A*, 234:1–23, January 1956.

[8] I. R. Paluch. The Entrainment Mechanism in Colorado Cumuli. *Journal of Atmospheric Sciences*, 36:2467–2478, December 1979.

[9] R. S. Scorer. *Dynamics of Meterorology and Climate*. John Wiley & Sons, 1997.

[10] J. S. Turner. Turbulent entrainment: the development of the entrainment assumption, and its application to geophysical flows. *Journal of Fluid Mechanics*, 173:431–471, 1986.

Oleg_Bakunin@yahoo.com

Percolation transport in random flows with weak dissipation effects

O.G. Bakunin

Russian Researc Center "Kurchatov Institute", Nuclear Fusion Institute, Moscow

Abstract In the present paper, we consider the influence of weak dissipative effects on the passive scalar behavior in the framework of continuum percolation approach. The renormalization method of a small parameter in continuum percolation models is reviewed. It is shown that there is a characteristic velocity scale, which corresponds to the dissipative process. The modification of the renormalization condition of the small percolation parameter is suggested in accordance with additional external influences superimposed on the system. In the framework of mean field arguments, the balance of correlation scales is considered. This gives the characteristic time that corresponds to the percolation regime. The expression for the effective coefficient of diffusion is obtained.

1. Introduction

The long-range correlations are responsible for the anomalous transport in complex systems. In spite of considerable progress attained in this field of research [1-6], the problem still awaits its complete solution. The variety of anomalous transport forms requires not only special description methods, but also an analysis of general mechanisms. There exist many methods to describe correlation effects: the direct calculation of correlation functions, the diffusive approximation of correlation effects in the framework of the hydrodynamic or kinetic description, the mean field approximation of mixing length etc. One of the simplest possibilities for the interpretation of anomalous transport models is based upon using the scaling conception. In the framework of scaling approximation, often it is possible to consider different aspects of anomalous transport by characteristic temporal and spatial scales. Thus, in terms of the Hurst number *H* one can represent the mean free path $R = \left\langle x^2 \right\rangle^{1/2}$ by the scaling, $R \propto t^H$, where $0 < H \leq 1$ [1]. Here *H=1/2* corresponds to the conventional diffusivity; $0 < H < 1/2$ describes subdiffusion; and $1/2 < H \leq 1$ corresponds to superdiffusion. On the one hand, there exist formal methods that allow relation of the Hurst exponent *H* to the values characterizing system physical properties. Thus, in the framework of the continuous time random walk (CTRW) approach, use is made of the model function $\psi(t)$ that describes the probability to make jump at the moment *t* [1,3]. For the power form

$$\psi(t) \propto 1/t^{\gamma+1} \tag{1}$$

, where $0 < \gamma < 1$, the simple relationship between the Hurst exponent *H* and the waiting time exponent γ: $H = \gamma/2$ can be used [1-3].

On the other hand, there exist fairly universal physical models that allow the description of anomalous transport by means of the analysis of stochastic layer evolution, the consideration of correlation scales dynamics, the analysis of stochastic instability etc. [5-9].

Naturally, the linear estimate of width growth of stochastic layer $\Delta \propto t$ is not universal. Thus, in the framework of percolation approach to the description of turbulent transport in two-dimensional flows, the estimate of stochastic layer width (the width of percolation streamline) Δ also plays a role of principle [4]. However here the main point is the renormalization condition [4,8-10] of the small percolation parameter ε that characterizes the nearness of the system to a percolation threshold

$$\Delta(\varepsilon)=\lambda\varepsilon. \tag{2}$$

Here λ is the characteristic spatial scale ($\lambda >> \Delta$). The "universality" of such an approach is discussed in [4,9]. The percolation model implies that there exists a percolation (fractal) streamline in the two-dimensional random flow under consideration, which embraces almost the whole plane. The convective transport of the passive scalar along this streamline defines the transport character in the system under analysis [4]. Percolation approach gives the simple topological model of behavior related to strong correlation effects to obtain dependences of transport coefficients on the parameters characterizing the common properties of a flow (velocity scale V_0, spatial scale λ, "seed" diffusion D_0 etc.). In this theory the correlation length $a(\varepsilon)$ is the

main magnitude characterizing the spatial scale of the system, which is located near the percolation threshold $\varepsilon \to 0$:

$$a = \frac{\lambda}{|\varepsilon|^{\nu}} \qquad\qquad L(a) \approx \lambda \left(\frac{a}{\lambda}\right)^{D_h} . \tag{3}$$

Here, $\nu = 4/3$ and $D_h = 1 + \dfrac{1}{\nu}$ are the percolation exponents that are exactly calculated for the two-dimensional case [4,11], λ is the geometric characteristic scale, and $L(a)$ is the length of the percolation streamline that is also expressed through the small parameter $\varepsilon \to 0$. To obtain the finite value of the small percolation parameter ε, the authors of Refs. [8] used mean field arguments. For the steady case in the presence of seed diffusion D_0, the main contribution in transport is defined by the balance of characteristic times. Thus, assuming that in the steady case the particle motion time along the percolation streamline $\tau_B \approx L/V_0$ has to be the same order as the characteristic diffusive time $\tau_D \approx \Delta^2 / D_0$ of the particle escape from the percolation (stochastic) layer Δ, the authors of Refs. [8] obtained the expression:

$$\Delta(\varepsilon) = \sqrt{\frac{D_0 L(\varepsilon)}{V_0}} . \tag{4}$$

Thus for the steady model [8] the small parameter is defined as a solution of the equation $\Delta(\varepsilon)=\lambda\varepsilon$,

$$\varepsilon = \left(\frac{1}{Pe}\right)^{\frac{1}{\nu+3}} = \left(\frac{D_0}{\lambda V_0}\right)^{3/13} . \tag{5}$$

Here $Pe = \dfrac{\lambda V_0}{D_0}$ is the Peclet number. To calculate the effective diffusion coefficient it is necessary to take into account that the percolation cluster occupies only a small fraction of the space. Therefore, the value

$$D_{eff} \approx \frac{a^2(\varepsilon)}{\tau(\varepsilon)} P_{\infty}(\varepsilon) \approx \frac{a^2}{\tau_B} \frac{\Delta(\varepsilon) L(\varepsilon)}{a^2} \approx V_0 \Delta(\varepsilon) . \tag{6}$$

can be the estimate of the effective diffusion coefficient. One can see that the stochastic (percolation) layer width $\Delta(\varepsilon)$ is the key parameter of the problem. Note, that percolation approach permits obtaining the transport estimates $D_{eff} \propto V_0^{10/13}$, which differ essentially from the conventional quasi-linear estimate $D_T \approx V_0^2 \tau$ [1-3]. Moreover, it is possible to consider different physical models (time dependence, drift effects, multiscale models by means of the renormalization of the small parameter [8-10].

2. Dissipation and renormalization of the small percolation parameter

In this section, we consider the influence of weak dissipative effects on the percolation layer width. The presence of even small dissipation can considerably change the character of streamlines behavior [4]. It is possible to introduce the rate of energy dissipation ε_K by analogy with isotropic turbulence theory [17], $\varepsilon_K = \left[\dfrac{m^2}{c^3}\right] = const$. Note, that in the framework of such an approach even simple dimensional estimate of the characteristic time $\tau_K \approx \left(\varepsilon_K k^2\right)^{-1/3}$ together with the Fourier representation of the Einstein-Smolukhowski non-local functional [1], yields the classical Richardson law [2,17] for the relative diffusivity: $R^2 \propto t^3$. Here k is the wave number.

In the percolation case under consideration, the weak dissipation leads to increasing the stochastic layer width. We can estimate this at the initial stage of the percolation process by the linear dimensional expression

$$\Delta \approx V_* t \approx \lambda \left(\frac{\varepsilon_K}{\lambda^2}\right)^{\frac{1}{3}} t . \tag{7}$$

Here $V_* \approx \dfrac{\lambda}{\tau_K}$ characterizes the rate of growth of the stochastic layer width, δ is the spatial dissipative scale.

Formally, the value δ can be considered as an independent parameter. However in the framework of the hierarchy of spatial scales [1,9] that corresponds to the percolation model [8]

$$\Delta \approx \lambda\varepsilon \ << \lambda << a \approx \frac{\lambda}{\varepsilon^{\nu}} << L \approx \frac{a}{\varepsilon} \tag{8}$$

the estimate $\delta \approx \Delta$ is fairly adequate to the weak dissipation since Δ is the less among spatial scales. Then simple calculations yield

$$\Delta \approx \lambda\left(\frac{\varepsilon_K}{\lambda^2}\right)^{1/5} t^{3/5}. \tag{9}$$

At the initial stage we deal with two competing processes: the increase of the correlation scale a due to growth of the distance passed by the test particle, and the decrease of the correlation scale due to the dissipative effects. Indeed in the case under consideration the dissipation leads to the increase of the stochastic (percolation) layer width $\Delta(t)$ and hence to the decrease of the correlation scale:

$$a_D(t) \approx \lambda\left(\frac{\Delta(t)}{\lambda}\right)^{-\nu} \approx \lambda\left(\frac{\lambda}{\lambda(\varepsilon_K/\lambda^2)^{1/5} t^{3/5}}\right)^{\nu}. \tag{10}$$

On the other hand it is necessary to take into account also increasing correlation scale a due to the percolation character of streamlines (3)

$$a_I(t) \approx \lambda\left(\frac{L(t)}{\lambda}\right)^{1/D_h} \approx \lambda\left(\frac{V_0 t}{\lambda}\right)^{1/D_h}. \tag{11}$$

Here the supposition was made that the test particle path at this stage is approximately ballistic $L(t) \approx V_0 t$.

In the framework of scaling arguments we consider the balance between these processes as the balance of the correlation scales $a_I(t_0) \approx a_D(t_0) \approx a$,

$$\left(\frac{\lambda}{\lambda(\varepsilon_K/\lambda^2)^{1/5} t_0^{3/5}}\right)^{\nu} \approx \left(\frac{V_0 t_0}{\lambda}\right)^{1/D_h}. \tag{12}$$

Here t_0 is the mean field estimate of the characteristic time that corresponds to the correlation scale balance. The solution of this equation yields

$$t_0 \approx \left(\frac{\lambda}{V_0}\right)^{\frac{5}{12}} \left(\frac{\lambda^2}{\varepsilon_K}\right)^{\frac{7}{36}}. \tag{13}$$

This expression allows us to define the small percolation parameter that characterizes analyzed model based on approximation (2) of the stochastic layer width,

$$\varepsilon = \frac{\Delta}{\lambda} \approx \left(\frac{(\varepsilon_K \lambda)^{1/3}}{V_0}\right)^{\frac{1}{4}}. \tag{14}$$

Now one can obtain the scaling for the percolation layer width

$$\Delta(t) \approx \left(\frac{\varepsilon_K}{\lambda^2}\right)^{1/5} t_0^{3/5} \approx \lambda\left(\frac{U}{V_0}\right)^{1/4}. \tag{15}$$

Here, $U = \left(\varepsilon_K \lambda\right)^{1/3}$ is the dimensional estimate of the characteristic velocity that is related to dissipative

effects. Note, that the real small percolation parameter $\varepsilon = \varepsilon_0^{1/4} = \left(\dfrac{(\varepsilon_K \lambda)^{1/3}}{V_0}\right)^{1/4}$ differs from the initial

dimensionless parameter $\varepsilon_0 = \dfrac{U}{V_0} = \dfrac{(\varepsilon_K \lambda)^{1/3}}{V_0}$. This is analogue to the known percolation results [9], where

the initial small parameter ε_0 differs from the real (renormalized) percolation parameter ε. Thus for example

in the steady case (5) $\varepsilon_0 = \dfrac{1}{Pe}$, whereas $\varepsilon = \left(\dfrac{1}{Pe}\right)^{\frac{1}{\nu+3}}$ [8].

3. Percolation estimates of transport effects

In the framework of percolation approach, the expression for effective diffusivity has the form (6), $D_{eff} \approx V_0 \Delta(\varepsilon)$ which mirrors the key role of the stochastic layer width Δ. This expression is similar to the convective cells estimate, where Δ depends only the model geometry, but in the percolation approach one deals with the dependence $\Delta = \Delta(\varepsilon)$. In the case under consideration, the expression for the small percolation parameter (14) is based on the supposition of smallness of the value $\dfrac{(\varepsilon_K \lambda)^{1/3}}{V_0} = \dfrac{U}{V_0}$, which characterizes the distortion of a pattern flow by dissipative effects. The substitution of (14) into (6) yields the expression for the effective diffusivity in the form

$$D_{eff} \approx V_0 \Delta(\varepsilon\ ) \approx V_0 \lambda \left(\frac{(\varepsilon_K \lambda)^{1/3}}{V_0}\right)^{\frac{1}{4}} \propto V_0^{3/4} \varepsilon_K^{1/12}\ . \tag{16}$$

The obtained dependence differs essentially from both the quasi-linear $D_T \approx V_0^2 \tau$ and the known percolation estimate (6) $D_{eff} \propto V_0^{10/13}$.

4. Conclusions

The influence of weak dissipative effects on the passive scalar behavior in the framework of percolation approach is considered in the paper. The renormalization method of a small parameter in continuum percolation models for two-dimensional random flows is reviewed.

References

[1] R. Balescu, Statistical dynamics, Imperial College Press,1997.
[4] M.B. Isichenko, Rev. Mod. Phys. 64 (1992) 961.
[5] M.F. Shiesinger, G.M. Zaslavsky, Levy flights and related topics in physics, Springer,
    1995.
[6] A.J. Majda, P.R. Kramer, Physics Reports 314 (1999) 237-574.
[7] G.M. Zaslavsky, M. Edelman, Chaos 10 (2000) 135.
[8] M.B. Isichenko, Ya.L. Kalda, E.V. Tatarinova, O.V. Telkovskaya, V.V. Yankov, Sov.
    Phys. JETP 69 (1989) 517.
[9] O.G. Bakunin, Plasma Phys. Control. Fusion. 45 (2003) 1909.
[10] O.G. Bakunin, Physics Uspekhi 46 (2003) 756.
[11] J. Feder, Fractals, Department of Physics University of Oslo, Norway. Plenum
     Press, New York, 1988.
[16] M.Vergassola, M. Avellaneda, Physica D 106 (1997)148.
[17] U. Frisch, Turbulence the Legacy of A.N. Kolmogorov, Cambridge, University Press
     1995.
[18] M.B. Isichenko, Ya.L. Kalda, J. Nonlinear Sci. 1 (1991) 255.
[19] O.G. Bakunin, Physica A 337 (2004) 27.
[20] O.G. Bakunin, Physics Letters A 322 (2004) 105.
[21] O.G. Bakunin, Plasma Physics Reports 29 (2003) 955.

e-mail: `mireille.boulet@cea.fr`

Three-dimensional numerical simulation of experiments on Richtmyer-Meshkov induced mixing with reshock

Mireille BOULET and Jérôme GRIFFOND [1]

[1] *CEA/DAM Ile-de-France BP 12 91680 Bruyères-le-Châtel FRANCE*

Abstract: Numerical simulation of turbulent Richtmyer-Meshkov shock tube experiments with two different chamber length are reported here.

1 EXPERIMENTAL SET-UP AND RESULTS

Shock tube experiments have been performed to study the shock induced mixing at an air-SF6 interface. The incident Mach 1.2 shock-wave in air is transmitted in the SF6 chamber of either $25cm$ or $30cm$ length; it reflects on the end-wall and interacts with the premixed interface. Initially, both gases are separated by a thin membrane maintained between two square wire meshes. The space between wires is small ($1.8mm$ and $1mm$) in order that the mixing becomes quickly turbulent. Using the initial growth of the mixing zone width as a reference velocity and mesh wire spaces as reference length, the reshock occurs at a dimensionless time around 100 to 200. Such long time developments are challenging for simulation.

Description and results of the experimental set-up are provided by Haas J.F., Counilh D. and Schwaederl L. (10th IWPCTM 2006).

Different criteria, see Fig. 1.1, can be applied to estimate the mixing zone width from schlieren photographs but whatever be the criterion used, two clear trends appears:

- the mixing zone width evolves like $t^{1/4}$ before reshock;
- the larger is the SF6 chamber, the later occurs the reshock, the larger is the growth rate after reshock.
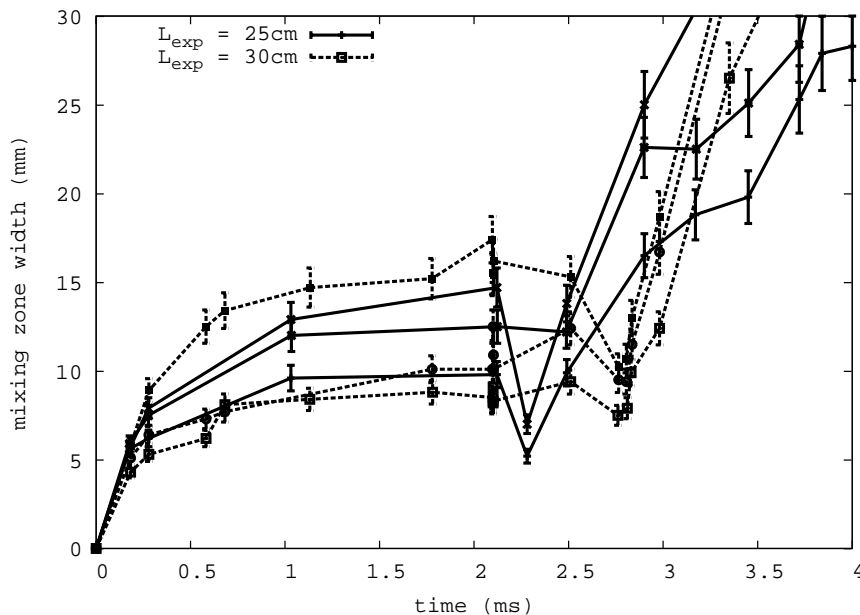
Fig. 1.1 –. *Experimental turbulent mixing zone width with both chamber length according to three criteria.*

2 CHARACTERISTICS AND VISUALIZATION OF SIMULATIONS

Simulations are performed with the TRICLADE parallel code which can solve the 3D Navier-Stokes equations for gas mixtures with high order numerical schemes. For the present simulations:

– 3D Euler equations with mixing described by a mass fraction giving the local properties of the mixture;
– 30 millions cells in the whole domain;
– 200 x 200 cells in each cross section ($d \times d$);
– 2 main wavelengths $\lambda = d/5$ and $\lambda = d/9$ parallel to the walls representative of approximately $1/50^{th}$ of experimental tube cross section
– simulation performed in 2 stages (see Fig. 2.2): one for each interaction, in the frame attached to the interface after interaction.
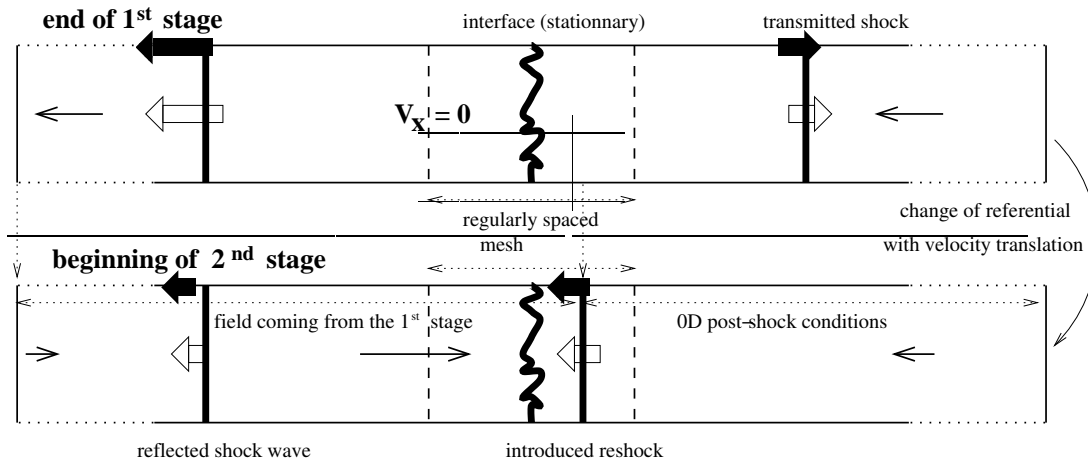
Fig. 2.2 –. *Principle of the 2 stages simulation procedure.*
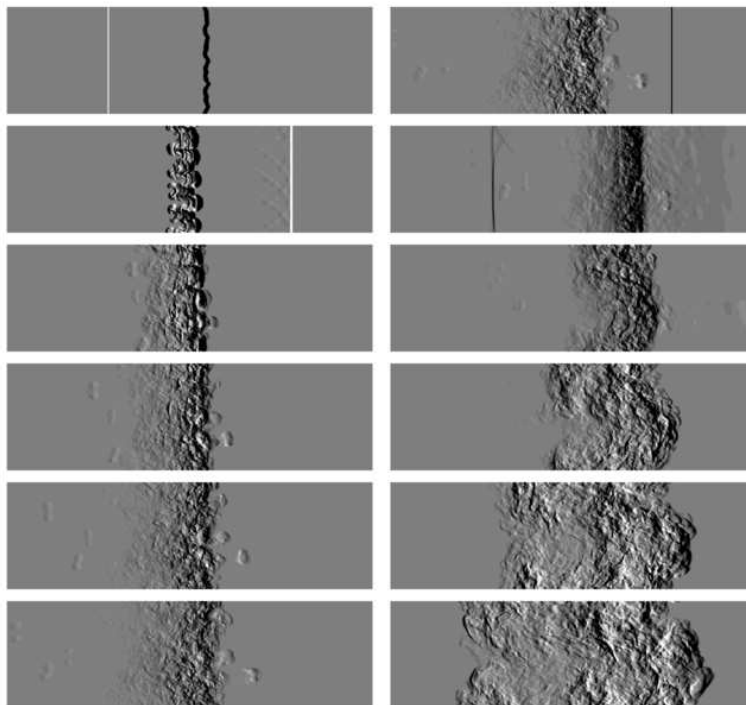
Fig. 2.3 –. *First interaction (left), and second interaction (right). Air is on the left of the pictures and SF6 on the right. First shock comes from the left, second comes from the right.*

Schlieren pictures are obtained from 3D numerical simulation, and shown in Fig. 2.3, by computing light rays deflection in one cross direction.

The first interaction is shown on the left of Fig. 2.3: it involves a Mach 1.2 shock wave in air with an Air-SF6 interface at rest (Atwood 0.67). The air bubbles on the SF6 side produce a clear front in the numerical schlieren images whereas the SF6 penetrating in the air side gives a dilute aspect without a well-defined mixing zone edge on the left. Vortex rings are thrown out of the mixing zone on both sides.

The second interaction is shown on the right of Fig. 2.3: it involves a Mach 1.3 reshock in SF6 with the mixing zone (Atwood -0.70). After compression of the mixing zone by the reshock, large structures of the size of the computational domain appear and develop quickly. After reshock, turbulent fine scales added on the growing large scales without isolated vortex rings produce schlieren visualizations that look completely different.

3 COMPARISONS TO EXPERIMENTS

(a) $t \approx 2.2ms$ (b) $t \approx 2.48ms$ (c) $t \approx 3.0ms$
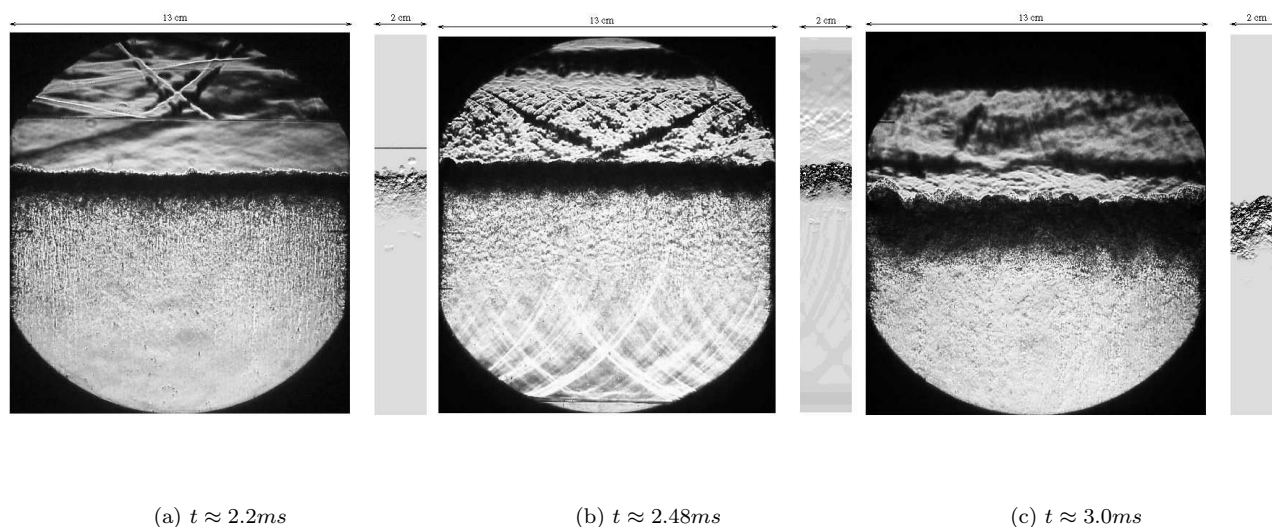
Fig. 3.4 −. *Comparison of experimental and numerical schlieren pictures just before reshock, a short time after reshock and later after reshock.*

Comparisons of experimental and numerical schlieren images, in Fig. 3.4, show the fraction of the tube that is really simulated. Two aspects can be noticed: contrary to simulation, no sign of vortex rings getting out of the mixing zone before reshock can be observed in photographs and both simulation and experiment display structures of larger and larger size after reshock.

(a)   (b)
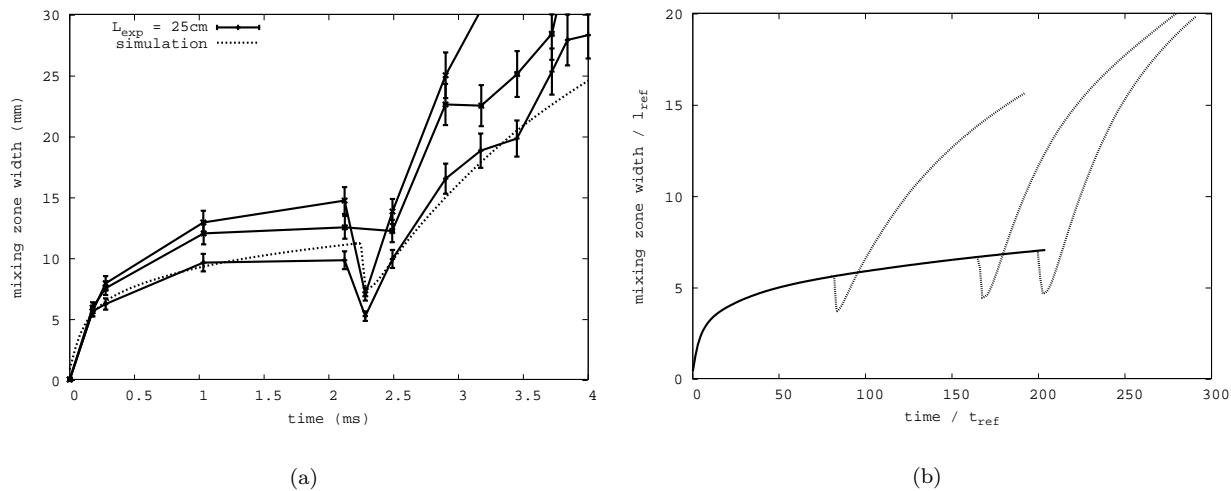
Fig. 3.5 –. *(a)-Comparison of experimental and numerical mixing zone width for the 25cm chamber. (b)-Numerical mixing zone width when the reshock is introduced at different times.*

The evolution of the mixing zone width is correctly reproduced by the simulation before and after reshock, see Fig. 3.5-(a). The criterion giving the smallest estimate (which should be free from boundary layer effects), at least, is close to the numerical one. Especially, the $t^{1/4}$ growth before reshock is obtained whereas more diffusive numerical computations predict a larger exponent.

Introduction of the reshock at different times in the simulation, see Fig. 3.5-(b), confirms qualitatively the experimental observation : the sooner the reshock occurs, the less the mixing zone grows after interaction. However, the experimental growth rate difference between both chambers of $25cm$ and $30cm$ length is larger than the numerical one.

4   CONCLUSION

The simulation of the effect of the time arrival of the reshock on the mixing zone width is a very challenging problem due to very long turbulent development between first and second interaction. Compared to the experiments, satisfactory results are obtained concerning the late-time $t^{1/4}$ growth rate of first-time shocked mixing layer. Like in the experiment, the larger growth rate is obtained when the reshock arrival occurs later. However, the difference between the observed growth rates is not as pronounced as in the experiment.

e-mail: `burton29@llnl.gov`

Large-eddy simulation of round turbulent jets using the Inertial LES method with multifractal subgrid-scale modeling

Gregory BURTON[1]

[1] *Lawrence Livermore National Laboratory, Livermore, CA 94550 USA*

Abstract: Large-eddy simulation of passive scalar mixing by a fully three-dimensional round incompressible turbulent jet is evaluated using the Inertial LES methodology with multifractal subgrid-scale modeling. The Inertial LES approach involves the direct calculation of the inertial term $\overline{u_i\,u_j}$ in the filtered incompressible Navier-Stokes equation and the scalar flux term $\overline{u_j\,\phi}$ in the filtered advection-diffusion equation, using models for the subgrid velocity field $\mathbf{u}^{sgs}$ and the subgrid scalar-concentration field ϕ^{sgs}. In this work, the models are based on the multifractal structure of the subgrid enstrophy $2\mathcal{Q}^{sgs}(\mathbf{x},t) \equiv \boldsymbol{\omega}^{sgs} \cdot \boldsymbol{\omega}^{sgs}$ and scalar-dissipation $\boldsymbol{\chi}^{sgs}(\mathbf{x},t) \equiv D\nabla\boldsymbol{\phi}^{sgs} \cdot \nabla\boldsymbol{\phi}^{sgs}$ fields, respectively. No artificial viscosity or diffusivity constructs are applied and no explicit dealiasing is performed. Numerical errors are controlled by the application of an adaptive backscatter limiter. The present work summarizes the initial evaluation of the Inertial LES approach in the context of the round turbulent jet, including examinations of jet self-similarity and the scale-to-scale distribution of kinetic and scalar energy in the jet far field. These inquiries confirm that the Inertial LES method accurately recovers the large scale structure of this complex turbulent shear flow.

1 INTRODUCTION

The free round turbulent jet is perhaps the most extensively studied of the canonical free turbulent shear flows. Turbulent jets are important in a variety of industrial applications, such as fuel injectors, furnaces and rocket engines, as well as in high energy-density phenomena such as astrophysical jets and inertial confinement fusion. The enormous range of length and time scales generated by such flows, however, makes high-resolution laboratory or field study of most of them difficult or impossible. The multiplicity of scales also prevents direct numerical studies (DNS) of such flows, since fully resolving all dynamically-significant scales would require computational power well beyond present-day capabilities. Currently, therefore, the most promising method to study such flows on the computer is through large-eddy simulation (LES), in which only the larger turbulent scales are calculated explicitly, while the smaller, unresolved scales are modeled. However, most presently-available modeling techniques lack the fidelity necessary for LES to become a more widely-accepted tool for scientific and engineering work.

2 INERTIAL LES METHOD

2.1 Multifractal subgrid modeling

Recently, Inertial LES with multifractal subgrid modeling has been proposed as a new, physically-based technique for obtaining high-fidelity large-eddy simulations [1, 2]. In this approach, the filtered Navier-Stokes momentum equation, given by

$$\frac{\partial \overline{u}_i}{\partial t} + \frac{\partial}{\partial x_j}\,\overline{u_i\,u_j} - \nu\,\frac{\partial^2 \overline{u}}{\partial x_j \partial x_j} = 0, \tag{2.1}$$

is solved by explicitly calculating the filtered inertial term $\overline{u_i\,u_j}$. Similarly, the filtered advection-diffusion equation, given by

$$\frac{\partial \overline{\phi}}{\partial t} + \frac{\partial}{\partial x_j}\,\overline{u_j\,\phi} - D\frac{\partial^2 \overline{\phi}}{\partial x_j \partial x_j} = 0, \tag{2.2}$$

is solved by explicitly calculating the filtered scalar-flux term $\overline{u_j\,\phi}$. This approach represents a "return-to-first-principles" in LES methodology, since the unclosed terms in (2.1) and (2.2) are calculated in their original

forms, *i.e.,* as nonlinear stresses, rather than as linear stresses modeled with the gradient-diffusion hypothesis, the approach taken by most current LES methods. The nonlinear terms may be expanded, giving

$$\overline{u_i\,u_j} \quad \equiv \quad \overline{\overline{u}_i\,\overline{u}_j} + \overline{\overline{u}_i\,u_j^{sgs}} + \overline{u_j^{sgs}\,\overline{u}_j} + \overline{u_j^{sgs}\,u_j^{sgs}} \tag{2.3}$$

$$\overline{u_j\,\phi} \quad \equiv \quad \overline{\overline{u}_j\,\overline{\phi}} + \overline{\overline{u}_j\,\phi^{sgs}} + \overline{u_j^{sgs}\,\overline{\phi}} + \overline{u_j^{sgs}\,\phi^{sgs}}\,, \tag{2.4}$$

indicating that the terms involve interactions between resolved and subgrid velocities and scalar fields. Thus, the Inertial LES approach requires models for the subgrid velocities u_j^{sgs} and scalar fluctuations ϕ^{sgs}.

Here, these subgrid models are derived from the multifractal structure present in hydrodynamic turbulence at inertial-range scales. This structure has been confirmed in numerous previous studies [7, 11]. Multifractal structure in the enstrophy field, $2\mathcal{Q}(\mathbf{x},t) \equiv \boldsymbol{\omega}\cdot\boldsymbol{\omega}$, is used first to develop an analytical model for the subgrid vorticity field $\boldsymbol{\omega}^{sgs}(\mathbf{x},t)$. The Biot-Savart law is then employed to relate the analytical model for $\boldsymbol{\omega}^{sgs}(\mathbf{x},t)$ to the subgrid velocity field $u_j^{sgs}(\mathbf{x},t)$. The analytical model for $u_j^{sgs}(\mathbf{x},t)$, in turn, may be simplified to obtain a computationally tractable model for the subgrid velocity field $u_j^{sgs}(\mathbf{x},t)$. A similar approach is taken to derive a model for the subgrid scalar-fluctuation field $\phi^{sgs}(\mathbf{x},t)$ from multifractal structure present in the scalar-dissipation field $\boldsymbol{\chi}(\mathbf{x},t) \equiv D\nabla\phi\cdot\nabla\phi$. Here, the Green's function operator is employed to relate an analytical model for the subgrid scalar-gradient field $\nabla\phi^{sgs}(\mathbf{x},t)$ to the subgrid scalar-fluctuation field $\phi^{sgs}(\mathbf{x},t)$, from which a computational model for $\phi^{sgs}(\mathbf{x},t)$ is derived. In their final forms, both models involve transforming the smallest-resolved scale Δ velocity and scalar fields, as

$$u_j^{sgs}(\mathbf{x},t) \quad \approx \quad \mathcal{B}\,u_j^{\Delta}(\mathbf{x},t) \tag{2.5}$$

$$\phi^{sgs}(\mathbf{x},t) \quad \approx \quad \mathcal{D}\,\phi^{\Delta}(\mathbf{x},t) \tag{2.6}$$

where $\mathcal{B}$ and $\mathcal{D}$ are functions of the number of subgrid scales within an LES grid cell. Detailed development of the subgrid velocity and scalar models are provided in [1] and [3]. Prior evaluation of the Inertial LES method indicates that it reproduces more accurately the local momentum and energy transfer between the resolved and subgrid scales than traditional subgrid modeling approaches [2, 3].

2.2 Backscatter limiting

Numerical errors in the Inertial LES method are controlled here by an adaptive backscatter limiter, a refinement of the technique introduced by Burton & Dahm [2]. That work demonstrated that numerical errors may be effectively controlled by selectively reducing the magnitude of those nonlinear stresses in (2.3) and (2.4) responsible for the reverse transfer of energy from the subgrid to the resolved field during a simulation. To implement such a limiter, the filtered inertial stresses $\overline{u_i\,u_j}$ responsible for backscatter of kinetic energy are first identified as those that satisfy

$$\overline{u_{(i)}\,u_{(j)}}\,S_{(ij)} > 0\,, \tag{2.7}$$

where $2\,S_{ij} \equiv (\partial u_i/\partial x_j + \partial u_j/\partial x_i)$ and where $(\,\cdot\,)$ indicates that no summation is implied. The magnitude of the stress components satisfying (2.7) then are reduced by a factor $C_{\mathcal{B}}$ giving

$$\widehat{\overline{u_i\,u_j}} \equiv C_{\mathcal{B}}\,\overline{u_i\,u_j}\,, \tag{2.8}$$

and the reduced inertial stress is then applied to the momentum update in (2.1). A similar strategy is applied to the passive-scalar equation of (2.2). There, backscatter of scalar energy will occur whenever

$$\overline{u_{(j)}\,\phi}\,\nabla\phi_{(j)} > 0\,. \tag{2.9}$$

Where (2.9) is satisfied, the magnitude of the scalar-flux component is reduced by a factor C_{ϕ} giving

$$\widehat{\overline{u_j\,\phi}} \equiv C_{\phi}\,\overline{u_j\,\phi}\,. \tag{2.10}$$

The reduced scalar-flux component is then applied to update the scalar field in (2.2). For both the momentum and the scalar updates, this strategy has the effect of canceling numerical errors arising during the simulation. In the current approach, the values $C_{\mathcal{B}}$ and C_{ϕ} are determined locally during the simulation.

3 COMPUTATIONAL METHOD

The numerical scheme consists of a standard pressure-correction algorithm on a regular cartesian mesh with primitive variables stored at staggered locations following the method of Harlow & Welch [9]. All spatial derivatives are discretized using 4th-order centered operators, while an explicit 3rd-order Runge-Kutta scheme is used for temporal integration. All simulations employ a resolution of $Nx \times Ny \times Nz \equiv 384 \times 128 \times 128$ points, with **x** the downstream direction. Cross stream directions are periodic over the interval $L = 2\pi$. This configuration permits an exact, direct solution of the Poisson equation using standard FFT methods. At the jet outflow, the nonreflective boundary condition of Tang & Grimshaw [13] is implemented. The jet inlet profile consists of a hyperbolic tangent function to which a small co-flow $U_{co} = 0.075\,U_o$ has been added. This has been shown to be a realistic approximation of the actual inlet found in round jets [8]. The inlet width is set at $D \equiv \pi/5$, which in conjunction with the velocity co-flow, has been shown to minimize the impact of the cross-stream periodicity on the downstream development of the jet [5]. All simulations are performed at a relatively high Re_D of $25,000$, which provides for significant unresolved turbulence in the jet's subgrid field.

4 RESULTS

The present work reports only on the initial validation studies of the Inertial LES method in the round turbulent jet configuration, focusing on the fidelity with which the large-scale features of the velocity and scalar fields are reproduced. Figure 1 shows two-dimensional extracts at the jet centerline in the $\mathbf{x}-\mathbf{z}$ plane for the vorticity magnitude field (*top*) and scalar-fluctuation field (*bottom*). These provide a qualitative assessment of the flow field generated by the Inertial LES method. In each frame, zero magnitude is depicted in black while the highest values are depicted in white. The graphics show the characteristic decay of the jet's core by $\sim 5D$ downstream. The angle subtended by the jet expansion cone from the centerline is estimated to be $13.4\,^{\circ}$, close to the value of $12\,^{\circ}$ reported by prior studies [6].

As the round turbulent jet is known to develop a scale-similar velocity profile in the far-field region [14], it is useful to examine how well the Inertial LES approach attains and preserves a self-similar state. Figure 2 illustrates four velocity-component profiles as functions of the radial-similarity variable $\boldsymbol{\eta} \equiv r/(x - x_o)$ at five planes, $x/D = [\,17.5, 20, 22.5, 25, 27.5, 30\,]$, in the far-field region (*clockwise, from upper left*): streamwise mean velocity $U_x(\boldsymbol{\eta})$, streamwise fluctuation velocity $u_x(\boldsymbol{\eta})$; radial fluctuation velocity $u_r(\boldsymbol{\eta})$; and azimuthal fluctuation velocity $u_\theta(\boldsymbol{\eta})$. Each of the depicted distributions shows good collapse at the given downstream planes, indicating that the Inertial LES system reaches and preserves self-similarity, consistent with prior experimental studies [10]. The relatively weaker convergence near the centerline of the jet reflects the smaller number of sampling locations at small $\boldsymbol{\eta}$ and would likely improve over longer simulation times. Figure 3 examines the self-similarity of the scalar concentration field as a function of $\boldsymbol{\eta}$ from statistics gathered at the same five cross-stream planes. Four moments of the scalar concentration field are evaluated (*clockwise, from upper left*): mean scalar concentration $\langle\phi\rangle(\boldsymbol{\eta})$; root-mean-square scalar fluctuations $\phi^{rms}(\boldsymbol{\eta})$; scalar skewness $\mathcal{S}^3(\boldsymbol{\eta})$; scalar flatness $\mathcal{K}^4(\phi)(\boldsymbol{\eta})$. As compared to the velocity field statistics, the radial distributions for the scalar-field statistics show better collapse at $\boldsymbol{\eta}$ values near the jet centerline.

Figure 4 illustrates extracts from timeseries data of the velocity (*top*) and scalar (*bottom*) fields on the jet centerline at $x/D = 27.5$, collected over approximately 1000 timesteps after the jet had reached a statistically-stationary state. Subtle differences can be detected between these timeseries profiles, as the scalar field appears to exhibit the "ramp-cliff" structures that typically characterize scalar fields driven by large-scale anisotropic forcing, like the present shear flow [15]. Figure 5 shows the power spectra for the full velocity and scalar timeseries data sets; (*left*) spectrum of the kinetic energy field vs. time, (*right*) spectrum of the scalar energy field $E_\phi(k)$ vs. time, where $2\,E_\phi = \boldsymbol{\phi}^2(t)$. A $-5/3$ reference slope is provided for comparison. Both figures indicate that the kinetic and scalar energy distributions slightly exceed the $k^{-5/3}$ scaling predicted by Kolmogorov theory [4].

The present investigation confirms that the Inertial LES method accurately recovers the significant large scale structure of both a fully three-dimensional round turbulent jet and the scalar concentration field mixed by it. In the future, the Inertial LES method with multifractal subgrid-scale modeling will be used to study passive-scalar mixing at high Schmidt number ($Sc \gg O(1)$) in a three-dimensional round turbulent jet.
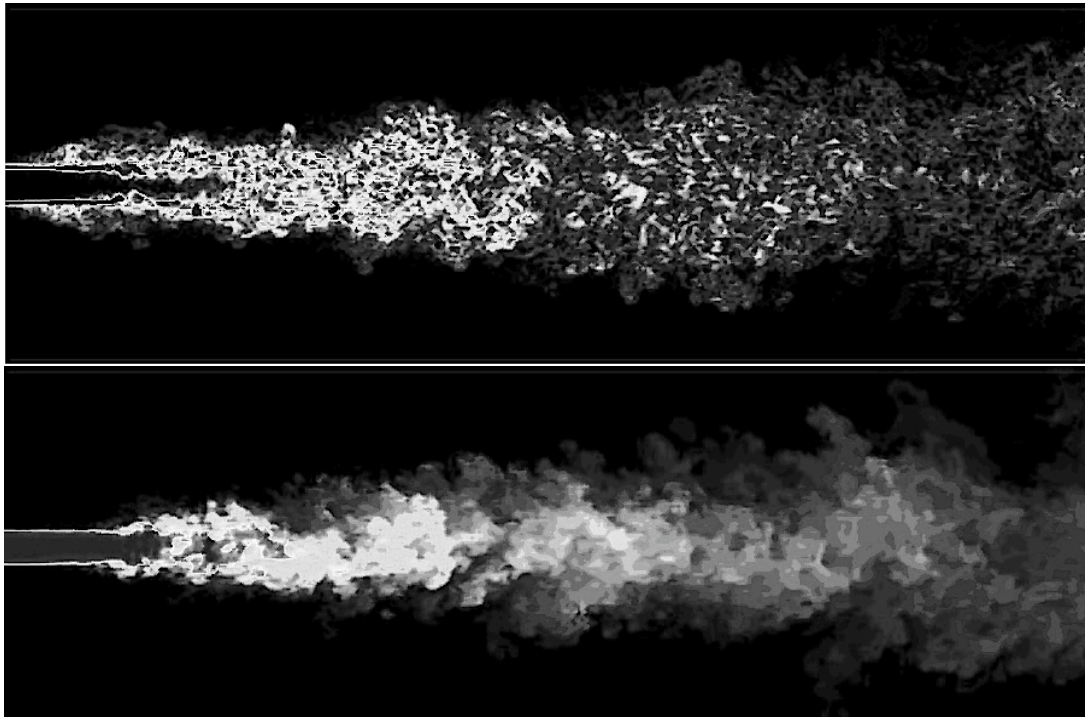
Fig. 4.1. Two-dimensional cross-sections from fully three-dimensional large eddy simulation of round turbulent jet at $Re_D \approx 25,000$ using the Inertial LES method with multifractal subgrid-scale modeling. *(Top)* Vorticity field magnitude with black as $|\omega| \equiv 0$ and white as $|\omega| \equiv 4.32$. *(Bottom)* Scalar fluctuation field with black as $\phi \equiv 0$ and white as $\phi \equiv 1$. From the jet virtual origin, the jet cone of expansion subtends an angle from the centerline of $\theta \approx 13.4\,^\circ$, close to the estimate of $\theta \approx 12\,^\circ$ reported in experimental studies by Dowling & Dimotakis [6].

REFERENCES

[1] Burton, G.C. and Dahm, W.J.A. 2005, Multifractal subgrid-scale modeling for large-eddy simulation. I. Model development and *a priori* testing. *Phys. Fluids* **17**, 075111.

[2] Burton, G.C. and Dahm, W.J.A. 2005, Multifractal subgrid-scale modeling for large-eddy simulation. II. Backscatter limiting and *a posteriori* evaluation. *Phys. Fluids* **17**, 075112.

[3] Burton, G.C. 2005, Large-eddy simulation of passive-scalar mixing using multifractal subgrid-scale modeling. *Annual Research Briefs*, Center for Turbulence Research, Stanford, CA

[4] Corrsin, S. 1951, On the spectrum of isotropic temperature fluctuations in isotropic turbulence. *J. Appl. Phys.* **22**, 469.

[5] da Silva, C.B. and Métais, O. 2002, Vortex control of bifurcating jets: A numerical study. *Phys. Fluids* **14**, 3798-3819.

[6] Dowling, D.R. and Dimotakis, P.E., 1990. Similarity of the concentration field of gas-phase turbulent jets. *J. Fluid Mech.* **218** 109-141.

[7] Frederiksen, R.D., Dahm, W.J.A. and Dowling, D.R., 1997, Experimental assessment of fractal scale similarity in turbulent flows. Part 3. Multifractal Scaling. *J. Fluid Mech.* **338** 127-155.

[8] Freymuth, P. 1966, On transition in a separated laminar boundary layer. *J. Fluid Mech.* **25**, 683.

[9] Harlow, F.W. and Welch, J.E. 1965, Numerical calculation of time-dependent viscous incompressible flow of fluids with free surface. *Phys. Fluids* **8**, 2182-2189.

[10] Hussein, H.J., Capp, S.P. and George, W.K. 1994, Velocity measurements in a high-Reynolds-number, momentum-conserving, axisymmetric, turbulent jet. *J. Fluid Mech.* **258**, 31-75.

[11] Meneveau, C. and Sreenivasan, K.R. 1991, The multifractal nature of turbulent energy dissipation. *J. Fluid Mech.* **224**, 429-459.

[12] Michalke, A. and Hermann, G. 1982, On the inviscid instability of a circular jet with external flow. *J. Fluid Mech.* **114**, 343.

[13] Tang, Y. and Grimshaw, R. 1996, Radiation Boundary Conditions in Barotropic Coastal Ocean Numerical Models. *J. Comp. Phys.* **123**, 96-110.

[14] Tennekes, H. and Lumley, J.L. 1972, A First Course in Turbulence. *MIT Press*, New York.

[15] Warhaft, Z. 2000, Passive scalars in turbulent flows. *Ann. Rev. Fluid Mech.* **32**, 203-240.
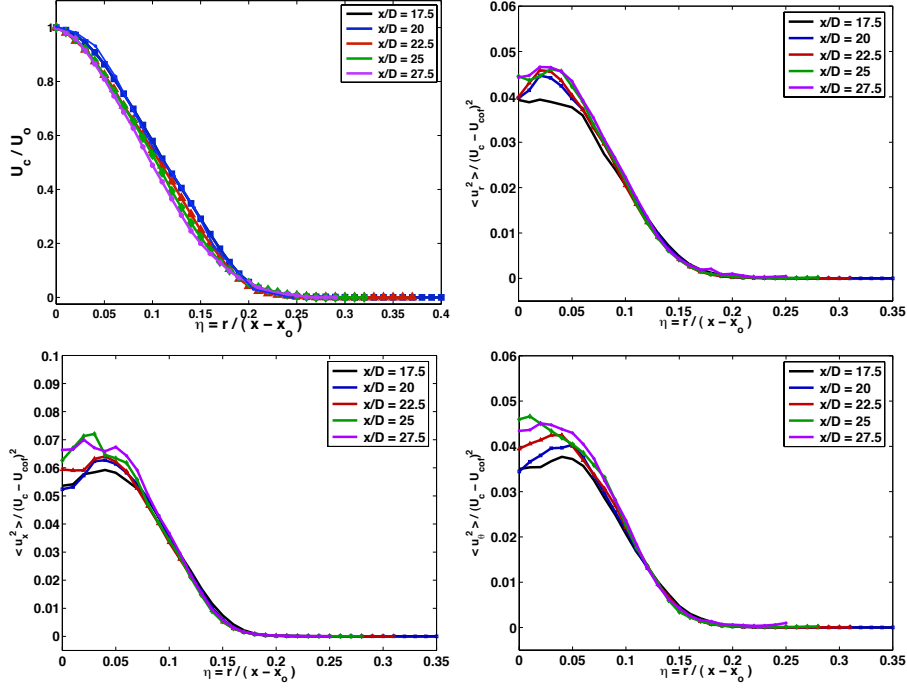
Fig. 4.2. Cross-stream profiles of the first four moments of the velocity fluctuation field vs. similarity variable $\eta \equiv r/(x - x_o)$. Clockwise from upper left: mean streamwise velocity, $\langle u \rangle(\eta)$; streamwise fluctuation, $u_x(\eta)$; radial velocity fluctuation, $u_r(\eta)$; azimuthal velocity fluctuation, (η). Reasonable collapse of the scaled cross-stream profiles is obtained at the five planes examined in the jet far field, $x/D = [\, 17.5,\, 20,\, 22.5,\, 25,\, 27.5,\, 30\,]$.
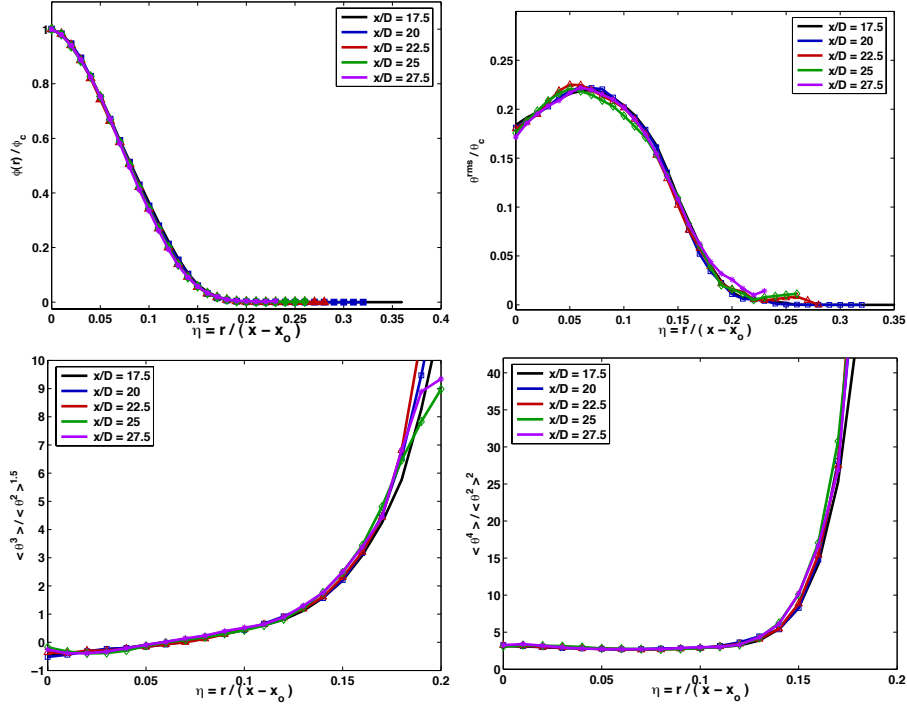
Fig. 4.3. Cross-stream profiles of the first four moments of the scalar concentration field vs. similarity variable $\eta \equiv r/(x - x_o)$. Clockwise from upper left: mean scalar concentration, $\langle \phi \rangle(\eta)$; scalar fluctuation r.m.s., $\phi'(\eta)$; scalar-fluctuation skewness, $\mathcal{S}^3(\phi')$; and scalar-fluctuation kurtosis, $\mathcal{K}^4(\phi')$.
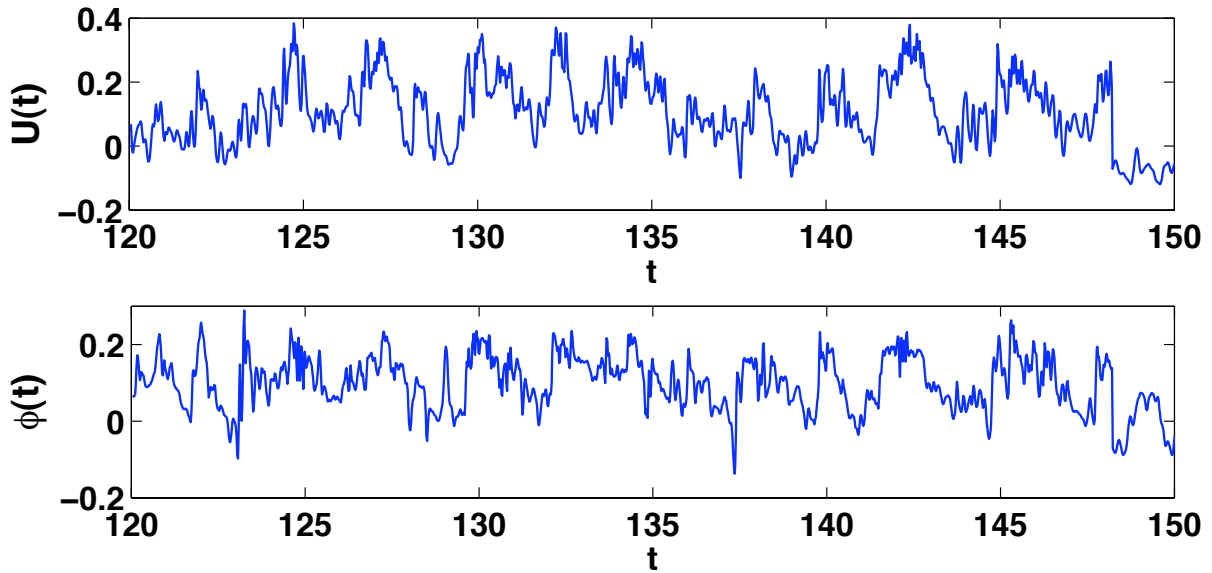
Fig. 4.4. Sample timeseries extracts of the stream-wise velocity field (*top*) and scalar concentration field (*bottom*) from fully three-dimensional large eddy simulation of round turbulent jet at $Re_D \approx 25,000$ using the Inertial LES method with multifractal subgrid-scale modeling. Illustrated timeseries were gathered at the jet centerline at the downstream plane $x/D = 27.5$. Note appearance of subtle "ramp-cliff" structures in the scalar timeseries, indicating large scale anisotropic forcing of the scalar field, as discussed in [15].
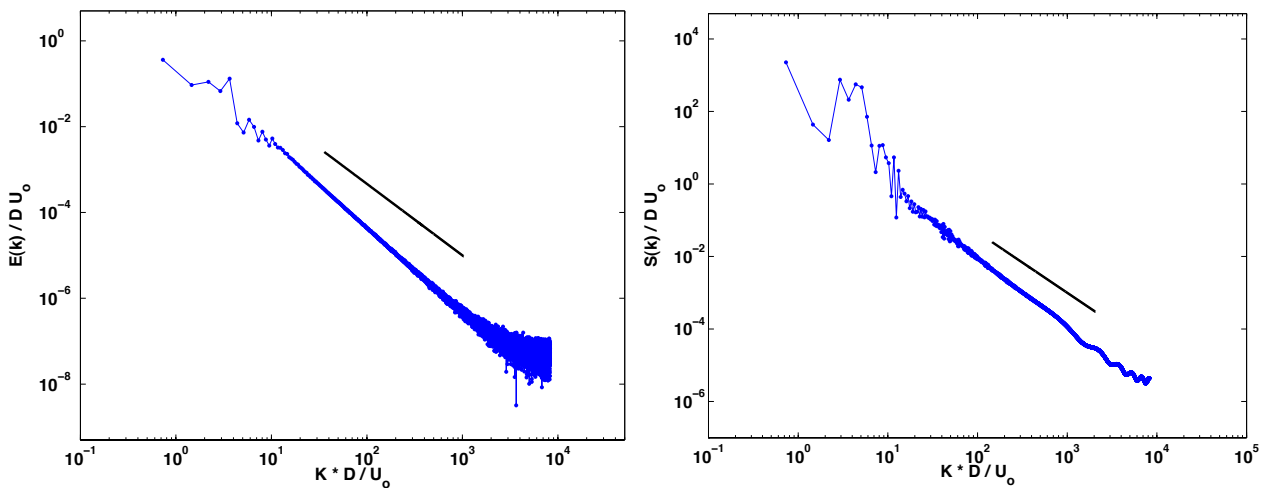
Fig. 4.5. Spectra from timeseries of the stream-wise velocity field (*left*) and scalar concentration field (*right*) from fully three-dimensional large eddy simulation of round turbulent jet at $Re_D \approx 25,000$ using the Inertial LES method with multifractal subgrid-scale modeling. Solid line in each frame provides a $-5/3$ slope for comparison, indicating that both spectra slightly exceed the value predicted by Kolmogorov theory [4].

e-mail: `bouquet@bruyeres.cea.fr`

Analytical Solutions of the Buoyancy – Drag Equation

Serge BOUQUET, Pierre GANDEBOEUF and Pierre PAILHORIES

CEA/DAM Ile de France, BP 12, 91680 Bruyères-le-Châtel, France

Abstract: The buoyancy – drag equation (BDE) describes the evolution of the mixing zone, at the interface of two fluids, due to Rayleigh-Taylor instabilities. In this paper, the integrability of the BDE is studied analytically. The general solution is derived for a constant acceleration whereas for accelerations varying like a power of time, we obtain a one-parameter family of solutions.

1 INTRODUCTION

The buoyancy – drag equation (BDE) [1-5] arises in the modeling of Rayleigh – Taylor instabilities (RTI) [5, 6]. In this process, a configuration consisting in two fluids with two different mass densities and separated by a smooth interface, becomes unstable provided the condition $\vec{\nabla}p.\vec{\nabla}\rho < 0$ is satisfied where p and ρ are respectively the instantaneous pressure and mass density of the material at the interface [6, 7].

RTI occur, for instance, in a glass experiencing the earth gravitation field, g, containing a layer of vinegar ("heavy fluid 2" with density ρ_2) located above a layer of oil ("light fluid 1" with density ρ_1) – see **Fig. 2.1a**. In that case, RTI lead to the formation of a mixing zone with vertical extension $h(t) = h_1(t) + h_2(t)$ where $h_1(t)$ and $h_2(t)$ correspond respectively to the "penetration depth" of dense fluid into the light one and to the "elevation" of light bubbles into the heavy material. When the heavy fluid penetrates into the light one, spikes (or filaments) form [8] and because of their small cross sections, they are submitted to a drag force that is much smaller than for the rising bubbles. The evolution is quite dissymmetric in strongly non linear regime and at high Atwood number, At (see below), and we have $h_1(t) > h_2(t)$.

The BDE corresponds to a zero-dimensional (0D) model, i.e., it does not take into account the inner spatial structure of the mixing zone with spikes and bubbles. However, this equation provides the time-dependence of each length $h_i(t)$; i = 1, 2; and therefore the time variation of the total thickness, h(t), of the mixing zone is easily computed. Moreover, although the BDE was initially found from phenomenological viewpoints, it can be shown that one deduces it from a theoretical approach based on Hamiltonian formalism [4, 9]. The BDE [1-5] is a second order differential equation (SODE) and it reads:

$$d^2h_i / dt^2 = B_i.\gamma(t) - C_i |dh_i / dt|.(dh_i / dt) / h_i(t) , \qquad (1.1)$$

where the parameters B_i and C_i correspond respectively to the buoyancy and drag coefficients that can be determined either from experimental [10] or theoretical considerations [11]. The quantity γ(t) is proportional to the product of the acceleration g(t) – which can depend explicitly on time in specific experiments [10] – by the well-known dimensionless Atwood number [6], $At(t) \equiv [\rho_2(t)-\rho_1(t)]/[\rho_2(t)+\rho_1(t)]$, computed at the interface of the two fluids. From now and for the sake of simplicity, although γ(t) takes into account the time variation of At(t), it will be called later on the acceleration instead of the quantity g(t).

In the following, we consider first (Sect. 2) the case of a constant acceleration $\gamma(t) = \gamma_0$ and the general solution for the thickness, h(t), of the mixing zone is derived. In a second step (Sect. 3), a special form for the time dependence of γ(t) is considered and a family of solutions is obtained. Finally, since the variables $h_i(t)$; i = 1, 2; are defined to be positive and assuming that they can only increase with time [we consider that the acceleration γ(t) remains positive and that no "de-mixing" process takes place], Eq. (1.1) simplifies in the new SODE:

$$d^2h / dt^2 = B.\gamma(t) - C.(dh / dt)^2 / h(t) , \qquad (1.2)$$

where the subscript "i" has been dropped. For either bubbles or spikes, the same SODE (1.2) is used except that for each structure the numerical values of the parameters B and C will not be the same.

2 GENERAL SOLUTION FOR A CONSTANT ACCELERATION

In this section, we consider the special case of a constant acceleration $\gamma = \gamma_0$. Under this assumption, Eq. (1.2) becomes autonomous, i.e., the coefficients do not depend anymore explicitly on the independent variable t. From this property, it follows that the differential order of (1.2) can be reduced by one [12-15] and from a SODE one obtains a first order differential equation (FODE) [14, 15]. This procedure provides the general solution of the time-independent BDE and although the asymptotic form of the solution for large value of t was found recently by Cheng et al. [5], it is the first time this general solution is derived, to our knowledge.

(a)

(b)
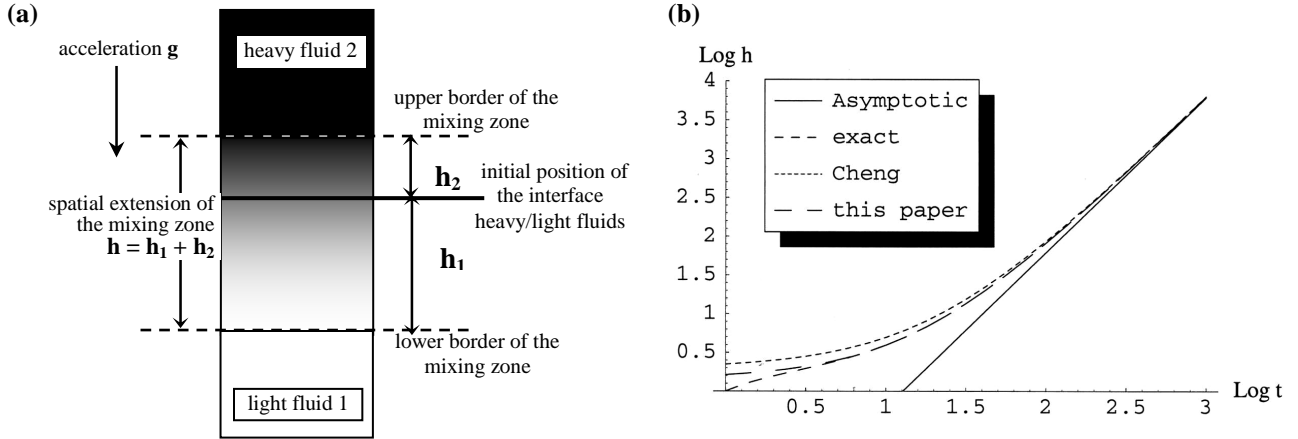
Fig. 2.1. (a) Sketch of two superposed layers of fluids with different densities. The dense and light fluids are respectively located in the upper and lower part of the box. The configuration experiences Rayleigh – Taylor instabilities and a mixing zone develops.
(b) Comparison between the result by Cheng et al. [5] (dotted line) and our result
(dashed line "this paper"). See the main text for further comments.

Since the acceleration is constant, the BDE admits a Lie point symmetry [12, 13], $S_1 = \partial/\partial t$, and it is invariant under the transformation $t \to \bar{t} = t + \Delta t$, $h(t) \to \overline{h(\bar{t})} = h(t)$ where Δt is an arbitrary value of time translation. The FODE is derived by introducing the new function (or dependent variable) $y(t) \equiv dh(t)/dt$ and Eq. (1.2) becomes:

$$y.(dy/dh) = B.\gamma_0 - C.y^2/h \ , \tag{2.1}$$

where the new independent variable is h instead of t. This FODE is linear w.r.t. y^2 and is integrable. The solution is $y^2 = h^{-2C}.\{[2B\gamma_0/(1+2C)].h^{1+2C} + K\}$ where K is an arbitrary integration constant. Keeping in mind that $y \equiv dh(t)/dt$ to come back to the height h(t) in terms of t, the general solution of Eq. (1.2) for $\gamma = \gamma_0$ writes in the closed form:

$$t - t_0 = \int_{h_0}^{h} dX \left[X^C / \left(M.X^{1+2C} + K \right)^{1/2} \right] , \tag{2.2}$$

where $M = 2B\gamma_0/(1+2C)$ and where t_0 is a second constant of integration related to h_0 through the definition $h(t=t_0) \equiv h_0$. The RHS of (2.2) corresponds to a well-known quadrature [16, 17] and the implicit form of (2.2) is $t-t_0 = G(h) - G(h_0)$ with $G(X) = \{X^{1+C}/[(1+C).(\varepsilon K)^{1/2}]\} \times {}_2F_1[1/2, (1+C)/(1+2C); (2+3C)/(1+2C); -\varepsilon.M.X^{1+2C}/K]$ where the function ${}_2F_1(a, b; c; x)$ is the Gauss hypergeometric function [16, 17] and the parameter ε is given by $\varepsilon = \text{sign}(K)$. This expression provides the general solution for h(t), and the two constants (K and t_0) allow to take any value for the initial position $h(t=0) \equiv (h)_0$ [this value should not be confused with h_0 which is the value of h for $t=t_0$!]and the initial velocity $[dh(t=0)/dt] \equiv (h')_0$ – it should be reminded that these two quantities are assumed to be positive in the present modeling. As far as we know, that is the first time Eq. (1.2) is solved analytically for $\gamma = \gamma_0$ without any constraints on the parameters B and C. As a result, in order that a theoretical approach describes accurately a specific experiment, the relevant values of the above parameters can be derived from a comparison between the general solution and experimental measurements (or data).

Moreover, the asymptotic behavior of the solution ($t \to +\infty$) can be obtained exactly from the analytical properties of the function G(X). Considering that X goes to infinity, the asymptotic expansion is, at first order in 1/t:

$$h(t) = \left\{ B.\gamma_0/[2(1+2C)] \right\}(t - t_0 + t_*)^2 + O(1/t) \ , \tag{2.3}$$

with $t_* = G(h_0) - \{(\varepsilon K/M)^{1/(2+4C)}/[(1+C).M^{1/2}]\}.\{\Gamma[(2+3C)/(1+2C)].\Gamma[-1/(2+4C)]\}/\Gamma(1/2)$ where $\Gamma(z)$ is the "gamma factorial function" of argument z [16, 17]. This expression is similar but is not identical to the result given by Cheng et al. [5] although in both cases the solution behaves asymptotically according to:

$$h(t) \approx \{B\gamma_0/[2(1+2C)]\}(t - t_0)^2 , \tag{2.4}$$

for $t \to +\infty$. We conclude that the fluid evolves like a free falling material experiencing a constant acceleration, in agreement with the fact that the acceleration γ is constant. This rather simple asymptotic time dependence has been found earlier by Cheng et al. [5], but in (2.4) the influence of the parameters B and C is clearly evidenced. The coefficient in the RHS of (2.4) is just proportional to M [see just below Eq. (2.2)] and two distinct systems with different values of both B and C will follow the same asymptotic law if M is kept invariant from one system to the other.

Generally, the heavy and light fluids do not satisfy $B_1 = B_2$, $C_1 = C_2$ and therefore M_1 is not equal to M_2. Nevertheless, in spite of this difference, we have $h_i(t) \sim t^2$ for each fluid (i = 1, 2) and the final result is that the total thickness h(t) of the mixing zone obeys the law $h(t) = h_1(t) + h_2(t) \propto t^2$. Notice that t_* provides the order of magnitude of the necessary time delay for the solution to reach the asymptotic behavior in t^2.

Finally, a comparison between various results is given in logarithmic scale in **Fig. 2.1b**. The straight line corresponds to the parabolic solution (2.4) and as t increases, the other curves converge towards this asymptotic behavior. The "short-dashed" line comes from the numerical integration of (1.2) with $\gamma = \gamma_0$; the dotted curve is obtained from the analytical approximation by Cheng et al. [5], and the "long-dashed" line corresponds to Eq. (2.3). It is found that (2.3) converges faster and closer towards solution (2.4) and, consequently, the result given by Eq. (2.3) is more accurate than the work presented in [5] for the current set of initial conditions.

3 SOLUTION FOR A TIME-DEPENDENT ACCELERATION

Now we move to the study of a time-dependent acceleration $\gamma(t)$. In that case Eq. (1.2) is no longer autonomous and in order to make easier our study, we are going to restrict ourselves to the special case:

$$\gamma(t) = \gamma_0.(t/t_0)^n, \tag{3.1}$$

where n is an arbitrary exponent, and where γ_0 and t_0 are two arbitrary constants (it should be noticed that these quantities do not have the same meaning as in Sect. 2). With this assumption Eq.(2) becomes:

$$d^2h/dt^2 = B.\gamma_0(t/t_0)^n - C.(dh/dt)^2/h(t) . \tag{3.2}$$

It depends explicitly upon time and the Lie point symmetry S_1 (see Sect. 2) does not exist anymore. However, one finds that it is invariant under the transformation $t \to \bar{t} = a^{-\alpha}t$, $h(t) \to \bar{h}(\bar{t}) = a^{-\beta}h(t)$ where "a" is the parameter of the transformation (it is a constant), provided the exponents α and β satisfy $\beta/\alpha = n+2$ [12-15].

It is not surprising to end up with this condition since the LHS of (3.2) and the second term of the RHS scale both like h/t^2. Requiring, in addition, that the time-dependent term $B\gamma_0(t/t_0)^n$ has to behave in the same way, one gets the above condition for the ratio β/α. As a consequence, a invariance transformation exists for any value of the exponent n and we are going to derive a solution h(t) in which n is a free parameter. Eq. (3.1) describes decreasing (resp. increasing) acceleration with time for n < 0 (resp. n > 0) and the special case studied in Sect. 2 is recovered for n = 0. Taking into account the degree of freedom of the parameters γ_0 and t_0, we may expect to be able to reproduce (or to fit) acceleration variations achieved in various experiments.

As we did it in Sect. 2, the transformation $(t, h) \to (\bar{t}, \bar{h})$ gives rise to a Lie point symmetry, namely, $S_2 = t.(\partial/\partial t) + (\beta/\alpha).h.(\partial/\partial h)$ given in Refs. [14, 15] and, although the structure of Eq. (3.2) is much more complex than the BDE we solved in the previous section, this symmetry makes possible the reduction of (3.2) to a FODE. In this process, the two invariants of the transformation have to be calculated. The first one is denoted I and noticing that $a = (t/\bar{t})^{1/\alpha} = (h/\bar{h})^{1/\beta}$, we find the relation $h/t^{\beta/\alpha} = \bar{h}/\bar{t}^{\beta/\alpha}$ and the corresponding invariant is $I = h/t^{n+2}$ [12, 14, 15]. Next, to obtain the second invariant J, one has to combine the derivative dh/dt and the time t. From the transformation, we have $d\bar{h}(\bar{t})/d\bar{t} = a^{\alpha-\beta}dh(t)/dt$ which is also $(d\bar{h}/d\bar{t})/\bar{t}^{(\beta/\alpha)-1} = (dh/dt)/t^{(\beta/\alpha)-1}$ and the invariant J is, therefore, $J = (dh/dt)/t^{n+1}$.

These invariants are the key elements to transform Eq. (3.2) in a FODE. The derivative dh/dt [resp. the solution h] expresses in terms of J [resp. I] and, consequently, the second derivative d^2h/dt^2 is changed in the first derivative dJ/dI. Finally, the FODE corresponding to (3.2) is:

$$\left[J / I - (n+2) \right](dJ / dI) = -C(J / I)^2 - (n+1).(J / I) + [B\gamma_0 /(t_0)^n] I . \qquad (3.3)$$

A straightforward family of solutions of this equation is $J = (n + 2).I$ leading to the linear ordinary differential equation $(dh/dt)/t^{n+1} = (n+2)(h/t^{n+2})$, the solution of which is given by $h(t) = h_0(t/t_0)^{n+2}$ where h_0 and t_0 are two arbitrary constants. This expression does not correspond to the general solution of (3.3), nevertheless it is valid for any value of the exponent n and it depends on the arbitrary parameter $h_0/(t_0)^n$. Moreover, setting n = 0 in Eq. (3.1), i.e., taking a constant acceleration γ_0, we obtain $h(t) \sim t^2$ [Eq. (2.4)]. We conclude, therefore, that for $\gamma \sim t^n$ the solution $h(t) \sim t^{n+2}$ can be considered as a direct generalization (or extension) of the behavior $h(t) \sim t^2$ obtained for t going to infinity.

4 CONCLUSION

In this paper, we have studied the buoyancy – drag equation (BDE) which describes the time evolution of the thickness h(t) of a region located at the interface of two fluids where the mixing of both fluids takes place. In this model, the mixing is assumed to be generated by the well – known Rayleigh – Taylor instability that occurs when a upper dense medium is located above a lower light fluid in an acceleration field, $\gamma(t)$, which is directed from top to bottom.

The BDE is a non-linear second order differential equation and it is shown that it possesses a Lie point symmetry $S = S_1$ (resp. $S = S_2$) for a constant acceleration $\gamma = \gamma_0$ [resp. $\gamma(t) \sim t^n$]. In both cases, the initial second order differential equation (SODE) can be transformed into a FODE (first order differential equation) and for the first case ($S = S_1$) the general solution of the BDE is derived analytically in a closed form. As far as we know, this is the first time this solution is found explicitly. In addition, it is obtained that for large time (t goes to infinity), the solution behaves according to $h(t) \sim t^2$ irrespectively of the initial conditions.

For $S = S_2$, we have not been able to derive the general solution, however a one parameter family of solutions has been obtained. Moreover, the thickness of the mixing zone increases as $h(t) \sim t^{2+n}$ (instead of t^2). This solution can be considered as a direct extension of the solution existing for the first case since for n = 0, the acceleration does not vary anymore with t and, in addition $h(t) \sim t^{2+n}$ simply reduces to $h(t) \sim t^2$.

Finally, according to us, the next step in this work corresponds to the study of the FODE for the two invariants I and J. We may expect finding solutions that differ from $J = (n + 2).I$ (case $S = S_2$) in order to go further and to extend the results presented in this paper.

REFERENCES

[1]   Youngs, D. L. 1989, Modelling turbulent mixing by Rayleigh – Taylor instability. *Physica D* **37**(1-3), pp. 270-287.
[2]   Alon, U., Hecht, J., Mukamel, D., Shvarts, D. 1994, Scale invariant mixing rates of hydrodynamically unstable interfaces. *Physical Review Letters* **72**(18), pp. 2867-2870.
[3]   Alon, U., Hecht, J., Hofer, D., Shvarts, D. 1995, Power laws and similarity of Rayleigh-Taylor and Richtmyer – Meshkov mixing fronts at all density ratios. *Physical Review Letters* **74**(4), pp. 534-537.
[4]   Ramshaw, J. D. 1998, Simple model for linear and non-linear mixing at unstable fluid surfaces with variable acceleration. *Physical Review E* **58**(5), pp. 5834-5840.
[5]   Cheng. B., Glimm. J., Sharp, D. H. 2002, Dynamical evolution of Rayleigh – Taylor and Richtmyer – Meshkov mixing fronts. *Physical Review Letters* **63**(3), pp. 036312.
[6]   Chandrasekhar, S. 1961, Hydrodynamic and Hydromagnetic Stability (Oxford University Press, Oxford, 1961).
[7]   Krishan, V. 1999, Astrophysical Plasmas and Fluids (Kluwer, Singapore, 1999).
[8]   Sharp, D., H. 1984, An overview of Rayleigh – Taylor instability. *Physica D* **12**(1-3), pp. 3-10.
[9]   Pailhoriès, P. and Van Renterghem, E. 2006, A mixing model based on the Hamilton's principle, *in proceedings of IWPCTM'10*, Paris, France, July 17-21, 2006, this issue.
[10]   Dimonte, G., 2000, Spanwise homogeneous buoyancy – drag model for Rayleigh – Taylor mixing and experimental evaluation. *Physics of Plasmas* **7**(6), pp. 2255-2269.
[11]   Oron, D., Arazi, L., Kartoon, D., Rikanati, A., Alon, U. and Shvarts, D. 2001, Dimensionality dependence of the Rayleigh – Taylor and Richtmyer – Meshkov instability : late time scaling laws. *Physics of Plasmas* **8**(6), pp. 2283-2289.
[12]   Olver, P. J. 1993, Applications of Lie Groups to Differential Equations (Springer, Berlin, 1993).
[13]   Ibragimov N. H. 1999, Elementary Lie Group Analysis and Ordinary Differential Equations (Wiley, New York, 1999).
[14]   Leach, P. G. L., Feix, M. R. and Bouquet, S. 1988, Analysis and solutions of a nonlinear second-order differential through rescaling and through a dynamical point of view. *Journal of Mathematical Physics* **29**(12), pp. 2563-2569.
[15]   Bouquet, S., Feix, M. R. and Leach, P. G. L. 1991, Properties of second-order ordinary differential equations invariant under time translation and self-similar transformation. *Journal of Mathematical Physics* **32**(6), pp. 1480-1490.
[16]   Gradshteyn, I., S. and Ryzhik, I. M. 1965, Table of Integrals, Series, and Products (Academic Press, New York, 1965).
[17]   Abramovitz, M. and Stegun, I. A. 1965, Handbook of Mathematical Functions (Dover, New York, 1965).

e-mail: `a.m.buyko@vniief.ru`

Results and Prospects of Material Strength Studies on Electrophysical Facilities based on Rayleigh-Taylor Instability Development in Liner Systems

Anatoly BUYKO[1], Vadim ZMUSHKO[1], Walter ATCHISON[2] and Robert REINOVSKY[2]

[1]*Russian Federal Nuclear Center – All-Russian Research Institute of Experimental Physics, Sarov, N.Novgorod reg., Russia*
[2] *Los Alamos National Laboratory, Los Alamos, NM, USA*

Abstract: Data of refined perturbation growth simulations of the three-layer cylindrical liner systems, tested during experiments with DEMG (Disk Explosive Magnetic flux compression Generator) to study the strength properties of copper and polyethylene at shockless pressures up to ~15 GPa, and preliminary simulation data of the same liner systems for the Atlas experiments to study the strength properties of copper at shockless compression to ~40 GPa are presented. The feasibility of similar strength experiments with quasi-isentropic material compression to ~ 2000 GPa using DEMGs is demonstrated.

1 INTRODUCTION

Magnetically imploded cylindrical liners can be used to study dynamic shear strength properties of materials based on the growth of initial perturbations during the Rayleigh-Taylor instability development in liner systems [1-7]. High-current capacitor banks (Pegasus-2, Shiva Star, Atlas, peak currents $I_{max} = 6 \div 30$ MA) and disc explosive magnetic generators (DEMGs, $I_{max} = 20 \div 70$ MA) are capable of driving cylindrical liner systems to a wide range of material pressures from ~1 GPa [2,3] to hundreds of GPa [5]. Numerical simulations of the experimental perturbation growth make it possible to test different dynamic strength models [3,7].

The 1998-1999 RUS-1,2,5 [2] experiments were focused on the strength properties of cylindrical current carrying liners having a radius of 2.4 cm and thickness of 0.5 mm and made from A995 analytically pure soft aluminum (99.995 % Al), ADO commercially pure aluminum and two high-strength aluminum alloys with magnesium (AMg-6) or zinc (V95) as major additives. The liners were driven by a ~ 6.5 MA current at a ~ 1 GPa magnetic pressure. We have managed to describe the experimental growth of initial perturbations by simulations [3] under some assumptions about conductivity and dynamic strength of the materials being tested. In these simulations, the characteristic yield strength of all the tested materials proved to be similar, 0.15-0.3 GPa, while their quasi-static (conventional) yield strengths differed up to 40 times. Thermal softening of the materials of interest due to their Joule heating complicated the analysis of these experiments.

As a result, VNIIEF suggested using cylindrical ponderomotive units (PU) with multi-layer liner systems [4,5] that preclude Joule heating of the materials being tested. Such liner systems were tested in the RHSR-1,2 (Russian High Strain Rate) experiments with 0.4 meter diameter DEMGs [6]. These experiments sought to validate the concept of using state-of-the-art electrophysical facilities to study dynamic strength properties of materials based on the perturbation growth in cylindrical liner systems. The preliminary analysis [6,7] of experimental data confirmed the possibility to use such liner systems for strength studies of high-density (copper) and low-density (polyethylene) materials. The experimental three-layer Al-CH$_2$-Cu (RHSR-1) and Al-H$_2$O-Cu (RHSR-2) liner systems with a current carrying aluminum piston liner (**Fig. 1.1**) provided isentropic compression of copper and polyethylene to design pressures of ~15 GPa. The radii of the boundaries between different materials in these liner systems were 2.4 ≈ 2.6 - 4.8 - 5.2 cm. On the outer surface of the Cu layer (R ≈ 2.6 cm) were machined axially symmetric sinusoidal perturbations with wavelengths of $\lambda = 2$ and 4 mm and full amplitudes (peak to valley) of $A_0 = 1.0$ mm (RHSR-1) and 0.6 mm (RHSR-2).
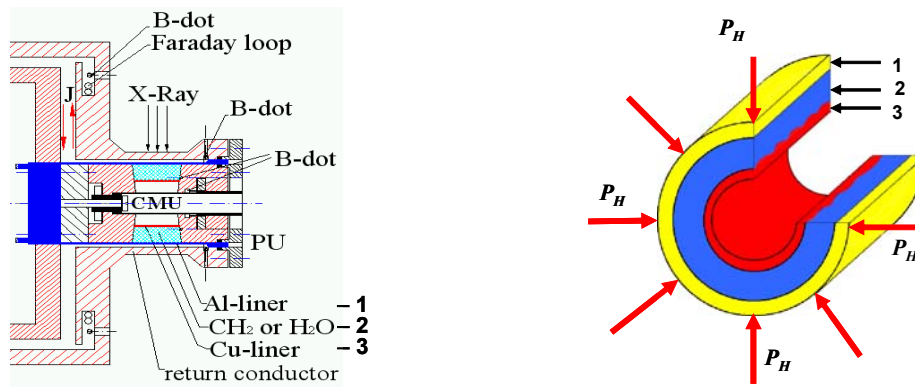
Fig. 1.1. Diagrams showing the PU with a three-layer liner system and its diagnostic suite in the RHSR-1,2 (left) experiments and how this liner system works (right). 1 – current carrying piston liner, 2 – working fluid: water in RHSR-2 or polyethylene in RHSR-1, 3 – Cu sample (Cu as reference material in RHSR-1)

The 0.4 meter diameter DEMGs equipped with an electrically exploding foil opening switches (FOS) in similar devices [5] are capable of compressing Cu liners to $P \approx 120$ GPa without shock and to hundreds of GPa with shock waves; at such pressures, materials start melting. In accordance with preliminary calculations, Atlas is capable of shock and shockless copper compression in similar liner systems to ~ 200 GPa and ~ 70 GPa, respectively. The physics of shock-drive liner systems has two major features that distinguish them from the system shown in **Fig. 1.1**: The current carrying liner 1 is an impactor, i.e. it is accelerated into a vacuum gap to impact the working fluid layer 2 and, through it, the liner of interest 3; the working fluid layer is placed next to the inner surface of the liner of interest 3 in order to preclude spallation in the latter. The anti-spall layer may also be required in the systems with piston liners.

Simulations of experimental devices as a whole are also important for the investigations in question as they provide rather accurate prediction of currents in liner PUs, which is of particular importance for "targeted" radiography (**Fig. 1.1**, left) of rapidly growing perturbation amplitudes in the liners. At VNIIEF, such simulations are performed with a 1D $(MHD)_n$ code developed on the basis of the UP technique [8] and 1D MHD approximation to simulate different pulse power systems and loads [2-7]. Thus, we also simulate essentially two-dimensional units of the devices, such as DEMG and quasi-spherical liners, by using prior 2D simulation data. 1D $(MHD)_n$ simulations of experimental devices generally provide high accuracy of current prediction. For example, in the RHSR-1, 2 experiments with a seven-module 0.4 meter diameter DEMG, the difference between experimental currents and pre-shot design simulations is ~ 3 percent [6].

Below are given the results of refined simulations (as against [7]) of experiments (**Fig. 1.1,** Section 2) and similar (Section 3) liner systems to study material strength properties under quasi-isentropic compression in DEMG and ATLAS experiments. 2D simulations use the MIMOZA Lagrange-Euler MHD code [9,3] using different strength models and equations of state (Mie-Grueneisen for copper and polyethylene, tabulated for water and hydrogen).

2 DYNAMIC STRENGTH OF COPPER AND POLYETHYLENE UNDER SHOCKLESS DRIVE TO 15 GPA

In earlier studies [4,5,7] we considered different strength models of copper and polyethylene, such as Glushak's (VNIIEF) and Steinberg's (LLNL) elasto-plastic strength models of copper, which gave ~ 3 times different calculated growths of perturbation amplitudes for the same copper liners [4,5]. The VNIIEF copper and polyethylene strength models we use have been validated in explosive perturbation growth experiments with flat copper and polyethylene slabs under shockless compression to ~ 40 GPa for Cu [10] and ~ 20 GPa for CH_2 (teams of Dr. Rayevsky and Dr. Solovyev). Let us give the major formulas and constants of these models given that the polyethylene model is viewed by the authors as "the first approximation…for preliminary calculations" (due to the lack of data).

In the elasto-plastic model for copper and polyethylene, the yield strength Y_{ep}, the shear modulus G, and Poisson's ratio ν are calculated using the formulas ([T]=^oK):

$$Y_{ep}\big|_{T<T_m} = Y_{ok} \cdot \left[1 + a\left(1 - e^{-b\varepsilon_p}\right)\right] \cdot (1 + \alpha P_x) \cdot \left(1 - \frac{T}{T_m}\right)^{\beta}, \quad Y\big|_{T \geq T_m} = 0 ,$$

$$G = \frac{3(1-2\nu)}{2(1+\nu)} \cdot \rho C_s^2, \quad \nu = \begin{cases} \nu_0\left[1 + \left((2\nu_0)^{-1} - 1\right)(T/T_m)\right], & T < T_m , \\ 0.5 , & T \geq T_m ; \end{cases}$$

$$Y_{ok} = \begin{cases} 73\,MPa, \\ 83\,MPa, \end{cases} \quad a = \begin{cases} 9.66, \\ 1.4, \end{cases} \quad b = \begin{cases} 1.5, \\ 5, \end{cases} \quad \alpha = \begin{cases} 0.11\,GPa^{-1}, \\ 0.2\,GPa^{-1}, \end{cases} \quad \beta = \begin{cases} 1.0, \\ 1.4, \end{cases} \quad \nu_0 = \begin{cases} 0.347, & Cu ; \\ 0.45, & CH_2 \end{cases}.$$

(1)

Here, ε_p and T are the degree of plastic deformation and temperature, P_x and T_m are the "cold" pressure (at $T = 0^0$ K) and the material's melting point determined by its density ρ (T_m according to Lindemann), $C_S = (\partial P / \partial \rho)_S^{0.5}$ is isentropic speed of sound ($P = P_x + P_T$, $P_T = 0$ at $T = 0^0$ K).

In the relaxation strength model, copper's yield strength Y_{rel} is derived from the following equations:

$$\dot{Y}_{rel} = 3G\dot{\varepsilon} - \frac{1}{\tau}\left(Y_{rel} - Y_{ep}\right), \qquad Y_{rel} \geq Y_{ep} , \qquad \tau = \tau_0 \left(1 + \frac{\dot{\varepsilon}}{\dot{\varepsilon}_0}\right)^{-0.5} ;$$

$$Y_{rel} = 3G\varepsilon_e , \qquad Y_{rel} < Y_{ep} ; \quad \tau_0 = 2 \cdot 10^{-6}\,s, \dot{\varepsilon}_0 = 0.25\,s^{-1}\,(Cu),$$

(2)

where $\dot{\varepsilon}$ and ε_e are the strain rate and the degree of elastic deformation, τ is the relaxation time of elastic stresses. With small values of $\dot{\varepsilon}$, model (2) transforms into elasto-plastic model (1):

$$Y_{rel} \approx Y_{ep} , \quad \left|\dot{\varepsilon}\right| << Y_{ep} / (3\tau G).$$

(3)

The perturbation growth on the Cu liner recorded in RHSR-2 proved to be generally close to the simulation (see **Figs. 2.1, 2.2**). This is an important result, because it could not be excluded before the experiment that water would have no high viscosity or even some strength, and we were not sure that the results obtained for copper and tested during explosive experiments [10] at shockless pressures as high as 40 GPa would be applicable to ~ 15 GPa pressures. This result allows us to consider copper as a reference material in the RHSR-1 experiment and learn about strength properties of polyethylene, for example by refining model (1) (1): $\alpha \approx 0.5$ GPa^{-1} (**Fig. 2.2**)$^{*)}$. At that, the highest characteristic yield strength of polyethylene is ~1 GPa (~100 times higher than the quasi-static value). On the whole, it is clear that other strength models of polyethylene, for instance, the visco-elasto-plastic model, should be considered in addition to model (1).

a) experiment   b) simulation   c)   d)
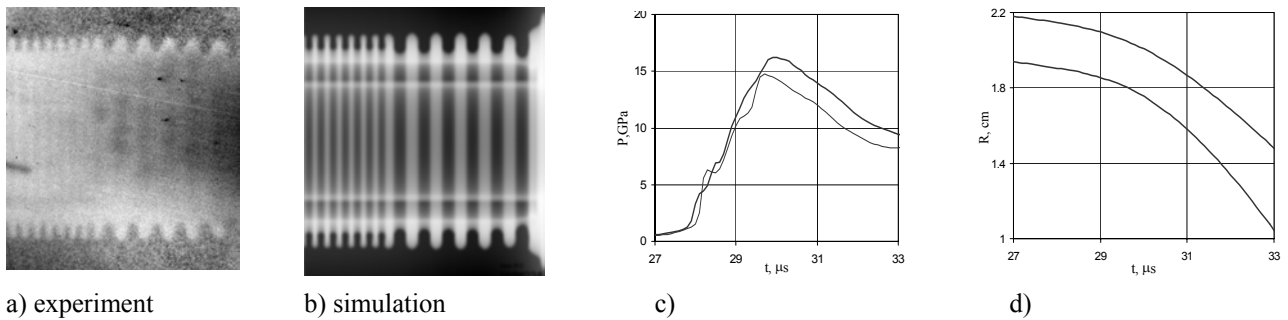
Fig. 2.1. Radiograms of the copper liner next to water (a, b); calculated pressures in perturbation peaks and valleys ($\lambda = 2$ mm) and average radii of the liner's boundaries (c, d)

$^{*)}$ Ref. [7] gave the value of $\alpha \approx 0.12$ GPa^{-1}, because as distinct from (1), the temperature softening was described by the formula $[1 - (T/T_m)^{\beta}]$, which is probably less preferable. Its use in (1) results in the overstated yield strength under normal conditions (~ 28 MPa instead of ~ 10 MPa).
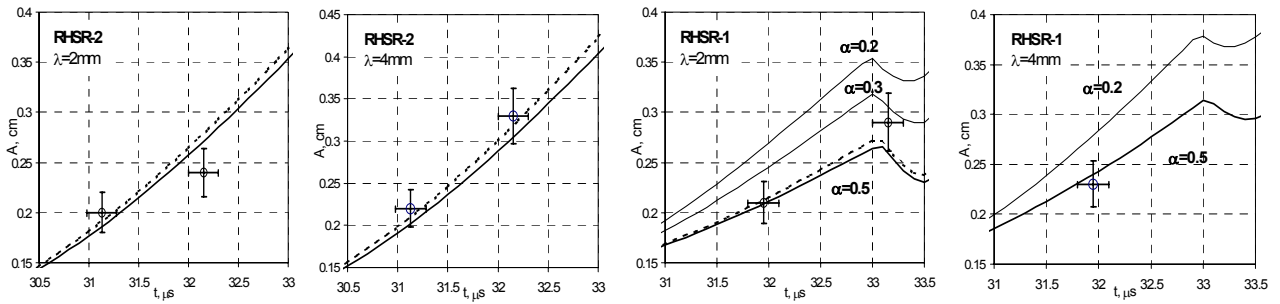
Fig. 2.2. Experimental data for the perturbation growth on the Cu liner in polyethylene (+) compared with simulations using the relaxation and elasto-plastic (dash line) copper strength models, parameter $\alpha = 0.2 - 0.3 - 0.5$ GPa^{-1} for polyethylene (RHSR-1), and current tables close to the experiment ($I_{max} = 33.4$ MA)

Fig. 2.2 indicates that the relaxation (2) or elasto-plastic (1) strength models of copper give almost identical computational perturbation growths on the Cu liner in accordance with (3). The characteristic computational values of deformation, strain rate and yield strength of copper are $\varepsilon \approx 130\%$, $\dot{\varepsilon} \approx 10^6 \sec^{-1}$, $Y_{Cu} \approx 1 GPa$ (they exceed the quasi-static yield strength of copper by a factor of ~ 15). Thus, copper strength models (1) – (2) suggest that the given strain rates have almost no effect on the strength properties of copper subjected to isentropic compression to ~ 15 GPa

3 SOME PROSPECTS OF MATERIAL DYNAMIC STRENGTH STUDIES

In the near future, we are going to study dynamic strength of copper at ~ 40 GPa shockless pressures and compare it with the results of explosive experiments [10] with flat slabs at similar shockless pressures. Of interest is additional validation of the copper strength models (1) – (2), since some questions remain open upon review of the shots [10] (for example, the experimental growth of 1 millimeter wavelength perturbations has not been determined through simulations). **Fig. 3.1** shows the results of perturbation growth simulations of two liner systems chosen for Atlas based on the 1D (MHD)$_n$ simulations of the devices similar to RUS-6,7 [4]. Liner system 1 has three layers (**Fig. 1.1**) with layer radii of $2.0 - 1.8 - 1.0 - 0.8$ cm and provides "single-peak" compression of the Cu liner, determined by the great thickness of the intermediate layer of water (8 mm). The PU current had a peak value of $I_{max} \approx 19$ MA at a charge voltage of Uo=185kV. The distinguishing features of liner system 2 as against **Fig.1.1** include the presence of a 5 millimeter anti-spall layer of water and "double peak" compression of the Cu liner, determined by the small thickness of the water layer, 3 mm ($I_{max} \approx 21.5$ MA, Uo=210 kV). The layers in these liner systems had the radii of $2.0 - 1.8 - 1.5 - 1.3 - 0.8$ cm. The outer surface of the cylindrical Cu liners had machined sinusoidal axially symmetric initial perturbations with $A_0 = 2a_0$ amplitude and $\lambda = 4 - 2 - 1$ millimeter wavelength.
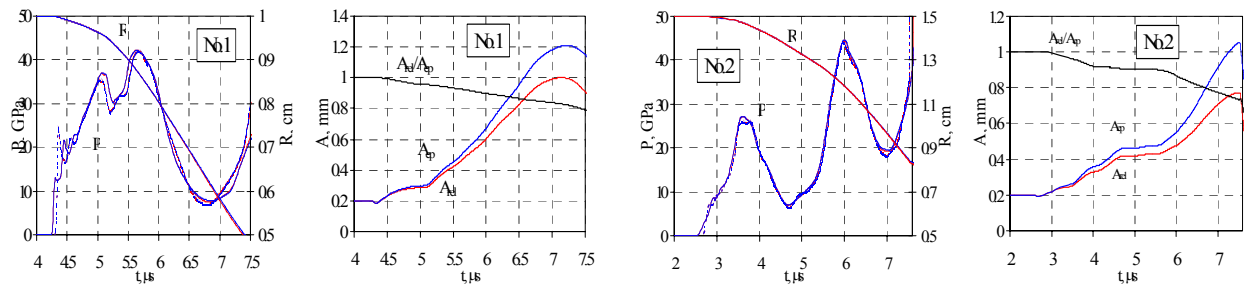
Fig. 3.1. Pressures $P_i(t)$ in perturbation peaks and valleys ($\lambda = 1$ mm) on the outer surface of the Cu liner; average radius R (t) of this surface and perturbation amplitudes $A_{rel}(t)$ and $A_{ep}(t)$ resulting from the simulations of liner systems 1 and 2 using the relaxation and elasto-plastic copper strength models

Fig. 3.1 indicates that the trend of the curves for perturbation amplitudes versus time *A(t)* corresponds to the driving pressure curves *P(t)*. In particular, "double-peak" pressures correlate with the two-stage perturbation growth *A(t)*. The difference between the computational perturbation amplitudes *A$_{ep}$(t)* and *A$_{rel}$(t)* given by the elasto-plastic and relaxation models is the higher, the smaller is the perturbation wavelength in liner systems 1 and 2:

$$\frac{\Delta A_{max}}{A_{max}} \approx \begin{cases} 17\% & - & 9\% & - & 4\%, & \sim 40\,GPa, & N\,1, \\ 26\% & - & 10\% & - & 5\%, & \sim 40\,GPa, & N\,2, \end{cases} \quad (4)$$

$$\lambda \qquad\quad 1 \quad - \quad 2 \quad - \quad 4 \;\; mm$$

where $A_{max} \equiv (A_{ep} - A_{rel})_{max}$, $A_{max} \equiv (A_{ep})_{max}$. It follows from this that with Atlas's possible perturbation amplitude measurement accuracy (~5%), which is higher than in [6,10], the growth of long-wavelength perturbations in the liner systems being considered would not allow us to give preference to any of the two copper strength models being used. Hence, of interest is the experimental growth of perturbations with the minimum wavelengths admissible for efficient radiography ($\lambda \le 2$ mm).

Fig. 3.2 gives simulation data of devices similar to the RHSR-2 device with the number of DEMG modules N = 7 and 15 (I_{max} = 31 and 47 MA). The working liquid of the devices' liner system is gaseous hydrogen at a pressure of 25 MPa, the radii of the liner surfaces are 2.4 – 2.6 cm (Cu) and 4.6 – 5.2 cm (Al). Such systems may produce higher isentropic compression (**Fig. 3.2 a**) of the driven Cu liner than the systems shown in **Fig. 1.1** : with N = 7 to ~ 40 GPa (compared to ~ 15 GPa in the RHSR-2 device) and can be used in the HS/HSR-101, 102 experiments on DEMG.

a)   b)   c)
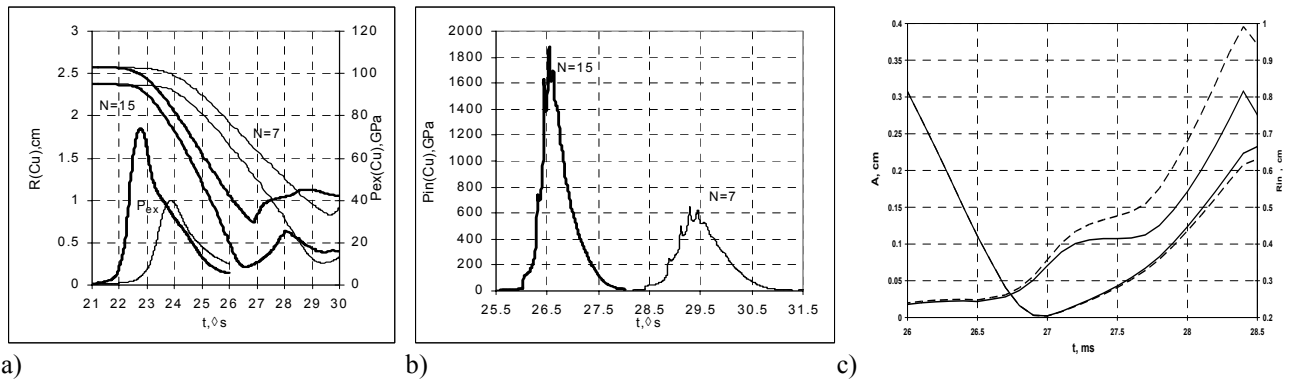
Fig. 3.2. Drive pressure P_{ex} (t) on the Cu liner, its surface radii (left) and slow-down pressure P_{in} (t) from simulations of the liner system with hydrogen in the devices similar to RHSR – 2 (N is the number of DEMG modules) – a, b; c - perturbation amplitude and average radius of the Cu liner's inner boundary given by the 2D simulations of the Al – H_2 – Cu– H_2 (N=15) liner system using the relaxation and elasto-plastic (dash line) copper strength models

During liner deceleration by compressed hydrogen pressure, the liner can undergo quasi-isentropic loading near the axis to pressures of 600 ÷ 1900 GPa with N = 7 ÷ 15 (**Fig. 3.2 b**),which is of interest for testing the material strength models with the highest possible quasi-isentropic pressures (**Fig. 3.2 c**). Here the characteristic computational values of deformation, strain rate and yield strength of copper are $\varepsilon \approx 170\%$, $\dot{\varepsilon} \approx 5 \cdot 10^6\,\text{sec}^{-1}$, $Y_{Cu} \approx 80\,GPa$ (they exceed the quasi-static yield strength of copper by a factor of ~ 1200). In this case, initial perturbations are machined on the inner surface of the liner of interest, as distinct from **Fig. 1.1**, and it is harder to record the growth of such perturbations than in the systems shown in **Fig. 1.1**, though it is possible [11]. Since the minimum radius R_{min} of the liner of interest can be many times smaller than the initial radius R_0 (in the systems shown in **Fig. 1.1**, $R_0 \approx 2\,R_{min}$ – see **Fig. 2.1 d**), may give experimental evidence on whether or not the difference between deformation parameters of flat and cylindrical liners correlates with the geometry-related difference between the deviator components of the stress tensor σ_{ik} and the shear strain tensor ε_{ik}. As distinct from shots [11], magnetically imploded outer liners produce uniform compression, which allows us to expect that perturbation amplitudes in the inner liner of interest will be measured with smaller errors.

Such VNIIEF-proposed liner systems can also be used to study compressibility of hydrogen and other gases at ~ 2000 GPa pressures and, probably, turbulent mixing of materials on the inner surface of the liner of interest.

4 SUMMARY

In general, the elasto-plastic and relaxation shear strength models of copper, that have been proposed at VNIIEF and validated through explosive experiments with up to ~ 40 GPa shockless pressures, proved to be applicable to strength description of copper at up to ~15 GPa shockless pressures. Both models give almost identical perturbation growth for the cylindrical Cu liner of interest bordering on water, which is close to the RHSR-2 experiment. Thus, according to the relaxation model being used, strength of copper under isentropic compression to ~15 GPa shows almost no response to the strain rate up to ~10⁶ s⁻¹.

As distinct from water, polyethylene strongly restrains the growth of perturbations on the Cu liner. This, in principle, allows us to get new data on dynamic strength of polyethylene from the RHSR-1 experiment, given the possibility to consider copper a reference material for material dynamic strength as demonstrated during RHSR-2. Pre-shot simulations of RHSR-1 were performed, which highlighted the necessity of substantial refinement or modification of the elasto-plastic strength model of polyethylene proposed earlier by VNIIEF as "the first approximation…for preliminary calculations" (due to the shortage of experimental data).

Results of simulations of RHSR-2-similar cylindrical candidate liner systems for the envisaged HS/HSR-101,102 experiments on Atlas are given. The objective of these experiments is to look at the dynamic strength of copper at shockless compression to ~40 GPa, to provide additional validation of the strength models of copper, and – probably – to reveal strain rate effects on the shear strength properties of copper. It is also important to improve the strength models of copper as the reference material for dynamic strength studies of low-density materials based on the perturbation growth in the liner systems similar to RHSR-1.

Two-liner gas-filled systems (Al-H_2-Cu-H_2) in devices similar to the RHSR-2 experiment are considered tentatively. Such devices are shown to be promising as applied to strength studies of high-density materials at up to ~ 2000 GPa quasi-isentropic pressures.

REFERENCES

[1] Buyko A.M. *et al.* Numerical studies of perturbation growth in liner systems including elasto-plastic properties of liners. *Workshop paper*, July 5-9, 1996, Los Alamos, USA.

[2] Buyko A.M. *et al.* Initial perturbation growth in magnetically imploded cylindrical liners made of aluminum and high-strength aluminum alloys (Principal Results of Joint LANL/VNIIEF Pegasus-2 Experiments). Proc. 7th IWPCTM, 1999, St.-Peterburg, Russia, pp. 149-154.

[3] Buyko A.M. *et al.*, 2D computations for perturbation growth of magnetically driven cylindrical aluminum and aluminum alloy liners, *Proc. 7th Int. Work. Phys. Compr. Turb. Mix.*, St.Petersburg, 1999, Ed. E.Meshkov, Yu.Yanilkin & V.Zhmailo, Sarov, 2001, pp.237-243.

[4] Buyko A.M. *et al.* Study of dynamic strength of copper in joint VNIIEF/LANL liner experiments on capacitor bank AT-LAS (RUS – 6, 7), *Proc. Int. Conf. Megagauss-9*, Moscow-St.-Petersburg, 2002, pp. 718-724.

[5] Buyko A.M. *et al.* Explosive magnetic liner systems to study dynamic strength of materials, *Proc. 14th IEEE Int. PPC*, Dallas, 2003, pp. 74-77.

[6] Arinin V.A. *et al.* A series of joint VNIIEF/LANL experiments on radiographic studies of perturbation growth at the interface of a polyethylene liner with polyethylene or water, *Proc. Int. Conf. Megagauss-10*, Berlin, 2004 pp. 348-353.

[7] Buyko A.M. *et al.* Dynamic Copper and Polyethylene Strength in Shockless Loading to 15 GPa According to the Data of Explosive Magnetic Experiments with Cylindrical Three-Layer Liner Systems, *Pres. 15th IEEE Int. PPC*, Monterey, 2005.

[8] Gavrilov N.F. *et al.* The UP-OK code for solving one-dimensional continuum mechanics problems by one-dimensional technique, *VANT, Series: Techniques and Codes for Numerical Simulation of Computational Physics Problems*, 1982, Vol. No. 3 (4), pp. 11-14

[9] Sofronov I.D. *et al.*, Program system MIMOZA: Solving multi-dimensional hydrodynamics problems, *Issues of Computer Simulation of Computational Mathematics and Computer Science*, Russia, Moscow – Arzamas-16, 1994.

[10] Rayevsky V.A. *et al.*, Studying Rayleigh-Taylor instability in copper and aluminum at pressures up to 45 GPa and deformation rates $10^5 – 10^8$ s^{-1}, *Pres. Int. Conf. 5th Khariton Scientific Talks*, Sarov, VNIIEF.

[11] Makarov Yu.M. *et al.*, Perturbation method to study shear strength of materials up to pressure ~ 300 GPa, *Pres. Int. Conf. 7th Khariton Scient. Talks*, Sarov, VNIIEF, 2005.

e-mail: `bcheng@lanl.gov`

An Overview of Mix Models

Baolian CHENG [1]

[1] *Los Alamos National Laboratory, Los Alamos, NM 87545*

Abstract: Fluid mixing is an important phenomenon in many physical applications from supernova explosions to inertial confinement fusion. In this paper, we present an overview on the current existing dynamic mix models in the scientific community, in particular, the multifluid interpenetration mix model, the phenomenological and hybrid turbulent mix models, the buoyancy drag model, and the large eddy simulation mix model. The similarities, distinctions, and connections between these models and their applications are discussed.

1 INTRODUCTION

Small perturbations in a multifluid systems grow due to buoyancy and shear driven instabilities at an interface between distinct fluids. These instabilities produce turbulent mixing zones consisting of bubbles of light fluid and spikes of heavy fluid, each penetrating into the opposite fluid. There are three major types of instabilities which play important roles in mix processes. The first type, called Rayleigh-Taylor (RT) instability [1], occurs when a fluid accelerates another fluid of higher density. The second instability, named Richtmyer-Meshkov (RM) instability [2], takes place when a shock wave accelerates a perturbed interface between two fluids of different densities. The third type is Kelvin-Helmholtz instability, which arises when a non-zero velocity gradient exists between the two fluids. These instabilities appear in technological applications, such as inertial confinement fusion (ICF) capsules, and in natural physical phenomena, such as supernova explosions in astrophysics. Studies of hydrodynamic instabilities have been carried out extensively in experiments [3–5], theories [3, 6–11] and numerical simulations [7, 11, 12], over many decades. Various models for fluid mixing have been proposed, from stochastic models describing the microstructure and evolution of the mixing region [7, 9–11, 13, 14] to models predicting the growth rate of instabilities and large structures in the mixing layer [13, 15–18]. In particular, current mix models include phenomenological turbulent mix models [7], hybrid turbulent mix models [10], BHR single fluid turbulence model, the ensemble-averaged microphysical model [14], multifluid interpenetration mix model [9], buoyancy-drag models [5, 16, 17], and the large-eddy simulation model. These models differ in the variables retained after averaging and in the closure assumptions introduced as constitutive laws required to complete the equations. Each model shows advantages and difficulties. Some of the difficulties are not removable, for example, a large set of undetermined model parameters, and lack of physical derivations of some model equations. In order to describe the chaotic mixing processes uniquely and predictively, it seems that a set of multifluid equations derived from first principles is strongly needed.

The main contribution of this paper is to present an overview of the various mix models, including their dynamical equations, closures, assumptions, and applications, so that users can choose the proper mix model for their problems. We will, especially, focus on the similarities, connections, and major differences between each class of the models in the discussion.

2 MIX MODELS

2.1 Phenomenological mix models

Phenomenological mix models often are not derived from first principles. The model equations are constructed empirically through comparisons between numerical simulations and experiments. Their capabilities rely on the flexibility of the model parameters and the phenomenological closure relationships. A typical model in this class is the Youngs' mix model [7] which was constructed under the guidance of numerical simulations and experimental data. The model equations have the following form

$$\frac{\partial}{\partial t}(\rho_r f_r) + \frac{\partial}{\partial x_j}(\rho_r f_r u_{rj}) = 0; \qquad (2.1)$$

$$\frac{\partial}{\partial t}(\rho_r f_r u_{ri}) + \frac{\partial}{\partial x_j}(\rho_r f_r u_{rj} u_{ri}) = -f_r \frac{\partial}{\partial x_i}p - m_r \frac{\partial}{\partial x_j}R_{ij} + \sum_s (D_{rsi} + M_{rsi}) + \rho_r f_r g_i; \tag{2.2}$$

$$\frac{\partial}{\partial t}(\rho_r f_r e_r) + \frac{\partial}{\partial x_j}(\rho_r f_r u_{rj}) = -h_r p_r \frac{\partial}{\partial x_j}\overline{u}_j + \frac{\partial}{\partial x_j}\left(\rho_r f_r D \frac{\partial e_r}{\partial x_j}\right) + \epsilon; \tag{2.3}$$

$$\frac{\partial}{\partial t}(\rho k) + \frac{\partial}{\partial x_j}(\rho k \overline{u}_j) = \frac{\partial}{\partial x_j}\left(\rho D_k \frac{\partial k}{\partial x_j}\right) + S_k - \epsilon, \quad \frac{\partial}{\partial t}L + u_{Lj}\frac{\partial}{\partial x_j}l = \frac{\partial}{\partial x_j}\left(D_L \frac{\partial L}{\partial x_j}\right) + S_L - e_L L, \tag{2.4}$$

and the phenomenological relationships to close this model are given by

$$\rho = \sum_r f_r \rho_r, \; \rho_{rs} \equiv (f_r \rho_r + f_s \rho_s)/(f_r + f_s), \; u_{ri} = \overline{u}_i + w_{ri}, \; \overline{u}_i \equiv \sum_r f_r \overline{u}_{ri}, \tag{2.5}$$

$$w_{ri} = -\frac{D}{f_r \rho_r}\frac{\partial}{\partial x_i}(f_r \rho_r), \; u_{ri} - \overline{u}_{ri} = w_{ri} + \frac{D}{f_r}\frac{\partial f_r}{\partial x_i}, \; D_{rsi} = c_1 \frac{\rho_{rs} f_r f_s}{L}|\vec{u_r} - \vec{u_s} + \vec{w_r} - \vec{w_s}|, \tag{2.6}$$

$$M_{rsi} = -c_a \rho_{rs} f_r f_s \left(\frac{D_r u_{ri}}{Dt} - \frac{D_s u_{si}}{Dt}\right), \; \frac{D_r u_{ri}}{Dt} \equiv \frac{\partial u_{ri}}{\partial t} + u_{rij}\frac{\partial u_{rj}}{\partial x_j}, \quad p = \sum_r h_r p_r, \; h_r = \frac{f_r/(\rho_r c_r^2)}{\sum_s f_s/(\rho_s c_s^2)}, \tag{2.7}$$

$$R_{ij} = \frac{2}{3}\rho k \delta_{ij} - 2\mu_t(\tilde{e}_{ij} - \frac{1}{3}\tilde{e}_{kk}\delta_{ij}), \; \tilde{e}_{ij} \equiv \frac{1}{2}\left(\frac{\partial \tilde{u}_i}{\partial x_j} + \frac{\partial \tilde{u}_j}{\partial x_i}\right), \; \tilde{u}_i = \sum_r f_r \rho_r u_{ri}/\rho, \tag{2.8}$$

$$\epsilon = 0.09\rho k^{1/2}/l_t, \; l_t = c_2 L, \; \mu_t = \rho k^{1/2}l_t, \; D = D_k = D_L = 2k^{1/2}l_t, \tag{2.9}$$

$$S_k = \sum_{r>s}(u_{si} - u_{ri})(M_{rsi} + D_{rsi}) - R_{ij}\tilde{e}_{ij}, \quad u_{Li} = \overline{u}_i + \sum_{r>s} f_r f_s(f_r - f_s)(u_{si} - u_{ri})/\sum_{r>s} f_r f_s, \tag{2.10}$$

$$S_L = \sum_{r>s} f_r f_s \sqrt{s}(u_{sj} - u_{rj}n_{rsj})/\sum_{r>s} f_r f_s, \; s \equiv \frac{2\rho_{rs}}{\rho_r + \rho_s}e_L = \frac{1}{3}e_{kk} - c_3|n_i e'_{ij}n_j|, \tag{2.11}$$

$$e_{ij} = \frac{1}{2}\left(\frac{\partial \overline{u}_i}{\partial x_j} + \frac{\partial \overline{u}_j}{\partial x_i}\right), \; e'_{ij} = e_{ij} - \frac{1}{3}e_{kk}\delta_{ij}, \; c_1 = a + bA, \; c_2 = c + dA, \; A \equiv \left|\frac{\rho_1 - \rho_2}{\rho_1 + \rho_2}\right|, \tag{2.12}$$

where ρ_r, u_{rj}, e_r and f_r, respectively express the mass density, velocity, energy density, and volume fraction of fluid r, the other detailed notations are explained in [7].

In this model, the unresolved parts (or the interactions between species) are closed by added mass, various (mass, thermal and turbulence) diffusions, drag, and turbulence dissipations, which are defined by more than ten phenomenological relationships and six adjustable model parameters (c_a, D, a, b, c, d). Because of a large degree of fine tuning, this model, in practice, works quite well in spite of its lack of rigorous derivation and some unusual terms in the equations which may not be explained physically. Therefore, such a model is an engineering model, and one never knows how many terms are enough and what their exact forms are to capture the real physics. This model, in general, is used to describe turbulent chunk mix phenomena in a system although the model equations are mathematically ill-posed in inviscid flows, due to the assumption of pressure and thermal equilibrium between the fluids. However, this mathematical instability is removed by the addition of a non-zero physical viscosity in the system.

2.2 Ensemble-average microphysical model

A typical model in this class was proposed by Glimm et al [11,14]. It is based on the formalism that is described by Drew via performing single-phase averages of the microphysical model (Euler equations) over an infinite ensemble of microscopic flow realizations. The closures for this model are in the interfacial quantities, *i.e.*, the interfacial velocity v^*, interfacial pressure p^*, and the interfacial energy rate $(pv)^*$. The model equations are given below

$$\frac{\partial \beta_k}{\partial t} = -v^* \frac{\partial \beta_k}{\partial z}, \quad \frac{\partial \rho_k}{\partial t} + \frac{\partial(\rho_k v_k)}{\partial z} = \frac{\rho_k(v^* - v_k)}{\beta_k}\frac{\partial \beta_k}{\partial z}, \tag{2.13}$$

$$\frac{\partial(\rho_k v_k)}{\partial t} + \frac{\partial}{\partial z}(\rho_k v_k^2 + p_k) = \rho_k g(t) + \frac{1}{\beta_k}\left[\rho_k v_k(v^* - v_k) + p^* - p_k\right]\frac{\partial \beta_k}{\partial z}, \tag{2.14}$$

$$\frac{\partial(\rho_k e_k)}{\partial t} + \frac{\partial}{\partial z}(\rho_k e_k v_k + p_k v_k) = \rho_k v_k g(t) + \frac{1}{\beta_k}\left[\rho_k e_k(v^* - v_k) + (pv)^* + p^* v_k - 2p_k v_k\right]\frac{\partial \beta_k}{\partial z}, \tag{2.15}$$

with phenomenological closures $\beta_1 + \beta_2 = 1$, $v^* = \mu_1^v v_2 + \mu_2^v v_1$, $p^* = \mu_1^p p_2 + \mu_2^p p_1$, $(pv)^* = \mu_1^{pv} p_2 v_2 + (1 - \mu_1^p - \mu_2^p) p_1 v_2 + \mu_2^{pv} p_1 v_1$, and assumed boundary conditions $(-1)^k dV_k/dt = C_k^b A g(t) - C_k^d [1 - (-1)^k A] \frac{V_k^2}{L_k}$. Where μ_i^v, μ_i^p, μ_i^{pv}, C_i^b, and C_i^d ($i = 1, 2$) are the free model parameters, and the flow velocity is assumed to be along the $\hat{z}$ direction. The definition of other quantities in the equations is explained in [14]. The difference between this model and the other models is that it assumes a buoyancy-drag equation for the moving boundaries (*i.e.,* mixing layers) and uses the incompressible self-similar solutions for the edge velocities of the mixing zone to close the interfacial quantities and then solves for the (internal) flow structures inside the mixing region. All other models determine the flow quantities at the edges only after the internal flow structure is solved. This model has been used to study multifluid chunk mix and instabilities (RT and RM) at the interfaces with less turbulence. In the incompressible limit ($\mu_i^v = V_{i'}/V_i$, $\mu_i^p = \rho_{i'}/\rho_i$, ..., and etc), this two pressure two temperature model reduces to only one free parameter (C_b^d) [14] from nearly eight adjustable model parameters. Therefore, this model is very effective for mix studies in incompressible fluids.

2.3 Multifluids interpenetration mix model

The multifluid interpenetration mix model was proposed by Scannapieco [9]. It was derived rigorously from the collisional Boltzmann equation in a self-consistent manner. The unresolved parts in this model are closed by equation of state and the microscopic collisional terms which are expressed as functions of a microscopic collisional frequency. The model contains only one adjustable parameter which is in the expression of the phenomenological collisional frequency and is to be determined by experimental data. This model describes mix driven by all types of instabilities including RT ($g_j = $ constant), RM (a shock or impulsive, $g_j = \delta(t)$), and Kelvin-Helmholtz instability. The dynamical equations in this mode are

$$\frac{\partial}{\partial t}\rho^s + \frac{\partial}{\partial x_j}\left(v_j^* \rho^s\right) + \frac{\partial}{\partial x_j}\left(\langle U_j^s\rangle \rho^s\right) = S_{\text{coll}}^s, \tag{2.16}$$

$$\frac{\partial}{\partial t}\left(\rho^s \langle U_j^s\rangle\right) + \frac{\partial}{\partial x_i}\left(v_i^* \rho^s \langle U_j^s\rangle\right) + \frac{\partial}{\partial x_i}\left(P_{ij}^s + R_{ij}^s\right) - \frac{\rho^s}{\rho^*}\frac{\partial}{\partial x_i}\left(P_{ij}^* + R_{ij}^*\right) + \rho^s \langle U_i^s\rangle\frac{\partial}{\partial x_i}v_j^* = \left(A_j^s\right)_{\text{coll}}, \tag{2.17}$$

$$\frac{\partial}{\partial t}e^s + \frac{\partial}{\partial x_j}\left(v_j^* e^s\right) + \frac{\partial}{\partial x_j}\left(\langle U_j^s\rangle e^s\right) + \frac{\partial}{\partial x_j}\left(Q_{Tj}^s + P_{ji}^s \langle U_i^s\rangle\right) + \left(P_{ij}^s + R_{ij}^s\right)\frac{\partial}{\partial x_i}v_j^* - \frac{\rho^s}{\rho^*}\langle U_j^s\rangle\frac{\partial}{\partial x_i}\left(P_{ij}^* + R_{ij}^*\right) = E_{\text{coll}}^s, \tag{2.18}$$

$$\frac{\partial}{\partial t}\rho^* + \frac{\partial}{\partial x_j}\left(v_j^* \rho^*\right) = 0, \quad \rho^*\left(\frac{\partial}{\partial t}v_j^* + v_i^*\frac{\partial}{\partial x_i}v_j^*\right) + \frac{\partial}{\partial x_i}\left(P_{ij}^* + R_{ij}^*\right) = 0, \tag{2.19}$$

$$\frac{\partial}{\partial t}e^* + \frac{\partial}{\partial x_j}\left(v_j^* e^*\right) + \frac{\partial}{\partial x_j}Q_{Tj}^* + \sum_s \frac{\partial}{\partial x_j}\left[\langle U_j^s\rangle\left(e^s + P^s\right) + \Pi_{ji}^s \langle U_i^s\rangle\right] + \left(P_{ij}^* + R_{ij}^*\right)\frac{\partial}{\partial x_i}v_j^* = 0, \tag{2.20}$$

where

$$S_{\text{coll}}^s = \sum_{s'} \delta M^s N^s \nu_{\text{eff}}^{ss'}, \quad \left(A_j^s\right)_{\text{coll}} = \sum_{s'} N^s M^s \left(\langle U_j^{s'}\rangle - \langle U_j^s\rangle\right)\nu_{\text{eff}}^{ss'}, \tag{2.21}$$

$$E_{\text{coll}}^s = \sum_{s'} \frac{N^s M^s \nu_{\text{eff}}^{ss'}}{M^s + M^{s'}}\langle M^{s'} U_j^{s'} U_j^{s'} - M^s U_j^s U_j^s\rangle, \quad \nu_{\text{eff}}^{ss'} \sim \frac{M^{s'}}{M^{s'} + M^s}\frac{|\vec{U}^s - \vec{U}^{s'}|}{\lambda^{ss'}}, \tag{2.22}$$

and $\lambda^{ss'} \equiv \lambda_c + \alpha^{ss'} \int |U_j^s - U_j^{s'}| dt$ are the phenomenological closures in which a binary collisional process is assumed. The detailed definition of each quantity in the model equations is given in [9]. This set of equations can be solved in a closed form and the dynamics of the fluid, in principle, is uniquely determined. This model has been used effectively to describe atomic mix between fluids and plasmas in which each species has its own pressure and temperature. Particularly, it works well for ICF capsules [19–21] .

2.4 Hybrid turbulent mix model

This model was proposed by Cranfill [10] and is based on the usual decomposition of the fluid properties into mean and fluctuating parts and is obtained from the Navier-Stokes equations. It divides the turbulent contributions to the bulk fluid into ordered convective and disordered diffusive parts. The ordered contributions

are given as the sums of the multifluid drift motions, while the disordered parts are described by a set of single-fluid turbulence equations. The merit of this model is to naturally combine the usual multifluid equations with a $k - \epsilon$ model of turbulence. The dynamical equations of this model are

$$0 = \frac{d}{dt}\rho + \rho\vec{\nabla}\cdot\vec{u}, \quad 0 = \rho\frac{d}{dt}\vec{u} + \vec{\nabla}\cdot(\mathbf{R}+\mathbf{P}), \quad 0 = \rho\frac{d}{dt}i + \vec{\nabla}\cdot(\vec{s}+\vec{q}) + (\mathbf{P}+\mathbf{Q}):\vec{\nabla}\vec{u} + P\vec{\nabla}\cdot\vec{w} - \rho\epsilon \quad (2.23)$$

for bulk fluid,

$$0 = \rho\frac{d}{dt}x_j + \vec{\nabla}\cdot(\rho x_j\vec{w}_j), \tag{2.24}$$

$$0 = \rho\frac{d}{dt}(x_j\vec{w}_j) + \rho x_j(\frac{d}{dt} + \vec{w}_j\cdot\vec{\nabla})\vec{u} + \vec{\nabla}\cdot(\rho x_j\vec{w}_j^2 + f_j\mathbf{R}_{dj} + f_j\mathbf{\Pi}_j) + f_j\vec{\nabla}P + \omega\rho x_j\vec{w}_j, \tag{2.25}$$

$$P_j(m_j,\theta_j) = P(\rho,i,x_1,x_2,\ldots), \quad T_j(m_j,\theta_j) = T(\rho,i,x_1,x_2,\ldots), \quad m_j = \rho x_j/f_j. \tag{2.26}$$

for multifluid interpenetration, and

$$0 = \rho\frac{d}{dt}k + \vec{\nabla}\cdot(\vec{\sigma}+\vec{\pi}) + (\mathbf{R}-\mathbf{Q}):\vec{\nabla}\vec{u} + (\vec{\nabla}P)\cdot\vec{w} + \rho\epsilon, \tag{2.27}$$

$$0 = \rho\frac{d}{dt}k_o + \vec{\nabla}\cdot(\vec{\sigma}_o+\vec{\pi}_o) + (\mathbf{R}_o-\mathbf{Q}):\vec{\nabla}\vec{u} + (\vec{\nabla}P)\cdot\vec{w} + \rho\phi_o + 2\omega\rho k_o + \rho\epsilon_o, \tag{2.28}$$

$$0 = \rho\frac{d}{dt}k_d + \vec{\nabla}\cdot(\rho k_d\vec{w} - C_{kd}\mathbf{D}_d\cdot\vec{\nabla}k_d) + \rho\phi_d - 2\omega\rho k_o + \rho\epsilon_d, \tag{2.29}$$

$$0 = \rho\frac{d}{dt}l + \vec{\nabla}\cdot(\rho l\vec{w} - C_{ld}\mathbf{D}_d\cdot\vec{\nabla}l) - C_{lo}\rho(l\vec{\nabla}\cdot\vec{u} + \sqrt{k_o+k_d}) \tag{2.30}$$

for single-fluid turbulence. The phenomenological closures for the model equations are $\vec{v}' = \vec{v} - \vec{u}$, $\vec{w} =< \vec{v}' >$, $\rho_j = x_j\rho$, $\mathbf{R} =< m\vec{v}'^2 >= \mathbf{R}_o + \mathbf{R}_d$, $\mathbf{R}_o = \sum_j f_j\mathbf{R}_{oj} = \rho x_j\vec{w}_j^2$, $\mathbf{R}_d = \sum_j f_j\mathbf{R}_{dj} = \frac{2}{3}\rho k_d\delta + \mathbf{\Gamma}_{dj}$, $\mathbf{\Gamma}_{dj} = -\eta_d[\vec{\nabla}\circ(\vec{u}+\vec{w}_j) - \frac{2}{3}\vec{\nabla}\cdot(\vec{u}+\vec{w}_j)\delta]$, $\eta_d = C_{\eta d}\omega^{-1}(\frac{2}{3}\rho k_d)$, $\mathbf{P} = \sum_j f_j(P_j\delta + \mathbf{\Pi}_j) = P\delta + \mathbf{\Pi}_o$, $\mathbf{\Pi}_0 \equiv \sum_j f_j\mathbf{\Pi}_j$, $\mathbf{\Pi}_j \equiv -\eta_j[\vec{\nabla}\circ(\vec{u}+\vec{w}_j) - \frac{2}{3}\vec{\nabla}\cdot(\vec{u}+\vec{w}_j)\delta]$, $\mathbf{Q} = \sum_j f_j\mathbf{\Pi}'_j$, $\mathbf{\Pi}'_j = -\eta_j(\vec{\nabla}\circ\vec{w}_j - \frac{2}{3}\vec{\nabla}\cdot\vec{w}_j\delta)$, $\mathbf{D}_d \equiv \omega^{-1}(\mathbf{R}_d+\mathbf{\Pi}_o) \equiv \sum_j f_j\mathbf{D}_{dj}$, $\mathbf{D}_{dj} \equiv \omega^{-1}(\mathbf{R}_{dj}+\mathbf{\Pi}_j)$, $\omega = \frac{2}{3}C_\omega\sqrt{k_o+k_d}/l$, $\vec{s} = \vec{s}_o + \vec{s}_d$, $\vec{s}_o = \sum_j \rho x_j\theta_j\vec{w}_j$, $\vec{s}_d = \sum_j f_j\vec{s}_{dj} = -f_j C_{id}(\frac{\partial i}{\partial T})_\rho\mathbf{D}_{dj}\cdot\vec{\nabla}T$, $\vec{q} = -<\kappa>\vec{\nabla}T$, $\vec{\sigma} == \vec{\sigma}_o + \vec{\sigma}_d$, $\vec{\pi} = \vec{\pi}_o + \vec{\pi}_d$, $\vec{\sigma}_o = \sum_j \frac{1}{2}\rho x_j w_j^2\vec{w}_j$, $\vec{\pi}_o = \sum_j f_j\mathbf{\Pi}_j\cdot\vec{w}_j$, $\vec{\sigma}_d + \vec{\pi}_d = \sum_j(\rho x_j k_{dj}\vec{w}_j + f_j\mathbf{R}_{dj}\cdot\vec{w}_j) + \sum_j f_j(\vec{\sigma}_{dj}+\vec{\pi}_{dj})$, $\rho k = \rho k_o + \rho k_d$, $\rho k_o = \sum_j \frac{1}{2}\rho x_j w_j^2$, $\rho k_d = \sum_j f_j\rho k_d$, $\rho\epsilon = \rho\epsilon_o + \rho\epsilon_d$, $\rho\epsilon_o = -\sum_j f_j\mathbf{\Pi}'_j:\vec{\nabla}\vec{w}_j$, $\rho\epsilon_d = \sum_j f_j\rho\epsilon_d$, $l \equiv k_d\sqrt{k_o+k_d}/\epsilon_d$, and $\rho\phi_o = \sum_j \vec{\nabla}\cdot(f_j\mathbf{R}_{dj})\cdot\vec{w}_j$, $\rho\phi_d = \sum_j f_j\mathbf{R}_{dj}:\vec{\nabla}(\vec{u}+\vec{w}_j)$. The nomenclature of this model is given in [22]. Clearly, this model has a number of phenomenological closure relationships and nine adjustable parameters. Generically, this model inherits all of the assumptions of the $k - \epsilon$ models, such as, isotropic and homogeneous turbulence. The unresolved parts in this model are closed by empirical expressions, drag, diffusions, and single fluid turbulence, as used in the phenomenological turbulent mix model in Section 2.1. But the difference between this model and the phenomenological turbulent mix model is that this model was derived from the Navier-Stokes equations. This model also suffers from ill-posedness because of the assumption of pressure and thermal equilibrium between the fluids in the system. The single fluid turbulence was not developed fast enough to remove it. In order to remove the ill-posedness, the pressure fluctuations in the mixing regions need to be taken into account. Recently, the author and Cranfill [22] have calculated the pressure fluctuations analytically by Green's function methods which will be implemented into this model. Finally, it is worthwhile to point out that if the disordered Reynolds stress tensor is ignored (*i.e.*, set $R_{dij} = 0$), this set of equations is similar to the dynamical equations of Scannapieco's multifluid interpenetration mix model.

2.5   Single fluid variable-density turbulence model

This model is also called the BHR model which was proposed by Besnard, Harlow, and Rauenzahn [8] and uses the Reynolds decomposition of the Navier-Stokes equations for a single field with potentially large density variations. This approach is compatible with the multiphase flow equations only in special cases. It could be

equivalent to multiphase model only when the fluid is nearly incompressible. A closed set of transport equations in this approach is given below

$$\frac{\partial}{\partial t}R_{ij} + \frac{\partial}{\partial x_n}(\tilde{u}_n R_{ij}) + R_{jn}\frac{\partial}{\partial x_n}\tilde{u}_i = \sum_s \left\{ a_i \left(\frac{\partial}{\partial x_j}\overline{P} - \frac{\partial}{\partial x_n}\overline{\tau}_{nj} \right) + C_{DR}\frac{\partial}{\partial x_m}\left[\frac{K}{\epsilon}R_{in}\frac{\partial}{\partial x_n}\left(\frac{R_{mj}}{\overline{\rho}} \right) \right] \right\}$$

$$- C_{1R}\frac{\epsilon}{K}\left(R_{ij} - \frac{1}{3}\delta_{ij}R_{nn} \right) - C_{2R}\left(R_{in}\frac{\partial}{\partial x_n}\tilde{u}_j + R_{jn}\frac{\partial}{\partial x_n}\tilde{u}_i - \frac{2}{3}\delta_{ij}R_{mn}\frac{\partial}{\partial x_n}\tilde{u}_m \right) - \frac{2}{3}\delta_{ij}\overline{\rho}\epsilon, \tag{2.31}$$

$$\frac{\partial}{\partial t}(\overline{\rho}\tilde{c}_i) + \frac{\partial}{\partial x_n}(\overline{\rho}\tilde{u}_n\tilde{c}_i) = \frac{\partial}{\partial x_n}\left(\overline{\rho}D\frac{\partial}{\partial x_n}\tilde{c}_i \right) + C_{Dc}\frac{\partial}{\partial x_n}\left(\frac{K}{\epsilon}R_{nm}\frac{\partial}{\partial x_m}\tilde{c}_i \right), \tag{2.32}$$

$$\frac{\partial}{\partial t}(\overline{\rho}a_i) + \frac{\partial}{\partial x_n}(\overline{\rho}\tilde{u}_n a_i) + \overline{\rho}a_n\frac{\partial}{\partial x_n}\overline{u}_n = b\left(\frac{\partial}{\partial x_i}\overline{P}\frac{\partial}{\partial x_n}\overline{\tau}_{ni} \right) - \frac{R_{in}}{\overline{\rho}}\frac{\partial}{\partial x_n}\overline{\rho}$$

$$+ C_{Da}\overline{\rho}\frac{\partial}{\partial x_m}\left[\frac{K}{\epsilon\overline{\rho}}\left(R_{in}\frac{\partial}{\partial x_n}a_m + R_{mn}\frac{\partial}{\partial x_n}a_i \right) \right] + \overline{\rho}\frac{\partial}{\partial x_n}(a_n a_i) - C_{1a}\overline{\rho}\frac{\epsilon}{K}a_i + C_{2a}\overline{\rho}a_n\frac{\partial}{\partial x_n}\tilde{u}, \tag{2.33}$$

$$\frac{\partial}{\partial t}b + \overline{u}_n\frac{\partial}{\partial x_n}b + \frac{b+1}{\overline{\rho}}\frac{\partial}{\partial x_n}(\overline{\rho}a_n) = \overline{\rho}C_{Db}\frac{\partial}{\partial x_n}\left[\frac{K}{\epsilon\overline{\rho}}R_{nm}\frac{\partial}{\partial x_m}\left(\frac{b+1}{\overline{\rho}} \right) \right] - C_{1b}\frac{\epsilon}{K}b, \tag{2.34}$$

$$\frac{\partial}{\partial t}(\overline{\rho}K) + \frac{\partial}{\partial x_n}(\overline{\rho}\tilde{u}_n K) + R_{nm}\frac{\partial}{\partial x_n}\overline{u}_m = a_n\frac{\partial}{\partial x_n}\overline{P} + \frac{\partial}{\partial x_n}\left(\mu_t\frac{\partial}{\partial x_n}K \right) - \overline{\rho}\epsilon, \tag{2.35}$$

$$\frac{\partial}{\partial t}(\overline{\rho}\epsilon) + \frac{\partial}{\partial x_n}(\overline{\rho}\tilde{u}_n\epsilon) + C_{1\epsilon}\frac{\epsilon}{K}R_{nm}\frac{\partial}{\partial x_n}\overline{u}_m = C_{3\epsilon}\frac{\epsilon}{k}a_n\frac{\partial}{\partial x_n}\overline{P} + C_{D\epsilon}\frac{\partial}{\partial x_n}\left(\frac{\overline{\rho}K^2}{\epsilon}\frac{\partial}{\partial x_n}\epsilon \right) - C_{2\epsilon}\frac{\overline{\rho}\epsilon^2}{K} - C_{4\epsilon}\overline{\rho}\epsilon\frac{\partial}{\partial x_n}\overline{u}_n, \tag{2.36}$$

where $a_i \equiv -\overline{u''}_i$, $u''_i = u_i - \tilde{u}_i$, $b = -\overline{\rho'\left(\frac{1}{\rho}\right)'}$ are respectively the associated velocity and the density self-correlation, and $\mu_t = C_\mu \overline{\rho}K^2/\epsilon$. This model has more than sixteen adjustable parameters and assumes incompressible fluctuation components, *i.e.*, $\frac{\partial}{\partial x_i}u'_i \equiv 0$. It is appropriate for variable-density turbulence when the fluctuating velocities are far subsonic which applies local pressure equilibrium among the different eddies and species over a distance small compared to the mean-flow gradients. In order to predict how the mean flow variations affect instabilities and to produce the statistical effects of instabilities, the fluids have to be nearly incompressible. This model can reduce to the multifluid equations only when the fluids are incompressible, which would be a problem for strongly shocked fluid systems.

2.6 Buoyancy-drag model

Various buoyancy-drag models have been proposed by numerous authors [?, 5, 16, 17] and widely used in one-dimensional studies of RT and RM instabilities. It is used to describe the dynamic position of the interface between two fluids, *i.e.*, the edges of a mixing zone resulting from Rayleigh-Taylor or Richtmyer-Meshkov unstable flows. The general dynamic equation is

$$(\rho_i + k_i\rho_{i'})\frac{dV_i}{dt} = (\rho_i - \rho_{i'})g(t) - (-1)^i\frac{C_i\rho_{i'}V_i^2}{|Z_i|}, \quad i = 1, 2 \ , \tag{2.37}$$

where the added mass coefficient, k_i, and the drag coefficient, C_i, are the model's phenomenological constants. For cylindrical bubbles and spikes, $k_i \sim 1$, and Eq. (2.37) becomes

$$\frac{dV_i}{dt} = (-1)^i A g(t) - (-1)^i C_i \frac{1 - (-1)^i A}{2}\frac{V_i^2}{|Z_i|}, \quad i = 1, 2 \ . \tag{2.38}$$

The solution of this model characterizes the average position and velocity of the envelopes of the mixing zone, but it can not tell about the detailed flow structure inside and outside of the mixing zone. For simple problems which are only concerned with the width of the mixing layer or a rough amount of mixing (assuming a uniform mix inside the mixing zone), this model serves the purpose. But for a 3-D mixing problem, this model is insufficient and suffers serious difficulties. The exact solution [17] for RT mixing shows that the RT mixing front grows exponentially at early times, then linearly during the intermediate stage with a dependence on initial conditions, and later reaches the self-similarity regime and grows with $\alpha A g t^2$. The usual $\alpha A g t^2$ solution is only a late time self-similar solution. The real physical process indeed undergoes a dynamic transition from initial condition dependence to independence.

2.7   Large-eddy simulations

Large-eddy simulation (LES) [23, 24] is an intermediate approach between DNS and RANS, capable of simulating flow features such as significant flow unsteadiness and strong vortex-acoustic couplings, with respect to accuracy and computational cost. In LES the large or grid scale motions which morphologically depend on the geometry of the flow via the boundary conditions, are explicitly modeled. These structures carry most of the kinetic energy and are responsible for most of the turbulent flux. The small or subgrid scale motions which are statistically steady and sufficiently far from boundaries or unaffected by the domain geometry, are modeled by a subgrid scale model. This approach tries to solve the filtered Navier-Stokes equations closed with a subgrid model for the turbulence stress tensor. The equations have the following forms

$$\frac{\partial}{\partial t}\overline{\rho} + \frac{\partial}{\partial x_j}(\overline{\rho}\tilde{u}_j) = 0, \quad \frac{\partial}{\partial t}(\overline{\rho}\tilde{u}_i) + \frac{\partial}{\partial x_j}(\overline{\rho}\tilde{u}_i\tilde{u}_j) + \frac{\partial}{\partial x_i}\overline{p} - \frac{\partial}{\partial x_j}\breve{\sigma}_{ij} = -\frac{\partial}{\partial x_j}(\overline{\rho}\tau_{ij}) + R_i, \qquad (2.39)$$

$$\frac{\partial}{\partial t}\breve{e} + \frac{\partial}{\partial x_j}\left[(\breve{e} + \overline{p})\tilde{u}_j\right] - \frac{\partial}{\partial x_j}(\breve{\sigma}_{ij}\tilde{u}_i) + \frac{\partial}{\partial x_j}\breve{q}_j = R_e, \qquad (2.40)$$

where

$$\breve{e} = \overline{p}/(\gamma - 1) + \frac{1}{2}\tilde{u}_i\tilde{u}_i, \ \overline{\rho}\tilde{T} = \gamma M^2\overline{p}, \ \breve{\sigma}_{ij} = (\tilde{\mu}/Re)\tilde{S}_{ij}, \qquad (2.41)$$

$$\tilde{\mu} = \mu(\tilde{T}), \ \tilde{S}_{ij} = \frac{\partial}{\partial x_j}\tilde{u}_i + \frac{\partial}{\partial x_i}\tilde{u}_j - \frac{2}{3}\delta_{ij}\frac{\partial}{\partial x_n}\tilde{u}_n, \ \tau_{ij} = \widetilde{u_i u_j} - \tilde{u}_i\tilde{u}_j, \qquad (2.42)$$

R_i is the subgrid term resulting from the nonlinearity in the viscous stress tensor, and R_e is the Reynolds number. The notation of the other quantities in the equations is explained in [23]. Clearly, the left side of the equations are the Navier-Stokes equations expressed in the filtered variables $(\overline{\rho}, \tilde{u}_i, \overline{p})$, the right hand are the subgrid terms and must be modeled. In this picture, the grid scale components are defined by the convolutions, such as $\overline{F} = G * F = \int G(\boldsymbol{x} - \boldsymbol{\xi}, \Delta)F(\boldsymbol{\xi}, t)d^3\boldsymbol{\xi}$, where a filter function G is needed and the filter function G is assumed to commute with $\frac{\partial}{\partial t}$ and $\frac{\partial}{\partial x_i}$. This assumption is invalid if (i) we consider boundaries and (ii) the filter is non-uniform. LES has been used to simulate jets, wakes, and flows in combustion and around moving vehicles. But in a more complex flow, and in realistic engineering applications, traditional filtering techniques have to be extended to non-uniform filters. This method would be very effective if the system has enough experimental data to validate it, such as, in ocean and atmosphere modeling. Otherwise, this method is less effective.

3   DISCUSSION

In the previous section, we discussed seven distinct mix models, four of which are similar. Each, given one, is capable of solving the detailed flow structure inside and outside the mixing region in 3-D, but the closures are quite different. For example, the Youngs phenomenological model is closed by added mass, diffusions, and turbulence models. The Ensemble-average microphysical model is derived from Euler equations and closed by interfacial quantities (v^*, p^*, and $(pv)^*$). The multifluid interpenetration mix model by Scannapieco is closed down to the atomic level by the microscopic collisional terms which are expressed as functions of a single microscopic collisional frequency, while the Hybrid model is closed by phenomenological drag coefficients, diffusions, and $k - \epsilon$ single-fluid turbulence model. The major differences between each model lie in the derivations of the model equations, the unique approach to introduce the closures, and the number of free model parameters. A detailed comparison between these models is displayed in Table I. From the table we see that among these models, the interpenetration mix model seems most attractive because this model, unlike the other models which have more than one free parameter and are closed by more than one phenomenological relationship, introduces only one phenomenological quantity, *i.e.* the collisional frequency, to describe the unresolved physics in the model at an atomic level. This phenomenological quantity characterizes the physical system. The advantage of doing this is to transform the model approximations from its governing equation level to the collisional terms, particularly, to a characteristic quantity for binary collisions. This technique enables us to minimize and improve the model approximations through a further detailed understanding of the physics of the particle collisional process which are known to change in the presence of additional physical processes, such as, magnetic fields, radiation, plasma, and turbulence, in terms of the collisional frequency and the mean free path. In this sense, we characterize this model more rigorous and more appealing than the other models. Clearly in the other models, if any parameter or any phenomenological closure is modified, all

Mix Model	Features	Model Closure	Number of Parameters	Application Limitation
Youngs' model	phenomenological not derived one p, one T	added mass, drag,diffusions, turbulence	7	multifluid mix with turbulence
Ensemble average model	from Euler Eqs. two ps, Ts	interfacial v^*, p^*, $(pv)^*$ incompressible buoyancy-drag Eq self-similar sol.	$1 \sim 2$ ($c_s = \infty$) > 3 (finite c_s)	multifluid chunk mix no turbulence
Scannapieco's model	from collisional Boltzmann Eq. two ps, Ts	collisional frequency in the collisional terms	1	multifluid atomic mix, plasma with part of turb.
Hybrid model	from Navier-Stokes Eqs.,one p, T, Fluid decomposed into ordered and disordered.	drag frequency, diffusions,$k - \epsilon$ single fluid turbulence	> 6	multifluid chunk mix with isotropic and homogeneous turbulence
BHR model	Navier-Stokes Eqs, Reynolds decomposition, mass weighted average, one p, T	gradient approx. engineering closure with model constants.	16	1 fluid variable density turb. very weakly compressible two fluids.
Buoyancy-drag model	phenomenological, from Newton's second law.	phenomenological constants: added mass, drag coeff..	2	1-D motion of edges of mix zone, no info on inside of mix zone.
LES model	filtered Navier-Stokes Eqs. solve the grid scale with a given filter.	subgrid scale model	filters > 3	1 fluid huge unsteadiness, strong vortex-acoustic couplings, uniform filter. less complex.

Table 2.1. A comparison between available mix models

of the model parameters or empirical relationships will need to be changed correspondingly which is a multi-dimensional problem. Here it is worthwhile to point out that if turbulence is not important in the physical system, in principle these models can be derived from one to another. But if it is not negligible to the physical system, then it has to be modeled correctly. However, for the turbulence in a mixing region, the simple single fluid turbulence $k - \epsilon$ models may not be adequate because (i) the fluid is not weakly compressible; and (ii) the turbulence may not be isotropic and homogeneous. The buoyancy-drag mix model can only be used to determine the width of the mixing zone but not the detailed structure of the flows inside and outside of the mixing zone. All of the mix models can reduce to this model under some simplifications [25]. Finally, the LES mix model is only effective if the filter function for the considered system is known and if the system has an abundance of experiment data to validate it. Otherwise the accuracy of the LES method is not guaranteed. In complex fluid system, a non-uniform filter will be required for the accuracy of the method.

ACKNOWLEDGEMENTS

REFERENCES

[1] Rayleigh, L. Investigation of the character of the equilibrium of an incompressible heavy fluid of variable density. In *Scientific Papers*, volume II, page 200. Cambridge Univ. Press, Cambridge, England, 1900. Taylor, G. I. 1950, The instability of liquid surfaces when accelerated in a direction perpendicular to their planes I. *Proc. R Soc. London A*, **201**,pp 192–196.

[2] Richtmyer, R. D. 1960, Taylor instability in shock acceleration of compressible fluids. *Comm. Pure Appl. Math.*, **13**, pp 297–319. Meshkov, E. E. 1969, *Izv. Akad. Nauk SSSR, Mekh. Zhidk. Gaz.*, **5**, p 151.

[3] V. Andronov, S. Bakhrakh, E. Meshkov, V. Mokhov, V. Nikiforov, A. Pevnitskii, and A. Tolshmyakov. 1982, An experimental investigation and numerical modeling of turbulent mixing in one-dimensional flows. *Sov. Phys. Dokl.*, **27**, pp 393–396; 1967, *Sov. Phys. JETP*, **44**, pp 424–427.

[4] K. I. Read. 1984, Experimental investigation of turbulent mixing by Rayleigh-Taylor instability. *Physica D*, **12**, pp 45–58.

[5] G. Dimonte. 1999, Nonlinear evolution of the RT and RM instabilities. *Phys. Plasmas*, **6**, pp 2009–2015.

[6] D. H. Sharp. 1984, An overview of Rayleigh-Taylor instability. *Physica D*, **12**, pp 3–18.

[7] D. L. Youngs. 1989, Modeling turbulent mixing by Rayleigh-Taylor instability. *Physica D*, **37**, pp 270–287; 1984, Numerical simulation of turbulent mixing by Rayleigh-Taylor instability. *Physica D*, **12**, pp 32–44.

[8] D. Besnard, F. Harlow, R. Rauenzahn, and C. Zemach. 1992, Turbulent transport equations for variable-density turbulence and their relationship to two-field models. LANL report LA-12303-MS.

[9] A. J. Scannapieco and B. Cheng, 2002, A multifluids interpenetra mix model. *Phys.Letts. A*, **299**, pp 49–64.

[10] C. W. Cranfill, 1992, A New Multifluid Turbulent-Mix-Model. *Los Alamos National Laboratory Report* LA-UR-92-2484.

[11] B. Cheng, J. Glimm, D. Saltz, and D. H. Sharp. 1999, Boundary conditions for a two pressure two phase flow model. *Physica D*, **133**, pp 84–105. Y. Chen, J. Glimm, D. H. Sharp, and Q. Zhang. 1996, A two-phase flow model of the Rayleigh-Taylor mixing zone. *Phys. Fluids*, **8**, pp 816–825.

[12] K. Mikaelian. 1990, RT and RM instabilities in multilayer fluids with surface tension. *Phys. Rev. A*, **42**, p 7211.

[13] N. Freed, D. Ofer, D. Shvarts, and S. Orszag. 1991, Two-phase flow analysis of self-similar turbulent mixing by Rayleigh-Taylor instability. *Phys. Fluids A*, **3**, pp 912–918. U. Alon, J. Hecht, D. Ofer, and D. Shvarts. 1995, Power laws and similarity of Rayleigh-Taylor and Richtmyer-Meshkov mixing fronts at all density ratios. *Phys. Rev. Lett.*, **74**, pp 534–538.

[14] J. Glimm, D. Saltz, and D. H. Sharp. Two-phase modeling of a fluid mixing layer. *J. Fluid Mech.*, 378:119–143, 1999.

[15] J. Glimm and D. H. Sharp. Chaotic mixing as a renormalization group fixed point. *Phys. Rev. Lett.*, 64:2137–2139, 1990.

[16] B. Cheng, J. Glimm, and D. Sharp. 2000, Density dependence of RT and RM mixing fronts. *Phys. Lett. A*, **268**,p 366.

[17] B. Cheng, J. Glimm, and D. Sharp. 2002, Dynamical evolution of the RT and RM mixing fronts. *Phys. Rev. E* **66**, 036312.

[18] B. Cheng, J. Glimm, and D. H. Sharp. 2002, Multi-temperature multiphase flow model. *Z. angew. Math. Phys.*, **53**, p 211.

[19] D. C. Wilson, A. J. Scannapieco, C. W. Cranfill et al. 2003, Degradation of radiatively driven inertial confinement fusion capsule implosions by multifluid interpenetration mixing. Phys. Plasmas **10**, p 4427.

[20] D. C. Wilson, C. W. Cranfill, C. Christensen, et al. 2004, Multi-fluid interpenetration mixing in directly driven ICF capsule implosions. Phys. Plasmas **11**, p 2723.

[21] C. R. Christensen, D. C. Wilson, C. W. Barnes, et al. 2004, The Influence of Asymmetry on Mix in Direct-Drive ICF Experiments. Phys. Plasmas **11**, p 2771.

[22] B. Cheng, C. Cranfill, and L. Turner, 2001, The characteristic analysis of a hybrid multifluid turbulent mix model. *LA-13851*. B. Cheng and C. Cranfill. 2004, Using the Green's function method to calculate pressure fluctuations in compressible multifluids. *The Proceedings of the 9th International Conference on the Physics of Compressible Turbulent Mixing*.

[23] B. Vreman, B. Geurts, H. Kuerten. 1997, Large-eddy simulation of the turbulent mixing layer. *J. Fluid Mech.* **339**, p 357.

[24] F.F. Grinstein, and G. Karniadakis. 2002, Alternative LES and hybrid RANS/LES. *J. Fluids Engineering,* **124**, p 821. C. Fureby, and G. Tabor. 1997, Mathematical and physical constraints on large-eddy simulations. *Theoret. Comput. Fluid Dynamics*, **9**, p 85.

[25] B. Cheng and A. J. Scannapieco. 2005, Buoyancy-drag mix model obtained by multifluid interpenetration equations. *Phys. Rev. E* **72**, 046310.

STUDY OF THE MECHANISM OF MAGNETIC FIELD DIFFUSION INTO LASER PLASMA

© 2006 A.V.Bessarab, G.A.Bondarenko, G.V.Dolgoleva, V.A.Zhmailo, V.V.Misko, A.V.Kunin, I.N.Nikitin, V.P.Statsenko, R.R.Sungatullin

Russian Federal Nuclear Center – All-Russian Research Institute for Experimental Physics, Sarov, Russia

The results of the study of the interactions of plasma formation (PF) occurring at laser irradiation of a spherical target in the background gas atmosphere and magnetic field on the Iskra-5 MKV-4 test bench are discussed.
The methods of magnetic and sensor diagnostics were employed for the study of plasma spreading dynamics in ≈ 300÷500 Oersted magnetic field.
The obtained results were compared with the computations obtained using different models of laser plasma diffusion in magnetic field.

The problem of plasma cloud interaction with external magnetic field is interesting in the terms of numerous applied and fundamental problems. These are, for example, the problems of plasma confinement in magnetic traps, dynamics of different plasma formations in the Earth's magnetosphere or interactions of Supernovas' remnants with interstellar magnetic filed.

During the last years the method of laboratory investigation using laser facilities has been applied for the investigation of these phenomena. The examples of such activities (along with detailed bibliography) are given in [1-9].

In these papers plasma deceleration by magnetic field and field perturbation at this plasma expansion are discussed in detail.

It was discovered in these experiments that interpenetration of spread plasma and magnetic filed was more noticeable than it could be expected basing on the "collision-wise" understanding of the diffusion coefficient.

This phenomenon was discovered in the investigations described in [4, 10], and was explained by the development of some types of "kinetic" instabilities [11] in spread plasma. In later papers [7, 9] it was considered similarly to the Rayleigh-Taylor instability basing on obtained experimental data.

In this work a semi-empirical model which joins both the above approaches is formulated basing on the earlier obtained results.

To prove the main assumptions of such model a number of experiments has been conducted at the MKV-4 test bench. They are similar by the design to the experiments earlier performed at the KI-1 test bench [2-5]. The main difference is in the parameters of the laser radiation (shorter wavelength and considerably higher power), as well as in the target types.

The experiments for the study of the properties of plasma cloud (PC) spread in external magnetic field were performed at the MKV-4 test bench located in a channel of the ISKRA-5 iodine laser facility[13].

The test bench is a cylindrical vacuum chamber (1.5 m long with the 1 m diameter), provided with the exhaust system, gas-letting system and laser radiation letting-in windows and equipped with a number of optical diagnostics instruments. In the experiments thin-wall spherical targets (polyparaxililen ($C_8H_8)_n$) were used. The pressure of the residual gas in the vacuum chamber was $P_o \sim 10^{-2}$ torr and $P_o \sim 10^{-5}$ torr. The laser energy was ≈ 500 J, the pulse duration was ≈ 0.5 ns. The homogeneous (axially) magnetic field with the strength of up to 500 Oersted was created in the chamber.

In the computations presented below the model of the magnetic field diffusion based on the supposition that the diffusion occurs as the result of the instability development in the studied plasma flows, was employed. Two types of such instabilities were considered: the kinetic and the hydrodynamic [11].

The strongly nonlinear "turbulent" phase of such instabilities is characteristic for these experiments. Similarly to hydrodynamics approximate semi-empirical approaches are used for its description in this work.

Deriving the equations for the magnetic field basing on these approaches is shown in the appendix.

The above mentioned experiments were conducted at two essentially different pressures of the atmosphere in the MKV-4 chamber. Hence, the computations of these experiments were performed using different approaches. The computations shown below refer to the experiments at the pressures 10^{-2} and 10^{-5} torr. Plasma deceleration at such pressures is mainly due to the magnetic field.

Earlier in paper [14] the physical model and the numerical technique for the computation of nonequilibrium low-density plasma flows in magnetic field were discussed. The model is based on the "three-flow" approximation used for the description of such flows.

In this work this model is extended with account for anomalous diffusion occurring due to the development of kinetic instabilities in the plasma electronic component. The results of paper [15] were used to determine the diffusion coefficient.

In Figs.1 and 2 the computed data is compared with those experimental (here, *L* is the distance between the measurement point and the target perpendicularly to nonpertrubed magnetic filed).
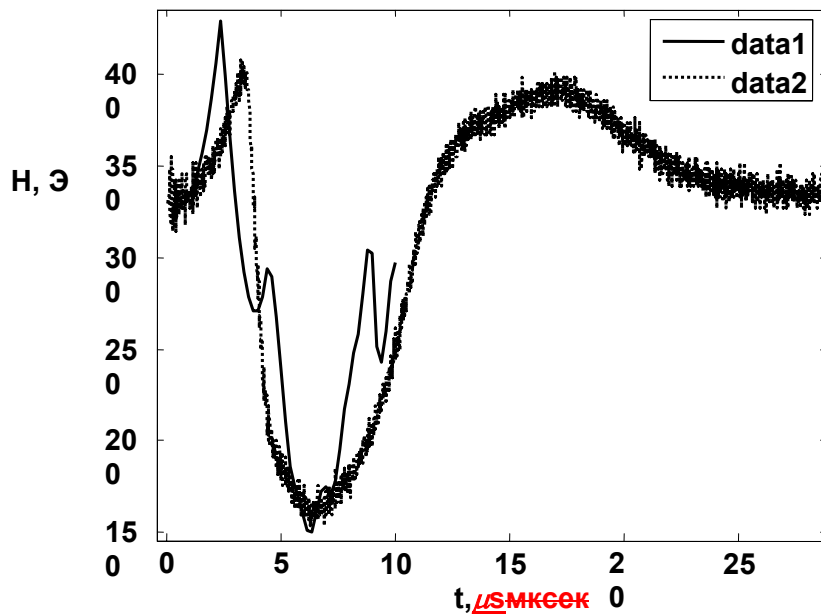
Fig. 1. Time dependence of the magnetic filed strength *H* at $p_0 \approx 10^{-5} torr$, *L*=21cm: 1 - computation, 2 – experiment.
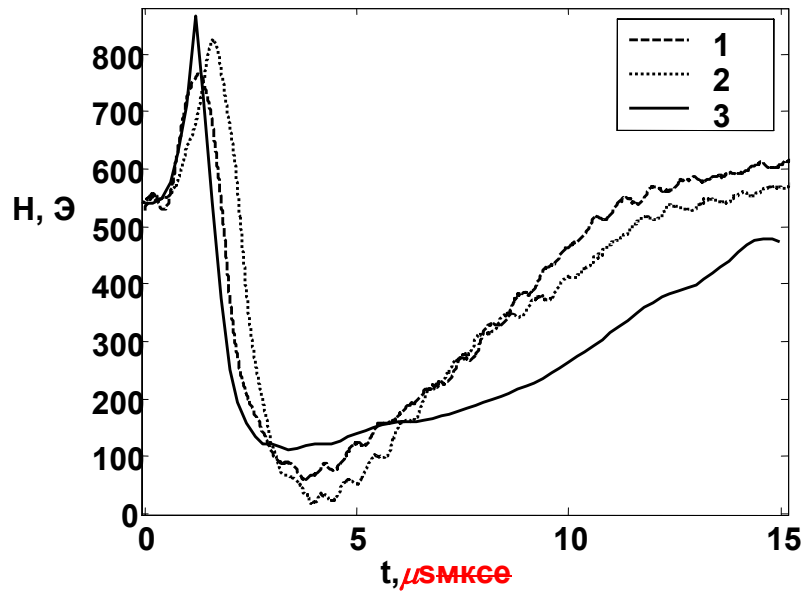
Fig.2. Dependence H(t) for the sensors L=10 см in the experiments at $p_0 \approx 10^{-2} torr$, H_0=540 oersted: 1,2 – two experiments' data, respectively, 3 – computation.

We can see that the used model allows obtaining reasonable agreement with the experimental data.

The hydrodynamic turbulence model [16,17] was used to describe the experiments at high pressures. The obtained results are planned to publish separately.

REFERENCES

[1]   D.W. Coopman, Phys. Fluids, 1971, v.14, p.1707.

[2]   Antonov V.M., Bashurin V.P., Golubev A.I. et al. PMTF, 1985, No 6, pages 6-9.

[3]   Antonov V.M., Bashurin V.P., Golubev A.I. et al. DAS USSR, 1986 vol.289, pages 72-75.

[4]   Zakharov Yu.P., Orishitch A.M., Ponomarenko A.G., Posukh V.G. FP, 1986, 12, pages 1170-1175.

[5]   Zakharov Yu.P., Orishitch A.M., Ponomarenko A.G., Posukh V.G. FP, 1988, 14, pages 203-210.

[6]   S. Kacenjar, M. Haussman, M.Keskinen et al., Phys. Fluids, 1986, 29, pp.2007-2012.

[7]   B.H. Ripin, J.D. Huba, E.A. McLean et al., Phys. Fluids, 1993, B5, pp.3491-3506.

[8]   Yu.P.Zakharov et al. Proceed. of 1996 Intern. Conf. On Plasma Physics (Nagoya,1996), v.2, p.1674 (1997).

[9]   Guy Dimonte and L.Wiley,Phys. Rev. Letters, 1991, v.67, pp.1755-1758.

[10]   D.W. Coopman, Phys. Fluids, 1976, v.19, pp.670-674.

[11]   Kadomtsev B.B. Kollektivnye yavleniya v plazme (Collective Phenomena in Plasma). Moscow, Nauka, 1988.

[12]   Bogunenko Yu.D., Bessarab A.V., Bondarenko G.A. et al. Issledovanie opticheskig svoistv neravnovesnoi plasmy v opytah na ustanovke MKV-4 (Investigation of Nonequilibrium Plasma Optical Properties on the MKV-4 Facility) Plasma Physics, 2005, volume 31, №8, pp.765-768.

[13]   V.I.Annenkov, V.A.Bagretsov, V.G.Bezuglov, et al. Impulsnyi lazer poshnost'yu 120 TV "Iskra-5" ("Iskra-5" 120 TW Pulse Laser). Kvantovaya electronika 1991. V.18. № 5. P.536.

[14]   Antonenko E.M., Bashurin V.P., Dolgoleva G.V., Zhmailo V.A. Metody rascheta "dvuhpotokovyh" techeniy neravnovesnoy plazmy v magnitnom pole (Computation Methods for "Bistream" Flows of Nonequilibrium Plasma in Magnetic Field). VANT, series Matematicheskoe modelirovanie fizicheskih protsessov (Mathematical Simulation of Physical Processes). Issue 1-2, 1995, pages 48-53.

[15]   Golubev A.I., Solov'ev A.A., Terekhin V.A. O besstolknovitelnom tormozhenii ionizirovannogo oblaka v odnorodnoy zamagnichennoi plazme (On Collissionless Stopping of Ionized Cloud in Homogeneous Magnetized Plasma). PMTF, 1978, N_o 5, pages 33-42.

[16]   R.C. Davidson, N.A Krall "Anomalous transport in high-temperature plasmas with application to solenoidal fusion systems", Nucl. Fus., vol. 17, N_o 6, p.1313, 1977.

[17]   Gubkov E.V., Yanilkin Yu.V., Zhmailo V.A. // Proc. of 8th International Seminar on Turbulent Mixing of Compressible Matter. 8th IWPCTM, Pasadena, USA, 2001.

[18]   Yanilkin Yu.V., Nikiforov V.V., Bondarenko Yu.A., Gubkov E.V., Zharova G.V., Statsenko V.P., Tarasov V.I. Two-parameter model and method for computations of turbulent mixing in 2D compressible flows // 5rd International Workshop on the Phisics of compressible turbulent mixing. Stony Brook, USA, 1995.

Stabilization of Wave Formation on a Contact Boundary of Metal Layers at an Oblique Impact During Kelvin - Helmholtz Instability Development

Oleg DRENNOV and Anatoly MIKHAILOV

Russian Federal Nuclear Center – VNIIEF 607190 Sarov Russia

Abstract The elimination effect of disturbances and mutual mixing on a contact boundaries of metal layers at oblique impact during Kelvin - Helmholtz instability development was established and investigated. Thin layers of metal coatings ($\Delta \sim 30$ μm) reduce amplitude of disturbance realization in 10-100 times and eliminate mutual mixing of contacting materials (eliminate the formation of a welded zone). This stabilizing effect is explained by physical properties of a metal coating as a whole. Under pulsed loading high dynamic strength characterizes these materials; that explains the stabilizing effect. Thermophysical limits for coating layers are pointed out.

1 INTRODUCTION

The oblique shock wave loading of the contacting layers with different dynamic rigidness is accompanied, in general, by the realization of material tangential flow along a contact boundary, which may result in Kelvin - Helmholtz instability development [1]. The wave formation and mutual material mixing process is extensively applied during explosion welding of metals [2]. However, in some cases the wave formation and intermixing in metal layers under oblique shock wave loading is unfavourable.

2 EXPERIMENTAL SCHEME

Plane metal layers (copper, brass, aluminium, magnesium and their combinations) loading by an oblique shock wave during explosive welding and various shields' effects on a contact boundary state after the loading were experimentally investigated. A traditional scheme of plane throwing during a sliding detonation of explosive charge was used. In fig.2.l a test arrangement scheme and the notation of characteristic parameters of throwing are presented. A fixed plate (5) is placed on a massive steel base (6). Above it a flying plate (3) is mounted at a specified angle α to the fixed plate plane. On a flying plate surface an explosive layer (1) is placed, where a plane sliding detonation wave is initiated. To prevent spallation events in a striker material, between it and an explosive layer a thin spacer (2) with a low acoustic impedance is placed [3]. On a contact surface of a fixed plate (*l-l'* plane in fig.2.l) a shielding layer (4) of 10 μm $< \Delta <$ 50μm thickness is predeposited. The loading regimes for all metal pairs tested were selected to form a cumulative jet in a contact point. A subsonic loading was realized: a contact point velocity is 2.5 mm/ μs $< \upsilon_c <$ 4.5 mm/μs; an impact angle is 12[°] $< \gamma <$ 25[°]. Of the samples, which have experienced the dynamic loading, the microsections were prepared, which were metallographically analysed at the zone of materials contact.
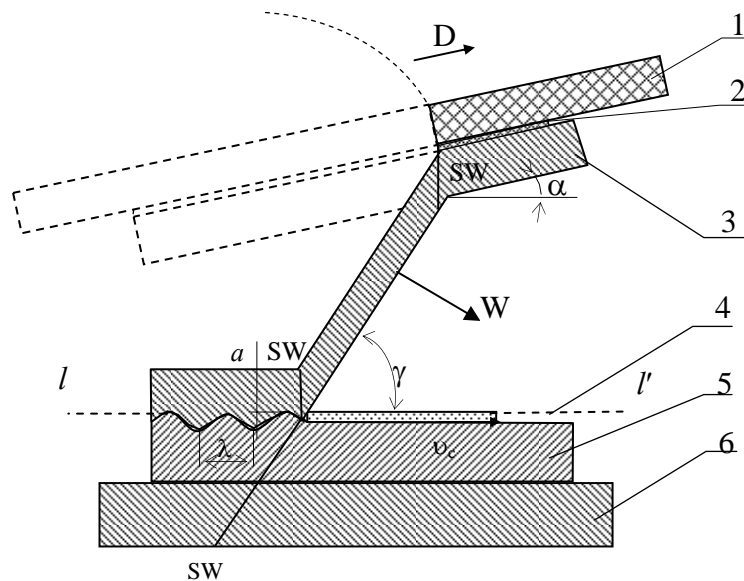
Fig.2.l. Test arrangement scheme

3 EXPERIMENTAL RESULTS

The stabilizing effect of thin metal coating on the explosive welding and disturbance evolution at a contact boundary was experimentally found. In fig.3.1 a photograph of a section of a contact boundary aluminium - aluminium (AlMn alloy) after high - speed oblique impact is shown. The explosive welding took place. In the vortex zones of wave crests the metals melt. The disturbance amplitude is $a \approx 400$ μm. In fig.3.2 the photograph of a contact boundary section of the same metal pair is shown under the loading through a magnesium coating layer $\Delta \approx 22$ μm thick. The disturbance amplitude decreased substantially, $a < 10$ μm. A welded joint between the metals is absent.

Fig.3.1. Contact boundary (increase 30 times)

Fig.3.2. Contact boundary (increase 30 times)

In fig.3.3 section of contact boundary copper - copper (Ml grade) is given. The explosive welding took place. The disturbance amplitude is $a \approx 350$ μm. In fig.3.4 section photograph of a contact boundary for the same pair is shown, but under the loading through a zinc layer $\Delta \approx 22$ μm thick. The disturbance amplitude decreased up to $a \approx 15$ μm. The explosive welding was not realized.
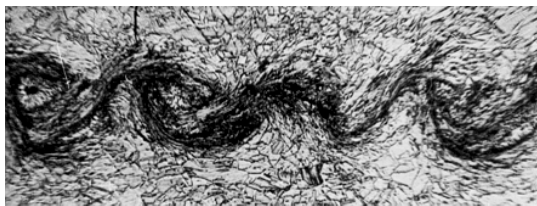
Fig.3.3. Contact boundary (increase 30 times)
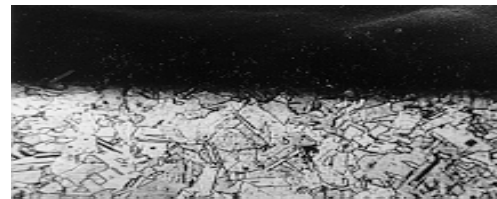
Fig.3.4. Contact boundary (increase 30 times)

It was noted that in all tests where a reliable stabilization of a contact boundary is seen, a metal structure of a fixed plate doesn't change.

In fig.3.5 the dependence of disturbance amplitudes on zinc coating thickness is shown for the contact boundaries of the following metal pairs; aluminium – aluminium (1), coppper - copper (2), aluminium - copper (3).
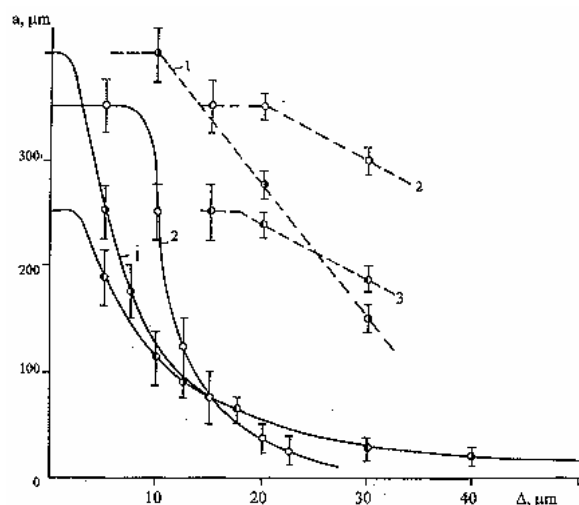
Fig.3.5. Dependence of disturbance amplitudes on coating thickness

The foils of the same materials and thickness are not characterized by the same strong stabilizing properties. The stabilizing properfis of zinc foil (dashed lines) are illustrated in the fig.3.5 too.

4 DISCUSSION OF RESULTS

The theory of non - connective component mixtures, developed by Morland [4] and Drumheller [5] can be applied to the metal coating layers. A mixture means a uniform, densely packed, insoluble distribution of solid microparticles in a continuum (liquid, gas). This theory postulates that only with very small dimensions of a final number of solid microparticles the effect of their dissociation is vivid. A microstructure of a separate microbody becomes dominant, that determines the peculiarities in dynamic loading of such mixtures.

A complex reaction of solid microparticles' mixture in a continuum due to dynamic loading results in a considerable difference between normal and tangential stresses and, as a consequence, in a big magnitude of dynamic yield strength (dynamic strength).

This theory data supported by the experiments with epoxide matrix, filled with aluminium microparticles of $2 \ \mu m \leq d \leq 8 \mu m$ diameter ($\rho \approx 0.9 \ \rho_0$ of aluminium) [6].

According to Drumheller concept, metal coatings will be characterized by high dynamic strength yield under dynamic loading, so their stabilizing effect is explained. In work [2] a semi - empiric relation, describing a function of wave - disturbance parameters (amplitude and wave length; a, λ) vs contact point velocity υ_c, density and strength properties (microhardness) of impacting metals is suggested. This relation shows that under equal conditions the disturbances on a contact boundary are lesser than there are stronger materials.

In a special test series, conducted accoding to the method described in work [7] dynamic yield strength of a copper coating was measured. Value $y \approx 2.5$ gpa was obtained under pulsed hydrodynamic pressure $p \approx 5$ gpa. This value considerably exceeds the dynamic yield strength for a copper continuum ($y \approx 0.7$ gpa under $p \approx 5$ gpa) and is the same as a dynamic yield strength for strenghth steel.

Thermophysical properties of a coating material affect the stabilization. In fact, ductile metal layers or simply thin metal layers can't acquire considerable dynamic yield strength value under pulsed loading since after complete layer melting intercrystal interactions do not manifest themselves. Fig. 3.5 shows that for a copper - copper pair a zinc layer $\Delta < 10$ μm thick does not stabilize a contact boundary. Evidently, it melts and takes part as a homogeneous continuum in boundary layers of loaded metals' mixing. A property of disturbance elimination on a contact boundary disappears.

In a series of unidimensional thermal calculations based on the main thermal conductivity equations [8] we obtained, that under the loading parameters described for $t \leq 5 \ \mu s$ (loading time) coating layers $\Delta \leq 10 \ \mu m$ thick, made of practically all metals, experience complete melting. A contact boundary is heated intensively as well, as a consequence. The materials mix. Only layers of fusible metals (tin, lead, cadmium, bismuth) having $10 \mu m < \Delta \leq 20 \mu m$ thickness melt completely. Coatings of tantalum, copper, nickel, titanium, aluminium, magnesium, zinc experience partial melting in a outer zone. Inner zone of a coating layer and boundary layers of a loaded sample are weakly heated and are characterized by the inherent original dynamic strength.

These test results give grounds to state that stabilization effect is determined by metal coating nature, its physical properties as a whole. Coating layer ρ density onstitutes (0.9-0.95) of density ρ_0 for a corresponding metal. The elementary micro volumes' cohesion is extremely weak, it is described by the bonds in dense packing. Disruption .strength is $\sigma < 0.01$ gpa for a copper coating of $\Delta \approx 20 \ \mu m$ thickness; and $– \ \sigma \leq 0.2$ gpa for a copper foil of the same thickness.

The most effective in stabilizing of a contact boundary are the coating layers, made of the metals with melting temperatures $t > 400°$ and low thermal conductivity (temperature conductivity coefficient $\text{æ}^2 < 10^{-4} \ m^2/s$).

5 SUMMARY

Thus, a method is suggested to eliminate an explosive welding and disturbances on a contact metal pair boundary in the process of oblique shock wave loading. Thin layers of metal coatings ($\Delta \approx 30 \ \mu m$) reliably stabilize a contact boundary and eliminate mutual intermixing of the metals under the loading. This coating property is explained by their high dynamic strength under the pulsed loading. Thermophysical properties of coating materials, contributing to the effective stabilization of a contact boundary are indicated.

REFERENCE

[1]   Hunt, J. 1968, Wave formation in explosive welding. *The Phyl. Mag.* **148**, p.669-680.}
[2]   Cowan, G. , Bergmann, O. and Holtzman, A. 1971, Mechanism of bond zone wave formation in explosion - clad metals. *Met. Trans.* **11,** pp.3145-3155.}
[3]   Glushak, B., Novikov, S., Pogorelov, A. and Sinitsyn, V. 1981, Study of initiation of TNT and TG 50/50 by shock waves having small durations. *FGV.* **6**, pp.90-95.}

[4]   Morland, L. 1972, A simple constitutive theory for a fluid - saturated porous solid. *J. of Geophys. Res.* **77**, pp.890-900.}

[5]   Drumheller, D. 1982, On the dynamical response of particulate - loaded materials. II.A theory with application to alumina particles in an epoxy matrix. *J. of Appl. Phys.* **2**, pp.957- 969.}

[6]   Chhabildas, L. and Swegl, J. 1982, On the dynamical response of particulate - loaded materials. I. Pressure-shear loading of alumina particles in an epoxy matrix. *J. of Appl. Phys*. **2**, pp.954-956.}

[7]   Bat'kov, Yu., Novikov, S., Sinitsyna, L. and Chernov, A. 1981, Study of shear stresses in metals at front of shock wave. *Strength problem*. **5**, pp.56-59.}

[8]   Godunov, S. 1979, Equation of mathematical physics. (Nauka, Moscow).

Instability of an Interface Between Steel Layers Acted upon by an Oblique Shock Wave

Oleg DRENNOV, Anatoly MIKHAILOV, Peter NIZOVTSEV and Victor RAEVSKII

Russian Federal Nuclear Center – VNIIEF 607190 Sarov Russia

Abstract This paper reports results of experiments in which development of instability was observed on the interface between two identical metals in tight contact with passage of an oblique shock wave through it. Numerical modeling of experimental results was performed by a two-dimensional Lagrangian procedure using an elastoplastic model with a functional dependence of the dynamic yield point on the state variables of the material. The calculations showed that perturbations develop only in the presence of a technological microgap of several tens of micrometers between the metal layers. Unloading of the material behind the oblique shock front into the gap gives rise to a considerable short-term velocity gradient. Simultaneously, near the interface behind the wave front there is a short-term loss of strength of the material due to thermal softening and the heterogeneous nature of the deformation.

1 INTRODUCTION

Hydrodynamic instabilities on interfaces between materials are of great theoretical and practical interest. The instabilities of interfaces between dissimilar materials under high-velocity flow conditions have long been known and have been studied on the bases of classical continuum mechanics. These studies are of interest for various modern engineering applications, for example, for the solution of the problem of inertial thermonuclear fusion. In particular, Kelvin-Helmholtz instability (shear instability) arises when the tangential velocity-field component undergoes a discontinuity in a continuous medium, resulting in an exponential growth of perturbations on the velocity-discontinuity surface [1].
Hydrodynamic instabilities have been adequately studied for liquids and gases. However, no adequate models have been developed to describe the development of instability in media possessing strength, compressibility, and viscosity, in particular, in metals.
Development of perturbations at an interface between two metal specimens upon passage of a shock wave with the front propagating at an angle to the interface (oblique shock wave) is most interesting in the case of identical materials. In the case of dissimilar materials, the conditions of Richtmyer-Meshkov and Kelvin-Helmholtz instabilities and, at an appropriate density ratio, Rayleigh-Taylor instability are satisfied. If two layers of the same metal are in tight contact (lack of a gap), the interface should be stable. Indeed, if shear strength is ignored, such an interface is fictitious, and flow singularities should not arise after shock-wave passage. If shear strength cannot be ignored, slippage of one layer relative to the other along the interface is possible.
A special case of instability development is the experimentally observed development of periodic perturbations on an interface between specimens of the same metal with passage of an oblique shock wave through it [2, 3].

2 EXPERIMENTAL RESULTS

A simplity loading scheme is given in fig.2.1. Two metal speciments have tight contact and are loaded by oblique shock wave.
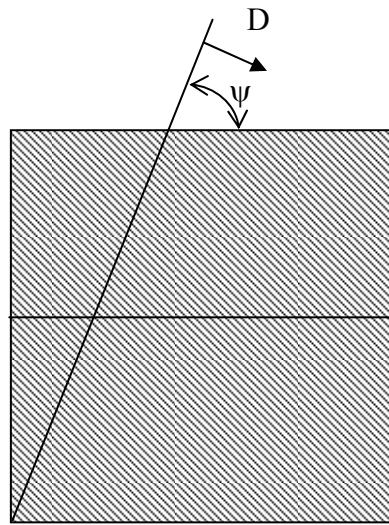
Fig.2.1. A simplity loading scheme

Figure 2.2 gives photograph of microsection of two steel samples' contact boundary (D is the velocity of the shock-wave front in metal and ψ is the slope of the front.).
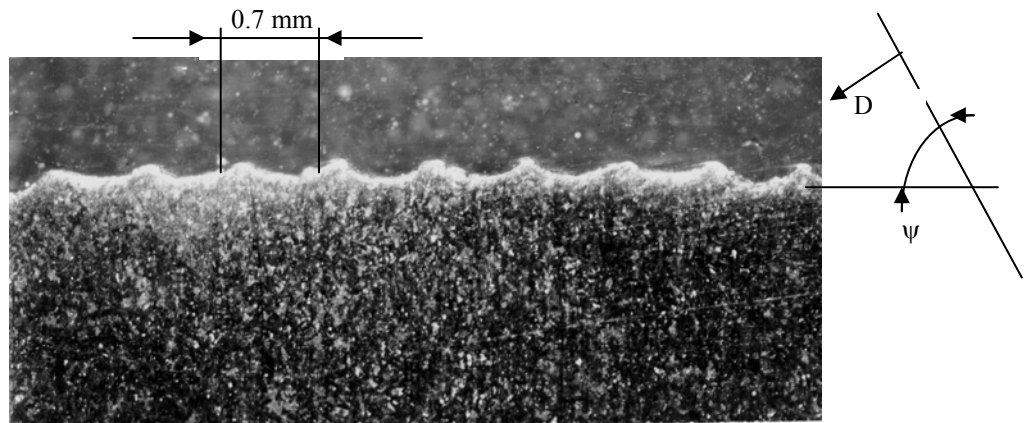
Fig. 2.2. Photograph of microsection of the samples contact boundary after shock – wave loading

The nearly sinusoidal perturbations have an amplitude $a \approx 0.06$ mm and a wave length $\lambda \approx 0.7$ mm. An drastic change of the starting structure of the steel is observed in the near-interface zone with a width $\Delta a \approx 0.02$ mm.

3 NUMERICAL SIMULATION OF THE LOADING PROCESS

The passage of an oblique shock wave through an interface between two identical metal specimens was studied by numerical calculations using a two-dimensional Lagrangian procedure [4]. The shock-wave parameters and the orientation of the front relative to the interface correspond to the data of the experiment in which perturbation growth was observed. The shock front pressure is p = 45 gpa. The shock wave entered the interface an angle $\psi = 70^0$. The numerical simulation was performed using an elastoplastic model with a functional dependence of the dynamic yield point on the state variables of the material (plastic strain rate, pressure, temperature). The relationship between the spherical components of the strain and stress tensors was derived using the Mie-Grüneisen equation of state.
The geometry of the computational domain (fig. 3.1) was close to the geometry of the experimental assembly.
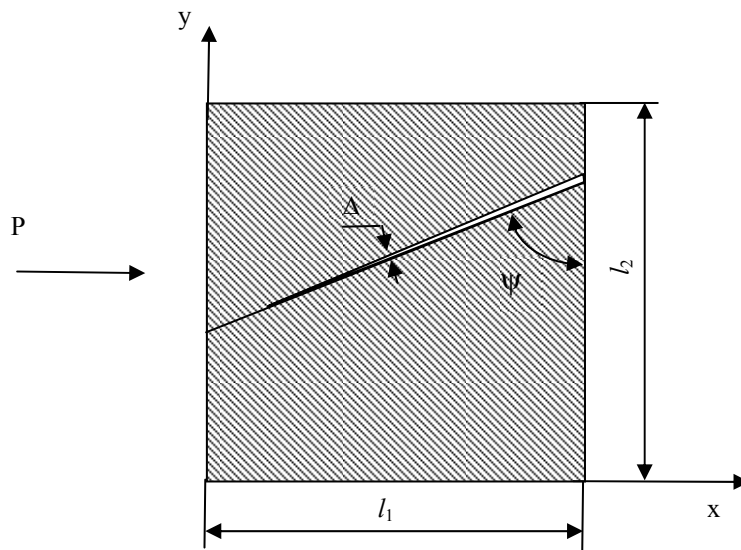
Fig. 3.1. Computational domain (p = 45 gpa, $l_1 = l_2 = 5$ mm, and $\psi = 70°$).

On the boundaries **y** = 0 and y = l_2, we imposed the rigid- wall condition. In the zone of interfaces, the characteristic size of the computational mesh is 5 μm. An oblique shock wave was simulated by constant pressure on the left boundary of the computational domain; i.e., in the computational scheme, a shock wave with a constant pressure p at the front was formed at the time t > 0. The calculations were performed for various magnitudes of the gap Δ between the surfaces. In the first series of calculations, a gap was absent, and the absolute slippage condition was specified on the interface; i.e., along the interface, the discontinuity of the shearing stress was equal to zero. In this case, $a/a_0 \approx 1$.

An incorporation of the gap into the computational scheme led to an increase in the rate of the relative displacement of the surfaces In the calculations with a gap the materials behave themselves as fluids with the equation of state of iron. Figure 3.2 gives a curve of the projection of the material's velocity onto the direction of the interface at boundary points of the section versus the coordinate x at the moment when the shock wave traveled a distance $x = 2.25$ cm.
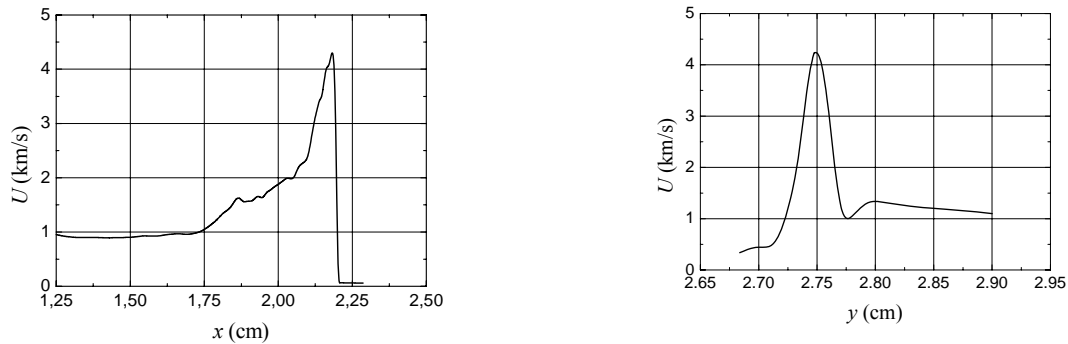
Fig. 3.2. Relative velocity of the material along the interface (Δ= 40 μm): (left) projection onto the *x* axis; (right) projection onto the *y* axis.

The maximum velocity is attained directly ahead of the shock-wave front and is $u_{max} \approx 4$ mm/μsec. The reason for such a velocity jump in the gap is the unloading of the material into the gap. The subsequent closure of the gap and deceleration of the unloaded material leads to a decrease in the velocity to the mean mass velocity u ≈ 1 mm/μsec in a time $\Delta t \approx 0.15$ μsec. The velocity jump gives rise to a short-term velocity gradient in the direction perpendicular to the interface.

In the region separated from the boundary by $\Delta y \approx \pm 0.25$ mm, the velocity gradient reaches a value $\sim 10 \mu sec^{-1}$. In the remaining region, a velocity gradient is absent. The velocity gradient in the region $\Delta y \approx \pm 0.25$ mm should lead to growth of perturbations whose wavelength is greater than the width of this region, i.e., $\lambda > 0.25$ mm. The calculations predicted the growth of propagation of exactly this wavelength: $\lambda = 0.2$-0.3 mm. Let us estimate the possible increase in the amplitude of these perturbations over the characteristic time of operation of the velocity gradient pulse $\Delta t \approx 0.15$ μsec ($\lambda \approx 0.3$ mm and $\Delta u = 3$ mmμsec) in hydrodynamic approximation [5]:

$$\frac{a}{a_o} \approx \mathrm{ch}\left(\Delta u \cdot \Delta t \, \frac{\pi}{\lambda} \right) \approx 60 \tag{3.1}$$

Thus, in the hydrodynamic approximation, a considerable growth of perturbations with wavelengths $\lambda > 0.3$ mm is possible. Perturbations with a wavelength $\lambda = 0.7$ mm build up more weakly: $a/a_0 \approx 4$.

Calculations with the yield point dependent on pressure and thermal energy were also performed. Such dependences for steel were obtained from results of measurements using the principal stress method [6].

In calculations without assigning initial perturbations, perturbation growth was not observed. Neither did development of perturbation occur when initial sinusoidal perturbations with an amplitude $a_o = 10$ μm. Probably, the reason for perturbation growth in a real system is a short-term decrease in shear strength behind the shock-wave front due to the formation of a system of localized shear bands with increased heating.

To verify this hypothesis, we performed calculations in which the yield point was artificially understated and given by

$$y = 0.045\left(1 - {e_t}/{e_m} \right) \; [\text{gpa}] \tag{3.2}$$

Here e_t is the thermal energy, e_m – is the energy of melting of the material.

In the calculations, perturbations with wavelengths $\lambda = 0.46$ and 0.7 mm increased by a factor of about 2.5. In these calculations, the magnitude of the initial gap was $\Delta \approx 20$ μm, which corresponds to the case where one surface having initial perturbations was actually pressed to the other.

4 SUMMARY

Thus, the calculations showed that the most probable reason for the development of perturbations during passage of an oblique shock wave through the interface of identical metals is the presence of a small microgap $\Delta = 20$-40 μm. The gap leads to the occurrence of a considerable but short-term velocity gradient along the interface, which, in turn, is responsible for perturbation propagation.

However, to recognize this explanation valid, one should also assume that short-term softening of the material due to the heterogeneous nature of the deformation occurs behind the shock- wave front.

REFERENCES

Birkhoff, H. 1960, Hydrodynamics. Study in Logic, Fact and Similitude, Princeton Univ. Press, Princeton, 243.

Drennov, O. 1999, Development of shear instability in metals. *Zh. Tekh. Fiz.* **2**, pp. 38-42. }

Drennov, O. 2001, Development of shear instability in media possessing strength. *Khim. Fiz.* **8**, pp. 86-89. }

Abakumov, I., Lebedev, A. and Nizovtseva, I. 1990, Rayleigh-Taylor instability in an elastoplastic medium. Numerical investigation. *Vopr. Atom. Nauki Tekh., Ser. Teor. Prikl. Fiz.*, **3**, pp. 14-19. }

Landau, L. and Lifshits, E. 1954, Mechanics of Continua, Gostekhteoretizdat, Moscow , 795.

Bat'kov, Yu., Glushak, B. and Novikov S. 1989, Strength of aluminum, copper, and steel at the front of a shock wave. *Comb. Expl. Shock Waves*, **5**, pp. 635-640. }

e-mail: `emeric.falize@cea.fr`

Kelvin-Helmholtz Instability in Astrophysical Jets

Émeric Falize[1], Serge Bouquet[1] and Claire Michaut[2]

[1] *Commissariat à l'Énergie Atomique, Département de Physique Théorique et Appliquée Île-de-France BP 12 91680 Bruyères-le-Châtel FRANCE*
[2] *Laboratoire de l'Univers et de ses Théories, UMR8102, Observatoire de Paris, 92195 Meudon, France*

Abstract: In this article, we study the influence of cooling on the Kelvin-Helmholtz instability in the context of astrophysical jets. It is quite obvious that cooling modifies the whole of the morphology and dynamics of jets. Adding cooling term can produce a new instability (thermal instability). This additional instability can play a fundamental role in the evolution of jets and can be an alternative model to understand the creation of overdensity regions (knots) in these jets.

1 INTRODUCTION

Jets are very common phenomena in the Universe. Both mysterious and fascinating, they leave all the theoreticians amazed about their nature. Though they may be found around supermassive black holes as well as around young stellar objects (YSO) [1], [2], they have common properties: the coherent structure on very large distance (the collimation problem) and the knotty structure. Regarding the collimation problem, there are two main models: the MHD model and the radiative one [4], [5], [6]. For the knotty structure there are also two approaches: the pulse concept [7] in which it is supposed that the object emits plasma regularly or the shear instability model [8], [9]. In this paper we focus on the second model, i.e., the shear or the so called Kelvin-Herlmholtz instability in the context of YSO jets where we include the radiative heating and cooling. It is clear that the YSO jets spread across Interstellar Medium (ISM) and consequently they may develop shear instability. It is the same thing in the case of galactic jets. We know that this type of jet is radiative (radiative energy losses) and the cooling can play, therefore, an important role in the morphologic and dynamic evolution of jets [10]. Thus we study the feedback of the radiative process in the development of Kelvin-Helmholtz instability. This work is achieved in slab case for the pinch and helical modes [11]. We consider a cylindrical jet, in order to compare with axisymmetric numerical simulations and various numerical works have shown differences between slab and axisymetric simulations [12]. In the first part we describe the model of young stellar object jets where we discuss different points (like thermal conductivity). Secondly, we study the linear stability of the flow and we derive the corresponding dispersion relation. Finally, we study the case where the jet is thermally unstable and an attempt to interpret the knotty structure as well as our conclusion are given.

2 DESCRIPTION OF YSO JETS

The YSO emit non relativist bipolar jets which are characterized by an internal Mach number ($M = v_{jet}/c_s^{int}$ with v_{jet} the speed of the jet and c_s^{int} the local sound velocity inside the jet) around 10 and a constrat of density about 1-10 [13]. These jets have a cooling factor [10] (denoted $\chi_c = d_{cool}/R_0$) which satisfies $\chi_c < 1$. In term of characteristic time, this corresponds to the ratio counter between: $0.1 < t_{cool}/t_{dyn} < 10$ where we define the cooling time by: $t_{cool} = P/[(\gamma - 1)\Lambda(\rho, P)]$ with Λ is the cooling function and t_{dyn} corresponds to the dynamical time. The quantities P, ρ and γ correspond respectively to the pressure, the density and polytropic index. We can see that radiative effects can modify the evolution of jets. The YSO jets are optically thin and we assume that the radiative transfer processes are negligible. Thus the radiative effect can be modelled by a simple gain or loss of entropy [14]. The equation of the model are:

$$\partial_t \rho + \frac{1}{r}\partial_r\left[r\rho v\right] = 0, \tag{2.1}$$

$$\rho\left[\frac{\partial}{\partial t} + (\vec{v}.\vec{\nabla})\vec{v}\right] = -\vec{\nabla}P, \tag{2.2}$$

$$\left[\frac{\partial}{\partial t} + (\vec{v}.\vec{\nabla})\right] P - \frac{\gamma P}{\rho} \left[\frac{\partial}{\partial t} + (\vec{v}.\vec{\nabla})\right] \rho = L(\rho, P), \tag{2.3}$$

where $\vec{v}$ is the fluid velocity and $L(\rho, P) = H(\rho, P) - \Lambda(\rho, P)$ with H the heating function and Λ is still the cooling function. In this model we do not introduce the heat conductivity effects because they are also negligible [15]. Different zones can develop the Kelvin-Helmholtz instabilty, like the contact between the cocoon and the jet or between ISM and the jet [16]. In this study, we do not introduce a transition zone. Such a zone stabilizes the wavelengths which are smaller than the thickness of this zone. These perturbations do not *"see"* the velocity discontinuity. Generally the cooling function can be approximated by a power-law model [17] in density and pressure (or temperature) but here we consider an arbitrary dependence. It is possible to extend this model to the other radiative cooling regimes [18]. Let us begin with the characterisation of the stationnary state. We consider a uniform plasma jet which moves at a uniform velocity in a uniform ISM at rest. This configuration is represented in the figure (2.1)
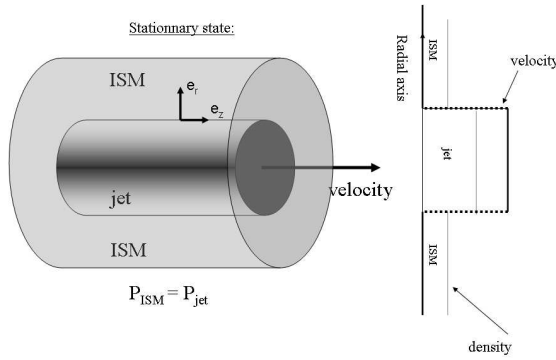
Fig. 2.1. Representation of the configuration and various physical profiles in the stationnary state. For the sake of simplicity, we ommitted the existence of the cocoon located between the jet and the ISM.

This system is Kelvin-Helmholtz unstable because we have a discontinuity of the velocity which can give rise to shear instabilities. First, we therefore study the linear stability of this flow.

3   PERTURBATION OF THE FLOW AND DISPERSION RELATION

We consider the linear stability analysis of the flow and we decompose all the physical fields, X, in the form $X = X_0 + \delta X$, where X_0 is the value for the stationnary configuration and where δX is the perturbation given by:

$$\delta X(r, z, \theta, t) = \tilde{x}(r) Exp[i(\omega t - kz - n\theta)] \tag{3.1}$$

where n is a relative integer, ω the pulsation, k the wave number, θ the angular component and $\tilde{x}(r)$ is the magnitude of the perturbation. For example [19], n=0 corresponds to the pinch mode, n=1 to the helical mode, n=2 to the elliptical mode and n=3 to the triangular mode. We can determine the evolution of different perturbations and obtain:

$$P = P_0 + Exp[i(\omega t - kz - n\theta)] \times \begin{cases} \tilde{P}_{jet}(r) \propto I_n(f_{jet}(k, w - kU)) \\ \tilde{P}_{ISM}(r) \propto K_n(f_{ISM}(k, w)) \end{cases} \tag{3.2}$$

where I_n and K_n are the two modified Bessel functions and the function f_i (i= jet or ISM) writes:

$$[f_i(k, x)]^2 = k^2 - \frac{\omega^2}{(c_s^i)^2} \frac{\omega - \mathbf{i}\omega_P^i|_{eq}}{\omega + \mathbf{i}\omega_\rho^i|_{eq}} \tag{3.3}$$

where c_s^i (i= jet or ISM) is the sound velocity in the different medium, $\omega_p^i = (\gamma - 1)[\partial L_i/\partial P]$ and $\omega_\rho^i = [\gamma - 1]/[(c_s^i)^2] \times [\partial L_i/\partial \rho]$; the subscript "eq" stands for "equilibrium" or "stationnary state". Now we impose

a continuous pression at the interface and the equality between the displacement inside and outside the jet in the r direction. These conditions, written below, lead to the dispersion relation:

$$\begin{cases} \tilde{P}_{jet}(R) = \tilde{P}_{ISM}(R) \\ [(v_r)_{jet}] / [\mathbf{i}(\omega - kU)] = [(v_r)_{ISM}]/[\mathbf{i}\omega] \end{cases} \tag{3.4}$$

where U is the jet velocity and the dispersion relation is:

$$\left[\frac{\omega}{\omega - kU}\right]^2 = \eta \frac{f_{ISM}(k,\omega)}{f_{jet}(k,\omega - kU)} \frac{I_n\left[f_{jet}(k,\omega - kU)\right] \dot{K}_n\left[f_{MIS}(k,\omega)\right]}{\dot{I}_n\left[f_{jet}(k,\omega - kU)\right] K_n\left[f_{MIS}(k,\omega)\right]} \tag{3.5}$$

This dispersion relation written in this form is very interesting because it is equivalent to the dispersion relation for polytropic cases [19]. The only difference for the polytropic case is that the function f_i reduces to:

$$[f_i(k,x)]^2 = k^2 - \frac{\omega^2}{(c_s^i)^2}. \tag{3.6}$$

Then it is possible to study the general dispersion relation (3.5) in various regimes. A specially interesting case appears where $kR_0 << 1$ since we have $Im(w) < 0$ and the gas is thermally instable [20], [21], [22]. Introducing dimensionless variables:

$$\bar{\omega} = \frac{R_0\omega}{U}, \bar{k} = R_0 k, M_i = \frac{U}{c_s^i} \tag{3.7}$$

where R_0 is the initial radius of jet and the equation (3.5) becomes:

$$\left[\frac{\bar{\omega}}{\bar{\omega} - \bar{k}}\right]^2 = \eta \frac{1}{\left[f_{jet}(\bar{k}, \bar{\omega} - \bar{k})\right]^2} \frac{2}{\left[\gamma_{Euler} + ln\left[f_{ISM}(\bar{k}, \bar{\omega})\right]\right]} \tag{3.8}$$

where γ_{Euler} corresponds to the Euler constant. We can re-write this relation in a polynomial form:

$$g(\bar{k})\bar{\omega}^4 + 2\bar{k}g(\bar{k})\bar{\omega}^3 + \left[\bar{k}^2 ln(\bar{k}) - g(\bar{k})\bar{k}^2 - 2\eta\right]\bar{\omega}^2 + 4\eta\bar{k}\bar{\omega} - 2\eta\bar{k}^2 = 0 \tag{3.9}$$

where

$$g(\bar{k}) = [M_{jet}]^2 \frac{\bar{\omega}_P^{jet}}{\bar{\omega}_\rho^{jet}} ln\left[\bar{k}\right] \tag{3.10}$$

It is possible to obtain four temporal branches for the pinch mode which is the "best" to develop thermal instability. These four branches are:

$$\bar{\omega}_1^\pm = \frac{\bar{k}}{2} + \frac{(2\sqrt{r} - p + 2y_0) \pm \sqrt{(2\sqrt{r} - p + 2y_0)^2 - 4(\sqrt{r} + \frac{q}{2(2\sqrt{r} - p + 2y_0)} + y_0)}}{2} \tag{3.11}$$

$$\bar{\omega}_1^\pm = \frac{\bar{k}}{2} + \frac{-(2\sqrt{r} - p + 2y_0) \pm \sqrt{(2\sqrt{r} - p + 2y_0)^2 - 4(\sqrt{r} + \frac{q}{2(2\sqrt{r} - p + 2y_0)} + y_0)}}{2} \tag{3.12}$$

$$r = -\frac{1}{4}\bar{k}^4 - \frac{9}{2}\eta\bar{k}^2 + \frac{1}{4}\bar{k}^4 ln\left[\bar{k}\right] - \frac{1}{4}\bar{k}^4 g(\bar{k}) \tag{3.13}$$

$$p = -\frac{3}{2}\bar{k}^2 - 2\eta + \bar{k}^2 ln\left[g(\bar{k})\right] - \bar{k}^2 g(\bar{k}) \tag{3.14}$$

$$q = \frac{5}{2}\bar{k}^3 + 6\eta\bar{k} + \bar{k}^3 g(\bar{k}) - \bar{k}^3 ln\left[\bar{k}\right] \tag{3.15}$$

and y_0 is a real solution of polynom (it is not written here but it can be easily derived):

$$8y^3 + 4(6\sqrt{r} - p)y^2 + 8(2r - p\sqrt{r})y - q^2 = 0 \tag{3.16}$$

One criterium [20] for thermal instability is that $[dP/d\rho]|_{L=cste} < 0$ which is equivalent to $\chi = [\omega_P/\omega_\rho] > 0$. Requiring therefore the condition $r < 0$, we are sure that the system is always unstable. In the figure (3.2) we represent the evolution of growth rate (in function of $\bar{k}$) for differents values of χ for a jet which is characterized by Mach number 10. We find a behaviour similar to that in the case of pure thermal instability.
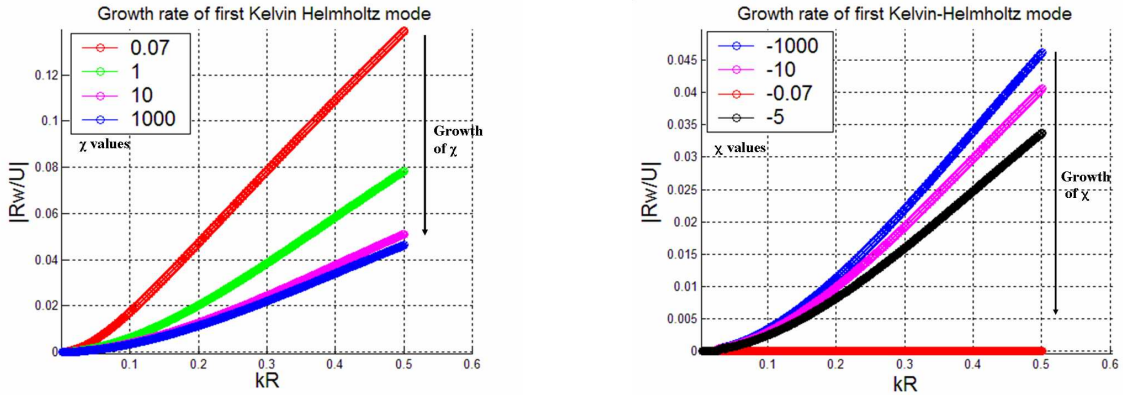
Fig. 3.2. Representation of growth rate of pinch mode. On the right figure the gas is thermally unstable, on left figure the gas is thermally stable.

4   ASTROPHYSICAL IMPLICATIONS AND CONCLUSION

As a conclusion, the thermal instability can play a major role in the Kelvin-Helmholtz instability and in the evolution of jets. This is very interesting as the pinch mode allows to form a knotty structure. The knots come from the fragmentation of gaz by thermal instability. Though it is a very simple model it can find different results that we obtain in the numerical simulation [15].

REFERENCES

[1]   Bally, J., Heathcote, S., Reipurth, B., Morse, J., Hartigan, P. and Schwartz, R., 2002. Hubble Space Telescope observations of proper motions in Herbig-Haro objects 1 and 2, *Astron. J.* 123:2627-2657

[2]   Bally, J., Reipurth, B. and Aspin, C., 2002. The highly collimated HH92 jet and parsec-scale outflow from IRAS 05399-0121, *Astrophys. J.* 574:L79-L82

[3]   Tsinganos, K. and Bogovalov, S., 2000. Magnetic collimation of the solar and stellar winds, *Astron. & Astrophys.* 356:989-1002

[4]   Shigemori, K., Kodama, R., Farley, D. R., Koase, T., Estabrook, K. G., Remington, B. A., Ryutov, D. D., Ochi, Y., Azechi, H. Stone, J. and Turner, N., 2000. Experiments on radiative collapse in laser-produced plasmas relevant to astrophysical jets, *Phys. Rev. E* 62:8838-8841

[5]   Falize, E. and Bouquet, S., 2007. Étude des jets astrophysiques et des jets de laboratoire I. Étude analytique de l'expansion et de la collimation radiative des jets. Confrontation aux expériences, *Rapport CEA in preparation*

[6]   Frank, A. and Mellama, G., 1997. Hydrodynamic collimation of YSO jets *Intern. Astron. Un. Symp.* 182-291

[7]   Raga, A. C. Canto, J., Binette, L. and Calvet, N., 1990. Stellar Jets with intrinsically variable sources, *Astrophys. J.* 364:601-610

[8]   Buhrke, T., Mundt, R. and Ray, T. P., 1988. A detailed study of HH34 and its associated jet, *Astron. & Astrophys.* 200:99-119

[9]   Micono, M., Massaglia, S., Bodo G., Rossi, P. and Ferrari A., 1998. Kelvin Helmholtz instabilities in stellar jets IV. On the origin of the emission knots, *Astron. & Astrophys.* 333:1001-1006

[10] Blondin, J. M., Fryxell, B. A. and Konigl, A., 1990. The structure and evolution of radiatively cooling jets, *Astrophys. J.* 360:370-386

[11] Hardee, P. E. and Stone, J. M., 1997. The stability of radiatively cooling jets. I. Linear Analysis, *Astrophys. J.* 483:121-135

[12] Downes, T. P. and Ray, T. P., 1998. Numerical simulations of the Kelvin-Helmholtz instability in radiatively cooled jets, *Astron. & Astrophys.* 331:1130-1142

[13] Remington, B. A., Drake, R. P. and Ryutov, D. D., 2006. Experimental astrophysics with high power lasers and Z pinches, *Rev. Modern. Phys.* 78:756-807

[14] Buchler, J. R., 1979. Radiation hydrodynamics in the fluid frame, *Journ. Quant. Spec. Rad. Transf.* 22:293-300

[15] Massaglia, S., Trussoni, E., Bodo, G., Rossi, P. and Ferrari, A., 1992. Radiative unstable modes in the jets of young stellar objects, *Astron. & Astrophys.* 260:243-249

[16] Hartigan, P., 1989. The visibility of the Mach disk and the bow shock of a stellar jet, *Astrophys. J.* 339:897-999

[17] Bertschinger, E., 1986. On the structure and stability of radiative waves, *Astrophys. J.* 304:154-177

[18] Drake, R. P., 2006. High-Energy density physics: Fundamentals, Inertial Fusion and Experimental Astrophysics, *Ed. Springer*

[19] Birkinshaw, M., 1996. Instabilities in Astrophysical Jets, *Astrophys. and Spac. Sc.* 242:17-91

[20] Field, G. B., 1965. Thermal instability, *Astrophys. J.* 142:531-567

[21] Balbus, S. A., 1988. On thermal instability and hydrostatic equilibrium in cooling flows, *Astrophys. J.* 328:395-403

[22] Balbus, S. A., 1986. Local dynamic thermal instability, *Astrophys. J.* 303:L79-L82

e-mail: `mmfran@lanl.gov`

Effects of different numerical interface methods on hydrodynamics instability

Marianne M. FRANCOIS, Edward D. DENDY, Robert B. LOWRIE, Daniel LIVESCU and Michael J. STEINKAMP

LOS ALAMOS NATIONAL LABORATORY Los Alamos NM 87545 U.S.A.

Abstract : We compare the effects of different numerical schemes for the advection and material interface treatments on the single-mode Rayleigh-Taylor instability, using the RAGE hydro-code. The interface growth and its surface density (interfacial area) versus time are investigated. The surface density metric shows to be better suited to characterize the difference in the flow, than the conventional interface growth metric. We have found that Van Leer's limiter combined to no interface treatment leads to the largest surface area. Finally, to quantify the difference between the numerical methods we have estimated the numerical viscosity in the linear-regime at different scales.

1 INTRODUCTION

The Rayleigh-Taylor instability (RTI) occurs in a variety of applications: astrophysics, inertial confinement fusion (ICF), and mixing, for example. Because of the importance of the RTI in many applications, it is important to understand, report and quantify the effects of the numerics on RTI simulations. In this study, we consider the single mode RTI and perform a series of numerical experiments using the RAGE hydro-code by varying the advection schemes and interface treatment. This study is organized as follows: In Section 2, we give a brief overview of the RAGE code, a description of our RTI problem setup and the different numerical options that we investigate. In Section 3, we show the density contours plots at different times and the time evolution of the interface growth and surface density metrics to investigate the differences between the numerical schemes. And in Section 4 we carefully evaluate the numerical viscosity in the linear regime.

2 THE RAGE HYDRO-CODE AND SINGLE MODE RTI PROBLEM SETUP

The RAGE hydro-code is a multi-material Eulerian code [1]. It solves the compressible-Euler equations using finite-volume high resolution Godunov schemes. RAGE uses the pressure-temperature equilibrium model.

In this work, we consider the single mode Rayleigh-Taylor instability between two fluids of density ratio 2. The computational domain is [0,1]x[-3,3]. The Atwood number A, defined as $A = (\rho_1 - \rho_2)/(\rho_1 + \rho_2)$, where ρ_1 is the density of the upper fluid and ρ_2 the density of the lower, with $\rho_1 > \rho_2$. Unless noted, throughout this study we used A=1/3. The gravity acceleration, g, is acting downward and is 0.1. Initially, the interface between the two fluids is perturbed. The initial interface position is given as $y(x) = a_0 \cos(2\pi x)$ with the amplitude perturbation $a_0 = 0.06$. The adiabatic constants for both fluids are $\gamma_1 = \gamma_2 = 1.4$. On the left and right sides of the domain we have periodic boundary conditions. Initially, the fluids have constant density and variable energy. The pseudo Mach number, defined as $M = \sqrt{g\lambda}/c$ where λ is the wave length and c is the speed of sound, is initially 0.21 for fluid 1 and 0.30 for fluid 2 at the interface. The mesh is uniform with equal spacing $\Delta x = \Delta y = 0.01$, i.e. the mesh size is 100x600.

We investigate the effects of different numerical schemes for advection and for modeling material interfaces. The following slope limiters (for the advection terms) are investigated: (1) zero slope, denoted in this paper by Ist order scheme, (2) minmod limiter denoted by MM and (3) Van Leer's limiter denoted by VL. For the interface treatments the following techniques are tested: (1) base capturing (denoted by noIP), (2) interface preserver (IP) (3) volume tracking or volume-of-fluid method (VOF) [3].

The interface preserver (IP) technique is based on a modified minmod limiter approach [1].This method is a capturing method that artificially steepens the slope so that the interface diffusion is limited to a fixed number of cells (about 3). For the base capturing method (noIP), the interface diffuses, there is no numerical interface 'steepener'. In the volume tracking method, the interface is reconstructed by piecewise linear planes (PLIC) method [2]. The material advection fluxes are estimated based on the geometrical reconstruction. This approach is considered a 'sharp' approach, i.e. the interface is located over one cell and thus there is no mass diffusion at the interface. However, the VOF approach is known to generate 'numerical surface tension' in regions where the interface curvatures are not resolved [2].

3 SINGLE MODE RTI SIMULATIONS RESULTS

The density contour plots at time t=5, 10, 15 and 20 are shown for the different schemes in Figure 3.1. From these figures we clearly observe the effects of the different schemes. The Ist order upwind scheme is very diffusive as expected. With high resolution methods, more complex structure develop in the flow compared to the Ist order scheme. The results of the VOF method are only considered with the Ist order scheme in our present comparison study.

In Figure 3.2 (a), the interface growth or mixing width, defined as the averaged bubble and spike amplitude is plotted versus time. We observe very slight difference between the interface growth results for the minmod and the Van Leer's limiters (high resolution method). We observe more difference between the results obtained with the Ist order scheme and the results obtained with the high resolution methods, as expected, since the Ist order scheme is more diffusive (less accurate) than the high resolution methods. The interface growth results with MM and VL shows a "reacceleration" that is not captured with the Ist order scheme.

In Figure 3.2 (b), the surface density function of the interface, i.e. a measure of the interface area, versus time is plotted. Compared to the interface growth metric, the surface density metric is expected to be more sensitive to differences in flow structures. The definition of the surface density function can be found in references [3]. In this work the surface density function $\langle \Sigma \rangle$ is computed as:

$$\langle \Sigma \rangle = \frac{\sum |\nabla f| P(0.4 < f < 0.6)}{N_{0.4 < f < 0.6}} \quad , \tag{3.1}$$

where f is the volume fraction, P is the probability of having an interfacial cell (a cell with 0.4<f<0.6) and N the number of interfacial cells.

For a given limiter (minmod or Van Leer), the surface density function is smaller when IP (interface preserver) is employed, showing the effect of sharpening the interface treatment. For the Ist order scheme, the VOF method gives the smallest surface density function, and IP gives a smaller surface density function than with noIP but larger than with VOF. For a given advection scheme, a sharper interface treatment leads to a smaller surface density function. For a given interface treatment, high resolution methods (MM and VL) have larger surfaces and have clearly more complex structures than the lower resolution scheme (Ist), as shown in the density contour plots of Figure 3.1.

As anticipated, the surface density function is found to be a more sensitive metric than the interface growth metric to reflect differences in the flow structure for the difference schemes. Next, we quantify the numerical viscosity in the linear regime.

4 EVALUATION OF NUMERICAL VISCOSITY IN LINEAR REGIME

In this section, we estimate the numerical viscosity in the linear regime by performing a series of simulation for different wave numbers k. The mesh size is 500x1000 and the computational domain is [0,1]x[-1,1]. The fluid density and adiabatic constants are the same as in the previous problem. The initial amplitude perturbation of the interface a_0 is chosen such that $a_0 k << 1$ holds. In the linear regime, for the inviscid case, The interface growth rate, denoted by n, for the inviscid case and with no physical surface tension, is:

$$n = \sqrt{A.g.k} \quad , \tag{4.1}$$

and for the viscous case (and with no surface tension) is approximated as [4]:

$$n_{viscous} = \sqrt{A.g.k - \nu^2 k^4} - \nu k^2 \quad , \tag{4.2}$$

where $\nu = (\mu_1 + \mu_2)/(\rho_1 + \rho_2)$.

In Figure 4.1 (a), we have plotted on the same figure the interface growth rate estimated from the RAGE simulations (represented by points) and the theoretical (represented by lines) growth rates for the inviscid and viscous cases at different wave numbers. The trend of the estimated growth rate does not follow the theoretical growth rates for the viscous cases. Therefore, we can state that the numerical viscosity effect on the growth rate does not have similar effect as a physical viscosity on all the scales (over the different wave numbers) on this mesh resolution. The combination of Van Leer's limiter with interface preserver gives growth rates that are the closest to the inviscid case. Recall that in the simulation we have no physical viscosity and the numerical viscosity that is present is highly nonlinear. Also, the wavenumber sensitivity of the numerical viscosity is expected, as it is well known that slope limiting is effectively a highly nonlinear viscosity that is large only at high wavenumbers. To quantify the numerical viscosity effect, we have plotted the time scale ratio between the numerical diffusion and the inviscid interface growth rate in Figure 4.1(b). From these two figures, we observe that the high resolution schemes (MM and VL) have smaller numerical viscosities compared to the Ist order scheme, as expected. We also observe that IP and VOF reduce numerical viscosity, but the main cause of the numerical dissipation is the advection scheme. We have also performed the same analysis for a case of A=5/7 and found similar results (not shown here).

(a) Ist order and noIP   (b) Ist order and IP   (c) Ist order and VOF

(d) MM and noIP   (e) MM and IP

(f) VL and noIP   (g) VL and IP
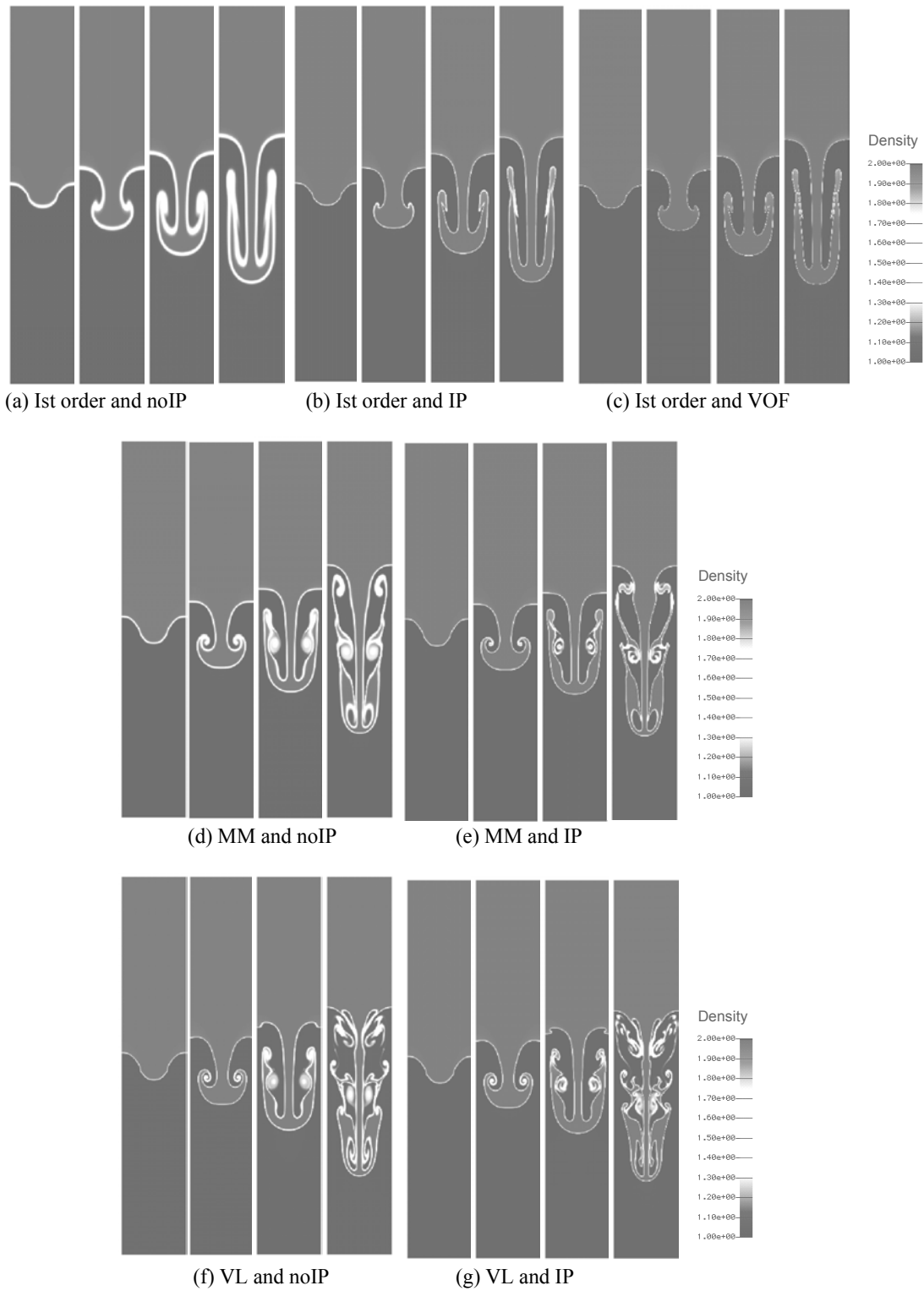
Fig. 3.1. Density contours at times t=5, 10, 15, 20 for the different schemes
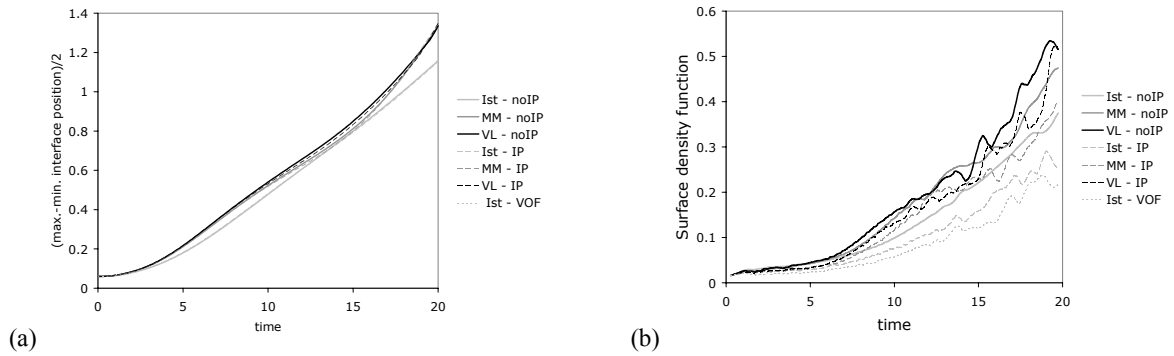
Fig. 3.2. Time evolution of (a) interface growth and (b) surface density
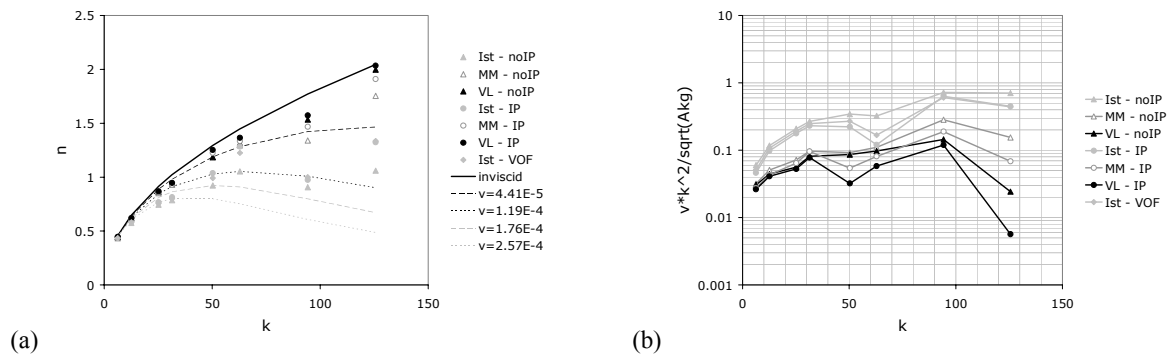
Fig. 4.1. (a) Theoretical and estimated growth rates and (b) time scale ratio
of numerical diffusion and inviscid interface growth rate, at different wave numbers

5 CONCLUSIONS

We have performed several numerical simulations with the RAGE hydro-code of single mode RTI using different numerical advection and interface treatment schemes. We have compared our simulations results by investigating the time evolution of the interface growth rate and surface density in both the linear and non-linear regimes. We have quantified the numerical viscosity in the linear regime. We have found (1) that the surface density function is a more sensitive metric to reflect the differences between the different schemes, (2) that 'sharper' interface treatment reduces the surface density function, (3) that the numerical viscosity does not have the same effect as a physical viscosity, (4) that interface preserver reduces the numerical viscosity (compared to no interface treatment) but (5) that the main cause of the numerical dissipation is the advection scheme.

REFERENCES

[1]   Gittings M., Weaver R., Clover M., Betlach T., Byrne N., Coker R., Dendy E., Hueckstaedt R., New K., Oakes W.R., Ranta D., Stefan R., 2006, The RAGE Radiation-Hydrodynamic Code, J. Comp. Phys., submitted, Los Alamos technical report, LA-UR-06-0027.
[2]   Rider W.J. and Kothe D.B., 1998, Reconstructing Volume Tracking, J. Comp. Phys., 141: 112-152.
[3]   Jaberi, F.A., Livescu D. and Madnia, C.K., 2000, Characteristics of Chemically Reacting Compressible Homogeneous Turbulence, Phys. Fluids, 12:1189-1209.
[4]   Duff R.E., Harlow F.H., Hirt C.W., 1962, Effects of Diffusion on Interface Instability between Gases, Phys. Fluids, 5:417-425.

e-mail: `gaysin@hitv.ru`

Rayleigh-Taylor Instability in Multichannel Gas-Vapour Discharge with Electrolyte Electrode at Atmospheric Pressure.

Azat GAYSIN[1], Almaz GAYSIN[1], Eduard SON[2], Fivzat GAYSIN[1].

[1]*Kazan State Technical University nam. A.N. Tupolev*
[2]*Moscow Physics-Techniques Institute (State University)*

Abstract: The experimental investigations of gas-vapor multichannel discharges with electrolyte jets at low and high voltages revealed the following features. The multichannel discharge propagates over the electrolyte surface when the solid electrode is immersed to electrolyte or is placed under the electrolyte jet. If the solid electrode is placed over the electrolyte surface transversal waves are induced and turbulent mixing of plasma and electrolyte occurs.

INTRODUCTION

The multichannel discharge with electrolyte jet as an electrode is of great interest in connection with study of physical processes and phenomena occurring on the plasma-electrolyte boundary. The objective of this work is investigation of instabilities of multichannel discharge where the solid is immersed to electrolyte, placed over the electrolyte surface, or is under the electrolyte jet.

DISCUSSION OF INVESTIGATION RESULTS

The surface of liquid metal is instable in electric fields with strength higher than critical $E_{cr} = (64\pi^2\alpha\rho g)^{1/4}$ (α – surface tension coefficient, ρ – liquid density, g – acceleration of free fall) due to instabilities like Raleigh-Taylor investigated theoretically by Thonks and Frenkel. Turbulent mixing occurs at the nonlinear stage of turbulence development.

We have studied multichannel discharges between electrolyte and solid electrodes, between electrolyte jet and solid electrode. The experimental set-up consists of electric power supply system (either high or low voltage), electrolyte bath, and measuring apparatus. The electrolyte-plasma boundary is observed visually and with high-speed digital camera DMC-FZ20 that allows getting pictures of various states of the boundary and filming processes development dynamics. The experiments show that at high currents (over 10 A) the foamy zone of turbulent mixing appears. The processes of mixing of plasma with electrolyte at wide range of discharge parameters were investigated. The characteristic features of physical processes and phenomena are revealed. Multichannel gas-vapor discharges between electrolyte jet and metal electrode at a wide current range (0.3 – 15 A), distances between electrodes from 2 to 170 mm, jet diameter from 1 to 10 mm, and pressure range 95 ÷ 105 kPa for various electrolyte composition (solutions of NaCl, KCl, NH_4Cl, $CuSO_4$ in purified water) and concentration are realized. The discharge properties significantly depend on jet diameter and its length, on electrolyte composition and concentration, as well as on electrode polarity. The processes in the boundary between electrolyte and plasma are investigated in the case of a multi-channel discharge with many jets at atmospheric pressure for various electrolyte compositions and concentrations. The discharge spatial structure was investigated. The voltage-current characteristics, spatial distribution of current density and temperature were obtained. Various types of self-sustained multichannel discharges between electrolyte jet and solid electrode are distinguished.

The basic results of experiments with high voltage multichannel discharges between solid and liquid electrodes are in following. If the solid electrode is placed above the electrolyte surface the transversal waves are induced on the liquid surface (Fig. 1a). The discharge channels disturb the surface and induce transversal waves that impose one onto another. Each channel generates electrolyte wave at some distance from the center. The disturbed surface region transforms to boiling foamy zone of turbulent mixing of plasma and electrolyte as current is increased (Fig. 1b and 1c). The critical value of current when transition to turbulent mixing current occurs is greater for an electrolyte cathode (Fig. 1c) than for electrolyte anode (Fig. 1b). The turbulent mixing of plasma and electrolyte is due not only to high value of electric field strength but also to electrolyte surface heating. Significant features of multichannel discharge are observed when the solid electrode is immersed to electrolyte. After switching the voltage during the time period of 5 – 10 s the jelly like colloid substance is formed. Chemical analysis showed that the electrolyte under discharge is alkali medium

(pH > 7) that can give off metal oxide hydrate due which the colloid substance is formed. The colloid substance is mixed with electrolyte. During the mixing gas bulbs are emerged inside the electrolyte and they go upwards, while the colloid substance by thin jets is deposited down. The multichannel discharge propagates between colloid substance jets and electrolyte (Fig. 1c and 1d), the discharge current increasing from 5 to 150 A. At the same time the discharge voltage decreases from 460 to 400 V. These changes in current and voltage are not due to supply voltage or ballast resistors adjustment.

a

b

c

d
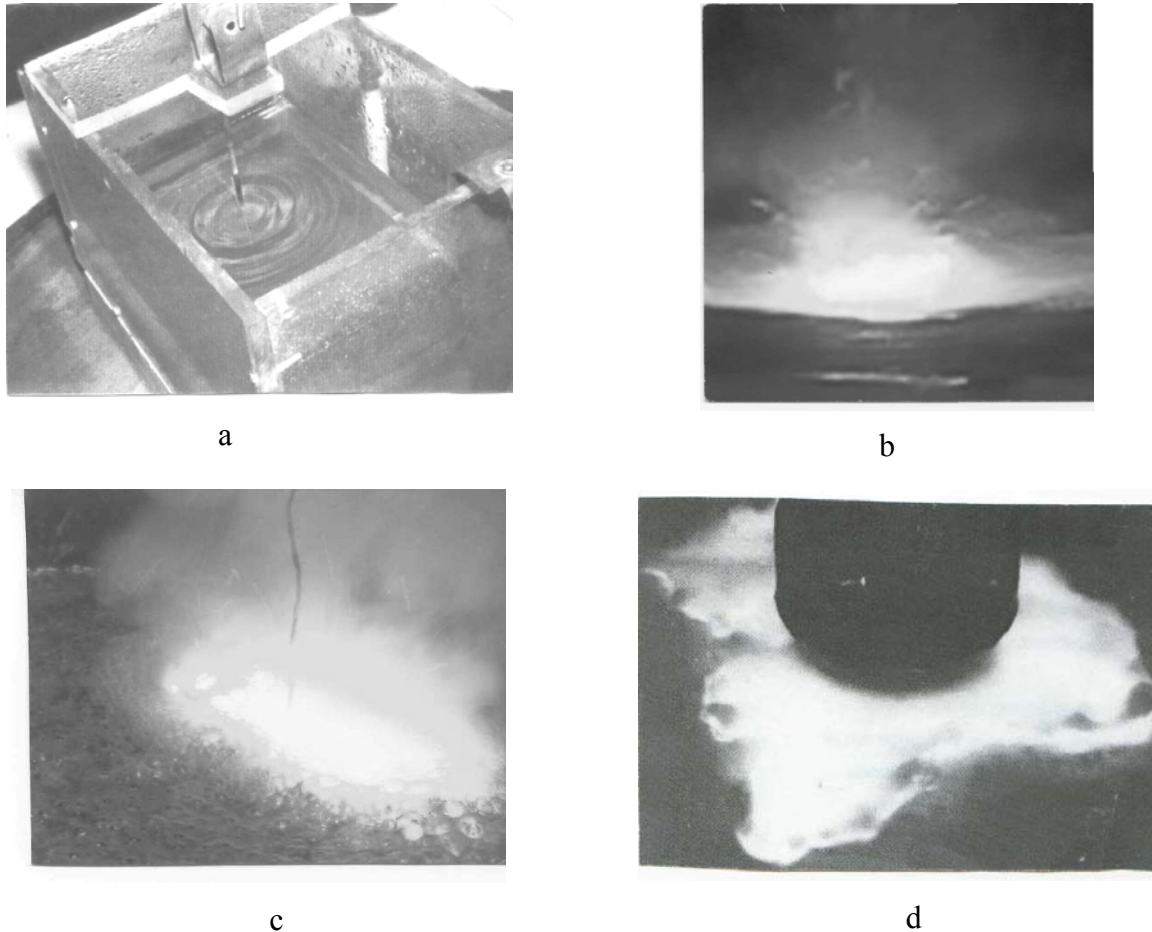
Fig. 1 Various forms of disturbances and instabilities on the plasma-electrolyte boundary.

SUMMARY

The turbulent mixing of plasma and electrolyte on the plasma-electrolyte boundary for DC multichannel discharge between solid and liquid electrodes is investigated. The various forms of electrolyte surface disturbances are revealed and their development and propagation processes observed.

REFERENCES

[1]   Gaysin F.M., Son E.E. Electrophysical processes in discharges with solid and liquid electrodes. Sverdlovsk: Urals University Publishing House, 1989. 432 p. (in Russian)
[2]   Gaysin F.M., Son E.E. Initiation and development of spatial discharge between solid and liquid electrodes.//Plasma Chemistry (Khimiya Plazmy), 1990. V. 16. P. 120. (in Russian)
[3]   Gaysin F.M., Son E.E. Gas-Vapor discharges between electrolyte cathode and metal anode at atmospheric pressure.// TVT (Teplofizika Vysokikh Temperatur). 2005. V.43 №1. P. 5 – 10. (in Russian)

e-mail: `glimm@ams.sunysb.edu`

Recent Progress in Turbulent Mixing

James GLIMM[1,2] and Xiaolin LI[1]

[1]*Stony Brook University, Stony Brook NY 11794-3600, USA*
[2]*Brookhaven National Laboratory, Upton NY, USA*

Abstract We present recent progress on turbulent mixing, jointly obtained with collaborators. We have an improved version of front tracking, improved physics models of Rayleigh-Taylor turbulent mixing, and agreement of simulations with experiment for immiscible experiments without surfactants and msicible fluids with mass diffusiion. We present improved closures for averaged equations. We use the experimentally validated simulations to validate the closures in the averaged equations. Issues of verification are also addressed.

1 INTRODUCTION

Our main result is validation of 3D turbulent mixing Rayleigh-Taylor simulations through comparison to laboratory experiments. The comparison is to the overall growth rate, α_b. This accomplishment is based on improved numerics (an improved version of Front Tracking), and improved physical modelling (surface tension effects for immiscible fluids and mass diffusion for air-helium miscible experiments). An overview of these results was presented in [1]. These validated simulations are used as a starting point for validation of an averaged equation fluid mixing model. We also compare our model closures to those of others, finding overall good agreement with the DNS data for both, but better agreement for the model we propose. We also present results from a statistical analysis of mixing rates and discuss a program for verification of turbulent mixing simulations.

2 IMPROVED NUMERICS

Two front tracking methods have been combined. Grid free tracking is based on marker particles which move freely through an underlying grid, and are connected, or organized, into triangulated surfaces to represent dynamic solution discontinuities. It is highly accurate. In contrast, grid based tracking projects the interface onto a reconstruction tied to the grid structure at each time step. It is robust but inaccurate. We use grid based tracking only locally during the bifurcations of the front, which makes the combined locally grid based tracking algorithm (LGB) essentially as accurate as the grid free tracking and as robust as grid based tracking [2]. The new algorithm greatly reduces surface smoothing, a numerical effect similar to surface tension. Standard benchmark tests in comparison to other interface methods such as volume of fluids and level sets show the advantage of front tracking [3].

A further improvement to the front tracking method, still in a development stage, is conservative and higher order tracking [4,5]. The schemes described above, as with all conventional methods, are zeroth order accurate locally near a discontinuity. Conservative tracking is based on tracking the space time discontinuity interface, and using finite volume difference methods in the irregular space time cells cut by the interface. This method is first and potentially second order accurate near the interface, and so it allows a greatly increased level of accuracy as the grid is refined.

3 IMPROVED PHYSICS MODELS AND NEW SIMULATIONS

We then add physical values of surface tension in models of mixing of immiscible fluids, and obtain Rayleigh-Taylor mixing growth rates (i.e., α_b) in agreement with experiment. See Table 3.1. Four simulations [6] span the range of dimensionless surface tensions in the experiments. One of these, ideal, with no surface tension, is significantly higher in its mixing rate than the experiments. The simulations show significant dependence of the mixing rate on the value of the surface tension. Only experiments without surfactant are included in Table 3.1.

We also modelled the Andrews-Banerjee air-helium splitter plate experiments, in which the dominant secondary physics effect is mass diffusion. Simulations [7] with the identical dimensionless value for mass diffusivity yield a maxing rate α_b identical to that of the experiment. See Table 3.1 and Fig. 3.1. Because of the very small value for the dimen-

sionless mass diffusion, representation of the diffusivity through a finite difference operator was not possible and instead, we introduced a subgrid model to implement this term in the continuity equation [8].

	Experiment	Simulation
Immiscible [9,10]	0.050-0.077	0.067
Miscible [11]	0.070	0.069

Table 3. 1. Comparison of experimental and simulation values for α_b.
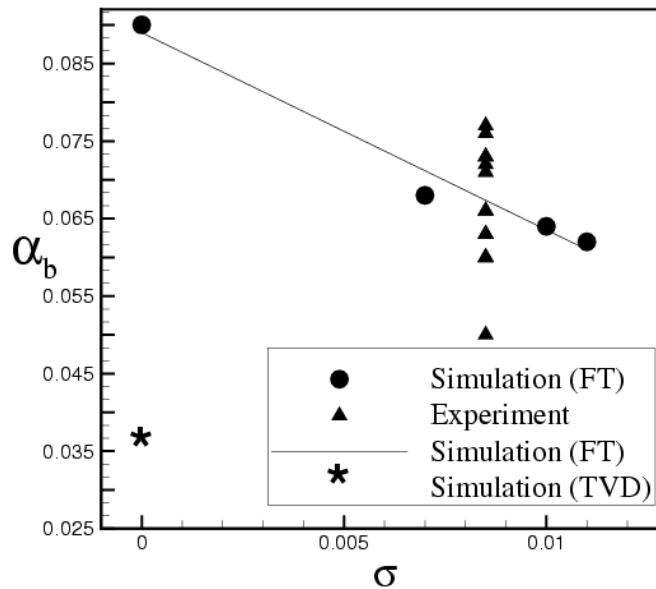
Figure 3.1. Plot of α_b vs. dimensionless surface tension. FronTier simulations pass through the experimental data points while the untracked TVD simulation, with ideal physics (no surface tension), yields a mixing rate about half the experimental value and about one third the front tracking value for ideal physics.

4 AVERAGED EQUATIONS AND CLOSURE

Averaged equations and closures are introduced based on a complete two fluid closure with independent velocities, pressures and energy for each phase. These models require expressions for the velocity, pressure and work evaluated at the interface as closure terms [12,13]. These quantities are denoted respectively $v^*, p^*, (pv)^*$. These quantities are written as convex sums of the corresponding pure phase quantities, with convex coefficients to be modeled. The models satisfy the following properties: 1. Hyperbolic stability, meaning real characteristics for time propagation, without appeal to diffusive terms. 2. Conservation of phase mass, total momentum, total energy, and a phase entropy inequality. Entropy conservation does not hold due the nonisentropic aspect of averaging. 3. Boundary conditions at the edges of the mixing zone. The closure describes a regime of imperfect mixtures, i.e. non-atomic mixture. The convex coefficients for the closures are themselves fractional linear expressions. This form for the convex coefficients was originally a guess, and in [12,13] was derived from manipulation of the exact (unclosed) equations. In the fractional linear expressions, two of the three independent parameters can be evaluated based on imposition of boundary conditions. The remaining condition is discussed below.

For adiabatic flows we also examine the entropy [13]. There are two possible entropies, namely as derived from direct averaging of the microphysical entropy and as derived from an equation of state from the averaged densities and

pressures. These two do not coincide in general, and only the former is guaranteed to be conserved. In fact, the second entropy, which is the one normally associated with the averaged equations, should not be conserved. The averaging process by itself is akin to mixing, and as such is non-isentropic. On this basis, even for smooth flows (without shocks), the entropy should be subject to an inequality, but should not be conserved.

The averaged equations are missing one condition at each edge of the mixing zone. This missing condition (an internal boundary condition) is associated with an incoming characteristic speed at the mixing zone edge from the single phase region associated with the phase which is missing there. To compensate for this missing information, and to complete the definition of the model, we couple the buoyancy drag equation [14] to the averaged equations at the two edges of the mixing zone. The buoyancy drag equation is a pair of phenomenological ordinary differential equations for the positions of each edge of the mixing zone. It has been considered by a number of authors, and in the form given in [14], it has one free parameter for each edge, a drag coefficient. Methods for chosing this drag coefficient have been addressed by a number of investigators including the authors and will not be examined here.

To illustrate this closure, we present the formulas for a representative case, namely v^*,

$$v^* = \mu_1^v v_2 + \mu_2^v v_2$$

where $v_k, k = 1, 2$ is the fluid velocity in phase k and μ_k^v are convex coefficients defined by the equation

$$\mu_k^v = \frac{\beta_k}{\beta_k + d_{k'}^v \beta_{k'}}$$

and $d_{k'}^v$ is a parameter to be determined. The identity $d_k^v d_{k'}^v = 1$ is enforced, so there is one free parameter to be chosen for each of the $v^*, p^*, (pv)^*$.

Extensions of these equations to three and more fluids was examined in [15]. In the 1D incompressible case, the equations admit closed form solutions [16,17].

5 VALIDATION OF MIX MODEL CLOSURES

The experimentally validated Rayleigh-Taylor simulations define an important data set. We use it to validate the closure terms for the averaged equations. Validation of the proposed closure relations relative to Richtmyer-Meshkov simulations is also discussed. From the previous section, we see that the closure model depends on three parameters, the $d_k^q, q = v, p, pv$. From analysis of the validated Rayleigh-Taylor simulations and from a simulation study of a circular Richtmyer-Meshkov mixing layer, we have determined that in most cases, the mixing coefficients are insensitive over a broad range of their values, and can be conveniently be set to 1. The only exception to this rule occurs for the velocity closure v^* and its parameter d_k^v for the case of Rayliegh-Taylor mixing. This parameter, however, is constrained in terms of the edge motions and is thus not a free parameter. Thus we see that the only free parameters in the model are the drag coefficients for the buoyancy drag equation coupled to the averaged equations.

For comparison to simulation data, we set the drag to yield agreement with the simulated edge position, and assess the degree to which the closure terms $v^*, p^*, (pv)^*$ agree with the direct computation of the interface quantities they are supposed to approximate. The overall error for each of the three terms is assessed in this comparison [18]. See Table 5.1. Additionally, we carry out the same comparison for the closure [19], for which the errors are larger.

Total	v^*	p^*	$(pv)^*$
11%	17%	0.0%	17%

Table 5.1. Relative errors in closure terms based on comparison to simulation data.

6 STATISTICAL ANALYSIS OF RT SIMULATIONS

We discuss mixture fractions and fluctuation spectra for the RT direct numerical simulations mentioned above, see [20].

The molecular mix fraction θ was computed for the three (ideal, surface tension and mass diffusion) simulations. As could be expected, due to the tracking of the interface and reduction of numerical mass diffusion, θ has a value zero for the first two simulations. To provide a comparison to work of others, we first averaged the simulation data over mesh blocks of size 1, ... , 8 and then recomputed θ using these values, on the coarse grid defined by the averaging process. Even the mesh block size 1 averaging changes θ, as in this case all partial cells with distinct fluids in separate components are replaced with a single mesh block average. We found that θ was a nearly monotone function of the block averaging size, and that the increase stabilized for an averaging length scale in the range $2\Delta x$ to $4\Delta x$, with a value in the range $\theta \approx 0.7 - 0.8$. These values for the mesh block averaged θ are consistent with values obtained by other investigators using untracked simulations.

The molecular mix fraction θ for the mass diffusion simulation is defined in terms of concentrations rather than volume fractions, in view of the physical mass diffusion contained in the simulation. These concentrations were not recorded during the simulation, but have been reconstructed from the densities assuming approximate incompressibility of the flow. For this simulation, the picture is different. The zero averaging (zero block size θ) is 0.7, already in approximate agreement with results of others, and is approximately stable after further block averaging of the data. Since the simulation differs from many in that its α agrees with experiment, we comment on this difference in comparing θ and α as measures of mixing. We have traced differences between our simulations and many untracked ones in the value of α as originating in numerical mass diffusion of the untracked simulations. The numerical mass diffusion is well reflected in a time dependent Atwood number $A(t)$, which is sensitive to the extremes of density contrast in a layer, while θ is defined in terms of averages. The many smaller bubbles, on the verge of elimination from the bubble mixing zone, are in fact diffused, while a few larger bubbles, to drive the mixing rate into the future, are not well mixed. The former dominate the definition of θ, while the latter dominate the definition of $A(t)$.

We also plotted the spectra for density, velocity and energy fluctuations, that is, a log log plot of fluctuations vs. wave number.

7 VERIFICATION FOR TURBULENT MIXING

We have proposed several concepts for verification, validation and uncertainty quantification. For complex problems, we favor a decomposition of the analysis into smaller components, with the uncertainties of the whole expressed as probabilities in a Bayesian framework and combined from the uncertainties of the components according to laws of probability. These ideas were tested in a simple (1D) framework [21] and found to be successful there. Within this framework, we allow for errors coming from the solution process as well as those introduced through initial conditions. Thus the solution framework not only is a transmitter of error (with possible amplification), but it also has the potential to create error. In the Bayesian framework, the essential inputs are the Bayesian prior and the Bayesian likelihood (of discrepancy between solution and observation). We develop numerically based models for this likehood, which are calibrated by ensembles of solutions and of solution errors, so that the error can be described by a PDF and the PDF has a basis in numerical studies of solution error. Other contributions to this likelihood can be treated in a similar manner.

For turbulent mixing, these issues become vastly more difficult. In earlier sections of this paper we have discussed issues related to validation of Rayleigh-Taylor mixing flows, that is, the agreement of simulations with experiment. Although we have achieved this goal, not all issues related to validation have been settled and so validation remains a partially open question.

Verification, the statement that the simulation is a mathematically correct solution of the equations being solved, is also difficult. For these flows and related Richtmyer-Meshkov mixing flows, the essential problem is that the flow becomes more complex under mesh refinement (until some extreme level of refinement is reached in which transport or scale breaking physics introduces a regularizing influence, and the underlying differential equations have changed). Thus verification, the issue of whether the equations as posed have been solved in a mathematically and computationally correct manner, is daunting, to say the least. To address this issue, we considered as a typical case a cylindrical Richtmyer-Meshkov unstable flow, formulated in 2D [22]. Because the problem was formulated in 2D, mesh refinement was feasible and could be pushed to a high degree. Because the problem was chaotic, new structures emerged in the solution under mesh refinement, and convergence under mesh refinement was problematic. In this sense the problem is representative of verification for turbulent mixing problems in general.

We address this problem through two methods. The two methods are related, as both serve to clarify and enhance the convergence properties of the solution, or even to define the convergence properties. The first method is linear and the second is nonlinear.

The first step is the introduction of solution functionals. These functionals involved some degree of averaging; the averaged functionals described the solution in a manner which was insensitive to the influence of the new, small scale structures introduced by mesh refinement. Typical functionals are averages over fixed size regions or over fixed rotational angles relative to the circular geometry.

A second essential step is the use of wave filters, to identify the principal shock and rarefaction waves of the problem. A wave filter is a post processing program which examines each location in space and time and each direction, for the presence of a shock wave. The detection is based on solving a local Riemann problem between states with positions displaced slightly in directions of the trial normal direction. When this Riemann problem yields a single strong wave with the other two waves weak, a local wave is identified. Variation of the allowed normal selects a maximum strength and a trial normal. These pointwise identified strong waves are assembled into curves (in 2D), allowing a further refinement to the local normal directions. The construction extends to 3D in principle. It assumes nothing special of the simulation, and so it could be applied to any fluid simulation. The wave filter can be thought of as a nonlinear solution functional, specially adapted to the physics of the problem, and in that sense the two steps are related.

The location of the contact waves (the location of the boundary between the heavy and light fluids) depends on the fact that the solution is tracked. These waves are determined dynamically within the calculation. The edges of the mixing zone are identified in terms of volume fractions of the heavy and light fluids. Errors in the convergence properties, that is, differences between solutions obtained at different levels of mesh, are divided into two types. The first is errors in the positions of the shock, rarefaction and mixing zone edges, that is, errors in the dominant wave structures of the problem. The second class of errors are the solution states values (pressure, density, velocity) at locations having the same flow history. Thus we examine and compare for convergence flow regimes having a similar history, such as the singly shocked heavy fluid in a single phase flow region, or the doubly shocked light fluid within the mixing zone. Through this use of the wave filters, we view the solution in a manner insensitive to the new structures which emerge at each new level of mesh refinement.

The major errors in the solution values occur within or near the dominant wave structures, due to position mismatch of the waves and due to the lack of numerical convergence of the solution near these points. It is well known that solution convergence is O(1) (non convergent) in a pointwise sense near major wave structures. So removing regions near these waves is important in assessing convergence properties (away from these waves).
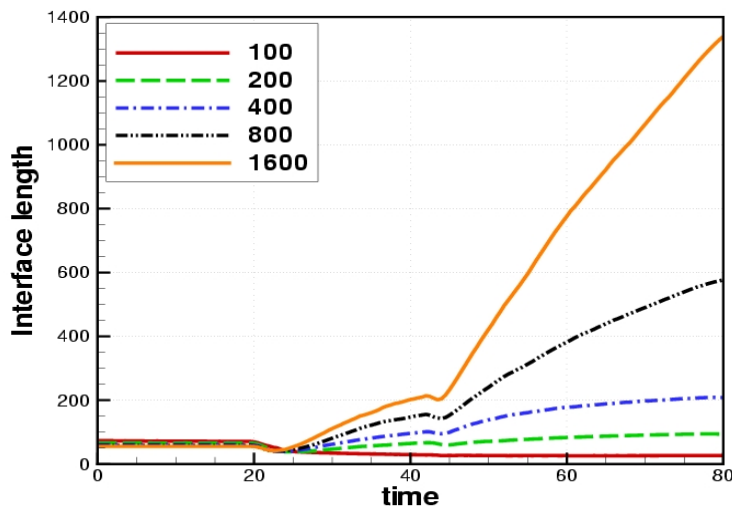
Figure 7.1. Interface length as a function of time, computed at five distinct mesh levels. The fractal property of the interface relative to mesh refinement is clearly visible from this plot. The indicated mesh numbers are the number of cells along the narrow dimension of the half circle.

Through these two main steps, we found convergence of the solution under mesh refinement for both wave location and solution value errors.

The total interface length (as a function of time) was recorded, and it was found not to converge under mesh refinement.

This is to be expected as there are no units of physical length in the simulation. Neither the global problem dimensions nor any microphysical scale have any meaning. All microphysical regularizing scales, such as physical mass diffusivity, viscosity, thermal conductivity, and surface tension have been set to zero. Thus the only regularization present comes from the grid. Quantities whose meaning depends on regularization thus may diverge under mesh refinement.

In Fig. 7.1 we present a plot of interface length vs. time for five different grid levels. If we model the length as an inverse power of Δx, namely $\Delta x^{-(1+\varepsilon)}$, we find ε increasing with time and positive after an initial time period. This fractal property of the interface raises obvious issues for mesh convergence of untracked simulations.

REFERENCES

[1]   Glimm, J. and Sharp, D. H., 2006. Simulation vs. theory vs. experiment for complex fluid mixing regimes, *in SIAM News*.

[2]   Glimm, J., Grove, J., Li, X.-L. and Tan, D., 2000. Robust computational algorithms for dynamic interface tracking in three dimensions, *in SIAM J. Sci. Comp*. **21**, pp. 2240-2256.

[3]   Du, J., Fix, B., Glimm, J., Jia, X., Li, X.-L., Li, Y. H and Wu, L., 2006. A simple package for front tracking*, in J. Comp. Phys*. **213**, pp. 613-628.

[4]   Glimm, J., Li, X.-L., Liu, Y.-J., Xu, Z. L. and Zhao, N, 2003. Conservative front tracking with improved accuracy. *SIAM J. Numerical Analysis* **41**, pp. 1926-1947.

[5]   Liu, J., Lim, H.-K., Glimm, J. and Li, X.-L., 2006. A conservative front tracking method in N-dimensions, *in J Sci Comp. In press.*

[6]   George, E., Glimm, J., Li, X.-L., Li, Y. H. and Liu, X. F., 2006. The influence of scale-breaking phenomen on turbulent mixing rates. *in Phys. Rev. E*. **73**, pp. 016304-1—016304-5.

[7]   Liu, X. F., George, E., Bo, W. and Glimm, J., 2006. Turbulent Mixing with physical mass diffusion, *in Phys. Rev. E* **73,** pp. 056301-1—056301-8.

[8]   Liu, X. F., Li, Y. H., Glimm, J. and Li, X.-L., 2006. A front tracking algorithm for limited mass diffusion, *in J. Comp. Phys.* In press.

[9]   Read, K. I., 1984. Experimental investigation of turbulent mixing by Rayleigh-Taylor instability, **in Physica D 12**, pp. 45-58.

[10] Smeeton, V. S. and Youngs, D. L., 1987. Experimental investigation of turbulent mixing by Rayleigh-Taylor instability, part 3, *AWE report number 0 35/87.*

[11] Banerjee, A. and Andrews, M. J., 2006. Statistically steady measurements of Rayleigh-Taylor mixing in a gas channel, *in Phys. of Fluids* **18**, pp. 35107-1.

[12] Jin, H. Glimm, J. and Sharp, D. H. Compressible two-pressure two-phase flow models, *in Phys. Lett. A*, **353**, pp. 469-474.

[13] Jin, H. Glimm, J. and Sharp, D. H. Entropy of averaging for compressible two-pressure two-phase flow models, *in Phys. Lett. A*. In press.

[14] Cheng, B. Glimm, J. and Sharp, D. H., 2002. Dynamical Evolution of the Rayleigh-Taylor and Richtmyer-Meshkov mixing fronts, *in Phys Rev E* **66**, pp. 1-7 paper No. 036312.

[15] Cheng, B., Glimm, J. Sharp, D.H. and Yu, Yan, 2005. A multiphase flow model for the unstable mixing of layered incompressible materials, *in Phys. of Fluids* **17** pp. 087102.

[16] Glimm, J., Saltz, D. and Sharp, D. H. , 1998. Statistical evolution of chaotic fluid mixing, *in Phys. Rev. Lett* **80**, pp. 712-715.

[17] Glimm, J. Saltz, D. Sharp, D. H., 1999. Twp-phase modeling of a fluid mixing layer, *in J. Fluid Mech*. **378**, pp. 119-143.

[18] Bo, W., Jin, H., Kim, D., Liu, X., Lee, H., Pestieau, N., Yu, Y., Glimm, J. and Grove, J. Compressible multi species multiphase flow models, 2006. *Stony Brook Technical Report,* to be submitted.

[19] Chinnayya, A, Daniel, E,. and Saurel, R. 2004, Modelling detonation waves in heterogeneous energetic materias, *J. Comp.. Phys.* **196**, pp. 490-538.

[20] Lee, H., H. Jin and Glimm, J., 2007. Notes on validation of turbulent mixing simulations for Rayleigh-Taylor instability, *Stony Brook University Technical Report,* to be submitted.

[21] Glimm, J. Grove, J. W., Kang, Y., Lee, T. Li, X., Sharp, D. H., Ye, K. and Zhao, M., 2005. Errors in numerical solutions of spherically symmetric shock physics problems, *in Contemporary Mathematics* **371**, pp. 163-179.

[22] Yu, Y., Zhao, M., Lee, T., Pestieau, Bo, W., Glimm, J. and Grove, J., 2006. Uncertainty quantification for chaotic computational fluid dynamics, *in J. Comp. Phys.* **217**, pp. 200-216.

/

Aluminum Rayleigh Taylor Strength Measurements and Calculations

M.J. Graham LINDQUIST[1], R.M. CAVALLO[1], K.T. LORENZ[1], S.M. POLLAINE[1], B.A. REM-INGTON[1], A.I. Lebedev[2] and V.A. RAEVSKY[2]

[1]LAWRENCE LIVERMORE NATIONAL LABORATORY 7000 East Avenue Livermore California 94550
[2]RUSSIAN FEDERAL NUCLEAR CENTER - VNIIEF, Sarov, Russia

Abstract: A traditional approach to the study of material strength has been revitalized at the Russian Federal Nuclear Center (VNIIEF). Rayleigh Taylor strength experiments have long been utilized to measure the material response of metals at high pressure and strain rates. A modulated (sinusoidal or sawtooth perturbation) surface is shocklessly (quasi-isentropically) accelerated by a high explosive (HE) driver, and radiography is used to measure the perturbation amplitude as a function of time. The Aluminum T-6061 targets are designed with several sets of two-dimensional saw-tooth perturbations machined on the loading surface. The HE driver was designed to reach peak pressures in the range of 200 to 300 kbar and strain rates in the range of 10^4 - 10^6 s^{-1}. The standard constitutive strength models, Steinberg-Guinan (SG) [1], Steinberg-Lund (SL) [2], Preston-Tonks-Wallace (PTW) [3], Johnson-Cooke (JC) [4], and Mechanical Threshold Stress (MTS) [5], have been calibrated by traditional techniques: (Hopkinson-Bar, Taylor impact, flyer plate/shock-driven experiments). The VNIIEF experimental series accesses a strain rate regime not attainable using traditional methods. We have performed a detailed numerical study with a two-dimensional Arbitrary Lagrangian Eulerian hydrodynamics computer code containing several constitutive strength models to predict the perturbation growth. Results show that the capabilities of the computational methodology predict the amplitude growth to within 5 percent of the measured data, thus validating both the code and the strength models under the given conditions and setting the stage for credible future design work using different materials.

1 INTRODUCTION

The evolution of a Rayleigh Taylor Instability (RTI) in metals has long been used to study and understand material strength under high pressure and high loading rates [6-9]. Under aggressive loading conditions, material strength serves to stabilize or retard instability-induced perturbation growth. An RTI occurs at a perturbed surface of a metal that has been accelerated by another material of a lower density. In Figure 1, a material (ρ_H) having a uniform frequency of small amplitude perturbations, with fixed wavelength, λ, is accelerated by low density, high--explosive (HE) products (ρ_L). Rather than uniform compression of the material surface, stress gradients are formed which induce plastic flow. Material moves from the valleys into the spike regions, increasing the amplitude of the original modulation. Spike growth continues, with increasing time, as illustrated in Figure 1. To assess the effect of material strength under RTI conditions, the evolution of the perturbation growth is used as a metric.
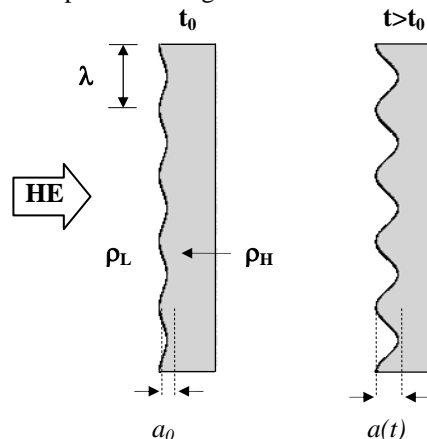
Figure 1. Schematic of RTI. a_0 is the initial amplitude of the perturbation, peak to valley. *A(t)* shows perturbation growth at later time.

During the decades that material strength has been studied, numerous experimental techniques have been developed to measure strength properties as functions of strain, pressure, temperature and strain rate. The data from Hopkinson-bar, Taylor impact and flyer plate/shock-driven experiments have all been used to formulate and validate constitutive strength models (SG, PTW, JC, MTS) widely in use in current hydrocodes. These experiments have largely been applied to physical problems where the strain and strain rate regimes are mostly less than 100 percent and less than $10^4 \, s^{-1}$, respectively. There are many applications where the RTI-induced strain exceeds 100 percent and strain rates are in the $10^4 - 10^8 \, s^{-1}$ range, for example, RTI in Inertial Confinement Fusion applications.

The VNIIEF RTI growth experiments are serving to provide the data necessary to validate existing strength models in the strain and strain rate regimes mentioned. The RTI growth experiments revitalized at VNIIEF are a technique initiated by Barnes, et al [6]. Barnes' idea is to smoothly accelerate a sinusoidally perturbed surface by the expansion of HE products across a void thus guaranteeing shockless (quasi-isentropic) loading to pressures in the hundreds of kilobar range. What we have investigated are a series of experiments which have attained 200 – 300 kbar peak pressures and strain rates in the range of $10^4 \, s^{-1}$ - $10^6 \, s^{-1}$. This is the first time since Barnes' [6] pioneering work in 1974 that experiments of this kind have been accomplished. We have performed a detailed numerical study to predict the perturbation amplitude using two constitutive strength models, namely, SG and PTW. The remainder of the article is dedicated to details of the experimental technique, the numerical results and justification for follow-on experiments at higher pressures and strain rates using different materials.

2 EXPERIMENTAL CONFIGURATION

The experimental setup is based on the original series of experiments formulated by Barnes [6] for the purpose of studying the growth (or lack thereof) of a sinusoidal perturbation imposed on a metal liner accelerated by HE products. It was shown that the perturbation growth is greatly moderated by the dynamic yield strength. In order to avoid the complications and heating caused by shock formation, the experiment was designed with a void between the HE driver and the target. The HE products cross the void and pile up on the side of the metal liner containing the small amplitude perturbations, providing a smooth rise to peak pressures. A schematic of the VNIIEF experimental design is provided in Figure 2.(a), (b), (c).
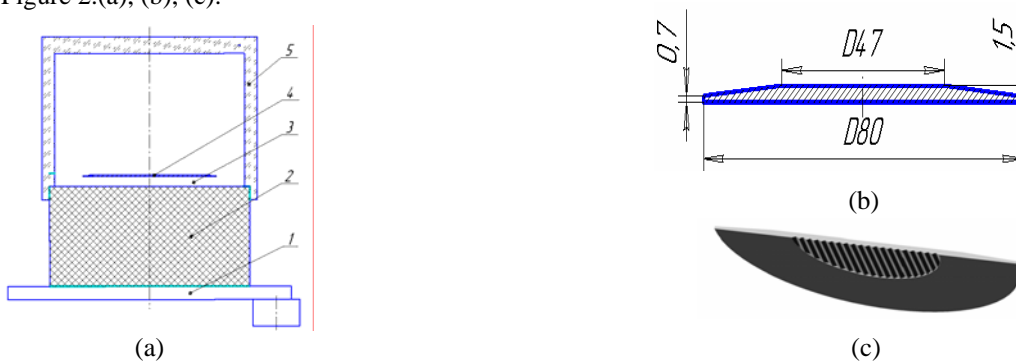
Figure 2. (a) Schematic of the experimental assembly (*1*) planar detonation wave generator, (*2*) HMX-based HE, (*3*) vacuum gap, (*4*) studied liner, Aluminum T-6061, and (*5*) sealing cylinder; (b) dimensions of aluminium liner; and (c) periodic perturbations machined on the loading surface of the aluminium.

The dimensions of the HE cylinder are diameter 120 mm and height 60 mm. The vacuum gap is fixed to be 3.5 mm. The aluminium sample was machined to a mean thickness of 1.5 mm in the central region, and had an overall diameter of 80 mm. The back side of the target is bevelled (such that the sample is thinner at the edges than in the center) in order to prevent bending due to lagging peripheral zones behind the central part of interest. The perturbations are located on the side of the target facing the HE. The composition of the HE governs the magnitude of the pressure. For the 300 kbar case, an HMX-based composition was used having density $\rho_0 = 1.885 \, g/cm^3$ and energy release Q = 6.1kJ/g. Results will also be shown for 200 kbar peak pressure, where a TNT/RDX-based composition was used having density $\rho_0 = 1.67 \, g/cm^3$ and energy release Q = 5.786 kJ/g. Due to the limitations of machining capabilities, the perturbations were chosen to be saw-tooth (Ideally, a sinusoidal modulation is preferred as it is considered a single frequency mode). For each of the liners studied, the wavelength of the perturbation, λ, is set at 2 mm. On each of the loading surfaces of the aluminium liners, a set of twenty wavelengths were machined. The perturbations are in two zones of 10 wavelengths each. The wavelength is fixed at λ = 2mm and the initial amplitude (peak to valley), A_0, in each of the zones of 10 are 0.06, 0.11, 0.15, 0.19, or 0.23 mm. Hence each sample provided information for two different initial perturbation amplitudes.

There were a total of seven experiments performed in this series, four of which were at 300 kbar peak pressure and three, at 200 kbar peak pressure. Perturbation growth was obtained by x-radiography; therefore, only one piece of data can be obtained from one experiment. A broad-band x-ray source having peak energies of 1 MeV and pulse widths of 100 ns (fwhm) was used in a side-on imaging arrangement. A sample of the X-ray photos of the aluminium liner at 300 kbar peak pressure is provided in Figure 3.
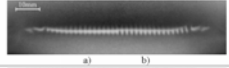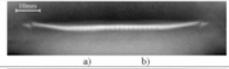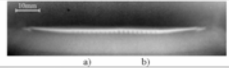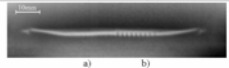
Zone	λ, mm	A₀, mm	S, mm	X-ray photo of studied plate	A, mm
a)	2	0.11±0.01	11±0.5		1±0.13
b)	2	0.15±0.01			2.13±0.18
a)	2	0.06±0.01	11±0.5		0.63±0.1
b)	2	0.11±0.01			0.9±0.09
a)	2	0.11±0.01	6.9±0.5		0.72±0.09
b)	2	0.15±0.01			1.24±0.10
a)	2	0.06±0.01	12±0.5		0.4±0.09
b)	2	0.15±0.01			1.96±0.14

Figure 3. X-ray results from aluminum experiments with peak pressures to 300 kbar. Sections a) and b) represent the zones of different initial perturbation amplitude. S (mm) is the position of the liner for a given x-ray image. A_0 (mm) is the initial peak to valley perturbation amplitude. A (mm) is the amplitude of the perturbation at the given position.

3 COMPUTATIONAL TECHNIQUE

A. Characterization of the Drive

Material strength is inferred from the RTI; however, it is critically important to correctly model the drive, or acceleration source of the aluminium liner, in order to accurately extract the material strength. The driver of the acceleration for the RTI comes from the stored chemical energy released from the HE, and therefore, the characterization of the pressure source is an integral part of the process. The JWL [10] equation of state, Equation (1), is a pressure-volume-energy equation most commonly and successfully used in the hydrocodes, where P is the pressure, ν is the relative volume, related by $\nu = V/V_0$, and V_0 is the initial volume, V, the time-evolved volume; A, B, R_1, R_2 and ω are constants. The parameters used for each HE are given in Figure 4.

$$P = A\left(1 - \frac{\omega}{R_1 v}\right)e^{-R_1 v} + B\left(1 - \frac{\omega}{R_2 v}\right)e^{-R_2 v} \quad (1)$$

	HMX	TNT/RDX
ρ_0 (g/cc)	1.895	1.67
A (Mbar)	8.478669	5.006074
B (Mbar)	0.2195808	0.1587606
R_1	4.50	4.50
R_2	1.50	1.50
ω	0.35	0.32
E_0 (Mbar)	0.1088	0.0873
$\Gamma_0 + 1$	3.814231	3.685124
U_s (cm/µs)	0.9000	0.7600

Figure 4. JWL parameters for HE

We performed a detailed one-dimensional (1D) numerical study to characterize the drive conditions, comparing the Pressure, Velocity and Position versus time with the gas dynamic calculations provided by VNIIEF for both HE drive conditions. An analytic equation of state was used for the Aluminum T-6061, with two different strength models: SG and PTW. Figure 5 shows that the 1D ARES SG calculations are in good agreement with the VNIIEF 1D representation. Calibration tests for the drive were performed by VNIIEF using thicker aluminium and incorporating manganin gauges to obtain in-situ pressure data. Velocimetry was not available at the time. Figure 5. (a) (b) (c) shows good agreement between the ARES calibration model and the VNIIEF drive characterization for the pressure, velocity and position of the loading surface of the aluminium versus time.

(a)   (b)   (c)
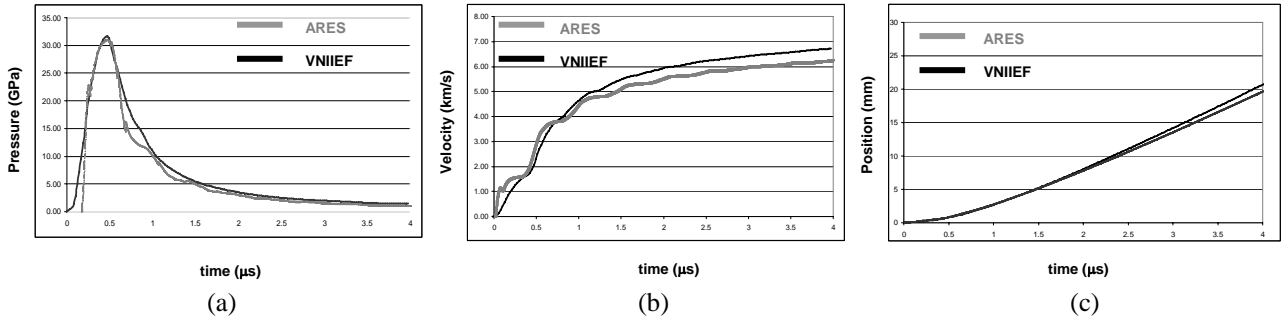
Figure 5. Comparision between ARES and VNIIEF drive conditions at the loading surface of the aluminium for the 300 kbar peak pressure experiments. (a) Pressure (GPa) vs. time (μs), (b) Velocity (km/s) vs. time (μs), and (c) Position vs. time (μs).

Very good agreement is shown at early time during the calculation, approximately 1 μs into the problem, with the deviation at late time being due to the material strength. The material strength consumes energy and helps to decelerate the plate.

B. Calculated two-dimensional Perturbation Growth

The initial conditions for the two-dimensional (2D) simulations were modelled after the experiment (Figure 6), using the drive calibrated in the 1D study. The full 2D calculations were performed using ARES, which is a massively parallel, multi-physics code. It is built on a multi-block Arbitrary Lagrangian Eulerian (ALE) hydrodynamics package and contains a wide array of physics models necessary for carrying out the HE driven material characterization experiments.
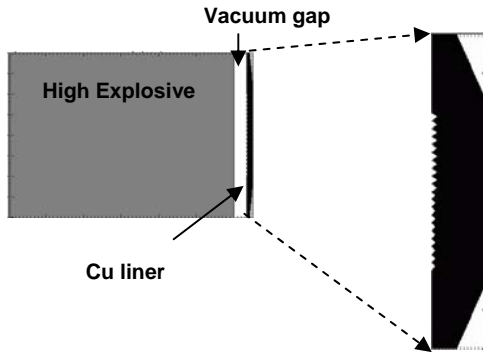
Figure 6. Schematic of the full 2D computational model, HE slab, vacuum gap and aluminium liner.

Each of the experiments was modelled with 120 zones per wavelength, with square zoning in the target, i.e., $\Delta x=\Delta y=1.67$ microns zoning in the metal. An analytic equation of state is used for the Aluminum T-6061. Two constitutive strength models were used to determine the material strength: Steinberg-Guinan [1] and Preston-Tonks-Wallace [3]. The SG model is an empirically based constitutive model with no explicit strain-rate dependence. Because of this feature, there has been some debate pertaining to the strain-rate regime in which SG is applicable. The SG equations are given in (2), (3), (4).

$$Y = Y_o f(\varepsilon_p) G(P,T) / G_o \qquad (2)$$

$$Y_o f(\varepsilon_p) = Y_o \left[1 + \beta(\varepsilon_p + \varepsilon_i) \right]^n \leq Y_{max} \qquad (3)$$

$$G(P,T) = G_o \left[1 + AP/\eta^{\frac{1}{3}} - B(T-300) \right] \qquad (4)$$

With *A* and *B* given,

$$A = \frac{1}{G_0} \frac{dG}{dP}$$

$$B = \frac{1}{G_0} \frac{dG}{dT}$$

$$\hat\tau = \hat\tau_s + \frac{S_0 - \hat\tau_y}{p} \ln\left[1 - \left[1 - \exp\left(-p\frac{\hat\tau_s - \hat\tau_y}{s_0 - \hat\tau_y} \right) \right] \exp\left\{ -\frac{p\theta_0\psi}{(S_0 - \hat\tau_y)\left[\exp\left(p\frac{\hat\tau_s - \hat\tau_y}{s_0 - \hat\tau_y} \right) - 1 \right]} \right\} \right] \qquad (5)$$

$$\hat\tau_s = \max\left\{ S_0 - (S_0 - S_\infty)\text{erf}\left[\kappa\hat T \ln\left(\frac{\gamma\dot\xi}{\psi} \right) \right], S_0\left(\frac{\psi}{\gamma\dot\xi} \right)^\beta \right\} \qquad (6)$$

$$\hat\tau_y = \max\left\{ y_0 - (y_0 - y_\infty)\text{erf}\left[\kappa\hat T \ln\left(\frac{\gamma\dot\xi}{\psi} \right) \right], \min\left[y_1\left(\frac{\psi}{\gamma\dot\xi} \right)^{y_2}, S_0\left(\frac{\psi}{\gamma\dot\xi} \right)^\beta \right] \right\} \qquad (7)$$

From shock wave experiments, it is often assumed that SL applies to strain rates up to 10^5 s^{-1}, beyond which SG applies and the strain rate becomes unimportant. Our calculations for Aluminum T-6061 using the SG constitutive model are shown in Figure 7. The PTW model (Equations 5, 6 and 7) is a physically based constitutive model with a thermal activation to phonon drag transition that takes effect at a specified strain rate in the 10^6 - 10^8 s^{-1} regime. Due to the scale-invariant nature of the PTW model, the authors claim it is valid for arbitrary strains, temperatures and strain rates [15]. The calculations for Aluminum T-6061 using the PTW strength model are also shown in Fig. 7. Simulations with either model (SG vs PTW) reproduce the observed results reasonably well.
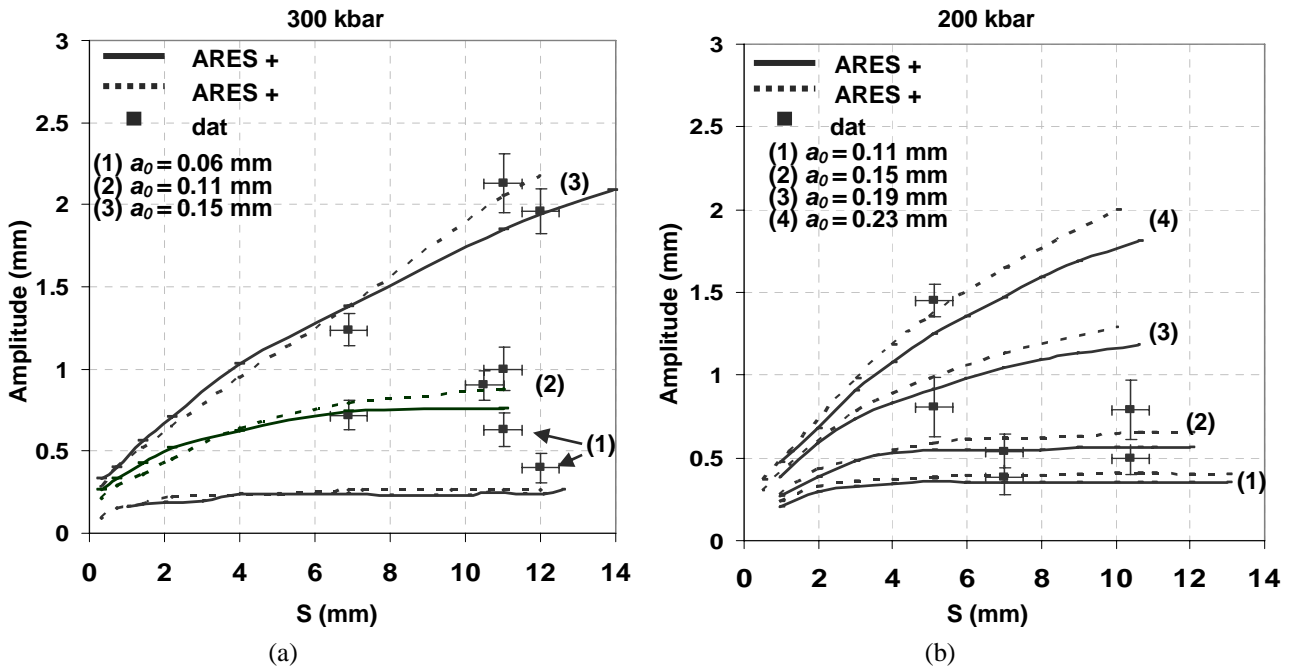
Figure 7. Perturbation amplitude vs. distance travelled. (a) P_{max} = 300 kbar (HMX driver), and (b) P_{max} = 200 kbar (TNT/RDX driver).

The results shown in Figure 7 represent the data from the seven experiments, ARES calculations with SG strength model and ARES calculations with PTW strength model. The ARES 2D simulations have predicted the material yield strength to within 5 percent of the measured data for all cases except the smallest initial amplitude case. The standard input parameters for the SG and PTW models were used for Aluminum T-6061. Since Aluminum T-6061 is a well-known substance, it is not surprising to find such good agreement. However, the fact that both of the material strength models were formulated from data with very different experimental techniques and strain less than 100 percent indicates that the strength models for Aluminum T-6061 implemented in our hydrocodes are well calibrated. These experiments have provided an excellent validation experimental set for Aluminum T-6061 in the given conditions.

We show in Fig. 8 predictions from the PTW model for flow stress for Al6061 at the representative conditions of P = 200 kbar, T = 400 K, $\rho/\rho_0 = 1.1$, $\varepsilon = 0.1$ (solid curve). [11] Flow stress is plotted versus log($d\varepsilon/dt$). The flow stress has been normalized by the value predicted by PTW at $d\varepsilon/dt = 1$ (but still at the above P, T, ρ/ρ_0, and ε). Also plotted is the result for thermal activation only (dashed) curve, turning off the contribution due to nonlinear phonon drag. In the thermal activation regime, PTW predicts flow stress increasing logarithmically with strain rate, $\sigma \sim \ln(d\varepsilon/dt)$, whereas in the nonlinear phonon drag regime, PTW assumes a power law dependence on strain rate, $\sigma \sim (d\varepsilon/dt)^\beta$, with $\beta \sim 1/4$. Note, using nominal input parameters for Al6061 for the PTW model, the transition from thermal activation to phonon drag occurs at strain rates of $\sim 10^8$ s^{-1}. Hence, the PTW model predicts that these HE-RT experiments, with strain rates in the 10^4-10^6 s^{-1} range, lie in the thermal activation regime. Also plotted in Fig. 8 (dotted curve) is the prediction from the SG model. The SG model is independent of strain rate, but is meant only for high strain rate applications, $d\varepsilon/dt > 10^4$ - 10^5 s^{-1}. Note also, for the conditions of these experiments, 10^4-10^6 s^{-1}, the PTW model predicts 10-20% greater strength, due to the strain rate dependence in the thermal activation regime. This is consistent with the simulated growth factors being slightly lower for the HE-RT experiments when the PTW model is used, compared to the SG model.
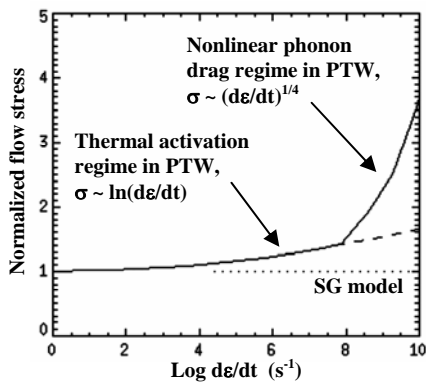
Figure 8. Normalized flow stress versus log(strain rate) from the PTW model versus the SG model.

There is a nearly 50 percent discrepancy between the calculations and the experimental data at 300 kbars for the smallest initial perturbation amplitude of 0.06 mm. We have found that this is due to the limitations of the machining accuracy. The VNIIEF machining error, at that time, was as much as 20 percent. We performed calculations incrementally increasing the initial amplitude from 0.06 mm to 0.08 mm and found good agreement when the initial perturbation amplitude has been arbitrarily set to 0.075 mm.

4 CONCLUSION

Modeling results show that the standard SG and PTW parameters for Aluminum T-6061 are sufficient to model the evolution of a RTI driven quasi-isentropically to pressures in the range 200 – 300 kbar, strain larger than 100 percent and strain rates to 10^6 s^{-1}. The simulated perturbation amplitude as a function of distance generally agrees well with the VNIIEF data. Future work will focus on higher pressures and strain rates, comparisons of BCC (such as vanadiuim) vs FCC (such as Al6061) materials, and different initial grain sizes. Understanding the effects of varying the peak pressure and strain rate is extremely important, to see how these constitutive models scale outside the regime in which they were calibrated.

ACKNOWLEDGEMENTS

[1] D.J. Steinberg, S.G. Cochran and M.W. Guinan, J. Appl Phys. **51**, 1496 (1980).
[2] D.J. Steinberg and C.M. Lund, J. Appl Phys. **65**, 1528 (1989)
[3] D.L. Preston, D.L. Tonks, and D.C. Wallace, J. Appl Phys. **23**, 211 (2003).
[4] G.R. Johnson, J.M. Hoegfeldt, U.S. Lindholm and A. Nagy, ASME J Eng Mater Tech **105,** 42 (1983).
[5] P.S. Folansbee and U.F. Kocks, Acta metal, **36**, 81 (1988).
[6] J.F. Barnes, P.J. Blewett, R.G. McQueen, K.A. Meyer and D. Venable, J. Appl Phys. **45**, 727 (1974).
[7] J.D. Colvin, M. Legrand, B.A. Remington, G. Schurtz and S.V. Weber, J. Appl Phys. **93**, 5287 (2003).
[8] D.H. Kalantar, B.A. Remington, E.A. Chandler, J.D. Colvin, D. Gold, K. Mikaelian, S.V. Weber, L.G. Wiley, J.S. Wark, A.A. Hauer and M.A. Meyers, J. Impact Engineer., **23**, 409 (1999).
[9] K.T. Lorenz, M.J. Edwards, S.G. Glendinning, A.F. Jankowski, J. McNaney, S.M. Pollaine and B.A. Remington, Phys. Plasmas, **12**, 056309 (2005).
[10] private conversation C. Souers.
[11] private conversation J.D. Preston.

e-mail: brian.grieves@awe.co.uk

2D Direct Numerical Simulation of Ejecta Production

Brian GRIEVES

AWE Plc, Aldermastion, READING, RG6 4PR, UK

Abstract: A 2D Eulerian code is used to calculate the shock induced ejecta produced from a metal surface using a typical random surface finish. This is an example of multimode Richtmyer-Meshkov instability at high Atwood number. The aim of this work is to calculate a 2D direct numerical simulation of ejecta and to compare with experimental results. © British Crown Copyright (2006/MOD)

1 2D EULERIAN CODE, PETRA

PETRA is a 2 dimensional Eulerian code [1]. It uses a rectangular grid with a Lagrangian calculation and then an advection step in each timestep. The Eulerian grid can be in several geometries; plane, axiysmmetric, spherical and cylindrical polar. The EOS variables are pressure, energy and density. The material options include strength and interface reconstruction is used.

This study uses fine zoned calculations to model the hydrodynamics involved in the production of ejecta. In this work we allow the mesh to move with the average local fluid speed in the direction of an incident shock (i.e. Lagrangian in the x-direction) which is driven by a time dependent pressure boundary condition.

2 A SIMPLE TEST PROBLEM

To demonstrate the method and to give some indication of what mesh size is needed we initially calculate a simple problem. In this case it is a block of lead with a groove cut in one side and is shown in **Fig 2.1**. An applied pressure on the opposite face drives a shock into the block which results in the production of ejecta. The applied pressure is high enough to melt the lead. The resultant jetting is seen experimentally [2]

P vs. t $\rightarrow$ Pb   Low-density gas
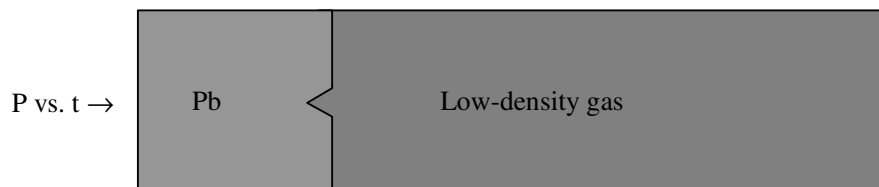
Figure 2.1: Set up of simple problem used to demonstrate the method.
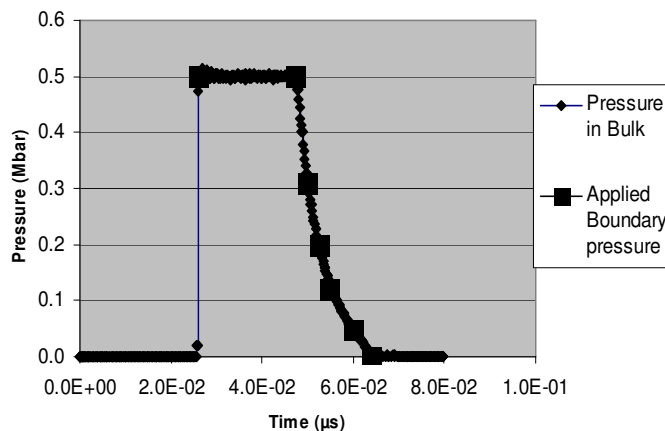
Figure 2.2: Comparison of applied pressure and the pressure in the Pb.

The shock is generated by applying a pressure boundary condition to the left hand edge of the metal block. However if a constant pressure is a applied then the rarefaction wave that reflects from the metal gas interface means a second shock is produced when it reaches the upstream boundary. The solution to this is to reduce the applied pressure as the rarefaction wave reaches the boundary. **Fig 2.2** shows the pressure in bulk sample of Pb and the applied boundary pressure. The resultant free surface velocity is shown in **Fig 2.3**.

95
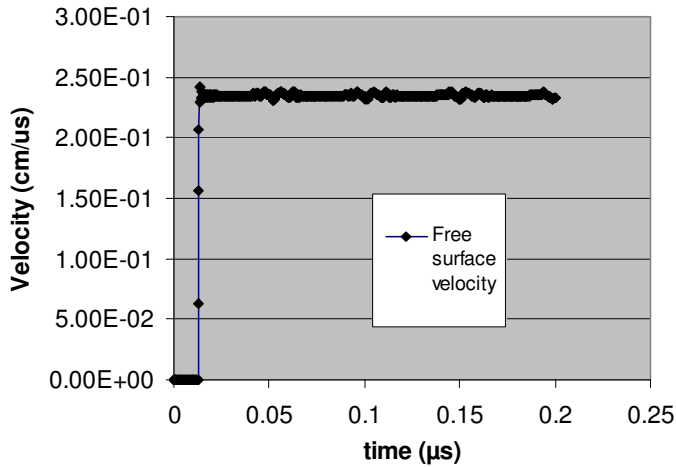
To analyse these calculations it is desirable to produce results which are more directly comparable with experiments. Some experimental results are represented by a plot of cumulative areal mass against velocity. The results of the groove problem are presented below (**Fig 2.4**) in this form. The velocity is scaled by the jump off velocity of the free surface (as determined by a 1D calculation.)

Figure 2.3: The Free surface velocity of the Pb sample.
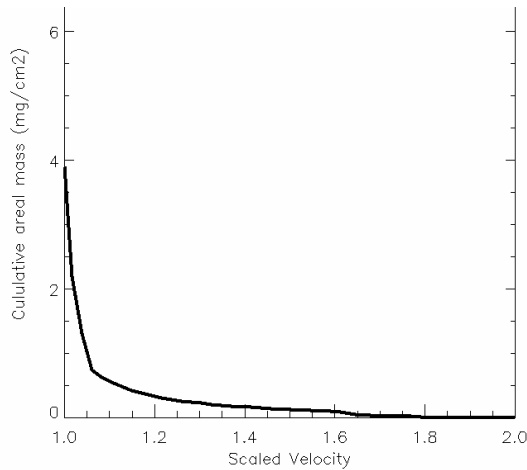
Figure 2.4: The cumulative areal mass against scaled velocity.

3 A MORE REALISTIC PROBLEM

A calculation with a surface finish typical of that expected in an experiment has been run. **Fig 3.1** shows the calculation after the shock has passed through the surface into the gas. The shock causes ejecta to form. The spikes shown here are the sources of the ejecta. The analysis of the ejecta calculation produces this plot of cumulative areal mass against the scaled velocity which is shown in **Fig 3.2**.

This shows the peak ejecta velocity is approximately 30% faster than the free surface and the total mass is approximately 3mg/cm^3. By repeating the calculations using measured surface roughness of a sample this curve could be compared with experiment. If the comparison is favorable then the calculation could be used to improve ejecta models as the simulations provide more detailed information than is available experimentally.
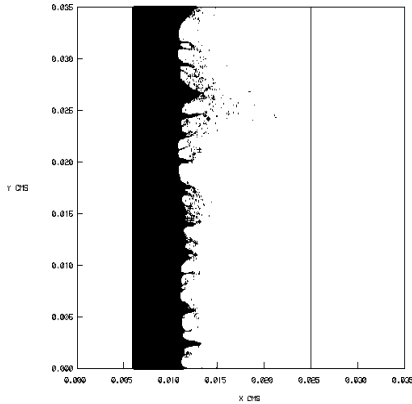
Figure 3.1: Formation of Ejecta
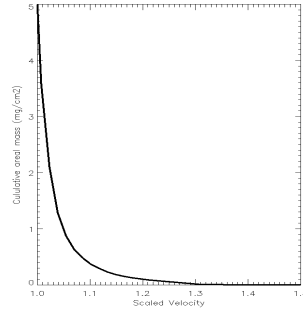
Figure 3.2: Areal mass distribution.

4 EXPERIMENT WITH A MACHINED SURFACE

Another approach to an experiment with a measured surface is to perform an experiment with a machined surface. One such experiment [3] consists of a HE driven aluminum flyer plate impacting onto a tin target. The surface of the tin target has a machined sinusoidal surface with a wavelength of 2.5mm and an amplitude of 0.2mm. This experiment was performed at the Los Alamos Neutron Science Center, proton radiography was used to diagnose the growth of the surface perturbations.

This experiment has been calculated on PETRA using the method described previously. **Fig 4.1** below shows how it is modeled.   The HE is represented by low density gas and the calculation starts with a mesh size of 20μm the Al impacting the Sn with an initial velocity of 4.5mm/μs. The middle four periods of the surface perturbation are modeled. **Fig 4.2** (from [3]) shows the result of the experiment. The middle frame on the bottom row is at a time of 28.9μs.

6mm	3.8mm		
Low-density gas (HE products)	Al 4.5 mm/μs	Sn	Low-density gas
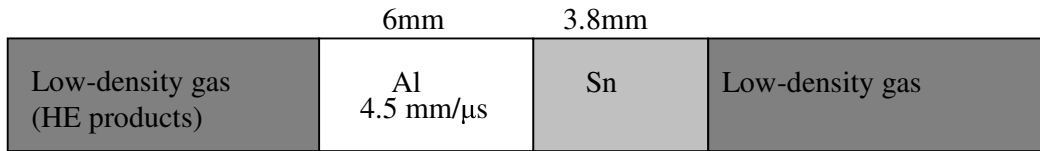
Figure 4.1: Diagram for the tin sinusoidal surface experiment calculation.
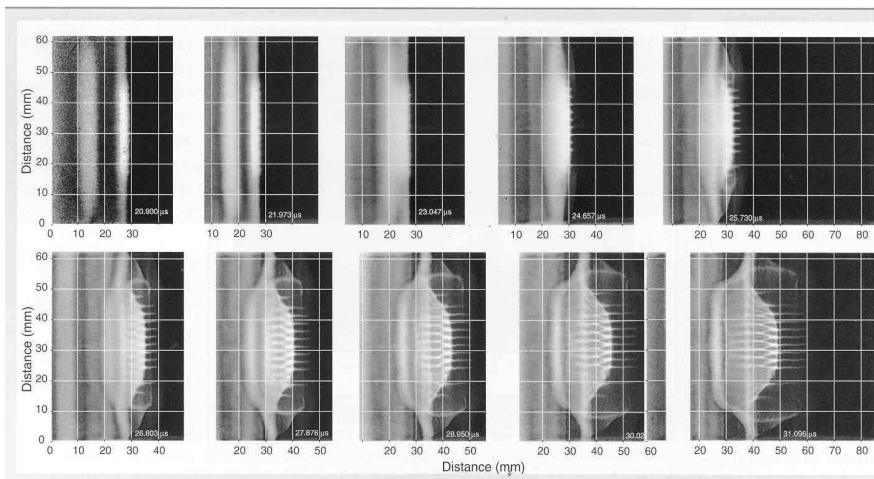
Figure 4.2: Experimental results (from Butler, 2005)

Fig 4.3 shows the calculation at a time of 28.9μs and it shows the main features of the experiment. There are long jets with smaller jets between them. The structure behind the jets is also represented.
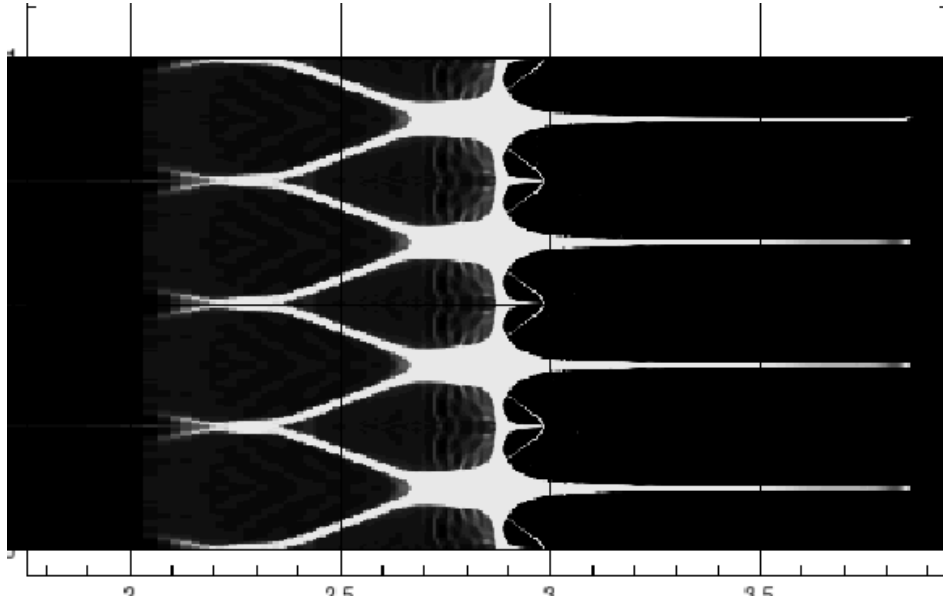
Figure 4.3: Calculational density plot at time of 28.9μs

6 CONCLUSIONS AND FURTHER WORK

We have shown that the method can be used to calculate ejecta. Plots of cumulative areal mass against velocity can be produced which can then be compared with experimental results. We need to identify experiments with a measured surface finish and model them using this method.

This method has also been used to calculate an experiment with a machined surface perturbation. In this case experimental results were available and the calculation agreed was in broad agreement with them. This gives us confidence that it is possible to use 2D simulations to model the production of ejecta.

Given that the calculations match the experiments then ejecta models to be improved using these computational results. These averaged models enable the properties and effects of ejecta to be calculated for problems that would be too computationally expensive using a fully resolved simulation.

REFERENCES

[1] Youngs, D.L. 1982 'Time-dependent multi-material flow with large fluid distortion.' In Numerical Methods for Fluid Dynamics, eds. K.W. Morton and M.J. Baines. Academic Press
[2] Asay, JR, et al, 1976,, 'Ejection of material from shocked surfaces', Appl. Phys. Lett. **29**, 284
[3] Buttler, W.T. 2005 'The Physics of Ejecta', Nuclear Weapons Journal, issue 1, LALP-05-067

e-mail: `jerome.griffond@cea.fr`

Linear interaction analysis for flow configurations involving mixtures of perfect gases

Jérôme GRIFFOND[1]

[1] *CEA/DAM Ile-de-France, BP 12, 91680 Bruyères-le-Châtel, FRANCE*

Abstract: Possible applications of the linear interaction analysis predicting the evolution of a small perturbation field interacting with a shock wave are presented for flow configurations involving mixtures of perfect gases.

1 LINEAR INTERACTION ANALYSIS

1.1 Principle

Linear interaction analysis is a theory aimed at predicting the evolution of a small perturbation field across a shock front. The pioneering work of Ribner [7] and Moore [6] relies on the identification by Kovasznay [5] of three wave families in uniform flow : shear, entropy and acoustic waves. The flow is assumed uniform upstream and downstream from the shock so that for small perturbations ($|g'/\bar{g}| \ll 1$), the fluctuation field can be written as a linear combination of each wave families in both region. The Rankine-Hugoniot jump relations written at the deformed shock front then allow to get the downstream amplitudes with respect to their upstream counterpart. Figure 1.1 sketches this procedure.
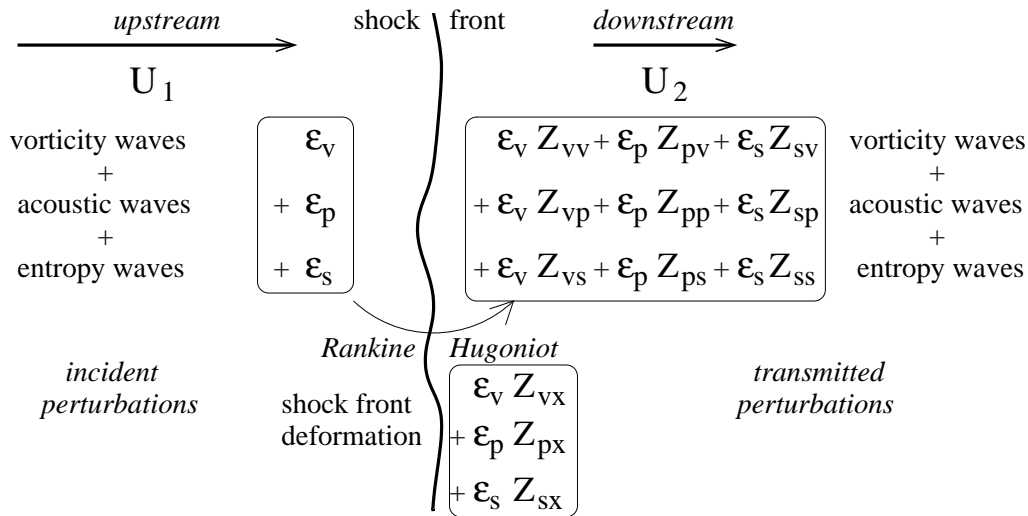
Fig. 1.1. Principle of the analysis of the interaction between a shock and a turbulent mixture. Picture of the interaction of a single non-acoustic wave with a shock front.

More precisely, Fourier decomposition is applied to the upstream field. Then, the downstream effect of single waves with different incidence angles α must be computed. Figure 1.2 shows a picture of such an interaction (for a non-acoustic wave with incidence angle α) and introduces the notations used in the following. Finally, backward Fourier transform can be used to get the downstream field in the physical space.

For our purpose of using LIA to treat mixtures, it must be kept in mind that all non-acoustic waves (the transmitted one and the created ones) are advected with material speed and remain completely correlated.
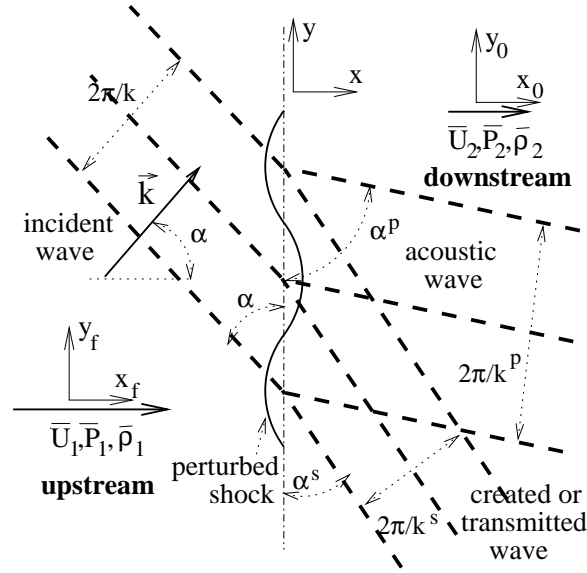
Fig. 1.2. Picture of the interaction of a single non-acoustic wave with a shock front.

1.2 Extension to mixtures of perfect gases

The extension to mixtures of perfect gases is more precisely described by the author in the reference [3]. The key points are:

- Mixture of 2 gases (a and b) described with a mass fraction c.

- Navier-Stokes equations + advection-diffusion equation for c.

- Non-constant mixture properties, molar weight $\mathcal{M}$ and constant volume specific heat C_v, given by

$$\mathcal{M} = \frac{\mathcal{M}_A \mathcal{M}_B}{c\mathcal{M}_B + (1-c)\mathcal{M}_A}, \; \gamma = \frac{cC_{v_A}\gamma_A + (1-c)C_{v_B}\gamma_B}{cC_{v_A} + (1-c)C_{v_B}}, \; C_v = cC_{v_A} + (1-c)C_{v_B}$$

A new wave family appears for concentration perturbation. The validity limitation for LIA is then given by

$$\frac{(\frac{1}{\mathcal{M}_A} - \frac{1}{\mathcal{M}_B})c'}{\frac{1}{\mathcal{M}_A}\bar{c} + \frac{1}{\mathcal{M}_B}(1-\bar{c})} \ll 1 \quad \text{and} \quad \frac{(C_{v_A} - C_{v_B})c'}{C_{v_A}\bar{c} + C_{v_B}(1-\bar{c})} \ll 1$$

The effect of the interaction of a single wave with the shock front can be described by transfer functions. The transfer functions $Z_c = (Z_{cv}, Z_{cs}, Z_{cp}, Z_{cx})^T$ relate the amplitudes of the downstream wave families to the upstream concentration perturbation. For each incidence angle α and shock Mach number M, Z_c is given by a 4×4 system:

$$AZ_c(\alpha) = B_{c_r}(\alpha)\frac{1/\mathcal{M}_A - 1/\mathcal{M}_B}{1/\bar{\mathcal{M}}} + B_{c_{C_v}}(\alpha)\frac{C_{v_A} - C_{v_B}}{\bar{C}_v}$$

The matrix A and vectors B_{c_r} and $B_{c_{C_v}}$ are given in [3], with a form similar to the one used by Fabre *et al.* [1] for single fluid applications.

2 APPLICATIONS

Different applications can be performed which can be divided into two classes

- interaction with upstream perturbations of finite spatial extension (for example with diffused bubbles of gases or a corrugated interface);

- interaction with an infinite upstream perturbation field with statistically homogeneous characteristics (for example a homogeneous turbulent field or a mixture without mean gradient).

2.1 Shock / spot interaction

The interaction of Mach 2 shock front with gaussian spots of concentration is shown in Fig. 2.3. In the case of the "molar weight" spot, both gases have equal specific heats C_v but different molar weights $\mathcal{M}$ and in the case of the "specific heat C_v" spot, both gases have equal molar weights $\mathcal{M}$ but different specific heats C_v. Figure 2.3 shows good agreement between numerical simulation with the TRICLADE code (top) and LIA (bottom).

In both cases, a primary vortex ring containing most of the circulation is created at the abscissa of spot center and a counter-rotating secondary vortex is created somewhat farther downstream. On the opposite, the radiated acoustic pressure waves are qualitatively different : the "molar weight" spot seems to radiate like a dipole and the "specific heat" spot like a monopole.

(a) "Molar weight" spot
(b) "Specific heat C_v" spot
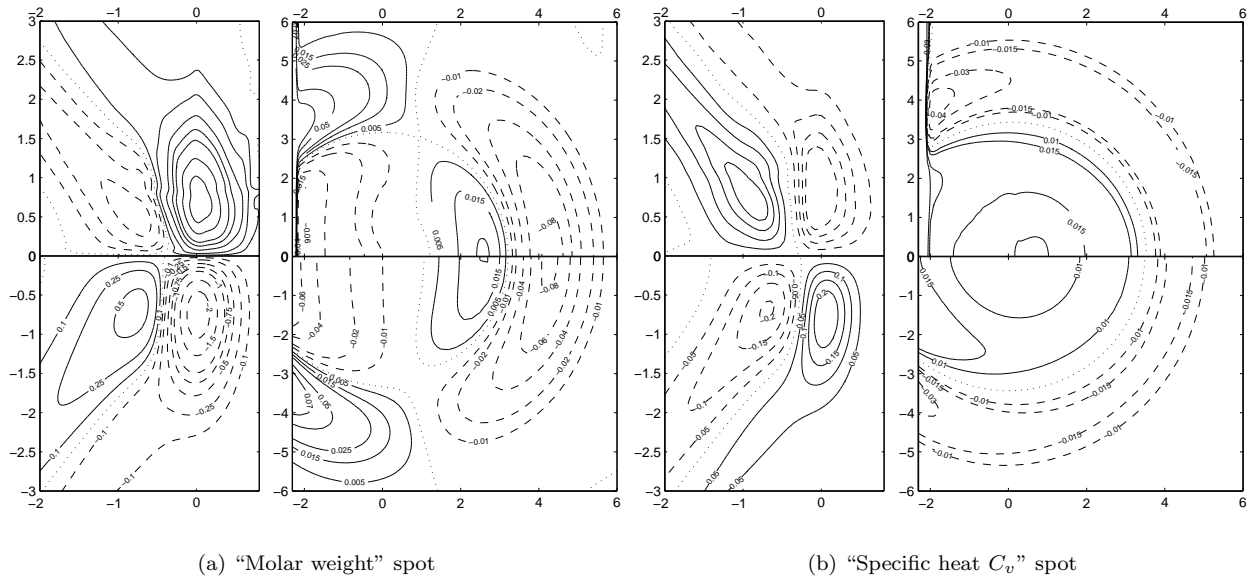
Fig. 2.3. Interaction of a Mach 2 shock wave with two kinds of spots. Vorticity field (on the left) and pressure field (on the right). Numerical simulation (top) and LIA results (bottom).

2.2 Richtmyer-Meshkov instability

LIA can be applied to Richtmyer-Meshkov instability by considering the a sinusoidal discontinuous concentration field (of corrugation amplitude a_0^- and regularized by a gaussian function giving a diffusion thickness δ).

LIA predicts the vorticity field *i.e.* the solenoidal part of the velocity field which is believed to be sufficient to predict the asymptotic linear growth rate of the interface (that is the growth rate after evacuation of the acoustic waves reverberating between the interface and the shock front but before nonlinear interactions can occur).

Figure 2.4-(a) shows a vorticity field computed from LIA which is larger close to the interface but has nonnegligible values on the side of the transmitted shock due to its relaxation after it has been corrugated by the interaction.
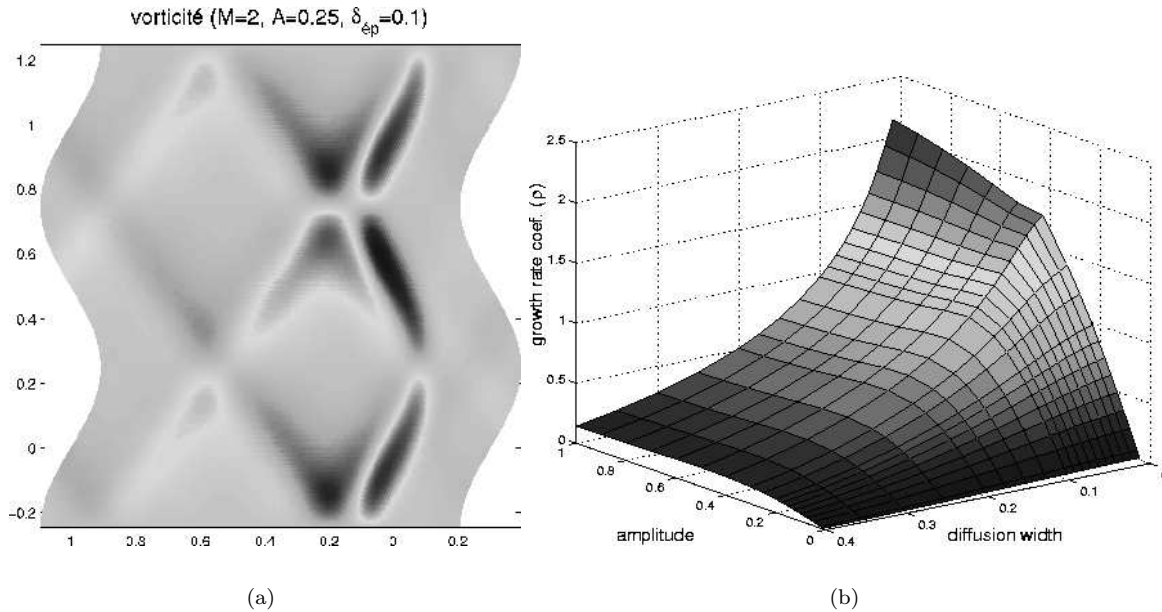
Fig. 2.4. (a)-Vorticity field for a "γ-perturbation"; (b)-growth rate for a ρ-perturbation as a function of the initial amplitude and diffusion thickness.

LIA is intersting in this case because its limitations are different from other theories: it is limited to gases with close properties ($\mathcal{M}_A \sim \mathcal{M}_B$, $\gamma_A \sim \gamma_B$: Atwood ≤ 0.1) but arbitrary corrugation amplitudes a_0^- and diffusion thickness δ can be treated. Figure 2.4-(b) shows the coefficient defining the growth rate as a function of both parameters.

More details can be found about this application in the reference [4].

2.3 Shock / turbulence-mixture interaction

The interaction of a Mach 2 shock wave with an inhomogenous mixture of gases at rest is shown in Fig. 2.5. The Reynolds average is denoted with $\bar{g}$ or $< g >$, the Reynolds fluctuation with g' and the Favre (density weighted) average with g''. The longitudinal Reynolds stress R_{ll} is $< v_l'^2 >$ and the transversal one R_{tt} is defined by the mean stress between both homogeneous directions.

In Fig. 2.5-(a), two regions can be seen downstream from the shock front : a near-field and a far field. The existence of the near field is due to evanescent pressure waves and transient correlation between acoustic and non-acoustic waves created in phase at the shock front.

Figure 2.5-(b) shows the evolution of the far field values of the Reynolds stresses and turbulent mass flux ($< v_l'' >$) with respect to the rms amplitude of the upstream density fluctuation.

Figure 2.5 shows good agreement between LIA and numerical simulation both in the near field and in the far field at weak amplitude, and good agreement in the far field over the whole range of density perturbations of the figure.

These results are of interest because they show that LIA can predict quantities involved in one-point turbulence models.
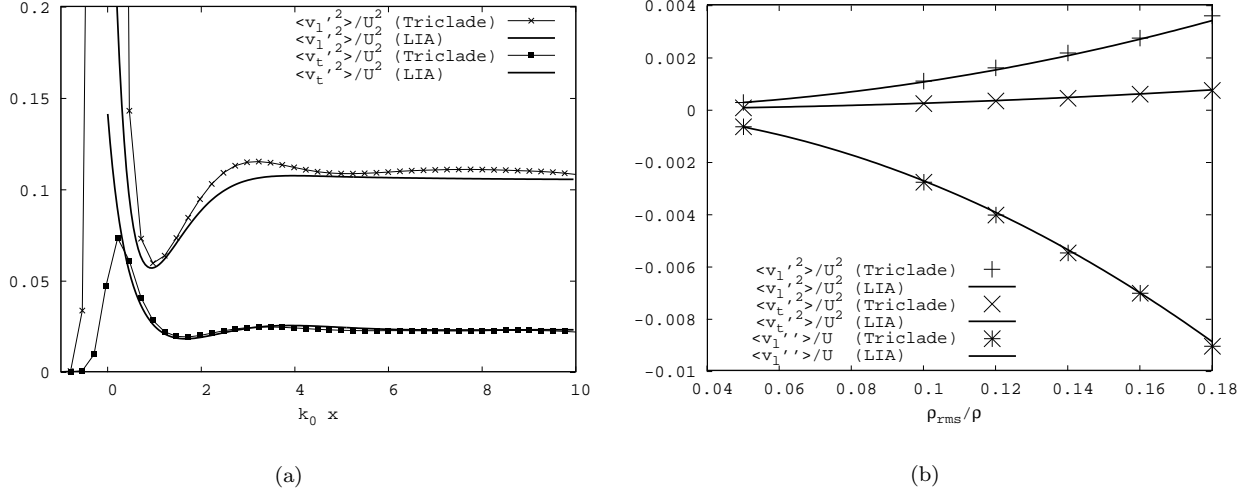
Fig. 2.5. (a)-Reynolds stresses versus the distance downstream from the shock front; (b) statistics in the far-field as a function of the amplitude of the density perturbation. Comparison: symbols- numerical simulation (TRICLADE), solid lines- LIA.

2.4 Turbulence modelling

For some compressible turbulence models, "jump relations" across the shock may be obtained.

For example, for the GSG model of O. Grgoire, D. Souffland and S. Gauthier [2] one can show

$$X_{downstream} = T(M).X_{upstream} \quad \text{with} \quad X = \left(\frac{R_{ll}}{\overline{U}^2}, \frac{\overline{u''}}{\overline{U}}, \frac{\overline{\rho'^2}}{\overline{\rho}^2}, \frac{R_{tt}}{\overline{U}^2} \right)$$

This result is valid only in the following limits :

- weak shock waves $(M - 1 \ll 1)$;

- weak turbulence $(X_i \ll 1)$,

the second one being the only assumption needed by LIA.

By varying the properties of the incident turbulent mixture, LIA allows to compute $X_{downstream}^{LIA}$ for a variety of upstream fields and compare it to $X_{downstream}$ predicted by the model. Then, it is possible to construct matrices from LIA giving $X_{downstream}^{LIA}$ as a function of $X_{ustream}^{LIA}$. Some further assumptions are needed to get a single matrix from LIA (instead of an infinity): particularly, we assume that the upstream wave amplitude is independent of the incidence angle α.

Finally, the matrix $T(M)$ for the turbulence model is not analytic but is obtained through an invertible transform from an analytic M_{GSG} matrix. The LIA transfer matrix can then be transformed into an M_{LIA} matrix which can be directly compared to the coefficients of the model.

The matrix M_{GSG} from the GSG model (in the weak shocks limit) for a Mach 1.2 shock wave is

$$M_{GSG} = \begin{pmatrix} 4 - \dfrac{4}{3}\gamma' & -2 + \dfrac{4}{3}\gamma^H & 0 & 0 \\ 1 - \gamma^u & 2 - \gamma^u & \gamma^u - 1 & 0 \\ 0 & 2 & 0 & 0 \\ \dfrac{2}{3}\gamma' & -\dfrac{2}{3}\gamma^H & 0 & 2 \end{pmatrix}$$

and the corresponding matrix M_{LIA} from LIA is

$$
M_{LIA} = \begin{pmatrix}
4 - \dfrac{4}{3}0.73 & -2 + \dfrac{4}{3}0.43 & 9 \times 10^{-3} & 0 \\
1 - 0.97 & 2 - 0.61 & 0.38 - 1 & 0 \\
10^{-3} & 2(1 - 0.98) & -1.7 \times 10^{-2} & 0 \\
\dfrac{2}{3}0.64 & -\dfrac{2}{3}0.39 & -3 \times 10^{-3} & 2
\end{pmatrix}
$$

This shows an approximate validation of the matrix structure and a possible identification of the constants. The most striking disagreements disappear with the improved model of Soulard and Souffland [8].

3 CONCLUSION

Extension of LIA to mixtures of perfect gases shows that two properties of the gases, the molar weight and the specific heat, produce their own effect on the field downstream of a shock wave.

LIA is limited to low Atwood numbers (for the molar weight and the specific heat) but a variety of configurations can be studied:

- interaction of a shock wave with a perturbation of finite longitudinal extension: application to the Richtmyer-Meshkov instability;

- interaction of a shock wave with an homogeneous turbulent mixture: application to turbulence modelling.

REFERENCES

[1] D. Fabre, L. Jacquin, and J. Sesterhenn. Linear interaction of a cylindrical entropy spot with a shock. *Phys. Fluids*, 13(8), 2001.

[2] O. Grégoire, D. Souffland, and S. Gauthier. A second-order turbulence model for gaseous mixtures induced by Richtmyer-Meshkov instability. *Journal of Turbulence*, 6(29), 2005.

[3] J. Griffond. Linear interaction analysis applied to a mixture of two perfect gases. *Phys. Fluids*, 17(8), 2005.

[4] J. Griffond. Linear interaction analysis for richtmyer-meshkov instability at low atwood numbers. *Physics of Fluids*, 18(5), 2006.

[5] L.S.G. Kovasznay. Turbulence in supersonic flow. *J. Aeronaut. Sci.*, 20:657–682, 1953.

[6] F.K. Moore. Unsteady oblique interaction of shock wave with a plane disturbance. Technical Report 1165, NACA, 1954.

[7] H. S. Ribner. Convection of a pattern of vorticity through a shock wave. Technical Report TN 2864, NACA, january 1953.

[8] O. Soulard and D. Souffland. Second-order turbulence model for predicting RMI driven turbulence: derivation of scalar flux and variance equations from a PDF approach. 10th IWPCTM, 2006.

ON IMPLICIT LARGE EDDY SIMULATION OF TURBULENT MIXING◆

Fernando F. GRINSTEIN, [1] Christer FUREBY, [2] Dimitris DRIKAKIS, [3] and David YOUNGS [4]

[1] Los Alamos National Laboratory, MS-B259, Los Alamos, NM 87545, USA; fgrinstein@lanl.gov
[2] The Swedish Defence Research Agency, FOI, SE-172 90, Stockholm, Sweden
[3] Aerospace Sciences Department, Cranfield University, Bedfordshire, MK43 0AL, UK
[4] AWE, Aldermaston, Reading, Berkshire, RG7 4PR, UK

Abstract: Conventional large eddy simulation (LES) and implicit LES (ILES) are tested in emulating the dynamics of transition to turbulence in the Taylor-Green vortex (TGV). A variety of subgrid scale (SGS) models and high-resolution numerical methods are implemented in the framework of both incompressible and compressible fluid flow equations. Comparisons of the evolution of characteristic TGV integral measures are made with direct numerical simulation (DNS) data. The computations demonstrate that the convective numerical diffusion effects in the ILES methods can consistently capture the physics of flow transition and turbulence decay without resorting to an explicit SGS model, while providing accurate prediction of established theoretical findings for the kinetic energy dissipation, energy spectra, enstrophy and kinetic energy decay. All approaches tested provided fairly robust computational frameworks.

INTRODUCTION

LES has emerged as the next generation simulation tool for handling complex engineering, geophysical, and astrophysical flows. In LES, large scale structures are resolved, the smaller flow features (presumably more isotropic and universal) are filtered out, and their effects are modeled (e.g., [1]). In ILES [2], the SGS physics is modeled implicitly through specific features of the non-oscillatory finite volume (NFV) algorithms on which the simulation model is based. ILES based on monotonicity preserving methods corresponds to the monotone [3] (or monotonically) integrated LES (MILES) approach [2,4-6].

ILES uses locally adaptive (dynamic) numerics to capture the inherent small-scale anisotropies of high-Re turbulent flows (e.g., worm vortices, shocks) and the viscosity independent dissipation characteristic of the inertial range cascade dynamics, ensuring nonlinear stability and positivity where physically needed. The use of conservative finite volume schemes in ILES provides the ability to capture the inherently discrete nature of laboratory observables (measurements always involve finite scales in space and time). By focusing on the inviscid inertial-range dynamics and on regularization of the under-resolved flow, ILES follows up very naturally on the historical precedent of using this kind of numerical schemes for shock capturing, based on requiring weak solutions and 2nd Law – entropy condition – satisfaction.

In this paper, we report a study of transition to turbulence in the TGV case [7] using conventional LES and ILES. Using the TGV, we aim to advance our understanding in relation to the properties of different high-resolution methods, especially with regards to their embedded nonlinear dissipation that acts as a dynamic SGS model in the ILES framework.

THE TAYLOR GREEN VORTEX

The TGV is a well-defined flow that has been used as prototype for vortex stretching, instability and production of small-scale eddies to examine the dynamics of transition to turbulence based on DNS [7]. As such, it can also be effectively used [9] as a convenient case to test the ability of explicit and implicit SGS modeling to allow the simulation of the basic empirical laws of turbulence (e.g., [8]), namely the existence of an inertial sub-range on the energy spectra for sufficiently high Re number and the finite (viscosity-independent) energy dissipation limit law.

We also revisit the ability of ILES based on locally monotonic NFV methods to reproduce established features of decaying turbulence. Positive evaluations of ILES in the turbulence decaying case have been previously reported [10-12]. On the other hand, poor ILES performances in this fundamental context using other popular shock capturing schemes [13] – e.g., MUSCL [14] with a minmod limiter – have been recently noted (Chapter 5 of [2]) as indicating that inherently more-diffusive features of certain numerical algorithms are not suitable for ILES.

The conventional wisdom is that numerical diffusion effects at the convection stage are undesirable and should be avoided. In the incompressible limit, the kinetic energy can be damped only by resolved (large scale) viscous effects, or by those introduced through explicit SGS models, and the kinetic energy should otherwise be conserved. In this context, integral measures in the TGV case have been used as reference to assess (presumably un-

---

wanted) numerical dissipation effects (e.g., [15]). This is in contrast with the ILES perspective here, where we demonstrate that the dominant SGS physics in the high-Re applications can be effectively emulated through use of convective numerical diffusion effects of certain algorithms.

The TGV configuration considered involves triple-periodic boundary conditions enforced on a cubical domain with box side length 2π cm using 64^3, 128^3, or 256^3 evenly spaced computational cells. The flow is initialized with the solenoidal velocity components, u=$U_o$sin(x)cos(y) cos(z), v =-$U_o$cos(x)sin(y)cos(z), w=0, and pressure given up to an additive constant P_o by a solution of the Poisson equation for the above given velocity field. We further select P_o=1.0 bar, mass density 1.178 kg/m^3, U_o=100 m/sec (corresponding to Mach number 0.28), and an ideal gas equation of state for air.

Using truncated series analysis techniques, an inviscid instability for the TGV system was identified with estimated onset at a non-dimensional time t*=ku_0t≈5.2 (the wavenumber k is unity here) [16]. These results were later questioned in [7], where it was pointed out that accuracy in the analytic continuation procedure used in [16] deteriorates too quickly to lead to a definite conclusion regarding their early prediction. Further estimates of t* based on DNS in the incompressible regime [7,17] reported a fairly consistent dissipation peak at t*~9, for Re=800, 1600, 3000, and 5000, where Re=u_o/(kv), and almost indistinguishable results for Re=3000 and 5000, suggesting that they may be close to a viscosity independent limit [8]. Although the existence of a finite-time singularity for finite Re, is not suggested by the cited observed (apparent) convergence, whether or not such singularity exists for the purely inviscid case remains unsettled and controversial (e.g., [15]).

By design, ILES emulates the dynamics of convectively dominated flows characterized by high (but finite) Re ultimately determined by the non-vanishing residual dissipation of the numerical algorithms. In the present work, ILES models nominally inviscid flow (when Euler based) or a linear viscous flow for which SGS effects are neglected (when Navier-Stokes based). ILES was tested on this TGV case using various algorithms, including FCT, Characteristics-Based Godunov (CBG), and Lagrange Remap (LR) methods. The FCT schemes considered involved the standard 4th order FCT algorithm [18], the 4th order three-dimensional (3D) monotone limiter FCT [19], and a 2nd order FCT using hybridization of first-order upwind and second order central differences (e.g., Chapter 4a of [2]). In the CBG scheme the fluxes are discretized at the cell faces using the values of the conservative variables along the characteristics (see [4,20] and Chapter 4a of [2] for details). Third-order variants of the fluxes can be obtained through flux limiting, based on the squares of second-order pressure or energy derivatives. The LR method by Youngs [21] (see Chapter 4c of [2] for further details), uses a non-dissipative finite difference method plus quadratic artificial viscosity in the Lagrange phase, and a 3rd order van Leer monotonic advection method [22], in the remap phase.

Figure 1 shows the TGV flow dynamics based on instantaneous visualizations from the present TGV simulations. The figure shows the initial TGV at t*=0, depicts the later transition to increasingly smaller-scale (but organized) vortices (top row), and then to the fully developed (disorganized) decaying worm-vortex dominated flow regime (bottom row), as characteristic of developed turbulence. Being representative of all methods discussed, the results shown here were generated with ILES using the 4th order 3D monotone FCT on the 128^3 grid. The snapshots are based on (ray tracing) volume renderings of λ_2 – the second-largest eigenvalue of the velocity gradient tensor [23], with hue and opacity maps chosen to be the same for all times, except for peak magnitude values (normalized by its value at t*=0), indicated at the lower right of each frame.

The evolution in time of the kinetic energy dissipation   , where   , denotes mean (volumetric average), is demonstrated in Figs. 2, including DNS results [17], and the 128^3 resolution ILES for FCT, CBG, and LR (Fig.2a); corresponding conventional LES results on the 128^3 grid are shown in Fig.2b, including the dynamic Smagorinsky subgrid viscosity model [24] (DSMG), the one-equation eddy-viscosity model [25] (OEEVM), and the Mixed Model [26] (MM), combining the OEEVM and the scale-similarity model. Fastest K decay at the dissipation peak (and peak mean enstrophy   in Fig.2c) corresponds to the onset of the inviscid TGV instability at t*≈9. The observed qualitative agreement between ILES, Mixed-Model LES, and previous high-Re DNS is quite good in predicting both the time and height of the dissipation peak for the large-Re limit; agreement is particularly good when comparing the (present) 128^3 results with the highest-Re DNS cases.

Actual values of Re characterizing the flow at the smallest resolved scales (e.g., Re$_\lambda$, based on the Taylor microscale) are not a priori available in LES or ILES. The predictions for the mean dissipation rate of the kinetic energy indicate that explicit and implicit subgrid viscosities act very similarly in predicting some sort of Re-independent regime asymptotically attained with increasing grid resolution. On the other hand, Re-dependent effects are clearly suggested associated with the lower predicted characteristic t* at dissipation peaks (as well as the wider peaks) with the coarser-grid simulations, a trend that is consistently exhibited by the DNS results as Re is lowered [7,8]. Moreover, we also find noticeable correlation between profiles of mean kinetic energy dissipation rates (Fig.2ab) and mean resolved enstrophy (Fig.2c), from various different ILES, LES, and grids, with actual peak values increasing with grid resolution. This observed correlation is qualitatively consistent with the expected relation (   ) for an incompressible fluid with Reynolds number Re. Thus, the relevance of using a characteristic Re that effectively increases with grid resolution is suggested by the analysis of our results.

Some obvious differences between the present ILES and conventional LES results compared to the DNS, such as the additional structure predicted near t*~5-6 in Figs. 2ab by some of the methods and other details, are attributed to specific aspects of the implicit SGS model provided by the various limiting algorithms, by the explicit

SGS models, and/or their actual implementation. For example, we speculate that the double-peaked structure of the dissipation near t*~9 predicted by the LR method is likely due to the dispersive properties of this scheme compared to the less dispersive FCT and CBG schemes. On the other hand the LR method is also the least dissipative of the compared methods, at least at early stages of the flow development; the peak enstrophy with LR is significantly higher, and up to t*~20 the decay rate of K* is slower compared to the other schemes.

Compensated three-dimensional velocity spectra for the 128^3 and 256^3 resolutions are shown in Fig. 2d. Higher wave-number modes are populated in time, through the virtually inviscid cascading process (Fig.1). As the size of the smallest scale structures approaches the cutoff resolution, kinetic energy is removed at the grid level through numerical dissipation. The velocity spectra consistently emulates a (–5/3) power law inertial subrange and self-similar decay, and the length of the simulated inertial subrange becomes longer with increasing resolution (and presumably larger associated effective Re). As the Kolmogorov spectra becomes well established in time it is associated at the smallest resolved scale with the more disorganized worm-vortex dominated flow regime (bottom row of Fig. 1) – as characteristic of developed turbulence (e.g., [27]).

The depicted self-similar decay in Fig. 2d suggests that the removal of kinetic energy by numerical dissipation may occur at a physically suitable rate. The decay rates are examined with more detail based on selected representative 128^3 data in Figs. 3a, where for reference, we have indicated slopes corresponding to power laws with exponents -1.2 and -2 through the mean value of K at the observed dissipation peaks, Fig.3a. All compared methods show decay rates consistent with each other and with the -1.2 law for times immediately after that of the dissipation peak at t*≈9, and with the -2 exponent for much later times. The power law – with -1.2 exponent, is the one generally accepted as characteristic of decaying turbulence (e.g., [28]). Figure 3b uses the FCT-based ILES data to illustrate the consistency of the latter power-law behavior vs. grid resolution. The *later* -2 exponent can be understood in terms of the expected saturation of the energy containing length scales reflecting that eddies larger than the simulation box side length cannot exist [29]. The results suggest that the latter power law changes are somewhat sensitive to the specifics of the flux-limiting numerics (e.g., nature of low and high order schemes and their interaction through the limiter, presence of Lagrange step in the algorithm) and explicit SGS models, as well as their actual implementations. This is an area which clearly warrants further studies.

CONCLUDING REMARKS

We have examined the behavior of classical LES methods and ILES based on different high-resolution monotonic schemes in the simulation of the TGV. The results show that numerical schemes such as tested here can provide a fairly robust LES computational framework to capture the physics of flow transition and turbulence decay without resorting to an explicit SGS model and using relatively coarse grids. The results show that the mean kinetic energy dissipation rate and enstrophy specifics depend somewhat on the detailed aspects of the SGS model provided implicitly by the various high resolution algorithms (or explicitly by the conventional LES methods), and by their actual implementations. The performance of LES and ILES approaches appears to be equally good for this application, and there is no discriminating characteristic favoring one or another. However, looking forward towards practical complex flows and regimes, the ability of ILES to offer a simpler computational environment should be clearly emphasized. ILES performance enhancements are possible through improved design of the SGS physics capturing capabilities. Thus, further investigations seeking a better understanding of the specific dissipation and dispersion properties of the different high-resolution schemes, and suitable testing and validation frameworks to establish a physical basis for the various possible choices, are clearly warranted in this context.

Most flows of practical interest feature coupled processes that introduce additional physical length sales and time scales to those of convection. These may occur strictly in the context of hydrodynamics, e.g., compressibility, rotation, stratification. Alternatively, these may include additional regimes of physics where the flow features are not necessarily dominated by large scale convection, such as scalar mixing, combustion, radiation transport, plasma physics and magneto-hydrodynamics. The presence of new physical scales will likely require adding specialized explicit SGS models to ILES, *as with any other conventional LES approach*, and determining when they are actually necessary is an important question in its own right. In particular, ILES formal and test studies need to be extended to establish how ILES methods treat turbulent mass-density and species-concentration fluctuations, the role of which is crucial for Kelvin-Helmholtz, Rayleigh-Taylor, and Ritchmyer-Meshkov, driven mix instabilities, and increasingly important for the higher Mach number regimes.

REFERENCES

[1] Sagaut P. 2005 *Large Eddy Simulation for Incompressible Flows*, 3rd Edition, Springer.
[2] Grinstein, F.F, Margolin, L.G., Rider 2007, W.J., Editors, *Implicit Large Eddy Simulation: Computing Turbulent Fluid Dynamics*, Cambridge University Press.
[3] Boris, JP, 1990, On large eddy simulation using subgrid turbulence models, in *Whither Turbulence? Turbulence at the Crossroads*, JL Lumley, ed., pp. 344-353, Springer.
[4] Drikakis, D.; 2003, *Progress in Aerospace Sciences*, **39**, 405-424.
[5] Grinstein, F.F. and Fureby, C. 2004, *Computing in Science and Engineering*, **6,** 37-49.
[6] Margolin, L.G., Rider, W.G. & Grinstein, F.F. 2006, *Journal of Turbulence*, **7**, 015.

[7] Brachet, M.E., Meiron, D.I., Orszag, S.A., et al. 1983, *J. Fluid Mech.* **130**, 411.

[8] Frisch, U. 1995 *Turbulence*. Cambridge University Press, Chapter 5.

[9] Drikakis, D., Fureby, C., Grinstein, F.F. & Youngs, D. 2007, Simulation of Transition and Turbulence Decay in the Taylor-Green Vortex, *Journal of Turbulence*, in press.

[10] Porter, D.H., Pouquet, A. & Woodward, P.R. 1994, *Phys. Fluids*, **6**, 2133.

[11] Fureby C. & Grinstein F.F., 2002, *J. Comput. Phys.*, **181**, p 68.

[12] Domaradzki, J.A., Xiao, Z. & Smolarkiewicz, P.K. 2003, *Phys. Fluids*, **15**, 3890-93.

[13] Garnier, E., Mossi, M., Sagaut, et al. 1999, *J. Comput. Phys.* **153**, 273-311.

[14] Van Leer, B. 1979, *J. Comput. Phys.* **32**, 101.

[15] Shu, C-W., Don, W-S., Gottlieb, et al. 2005, *J. Scientific Comput.*, **24**, pp. 1-27.

[16] Morf, R.H., Orszag, S.A. & Frisch, U. 1980, *Phys. Rev.* **44**, 572.

[17] Brachet, M.E. 1991 *Fluid Dynamics Research* **8**, 1.

[18] Boris, J.P. & Book, D.L. 1973, *J. Comput. Phys.* **11**, 38.

[19] DeVore, C. R. 1998, An Improved Limiter for Multidimensional Flux-Corrected Transport, NRL Report NRL-MR-6440-98-8330, Washington DC.

[20] Drikakis, D. & Rider, W. 2004, *High-Resolution Methods for Incompressible and Low-Speed Flows,* Springer.

[21] Youngs, D.L. 1991, *Phys. Fluids* **A3**, 1312-1320.

[22] van Leer, B. 1977, *J. Comput. Phys.* **23**, 276-299.

[23] Jeong, J. & Hussain, F. 1995, J. Fluid Mech. 285, 69.

[24] Germano, M., Piomelli, U., Moin, P. & Cabot, W.H. 1994, *Phys. Fluids* **A3**, 1760.

[25] Schumann, U. 1975, *J. Comput. Phys.* **18**, 376.

[26] Bardina, J., Ferziger, J.H. & Reynolds, W.C. 1980 Improved Subgrid Scale Models for Large Eddy Simulations. AIAA Paper No. 80-1357.

[27] Jimenez, J., Wray, A., Saffman, P. & Rogallo, R. 1993 *J. Fluid Mech.* **255**, 65.

[28] Lesieur, M. & Ossia, S. 2000, *Journal of Turbulence*, **1**, 007, pp 1-25.

[29] Skrbek, L. & Stalp, S.R. 2000, *Phys. Fluids* **12**, 1997.
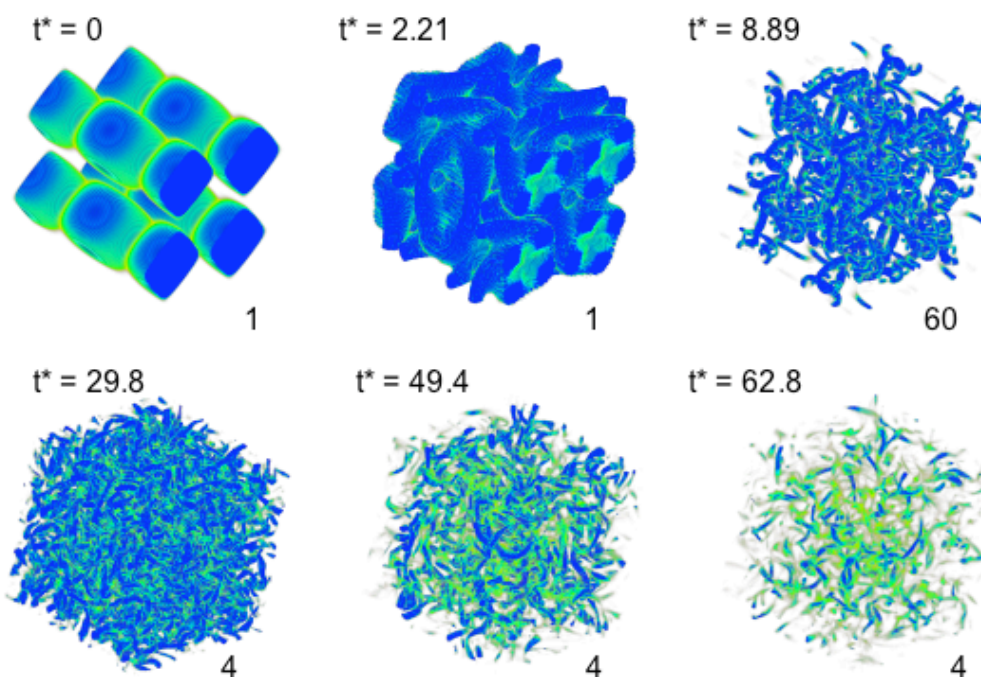
Figure 1. Flow visualizations of the Taylor Green Vortex flow using volume renderings of l_2 – the second-largest eigenvalue of the velocity gradient tensor. The results shown here, being representative of al methods discussed, are from the 4th order 3D monotone FCT on the 128^3 grid.
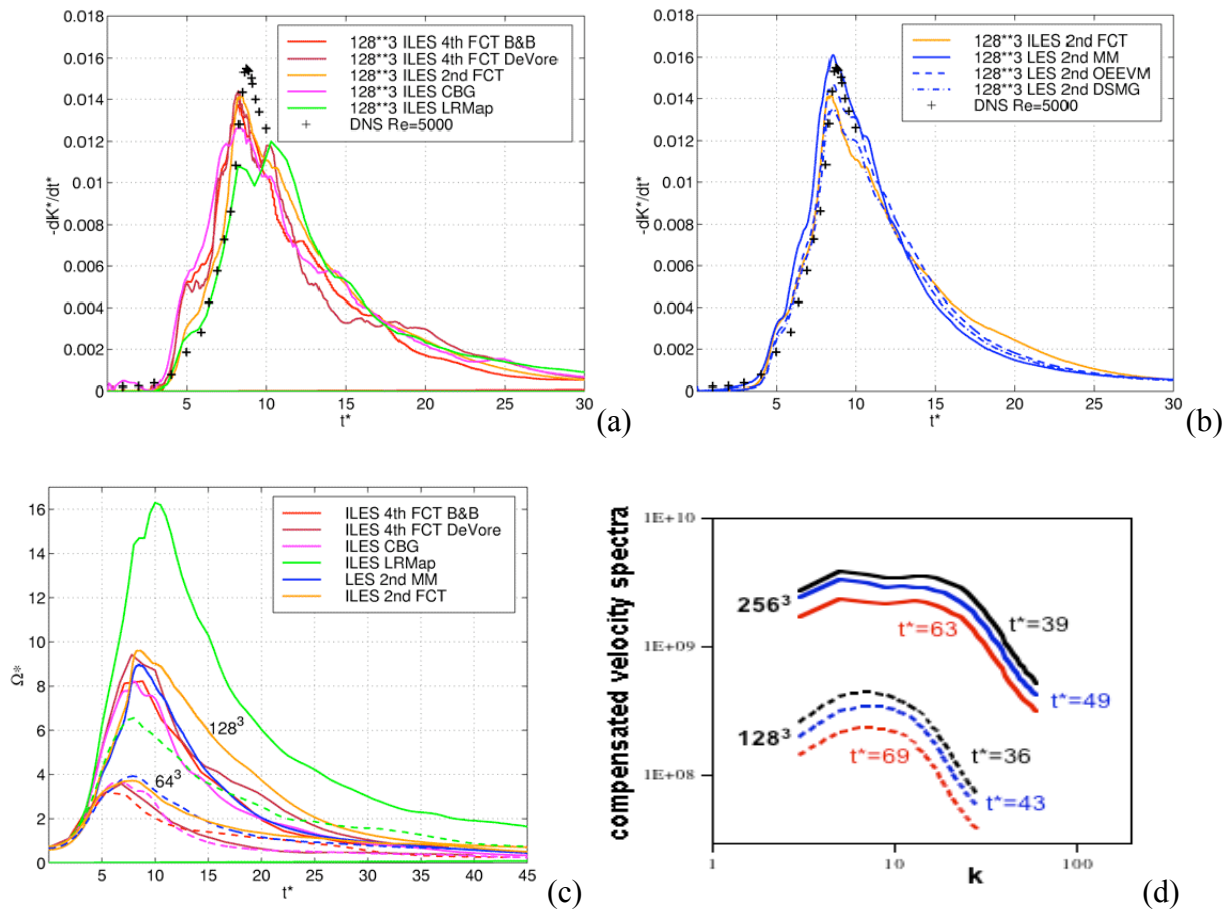
Figure 2. Mean kinetic energy dissipation rate –dK/dt from (a) 128^3 ILES and MM LES simulations, and (b) 128^3 conventional LES vs. high-Re DNS [17]; (c) evolution of the mean enstrophy on 64^3 and 128^3 ILES and LES. (d) ILES compensated three-dimensional velocity spectra $k^{+5/3} E(k)$ for 4th order DeVore FCT.
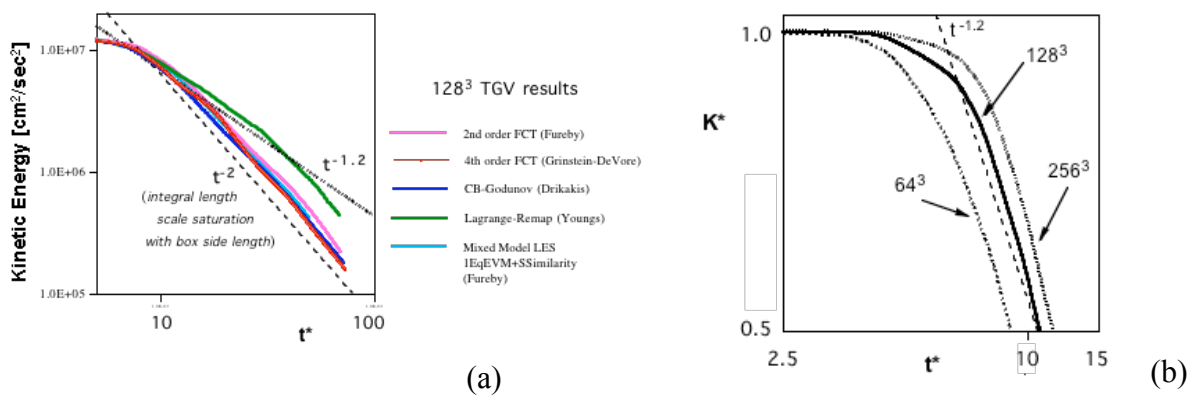
Figure 3. Volumetrically averaged kinetic energy decay in time. (a) comparative power law behaviors vs. various ILES methods and the MM LES; (b) kinetic energy decay vs. grid resolution, based on 4th order FCT simulation data; scale in both axis is logarithmic.

e-mail: `ghazak@netvision.net.il`

Correlations in the mixed state induced by the Rayleigh-Taylor instability

G. Hazak

Physics Department, Nuclear Research Centre, Negev P.O. Box 9001 Beer-Sheva, 8405, Israel.

Abstract: An expression is derived for the pressure as a functional of the velocity and density fields for incompressible fluids with large spatial variations in the density. The expression indicates that the average pressure induced by an eddy immersed in a "sea" of spatial density fluctuations decays exponentially, with the density correlation length as the decay length. The exponential fall off is in agreement with results found in the analysis of experimental and direct numerical simulation results of the mixed state induced by the Rayleigh-Taylor instability (G. Hazak, Y. Elbaz, J. H. Gardner , A. L. Velikovich, A.J. Schmitt and S. T. Zalesak, Phy. Rev. E 73, 047303 (2006)). This result is in contrast with the constant-density case where the pressure of an eddy, and consequently also correlations fall off as some power of the distance (G. K. Batchelor and I Proudman Phil. Trans. Roy. Soc. A, **248**, 369 (1956)).

1 INTRODUCTION

In the theory of hydrodynamic turbulence, in incompressible fluids, it is assumed that the system is initiated with a uniform density. Incompressibility keeps the density uniform (although the turbulent velocity field may be inhomogeneous, even on the average). The assumption of uniformity of mass density has far reaching consequences. For example, with homogeneous mass density, in the limit of vanishing molecular viscosity, vortex stretching is the only source for vorticity in three dimensional (3D) systems , and nonexistent in two dimensional (2D) flows. i.e. vorticity is conserved in 2D. This is the origin of the difference between the energy spectra of 2D and 3D turbulence[1]. Density variation, introduces an additional source (by interaction with the pressure gradients) and vorticity is not conserved even in 2D. Clearly in cases , where density variation governs the dynamics (e.g. turbulence and mixing, induced by Rayleigh-Taylor instability(RTI)[2],[3],[4]) some of the intuition and theoretical tools of turbulence with uniform density are not applicable.

In the case of uniform density, one may express the pressure as a functional of the velocity field[5]. In turbulence theory this is used to rewrite the velocity-pressure-gradient correlation tensor in terms of velocity and velocity gradients correlations. This step enables a systematic approach to the closure problem. (see for example, [6],[1],[7]). Surprisingly, no such expression for the pressure exists in the literature for the case of incompressible fluids with spatial variations in the density.

In the present work a formula is derived, for the pressure in terms of the density and velocity fields, for incompressible fluids with variable-density. This formula is used for the derivation of an expression for the average pressure induced by a "test eddy" immersed in a "sea" of density fluctuations. The result indicates that the pressure (and therefore also correlations) decays exponentially as a function of the distance from the eddy's position, with the density correlation length as the decay length. The exponential fall off is in agreement with results found in the analysis of experimental and direct numerical simulation results of the mixed state induced by the Rayleigh-Taylor instability[8]. This result is in contrast with the constant-density case where the pressure of an eddy, and consequently also correlations fall off as some power of the distance [5,9].

The basic set of Navier-Stokes equations with the boundary conditions which will be used in the present work will be described in section (2) . Section (3) will be devoted to the pressure formula and some of its consequences.. Summary and discussion will be given in section (4).

2 THE BASIC EQUATIONS

Consider a system of an incompressible fluid which is immersed in a gravitational field. The system is initiated in an hydrostatic equilibrium which, at $t = 0$, is perturbed at the $z = 0$ plane. (For simplicity the treatment is in planar geometry). Assume that the pressure, $p(\vec{r}, t)$ velocity $\vec{u}(\vec{r}, t)$ and density $\rho(\vec{r}, t)$ are periodic in the x, y coordinates and that at large enough distance from the $z = 0$ plane hydrostatic equilibrium is maintained at all relevant times with a constant pressure gradient and density. Formally this requirement reads as $\rho(x, y, z \to \infty, t) \to \rho^{(1)}$,
$\rho(x, y, z \to -\infty, t) \to \rho^{(2)}$ and

$$\left[\tfrac{\partial}{\partial \vec{r}} p \right]_{z \to \infty} \to -\rho^{(1)} g \hat{z} \tag{2.1}$$

$$\left[\tfrac{\partial}{\partial \vec{r}} p \right]_{z \to -\infty} \to -\rho^{(2)} g \hat{z} \tag{2.2}$$

The Navier-Stokes equation and the incompressibility condition for this system are:

$$\rho(\vec{r}, t)\left(\tfrac{\partial}{\partial t} \vec{u} + \vec{u} \cdot \tfrac{\partial}{\partial \vec{r}} \vec{u} + g \hat{z} - \nu \tfrac{\partial}{\partial \vec{r}} \cdot \tfrac{\partial}{\partial \vec{r}} \vec{u} \right) = -\tfrac{\partial}{\partial \vec{r}} p \tag{2.3}$$

and

$$\tfrac{\partial}{\partial \vec{r}} \cdot \vec{u} = 0 \tag{2.4}$$

Where g is the gravitational acceleration and $\rho \nu$ is the molecular viscosity.

3 A FORMULA, FOR THE PRESSURE IN TERMS OF THE DENSITY AND VELOCITY FIELDS, FOR IN-COMPRESSIBLE FLUIDS WITH VARIABLE-DENSITY.

Operating with $\tfrac{\partial}{\partial \vec{r}} \cdot$ on the Navier-Stokes equation , one gets an equation for $\tfrac{\partial}{\partial \vec{r}} \cdot \vec{u}$:

$$\rho\left(\tfrac{\partial}{\partial t} + g \hat{z} - \nu \tfrac{\partial}{\partial \vec{r}} \cdot \tfrac{\partial}{\partial \vec{r}} \right) \tfrac{\partial}{\partial \vec{r}} \cdot \vec{u} = -\rho \tfrac{\partial}{\partial \vec{r}} \cdot \tfrac{1}{\rho} \tfrac{\partial}{\partial \vec{r}} p - \rho \tfrac{\partial}{\partial \vec{r}} \cdot \left(\vec{u} \cdot \tfrac{\partial}{\partial \vec{r}} \vec{u} \right) \tag{3.1}$$

Initiating the system with a divergenceless velocity field, $\tfrac{\partial}{\partial \vec{r}} \cdot \vec{u}(\vec{r}, t = 0) = 0$, the solution of equation (3.1) will be $\tfrac{\partial}{\partial \vec{r}} \cdot \vec{u}(\vec{r}, t) = 0$ at all times *if and only if the right hand side vanishes* [10], i.e. *if and only if* the pressure obeys the equation:

$$\rho \tfrac{\partial}{\partial \vec{r}} \cdot \tfrac{1}{\rho} \tfrac{\partial}{\partial \vec{r}} p = -\rho \tfrac{\partial}{\partial \vec{r}} \cdot \left(\vec{u} \cdot \tfrac{\partial}{\partial \vec{r}} \vec{u} \right) \tag{3.2}$$

For a given velocity field and density distribution, equation (3.2) , together with the requirement that p is periodical in the x, y plane and the boundary conditions (2.1), (2.2) uniquely determine the pressure gradient.

In the case of constant-density fluid where $\rho^{(1)} = \rho^{(2)}$ and $\tfrac{\partial}{\partial \vec{r}} \rho = 0$, equation (3.2) is just the Poisson's equation and the pressure formula is well known [5],[10],[1]:

$$\tfrac{1}{\rho} \tfrac{\partial}{\partial \vec{r}} p = \tfrac{1}{\rho} \int_V \left(\tfrac{\partial}{\partial \vec{r}} \tfrac{1}{4\pi} \tfrac{1}{|\vec{r} - \vec{r}'|} \right) \rho\left(\tfrac{\partial}{\partial \vec{r}'} \cdot \left(\vec{u} \cdot \tfrac{\partial}{\partial \vec{r}'} \vec{u} \right) \right) d^3 \vec{r}' - g \hat{z} \tag{3.3}$$

The solution for the variable density case is:

$$\tfrac{1}{\rho(\vec{r})} \tfrac{\partial}{\partial \vec{r}} p = \int_V \tfrac{1}{\rho(\vec{r})} \tfrac{\partial}{\partial \vec{r}} G(\vec{r}, \vec{r}') \rho(\vec{r}') \tfrac{\partial}{\partial \vec{r}'} \cdot \left(\vec{u} \cdot \tfrac{\partial}{\partial \vec{r}'} \vec{u} \right) d^3 \vec{r}$$
$$+ \int_V \tfrac{1}{\rho(\vec{r})} \tfrac{\partial}{\partial \vec{r}} G(\vec{r}, \vec{r}') \vec{A}(\vec{r}') d^3 \vec{r}' \cdot \left(\tfrac{1}{2}\left(\rho^{(1)} + \rho^{(2)} \right) g \hat{z} \right) - \tfrac{1}{2} \tfrac{1}{\rho(\vec{r})} \left(\rho^{(1)} + \rho^{(2)} \right) g \hat{z} \tag{3.4}$$

where, $G(\vec{r}, \vec{r}')$ is defined by :

$$G(\vec{r}, \vec{r}') = \int \tfrac{1}{4\pi} \tfrac{1}{|\vec{r} - \vec{r}''|} \left\{ \delta^3(\vec{r}'' - \vec{r}') - Q(\vec{r}'', \vec{r}') + \int Q(\vec{r}'', \vec{r}''') Q(\vec{r}''', \vec{r}') d^3\vec{r}''' - .. + ... \right\} d^3\vec{r}'' \tag{3.5}$$

$\delta^3(\vec{r})$ is the Dirac delta function, also

$$Q(\vec{r}'', \vec{r}') \equiv \vec{A}(\vec{r}'') \cdot \left(\tfrac{1}{4\pi} \tfrac{\partial}{\partial \vec{r}''} \tfrac{1}{|\vec{r}'' - \vec{r}'|} \right) \tag{3.6}$$

and

$$\vec{A} \equiv \tfrac{1}{\rho(\vec{r})} \tfrac{\partial}{\partial \vec{r}} \rho(\vec{r}) \tag{3.7}$$

The validity of solution (3.4) may be checked directly, by verifying that G is the solution of the equation:

$$\rho \frac{\partial}{\partial \vec{r}} \cdot \frac{1}{\rho} \frac{\partial}{\partial \vec{r}} G(\vec{r}, \vec{r}^{'}) = -\delta^3(\vec{r} - \vec{r}^{'}) \tag{3.8}$$

and that the divergence of relation (3.4) yields equation (3.2). To check that this solution also obeys the boundary conditions (2.1),(2.2), notice that as $z \to \pm\infty$ the integral part of it tends to $\mp \frac{1}{2} \frac{1}{\rho(\vec{r})}\left(\rho^{(1)} - \rho^{(2)}\right)$.

The effect of density variations on the pressure manifests itself mainly in the replacement of the Green's function of Poisson's equation; $G_0(\vec{r}, \vec{r}^{'}) = \frac{1}{4\pi} \frac{1}{|\vec{r} - \vec{r}^{'}|}$ in equation (3.3) by $G(\vec{r}, \vec{r}^{'})$.

Note that unlike G_0, which is independent of fluid variables, G depends on the density (but not on the velocity field).

In treating turbulence, one considers an ensemble of systems which differ from one another in the microscopic details but are macroscopically indistinguishable, all obeying the Navier-Stokes equation. In the following, angular brackets will denote average over the ensemble and δ denotes the fluctuating part, e.g. $\delta\tilde{u} \equiv \vec{u} - \langle\vec{u}\rangle$. The pressure formula for constant density (equation (3.3)) tells us that the ensemble average $\langle(\delta\tilde{u}(\vec{r}_1,t)) p(\vec{r}_1,t)\rangle$ involves the *two-point* correlation of $\left\langle(\delta\tilde{u}(\vec{r}_1,t))\left(\frac{\partial}{\partial \vec{r}_2} \cdot \left(\vec{u}(\vec{r}_2,t) \cdot \frac{\partial}{\partial \vec{r}_2} \vec{u}(\vec{r}_2,t)\right)\right)\right\rangle$. This observation is the starting point for all systematic modeling efforts of turbulence in homogeneous and inhomogeneous incompressible fluids (see for example section 5.1 in [5], section 2.1 in [11], section 2.5 and 11 in [10] and sections 1.7 and 6.3.4 in [1], chapter 6 in [7] and [12]). In contrast, the pressure formula (3.4) (with definition (3.5)) for variable-density tells us that the correlation $\langle(\delta\tilde{u}(\vec{r}_1,t)) p(\vec{r}_1,t)\rangle$ will involve also $3, 4,$ and infinite number of points correlations, the $n-$ point correlation involves two points attached to $\vec{u}(\vec{r}_1,t)$ and $\left(\frac{\partial}{\partial \vec{r}_2} \cdot \left(\vec{u}(\vec{r}_2,t) \cdot \frac{\partial}{\partial \vec{r}_2} \vec{u}(\vec{r}_2,t)\right)\right)$ and $n-2$ points attached to $\left(\frac{1}{\rho(\vec{r}_3)} \frac{\partial}{\partial \vec{r}_3} \rho(\vec{r}_3)\right)...\left(\frac{1}{\rho(\vec{r}_n)} \frac{\partial}{\partial \vec{r}_n} \rho(\vec{r}_n)\right)$. To further analyze the behavior of the pressure, one may rewrite equation (3.2) in the form:

$$\frac{\partial}{\partial \vec{r}} \cdot \frac{\partial}{\partial \vec{r}} p - \left(\frac{1}{\rho} \frac{\partial}{\partial \vec{r}} \rho\right) \cdot \frac{\partial}{\partial \vec{r}} p = -\rho \frac{\partial}{\partial \vec{r}} \cdot \left(\vec{u} \cdot \frac{\partial}{\partial \vec{r}} \vec{u}\right) \tag{3.9}$$

, $G(\vec{r}, \vec{r}^{'})$ (which is the Green's function of this equation) describes a pressure wave induced at $\vec{r}$ by an eddy (A localized distribution of $\rho \frac{\partial}{\partial \vec{r}} \cdot \left(\vec{u} \cdot \frac{\partial}{\partial \vec{r}} \vec{u}\right)$) at $\vec{r}^{'}$. The term $\left(\frac{1}{\rho} \frac{\partial}{\partial \vec{r}} \rho\right) \cdot \frac{\partial}{\partial \vec{r}} p$, on the left hand side, represents a secondary source due to interaction of the wave with a density variation. The total pressure is represented by the "Dressed" Green's function $G(\vec{r}, \vec{r}^{'})$ as the sum of infinite number of contributions. The first term corresponds to the "direct" wave described by the "bare" Green's function $G_0 = \frac{1}{4\pi} \frac{1}{|\vec{r} - \vec{r}^{'}|}$. The second contribution is the correction due secondary source generated by the interaction of the direct wave with a density fluctuation at $\vec{r}^{''}$. In general the $n+1$ order correction is due to the source generated by the interaction of the n order wave with the density fluctuations. Consider an isolated eddy immersed in a statistically uniform "sea" of density fluctuations. (no gravitational field). The ensemble averaged pressure due to this source is, $\langle G(\vec{r}, \vec{r}^{'})\rangle$. It is plausible that odd order terms are washed out in the averaging process and we are left with:

$$\langle G(\vec{r}, \vec{r}^{'})\rangle = \int \frac{1}{4\pi} \frac{1}{|\vec{r} - \vec{r}^{''}|} \left\{ \delta^3(\vec{r}^{''} - \vec{r}^{'}) + \right.$$

$$\int \left\langle \frac{1}{\rho(\vec{r}^{''})} \frac{\partial}{\partial \vec{r}^{''}} \rho(\vec{r}^{''}) \cdot \left(\frac{1}{4\pi} \frac{\partial}{\partial \vec{r}^{''}} \frac{1}{|\vec{r}^{''} - \vec{r}^{'''}|}\right) \frac{1}{\rho(\vec{r}^{'''})} \frac{\partial}{\partial \vec{r}^{'''}} \rho(\vec{r}^{'''}) \right\rangle \cdot \left(\frac{1}{4\pi} \frac{\partial}{\partial \vec{r}^{'''}} \frac{1}{|\vec{r}^{'''} - \vec{r}^{'}|}\right) d^3\vec{r}^{'''} + .. + ... \left.\right\} d^3\vec{r}^{''} \tag{3.10}$$

.

The term

$$\vec{w} \equiv \left\langle \frac{1}{\rho(\vec{r}^{''})} \frac{\partial}{\partial \vec{r}^{''}} \rho(\vec{r}^{''}) \cdot \left(\frac{1}{4\pi} \frac{\partial}{\partial \vec{r}^{''}} \frac{1}{|\vec{r}^{''} - \vec{r}^{'''}|}\right) \frac{1}{\rho(\vec{r}^{'''})} \frac{\partial}{\partial \vec{r}^{'''}} \rho(\vec{r}^{'''}) \right\rangle \tag{3.11}$$

is a function of $\vec{r} - \vec{r}'$. To further examine the pressure wave described by equation (3.4) I suggest the anszatz $\vec{w}(r - \vec{r}') \Box \frac{A^2}{\lambda_T^2} \int i\vec{k} \frac{1}{k^2} e^{-i\vec{k}\cdot(r - \vec{r}')} d^3\vec{k}$, where λ_T is the correlation length of the density fluctuations, and $A \equiv \frac{\rho^{(1)} - \rho^{(2)}}{\rho^{(1)} + \rho^{(2)}}$ is the Atwood number. With this anszatz one gets:

$$
\begin{aligned}
\left\langle G(\vec{r} - \vec{r}') \right\rangle &= \int \left\langle G(k) \right\rangle e^{i\vec{k}\cdot(\vec{r} - \vec{r}')} d^3 k \\
&= \int \frac{1}{k^2} \left(1 - \frac{A^2}{k^2 \lambda_T^2} + ..\right) e^{i\vec{k}\cdot(\vec{r} - \vec{r}')} d^3 k \\
&= \int \frac{1}{k^2 \left(1 + \frac{A^2}{k^2 \lambda_T^2}\right)} e^{i\vec{k}\cdot(\vec{r} - \vec{r}')} d^3 k \\
&= \frac{1}{4\pi} \frac{e^{-|A||\vec{r} - \vec{r}''|/\lambda_T}}{|\vec{r} - \vec{r}''|}
\end{aligned}
\tag{3.12}
$$

Since the communication between points is governed by the pressure, it is plausible that two-point correlations will also fall off exponentially with the distance between the points. An exponential behaviour was indeed found recently in the analysis of experimental and direct numerical simulation results of the mixed state induced by RTI[8].

4 SUMMARY AND DISCUSSION

The main result of the present work is in formula (3.4) which represents the pressure p in a variable-density incompressible fluid as a functional $\tilde{p}(\vec{u}, \rho)$ of the velocity field $\vec{u}$ and the density distribution ρ. In the case of constant density the functional is well known and serves as a major tool in handling the closure problem in turbulence. Formula (3.4) now enables similar treatments also of the problem of turbulent RTI mixing. The pressure formula predicts that the pressure induced by an eddy immersed in a "sea" of density fluctuations decays exponentially, with the density correlation length as the decay length. This result is in contrast with the constant-density case where the pressure falls off as some integral power of the distance[5]. It is plausible that this will induce an exponential behaviour of all correlations in the system (including, when solved in a self consistent manner, the correlation of density fluctuations). An indication of this exponential behaviour was recently found in the analysis of experimental and direct numerical simulation results of the mixed state induced by RTI[8]. This exponential (rather than algebraic) fall off of correlations, has an implication also on the existence of some dynamic invariants in the system [9].

REFERENCES

[1] *Turbulence* by P.A. Davidson (Oxford University press 2004).

[2] Lord Rayleigh,Scientific Papers (Cambridge University Press,Cambridge,1900),Vol.II,p.200;G.I.Taylor, Proc.R.Soc.London A 201,192 (1950).

[3] Youngs D.L. Physica D **12**, 32 (1984).

[4] Youngs D.L. Physica D **37**, 270 (1989).

[5] G. K. Batchelor *The theory of homogeneous turbulence* (Cambridge 1953).

[6] Chou P. Y. Quart. Appl. Math. **3**, 38 (1945).

[7] David LC. Wilcox *Turbulence modeling for CFD* (DCW industries,1993).

[8] G. Hazak, Y. Elbaz, J. H. Gardner , A. L. Velikovich, A.J. Schmitt and S. T. Zalesak, Phy. Rev. E 73, 047303 (2006).

[9] G. K. Batchelor and I Proudman Phil. Trans. Roy. Soc. A, **248**, 369 (1956).

[10] Stephen B. Pope *Turbulent flows* (Cambridge University press, 2000).

[11] Uriel Frisch *Turbulence The Legacy of A.N. Kolmogorov* (Cambridge University press, 1995).

[12] J. L. Lumley Adv. Appl. Mech. **18**, 123 (1978).

e-mail: nhearn@uchicago.edu

FLASH Code Simulations of Laser-Driven Rayleigh-Taylor and Richtmyer-Meshkov Experiments on OMEGA

Nathan C. HEARN[1], Tomasz PLEWA[1], R. Paul DRAKE[2] and Carolyn KURANZ[2]

[1] *ASC Flash Center, University of Chicago, Chicago, Illinois, U.S.A.*
[2] *Space Physics Research Laboratory, University of Michigan, Ann Arbor, Michigan, U.S.A.*

Abstract:
The ASC Flash Center is using its FLASH adaptive mesh refinement code to perform simulations of the high energy density hydrodynamic processes that occur within supernovae. Observations of core-collapse supernova events suggest that mixing processes play a critical role in the distribution of elements after the explosion. Since the elements are initially separated into shells that are nearly spherical, Rayleigh-Taylor and Richtmyer-Meshkov instabilities may provide the mechanism for this mixing.

An ongoing series of experiments on the OMEGA laser is aimed to study such shock-induced mixing processes in a two-fluid medium. In these experiments, the interface between the two media is planar with sinusoidal perturbations, where one or more perturbation modes are present.

Here we present a set of two- and three-dimensional comparisons between FLASH simulations and the two-media mixing experiments. With the help of high-resolution numerical models, we evaluate the differences in mixing efficiencies obtained in two and three dimensions. Finally, the dependence of mixing on the form of the perturbations is discussed.

1 INTRODUCTION

Fluid instabilities may play an important role in supernova explosions. Supernova progenitors are massive stars, with layers of different elements arranged in concentric shells. The interfaces between the shells are subject to Richtmyer-Meshkov and Rayleigh-Taylor instabilities seeded by perturbations and triggered by the the passage of blast waves during the explosion. Such instabilities lead to mixing processes that may be responsible for the observed transport of material in core-collapse supernovae.

The FLASH code [6] is an Eulerian hydrodynamics program with adaptive mesh refinement that was developed for the primary purpose of modeling supernova explosions. As such, FLASH must include a number physical phenomena on a wide range of spatial and temporal scales, including hydrodynamics, gravity, and nuclear burning. Careful validation of each of these components is essential for gaining confidence in applying the FLASH code to situations inaccessible to experiment (see [2], [7]).

2 FLASH CODE VALIDATION

Because of the magnitude of the scales involved in supernova explosions, FLASH validation relies on the use of surrogate systems that yield similar behavior, but are manageable within a laboratory setting. A method for scaling the dimensions of a polytropic fluid is described by [13]. As long as no significant differences exist in the dimensionless quantities describing the supernova and the experiment (see [1]), we can confidently use laboratory fluid experiments to validate FLASH for supernova dynamics.

The current project focuses on the evolution of the mixing layer in Rayleigh-Taylor unstable media. The laboratory experiments are inherently three-dimensional, as are the physical processes within a supernova, so three-dimensional simulations are crucial. Analysis of less-expensive, two-dimensional problems provide valuable insight into the performance of the FLASH code, whereas the geometry of three-dimensional runs permits more complex behavior. This 3D behavior includes significantly faster mixing layer growth as demonstrated in [9].

3 OMEGA LASER EXPERIMENTS

The experiments being run on the OMEGA laser (see [5], [10]) involve a solid cylinder with a diameter of 900 μm. One end of the cylinder is composed of polyimide (1.41 g cm^{-3}), while the other end is a lower density carbon foam (0.05 g cm^{-3}). The interface between the two components is a plane transverse to the cylinder axis onto which sinusoidal perturbations are imposed (see Figure 3.1). The target is encased in a polyimide tube roughly 25 μm thick.
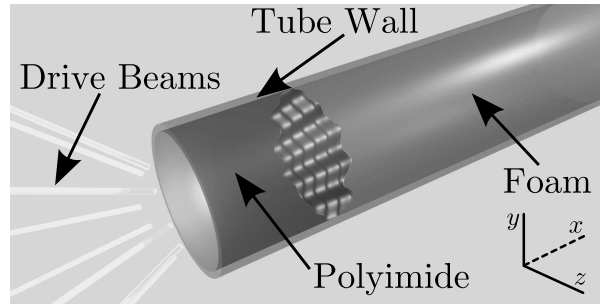
Fig. 3.1. Illustration of the experimental setup. A simplified version of the target cylinder is shown, with the OMEGA drive beams inducing a planar blast wave in the polyimide. The blast wave travels into the foam, triggering Richtmyer-Meshkov and Rayleigh-Taylor instabilities in the interface between the two media. Within this paper, the coordinate axes are defined such that the x-axis runs along the length of the cylinder, while the y- and z-axes are tranverse to the cylinder's axis.

Each simulation and experimental run has a primary perturbation mode (71 μm wavelength) that varies along both transverse axes:

$$\delta x_1(y, z) = (2.5 \ \mu\text{m}) \cos \frac{2\pi y}{71 \ \mu\text{m}} \cos \frac{2\pi z}{71 \ \mu\text{m}} \tag{3.1}$$

"Single-mode" simulations and experiments have only the primary perturbation mode. "Double-mode" simulations and experiments have an additional perturbation that varies only along one of the transverse axes. In this paper, we are concerned with a secondary perturbation wavelength of 213 μm:

$$\delta x_2(y, z) = \delta x_1(y, z) + (2.5 \ \mu\text{m}) \cos \frac{2\pi y}{213 \ \mu\text{m}} \tag{3.2}$$

The OMEGA experiments use laser ablation to form a nearly planar shock wave at the polyimide end of the tube. The laser pulse is brief enough that radiative transport subsides and the shock wave evolves into a planar blast wave (see [3]) before the shock front reaches the material interface. When the shock wave travels across the interface, the perturbations and the jump in density conspire to induce vorticity in the velocity field. Meanwhile, material behind the shock is subject to a rarefaction wave due to material exiting the tube at the drive end. The pressure and density gradient produced by the rarefaction provides the deceleration necessary for the growth of Rayleigh-Taylor instabilities seeded by the perturbations and the vorticity. However, unlike classical RTI, the gradients producing the acceleration field are not spatially uniform, but decrease with distance from the shock front.

4 FLASH SIMULATIONS

A set of simulations of the OMEGA experiments were run with the FLASH code, exploring different resolutions and different perturbation modes (single and double) in both two and three dimensions. (For the 2D simulations, the z-dependence of the perturbations was ignored.) The resolutions used are denoted L15, L30, and L60, corresponding to approximately 15, 30, and 60 mesh cells per primary (71 μm) wavelength at the finest level of refinement.

The simulations included a model of the polyimide and foam cylinder onto which the pressure, density, and velocity field from a one-dimensional HYADES simulation was imposed. The HYADES simulation included a model of radiation transport from the laser, and was run long enough (1.5 ns) for the radiative effects from the laser to subside, but not long enough for the shock wave to reach the interface. The polyimide–foam interface
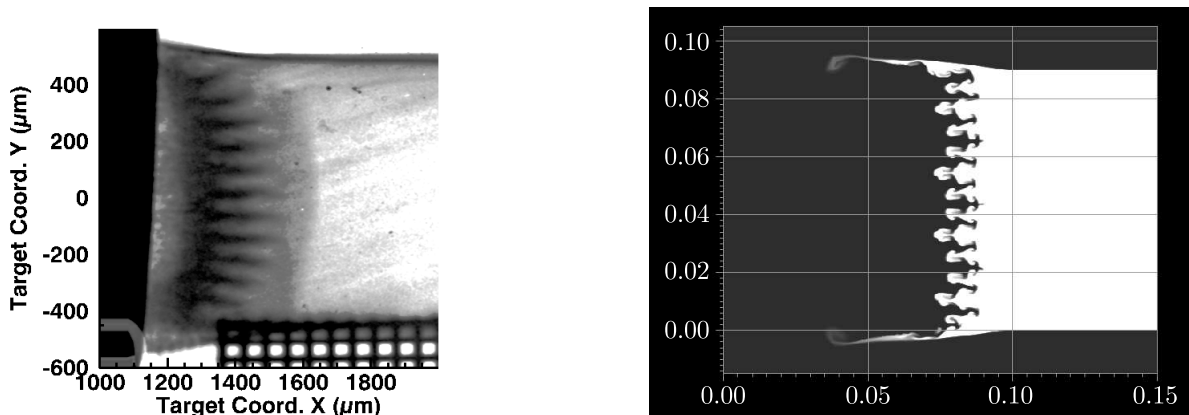
Fig. 4.2. *Left*. Radiograph image from an OMEGA experiment. This image shows the state of a double-mode experiment at a time of 17 ns. The mixing layer (Rayleigh-Taylor spikes) is visible as the dark, comb-shaped structure across the width of the tube; the shock front can be seen just to the right. We also note the expansion of the tube wall behind the shock wave, as well as the large-scale curvature in both the shock front and the mixing layer. The grid in the lower-right corner is a gold mesh used for spatial calibration. *Right*. The state of an L30 double-mode simulation at 12 ns. Here, the mass fraction of polyimide is shown for a slice through the middle of the volume, with darker shades denoting higher polyimide concentration, and lighter shades denoting higher foam concentration. (The coordinate scale is centimeters.) The polyimide bars above and below the foam region represent the tube walls; we note the expansion of the tube walls around the mixing layer. The shock, which appears in density and pressure, is not visible here.

was then perturbed with the same pattern as the experiment. An image from a 3D double-mode simulation at L30 is shown in Figure 4.2.

High-pressure Hugoniot data for polyimide has been published by [14]. However, as little other information exists about these materials in this regime, we have chosen to model these fluids with an ideal gas equation of state and a fixed value for the adiabatic index, γ. During the experiment, the materials transition to a partially ionized state. Thus, the appropriate γ values will be softer than 5/3 (see [3]); we have chosen a value of 1.4 for both species.

The FLASH code does not have a tensile strength model. To approximate the polyimide tube surrounding the cylinder, the computational volume outside of the cylinder (larger than the thickness of the real tube by a factor of four) was filled with polyimide. The simulation was then run with "outflow" (zero gradient) boundary conditions. The tube could then expand with some resistance, as occurs in the experiment (see Figure 4.2).

Plots of the polyimide mass fractions for 2D single- and double-mode simulations at resolution L60 are displayed in Figure 4.3. These plots show a subset of the computational volume about the fluid interface at three different points in time after the shock wave has passed by.

Figure 4.4 shows polyimide mass fraction plots for the 3D single- and double-mode simulations at L60. The plots are derived from slices through the center of the volume parallel to the x-y plane. The value for the z coordinate was chosen to maximize the amplitude of the 71 μm perturbation, enabling direct comparisons with the 2D plots. The times and spatial coordinates were chosen to be the same as those of Figure 4.3.

5 MIXING LAYER GROWTH

The primary metric chosen for this analysis was the width of the mixing layer as a function of time. Here, the mixing layer was determined by randomly sampling the volume a different y- and z- values, and finding the minimum and maximum x-values for which the polyimide mass fraction passed through 50%. Thus, we end up with an approximation for the maximum extent of mixing, but we do not account for the distribution of matter throughout the mixing layer. (More recent analysis methods are described in Section 6.) The evolution of the simulated mixing layers is shown in Figure 5.5.

Overall, the simulation curves are parallel to those of the experiment, suggesting that the mixing layer growth rates are close to those of the experiment at the times of observation. The expected trends are also seen, with 3D growth rates being faster than 2D, and double-mode being faster than single-mode. The curves for the 2D simulations show some signs of convergence with resolution, but convergence is unclear for the 3D

2D Single Mode Simulation   2D Double Mode Simulation
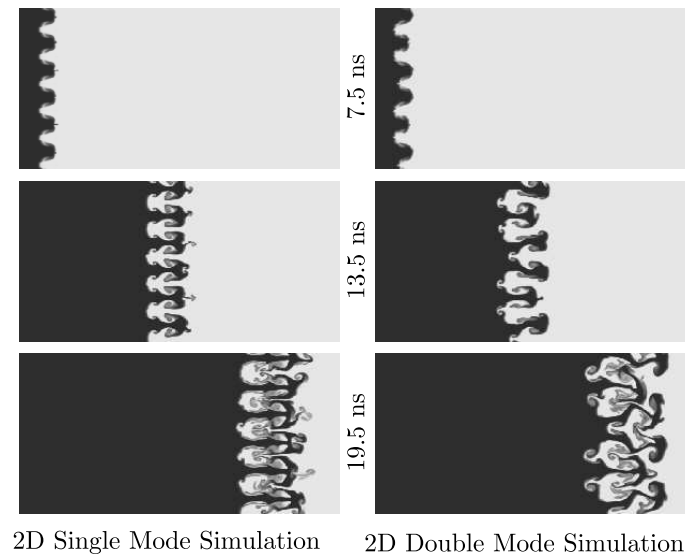
Fig. 4.3. Images from 2D FLASH simulations. Here we show the mass fraction of polyimide material about the mixing layer at three different times for single-mode (left) and double-mode (right) simulations. Dark regions denote high polyimide concentration, while light regions denote low concentration.

3D Single Mode Simulation   3D Double Mode Simulation
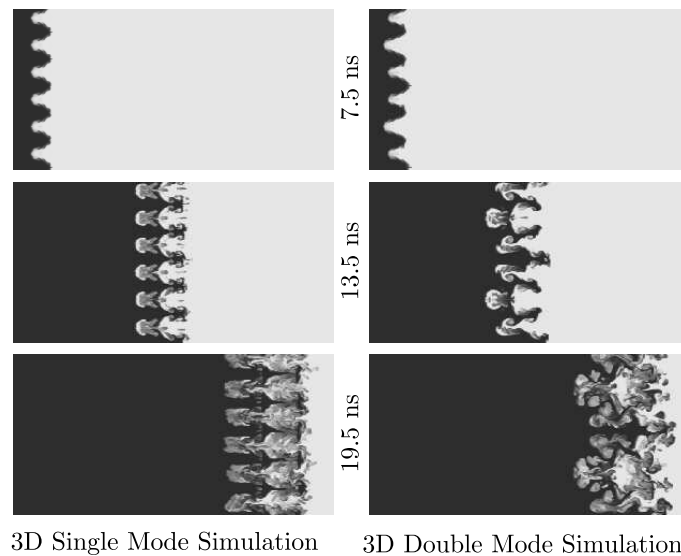
Fig. 4.4. Images from 3D FLASH simulations. Slices through the center of the volume are shown, colored according to polyimide mass density, as in Figure 4.3. We note the agreement with the 2D simulations in the position of the mixing layer along the cylinder axis. However, the 3D simulations show longer, narrower spikes that result in the enhanced mixing layer growth rate.

simulations. The jitter seen in the curves is likely due to the random sampling used. Both of these issues may be resolved with more sophisticated metrics, as discussed in Section 6.1.

6 DISCUSSION

There are a number of points where the simulations find agreement with the experiment and previous theoretical work. From the mixing layer growth plots (Figure 5.5) and the interface morphology (Figures 4.2, 4.3, and 4.4), we note the following:

- 3D simulations exhibit faster mixing layer growth than 2D, in agreement with [9]
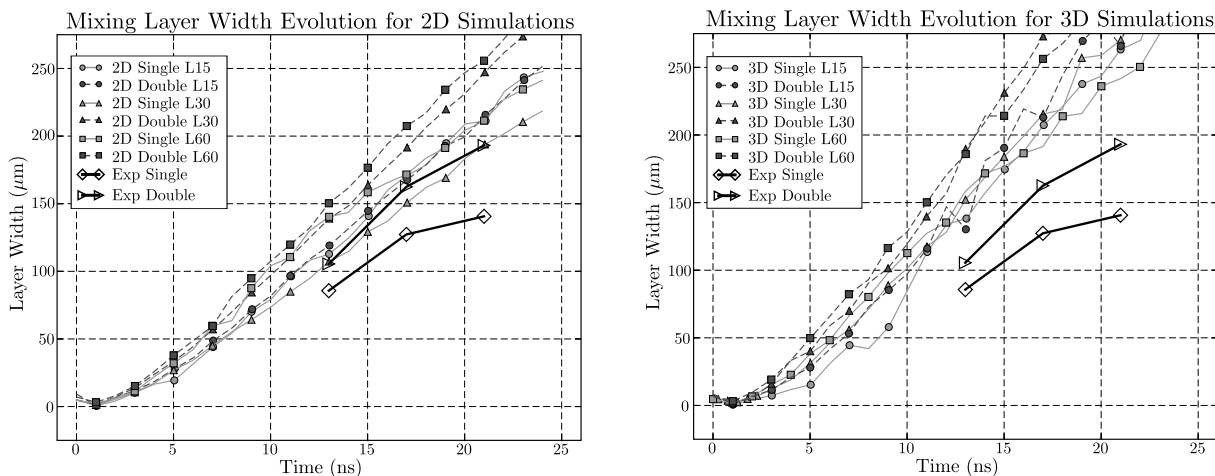
Fig. 5.5. Mixing layer growth rate curves. The mixing envelope widths for the 2D and 3D simulations are shown in the left and right panels, respectively. In each plot, the three single-mode simulations are shown in light gray, and the three double-mode simulations are shown in dark gray. Each plot also includes preliminary experimental values for the single- and double-mode widths in black.

- Double mode perturbations yield faster initial growth than single-mode, as in the experiment and [12]

- Expansion of the tube wall is seen in the simulations, as in the experiment

However, there are still a number of disagreements that we find between the simulations and the experiment. The most significant of which are:

- Simulations do not account for the large-scale curvature of the mixing layer

- 3D simulations exhibit faster mixing layer growth than seen in the experiment

These disagreements may be due to a number of factors. Any comparison of simulations and data must acknowledge that fundamental deficiencies exist in any numerical algorithm. Our primary task is to determine whether any such deficiencies are a significant contributor to the observed errors. Other possible causes can be classified as inadequate analysis metrics or errors in simulation parameters and initial conditions.

6.1 Improved Metrics and Analysis

We are improving our analysis techniques for computing the mixing layer width, exchanging the random sampling method for one that uses all of the data for a central core of the tube. In doing so, we are looking at internal structure for determining the boundary of the mixing layer. Ultimately, these techniques will enable us to validate the code on much smaller scales, directly comparing structures in the simulation and the experiment.

We are also investigating verification of the FLASH simulations against linearized analytic models of Rayleigh-Taylor growth. Since classical RT models have uniform acceleration fields to drive the instability, a "correction" that removes the expansion due to the non-uniform acceleration must be applied to the simulation (see [11]). This correction will essentially put the simulations on the same footing as are used in the linear models.

6.2 Refining the Simulations

The choice of adiabatic index values for the materials can influence the shock speed and the growth of the perturbations, especially at early times. The γ's used for these simulations represent an estimate of the proper parameter for the equation of state. An exploration of different values of γ for polyimide can be found in [11]; we are building this work by using Bayesian design-of-experiments techniques (see, for example, [8]) to tune separate values for the polyimide and the foam.

The tube wall used in the simulations did not produce the large-scale curvature of the mixing layer seen in the experiments. As suggested by the simulations of [11], the likely cause of the curvature is the non-planar

driving produced by the lasers. New, two-dimensional HYADES simulations of the laser interaction are being run, which will provide us with more-realistic initial conditions for the simulations.

The initial conditions may also be improved by including the contribution of "noise" in the perturbations used. The manufacturing process produces low-amplitude, fine-scale artifacts on the polyimide-foam interface. We are characterizing this noise, and we will determine whether it is a contributor to the dynamics of the mixing layer. If so, it will be included as part of our interface perturbations.

ACKNOWLEDGMENTS

REFERENCES

[1] Buckingham, E., 1914. On physically similar systems; illustrations of the use of dimensional equations. *Phys. Rev.* **4**, pp. 345-376.

[2] Calder, A. C., Fryxell, B., Plewa, T., Rosner, R., Dursi, L. J., Weirs, V. G., Dupont, T., Robey, H. F., Kane, J. O., Remington, B. A., Drake, R. P., Dimonte, G., Zingale, M., Timmes, F. X., Olson, K., Ricker, P., MacNeice, P., and Tufo, H. M., 2002. On validating an astrophysical simulation code. *Astrophys. J. Suppl.* **143**, pp. 201-229.

[3] Drake, R. P., 2006. High Energy Density Physics: Intertial Fusion and Experimental Astrophysics, *Springer Verlag.*

[4] Drake, R. P., Carroll III, J. J., Smith, T. B., Keiter, P., Glendining, S. G., Hurricane, O., Estabrook, K., Ryutov, D. D., Remington, B. A., Wallace, R. J., Michael, E., and McCray, R., 2000. Laser experiments to simulate supernova remnants. *Phys. Plasmas* **7**, pp. 2142-2148.

[5] Drake, R. P., Leibrandt, D. R., Harding, E. C., Kuranz, C. C., Blackburn, M. A., Robey, H. F., Remington, B. A., Edwards, M. J., Miles, A. R., Perry, T. S., Wallace, R., Louis, H., Knauer, J., and Arnett, D., 2004. Nonlinear mixing behavior of the three-dimensional Rayleigh-Taylor instability at a decelerating interface. *Phys. Plasmas* **11**, pp. 2829-2837.

[6] Fryxell, B., Olson, K., Ricker, P., Timmes, F. X., Zingale, M., Lamb, D. Q., MacNeice, P., Rosner, R., Truran, J. W., and Tufo, H., 2000. FLASH: an adaptive mesh hydrodynamics code for modeling astrophysical thermonuclear flashes. *Astrophys. J. Suppl.* **131**, pp. 273-334.

[7] Hearn, N. C., Plewa, T., Drake, R. P., and Kuranz, C., 2006. FLASH code simulations of Rayleigh-Taylor and Richtmyer-Meshkov instabilities in laser-driven experiments. *Astrophys. & Space Sci.*, accepted for publication.

[8] Heitmann, K., Higdon, D., Nakhleh, C., and Habib, S., 2006. Cosmic calibration. *Astrophys. J.* **646**, pp. L1-L4.

[9] Kane, J., Arnett, D., Remington, B. A., Glendinning, S. G., Bazán, G., Müller, E., Fryxell, B. A., and Teyssier, R., 2000. Two-dimensional versus three-dimensional supernova hydrodynamic instability growth. *Astrophys. J.* **528**, pp. 989-994.

[10] Kuranz, C. C., Drake, R. P., Donajkowski, T. L., Dannenberg, K. K., Grosskopf, M., Kremer, D. J., Krauland, C., Marion, D. C., Robey, H. F., Remington, B. A., Hansen, J. F., Blue, B. E., Knauer, J., Plewa, T., and Hearn, N., 2006. Assessing mix layer amplitude in 3D decelerating interface experiments. *Astrophys. & Space Sci.*, accepted for publication.

[11] Miles, A. R., Braun, D. G., Edwards, M. J., Robey, H. F., Drake, R. P., and Leibrandt, D. R., 2004. Numerical simulation of supernova-relevant laser-driven hydro experiments on OMEGA. *Phys. Plasmas* **11**, pp. 3631-3645.

[12] Miles, A. R., Edwards, M. J., Blue, B., Hansen, J. F., Robey, H. F., Drake, R. P., Kuranz, C., and Liebrandt, D. R., 2004. The effect of a short-wavelength mode on the evolution of a long-wavelength perturbation driven by a strong blast wave. *Phys. Plasmas* **11**, pp. 5507-5519.

[13] Ryutov, D., Drake, R. P., Kane, J., Liang, E., Remington, B. A., and Wood-Vasey, W. M., 1999. Similarity criteria for the laboratory simulation of supernova hydrodynamics. *Astrophys. J.* **518**, pp. 821-832.

[14] Takamatsu, K., Ozaki, N., Tanaka, K. A., Ono, T., Nagai, K., Nakai, M., Watari, T., Sunahara, A., Nakano, M., Kataoka, T., Takenaka, H., Yoshida, M., Kondo, K., and Yamanaka, T., 2003. Equation-of-state measurements of polyimide at pressures up to 5.8 TPa using low-density foam with laser-driven shock waves. *Phys. Rev. E* **67**, pp. 056406-1-5.

e-mail: `nail-inogamov@yandex.ru`

Richtmyer-Meshkov Turbulence

Nail INOGAMOV[1]

[1]*L.D. Landau Institute for Theoretical Physics, Moscow, Russian Federation*

Abstract: There are the power-law dependences $z = h_+(t) = q_+ t^{\theta_+} > 0$, $-z = h_-(t) = q_- t^{\theta_-} > 0$ describing the expansion of the Richtmyer-Meshkov turbulent mixing fronts into dense "upper" (+) and less dense "lower" (-) substances. An analysis presented below shows that $\theta_+ = \theta_-$ (density asymmetry is in the ratio q_-/q_+) and the exponents θ_+, θ_- do not depend on the density ratio $\mu \in [0,1]$ of these substances. The analysis gives also values $\theta_{2D}^{sp} = 2/5$ ($\theta = \theta_+$) for the 2D geometry and $\theta_{3D}^{sp} = 1/3$ for the 3D geometry. These values correspond to the most important case of *spontaneous* Richtmyer-Meshkov turbulence which grows from short-wavelength initial perturbations without or with insignificant initial long-wavelength perturbations. On the contrary the development of the *stimulated* Richtmyer-Meshkov turbulence is controlled { $\theta_{2D}^{st} = 1/(\beta + 5/2)$, $\theta_{3D}^{st} = 1/(\beta + 3)$ } by the long-wavelength $k \to 0$ initial (before a passage of a shock wave) spectrum $\eta_k \propto k^{\beta}$ of surface perturbations. The values 2/5, 1/3 may be obtained from the expressions $\theta^{st}(\beta)$ when $\beta = 0$. The major achievement of the study is not, of course, a derivation of the simple expressions $\theta^{st}(\beta)$, but the demonstration how the general arbitrary short-wavelength initial perturbations create the long-wavelength tail with the exponent $\beta = 0$.

1 INTRODUCTION

Development of the Richtmyer-Meshkov instability in the case of large Reynolds numbers leads to Richtmyer-Meshkov turbulence. The problem concerning the asymptotical (this means at $t \to \infty$) expansion in space of such turbulence is of fundamental importance. At late stage compressibility effects become negligible. Therefore we can consider Richtmyer-Meshkov turbulence around a contact boundary between two incompressible media - the asymptotical power law dependences

$$h_{\pm} \propto t^{\theta_{\pm}} \tag{1.1}$$

are the same for the compressible Richtmyer-Meshkov turbulence and for the incompressible Richtmyer-Meshkov turbulence. Morphologically the mixing region is a layer expanding with time t. The mixing layer "upper" and "lower" boundaries are $z = h_+(t)$ and $z = h_-(t)$, where z is a "vertical" or longitudinal axis normal to the layer (it is the direction of the fronts propagation). Let the upper substance to be denser than the lower one. Let's denote by $\mu = \rho_l / \rho_h$ the density ratio of light (l) and heavy (h) fluids.

Dynamical interaction through a whole mixing layer $h_- < z < h_+$ bands both fronts together for $\mu \neq 0$ cases. Therefore we have $\theta_+ = \theta_-$ for the $\mu \neq 0$ cases.

Mixing with "vacuum" - when $\mu = 0$ - is a special case. The jets thrown into vacuum ($\rho_l = 0$) lose their links or ties with the dense semi-space. They do not affect dynamics of bubbles near the perturbed boundary of this semi-space. They keep in time their velocities gathered during a process of their separation from the semi-space and ejection into vacuum. Therefore positions of the jets are $z \propto t$. Conditionally in this sense it may be said that $\theta_- = 1$. At the same place it should be emphasized that asymptotical profiles (e.g., density profile) for the $\mu = 0$ case are self-similar with

the "heavy front" power-law exponent θ_+ : $\left\langle \rho(x,y,z,t) \right\rangle_{x,y} = \overline{\rho}(z,t) \rightarrow \rho_{ss}(z/t^{\theta_+})$ when $t \rightarrow \infty$, here $\left\langle \ \right\rangle_{x,y}$ means averaging in the transverse plane, and the subscript "ss" denotes "self-similar". Only small part of mass (thrown at early stages of "mixing with vacuum") located near the "light front" h_- can not be described by the "θ_+ self-similarity" $(z,t) \rightarrow z/t^{\theta_+}$. This part forms the non self-similar "tail" of ejected matter. This "tail" resembles kinetic (non-hydrodynamical collisionless) tail of hydrodynamic wave of gas expansion into vacuum.

Large scale structures define an expansion of the mixing layer. The conceptions "mixing layer" and "large scale structures" are inseparable. In the pair "mixing layer"-"large scale structures" the second is more substantial and definitive. {The mixing layer $z \in [h_-, h_+]$ is composed from chunk to molecular mixtures. The problem of a mixture composition at small space scales needs a separate treatment.}

The instant transverse scale $\overline{\lambda}$ of the large structure grows with time similarly to the growth of the penetration depth: $\overline{\lambda}(t) \simeq h_+(t)$. Let's consider the spectrum $f(z,t,k_x,k_y)$ of some value (e.g., velocity, mixture composition or pressure) in the 3D case at the transverse plane $z = 0$ (at $t = 0$ this plane separates contacting substances). The spectrum consists of the long wavelength linear $0 < \lambda < \overline{\lambda}$ and the short wavelength nonlinear ("saturated") $\overline{\lambda} < \lambda < \infty$ spectral parts, where $\lambda = 2\pi/k$, $k = \sqrt{k_x^2 + k_y^2}$.

The instant expansion rates $\dot{h}_\pm(t)$ are defined by a group of the largest nonlinear modes with wavelengths $\lambda \simeq \overline{\lambda}$ - the largest developed scale at this instant $t(\overline{\lambda})$. At the next instant $t_1 = t(\overline{\lambda}_1) > t(\overline{\lambda})$ the next large scale mode $\overline{\lambda}_1 > \overline{\lambda}$ appears or (i) from amplifying of small amplitude perturbation λ_1 in the long wavelength spectrum linear for $t < t_1$ or (ii) from harmonic beating and amplifying of nonlinear modes $\lambda \cong \overline{\lambda}$. The way (i) with linear growth of the mode λ_1 during the time interval $t \rightarrow t_1$ presents development of the *stimulated* turbulence if the long wavelength part of the spectrum corresponds to the initially imposed perturbation spectrum. The way (ii) with self-development $\overline{\lambda} \rightarrow \overline{\lambda}_1$ of leading or dominating large scale $\overline{\lambda}(t)$ is the way of development of the *spontaneous* turbulence. In this sense Richtmyer-Meshkov and Rayleigh-Taylor turbulences are qualitatively similar.

Two main theoretical approaches and powerful modern experimental [1,2] and computational techniques [3] were applied to define the exponent θ . The first group of the theoretical approaches use K, K-L, K-ε or buoyancy-drag models (see, e.g., [1,2]). The second group base their work on the two–bubble interaction or the bubble shell models [4-6]. Both groups describe phenomenon by fitting experimental results with phenomenological parameters. The "K-approaches" exploit an energy equation for the turbulent kinetic energy K with the Kolmogorov viscous energy loses $\dot{E}_{visc}$. The buoyancy-drag approach is based on a force balance between the buoyancy and the decelerating hydro-resistance force connected with ram pressure. The K- and the buoyancy-drag approaches are qualitatively similar – the resistance to the bubble motion plays the same role as the viscous loses. The force balance may be transformed into the form of the energy equation $dv/dt \rightarrow vdv/dt \rightarrow dK/dt$. Deceleration of the "$\overline{\lambda}$ -bubbles" of the large scale structure by the ram resistance converts kinetic energy of potential bubble streamline motion into kinetic energy of vortices. After that the vortical kinetic energy dissipates somehow. Therefore all of the first group models may be called local (on the scale $\overline{\lambda}$) dissipative models. The shell model describes the enlargement of the leading scale $\overline{\lambda}$ due to bubble merging. Both theoretical groups give approximate values $\theta_\pm(\mu)$ which may differ for the "+" and "–" directions and depend on the ratio μ .

Unfortunately, it is necessary to say that the local dissipative approach (useful for description of Rayleigh-Taylor and Kelvin-Helmholtz turbulences) is inapplicable for the description of the scaling of the Richtmyer-Meshkov turbulence. The point is not that it is approximate or phenomenological. The point is that it offers wrong physical assumptions for the description of the phenomenon. For example, in the K-approaches peoples adjust the value $\Delta\theta_{visc}$ in the relation

$\theta = 2/3 - \Delta\theta_{visc}$ using experimental values for the exponent θ (the K-approaches may be used only in the 3D case where the Kolmogorov dissipation exists). But the reason for the exponent θ_{3D} to be 1/3 is not that the dissipation $\Delta\theta_{visc}$ equals to 1/3. It will be clear below that the values 2/5 and 1/3 result from statistics of momentum in all scales $[\overline{\lambda}, \infty]$ interacting simultaneously and not from energy loses.

The shell models [4-6] are better. Some statistical information about the transverse structure is presented. One disadvantage of the shell models is connected with their approximate nature. This follows from the phenomenological description of propagation of bubbles and their merging. Using of only pair bubble interaction (local $\overline{\lambda}$-scale interaction) is another disadvantage. In the Richtmyer-Meshkov case it is necessary to include simultaneous interaction in all scales $[\overline{\lambda}, \infty]$ (pairs, quartettes, octettes and so on). Because this wide scale interaction produces velocity cell structure like a geometric series (see below).

2 CREATION OF HIERARCHICAL VELOCITY FIELD BY SHOCK IMPACT

We have to study the scaling at the late times $t \gg \lambda_0 / w_0$ at large distances $\Delta r \gg \lambda_0$ in the case when influences of compressibility, viscosity, or surface tension are negligible. The quantities λ_0 and w_0 are average transverse scale of the arbitrary short-wavelength initial perturbation and average initial (after passage of shock through perturbed boundary) velocity. {The 3D x, y, z-components of velocity are u, v, w. In 2D the components are x, z and u, w. } Motion after impact acceleration depends on the perturbation. General dynamics is initiated by the perturbation of general form. General multimode motion is turbulent motion. The most interesting is the case when turbulent motion develops from the general arbitrary short-wavelength perturbations. Such perturbations have some average scale λ_0 and they are transversally homogeneous. Let us call them random-periodic functions (RPF). An example of the function for 2D case is presented
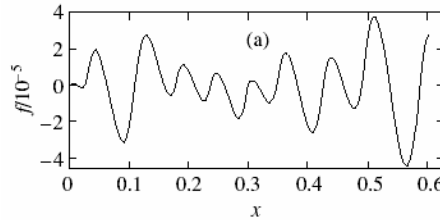
Fig. 2.1. Random walk of RPF describing initial perturbed contact surface of general form

in Fig. 2.1. Randomness and periodicity of the RPF are equally important. Periodicity ensures transverse homogeneity while randomness extends the function to broad class of arbitrary perturbations. The solitary and the periodic functions correspond to very restricted classes of initial data in comparison with the RPF. They are or transversally inhomogeneous (the solitary functions) or present special kind of initial perturbation (the periodic functions).

In the Section 2 we have to show how the contact boundary perturbed by the RPF "refracts" the shock impact into hierarchical cell velocity field shown in Fig. 2.2. Let's begin with a short description of the two main properties of the RPF:
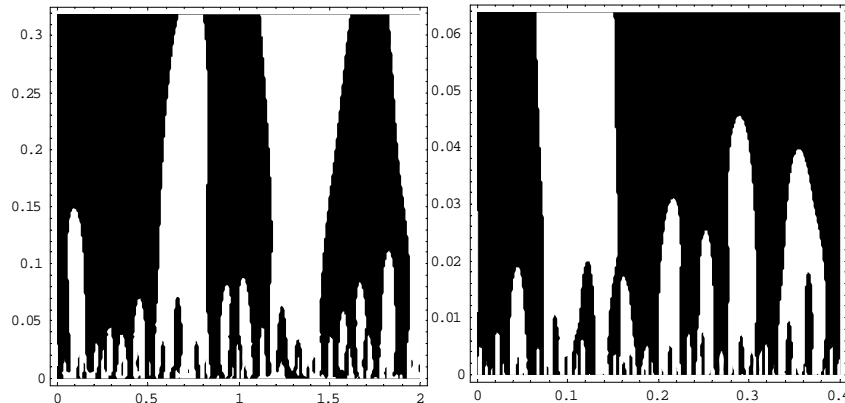
Fig. 2.2. The hierarchical cell velocity field created by shock passage "through the RPF". The cell net forms geometric series. The right picture is the five times enlarged left bottom pierce of the left picture (comp. digital marking of the axes)

the "loss of memory" when we shift the RPF transversally to several average lengths λ_0 and the asymptotical behaviour of long-wavelength ($k \to 0$) tail of the Fourier transformation of the RPF [5]. The correlation function (2.1) is

$$K(x) = \frac{\int\limits_0^{2\pi} f(x')f(x'-x)dx'}{\int\limits_0^{2\pi} [f(x')]^2 \, dx'} \tag{2.1}$$

presented in Fig. 2.3. The left picture in this Figure shows one realization of the correlation function $K(x)$, while the
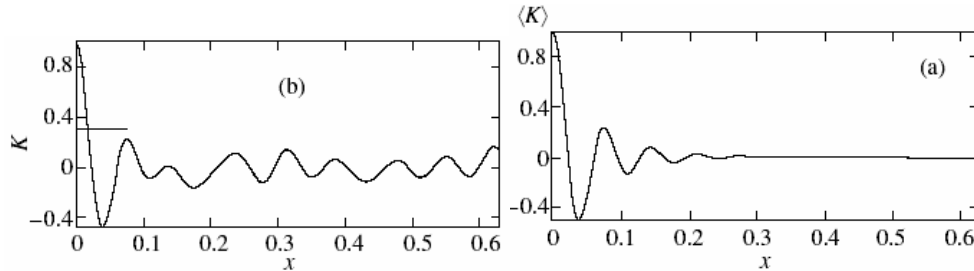
Fig. 2.3. The correlation properties of the RPF. One realization (left) and averaged after many realizations (right). We see that the correlation between the successive "bumps" of the RPF decays at a distance $\sim \lambda_0$ (comp. with Fig. 2.1)

right picture presents the curve $K(x)$ averaged after the 4000 realizations. The RPF with the length $\lambda_0 = L/100$ at the interval $[0, L], L = 2\pi$ has been taken for the example shown in Figs. 2.1 and 2.3. The periodic boundary conditions have been applied at the interval end points. As $\lambda_0 \ll L$ the periodic conditions at the interval ends do not influence the statistical properties of the RPF. The integrals in the definition (2.1) of correlation function $K(x)$ are taken over the interval $[0, L]$.

The spectrum of the RPF is shown in Fig. 2.4. The left picture corresponds to the example of the RPF presented in Fig. 2.1. The right picture is obtained after averaging over 4000 realizations. The main thing is that the long-wavelength ($k \to 0$) asymptotic $f_k \to k^\beta$ has the exponent $\beta = 0$. As we will see this long-wavelength tail defines the rate of expansion of the mixing layer at late time and therefore it defines the exponent θ (1.1). The "shoulder" $\beta = 0$,
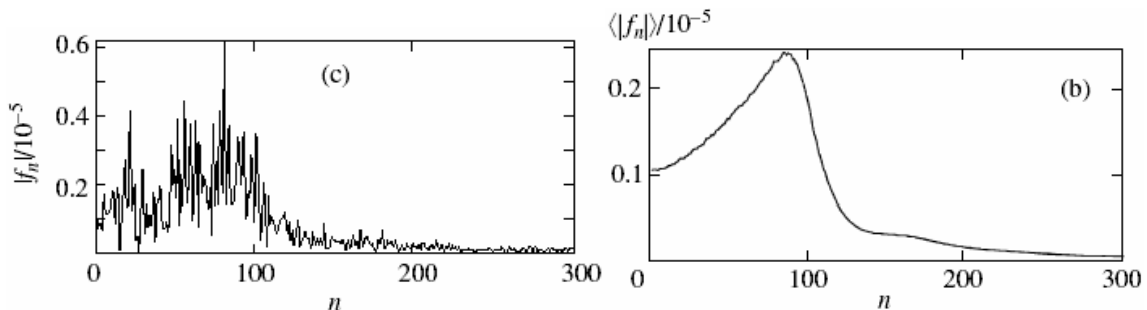
Fig. 2.4. The spectrum of the RPF. The long-wavelength tail of this spectrum defines the exponent θ

$k \to 0$ in the spectrum appears due to decay of correlation (Fig. 2.3) between the "bumps" in the chain of the "bumps" of the RPF. The long range correlations increase the β, and thus decrease the influence depth and the mixing rate θ.

It is important to consider the case when the initial amplitudes of perturbations are small $|\nabla_\perp \eta| \ll 1$ because in the opposite case of the large amplitude perturbations the universal dynamics is absent. This means that the inclination or tangent angles of the perturbed contact surface are infinitesimal and the perturbation are linear. Here $\eta(x)$, $\eta(x,y)$ are the initial contact boundaries, $\nabla_\perp = \{\partial/\partial x, \partial/\partial y\}$. The arbitrary initial perturbation may be decomposed into the linear superposition of harmonics in the case of the infinitesimal perturbation.

Let us apply the Richtmyer formula (2.2) to all harmonics in the superposition. Here w_n is the Fourier amplitude of the

$$w_n = F \, \mathrm{At} \, n\eta_n \, W_{SW} \tag{2.2}$$

n-th harmonics of the vertical velocity, F is the non-dimensional coefficient, At is the Atwood number, η_n is the n-th harmonics of the initial surface perturbation, and W_{SW} is the velocity "jump" of the unperturbed contact after passage of shock. The velocity harmonics w_n are created by shock impact from the surface perturbations η_n. It is important that the coefficient F does not depend on wavelength. Therefore the velocity field after shock impact is given by the linear superposition $\sum w_n \propto \sum n\eta_n$ of the $n\eta_n$ terms. The velocity amplitudes w_n are proportional to wave number n as the amplitudes η_n do not depend on n. The phases of the harmonics n are random.

The differences in the velocity fluctuations at the scale λ in the plane $z = $ const are given by the expression (2.3)

$$w_\lambda(z,t) = \left\langle \left| \vec{v}(\vec{r},t) - \vec{v}(\vec{r}-\vec{\lambda},t) \right| \right\rangle \tag{2.3}$$

where vectors $\vec{r}$ $\{x,y\}$ 2D or $\{x,y,z\}$ 3D have the same value of the coordinate z. The fluctuations of the velocity components (e.g., w_λ) are of the same order as fluctuations of velocity v_λ, $v = |\vec{v}|$, $\lambda = |\vec{\lambda}|$. The fluctuations (2.3) and the Fourier amplitudes w_n are connected

$$w_\lambda \simeq \sqrt{n} \, w_n , \tag{2.4}$$

where $n = n_\lambda = L/\lambda$. From the equation (2.2) $w_n \propto n$ and (2.4) we obtain that

$$w_\lambda \propto n^{3/2} \propto 1/\lambda^{3/2} . \tag{2.5}$$

The example of the 2D velocity field with $w_n \propto n$ and $w_\lambda \propto \lambda^{-3/2}$ is shown in Fig. 2.2. The field was presented by the sum $w(x,z) = \sum_{n=1}^{N} n\cos(nx + \psi_n)\exp(-nz)$ with $N = 1000$, $L = 2\pi$, $\lambda_0 = L/N = 2\pi/N$, and the random phases ψ_n. The left picture is the frame $2\times[2/(2\pi)]$ of the upper semi-space $z > 0$. In the black areas the vertical velocity is negative $w < 0$ and in the white – positive.

The dependence (2.5) defines the decay of velocity field from the boundary into the bulk of fluid $w(x,z) \propto 1/z^{3/2}$ (the sum $\sum n\cos(nx + \psi_n)e^{-nz}$ decays as $z^{-3/2}$). We have $dh/dt \simeq w(x,z)|_{z\simeq h} \simeq 1/h^{3/2}$, where h is the mixing front position. Therefore the exponent (1.1) is $\theta_{2D} = 2/5$. Similar calculation in 3D gives $\theta_{3D} = 1/3$.

3 VARIATION OF THE CELL VELOCITY FIELD IN TIME AND LOGARITHMIC CORRECTIONS

Let us consider time dependence of velocity in a point Λ remote from the boundary $w_\Lambda(\tau) = w(\vec{r}_\perp^{\,fix}, z = \Lambda, t)$ as a function of "logarithmic" time $\tau = \log(t/t_0 + 1)$, where $t_0 = \lambda_0 / w_0$, w_0 is the average velocity of the boundary after impact. Before the shock arrival the contacting fluids are at rest, $w_\Lambda(0) = 0$. The shock quickly (in the incompressible case) creates the cell velocity field: $w_\Lambda(+0) \propto 1/\Lambda^{3/2}$. This is the "Richtmyer jump" $w_\Lambda(0) \rightarrow w_\Lambda(+0)$. During the time interval $\sim t_0$ after the shock impact the almost plane at $\tau = +0$ boundary deforms into the nonlinearly $|\nabla_\perp \eta| \sim 1$ perturbed surface. The large scale bubble structure with the dominant scale λ_0 appears. The duration t_0 is the one rotation time for vortices of the scale λ_0.

The imprint pressure of groups of λ/λ_0 bubbles changes the cell velocity field during the time interval $\sim t_0$. Here $\lambda \in [\lambda_0, \infty]$ is the size of the group. It will be described below how the imprint pressure works. The change of velocity Δw_Λ in the point $\{\vec{r}_\perp^{\,fix}, z\}$ is $\Delta_1 w_\Lambda = \xi_1 w_\Lambda(+0)$, where the coefficient ξ_1 may be positive or negative, $|\xi_1| \simeq 1$. This is the result of momentum creation by the imprint pressure during the first time step $\Delta\tau$ from $\tau = +0$ to $\tau = 1$. During the second time step $\Delta\tau = 1$ from $\tau = 1$ to $\tau = 2$ the dominant scale of large structure enlarges several (q) times $\lambda_0 \rightarrow q\lambda_0$. The imprint pressure of the groups of $\Lambda/(q\lambda_0)$ bubbles again changes velocity in the chosen point $w_\Lambda(\tau = 2) = w_\Lambda(+0) + \Delta_1 w_\Lambda + \Delta_2 w_\Lambda$, $\Delta_2 w_\Lambda = \xi_2 w_\Lambda(+0)$, where the coefficient ξ_2 may be positive or negative, $|\xi_2| \simeq 1$.

After m of such steps the dominant scale is $q^{m-1}\lambda_0$ while the velocity in the chosen point is
$w_\Lambda(\tau = 2) = w_\Lambda(+0) + \Delta_1 w_\Lambda + \Delta_2 w_\Lambda + ... + \Delta_m w_\Lambda$, $\Delta_m w_\Lambda = \xi_m w_\Lambda(+0)$, where $\xi_m <$ or > 0, $|\xi_m| \simeq 1$. There are three possibilities: (a) the sum $s = \xi_1 + \xi_2 + ... + \xi_m$ is less than 1, (b) the terms are $|\xi_m| \simeq 1$ and the signs of the terms ξ_m randomly changes, and (c) the terms are $|\xi_m| \simeq 1$ and all signs of the terms are the same. Then for the velocity field and the growth (1.1) of the mixing layer in 2D and 3D cases we have respectively

$$w_\Lambda \simeq (\lambda_0/\Lambda)^{3/2} w_0 \rightarrow h \simeq (\lambda_0^{3/2} w_0)^{2/5} t^{2/5} \leftrightarrow (\lambda_0^2 w_0)^{1/3} t^{1/3},$$

$$w_\Lambda \simeq \sqrt{\log\frac{\Lambda}{\lambda_0}} (\lambda_0/\Lambda)^{3/2} w_0 \rightarrow h \simeq (\lambda_0^{3/2} w_0)^{2/5} \left(\log\frac{t}{t_0}\right)^{1/5} t^{2/5} \leftrightarrow (\lambda_0^2 w_0)^{1/3} \left(\log\frac{t}{t_0}\right)^{1/6} t^{1/3},$$

$$w_\Lambda \simeq \log\frac{\Lambda}{\lambda_0} (\lambda_0/\Lambda)^{3/2} w_0 \rightarrow h \simeq (\lambda_0^{3/2} w_0)^{2/5} \left(\log\frac{t}{t_0}\right)^{2/5} t^{2/5} \leftrightarrow (\lambda_0^2 w_0)^{1/3} \left(\log\frac{t}{t_0}\right)^{1/3} t^{1/3}.$$

4 MULTIBUBBLE GROUPS AND THEIR IMPRINT/INDENTATION PRESSURE

Let's consider the current stage $\lambda_{curr} = q^m \lambda_0$, $\tau_{curr} = m\log q + C$, $\lambda_0 \ll \lambda_{curr} \ll \Lambda$ of the enlarging in the process of the inverse cascade, here λ_{curr} is the current or the present size of the dominant scale of the large scale structure at the instant τ_{curr}, or $t_{curr} \simeq q^m t_0$. This is the m-th generation in the sequence of pair merging. The value $C \simeq 1$ is a constant. The particular deposit into momentum $\rho\Lambda^2(\Delta_m w_\Lambda)$ of the cell $\Lambda \times \Lambda$ (2D) during the time interval

$[\tau_m - 1, \tau_m]$ is produced by the action of the bubbles/vortices of the size λ_{curr}. The *coordinated* action of the group (the "Λ-group") of the Λ / λ_{curr} bubbles creates this deposit (see prev. Section).

The momentum is changed by force. In the Richtmyer-Meshkov case the only force is the pressure force (gravity is absent). The change in momentum is due to *imprint* or *indentation* pressure of the "Λ-group". How the indentation or imprint pressure is produced? The ram pressure decelerates the bubble but the indentation of the bubble also raises pressure in surrounding fluid. The pressure increase is of order of the ram pressure. The size of the increased pressure region is of order of the bubble size. In the case of the coordinated Λ-group of the bubbles the size of the region with increased pressure is of order of $\Lambda \times \Lambda$. The periodic bubble array increases pressure at infinity $z = \pm\infty$ because all bubbles are long-range correlated and the transverse size of the array is infinitely large, see Fig. 4.1.
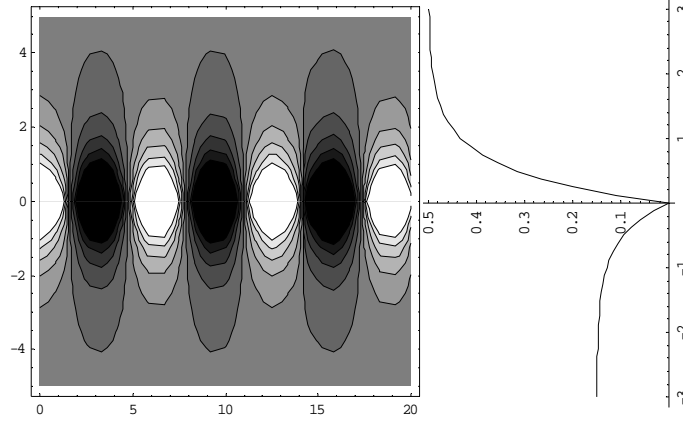
Fig. 4.1. To the left: the vertical velocity contours for the instant $t = +0$ after the shock impact onto the periodically disturbed contact with small initial surface amplitude [7]. To the right: the p (the horizontal axis) on z (the vertical axis) dependence (the pressure "well", p does not depend on x at $t = +0$) for the case shown in the left picture. There are $p(+\infty) = \rho_h w^2 / 2$, $p(0) = 0$, $p(-\infty) = \rho_l w^2 / 2$, where w is the bubble rise velocity at $t = +0$

The Λ-groups are responsible for velocity changes Δw_Λ at the vertical distance Λ from the contact. The increment Δw_Λ is produced by statistical inequality of the Λ-groups. The mean value of the force acting on the horizontal distance Λ is $\simeq (\rho_h - \rho_l) w^2 \lambda_{curr} (\Lambda / \lambda_{curr})$, where w is the average current velocity of bubble penetration. Due to inequality of the Λ-groups the amplitude of fluctuations of this mean force is $\simeq (\rho_h - \rho_l) w^2 \lambda_{curr} (\Lambda / \lambda_{curr})^{1/2}$. The Λ-groups of the λ_{curr} bubbles acts during the time interval $[\tau_m - 1, \tau_m]$. After that time interval the dominant bubbles are changed due to the currently going process of the enlarging. This may induce the changes in the phases of the cell pressure field. The momentum creation during this time interval in 2D geometry is $(\rho_h - \rho_l) \Lambda^2 (\Delta_m w) \propto \Lambda^{1/2} (t_m - t_{m-1})$. The main l.h.s. and r.h.s. factors in this equation are $\Lambda^2 (\Delta_m w) \propto \Lambda^{1/2}$ - surface Λ^2 (or volume in 3D) versus statistics $\sqrt{\Lambda}$. From this the desired relation $\Delta_m w \propto \Lambda^{-3/2}$ follows.

5 THE LONG-WAVELENGTH TAIL STIMULATING THE INVERSE CASCADE OVERTAKING THE SPONTANEOUS INVERSE CASCADE AND THE LIMIT OF SUCH STIMULATION – HOMOGENEOUS NOISE

In the spontaneous Richtmyer-Meshkov turbulence the long-wavelength tail is formed due to an interference of random modes of scale λ_{curr}. Its $k \to 0$ asymptote is $\eta_k^{sp} \propto k^\beta$ with $\beta = 0$ for the surface perturbations η for both 2D and 3D cases. In 3D the k is $\sqrt{k_x^2 + k_y^2}$. The upper superscript "sp" means spontaneous. Let's impose additional long-wavelength perturbations with the Fourier spectrum $\eta_n^{st} = (\lambda_*^{\beta+3/2} / L^{\beta+1/2})(\varsigma_n \cos\psi_n) n^\beta$ (2D), $\eta_\lambda^{st} \propto n^\beta$ (3D). Its variations at distance λ are $\eta_\lambda^{st} = (\lambda_*^{\beta+3/2} / L^{\beta+1/2}) n^{\beta+1/2} \simeq \sqrt{n} \eta_n^{sp}$ in 2D case and $\eta_\lambda^{st} \propto n^{\beta+1} \simeq n \eta_n^{sp}$ in 3D. Its

relative variations are $\varepsilon_\lambda^{st} = \eta_\lambda^{st} / \lambda \simeq (\lambda_* / \lambda)^{\beta+3/2}$ (2D), $\varepsilon_\lambda^{st} \simeq (\lambda_* / \lambda)^{\beta+2}$ (3D). Here the "st" is "stimulated", λ_* is the shortest considered wavelength, for simplicity the discrete representation with integers $n = L / \lambda_n$ equivalent to the wavenumbers $k = 2\pi / \lambda$ is used, L is the transverse box size, $L = 2\pi$, $\lambda_* \ll L$, $k_{3D} = \sqrt{k_x^2 + k_y^2}$, $\langle \varsigma_n \rangle = 1$, ψ_n are random phases. The rate of stimulated expansion is $\theta^{st} = (\beta + 5/2)^{-1}$ (2D) { $\theta^{st} = (\beta + 3)^{-1}$ (3D)}.

It is obvious that the interval of values β is $-3/2 < \beta < 0$ (2D) { $-2 < \beta < 0$ (3D)}. The stimulation is stronger if the exponent β is smaller. The weakest stimulation is $\beta = 0$. It has the same expansion rate as spontaneous turbulence. The strongest possible stimulation has $\beta = \beta_{homo} = -3/2$ (2D) { -2 (3D)}. It corresponds to the homogeneous noise. It is homogeneous at all scales λ, because in this case the relative changes $\varepsilon_\lambda^{st} = \eta_\lambda^{st} / \lambda$ are the same for all scales (the homogeneous noise is of course transversally homogeneous as all considered perturbations). Stronger perturbation can not be imposed. The perturbation with $\beta < -3/2 \{ < -2 \}$ strongly distorts the unperturbed state. In this case the initial state far deviates from the state with two semi-infinite spaces separated by almost plane boundary.

6 DISTURBANCES HOMOGENEOUS IN ALL WAVELENGTHS/SCALES – HONOGENEOUS NOISE

It should be emphasized that the homogeneous noise is nondimensional. It does not contain the dimensional scale λ_*. The stimulative non-homogeneous ($\beta_{homo} < \beta$) spectra contain the scale λ_*. The spontaneous case is also non-homogeneous. Its scale is λ_0. The exponent θ of the rate of expansion (1.1) in the homogeneous case is $\theta = 1$ (2D, 3D) [6]. It corresponds to the fastest possible rate of large scale mixing.

7 SUMMARY

Development of Richtmyer-Meshkov mixing from the random perturbations of *general* form has been considered. General or typical forms means that the perturbation is transversally *homogeneous* and has some *finite* transverse scale (scale of initial roughness of the contact). Corresponding motion has been called *spontaneous* Richtmyer-Meshkov turbulence. Its expansion exponents are $\theta = 2/5$ (2D) and $\theta = 1/3$ (3D) (Section 2). They are the same for the upper and lower expansion fronts and do not depend on the density ratio. The expansion law $h \propto t^\theta$ may have the logarithmic corrections: $h \propto (\log t)^\phi t^\theta$ (Section 3). The *spontaneous* and *homogeneous* turbulences are the most interesting cases. The first starts from small scale roughness (Sections 2,3,4) while the other is of the nondimensional nature and does not have any distinctive scale (Sections 5,6). They form two limits for the stimulated Richtmyer-Meshkov mixing.

REFERENCES

[1]   Dimonte, G., Ramaprabhu, P. and Andrews, M. 2004. Dependence of self-similar Rayleigh-Taylor growth on initial conditions. 9th International Workshop on the Physics of Compressible Turbulent Mixing, Cambridge, UK, 19-23 July 2004, Abstracts, p. 26; http://www.damtp.cam.ac.uk/iwpctm9/

[2]   Dimonte, G. 2004. Spanwise homogeneous buoyancy-drug model for Rayleigh-Taylor mixing and experimental evaluation. *Phys. Plasmas* 7, pp. 2255-2269.

[3]   Youngs, D.L. 2004. Effect of initial conditions on self-similar turbulent mixing. 9th International Workshop on the Physics of Compressible Turbulent Mixing, Cambridge, UK, 19-23 July 2004, Abstracts, p. 123; http://www.damtp.cam.ac.uk/iwpctm9/

[4]   Shvarts, D., Oron, D., Kartoon, D. et al. 2000. Scaling laws of nonlinear Rayleigh-Taylor and Richtmyer-Meshkov instabilities in two and three dimensions. *C.R. Acad. Sci. Paris*, t. **1**, Serie IV, pp. 719-726.

[5]   Inogamov, N.A., Oparin, A.M., Dem'yanov, A.Yu., Dembitskii, L.N., and Khokhlov, V.A. 2001. On stochastic mixing caused by the Rayleigh-Taylor instability. *Journal of Experimental and Theoretical Physics*, **92**(4), pp. 715-743.

[6]   Inogamov, N.A. 1999. The Role of Rayleigh-Taylor and Richtmyer-Meshkiv Instabilities in Astrophysics: An Introduction. *Astrophysics and Space Physics Reviews*, **10**, part 2, pp. 1-335.

[7]   Inogamov, N.A. and Oparin, A.M. 1999. Three-dimensional array structures associated with Richtmyer–Meshkov and Rayleigh–Taylor instability. *Journal of Experimental and Theoretical Physics*, **89**(3), pp. 481-499.

e-mail: `nail-inogamov@yandex.ru`

Gravitational and Shear Turbulence of Two-Phase System Flowing Through Wide Inclined Pipes

Alexander DEMIANOV[1], Nail INOGAMOV[2] and Alexei OPARIN[3]

[1]Moscow Institute for Physics and Technology, Dolgoprudnii, Moscow region, Russian Federation
[2]Landau Institute for Theoretical Physics, Chernogolovka, Moscow region, Russian Federation
[3]Institute for Computer Aided Design, Moscow, Russian Federation

Abstract: The IWPCTM have started from considering Rayleigh-Taylor and Richtmyer-Meshkov instabilities. After some delay problems concerning Kelvin-Helmholtz instability and shear mixing also have been included. In applications there are the cases where a combination of Rayleigh-Taylor and Kelvin-Helmholtz instabilities (gravity and shear mixing together) appears. But another case is much more important for applications. In this case Kelvin-Helmholtz instability competes with internal gravity waves (shear mixing against stabilizing influence of buoyancy factor). In the last case there is the critical (or threshold) value of Richardson number which separates stable (shear is weaker than gravity stabilization) and unstable (shear is stronger than gravity stabilization) cases. Very interesting situation arises when we consider transport of two-phase system through wide pipes. Here some surprising flows exist which combine Richardson like flow (shear against gravity waves) together with Rayleigh-Taylor type flow with rising up bubbles of light fluid. There are gas-liquid and liquid-liquid cases. They differ in density ratio μ of light to heavy phases. A wide pipe means that capillary scale is much less than a pipe diameter D. There are beautiful regimes with large (many pipe diameters) gas pockets separated by liquid slugs in the gas-liquid case. There are interesting changes of regimes when a ratio of transportation velocity $v_Q = Q/S$ to gravitational velocity $v_g = \sqrt{(1-\mu)gD}$ varies, where Q is the volumetric flowrate, S is the cross-section area. Flow changes from slug to churn and to annular flow as the ratio v_Q / v_g grows. In this report we will present short review of known results and what was done new by us.

1 INTRODUCTION

There is wide scope of important topics considered by the IWPCTM. It is written "this workshop focuses on fundamental aspects of turbulent mixing in flows subject to destabilising acceleration". It is known also that the shear mixing by Kelvin-Helmholtz instability is among the topics of the workshop. This is exactly the set of physical ingredients which are important for studies concerning motion of two-phase mixtures in pipes. In the Rayleigh-Taylor problem we have vertical "pipe" filled with light and heavy fluids below and above initially plane contact boundary. For the vertical pipe the inclination angle is $\alpha = 90^0$. Similar problem is studied for the inclined ($-90^0 \leq \alpha \leq 90^0$) pipes transporting two-phase mixtures. Negative and positive inclinations correspond to downward and upward motion, respectively.

In the pipes there is *flow* of light and heavy phases. This is important complicative difference with the more simple case of the Rayleigh-Taylor instability where light and heavy phases only interpenetrate each other. This means that in the Rayleigh-Taylor case the parts of light and heavy substances located far from the mixing region are at rest relative to the pipe walls – volumetric flowrate of mixture through pipe is absent. In the Rayleigh-Taylor or Richtmyer-Meshkov cases we study the Cauchy problem - the problem with initial data where interpenetration gradually develops in time. In the two-phase hydraulics the "steady in average" problem of transportation of turbulent two-phase systems is interesting. In this problem the flowrates of the phases are fixed in time but flow fluctuates significantly around its mean values at frequencies $\sim v_Q / D$, $\sim v_g / D$.

We think that the two-phase hydraulics may be used for testing of computer algorithms and codes. Indeed, there are serious questions about description of the rate of transformation of chunk mixture into molecular mixture by numerical codes. This rate influences the computer estimates of the alpha coefficient ($h_+ = \alpha_+ \text{At} g t^2$) for Rayleigh-Taylor self-similar ($h/t^2 \propto g$) mixing [1,2]. It may be so that too low values of the alpha coefficient ($\alpha_+ \approx 2\%$) appear due to

too high fine mixing rate in the computer simulations [1]. {Another plausible suggestion explains slow mixing in computer simulations by presence of the almost inevitable small amplitude long-wavelength noise in the experimental device [1,2]}. Similar problems with mixing of light and heavy phases and with back separation of them exist in the two-phase hydraulics (there are Taylor bubbles with sizes $\simeq D$ at Weber numbers $We \sim 10^4$). It is not well understood how these mixing and separation depend on the number We which characterizes the importance of surface tension.

2 LARGE OR TAYLOR BUBBLES IN RAYLEIGH-TAYLOR INSTABILITY AND IN INCLINED PIPES

Analysis of development of bubble and jet structure after periodic perturbation is basic in the theory of Rayleigh-Taylor instability. Let's consider 2D case with small density ratio $\mu = \rho_l / \rho_h$ and impose velocity perturbation with the x-component of velocity $\propto \cos(\pi y / D)$ onto the initially plane contact $x = 0$ separating ρ_l, ρ_h fluids. Then periodicity on the axis y and symmetry $y \to -y$ allows to restrict the region of motion to the "pipe" (the strip) $0 < y < D$, $-\infty < x < \infty$, where x and y are the longitudinal and transverse axes. Let the sign of longitudinal velocity is positive at the x-axis. Then the half of the bubble will rise up along the x-axis while the half of the jet will go down along the straight line $y = D$. Similar picture for the inclined pipe is shown in Fig. 2.1. In the inclined case the
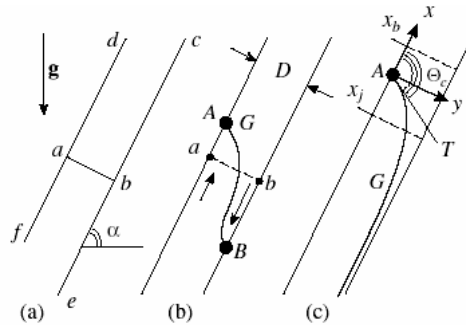
Fig. 2.1. The initial (a), the transition (b), and the final steady-state (c) stages of development of the bubble-jet pair

axes x, y are not the vertical and horizontal axes but they remain the longitudinal and transverse axes. After some transition the steady-state stage with steady shape of the bubble nose and constant bubble rise velocity $u(\alpha)$ establishes. In Fig. 2.2 (left) development of the bubble-jet pair for inclinations $0^0, 30^0, 90^0$ is presented (arrows are the $\vec{g}$ vectors) [3,4]. The evolution (c) corresponds to the Rayleigh-Taylor case. The mushroom size grows with inclination. The thin
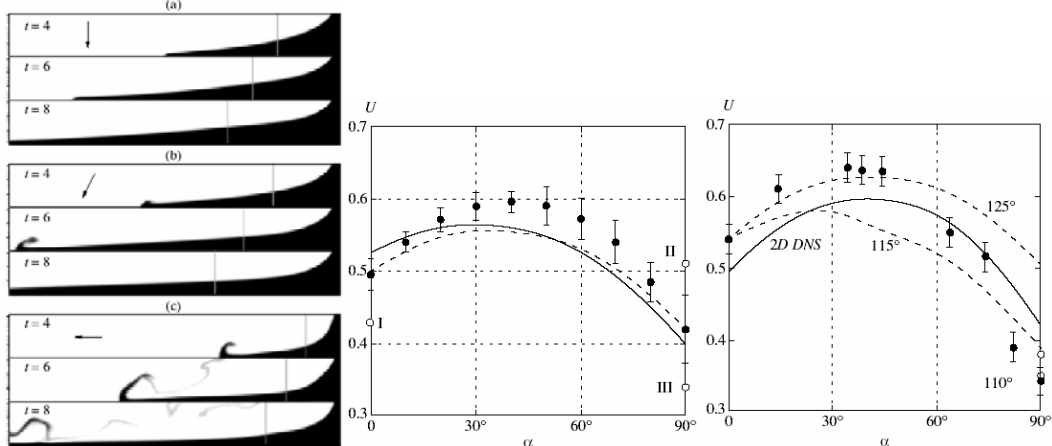
Fig. 2.2. Transition to the steady-state for various inclinations (left). The function $u(\alpha)$ in 2D (middle) and 3D (right)

transverse straight line shows the position of the initial plane. All bubble tips at different time instants are shifted to the same position on the x-axis. The inclination dependence of steady longitudinal rise velocity $u(\alpha)$ of the Taylor bubble is shown in Fig. 2.2 (middle and right).

3 TAYLOR BUBBLE, ITS TRACE BEHIND AND THE "TRAIN" OF SUBSEQUENT TAYLOR BUBBLES

Above the simplest case has been considered {an infinitely long bubble rising in a pipe in fluid which is at rest at infinity $\vec{v}(x = +\infty, y, t) \equiv 0$ }. Flow around the finite bubble (Fig. 3.1) rising in still fluid $\vec{v}(x = \pm\infty, y, t) \equiv 0$ is more complex. Flow near the nose and rise velocity don't depend on the length of the bubble if this length is larger than few D. But now the trace appears. Matter in the narrow jet streaming around the bubble is accelerated up to high velocities.

Fig. 3.1. Transition to steady-state rise. One finite bubble in the "infinitely" long pipe, $\alpha = 45^0$, $\mu = 0.1$

Therefore there is a long (several tens of D) trace behind the bubble. Let there is flowrate of heavy fluid $Q = v_Q S$, $u(x = \pm\infty, y, t) = v_Q$. There is no difference with the case in Fig. 3.1 (after Galilean transformation) if the pipe walls are ideal (without friction) as in the case of Rayleigh-Taylor half of the bubble (Fig. 2.2, left, c) where the walls are lines of symmetry. In viscous fluid (no-slip walls) there are some insignificant modifications. Real complexity begins when flowrates of both phases Q_l, Q_h are non zero. The situations are very different for liquid-liquid $\mu \sim 1$ and gas-liquid $\mu \ll 1$ systems. Here only the most difficult case $\mu \ll 1$ is considered. Complexity is connected with finite flowrate of gas phase Q_l. Flowrate Q_h of liquid (heavy) phase is less important. Let's consider motion of two bubbles

Fig. 3.2. Two bubbles in the long pipe, $\alpha = 45^0$. (1) Initial state, (2) non-interacting bubbles {non-interacting because the trace of the upper bubble is shorter than the liquid slug between the bubbles}, (3) the influence of the trace of the upper bubble on the lower bubble begins, (4,5) due to shear in the trace of the upper bubble the lower bubble rises faster than the upper bubble – the distance separating them decreases, (6) merging of two bubbles into one bubble

in still liquid in infinitely long pipe (Fig. 3.2) $u(x = \pm\infty, y, t) = 0$ before the consideration of the case $Q_l \neq 0$. The figure 3.2 explains how instability in the chain (or "train") of bubbles works (Fig. 3.3). The chain consists of equal gas bubble – liquid slug pairs. The chain corresponds to the case $Q_l \neq 0$. Instability of the periodic chain appears if the pairs in the chain are not exactly equal. Development of this instability leads to merging of neighbour bubbles into one bubble. Thus the lengths of the bubbles and the lengths of the liquid slugs grow. Influence of the upper bubble on the lower one weakens when length of the slug increases. This decreases the increment of the merging instability. Trains with very long bubbles and very long slugs (many tens of D) establish in that way.

The figure 3.3 presents important model of the train with equal pairs. In incompressible fluid this train corresponds to the periodic bubble-slug chain. We consider one link of this periodic chain. It includes one bubble and one slug. We

Fig. 3.3. Establishing of steady-state flow of the periodic slug chain, $\alpha = 20^0$. Time increases from the upper to the lower frame

take a pipe and impose periodic boundary conditions at the pipe ends (compare – in the cases shown in Figs. 3.1, 3.2 the pipe ends are closed). Thus we obtain periodic model of the infinitely long chain with equal links. In sequence of Figs. 3.3 we see how the bubble exits from the right end of the pipe interval and simultaneously its nose appears at the left end. It is necessary to consider two bubbles and two slugs in the pipe interval with periodic boundary conditions at the ends to explore the merging instability in the periodic chain (two slightly different links in one interval, difference between links grows due to development of the merging instability). Results of this simulation need separate presentation.

Analysis of results for the periodic chain (Fig. 3.3) shows that steady-state bubble rise velocity $u(L_{slug}, L_{bubb}, \alpha)$ in

the chain is very significantly larger (2-3 times) than velocity $u(\infty, \infty, \alpha)$ for the solitary bubble shown in Figs. 2.2.

This is due to shear created by the upper bubble. At the same time it should be emphasized that velocity $u(\infty, \infty, \alpha)$ is

rather insensitive to the inclination and even to dimension! The 3D case shown in Fig. 2.2 corresponds to the cylindrical pipe. One of us (A.M.O.) is grateful to the Russian Foundation for Basic Research (project No. 06-01-00558) for support.

REFERENCES

[1]   Youngs, D.L. 2004. Effect of initial conditions on self-similar turbulent mixing. 9th International Workshop on the Physics of Compressible Turbulent Mixing, Cambridge, UK, 19-23 July 2004, Abstracts, p. 123; http://www.damtp.cam.ac.uk/iwpctm9/

[2]   Dimonte, G., Ramaprabhu, P. and Andrews, M. 2004. Dependence of self-similar Rayleigh-Taylor growth on initial conditions. 9th International Workshop on the Physics of Compressible Turbulent Mixing, Cambridge, UK, 19-23 July 2004, Abstracts, p. 26; http://www.damtp.cam.ac.uk/iwpctm9/

[3]   Inogamov, N.A. and Oparin, M.A. 2003. Bubble motion in inclined pipes, *JETP*, **97**(6), pp. 1168-1185.

[4]   Inogamov, N.A. and Oparin, M.A. 2003. Wedge and conic singularities on the free surface of a fluid: the dynamics of Rayleigh-Taylor bubbles and bubbles near the wall of an inclined tube, *Doklady Physics*, **48**(10), pp. 576-579.

Numerical Simulation of the Experimental Richtmyer-Meshkov Instability[1]

Jing-Song Bai, Li-Yong Zou, Ping Li, Duo-Wang Tan, Wang Tao and Chen Sen-Hua

National Key Laboratory of Shock Wave and Detonation Physics, Institute of Fluid Physics, CAEP, P.O. Box 919-105, Mianyang, Sichuan, P. R. China, 621900

bjsong_mail@21cn.com

Abstract:

In this paper, the code MFPPM (Multi-Fluid Parabolic Piecewise Method) employs to simulation of the Richtmyer-Meshkov instability (RMI). The basic algorithm is an operator split two-step high-order Godunov PPM method. The algorithm captures, but does not track, the interfaces between distinct materials while maintaining a VOF representation of the constituent materials. We simulated the two experimental modes, one is from Ref [3] and the other is from our Laboratory for Shock wave and Detonation physics (LSD). We also described our experiments and applied the MFPPM to simulation of the instability of the jelly surfaces under the imploding drive. Shape, position, velocity and acceleration of the outer and the inner surfaces at top-bottom of the jelly experimental and numerical results are given. For analyzing the numerical particularly and comparing to the experimental results, the basic physics phenomena and numerical images are excellent consistent each other.

Key Words: Richtmyer-Meshkov Instability , PPM, MultiFluid, VOF

Experiments and numerical simulations are important implements in researching of the RMI [1,2]. Jelly experiment is one of the basic experiments for RMI. Also, various techniques emerged to predict the position of the instability interfaces during the solution in time and fall into of two categories. These are interface tracking methods, including moving mesh, front tracking and particle tracking schemes; and interface capturing method, which include volume of fluid (VOF) and level set techniques. We study jelly experimentally and numerically to learn how mix develops in cylindrical geometry. In this paper we study RMI in cylindrical geometry. We applied the high-resolution compressible multi-fluid PPM method to simulation of the instability of the jelly surfaces under the imploding drives. To verify our code MFPPM [6], we simulate two experiments from Ref [3], and obtain the numerical results of the jelly agreement with that experiment and simulation. Our experiment is different from Ref [3], which the outer and the inner surfaces of the jelly are set by mode numbers 10, amplitude 1 mm in top-top and top-bottom initially. Emphasis is on feed-thru of perturbations from one surface to another in cylindrical geometry. Shape, position, velocity of the outer and the inner surfaces of the jelly computational results are given; radius of the inner and outer surface and the basic physics phenomena of the jelly are consistent with our experiment well.

The code MFPPM employs an operator-split piece-wise parabolic method [4], which is part of the family of higher-order Godunov methods. This method accurately follows shocks by reducing the diffusion present at the discontinuity. The basic algorithm of the MFPPM is a two-step Euler higher-order finite volume scheme to the multi-fluid hydrodynamic equations system. The first step is Lagrange step in which the computation cells distort to follow the material motions, and the second step is Remap step where the distorted cells are mapped back to the Euler mesh. This two-step Lagrange/Remap algorithm can be divided into a four-step calculations: ① the piecewise parabolic interpolation of physical quantities, ②

---

approximately solving Riemann problems, ③ evolution of the Lagrange equations and ④ mapping the physical quantities back onto the Euler meshs. The multi-fluid interfaces are captured by using the volume of fraction (VOF) method [5]. We extend the process to 2D and 3D cases by using the operator-split techenique.

The first computational experimental model from Ref [3] is simulated by MFPPM. The cylindrical jelly is imploded by an explosive gas such as oxyacetylene. The thickness of the jelly is 1.5 cm with an outer radius of 5.5 cm. The oxyacetylene explosion as an energy source which was added to the gas (adiabatic index $\gamma = 1.21$) over a 10 μs period to bring it up to a pressure of 16.5 atmospheres. A sinusoidal perturbation having the form $\eta_0 \cos(m\theta)$ was added to the outer surface of the jelly. The amplitude η_0 is set 0.1 cm, while the mode number m was chosen to be 6 (only single-mode perturbations were applied). In Fig.1 we show snapshots of the Ref [3] and MFPPM simulation, and in Fig. 2 we show the evolution of the inner and outer surface perturbations as functions of time. We see that there is good agreement between simulation and experiment.
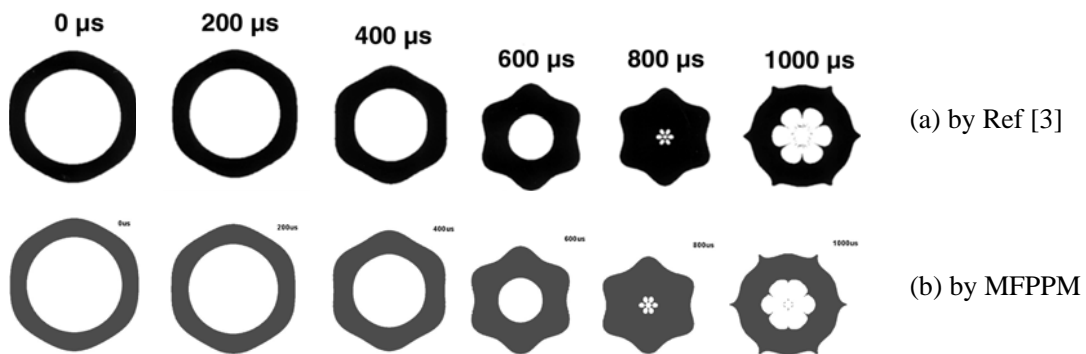
Fig.1 Snapshots of the implosion and bounce of the jelly as calculated by Ref [3] and MFPPM.
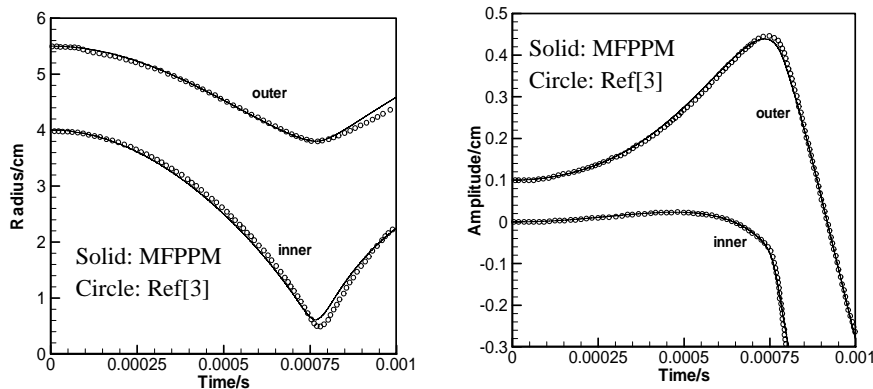
Fig.2 Comparison of the radius and amplitude of the jelly as function of time.

The second computational experimental model is from our LSD. The outer and the inner surfaces are both set sinusoidal perturbation and amplitude 0.1 cm with top-top and top-bottom initially, while the mode number m was chosen to be 10. Emphasis is on feed-thru of perturbations from one surface to another in cylindrical geometry. In Fig.3 we show the MFPPM simulation results, include evolution of the inner and outer surface perturbations amplitude, radius, velocities and accelerations as functions of time. Especially, the radius of the inner and outer surface experiment and numerical results are given in Fig.3 (a). It is shown that the inner surfaces are good agreement with our experiment, and the outer surfaces are poor at the time great than 820μs (may be invisible of mixing). In the top-top model, the radius of the inner surface reaching a maximum value of 0.548cm at time 763.88μs, and the outer surface reaching a maximum value of 3.905cm at time 752.04μs. Also in the top-bottom model, the radius of the inner surface reaching a

maximum value of 0.388cm at time 757.33µs, and the outer surface reaching a maximum value of 3.902cm at time 745.17µs. For the perturbation of amplitude in these two models, see Fig. 3(b), the outer surface has a perturbation of amplitude 0.1cm which grows during the implosion reaching a maximum value of 0.603cm in top-top and value of 0.629cm in top-bottom, after which it undergoes a large phase reversal. This reversal results from the bounce which can be thought of as an impulse which "shocks" the jelly radially outward and hence proceeds from a heavy fluid (jelly) to a lighter fluid (oxyacetylene) at the outer surface, hence the Richtmyer-Meshkov-instability-induced phase reversal. The evolution of the inner-surface perturbation, however, is more subtle: the first is phase reversal and decreases, passes through zero, and has the opposite phase before bounce, then increasing to a maximum value of 0.165cm in top-top and value of 0.16cm in top-bottom, after which it undergoes another phase reversal. A strange phenomenon of the third phase reversal appeared in the top-bottom of inner-surface perturbation (unknown).
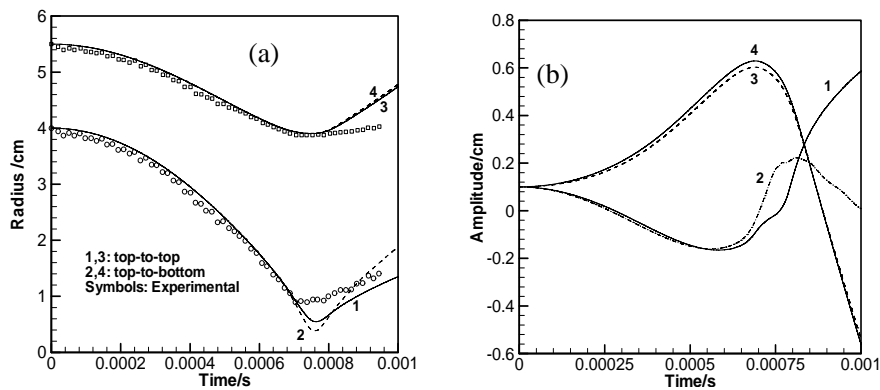
Fig. 3 MFPPM simulation results, as well as it compare the radius of jelly with our experiment.
(1,2: inner;   3,4: outer;   1,3: top-top;   2,4: top-bottom;   in (a) circle and square are experimental)

The velocity of the outer and the inner surfaces of the jelly computational results in top-top and top-bottom by MFPPM are given in Fig.4. It is shown that the evident difference appeared at the bottom of the inner surface in our two models. We can see the position presents at the thickest of the jelly, may be a strong shock wave focus from the outer and inner surface perturbations. Next, we given two images in our experiments at time 400µs, and corresponds simulation by MFPPM in Fig. 5.
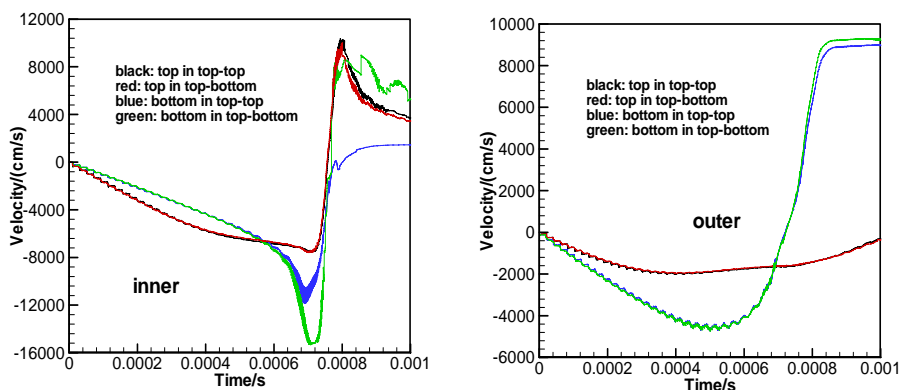
Fig.4 Resultant velocity of the jelly as function of time by MFPPM.

(a) top-top   (b) top-bottom
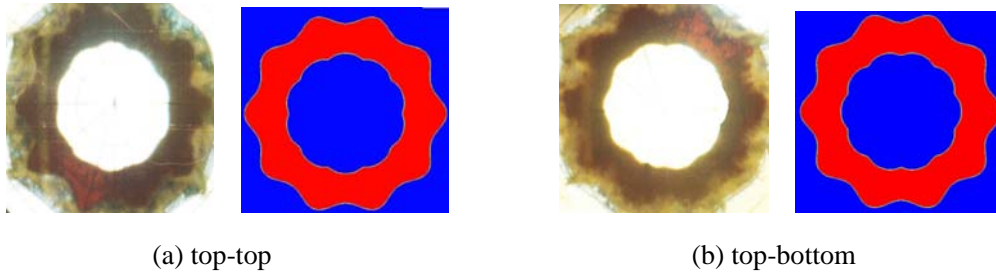
Fig.6 Comparison of our experimental and calculated by MFPPM snapshot at 400μs.

Summary of this paper. The jelly technology has distinctive advantages in 2D hydrodynamic instability studies, especially for converging implosion. It can be used to verify the theoretical models and numerical codes quantitatively. The 2D numerical simulation can reproduce correctly the complicated experimental process. Its results accord with the experiment quantitatively for the linear stage, and qualitatively for the nonlinear stages. In the experiments on the interaction of perturbations on outer and inner boundaries, an interesting phase reverse of inner perturbation has been observed.

References

1   R D Richtmyer. Taylor instability in shock acceleration of compressible fluids, 1960, Pre Appl Math 13,297.

2   E E Meshkov. Instability of the interface of two gases accelerated by a shock wave, 1969, Fluid Dyn. 4,101.

3   Hirt C W and Nichols B D. 1981, *J Comput Phys*, 39,201

4   Colella P, Woodward P. The Piecewise Parabolic Method (PPM) for gas dynamical Simulations[J] . J comput Phys, 1984, 54: 174-201

5   K O Mikaelian. Rayleigh-Taylor and Richtmyer-Meshkov Instabilities and Mixing in Stratified Cylindrical Shell, UCRL-JRNL-204014, Lawrence Livermore National Laboratary, 2004

e-mail: `Georges.Jourdan@polytech.univ-mrs.fr`

Experimental observations of the reflected shock effects on an accelerated gas bubble interface

Guillaume LAYES[1], Christian MARIANI[1], Georges JOURDAN[1], Lazhar HOUAS[1], François RENAUD[2] and Denis SOUFFLAND[2]

[1] *Polytech'Marseille - Dpt Mécanique Energétique, IUSTI/UMR CNRS 6595, Université de Provence, Technopôle de Château-Gombert, 5 rue Enrico Fermi, 13013 Marseille, FRANCE*
[2] *CEA/DAM Île-de-France BP 12 91680 Bruyères-le-Châtel, FRANCE*

Abstract: An experimental investigation of the shock and re-shock gas bubble interactions have been undertaken in a shock tube coupled with a high speed camera shadowgraph device. Positive, negative and close to zero density jumps across the bubble interface have been considered. Qualitatively, observations show, in all cases, a deceleration, even a stop, for the close density case, of the inhomogeneity and an increase of the mixing process after the re-shock bubble interaction.

1 INTRODUCTION

The interaction of a plane shock wave with a single spherical gaseous inhomogeneity is an example of shock-induced Richtmyer-Meshkov instability with large initial distorsions of the gas interface which is materialized, here, by a soap film. Except the axisymmetric geometry, soap bubble is more acceptable (less effects on the flow) than a mylar or nitrocellulose membrane usually used in plane configuration. These phenomena of shock-accelerated gas flows arise in inertial confinement fusion, supersonic combustion or supernova astrophysics. The aim of the present experimental work is to understand the influence of a re-shock on a previously accelerated inhomogeneity. It follows a previous study focussed on the incident shock wave acceleration of the bubble [1], [2].

2 EXPERIMENTS

Experiments were conducted in the T80 shock tube, previously used for incident shock/bubble interaction experiments. In the present work, to anticipate and to be able to observe the interaction between the reflected shock wave and the distorting bubble, the end-wall was moved in order to reduce the experimental chamber length from 80 cm to 35 cm. A high speed shadowgraph picture device was coupled with the shock tube and allows to observe the interaction process on a 30 cm long field by taking 100 frames during 7 ms (70 μs between 2 consecutive frames). We have investigated close to zero, negative and positive density jumps across the interface. To obtain such density gradients, bubbles were filled respectively with nitrogen, helium and krypton. The surrounding gas was always air at atmospheric pressure and ambiant temperature. Regarding to the results obtained previously [1], [2], we chose to investigate only two Mach number values: 1.2 and 1.7.

2.1 Close density configuration: Nitrogen bubble in air (A= -0.05)

In such a configuration, after the incident shock wave passage, the bubble is only submitted to a compression which only affects both bubble length and height, i.e. its diameter. During such a rapid stage, the bubble is also set into motion. The velocity value reached at the end of the compression phase is very close to that of the main flow. The reflected shock then interacts with a stabilized inhomogeneity which is one more time submitted to a new compression. After that, we can observe that the main part of the bubble is stopped, whereas the upstream interface tends to follow the shock wave direction. In fact, we have shown [3] that the nitrogen acts as a light bubble gas at long time, with the appearance of a small penetrating jet due to the light generation of vorticity. Furthermore, the interface is no more smooth and turbulent structures appear, what proves that the second interaction intensifies the mixing. Note that, for a lower Mach number, we have observed a velocity reduction of the bubble. However, the re-shock does not completely stop the inhomogeneity motion.

Fig. 2.1. Experimental shadowgraph pictures of a shocked and re-shocked nitrogen bubble ($D_0 = 4.4$ cm) for incident shock wave Mach number of 1.61 (run ♯ 318).

Fig. 2.2. Experimental shadowgraph pictures of a shocked and re-shocked helium bubble ($D_0 = 3.9$ cm) for incident shock wave Mach number of 1.73 (run ♯ 319).

2.2 Heavy/light configuration: Helium bubble in air (A= -0.8)

During heavy/light configuration interaction, we can observe a compression phase followed by a distortion phase due to vorticity which leads to the reversal of the bubble and then the formation of a double vortex ring.

During the incident reversal phase, an air jet emerges from the upstream vortex ring, where a great quantity of vorticity is concentrated. This downstream ring goes faster than the main air flow, whereas the upstream one travels at a velocity close to that of the surrounding flow. Moreover, for the present experiments, due to the relative high shock wave strength, the downstream ring is bigger than the upstream one. About 430 μs after the incident acceleration, the interaction with the reflected shock wave takes places with the compression of the downstream vortex ring which keeps its travelling forward. 60 μs later, the reflected shock interacts with the upstream vortex ring, involving its compression and its stop in motion. On the picture movie, we clearly observe that the downstream vortex ring motion direction remains the same (forward) whereas the upstream one is the opposite (back). As initial vorticity generated by the incident shock wave mainly concentrates on the downstream vortex ring, its effects are not counterbalanced by those of reflected shock generated vorticity. On the other hand as there is very less vorticity in the upstream ring, the reflected shock wave effects are dominant. To summarize, after the reflected shock wave passage, a compression phase occurs, followed by a generation of vorticity, depending on the considered part of the bubble. The more vorticity there is in the considered vortex ring, the more competition there is between initially generated vorticity and reflected secondary deposited one. Thus, the high initial vorticity area is not stopped by the reflected shock effect but only slowed down. On the other side, the low initial vorticity one is stopped and sets out again even in opposite direction. Experiments at lowest Mach number give similar behaviors even if they are less visible.

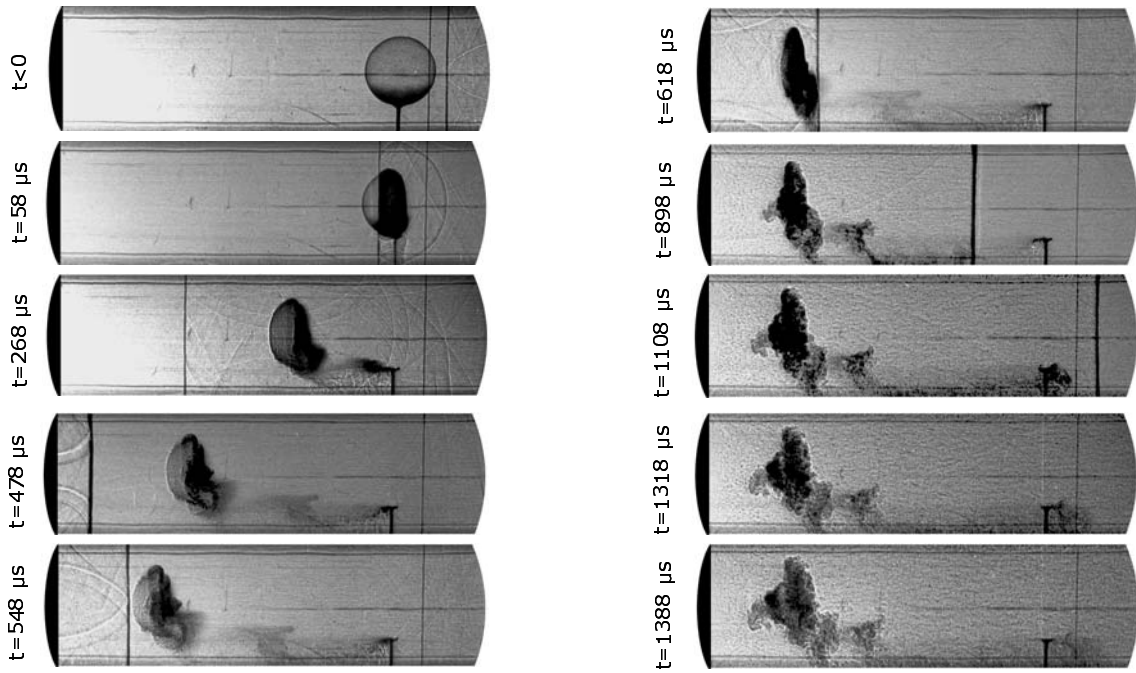### 2.3   Light/heavy configuration: Krypton bubble in air (A= 0.4)
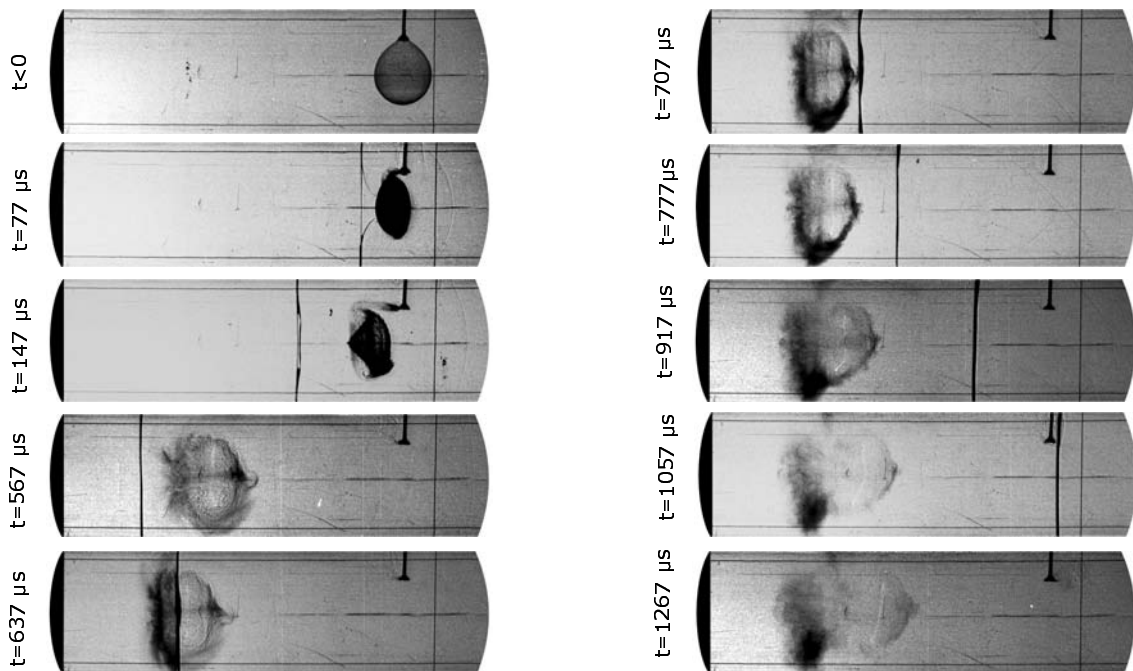
Fig. 2.3. Experimental shadowgraph pictures of a shocked and re-shocked krypton bubble (D_0 = 3.9 cm) for incident shock wave Mach number of 1.59 (run ♯ 321).
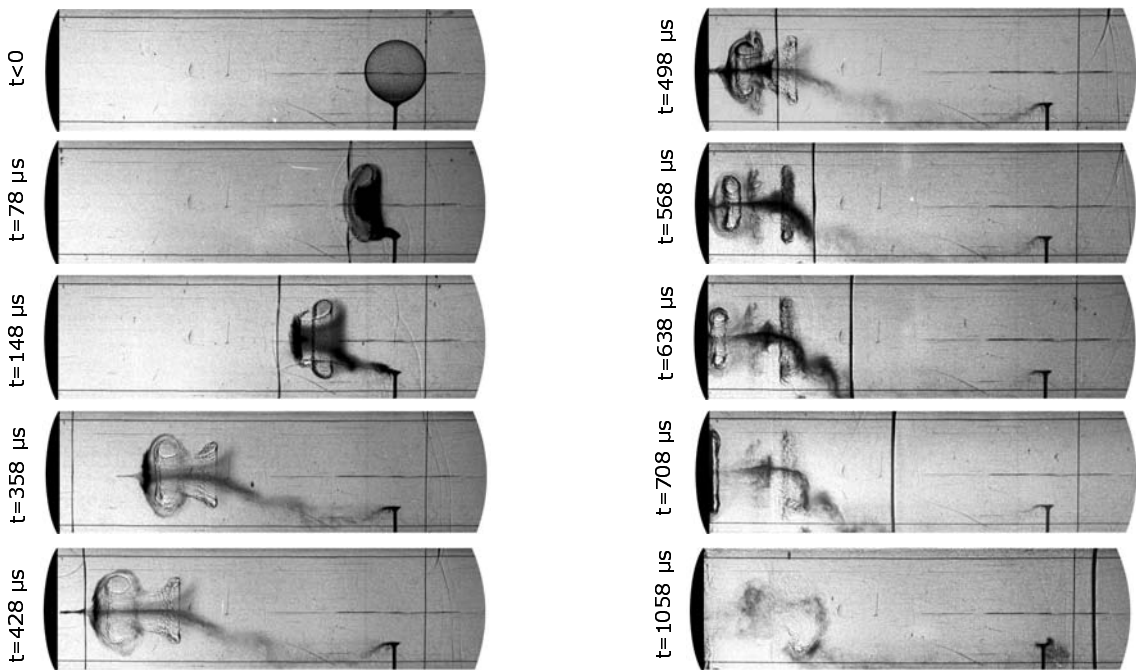
During the incident shock wave interaction with a heavy gas bubble, we can observe also a compression phase followed by a vorticity generation. If the compression phase is similar than the previous case, the difference occurs during the second one. This comes from the generated vorticity which rotating sense is now opposite. This results from the change of the density gradient direction whereas the pressure gradient remains the same. We observe now the formation of filaments on the boundary of the bubble. They roll up on themselves and thus create a vortex ring on the front of the inhomogeneity which grows up whereas the body of the inhomogeneity decreases. Near the vortex, an area of turbulence and mixing also develops. Just before the second interaction, the inhomogeneity has reached its final shape. About 630 μs after the initial acceleration, the passage of the reflected shock wave implies a compression and a stop in the bubble motion. The vortex ring after stretches

but its front interface stays at the same abscissa and only the rear interface seems to go back. Due to this process of stretching , mixing occurs and it then becomes harder to distinguish one gas from the other as an homogenous media appears. Lower Mach number experiments are less interesting because the interaction with the reflected shock wave occurs when the initial deformation process only begins.

3   SUMMARY

An experimental investigation of the shock and re-shock gas bubble interaction has been undertaken in a shock tube coupled with a high speed camera shadowgraph device. Positive, negative and close to zero density jumps across the bubble interface have been considered. Observations show in all cases, first, an increase of the mixing process after the re-shock bubble interaction. This is especially distinguishable in area initially poor in vorticity. Second, a strong or weak, decrease of the bubble motion has also been observed for all the studied configurations. We found that the higher the vorticity concentration is, the lower the area is slowed. For the experimental conditions considered, we point out the difference in area behavior regarding to their initial concentration in vorticity deposited by the incident shock. The more vorticity in an area there is, the less it is affected by the re-shock.

REFERENCES

[1] Layes G., Jourdan G., Houas, L., 2003. Distortion of a spherical gaseous interface accelerated by a plane shock wave. *Phys. Rev. Lett.* **91**.

[2] Layes G., Jourdan G., Houas, L., 2005. Experimental investigation of the shock wave interaction with a spherical inhomogeneity. *Phys. Fluids* **17, 2**.

[3] Layes G., 2004. Etude expérimentale de l'interaction d'une onde de choc avec une bulle de gaz différent du gaz porteur. *PhD thesis*, Université de Provence, Marseille, France.

e-mail: `V.I.Kozlov@vniief.ru`

Non-steady Turbulent Flows' Simulation on the Base of Modified Nikiforov Model

V.I. KOZLOV AND I.V. SAPOZHNIKOV

RFCN-VNIIEF, 607190, Sarov, Nizhni Novgorod region, Russia

Abstract: Modified Nikiforov model is described in which turbulence energy dissipation rate change in SW is determined by longitudinal turbulence macro-scale change with the assumption of turbulent eddies freezing into the fluid. This provides as rapid difference solution convergence so well enough agreement with experimental data. New expressions of turbulent diffusion and turbulent energy exchange' correlations are proposed in which a limit transfer to the case of negligible density fluctuations exists. To initialize TM calculations an algorithm based on the model of small short-wave perturbation growth is proposed.

1 INTRODUCTION

Turbulent flows realized in various devices (for example, such as laser targets in inertial fusion and explosive magnetic generators) are characterized by very high Reynolds numbers Re~$10^5 \div 10^8$, while only relatively simple flows at Re~10^3 are accessible for DNS so practical engineering calculations are based on various turbulence models. Thus Nikiforov semi-empirical turbulent mixing model [1] being among Reynolds stress models is widely used in VNIIEF. In the report we describe some problems appeared with using of Nikiforov model and a model modification which permits to solve these problems. Results of several test simulations show that modified Nikiforov model provides with more physically correct description of the wide class of turbulent flows.

2 NIKIFOROV MODEL FEATURES AND ITS USING PROBLEMS

In Nikiforov model [1] turbulent flow is characterized by density, pressure and temperature averaged over flow realizations' ensemble and velocity, specific internal energy and turbulent mixture species' mass concentrations Favre averaged with density as weight function. Turbulence is described by Reynolds turbulent stresses tensor, turbulence energy tensor, total turbulence energy with account of density fluctuations' effect, turbulence energy dissipation rate, turbulent mass flux and density fluctuations' intensity.

Equations of evolution deduced from mass and momentum conservation are used for turbulent quantities in the model. Representation of turbulent fluxes (third order correlations) contains both turbulent diffusion of small-scale eddies and convective transfer of large-scale energetic eddies. Compressibility, thermal expansion of multi-species mixture and density fluctuations effect on the departure of turbulent mixture moles' acceleration from gas-dynamic acceleration are accounted for in the model.

Practice of Nikiforov model using showed that this model gives satisfactory description of gas and plasma turbulent flows if difference grids used for computation are not too detailed. At the same time calculations accomplished on detailed grids to increase its accuracy and simulation of experiments with measuring of flow velocity revealed some problems of Nikiforov model. In the case of flows with SW this is a strong dependence of difference solution of model equations upon difference grid while calculated evolution of turbulent quantities does not agree with measurements. Besides this the model gives too high TMZ growth rate for incompressible liquids (by 2-3 times greater than experimental data). At last in the model there is no physically adequate way to initialize turbulent mixing simulation (or to set a beginning moment of turbulent mixing calculation and initial turbulent quantities distributions on this moment

Said is illustrated by Fig. 2.1 where the results of simulations are shown for cylindrical Meshkov experiment [1] where TM was observed on cylindrical helium-air interface accelerated by converging SW. Calculations were accomplished on a series of grids with mesh refinement up to 32-fold while initial TMZ width (where initial density fluctuations intensity was set) was conserved. It's seen that calculated zone width does not practically depend on difference grid only until reflected SW arrives on zone while zone width agrees well with the experiment. Turbulence suppression behind SW occurs after TMZ interaction with reflected SW and this suppression is more as mesh size is less.

3 MODEL MODIFICATION

Thus difference solution of model equation does not converge in simulation of flows with SW (more exactly, solution behind SW degenerates into trivial one in the limit of grid with infinitesimal meshes). This defect is caused by following features of Nikiforov model. Turbulence effect on difference SW structure is negligible so SW width is completely determined by dissipation and dispersion of difference scheme used. Balance equations of all turbulent quantities except for turbulence dissipation rate Q are linear in gas-dynamic gradients so these quantity changes in SW do not practically depend on mesh size (to prove this one must use reference frame where SW is fixed and integrate balance equations on shock transition). At the same time balance equation of Q is quadratic in gas-dynamic gradients so dissipation rate change in SW is inversely proportional to SW width or mesh size. Thus turbulence energy does not change and dissipation rate increases behind SW with grid refinement. This results in turbulence suppression behind SW for detailed enough difference grid. To eliminate this model defect a modification was proposed in [2] in which Q change in SW is determined by turbulence energy e and longitudinal turbulence macro-scale L_t' changes with the assumption of turbulent eddies freezing into the fluid. Such modification provides for both rapid difference solution convergence and well enough agreement with experimental data.

Too high growth of incompressible liquids TMZ is caused in Nikiforov model by following reasons. Values of some model constants were chosen arbitrarily in correlations accounting for density fluctuations effect (such as energy exchange tensor and generation terms in balance equation of turbulence dissipation rate). At that model constant in turbulent diffusion coefficient was calibrated on the basis of simulation results for gas tests where the mean strain rate influence (that is <u>velocity fluctuations</u> influence) is the leader effect. At the same time the buoyancy force influence (that is <u>density fluctuations</u> influence) is the leader effect in experiments with incompressible liquids mixing. As a result of incorrect choice of model constants turbulent quantities balance does not agree with phenomenon physics in this case.

In Nikiforov model a representation

$$L_{ik} = \gamma \frac{Q}{e}\left(e_{ik} - \frac{1}{3}e_{mm}\delta_{ik} \right) \tag{3.1}$$

is used for the energy exchange tensor where γ is a function accounting for gas-dynamic gradients' effect on energy exchange rate. In modified model expression

$$\gamma = \gamma_0 + \gamma_1 X_t \tag{3.2}$$

is used where

$$X_t = -2\frac{V_{ik}e_{ik}}{Q} + \frac{f_1 \vec{G}\vec{W}}{Q}. \tag{3.3}$$

Here V_{ik} is strain rate tensor, $e_{ik} = \langle u'_i u'_k \rangle / 2$ is "turbulent energy" tensor, $\vec{G} = \nabla P / \rho$, $\vec{W} = \langle \rho' \vec{u}' \rangle / \rho$, f_1 is a function accounting for density fluctuations' effect on turbulent mixture moles' acceleration. Parameter X_t characterizes sui generis turbulence sub-criticality (if $X_t > 1$ then turbulence develops, if $X_t < 1$ then turbulence is suppressed) as it's seen from turbulence energy balance equation

$$\cdot \frac{de}{dt} = Q\{X_t - 1\}. \tag{3.4}$$

$\gamma_0 = 2$ and $\gamma_1 = 1/4$ values were chosen in (3.2) on the basis of simulation of turbulence deformation in tunnel with variable cross-section [3].

If incompressible liquids' mixing develops under constant gravity than longitudinal turbulence macro-scale satisfies inequalities

$$0 < \frac{dL_t}{dt} \le \frac{dL_{TMZ}}{dt} \tag{3.5}$$

where $L_t = \left(2e\right)^{3/2} / Q$ and $L_{TMZ} = \beta A g t^2$. From this one can get a Q balance equation term

$$\frac{dQ}{dt} \approx \frac{3}{2} f_1 \vec{G} \vec{W} \frac{Q}{e},$$ (3.6)

which accounts for the buoyancy forces' effect and contribution of which is about 1.5 times greater than it was in initial model.

At last in the modified model there is a new representation of turbulent diffusion coefficient

$$D_t = \mu_t \frac{ee_1}{Q} + \tilde{\beta} \frac{\rho'}{\rho} |\vec{W}| L_t \approx \mu_t \frac{ee_1}{Q} + \beta f_1 \frac{e^{3/2}}{Q} |\vec{W}|,$$ (3.7)

which is similar to turbulence diffusion in two-phase heterogeneous turbulence models [4]. The first term corresponds to turbulent diffusion in the case of infinitesimal density fluctuations and value used in k-ε model is taken for constant $\mu_t = 0.09$. The second constant value $\beta = 0.675$ was calibrated against simulations' results for water and Freon mixing under the constant acceleration in experiments [5]. It is about of value used in two-phase heterogeneous turbulence models.

4 AN INITIALIZATION OF TM CALCULATION

In Nikiforov model to initialize TM calculation in the case of Richtmyer-Meshkov or Raleigh-Taylor instabilities non-zero density fluctuations' intensity values

$$R_0 = \left\langle \rho'^2 \right\rangle / \rho^2 = 0.01 \div 0.02 (\delta - 1)^2 / \delta$$ (4.1)

are posed in some moment in narrow layer nearby the interface while all other turbulent quantities are supposed to be equal to background values (here δ is density ratio). This method has some disadvantages from physical point of view. So an initialization moment, initial level of density fluctuations and initial TMZ width are not exactly determined by it. A choice of these values depends practically entirely on intuition and experience of the researcher. This method works most surely in the case of pure Raleigh-Taylor instability under constant acceleration.

In modified model an evolution of single-mode short-wave interface perturbation with initial amplitude a_0 and wave number k is considered. Toward this end an approximate model

$$\dot{a} = V,$$ (4.2)

$$\dot{V} = -Agka - \frac{\sigma k^3 a}{\rho_1 + \rho_2} - 2\nu k^2 V \text{ if } |ka| < 0.4,$$ (4.3)

$$\dot{V} = -\frac{Agka}{0.6 + |ka|} - \frac{\sigma}{\rho_1 + \rho_2} \cdot \frac{k^3 a}{1 + (|ka| - 0.4)^3} - \frac{2\nu k^2 + C_d k (|ka| - 0.4) |V|}{1 + (|ka| - 0.4)^2} V \text{ if } |ka| \ge 0.4$$ (4.4)

is used in which molecular viscosity ν and surface tension σ are accounted for. Here $g \equiv -\dot{U}_I$ is an effective gravity (where U_I is velocity of the interface under consideration) and $C_d = 1.5$.

An initialization moment of the TM calculation is determined by condition

$$\text{Re} = \frac{|aV|}{\nu} \ge \text{Re}_{crit} \approx 2500$$ (4.5)

where a and V are an amplitude and a growth rate of the perturbation, ν is n effective viscosity of initial mixture. Non-zero initial values of all turbulence quantities are assigned in the layer $|r_j - r_I| \le a$ nearby interface under investigation and initial values are determined by a and V values.

5 SIMULATIONS' RESULTS

Fig. 5.1 shows results of Meshkov cylindrical experiment [1] simulations which are analogous to those shown on Fig. 2.1 (an initial perturbation is determined by $a_0 = 35$ μm and $k \approx 31$ cm^{-1}). It's seen that the model modification provides

for both difference solution convergence and well enough agreement with the experiment.

Fig. 5.2 shows simulation results of experiments [5] in which mixing of water and Freon was investigated under various accelerations of effective gravity. An initial perturbation amplitude $a_0 = 1$ μm was used in simulation (which is a size of micro-in-homogeneities being always in technically pure water) and wave-number corresponds to the quickest mode.

Fig. 5.3 shows simulation results for Meshkov experiment with TMZ merging [1] in which TM development on two flat helium-air interfaces placed nearby and accelerated by flat SW was investigated. It' seen that TMZ merging occurs in initial Nikiforov model visibly later than in the experiment while total TMZ width is less than in the experiment. Model modification gives well enough agreement with the experiment. Notice that TM calculation begins in modified model only after reflected SW passes through both interfaces.

Fig. 5.4 and 5.5 show simulation results for an experiment in which TM development is caused by SW (with M = 1.45) passing through a flat air-SF_6 interface [6] (instantaneous flow velocity was measured in this experiment by laser Doppler velocimetry). It's seen that calculated TMZ width is less by 20% than experimental while a variance of the axial gas mixture velocity is 3 times greater than measured one after reflected SW passing through TMZ. This discrepancy is probably related with following. In the experiment velocities of doped particles were measured by laser Doppler velocimetry and so the axial velocity variance for doped particles was determined while Nikiforov model gives the axial velocity variance for gas mixture. At the same time it's known that velocity of heavy particles moving in fast oscillating flow of light gas differs from gas velocity and, as consequence, axial velocity variances also differs for particles and bearing gas. One can get approximate evaluation for transition coefficient from gas to particle axial velocity variance which is

$$k_{eff} \equiv \frac{\langle u_x'^2 \rangle}{2e_1} \approx \frac{1}{1 + (\omega\tau)^2} \, , \qquad (5.1)$$

where $\omega \approx Q/e$ is turbulent velocity fluctuations' frequency, $\tau \equiv 2\pi(\rho_P + \rho/2)R^2/9\mu$ is a velocity relaxation time for particles with radius R and density ρ_P, ρ and μ are density and dynamical viscosity of gas mixture. Corresponding results for soot particles ($\rho_P = 2$ g/cm^3 and $R = 2$ μm) are shown by the Fig. 5.5. It's seen that well enough agreement with data [6] is obtained now.

5 SUMMARY

We proposed the modification of Nikiforov model which provides for rapid convergence of model equations' difference solution and the method of TM calculation initialization based upon evolution analysis of interface small short-wave perturbation. Simulation results for some test experiments agree well enough with experimental data.

REFERENCES

[1]   Andronov V.A., Bakhrakh S.M., Meshkov E.E., Nikiforov V.V., Pevnitskii A.V., Tolshmyakov A.I. 1982, An experimental investigation and numerical modeling of turbulent mixing in one-dimensional flows. *DAN* **264**, No. 1, pp. 76-82.

[2]   Kozlov V.I. 2006, Simulation of SW/turbulence interactions. 10th *IWPCTM*, Paris, France, July 17-21 2006.

[3]   Uberoi M.S. 1956, Effect of wind-tunnel contraction on free-stream turbulence. *J. of Aeronautical Sciences*, **23**, No, 8, p. 754.

[4]   Ilić M., Wörner M., and Cacuci D.G. 2004, Balance of liquid-phase turbulence kinetic energy equation for bubbly-train flow. *Journal of Nuclear Science and Technology*, **41**, No. 3, p. 331-338.

[5]   Dimonte G. and Schneider M. 1996, Turbulent Rayleigh-Taylor instability experiments with variable acceleration. *Phys. Rev. E*, vol. 54, No. 4, pp. 3740÷3743.

[6]   Poggi F., Thorembey M.-H., Rodriguez G. 1998, Velocity measurements in gaseous mixtures induced by Richtmyer-Meshkov instability. *Phys. Fluids*, v. 10, № 11, pp. 2698-2700
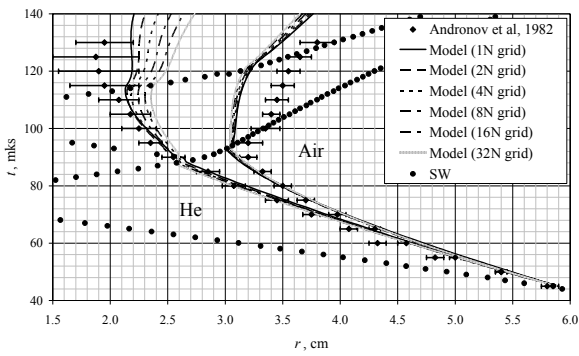
Fig. 2.1. r-t diagrams of TMZ bounds in Meshkov cylindrical experiment (initial Nikiforov model)
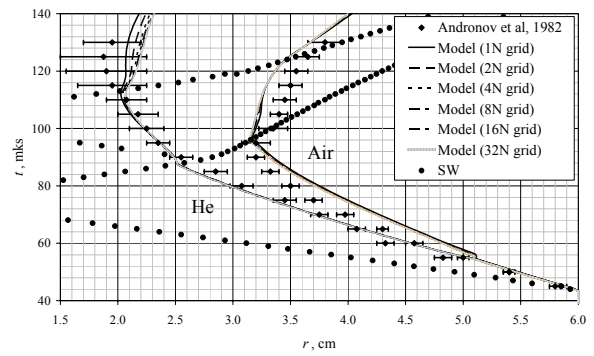
Fig. 5.1. r-t diagrams of TMZ bounds in Meshkov cylindrical experiment (modified model)

Fig. 5.2. Location of water front in Freon versus distance passed by the experimental ampoule for various ampoule acceleration laws (modified model)

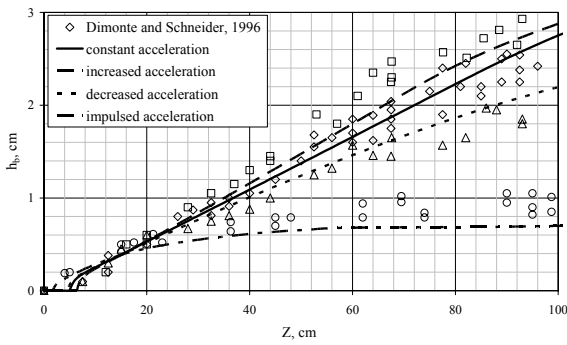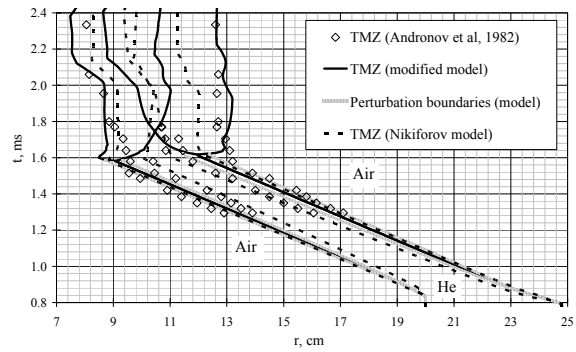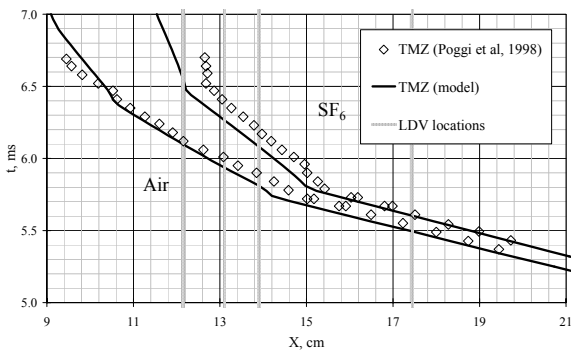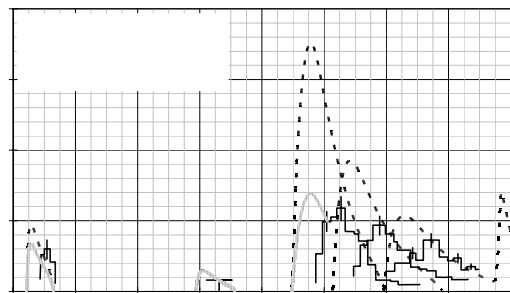**Fig. 5.3.** r-t diagrams of TMZ bounds in Meshkov flat experiment with two TMZ merging

Fig. 5.4. r-t diagrams of TMZ bounds in flat experiment with velocity measurements (modified model)

e-mail: `V.I.Kozlov@vniief.ru`

Simulation of SW/Turbulence Interactions

V.I. KOZLOV

RFCN-VNIIEF, 607190, Sarov, Nizhni Novgorod region, Russia

Abstract: Turbulence energy dissipation rate behind difference SW is shown for Nikiforov model to be inversely proportional to SW width while all other turbulence quantities do not depend practically on difference grid. In the case of grids detailed enough it causes almost complete suppression of turbulence behind SW. Model modification is proposed to eliminate this defect and to get good agreement with experiment.

1 INTRODUCTION

SW/turbulence interactions are interesting from both practical (flow around supersonic aircraft) and theoretical (plasma spread from supernova explosion) points of view. Many experimental, theoretical and numerical papers are devoted to investigation of this problem. Here it is considered on the base of Nikiforov model [1] which is among models with Reynolds stresses and accounts for effects of compressibility and density fluctuations.

2 CONVERGENCE OF NIKIFOROV MODEL'S DIFFERENCE SOLUTION

In a shock transition turbulent stresses are negligible in comparison with momentum flux that is turbulence has practically no effect on the average flow in the shock transition in the case of Reynolds stresses' models. As a result the difference shock structure and, in particular, its width l_{SW} depend only dissipation and dispersion of difference scheme and specific numerical viscosity in use. At that relation $l_{SW} \approx (4 \div 6)\, \Delta x$ holds true with good accuracy where Δx is characteristic size of meshes in the shock transition.

In Nikiforov model balance equations of all turbulent quantities except of turbulence energy dissipation rate Q are linear in mean gas-dynamic quantities' gradients and equation for Q is quadratic in these gradients. Turbulent quantity change in SW is determined by integration of its balance equation over the shock transition. As a result turbulent quantities' changes in difference SW are qualitatively described with meshes refinement ($\Delta x \rightarrow 0$) by relationships

$$\Delta e_1 = o\left(\Delta x^0\right),\ \Delta e_2 = o\left(\Delta x^0\right),\ \Delta W = o\left(\Delta x^0\right),\ \Delta R = o\left(\Delta x^0\right),\ \Delta Q = O\left(\Delta x^{-1}\right). \tag{2.1}$$

Here e_1 and e_2 are mean squares' halves of longitudinal and transversal velocity fluctuations, W is turbulent mass flux velocity, R is density fluctuations' intensity. Thus in Nikiforov model dissipation rate behind SW increases monotonically in reversal proportionality to SW width while difference grid being refined. This results in considerable turbulence suppression behind SW as turbulence kinetic energy change being practically invariable. Thus TMZ growth rate decreases significantly after passing of intensive SW through the zone in the case of simulations with using of difference grids detailed enough.

3 MODEL MODIFICATION

Turbulence kinetic energy change in SW is shown by calculations to be correctly described by Nikiforov model. So to provide convergence of model difference solution in SW one needs a new balance equation of Q which will be linear in gas-dynamic gradients. It can be gotten on the base of following consideration.

Let's suggest that relationship

$$Q \approx \frac{u'^3}{\Lambda} = \frac{(2e)^{3/2}}{\Lambda} \tag{3.1}$$

holds true in SW. Here $e = e_1 + e_2$ is turbulence kinetic energy, Λ is longitudinal turbulence macro-scale. Longitudinal macro-scale is about size of eddies which contain basic part of turbulence energy. Let's also suggest that these eddies are frozen into the fluid moving through SW then one can get equation

$$\frac{dQ}{dt} \approx \frac{3}{2}\frac{Q}{e}\left\{\frac{de_1}{dt} + 2\frac{de_2}{dt}\right\} - Qdiv\vec{V} \tag{3.2}$$

by logarithmically differentiating the freezing-in condition $\rho\Lambda \approx const$ and using (3.1). This equation describes dissipation change in SW. To determine those meshes which are in shock transition following condition is used in calculations. Total change of mass velocity in SW is $\Delta V \approx -\Lambda div\vec{V}$ and at the same time $-\Delta V \square C_S$ where C_S is local sound speed. On the other hand $|\Delta V| \square C_S$ in weak-compressible flows and $\Delta V/C_S > 0$ in rarefaction waves. Therefore condition

$$X = -\frac{\Delta V}{C_S} \square -\frac{e^{3/2}div\vec{V}}{QC_S} \geq X_{SW} \tag{3.3}$$

holds true in shock transition meshes where X_{SW} is model parameter ($X_{SW} \approx 0.1$ on the base of calculations' results).
In Nikiforov model balance equations of some turbulent quantities as they are deduced from mass and momentum conservation there is density gradient. Nikiforov suggested that turbulent mixture moles move adiabatically in developed turbulence so adiabatic density "gradient" $A = \left\{(\partial\rho/\partial P)_S \nabla P - \nabla\rho\right\}/\rho$ is used in [1] instead of relative density gradient $-\nabla\rho/\rho$. In this way non-physical turbulence development is suppressed in stably stratified flows. However moles' entropy is increased as they pass through SW so in modified model very relative density gradient is used in SW meshes.

4 SIMULATIONS' RESULTS

Modification efficiency is illustrated by simulations of an experiment [2] in which isotropic turbulence and steady SW (with $M \approx 3$) interaction was investigated. In simulations $e_1 = e_2 = 0.6723$ m^2/s^2, $Q = 0.2496 \times 10^4$ m^2/s^3, W = 0, R = 0.5×10^{-8} were set before SW. They were calculated on the base of mean square of longitudinal velocity fluctuations and longitudinal macro-scale' values before SW measured in [2].
Fig. 4.1 shows evolutions of mean square of longitudinal velocity fluctuations and turbulence anisotropy that is ratio of root-mean-square values of longitudinal and transversal velocity fluctuations. They were obtained in simulations with using of initial Nikiforov model [1]. (Sequence of difference grids 1N, 2N, 4N, 8N, 16N was used in these simulations in which every grid had doubled number of meshes as compared with previous one. The coarsest grid 1N had 200 meshes and initial meshes' size was 1.5 mm that is 2 times less than SW width in [2].) One sees that difference solution convergence is absent in these simulations and turbulent quantities' evolutions differ even qualitatively from experiment. Rapid turbulence degeneration behind SW shows significant overstating of dissipation rate change in SW.
Fig. 4.2 shows results of similar simulations with using of modified model. Now both rapid convergence of difference solution and well enough agreement with measurements [2] are obtained.
Fig. 4.3 shows evolution of spatial integral turbulence scale obtained on the base of modified model. It should be noted that temporal autocorrelation of longitudinal velocity fluctuations was measured in [2] and temporal integral scale T was calculated using it. Spatial integral scale L was calculated on the base of T using Taylor hypothesis $L = U_x T$. In simulations estimation $T \square e_1/Q$ was used for temporal scale. It's seen that modified model provides good agreement of this parameter with [2] (some descreapency for X > 1 cm is explained by 2D effects).
Fig. 4.4 shows dependence of turbulence kinetic energy amplification just behind SW on density fluctuations' intensity before SW obtained using modified model. Besides of R$_0$ non-zero values of $W = \pm\sqrt{2 \cdot R \cdot e_1}$ were set before SW in these simulations. It's seen that positive correlation $W = \overline{\rho'u_x'}/\overline{\rho}$ before SW causes additional turbulence amplification in SW while negative one inhibits turbulence amplification (it agrees with DNS results [3]).

5 SUMMARY

Modification of Nikiforov model is proposed which provides rapid convergence of model difference solution. Simulations' results agree well enough with experimental data. Also this modification describes correctly influence of density fluctuations before SW on turbulence amplification.

REFERENCES

[1]   Andronov V.A., Bakhrakh S.M., Meshkov E.E., Nikiforov V.V., Pevnitskii A.V., Tolshmyakov A.I. 1982, An experimental investigation and numerical modeling of turbulent mixing in one-dimensional flows. *DAN* **264**, No. 1, pp. 76-82.

[2]   Barre S., Alem D. and Bonnet J.P. 1996, Experimental Study of a Normal Shock/Homogeneous Turbulence Interaction. *AIAA Journal* **34**, No. 5, pp. 968-974.

[3]   Mahesh K., Lele S.K. and Moin P. 1997, The influence of entropy fluctuations on the interaction of turbulence with a shock wave. *Journal of Fluids Mechanics* **334**, pp. 353-379.
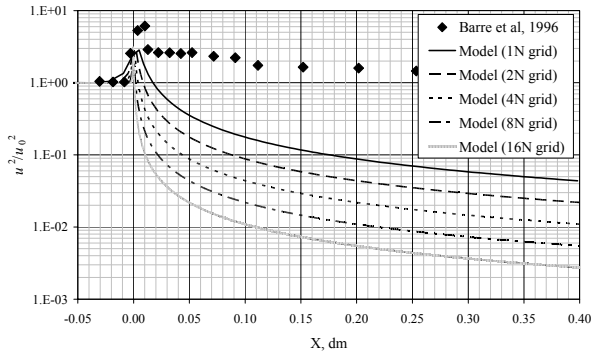
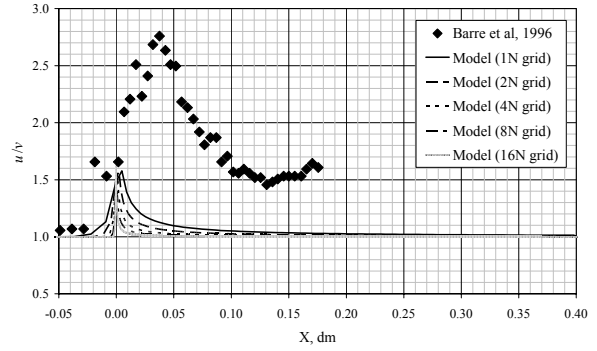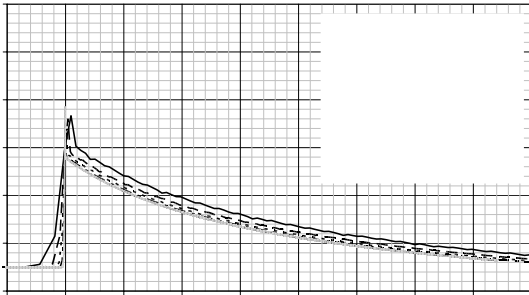**Fig. 4.1.a.** Evolution of $\overline{u_x'^2}$ in SW (initial Nikiforov model)

Fig. 4.1.b. Evolution of $\sqrt{\overline{u_x'^2}/\overline{u_y'^2}}$ in SW (initial Nikiforov model)

Turbulent mixing evolution caused by the passage of a non-stationary shock wave through an interface separating gases with different densities

Yury KUCHERENKO[1], Sergey BALABIN[1], Oleg SHESTACHENKO[1], Anatoly PYLAEV[1] and Oleg SCHILLING[2]

[1] *Russian Federal Nuclear Center – VNIITF, Snezhinsk, Chelyabinsk region, Russia*
[2] *Lawrence Livermore National Laboratory, Livermore CA 94550, USA*

Abstract: Experimental results for turbulent mixing caused by the combined action of the Richtmyer-Meshkov and Rayleigh-Taylor instabilities following the passage of a non-stationary shock wave through an interface separating two gases with different densities are presented. The experiments were performed with combinations of gases having Atwood numbers $A = 0.2$ and $A = 0.8$. The Schlieren method was used to record the turbulent mixing in the region of the contact boundary. The turbulent mixing zone width was determined in the light and heavy gases at different instants of time. The dependence of the mixing zone size on time was determined.

1. INTRODUCTION

The Multifunctional Shock Tube [1,2] was used to experimentally investigate turbulent mixing caused by the successive action of the Richtmyer-Meshkov and Rayleigh-Taylor instabilities at the RFNC-VNIITF together with LLNL on ISTC Project 2716. A non-stationary shock wave was generated in the shock tube to create the conditions for development of both the Richtmyer-Meshkov and Rayleigh-Taylor instabilities following the shock passage through the interface separating different density gases. The non-stationary shock wave initiates the Richtmyer-Meshkov instability, and during the subsequent accelerated motion of the contact boundary, if the shock wave travels from a heavy gas into a lighter one, turbulent mixing caused by the Rayleigh-Taylor instability develops. Stochastic perturbations at the interface are a "seed" for the turbulent mixing evolution. Such perturbations (i.e., arising from the interface geometry and the light and heavy gases velocities) form after a shock wave passage through the interface. The dynamics of perturbation formation relates to the process of destruction of a separating membrane which is directly in contact with the light and heavy gases, and separates them before the unstable state arises. The occurrence of the initial stochastic perturbations of the velocity near the interface is one of the characteristics of the experiments.

2. THE EXPERIMENTAL CONFIGURATION AND THE DIAGNOSTIC TECHNIQUES

The physical and functional schemes of the experiments are presented in Fig. 2.1 and Fig. 2.2. The Multifunctional Shock Tube (MST) was assembled in different sections. The sections form a channel of a square cross-section of sizes $y_k \times z_k = 13.8$ cm $\times$ 13.8 cm. Different one-dimensional gas dynamic flows were realized in the MST channel.

The sections G_1 and G_2 were filled with a light gas of density ρ_1 and a heavy gas of density ρ_2, respectively. The sections with the working gases (WG) were filled by blowing gas in, displacing the air by the light and heavy gases. The composition of the resulting gas mixture was tested by the gas purity control system. The gas filling process was stopped when the air content in the mixture was less than 3%.

The measuring section equipped with optical windows allowed the possibility of taking photo images of the turbulent mixing zone in the region of the interface and determine its size $L(t)$ at different instants of time using the Schlieren method (IAB-451 device).

To check the realized gas dynamic flow in the MST from one experiment to another, the sensors τ_i SW were placed in the G_1 and G_2 sections. These sensors timed the shock wave arrival τ_i at the given coordinate $x = x_{\tau i}$ (see Fig.2.1).

In the plane $x = x_{CB}$ of the WG separating membrane section, a nitrocellulose film of thickness ~ 1 μm was placed against a grid consisting of strong thin strings (the metallic string diameter was $\text{ø}d = 0.005$ cm, and the grid cell size was $\Delta y_{HB} \times \Delta z_{HB} = 0.6$ cm $\times$ 0.6 cm). The initial perturbation zone of size L_0 formed at the plane $x = x_{CB}$ following shock wave passage. The perturbation zone formed in the course of the small-scale destruction of the nitrocellulose film. The maximum size of fragments from the destruction of the nitrocellulose film was $\Delta y_{HB} \times \Delta z_{HB}$ ($\Delta y_{HB} = \Delta z_{HB} \ll y_k$).

The GEM section was filled by a Gaseous Explosive Mixture (GEM) consisting of the stochiometric composition of hydrogen and oxygen, $H_2 + 0.5\,O_2$.

Lavsan films of thickness 50 μm were placed in the planes $x = x_1$ and $x = x_2$ of the GEM membrane 1 and membrane 2 sections respectively. These films leaned against the grids made of thin metallic strings of cell size 1.2 cm $\times$ 1.2 cm and confined the volume occupied by the gaseous explosive mixture. The metallic grids allowed the possibility of small-scale destruction of the lavsan films by a shock or detonation wave. This ensured the one-dimensionality of the gas dynamic flow near the interfaces $x = x_1$ and $x = x_2$.
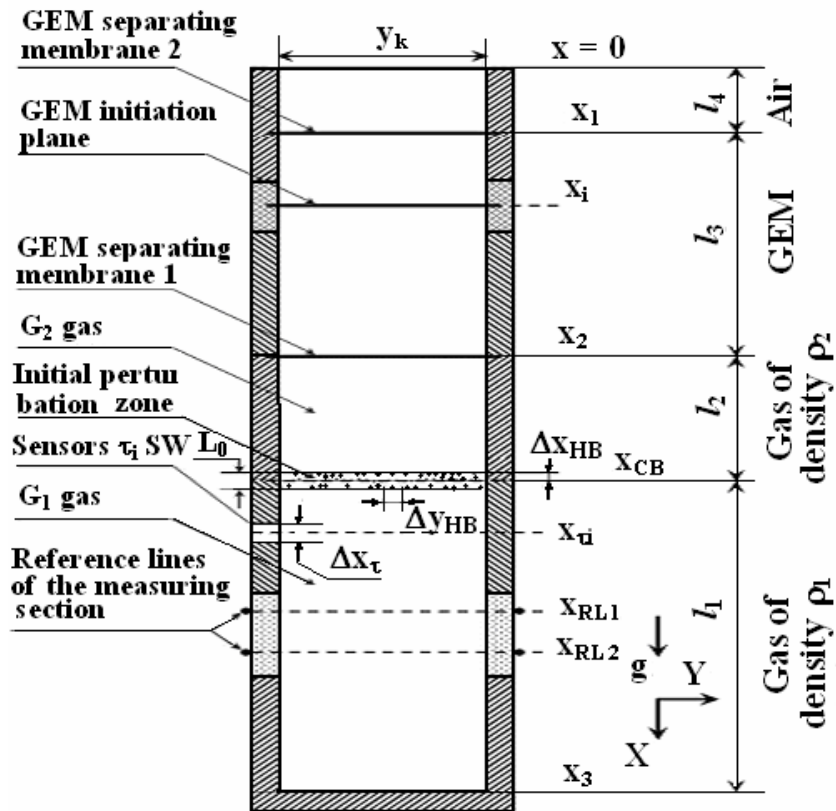
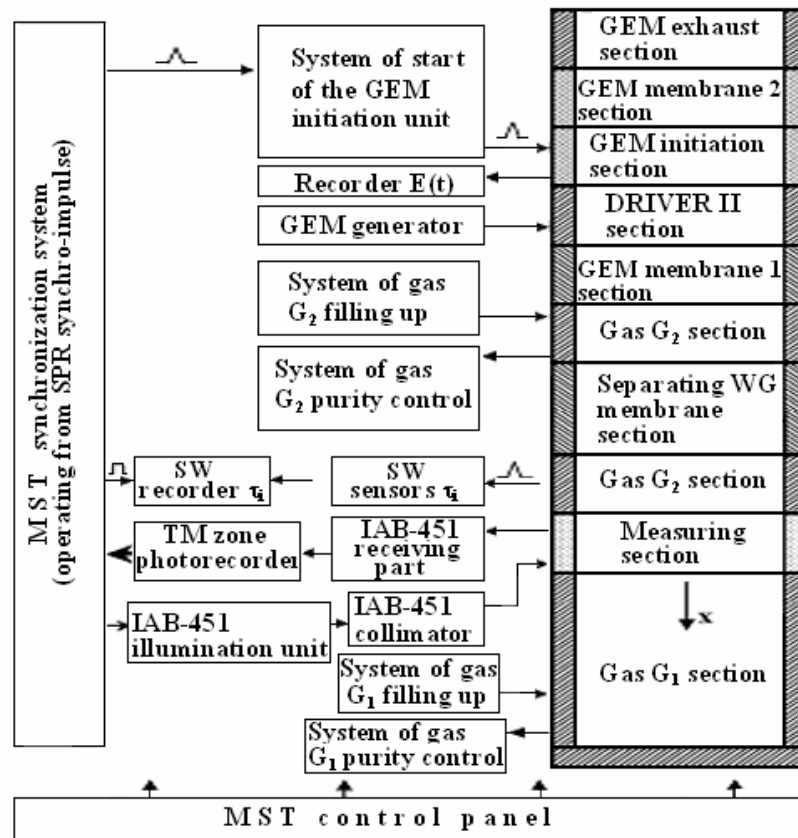**Fig. 2. 1.** Physical schematic of the MST experiments on turbulent mixing

Fig. 2. 2. Functional schematic of the MST experiments on turbulent mixing

In the plane $x = x_i$ of the GEM initiation section, there were 23 copper conductors of diameter 0.01 cm, length $y_k = 13.8$ cm, and spacing 0.6 cm (which were isolated from metallic parts of the MST for 50 kV voltage). The rapid parallel electric burst of the conductors was produced by the GEM initiation unit (burst time is 0.4 μs, with an energy release of 1.4×10^3 J). This provided the initiation of detonation in the plane $x = x_i$. The development of the shock wave flow in the MST began from the moment of the electric burst of the conductors ($t = 0$). This moment of time was detected by the recorders τ_i SW that allowed the times τ_i to be determined with high accuracy. In addition, the value of the electric burst energy was determined in each experiment. This allowed a determination of whether the initiator operation was as expected.

The initial coordinates of all of the contact boundaries (interfaces) which influence the gas dynamic flow in the MST and the initial dimensions of the regions occupied by the different gases in the MST channel are given in Table 2.1.

x_1, cm	x_i, cm	x_2, cm	x_{CB}, cm	x_3, cm	l_1, cm	l_2, cm	l_3, cm	l_4, cm
18.2	19.8	98.8	203.8	566.8	363	105	80.6	18.2

Table 2. 1. The initial coordinates of the contact boundaries

The MST and the ambient air were connected by the GEM exhaust section, through which the detonation products escaped into the air.

3. EXPERIMENTAL RESULTS

Two series of experiments with gases of different Atwood numbers were performed (see Table 3.1).

Series No	Atwood number	Gas characteristics under normal conditions			
		G_1 gas		G_2 gas	
		Gas	$\rho_1 \times 10^{-3}$, g/cm³	Gas	$\rho_2 \times 10^{-3}$, g/cm³
I	0.21	Air	1.29	Carbon dioxide (CO₂)	1.98
II	0.82	Helium (He)	0.178	Argon (Ar)	1.78

Table 3. 1. The gas parameters in the experiments

The geometry of the experiments described above was the same for all of the experiments. The initial pressure and temperature of the gases and the mixtures placed in the MST channel were equilibrated to the pressure and temperature of the ambient air ($P = 0.97$ atm, $T = 293^0$ K).

The one-dimensional codes ERA, VOLNA and MAHAON [3–5] were used to simulate the shock wave flow evolution following the GEM detonation. To calibrate the codes and confirm the simulation results, the shock wave hodographs in the G_1 and G_2 sections were measured by the τ_i SW sensors. Figures 3.1–3.4 show the *x-t* diagrams of the shock wave in the MST channel and the time dependences of the velocity of the working gases contact boundary $U_{CB}(t)$ for the series I and II experiments. The turbulent mixing near the contact boundary was recorded from the moment of arrival of the first shock wave at the contact boundary ($t = \tau_1$) to the moment of arrival of the reflected shock wave from the plane $x = x_3$ at this boundary ($t = \tau_2$).

As mentioned above, the visualization of the turbulent mixing near the working gas contact boundary was accomplished using the Schlieren method. Characteristic photographic images of the turbulent mixing regions are presented in Fig. 3.5 for series I and in Fig. 3.8 for series II. The following peculiarities of the flows are noteworthy. The following are observed for small displacements of the contact boundary ($\Delta x_{CB} < 60$ cm):
- turbulent mixing zone (5);
- fronts (1) and (2) of the mixing in the light gas and the heavy gas, respectively;
- scaled reference lines (4);
- layer (6) consisting of fragments of the destroyed nitrocellulose film which gradually expands and leaves the turbulent mixing zone behind;
- interference wave field (7), which arose at the initial instant of time when the shock wave passed through the metallic grid at the contact boundary (it formed as a result of the addition of numerous waves reflected from the metallic strings of the grid; the amplitude of these waves and their decay factor depend on the string diameter).

The following are observed for intermediate displacements of the contact boundary (60 cm $< \Delta x_{CB} < 110$ cm):
- fronts (1) and (2) of the mixing in the light gas and the heavy gas, respectively;
- wall flow (3) (the development of this flow near the walls is associated with a "friction" of the mixing zone as it moves along the MST channel, and its development with time made visualization of the mixing front in the heavy gas difficult).

Air	H$_2$+ 0.5O$_2$	CO$_2$	Air
14	*13*	*12*	*11*
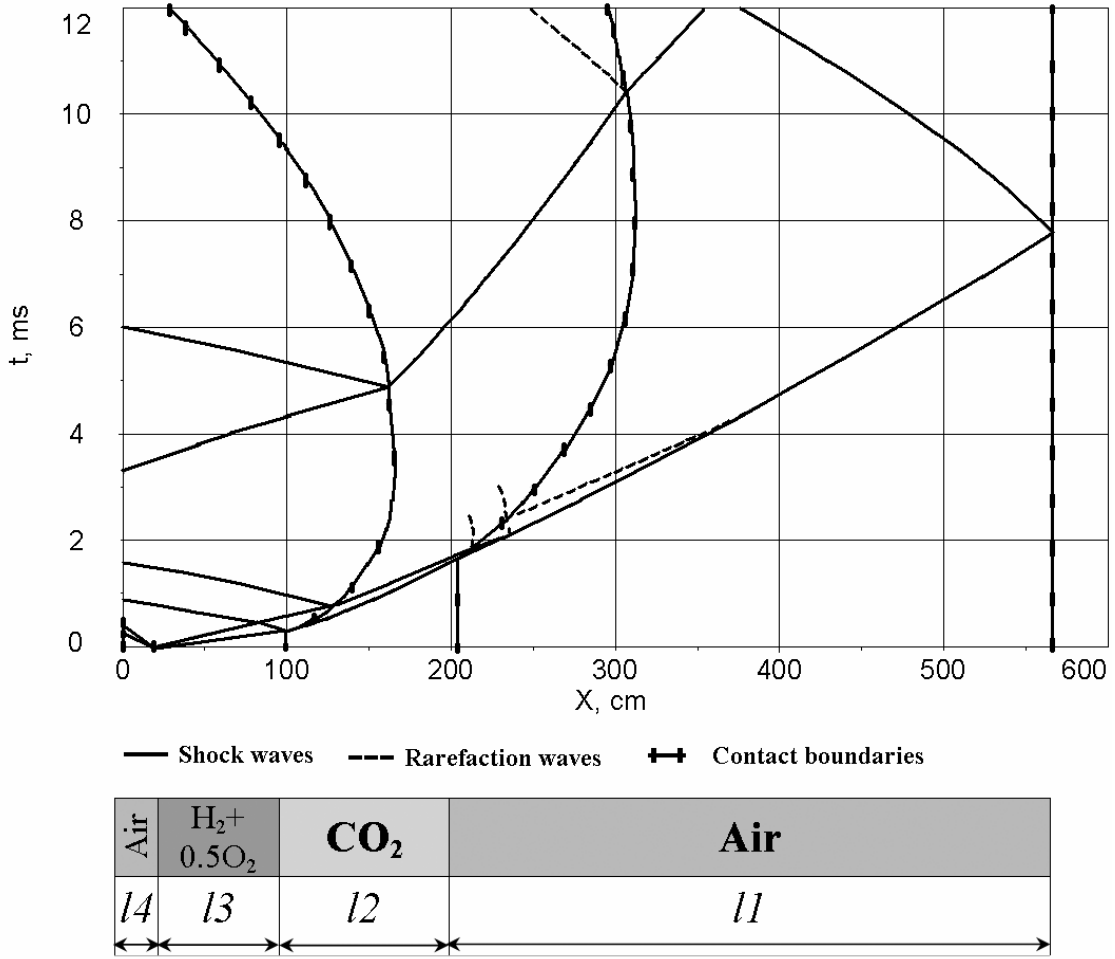
Fig. 3. 1. *x-t* diagram of the shock wave flow in the MST channel for series I experiments
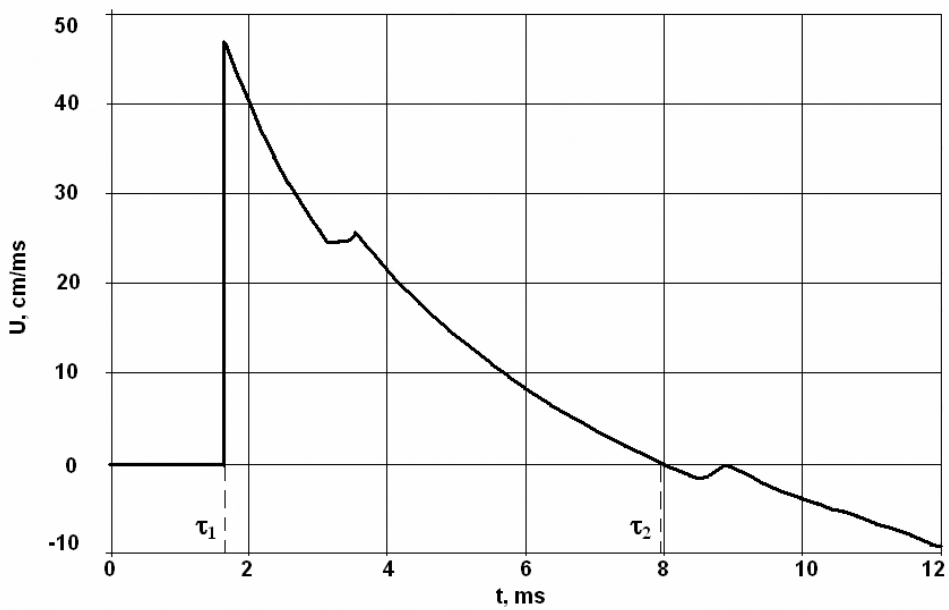
Fig. 3.2. Time-dependence of the contact boundary velocity U$_{CB}$(t) for series I experiments
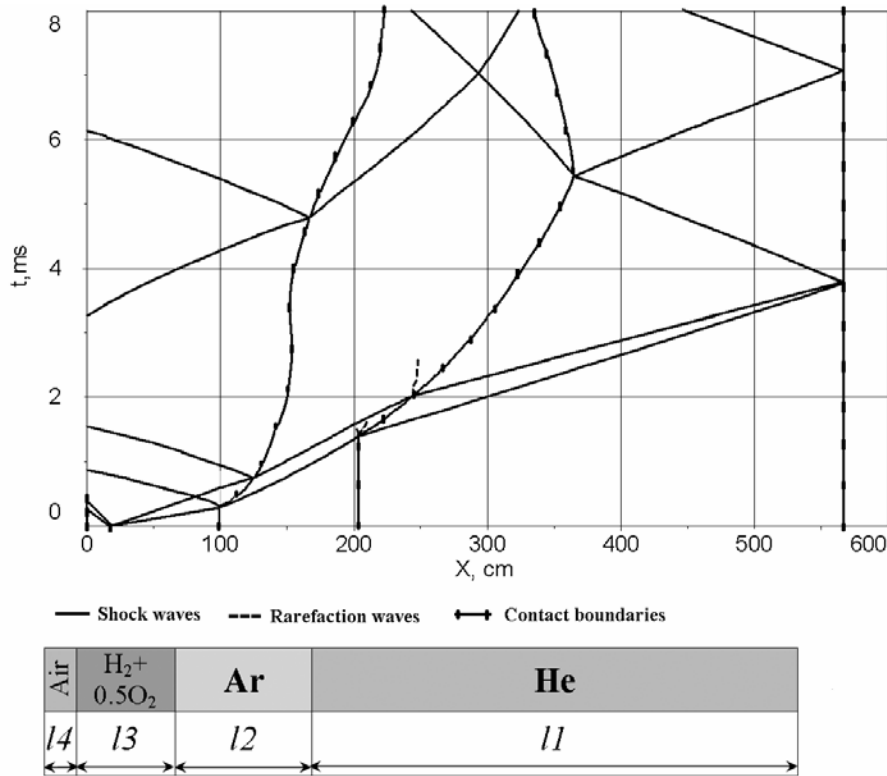
Fig. 3.3. *x-t* diagram of the shock wave flow in the MST channel for series II experiments
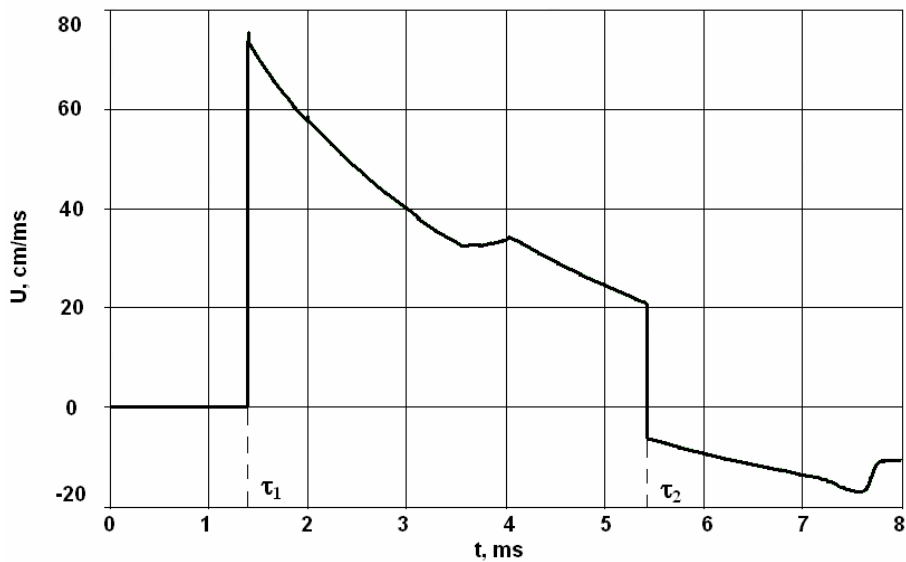
Fig. 3.4. Time-dependence of the contact boundary velocity $U_{CB}(t)$ for series II experiments

For large displacements of the contact boundary ($\Delta x_{CB} > 110$ cm), either the mixing front of the light gas in the heavy one or the mixing front of the heavy gas in the light one was recorded, as for such large displacements the size of the mixing zone exceeds that of the optical window through which the recording occurs.

The mean values of $x_{21}(t)$-coordinate of the mixing front in the light gas and $x_{12}(t)$-coordinate of the mixing front in the heavy gas were determined by the photographic images. The mean size of the turbulent mixing zone **L** was determined as **L(t) = $x_{21}(t) - x_{12}(t)$**. Averaging was performed over 16 experiments for each instant of time. The mixing front coordinates were determined by zero concentrations of the heavy gas and the light gas, respectively. Neither the layer of

the destroyed nitrocellulose film nor the wall flow hampered the determination of the position of the mixing front in the light gas. However, the determination of the position of the mixing front in the heavy gas was difficult beyond a certain time due to the wall flow.

The obtained time dependences of the averaged values $x_{21}(t)$, $x_{12}(t)$, and $L(t)$ for the two series of experiments are presented in Figs. 3.6, 3.7 and in Figs. 3.9, 3.10. The calculated trajectory of the contact boundary $x_{CB}(t)$ (solid line) and the experimentally measured time τ_1 of the shock wave arrival at the contact boundary are presented in the same figures.

All of the experiments were performed using the following parameters of the working gas separating membrane:

- Nitrocellulose film thickness $\Delta l_f = 1$ μm;
- Grid cell size $\Delta y_{HB} = \Delta z_{HB} = 0.6$ cm;
- Metallic string diameter 0.005 cm.

Fig. 3.5. Characteristic photographic images of the turbulent mixing regions in the series I experiments (CO_2 – air: 1- mixing front in the light gas; 2- mixing front in the heavy gas; 3- wall flow; 4- scaled reference lines; 5- turbulent mixing zone; 6- nitrocellulose film fragments; 7- wave field)
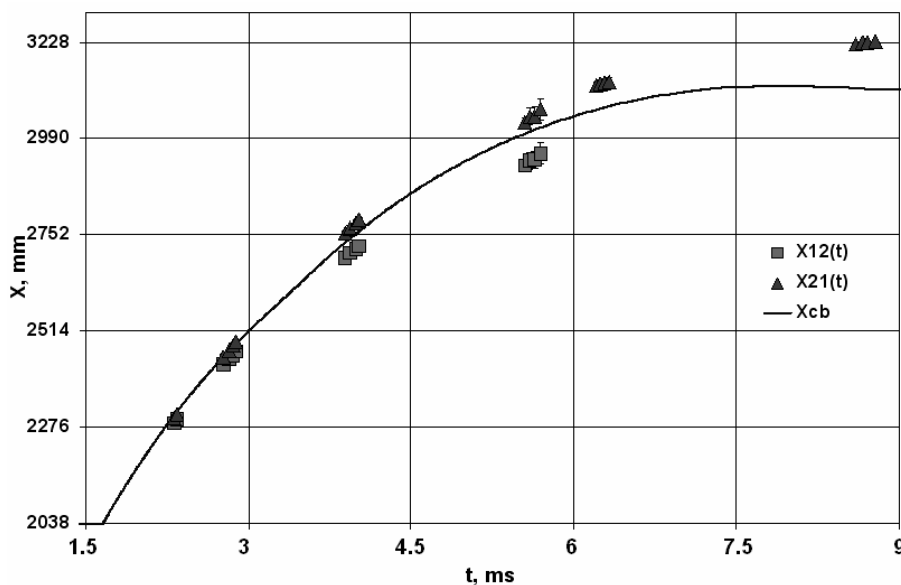
Fig. 3.6. Time-dependence of the mean values the mixing front coordinates $x_{1.2}$ and $x_{2.1}$, and the calculated coordinate of the contact boundary x_{CB} for series I experiments

153
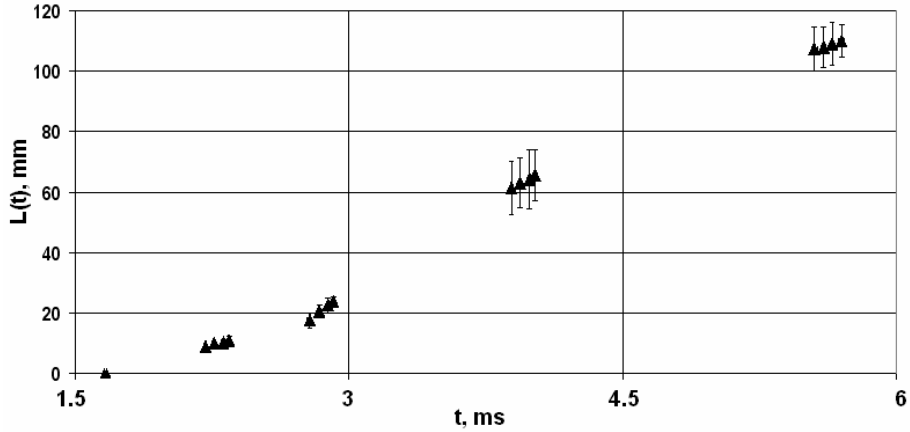
Fig. 3.7. Time-dependence of the mean value of the turbulent mixing zone L(t) for series I experiments

All of these parameters influence the formation of the initial stochastic perturbation zone caused by the shock wave passage through the working gas interface. In fact, the pressure drop required to destroy the nitrocellulose film depends on its thickness, the maximum size of fragments of the nitrocellulose film depends on the grid cell size, and the amplitude and decay factor of the interference wave field depend on the metallic string diameter.

Special experiments were performed to clarify the influence of the working gas separating membrane parameters on the measured widths L(t). The working gas separating membrane parameters were varied within the ranges $1~\mu m \leq \mathit{\Delta l_f} \leq 4$ μm, $0.3~cm \leq \mathbf{\Delta y_{HB}} \leq 2.4~cm$, and $0.001~cm \leq \mathbf{\o d} \leq 0.12~cm$. These experiments showed that the turbulent mixing zone size increased with increasing $\mathit{\Delta l_f}$, $\mathbf{\Delta y_{HB}}$, and $\mathbf{\o d}$. This is clearly associated with the increase of the initial scale of the stochastic non-uniformities and both the velocity and pressure fluctuations (initial perturbations) near the interface. In these experiments, the mean size of the turbulent mixing zone increased by 2σ (σ is the mean-square deviation) for the following parameters of the working gas separating membrane: $\mathit{\Delta l_f}^* \approx 3~\mu m$; $\mathbf{\Delta y_{HB}}^* \approx 1.2~cm$, and; $\mathbf{\o d}^* \approx 0.08~cm$. This result showed that the chosen parameters of the working gas separating membrane ensured acceptable small-scale initial stochastic perturbations near the interface in the series I and II experiments.
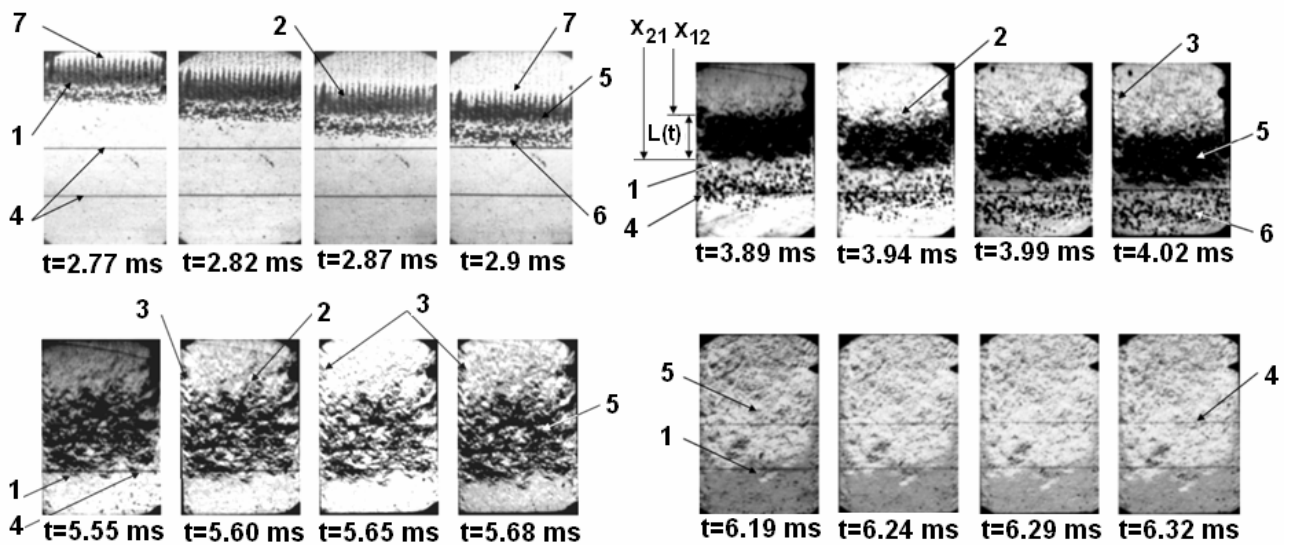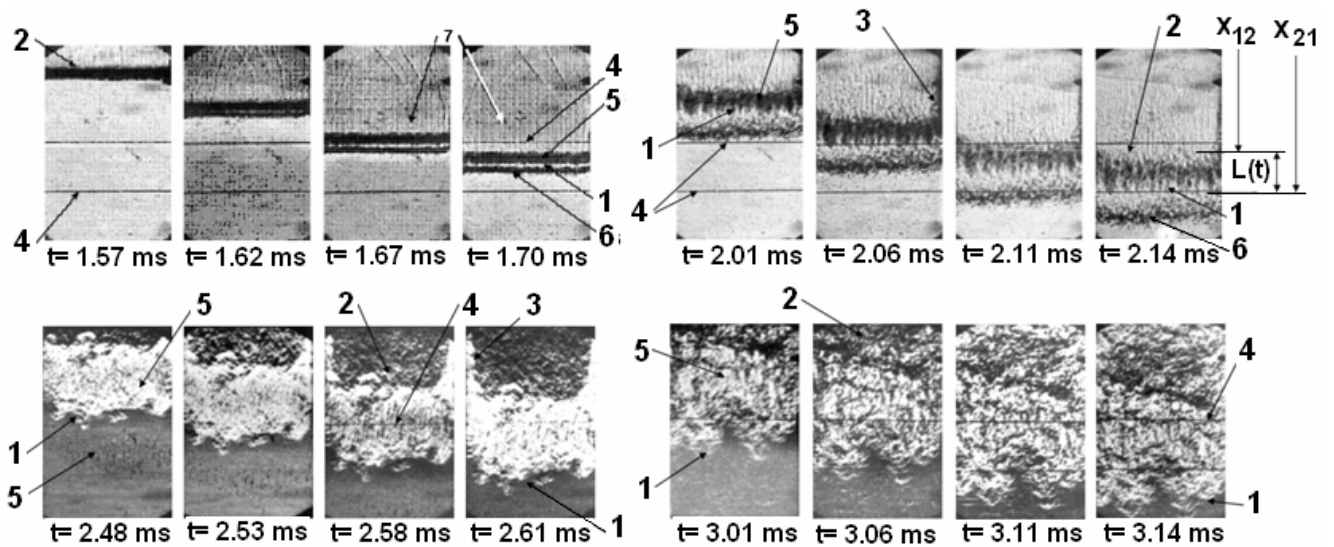

Fig. 3.8. Characteristic photographic images of the turbulent mixing regions in the series II experiments (Ar – He: 1- mixing front in the light gas; 2- mixing front in the heavy gas; 3- wall flow; 4- scaled reference lines; 5- turbulent mixing zone; 6- nitrocellulose film fragments; 7- wave field)
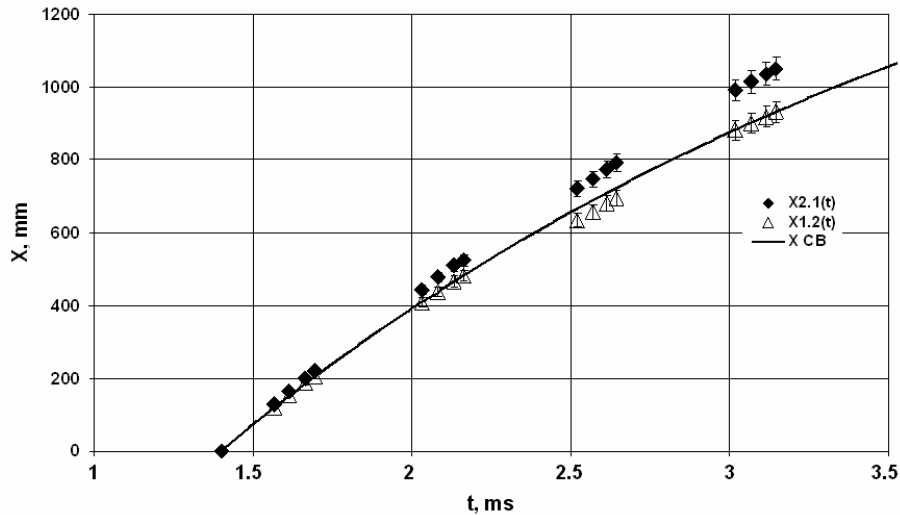
Fig. 3.9. Time-dependence of the mean values the mixing front coordinates $x_{1.2}$ and $x_{2.1}$, and the calculated coordinate of the contact boundary x_{CB} for series II experiments
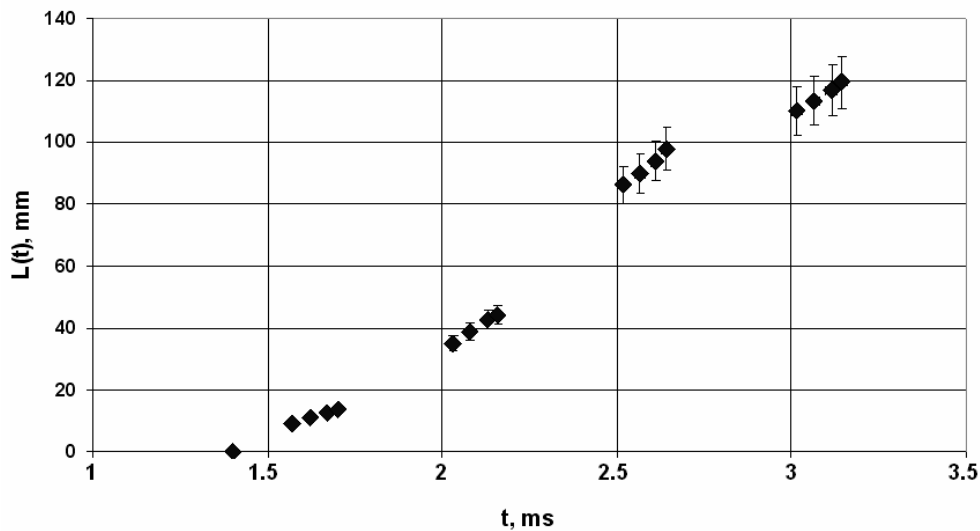
Fig. 3.10. Time-dependence of the mean value of the turbulent mixing zone L(t) for series II experiments

4. CONCLUSION

The first experimental investigation into the turbulent mixing evolution caused by non-stationary shock wave passage through an interface separating two different density gases has been carried out using the Multifunctional Shock Tube. The decaying shock wave accelerated the interface, thereby creating conditions for the development of both the Richtmyer-Meshkov and Rayleigh-Taylor instabilities. The experiments were performed using two pairs of gases with Atwood numbers $A = 0.2$ and $A = 0.8$. Initial small-scale stochastic perturbations were present at the interface separating the gases. The time-dependence of the mean values of the turbulent mixing zone size were measured.

ACKNOWLEDGEMENT

REFERENCES

[1] Kucherenko Yu., Shestachenko O., Piskunov Yu., Sviridov E., Medvedev V., Baishev A., 2001. Experimental Investigation into the Evolution of Turbulent Mixing of Gases by Using the Multifunctional Shock Tube, *in proceedings of the 8th International Workshop on the Physics of Compressible Turbulent Mixing*, Pasadena (USA), CD, E38.

[2] Kucherenko Yu., Shestachenko O., Balabin S., Pylaev A., 2003. RFNC-VNIITF Multifunctional Shock Tube for Investigating the Evolution of Instabilities in Non-stationary Gas Dynamic Flows. *Laser and Particle Beams* **21**, *pp.* 381–384.

[3] Barysheva N., Zuev A., Karlikhanov N. et al, 1982. Implicit schemes ERA for numerical modeling of physical processes in laser plasma. *Computational Mathematics and Mathematical Physics* **22**, *pp.* 401–410.

[4] Kuropatenko V., Kovalenko G., Kuznetcov V. et al, 1989. Program complex "VOLNA" and non uniform difference method for calculation of non-stationary motions of compressible continuous media. *VANT, Series: Mathematical modeling of physical processes, Issue 2, pp. 9–25.*

[5] Bokov D., 2004. Characteristic directions approach to solving scalar one-dimensional nonlinear advection equation with non-convex flow function. *Applied Numerical Analysis and Computational Mathematics* **1**, *pp.*113–127.

e-mail: `marc-antoine.lafay@cea.fr`   e-mail: `benjamin.le.creurer@gmail.com`   e-mail: `serge.gauthier@cea.fr`

Compressibility effects on the Rayleigh-Taylor instability

M.-A. LAFAY[1], Benjamin LE CREURER[2] and Serge GAUTHIER[1]

[1] *CEA/Bruyères-le-Châtel BP 12 91680 Bruyères-le-Châtel FRANCE*
[2] *Previous address: CNRS-LIMSI/Mechanical Department BP 133 91403 Orsay Cedex FRANCE*

Abstract: Compressibility effects of the Rayleigh-Taylor instability are investigated. The linear eigenvalue problem is solved numerically with a self-adaptive multidomain highly accurate Chebyshev method. Quantitative results are obtained for a wide range of parameter values. Two types of "compressibilities", static and dynamic, have been distinguished. The effect of transport coefficients is also studied. These findings are confirmed by nonlinear numerical simulations with the full Navier-Stokes equations.

1 INTRODUCTION

Although the Rayleigh-Taylor instability (RTI) has been the object of numerous studies for decades, compressibility effects in RTI are still an open problem. One has to distinguish two types of "compressibilities". The first one, called "static compressibility" is due to the variable density of the fluid. In an acceleration field, it results a stratification quantified by the density gradient length scales, $L_{\rho_{H,L}} = |d \ln \rho_{H,L}/dz|^{-1}$, of the heavy and light fluid, respectively. The second one, called "dynamic compressibility" is essentially an effect of the equation of state. For a perfect gas equation of state, this effect is governed by the adiabatic index γ. In previous works, these two compressibility effects were not clearly identified. This leads to some misunderstanding [1,2]. Actually there are several "compressible Rayleigh-Taylor instabilities", depending on the thermodynamical hypotheses made on the equilibrium state and the perturbations. Notations and details on the modeling are recalled in Ref. [3].

There are several cases where the problem can be solved analytically. Mathews and Blumenthal [4], Baker [5] and Ribeyre *et al.* [6] solved the configuration where both the basic state and the perturbations are isothermal. Bernstein and Book [7] solved the stability problem for perfect fluids for an isothermal basic state and isentropic perturbations. Recently Livescu [8] solved this configuration with surface tension. Lezzi and Prospereti [9] solved the case of isentropic basic state.

2 PHYSICAL MODEL AND GOVERNING EQUATIONS

We use the Navier-Stokes equations that are made dimensionless with the following four reference quantities *(i)* length: L_y (the horizontal length of the box), *(ii)* time: $(L_y/g)^{1/2}$ (g is the acceleration), *(iii)* mass: $(\rho_H(0^+) + \rho_L(0^-))/2\, L_y^3$, (where the densities are taken on each side of the interface) *(iv)* temperature: $T_r = \overline{T}$, the uniform temperature. The reference of pressure is given by the equation of state. The full Navier-Stokes writes [10]:

$$\partial_t \rho + \partial_j(\rho\, u_j) = 0, \tag{2.1a}$$

$$\partial_t u_i + u_j \partial_j u_i = -\frac{1}{Sr\,\rho}\partial_i p + \frac{1}{Re\,\rho}\partial_j \sigma_{ij} - \delta_{i2}, \tag{2.1b}$$

$$\partial_t T + u_j \partial_j T = \frac{\gamma_r - 1}{\rho\,C_v} p\, \partial_j u_j - \frac{\gamma_r - 1}{\rho\,C_v}\frac{Sr}{Re}\sigma_{ij}D_{ij} + \frac{T}{\rho\,C_v}\frac{d_c C_v}{Re\,Sc}\partial_{jj}^2 c + \frac{\gamma_r}{Re\,Pr\,\rho\,C_v}\partial_{jj}^2 T, \tag{2.1c}$$

$$\partial_t c + u_j\,\partial_j c = \frac{1}{Re\,Sc}\partial_{jj}^2 c, \tag{2.1d}$$

The total density profile is built with the regularized Heaviside functions $H_{\pm}(z) = (1 \pm \mathrm{erf}(z/\delta))/2$, where the parameter δ represents the width of the initial pseudo-interface thickness. It writes

$$
\begin{aligned}
\overline{\rho}(z) &= \overline{\rho}_H(z) + \overline{\rho}_L(z) \\
&= (1 + A_t)\exp(A_- z)H_+(z) + (1 - A_t)\exp(A_+ z)H_-(z),
\end{aligned}
\tag{2.2}
$$

where $A_{\pm} = -Sr/(1 \pm A_t)$. The concentration profile is

$$\overline{c}(z) = (1 + A_t) \exp(A_- z) H_+(z)/\overline{\rho}(z). \tag{2.3}$$

Pressure is calculated from Eq. (2.1b) as $\overline{p}(z) = -Sr \int \overline{\rho}(z) \, dz$, one obtains

$$\overline{p}(z) = \overline{p}_b \quad + \quad (1 - A_t^2) \Bigg[\exp(A_- z) H_+(z) + \exp(A_+ z) H_-(z)$$
$$- \quad \frac{1}{2} \exp\left(A_-^2 \, \delta^2/4\right) \operatorname{erf}\left(\frac{z}{\delta} - \frac{A_- \delta}{2}\right) + \frac{1}{2} \exp\left(A_+^2 \, \delta^2/4\right) \operatorname{erf}\left(\frac{z}{\delta} - \frac{A_+ \delta}{2}\right) \Bigg]. \tag{2.4}$$

The integration constant $\overline{p}_b$ is adjusted in such a way that $\overline{T}(z_b) = 1$. The temperature is then recalculated from these quantities.

3 THE NUMERICAL METHOD

A stability code analysis, based on the normal mode method and called SPECLMD, has been developed to study the stability of the equilibrium profile given by Eqs. (2.2)–(2.4). In this approach, dependent variables are supposed to behave as $\varphi(y, z, t) = \overline{\varphi}(z) + \widehat{\varphi}(z) \, e^{\mathrm{i} k \, y} \, e^{\sigma \, t}$, where $\varphi = (\rho, \ u_i, \ T, \ c)^T$. The quantities $\overline{\varphi}$ and $\widehat{\varphi}$ denote the equilibrium state and the corresponding perturbation, respectively. The real wave number is k and the complex growth rate is σ. With solutions of the previous form, the initial boundary value problem of the linearized Navier-Stokes equations (2.1) reduces to the generalized linear eigenvalue problem

$$A \, \widehat{\varphi} = \sigma \, B \, \widehat{\varphi}. \tag{3.1}$$

The matrices A and B are 5×5 block matrices for two-dimensional geometry. They depend on the steady state defined by Eqs. (2.2)–(2.4) and on the first and second derivative operators, D_z and D_z^2. Boundary and continuity conditions are enforced with the penalty method. The numerical method used a self-adaptive pseudo-spectral algorithm [11–13]. The eigenvalue problem (3) is usually solved with a global LZ method available through the IMSL library that provides both the eigenvalues and the eigenvectors. The whole method has been validated on various perfect fluid configurations for which exact solutions are known [4]. In particular a configuration where the Atwood number A_t is equal to 0.99 (the density ratio is then equal to 199) has been computed accurately. The numerical values of the dimensionless coefficients have been chosen in such a way that the flow is both quasi-inviscid and quasi-isothermal. The eigenvalue σ obviously depends on the numerical width δ of the density gradient and we have carried out several calculations versus this parameter. It turns out that the eigenvalue σ depends linearly on the thickness δ and extrapolation at $\delta = 0$ gives the value $\sigma(\delta = 0)$, which when compared with the exact value, leads to an accuracy of $0.7 \, 10^{-4}$. This calculation has been carried out with 16 subdomains with 50 Chebyshev collocation points. This result has been obtained with a 32 significant-digit floating-point representation [13, 14].

4 LINEAR STABILITY RESULTS

A systematic parameter study has been conducted in order to understand the various effects that play a role in the compressible Rayleigh-Taylor instability. In the following, the stratification of the initial equilibrium profile, through the parameter Sr, the compressibility, through the γ-indices, the confinement of the fluid layer (L_z) and the effects of the transport coefficients through the Reynolds (Re), Schmidt (Sc) and the Prandtl (Pr) numbers are investigated. The effect of stratification is first studied. Results of the linear stability analysis are represented in Fig. 4.1 for stratification parameter values Sr ranging from 0.05 to 8. The density gradient length scales $L_{\rho_{H,L}} = (1 \pm A_t)/Sr$ are given in Table 4.1. For small values of the stratification, only very small wave numbers are close to density gradient length scales. Consequently the dispersion curve is not affected by the stratification. On the contrary, for values of Sr close to 1, the length scale of the heavy fluid becomes comparable to the horizontal size of the box. As a result, influence of the stratification becomes more pronounced. The dispersion curves are approximately symmetric with respect to the maximum, so that large and small scales are affected by stratification in a symmetrical way. Consequently the wave number of the most unstable mode does not vary much with the stratification.
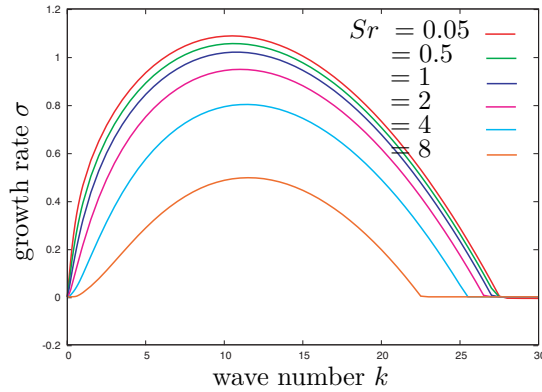
Fig. 4.1. Dispersion curves for various values of the stratification parameter Sr.

Sr	L_{ρ_H}	L_{ρ_L}
0.05	$0.250\,10^2$	$0.150\,10^2$
0.50	$0.250\,10^1$	$0.150\,10^1$
1.00	$0.125\,10^1$	0.750
2.00	$0.625\,10^1$	0.375
4.00	0.312	0.187
8.00	0.156	$0.937\,10^{-1}$

Table 4.1. Density gradient length scales of the heavy and light fluid versus the stratification parameter Sr.
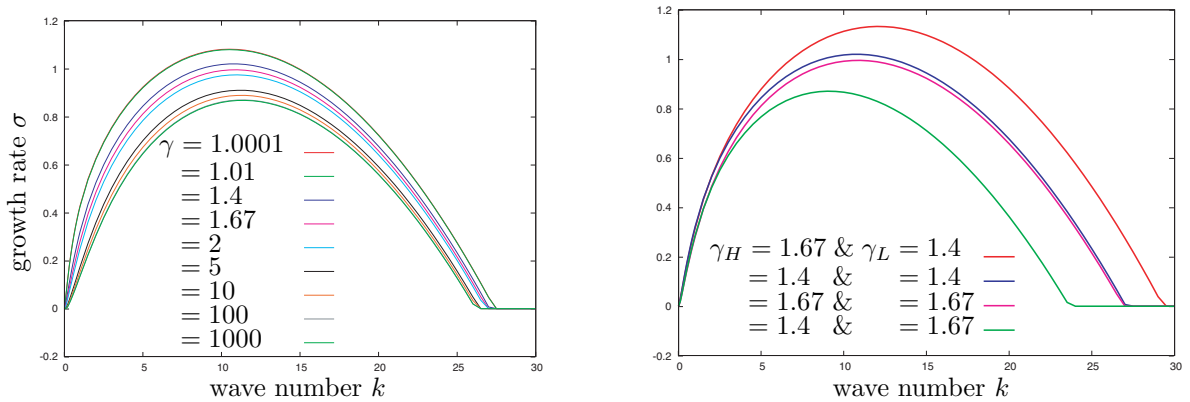
Fig. 4.2. Dispersion curve for various values of the adiabatic index $\gamma = \gamma_H = \gamma_L$ (left) with $A_t = 0.25$, $Sr = 1$, $Re = 400$ and $Pr = Sc = 0.7$; Dispersion curve for different adiabatic indices $\gamma_H \neq \gamma_L$ (right).

The results for the compressibility through the γ-indices are reported in Figs. 4.2. On the left part of this figure, the γ's of both fluids are equal. In that case, we observe that compressibility destabilizes the Rayleigh-Taylor flow. However the overall effect is small since the growth rate varies of 20% for γ values ranging from 1.0001 to 1000. In other words, the instability is not strongly affected as long as both fluids have the same compressibilities. A different result is obtained when compressibilities of the two fluids are not equal (see Fig. 4.2 (right)). In these cases, a heavy incompressible fluid (large γ_H) over a compressible light fluid (small γ_L) is more unstable than the standard configuration. In the same way a heavy compressible fluid (small γ_H) over an incompressible (large γ_L) light fluid is more stable than the standard configuration.

The influence of the confinement is given in Fig. 4.3 where dispersion curves for box sizes are ranging from 5 to 0.156. Wave numbers of the perturbation that are of the order of the wave numbers associated with the vertical thicknesses of the heavy and light fluids are affected (see Table 4.2). As a result, large scales are first stabilized as the size of the box is decreasing. Dispersion curves are non-symmetric with respect to the wave number of the most unstable mode. For very small aspect ratios, large scales are weakly unstable and the wave

	L_z	$2\pi/L_{zH}$	$2\pi/L_{zL}$
L_z	5.000	$0.228\,10^1$	$0.279\,10^1$
$L_z/2$	2.500	$0.457\,10^1$	$0.558\,10^1$
$L_z/4$	1.250	$0.914\,10^1$	$0.112\,10^2$
$L_z/8$	0.625	$0.183\,10^2$	$0.223\,10^2$
$L_z/16$	0.312	$0.366\,10^2$	$0.446\,10^2$
$L_z/32$	0.156	$0.731\,10^2$	$0.894\,10^2$

Table 4.2. Wave numbers associated with the vertical thicknesses of the heavy and light fluids, respectively.

numbers of the most unstable mode and the cutoff are shifted to the small scales.
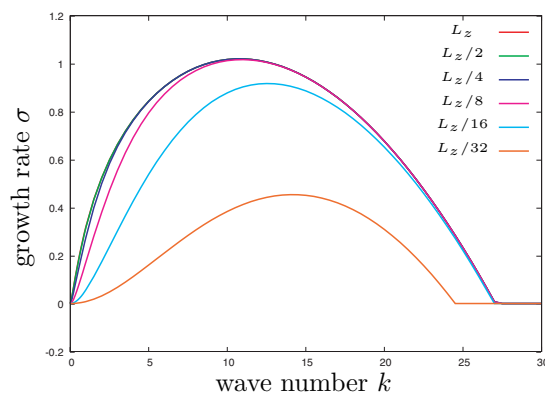
Fig. 4.3. Dispersion curve for various values of the aspect ratio with $A_t = 0.25$, $Sr = 1$, $Re = 400$, $Sc = Pr = 0.7$ and $\gamma_H = \gamma_L = 1.4$.

Influence of the transport coefficient has also been investigated. Results are reported in Figs. 4.4 and 4.5. The influence of transport coefficients are roughly the same: the cutoff wave number strongly depends on the dimensionless transport coefficients Re, Sc and Pr numbers. At large scales, the growth rate follows the law of the corresponding compressible perfect fluid.
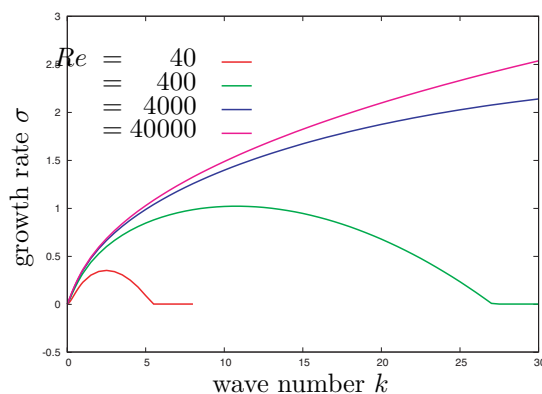
Fig. 4.4. Dispersion curve for various values of the Reynolds number

5   NONLINEAR NUMERICAL SIMULATIONS

The results obtained within the linear regime are checked with respect to those obtained in the nonlinear regime where numerical simulations of the complete Navier-Stokes have been used. Only few results are presented here. Fig. 5.6 displays single-mode simulations for four different values of the stratification parameter Sr. Inhibition of the instability by the stratification is obvious in these concentration fields. Fig. 5.7 shows concentration and
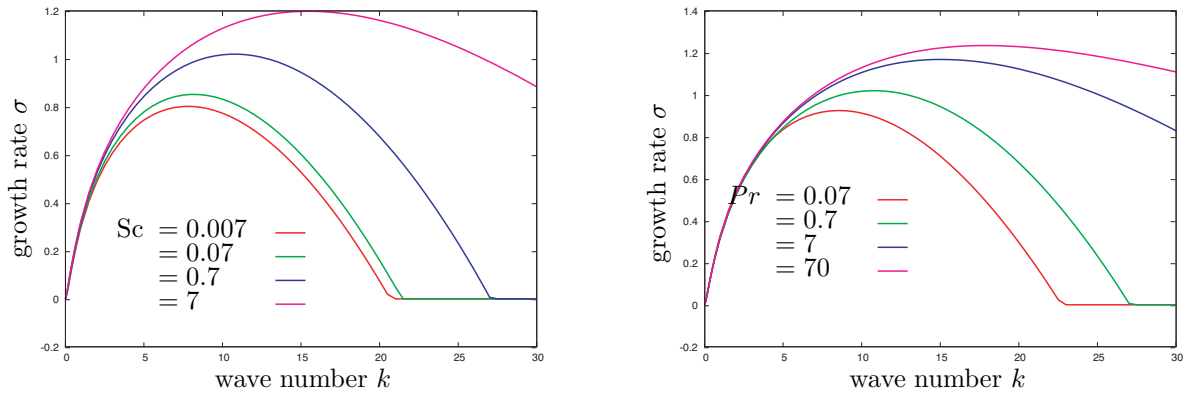
Fig. 4.5. Dispersion curve for various values of the Schmidt number Sc (left) with $A_t = 0.25$, $Sr = 1$, $Re = 400$, $Pr = 0.7$ & $\gamma_H = \gamma_L = 1.4$; Dispersion curve for various values of the Prandtl number Pr.
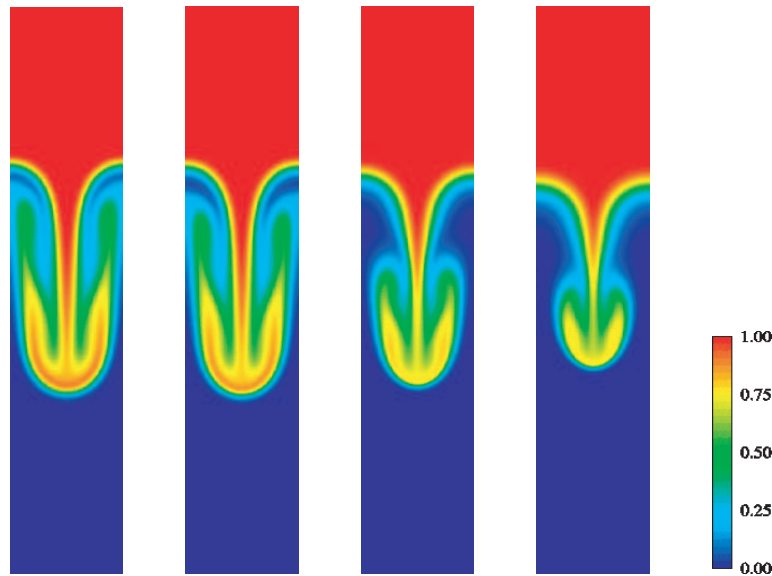
Fig. 5.6. Influence of the stratification: Concentration field at $t = 10$. Four values of the stratification parameter $Sr = 0.005$, $Sr = 0.05$, $Sr = 0.5$ and $Sr = 1$.

density fields for four different compressibilities. For the ($\gamma_H = 5$, $\gamma_L = 5/3$) and ($\gamma_H = 5/3$, $\gamma_L = 5$) cases the nonlinear behavior agree with the linear stability results, *i.e.*, the more the heavy fluid is incompressible, with respect to the light one, the more the configuration is unstable. However for the ($\gamma_H = 5/3$, $\gamma_L = 5/3$) and ($\gamma_H = 5$, $\gamma_L = 5$) configurations, the result is different. In a first step, the linear behavior is confirmed by the simulation of the full Navier-Stokes equations, *i.e.*, the compressible configuration grows faster than the incompressible configuration. However in the nonlinear regime, the incompressible configuration grows faster than the compressible configuration (see Fig. 5.7 second and third concentration and density fields).

6 SUMMARY

The linear Rayleigh-Taylor problem for two compressible fluids has been solved for a wide range of parameter values. A self-adaptive Chebyshev method allows us to obtain accurate and reliable results. The effects of stratification on the one hand and compressibility, due to the equation of state, on the other hand, have been clearly distinguished. Nonlinear numerical simulations with the complete Navier-Stokes equations confirm these trends.
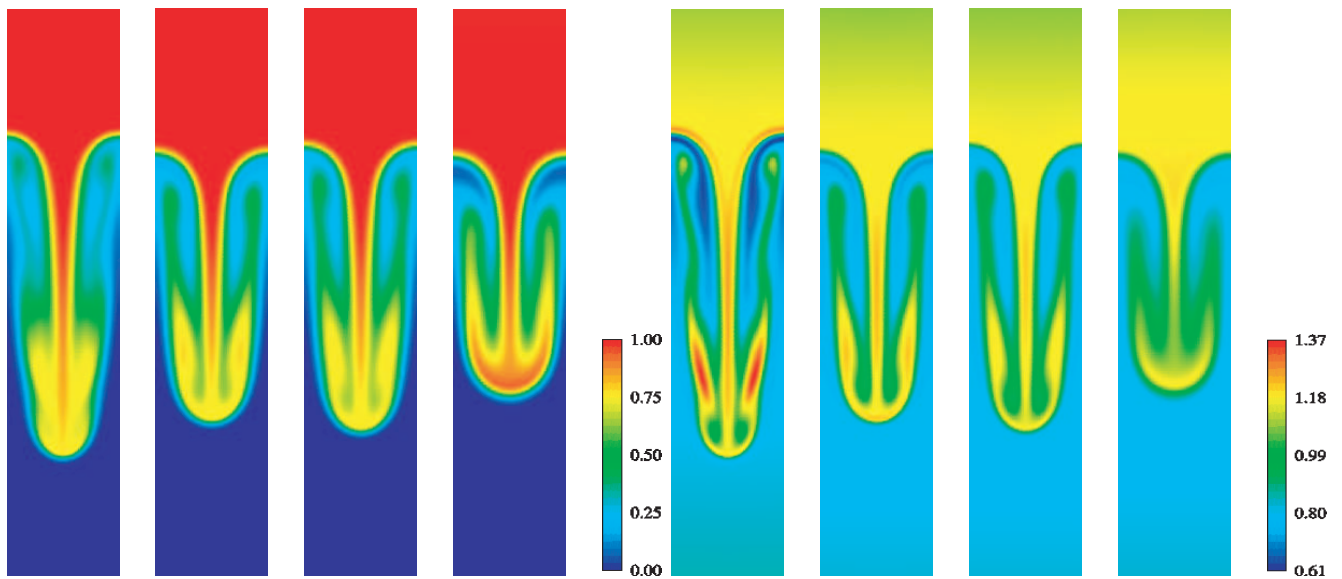
Fig. 5.7. Influence of the compressibilities: concentration fields with $A_t = 0.25$, $Sr = 0.05$ for four different compressibilities: $(\gamma_H = 5,\ \gamma_L = 5/3)$, $(\gamma_H = 5/3,\ \gamma_L = 5/3)$, $(\gamma_H = 5,\ \gamma_L = 5)$, $(\gamma_H = 5/3,\ \gamma_L = 5)$ (left); density fields (right).

REFERENCES

[1] D. Livescu, 2005, Comment on "Compressible Rayleigh-Taylor instabilities in supernova remnants". *Phys. Fluids* **17**, pp. 069101–1–2.

[2] X. Ribeyre, V.T. Tikhonchuk and S. Bouquet, 2005, Response to "Comment on 'Compressible Rayleigh-Taylor instabilities in supernova remnants' ". *Phys. Fluids* **17**. pp. 069102–1.

[3] B. Le Creurer and S. Gauthier, Pseudo-spectral simulation of the overturning process due to Rayleigh-Taylor instability for compressible miscible fluids. This volume.

[4] W.G. Mathews, and G.R. Blumenthal, 1977, Rayleigh-Taylor stability of compressible and incompressible radiation-supported surfaces and slabs : application to QSO clouds. *Ap. J.* **214**, 10–20.

[5] L. Baker, 1983, Compressible Rayleigh-Taylor instability. *Phys. Fluids* **26**, pp. 950.

[6] X. Ribeyre, V.T. Tikhonchuk and S. Bouquet, 2004, Compressible Rayleigh-Taylor instabilities in supernova remnants. *Phys. Fluids* **16**, pp. 4661–4670.

[7] I.B. Bernstein and D.L. Book, 1983, Effect of compressibility on the Rayleigh-Taylor instability. *Phys. Fluids* **26**, pp. 453–458.

[8] D. Livescu, 2003, Compressibility effects on the Rayleigh-Taylor growth between immiscible fluids. *Phys. Fluids* **16**, pp. 118–126.

[9] A. M. Lezzi and A. Prosperetti., 1989, Rayleigh-Taylor instability for adiabatically stratified fluids. *Phys. Fluids A* **11**, pp. 1784–1795.

[10] B. Le Creurer, and S. Gauthier, A return toward equilibrium in a two-dimensional Rayleigh-Taylor instability for compressible miscible fluids. Submitted to *Phys. Rev. E*.

[11] H. Guillard, J.-M. Malé and R. Peyret, 1992, Adaptive spectral methods with application to mixing layer computations. *J. Comput. Phys* **102**, pp. 114–127.

[12] F. Renaud and S. Gauthier, 1997, A Dynamical Pseudo-Spectral Domain Decomposition Technique: Application to Viscous Compressible Flows. *J. Comput. Phys.* **131**, pp. 89–108.

[13] S. Gauthier, B. Le Creurer, F. Abéguilé, C. Boudesocque-Dubois, J.-M. Clarisse, 2005, A self-adaptive method decomposition method with Chebyshev method. *Int. J. Pure Appl. Math.* **24**, pp. 553–577.

[14] B. Le Creurer, 2005, Simulations numériques pseudo-spectrales de l'instabilité de Rayleigh-Taylor pour des fluides compressibles. PhD thesis, CEA-Université de Marne-la-Vallée.

An overview of the 2SFK model

Nicolas Lardjane & Olivier Poujade[1] and Antoine Llor[2]

[1] *Commissariat à l'Energie Atomique,*
Centre DAM Ile de France, FRANCE
nicolas.lardjane@cea.fr, olivier.poujade@cea.fr

[2] *Commissariat à l'Energie Atomique,*
Siège, 31-33, rue de la fédération, 75752 Paris Cedex 15, FRANCE
antoine.llor@cea.fr
http://www.cea.fr/

Abstract: In this poster, we present the 2SFK model, already introduced in Pasadena [Llor & Bailly, 2001] and also in Cambridge [Llor, Bailly & Poujade, 2004]. 2SFK is a statistical RANS model aimed at simulating developed turbulent mixing due to gravitational and shearing instabilities at the interface of two fluids (Rayleigh-Taylor, Richtmyer-Meshkov and Kelvin-Helmholtz). The basic idea behind the 2SFK concept, which stands for 2 Structures, 2 Fluids and 2 turbulent fields (K-ϵ), is that the dynamic evolution of the mixing zone is driven by usual buoyancy-drag balance acting on the large turbulent eddies which form the structures: bubbles on one side and spikes on the other side. The first part of this poster summarizes the main ideas and the methodology to build up a coherent set of equations (least action principle and an extension of the thermodynamics of irreversible processes to statistical models). The model is adjusted by two constants (C_d: drag, C_s: sifting diffusion). The second part deals with the calibration of these constants. It is performed in two steps: (i) a 0D analysis (in which all fields in the equations are replaced by "simple" and "reasonable" guess) gives a coarse estimate of the search area in the (C_d, C_s) space, and (ii), by refined scanning within the delimited area where the outcomes of 1D numerical simulations of the 2SFK model (growth rates for spikes and bubbles in the mixing zone as given by a code) are compared to expected experimental results (LEM results). The best fit gives the model constants C_d and C_s. The last part is devoted to the results of the model for the single set of constants that passes the previous tests. We compare growth rate of bubbles and spikes given by 2SFK with LEM results at Atwood numbers ranging from 0.1 to 0.9 [Dimonte, 2000]. We also compare the ratio of the bubble length with the size of large eddies on the bubble side $L_b/\langle\lambda\rangle$ [D. Oron et al., 2001]. Various profiles (volume fraction, kinetic turbulent energy, eddies length scale ...) within the mixing zone highlight the advantages of the 2SFK model.

1   THE 2SFK MODEL

The 2SFK model is a RANS (Reynolds Averaged Navier Stokes) model. It describes the evolution of a turbulent mixing layer between two fluids (heavy and light). This mixing layer may have been triggered by 3 types of instability: Rayleigh-Taylor, Richtmyer-Meshkov or Kelvin-Helmholtz, for which it is crucial to capture the following:

- the directed transport by a two fluid approach,

- the natural buoyancy force (in opposition to artificial terms that need to be added in a one fluid approach),

- the turbulence diffusion by including the k-ε features,

- the mixing rate and exchange of fluids between structures,

- the geometrical aspect of the turbulent structures.

We will label the fluids by the roman letter m where $m \in \{1, 2\}$ for light (1) and heavy (2) fluid. At the initial time, before any instability creates the mixing zone, the turbulent structure $-$ is merged with the fluid 1 and structure $+$ with fluid 2. When any of the 3 instabilities described above starts, the turbulent structures do not have any reason to evolve in the same way the fluids do. But fluids exchange at the border of the turbulent

structures (cf. figure 3.5). This effect is taken care of by the so called exchange term Ψ in the following set of equations:

$$D_t^{\pm}\left(\alpha^{\pm}\rho^{\pm}\right) = \mp\Psi \tag{1.1}$$

$$D_t^{\pm}\left(\alpha^{\pm}\rho^{\pm}C_m^{\pm}\right) = \mp\Psi_m + \Phi_{j,j}^{m\pm} \tag{1.2}$$

$$D_t^{\pm}\left(\alpha^{\pm}\rho^{\pm}H^{\pm}\right) = -\alpha^{\pm}P,i \mp R_{ij,j}^{\pm} \mp (\Psi_i + D_i) \tag{1.3}$$

$$D_t^{\pm}\left(\alpha^{\pm}\rho^{\pm}E^{\pm}\right) = +\alpha^{\pm}\rho^{\pm}\varepsilon^{\pm} \mp \Psi_E + \Phi_{j,j}^{E\pm} \tag{1.4}$$

$$D_t^{\pm}\left(\alpha^{\pm}\rho^{\pm}k^{\pm}\right) = \Pi^{\pm} - \alpha^{\pm}\rho^{\pm}\varepsilon^{\pm} \mp \Psi_k + \Phi_{j,j}^{k\pm} \tag{1.5}$$

$$D_t^{\pm}\left(\alpha^{\pm}\rho^{\pm}\varepsilon^{\pm}\right) = C_{\varepsilon_1}\frac{\varepsilon^{\pm}}{k^{\pm}}\Pi^{\pm} - C_{\varepsilon_2}\frac{\varepsilon^{\pm}}{k^{\pm}}\alpha^{\pm}\rho^{\pm}\varepsilon^{\pm} \mp \Psi_\varepsilon + \Phi_{j,j}^{\varepsilon\pm} \tag{1.6}$$

There are two k-ε fields, one for each type of turbulent structure $\pm$. Each of these fields are evolved using the standard k-ε equations of Launder & Spalding. The exchange of the generic physical value A between structures is a first order closure of the type $\alpha^+\rho^+A^+ - \alpha^-\rho^-A^-$. The associated exchange rate depends on the turbulent physical values $k^{\pm}$ and $\varepsilon^{\pm}$. In addition to the standard k-ε constants hidden in the closure of flux terms there are three adjustable constants. The one called C_{ε_c}, which is common to all exchange terms, is fixed by asymptotic assumptions. There are experimental constraints and physical requirement (positivity of turbulent production $\Pi^{\pm}$) that fixes the value. The two other adjustable constants, called C_d (for drag) and C_s (for sifting), act on the drag term $(\Psi_i + D_i)$ in the momentum equation and on diffusion fluxes $\Phi_{j,j}^{A\pm}$.

2 CALIBRATION OF THE MODEL CONSTANTS

We have compared the 2SFK model results to the LEM experiment results for Rayleigh-Taylor and Richtmyer-Meshkov. In order to find the correct values of C_d and C_s that allow the model to be in agreement with experimental results we have proceeded in two steps:

- first: at low Atwood numbers, the 2SFK model has been reduced to a set of ODEs with the help of a "0D" projection. This simplified system depends on C_d and C_s and evolves bulk physical values like "bubble length" and "spike length". Given the experimental bubble growth rate from LEM experiments, we find a region of potential calibration in the (C_d, C_s) plane.

- second: we search more precisely within this narrow region using the full set of PDEs (1D code Lagrange, remap). A region of acceptable values can be drawn on a (C_d, C_s) plane for RT and RM experiments. The model is said to be valid if these two regions intercept and the correct value of C_d and C_s must be taken from there.

The final set of constants comes from the restitution of bubble and spike growth rates of LEM experiments (RT and RM) within 15% for Atwood numbers from 0.0 to 0.9.

3 RESULTS FOR THE RAYLEIGH-TAYLOR INSTABILITY

The results of several 1D simulations at Atwood numbers 0.2 to 0.9 is now presented for the RTI. The bubble (α_b) and spike (α_s) coefficients, cf. figure 3.1, are in good agreements with LEM results [3]. The ratio of bubble length to the turbulence length scale, cf. figure 3, is nearly constant around 1.5 value as expected from [4]. At last, we show instantaneous profiles for the volumic fraction of fluid and structure at Atwood numbers 0.2 (cf. figure 3.3) and 0.9 (cf. figure 3.4). The fluid profiles are in agreement with known results : linear at low Atwood numbers.

REFERENCES

[1] A. Llor & P. Bailly, *A new turbulent two-field concept for modeling Rayleigh-Taylor, Richtmyer-Meshkov and Kelvin-Helmholtz mixing layers*, Laser Part. Beams **21**, 311 (2003).

[2] A. Llor, P. Bailly & O. Poujade, *Derivation of a minimal 2-structures, 2-fluids and 2-turbulence (2SFK) model for gravitationally induced mixing layers*, Proceedings of the IWPCTM **9**.

[3] G. Dimonte, *Spanwise homogeneous buoyancy-drag model for Rayleigh-Taylor mixing and experimental evaluation*, Phys. Plasma **7**, 2255 (2000).

[4] D. Oron, L. Arazi, D. Kartoon, A. Rikanati, U. Alon & D. Shvarts,*Dimensionality dependance of the Rayleigh-Taylor and Richtmyer-Meshkov instability late-time scaling laws*, Phys. Plasma **8**, 2883 (2001).

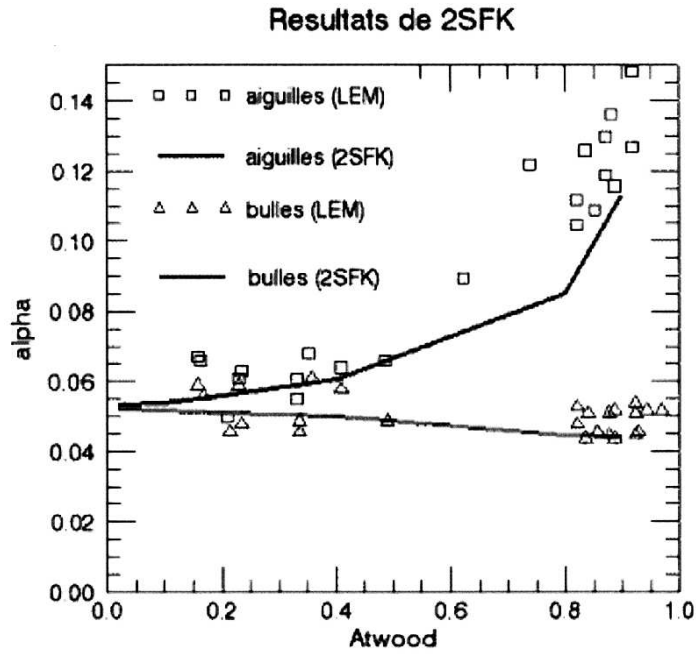**Fig. 3.1.** Bubble and spike growing coefficient versus Atwood number in comparison with LEM results
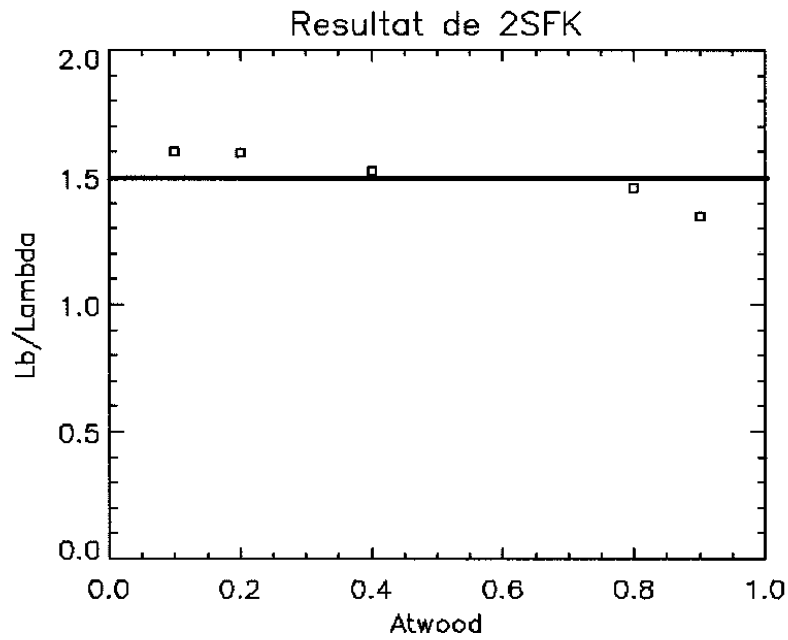

Fig. 3.2. Bubble size over turbulence length scale versus Atwood number
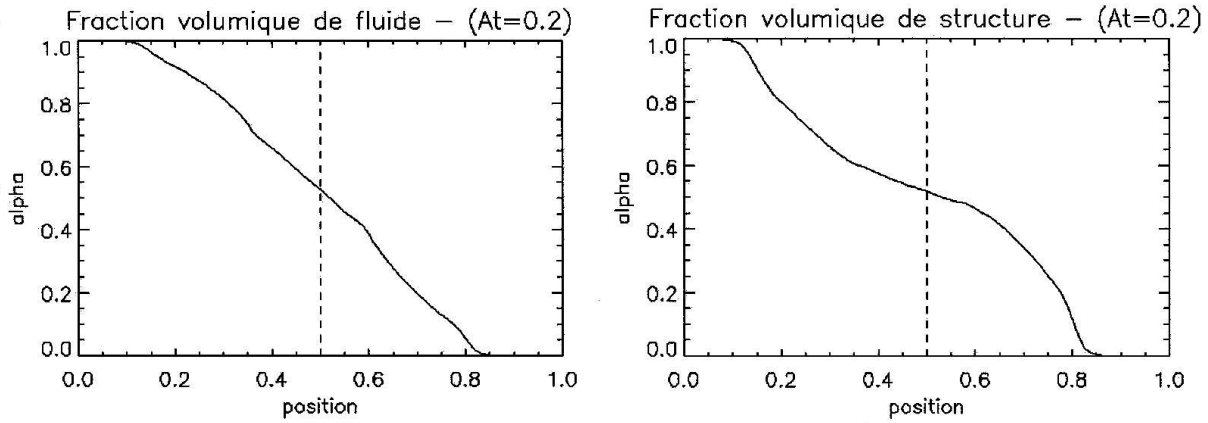
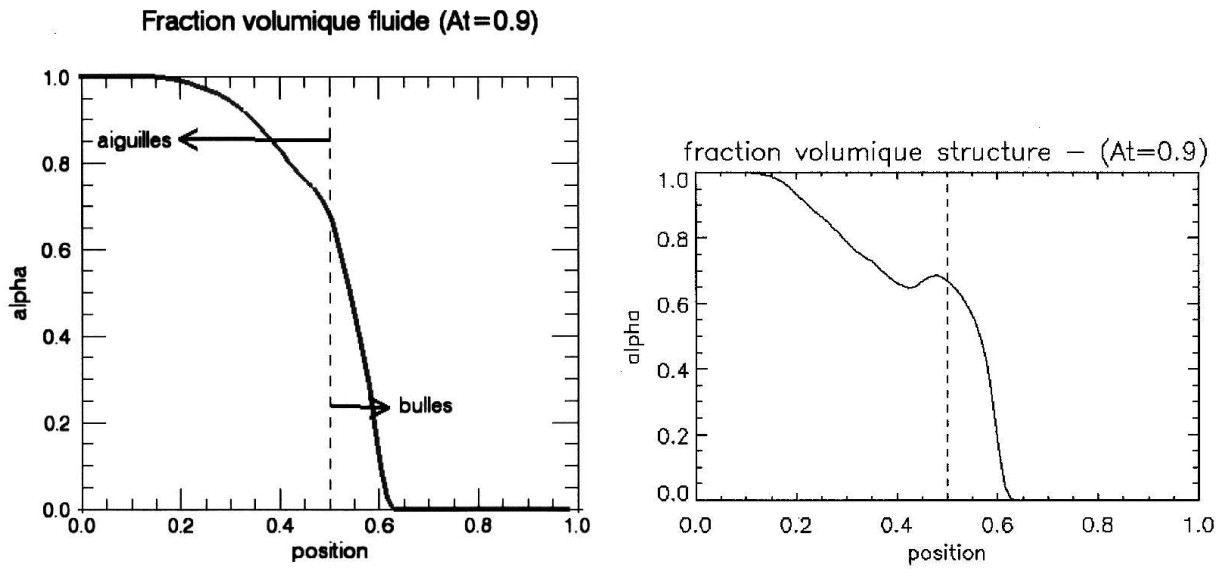**Fig. 3.3.** Profiles of volumic fraction of fluid (left) and structure (right) @ At=0.2

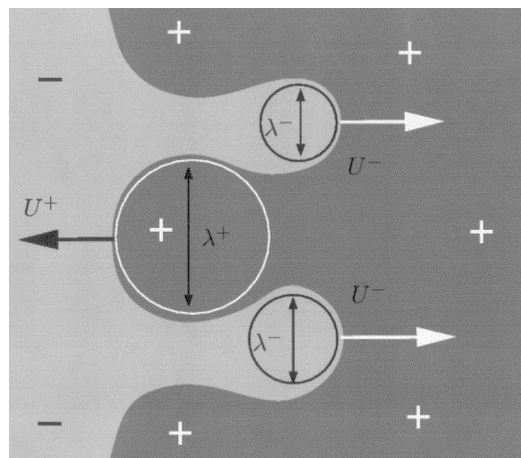**Fig. 3.4.** Profiles of volumic fraction of fluid (left) and structure (right) @ At=0.9

Fig. 3.5. The structure concept

e-mail: nicolas.lardjane@cea.fr

Effective performance of improved WENO schemes

Nicolas LARDJANE[1], Ludivine GOUGEON[2] and Ivan FEDIOUN[2]

[1]*CEA/DAM Ile de France BP 12 91680 Bruyères-le-Châtel France*
[2]*LCSR/CNRS, 1c avenue de la Recherche Scientifique, 45072 Orléans CEDEX 2, France*

Abstract: In this document we analyse the effective performance of WENO [1] schemes of order 3, 5, 7, 9, 11, and we present an extension to multi-species simulations. This analysis is performed through numerical experiments on: asymptotic linear analysis of the effective modified wave number, mono and multi-species elementary test cases (Sod, RT, flame), an adaptation of Pasadena's test case #2 in 2D.

1 INTRODUCTION

Due to its simplicity, Monotone Integrated Large Eddy Simulation (MILES) has become a standard way of LES. This form of LES is intended to capture the correct flow energy up to some scale in the inertial range and then dissipate it at a non linear rate depending on the numerical dissipation of the scheme. Very long time simulations should then use highly accurate schemes in conjunction with fine enough grids to ensure that results are not polluted by the numerics. From our experience on Kelvin-Helmholtz instabilities [2], WENO schemes are good candidates for MILES but, in their initial form, they still suffer from a relatively poor resolution of contact discontinuities (with smearing for larger time), and may not always preserve monotonicity. Recent work of [3] and [4] allowed to fix these two key points, leading to a nearly optimal numerical scheme. Here, we present numerical experiments with schemes of order 3, 5, 7, 9, 11.

2 WENO BASICS

The WENO idea consists in approximating a spatial derivative in a conservative form with the highest possible order for an imposed stencil size. One is then looking for an interfacial value knowing mean values of a discrete function on a given stencil. This is done by using a convex combination of all interpolated values obtained at order k on different stencils around the point of interest to get a final order of 2k-1. A complete description of WENO schemes is included in the review article [1]. Inside WENO class of methods, two principal approaches can be distinguished: upwinding in which the eigensystem is extensively used, and centered scheme family , in which the eigensystem is ignored. The latter form is straightforward even for complex sets of equations while the former is more accurate but needs more CPU time. In this study, we restrict ourselves to the classical direct and characteristic finite differences schemes with Lax-Friedrichs flux splitting for upwinding.

3 LINEAR ANALYSIS

The linear analysis of WENO schemes is based on the modified wave number (MWN) concept [2]. It gives an idea of the resolving efficiency of the scheme in 1D and of the anisotropic directional damping in 2D. In 1D, we examine the response of the derivation operator to a single frequency. Since the scheme is really non linear, other frequencies may appear, but with smaller amplitude and not considered here. A single mode $F_k(x) = \hat{F}_k e^{jkx}$ is derived numerically on

an uniform mesh of size N with periodic boundary conditions to get $\delta F_k / \delta x = F_k^{'}(x) = \sum_{n=-N/2}^{N/2} \hat{F}_k^{'}(n) e^{jnx}$. Then, we

impose $F_k^{'}(x) = jk_k^{'}\hat{F}_k e^{jkx}$, where $k_k^{'} = k_L^{'}(k) + k_{NL}^{'}(k)$ is the modified wave number, and $k_L^{'}(k) = -j\hat{F}_k^{'}(k)/\hat{F}_k$ is the linear MWN ($w' = k_L^{'}\Delta x$ is the scaled linear MWN, independent of the grid mesh). The phase error, $\Re(k_k^{'})$, and the amplification factor, $\Im(k_k^{'})$ (negative for stability), are plotted on **Fig. 1**. One can note that the 11th order (k=6) scheme shows a possible unstable behaviour and the smoothness indicator of WENO schemes are in default for sub-multiples of $w = \pi$. The damping of higher frequencies is the main source of numerical errors. For the 9th order scheme (k=5), about 1/3 of the full wavenumber range is accurately captured. The 2D analysis,

not shown here, reveals large directional errors, mainly in the diagonal direction, which may cause difficulties to handle cylindrical/spherical geometries on Cartesian grids.

4 NON REACTIVE EULER SIMULATIONS

The single species Sod (1D) and monomode Raleigh-Taylor (2D) test cases confirmed that going to higher order schemes provides sharper profiles for the contact discontinuity without any artificial technique (ACM, anti-diffusive …). Furthermore, results from the characteristic reconstruction are more accurate. A 2D multi-mode Rayleigh-Taylor case, inspired from **IWPCTM8** test case #2 for a mono-species configuration at Atwood number 0.5, demonstrates the ability of the WENO procedure to capture the development of instabilities even at very low spatial resolution which is crucial for LES simulations, cf. **Fig. 2**.

When one goes to multi-species Euler simulations, two main difficulties arise. The first one is the **mass fraction positivity** problem (which has been fixed by Larrouturou [5]). The second one is the emergence of **pressure oscillations at contact discontinuities** when γ is not constant (at our knowledge this problem is still open in the conservative case). We do not focus on this second point, expecting small effects on our results. **Larrouturou's idea** is to use a flux for the species directly linked to the full mass flux so that the mass fraction $Y_i = (\rho Y)_i / \rho_i$ is coherent and remains bounded under some time step condition. The application to the WENO formalism leads to the evaluation of $Y_{i+1/2}$ at the same order as the hydro scheme and, most of all, we have to insure that $\sum_{j=1}^{Nsp} Y_{i+1/2}^j = 1$. This last condition is fulfilled by choosing the same non-linear WENO weights for all species. Furthermore, we apply some limitation on the interpolated value $Y_{i+1/2}$ to avoid the generation of new extrema. This method can be applied to the direct procedure or to the characteristic one where we may assume either a full characteristic decomposition (CPU time consuming when dealing with a large number of species) or an approximate characteristic projection based on the mono-species case (may introduce large errors when variable thermodynamic coefficients are taken into account). The 1D bi-species Sod case shows only little difference on Y between those methods. A 2D bi-species Rayleigh-Taylor problem (O_2/N_2 mixture with same $\gamma = 1.4$) reveals that the characteristic WENO is much more accurate than the direct reconstruction procedure and that the full or approximate characteristic methods are in good agreement due to the fixed value of $\gamma = 1.4$, cf. **Fig. 4**.

5 REACTIVE EULER SIMULATIONS

We test now the ability of WENO schemes to handle complex physics (variable thermodynamic properties and large number of species). Here the two main difficulties arise from stiff source terms and the great number of species for detailed chemistry. For all our reactive simulations we consider the Air/H_2 combustion with the detailed chemical model of Dagaut, involving 9 species H, H_2, O, O_2 OH, H_2O, HO_2, H_2O_2, N_2 and 34 elementary reactions (17 reversible). Nitrogen serves as a third-body in 8 elementary reactions. We use the JANAF database for all species thermodynamic properties (Cp are polynomial functions of temperature). The results of a typical laminar 1D premixed flame, not shown here, reveal that: the direct reconstruction is unstable unless Larrouturou's fluxes are used for the species, and that the delay of ignition may be slightly different, depending on the order of the scheme (i.e. numerical viscosity). A 2D cylindrical laminar flame with periodic boundary conditions shows that directional diffusion strongly affect the topology of the flame unless the highest 9th order scheme is used in conjunction with Larrouturou's fluxes for species in full characteristic reconstruction, cf. **Fig. 3**.

REFERENCES

[1]   Shu, C.-W., 1997. Essentially non-oscillatory and weighted essentially non-oscillatory schemes for hyperbolic conservation laws. *NASA/CR-97-206253, Icase Report 97-65.*

[2]   Lardjane, N. 2002, Etude théorique et numérique des écoulements cisaillés libres à masse volumique fortement variable. *PhD Thesis, University of Orleans France.*

[3]   Balsara, D.S. and Shu, C.-W., 2000. Monotonicity preserving weighted essentially non-oscillatory schemes with increasingly higher order of accuracy. *J. of Comp. Phys.* **160**, pp. 405-452.

[4]   Xu, Z. and Shu, C.-W., 2005. Anti-diffusive flux corrections for high order finite difference WENO schemes. *J. of Comp. Phys.* **205(2)**, pp. 458-485.

[5]   Larrouturou, B., 1991. How to preserve mass fraction positivity when computing compressible multi-component flows. . *J. of Comp. Phys.* **95(1)**
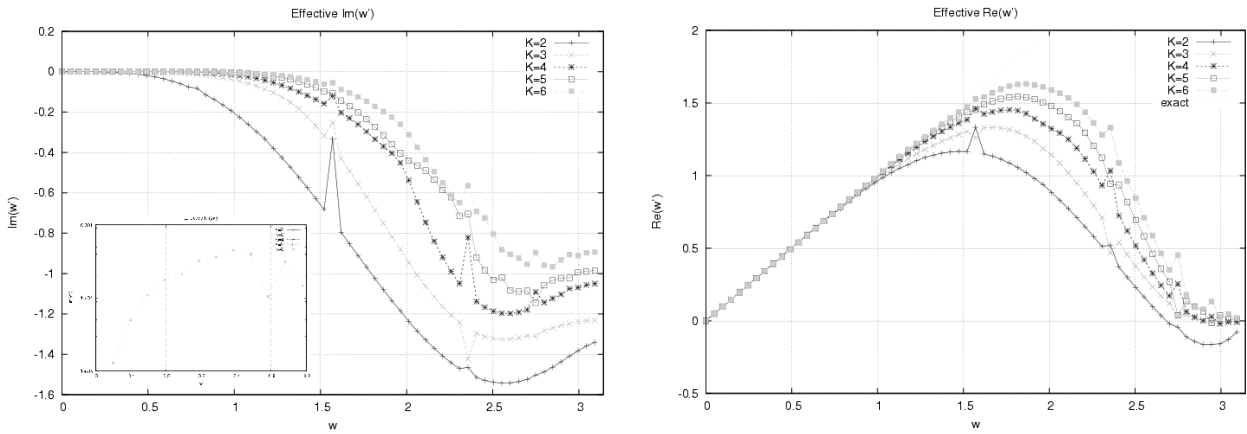
FIGURES

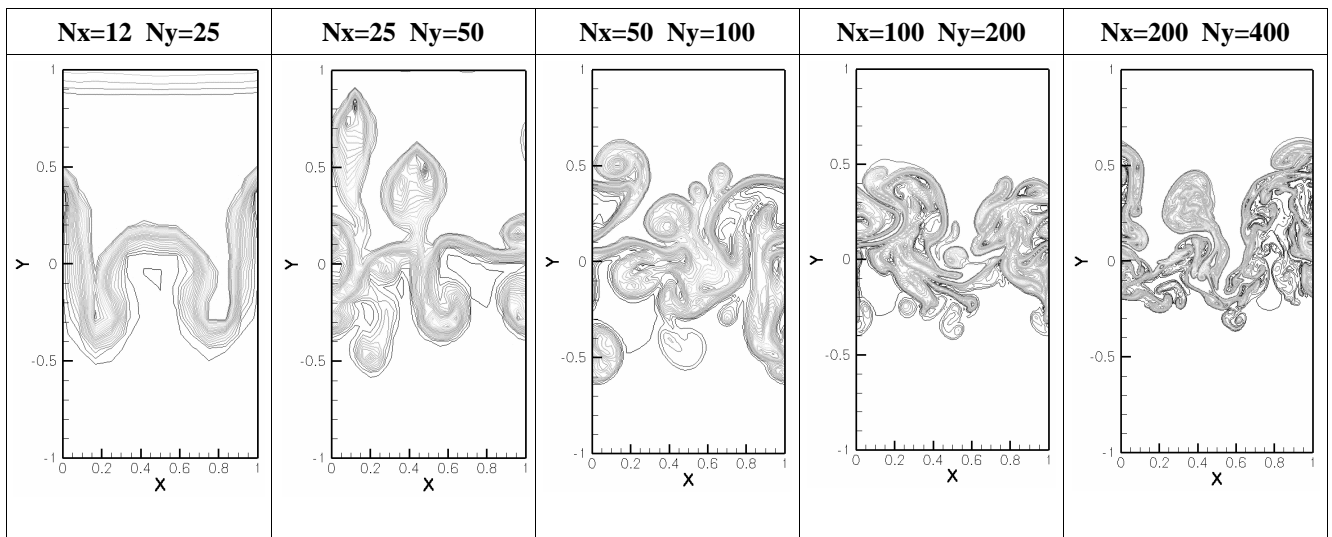Fig. 1. Linear effective modified wave number for various order of the WENO procedure

Fig. 2. Same iso-level of density for the k=5 WENO-characteristic scheme at various spatial resolutions
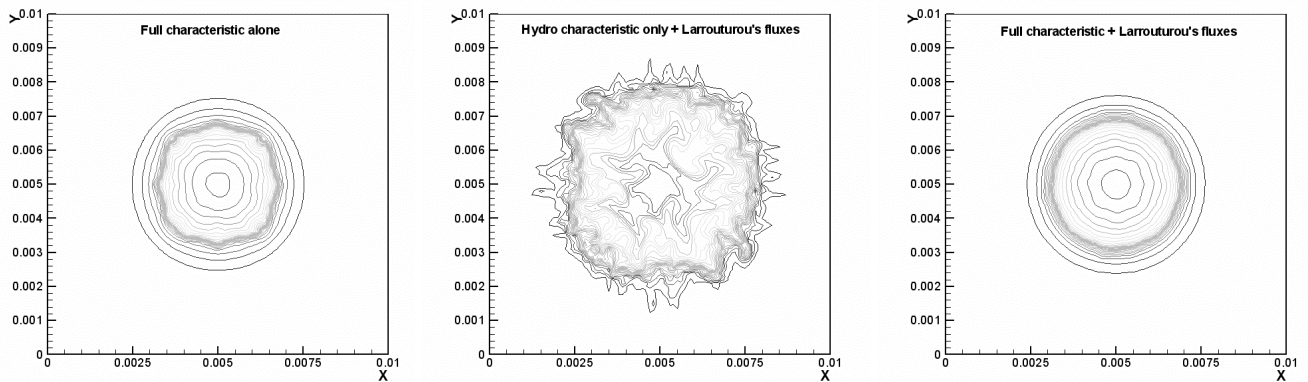

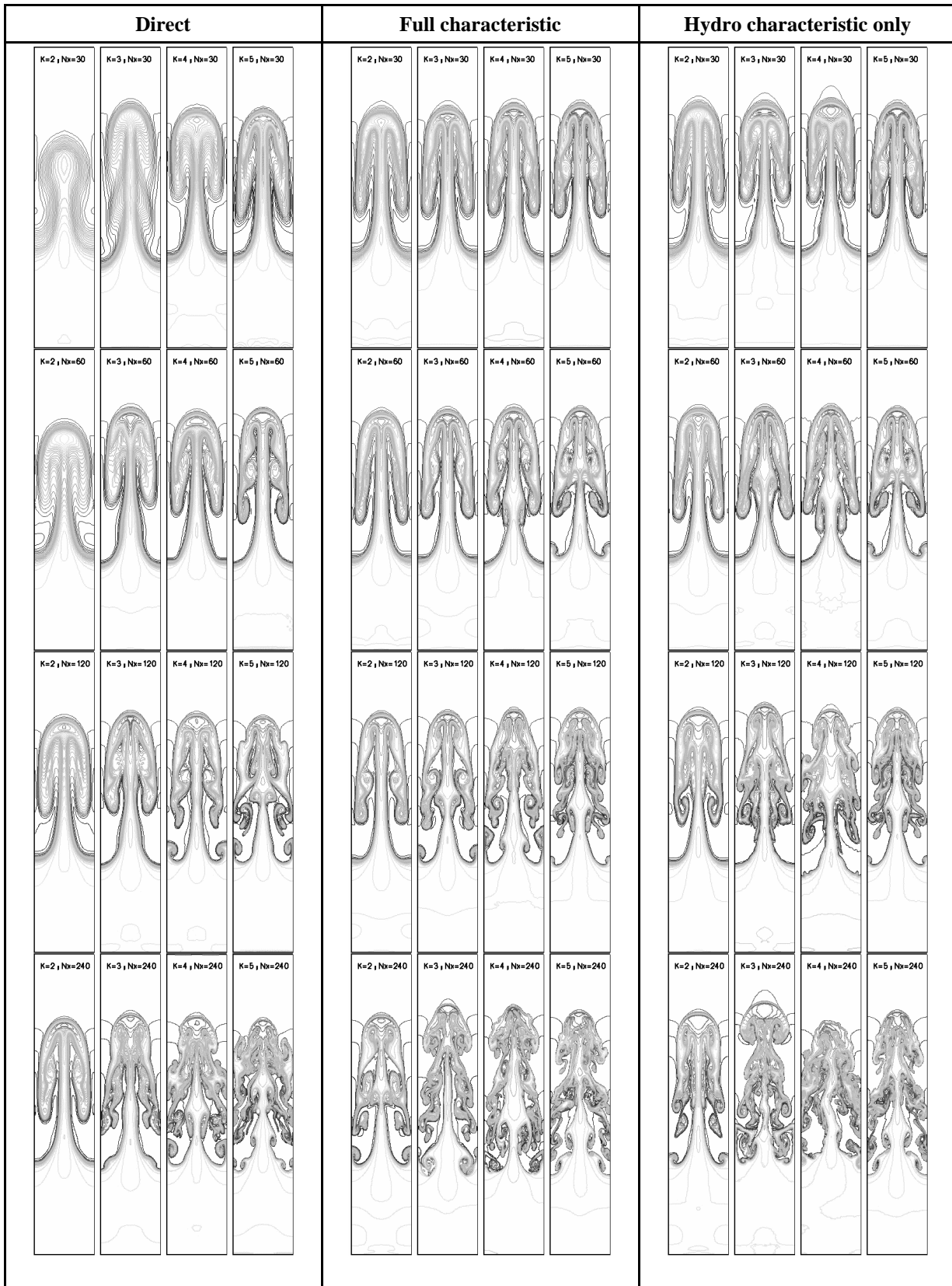Fig. 3. Iso-levels of temperature (300 to 2500K) for the cylindrical flame

Fig. 4. Effect of resolution, order and reconstruction for the WENO procedure

e-mail: `A.G.W.Lawrie@damtp.cam.ac.uk`

Rayleigh-Taylor Driven Mixing in a Multiply Stratified Environment

Andrew LAWRIE[1] and Stuart DALZIEL[1]

[1] *Department of Applied Mathematics and Theoretical Physics, University of Cambridge, United Kingdom*

Abstract: The turbulent mixing of stratified fluids is of concern in many fields. This paper presents the results of both numerical and experimental investigations of mixing processes in an environment where stable and unstable interfaces are interleaved. The simplest example is a three-layer problem, with an stable interface lying beneath a Rayleigh-Taylor unstable one. Direct visualisation of the mixed fluid is achieved using LIF techniques on a chemically reactive fluorescent dye. On the numerical side, recent developments enable us to capture with some validity the physics of mixing generated by the unstable layer. In the Rayleigh-Taylor context, the ILES approach is of interest because of its computational efficiency. ILES simulations are shown in this paper to have good quantitative agreement of mixing behaviour with complementary experiments.

1   INTRODUCTION

The driving instability in the present study has been a focus for scientific curiosity since Rayleigh [13] when the problem of dense fluid above less dense fluid in a gravitational field was first considered. Such instability is observed in a variety of fluids with applications ranging from geophysical and astrophysical to industrial fluid systems. Understanding the suppression of turbulent mixing by stable density stratification also has implications for geophysical systems and potential industrial application, and the interleaved heavy-light-heavy problem configuration of [6] considered here is an appropriate case study, since turbulence generated by the development of the unstable interface induces mixing across the stable interface. The ability of modern numerical techniques to capture the flows with such varied mixing characteristics is not yet confirmed, and this is a focus of current investigation.

1.1   Computational Approach

Despite the approximately exponential growth in computing power over time, numerical simulation of Rayleigh-Taylor instability remains a challenging problem. An approach called Implicit Large Eddy Simulation (ILES) is used in this paper, with the code of [1]. Historically, the approach originated from the surprisingly successful application of modern numerical methods for compressible gas dynamics to problems involving intense mixing. Total Variation Diminishing (TVD) methods (eg. [9]) were developed as a (non-linear) means of controlling truncation error terms in numerical algorithms. Dispersive error (odd order truncation error terms) manifests itself as spurious oscillations around discontinuities and high gradients. Such errors could be eliminated by using a numerical scheme which interpolates, using some empirically derived function, between low and high order. Increased diffusive error (even order truncation error terms), although undesirable in regions of high gradient, is accepted as a consequence, since it has a physical analogue.

The physical relevance of diffusion associated with high gradients motivated the change in application from wave-dominated to highly turbulent flows. It is well known that high gradients are smoothed by viscous effects in a real flow, and the observation that TVD methods also smoothed gradients led to the birth of ILES. Without explicitly applying viscous terms, real flows could be simulated with plausible results (eg. [3, 12, 15]). Effectively, the numerical error replaces a conventional 'eddy-viscosity' sub-grid scale model, and performs a similar function. However, a better understanding of the numerical analysis of ILES for mixing problems is only now being developed (see [11]).

1.2   Experimental Method

While in a broad range of fields much experimental work has focussed on the physics of mixing, obtaining direct visualisation of the mixing process is much less common. Light/Laser-Induced Fluorescence (LIF) techniques

have been used in the past for this purpose in miscible liquid shear flows, eg. [7], and more recently also a hybrid fluorescence/phosphorescence technique in gaseous shear flows (see [4]), but in Rayleigh-Taylor driven mixing there seem not to be comparable experiments. Experiments using pH indicators in the Rayleigh-Taylor context to mark mixed fluid have been performed before (see [10]); the present work extends this concept by using a fluorescent pH indicator, hence permitting detailed LIF visualisation of the actual mixing within the 'mixing region' and furthering understanding of its structure.

The experiments in the current study were conducted using developments of apparatus and techniques which have been applied previously by [2], [3] and [6]. The principal feature of the experimental rig is a horizontal barrier to provide initial separation of fluids across an unstable interface. Using a technique devised by [8], the barrier can be removed from the tank without applying the resulting shear to the fluid. The fluorescent dye
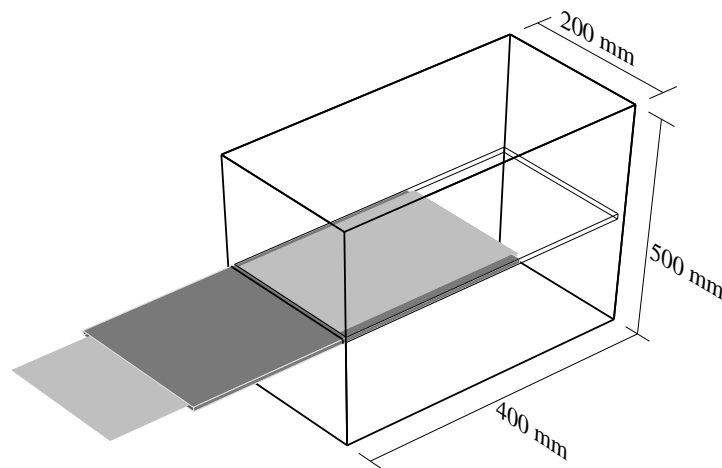
Fig. 1.1. Sketch of experimental apparatus. The hollow stainless steel barrier is shown as dark grey and the nylon fabric as light grey.

used in these experiments is 2,3,5,6-dibenzo pyridine, which absorbs light in the ultraviolet wavelength range, but its emission wavelength is pH dependent. Above pH 5 [14], the emission is violet blue, but below pH 5 the emission is cyan-green. By appropriately filtering the emitted light before reaching the CCD camera, a signal is only received in areas of mixed fluid. The light sheet, provided by a pair of xenon arc lamps, is thin relative to the dynamics of the flow, so the internal structure of the mixing in a two-dimensional cross-section can be examined. The ratio of advection to reaction timescales is very large, and the temperature changes due to the chemistry are negligible, so the reaction itself plays no dynamic role in the fluid mechanics. Acid is added to one (salt solution) fluid layer, the fluorescent dye to another. Refractive indices are matched using alcohol. The initial densities are set by the combination of acid and salt, and densities measured using a Paar density meter.

2 OBSERVATIONS ON RAYLEIGH-TAYLOR MIXING

As a starting point for validation of the numerical simulation, detailed experimental work was focussed on the Rayleigh-Taylor component of the flow, since ILES has been found to work well for this problem. Direct comparison of experiment and simulation is not strictly appropriate because there are significant unsimulated effects in the experiments, such as asymmetries and large scale motions introduced in the experiment by the barrier removal, and discrepancies due to the random perturbation which initialises the simulation. However, a virtual time origin can be derived from the comparison of growth profiles. The experimental results have been spatially filtered down to the same resolution as the simulation, and an equivelant diagnostic used to present

the simulations. A dual time-sequence of images in figure 2.2 compares the evolution of the flow. As is evident
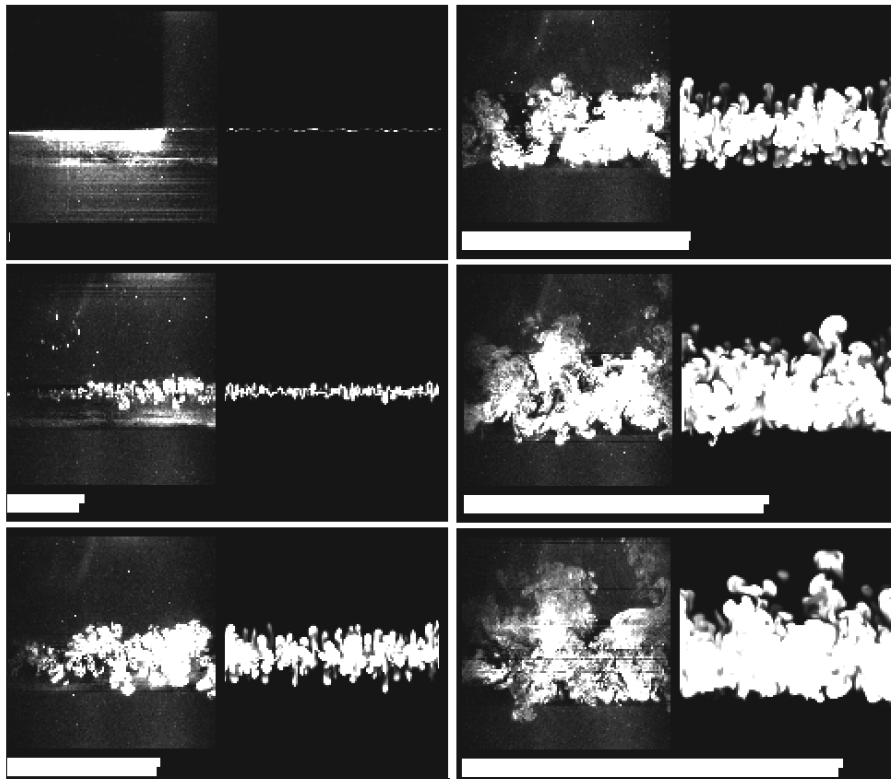
Fig. 2.2. Time series charting the flow evolution in experiment and simulation, using a comparable diagnostic. The white bar indicates the progress of nondimensional simulation time from 0 to 5. The experimental time origin has been shifted to account for the initialisation differences between experiment and simulation.

from figure 2.2, the simulation does not explicitly capture the smallest scales of the flow that are visible even in the filtered experimental time series. However, the mesh size (160x80x200) in the simulation is chosen such that the energy dissipation by numerical error (the implicit sub-grid scale model) in some way approximates the energy dissipation by 'turbulent diffusion' (nature's sub-grid scale model). By matching the rate of energy dissipation, one might expect the simulation flow statistics to converge on the experiment, and hence the mixing statistics, which can be directly derived by image analysis, should match well. Figure 2.3 shows the evolution of
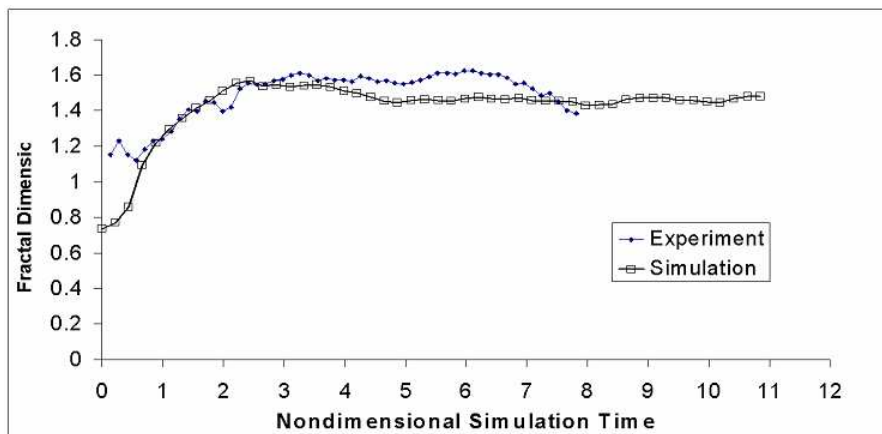
Fig. 2.3. Comparison of fractal dimension evolution in time.

the fractal dimension in time, calculated using the box-counting algorithm of [3] applied to the boundary of the

mixed region as obtained directly from the experimental and simulation images. Qualitatively, the simulation prediction provides a good approximation to the experiment. Discrepancies at very early time are due in part to the differing initialisation, and also (in the simulation case) errors in computing the fractal dimension near the limiting case of a one-dimensional line. As the Rayleigh-Taylor instability grows in time, the range of scales in the turbulence grows and an inertial range begins to develop, with a corresponding increase in the fractal dimension. After non-dimensional time $\tau = 4$ (based on the Atwood number of the unstable interface, the thickness of the middle layer and gravitational acceleration), the fractal dimension ceases to grow and fully developed turbulence is established. [5] proved a simple algebraic relationship between the slope of the power spectrum of a two-dimensional entity and its fractal dimension. The extrapolation to three dimensions suggests that the fractal dimension of about 1.6, as seen in the present study, approximates a $P(k) = k^{-\frac{5}{3}}$ spectral slope surprisingly well. A more direct evaluation of the mixing process can be obtained by considering
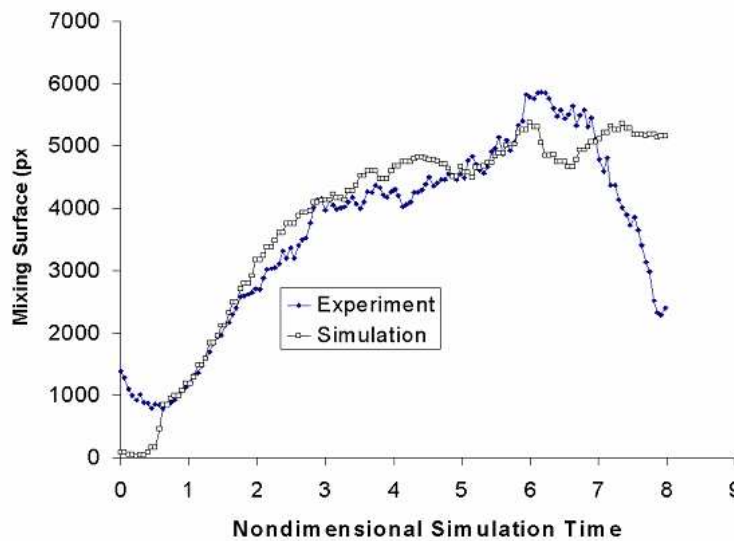
Fig. 2.4. Evolution of mixing surface area in time. The length of the two-dimensional cross-section through the surface is measured by pixel count. Close agreement between experiment and simulation is achieved.

the surface area over which mixing takes place, and the enclosed volume of mixed fluid which grows in time as the mixing front advances. The planar analogue of the surface area (the length by pixel count of the enclosing contour) is shown in figure 2.4 and is defined as the boundary of a region where pixel intensity is greater than a threshold. The corresponsing volume is shown in figure 2.5 As before, the processing is performed on the filtered experimental data, for valid comparison with the simulation. The threshold is chosen for convenience, to avoid contaminating the image analysis with digital noise. However, signal intensity (in the absence of other effects) is linear in the local dye concentration, so as further mixing takes place towards later times, the signal intensity of this mixed fluid reduces, until it eventually falls below the noise threshold. Since this effect is not included in the simulation diagnostic, the experimental and simulation curves diverge at late time.

3 CONCLUSIONS

An experimental technique has been presented for directly visualising regions of molecularly mixed flow in miscible liquid flows. Particular attention has been paid to the early time evolution of the Rayleigh-Taylor instability, obtaining quantitative measurements from a novel perspective on a widely studied problem. Previous work by [10] on chemical indicators of molecular mixing has been developed in this study by gaining a first insight into the detailed structure of the mixing region. ILES numerical simulations have been performed which show comparable mixing behaviour to the experiments, when considering fractal dimension, mixing surface and mixed volume.
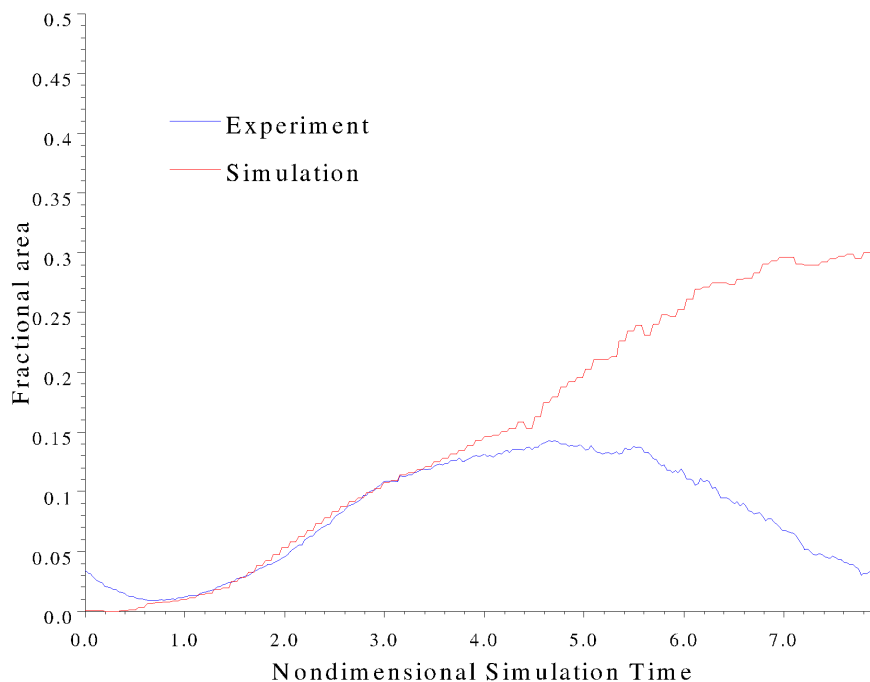
Fig. 2.5. Evolution of mixed volume in time. The independent variable is measured as a fraction of total area. Agreement is good until the dilution of fluid in the experiment is such that recovered signal intensity is of the order of the noise threshold.

4   ACKNOWLEDGEMENTS

REFERENCES

[1] Almgren, A. S., Bell, J.B., Colella, P., Howell, L. H., and Welcome, M. L., 1998. A conservative adaptive projection method for the variable density incompressible Navier Stokes equations. *J. Comp Phys.*, 142:1-46

[2] Dalziel, S. B., 1993. Rayleigh-Taylor instability: experiments with image analysis. *Dyn. Atmos. Oceans*, 20:127-153

[3] Dalziel, S. B., Linden, P. F., and Youngs, D. L., 1999. Self-similarity and internal structure of turbulence induced by Rayleigh-Taylor instability. *J. Fluid Mech.*, 399:1-48

[4] Hu, H. and Koochesfahani, M. M., 2002. A novel method for instantaneous, quantitative measurement of molecular mixing in gaseous flows. *Exp. Fluids*, 31:202-209

[5] Hunt, J. C. R., and Vassilicos, J. C., 1991. Kolmogorov's contributions to the physical and geometrical understanding of small-scale turbulence and recent developments. *Proc. R. Soc. Lond.*, 434:183-210

[6] Jacobs, J. W. and Dalziel, S. B., 2005. Rayleigh-Taylor instability in complex stratifications. *J. Fluid Mech.*, 542:251-279

[7] Koochesfahani, M. M., and Dimotakis, P. E., 1985. Mixing and chemical reactions in a turbulent liquid mixing layer. *J. Fluid Mech.*, 170:83-112

[8] Lane-Serff, G. F., 1989. *Heat flow and air movement in buildings.* PhD thesis, DAMTP, University of Cambridge, UK.

[9] Leveque, R., editor, 1992. *Numerical methods for conservation laws.* Birkhauser

[10] Linden, P. F., Redondo, J. M., and Youngs, D. L., 1994. Molecular mixing in Rayleigh-Taylor instability. *J. Fluid Mech.*, 265:97-124

[11] Margolin, L. G., Rider, W. J., and Grinstein, F. F., 2006. Modeling turbulent flow with implicit LES. *J. Turbulence*, 7:1-27

[12] Ramaprabhu, P., Dimonte, G., and Andrews, M. J., 2005. A numerical study of the influence of initial perurbations on the turbulent Rayleigh-Taylor instability. *J. Fluid Mech.* 536:285-319

[13] Rayleigh, L., 1883. Investigation of the character of the equilibrium of an incompressible heavy fluid of variable density. *Proc. Lond. Math. Soc.*, XIV:70-177

[14] Weast, R. C., editor, 1971. *Handbook of Chemistry and Physics.* CRC Press, 52nd edition.

[15] Youngs, D. L., 1994. Numerical simulation of mixing by Rayleigh-Taylor and Richtmyer-Meshkov instabilities. *Laser and Particle Beams*, 12:725-750

e-mail: `benjamin.le.creurer@gmail.com`   e-mail: `serge.gauthier@cea.fr`

Pseudo-spectral simulation of the overturning process due to Rayleigh-Taylor instability for compressible miscible fluids

Benjamin LE CREURER[1] and Serge GAUTHIER[2]

[1] *Previous address: CNRS-LIMSI/Mechanical Department BP 133 91403 Orsay Cedex FRANCE*
[2] *CEA/Bruyères-le-Châtel BP 12 91680 Bruyères-le-Châtel FRANCE*

Abstract: A Fourier-Chebyshev pseudo-spectral numerical method is used to perform 2D simulations of the Rayleigh-Taylor instability. Interface is disturbed by a single-mode perturbation. This long time-integrated simulation is pursued until a return toward the mechanical equilibrium. Thanks to the physical model and parameter set on the one hand, and to the highly accurate method on the other hand, an acoustic wave system is exhibited. The beginning of a multimode simulation is also presented.

1 INTRODUCTION

Superposition of a heavy fluid above a lighter one in a constant acceleration field depicts a hydrodynamic unstable configuration called the Rayleigh-Taylor (R-T) instability. The interest of R-T instability goes beyond inertial-confinement fusion and Astrophysics, even if these concerns are dominant in today studies. This is a basic problem in fluid dynamics. Although this instability is studied for decades it is still an open problem in several aspects. In order to investigate the physics of the R-T-instability the Navier-Stokes (NS) equations should be preferred since they take into account diffusion effects. These transport coefficients are associated with cutoff wave numbers in the linear regime as well as in the fully developed turbulent regime. In this way, when the NS equations are solved with an accurate numerical scheme, one obtains the physical damping rates. Direct numerical simulations are needed in some situations: low Reynolds number flows such as single mode instability or multimode transitional flows at large Reynolds numbers. Even though these simulations are very demanding in terms of computational resources, they also bring reference solutions for turbulence modeling and subgrid-scale models for LES. It appears that DNS of R-T-compressible mixing layers, based on the complete NS equations, and solved with a high order numerical scheme, are still lacking. We do believe that an effort has to be made in that direction. This is the reason why we have developed, over the last few years, a Chebyshev-Fourier spectral numerical method for subsonic mixing compressible flows where stiff and unsteady gradients are present (AMÉNOPHIS code) [1, 2]. In this paper we present two-dimensional direct numerical simulations of compressible miscible fluids of a R-T-instability where viscosity, thermal conductivity and species diffusion coefficients are taken into account. These simulations, started from rest, are initialized with a single-mode density perturbation and they lead toward the hydrostatic equilibrium state. A system of 1D-acoustic waves is exhibited in the final stage. Moreover the physical damping rate of the acoustic waves is also recovered. A multimode simulation is also carried out from rest to a nonlinear behavior. In that case, the initial perturbation is a solenoidal velocity field. These simulations show that flows with strong unsteady gradients can be handled by spectral methods.

2 PHYSICAL MODEL AND GOVERNING EQUATIONS

2.1 Physical model

Choose is made to describe the mixing of two perfect *miscible* gases within the single-fluid approximation. We assume the additivity of extensive variables and the local thermal equilibrium hypothesis [3–5]. It follows that

$$p = p_1 + p_2, \quad \rho = \rho_1 + \rho_2 \quad \text{and} \quad T = T_1 = T_2, \tag{2.1}$$

Concentration c is defined as

$$\rho_1 = \rho\, c \quad \text{so } \rho_2 = (1 - c)\rho. \tag{2.2}$$

The partial pressure reads

$$p_i = \rho_i \frac{\mathcal{R}}{\mathcal{M}_i} T = (\gamma_i - 1)\rho_i C_{v_i} T, \quad (i = 1, 2) \tag{2.3}$$

with C_v is the specific heat at constant volume and γ the ratio of specific heats. The molar weights are $\mathcal{M}_1$ and $\mathcal{M}_2$. Moreover if one states equality of pressures on both sides of the pseudo-interface, it comes

$$A_t \equiv \frac{\rho_1(0^+) - \rho_2(0^-)}{\rho_1(0^+) + \rho_2(0^-)} = \frac{\mathcal{M}_1 - \mathcal{M}_2}{\mathcal{M}_1 + \mathcal{M}_2}. \tag{2.4}$$

2.2 Governing equations

The motion takes place in a 2D closed rectangular box of dimensions $L_y \times L_z$ with $L_z \equiv z_t - z_b$. The flow is governed by the full NS equations closed with Eqs. (2.3) and (2.1). Boundary conditions are periodic in the horizontal y-direction for all quantities, and of Neumann (Dirichlet, resp.) type in the vertical z-direction for the velocity $u_1 = u_y$ ($u_2 = u_z$, resp.), the concentration and the temperature. Once making NS equations dimensionless, it comes

$$\partial_t \rho = -\partial_j \rho u_j, \tag{2.5a}$$

$$\partial_t u_i - \frac{1}{Re\,\rho}\partial_j \tau_{ij} = -u_j \partial_j u_i - \frac{1}{Sr\,\rho}\partial_i p - \delta_{i2}, \tag{2.5b}$$

$$\partial_t T - \frac{\gamma_r}{Re\,Pr\,\rho C_v}\partial_{jj}^2 T = -u_j \partial_j T - \frac{1}{\rho C_v}\left(-(\gamma_r - 1)p\partial_j u_j + (\gamma_r - 1)\frac{Sr}{Re}\tau_{ij}D_{ij} - T\frac{1}{Re\,Sc}d_c C_v \partial_{jj}^2 c\right), \tag{2.5c}$$

$$\partial_t c - \frac{1}{Re\,Sc\,\rho}\partial_{jj}^2 c = -u_j \partial_j c, \tag{2.5d}$$

plus the equation of state for a mixing of perfect gases

$$p = (1 + A_t - 2A_t\,c)\,\rho T, \tag{2.6}$$

where $d_c C_v$ is the C_v derivative versus the concentration, $\tau_{ij}D_{ij}$ denote the dissipation function. The four reference scales are $L_r \equiv L_y$ for length; $t_r = (L_y/g)^{1/2}$ for time; $\rho_r L_r^3 = \frac{1}{2}(\rho_1(0^+) + \rho_2(0^-))L_r^3$ for mass and $T_r = \overline{T}$ for temperature (see Ref. [5] for details). The dimensionless numbers Reynolds Re, stratification Sr, Schmidt Sc, Prandtl Pr are defined as

$$Re = \frac{\rho_r\,g^{1/2}\,L_r^{3/2}}{\mu}, \qquad Sr = \frac{g\,L_r}{\mathcal{R}\,T_r/\mathcal{M}_r}, \qquad Sc = \frac{\mu}{\rho\,D} \qquad \text{and} \quad Pr = \frac{\mu\,\gamma\,C_{v,r}}{\kappa}, \tag{2.7}$$

where the transport coefficients μ, κ and D denote the viscosity, thermal conductivity and mass diffusion, respectively. τ_{ij} is the stress tensor (defined within the Stokes relation).

3 NUMERICAL METHOD AND SELF-ADAPTIVE METHOD

The features of the numerical method are summarized here (more details can be found in Refs. [5, 8] and references therein)

1. Physical quantities $\varphi = \rho$, u_i ($i = 1, 2$), T and c are expanded on Fourier series along the homogeneous y-direction and on Chebyshev polynomials along the z-inhomogeneous direction.

2. A non-overlapping domain decomposition is used in the z-direction and a coordinate transform is defined in each subdomain. Both the location of the numerical interfaces and the mapping parameters are dynamically adapted by minimizing some error of a linear combination of the calculated solution [2, 7].

3. Temporal discretization is performed with a semi-implicit three-step second-order Runge-Kutta scheme in a low storage formulation. Because of the domain decomposition, diffusive terms are handled implicitly through a splitting [2]. The time step is evaluated with uncoupled and unidimensional stability criteria.

4   SIMULATION RESULTS

4.1   A single mode simulation

We have carried out 2D numerical simulations started from rest toward mechanical equilibrium. The interface between the two fluids is initially perturbed through the density field [1,4,5]. The physical parameters are the following ones: $A_t = 0.20$, $Sr = 0.04$, $Re = 400$, $Sc = 20$, $Pr = 2$, $\gamma_i = 5/3$. The thickness of the interface is initially $\delta = 0.031$ [6]. The wavelength and the amplitude are $\lambda = 1$ and $a_0 = 0.052$, respectively. The spatial resolution is 5 subdomains with 64 collocation points and 128 points in the Fourier direction. Two simulations
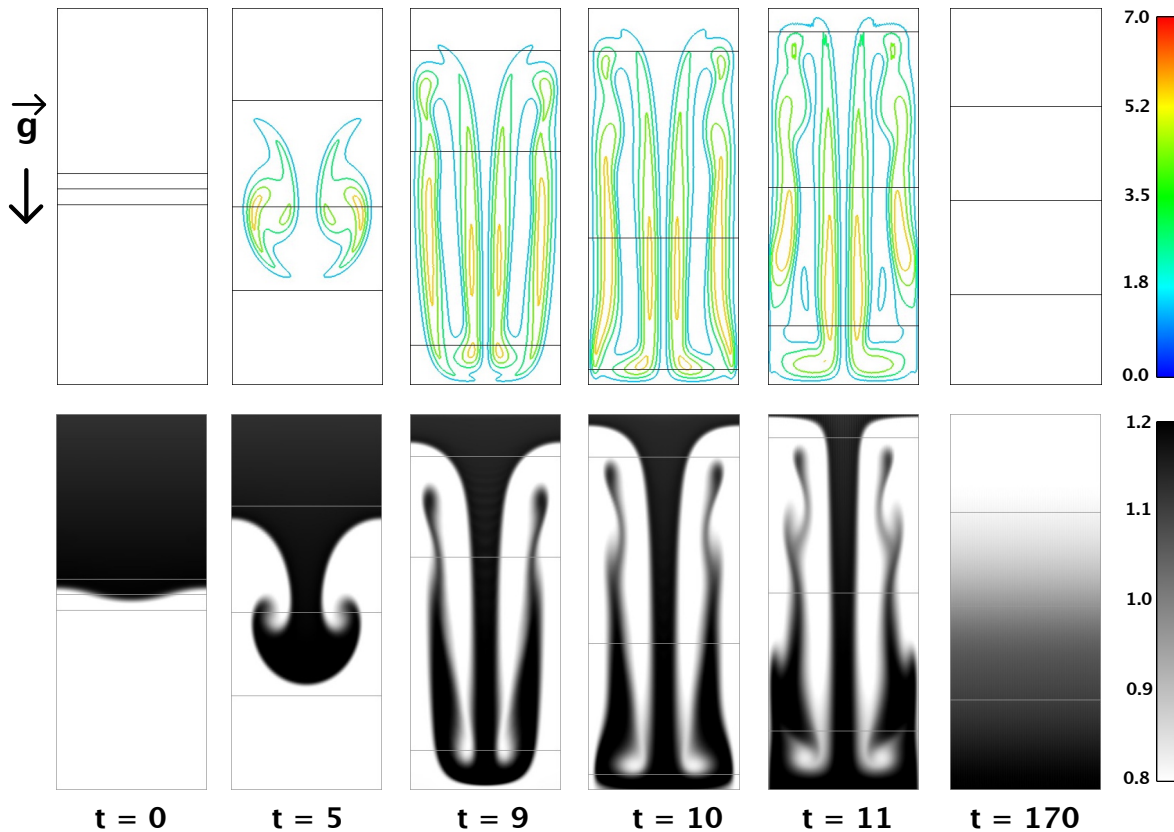
Fig. 4.1. Single mode simulation: vorticity (top) and density (bottom) fields at six different times.

have been carried out. The first one with an aspect ratio of 2.5 and the second one with an aspect ratio of 5. Results of the simulation are presented in Fig. 4.1. The mushroom reaches the bottom of the box at $t \approx 9.5$ and the flow overturn is observed at $t = 15$. The time step evolution is displayed in Fig. 4.2 (left). It varies of two orders of magnitude during the simulation. When the mushroom reaches the bottom of the box, the self-adaptive procedure brings a lot of collocation points in the vicinity of the boundary. As result, the time step decreases. The evolution of the numerical interface locations are given in Fig. 4.2 (center). They follow the main gradients of the fields. Notice the evolution of the interfaces that follow, at the very beginning, the acoustic perturbations. When the structure spreads all over the box, interface locations reach approximately constant values, close to a quasi-uniform distribution of the subdomains. The norm of the test-function is also displayed in Fig. 4.2 (right). Recall that this norm is an indicator of the interpolation error. This norm reaches very high levels at the beginning of the simulation and when the mushroom reaches the bottom of the box. Afterward, the norm slightly decreases showing that the gradients have been smoothed and, consequently, that the accuracy is better. The results of the linear regime are represented in Fig. 4.3. On the left, the growth rate and on center and on the right, the Fourier modes of the isoline $c = 0.5$. Later in time, at the end of the overturn process, the flow recovers a one-dimensional structure by time $t_{1D} \approx 150$. The kinetic energy, E_k, reaches a maximum at time $t \approx 10.4$ and then quickly decreases until $t \approx 120$ and then oscillates at high
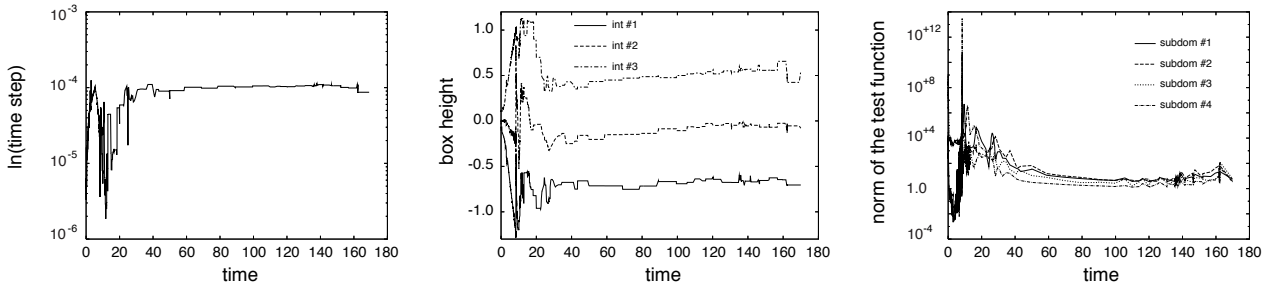
Fig. 4.2. Single mode simulation: evolution of the time step (left), the interface locations (center) and the norm of the test-function in each subdomain (right).
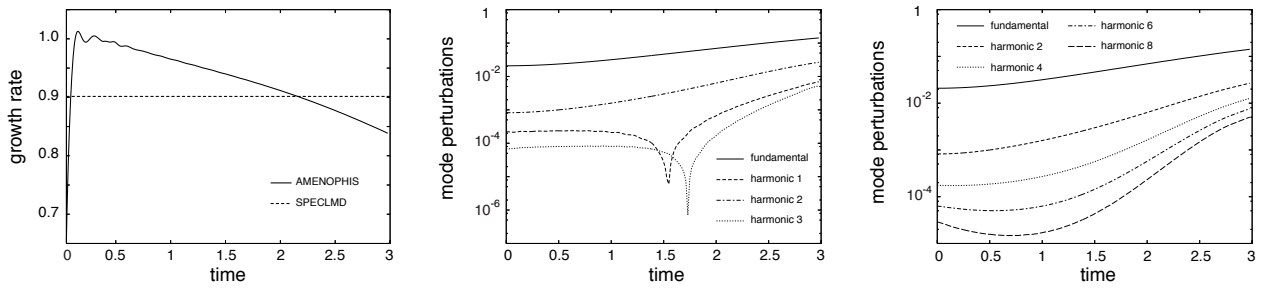
Fig. 4.3. Single mode simulation: growth rate of the perturbation versus time t (left) obtained from AMÉNOPHIS data (solid line) and calculated with the normal mode analysis code SPECLMD (dotted line) [5,6]; Fourier modes of the isoline $c = 0.5$, the fundamental and the first three harmonics (center) and the even harmonics (right).
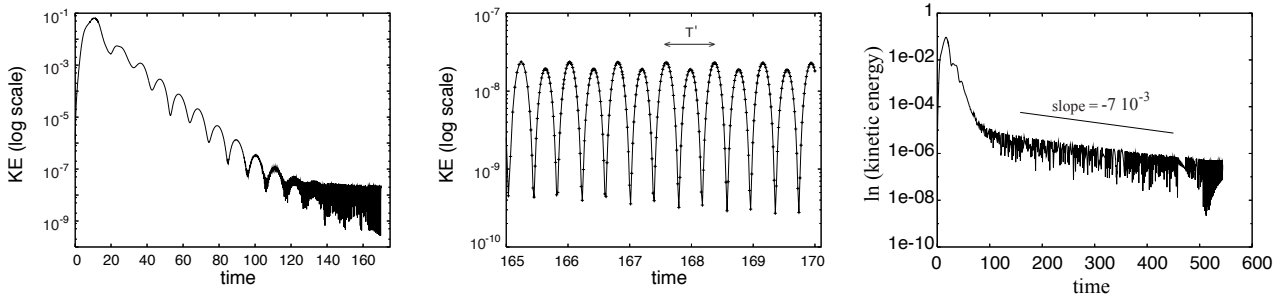
Fig. 4.4. Single mode simulation: kinetic energy (left); zoom of the previous figure (center); kinetic energy in the large box (right).

frequency but the mean value still decreases so that the flow slowly tends toward the equilibrium state as can be seen in Fig. 4.4 (left). A zoom is displayed in Fig. 4.4 (center) from which the period of these waves can be determined. Each point in this curve corresponds to a record data time. The question is of course the nature of these waves. Since dispersion relation for acoustic waves is $\omega = k\,c_S$ while $\omega = \sqrt{k}$ for gravity waves, we have carried out a second simulation in which the vertical size has been doubled. The period of the resulting 1D waves is also doubled [see Fig. 4.4 (right)], proving the acoustic nature of these waves. We have also represented, in this figure, the scaling law $E_k(t) = \exp\left(-2\,k^2/Re\,t\right)$ with $2\,k^2/Re = 7.89\,10^{-3}$ obtained from Eq. (2.5b) by retaining only the temporal derivative and the viscous term. We see clearly that the kinetic energy follows closely this damping rate. It also shows that the one-dimensional wave-system is damped by the physical viscosity, i.e., the numerical dissipation of the pseudo-spectral Chebyshev-Fourier method is negligible. The space-time evolution of kinetic energy is displayed in Fig. 4.5 (right). Recall that, for this time interval,
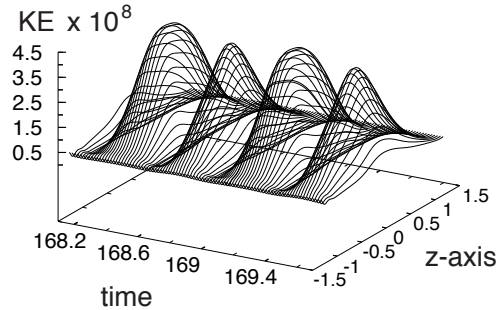
Fig. 4.5. Single mode simulation: Space-time variations of the kinetic energy E_k versus the altitude z and time for $168.2 \leq t \leq 169.5$.

the contribution of the y-component of the velocity to the kinetic energy E_k, is negligible. Thus this figure represents the kinetic energy associated with the one-dimensional wave system.

4.2 A multimode simulation
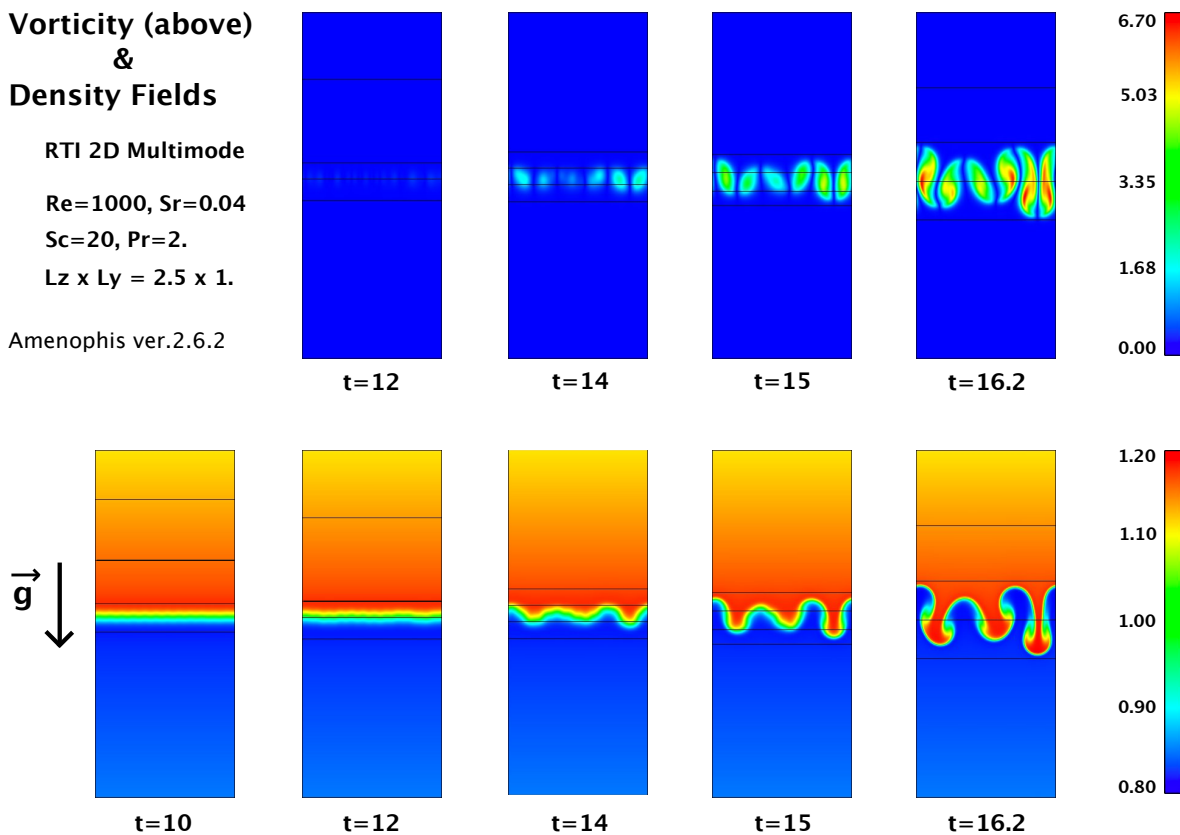
Fig. 4.6. Multimode simulation: vorticity (top) and density (bottom) fields at five different times.

We also present the beginning of a multimode simulation. Results of the simulation are presented in Fig. 4.6. The initial perturbation is a solenoidal velocity field obtained from a potential vector [9]. The physical parameters are the same as above except that the Reynolds number is now taken equal to 1000. The spatial resolution is 5 subdomains with 64 collocation points and 512 points in the Fourier direction. The
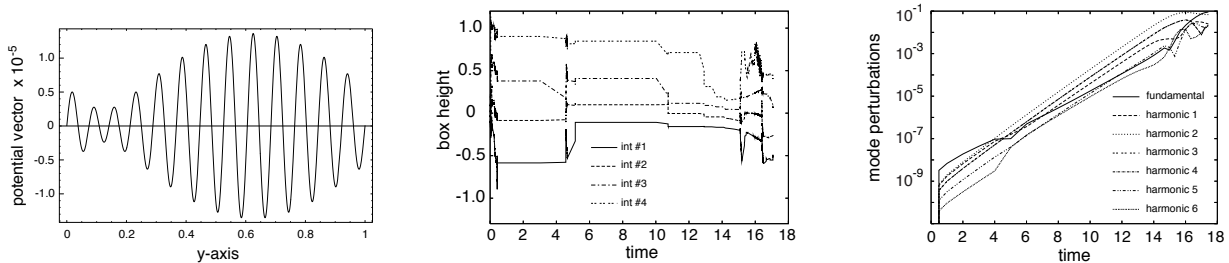

Fig. 4.7. Multimode simulation: profile of the potential vector (left); locations of the interfaces (center) and evolution of the Fourier modes of the isoline $c = 0.5$ (right).

evolution of the numerical interfaces are displayed in Fig. 4.7 (center) with the Fourier modes of the isoline $c = 0.5$ (right).

5 CONCLUSIONS

We have carried out two-dimensional numerical simulations of the Rayleigh-Taylor instability, for a compressible binary mixture of viscous fluids starting from rest until the return toward mechanical equilibrium where a system of acoustic waves takes place. The full Navier-Stokes equations with constant transport coefficients have been used. From a numerical point of view, we have shown, through a multidomain self-adaptive method, that spectral discretizations can handle strong moving gradients, such as those occurring in Rayleigh-Taylor flows. A linear stability analysis has been performed with the code SPECLMD. This code also uses the multidomain self-adaptive method, and gives the dispersion curve together with the eigenfunctions. Finally a numerical simulation with a multimode initial perturbation has been carried out. Next steps will be 2D and 3D high Reynolds number multimode simulations.

REFERENCES

[1] E. Fournier, S. Gauthier and F. Renaud, 2001, 2D pseudo-spectral parallel Navier-Stokes simulations of compressible Rayleigh-Taylor instability. *Comput. & Fluids* **31**, pp. 569–587.

[2] F. Renaud and S. Gauthier, 1997, A Dynamical Pseudo-Spectral Domain Decomposition Technique: Application to Viscous Compressible Flows. *J. Comput. Phys.* **131**, pp. 89–108.

[3] C. Mügler, and S. Gauthier, 2000, Two-dimensional Navier-Stokes simulations of gaseous mixtures induced by Richtmyer-Meshkov instability. *Phys. Fluids* **12**, pp. 1783–1798.

[4] B. Le Creurer, 2005, Simulations numériques pseudo-spectrales de l'instabilité de Rayleigh-Taylor pour des fluides compressibles. PhD thesis, CEA-Université de Marne-la-Vallée.

[5] B. Le Creurer, and S. Gauthier, S., A return toward equilibrium in a two-dimensional Rayleigh-Taylor instability for compressible miscible fluids. Submitted to *Phys. Rev. E.*

[6] M.-A. Lafay, B. Le Creurer and S. Gauthier, Compressibility effects on the Rayleigh-Taylor instability. This volume.

[7] H. Guillard, J.-M. Malé and R. Peyret, 1992, Adaptive spectral methods with application to mixing layer computations. *J. Comput. Phys* **102**, pp. 114–127.

[8] S. Gauthier, B. Le Creurer, F. Abéguilé, C. Boudesocque-Dubois, J.-M. Clarisse, 2005, A self-adaptive method decomposition method with Chebyshev method. *Int. J. Pure Appl. Math.* **24**, pp. 553–577.

[9] C.P. Verdon, R.L. Mc Crory, R.L. Morse, G.R. Baker, D.I. Meiron, and S.A. Orszag, 1983, Nonlinear effects of multifrequency hydrodynamic instabilities on ablatively accelerated thin shells. *Phys. Fluids* **25**, pp. 1653–1674.

The development of turbulent mixing zone at laser acceleration of thin foils.

Ivan G. Lebo[1,2] &Vladimir D. Zvorykin[2]

1. Technical University-MIREA,
pr. Vernadskogo, 78,Moscow, RUSSIA
lebo@mirea.ru

2. Lebedev Physical Instituite,
Leninski pr., 53, Moscow, RUSSIA
lebo@sci.lebedev.ru

Introduction.

The study of instability of an interface between two media in the field of constant (Rayleigh-Taylor instability-RTI (Taylor, 1950)) and pulsed (Richtmyer-Meshkov instability-RMI (Richtmyer, 1960, Meshkov, 1969)) acceleration is a fundamental problem of fluid and gas mechanics. The solution of this problem is high impertant for Inertial Confinement Fusion (ICF). A shock tube was used in an invistigation of these instabilities in our early publications (Aleshin, 1987, 1990). In 2000 we have proposed the concept of laser-driven shock tube for the hydrodynamic instability investigations (Zvorykin, 2000).

Paper presents the results of experimental and numerical investigations of the development of turbulent mixing zone at laser acceleration of thin films in air. The experiments have been made at KrF laser "GARPUN" (Lebedev Physical Institute, Moscow). We have compared the experimental data with the results of 2D numerical simulations. In order to describe the turbulent mixing we have used the model of turbulent diffusion (Belen'ki, 1965) and have got good agreement between experimental and numerical results.

Concept of laser-driven shock tube.

The design of such laser-driven shock tube (LST) is based on use of following basic components: 1) the powerful ultraviolet laser with pulse duration of 100 ns, 2) special focus system (multielement prism raster and lens, which obtain high uniformity of irradiation in focus plane (focal spot has a size ~ 2x2 cm), 3) shock tube cell, 4) 2D numerical codes for description of physical processes in LST.

"GARPUN" laser installation and experimental procedure.

A multistage KrF laser "GARPUN" was used in experiments. The laser facility consists of discharge-pumped EMG 150 TMSC eximer master oscillator and two electron-beam-pumped modules. In injection-controlled operation, the laser generates pulses of 100 J energy, 100 ns duration and radiation divergence 0.1 mrad. The targets are set inside an

evacuated chamber filled with air or noble gas, whose pressure is varied in the range P_0=0.0002-1 bar.

Focusing system combined a multi-element prism raster and a lens. By splitting an incident laser beam with a cross section of 10x10 cm2 into 25 individual 2x2 cm^2 beamlets and overlapping them at a focal plane this system provides non-uniformity less then a few per cent across the square spot. The hydrodynamics of laser plasma and shock waves were investigated by a streak camera or high-speed photo-chronograph with slit-scanning of images by means of rotating mirror. The shlieren and shadow techniques with a quasi-steady collimated probe beam produced by a capillary-discharge light source where combined with the high-speeded slit-scanning recording of images of laser plasma in self-luminescence.

2D Lagrange code "ATLANT-C"

Numerical simulations were carried out with the 2D hydrodynamic code "ATLANT-C" in cylindrical Lagrangian coordinates (Iskakov, 2000). This code is destined for simulation of flows gas and laser plasma in a broad range of initial condition. The axial symmetry of the processes is suggested. Either a tree- or two-temperature model with consideration for the self-radiation losses of plasma is useful, depending on the specific problem. The energy transfer by the electrons, ions, and self-radiation of plasma is taken into account. The plasma quasi-neutrality is assumed. The model of the mean degree of ionization is considered. The variations of the degree of ionization are considered to be caused by the electron impact, three-body recombination, and radiative recombination in every Lagrange cell.

Laser-acceleration of thin film.

Laser acceleration of thin films is a classic case where R-T and R-M instabilities would occur. We have irradiated thin CH film (with thickness d=3-10 μm) by means of KrF laser. Fig.1 shows the expansion of accelerated layer in vacuum (case a) and shock wave and layer in atmospheric air (case b). The initial thickness of CH film was 5 μm and incident laser intensity q=0.5 GW/cm^2.

Fig.1. Acceleration of 5 μm CH film by laser with intensity ~ 0.5 GW/cm^2 in vacuum (a) and ambient air (b).
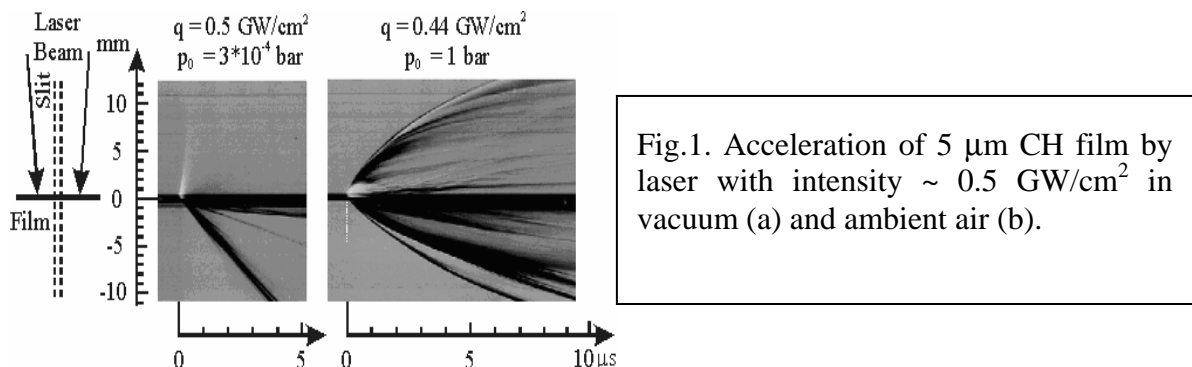
To investigate the evolution of the hydrodynamic flow and instability development during laser-film interaction we rotated the images by an angle of 90°, so that the slit of the photo-chronograph was set parallel to the film surface at various distances behind it.

Fig.2 illustrates the comparison of numerical results (solid line) and experimental data. Initial velocity of forward SW measured in the experiments are somewhat less then the calculated values. The reason for this discrepancy might be a partial reflection of laser radiation, which was not accounted in numerical simulations.
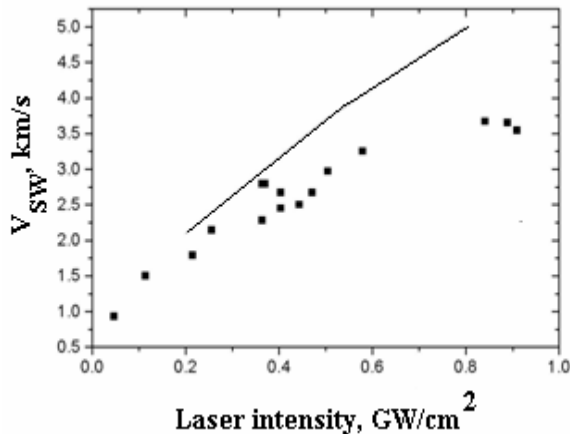
Fig.2. Initial velocity of forward SW in atmospheric air as function of laser intensity generated by CH-film of thickness 5 μm. Comparison of experimental and numerical results.

Fig.3 demonstrates the influence of initial in homogeneities of laser irradiation on the instability development. Fig. illustrates the images at slit distance 3.5 mm. In the second case we have used a wire grid with mesh sizes of 0.7x0.7 mm^2 and irradiated the film through the grid. It was set at the distance of about 1 cm in front of irradiated film.
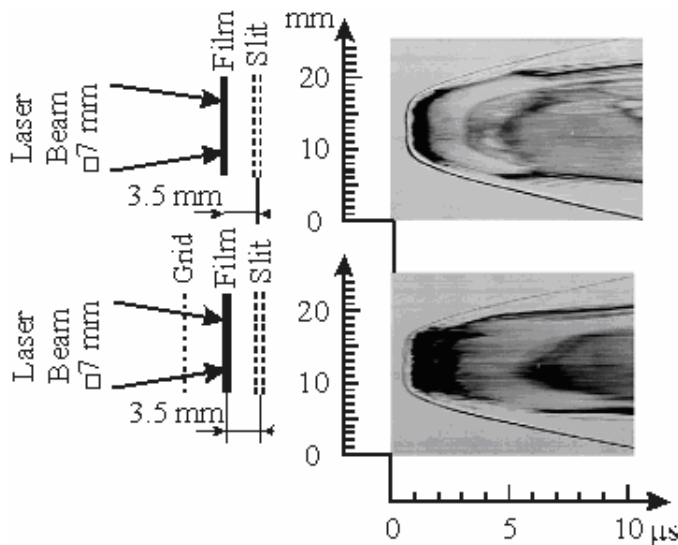
Fig.3. Slit-scanning recorders of laser interaction with 5 μm film.in atmospheric air with uniform irradiation (upper) and with non-uniformities (lower).

The slit was placed at a distance of 3.5 mm. We have modelled the acceleration of film with help of "ATLANT-C" code. Fig.4 illustrates density profiles along 0Z axes (a)

and distance (Z) and velocity (V) of maximum density of nonevaporated layer as function of time (b).
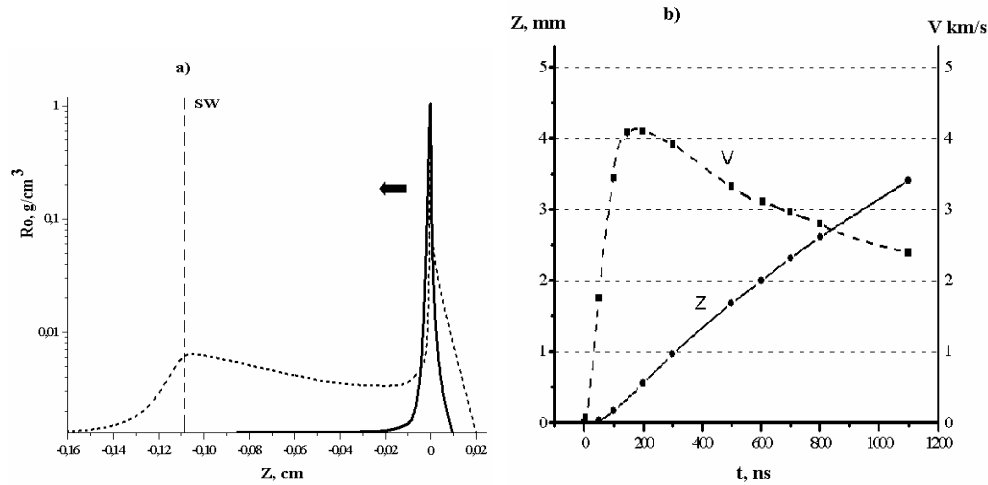
Fig.4. Density profiles along 0Z axes for two times moments, t=100 ns (solid line) and t=1100 ns (dashed line). The density maxima are superposed at one point. The vertical dashed line is the position of shock wave front at t=1100 ns. The arrow is the direction of the layer flight (a). The distance (Z) and density maximum velocity (V) as function of time (b).

At t~1100-1200 ns the "pick of density" flies near slit (see Fig.4b) for 0.5 μs (see Fig3a) with a velocity 2.5 km/s. As the result, the thickness of nonevaporated layer is ~ 1.3 mm. The suitable data from numerical simulation is about 0.2 mm (see Fig.4a).We explain such "widening" of layer as consequence of turbulent mixing effect.

Direct numerical simulation of the turbulent mixing in laser targets seems to be very laborious process even with up-to-date supercomputers. To estimate this effect we have developed a numerical model, which is based on the ideas of turbulent diffusion (Belen'ki, 1965). The turbulent diffusion equation has the following form: $\dfrac{\partial \rho}{\partial t} = \dfrac{\partial}{\partial z}(D_m \dfrac{\partial \rho}{\partial z})$,

ρ- density, D_m – coefficient of turbulent mixing, $D_m = l_p^2 (-\dfrac{\partial \ln \rho}{\partial z} \cdot \dfrac{\partial P}{\rho \partial z})^{0.5}$;

l_p − a scale of turbulent pulsation, P- pressure. The term $-\dfrac{\partial P}{\rho dz} = g$, where g is the average means of no evaporated layer acceleration, $L_\rho = 1/\dfrac{\partial \ln \rho}{\partial z}$ − density gradient scale.

From "ATLANT"-code simulations $g_1 = +(3\text{-}4)\cdot 10^{12}$ cm/s^2 at the first stage. The rear side of layer is unstable at the second stage, $g_2 = -(1\text{-}2)\cdot 10^{11}$ cm/s^2. Following

Belen'ki&Fradkin $l_p \approx \alpha L_{mix}$, where α- is self-consistent parameter and should be defined a priori. We have used the comparisons of experimental data and the results of numerical simulations to define this parameter. We have solved numerically the equation (1) with take into account (2). The value of $L_{mix} = \left| \int_{Z_1}^{Z_2} dz \right|$, $Z_1(t)$- position of maximal density, $Z_2(t)$- position, where $\rho(z)=\rho_0$. In the first stage (0<t<100 ns), $g_1 = +3,4*10^{12}$ cm/s^2 and $L_{mix}(t)$ is on the right side from maximal density. In the second stage (t>100 ns), $g_2=-10^{11}$ cm/s^2 and $L_{mix}(t)$ is defined on the left side of maximal density. Initial density profile is

$$\rho(z) = \begin{cases} \rho_0 + 0.5a_0(1+\cos(\dfrac{\pi z}{\lambda}), & |z| \le \lambda \\ \rho_0, & |z| \notin [-\lambda,+\lambda] \end{cases}$$

Parameters: $\rho_0=1.3\cdot10^{-3}$ g/cm^3, $\lambda= 20$ μm, $a_0=1000$, we have varied parameter α in our simulations.

Figure 5 illustrates the results of numerical simulations for the cases of α=0.16, 0.2 and 0.27.
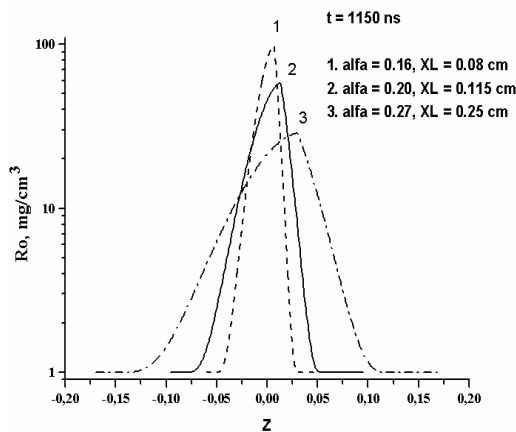
Fig.5. Results of numerical simulations of Eq. of turbulent diffusion, $\rho_0=1.3\cdot10^{-3}$ g/cm^3, $\lambda= 20$ μm, $a_0=1000$, α=0,27. XL- is the width of layer at suitable t

In order to describe the second experiment (with non-uniform irradiation of the film through the grid), we have supposed, that the scale of turbulent pulsation is $l_P = 0.7$ mm (the scale of grid cell in our experiment). We have solved numerically Equation (1) and have got suitable agreement with experimental data (see, Fig.6).
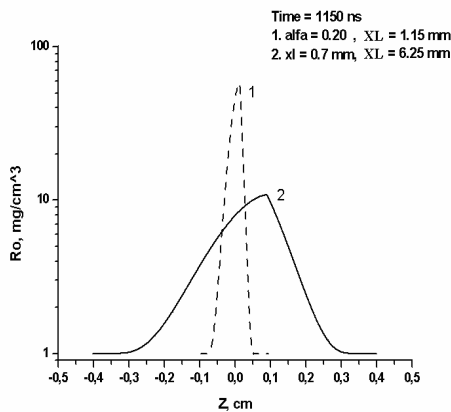
Fig.6. Results of numerical simulations: variant 1 with α=0.2 and variant 2 with l_p=0,7 mm.

Conclusions.

The problem of description of the turbulent mixing development is very important in Laser Thermonuclear Fusion. The different approximate models are developed to estimate the influence this phenomenon in laser targets. We have developed some simple model based on Belen'ki&Fradkin theory of turbulent diffusion. It has allowed us to get a good agreement between computational and experimental data and verified self-consistent parameter α.

References

1. Taylor G. 1950. The instability of liquid surfaces when accelerated in a direction perpendicular to their planes. Proc. Of Roy. Soc. Ser. A, V.201, p.192

2. Richtmyer R.D. 1960. Taylor instability in shock acceleration of compressible fluids. Commun. Pure Appl. Math., V.13, p.297

3. Meshkov E.E.1969, The instability of interface of two gases, accelerated by shock wave. Izvestiya Akademii Nauk SSSR. Ser. Mekh. Zhidkosti I gaza. V. 5, p.151 (in Russian).

4. Aleshin A.N. et al. 1987. Influence of interaction of a shock wave with a region of contact of two fluxes of different density on the rate of mixing. Sov. J. Quantum Electron.. V.17(11), p.1465

5. Aleshin A.N. et al. 1990. The investigation of linear, nonlinear and transition stages of Richtmyer-Meshkov instability development. Dokladi Akademii Nauk SSSR, V.310, N5, p.1105 (in Russian).

6. Zvorykin V.D. &Lebo I.G., 2000 Application of high-power KrF laser for the study of supersonic gas flows and the development of hydrodynamic instabilities in layered media; Quantum Electronics, **30**, 540-544

7. Belen'ki S.Z. & Fradkin E.S. 1965, Theory of turbulent mixing . Trudi FIAN 29, 207-233

8. Iskakov A.B., Lebo I.G., Tishkin V.F., 2000, 2D Numerical simulation of high-power pulses with plane targets using the "ATLANT-C" Lagrangian code. J. Russian Laser Research, 21, 247

e-mail: `leinov@bgu.ac.il`

Experimental investigation of hydrodynamic instability induced by multiple accelerations of a contact surface between two fluids

Eli LEINOV[1], Asaf FORMOZA[1], Oren SADOT[1,2], Arnon YOSEF-HAI[2], Guy MALAMUD[2], Yonatan ELBAZ[2], Aryeh L. LEVIN[1,2], Dov SHVARTS[2] and Gabi BEN-DOR[1]

[1] *Pearlstone Center for Aeronautical Engineering Studies, Dept. of Mech. Eng., Ben-Gurion University of the Negev, Be'er-Sheva 84015, Israel*
[2] *NRCN Be'er-Sheva 84190, Israel*

Abstract: Experimental investigation of the Richtmyer-Meshkov instability in a multiple acceleration conditions have been conducted in a shock tube apparatus. The instability is generated by an incident shock wave which ruptures a thin nitrocellulose membrane that separates initially air from SF_6 in the test section of a shock tube. The incident shock-wave reflects from the end-wall of the test-section and strikes the turbulent mixing zone evolving on the contact surface between the gases. The passage of the reflected shock wave causes a dramatic increase in the growth rate of the instability. The instability evolution was measured using a schlieren diagnostic technique. Two gas configurations were used – light/heavy (air/SF_6) and heavy/light (SF_6/air) – in order to study the influence of the reflected shock-wave arrival time at the turbulent mixing zone on the growth rate after the passage of the reflected shock-wave. The length of the test section was changed (between $80mm$ to $172mm$) in order to impose different arrival times, thus allowing the turbulent mixing zone to evolve into different widths before the arrival of the reflected shock wave. The results indicated that the length of the test section had no effect on the growth rate.

1 INTRODUCTION

When the interface separating two fluids of different densities is accelerated impulsively by a shock wave (SW) for example, a hydrodynamic instability, known as the Richtmyer-Meshkov Instability (RMI) [1,2], is developed. Small perturbations initially present on the interface separating the two fluids will grow first linearly, then at late time, nonlinear development of the perturbation will take place and subsequent transition to turbulence will occur.

The RMI has been described theoretically through the linear [1], nonlinear [3,4] and late nonlinear stages [4-6] for a single SW passing through the contact surface separating the two fluids and initiating the instability. Experiments have been conducted for initial single mode perturbation [2,7-8] and for initial multimode perturbation [4,9]. Most of the experimental researches have focused on the evolution of the instability after the passage of a single shock-wave; while some experimental results have reported on the instability growth rates after re-shock [10-12]. After passing through the contact surface, the shock wave is reflected from the shock tube end-wall and hits the perturbed contact surface again, enhancing the mixing process. The passage of the reflected shock through the contact surface creates a secondary reflected wave, which can be either a refraction wave or a compression wave (a shock wave) depending on the gas combination. This wave hits the unstable contact surface once again after reflecting from the end-wall. The end-wall distance from the initial contact surface position controls the duration of the above-described interaction with waves.

A complementary numerical study was conducted and compared with the experimental results reported in the present study yielding good agreement [13].

2 EXPERIMENTAL APPARATUS

The experiments were performed in a $5.5m$-long horizontal double-diaphragm shock tube with an $8cm$ x $8cm$ cross section, at Mach number of M~1.2. In order to generate a shock wave having a Mach number of about 1.2, the driver section was filled with air to a pressure of approximately 3 atmospheres. Then an electrically controlled striking pin ruptured a $75\mu m$ Mylar diaphragm which divided the driver section from the driven section of the shock tube. The strength and velocity of the shock wave were measured with flush-mounted piezoelectric pressure transducers on the shock-tube wall. The arrival of the shock wave at the first transducer was also used to trigger the diagnostic timing sequence. The test section was located at the end of the driven section. Transparent windows were built into the side walls of the test section, allowing recording of the experiments using a schlieren technique. The height of the test-section windows spanned the entire $8cm$ height of the test section, their length was $40cm$ and the frame holding the membrane was lo-

cated at the test-section center. The length of the test section could be changed by shifting the end-wall backwards or forward on a horizontal shaft.

The membrane which divided the test section from the driven section was prepared by dropping a small amount of mixture calibrates monomer and thinner onto a surface of water bath. After permitting the mixture to polymerize, a thin membrane layer was lifted from the water using an 8*cm* x 8*cm* aluminum frame. The membrane-carrying frame was placed in the proper position in the test-section of the shock tube. The gases on both sides of the membrane were at atmospheric pressure. The light gas in the experiments was air and the heavy gas was sulfur hexafluoride (SF_6). Hence, the Atwood number was 0.67.

The light source for the schlieren photographs was a Nd:Yag frequency doubled laser pulsed in the green region (532*nm*) at intervals of 56*μs* with energy of approximately 2.4*mJ* per pulse. The 1*mm* diameter laser beam was expanded by a telescope to a diameter of about 20*cm* in order to fill most of the test section window. The location of the laser beam along the 20*cm* window length could be selected at will. A shutter at the focus of the telescope blocks the beam except for a very short time during which the experiment was conducted. The parallel laser beam passed through the test section and is then focused by a concave mirror onto a knife-edge. A shutter-less rotating-prism camera recorded the schlieren photographs. Further information of the experimental apparatus and technique is available in [14].

3 EXPERIMENTAL RESULTS

Two experimental gas configurations were used in order to study the effect of the re-shock arrival time at the TMZ on the growth rate of the TMZ. In the first gas configuration, the incident shock wave traveled from the light gas to the heavier gas (air/SF_6 case), and in the second gas configuration, the incident shock wave traveled from the heavy gas to the lighter gas (SF_6/air). The first experimental configuration was conducted with four different distances of the end-wall of the test-section from the initial position of the membrane: 80*mm*, 98*mm*, *131mm* and *172mm*, while the second configuration was conducted with two different distances: 80*mm* and *169mm*. The different test-section end-wall distances introduce different time delay for the turbulent mixing zone (TMZ) to evolve before the arrival of the re-shock from the end-wall of the test-section.

3.1 LIGHT/HEAVY GAS CONFIGURATION

A sequence of schlieren photographs from a single experiment in the light/heavy gas configuration (the incident shock wave travels from left to right) with a random-mode initial condition is presented in Fig. 3.1.
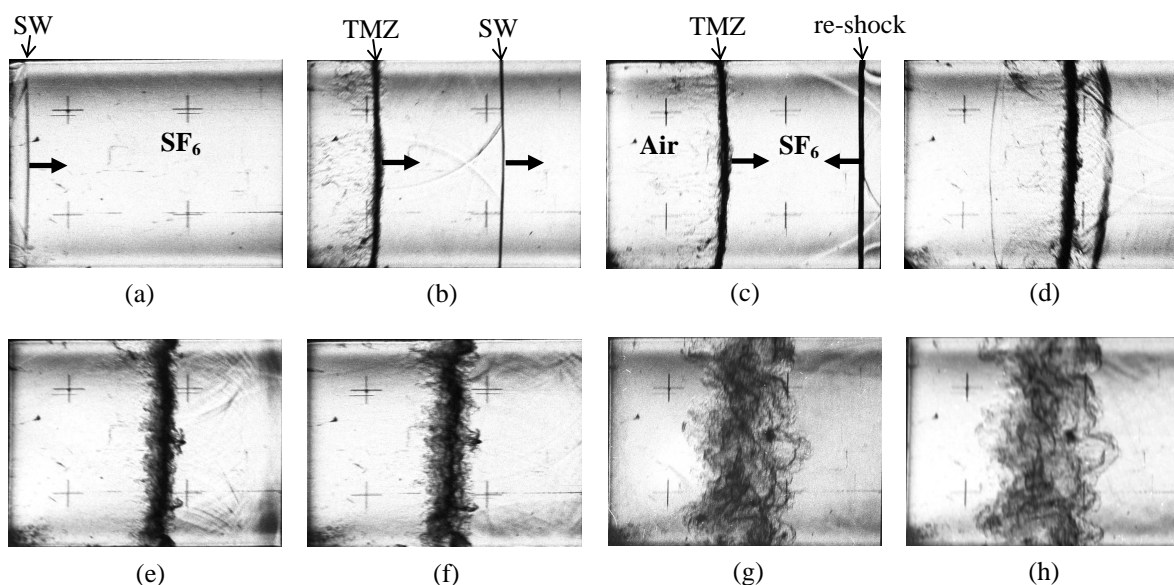
Fig. 3.1. Schlieren images from a light to heavy gas configuration (air to SF_6) experiment. (a) $t = 0.01$ms; (b) $t = 0.34$ms; (c) $t = 0.56$ms; (d) $t = 0.90$ms; (e) $t = 1.07$ms; (f) $t = 1.29$ms; (g) $t = 1.74$ms; (h) $t = 1.96$ms.

Each frame in Fig. 3.1 captures the test-section of the shock-tube. The test-section was filled with SF_6, which was separated from air filling the driven-section of the shock-tube by a thin nitrocellulose membrane (not evident in the frame).

The incident SW ruptured the membrane and traveled from left to right in the test section (Fig. 3.1a), a perturbed contact surface followed it (Fig. 3.1b). The SW stroked the end-wall (not evident in the frame) and reflected towards the TMZ (Fig. 3.1c). The reflected shock wave stroked the TMZ, transmitted leftward and reflects back towards the end-wall as a rarefaction wave (Fig. 3.1d). The dramatic increase in the growth rate of the TMZ is evident thereafter in the following images (Figs. 3.1e-h).

A plot of the measured time dependent TMZ thickness at different interface positions for four end-wall distances is presented in Fig. 3.2. The time in Fig. 3.2 is shifted so that t=0 corresponds to the re-shock striking the TMZ time. The time shift is obtained by subtracting the minimum measured TMZ width after being re-shocked for the first time from the real experimental time. The left vertical solid lines in the figures correspond to the moment the reflected shock waves strike the TMZ, so it is the time just prior to minimum measured TMZ width.

The re-shock strike deposits more energy in the TMZ, thus enhancing mixing. The second vertical solid lines in the figures represents the time at which the rarefaction wave hits the perturbed interface. The black solid lines in Figs. 3.2a-d correspond to a least square fit has been applied to the data – a power law fit for the evolution before the re-shock arrival at the TMZ, while post re-shock a linear fit has been applied to the data as it seemed the most appropriate to capture the phenomena.

Fig. 3.2. The measured TMZ widths as a function of shifted time for different end-wall positions (light/heavy gas configuration): (a) 80mm, (b) 98mm, (c) 131mm, (d) 172mm

The growth rate of the TMZ after being stroked by the incident shock wave is independent of the location of the end-wall and hence is the same for all four cases. However, the TMZ widths obtained in the four different end-wall distances at the time they were hit by the re-shock were different. The farther the end-wall was placed, the wider the TMZ

width was by the time the re-shock stroked it. In spite of that, it is clearly seen in Fig. 3.2a-d that the growth rate of the TMZs after being stroked by the re-shock are the same.

3.2 HEAVY/LIGHT GAS CONFIGURATION

The plots of the measured TMZ thickness at different interface positions for two end-wall distances in the heavy/light gas configuration are presented in Figs. 3.4(a-b).
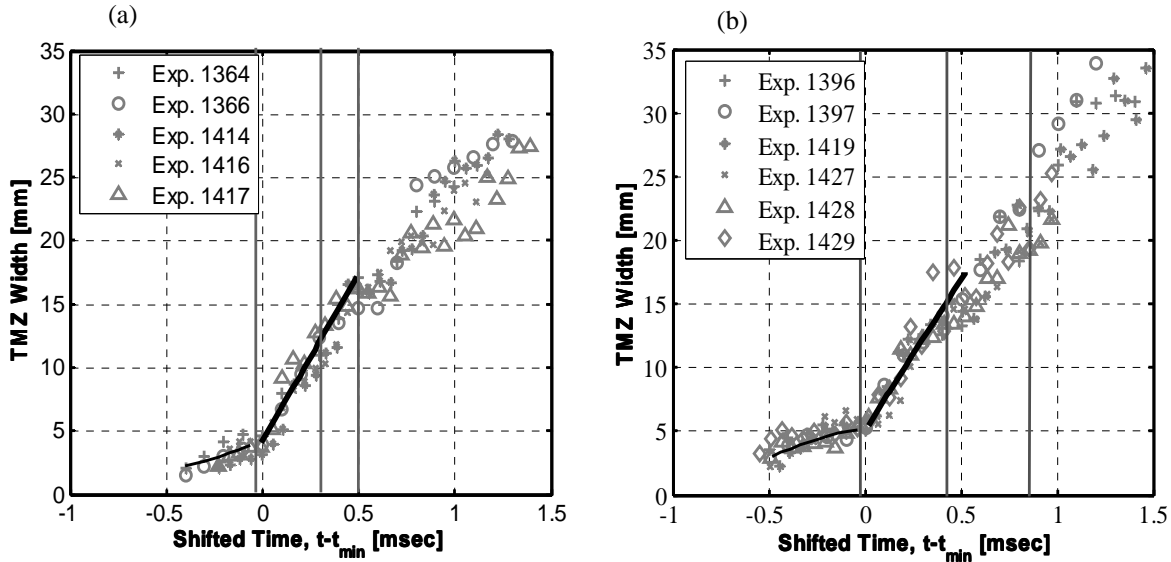
Fig. 3.3. The measured TMZ widths as a function of shifted time for different end-wall positions (heavy/light gas configuration): (a) 80mm, (b) 169mm.

The time shift in fig. 3.3(a-b) was obtained in a similar manner as the time shift in Fig. 3.2. The solid vertical lines appearing in the figures correspond, from left to right, to the incident SW, the first re-shock and the second re-shock respectively.

In the heavy/light gas configuration we can see that again the growth rate of the TMZ widths obtained for two different end-wall distances at the time they were hit by the re-shock were different. However the growth rate of the TMZs after being stroked by the re-shock is similar.

4 DISCUSSION

Two experimental configurations were used in order to study the effect of the TMZ width at the re-shock arrival time on the TMZ growth rate thereafter. The TMZ growth rates after the re-shock passage appears to be linear in time. The linear fits of the width measurements reveal a similar growth rates after the re-shock.

The mean growth rates for the four end-wall distances in the light/heavy gas configuration (Air/SF_6) and two end-wall distances in the heavy/light gas configuration (SF_6/Air) set of experiments are summarized in table 4.1.

Gas configuration	End-wall distance [mm]	Growth rate [m/s]	Error
Air/SF_6	80	22.91	± 2.04
	98	25.66	± 2.07
	131	24.90	± 2.12
	172	24.20	± 2.02
SF_6/Air	80	25.73	± 3.59
	169	23.93	± 5.56

Table 4.1. A summary of the mean growth rates measurements for four end-wall distances in the light/heavy gas configuration (Air/SF_6) and two end-wall distances in the heavy/light gas configuration (SF_6/Air).

It can be clearly seen from table 4.1 that the growth rates in all of the distances and in both gas configurations are alike within the error limits. The errors in the growth rates values were evaluated using a standard least-mean-squares procedure.

Figure 3.4a summarizes the results of the widths measured for the four different cases in the light/heavy configuration and figure 3.4b summarizes the results of the widths measured for the two different cases in the heavy/light configuration.

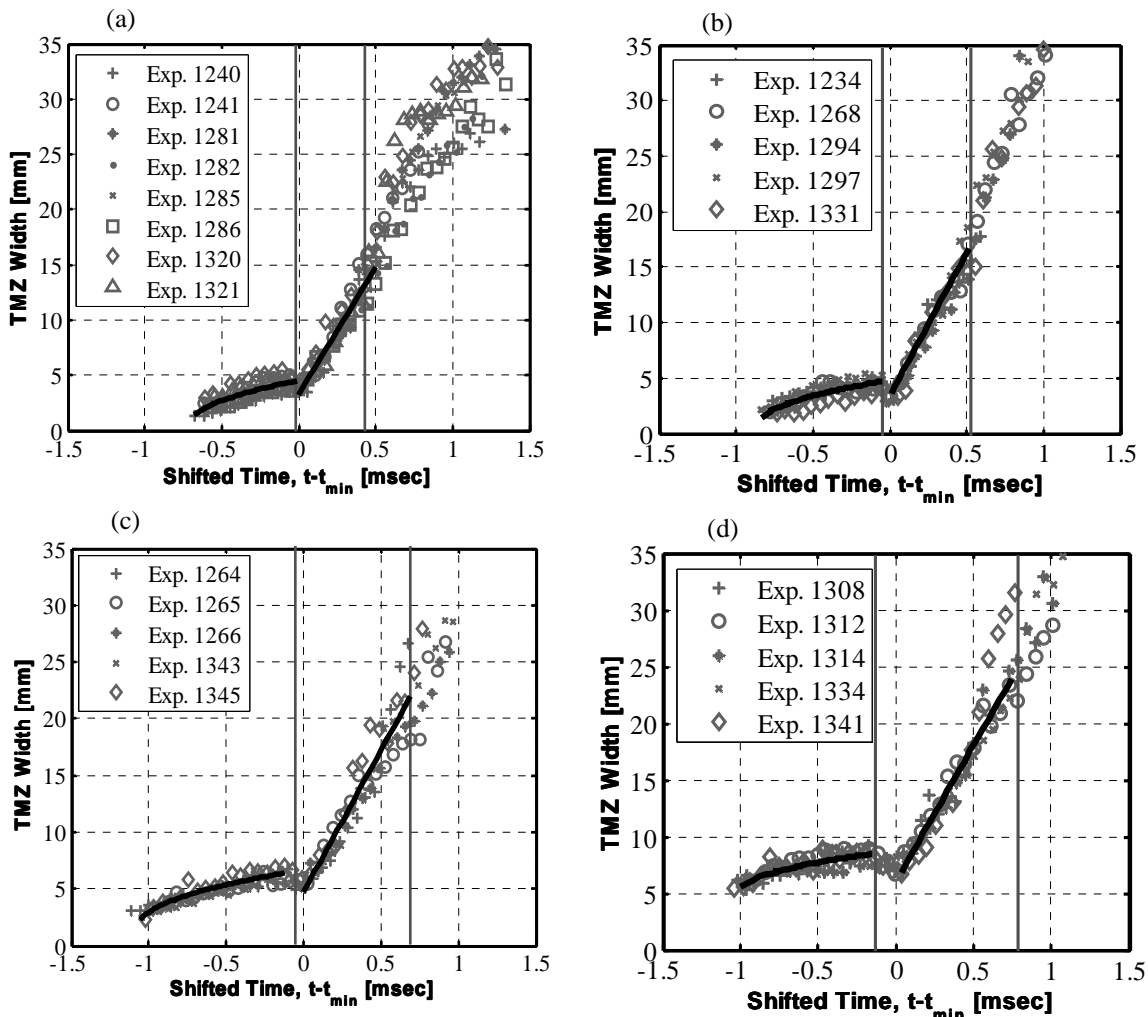(a)   (b)
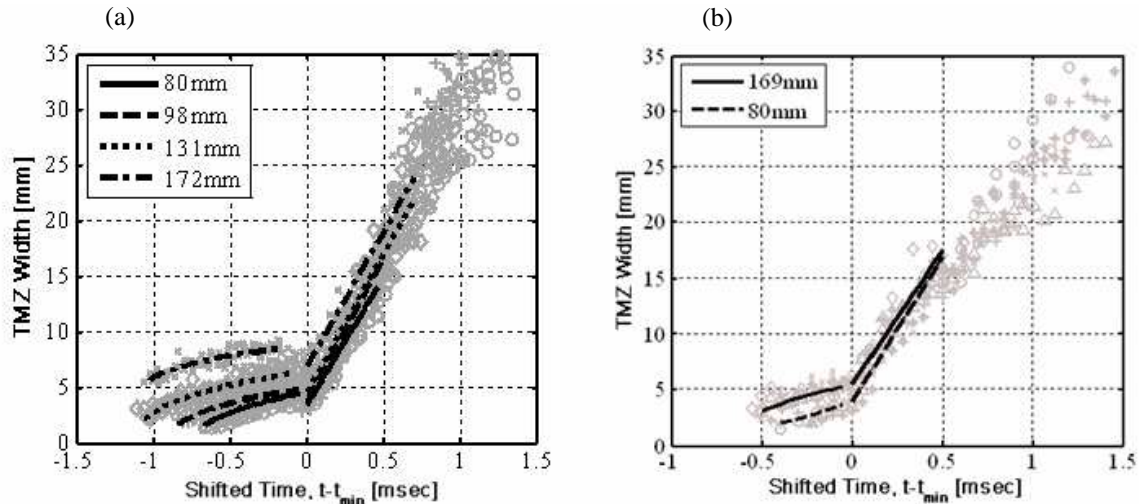
Fig. 3.4. Experimental measurements of TMZ widths as a function of shifted time for different end-wall positions:
(a) Light/Heavy gas configuration. (b) Heavy/Light gas configuration.

The Atwood number in both gas configurations was the same (0.67) but with opposite sign, thus the perturbed contact surface between the gases was overtaken by different wave combinations, i.e., in the light/heavy case the perturbed interface experienced the passage of the incident SW, followed by the re-shock, followed by reflected rarefaction wave, while in the heavy/light case the perturbed interface experienced the passage of the incident SW, followed by the re-shock, followed by another reflected shock wave. Though the perturbed interface experienced different wave combinations, the TMZ growth rate was similar.

5 SUMMARY

An attempt was made to understand the effect of the length of the test section on the Richtmyer-Meshkov instability evolution in a shock tube facility. The length of the test section was changed by shifting the end-wall position. All the other conditions of the experiments were identical.

Six sets of shock tube experiments with different lengths of the test section and different gas configurations were conducted in order to define whether the length of the test section, i.e., the time of re-shock arrival to the TMZ has an effect on the Richtmyer-Meshkov instability evolution. Different arrival times of the re-shock at the TMZ dictated different widths of TMZ, i.e., different initial conditions. It was found that though the TMZ evolved into different widths, its growth rate post re-shock passing through it, was practically the same. Thus, the growth rate following the re-shock does not depend on the size of the mixing zone when it is re-shocked and grows linearly in time.

Further work should be done in order to understand the relation between the re-shock strength and the TMZ growth rate.

REFERENCES

[1]   Richtmyer, R.D., 1960, Taylor instability in shock acceleration of compressible fluids. Comm. Pure Appl. Math. **13**, 297.
[2]   Meshkov, E.E., 1969, Instability of the interface of two gases accelerated by a shock wave. Sov. Fluid Dyn. **4**, 101.
[3]   Zhang, Q. and Sohn, S. I., 1997, Nonlinear theory of unstable fluid mixing driven by shock wave. Phys. Fluids **9**(4), 1106-1124.
[4]   Sadot, O., Erez, L., Alon, U., Oron, D., Levin, L.A., Erez, G., Ben-dor, G. and D. Shvarts, 1998, Study of nonlinear evolution of single-mode and two-bubble interaction under Richtmyer-Meshkov instability, Phys. Rev. Letters **80**, 1654-1657.
[5]   Hecht, J., Alon, U. and Shvarts, D., 1994, Potential flow models of Rayleigh-Taylor and Richtmyer-Meshkov bubble fronts. Phys. Fluids **6**(12), 4019-4030.

[6]   Alon, U., Hecth, J., Ofer, D. and Shvarts, D., 1995, Power laws and similarity of Rayleigh-Taylor and Richtmyer-Meshkov mixing fronts at all density ratios. Phys. Rev. Lett. **74**, 534-537.

[7]   Benjamin, R. 1992. in *Advances in Compressible Turbulent Mixing*, Eds. by Dannevick, W.P., Buckingham, A.C. and Leith, C.E., 341-348.

[8]   Sadot, O., Erez, L., Oron, D., Erez, G., Ben-Dor, G., Alon, U., Levin, L.A. and Shvarts, D., 2000, Studies on the nonlinear evolution of the Richtmyer-Meshkov instability. Appl. J. Suppl. **127**(1), 469-473.

[9]   Dimonte, G., Frerking, C.E. and Schneider, M., 1995, Richtmyer-Meshkov instability in the turbulent regime. Phys. Rev. Lett. **74**(24), 4855.

[10]   Nikiforov, V.V., Andronov, V.A. and Razin, A.N., 1995, Development of a turbulent mixing zone driven by shock wave. 1995, Sov. Phys. Dokl. 40(7).

[11]   Brouillette, M. and Sturtevant, B., 1993, Experiments on the Richtmyer-Meshkov instability: Small-scale perturbations on a plane interface. Phys. Fluids A **5**, 916.

[12]   Chebotareva, E.I., Aleshin, A.N., Zaytsev, S.G. and Sergeev, 1999, Investigation of interaction between reflected shocks and growing perturbations on an interface. Shock Waves **9**, 81-86.

[13]   Malamud, G., Elbaz, Y., Leinov, E., Formoza, A., Sadot, O., Shvarts, D. and Ben-Dor, G., 2006, to appear in *Proc. 10th Int. Workshop Phys. Compressible Turbulent Mixing*, 17-21 July 2006, Paris, France, Eds. by: Legrand, M. and vanden-boomgarde, M..

[14]   Erez, L., Sadot, O., Oron, D., Erez, G., Levin, L.A., Shvarts, D. and Ben-Dor, G., 2000, Study of the membrane effect on turbulent mixing measurements in shock tubes. Shock Waves **10**, 241-251.

e-mail: `stephane.liberatore@cea.fr`

Analytical Modeling of Magnetic Rayleigh-Taylor Instabilities in Compressible Fluids

Stéphane LIBERATORE[1] and Serge BOUQUET[1]

[1] *CEA/DAM Île-de-France BP 12 91680 Bruyères-le-Châtel FRANCE*

Abstract: The magnetic Rayleigh-Taylor instability (RTI) is investigated in the case of compressible plasmas. The goal of this work is highlighting the influence of both the magnetic field and the compressibility of the material on the growth rate of the RTI, compared to the classical growth rate derived for incompressible fluids. Our analytical and linear models are built up in the framework of the ideal magnetohydrodynamics theory. Two general dispersion relations are obtained : 1)- One for stratified fluids, including compressible (denoted CS) and incompressible (denoted IS) and 2)- One for incompressible uniform density fluids, including finite mass (denoted Ifm) and infinite (denoted I). Comparisons of those various configurations are performed and several differences are pointed out. The main results, for magnetized fluids, are : the CS case produces growth rates larger than for the IS and Ifm configurations (both incompressible) but weaker than the I situation; and the stratification weakens the RTI.

1 INTRODUCTION

The Rayleigh-Taylor instability (RTI) occurs when a heavy fluid is decelerated by a light one in the laboratory frame. It is a very common phenomenon, studied either in physics (inertial confinement fusion [1] for example) or in astrophysics (supernova [2], supernova remnant [3, 4] (SNR), HII regions [5] for example).

Let us focus especially to the case of SNR's [6,7]. A few hundreds of years after the explosion of a supernova (both types I and II), the resulting ejecta (hot plasma ejected during the explosion) begin to be decelerated by the low density compressible interstellar medium (ISM) which, in addition, experiences an ambiant magnetic field (**B**). As a consequence, one has to deal with a SNR (expanding ejecta in the ISM) which is unstable with respect to the buoyancy inter-exchange condition. It turns out, therefore, that the RTI takes place in a magnetized compressible medium.

The ideal magnetohydrodynamics (IMHD) is a good theory for SNR's. It is valid if a characteritic scale length of the system is much more greater than the ion Larmor radius and the ion inertial length [8] (i.e. derived from the ion plasma frequency). This is the case of SNR in the pre-Sedov phase when the RTI occurs. As outlined by several authors [6,7], in this phase, **B** is important because it provides an effective coupling between the material of the SNR and the interstellar medium. The magnetic field makes that the mean free path of the ions is small enough and, as a consequence, the hydrodynamic treatement is valid.

Chandrasekhar [9] established a detailed treatment of RTI in the context of IMHD, for different assumptions, especially in the case of incompressible and magnetized fluids. The purpose of this paper is to consider the compressibility in a magnetized medium. It introduces two difficulties: 1). $\nabla.\mathbf{V} \neq 0$ (compressibility); 2). $\rho_0 \equiv \rho_0(z) \neq$ constant (stratification), where **V** is the fluid velocity and $\rho_0(z)$ the equilibrium stratified, compressible density profile in an acceleration field **g**. The z-axis is along, but opposite to, the direction of this acceleration. In the case described by Chandrasekhar [9], where $\nabla.\mathbf{V} = 0$ (incompressibility) and $\rho_0 \equiv$ constant (no dependence upon z), those two difficulties do not appear. It leads to solutions in exponential form for the z-dependence. Nevertheless, for the stratified (compressible or incompressible) cases, this dependence is no longer valid and the solution is quite different.

Hence, two analytical dispersion relations are studied:
1). one for stratified fluids, in which, via a parameter (denoted i_c and explicited hereafter), the assumptions of compressible or incompressible fluid can be used;
2). one for uniform density fluids, in which, via a typical scale (denoted h and also explicited hereafter), finite mass or infinite mass effects can be included.
Those two approaches will allow to analyse physical effects on the RTI of the compressibility and the stratification, in magnetized fluids.

2 ANALYTICAL MODELS IN IDEAL MHD THEORY

The case of two superposed semi-infinite fluid slabs, imbedded in a magnetic field, separated by an interface at $z = 0$ is considered (see figure 2.1.(b)). The fluids are subject to a constant gravitational acceleration (or a gravity-like field -it can be, for example, the deceleration of a supernova remnant-) $\mathbf{g} = (0, 0, -g) = -g\mathbf{e_z}$, perpendicular to the contact discontinuity (CD) surface separating the two superposed plasma fluids. The cartesian system $(\mathbf{e_x}, \mathbf{e_y}, \mathbf{e_z})$ is used. The CD is, for the medium at rest, perpendicular to the $\mathbf{e_z}$ direction.

Each medium is assumed to be an isothermal ideal gas. For each, the motion is described by the set of equations of IMHD theory, i.e., the equations of mass and momentum conservation, the Faraday law, the $\mathbf{B}$ flow conservation law and the equation of state, namely:

$$\frac{\partial \rho}{\partial t} + \nabla.(\rho \mathbf{V}) = 0, \tag{2.1}$$

$$\rho \left[\frac{\partial \mathbf{V}}{\partial t} + (\mathbf{V}.\nabla)\mathbf{V} \right] = \rho \mathbf{g} - \nabla P + \frac{1}{\mu_0}(\nabla \times \mathbf{B}) \times \mathbf{B}, \tag{2.2}$$

$$\nabla \times (\mathbf{V} \times \mathbf{B}) = \frac{\partial \mathbf{B}}{\partial t}, \tag{2.3}$$

$$\nabla.\mathbf{B} = 0, \tag{2.4}$$

$$P = \rho C_s^2, \quad \text{with} \quad C_s^2 \propto T_0, \quad \text{and} \quad \nabla.\mathbf{V} \neq 0 \quad \text{or} \quad P \neq \rho C_s^2 \quad \text{and} \quad \nabla.\mathbf{V} = 0, \tag{2.5}$$

where t is the time, and ρ, P, $\mathbf{V}$, $\mathbf{B}$ are the density, the pressure, the velocity of the gas and the magnetic field respectively; T_0 is the constant gas temperature and C_{s} the isothermal sound velocity.

For an incompressible medium, $\nabla.\mathbf{V} = 0$ and the state equation is not usefull. Conversely, in a compressible medium $\nabla.\mathbf{V} \neq 0$ and the state equation is necessary. A unique parameter i_c will be introduced in order to solve the problem simultaneously in the IS ($i_c = 0$) and the CS ($i_c = 1$) cases.

The equilibrium state is sketched in the figure 2.1.(b). At $z = 0$ (CD) the density of the upper medium $(+)$ is greater than that of the lower medium $(-)$: $\rho_0^+(0) > \rho_0^-(0)$. *This condition allows the apparition of the RTI.* In stratified media, $\rho_0 \equiv \rho_0(z) \neq$ constant. In uniform density fluids $\rho_0(z) =$ constant for all z.

A *perturbation method* is used. The system of IMHD equations is linearly perturbed (all physical quantities Q are separated into two part : $Q = Q_0 + Q_1$, where Q_0 corresponds to the non-perturbed quantity and Q_1 is the linear perturbation) and reduced to a linear, homogeneous differential equation. When a perturbation is applied everywhere, the deformed CD is Rayleigh-Taylor unstable. Using the boundary conditions (continuity of P and $v_z = \mathbf{V}.\mathbf{e_z}$ accross the CD surface), a dispersion relation is obtained in order to show the role of the magnetic field, in a compressible medium, on the RTI. (For a detailed treatment see [10]).

Two general dispersion relations are obtained:
• one for stratified fluids, including CS ($i_c = 1$) and IS ($i_c = 0$) cases:

$$\left[\frac{\alpha - 1}{\alpha} - \zeta_1^+ + \frac{\zeta_1^-}{\alpha} - (\zeta_1^+ + 2m^+)\sqrt{K} - \frac{\Phi^-}{2\alpha}(\zeta_1^- + 2m^-) \right] F_2^- + (\zeta_1^+ + 2m^+) \left(\frac{K + \sqrt{K} - \dfrac{\zeta_2^+}{\zeta_1^+}}{2\sqrt{K} + 1} \right) \frac{\zeta_1^+ F_2^- F_{22}^+}{2m^+ F_2^+}$$

$$+ \left(\zeta_1^- + 2m^- \right) \left(\frac{\Phi^-}{4} - \frac{\alpha_T^2 K}{\Phi^-} \right) \frac{2m^- F_{22}^-}{\alpha \zeta_1^-} = 0, \tag{2.6}$$

where $\zeta_{1,2}^{+;-}$ are depending on i_c (see below);
• one for incompressible uniform density fluids, including Ifm and I cases:

$$W = \frac{1}{\alpha \tanh^{-1}(\sqrt{K}) + 1} \left[(\alpha - 1)\sqrt{K} - 2\alpha K \left(m^+ \tanh^{-1}(\sqrt{K}) + m^- \left(\frac{1 + m^+}{1 + m^-} \right) \right) \right]. \tag{2.7}$$

where $K \propto k^2$ and $W \propto \omega^2 > 0$ are two dimensionless numbers, k is the wave vector module and ω the growth rate so that $Q_1(x, z, t) = \tilde{Q}_1(z)\exp(ikx + \omega t)$. For an unstable configuration $\omega > 0$. Three parameters $\alpha = \rho_0^+(0)/\rho_0^-(0) > 1$ and $m^\pm = B_0^{\pm 2}/(2\mu_0 P_0^\pm(0)) = P_{0\mathrm{mag}}^\pm(0)/P_0^\pm(0)$ are called respectively the density and the magnetic numbers. With above numbers, other expressions are also used : $\alpha_T = \alpha(1 + m^+)/(1 + m^-)$; $F_2^+, F_{22}^+, F_{22}^-, F_2^-$ which are specific Hypergeometric Functions; $\zeta_1^+ = W/(K + i_c W)$; $\zeta_1^- = W/(\alpha_T K + i_c W)$; $\zeta_2^+ = W + 1 - i_c$; $\zeta_2^- = \alpha_T W + 1 - i_c$; $\Phi^- = 1 + \sqrt{\Delta^-}$; $\Phi^+ = 1 + \sqrt{\Delta^+}$; $\Delta^- = 1 + 4\zeta_2^-/\zeta_1^-$; $\Delta^+ = 1 + 4\zeta_2^+/\zeta_1^+$.

For $m \longrightarrow 0$, the hydrodynamic dispersion relations are recovered: (2.6) and (2.7) give rise to the Ribeyre's relations [11]. Ribeyre et al. have introduced the finit mass effect (i.e. the mass of the upper fluid is finite) in their incompressible non-stratified model. This effect is included in the relation (2.7) by means of h (the scale height of ρ_0^+), knowing that $K = h^2 k^2$. This mass is supposed to be the same as the compressible fluid. Furthermore, more generality is obtained since from a problem with six physical parameters (B_0^+, B_0^-, C_s^+, C_s^-, $\rho_0^+(0)$, g, - $\rho_0^-(0)$ is deduced from the hydrostatic equilibrium -) we have now just three dimensionless parameters (m^+, m^- and α).
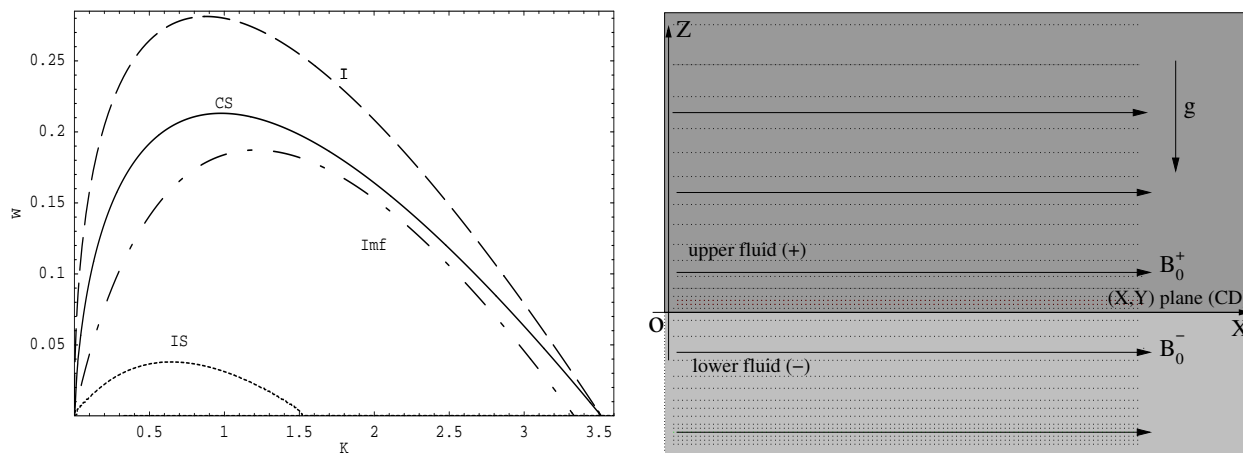
Fig. 2.1. (a) Dimensionless growth rate W versus dimensionless wave number K in four cases: solid line corresponds to the compressible case (CS); dotted line to the incompressible stratified case (IS); dashed line to the incompressible non-stratified case (I); and dash-dotted line to the incompressible finite mass case (Ifm). (For those curves, $\alpha = 4$ and $m^+ = m^- = 0.1$). **(b)** Stratification and magnetic field sketch.

3 EFFECTS OF COMPRESSIBILITY AND STRATIFICATION ON MAGNETIC RTI: RESULTS

Figure 2.1.(a) shows some dimensionless growth rate profiles W versus the normalized wave number K calculated numerically (with Mathematica) from the implicit dispersion relation (2.6) for the stratified cases, and directly with the explicit dispersion relation (2.7) for the non-stratified cases. Four configurations are plotted with respect to the notations: the CS growth rate (solid line) denoted W_{CS}; the IS growth rate (dotted line) denoted W_{IS}; the I growth rate (dashed line) denoted W_I (similar to the Chandrasekhar's relation [9]) and the Ifm growth rate (dash-dotted line) denoted W_{Ifm}.

In a first approach, the I and CS cases are compared and three observations can directly be outlined: 1) $W_I > W_{CS}$, whatever the wave number K is; 2) the cut off wave number K_{C_I} is equal to $K_{C_{CS}}$, this is demonstred analytically in [10]; 3) the wave numbers K_{max} of the maximum growth rates are close to each other. At first sight, it seems that compressibility weakens the unstable wavelength.

In a second approach, IS and CS cases are compared in order to distinguish the stratification and the compressibility effects. On one hand, Figure 2.1.(a) shows that $W_{IS} < W_{CS}$ and $K_{C_{IS}} < K_{C_{CS}}$: *the compressibility increases* at the same time *the instability* and *the cut off wave number*. On the other hand, since $W_{IS} < W_I$ and $W_{IS} < W_{Ifm}$, *the stratification weakens the instability*. This detailed comparison is done with two peculiar values of α and m ($\alpha = 4$ and $m = 0.1$). However, we have checked over that the above conclusions are recovered for a broad range of α and m.

The unstabilizing effect of the compressibility can be understood as follows: when the lighter (respectively the heavier) fluid goes to a higher (resp. lower) level, because of the instability, it must expand (resp. compress) in order to adjust the interface pressure to equal that of the other fluid. After this expansion (resp. compression) the elevated (resp. descended) fluid is less dense (resp. denser) than in the IS case, the resulting buoyancy will continue to drive up (resp. down) and, therefore, will drive the IRT more speedly.

Moreover, stratification weakens the instability but without stabilizing: in the purely hydrodynamic case, there are neither a maximum nor a cut off wave number and so the system is Rayleigh-Taylor unstable for

all wavelengths. Actually, the stabilizing effect is directly linked with the magnetic field **B**. Further, when **B** is taken into account, as showed by the comparison of the IS with the I cases, the stratification changes significantly K_C and K_{max}. As a consequence, **B** and the stratification are intrinsicly linked.

Finally, since the Ifm and CS cases have the same upper masses (medium +), the comparison $W_{CS} > W_{Ifm}$ seems to be more relevant that $W_{CS} < W_I$ but we must pay attention that contrary to above (where W_{IS} is always smaller than W_{CS}, W_I and W_{Ifm}) the result $W_{Ifm} < W_{CS} < W_I$ depends on parameters α and m. There are other values for which the curves intersect : for instance, for $m = 0.04$ and $\alpha = 4$, $W_{Ifm} < W_{CS}$ for $K < 3$ and $W_{Ifm} > W_{CS}$ for $K > 3$.

4   CONCLUSION

The magnetic field has a stabilizing role in RTI, whatever the compressibility is. The compressibility has to be distinguished from the stratification: the stratification weakens the instability and, the compressibility has a unstabilizing effect.

REFERENCES

[1] Lindl, J., 1995, Development of the indirect-drive approach to inertial confinement fusion and the target physics basis for ignition and gain, *Physics of Plasmas*, **2**, pp. 3933-4024

[2] Fryxell, B., Mueller, E., Arnett, D., 1991, Instabilities and clumping in SN 1987A. I. Early evolution in two dimensions, *The Astrophysical Journal*, **367**, pp. 619-634

[3] Chevalier, R.A., Blondin, J.M., 1995, Hydrodynamic instabilities in supernova remnants: early radiative cooling, *The Astrophysical Journal*, **444**, pp.312-317

[4] Jun, B.-I., Norman, M.L., Stone, J.M, 1995, A Numerical Study of Rayleigh-Taylor Instability in Magnetic Fluids, *The Astrophysical Journal*, **453**, pp. 332-349

[5] Williams, R.J.R., Ward-Thompson, D., Whitworth, A. P., 2001,Hydrodynamics of photoionized columns in the Eagle Nebula, *Monthly Notices of the Royal Astronomical Society*, **327**, pp. 788-798

[6] Woltjer, L.,1972, Supernova Remnants, *Annual Review of Astronomy and Astrophysics*, **10**, pp.129-158

[7] Chevalier, R.A., 1977, The interaction of supernovae with the interstellar medium, *Annual Review of Astronomy and Astrophysics*, **15**, pp. 175-196

[8] Huba, J.D., Winske, D., 1998, Rayleigh-Taylor instability: Comparison of hybrid and nonideal magnetohydrodynamic simulations, *Physics of Plasmas*, **5**, pp. 2305-2316

[9] Chandrasekhar, S., 1961, *Hydrodynamic and hydromagnetic stability*, International series of monographs on physics, Oxford University Press

[10] Liberatore, S., Bouquet, S., Analytical Modeling of Magnetic Rayleigh-Taylor Instabilities in Compressible Fluids, in preparation

[11] Ribeyre, X., Tikhonchuk, V.T., Bouquet, S., 2004, Compressible Rayleigh-Taylor instabilities in supernova remnants, *Physics of Fluids*, **16**, pp.4661-4670

e-mail: `livescu@lanl.gov`

Characteristics of buoyancy-driven, variable density turbulence

Daniel LIVESCU and J.R. RISTORCELLI

Los Alamos National Laboratory, Los Alamos, NM 87545, USA

Abstract: Buoyancy generated motions in an unstably stratified field composed of two incompressible miscible fluids with different densities, as occurs in the Rayleigh-Taylor instability, are examined. No Boussinesq approximation is made so that high Atwood numbers are allowed. The statistically homogeneous case (in which all moment equations become ordinary differential equations) is considered as a unit problem for variable density turbulence. It involves both the transition to turbulence and the decay of turbulence as the friction forces overcome buoyancy generation. The flow starts with zero solenoidal velocity in a non-premixed state and turbulence is generated due to the baroclinic production of vorticity and eventually dies as the two fluids become molecularly mixed. Results from Direct Numerical Simulations are used to follow the turbulence birth-life-death process and examine the influence of various parameters on the flow evolution and mixing. Simulations with resolutions up to 1024^3 are presented. It is shown that the rate of conversion of potential energy into kinetic energy, as well as between Favre mean and turbulent kinetic energies, is mediated by the mass flux so that the mass flux is likely the most important quantity to predict in lower dimensional models.

1   INTRODUCTION

Mixing to molecular scale in the presence of turbulence induced stirring is an important process in many practical applications. In general, the fluids participating in the mixing have different densities and we refer to such flows as variable density (VD) flows. In these flows, the specific volume changes in both time and space depending on the amount of each fluid in the mixture and the resulting velocity field is not divergence free even for constant density fluids. VD mixing is encountered in atmospheric and ocean flows, combustion and many flows of chemical engineering interest, astrophysical flows, etc. In many of these flows the turbulence is driven by acceleration (e.g. gravity in geophysical and astrophysical flows) which leads to differential forces as the density is not uniform.

Here we consider a simple form of multi-material mixing which involves two miscible fluids with different microscopic densities [1,2], in the presence of a constant acceleration, as occurs in the Rayleigh-Taylor (RT) instability. The properties of the turbulence and mixing in such flows, when they have been studied, are typically obscured by the presence of inhomogeneities due to edge effects and walls. The current investigation focuses on the nonlinear dynamics and statistics of buoyantly driven turbulence in the statistically homogeneous configuration. As such the new nonlinearities due to very large density variations in the advective terms of the Navier Stokes equations become important. The problem is an extension of the buoyantly generated turbulence in a Boussinesq fluid studied in [3] and in a VD fluid examined in [4].

2   PROBLEM FORMULATION

The equations describing the mixing between two miscible fluids with different microscopic densities, ρ_1 and ρ_2, are the Navier-Stokes and continuity equations. For binary mixing, the mass fraction of the two fluids can be recovered uniquely from the density. After non-dimensionalizing with $\rho_0 = 0.5(\rho_1 + \rho_2)$, reference velocity, U_0, and length, L_0, the equations can be written as (see [2]):

$$\rho_{,t}^* + (\rho^* u_j^*)_{,j} = 0 \tag{2.1}$$

$$(\rho^* u_i^*)_{,t} + (\rho^* u_i^* u_j^*)_{,j} = -p_{,i}^* + \tau_{ij,j}^* + \frac{1}{Fr^2}\rho^* g_i \tag{2.2}$$

$$u_{j,j}^* = -\frac{1}{Re_0 Sc} \ln \rho_{,jj}^* \tag{2.3}$$

with $\tau_{ij}^* = \frac{1}{Re_0}(u_{i,j}^* + u_{j,i}^* - \frac{2}{3}u_{k,k}^*\delta_{ij})$. The primary dependent variables are the density ρ^*, velocity in the x_i direction u_i^*, and pressure p^*. The superscript * is used to denote total instantaneous (mean plus fluctuation) values. The nondimensional parameters in equations (2.1)-(2.3) are the computational Reynolds number, $Re_0 = \rho_0 L_0 U_0/\mu_0$, Schmidt number, $Sc = \mu_0/\rho_0 D_0$, and Froude number, $Fr^2 = U_0^2/gL_0$, with g the magnitude of the gravitational acceleration taken to be constant. g_i are the components of the unit vector in the direction of gravity. The dynamic viscosity μ_0 is assumed constant and is the same for both fluids. Capital roman letters, angle brackets, or overbars are used to denote mean values and lower case letters (Roman or Greek) or primes to denote fluctuations. Thus, the instantaneous velocity, density, pressure, and specific volume are decomposed as $u_i^* = U_i + u_i$, $\rho^* = \overline{\rho} + \rho$, $p^* = P + p$, and $v^* = V + v$, respectively.

Equations (2.1)-(2.3) are those governing the flow generated by the variable density Rayleigh-Taylor (VD-RT) instability [5]. In this study the equations are solved in a triply periodic domain, corresponding to a statistically homogeneous flow, and the averages are calculated as volume averages. Such a configuration eliminates the complications due to the presence of non-periodic boundaries while allowing fundamental turbulence studies in the presence of buoyancy and VD effects in the context of mixing between initially segregated materials. From a physical viewpoint, the flow corresponds to the inner region of a fully developed RT mixing layer. From the modeling viewpoint this is a benchmark problem which any turbulence model for VD-RT should handily predict. In addition, moment closures (e.g. [1]) become ordinary differential equations, which are much easier to assess and test than the partial differential equations encountered in a RT configuration. From a flow physics point of view this benchmark problem allows us to study the peculiar nature of the mixing between two different density fluids.

In VD turbulence with arbitrary boundary conditions, the two first order moments, the mean pressure gradient, $P_{,i}$, and the mean specific volume, V, are dynamical variables evolving as the mixing proceeds. For periodic boundary conditions though, the mean pressure gradient can be determined up to a constant gradient which is a free parameter. This is chosen such that the energy conversion of potential to kinetic energy is maximized (see [2]) and leads to:

$$P_{,i} = \frac{1}{V}(g_i + <u_i u_{j,j}> - <vp_{,i}> + <v\tau_{ij,j}>) \tag{2.4}$$

$$U_{i,t} = 0 \tag{2.5}$$

whereas the mean specific volume can be related to the density specific volume correlation:

$$\overline{\rho}V = 1 - <\rho v> \tag{2.6}$$

which holds for any VD flow. In the Boussinesq case, $P_{,i}$ and V are constant in time, which is an important difference compared to the VD case.

3 NUMERICAL APPROACH

Equations (2.1)-(2.2) are solved in a triply periodic domain using a pseudo-spectral algorithm. The derivatives are calculated in Fourier space and the nonlinear terms evaluated in real space. The equations are time advanced using the pressure projection method. The numerical algorithm introduces several improvements over the existing approaches, as detailed in [2]. Thus, the pressure step is treated exactly, without additional temporal integration errors. In addition, condition (2.5) imposes a constrained between the mean and fluctuating momentum which needs to be satisfied as the equations are numerically integrated (see [2] for details).

3.1 Initial conditions and simulation cases

The density field is initialized as random blobs of pure fluids, corresponding to a double-delta PDF. The velocity field is initialized with a zero solenoidal part and dilatational part given by:

$$u_i = -\frac{1}{Re_0 Sc}(\ln\rho^*)_{,i} \tag{3.1}$$

which satisfies (2.3). Table 3.1 provides relevant information for the cases studied.

In order to facilitate comparisons with RT experiments, table 3.1 also provides the initial buoyancy Reynolds number, $Re_b = Re_0\sqrt{A/Fr^2 L_\rho^3}$ based on the initial density integral scale, L_ρ as length and $\sqrt{A/Fr^2 L_r ho}$ as

case#	A	$1/Fr^2$	Sc	Re_0	Re_{b_0}	$\frac{\langle \rho^2 \rangle}{\bar{\rho}^2}\vert_{t=0}$	$<\rho v>\vert_{t=0}$	Resolution
1	0.05	1.0	1.0	250	11	0.0024	-0.0024	256^3
2	0.25	1.0	1.0	250	26	0.057	-0.061	256^3
3	0.5	1.0	1.0	250	37	0.22	-0.29	256^3
4	0.05	10.0	1.0	250	35	0.0024	-0.0024	256^3
5	0.05	1.0	1.0	833	37	0.0024	-0.0024	256^3
6	0.25	1.0	1.0	833	87	0.06	-0.064	512^3
7	0.05	1.0	1.0	1667	73	0.0024	-0.0024	512^3
8	0.25	1.0	1.0	1667	174	0.061	-0.0066	1024^3

Table 3.1. Parameters for the DNS cases.

velocity scales. In terms of dimensional quantities, these scales are L_{0_ρ} and $\sqrt{AgL_{0_\rho}}$, respectively, so that the buoyancy Reynolds number $Re_{b_0} = \frac{\rho_0 \sqrt{AgL_{0_\rho}^3}}{\mu_0}$.

To reduce statistical variability, each simulation is repeated several times with initial conditions generated using a different random number seed. All data presented represent averages over 5 to 10 realizations. The high Reynolds number cases 7 and 8 were only performed up to the time when the kinetic energy peaks, $t/t_r \approx 2.5$ (see below).

4   FLOW EVOLUTION

The initial velocity field is very low magnitude as it is set only by the dilatational field which is small for the simulations considered. Due to the body force the two fluids move in opposite directions. Small and large scale fluctuations in the velocity and density fields are generated by nonlinear interactions, increasing the turbulent kinetic energy, $E_K = \langle \rho^* u_i u_i \rangle / 2$ (figure 4.1 a). Simultaneously, the fluids in contact molecularly mix. The amplification of the fluctuating strain field by baroclinic generation increases the interfacial area between the two fluids and the molecular mixing is accelerated. As the fluids become molecularly mixed the viscous forces overcome the buoyancy forces reduced by mixing and the turbulence begins to decay. At some late time only the relatively large scale regions survive; the small scale density fluctuations have been smoothed out by molecular diffusion. Buoyancy forces still feed the slowly decaying large scale components of the motions but not enough to overcome the viscous forces and the turbulence goes through a slow death.
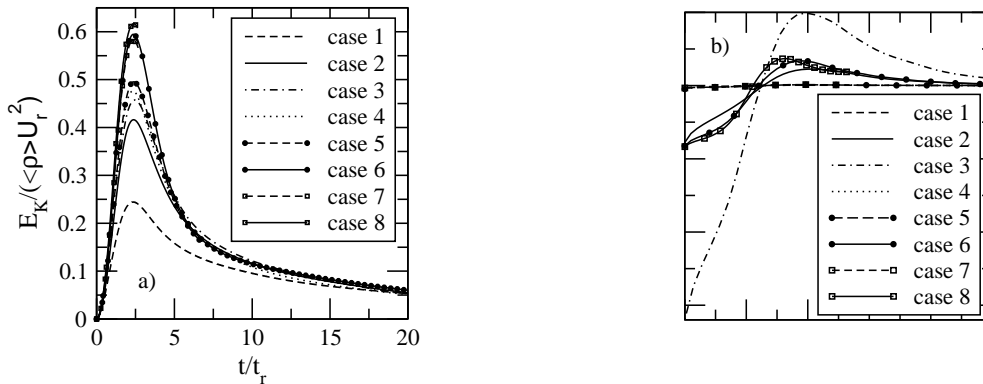
Fig. 4.1. Time evolution of a) turbulent kinetic energy and b) mean pressure gradient normalized by the pressure head

To compare different cases, the results are plotted in terms of the nondimensional velocity, $U_r = \sqrt{A/Fr^2} = \sqrt{AgL_0}/U_0$, and time scales, $t_r = \sqrt{Fr^2/A} = \sqrt{L_0/(Ag)}/(L_0/U_0)$, that characterize the balance between buoyancy and nonlinear forces. This scaling collapses the data better than the scaling based on the linear stability problem used by [6]. The scales used here are similar to those used in [3] with A replacing the initial magnitude of the density fluctuations. Note that the present simulations have similar initial density lengthscales with only small differences due to the smoothing of the initial density field performed by diffusion. The scalings

proposed above may change for different initial length scales or Schmidt numbers.

In the Boussinesq case, the mean pressure gradient is constant in time and equal to the hydrostatic head $\frac{1}{Fr^2}\overline{\rho}g_i$. In the VD case the mean pressure is a dynamical quantity and evolves as the mixing progresses (see figure 4.1 b)). As the mixing evolves and $\rho/\overline{\rho} \to 0$, $V \to 1/\overline{\rho}$, the mean pressure becomes hydrostatic. For the flow considered here, the specific volume pressure gradient correlation, $\langle vp_{,i} \rangle$, is primarily responsible for the non-Boussinesq behavior of the mean pressure gradient. After the initial moment most of energy resides in the solenoidal component and the pressure plays a role similar to that in incompressible flows: it reduces the velocity magnitude in the direction driven by gravity by transferring energy in the other two directions. The pressure gradient is positive in the rising low density regions and negative in the falling high density regions. Since the specific volume is negatively correlated to the density, it yields that $\langle vp_{,i} \rangle > 0$, acting as a production term for the mean pressure gradient in the VD case. At early times, the specific volume is larger than 1 and the mean pressure gradient is lower than the hydrostatic value. Later, as V decreases, the mean pressure gradient becomes larger than the hydrostatic head. Interestingly, $P_{,3}$ crosses the hydrostatic pressure value for all cases at about the same time, before the kinetic energy peaks.

Inspection of figure 4.1 b) indicates that non-Boussinesq effects are strongly dependent on Atwood number. Further increase in the non-Boussinesq effects can be obtained by increasing Re_0 or Sc. The current simulations are only modestly non-Boussinesq. Even so it is possible to conclude that non-Boussinesq effects, only modestly important at the current Atwood numbers and initial conditions, will be especially important at higher A and Sc.

5   ENERGY TRANSFER RATES

The rate of conversion of potential energy to kinetic energy is an important feature of buoyancy driven flows. In this section it is shown that the sole mechanism by which the potential energy is converted to kinetic energy is the mass flux. In more conventional turbulent flows the Reynolds stresses contracted on the mean velocity gradient extract energy from the mean velocity field at large scales and then the energy cascaded down to small scales where it is viscously dissipated. Here the potential energy of the unstable stratification is converted into kinetic energy by buoyancy forces. As a consequence, the kinetic energy is fed at a range of scales.

The available potential energy per unit volume in a volume $\mathcal{V}$ is given by:

$$E_p^*(t) \quad = \quad -\frac{g_i}{\mathcal{V}\ Fr^2} \int_{\mathcal{V}} (\rho^* - \overline{\rho})\, x_i \, \mathrm{d}\mathcal{V}. \tag{5.1}$$

Here $E_p^*(t)$ is the potential energy nondimensionalized by $\rho_0 U_0^2$. In the fully mixed state, which corresponds to the stable configuration, $E_p^* = 0$. The rate of change of the potential energy is the sum of the time rate of change of potential energy inside the control volume and the flux of potential energy through the boundaries:

$$\mathcal{E}_{,t} = E_{p,t}^* + \mathcal{F}_{E_p^*} \tag{5.2}$$

Using the definition of the potential energy (5.1) and after averaging, $\mathcal{E}_{,t}$ can written as [2]:

$$\langle \mathcal{E} \rangle_{,t} = -\frac{g_i}{Fr^2} \langle \rho^* u_i \rangle \tag{5.3}$$

The rate change of kinetic energy per unit volume is obtained by multiplying the momentum equation (2.2) by u_i and averaging:

$$E_{K,t} = \frac{g_i}{Fr^2} \langle \rho^* u_i \rangle + \langle pu_{j,j} \rangle - \langle u_{i,j}\tau_{ij} \rangle \tag{5.4}$$

The first term, proportional to the mass flux, is precisely the rate of change of potential energy with opposite sign. Thus, the mass flux term represents the reversible transfer of energy between potential and kinetic forms. The mass flux is the sole mechanism by which the potential energy is converted into kinetic energy. The last two terms are the pressure dilatation and viscous dissipation. For the simulations considered $\langle pu_{j,j} \rangle$ is small except at the initial instant when it is the only non-zero term in the equation. After this initial instant the two important terms in the equation above are buoyancy production (proportional to the mass flux) and the viscous dissipation.

In contradistinction, for a Boussinesq fluid the rate of change of potential energy can be shown to be:
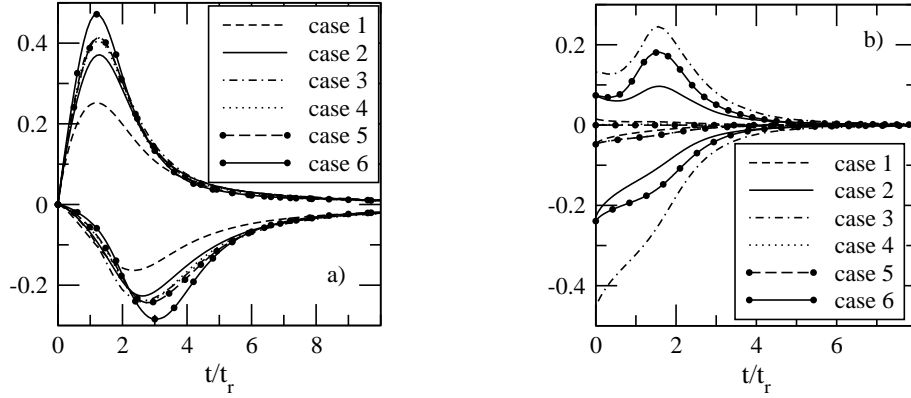
Fig. 5.2. a) Time evolution of the terms in the kinetic energy equation (5.4) scaled by $\overline{\rho} U_r^2 / t_r$. Production buoyancy term $\frac{g_i}{Fr^2} \langle \rho^* u_i \rangle$ upper curves, viscous term $-\langle u_{i,j} \tau_{ij} \rangle$ lower curves. b) Terms in the mass flux transport equation (5.8) normalized by U_r/t_r. The positive terms correspond to $\frac{\overline{p}}{1 - \langle \rho v \rangle} \langle v p_{,3} \rangle$ and the negative terms to $-\frac{\overline{p}}{1 - \langle \rho v \rangle} \langle \rho v \rangle \frac{g_3}{Fr^2}$

$$\mathcal{E}_{,t} = -\frac{g_i}{\mathcal{V} \, Fr^2} \int_{\mathcal{V}} [\rho^* u_i - \frac{1}{Re_0 Sc} \rho_{,j}^*] \mathrm{d}\mathcal{V} + \frac{g_i}{\mathcal{V} \, Fr^2} \int_{\mathcal{S}} [\overline{\rho} u_j - \frac{1}{Re_0 Sc} \rho_{,j}^*] \, x_i \mathrm{d}\mathcal{S}_j \tag{5.5}$$

while the rate of change of the kinetic energy is given by (5.4) with $\langle p u_{j,j} \rangle = 0$. There is an additional irreversible loss of potential energy by molecular diffusion and additional diffusive transfer through the boundaries not present in the VD case. Unlike VD, the Boussinesq approximation allows molecular diffusion in the absence of fluid motion. While the point is generally important, it is not relevant to the current triply homogeneous configuration, in which the extra diffusive terms in (5.5) vanish after ensemble averaging.

Figure 5.2 a) shows the evolution of the terms in the kinetic energy equation (5.4). Similar to the evolution of the kinetic energy, the buoyancy production term increases initially as the two fluids are accelerated, reaches a maximum and decreases as the fluids molecularly mix. As expected, the magnitude of the peak is larger as Re_{b0} is increased. A similar behavior is obtained for the evolution of the viscous dissipation. At late times the results are similar suggesting that in the buoyancy force scaling they are only weakly influenced by the parameters considered. Interestingly, since the results for cases 3 and 4 with the same A/Fr^2 are close, figure 5.2 indicates that the mass flux itself has a weaker dependence on the gravitational acceleration than on the Atwood number.

The VD problem is more conveniently treated using Favre averages: $\overline{\rho} \tilde{U}_i = \langle \rho^* u_i^* \rangle$. Here $U_i = 0$ and $\tilde{U}_i = a_i$, where $a_i = \langle \rho u_i \rangle / \overline{\rho}$. The Favre turbulent kinetic energy is $\overline{\rho} \tilde{k} = 1/2 \, R_{jj}$ where the Reynolds stresses are defined as $R_{ij} = \langle \rho^* u_i'' u_i'' \rangle$ with $u_i'' = u_i^* - \tilde{U}_i$. The relation between the Favre turbulent kinetic energy and the kinetic energy per unit volume, E_K, is $\overline{\rho} \tilde{k} = E_K - \tilde{K}$ where $\tilde{K} = \overline{\rho} \tilde{U}_i \tilde{U}_i / 2$ is the Favre mean kinetic energy.

$$\tilde{K}_{,t} = a_i [\overline{\rho} \frac{g_i}{Fr^2} - P_{,i}] \tag{5.6}$$

$$\overline{\rho} \tilde{k}_{,t} = a_i P_{,i} + \langle p u_{j,j} \rangle - \langle u_{i,j} \tau_{ij} \rangle \tag{5.7}$$

In a Favre average setting, the energy conversion is from potential to the Favre mean kinetic energy, $\tilde{K}$, by $\frac{g_i}{Fr^2} a_i \overline{\rho}$ and then to the Favre turbulent kinetic energy, $\tilde{k}$, by the production term $a_i P_{,i}$. Thus the mass flux mediates both the transfer of energy from potential to Favre mean kinetic energy and from here to Favre turbulent kinetic energy. Even for cases with small mass flux, a_i multiplies $P_{,i}$, a large term, to give the transfer between Favre mean and turbulent kinetic energies. The mass flux is likely the single most important item to predict in low dimensional models if one needs to capture accurately the conversion of potential to kinetic energy. The rate of energy conversion dictates the growth rate of the RT mixing layer, so that there is a direct connection between the mass flux and the growth rate which further emphasizes the importance of the mass flux.

The time evolution of the mass flux can be inferred from the kinetic energy production term, $\frac{g_i}{Fr^2} a_i \overline{\rho}$, shown in figure 5.2 a), since the only non-zero component is a_3 for the cases considered. Substituting for the mean pressure gradient, the mass flux equation can be written as:

$$\overline{\rho} a_{i,t} = -\frac{\overline{\rho}}{1 - \langle \rho v \rangle} \left(\langle \rho v \rangle \frac{g_i}{Fr^2} + \langle u_i u_{j,j} \rangle - \langle v p_{,i} \rangle + \langle v \tau_{ij,j} \rangle \right). \tag{5.8}$$

The terms on the right hand side of (5.8) are buoyancy production, velocity dilatation and specific volume pressure gradient and stress covariances. The density specific volume correlation, while important since it mediates the mass flux production, also follows the mixing progress. Figure 5.2 b) shows the two important terms in the equation, buoyancy production and specific volume pressure gradient correlation. Neither term is zero initially and the mass flux is both generated and destroyed from the initial instant. Consistent with the results above, the terms in the mass flux equation increase their magnitude with the static initial Reynolds number Re_{b0}. Also, similar to the mass flux, the terms in Figure 5.2 b) are less sensitive to changes in Froude number than in the Atwood number (compare cases 1, 3, and 4). The buoyancy production directly depends on the density volume correlation, $\langle \rho v \rangle$, which changes during the evolution of the flow. In the Boussinesq case the energy conversion is also accomplished by the mass flux but the production of the mass flux is moderated by a mixing mechanism that is fundamentally different. In that case, the density variance mediates the production of the mass flux. The mass flux equation highlights the interdependence between the buoyancy force on the mixing progress. Different measures for the evolution of mixing are presented and discussed in [7].

6   SUMMARY AND CONCLUSIONS

Simulations of the benchmark problem of homogeneous buoyantly driven variable density turbulence have allowed a study of the coupling between scalar mixing and its influence on the hydrodynamics. The current flow has been designed to have the largest mass flux possible and is, as a consequence, the maximally non-equilibrium flow possible for this configuration. It is useful to view this benchmark flow as characteristic of the interior of a fully developed RT layer: a RT layer at a time at which there is little pure fluid crossing the centerline because the layer is wide and mixing takes place before the fluid crosses the centerline.

The results of our study of buoyantly driven VD transition and turbulence permit several observations and generalizations: a) The mass flux is its own dynamical variable and is likely the single most important dynamical quantity to predict in low dimensional models in order to simulate the conversion of potential to kinetic energy. b) The mean pressure gradient in VD is not hydrostatic (as in a Boussinesq fluid) and is a dynamically evolving quantity. The mean pressure gradient is intimately coupled to material mixing through the specific volume pressure correlation. c) The short time evolution and transition of the flow is crucially dependent on a static or quiescent initial Reynolds number that sets the maximum kinetic energy attained. This is also seen in RT flows and for a Boussinesq fluid [3]. Interestingly, in scaled time, the kinetic energy maxima occur at approximately the same time, (≈ 2.5), for all simulations, regardless of Re_{b0}. The buoyancy force scaling also collapses the long time evolution of the flow.

REFERENCES

[1] Besnard, D., Harlow, F. H., Rauenzahn, R. M. and Zemach, C., 1992. Turbulence transport equations for variable-density turbulence and their relationship to two field models, *LANL Tech. Rep., IA-12303-MS.*

[2] Livescu, D. and Ristorcelli, J. R., 2006. Buoyancy driven, variable density turbulence, submitted to *J. Fluid Mech., LANL Tech. Rep. LA-UR-06-7190.*

[3] Batchelor, G. K., Canuto, V. M. and Chasnov, J. R., 1992. Homogeneous, buoyancy-generated turbulence, *J. Fluid Mech.* **235**, pp. 349-378.

[4] Sandoval, D. L., Clark, T. T. and Riley, J. J., 1996. Buoyancy generated variable density turbulence, In *Proceedings of the IUTAM Symposium on variable density low speed flows*, pp. 847-864, Kluwer.

[5] Cook, A W. and Dimotakis, P. E., 2001. Transition stages of Rayleigh-Taylor instability between miscible fluids, *J. Fluid Mech.* **443**, pp. 69-99.

[6] Ristorcelli, J. R. and Clark, T. T., 2004. Rayleigh-Taylor turbulence: Self-similar analysis and direct numerical simulations, *J. Fluid Mech.* **507**, pp. 213-253.

[7] Livescu, D. and Ristorcelli, J. R., 2007. Mixing characteristics in buoyancy driven, variable density turbulence, to be submitted.

e-mail: `jrrj@lanl.gov`

An eddy viscosity expression for Favre averaged Reynolds stresses in variable density turbulence

J.R. RISTORCELLI and Daniel LIVESCU

Los Alamos National Laboratory, Los Alamos, NM 87545, USA

Abstract: The analysis is motivated by the fact that the Boussinesq eddy viscosity model (BEVM) is a poor and, for variable density flows with body forces or large pressure gradients, a demonstratably wrong approximation. An eddy viscosity, as simple as the well known Boussinesq approximation, yet suitable for nonequilibrium variable and constant density flows, is derived. The result highlights the mass flux mean pressure gradient dyad plays in generating the Favre Reynolds stresses. The model is derived using a leading order isotropic truncation of the Favre averaged Reynolds stress equations. Constant density closures for the pressure strain covariance are used to close the algebraic expression for the anisotropy tensor. The resulting non linear equation is quadratic and the final expression is bounded for arbitrary mean velocity gradient, mass flux, and mean pressure gradient as might be seen in flows with shocks. The variable density eddy viscosity is tested in a non-equilibrium bouyantly driven flow.

1 INTRODUCTION

The derivation of an eddy viscosity type model for the Favre Reynolds stress in a variable density turbulence is given. The work is motivated by the fact that the Boussinesq eddy viscosity model (BEVM) is a demonstratably wrong approximation for variable density flows with body forces or large pressure gradients. In this modestly more rigorous variable density eddy viscosity model the direct dependence of the Reynolds stresses on the mass flux and the mean pressure gradient is shown. In the context variable density moment closures flows it shown that, as long as there are large density fluctuations, a mass flux equation is required to predict the Reynolds stresses.

2 PROBLEM FORMULATION AND BOUSSINESQ DISCUSSION

Several definitions are first given. The Favre Reynolds stress R_{ij}

$$R_{ij} = \langle \rho^* u_i'' u_j'' \rangle = \bar{\rho} \langle u_i u_j \rangle - \bar{\rho} a_i a_j + \langle \rho u_j u_j \rangle, \qquad R_{kk} = 2\bar{\rho}\tilde{k} . \qquad (2.1)$$

are given. The instantaneous velocity and density fields are written $u_i^* = U_i + u_i = \tilde{U}_i + u_i''$ and $\rho^* = \bar{\rho} + \rho$. Note that $u_i'' = u_i - a_i$ where $\langle u_i \rangle = 0$ and a_i is the normalized mass flux. The mass flux is

$$a_i = \frac{\langle u_i \rho \rangle}{\bar{\rho}} = -\langle u_i'' \rangle \qquad \Rightarrow \qquad \tilde{U}_i = U_i + a_i \qquad (2.2)$$

The operation $\langle ... \rangle$ is an ensemble average or, in the case of canonical RT, an area average. The anisotropy tensor based on R_{ij}, Lumley (1978), is written

$$b_{ij} = \frac{R_{ij}}{R_{kk}} - \frac{1}{3}\delta_{ij} \qquad (2.3)$$

where $R_{kk} = 2\bar{\rho}\tilde{k}$ is twice the Favre kinetic energy of the turbulence. For readers not familiar with the use of the anisotropy tensor the following facts are noted: The anisotropy tensor b_{ij} is bounded: $-\frac{1}{3} \leq b_{ij} \leq \frac{2}{3}$. The limit $b_{\alpha\alpha} - \frac{1}{3}$ corresponds to no energy in the (α, α) component of b_{ij}. The limit $b_{\alpha\alpha} = \frac{2}{3}$ corresponds to all the energy in α component, ie. a one-dimensional flow. The limit $b_{\alpha\alpha} = 0$ corresponds, of course, to isotropic turbulence. It is the bounded nature of this quantity that leads to useful computationally bounded properties of the model to be derived.

Replacing the Reynolds stress by its magnitude, $2\bar{\rho}\tilde{k}$ and its orientation, b_{ij}, serves to discriminate between two classes of physics and simplifies the modelling procedure allowing more rigourous results and highlighting the assumptions.

An evolution equation for R_{ij} is, from Besnard, Harlow, Rauenzahn and Zemach (1992), or from Adumitroaie, Ristorcelli and Taulbee (1996)

$$\frac{\partial}{\partial t} R_{ij} \quad + \quad (\tilde{U}_k R_{ij})_{,k} + R_{ijk,k} \;=\; P_{ij} \;+\; \Pi_{ij} \;-\; \varepsilon_{ij} \;-\; T_{ijk,k} \tag{2.4}$$

$$P_{ij} \quad = \quad -R_{ik}\tilde{U}_{j,k} - R_{jk}\tilde{U}_{i,k} + a_i P_j + a_j P_i \tag{2.5}$$

The production term, P_{ij} represents a transfer of turbulence to and from the mean Favre energy. The other terms on the right hand side of the R_{ij} equation, relevant to our goal, are

$$\varepsilon_{ij} \quad = \quad 2\mu\langle u_{i,n}\, u_{j,n}\rangle + \frac{2}{3}\langle s_{ij}d\rangle \qquad P_j = P_{,j} - \bar{\tau}_{kj,k} \qquad \Pi_{ij} = \langle p(u_{i,j} + u_{j,i})\rangle \tag{2.6}$$

and $\varepsilon_{jj} = 2\varepsilon + \frac{2}{3}\mu\langle d^2\rangle$. From the equation for R_{ij} an equation for b_{ij} is easily derived. This is underatken shortly.

2.1 Some Boussinesq shortcomings

The usual Boussinesq eddy viscosity model (BEVM) for the Reynolds stresses can be written in terms of b_{ij} as

$$R_{ij} - \frac{2}{3}k\delta_{ij} = -C_\mu \frac{k^2}{\varepsilon} S_{ij}^D \qquad \Rightarrow \qquad b_{ij} = -C_\mu \frac{k}{\varepsilon} S_{ij}^D = -G_1 S_{ij} \tag{2.7}$$

identifying $G_1 = C_\mu$ as the linear eddy viscosity coefficient and S_{ij} is the nondimensional strain rate tensor. The BEVM model shortcomings can be summarized as follows:

1. If a mean shear is not the major production mechanism the BEVM is not an accurate model. If the mean flow is primarily a strain flow the BEVM is not useful.

2. If a prediction of the normal stresses is required the BEVM is not useful whether or not the mean shear is the primary production mechanism.

3. If the flow has important non-equilibrium effects the BEVM is problematic as it can be computationally unbounded.

4. If one needs to predict a variable density buoyancy or pressure gradient driven turbulence the BEVM is not a poor model – it is a wrong model; there is no dependence on the mean pressure gradient as can easily be shown to be required. In RT flows, where there is no mean velocity gradient, it predicts an isotropic turbulence which is contrary to what is observed.

These points and additional shortcomings are enumerated in more detail in Ristorcelli, Livescu, Hjelm (2005). The weaknesses of the BEVM, which are not pertinent in many unidirectional aerodynamic simple shears for which the BEVM predicts the production adequately, are important in RT and RM turbulence. In such flows the Bousssinesq model does not contain even the leading order physics.

For canonical the RT and RM problems the off-diagonal terms of anisotropy tensor are zero indicating that there are no turbulent shear stresses. An eddy diffusivity such as those used in standard $k - \varepsilon$ models cannot predict such a flow. It is in fact the mean pressure gradient that drives RT turbulence. See Ristorcelli and Clark (2003) for b_{ij} values found in RT flows.

3 AN ALGEBRAIC TENSOR EQUATION FOR THE STRESS ANISOTROPY

The simplest of algebraic stress modeling *ansatzen* is $\frac{D}{Dt}\, b_{ij} = 0$. This can be understood as assuming that b_{ij} has no inertia and adjusts instantaneously to the local forces appearing in the b_{ij} evolution equation. Such an *ansatz* produces a model for b_{ij} directly from its evolution equations:

$$\frac{D}{Dt}\, R_{ij} = [\,b_{ij} + \frac{1}{3}\delta_{ij}]\frac{D}{Dt}\, R_{kk} \qquad \Rightarrow \qquad b_{ij} + \frac{1}{3}\delta_{ij} \;=\; \frac{\frac{D}{Dt}\, R_{ij}}{\frac{D}{Dt}\, R_{kk}} \;. \tag{3.1}$$

One sees that the deviation from isotropy is proportional to ratio of the rates of change of the Reynolds stresses to its trace. The Favre Reynolds stress anisotropy is then written as

$$b_{ij} = \frac{P_{ij} + \Pi_{ij} - T_{ijk,k} - R_{ijk,k} - \varepsilon_{ij}}{P_{qq} + \Pi_{qq} - T_{qqk,k} - R_{jjk,k} - 2\varepsilon} - \frac{1}{3}\delta_{ij} . \tag{3.2}$$

Taking the homogeneous limit $(...)_{,k} = 0$ produces the ASM (algebraic strees model) *ansatz*:

$$b_{ij} = a_P\left[\frac{P_{ij} + \Pi_{ij} - \varepsilon_{ij}}{P_{kk} + \Pi_{kk} - \varepsilon_{kk}} - \frac{1}{3}\delta_{ij}\right] . \tag{3.3}$$

Where $a_P \leq 1$ is number reflecting what we don't know, what we have neglected or what we will neglect. By construction b_{ij} is realizable. As a consequence the Reynolds stresses will be realizable, in the sense Schuman (1977), if $R_{nn} > 0$. Setting $\varepsilon_{ij} = 2\varepsilon(d_{ij} + \frac{1}{3}\delta_{ij})$ and re-arranging produces

$$b_{ij}[P_{kk} + \Pi_{kk} - 2\varepsilon] = a_P[P_{ij} - \frac{1}{3}P_{kk}\delta_{ij} + \Pi_{ij} - \frac{1}{3}\Pi_{kk}\delta_{ij} + 2\varepsilon d_{ij}] . \tag{3.4}$$

The above equation (3.4) is the ASM equation. It is, due to the appearance of b_{ij} in P_{ij}, a nonlinear equation for b_{ij}.

In nondimensional units

$$\tilde{U}_{i,j} = \frac{\varepsilon}{\bar{\rho}\tilde{k}}[S_{ij} + W_{ij} + \frac{1}{3}D\delta_{ij}] = \frac{2\varepsilon}{R_{nn}}[S_{ij} + W_{ij} + \frac{1}{3}D\delta_{ij}] \tag{3.5}$$

$$R_{nn} = 2\bar{\rho}\tilde{k} \qquad \varepsilon_{ij} = 2\varepsilon(d_{ij} + \frac{1}{3}\delta_{ij}) \qquad 2\varepsilon = \varepsilon_{kk} \tag{3.6}$$

$$2\varepsilon A_{ij} = a_i P_j + a_j P_i - \frac{2}{3}a_k P_k \delta_{ij} \tag{3.7}$$

$$R_e = \frac{P_{kk}}{2\varepsilon} + \frac{\Pi_{kk}}{2\varepsilon} - 1 = \frac{a_q P_q}{\varepsilon} - 2b_{pk}S_{pk} - \frac{2}{3}D + \frac{\Pi_{kk}}{2\varepsilon} - 1 \tag{3.8}$$

and the ASM (3.4) equation becomes the nonlinear matrix equation:

$$b_{ij}R_e = -a_P\left[\frac{2}{3}S_{ij} + b_{ik}S_{jk} + b_{jk}S_{ik} - \frac{2}{3}b_{pq}S_{pq}\delta_{ij} - A_{ij} - \frac{1}{2\varepsilon}(\Pi_{ij} - \frac{1}{3}\Pi_{kk}\delta_{ij})\right.$$
$$+ \left. b_{ik}W_{jk} + b_{jk}W_{ik} + d_{ij} + \frac{2}{3}b_{ij}D\right] \tag{3.9}$$

Here R_e is the departure from equilibrium ratio. The nonlinear equation (3.9) is the starting point for an explicit expression for b_{ij}. Closures for d_{ij} and Π_{ij} are required. We shall take $\Pi_{kk} = 0$ corresponding to solenoidal velocity fluctuations. For $a_P = 1$ the dependence of the equation on D falls out; D is rigorously neglected. In the interset of simplicity the high Reynolds number limit is taken, $d_{ij} = 0$.

An ASM tensor basis at most bilinear in $\mathbf{A}, \mathbf{S}, \mathbf{W}$ is the simplest solution to the above equation:

$$b_{ij} = G_1 S_{ij} + G_2[S_{ik}W_{kj} - W_{ik}S_{kj}] + G_3[S_{ij}^2 - \frac{1}{3}\mathcal{S}^2\delta_{ij}] + G_4 A_{ij}$$
$$+ G_5[A_{ik}W_{kj} - W_{ik}A_{kj}] + G_6[S_{ik}A_{kj} + A_{ik}S_{kj} - \frac{2}{3}\mathcal{AS}\delta_{ij}] \tag{3.10}$$

Solutions for the G_i as a function of the invariants were given by Ristorcelli (2004). It can be shown, see Ristorcelli (2004), the G_1 and G_4 terms are the largest in the above ASM solution expression. An EVM, corresponding to the retention of the G_1 and G_4 terms, is derived shortly.

4   AN EDDY VISCOSITY MODEL FOR VDT

To obtain an eddy viscosity type expression for variable density turbulence one truncates the ASM equation (3.9) by neglecting terms on the right hand side in the anisotropy tensor with respect to terms retained:

$$b_{ij}R_e = -a_P\left[\frac{2}{3}S_{ij} - A_{ij} - \frac{1}{2\varepsilon}\Pi_{ij}\right], \qquad R_e = \frac{P_{kk}}{2\varepsilon} - 1 = \frac{a_q P_q}{\varepsilon} - 2b_{pk}S_{pk} - 1 . \tag{4.1}$$

The truncation is called the weakly anisotropic limit and it has repercussions: the model coming from an equation so drastically truncated cannot predict highy anisotropic states. RT at early time is not weakly anisotropic; such a tactic is required to obtain an EVM – a simplistic model for a complex problem. This means that VD EVM will not be able to predict the almost 1D turbulence seen at the inception of the RT flows as the heavy fluid punches through the light fluid.

Using the standard constant density models for Π_{ij}, Ristorcelli et al. (2005), and simple shear data the variable density turbulence eddy viscosity approximation is

$$b_{ij} = -\frac{1}{R}\left[C_S S_{ij} - C_A A_{ij}\right] \tag{4.2}$$

$$R = \frac{a_q P_q}{\varepsilon} - 2b_{pk}S_{pk} - 1 + \frac{1}{2}a_P C_{S1} = A - 1 + \frac{1}{2}a_P C_{s1} - 2b_{pk}S_{pk} \tag{4.3}$$

$$C_S = a_P\left(\frac{2}{3} - \frac{1}{2}C_2\right) \qquad C_A = a_P(1 - C_{IPM}) \tag{4.4}$$

$$C_{S1} = 3.4, \qquad a_P = 0.85 \qquad C_2 = 0.82 \qquad C_{IPM} = 0.6. \tag{4.5}$$

For canonical RT and RM the largest term in (4.2) is the A_{ij} term. In as much as it involves the mass flux it becomes clear that any "first principles" moment closure will require an equation for the mass flux. The term R is (approximately) the production dissipation ratio and is a measure of non-equilibrium. In the flow against which this model will be tested R varies by two orders of magnitude: in RT, depending on ICs the term may be as large as 100 at early time indicating the very important nonequilibrium nature of the evolving RT layer. The point is that by working with a naturally bounded quantity we assure realizability of b_{ij} when S_{ij} and A_{ij} are large. This also assures a more computationally robust model.

A closed expression for R is required. Contracting both sides on S_{ij} and noting that $b_{ij}S_{ij} = A + \frac{1}{2}a_P C_{S1} - 1 - R$ produces the quadratic and the solution is

$$R^2 - R(A - 1 + \frac{1}{2}a_P C_{s1}) - 2(C_A \mathcal{S}^2 - C_A \mathcal{A}\mathcal{S}) = 0 \tag{4.6}$$

$$R = \frac{A - 1 + \frac{1}{2}a_P C_{s1}}{2}\left[1 + \sqrt{1 + 8\frac{(C_S \mathcal{S}^2 - C_A \mathcal{A}\mathcal{S})}{(A - 1 + \frac{1}{2}a_P C_{s1})^2}}\ \right]. \tag{4.7}$$

where $\mathcal{S}^2 = S_{ij}S_{ij}$ and $\mathcal{A}\mathcal{S} = A_{ij}S_{ij}$. The plus sign has been chosen in the root to make the limit $(C_S\mathcal{S}^2 - C_A\mathcal{A}\mathcal{S}) \to 0$ meaningful (non singular for individual components of the anisotropy tensor). As is clear from the quadractic equation $R \neq 0$ given this choice and (4.2) is not singular.

Note that the numerator and denominator scale the same way leaving the eigenvalue finite and bounded. It is of concern that the model does not violate realizability. Taking consecutively the three limits, $A \to \infty$, $S \to \infty$, $S = A \to \infty$, one obtains, respectively, $b_{11}^\infty = 0.226$, $b_{11}^\infty = 0.270$, and $b_{11}^\infty = 0.25 \pm 0.15$. These are within realizability bounds. In fact they indicate that a realizability limit cannot be attained let alone violated. It is noted that the predicted b_{11}^∞ are rather small; one might expect to peg $b_{11} \to \frac{2}{3}$ in these asymptotic limits. Simulations at early time show $b_{11} \approx 0.6$. This is to be expected for such a simplified procedure for several reasons: 1) terms in the anisotropy and the anisotropy of the production are neglected, 2) only the lowest order isotropic terms in the most rudimentary form of a pressure strain model is kept.

The model is compared in the Figure against simulations for bouyantly driven homogeneous variable density turbulence, Livescu and Ristorcelli (2006). The comparison is good. In fact when compared to the Boussinesq model, which predicts an isotropic state with $b_{11} = 0$ which is never observed [Ristorcelli and Clark (2004)], the results are a substantial improvement. At least the model is consistent with observations and the dynamical balance of the second order moment equations. The model has also been compared to RT in Ristorcelli et al. (2006). In both these flows b_{ij} is not dynamically significant: b_{ij} is not necessary to predict the flows evolution. When a buoyantly driven flow is sheared or strained b_{ij} will then be dynamically significant.
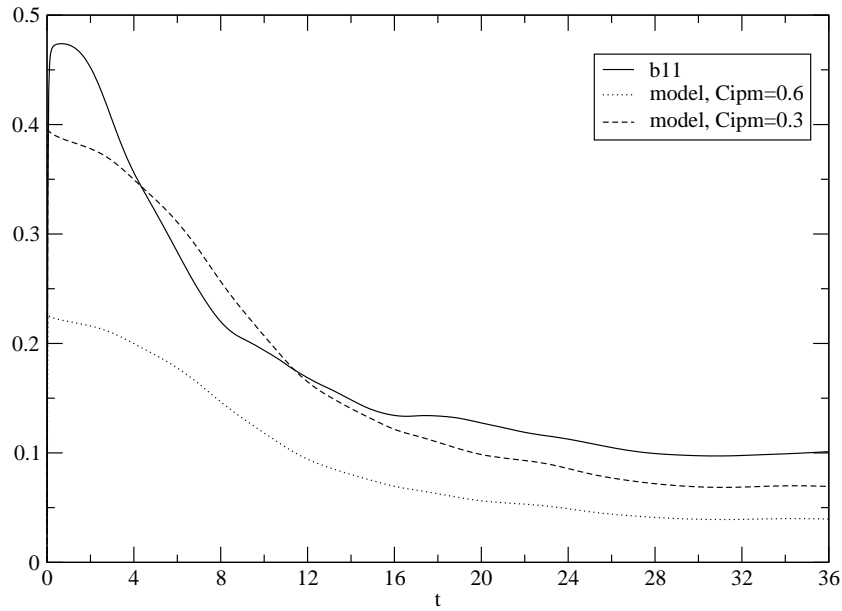
Fig. 4.1. Vertical anisotropy, b_{11}, of the turbulence as function of time for $A = 0.25$; model and DNS comparison.

REFERENCES

[1] Adumitroale, V. Ristorcelli, J.R.; Taulbee, D.B., 1999. Progress in Favre-Reynolds stress closures for compressible flows.

[2] Besnard, D., Harlow, F. H., Rauenzahn, R. M. and Zemach, C., 1992. Turbulence transport equations for variable-density turbulence and their relationship to two field models, *LANL Tech. Rep., IA-12303-MS.*

[3] Pope, S. 1976. A more general effective eddy viscosity hypothesis.

[4] Livescu, D. and Ristorcelli, J. R., 2006. Buoyancy driven, variable density turbulence, submitted to *J. Fluid Mech., LANL Tech. Rep. LA-UR-06-7190.*

[5] Lumley, J.L. 1978.Computational modeling of turbulent flows. Adv. Appld. Mech. 18:123.

[6] Ristorcelli, J.R., Livescu, D., Hjelm, N., 2004. An eddy viscosity expression for Favre averaged Reynolds stresses in variable density turbulence.*LANL Report: LA-UR-05-5837.*

[7] Ristorcelli, J.R., 2004. An explicit algebraic stress model for the Favre Reynolds anisotropy in variable density flows. *LANL Report LA-UR-04-6391.*

[8] Ristorcelli, J. R. and Clark, T. T., 2004. Rayleigh-Taylor turbulence: Self-similar analysis and direct numerical simulations, *J. Fluid Mech.* **507**, pp. 213-253.

[9] Schuman, U., 1979. Realizability of Reynolds stress models. Phys. Fluids 20:721-725.

e-mail: `virginie.lombard@cea.fr`

Kovásznay modes in stability of self-similar ablation flows

Virginie LOMBARD[1], Carine BOUDESOCQUE-DUBOIS[1], Jean-Marie CLARISSE[1]
and Serge GAUTHIER[1]

[1] *CEA/DAM Île-de-France BP 12 91680 Bruyères-le-Châtel FRANCE*

Abstract: Exact self-similar solutions of gas dynamics equations with nonlinear heat conduction for semi-infinite slabs of perfect gases are used for studying the stability of ablative flows in inertial confinement fusion. Both the similarity solutions and their linear perturbations are numerically computed with a dynamical multidomain Chebyshev pseudo-spectral method. Laser-imprint results, showing that maximum amplification occurs for a laser-intensity modulation of zero transverse wavenumber have thus been obtained [1]. Here we pursue this approach by proceeding to an analysis of the perturbations in terms of Kovásznay modes [2]. Focusing on the acoustic mode we have derived its exact propagation equation and, through an analysis of its source terms, obtained approximate equations for the different flow regions.

1 INTRODUCTION

The stability of ablative flows is of importance in inertial confinement fusion (ICF). Implosions of spherical capsules are highly non uniform and unsteady complex flows, hence rendering their stability analysis arduous. Most of the theories devoted to ICF target hydrodynamic stability has dealt with the "ablative Rayleigh Taylor" (RT) instability which occurs during the shell acceleration phase. Numerous analytical models have thus been established for steady ablative flows of unbounded fluid domains in a uniform and constant inertial force field, under incompressible or isobaric approximations. Such models have permitted a better understanding of this rather complex instability in the case of steady ablation front. Here we consider the stability of exact one-dimensional (1D) self-similar ablation flows, relevant to the so-called "shock transit time". Our approach is to describe accurately linear perturbations of exact solutions of the 1D Euler equations with nonlinear thermal conduction, and for this, to use adaptive multidomain Chebyshev spectral methods for computing both the mean flow and its 3D perturbations [1], hence avoiding the flaws of overly dissipative and dispersive numerical schemes found in ICF hydrocodes. Linear perturbation responses for ablation flows relevant to ICF are produced while taking into account—without any restriction, yet within a simplified setting—unsteadiness, compressibility and small-scale nonlinear heat-conduction effects. In this paper, we report on results regarding self-similar ablative flows due to radiative heat conduction and an analysis in terms of Kovásznay modes of laser-imprint results in the case of unsteady mean flow. As a first step, we focus on the acoustic mode, derive the exact acoustic wave equation, study acoustic source terms and exhibit approximate acoustic wave equations.

2 MEAN FLOW

2.1 EQUATIONS AND BOUNDARY CONDITIONS

Consider the 1D motion in the x direction of a compressible, inviscid, heat conducting fluid with a polytropic equation of state $p = \rho\,R\,T$, $\mathcal{E} = C_v\,T$, $C_v = R\,/\,(\gamma - 1)$. The equations of motion, written in terms of the Lagrangian coordinate m such that $\mathrm{d}m = \bar{\rho}\,\mathrm{d}x$, read

$$\frac{\partial}{\partial t}\left(\frac{1}{\bar{\rho}}\right) - \frac{\partial \bar{v}_x}{\partial m} = 0, \qquad\qquad \frac{\partial \bar{v}_x}{\partial t} + \frac{\partial \bar{p}}{\partial m} = 0,$$

$$\frac{\partial}{\partial t}\left(\frac{1}{2}\bar{v}_x^2 + \bar{\mathcal{E}}\right) + \frac{\partial}{\partial m}\left(\bar{p}\bar{v}_x + \bar{\varphi}_x\right) = 0, \quad \text{with} \quad \bar{\varphi}_x = -\bar{\chi}\,\bar{\rho}^{1-\mu}\,\bar{T}^{\nu}\,\frac{\partial \bar{T}}{\partial m}, \quad \mu \geq 0,\ \nu \geq 1. \tag{2.1}$$

In these equations, $\bar{\rho}$ denotes the density, $\bar{v}_x$ the longitudinal velocity, $\bar{p}$ the pressure, $\bar{T}$ the temperature, $\bar{\varphi}_x$ the nonlinear heat-flux, R the perfect gas constant and $\bar{\mathcal{E}}$ the specific internal energy. At t = 0, the fluid of uniform density is assumed to occupy the half-space $m \geq 0$, while a nonlinear heat-flux starts being applied along the plane $m = 0$. Initial conditions are of the form

$$\bar{\rho}(m,0) = \bar{\rho}_{\rm i}, \quad \bar{v}_x(m,0) = 0, \quad \bar{T}(m,0) = 0, \quad \text{for} \quad m \geq 0, \tag{2.2}$$

while boundary conditions are written as

$$\bar{p}(0,t) \;=\; \bar{p}_* \,(t/t_*)^{2(\alpha-1)}, \quad \bar{\varphi}_x(0,t) \;=\; \bar{\varphi}_* \,(t/t_*)^{3(\alpha-1)}, \quad \text{with} \quad \alpha = (2\,\nu - 1)/(2\,\nu - 2), \tag{2.3}$$

where $\bar{p}_*$, $\bar{\varphi}_*$ and t_* are some characteristic pressure, heat flux and time. With these initial and boundary conditions, system (2.1) admits a self-similar formulation. Introducing the self-similar variable $\xi = m\,t^{-\alpha}$, similarity solutions come as

$$\bar{\rho}(m,t) = \bar{G}(\xi), \quad \bar{v}_x(m,t) = t^{\alpha-1}\bar{V}(\xi), \quad \bar{T}(m,t) = t^{2(\alpha-1)}\bar{\Theta}(\xi), \quad \bar{\varphi}_x(m,t) = t^{3(\alpha-1)}\bar{\Phi}(\xi). \tag{2.4}$$

where the vector of unknowns $\mathbf{Y} = (\bar{G}\ \bar{V}\ \bar{\Theta}\ \bar{\Phi})^{\mathsf{T}}$ satisfies a system of ordinary differential equations,

$$\frac{d\,\mathbf{Y}}{d\xi} = \boldsymbol{\mathcal{F}}(\mathbf{Y}, \xi), \tag{2.5}$$

with boundary conditions

$$\bar{G} \;=\; 1, \quad \bar{V} \;=\; 0, \quad \bar{\Theta} \;=\; 0, \quad \text{as} \;\; \xi \to \infty, \tag{2.6}$$

$$\bar{P} = \bar{G}\bar{\Theta} = \mathcal{B}_p, \quad \bar{\Phi} = \mathcal{B}_\varphi, \quad \text{for} \;\; \xi = 0, \tag{2.7}$$

$\mathcal{B}_p$ and $\mathcal{B}_\varphi$ being dimensionless numbers based on $\bar{p}_*$ and $\bar{\varphi}_*$ respectively. The components $\mathcal{F}_i$ of $\boldsymbol{\mathcal{F}}$ are given by

$$\mathcal{F}_1 \;=\; \bar{G}^2\,N/D, \quad \mathcal{F}_2 \;=\; \alpha\,\xi\,N/D, \quad \mathcal{F}_3 \;=\; -\,\bar{G}^{\mu-1}\,\bar{\Theta}^{-\nu},$$
$$\mathcal{F}_4 \;=\; [\alpha\xi\mathcal{F}_3 \,-\, 2(\alpha-1)\bar{\Theta}]\,/\,(\gamma-1)\,-\,\alpha\xi\bar{G}\bar{\Theta}N/D, \tag{2.8}$$

with

$$N = (\alpha-1)\bar{V} + \bar{G}\,\mathcal{F}_3, \quad D = \alpha^2\xi^2 - \bar{G}^2\bar{\Theta}.$$

The singularity $D = 0$ of (2.5) corresponds to an isothermal characteristic curve, say $m/t^\alpha = \xi_s$, of the (m,t)-plane, which is circumvented by introducing an isothermal shock wave at $\xi = \xi_s$. Such a shock wave may be held to be a non-isothermal shock bounding the disturbed region. Henceforth the boundary conditions (2.6) are replaced by the non-isothermal Rankine-Hugoniot conditions, at $\xi = \xi_s$, thus defining, along with Eq. (2.7), a nonlinear eigenvalue problem for system (2.5). The method of solution consists of a finite-difference shooting procedure followed by a relaxation process coupled to an adaptive multidomain Chebychev spectral method [3].

2.2 RESULTS

Previous studies [1, 4, 5] have dealt with electron heat conduction solutions. We have chosen here to consider the case of radiative heat conduction for which the two exponents of the heat conductivity coefficient (2.1), are : $\mu > 1$ and $\nu > 3$, instead of $\mu = 0$ and $\nu = 2.5$ for electron heat conduction. The density, velocity, heat-flux and pressure reduced function profiles are given in Fig. 2.1. One can distinguish the four regions of the flow (from left to right): *(1)* a low density region (with a high temperature) between the origin and the ablation front, *(2)* a thin layer corresponding to the **continuous** thermal front, *(3)* the shocked region (cold and quasi-isothermal) where the density decreases slightly and the velocity is almost constant and *(4)* a region upstream of the shock wave where the fluid is at rest and the temperature zero as it is required by the self-similarity analysis. Notice that the front is very steep, hence difficult to capture numerically. This steepness at the ablation front, due to the temperature and density exponents, is noticeable on Mach and Péclet number profiles (Fig. 2.2).
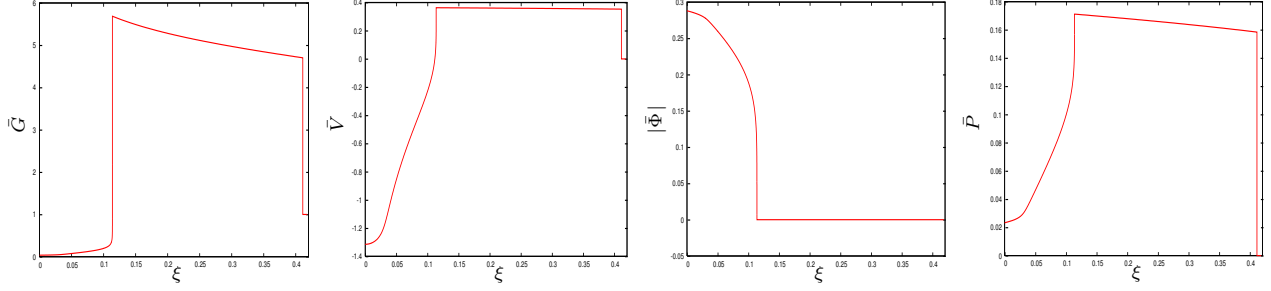
Fig. 2.1. Spatial profiles in the ξ-variable of the reduced functions for (from left to right) the density, velocity, heat-flux and pressure.
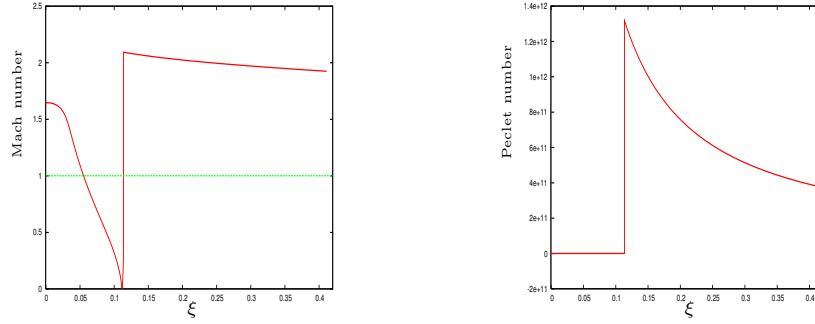

Fig. 2.2. Isentropic Mach and Péclet number profiles.

3   PERTURBED FLOW

3.1   EQUATIONS AND BOUNDARY CONDITIONS

The equations for the linear perturbations are written using an Eulerian description, in the (m, y, z)-coordinate system, as

$$\frac{\partial \rho}{\partial t} + \bar{\rho} \left(\frac{\partial \bar{\rho}}{\partial m} \, v_x + \bar{\rho} \frac{\partial v_x}{\partial m} + \frac{\partial \bar{v}_x}{\partial m} \, \rho + \nabla_\perp \cdot \vec{v}_\perp \right) = 0, \tag{3.1a}$$

$$\frac{\partial v_x}{\partial t} + \bar{\rho} \frac{\partial \bar{v}_x}{\partial m} \, v_x + \frac{\partial p}{\partial m} - \frac{\partial \bar{p}}{\partial m} \, \frac{\rho}{\bar{\rho}} = 0, \tag{3.1b}$$

$$\frac{\partial \vec{v}_\perp}{\partial t} + \frac{1}{\bar{\rho}} \, \nabla_\perp p = \vec{0}, \tag{3.1c}$$

$$C_v \left(\frac{\partial T}{\partial t} + \bar{\rho} \frac{\partial \bar{T}}{\partial m} \, v_x \right) + \bar{\rho} \frac{\partial \bar{v}_x}{\partial m} \, T + \bar{p} \frac{\partial v_x}{\partial m} + \frac{\partial \varphi_x}{\partial m} - \frac{\partial \bar{\varphi}_x}{\partial m} \, \frac{\rho}{\bar{\rho}} + \frac{(\bar{p} \nabla_\perp \cdot \vec{v}_\perp + \nabla_\perp \cdot \varphi_\perp)}{\bar{\rho}} = 0, \tag{3.1d}$$

where $\nabla_{\perp\cdot} = (\partial_y \cdot, \partial_z \cdot)^{\mathsf{T}}$. The above system of partial differential equations in physical space is replaced by a 1D system in the yz-Fourier space, consisting of (3.1a), (3.1b), (3.1d) along with

$$\partial_t \left(\nabla_\perp \cdot \vec{v}_\perp \right) - k_\perp^2 \, p/\bar{\rho} = 0, \quad \text{with } k_\perp = \sqrt{k_y^2 + k_z^2}, \tag{3.2}$$

where the same notation has been used for a quantity and its Fourier transform. Boundary conditions are provided at $\xi = 0$ by imposing arbitrary time-dependent density and incident heat-flux perturbations, and at the shock front ($\xi = \xi_s$) by the non-isothermal Rankine-Hugoniot conditions for linear perturbations. System (3.1a), (3.1b), (3.1d) and (3.2) is solved in the coordinate system ($\xi = m \, t^{-\alpha}, \, k_\perp$). Numerical approximation in the ξ variable is carried out with the same multidomain collocation spectral method as that used for the mean flow, while time integration is performed using an operator-splitting approach. In effect, the system of PDEs is decomposed into a first-order hyperbolic system and a second-order parabolic equation, boundary conditions being then spread over these two subsystems. This splitting is implemented at each step of a three

step second-order semi-implicit Runge-Kutta scheme. The hyperbolic system is integrated using the explicit part of this scheme [3,6], while the complete scheme is used for the parabolic system [7].

3.2 RESULTS

Laser nonuniformities and target surface roughness are the two major sources of perturbation growth in ICF pellet implosions. Here, we only consider nonuniform laser ablation by laser irradiation nonuniformities of otherwise perfectly smooth target. The flux perturbation, imposed at the boundary $\xi = 0$—here taken to be the energy deposition surface—, is chosen to be the following

$$\varphi_x(\xi = 0, t) = \bar{\varphi}_x(m = 0, t)\,\Pi_\varphi(t;\theta) \equiv t\,\mathcal{B}_\varphi\,\Pi_\varphi(t;\theta) \quad \text{with} \quad \Pi_\varphi(t;\theta) = \left[1 - 2\left(1 + \exp\theta(t - t_{\mathrm{i}})\right)^{-1}\right], \quad (3.3)$$

where t_{i} is the simulation starting time and θ is a free parameter controlling the rise of the heat-flux perturbation. Computations have been performed for a configuration with $t_{\mathrm{i}} = 0.1$ and $\theta = 100$ for transverse wavenumber values in the range: $0 \leq k_\perp \leq 100$.

3.2.1 LASER IMPRINT RESULTS

Computations for different values of the heat-flux perturbation rise-time parameter θ lead to the same conclusions [1,4,5]. Time evolutions of $\widehat{G} = \max_\xi |\rho|(t, k_\perp)$, *i.e* overall flow density perturbation extrema, are shown for all the wavenumbers considered here in Fig. 3.3. A noticeable feature of this amplification sheet is that its maximum level is reached for $k_\perp = 0$. For small values of the transverse wavenumber $k_\perp$, after a period of pure growth, the quantity $\widehat{G}$ stays nearly constant. For increasing values of $k_\perp$, the duration of the growth period shortens as a transient attenuation regime sets in, itself followed by a persisting oscillatory regime of smaller amplitudes. The transition between these two regimes defines wavenumbers which evolve like $t^{-4/3} \equiv t^{-\alpha}$, indicating that damping mechanisms are essentially governed by thermal conduction (α only depends on ν).
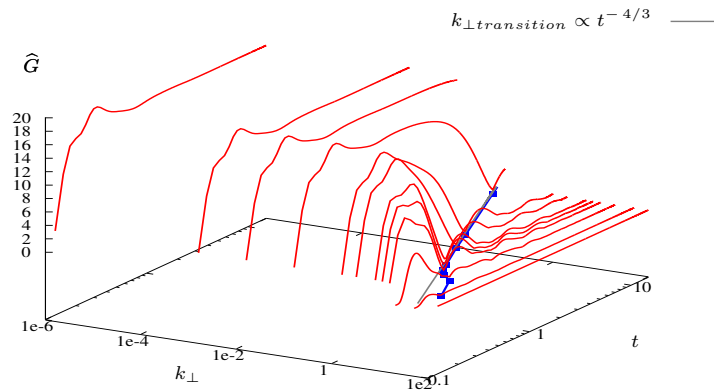

Fig. 3.3. Maximum of the density perturbation versus time and wavenumber.

Ablation-front distortion results (Fig. 3.4) illustrate the disparity, up to seven decades, in ablation-front distortion responses. Moreover we notice a highly oscillatory regime at very low level for large wavenumbers $k_\perp$ (Fig. 3.4a). Depending on the relative heat conduction zone thickness $k_\perp l_{\mathrm{con}}$, three regimes of the ablation-front distortion amplitude are identified: a regime of algebraic growth ($\propto t^{\frac{4}{3}}$) for $k_\perp l_{\mathrm{con}} \ll 1$, a regime of modulated amplitude oscillations for $1 \lesssim k_\perp l_{\mathrm{con}} \lesssim 10^3$, and a damped oscillatory regime. The fact that the oscillation frequencies become proportional to $k_\perp$ as $k_\perp \nearrow$ indicates that, in this regime, perturbations tend to be of acoustic type, hence justifying taking into account the compressibility of the flow and focusing at first on acoustic mode.
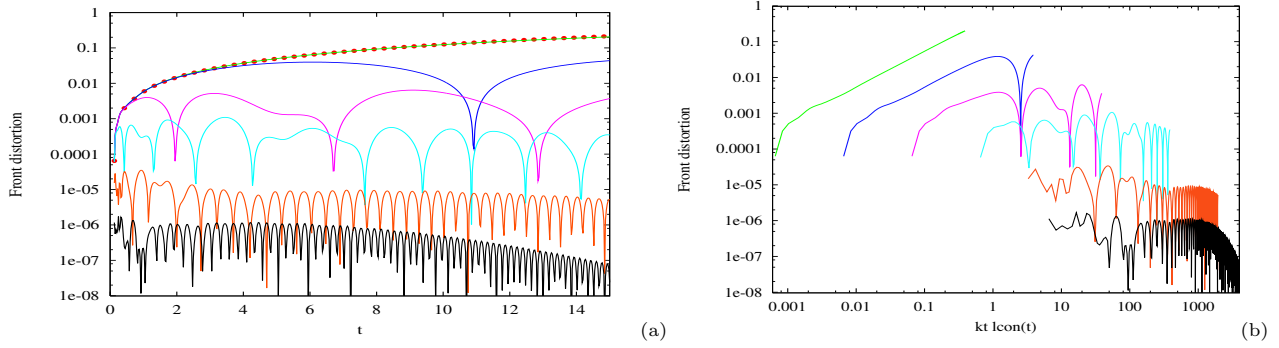
Fig. 3.4. Dimensionless plots of the ablation-front distortions vs (a) time and (b) the relative conduction zone thickness $k_\perp l_{con}$, for from (top to bottom) wavenumbers $k_\perp = 0$ (plot (a) only), 0.01, 0.1, 1, 10, 50, and 100.

3.2.2 KOVÁSZNAY ACOUSTIC MODE

An exact propagation equation for the acoustic perturbation has been derived for the present (unsteady and nonuniform) self-similar flows with, on the left-hand side, d'Alembert's operator, and on the right-hand side, 51 source terms, written in a compact form. This equation reads

$$\Box p \equiv \left[\frac{\partial^2}{\partial t^2} - \gamma \bar{p} \bar{\rho} \left(\frac{\partial^2}{\partial m^2} - \frac{k_\perp^2}{\bar{p}^2} \right) \right] p = f(\rho) + g(v_x) + k_\perp h(\nabla_\perp . \vec{v}_\perp) + q(p, T; k_\perp). \qquad (3.4)$$

Restricting ourselves to the case $k_\perp = 0$, the remaining 32 source terms are gathered in three groups: $f(\rho)$, $g(v_x)$ and $q(p, T; 0)$. Space-time evolutions of these source terms (Fig. 3.5) and analysis of their relative weight lead to approximate acoustic propagation equations for the different regions of the flow. Three regions in space—the shocked region, the ablation layer and the conduction zone (from the origin to the ablation front)—and two regions in time—short and long times—stand out (Fig. 3.5). In particular, it turns out that the acoustic excitation phenomenon takes principally place in the conduction zone and at the ablation front. In effect, for the shocked region, the sum of source terms is almost equal to zero, so that, we are dealing with an almost free propagation with associated approximate equation

$$\Box_{(k_\perp = 0)} p = 0. \qquad (3.5)$$

In the conduction zone, source terms exhibit complex patterns for short times while, for long times, become smooth and follow lines of constant ξ. A similar behaviour is observed for the ablation layer. For these two regions, the contributions of the different terms in each group have been evaluated and compared, leading to retaining only the dominant terms, and consequently approximate acoustic propagation equations. So in the conduction zone, the dominant terms of $f(\rho)$ and $q(p, T; 0)$ are the most influential, so that we obtain the equation

$$\Box_{(k_\perp = 0)} p = \tilde{f}(\rho) + \tilde{q}_c(p, T; 0), \qquad (3.6)$$

where $\tilde{f}$ indicates that we only retain the dominant term contribution.

For the ablation zone, many source terms are involved but sources stemming from nonlinear advection terms and nonlinear heat conduction dominate, leading to the approximate equation

$$\Box_{(k_\perp = 0)} p = \tilde{g}(v_x), + \tilde{q}_a(p, T; 0). \qquad (3.7)$$

4 SUMMARY

In this paper, we have presented a self-similar ablation flow due to radiative heat conduction, and some new results concerning the first analysis of laser imprinting based on a dynamic solution, revealing that maximum perturbation amplitudes in the thin ablation layer are reached for transverse wavenumber $k_\perp = 0$, and that perturbations are of acoustic type. Preliminary analysis of the Kovásznay acoustic mode has lead to identify the dominant acoustic source terms for the different flow regions for which approximate acoustic propagation
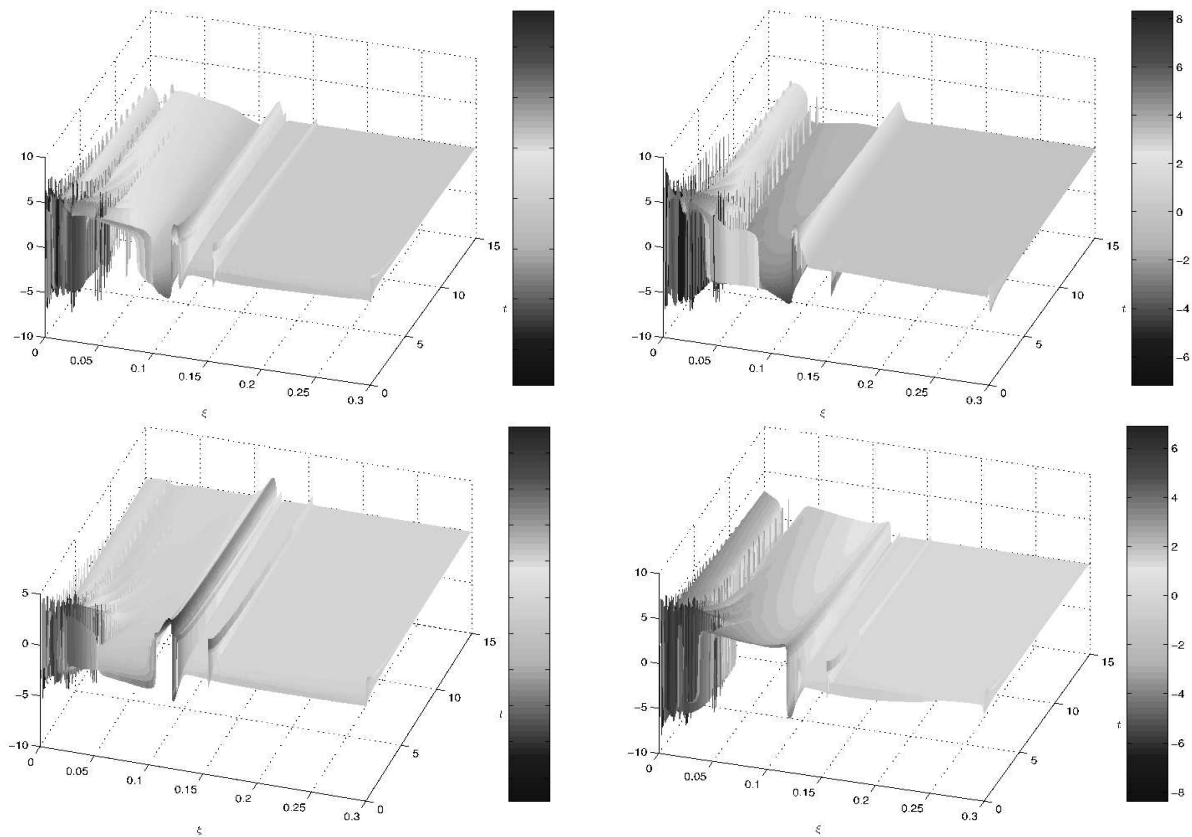
Fig. 3.5. Space-time evolutions of source terms of the acoustic propagation equation, respectively (from left to right and top to bottom), sum of source terms, q-group, g-group and f-group.

equations have been proposed. This analysis shall be completed for $k_\perp \neq 0$ and for the vorticity and entropic mode.

The authors are grateful to Miss V. Gognet for carrying out the Kovásznay acoustic mode computations.

REFERENCES

[1] F. Abéguilé, C. Boudesocque-Dubois, J-M. Clarisse, S. Gauthier, Y. Saillard. Linear perturbation amplification in ICF self-similar ablation flows. *Phys. Rev. Lett.*, 97:035002, 2006.

[2] B.T. Chu and L.S.G. Kovásznay. Non-linear interactions in a viscous heat-conducting compressible gas. *J. Fluid Mech.*, 3:494–514, 1958.

[3] S. Gauthier, B. Le Creurer, F. Abéguilé, C. Boudesocque-Dubois, J.-M. Clarisse. A self-adaptive domain decomposition method with Chebyshev method. *Int. J. Pure Appl. Math.*, 24:553–577, 2005.

[4] F. Abéguilé, C. Boudesocque-Dubois, J-M. Clarisse, S. Gauthier. Linear perturbation amplification in self-similar ablation flows of inertial confinement fusion. In *IWPCTM9*, 2004.

[5] J.-M. Clarisse, C. Boudesocque-Dubois, S. Gauthier, F. Abéguilé. Linear perturbation amplification in ICF self-similar ablation flows. *J. Phys. IV France*, 133:111–115, 2006.

[6] C. Boudesocque-Dubois, J.-M. Clarisse and S. Gauthier. A spectral Chebyshev method for linear stability analysis of one-dimensional exact solutions of gas dynamics. *J. Comput. Phys.*, 184:592–618, 2003.

[7] F. Abéguilé. *Étude de l'instabilité hydrodynamique d'écoulements autosemblables d'ablation*. Thèse de doctorat, Université de Paris 6, 2004.

e-mail: `guymala@bgu.ac.il`

Two- and Three-Dimensional Numerical Simulations of the Interaction of a Richtmier-Meshkov Instability Induced Turbulent Mixing Zone with Several Re-shocks.

G. Malamud[1,2], Y. Elabz[2], E. Leinov[1], A. Formoza[1], O. Sadot[1,2], D. Shvartz[1,2] and G. Ben-Dor[1]

[1]Department of Mechanical Engineering, Ben-Gurion University of the Negev, Beer-Sheva, Israel
[2]Physics Department, Nuclear Research Center, Negev, Israel

Abstract: Two- and three-dimensional direct numerical simulations (DNS) were preformed in order to study the dependence of the turbulent mixing zone growth rate on the perturbation initial spectrum when it is accelerated by several waves. Good agreement was achieved for initial spectrums containing large enough wave-lengths (i.e., a few mm). The DNS results were compared to the experimental results presented in Ref. [2], and good agreement is evident. A clear dimensionality (e.g., 2D or 3D) effect was found, expressed in the initial perturbation spectrum required for achieving good agreement with the experimental results.

1 INTRODUCTION

The shock wave interaction with a turbulent mixing zone (TMZ) has gained much attention over the past decades, due to its importance in physical systems such as inertial confinement fusion (ICF) and astrophysical phenomena (e.g., supernova). Although good understanding of the TMZ evolution due to a single shock wave interaction is now at hand, not much information is available about the development characteristics of the TMZ when it is accelerated by multiple shock waves, with random initial perturbations. There are several experimental studies addressing this problem [1, 2, 3, 4], which show that the TMZ growth rate following a re-shock impact increase sharply. A detailed comparison between the experimental results shows that the TMZ growth rate after the re-shock impact does not depend on the shock tube end-wall distance. It should be mentioned, that similar quantitative growth rates following the re-shock impact were achieved in different experimental facilities [1, 2, 3]. However, these experimental results were restricted mainly to the TMZ width development in time. Hence, very little is known about the initial conditions on the membrane separating the light and heavy gases and about the internal physical behavior of the TMZ. On the other hand, numerical simulations presented in literature do not reproduce in general the TMZ growth rate after the re-shock impact [5]. Therefore, it is needed to find the TMZ growth rate dependence on the initial condition (i.e., initial spectrum and amplitude) and geometry (i.e., 2D and 3D).

In the present study this problem is investigated by direct 2D and 3D numerical simulations of a shock tube system, where the TMZ is initially created by an incident shock wave and then interacts with a reflected re-shock from the shock tube end-wall. The Numerical simulations are compared with the experimental results of Ref. [2]. The shock tube apparatus used in the experiments is described in Ref. [2]. A shock wave passes an air/SF_6 (light/heavy configuration, initial shock wave Mach number M_i=1.2) or an SF_6/air (heavy/light configuration, initial shock wave Mach number M_i=1.5) interface (Atwood number A=0.67) where the fluids were separated by a thin membrane, on which the initial perturbation was randomly created. The shock tube end-wall was placed 80 mm downstream of the thin membrane.

2 Numerical Codes

All the presented simulations were preformed with LEEOR2D (Ref. [6]) and LEEOR3D, which are finite volume ALE (Arbitrary Lagrangian Eulerian) hydrodynamic codes with interface tracking capability; solving the Euler equations (viscosity effects are assumed to be negligible). The simulations were preformed using a minimum of 8 numerical nodes per wave-length at t=0. Hence, a satisfactory numerical description of the growing instability was achieved.

3 Two-dimensional Numerical Simulations

In the first stage, we conducted two-dimensional DNS, using several initial conditions which differed from each other by $\langle \lambda \rangle^0$ (average wave-length at t=0), using initial amplitude to wave-length ratio $\left(a \middle/ \langle \lambda \rangle^0 \right)$ of roughly 0.05. The initial amplitude for the calculations was derived from:

$$a_k(x) = \xi \left(\sum_{k_{min}}^{k_{max}} a_k \cos\left(\frac{x\pi}{d} k \right) \right) \qquad (1)$$

Where a_k is the wave number $k = 2\pi/\lambda$ random amplitude, x is the space coordinate, d is the domain width and $\xi = \varepsilon / \sum_k a_k$ is a normalization parameter.

The two-dimensional numerical simulations were preformed for the heavy/light and light/heavy configurations presented in [2]. The domain width was 4 cm, and two initial spectra were simulated: $0.5 < \lambda < 6.5$ mm and $0.5 < \lambda < 2.5$ mm ($\langle \lambda \rangle = 3.5$ and 1.5 mm, respectively).

The results revealed a clear dependence of the growth rate following the re-shock impact on the initial perturbation spectrum. A comparison between the two-dimensional numerical and experimental results is presented in Fig. 3.1, for the SF_6/air (heavy/light) (a) and air/SF_6 (light/heavy) configurations where the shock tube end-wall is 80 mm downstream of the initial location of the membrane. It can be seen that the growth rate following the re-shock impact increases with the initial average wave-length and that the $\langle \lambda \rangle = 3.5$ spectrum is in very good agreement with the experiments, both for the heavy/light and light/heavy configurations. It should be noted, that same quantitative agreement was achieved (with the same initial perturbation spectrum) with the experimental results presented in Ref [1].
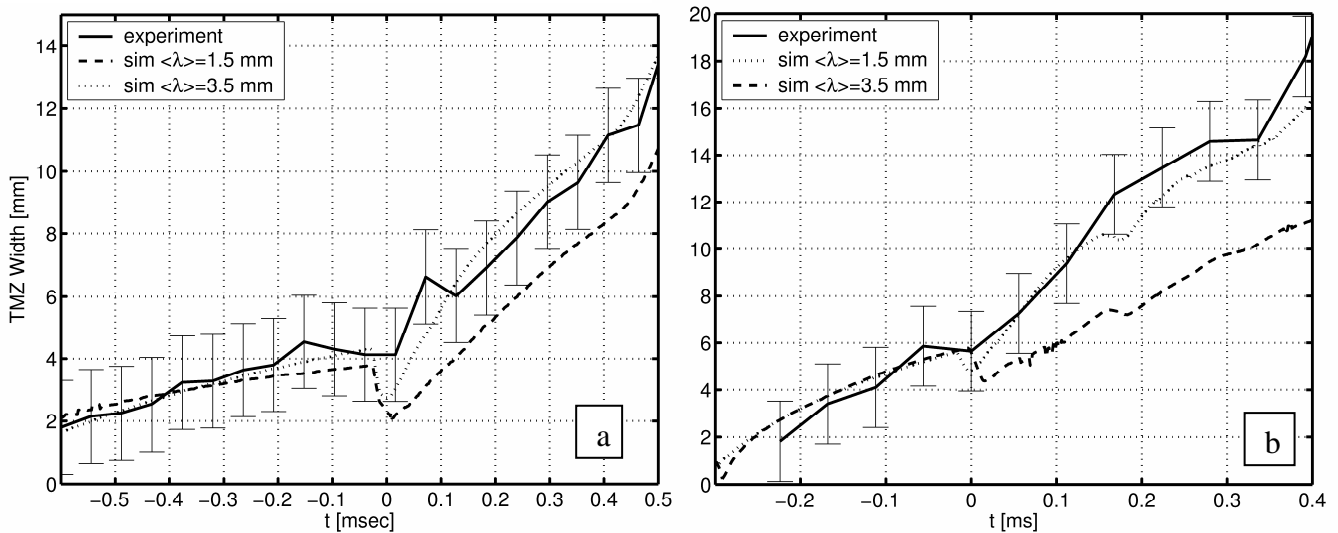

Fig. 3.1: TMZ width vs. time, for the light/heavy (a) and heavy/light (b) configuration (M_i=1.2 and 1.5, respectively, end wall at 80 mm) as was obtained experimentally [2] (smooth lines) and by two-dimensional numerical simulation with $\langle \lambda \rangle^0 = 1.5$ and $\langle \lambda \rangle^0 = 3.5$ mm (dashed and dotted lines, respectively). t=0 denotes the re-shock arrival to the interface.

The SF_6/air interface at different times is presented in Fig. 3.2 (t=0 marks the arrival time of the re-shock to the TMZ). Until the re-shock impact, no dominant bubble merging mechanism is evident (Fig. 3.2a-3.2b). It can be seen clearly, that shortly after the re-shock impact, large-scale structures evolve rapidly and dominant the TMZ structure, without any significant change in the average wave-length.

A comparison between the numerical simulation results for both spectra (e.g., $\langle \lambda \rangle^0 = 3.5$ and $\langle \lambda \rangle^0 = 1.5$) is presented in Fig. 3.3. It can be seen that the $\langle \lambda \rangle^0 = 3.5$ TMZ contains structures with wave-lengths of the order $< \lambda > \sim 5$ mm, while the $\langle \lambda \rangle^0 = 1.5$ contains wave-lengths of the order $< \lambda > \sim 2$ mm. since no dominant bubble merging occurs, this difference in the perturbation spectra sets the difference in the TMZ growth rate.

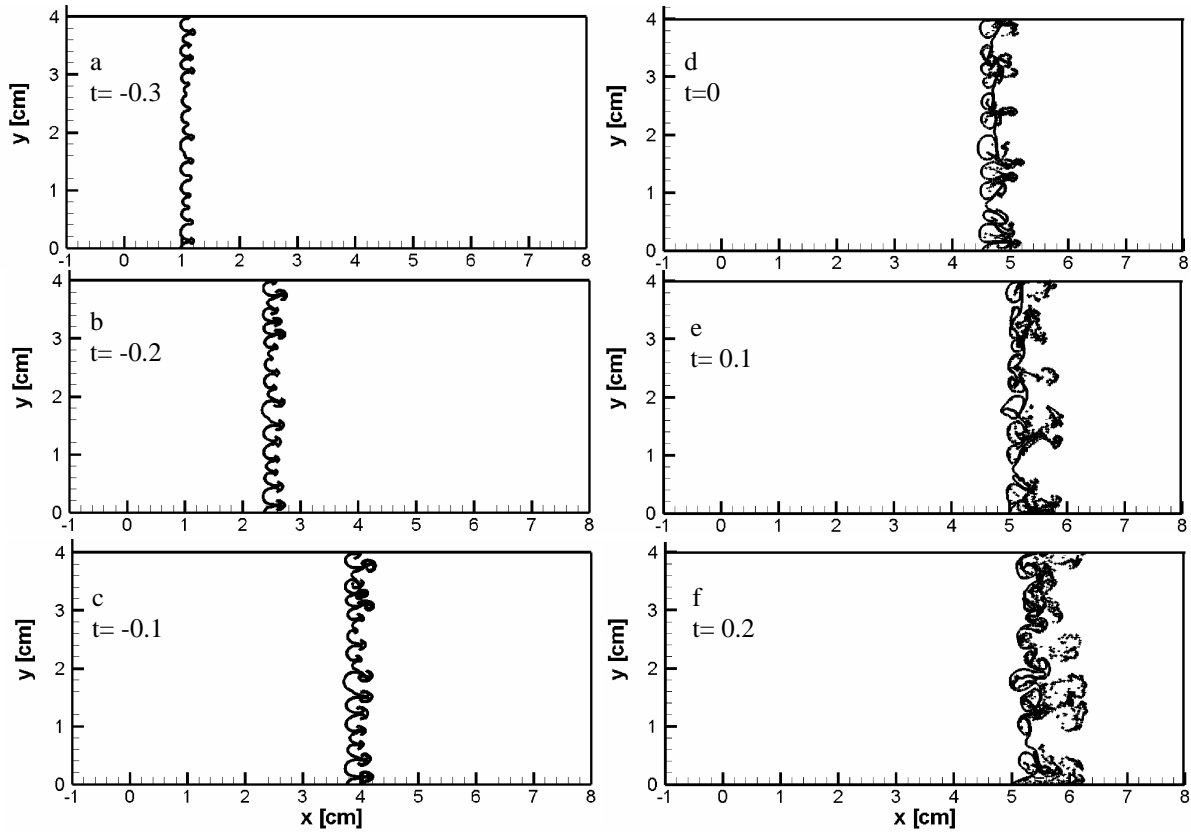**Fig. 3.2:** SF$_6$/air interface at different times (t=0 represents the re-shock impact) for the SF$_6$/air (heavy/light configuration, M$_i$=1.5, end wall at 80 mm) with initial perturbation spectrum of $\langle \lambda \rangle^0 = 3.5$.
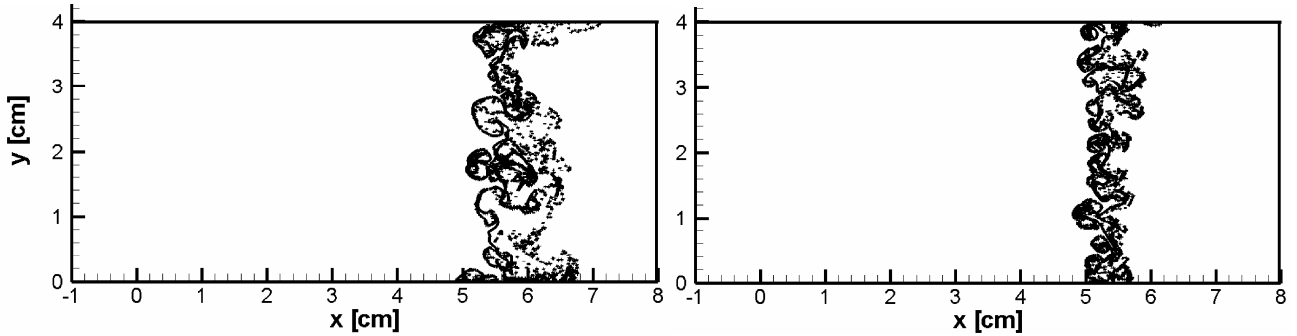
Fig. 3.3: SF$_6$/air interface extracted from the numerical simulations for the SF$_6$/air (heavy/light configuration, M$_i$=1.5, end wall at 80 mm) with initial perturbation spectrum of $\langle \lambda \rangle^0 = 3.5$ (a) and $\langle \lambda \rangle^0 = 1.5$ (b) 0.5 ms after re-shock interaction with the TMZ.

4 Three-dimensional numerical simulations

After achieving good agreement for the two-dimensional numerical simulations, some three-dimensional simulations were performed, for the heavy/light (SF$_6$/air) case, in which the initial perturbation amplitude was:

$$a_0\left(x,y\right) = \sum_{kx,ky} a_k \cos(\phi_x)\cos(\phi_y) + b_k \cos(\phi_x)\sin(\phi_y) +$$
$$c_k \sin(\phi_x)\cos(\phi_y) + d_k \sin(\phi_x)\sin(\phi_y) \tag{2}$$

Where $\phi_x = \dfrac{2\pi}{L} x k_x$, $\quad \phi_y = \dfrac{2\pi}{L} y k_y$ and a_k, b_k, c_k, d_k are random factors.

The simulations were preformed by means of LEEOR3D, with a 5x5 mm^2 domain cross section and a resolution of 60x60 computational nodes. In order to find the TMZ growth rate dependence on the initial perturbation spectrum, three-dimensional simulations, with $\lambda_{min} = 0.3$ mm and $\lambda_{max} = 5$, 2.5 and 1.25 mm, resulting with $\langle\lambda\rangle^0 = 2.6$, 1.5, 0.8 mm, respectively, were performed. Note that the wave-lengths for the three-dimensional case are were calculated from: $\sqrt{S/N}$, where S and N denote the total domain area and the number of bubbles.

In Fig. 4.1, the SF$_6$/air interface from the $\langle\lambda\rangle^0 = 2.6$ mm numerical simulation is presented at different times. It can be seen, that while the initial perturbation contains a large number of bubbles, ~120, (Fig. 4.1a), a rapid inverse cascade (e.g., bubble competition) reduces the number by a factor of 1/3 to ~40 (Fig. 4.1b-d) when the re-shock arrives at the interface. This number continues to reduce slowly (Fig. 4.1e to 4.1f), and the growth rate following the re-shock remains constant, with dominant wave-lengths of approximately 2 mm.

Fig. 4.1: SF$_6$/air interface at different times (t=0 marks the re-shock impact) for the SF$_6$/air (heavy/light configuration, M$_i$=1.5, end wall at 80 mm) with initial perturbation spectrum of $\langle\lambda\rangle^0 = 2.6$ mm.
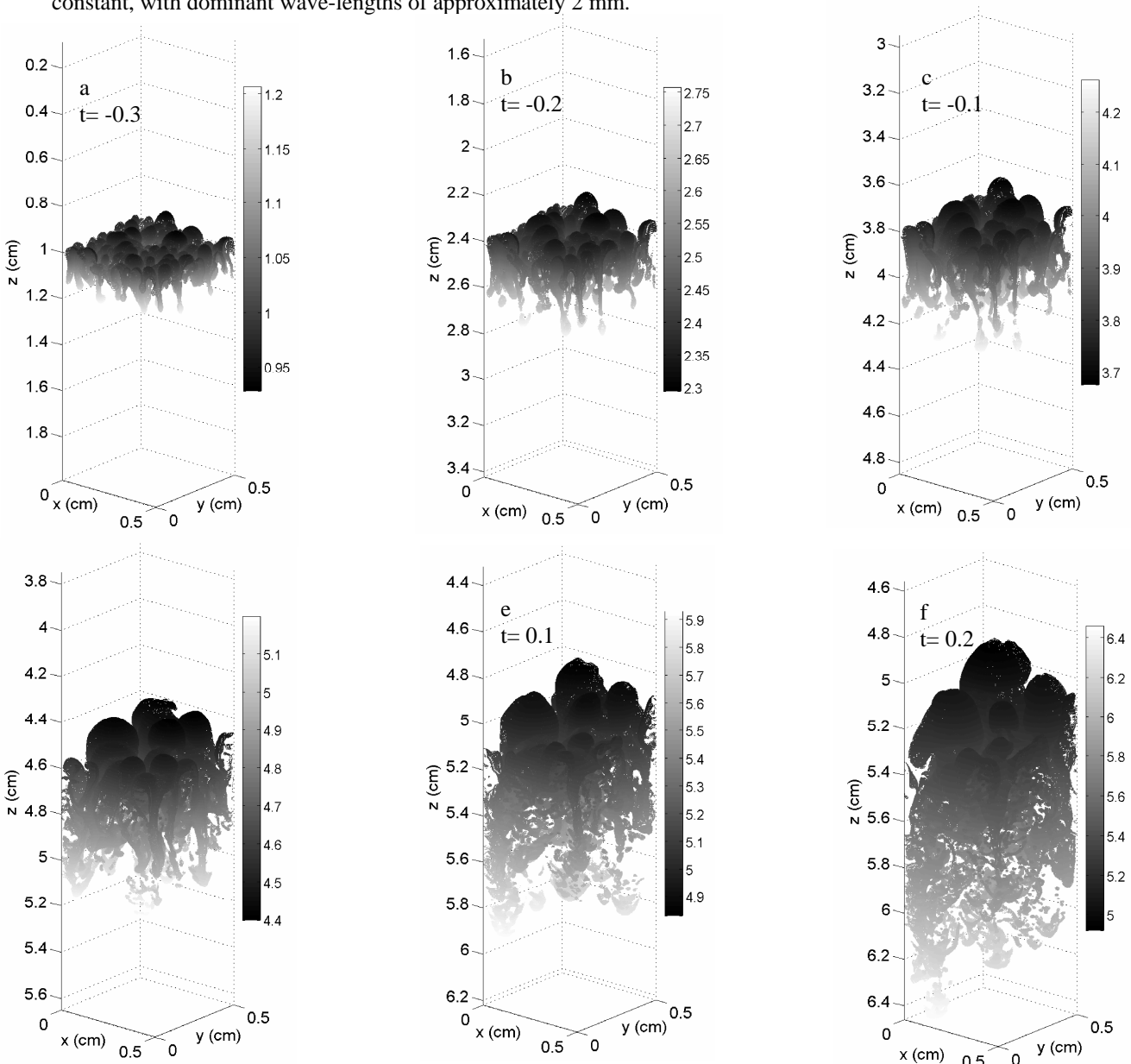
The TMZ width as a function of time as obtained in the three-dimensional numerical simulations and in the experiment is presented in Fig. 4.2. All the numerical calculations agree well with the experimental data before the arrival of the re-shock to the TMZ. It is also evident that when the initial perturbation spectrum contains large enough wave-lengths ($\langle \lambda \rangle^0 = 1.5$ and 2.6 mm, dashed and dotted lines, respectively), very good agreement is obtained after the re-shock arrival at the interface. When the initial perturbation spectrum is built from shorter wave-lengths ($\langle \lambda \rangle^0 = 0.8$ mm), the calculated TMZ fails to match the experimental results after the re-shock.
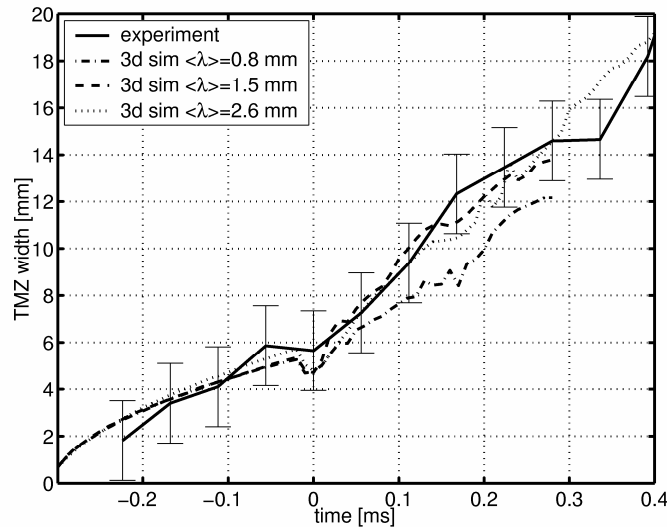

Fig. 4.2: TMZ width vs. time, for the heavy/light configuration (SF$_6$/air, M$_i$=1.5, end wall at 80 mm) as was obtained experimentally [2] (smooth line) and by three-dimensional numerical simulations with and $\langle \lambda \rangle^0 = 2.6, 1.5$ and 0.8 mm (dotted, dashed and dot-dashed lines, respectively). t=0 marks the re-shock arrival at the interface.

In order to enhance the difference between the two-dimensional and the three-dimensional simulations, the TMZ width as a function of time for $\langle \lambda \rangle^0 = 1.5$ mm, in both 2D and 3D, is presented in Fig. 4.3. It can be seen that while the three-dimensional simulation is in good agreement with the experiment, the two-dimensional simulation does not predict the correct growth rate after the recheck arrival at the interface.
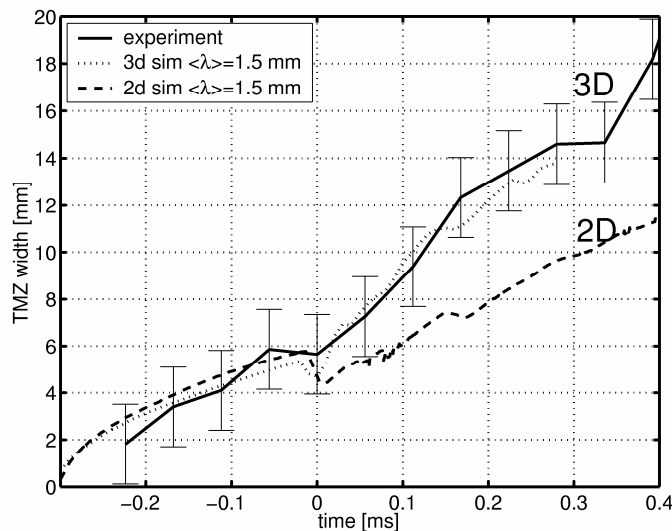

Fig. 4.3: TMZ width vs. time, for the heavy/light configuration (SF$_6$/air, M$_i$=1.5, end wall at 80 mm) as was obtained experimentally [2] (smooth line) and by the two- and three-dimensional numerical simulations with and $\langle \lambda \rangle^0 = 1.5$ mm (dotted and dashed lines, respectively). t=0 marks the re-shock arrival at the interface.

8 SUMMARY

Two- and three-dimensional numerical simulations were preformed in order to investigate the effect of the initial perturbation spectrum and geometry (2D or 3D) on the turbulent mixing zone growth rate in the case of multiple accelerations (e.g., shock tube with re-shock).

• It was found that both the 2D and the 3D simulations reproduce the experimental results of Ref. [2] for initial perturbation spectra containing large enough wave-lengths ($\langle \lambda \rangle^0 = 1.5$ and 3.5 mm for 3D and 2D, respectively).

• The reason for the difference in the initial spectrum required for good agreement with the experiments for the two- and three-dimensional simulations is that in the three-dimensional case, an efficient inverse cascade (e.g. bubble competition) process takes place in the TMZ, resulting a rapid increase in the average wave-length prior to the re-shock.

• Since the velocity of the bubbles and spikes depends on the wave length and on the geometry (e.g. 2D or 3D), the three dimensional TMZ tends to grow faster from the two dimensional (for a given wave length).

• Following the re-shock, no bubble competition is evident and the dominant medium wavelengths (~5 mm for 2D and ~2 mm for 3D) control the TMZ growth.

REFERENCES

[1]   V.A. Andronov, S.M. Bakhrakh, E.E. Meshkov, V. V. Nikiforov, A.V. Pevnitskii & A.I. Tolshmyakov, Sov. Phys. Dokl., **35**: 159 (1976).

[2]   E. Leinov, A. Formoza, O. Sadot, A. Yosef-Hai, G. Malamud, Y. Elabz, A. Levin, D. Shvarts & G. Ben-Dor, 10ᵗʰ IWPCTM, Paris, France.

[3]   F. Poggi, M.H. Thormbey & G. Rodriguez, Phys. Fluids **10**, 2698 (1998).

[4]   D. Shvarts, O. Sadot, L. Erez, D. Oron, U. Alon., G. Hanoch, G. Erez, G. Ben-Dor & L. A. Levin, 6ᵗʰ IWPCTM, Eds. G. Jourdan & L. Houas, pp. 464, Marseille, France, (1997).

[5]   D.L. Youngs, Physica D **12**, 32 (1984).

[6]   G. Malamud, A. Levy & D. Levi-Hevroni, AIAA J. **41**: 4, 663 (2003).

e-mail: `Christian.Mariani@polytech.univ-mrs.fr`

Experimental investigation of the interaction of a plane shock wave with spherical and sinusoidal gaseous interfaces

Christian MARIANI[1], Guillaume LAYES[1], Georges JOURDAN[1], Lazhar HOUAS[1] and Marc VANDENBOOMGAERDE[2]

[1] *Polytech'Marseille - Dpt Mécanique Energétique, IUSTI/UMR CNRS 6595, Université de Provence, Technopôle de Château-Gombert, 5 rue Enrico Fermi, 13013 Marseille, FRANCE*
[2] *CEA/DAM Île-de-France BP 12 91680 Bruyères-le-Châtel, FRANCE*

Abstract: We present the first results of two new studies concerning the Richtmyer-Meshkov instability. The first one consists in the observation with a laser sheet device of the deformation of a seeded gas bubble by a shock wave. The second one deals with the impulsive acceleration of a sinusoidal gaseous interface materialized by a nitrocellulose microfilm put on a computer designed grid. For each case, two gas couples, both heavy/light and light/heavy configurations, were tested with a weak shock wave (M=1.16±0.01).

1   INTRODUCTION

The mixing process between two gases, the interface of which is accelerated by a plane shock wave, has been the subject of a lot of studies for the last century, especially since it is known that the Richtmyer-Meshkov instability development is partly responsible for the loss of energy which prevent the Inertial Confinement Fusion. Several campaigns of experiments have been performed in our laboratory with different shapes and configurations of gaseous interfaces and with different visualization devices.

Concerning the acceleration of a gas bubble by a plane shock wave and in the continuity of a comprehensive study made with shadowgraph visualization [1,2], a campaign of runs is now carried out with pure two dimensional laser sheet visualization.

As regards the interaction of a plane shock wave with a sinusoidal gaseous interface, the present experiments concern two test gases initially separated by a thin nitrocellulose membrane put on a grid. This sinusoidal grid which was build with one's hand in a previous campaign [3], is now designed with computer and build by stereolithography. The present work gives the first results of these two studies.

2   EXPERIMENTAL SETUP

The experiments are performed in our horizontal 20 cm×20 cm square cross section shock tube.
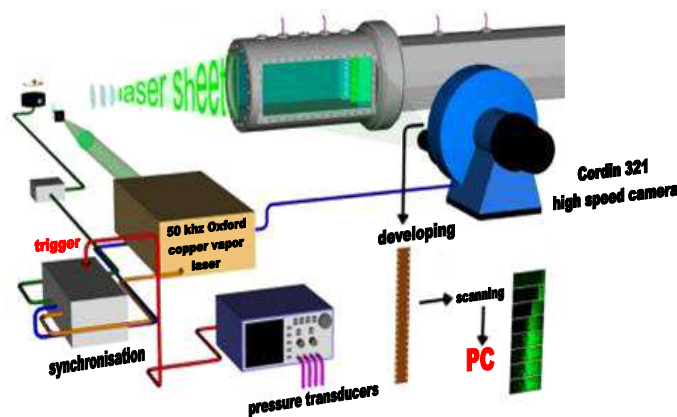

Fig. 2.1. Schema of the laser sheet visualisation.

The high pressure, low pressure and experimental chambers are respectively 1.65 m, 5 m and 0.48 m long. T200 shock tube allows to generate shock wave which Mach number range from 1.1 to 3. It is coupled with a laser sheet visualization device (figure 2.1) with a pulsed copper vapor laser (frequency ranges from 2 to 50 kHz), an optical system to transform the laser beam in a laser sheet and a high speed rotating drum camera (which turns up to 300 m/s). All this allow to obtain about 50 frames spaced by 500 μs to 20 μs. Dynamic PCB pressure gauges give temporal evolution of the pressure and set off the measurements.

3 SPHERICAL GASEOUS INTERFACE EXPERIMENTS

In the previous work of Layes et al. [1, 2], using a shadowgraph visualization device, the superposition on a frame of the phenomena along the test chamber section width induced a difficult distinction of bubble structures especially for low Atwood number and for a long time after the incident acceleration. To prevent this problem, experiments are now performed with laser sheet visualization. The use of this diagnostic needs to seed one of the two test gases. We decide to seed the bubble gas using a solution of titanium chlorid which reacts with water giving in particular a white smoke of titanium dioxide (*cf.* figure 3.2). The bubble test gas passes in titanium chlorid solution and takes a few fumes with it. As the bubble is blowing, these fumes react with the soap water and gives the seeding particles of titanium dioxide. The initial bubble diameter is about 40 mm and the soap solution is a mix in equal division of soap, glycerin and water. Concerning the other experimental parameters, the incident shock wave Mach number is about 1.15, the laser frequency is 10 kHz and the camera speed is 180 m/s (1 frame per 100 μs).
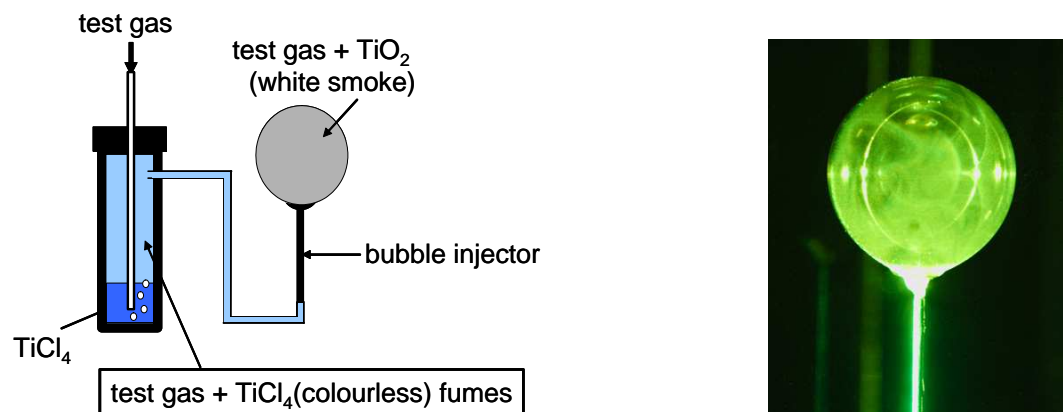

Fig. 3.2. Schema of the device to blow a seeded bubble and picture of a seeded bubble.

Figure 3.3 shows a comparison of shadowgraph and laser sheet diagnostics. For same deformation stages of a krypton bubble, frontiers of post shock structures (vortex rings, soap filaments and soap jet) are clearer with the laser sheet observation. This could be explained by the decrease of density gradient as the gases mix, insofar as smaller the density gradient is, worse is the contrast of the shadowgraph frames. However, we have to notice that the soap much diffracts the laser light and this harms the pictures contrast.

In a more quantitative way, we measure the bubble length (between the extremal bubble gas abscissa) and plot its dimensionless evolution (dividing the length by the initial diameter D_0 and time by the ratio $\frac{D_0}{U_f}$ where U_f is the flow velocity). If we compare the evolution of this characteristic size of the bubble measured both laser sheet or shadowgraph techniques (figure 3.4), a divergence of results appears with time. Here again, the difference of contrast should be responsible of this and the fact that the disagreement is earlier in the case of the krypton bubble than in that of the helium one is a further proof of it.

Shadowgraph
Run T80#222:   M=1.07

Laser sheet
Run T200#108:   M=1.13
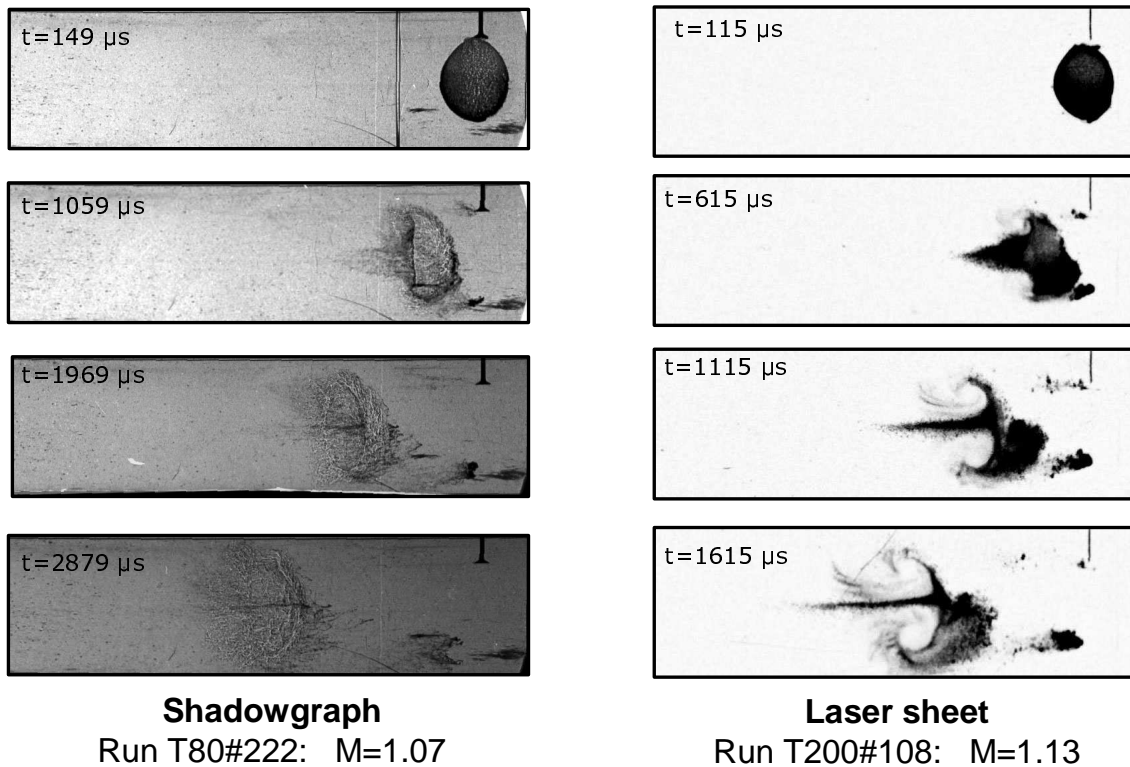
Fig. 3.3. Shadowgraph and laser sheet frames for same stages of bubble deformation.
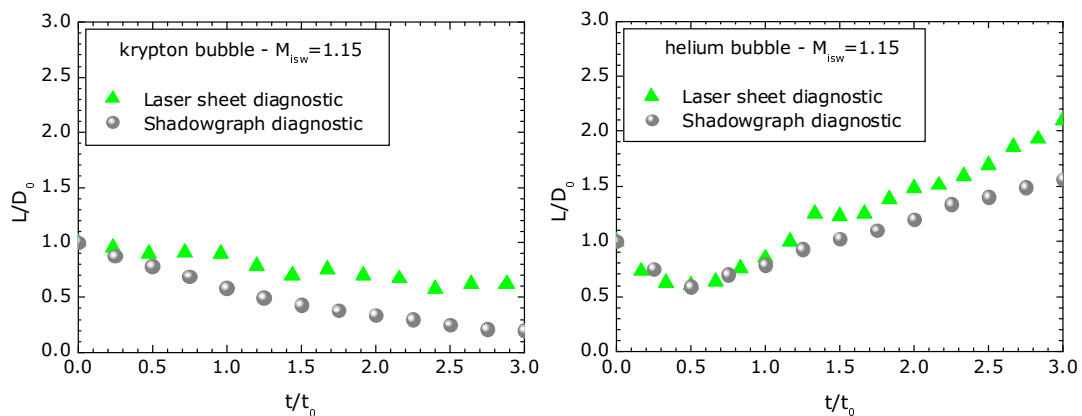
Fig. 3.4. Dimensionless temporal evolution of krypton and helium bubble lengths: comparison of shadowgraph and laser sheet results (D_0 is the initial bubble diameter and $t_0 = \frac{D_0}{U_f}$ where U_f is the flow velocity)

4 SINUSOIDAL GAS INTERFACE EXPERIMENTS

Unlike the previous experiments of Jourdan and Houas [3], we here used a double layer nitrocellulose membrane supported by a computer-aided designed grid which is also a perfect sinusoidal one. This grid which has been obtained by the stereolithography technique allows to have a better knowledge of the initial conditions. Therefore, the comparison between experiments should be easier.

As regards the experimental parameters, we have studied a light/heavy case with air/SF_6 interfaces accelerated by a shock wave of Mach number of about 1.15. Two kinds of perturbations have been used to completely follow the linear and the earlier non linear stages of the instability. The first is characterized by an initial

amplitude of 3 mm and a wave length of 80 mm. The second is characterized by an initial amplitude of 6 mm and a wave length of 120 mm. The runs were made with a laser frequency of 10kHz, a camera speed of 180 m/s and after an air seeding time of 15 minutes with incense smoke.

Fig. 4.5. Grid designs using the software CATIA (grid 1: λ_0=80mm - $\eta_0 = 3$mm , grid 2: λ_0=120mm - $\eta_0 = 6$mm).

Fig. 4.6. Polyacrilamid grids (grid 1: λ_0=80mm - $\eta_0 = 3$mm , grid 2: λ_0=120mm - $\eta_0 = 6$mm).

Laser sheet pictures in figure 4.7 show the interface evolution for the two initial sinusoidal configurations. This evolution consists in an increase of the initial perturbations. We can see the presence of membrane particles which more diffract the laser light along the interface contours.

Run T200#114 : grid 1 - air/SF$_6$ - M$_{isw}$=1.17   **Run T200#117** : grid 2 - air/SF$_6$ - M$_{isw}$=1.16
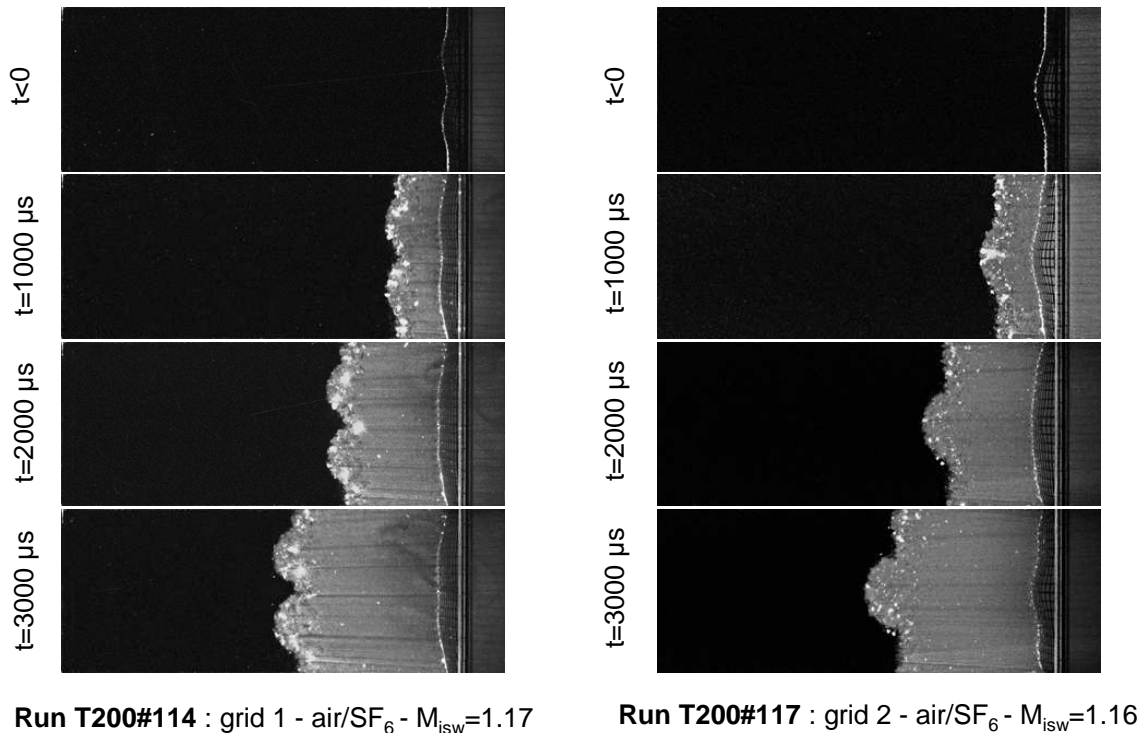
Fig. 4.7. Laser sheet frames of interactions between a 1.15 Mach number shock wave and two different seeded air/SF$_6$ sinusoidal interfaces

In figure 4.8 are plotted the dimensionless peak to peak amplitudes of the perturbations compared with the linear theory. For grid 1, this dimensionless peak to peak amplitude can be measured twice from the abscissa

difference between the minimum in the middle of the tube and the two maxima. The two other minima near the walls are not used to prevent the effects of the interfacial mode change (from sinusoidal to plane meshes). For grid 2, we measure the peak to peak amplitude between the maximum in the center and each minimum near the walls, calculate the average of the two values and divide it by two. The graphics in figure 4.8 have been obtained from two different experiments for each sinusoidal case. They show the good reproducibility of the experiments. Clearly, the measured growth rate is lower than that of the linear theory quickly after the passage of the incident shock wave. This is doubtless the effects of the nitrocellulose particles. But this disagreement with the linear theory is greater in the experiments with grid 2. The only one centered perturbation geometry maybe generates less vorticity in the hollow, near the wall, which could explain this lower growth rate.
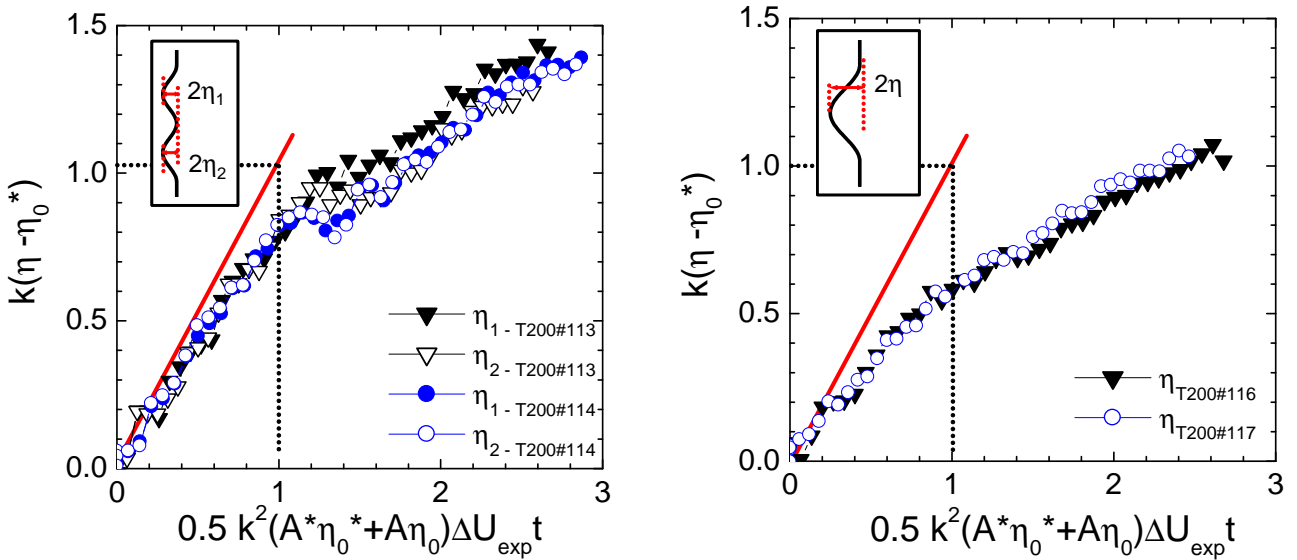

Fig. 4.8. Dimensionless temporal evolution of the growth rate of the perturbation for two different initial sinusoidal interfaces

5   SUMMARY

The first experiments of the shock wave/gas bubble interaction let predict that future measurements of some of the characteristic sizes of the bubble will be more accurate with the laser sheet diagnostic. The perspectives are to made a comprehensive study changing the gas configuration and the incident shock wave velocity. Moreover, in the future work, we will have to reduce the soap deposit because of the great diffraction of the laser light by water and we would like increase the bubble size.

Concerning the shock wave/sinusoidal gas interface interaction, the use of a grid obtained by stereolithography allows more accurate dimensions of the initial perturbations and also a better knowledge of the initial conditions. However, the first measurements show that the presence of membrane particles seems to reduce to growth rate of the perturbations in comparison with the linear and non linear theories. In this way, the perspectives to give to this investigation could be to reduce the membrane effects using a simple layer of nitrocellulose membrane and a higher shock wave Mach number.

REFERENCES

[1] Layes, G., Jourdan, G., and Houas, L. 2003, Distorsion of a spherical gaseous interface accelerated by a plane shock wave. *Phys. Rev. Lett.*, **91**, 17, pp. 174502.1-174502.4

[2] Layes, G., Jourdan, G., and Houas, L. 2005, Experimental investigation of the shock wave interaction with a spherical inhomogeneity. *Phys. Fluids*, **17**, 2, pp. 028103.1-028103.4

[3] Jourdan, G. and Houas, L. 2005, High-amplitude single-mode perturbation evolution at the Richtmyer-Meshkov instability. *Phys. Rev. Lett.*, **95**, 20 , pp. 204502.1-204502.4

e-mail: `Christian.Mariani@polytech.univ-mrs.fr`

Comparison of hot wire and laser Doppler measurements in shock-induced mixing zones

Christian MARIANI[1], Laurent SCHWAEDERLÉ[1], Georges JOURDAN[1] and Lazhar HOUAS[1]

[1] *Polytech'Marseille - Dpt Mécanique Energétique, IUSTI/UMR CNRS 6595, Université de Provence, Technopôle de Château-Gombert, 5 rue Enrico Fermi, 13013 Marseille, FRANCE*

Abstract: We have conducted two similar RMI induced air/SF_6 mixing experiments on two shock tubes using two different diagnostics : the constant temperature hotwire anemometer (CTHWA) at IUSTI and the laser doppler velocimeter (LDV) at CEA/DIF. First comparisons of the CTHWA and LDV raw signals, before reflected shock, on shocks and mixing zone passage times, indicate a good agreement between the two experiments undertaken on different shock tube apparatus.

1 INTRODUCTION

This paper presents the works carried out at Université de Provence [1] and the Commissariat l'Energie Atomique [2] on the Richtmyer-Meshkov instability (RMI) of gaseous interfaces in shock tubes and on the turbulent mixing zones arising from it. The RMI occurs when a shock wave refracts on an interface of gases of different densities materialized by a very thin membrane. On average, the shock and the interface are coplanar but any geometrical perturbations on, say, the gaseous interface, either set initially or created at shock passage, will lead to locally non parallel pressure and density gradients. This generates a sheet of vorticity on the interface which deforms it and leads to a turbulent mixing layer. This mixing layer can then be excited by subsequent waves, first and most strongly by the refracted shock after its reflection on the shock tube end wall. This planar shock-interface interaction followed by re-shock excitation is analogous to the dynamics of the interface between thermonuclear fuel and shell material occuring in inertial confinement fusion targets with spherical imploding incident shock and exploding reflected shock. Since mixing may impede the fusion process, it is important to predict it with modelling. Shock tube mixing experiments are carried out in order to help the modelling effort. We have been investigating, during the two last decades, the mixing zone in shock tube by various techniques, schlieren and shadowgraph visualizations, x-ray average density measurements, differential interferometry, laser-doppler velocimetry at CEA, schlieren and shadowgraph visualisations, average density measurements by infrared laser emission and absorption and hot wires at IUSTI.

2 PRESENT EXPERIMENTS

In the present experiments, the air/SF_6 interface is initially materialized by a thin nitrocellulose microfilm maintained next to a metallic wire mesh with a wire spacing of 1.8 mm. Thus the forcing wavelength of the RMI is 1.8 mm in both transverse directions with an unmeasured initial amplitude estimated at 1-3 mm. The length of the SF_6 chamber was 250 mm for the two experimental apparatus described below. For this fast to slow case, the Mach 1.2 incident shock wave in air refracts as a Mach 1.3 shock in SF_6 accelerating the flow to about 70 m/s. The refraction of the reflected shock of Mach 1.3 reverses the flow to about -25 m/s. The subsequent rarefaction wave brings the gases to a velocity of 10 m/s.

2.1 Experimental set-up installed at IUSTI

At IUSTI, the horizontal 85 mm by 85 mm shock tube is equiped with three hot wire probes supported close to the test section center by prongs inserted from the end plate as shown in Fig. 2.1. Each wire can be set at a different abscissa, thus each shock tube run provides three heat transfer measurements. The CTHWA output voltage is a fonction of local gas characteristics: velocity, density, temperature, viscosity and heat conductivity [1]. Using Wilke and Vassilievski laws for the transport coefficients in the mix and a simplifying hypothesis on temperature variation, this voltage depends on velocity and concentration. For sampled instants we calculate all possible values of hot wire signal for a logical range of velocity and concentration in the mix

then match it to the experimental signal to obtain a probable pair of velocity and concentration. We found that the evolution of the concentration profile is much less sensitive to the range of velocity then the velocity profile. The CTHWA is a good mixing zone dectector. However, the intrusive nature of the CTHWA makes it less useful for the reshocked mixing zone because the reflected shock waves propagates along the prongs and the wire is located in the wake of its support. The frequency response of the hot wire is also limited to 80 kHz.
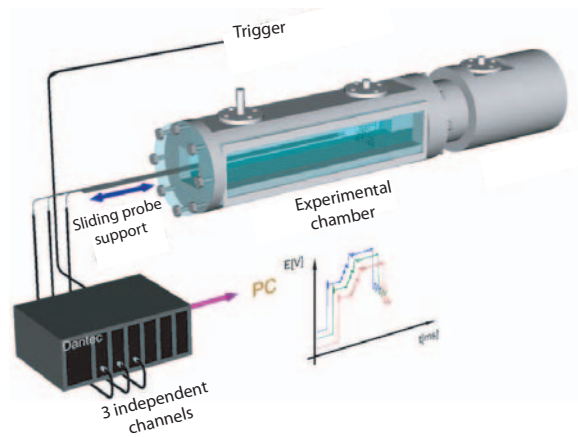
Fig. 2.1. Observation section and hot wire anemometer setup on IUSTI shock tube.

2.2 Experimental set-up installed at CEA

At CEA/DIF, as we can see in Fig. 2.2, we use a two component LDV in a vertical 130 mm by 130 mm shock tube to obtain axial and transversal velocity components at various abcissa along the shock tube. Prior to the
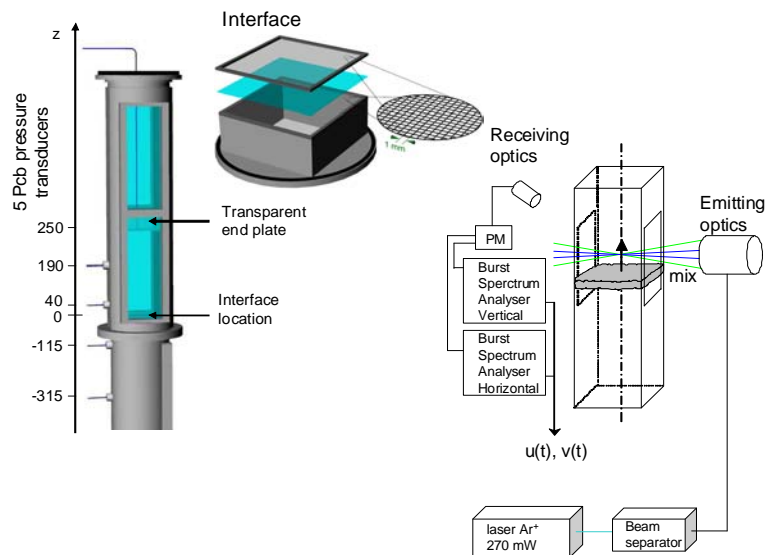
Fig. 2.2. Observation section and laser doppler anemometer setup on CEA shock tube.

run, air and SF_6 are seeded with incense smoke and olive oil droplets respectively. The LDV provides a velocity data point whenever a particle crosses the measuring volume (intersection of two pairs of laser beams) and the Doppler shifted light diffused from it reaches the receiving optics. We found that the membrane fragments

reduce the data rate in the mixing zone. Many identical runs are needed at each location to obtain velocity profiles in the mix [2].

2.3   First comparisons

Figure 2.3 presents a superposition of CTHWA and LDV raw signals obtained, respectively, on IUSTI and CEA shock tubes, for similar conditions, i.e., an air/SF_6 interface, materialized by a 0.5 μm nitrocellulose microfilm, accelerated by a 1.2 shock wave Mach number. Note that, the SF_6 chamber is 250 mm in both
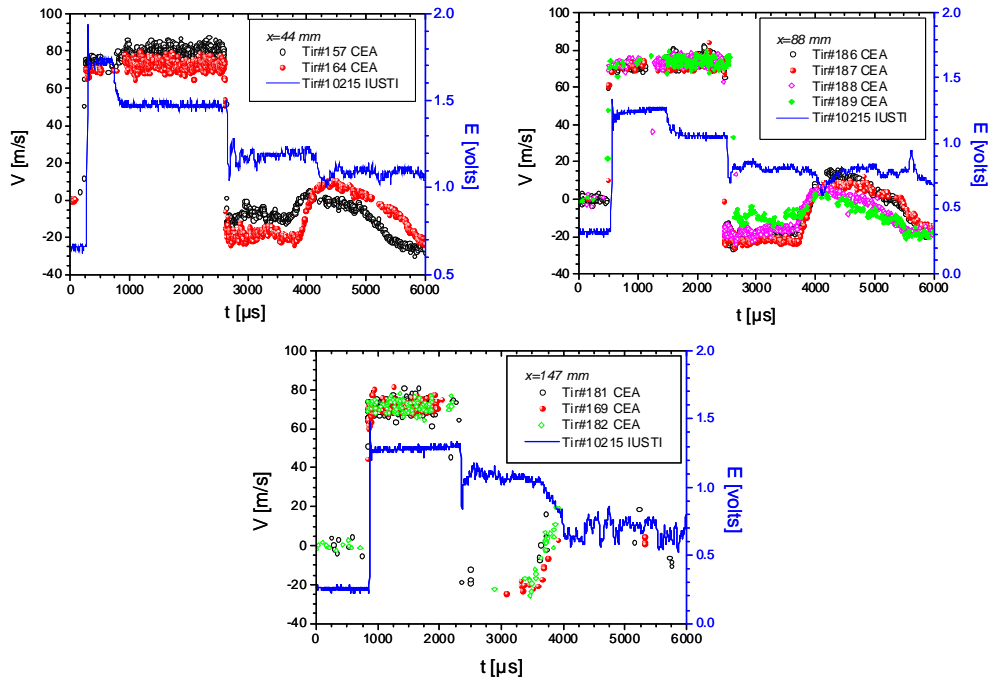

Fig. 2.3. Comparison of CTHWA and LDV raw signals obtained for similar conditions (air/SF_6, M_{is}=1.2).

cases and the shock tube cross sections is 85×85 mm^2 at IUSTI and 130×130 mm^2 at CEA. This comparison has been obtained for three different locations (44 mm, 88 mm and 147 mm) from the initial position of the interface, the last one corresponding, approximatively, to the abscissa of reshock-interface interaction. The mixing zone passes at the two first measurement locations at 70 m/s shortly before the reshock and returns some time after reshock at low velocity. Before reflected shock (at 44 mm, 88 mm), the CTHWA detects the mixing zone as a clear drop of signal, while the LDV indicates its passage by a relative rarity of velocity points. Although the correspondence of passage times of the different singularities of the flow is relatively in good agreement, the mixing zone passage occurs later at IUSTI than CEA, probably reflecting small differences in gas composition and shock wave strength. However, if the CTHWA allows a clear detection of the mix boundaries (before the reshock), with LDV in the first mixing zone passage, a dramatic reduction of the acquisition rate is observed, presumably because of the interception of the laser beams by the membrane fragments, and cannot be reasonably exploited. As we said above, many identical runs are needed at each location to obtain informations on the mixing velocity. In order to still confront two experiments undertaken on different apparatus we have compared the experimental x-t diagrams and mixing zone thickness obtained from schlieren visualization at CEA and from CTHWA signals at IUSTI in Figure 2.4. These two graphs confirms the good agreement of experiments of CEA and IUSTI and allows us to think that the two techniques, although presenting each one advantages and disadvantages, are complementary. We conceptually combine the two diagnostics by using the range of velocities measured with the LDV in one experiment for determining with the inverse method for CTHWA, the evolution of the concentration in the other.
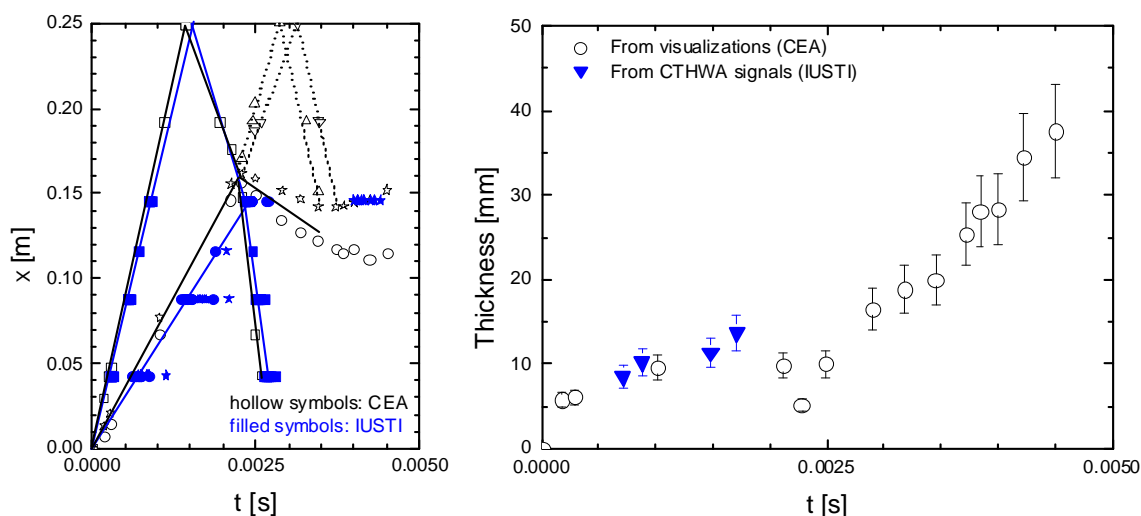
Fig. 2.4. Comparison of x-t diagrams and mixing zone thickness obtained from schlieren visualizations (CEA) and CTHWA signals (IUSTI) for similar conditions (air/SF$_6$, M$_{is}$=1.2).

3 SUMMARY

This work presents two methods for point measurements in mixing zones induced by Richtmyer-Meshkov instability in shock tubes. The constant temperature hot-wire anemometer exploited at IUSTI is an intrusive technique, but allows a clear detection of the mixing zone boundaries. Concentration profiles can be obtained by the inverse method in which concentration is allowed to vary between 0 and 1 and the velocity between set values. For these reasons only qualitative results for velocity can be obtained. However, as pointed out above, the CTHWA method is more useful before reflected shock for volume fraction estimates than the LDV technique in which only few data points could be obtained in the first mixing zone passage, presumably because membrane fragments intercept the laser beams. The Laser Doppler velocimeter developed at CEA can give precise information on velocity providing turbulent kinetic evaluation but remain a very tedious work : several tens identical shock tube shots at each locations are needed for statistical convergence. However, contrary to the CTHWA, LDV is more useful for the measurement of velocity after reshock. Here, preliminary LDV results are compared to hot wire results and show a good agreement with the two techniques. So, we wish to really combine the diagnostics on the same shock tube run by positioning next to each other the hot wire (2.5 mm long and 5 μm in diameter) and the LDV measuring volume (0.2 mm wide and 1-5 mm long). Thus each velocity data point from the LDV will remove this unknown from the CTHWA equation to yield the concentration. This would probably be difficult as the hot wire might be coated by the droplets and often destroyed by the membrane fragments.

REFERENCES

[1] Jourdan G., Schwaederlé L., Houas L., Haas J.F., Aleshin A.N., Sergeev S.V. and Zaytsev S.G., 2001. Hot wire method for measurements of turbulent mixing induced by Richtmyer-Meshkov instability in shock tube. *Shock waves* **11**, 189-197.

[2] Poggi F., Thorembey M.H. and Rodriguez G., 1998. Velocity measurements in turbulent gaseous mixtures induced by Richtmyer-Meshkov instability. *Phys. Fluids* **10, 11**, 2698-2700.

e-mail: ololeg@vniief.ru

On The Possibility Of Hydrodynamic Instability Growth Studies In 2D Flows

Yu.B.BAZAROV[1], S.E. KURATOV[1], D.E. MESHKOV[2], E.E. MESHKOV[1], O.V. OLKHOV[1], S. Yu. SEDOV[1], V.S. SIVOLGIN[2]

[1]Russian Federal Nuclear Center – VNIIEF, pr. Mira, Sarov, Nizhni Novgorod Region, Russia
[2]Sarov Lyceum №15, Sarov, Nizhni Novgorod Region, Russia

Abstract: It is shown that it is possible to study the generation and growth of gravitational and shear instabilities in 2D geometry in experiments with different-volume gas bubbles floating in water.

1 INTRODUCTION

It is important to understand the influence of the scale factor on the character of Rayleigh - Taylor (RT) turbulent mixing development at a gas - liquid interface. Therefore, it is interesting to study interactions between small-scale and large-scale initial perturbations and, in particular, interactions of turbulent mixing with large-scale initial perturbation in experiments.

This problem was studied theoretically in Inogamov et al. works [1]. Theoretical analysis was based on numerical simulations and it confronted significant difficulties, part of which are not related to physical problems, but are attributed to rather limited capabilities of numerical algorithms and computing resources. So, it is necessary to have experimental data on the development of the many-mode perturbations. Unfortunately, for the time being there is lack of such data. Some attempts to study the effect have been made earlier. In particular, in the 1990s, VNIIEF carried out some experimental and theoretical investigations on interactions between large-scale perturbations at gas interfaces and the turbulent mixing zone under ISTC project #29 [2, 3].

Experimental investigations have been further developed by the Hydrodynamic Educational Research Laboratory at the Sarov Physics & Technical Institute (SarFTI) in conjugation with a team of senior students from Sarov lyceum №15 over the last three years [4-7]. In order to study many-mode perturbation harmonics interaction, it was proposed to look at the perturbation development on the cupola of air bubbles floating in water. In this case, the bubble movement has an essentially 2D character, which allows studying the Rayleigh–Taylor instability in two dimensions.

In the first series of experiments, a technique was developed to produce air bubbles of several cubic centimeters in volume in a square-section (10x10-cm) vessel filled with water and to record their floating using an amateur video camera [4]. This technique was used later to study the process of bubble passing through an interface between two immiscible liquids [5].

Further upgrades to the technique in 2004-2005 made it possible to produce as large bubbles as 1 liter in volume and to learn how vortex rings form from large bubbles and how their rise velocity changes at their transformation and collapse [6].

The use of the VS-FAST high-speed video camera with a frequency of 500 frames per second made the experiments more informative and provided better insight into the mechanisms, by which vortex rings form from large bubbles and the process of instability development on the bubble surface at the initial stage of flow. The results of these experiments were used as a test for 2D computations [7].

A characteristic property of the flow emerging around a rising bubble is the unusual behavior of the Rayleigh–Taylor instability on the bubble cupola. Due to stabilization factors attributed to surface tension and shear flow on the bubble surface, the initial perturbations on the upper side of the bubble develop in an unusual manner - they grow and seem to slide down from the bubble, thus forming a stable smooth cupola [6, 7].

Today almost all Rayleigh–Taylor instability experiments are carried out in different geometries: flat, cylindrical or spherical; but flows in these experiments are on average one-dimensional (see, for example, flat case [8], cylindrical – [9], spherical – [10]). Certainly, RT instability and turbulent mixing have a 3D nature, but in all these cases the way the unstable interface moves on average depends on one coordinate.

At the same time the flow around the floating bubble is on average two-dimensional, and so there is a possibility to study the Rayleigh–Taylor instability in 2D.

The mentioned features of instability development with stabilizing factors illustrate the experimental results given below. In addition, the experimental setup developed can be used to look at more complex 2D and 3D instable flows.
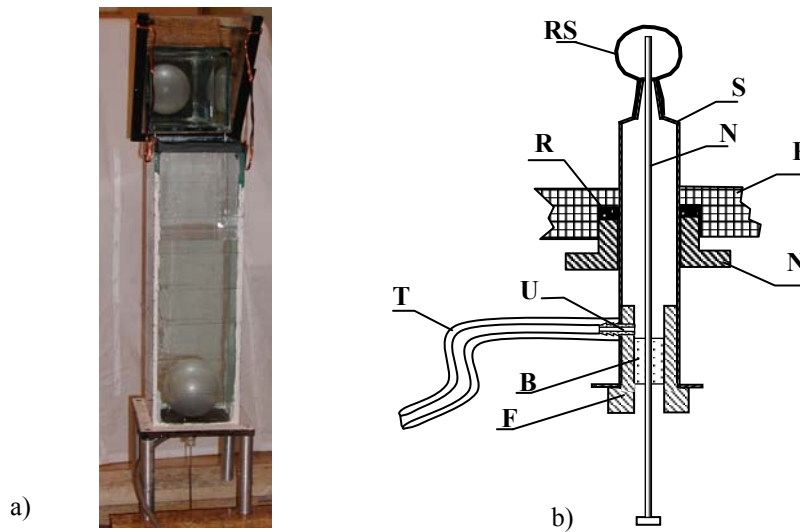
2 EXPERIMENTAL TECHNIQUE

Fig. 2.1. a) General view of the experimental setup, b) diagram of the bubble making unit. **RS**- rubber shell; **S**- syringe case; **Ne** - needle; **T** - rubber tube; **P**- vessel bottom (textolite); **N** - nut ;**R** – sealing rubber; **B** – rubber; **FP** – plexiglas plug; **U** - connection

The experimental setup is a square-section channel with window glass walls (**Fig. 2.1a**). It rests upon a textolite support. There is a bubble making unit at the bottom (**Fig. 2.1b**). Its central part is a syringe case, which is fastened in a plate. There is a small piece of the rubber shell attached to the upper part of the syringe by means of an adhesive tape. A plexiglass plug with a rubber gasket from an eraser is inserted into the bottom part of the syringe. There is a connecting pipe communicating with an automobile pump by means of a hose on the side of the syringe. A needle of necessary length is put into the rubber gasket. The experimental technique is in detail described in Ref. [4].

In the experiment, a rubber balloon of desired size was inflated. Then, the rubber shell was broken with the needle at its pole; shell fragments slid down along the water-air interface and produced an air bubble.

The rising bubble and the flow thus produced were recorded using the VS-FAST high speed camera a frequency of about 500 frames per second.

This method is the development of the technique developed at VNIIEF in the 1970s [12].

3 EXPERIMENTAL RESULTS

Fig. 3.1 shows typical frames obtained in the surface perturbation development experiments with the floating air bubble.

The frames clearly show how short wave-length perturbations emerge on the outer bubble surface as the bubble starts rising. These perturbations result from the surface deformation of the bubble, when the rubber shell slides down its surface. These perturbations keep on growing without changing their mode up to t≈30 ms. But then, beginning with t≈40 ms, one can see the perturbation spectrum to change – instead of many initial perturbations only a few fairly large bubbles begin to predominate. The perturbation mode continues to change, and as a result at t≈100..200 ms we have only the perturbations, the scales of whose wavelengths are comparable to the size of the bubble itself.

In accordance with the classical Rayleigh–Taylor instability theory, the increment of short wavelength perturbations is greater than that of large wavelength ones. At the same time, due to the uncommon flow geometry, one can observe the prevailing growth of those particular low-frequency harmonics. In this case, this is a manifestation of non linear effect of sub-harmonic instability [1]. This kind of instability was studied earlier only in theory using numerical simulations. The experimental layout developed enables gaining experimental data on the perturbation development.

The experimental setup produces a flow, which is somewhat different from 2D, because the channel, in which the bubble floats, has a square section. Replacing this channel is replaced with a cylindrical one will offer a tool for studying perturbations in purely 2D flows.
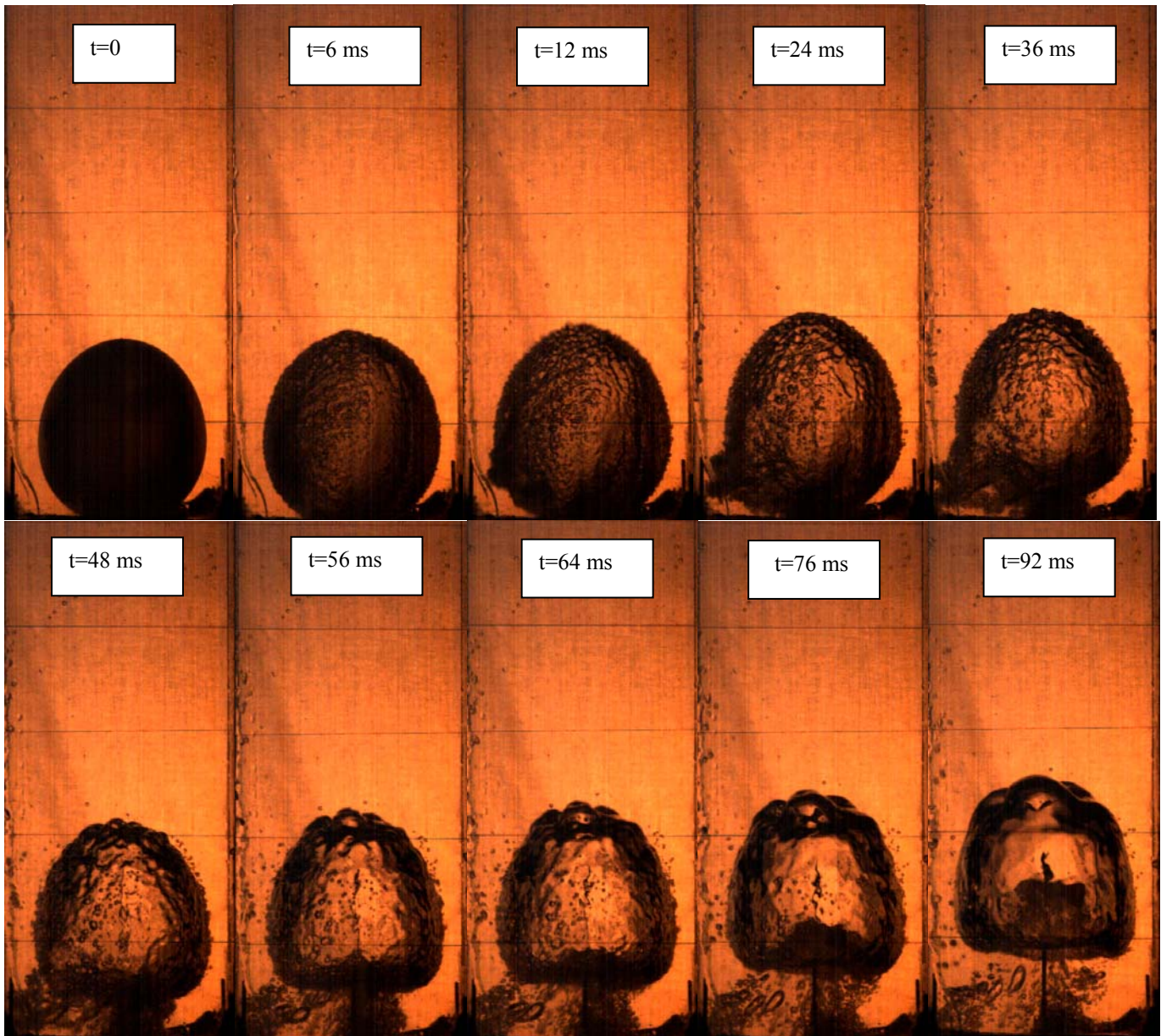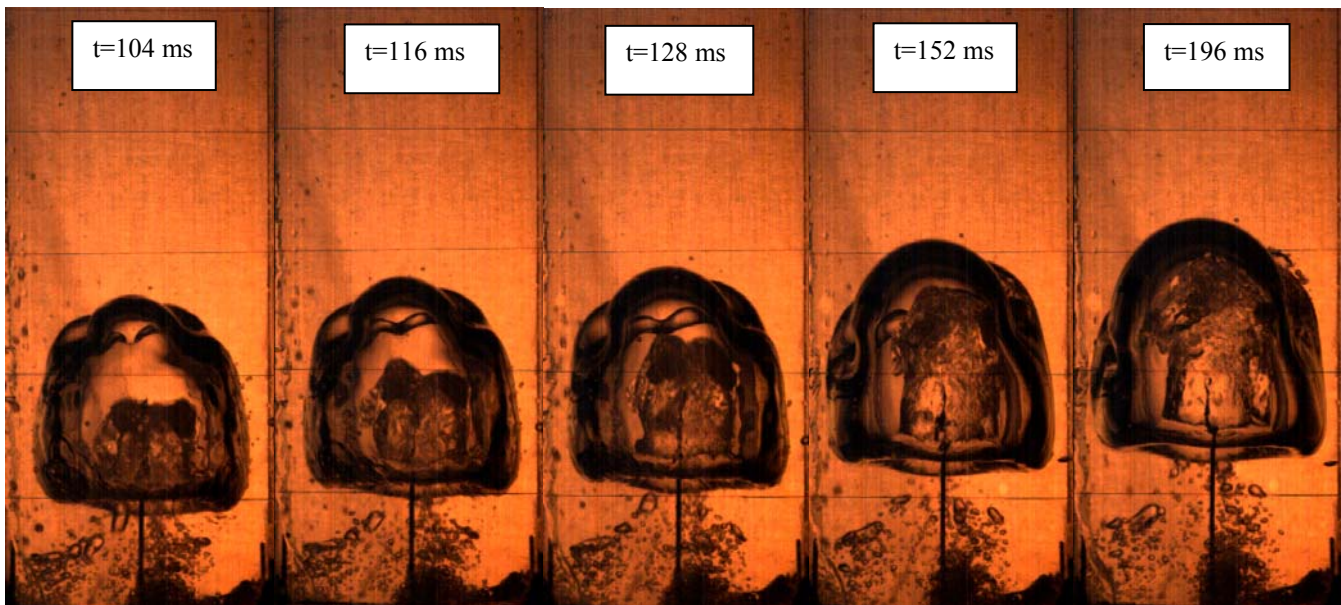
Fig.3.1. Perturbation development on the of the bubble floating in the square channel surface

Continuation of **Fig. 3.1**. Perturbations development on the surface of bubble floating in square channel

4 CONCLUSION

An experimental technique to study the Rayleigh - Taylor instability in a 2D flow produced by a large (~1 l) rising air bubble was developed.

A number of experiments were conducted. Data on local 2D perturbation development was obtained. The experiments also provided data on the mechanism of stabilization of the Rayleigh - Taylor instability on the cupola of the rising bubble.

Thus, the technique developed makes it possible to study the features of Rayleigh - Taylor instability development in a 2D flow.

REFERENCES

[1]. Inogamov N.A., Demyanov A.Yu., Son E.E. 1999. Hydrodynamic of mixing: Moscow, MFTI publ. (*In Russian*)

[2]. Bashurov V.V. Bondarenko Yu.A., Gubkov E.V., Dudin V.I., Poduvalov A.N., Sanin A.A., Stenin A.M., Til'kunov V.A., Tolshmyakov A.I., Trofimova L.Ya., Yanilkin Yu.V. 1996. Experimental investigation of two-dimensional perturbation development accelerated by series of shocks. *Preprint* 45-96 *VNIIEF* (*In Russian*)

[3]. Dudin V.I., Meshkov E.E., Poduvalov A.N., Til'kunov V.A., Tolshmyakov A.I., Holkin S.A., Yanilkin Yu.V. 1996. Investigations into perturbations growth and turbulent mixing on the gas-gas interface by laser knife method. *Preprint* 49-96 VNIIEF (*In Russian*)

[4]. Sivolgin V.S., Meshkov D.E. 2004. Development of the technique of carrying out of large-scale underwater experiment on small experimental setup. *Vestnik Sarovskogo PhizTeha.* **7**, *pp.* 46-50 *(in Russian)*

[5]. Marmyshev V.V., Meshkov D.E., Meshkov E.E., Ognev E.L., Sivolgin V.S., Shapovalov Ya.S. 2005. Transition of gas bubble through the interface between insoluble liquids. *Vestnik Sarovskogo PhizTeha.* **9**, pp. *21-25 (in Russian)*

[6]. Meshkov D.E., Meshkov E.E., Sivolgin V.S. 2005. Research of the character of flow depending on volume of floating air bubble. *Vestnik Sarovskogo PhizTeha.* **8**, pp. *68-73 (in Russian)*

[7]. Bazarov Yu.B., Meshkov D.E., Meshkov E.E., Sedov S.Yu., Sivolgin V.S. 2006. Vestnik Sarovskogo PhizTeha. **10**, *, to be published (in Russian)*

[8]. Bliznetsov M.V., Meshkov E.E., Nevmerzhitskij N.V., Nizovtsev P.N., Sen'kovskyi E.D., Sotskov E.A., Tochilina L.V. 1999. On possibility of modeling some aspects of Rayleigh - Taylor instability in solids. *VANT, ser. TPF.* **3**, p.4-57 (in Russian)

[9]. Kamchibekov M.D., Meshkov E.E., Nevmerzhitskij N.V., Sotskov E.A. 1996. Turbulent mixing on the cylindrical gas-liquid interface. *Preprint* 46-96 VNIIEF (*In Russian*)

[10]. Meshkov E. E., Nevmerzhitsky N. V., Zmushko V. V. 1997. On Possibilities of Investigating Hydrodynamic Instabilities and Turbulent Mixing Development in Spherical Geometry. *The Proc. of the 6th IWPCTM*. Marseille, France. Editors L.Houas & G.Jourdan, P.343.

[11]. Meshkov E.E. 2006. Investigations of hydrodynamic instabilities in laboratory experiments. Sarov, 138 (In Russian)

[12]. I.G. Zhidov, E.E.Meshkov, V.V.Popov, V.G.Rogachov, A.I.Tolshmyakov. 1977. Vortex ring generation in large air bubble rise up process in water. *PMTF*, **3**, p.75-78, *(in Russian)*.

E-mail: meshkov@sarfti.ru

Self-Organizing of Fibre-Like Structures in Turbulent Gas and Dust Cloud

Yu.B.Bazarov[1], A.E.Levushov[1,2], E.E.Meshkov[1,2], A.A.Polovnikov[1]

[1]Russian Federal Nuclear Center –Institute of Experimental Physics (VNIIEF),

[2]Sarov Physical and Technical Institute (SarFTI)

Abstract: The phenomenon of self-organizing of a fibre-like structures in a gas and dust turbulent mixing zone in experiments on a shock tube was observed. The zone of mixing is formed on the surface of a layer of the dust media, accelerated by pressure of products of a detonation of a mix of acetylene with oxygen in the closed channel of a shock tube of square cross section.

1 INTRODUCTION

1 Since the end 1990-s in VNIIEF and from the beginning of XXI century in educational-research hydrodynamic laboratory in SarFTI the works connected to application of hydrodynamic instabilities and turbulent mixing researches results for the decision of some practical problems in which instability play a positive role are carried out [1]. One of directions of these works are researches of opportunities of restriction of action of explosion by means of layers of the friable media. During these researches in experiments on a shock tube the phenomenon of self-organizing of fibre-like structures in turbulent gas and dust cloud was observed.

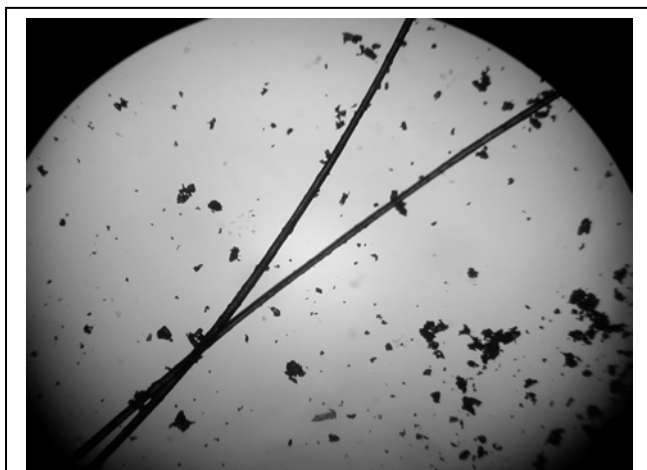Results of these experiments are submitted below.

Fig. 1. A microphoto of particles of a dust. For scale in a photo two hair ~60 microns in diameter are presented.

2. Experiments were carried out on the shock tube that similar shock tube described in [2]. The shock tube has been executed from plexiglas and had square cross section 4x4 sm^2. In the beginning and in the end the shock tube has been limited by rigid walls. The tube placed vertically. The dust layer on thin (~1 microns) mylar film separated a shock tube on two compartments: lower - *the chamber* (2 cm), and top - *the channel* (10 cm). On fig.1 the microphoto of particles of a dust is presented. In the channel there was air at atmospheric pressure. The chamber was filled by a stoichiometric mixture of acetylene with oxygen by gating through it of mix volume in ~ 10 times exceeding volume of the chamber. The detonation of a mixture was initiated synchronously in 5x5 = 25 points equally spaced for the wall area, limiting the chamber from below. In each point the mix was initiated by electric explosion of the wire bridge. Duration of a high-voltage electric pulse made a few microseconds.

The flow in a shock tube was registered in passing through light by means of high-speed camera SFR and digital videocamera SENSYCAM in a mode of one high resolution frame.

3. Fig. 2 and 3 a sequences of camera SFR images showing the development of fibre-like structures in two experiments on a shock tube are presented.

Development of flow in a shock tube can be divide conditionally into three stages:

a)Acceleration of a dust layer by pressure of detonation products of a mix (by estimation [3] initial equilibrium pressure ~ 1,7 МПа, temperature 4000°С, products of a detonation shine brightly enough for high speed photography of flow without additional light sources [4]);

| t = 0,1 ms | 0,3 ms | 0,51 ms | 0,71 ms | 0,91 ms | 1,12 ms |
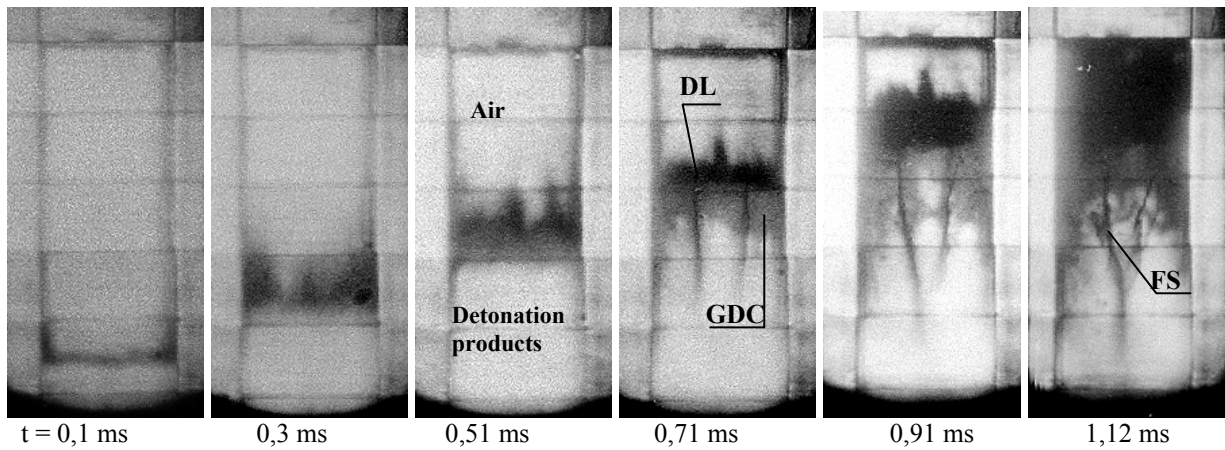
Fig. 2. Formation of fibre-like structures in gas and dust cloud (experiment № 04-03-04/4). The DL-layer of a dust (dark area), on its top edge Raileigh--Taylor instability develops; GDC-transparent gas and dust cloud; FS-fibre-like structures.

| 0,16 ms | 0,49 ms | 0,82 ms | 1,15 ms | 1,48 ms | 1.81 ms |

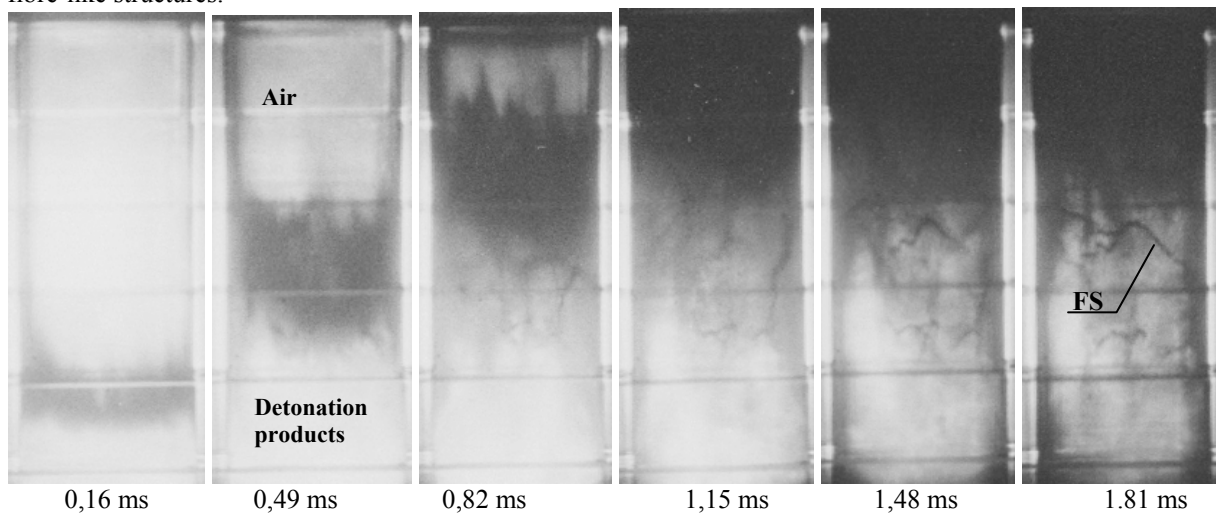**Fig. 3.** Formation fibre-like structures in gas and dust cloud (experiment 28-10-04/1).
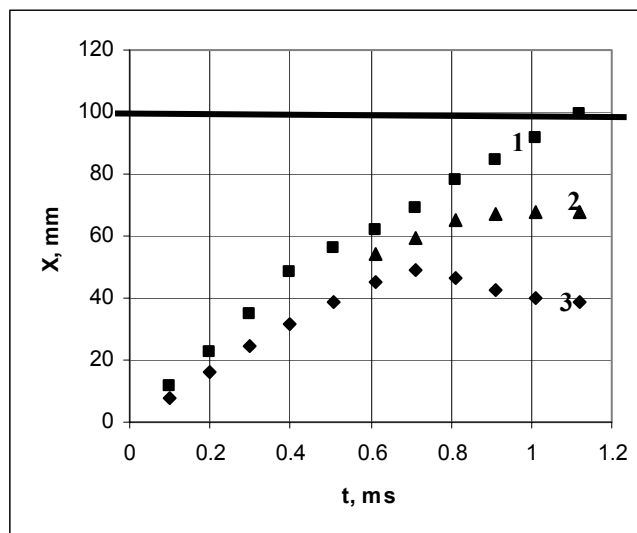

Fig. 4. *X-t* the diagram of flow in experiment of 04-03-04/4. 1-top boundary of a layer of a dust (average position); 2-bottom boundary of a layer of a dust (dark area); 3-bottom boundary gas and dust clouds.

b)Deceleration a layer under action of increasing pressure of compressed air;

c)Formation of gas and dust cloud with formation of fibre-like structures. Thus the second and third stages in time are imposed one on another.

The stage of acceleration is rather short-term. The layer is accelerated till the velocity about 100 m/s and then its velocity constantly falls (fig. 4). During layer deceleration a Raileigh--Taylor instability develops on the top edge of a layer. During flight of a layer pressure of detonation products falls, and air pressure in the channel increases and at the certain stage air pressure becomes higher than pressure of detonation products. Thus intensive leakage of air through a flying layer begins, carrying of particles of a dust by a stream of air should begin and as a result formation and growing gas and dust cloud. In this cloud fibre-like structures are formed.

Whereas the gasdynamic the nature of mechanisms of formation gas and dust cloud does not cause doubts (air filters through a layer of a dust and carries away behind itself of a particle of a dust) the nature of formation fibre-like structures is represented mysterious and can be hardly explained only by gasdynamic mechanisms

In experiment № 04-03-04/4 (fig. 2, 4) in the beginning two jet-like formations are formed in a field gas and dust cloud. It is not jets (in the true sense of the word) for two reason: a) the gas jet in another gas inevitably spreads, forming a torch (the running jet) and b) the gas jet is hardly capable to be bent. Fiber structures are formed on the basis of the specified pseudo-jets. In time these structures are shown more clear, getting more precise outlines and then are gradually washed away, and on their background there is a number of the new, finer fibres oriented in a cross-section direction.

In experiment № 28-10-04/1 (fig. 3) is observed a little bit other picture - here fibre-like structures are formed more likely in a horizontal direction.

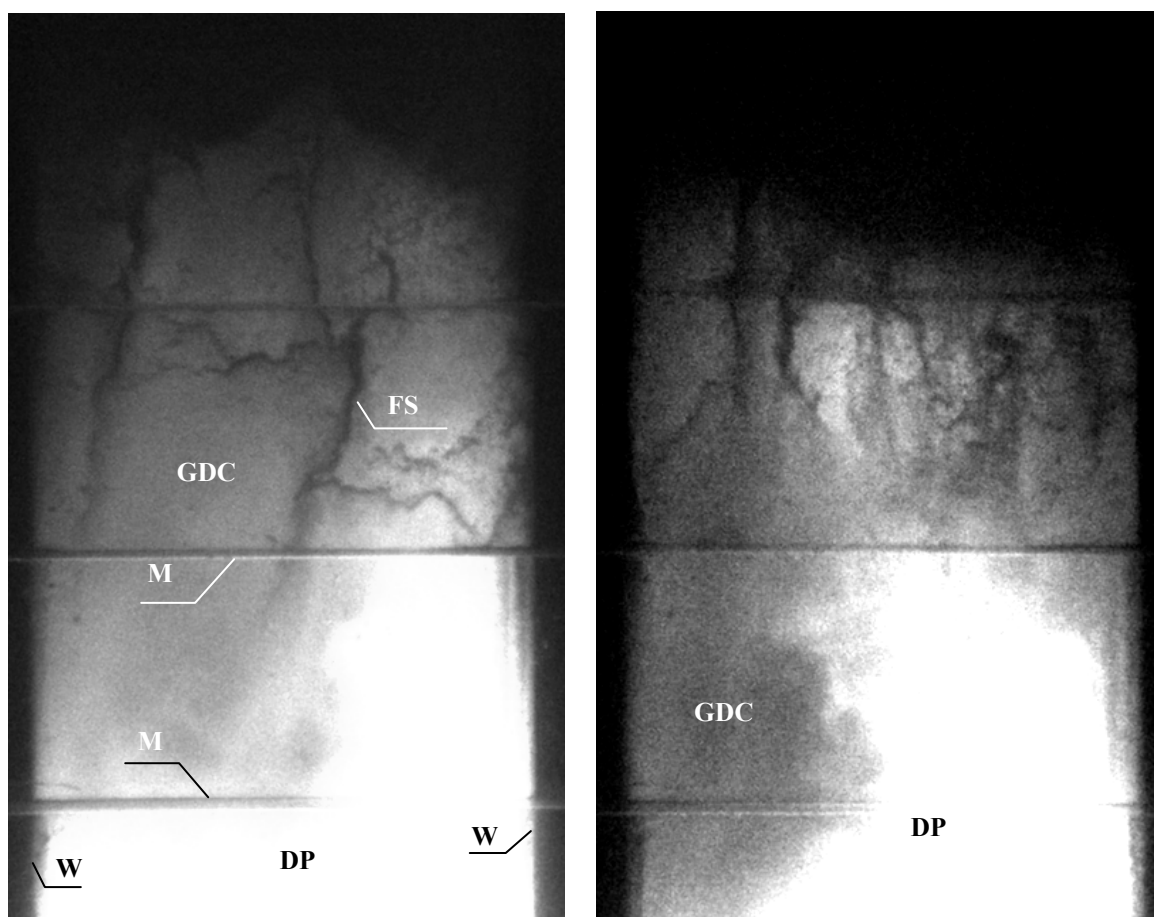**Fig. 5.** Instant photos of flow in the channel of a shock tube in passing light. GDC - gas and dust cloud; DP- detonation products of a acetylene with oxygen mix; C - wall of the channel of a shock tube; M-mark lines; FS- fibre-like structures.

Clear images of the fibre-like structures gives instant photos (fig. 5) of flow at the moment of time t = 1000 μs after initiation of a gas mixture detonation in the chamber of the shock tube. These photos was made by camera SENSYCAM. Here fibre-like structures are presented oriented both along the channel and in cross-section and other directions. It is possible to estimate characteristic diameter of "fibres" on this photo (0,5÷0,2 mm), basing on known distance between mark lines (20 mm).

Similar structures (*filament turbulence*) are formed from fine bubbles in vortical flows in water [5].

It is possible, that dielectric dust particles can be electrified during acceleration and decceleration of dust layer in a shock tube, to be grouped in vortical strings turbulent gas and dust cloud and then to be united under action of electrostatic forces just as there are " Lichtenberg figures" form on the charged surface of dielectric when depositing powder on it [6].

On the other hand, similar fibre-like structures structures are observed at a birth of stars from diffused media of gas and dust clouds [7], though this similarity can be only external. S.Boldyrev (the Chicago University branches of astronomy and astrophysics member) in the message by an e-mail also are marked with external similarity observable on fig. 5 fibre-like structures with the similar structures formed in turbulent interstellar molecular clouds.

The "observable" fibres formed in turbulent gas and dust cloud have fractal structure, it is possible to note also formation of the clusters having fractal structure, from particles of free carbon behind front of a detonation of the condensed explosives [8].

Many respondents as in Russia, and abroad have been acquainted (orally and by e-mail) with a photo presented on fig.5. All of them authors express the gratitude for useful discussions.

7 References

1. E.Meshkov On new possible directions of hydrodynamic instabilities and turbulent mixing investigations for the solution some practical problems. *Abstracts of the papers of the 9ᵗʰ IWPCTM, Cambridge, UK, 19-23 July 2004, p.74.*

2. M.Bliznetsov, I.Zhidov, E.Meshkov, N.Nevmerzhitskii, E.Sen`kovskii, E.Sotskov. Development of the Rayleigh-Taylor Instability at the Boundary of a Friable Medium Layer Acclerated by a Compressed Air Flow. *Technical Physics Letters. Vol.28, N1, 2002, pp.80-81*

3. Yu.A.Vlasov, S.I.Gerasimov, E.V.Gubkov, V.I.Dudin, V.P.Copushev, E.E.Meshkov, A.A.Nikulin, V.P.Ryabov, V.A.Til`kunov. Shock tube with explosive gas driver. // VNIIEF Preprint 47-96, 1996

4. V.I.Kozlov, A.E.Levushov, E.E.Meshkov. //The Proc. of the V Khariton Readings ed. By Dr.Mikhailov, Sarov, 2003, pp.410-414 (in Russian).

5. http://milou.msc.cornell.edu/cavitation.html (Filaments in Turbulence)

6. Jearl Walker.// Scientific American, Vol.258, No.4, 1988.

7. A.V. Kolesnichenko, M.Ya.Marov, Turbulence of Multicomponent Media. // MAIK, Nauka, M, 1999г, (in Russian).

8. A.P.Ershov, A.L.Kupershtrokh.. //Abstracts of III Int. Conf. «Lavrent`ev Readings», Novosibirsk, 1990, p.100, (in Russian).

E-mail: meshkov@sarfti.ru

Research of the Character of Flow Depending on Volume of Floating Air Bubble

E.E.Meshkov[1, 2], D.E.Meshkov[3], V.S.Sivolgin[3]

[1]Russian Federal Nuclear Center –Institute of Experimental Physics (VNIIEF)

[2]Sarov State Physical and Technical Institute (SarFTI)

[3]Lyceum 15, Sarov

Abstract: The technique is developed and research of change of character of flow was carried out at rising an air bubble in the vertical pipe of square section filled with water, depending on volume of a bubble.

Possible connection of change of observable in experiments bubble rise speed during its transformation in a vortical ring with growth rate of single perturbation a gas - liquid interface at RT-mixing is discussed.

1 INTRODUCTION

1. In 2003 year a group of students of Sarov lyceum №15 on the basis of educational-research hydrodynamic laboratory in Sarov Physics & Technical Institute (SarFTI) had started development of a technique to perform large-scale underwater experiment [1] with the purpose of checking the hypothesis about the influence of scale factor on character of development of a Rayleigh - Taylor (RT) mixing at a gas - liquid interface [2]. At the first stage on the basis of laboratory model the technique of getting small air bubbles of specified volume rising in a pipe of square section with transparent walls has been developed.

After completion of this technique the opportunity of getting of air bubbles with volume up to 1 litres and more was realized. In experiments [1] bubbles with volume up to 2.5 cm^3 turned out, during rise bubbles got jellyfish form. It is known, that with increase in volume of a bubble, from some volume the bubble gets the shape of a vortical ring [3]. The experiments resulted below show, that at rise of such bubbles in a pipe of square section, there are essential changes in character of flow. Similar features can influence the character of flow in pipelines with liquids and gas inclusions in it.

2. In fig.1,a the photo of experimental setup is presented. It is square section pipe made by window glass installed on a textolite plate.

In fig. 1,b the scheme of the experimental device for producing air bubbles of the volume more than 1 litres is presented. The case of syringe S is fixed in textolite plate P, which is the bottom of a vessel. Between the plate and the syringe is the rubber R which at twisting a nut N fixes the syringe and seals a backlash. On the top part of the syringe there is a small piece of rubber RS fixed by an adhesive tape. The plug made by plexiglas FP is inserted into the bottom part of the syringe in which elastic band B made from eraser which seals hole is inserted. A connection U which joins the rubber tube T connected to the automobile pump is attached to the case of the syringe. The needle Ne of necessary length is inserted into elastic band B.

During the experiment (fig. 2) a balloon of rubber of the necessary volume was inflated. Further a rubber shell was broken by a needle at its pole; thus the remains of the shell are reduced in length and slide off along water-air interface, forming a bubble.

Registration of the process of bubble rising in water was carried out by a video camera SONY DCR-TRV25E. Experimental registration of flow was conducted not only in horizontal direction through a wall of a vessel, but also simultaneously in vertical direction through a mirror, attached above vessel (fig. 1, a).

3. In the first series of experiments the vessel with the channel section 10x10 cm^2 was used. A series of experiments was carried out in which the volume of bubbles varied from 0.05 to 1.2 litres.

Fig. 1. a) General view of the experimental setup, b) the scheme of the device for making bubbles. **RS**- the rubber shell; **S**- case of a syringe; **Ne** - the needle; **T** - rubber tube; **P**-the bottom of a vessel (textolite); **N**-the nut ; **R** – sealing rubber; **B** – the rubber; **FP** – plug of plexiglas; **U** - connection
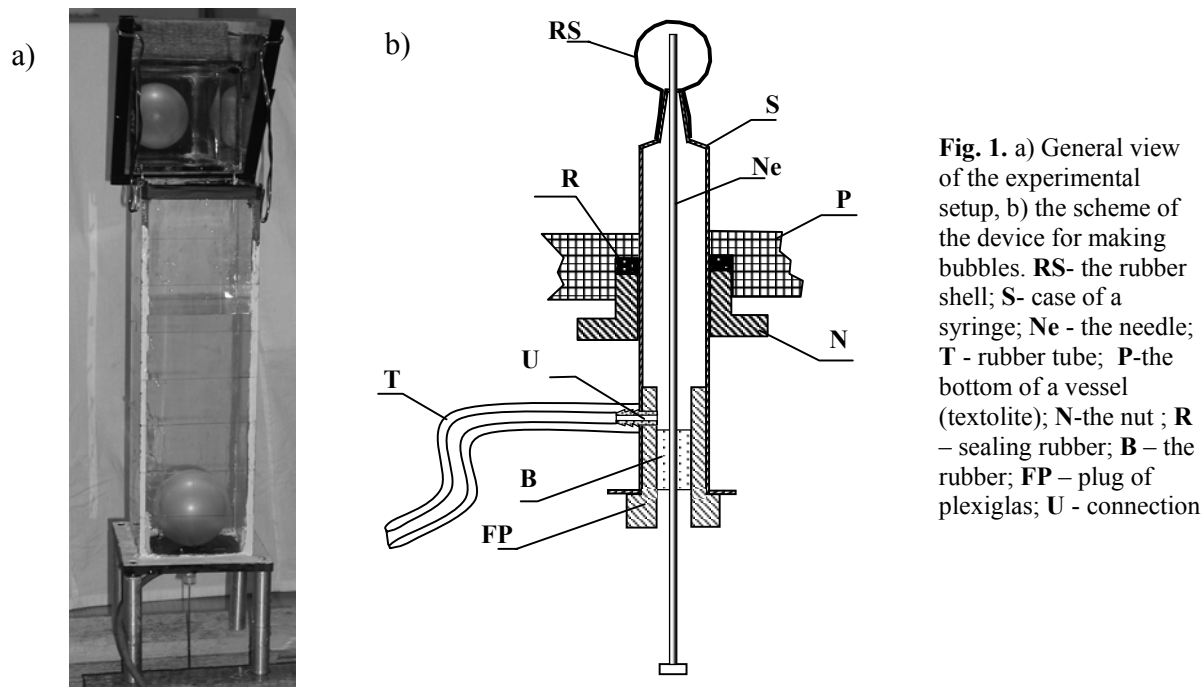
Fig. 2. Conduct of experiment
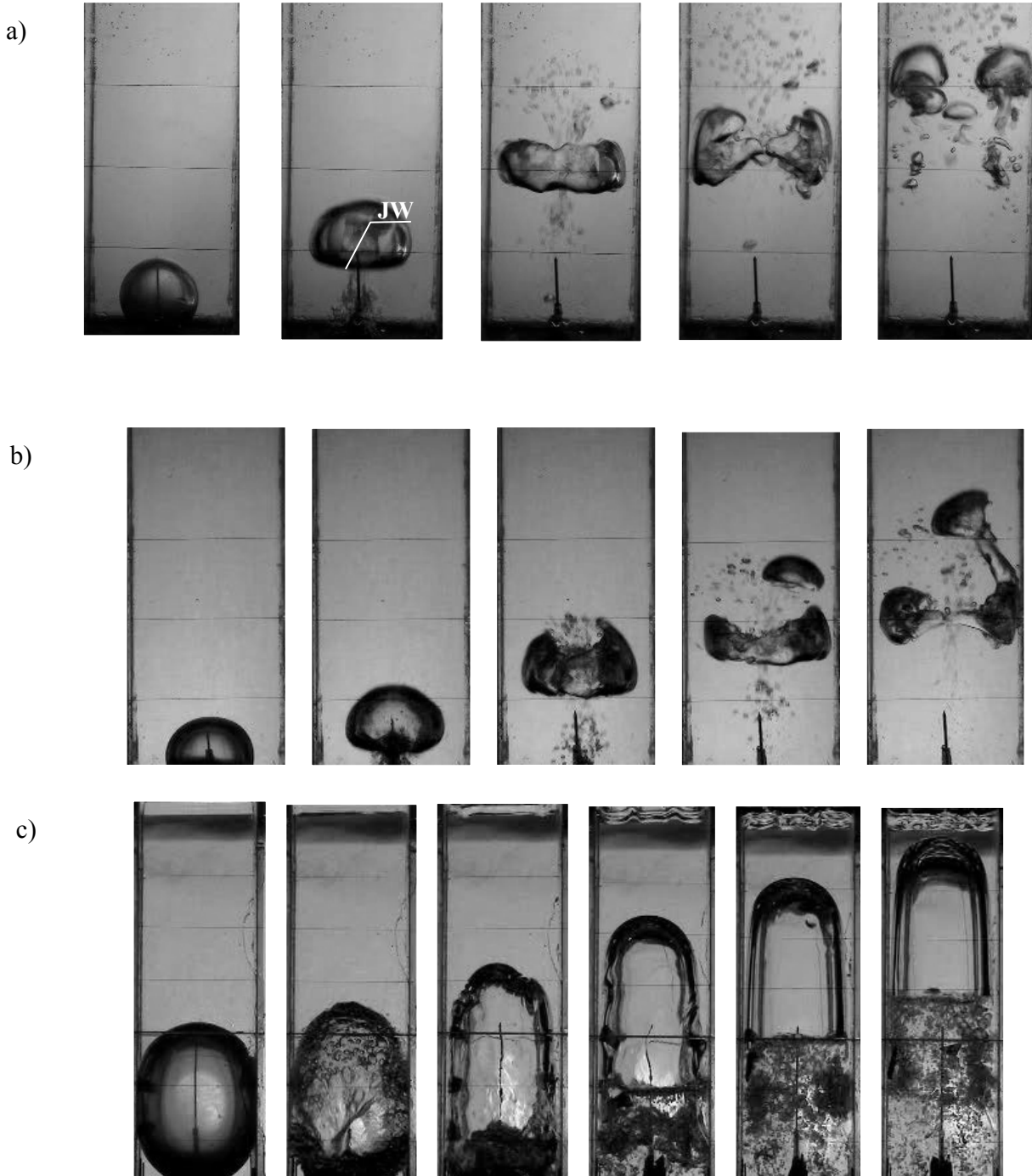
Fig.3. Change of character of flow depending on volume of a bubble. At small volumes ~0.05 litres (a) the bubble rises with the subsequent formation of it the vortical ring. The ring gradually extends and then collapses. At the same volume of a bubble we can observe a completely different picture (b). Here at formation of a ring in the top part of a bubble separates a little bubble looks like a mushroom hat which then again incorporates to a ring from which it separated. At volume ~1.2 litres (c)) the top part of a bubble is gradually leveled, forming a smooth dome. Formation of a ring in this case does not occur.
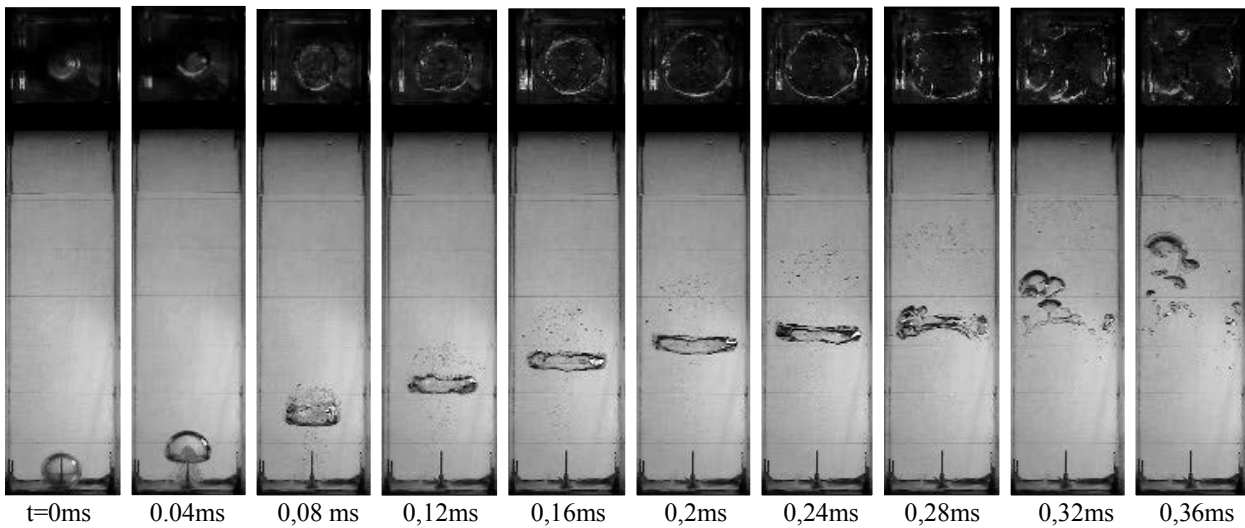
Fig.4. Frames of rise and transformation of a bubble (V ≈ 0.03 litres) (exp.205). In the initial stage of rise the bubble is transformed into a vortical ring. This process is observed both in horizontal projection, and in a projection along the vertical axis (through a mirror).
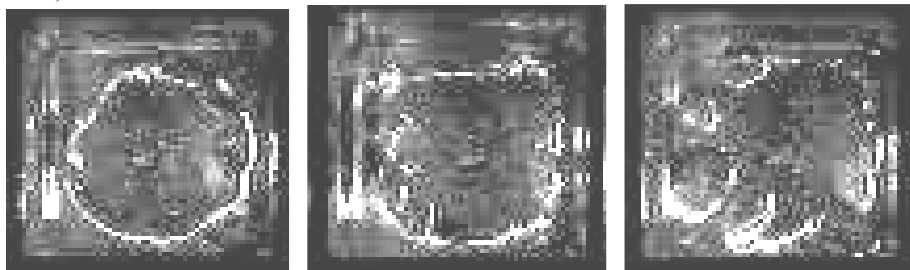
Fig.5. Process of destruction of a vortical ring (exp.205) (at registration on vertical axis through a mirror) for the moments of time t=0.24; 0.28 and 0.32 s, accordingly.
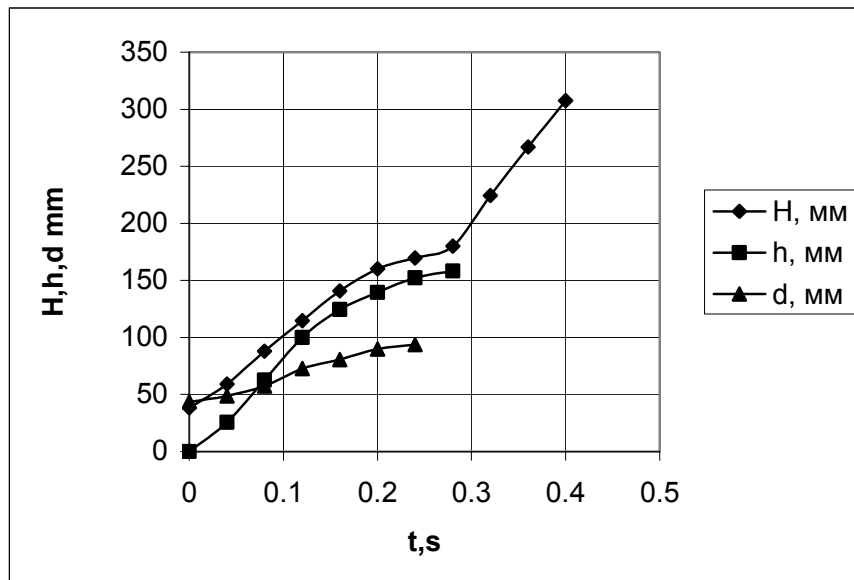
Fig.6. The *X-t* diagram of rise and transformation of a bubble (*V* = 0.03 litres) (exp.205).

Remember that in paper [1] research of the character of rise in water of a bubble up to 2.5 cm^3 volume have been carried out. In process of rise, the bubbles of such volumes got into jellyfish shape, without collapsing. Also it rose at constant speed.

With volume increase of a bubble the picture of rise sharply changes. It can be observed in fig. 3 where typical experiments from the first series are presented. The rising bubble with volume ~0.05 litres is very quickly transformed into a vortical ring (fig. 3, a). The vortical ring is formed after the jet of water (JW) - the jet of water penetrating a bubble from below upwards, breaks through the top surface of the bubble. Apparently, the jet of water is a cumulative jet which is formed owing to cylindrical stream of the water which are flowing round a rising bubble converging under a bubble.

An unusual picture is observed in the second experiment (fig. 3, b). Here at formation of a ring in the top part of a bubble a smaller bubble separates that looks like a mushroom hat which then again incorporates in to the ring from which it separated.

In experiment with a bubble with volume ~ 1.2 litres which besides has the ellipse shape, extended along a vertical, there is completely different flow pattern (fig. 3, c). Here the jet of water though starts to be formed, but does not catch up with the top border of a bubble. And the vortical ring in this case is not formed. An obstacle for development of the jet of water in this case most likely are two reasons: a) disturbance of cylindrical symmetry of converging flow under a bubble; during the initial moments of time water flows downwards only in four angular passes formed by walls of the vessel and the surface of a bubble, and b) the form of a bubble extended on a vertical. Initial perturbation of the surface of the bubble, caused by movement of the fragments of a rubber balloon, are smoothed out and, as a result, ideally smooth bubble with practically flat form of the bottom is formed. It is necessary to note especially the effect of suppression of RT-instability on the dome of a bubble during the initial moments of rise of a bubble. Initial perturbation of the surface at top of a bubble start to develop, but with rise of a bubble they "are gradually rolled" downwards, forming a smooth dome. The effect of stabilization of RT-instability in this case, apparently, is determined by action of a surface tension and shift flow of water on the surface of a bubble.

In the second series of experiments the experimental setup was modified and the cross-section of the vessel was increased to 11x11cm^2. Besides, registration of flow was conducted not only in horizontal direction through a wall of a vessel, but also simultaneously in vertical direction through a mirror, attached above the vessel (fig. 1, a)

In fig. 4 the visual record of rise and transformation of a bubble (V≈0.03 litres) is shown. In the initial stage of rise the bubble is transformed into a vortical ring. This process is observed both in horizontal projection, and in a projection along vertical axis (through a mirror).

During rise the ring extends and, finally, rests against the walls of the vessel. Thus the ring tends to take the square shape of the channel of the vessel and therefore collapses into separate bubbles of different volumes. This process can be well observed in fig. 5 where results of registration of a ring in vertical projection through a mirror are presented larger scale. It is interesting to note, that from the area of a ring in the top right corner of the image, on a having the square shape of walls of a vessel, the air flows over to the areas of the ring, still keeping the circular shape, the largest bubbles are here again formed.

In *the X-t* diagram (fig. 6) the dependences of height of top border *H*, the bottom border *h* and the cross-section volume *d* of bubble (and then the rings) on time *t* are presented.

Speed of the rising bubble constantly varies. In the initial stage the speed of the rising ring is ~0,68 m/s, after formation of the ring it gradually falls down to ~0.25 m/s, and then, after it's destruction, speed of rise again sharply grows up to ~1,06 m/s.

Results of the experiments described above represent first of all interest from the point of view of understanding of processes of flow of a liquid with gas inclusions on pipelines; and, in particular, influences of the shape of pipe cross-section on these processes.

At the same time the observable transformations of the rising bubbles, change of speed of rise of a bubble and then a vortical ring and influence on these processes of walls of a vessel can relate to development of a turbulent mixing zone on a gas-liquid interface. Earlier change of the form of a bubble of single perturbation on RT-unstable a gas-jelly interface and the tendency of its transformation into a vortical ring both in experiments [4], and in calculations [5] was already observed. In calculations [6] and experiments [7] the problem of joint development and interaction of single perturbation and a turbulent mixing zone on RT-unstable interface with Atwood number ~1 is investigated. In these calculations and experiments essential excess of growth rate of single perturbation is received in comparison with a turbulent mixing zone. On the basis of these results it is supposed, that single perturbation under some conditions can not be absorbed by a

turbulent mixing zone at unlimited space and time scales of flow. At the same time it is necessary to note, that in calculations [6] and experiments [7] the process of formation of a vortical ring in process of a bubble of single perturbation has not been completed.

We could see from above mentioned experiments that with formation of a vortical ring the speed of its rise decreases by ~2.7 times. Therefore there is a question: whether growth rate of single perturbation after formation of a vortical ring will decrease accordingly. In this case the assumption of possible unlimited growth of single perturbation [6] will need more proofs.

In summary authors express gratitude to V.A.Zhmajlo and V.S.Statsenko's for useful discussions.

7 References

1. V.S. Sivolgin, D.E.Meshkov. Development of the technique of carrying out of large-scale underwater experiment on small experimental setup. //Vestnik Sarovskogo FizTekha. №7, 2004, pp. 46-50 (in Russian)

2. E.E.Meshkov, N.V.Nevmerzhitskij, V.G.Rogachov, Yu.V.Yanilkin. Potential role of scaling factor in turbulent mixing problem. //Proc. of Int. Conf. "V Khariton's Topical Scientific Readings", Sarov, Russia. Editor A.L.Mikhailov, 2003, pp. 415-418 (in Russian).

3. I.G. Zhidov, E.E.Meshkov, V.V.Popov, V.G.Rogachov, A.I.Tolshmyakov. Vortex ring generation in large air bubble rise up process in water.// PMTF, №3, pp.75-78, 1977 (in Russian).

4. E.E Meshkov, N.V,Nevmerzhitsky V.A.Pavlovskii, V.G.Rogatchev, and I.G.Zhidov Jelly Technigue Applications in Evolution Study of Hydrodynamic Instabilities on Unstable Plane and Gylindrical Surfaces. // Proc. of the 5th IWPCTM. University at Stony Brook, New York, USA. Editors R.Young, J.Glimm & B.Boston, 1995, pp.243-250.

5. V.N.Motlokhov, V.A.Pavlovskii, V.V.Rasskazova, V.G.Rogatcvev, A.N.Shaporenko. Numerical Simulation of the Perturbation Growth on Unstable Plane and Cylindrical Interfaces. // Proc. of the 5th IWPCTM. University at Stony Brook, New York, USA. Editors R.Young, J.Glimm & B.Boston, 1995, pp.367-371.

6. V.A.Raevskyj, S.N.Sinitsina, Yu.V.Yanilkin. Numerical simulation of influence of turbulent mixing zone on local perturbation growth under Rayleigh-Taylor instability conditions. //Proc. of Int. Conf. "V Khariton's Topical Scientific Readings", Sarov, March, 17-21, 2003. Editor A.L.Mikhailov, pp. 366-372. (in Russian).

7. V.A.Sotskov, N.V.Nevmerzhitskij, E.E.Meshkov, M.V.Bliznetsov, A.O.Drenov, E.D.Senkovskij. Investigation single perturbation development and its interaction with turbulent mixing zone on a gas-jelly interface. Proc. of Int. Conf. "V Khariton's Topical Scientific Readings", Sarov, Russia. Editor A.L.Mikhailov, 2003, pp. 362-366 (in Russian).

E-mail: meshkov@sarfti.ru

First Mix Experiments on the Cylindrical Acetylene Shock Tube

Yu.V.Alekhanov[2], A.E.Levushov[1, 2], A.I.Logvinov[1, 2], S.A.Lomtev[2], E.E.Meshkov[1, 2], A.A.Polovnikov[1], E.A.Polovnikov[1]

[1]Russian Federal Nuclear Center –Institute of Experimental Physics (VNIIEF),

[2]Sarov Physical and Technical Institute (SarFTI)

Abstract: The technique of research of development of a turbulent mixing on gas - gas interface in cylindrical geometry by means of the cylindrical acetylene shock tube is developed. This shock tube was constructed in accordance with the outline: *an exploded wire on a symmetry axis - a cylindrical volume of a mixture of acetylene with oxygen (confined by thin film (~1μ)) - a cylindrical layer of air - a cylindrical rigid wall*. A preliminary series of experiments which results confirms operability of this technique was carried out. The first results of measurements of a turbulent mixing zone on interface: *mixture detonation products - air* in cylindrical geometry are presented.

1 INTRODUCTION

1. Experiments on research of the instability induced by a shock wave and of the accompanying turbulent mixing carried out in VNIIEF on an air driver shock tube [1,2], have initiated a lot of similar researches. A steady and universal interest in similar experiments is due to the fact that their results are widely used for verification of theoretical models of turbulent mixing development, and, on the other hand, to their self-descriptiveness, simplicity and availability. Later a technique has been developed for research of a turbulent mixing on a cylindrical interface between gases of different density, accelerated by a converging shock wave [3-6]; in these experiments the converging shock wave was created by electric explosion of a row wires. The development of modifications of shock tubes and similar devices for research of the instability developing in cylindrical and spherical geometries is also described in papers [7-12].

In VNIIEF, since the middle of the 1990s of the last century, they have been developing a technique of a shock tube with a driver of a shock wave as a mix of acetylene and oxygen [13-16]. In these works, experiments were carried out in a shock tube with a channel of a constant section in geometry: *rigid wall 1 - (thin) layer of a gas mix - air - rigid wall 2*. Detonation is initiated synchronously in many points regularly located on rigid wall 1. The initial density of air *(ρ_0=1,2g/l)* is approximately equal to the initial density of the mix *(ρ_0=1,35g/l)*, and during the expansion the density of the detonation products falls ~10 times, while the interface of the detonation products moves with deceleration. As a result, at the initial stage of the flow, the interface between these gases is stable by Rayleigh-Taylor (the acceleration is directed from the heavier gas to the lighter one) and the development of a turbulent mixing zone on the interface begins only after is impacted by the shock wave reflected from rigid wall 2. By then, the film that separated gases, has been completely destructed by the high temperature of the detonation products.

At the same time it is necessary to note, that [13] the possibility has already mentioned to use the given scheme not only in flat, but also in cylindrical and spherical geometry. In this case, the role of rigid wall 1 in a cylindrical configuration is played by an axis of symmetry and, in a spherical configuration, the center of symmetry.

Work [16] describes results of the experiments which demonstrated the opportunity to initiate a divergent cylindrical detonation wave in a gas mix by electric explosion of a long thin wire. This circumstance has been used for development of a cylindrical shock tube which is based on the following simple scheme: *electrically exploded wire along the tube axis - a cylindrical volume of a mix of acetylene and oxygen (limited by a thin (~1μ) film) - a cylindrical layer of air – a cylindrical case (a rigid wall).*

2. The scheme of a cylindrical shock tube with a driver of a shock wave as detonation products of acetylene and oxygen mixture is shown on fig. 1. A general view of the experimental installation and data-acquisition equipment is shown on a photo on fig. 2.
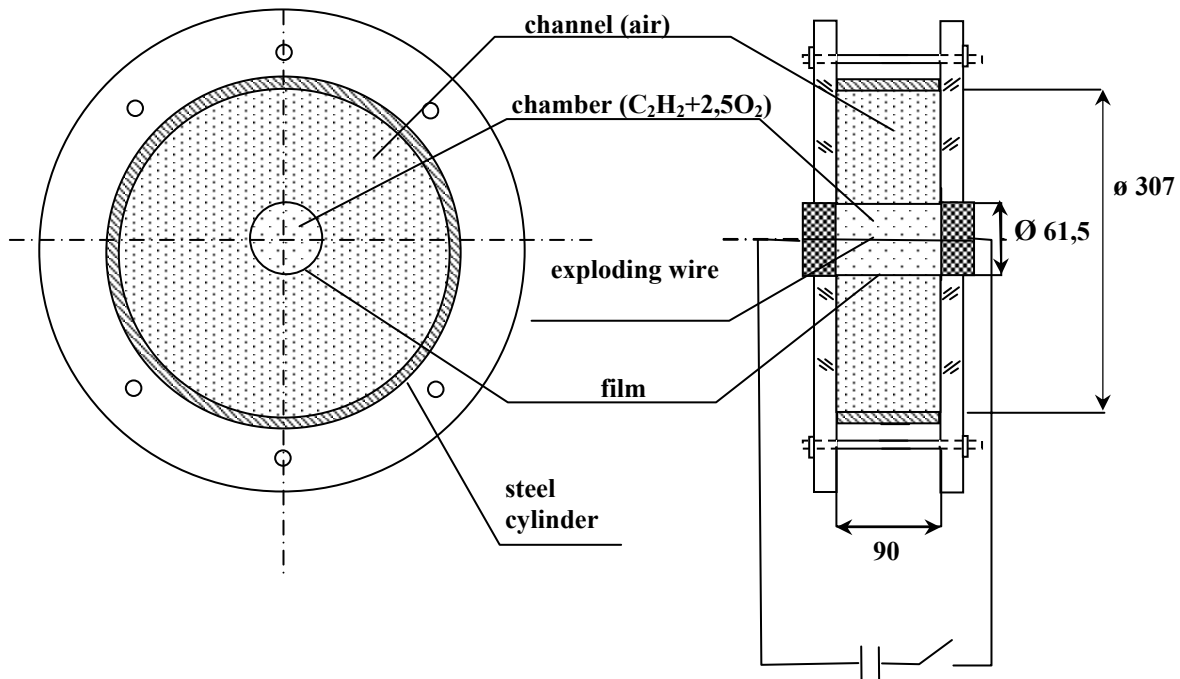
Fig. 1. The scheme of a cylindrical shock tube
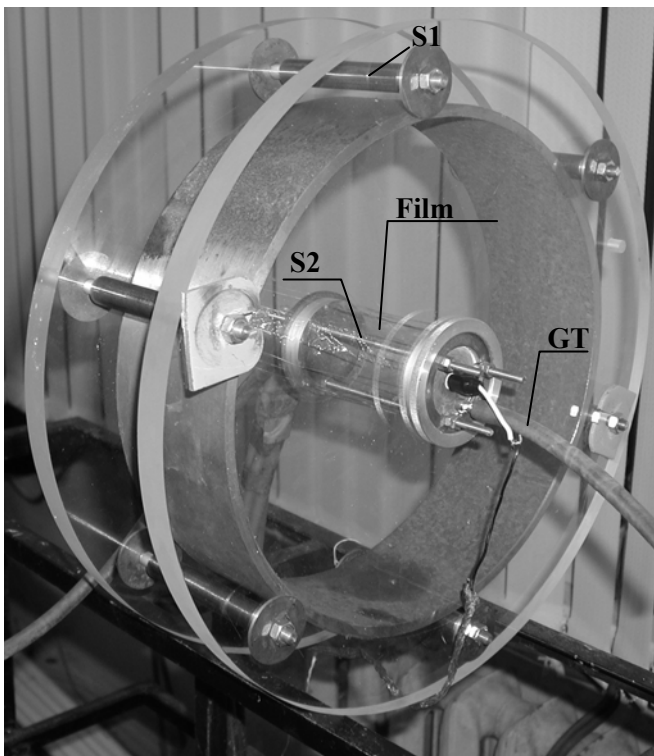
Fig. 2. Photo of a cylindrical shock tube. S1 - six studs fastening the case of the channel; S2 - three studs fastening the chamber; GT - gas tube.

A shock tube case is a piece of a cylindrical steel tube with an internal diameter of 307 mm, thickness of the wall of 8 mm and length of 90 mm. On both ends, the tube case is limited by to plexiglas plates with a thickness of 20 mm. Plates are tightened with six M8 steel studs. In assembly the lateral plates (windows) and the cylindrical case form the channel of the cylindrical shock tube.

Along the axis of the assembly, there is a hole housing a cylindrical chamber desined as two end walls inter-connected by 12 steel strings (with a 1 mm diameter). The end walls and the strings form a skeleton which was covered by a thin (~1 microns) film forming closed volume of the chamber. The chamber has a diameter of 61.5 mm. In the

development of the experimental technique it transpired, that the steel strings are not a reliable enough device for fastening the chamber, and additional three end – wall fastening steel studs with a diameter of 5 mm had to be installed.

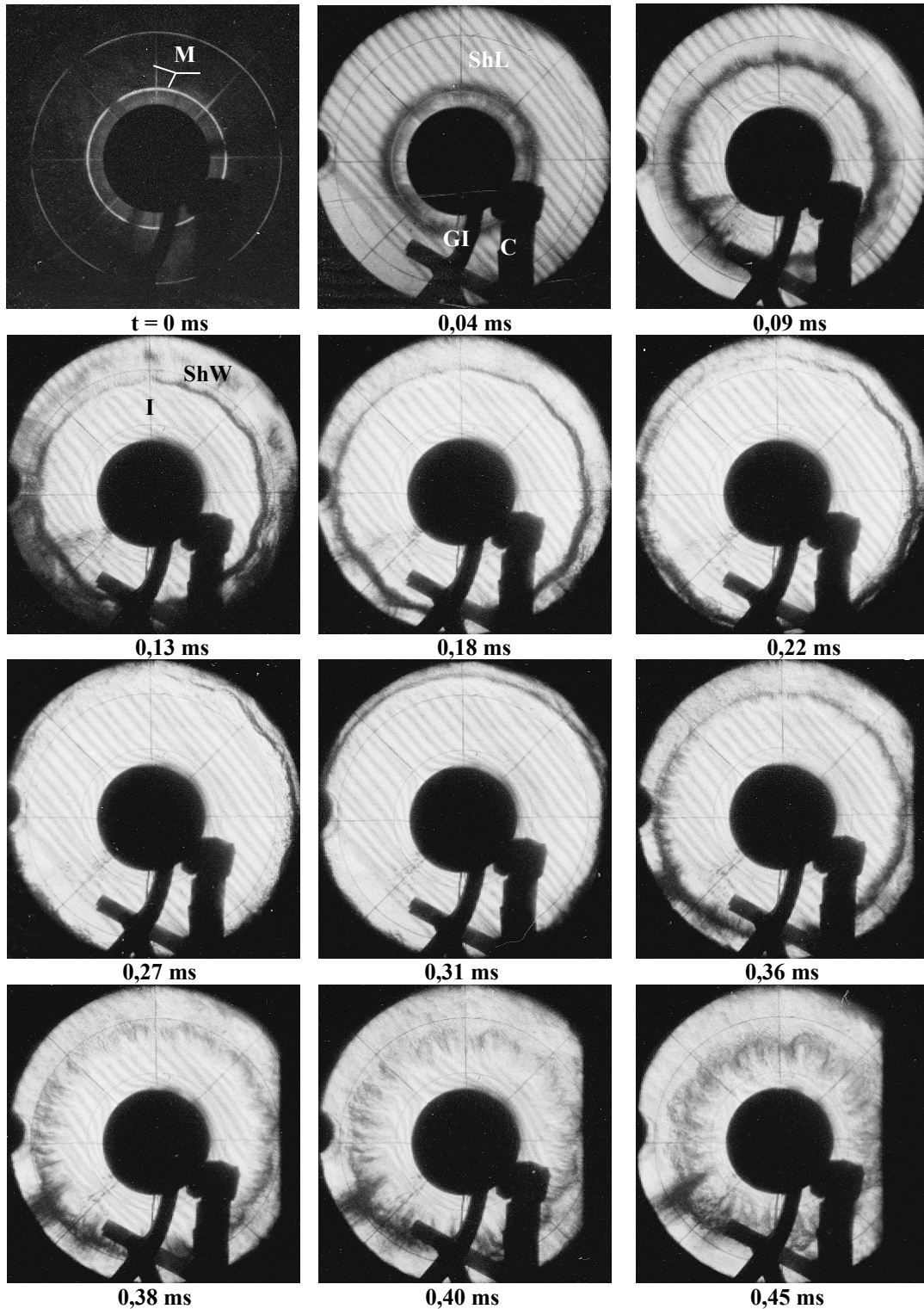|		
t = 0 ms	**0,04 ms**	**0,09 ms**
0,13 ms	**0,18 ms**	**0,22 ms**
0,27 ms	**0,31 ms**	**0,36 ms**
0,38 ms	**0,40 ms**	**0,45 ms**

Fig. 3. Photo of the experiment with the cylindrical shock tube
Legend: M - mark lines; GI - gas inlets; C - high-voltage pulse cable to a exploding wire; ShL - shadows of out-of-focus lattices [17]; I - interface between detonation products and air; ShW - shock wave. Time is counted from the moment of the mix detonation initiation in the chamber.
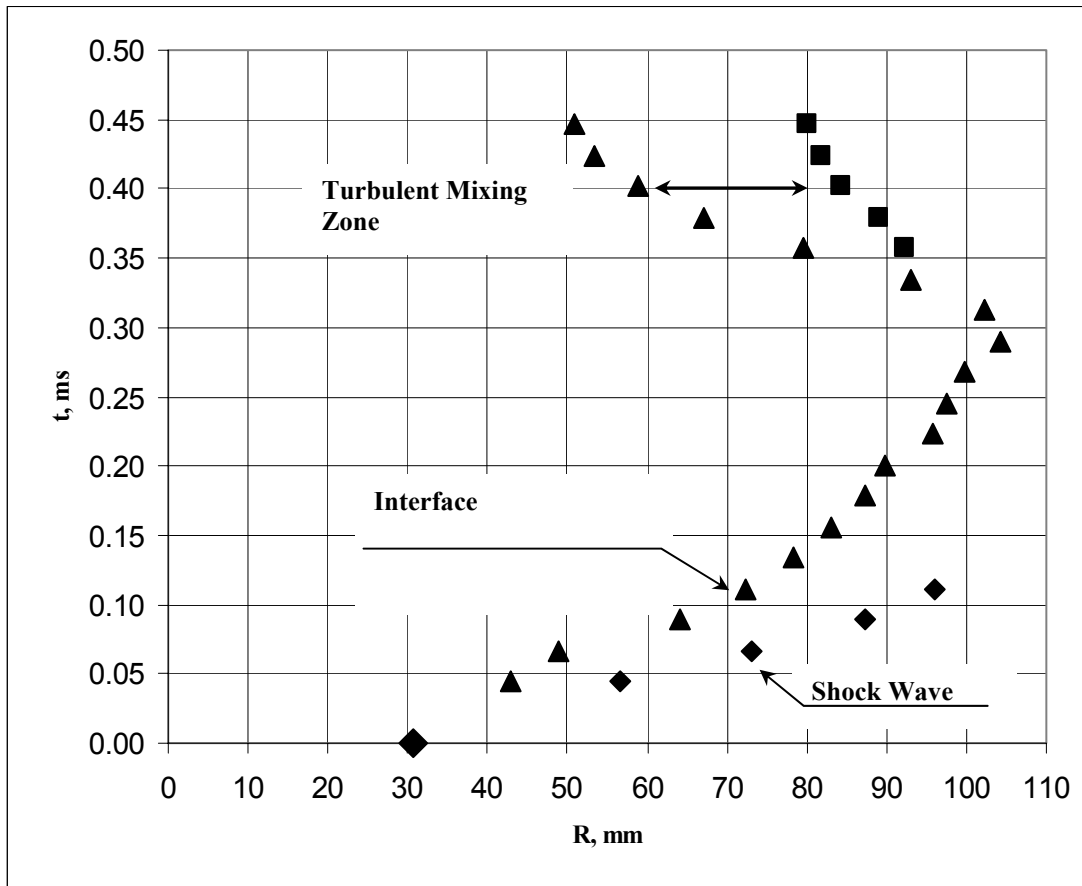
Fig. 4. *R-t* diagram of the flow in the cylindrical shock tube

Before the carrying out of the experiment, the internal volume of the chamber is filled, through gas inlets in end walls, by acetylene - oxygen mixture ($C_2H_2+2,5O_2$). The filling is carried out by pumping some 1.5 liter of the mixture through the volume of the chamber. In the channel, there is air at atmospheric pressure.

Detonation of the mixture is initiated by electric explosion of a wire stretched along the chamber axis.

Visualization of the flow is carried out by IAB-451 shadow installation by a method of out-of-focus lattices [17]. Registration of the flow is carried out by high-speed camera (SFR).

Negatives of experimental frames are scanned by ScanWit 2740s scanner. At that files are produced with an image of separate frames in PCX format, which are processed on a personal computer by an AUTOVIEW, PHOTOSHOP and EXCEL software packages.

3. Fig. 3 shows the results of one of the experiments carried out by the described technique and the measuring results presented as *R-t* diagrams (fig. 4).

As in the case of the experiments on a usual shock tube [13-16] at the initial stage of the flow, before shock wave reflected from a rigid wall (t <0.3 ms) reaches the interface, the mixing zone on the interface practically does not develop. The turbulent mixing zone starts developing intensively after it is reached by the reflected shock wave (t> 0.3 ms).

The experimental results quite unequivocally confirm an opportunity the possibility to use the given technique for research of processes of a turbulent mixing zone developing on a gas - gas interface in a cylindrical geometry. At that, it is necessary to note that, in comparison with the experiments the cylindrical shock tube [3-6] conducted in the 1970s years of the last century, the given technique has a member of essential differences and, in some respects, advantages:

1. In the described technique, the film is destructed and turns to smoke at the initial stage of flow and therefore does not influence the development of a turbulent mixing zone at the initial stage of flow.

2. The distance between the side walls of the cylindrical shock tube channel in experiments [3-6] was 2 cm; in this case, it makes 9 cm and can be additionally increased without much work and, in that way, the role of wall effects is significantly reduced. The wide – range variation of the distance between the end walls makes it possible to investigate

the role of wall effects. In addition to the aforesaid, it is possible to state, that in this case, the problem of increasing the cross-section section scale is solved easier than in the case of a usual shock tube.

3. It is possible to conduct a research of the development of a large-scale perturbation (for example, by displacing the chamber in relation to the case or by initiating disturbances on a cylindrical rigid wall.)

Thus, the technique is developed for research of the development of a turbulent mixing zone on a gas - gas interface in a cylindrical geometry by means of a cylindrical shock tube constructed according to the scheme: *an exploded wire along the axes of symmetry - a layer of a mix of acetylene and oxygen (limited by a thin (~1μ) film) - a layer of air - a cylindrical case (a rigid wall).*

The developed technique has essential differences and certain advantages in comparison with the technique of research by means of a cylindrical shock tube with a shock wave driver in the form of exploded wires [3].

7 References

1. Meshkov E.E., 1969. Instability of the interface of two gases accelerated by a shock wave. *Izy. Akad. Nauk. SSSR. Mekh. Zhidk. Gaza. Vol. 4, pp. 151. [Russian: Izy. Acad Sci. USSR. Fluid Dyn. Vol. 4. P. 101].*

2. Andronov V.A., Bakhrakh S.M., Meshkov E.E. et al., 1976. Turbulent mixing at contact surface accelerated by shock waves. *Sov. Phys. JETP, Vol. 44, N 2, pp. 424-427.*

3. Andronov V. A., Bakhrakh S.M., Meshkov E.E., Nikiforov A.V., Pevnitskii A.V., Tolshmyakov A.I., 1982 An experimental investigation and numerical modeling of turbulent mixing in one-dimensional flows. *Sov. Phys. Dokl., Vol. 27, pp. 393.*

4. Meshkov E.E., Nikiforov V.V.,. Tolshmyakov A.I., 1997. Investigation into Turbulent Mixing Development at the Gas-Gas Interface Driven by a Convergent Cylindrical Shock Wave. *The Proc. of the 6th IWPCTM. Marseille, France. Editors L.Houas & G.Jourdan, pp.348.*

5. Meshkov E.E., A.L. Tolshmyakov., 1999. Study of the effect of eccentricity in converging shock on light-gas compression by a heavy one for cylindrical geometry. *Proc. of the 7th IWPCTM. St-Petrsburg, Russia, Edited by E.Meshkov, Yu.Yanilkin & V.Zhmailo, pp.98-103.*

6. Tolshmyakov A.I., Meshkov E.E., 1989. Pertrubation growth on interface driven by cylindrical, converging shock. FGV, N 3 (in Russian).

7. D.A.Holder, A. V. Smith, M.K.Philpott, D.B.Miller. First Mix Experiments on the AVE Convergent Shock Tube. *Proc. of the 7th IWPCTM. St-Petrsburg, Russia, Edited by E.Meshkov, Yu.Yanilkin & V.Zhmailo, pp.28-32.*

8. D.A.Holder, D.A., Smith, A.V., Barton, C.J. and Youngs, D.L., 2003. Mix experiments using a two-dimensional convergent shock-tube. *Laser and Particle Beams 21, pp. 403-409.*

9. C J Barton, D A Holder., 2004. Convergent shock tube: new design, first results. *Abstracts of 10th IWPCTM, Cambridge, UK, pp.12.*

10. S.H.R.Hosseini and K. Takayama., 2001. Interaction of Converging Shock Waves With Cylindrical Heavy Gas Interfaces in an Eccentric Arrangement. *Abstracts of 8th IWPCTM, December 9-14, Pasadena, California, USA, pp.21.*

11. S. H. R. Hosseini and K. Takayama., 2001. Production of Diverging and Converging Spherical Shock Waves and Eccentric Interaction of Converging Shock Waves with Cylindrical Interfaces. *Abstracts of 8th IWPCTM, December 9-14, Pasadena, California, USA, pp.20,21 (Proc. of 8th IWPCTM, file e15.pdf)*

12. S.H.R. Hosseini, K. Takayama, T. Saito., 2004. Study of converging reflected shock waves and Richtmyer-Meshkov instability in spherical geometry. *Abstracts of 10th IWPCTM, Cambridge, UK, pp.45.*

13. Meshkov E.E., 1995. One Approach to the Experimental Study of Hydrodynamic Instabilities:Creation of a Gas-Gas Interface Using the Dynamic Technique. *The Proc of the 5th IWPCTM, Stony Brook, USA, pp.237.*

14. Yu.Vlasov, S.Gerasimov, E.Gubkov, V.Dudin, V.Kopyshev, E.Meshkov, A.Nikulin, V.Ryabov, V.Til'kunov., 1996. Shock tube with GM as a driver. *Preprint VNIIEF, №47-96, pp 38.*

15. V.I.Dudin, E.V.Gubkov, E.E.Meshkov, A.A.Nikulin, A.L.Stadnik, V.P.Statsenko, V.A.Til'kunov, Yu.AVlasov, Yu.V.Yanilkin, V.A.Zhmailo., 1996. The perturbations and turbulent mixing evolution at the plane gas-gas interface in shock-tube experiments with GEM as a driver. *Preprint VNIIEF, №50-96, pp.42.*

16. M. Bliznetsov, V. Dudin, O. Krivonos, A. Levushov, E.E. Meshkov, V. Fadeev., 2004. Development of 2-d perturbations of gas-gas interface in experiments on the shock tube with the gem driver. *Abstracts of 9th IWPCTM Cambridge, UK 19-23 July pp.14.*

17. A. Levushov, A. Logvinov, E. Meshkov & V. Popov., 2004. Application of Ronchi metod for visualization of a turbulent mixing zone in shock tube experiments. *Abstracts of 9th IWPCTM Cambridge, UK 19-23 July pp.67.*

e-mail: `pmiller@llnl.gov`

Bubble Counts for Rayleigh-Taylor Instability Using Image Analysis

Paul L. MILLER[1], Abel GEZAHEGNE[1], Andrew COOK[1], William CABOT[1], and Chandrika KAMATH[1]

[1]*Lawrence Livermore National Laboratory*

Abstract: We describe the use of image analysis to count bubbles in 3-D, large-scale, LES [1] and DNS [2] of the Rayleigh-Taylor instability. We analyze these massive datasets by first converting the 3-D data to 2-D, then counting the bubbles in the 2-D data. Our plots for the bubble count indicate there are four distinct regimes in the process of the mixing of the two fluids. We also show that our results are relatively insensitive to the choice of parameters in our analysis algorithms.

1 BUBBLE-IDENTIFICATION ALGORITHM

The three-dimensional data from the simulations are converted through a series of steps to two-dimensional data for analysis. A region-growing approach is first used to define the mixing region from the density field. The data volume is then processed to produce a "top-down" image of the height of the top surface of the three-dimensional mixing region defined by the region-growing method. To locate bubble structures in the surface depicted in the height map, the magnitude of the X-Y velocity is computed, and localized nodes of zero X-Y velocity magnitude are used to identify the tips of bubbles. See Figs. 1.1 and 1.2.

| (a) | (b) | (c) |
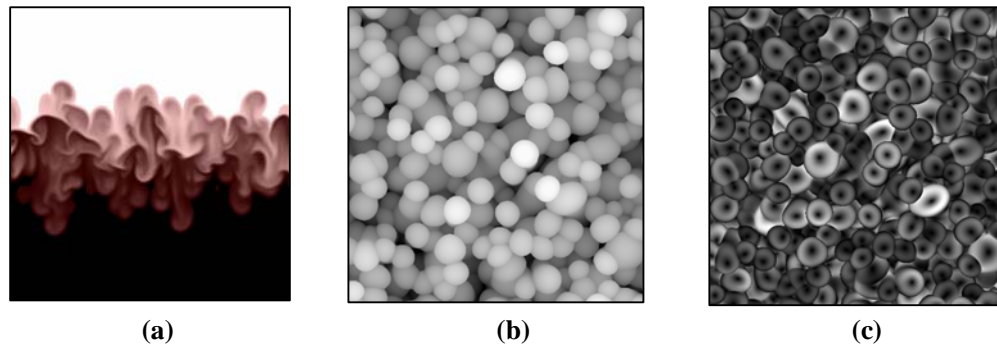
Fig. 1.1. DNS at t / τ = 6.25. Only 1/36 of the area of the data is displayed. (a) 2-D slice of density, where the gray regions are identified by the 3-D region-growing method. (b) The height of the bubbles as seen in the top view obtained from 3-D region growing. (c) Magnitude of the X-Y velocity at the bubble boundary.

| (a) | (b) | (c) |

Fig. 1.2. Sub-images from the DNS, with the bubble tips identified, for t / τ of (a) 2.25, (b) 5.625, and (c) 14. A bubble tip is the centroid of a region where both the magnitude of the X-Y velocity and the height variation are small. Only 1/36 of the area of the data is displayed.

2 SENSITIVITY TO THRESHOLD

The method we employ to determine the location of bubble structures is necessarily subjective. We used visualization to verify the results from the algorithms as they were developed and refined, and took the approach that a bubble is a structure that mani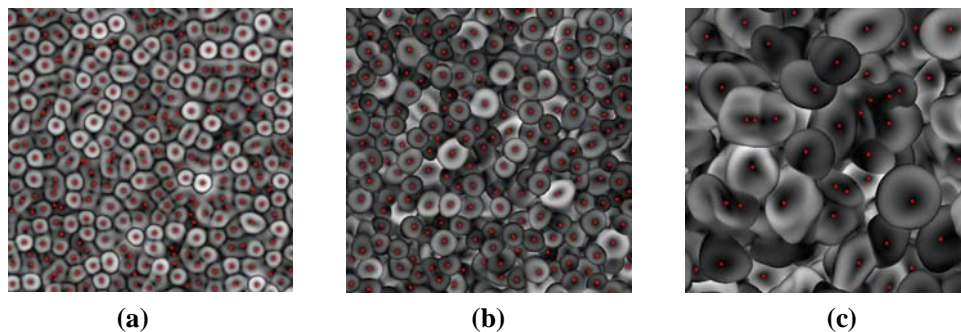fests itself near the top region of the mixing layer, has a characteristic domed feature, and is something that a person viewing an image can recognize intuitively. These assumptions work well at the early times in the flow development, but are strained at late time when the flow morphology becomes quite complicated.

We explored the dependence of the final bubble counts on the threshold used in the region-growing step. For a subset of simulation times, the threshold was varied and the resulting bubble tips on the top-down images were judged by eye for whether the result was consistent with what our eye discerned in the structure. Upper and lower bounds were determined, and the dependence of the upper and lower bounds on the final bubble counts was determined (Figs. 2.1 and 2.2). The differences resulting from the extremes of the thresholds are observed to be relatively small when considering the slopes of the bubble count curves. For the primary analysis, a logarithmic function was constructed that represented a reasonable range of threshold values. The increase in the threshold with time is reflective of the varying impact of diffusion on the bubble front.
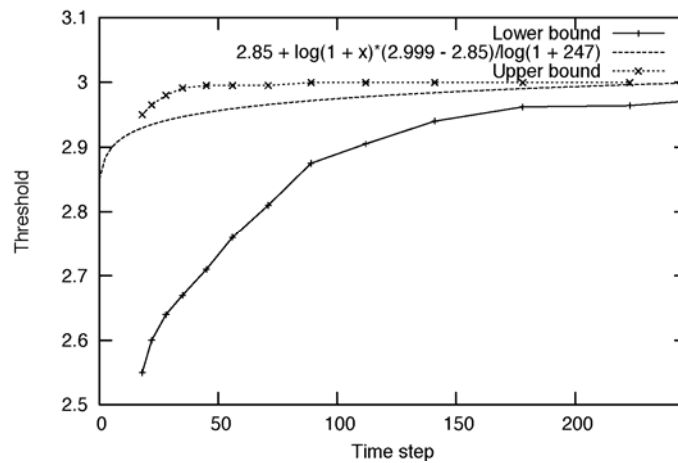

Fig. 2.1. Empirical range of thresholds observed to result in similar bubble identification (DNS).
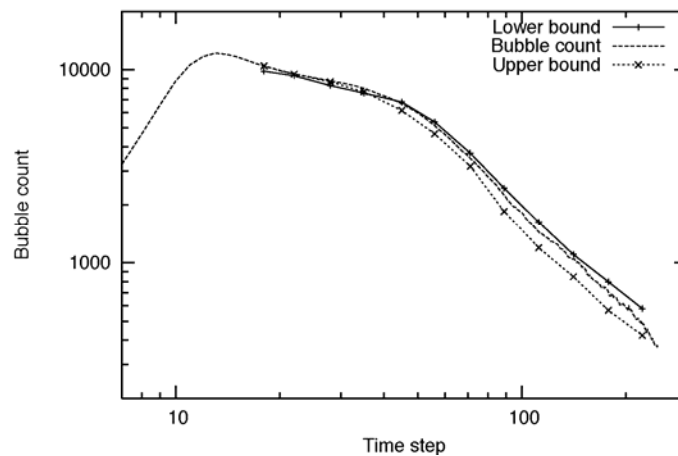

Fig. 2.2. The number of bubbles identified using the extreme thresholds in Fig. 2.1, as well as the result using the intermediate function-defined threshold values.

3 BUBBLE COUNTS

The bubble-identification algorithm was used to analyze data from two large-scale numerical simulations of the Rayleigh-Taylor instability, a Large-Eddy Simulation (LES) [1] and a Direct Numerical Simulation (DNS) [2]. The results are displayed in Figs. 3.1 and 3.2. Using log-log scales accentuates possible power-law scaling of the bubble count vs. nondimensional time (defined in [1]). Note that the log scales over-emphasize very early times. Also, the absolute value of the bubble count scale is arbitrary, simply reflecting the size of the analyzed domain.

Four regions emerge exhibiting different power-law behaviors, as indicated by the included line fits. The fit parameters are listed as measures of the curve slopes. The four regions are reminiscent of behavior observed previously [1] in other statistics of the mixing layer, such as the mixedness parameter and the growth rate. Roughly speaking, the four regions correspond to, from left to right, (1) early independent bubble growth, (2) nonlinear interactions between the growing structures, (3) a transition, and (4) fully turbulent regime. The more accentuated bump in the LES results (shallower region 3 slope) is not entirely understood, but may be related to a difference in effective Schmidt numbers between the two cases. Note the slopes do not drop below -2.28.
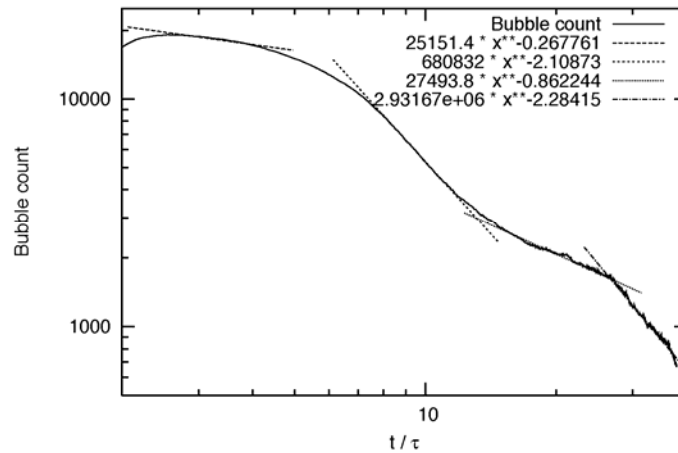

Fig. 3.1. Bubble counts for the LES, 1152^3 grid, 759 time steps, 30 terabytes of data.
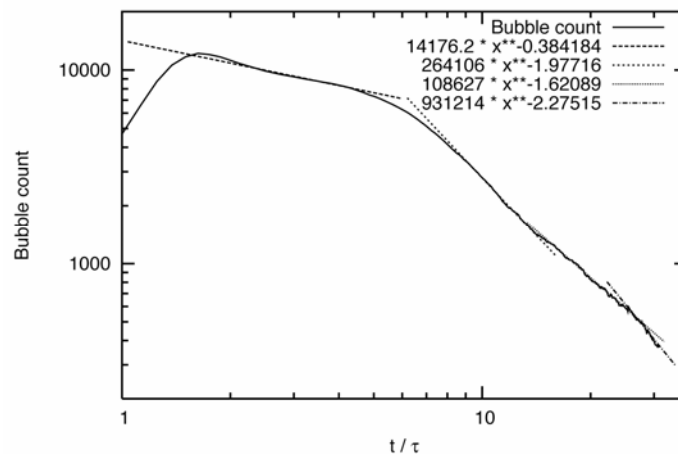

Fig. 3.2. Bubble counts for the DNS, 3072^3 grid, 248 time steps, 80 terabytes of data.

4 SUMMARY

In conclusion, we have developed a method for the identification of bubble structures in simulations of Rayleigh-Taylor instability, and applied the method to count bubbles in two large-scale data sets. We investigated the sensitivity of the results to the use of a subjective threshold, and found it has little influence on the power-law behavior of the bubble counts. Likewise, there are some differences in details, but the general conclusions hold for both the LES and the DNS datasets.

The log-log plots of bubble counts vs. nondimensional time exhibit four distinct regions. These regions correspond to qualitatively different bubble behavior. At the earliest times, the bubbles are very distinct and grow in a quasi-independent manner. Subsequently, the bubbles begin to interact, develop mushroom-cap rollups, and their stems begin to tilt and then intertwine with neighboring bubbles. The pattern soon becomes much more complex, and then undergoes a transition to a fully turbulent state. At the latest times, the mixing layer boundary has a wide spectrum of length scales represented in its structure, with bumps upon bumps, and a simplified concept of an idealized bubble becomes increasingly questionable.

The power-law scaling of these bubble counts has implications for bubble-based models of Rayleigh-Taylor instability. In particular, if the bubbles "tile" the area, then the number of bubbles should scale like the inverse of the square of the bubble radius. If it is further assumed that the characteristic bubble radius scales proportional to the layer width, and the mixing layer width scales like t^2, then the number of bubbles should be proportional to t^{-4}, i.e., a slope of -4 on the log-log plots of bubble count vs. time. Likewise, alternative scalings of the bubble radius will produce other power laws.

Our results do not exhibit slopes nearly as negative as -4, so we conclude that the destruction of bubbles (by whatever means, such as merging or competition) is slower than suggested by a bubble radius proportional to the layer width.

We have employed another analysis approach to the bubble-counting problem, with similar findings, that appears elsewhere in this Proceedings [3].

REFERENCES

[1]   Cook et al., *The mixing transition in Rayleigh-Taylor instability*, JFM **511** (2004), 333 - 362.
[2]   Cabot and Cook, *Reynolds number effects on Rayleigh-Taylor instability with possible implications for type-1a supernovae*, Nature Physics **2** (2006), 562 - 568.
[3]   Miller, et al., *Application of Morse Theory to Analysis of Rayleigh-Taylor Topology*, elsewhere in this Proceedings.

e-mail: `pmiller@llnl.gov`

Application of Morse Theory to Analysis of Rayleigh-Taylor Topology

Paul L. MILLER[1], Peer-Timo BREMER[1], William CABOT[1], Andrew COOK[1], Daniel LANEY[1], Ajith MASCARENHAS[1], and Valerio PASCUCCI[1]

[1]*Lawrence Livermore National Laboratory*

Abstract: We present a novel Morse Theory approach for the analysis of the complex topology of the Rayleigh-Taylor mixing layer. We automatically extract bubble structures at multiple scales and identify the resolution of interest. Quantitative analysis of bubble counts over time highlights distinct mixing trends for a high-resolution Direct Numerical Simulation (DNS) [1].

1 THE MORSE COMPLEX

We partition the mixing layer from a DNS of Rayleigh-Taylor instability [1] using a fundamental topological construct called a Morse complex. Given a function F(x) on a surface S (see Fig. 1.1), the Morse complex partitions S into regions in which all steepest ascending lines end at a single maximum. The domain S for this application is the levelset *density = 2.98*. The density in the problem ranges from 1.0 to 3.0. The function F(x) is the axis opposite to gravity.

The resulting Morse complex is a patchwork depiction of the isosurface in which each patch is assigned a color (Fig. 1.1, center), and the feature in the middle of the patch may be considered a bubble. For more complicated surface structure, as occurs later in the development of the flow, the structures are less distinct. The surface exhibits bumps upon bumps, and the concept of a simple bubble is not applicable.
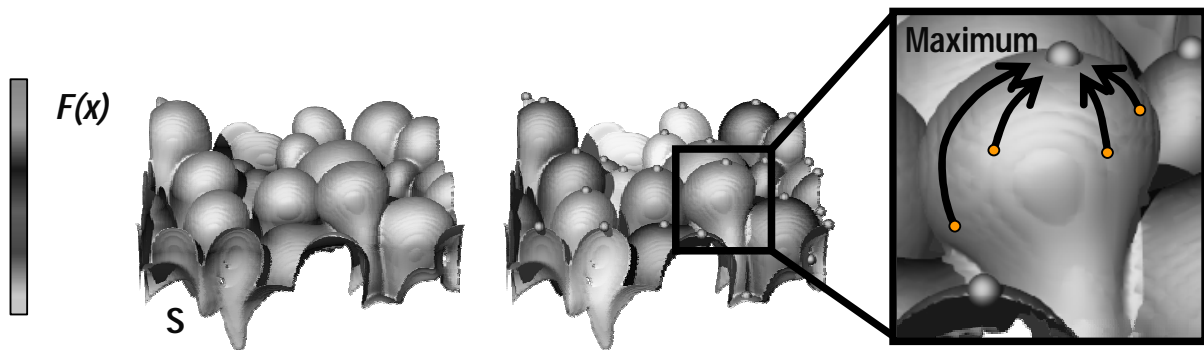
Fig. 1.1. F(x), indicated by the color bar, shown on a surface S (left); Morse complex cells indicated by distinct colors (center); in each Morse complex cell, all steepest ascending lines converge to one maximum (right).

2 TOPOLOGICAL PERSISTENCE

To handle the additional late-time (multi-scale) structure within a bubble framework, we incorporate the concept of *topological persistence*. The topological features are ranked by persistence, the difference in F(x) between a maximum and an adjacent saddle. Persistences *p1* and *p2* of two features are shown below (Fig. 2.1). We remove lower persistence features by contracting pairs of adjacent maxima into one. The corresponding Morse cells are merged to form a coarser partitioning of the domain.
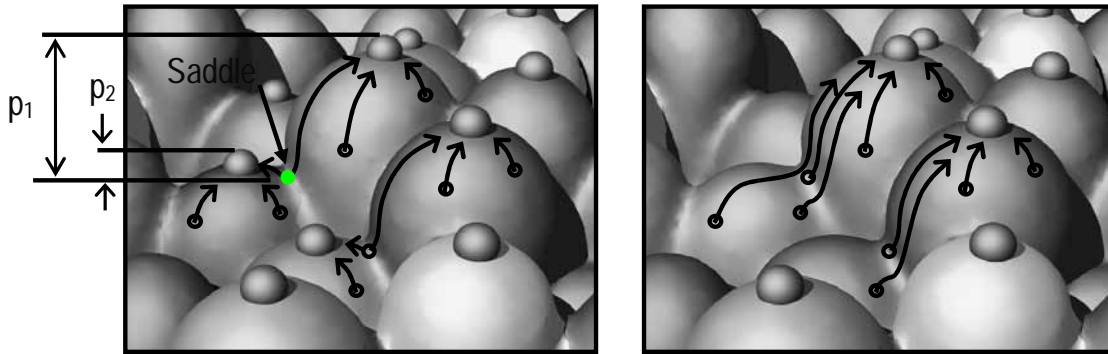
Fig. 2.1. Contracting low-persistence critical points reduces the Morse complex into a tiling that segments *S* into bubbles.

3 TEMPORAL REALIZATIONS

The Morse-complex approach was applied to the DNS data over a range of simulation times. Examples of the color-coded surface at a variety of times are shown in Figs. 3.1 and 3.2. A reduced version of the entire surface is at the upper left in Fig. 3.1, along with close-ups and a three-dimensional rendition. These visualizations were used for validation of the bubble-identification algorithm, which also produced bubble counts as a function of time.

$$t/\tau = 1.25 \qquad t/\tau = 2.50 \qquad t/\tau = 6.50 \qquad t/\tau = 11.00$$
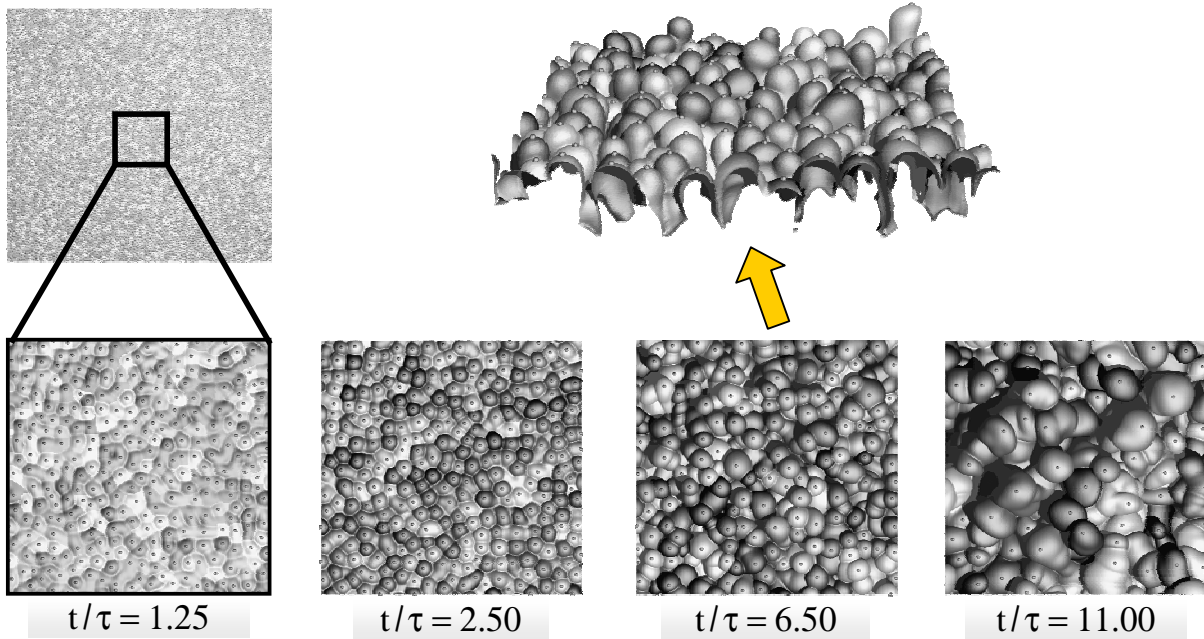
Fig. 3.1. Images of the bubble surface at four select times, enlarged to show just 4% of the total area (top left). The third time realization is also displayed in a three-dimensional rendition.

$$t/\tau = 19.0 \qquad\qquad t/\tau = 30.75$$
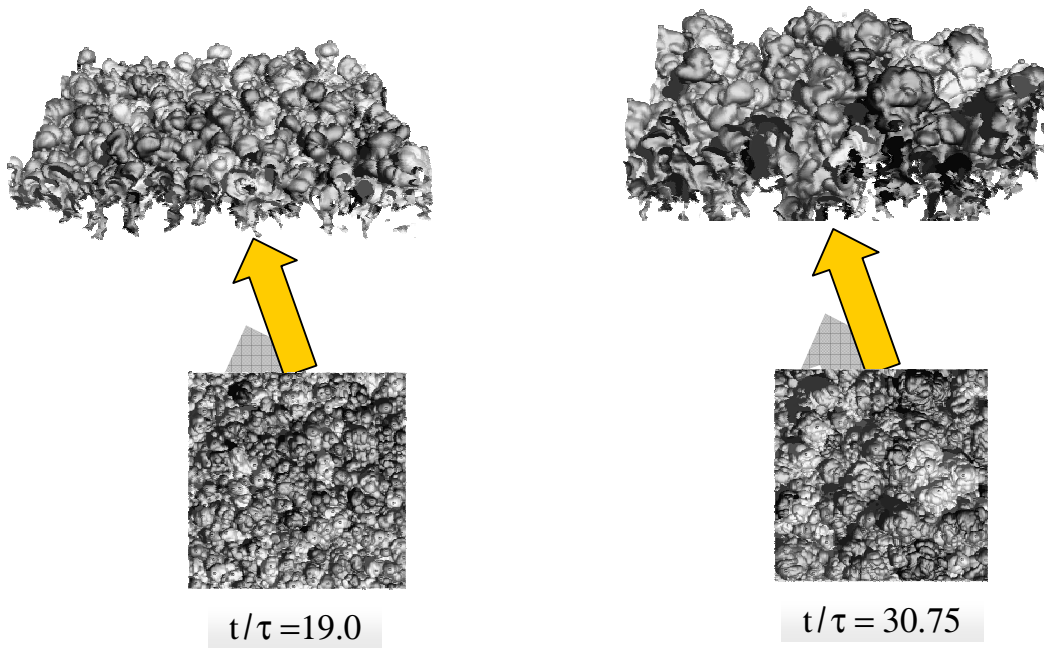
Fig. 3.2. Images of the bubble surface at two additional select times, showing 60% of the total area.

4 QUANTITATIVE TIME ANALYSIS

We analyze trends in a DNS Rayleigh-Taylor simulation (Cabot and Cook, 2006) by counting bubble structures. Shown are the number of Morse maxima vs. nondimensional time (green plot), and the local slope of that curve (red plot). The slope curve highlights several stages in the development of the interface topology, suggestive of earlier findings [2].
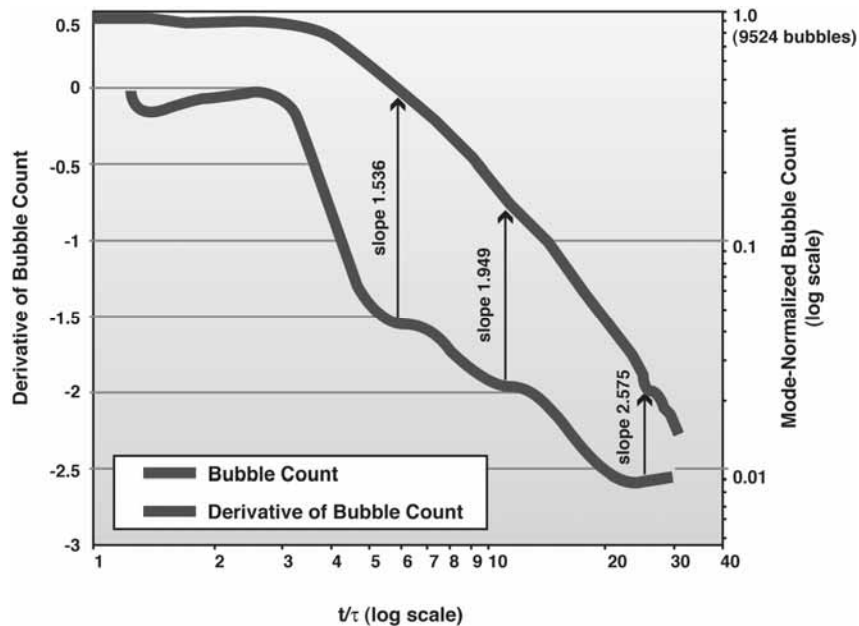
Fig. 4.1. Bubble count vs. time and the corresponding derivative curve.

5 SUMMARY

We have applied the Morse-complex approach to the analysis of simulation data of a Rayleigh-Taylor flow. Bubble counts derived from the analysis display a series of stages, or regimes, for the flow, much as regimes of the flow have been identified previously [2]. At the earliest times, the bubbles grow in an essentially independent manner, followed by a period of interaction during which they begin to feel the presence of their neighbors, develop roll-ups, and become much more convoluted. That is followed by a stage of weak turbulence that transitions to fully turbulent, late-time behavior. It is interesting to observe the regimes manifest themselves in the bubble-count statistics, which was unexpected.

One of our primary interests in pursuing this work was to explore the scaling of the number of bubbles with time. We find that the power-law behavior of the bubble count is much less steep power laws than may have been anticipated. The power-law scaling of these bubble counts has implications for bubble-based models of Rayleigh-Taylor instability. In particular, if the bubbles "tile" the area, then the number of bubbles should scale like the inverse of the square of the bubble radius. If it is further assumed that the characteristic bubble radius scales proportional to the layer width, and the mixing layer width scales like t^2, then the number of bubbles should be proportional to t^{-4}, i.e., a slope of -4 on the log-log plots of bubble count vs. time. Likewise, alternative scalings of the bubble radius will produce other power laws.

Our results do not exhibit slopes nearly as negative as -4, so we conclude that the destruction of bubbles (by whatever means, such as merging or competition) is slower than suggested by a bubble radius proportional to the layer width. We have employed another analysis approach to the bubble-counting problem, with similar findings, that appears elsewhere in this Proceedings [3].

REFERENCES

[1]   Cabot and Cook, *Reynolds number effects on Rayleigh-Taylor instability with possible implications for type-1a supernovae*, Nature Physics **2** (2006), 562 - 568.
[2]   Cook, et al., *The mixing transition in Rayleigh-Taylor instability*, JFM **511** (2004), 333 - 362.
[3]   Miller, et al., *Bubble Counts for Rayleigh-Taylor Instability Using Image Analysis*, elsewhere in this Proceedings.

e-mail: `bonazza@engr.wisc.edu`

Shock accelerated two-dimensional interface

Bradley MOTL[1], John NIEDERHAUS[1], Jason OAKLEY[1], Devesh RANJAN[1], Mark ANDERSON[1], Riccardo BONAZZA[1] and Jeffrey GREENOUGH[2]

[1] *University of Wisconsin-Madison, Madison, WI 53706 USA*

[2] *Lawrence Livermore National Laboratory, Livermore, CA 94550 USA*

Abstract: Richtmyer-Meshkov (RM) experiments for a two-dimensional membraneless, sinusoidal gas interface are carried out in a vertical shock tube [1] for an Atwood number ($A = (\rho_1-\rho_2)/(\rho_2+\rho_1)$) of approximately A=0.68 and shock strengths of M=1.26 and M=2.05. The interface is created by continuously flowing gases from opposite ends of the shock tube, light from the top and heavy from the bottom. The two flows form a planar stagnation surface and exit the shock tube through slots in the test section walls. The interface is then given a near sinusoidal perturbation by oscillating rectangular pistons embedded within the shock tube walls. The light gas is N_2 seeded with either acetone (imaged utilizing planar laser-induced fluorescence) or smoke (imaged with Mie scattering) and the heavier gas is SF_6. Growth rates and density field measurements are compared to numerical simulations using the *Raptor* code (LLNL). *Raptor* uses the Piecewise Linear Method (PLM) with Adaptive Mesh Refinement (AMR) to solve the Navier-Stokes equations. Good agreement between the experimental and *Raptor* simulations is achieved. The Mikaelian model predicts the experimentally observed and numerically simulated amplitude growth rate data well, for both the M=1.26 and M=2.05 cases.

1 INTRODUCTION

Shock-driven hydrodynamic instabilities are present in multi-component flows subjected to acceleration by shock waves. Vorticity is baroclinically deposited on a material interface during shock passage due to the misalignment of pressure and density gradients, causing the interface to become unstable and deform. The geometric features of the deformed interface and mixing zone are studied for a planar interface with a small-amplitude sinusoidal perturbation. This class of problems is called the Richtmyer-Meshkov (RM) [2] [3] instability. The evolution of the RM instability starts with the deposition of vorticity on the interface which causes the initial amplitude of the perturbation to grow linearly. The linear amplitude growth is followed by a nonlinear growth regime. This is followed by a regime that is influenced by the Kelvin-Helmholtz instability, which causes roll-up structures on each side of the heavy fluid spike and results in the formation of mushroom-shaped structures. The complex nature of these vortices ultimately leads to the development of a turbulent mixing zone. The RM instability plays an important role in the field of inertial confinement fusion (ICF) because it is responsible for lowering the ICF energy yield by creating unwanted mixing of the pellet shell with the nuclear fuel [4]. The RM instability also plays a role in supernova expansion [5], where shock waves traverse interstellar density non-uniformities.

2 EXPERIMENTAL SETUP

The experimental study is carried out at the Wisconsin Shock Tube Laboratory. The shock tube is oriented vertically, fires downward, and has a total length of 9.13 m. The driver section has a circular cross section with a radius of 0.41 m, while the driven section has a square inner cross section with 0.25 m sides [1]. A high-pressure boost tank is connected to the driver section by a pneumatically-driven fast-opening valve to control the diaphragm rupture time. Piezoelectric pressure transducers mounted along the shock tube side walls are used to trigger the controlling electronics and to measure the shock speed. The method of interface preparation is similar to the one used by Jones and Jacobs [6]. The interface section of the shock tube, shown in Fig. 2.1, accommodates two rectangular 5.08×25 cm aluminum pistons which have slots that are connected to a vacuum pump that is set to an outflow rate of 6.67×10^{-4} m^3/s. Sulfur hexafluoride is introduced into the bottom of the shock tube at a flow rate of 1.55×10^{-4} m^3/s, and nitrogen seeded with acetone or smoke is introduced into the shock tube just below the diaphragm at a rate of 5.13×10^{-4} m^3/s. The differences in flow rates account for different shock tube volumes above and below the interface.
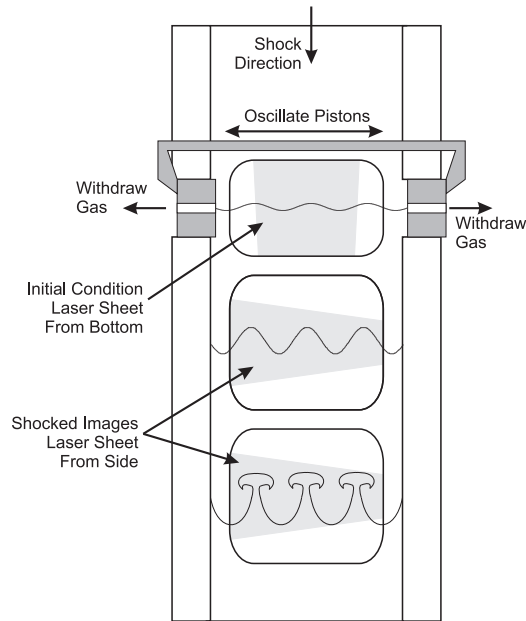
Fig. 2.1. Schematic of the interface section with piston system, and imaging windows.

Acetone seeding is performed by running nitrogen through two consecutive acetone baths that are kept at a constant temperature. On average, the mole fraction of acetone in the nitrogen/acetone mixture is 0.11. The pre-shock Atwood number for this interface is 0.64. Smoke seeding is performed by introducing smoke from a port approximately 2 m above the interface. The pre-shock Atwood number for the smoke-seeded N_2 over SF_6 is 0.68. The gases are continuously flowed for 45 minutes at which point a flat interface with an approximately 1 cm-thick diffusion layer is achieved. To generate a 2-D perturbation on the interface, the pistons are driven by a stepper motor at a frequency that creates a standing wave. In a nitrogen-acetone mixture, the pistons are oscillated at a frequency of 1.9 Hz for three revolutions (λ=90 mm wave) or 2.6 Hz for four revolutions (λ=180 mm wave). For the smoke seeded case, the pistons are oscillated at 2.1 Hz for three revolutions (λ=170 mm wave). The total piston travel is 2.86 cm. For the case of acetone seeding, planar laser-induced fluorescence (PLIF) is used to produce one pre-shock initial condition image and two post-shock images. For the case of smoke seeding, Mie scattering is utilized to generate one pre-shock and one post-shock image. All pre-shock and post-shock images are corrected for laser beam divergence and attenuation. A region of interest is extracted from a raw image, including either the entire width of the shock tube, or a single wavelength of the perturbation. The image is first corrected for divergence with a conformal mapping algorithm that conservatively maps diverging light rays to parallel columns, and then corrects for laser attenuation (due to absorption) by integrating Beer's Law along these columns. The image is then remapped to physical space, and convolved with a five-pixel Gaussian distribution, to reduce the levels of fine-scale noise in the image due to artifacts of the imaging technique.

3 NUMERICAL SIMULATION

The experimental configuration described in the previous section is simulated numerically in 2-D using an adaptive Eulerian hydrodynamics code called *Raptor*. Numerical integration of the 2-D compressible Euler equations is accomplished using an operator-split, second-order Godunov method. The basic kernel is the piecewise linear method (PLM) of Colella (1985) [8], which is a higher-order extension of the well-known MUSCL algorithm of van Leer (1979) [9]. Multifluid capturing capability is added to the scheme by adopting a volume-of-fluid technique similar to that described by Miller and Puckett (1996) [10], which allows two fluids with distinct adiabatic exponents to be included in the calculation.

The integration kernel is embedded within the block-structured adaptive mesh refinement (AMR) framework of Berger and Oliger (1984) [11], to maximize spatial resolution and accuracy for regions of interest that

move across the Eulerian mesh. The AMR technique has been used extensively in shock hydrodynamics computations, and its implementation has been discussed in detail by Berger and Colella (1989) [12] and Bell *et al.* (1994) [13]. The region of interest in the flow considered here includes the interface and regions containing shocks or rarefactions near the interface. This is enforced by applying a dual refinement criterion, based on both proximity to the interface and the local magnitude of the density gradient.

Calculations for the 2-D Richtmyer-Meshkov instability using *Raptor* are set up on a Cartesian mesh representing the midplane of the shock-tube flow field. A coordinate system is defined whose x-axis is coincident with the shock tube long axis, and whose y-axis is transverse. The physical dimensions of the domain are 25.4×330.2 cm, and the base grid size is 416×32. Two levels of AMR are applied, with a refinement ratio of 4 each, yielding an effective resolution of Δ=0.05 cm, which implies that approximately 310 highest-level grid cells are subtended by a distance equal to the dominant-mode wavelength, λ=15.45 cm. Symmetry boundary conditions are applied on the y=0 and y=25.4 cm boundaries to allow wave reflections at the shock tube side walls, and inflow/outflow conditions are applied on the axial boundaries to maintain constant driving pressure and allow waves to exit the domain smoothly (no endwall is included).

In the initial condition, regions of pure nitrogen (γ=1.399, ρ=1.130 kg/m^3) and pure SF$_6$ (γ=1.094, ρ=5.892 kg/m^3) are initially separated by a diffuse interface oriented normal to the x-direction. The 10%-90% thickness of the diffusion-layer region (tanh profile) at the interface in the initial condition is approximately 0.2 cm for the M=2.05 smoke seeded case. A perturbation is imposed on the interface by superposing a series of Fourier modes extracted from averaged measurements of experimental initial conditions. The Fourier spectrum is dominated by a single mode of wavelength λ, though 20 modes are present in the spectrum.

A planar shock wave approaches the interface along the x-direction. The shock wave is given a strength of M=2.05 by specifying the appropriate pressure, density, and velocity in the shocked-gas region. The development of the flowfield is tracked at closely-spaced time intervals during and after the impact of the shock on the interface. Visualizations of the accelerated interface and characterizations of the Richtmyer-Meshkov growth obtained from the resulting datasets are shown below and compared in detail with experimental results.

4   RESULTS

In order to analyze the experimental data with *Raptor* and several analytical models, this study utilizes the non-dimensional parameters proposed by Jacobs and Krivets [7]. The non-dimensional amplitude is given as:

$$a = k(\eta - \eta_0^1) \tag{4.1}$$

where k is the wavenumber ($2\pi/\lambda$), η is the perturbation amplitude (measured as half the peak to peak amplitude), and η_0^1 is the post-shock initial amplitude. The non-dimensional time is given as:

$$\tau = k\dot{\eta}_0 t \tag{4.2}$$

where $\dot{\eta}_0$ is the initial growth rate, and is approximated [7] by:

$$\dot{\eta}_0 \approx k\eta_0^1 A^1 V_0 \tag{4.3}$$

where A^1 is the post-shock Atwood number and V_0 is the velocity jump of the interface due to the impulsive acceleration of the shock.

One pre-shock and two post-shock images are obtained per experiment for the M=1.26 case where the N$_2$ is seeded with acetone. Figure 4.2 is a non-dimensional time sequence of experimental images from a single experiment. The images only represent a small region of the imaging plane (10 cm in width).

Figure 4.2 shows that by τ=4.66, the growth of the instability has proceeded far into the nonlinear growth regime and by τ=8.79, fully developed mushroom structures are present. *Raptor* accurately predicts the overall shape and size of the perturbation, however, *Raptor* is not able to resolve the small-scale secondary instabilities that appear on the "mushroom" structure at τ=8.79. These secondary instabilities suggest that the transition to a turbulent mixing zone is starting to occur.

One pre-shock and one post-shock image is obtained per experiment for the M=2.05 case where the N$_2$ is seeded with smoke. Figure 4.3 is a non-dimensional time sequence of experimental images from multiple experiments. The field of view spans 22.5 cm.

Figure 4.3 shows that once again *Raptor* accurately predicts the overall shape and size of the perturbation for the $M = 2.05$ case. Figure 4.3 also indicates that, for increased shock strength, geometric features similar

τ=0.00 $\qquad\qquad$ τ=4.66 $\qquad\qquad$ τ=8.79
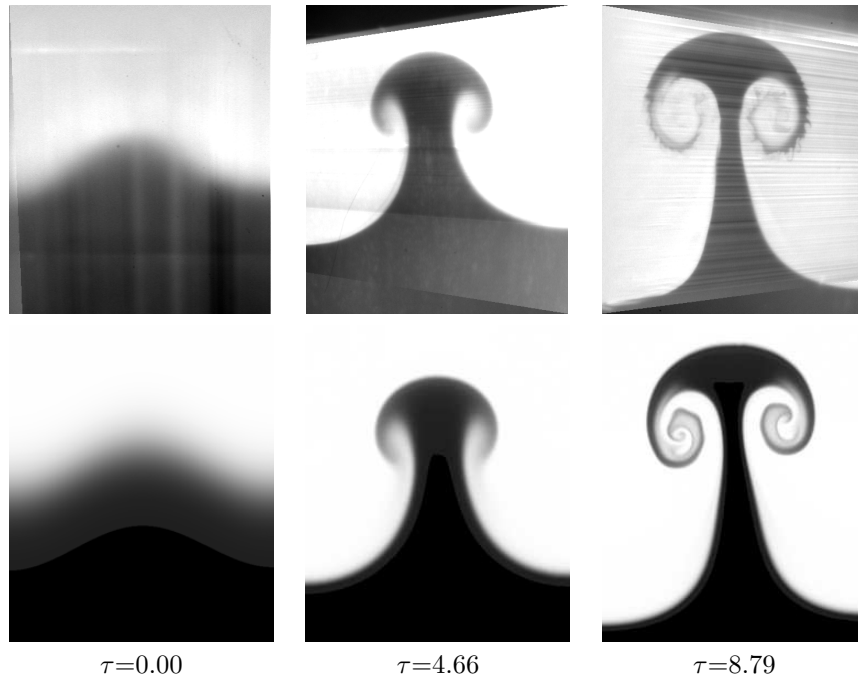
Fig. 4.2. Non-dimensional time sequence of M = 1.26 experimental images (top row) and computational images (bottom row).

τ=0.00 $\qquad\qquad$ τ=1.54 $\qquad\qquad$ τ=3.29 $\qquad\qquad$ τ=3.98
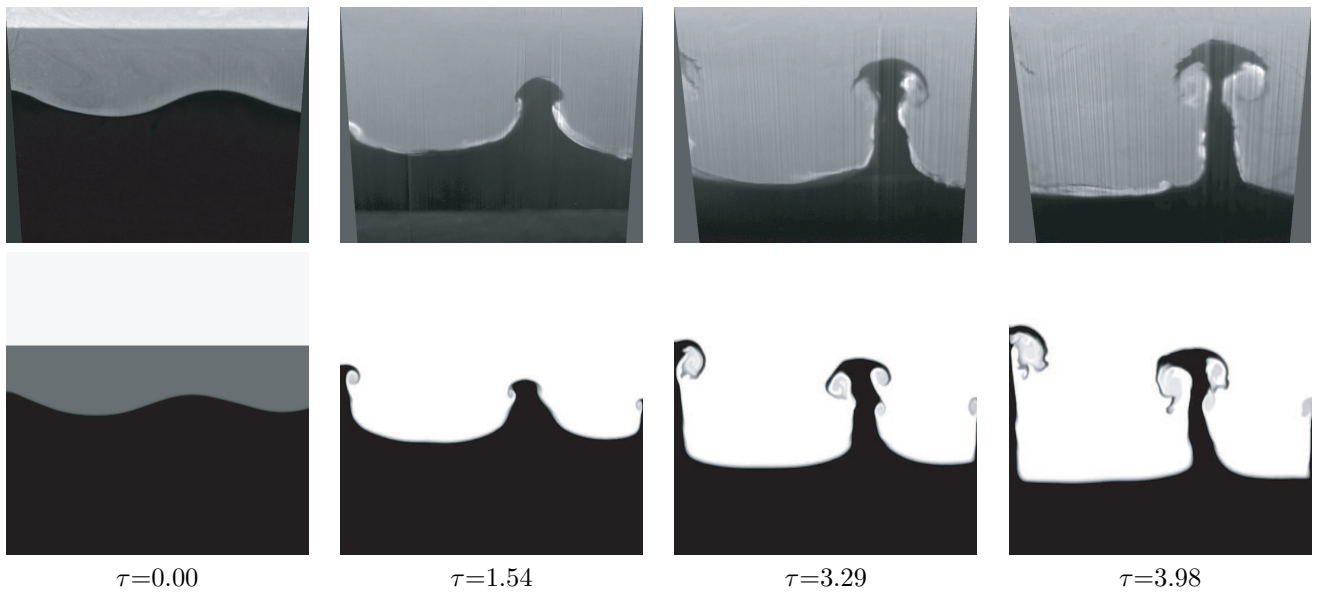
Fig. 4.3. Non-dimensional time sequence of M = 2.05 experimental images (top row) and computational images (bottom row).

to those observed in the M=1.26 case appear at earlier non-dimensional times. In particular, roll-up features appear as early as τ=3.98 in the M=2.05 experiments, but are not distinctly seen until much later in the M=1.26 case. Figure 4.3 shows that at late times, the downward-growing N_2 bubble flattens near the base of the "mushroom" structure for τ=3.29 and 3.98. This feature is further demonstrated by the τ=3.98 computational image.

The experimental data is compared to three nonlinear, analytical perturbation amplitude growth models.

The empirical model of Sadot *et al.* [14] utilizes experimental parameters and requires knowledge of the initial perturbation spectrum. In the present study, the model of Sadot *et al.* is implemented for the case of an initially single-mode perturbation. The Mikaelian [15] model is an explicit, analytic expression for the evolution of a two-dimensional, single mode interface. Lastly, the Dimonte and Schneider [16] model is a power law model that is designed for a broadband multi-mode initial condition.

The experimental amplitude is non-dimensionalized using Eq. 4.1 and plotted versus the non-dimensional time given in Eq. 4.2. Figure 4.4 compares the experimental data to the analytical models described above as well as the *Raptor* data for the M=1.26 case, while Fig. 4.5 compares the M=2.05 data.
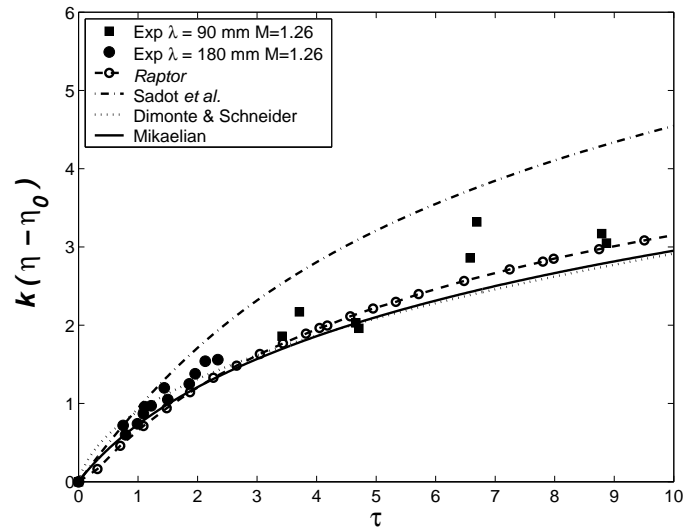
Fig. 4.4. A plot of non-dimensional experimental amplitude versus time compared to results obtained from various analytical models and *Raptor* for the M=1.26 case.
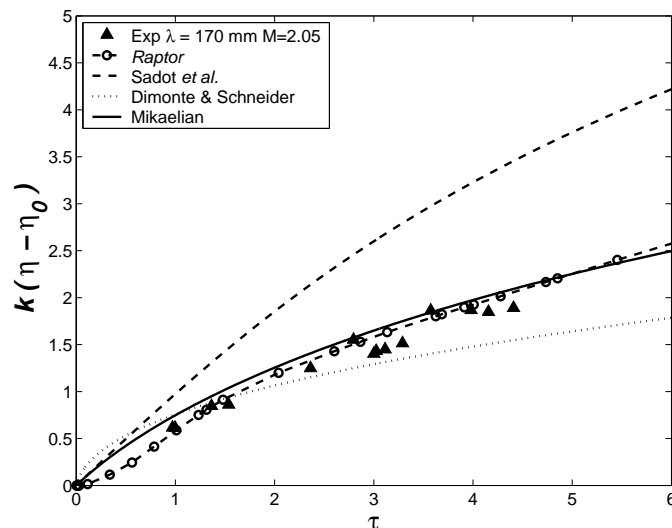
Fig. 4.5. A plot of non-dimensional experimental amplitude versus time compared to results obtained from various analytical models and *Raptor* for the M=2.05 case.

The Sadot *et al.* model consistently over-predicts the experimental and computational growth for both cases, whereas both the Mikaelian and Dimonte and Schneider models more accurately represent the M=1.26 experimental data as shown in Fig. 4.4. However, at late non-dimensional times, both of these models seem to

under-predict the experimental data, though it is difficult to make any firm conclusion due to the small number of data points at $\tau > 6.0$. For the case of M=2.05, the experimental data shown in Fig. 4.5 falls between the Mikaelian model (which tends to over-predict the growth) and the Dimonte and Schneider model (which tends to under-predict the growth). The M=2.05 *Raptor* data is best fit by the Mikaelian model, although it slightly over-predicts the growth for $\tau < 5.0$.

5 SUMMARY

The Richtmyer-Meshkov instability is experimentally investigated for a nitrogen (seeded with either acetone or cigarette smoke) over sulfur hexafluoride gas pair at M=1.26 and 2.05. Experimental images are compared to density field plots generated by the hydrodynamic code *Raptor* while non-dimensional growth rate plots are compared to *Raptor* and several models. *Raptor* accurately predicts the overall shape and size of the perturbation, however, for late non-dimensional times at M=1.26, the grid used for the calculations is not adequate to completely resolve small-scale secondary instabilities that appear in the experimental image. The experimental and computational non-dimensional growth rate data are modeled well by the Mikealian model. Future work will extend the experimental Mach number parameter space to approximately M=3.0, as well as the investigation of additional gas pairs.

REFERENCES

[1] Anderson, M.H., Puranik, B.P., Oakley, J.G., Brooks P.W., Bonazza, R., 2000. Shock Tube Investigation of Hydrodynamic Issues Related to Inertial Confinement Fusion, *Shock Wave.* **10**(5), pp. 377-387.

[2] Richtmyer, R.D., 1960. Taylor instability in shock accleration of compressible fluids, *Commun. Pure Appl. Math.* **13**, pp. 297-319.

[3] Meshkov, Ye.Ye., 1970. Instability of a shock wave accelerated interface between two gases, *NASA Technical Translation.* NASA TT F-13,074.

[4] Kilkenny, J.D., *et al., 1994. A review of the ablative stabilization of the Rayleigh-Taylor instability in regimes relevant to inertial confinement fusion,* Phys. Plasmas. *1(5), pp. 1379-1389.*

[5] Jun, B., Jones, T.W., Norman, M.L., 1996. Interaction of Rayleigh-Taylor fingers and circumstellar cloudlets in young supernova remnants, *The Astrophysical Journal.* **468**, pp. L59-L63.

[6] Jones, M.A., Jacobs, J.W., 1997. A membraneless experiment for the study of Richtmyer-Meshkov instability of a shock-accelerated gas interface, *Physics of Fluids.* **9**(10), pp. 3078-3085.

[7] Jacobs, J.W., Krivets, V.V., 2005. Experiments on the late-time development of a single-mode Richtmyer-Meshkov instability, *Physics of Fluids.* **17**, 034105.

[8] Colella, P., 1985. A direct Eulerian MUSCL scheme for gas dynamics, *SIAM J. Sci. Stat. Comput.* **6**(1), pp. 104-117.

[9] van Leer, B., 1979. Towards the ultimate conservative difference scheme, *J. Comput. Phys.* **32**, pp. 101-136.

[10] Miller, G.H., Puckett, E.G., 1996. A higher-order Godunov method for multiple condensed phases, *J. Comput. Phys.* **128**, pp. 134-164.

[11] Berger, M., Oliger, J., 1984. Adaptive mesh refinement for hyperbolic partial differential equations, *J. Comput. Phys.* **53**, pp. 484-512.

[12] Berger, M., Colella, P., 1989. Local adaptive mesh refinement for shock hydrodynamics, *J. Comput. Phys.* **82**(1), pp. 64-84.

[13] Bell, J.B., Berger, M., Saltzman, J.S., Welcome, M., 1989. Three dimensional adaptive mesh refinement for hyperbolic conservation laws, *SIAM J. Sci. Comput.* **15**, pp. 127-138.

[14] Sadot, O., Erez, L., Alon, U., Oron, D., Levin, L.A., Erez, G., Ben-Dor, G., Shvarts, D., 1998. Study of nonlinear evolution of single-mode and two-bubble interaction under Richtmyer-Meshkov instability, *Phys. Rev. Let.* **80**(8), pp. 1654-1657.

[15] Mikaelian, K.O., 2003. Explicit expressions for the evolution of single-mode Rayleigh-Taylor and Richtmyer-Meshkov instabilities at arbitrary Atwood numbers, *Phys. Rev. E* **67**(2), pp. 026319-1 - 026319-7.

[16] Dimonte, G., Schneider, M., 2000. Density ratio dependence of Rayleigh-Taylor mixing for sustained and impulsive acceleration histories, *Phys. Fluids* **12**(2), pp. 304-320.

Turbulent Mixing of Two Fluids of Different Density and Speed, Moving in a Field of Gravity

V.E.Neuvazhayev
Chief Researcher
Doctor of Physics and Mathematics, Professor
E-mail: v.e.neuvazhayev@vniitf.ru

T.V.Zabolotnikova
Junior Researcher
E-mail: t_v_zab@vniitf

Academician E.I.Zababakhin All –Russian Scientific Research Institute of technical Physics
Snezhinsk, 456770, Russia, P.O.Box 245, Phone +7(35146)54367, Fax +7(35146)55566,
E-mail: otdeldo@vniitf.ru

Two fluids of different density are in gravity field and move one relative to another with different speed. The interface is unstable; it is destroyed, and turbulent mixing appears.

The theoretical study of the turbulent mixing appearing as a result of the joint action of the shear and gravity instabilities is presented in the paper. Based on the kε- model there was defined the analytical formula for the width of the turbulent mixing zone in relation to the initial parameters of the task: Atwood Number $A=(\rho_1-\rho_2)/(\rho_1+\rho_2)$, Number $A_u=(U_1-U_2)/(U_1+U_2)$, acceleration g and initial roughness L_0, where U_1 and U_2, ρ_1 and ρ_2 are the velocities and densities of the fluids, respectively.

The formula for the width of the turbulent mixing zone was found in [1] based on the lv-model without taking into account the dissymmetry of the mixing, though in reality (according to experiments) the mixing takes place asymmetrically –the intensity of the mixing is higher toward the lighter substance than that toward the heavier one. The kε- model is considered in this paper, and the dissymmetry of the mixing is taken into account. Also there are derived formula is compared with the known experimental data and numerical calculations without taking into account the gravity force.

The kε- model equations for stationary flow of the incompressible liquids will be written as follows according to [2]:

$$U\frac{\partial \rho k}{\partial x} + V\frac{\partial \rho k}{\partial y} = D\frac{\partial \rho}{\partial y}g + \alpha_2 \rho D\left(\frac{\partial U}{\partial y}\right)^2 - \rho\varepsilon \qquad . (1)$$

$$U\frac{\partial \rho\varepsilon}{\partial x} + V\frac{\partial \rho\varepsilon}{\partial y} = C_\mu C_{\varepsilon 1} k\frac{\partial \rho}{\partial y}g + C_\mu C_{\varepsilon 1}\alpha_2 \rho k\left(\frac{\partial U}{\partial y}\right)^2 - C_{\varepsilon 2}\rho\frac{\varepsilon^2}{k}. \qquad (2)$$

The diffusion terms are not taken into account as they are small relative to source terms – the

first and second terms in the right part of the equations (1),(2) for this problem. Here

$C_\mu, C_{\varepsilon 1}, C_{\varepsilon 2}, \alpha_2$ are the constants of the kε- model, g is acceleration of gravity, U, V are the

components of the velocity, k is the kinetic energy of the turbulence, ε is the velocity of the

energy dissipation, $D = C_\mu \dfrac{k^2}{\varepsilon}$ is the coefficient of the turbulent diffusion. The system is added

with the averaged equations of the gas dynamics [1].

$$\frac{\partial}{\partial x}\rho U + \frac{\partial}{\partial y}\rho V = 0 \quad U\frac{\partial \ln \rho}{\partial x} + V\frac{\partial \ln \rho}{\partial y} = \frac{\partial}{\partial y}\left(D\frac{\partial \ln \rho}{\partial y}\right) \quad U\frac{\partial U}{\partial x} + V\frac{\partial U}{\partial y} = \alpha_2 \frac{1}{\rho}\frac{\partial}{\partial y}\left(D\rho\frac{\partial U}{\partial y}\right)$$

Initial conditions: $\rho(0,y) = \begin{cases} \rho_1 & y > 0 \\ \rho_2 & y < 0 \end{cases}$ $\qquad U(0,y) = \begin{cases} U_1 & y > 0 \\ U_2 & y < 0 \end{cases}$

In order to solve this system the following assumption were made. It is assumed that k and ε are the constants along axis y within the mixing zone. And it is assumed that D is broken in point y=0 and is equal to:

$$D = \begin{cases} C_\mu \dfrac{\overline{k}^2}{\overline{\varepsilon}}, & if \quad y > 0 \\[3mm] C_\mu \beta_2 \dfrac{\overline{k}^2}{\overline{\varepsilon}}, & if \quad y < 0 \end{cases}$$

where $\overline{k}, \overline{\varepsilon}$ are the mean values of the turbulence kinetic energy and dissipation, respectively, on mixing zone $[-L_2, L_1]$, β_2 is new empirical coefficient. We suppose that in the model equations velocity before derivatives equals $U_0 = \dfrac{\rho_1 U_1 + \rho_2 U_2}{\rho_1 + \rho_2}$. Also we suppose that $V = -D\dfrac{\partial \ln \rho}{\partial y}$.

The formula for calculation of the width of the turbulent mixing zone is:

$$L = L_0 + \frac{\left(1+\sqrt{\beta_2}\right)}{12}\frac{\left(2C_{\varepsilon 2}-3\right)^2}{4C_{\varepsilon 2}-3}C_\mu g\sqrt{\beta_2}A_0\Phi(\eta_1)\cdot\left(\frac{x}{U_0}\right)^2 +$$

$$+\sqrt{\frac{2\left(2C_{\varepsilon 2}-3\right)^2}{3C_{\varepsilon 2}}C_\mu\left(1+\sqrt{\beta_2}\right)^2 Q_0\eta_1^2 + \frac{C_\mu\left(2C_{\varepsilon 2}-3\right)^2}{3\left(4C_{\varepsilon 2}-3\right)}\left(1+\sqrt{\beta_2}\right)\cdot g\sqrt{\beta_2}A_0\Phi(\eta_1)L_0}\cdot\frac{x}{U_0}$$

where $Q_0 = \left(\dfrac{U_1-U_2}{1+\sqrt{\beta_2}}\right)^2 \dfrac{\left(1-A^2\right)\sqrt{\beta_2\alpha_2}}{16\sqrt{2}}\Phi\left(\sqrt{2}\dfrac{\eta_1}{\sqrt{\alpha_2}}\right)\left(1 - \dfrac{A_0\left(1-\sqrt{\beta_2}\right)}{2\sqrt{2}\Phi\left(\sqrt{2}\dfrac{\eta_1}{\sqrt{\alpha_2}}\right)}\right),$

$A_0 = \dfrac{\rho_1 - \rho_2}{\rho_1 + \rho_2\sqrt{\beta_2}}$.

Here dissymmetry is taken into account.
When dissymmetry is not taken account ($\beta_2 = 1$) this formula is:

$$L = L_0 + \frac{\left(2C_{\varepsilon 2}-3\right)^2}{6\left(4C_{\varepsilon 2}-3\right)}C_\mu gA\Phi(\eta_1)\left(\frac{x}{U_0}\right)^2 +$$

$$+\sqrt{\frac{B_0 C_\mu\left(2C_{\varepsilon 2}-3\right)^2\left(1-A^2\right)\left(U_1-U_2\right)^2\eta_1^2}{24C_{\varepsilon 2}} + \frac{2C_\mu gA\Phi(\eta_1)\left(2C_{\varepsilon 2}-3\right)^2 L_0}{3\left(4C_{\varepsilon 2}-3\right)}}\cdot\frac{x}{U_0}$$

In case when acceleration equation zero, and if we pass to a new system of coordinates based on the motion of mass center: $\tilde{x} = \dfrac{|U_1 - U_2|}{U_0}x$. We received the same formula as in [1] namely:

$$\frac{dL}{d\tilde{x}} = \frac{\alpha_u}{2}\sqrt{1-A^2} \qquad\qquad (3).$$

The difference is that coefficient α_u depends on the Atwood Number:

$$\alpha_u = \eta_1 \cdot \left|2C_{\varepsilon 2} - 3\right| \cdot \left(\frac{\beta_2 \alpha_2}{2}\right)^{1/4} \cdot \sqrt{\frac{C_\mu}{6C_{\varepsilon 2}} \cdot \Phi\left(\sqrt{2}\,\frac{\eta_1}{\sqrt{\alpha_2}}\right)\left(1 - \frac{A_0\left(1 - \sqrt{\beta_2}\right)}{2\sqrt{2}\Phi\left(\sqrt{2}\,\frac{\eta_1}{\sqrt{\alpha_2}}\right)}\right)} \cdot$$

The value β_2 found in [3] is: $\sqrt{\beta_2} = \left(1+A\right)^{0.45}$. Values C_μ и $C_{\varepsilon 2}$ were taken $C_\mu = 3.5$ and $C_{\varepsilon 2} = 1.85$ as in [3]. Constant α_2 was selected in such a way so that formula (3) satisfies the experiments and numerical calculations. There was found agreement with experiment [4] in case $C_\mu = 3.5$, $C_{\varepsilon 2} = 1.85$ and $\alpha_2 = 2$. Also the formula is agreed satisfactorily with results of the direct numerical calculation [5]. Introduction of dissymmetry improved the agreement of the exact result with the numerical one.

The comparison plot of the derived formula for different values of constant α_2 and earlier numerical [5,6,7] and experiment data [4,8] is presented below. Also there is presented the comparison plot of the derived formula taking and not taking into account the dissymmetry of the mixing.

Fig1: Dependence $\dfrac{dL}{d\tilde{x}}$ of on Atwood Number « ▲ » are calculation results [5],

« * » are experiment data [4], « + » are calculation data [8], «◆» are derived by 2D method "EGAK" data [6], « ► » are derived by 3D method "TREK" data [7],

« —— 1» - is formula (3) for $C_\mu = 3.5$, $C_{\varepsilon 2} = 1.85$, $\alpha_2 \approx 0.32$

« —— 2» - is formula (3) for $C_\mu = 3.5$, $C_{\varepsilon 2} = 1.85$, $\alpha_2 \approx 0.7$

« —— 3» - is formula (3) for $C_\mu = 3.5$, $C_{\varepsilon 2} = 1.85$, $\alpha_2 \approx 0.13$

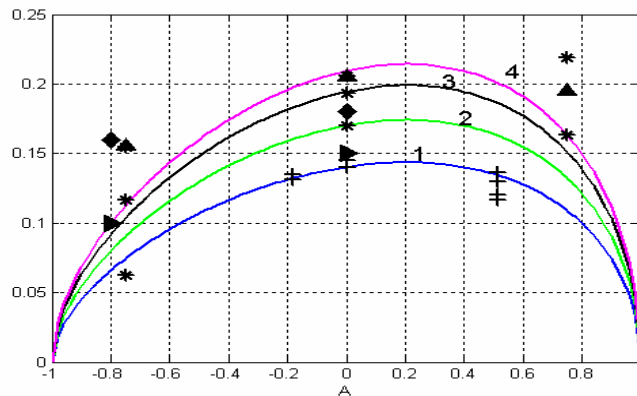« —— 4» - is formula (3) for $C_\mu = 3.5$, $C_{\varepsilon 2} = 1.85$, $\alpha_2 \approx 2$.
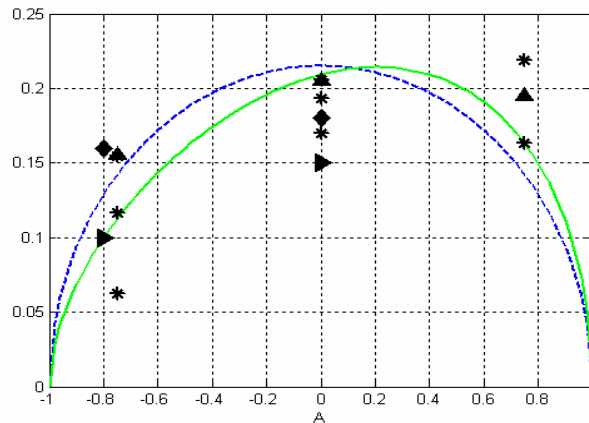
Fig2: Dependence $\dfrac{dL}{d\tilde{x}}$ of on Atwood Number « ▲ » are calculation results [5],

« * » are experiment data [4], « ◆ » are derived by 2D method "EGAK" data [6], « ► » are derived by 3D method "TREK" data [7], « ————— 1» - is formula (3) for $C_\mu = 3.5$, $C_{\varepsilon 2} = 1.85$, $\alpha_2 \approx 2$, « ————— 2» - is formula for $C_\mu = 3.5$, $C_{\varepsilon 2} = 1.85$, $\beta_2 = 1$, $B_0 \approx 0.94$.

Reference
1. V.E. Neuvazhayev, Turbulent Mixing of Two Fluids Moving in Gravitation Field, 6th International Workshop on the Physics of Compressible Turbulent Mixing, Marseil, 1997,P362.
2. V.E. Neuvazhayev, V.G.Yakovlev, Turbulent Mixing of Two Fluids for Arbitrary Low of the Acceleration, PMTF,2001,V.42,N4,P11-19
3. V.E. Neuvazhayev, V.G.Yakovlev, Description of the Gravitation Turbulent Mixing Based on kε- model , VANT, series of The Theoretical and Applied Physics, 1986,pablication 1,P28
4. Brown G.L., Roshko A. On Density Effects and Large Structure in Turbulent Mixing Layers. Journal of Fluid Mechanics, 1974, Vol 64(4), P775 – 815
5. N.S.Es'kov, A.S.Kozlovskih, D.V.Neuvazhayev. The Numerical Simulation of The Fully Developed Turbulence,PMTF,2000,P77
6. S.M.Bahrah, V.A.Zhmailo, V.P.Stasenko, Yu.V.Yanilkin, Numerical Simulation of Turbulent Mixing in Shear Flows, C. Numerical Methods of The Continuum Mechanics, 1983, V14, N2,P11-27
7. A.A. Stadnik, V.P.Statsenko, Yu.V.Yanilkin, V.A. Zhmailo, Direct Numerical Simulation of Turbulent Mixing in Shear Flows, Laser and Particle Beams, 1997,V15(1), P115-125
8. O.V. Yakovlevskiy. To Question about the Thickness of the Turbulent Mixing Zone in the Interface of Two Gas Fluids of the Different Speed and Densities, news AS USSR, Tectonic Science Department, 1958,N10, P153-155.

e-mail: `root@gdd.vniief.ru`

Study of Turbulent Mixing Development And Perturbations Growth in gases with increased Compressibility at Mach Numbers of Shock Wave from 2 till 9

Nikolay V. NEVMERZHITSKY, Alexander N. RASIN, Evgeny A. SOTSKOV, Evgeny D. SENKOVSKY, Olga L. KRIVONOS, Larisa V. TOCHILINA, Vyacheslav I. DUDIN, Andrey A. NIKULIN, Vasily A. USTINENKO

RFNC-VNIIEF, Sarov, Russia

Abstract: The experimental results are presented concerning the study of turbulent mixing development and the growth of two-dimensional local perturbations at Richtmayer-Meshkov instability at contact boundaries of gases (IG) with different density. The experiments were performed on a shock tube. Turbulent mixing (TM) was studied in gas layers at the interfaces: air–Elegas (SF_6), helium–SF_6, air-CO_2, air-helium of perturbations– at the air-–SF_6 interface. Shock wave Mach number was in the second gas $M_2 = (1.6 \div 9)$.

As a consequence, the mixing zone thickness increases with increase in shock wave Mach number M_2 at the interface Air-SF6. It is seen that a forward front of TM approaches a shock wave. Shock wave front is distorted at $M_2 \approx 9$ in SF_6. This can be connected with intensive interaction between vortexes and shock wave surface in the vicinity of CB (contact boundary) because of high compressibility of SF_6. Large-scale perturbations growth changes at the air- SF_6 interface with increase in Mach number.

1 INTRODUCTION

Hydrodynamic instabilities such as Raylegh-Taylor [1], Richmayer-Meshkov (RM) [2, 3] play a leading role in many fields of research, for example, in astrophysics, aerohydrodynamics, gas dynamics, in inertial thermonuclear fusion etc. To analyze a growth of instabilities and a subsequent transfer to turbulent mixing (TM), both numerical simulation methods and various semi-empirical models of turbulence are developed. At present several program packages have been created with regard to TM in VNIIEF to model two-dimensional flows. In these program packages TM evolution is calculated using V.V.Nikiforov's model. As this takes place, in some techniques Euler(ian) approach is used, in the others – Eulerian-Lagrangian approach. To test available two-dimensional techniques, some experimental studies can be fulfilled.

A number of experimental works is known, in which turbulent mixing development was investigated at the interface of gases at Mach numbers of a shock wave (SW) $M \leq 5$ (for instance, [3÷5]). In particular, in [6] it is noticed that in highly compressible gases TM may lead to distortion of SW surface. However, available experimental data are not sufficient for detailed understanding of physics of this process. Starting since 2002 the authors have been performing experimental, theoretical and numerical research of TM development at varied Mach numbers of SW. A part of the obtained results has been published in [7]. In the current paper the results are presented of additional studies in this field.

2 EXPERIMENTAL APPARATUS SCHEME

Experiments were conducted in a shock tube such as [8]. Shock tube scheme is presented in fig. 2.1. The shock tube consists of high pressure chamber (driver) 2 and low pressure chamber 3. The chambers are separated from each other by the help of a diaphragm made of lavsan thick up to 100-150 μm. A measuring section 4 is connected with the low pressure chamber.

The low pressure chamber was filled with helium (He) or air; the measuring section – SF_6, CO_2, or He under atmospheric conditions. Gases were separated initially by the help of a polymer film ≈ 1 μm thick. In some experiments local perturbations were formed at the air- SF_6 interface (s. fig. 2.1 versions I b-I c). The high pressure chamber was filled with acetylene/air mixture (combustible gas mixture -CGM) at the certain pressure P_0 (up to 9.5 atm), or compressed air up to pressure P_0=4.5 atm. Detonation of CGM was realized by pulsed electro spark discharge on rigid wall 1. Sizes L_{CGM} and L are varied ($L_{CGM} = 200 \div 450$ mm; $L = 800 \div 1520$ mm).
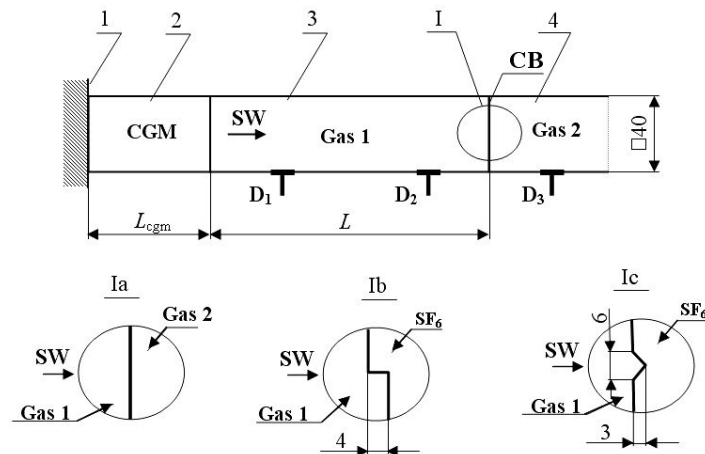
Fig. 2.1. Experimental setup (sizes in mm): 1 – rigid wall; 2 – high-pressure chamber; 3 – low-pressure chamber; 4 – measuring section

3 OPERATION OF THE APPARATUS

After initiating combustible gas mixture (CGM) a detonation wave is propagated in the high pressure chamber. When this detonation wave enters a diaphragm the latter fails and a shock wave propagates in gas 1. As a result of interaction between SW and a contact boundary (CB) a shock wave is formed going towards gas 2, and a reflected wave (shock wave or rarefaction wave), which goes to gas 1, is also formed. After destructing a separating film CB of gases accelerates, with the result that Richmayer-Meshkov instability arises in it, which causes perturbations growth and subsequent formation of turbulent mixing zone (TMZ).

The variation of CGM pressure has made it possible to obtain shock waves having a varied intensity. The flow has been recorded through the schlieren method by the use of a rapid movie camera in frame-by-frame mode and in slot image scanning mode. Shock wave velocity in gas 1 has been determined using sensors-markers D_1 и D_2, in gas 2 – by the help of moving image frames of experiments and sensor D_3.

Three sets of experiments have been fulfilled. In the first set of experiments the film dividing gases 1 and 2, has a flat surface (s. fig. 2.1 scheme Ia) for creating a flow similar to a one-dimensional flow. The second and the third sets of experiments have been implemented to study the growth of two-dimensional perturbations. In the second set of experiments the film takes the form of a rung (stair) (see on fig. 2.1 scheme Ib), in the third set of experiments the film has initial perturbations in the form of a triangular profile (see on fig. 2.1 scheme Ic).

4 TURBULENT MIXING DEVELOPMENT

Figures 4.1, 4.2 demonstrate slot moving image frames and frame-by-frame moving image frames of some experiments. Gas dynamical calculations of the flow were conducted by using one-dimensional techniques «VIKHR» [9].

From moving image frames we notice that:

- At the same Mach number (M_1) of SW in gas 1 (air) in gas 2 (He, CO_2, SF_6) various Mach members are realized (M_2) and various compression of gases, this causes a different character of TM development in the final analysis (see fig. 4.1 a, b, c);
- With increase in M_2 contact boundary of gases and, respectively, a front of TMZ approach a shock wave front due to high compressibility of gases- at high M_2 by the moment of completion of visualization of the process an optical gap is not observed between SW and a forward shock wave front of TM in experiments Air-SF_6 (X_1) (s. figures 4.1 d, e);
- With increase in M_2 in Air -SF_6 experiments optically observed width of TMZ increases (s. figures 4.1, 4.2).

In experiments №414, 415 in zone Z (figures 4.1 d, e) one observes distortion of SW front traveling on SF_6. Analogous distortion of SW front is observed in SF_6 in experiment №424 when recording a flow in frame-by-frame mode (fig. 4.2 b). Front distortion can be connected with intensive interaction between turbulent vortexes and shock wave due to the vicinity of CB (contact boundary) and SW. It should be noted that in experiment №423 (figure 4.1 f), in which the thick dividing film (50 µm) was located at CB, we did not observe any distortions of SW– in this experiment the thick film did not fail, and TM was not practically developed at CB. (The film was cut along the perimeter of a channel of the measuring section and it moves after SW with mass velocity of flow).
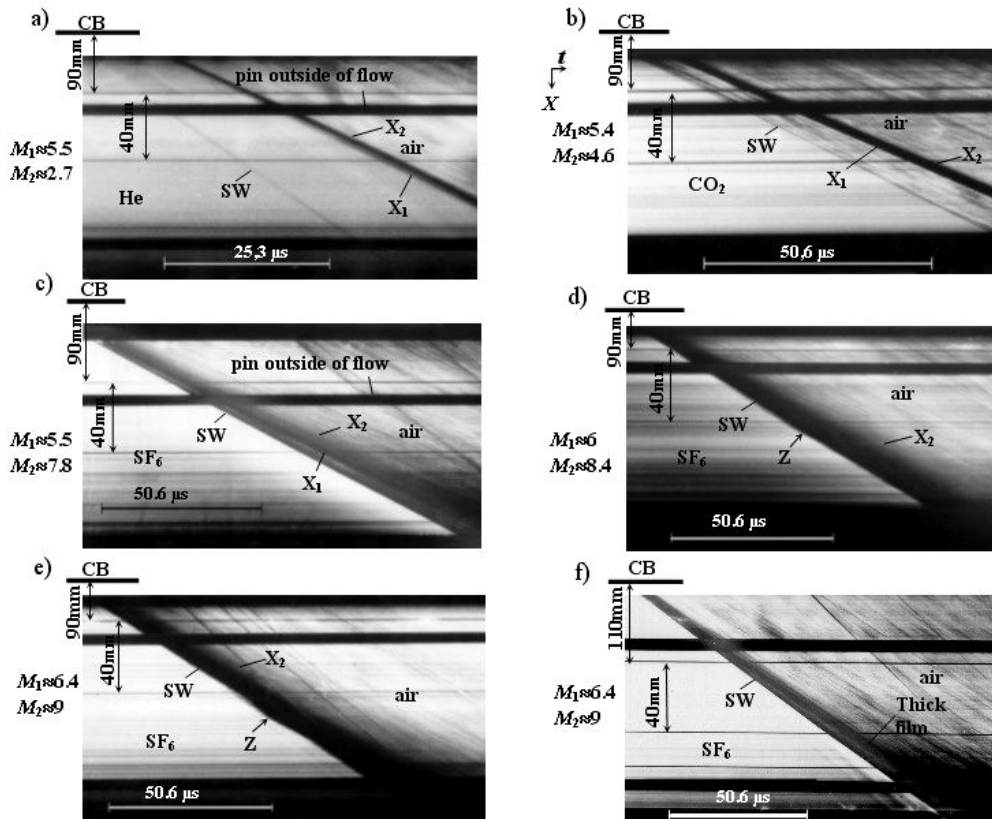
Fig. 4.1 – Slot moving image frames of the experiments: a) experiment №404 (air - He), b) experiment №413 (air - CO_2), c) experiment №409 (air –SF_6), d) experiment №414 (air –SF_6), e) experiment №415 (air –SF_6), f) experiment №423 (air – SF_6 with a thick dividing film).
Designations: Z – distorted shock front; X_1 – forward front of TMZ (turbulent mixing zone); X_2 – back front of TMZ
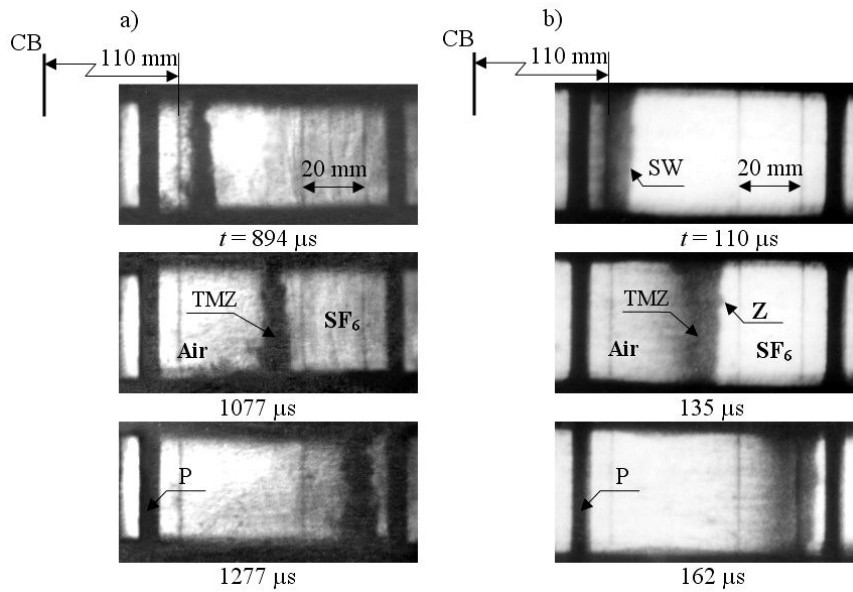
Fig. 4.2. Frame-by-frame moving image frame of flow at air- SF_6 interface:
a) experiment № 510 ($M_2 = 1.7$, SW on the right– outside of a frame);   b) experiment № 424 ($M_2 = 8.5$).
Designations: P – pin (outside (of) flow), Z – distorted shock front; t – time is reckoned from arrival of SW at CB

5 ANALYTICAL CALCULATIONS OF TMZ WIDTH

To describe evolution of TMZ let us use one of the versions of k-ε model [10]. In accordance with [10] the dependence of turbulent mixing zone upon time may be assessed through the following expression:

$$L = \frac{4}{k}\left[1 + \frac{a_*|A_+|Uk}{5.5p}(t - t_0)\right]^P, \qquad . \qquad (5.1)$$

where $k = \dfrac{2\pi}{\lambda}$ – wave number, U – CB (contact boundary) velocity, λ – wave length, A_+, $a_* = a_0\left(1 - \dfrac{U}{D}\right)$ – Atwood

number and perturbations amplitude after the interaction of SW (shock wave) with CB, time $t_0 = \dfrac{\mathrm{Re}_* \nu}{4(a_* A_+ Uk)^2}$.

The values $\mathrm{Re}_* \approx 10^4$, $\nu \approx 0.1 \times 10^{-5}$ m^2/s are used for transition Reynolds number and kinematic viscosity.

Figure 5.1 presents the dependencies upon the time of a width of TMZ obtained in calculation by formula (5.1) and in experiment. The results of fig. 5.1 a, b demonstrate that at a relatively large Atwood number a growth velocity of TMZ width in formula (1) depends on the index of power P with increase in M_2 (such dependence is observed in experiments with CB helium -SF$_6$). This dependence is not observed at a small Atwood number in the range M_2 from 2.6 to 4.6 (s. fig. 5.1 c). It is impossible to determine an exact value of index of power in (1) in the absence of exact initial values of amplitude and perturbations length.
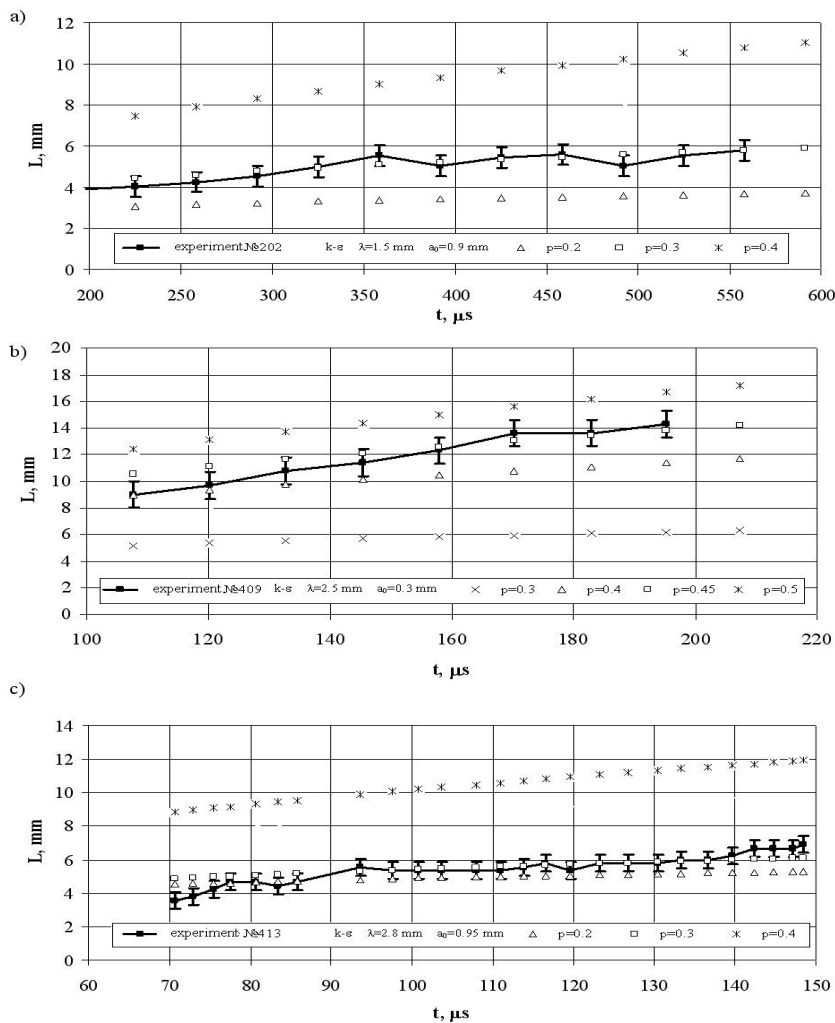

Fig.5.1. Growth of TMZ width: a) experiment №202 ($A \approx 0.83$, $M_2 \approx 1.8$);   b) experiment №409 ($A \approx 0.89$);
c) experiment №413 ($A = 0.32$) (time t is reckoned from the moment of coming SW to the contact interface)

6 PERTURBATIONS GROWTH

Figure 6.1 demonstrates some moving image frames of the growth of 2D perturbations from CB bend (rung\stair) and of the growth of 2D perturbations in the shape of triangular profile at various Mach numbers of SW. It can be seen from moving image frames demonstrated in fig. 6.1 that a vortex is developed at $M_2 \approx 1.6$ from 2D perturbations in the form of a rung (stair) before the moment of the completion of the experiment ($t \approx 458$ μs). One can observe the development of jet and vortex at $M_2 \approx 3.7$, at $M_2 \approx 9.5$ – only the development of a jet. When increasing M in relatively highly compressible gas SF$_6$ a vortex is changing promptly into a jet.

The growth of 2D perturbations in the shape of triangular profile (groove) depends also on SW Mach number in the highly compressible gas: at $M \approx 1.7$ perturbations are growing in the form of two vortexes in frontal projection. With increase in $M_2 \approx$ up to 3.7 – an actively growing turbulent mixing zone is dissipating vortexes partially, and at $M \approx 9$ the evident perturbations growth is not observed even after separation of SW from CB.
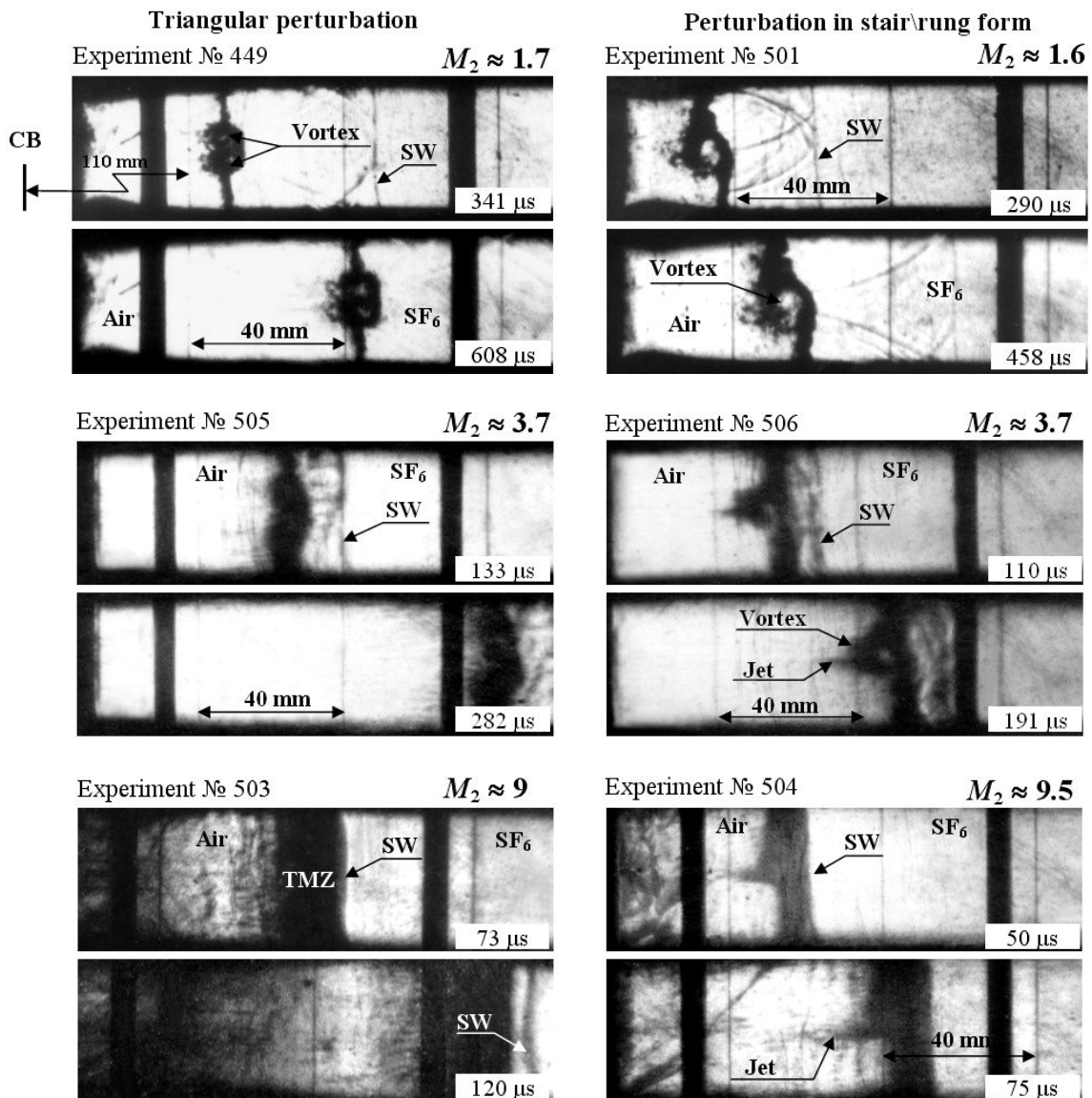

Fig. 6.1. Moving image frames of the experiments on perturbations growth at air- SF$_6$ interface (time is reckoned from SW arrival at CB): SW – shock wave; TMZ – turbulent mixing zone

7 CONCLUSIONS

It may be concluded in accordance with a series of experimental studies that a growth velocity of TMZ width increases at relatively high Atwood numbers with increase in Mach number of SW.

A shock wave front distorts strongly in highly compressible gas SF_6 at $M \approx 9$. This phenomenon results from active interaction of vortexes with the surface of SW close to CB. As SW Mach number increases, life time of vortexes to be formed in salient points of the Air– SF_6 interface, decreases (vortexes are dissipated quickly and merged into turbulent mixing zone).

Authors are indebted to E.E. Meshkov and V.A. Raevsky for their showed interest and helpful discussions.

REFERENCES

[1]   Taylor, G.I. 1950. The instability of liquid surfaces when accelerated in a direction perpendicular to their planes. *I. Proc.Roy.Soc.* **A201**, p.192.

[2]   Richtmyer, R.D. 1960. Taylor instability in shock acceleration of compressible fluids. *Commun. Pure Appl. Math.* **13**, p.297.

[3]   Meshkov, E.E. 1969. Instability of the interface of both gases accelerated by shock wave. *NEWS AH Soviet Union,* MZHG. №5, pp.151-158.

[4]   Zaytsev, S.G., Lazareva, E.V., Chernukha, V.V., Belyaev, V.M. 1985. Intensification of turbulent mixing at the boundary of media with different density as shock wave passes through the interface. *DAN Soviet Union.* **283**, №1, p.94-98.

[5]   Dudin, V.I., Meshkov, E.E.,A.N.Poduvalov et al. 1996. The study of development of perturbations and turbulent mixing at gas-gas interface using the method of laser blade. Preprint, *RFNC-VNIIEF.* № 49-96.

[6]   Inogamov, N.A., Demianov, A.Yu., Son, E.E. 1999. Mixing hydrodynamics. *Publishing House MFTI*, Moscow, p.464.

[7]   Bliznetsov, M.V., Nevmerzhitsky, N.V., Rasin A.N., et al. 2004. Study of Turbulent Mixing Development at the Interface Gas-Gas at Mach Numbers by Shock Wave from 2 till 9. *The Proc of the 9th IWPCTM*, England, Cambridge, July, 2004, in print.

[8]   Rakhmatulina, Kh.A., Semenova, S.S. 1962. Shock tubes. *Foreign literature*, Moscow, p.699.

[9]   Andronov, V.A., Kozlov, V.I., Nikiforov, V.V., Razin, A.N., Yudin, Yu.A. 1994. Techniques for calculation of turbulent mixing in one-dimensional flows (VIKHR technique). *Questions of Atomic Science and Engineering.* Series: Mathematical simulation (modeling) of physical processes. № 2, p.59.

[10]   Avramenko, M.I. 1998. About k-ε turbulence model. *Publishing House HAZW-VNIITF*, Snezhinsk, p.76.

e-mail: `root@gdd.vniief.ru`

Turbulent Mixing Development at Gas/Liquid Interface, when Changing the Atwood Number from +0.9 to -0.2

Nikolay V. NEVMERHZITSKIY, Alexsander N. RASIN, Evgeny A. SOTSKOV, Evgeny D. SENKOVSKIY, Olga L. KRIVONOS, Larisa V. TOCHILINA, Vasily A. USTINENKO

RFNC-VNIIEF, Sarov, Russia

Abstract: The paper presents experimental and 1D computational data on turbulent mixing development at gas/liquid interface, when the Atwood number is a variable (A). Water was used as the liquid and hexasulphurflorine (SF_6) or xenon (Xe) was used as the gas. The water layer was accelerated in the channel Ø50 mm with the gas compressed by a hard piston. During the compression of the gas its density rose thus leading to changing the Atwood number at the matter interface from +0.9 to -0.2, i.e.: experimentally xenon was compressed up to the density of ≈300g/l, while hexasulphurflorine – up to 1400 g/l. The pressure in the compressed gas reached ≈500 atm and the layer acceleration reached 1 mln m/s^2.

The experiments with xenon showed that the constant, which characterizes the rate of the gas front penetration into the liquid, is 0.02±0.01. In the experiments using hexasulphurflorine the gas front penetration into the liquid stops at negative Atwood numbers, though the mixing zone formed at $A>0$ continues to expand slowly into the SF_6.

1 INTRODUCTION

Turbulent mixing (TM) of matters, which occurs during the development of the Relay-Tailor and Richtmeier-Meshkov instabilities at the interfaces of matters with different densities [1,2,3], in particular leads to efficiency reduction of inertial confinement fusion targets. Presently, there is no reliable theory to describe such phenomena. For this particular reason in regard to the analysis of instability development and further transition to TM there are developed direct numerical computational methods, as well as different semi-empirical turbulence models. The both of those require calibration based on experimental data.

As is known to the authors, practically all experimental studies on TM development at a gas/liquid interface are performed for considerable density drops at the contact boundary, i.e. at the Atwood number close to unity [4]. TM at a gas/liquid interface is interesting especially at a small densities drop, even when a gas density becomes larger than that of a liquid. The present paper describes the outcome of several such experiments, as well as the respective numerical simulation data.

2 EXPERIMENTAL

The experimental facility layout is shown in fig. 2.1. The facility includes a chamber of combustible gas mixture (CGM); destructible diaphragm made of Dacron, stiff piston (organic glass), accelerating channel and substrate made of cloth laminate (water is pored onto the substrate). For a partial extinguish of shock waves the upper part of the piston is made of foam plastic ($\rho \approx 0.25$ g/cm^3). The thickness of a cut out edge of the substrate varied from 0.7 to 1.5 mm. The lower side of the tube is open: it is connected with the atmosphere. The water layer mass with the substrate is ≈101 g.

The volume of the channel between the water layer and stiff piston was filled with xenon or SF_6 gas, the CGM volume was filled with the mixture of acetylene and oxygen of non-stoichiometric composition. The initial pressure of the compressible gas varied from 2 to 4 atm.

After the CGM explosion the diaphragm was destroyed and the piston accelerated and compressed the gas beneath it. When reaching the gas pressure higher than the critical one ($P \approx 30$-100 atm), the substrate flange was cut out and the water layer with the substrate was accelerated in the vertical downward direction. The variation of the compressible gas initial pressures, explosive mixture and thickness of the cut out substrate flange allowed us to obtain both pulsed and growing acceleration in the experiments. The process of the layer acceleration and instability development was recorded by a fast camera in a transient light.
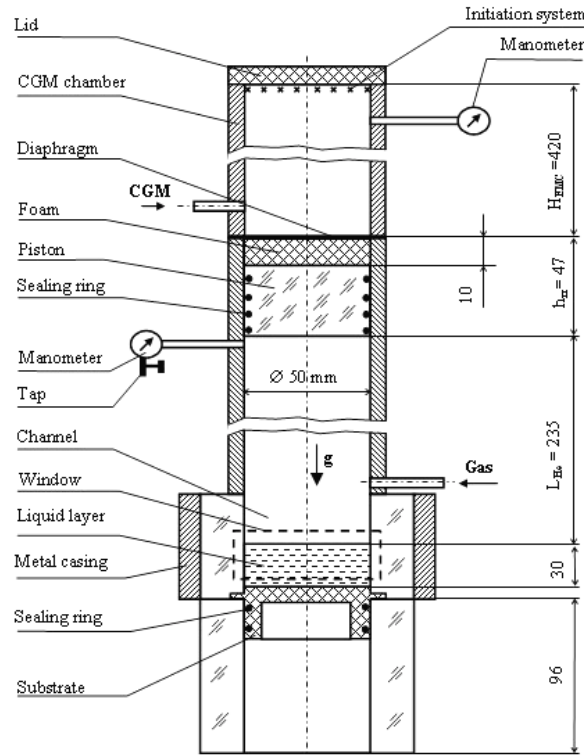
Fig 2.1. Experimental facility, sizes in mm

3 EXPERIMENTAL DATA

In figs. 3.1÷3.2 there are shown several frames recorded during the experiments, the plots $g = g(\sqrt{2S})$, $A = A(\sqrt{2S})$, the plots of the dependence of gas penetration depth into the liquid, as well as h and complete mixing zone width growth H on the layer displacement S in the form: $\sqrt{h}(\sqrt{A \cdot 2S})$, $\sqrt{H}(\sqrt{A \cdot 2S})$, correspondingly. When calculating the Atwood number $A = (\rho_g - \rho_w)/(\rho_g + \rho_w)$ the water density was considered to be equal to ρ_w=1000 g/l. The compressed gas density ρ_g was defined in accordance with [5,6] by the pressure and temperature values calculated in the adiabatic approximation by the layer acceleration and mass.

At the dependencies $\sqrt{h}(\sqrt{A \cdot 2S})$, $\sqrt{H}(\sqrt{A \cdot 2S})$ there are observed the parts close to linear ones. These might be interpreted as a well established mixing development mode. A tangent square of the above mentioned parts' slope angle towards the abscissa axis characterizes the rate β of the gas front penetration into the liquid, or rate β_H of the TM zone complete width growth in the expressions: $h = \beta_h \cdot A \cdot gt^2$, $H = \beta_H \cdot A \cdot gt^2$.

From the frames and plots it is obvious that:

• Mixing zone (as in similar experiments with helium [4]) has a small-scale structure: there are no big jets or bubbles (see figures 3.1a and 3.2a);

• Minimum Atwood number in the experiments with Xe reaches $A \approx 0.53$, in so doing the constant characterizing a penetration rate of gas front into liquid is 0.02±0.1 as in experiments with helium[4];

• In the experiments with SF_6 the Atwood number is decreased to $A \approx -0.2$, and then it increases up to $A \approx 0.8$: SF_6 is compressed up to the density more than water density, i.e. the situation is implemented, when the acceleration is directed from the heavy substance towards the light one, in this situation the interface of substances must be stable. As this takes place, the zone of turbulent mixing formed at $A>0$ continues to expand slowly into SF_6 (β_H=0.07, see fig. 3.3).

Fig 3.1. Experimental data for xenon: a) experimental frames; b) dependence of g on $\sqrt{2S}$; c) nature of the Atwood number changing at the xenon/water interface; d) dependencies $\sqrt{h}$ on $\sqrt{A \cdot 2S}$. Denominations: St- substrate; P – piston; TMZ – turbulent mixing zone; S – path traveled by the layer, LP – spontaneous local perturbations
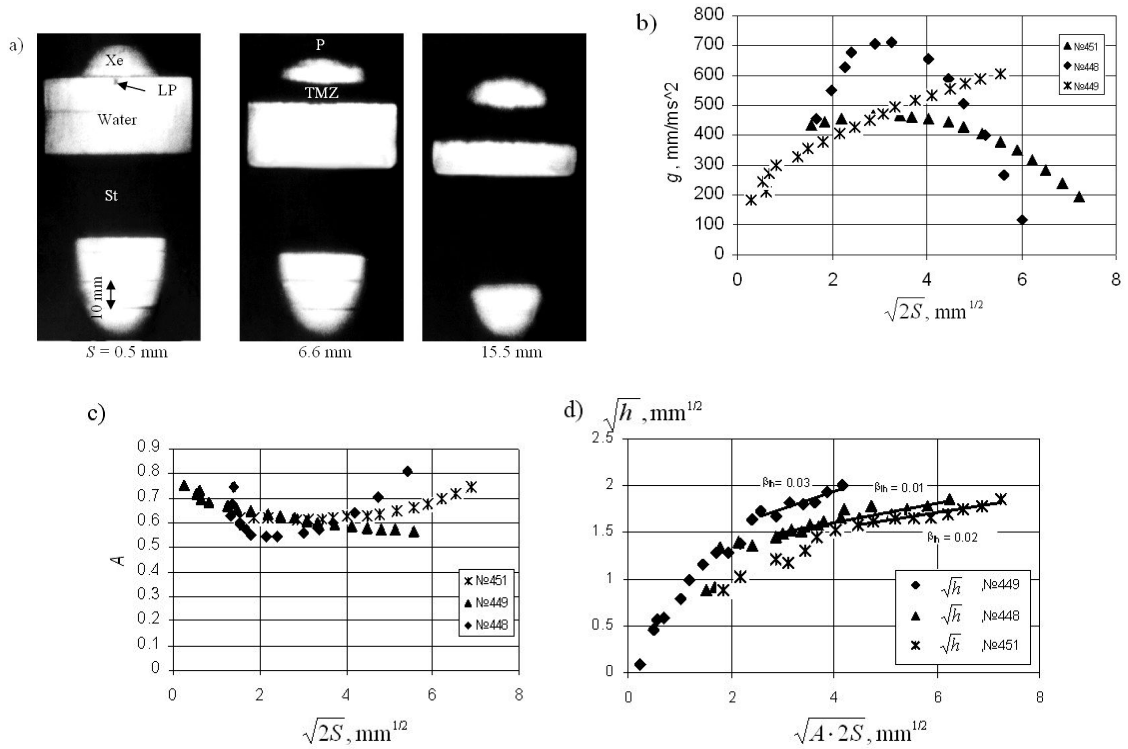

Fig 3.2. Experimental data for SF_6: a) experimental frames; b) dependence of g on $\sqrt{2S}$; c) nature of the Atwood number changing at the SF_6/water interface. Denominations: St- substrate; P – piston; TMZ – turbulent mixing zone; S – path traveled by the layer, LP – spontaneous local perturbations
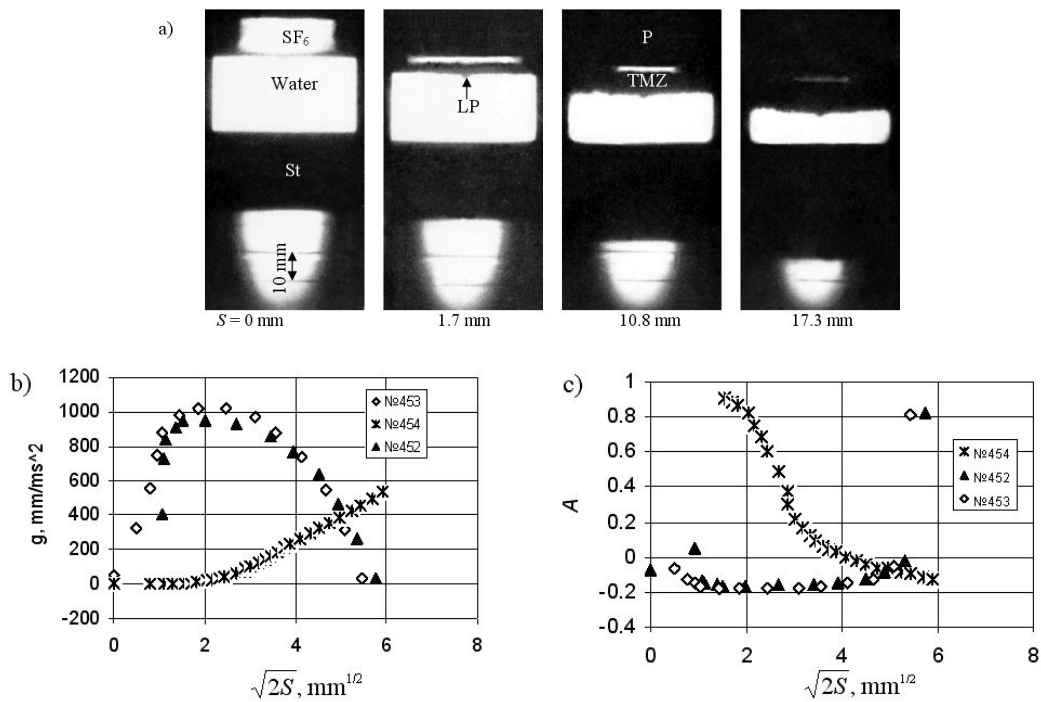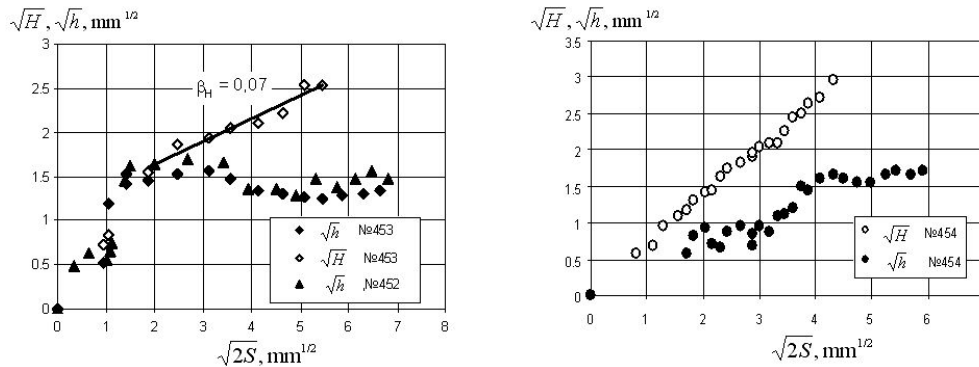
Fig 3.3. Experimental data for SF_6: dependencies $\sqrt{h}$ and $\sqrt{H}$ on $\sqrt{2S}$

4 COMPUTATIONAL DATA

Numerical simulation of TM at the interface $Xe-H_2O$ was ID using the code "Vortex" [7].
The heat conductivity processes and friction of the piston motion were not accounted for in the computations.
It is possible to assume experimentally the foam plastic presence at the piston and friction between the piston and channel walls leads to adiabatic compression of Xe layer.
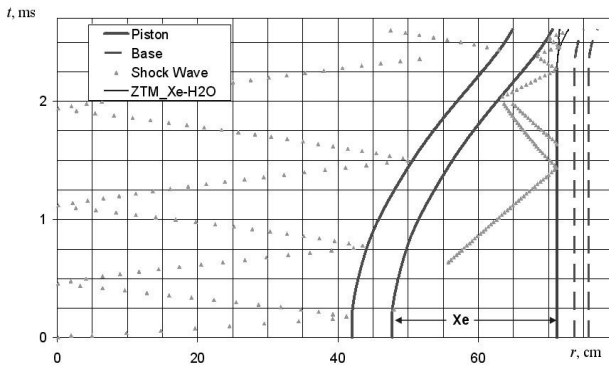

Fig. 4.1. r-t diagram of the interfaces and shock wave motion
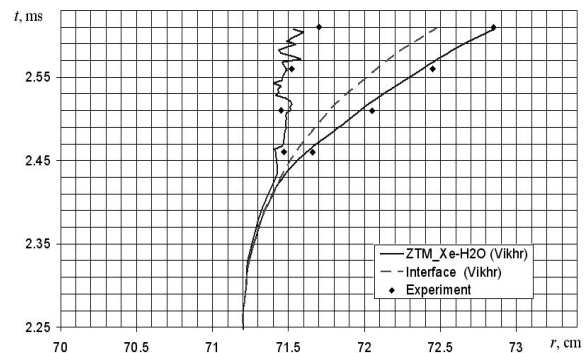
Fig. 4.2. r-t diagram of the $Xe-H_2O$ mixing zone boundaries and contact interface (CI)

5 SUMMARY

The experimental data were obtained on TM development at the liquid layer interface accelerated with the compressed gas, while the Atwood number changed from $\approx+0.9$ up to ≈-0.2. Experimentally, it was found that at negative Atwood numbers the gas penetration into the liquid stops, but the TM zone formed at $A>0$ continued to expand into the gas. The experimental data (Xe) agree well with the ID calculations.

REFERENCES

[1]   Lord Rayleigh. 1883, *Proc. London Math. Soc.* **14**, p.170.
[2]   Taylor, G.I. 1950. *Proc. Roy. Soc.* **A201**, p. 192.
[3]   Meshkov, E.E. 1969, Bulletin if the Academy of Sciences of the USSR, *MZhT*, **5**, pp. 151-158.
[4]   Bliznetsov, M.V., Nevmerzhitskiy, N.V., Sotskov, E.A. et al. 2003, Abstracts of the presentations for the V Scientific Khariton Readings: "Matters, Materials and Structures at Intensive Dynamic Loads" (*V Scientific Khariton Readings, Russia, Sarov, 17-21 March*).
[5]   Zherdev, E.P., Ulybin, S.A. 1973, Thermophysical properties of gases, "*Nauka*", Moscow, pp. 99÷104.
[6]   Zubarev, V.N., Kozlov, A.D., Kuznetsov, V.M. et al. 1989, Collected papers: Thermophysical properties of gases at high temperatures and gases, "*EnergoIzdat*", p.232.
[7]   Andronov, V.A., Kozlov, V.I., Nikiforov, V.V., Razin, V.V., Yudin, Yu. A. 1994, *VANT*, Series "Mathematical Modeling of Physical Processes, **2**, p.59.

e-mail: `root@gdd.vniief.ru`

Study of viscosity effect on turbulent mixing development at the gas/liquid interface

Maksim. V. BLIZNETSOV, Nikolay V. NEVMERHZITSKIY, Evgeny A. SOTSKOV, Larisa V. TOCHILINA, Valentin I. KOZLOV, Alexander K. LYCHAGIN, Vasily A. USTINENKO

RFNC-VNIIEF, Sarov, Russia

Abstract: We present the results of the experimental study of viscosity effect on turbulent mixing development (TM) occurring at Richtmayer-Meshkov instability at the boundary of a liquid layer accelerated by compressed gas.

In the experiments dynamic viscosity of liquid has varied from $\mu=1$ cP to $\mu=1.480$ cP. As liquid we used: water, glycerol, aqueous solution of glycerol having known viscosity. The value of acceleration of a liquid layer has amounted to: $g \cong 10^3 g_0$ and $g \cong 10^5 g_0$ ($g=9.8$ m/s^2). As gas we used helium compressed previously up to pressure $4.5 \div 500$ atm.

It has been demonstrated that when changing liquid viscosity a mixing zone structure changes. This influences on a mixing character of substances.

1 INTRODUCTION

So far as the authors know, in the course of interpretation of all experimental studies of turbulent mixing development at the gas/liquid interface and the liquid/liquid interface, stemming from R-T [1,2] instability the influence of molecular viscosity is believed to be negligible [3,4] thanks to a rather considerable value of turbulent Reynolds number (Re=$10^3 \div 10^4$). However, when comparing dynamics of turbulent mixing zone (TMZ) at low ($g \cong 10^2 g_0$, Re of the order of 10^3) and increased ($g \cong 10^5 g_0$, Re of the order of 10^5) accelerations of water layer [5] it has been showed that with increasing g TMZ becomes small-scale, a penetration rate of a gas front into liquid decreases more than twice. In [6] we have obtained that with decreasing Re from $2 \cdot 10^5$ to $1.4 \cdot 10^6$ a penetration rate of light substance into a heavy one decreases approximately twice. These effects can be connected with the influence of surface tension and viscosity on the structure of a turbulent mixing zone. This calls for further study. As this takes place, in viscous fluids a transition stage is of some interest: from perturbations growth to the turbulent mixing, on which the influence of viscosity can be the most significant. To study these matters, we have performed a series of experiments, their set-up and results are presented in this paper.

2 EXPERIMENTAL TECHNIQUE

The experiments with the acceleration $g \approx 10^3 g_0$ have been conducted in conformity with the scheme of figure 2.1a.

The instrument consists of a compressed gas chamber, a clear accelerating channel, transparent container made of Plexiglas and a failed diaphragm closing a lower channel end hermetically.

A layer mass together with a container has amounted to ≈ 70 g. To give initial perturbations, on a free surface of the layer we have placed randomly $40 \div 50$ solid particles (grain size – 0.4 mm, density is 0.91 g/cm^3). A chamber and a channel beneath a container have been filled with compressed helium with equal pressure (P=5.5 atm gauge (gauge atmosphere)). Then a diaphragm is failed - gas from under the container goes to atmosphere, the latter accelerates down under pressure above the container.

The experiments with the acceleration $g \cong 10^5 g_0$ have been conducted in conformity with the scheme of figure 2.1b.

The instrument consists of a compound accelerating channel, a chamber of gas explosive mixture (GEM), a cap, a rigid piston (polyethylene), a failed diaphragm and a substrate (textolite). The lower end of the channel is open: it is connected with atmosphere.

A layer mass together with a substrate has amounted to ≈ 120 g.

A channel between a layer and a rigid piston has been filled with helium at the initial pressure P=3.5 atm gauge (gauge atmosphere), a chamber with gas explosive mixture has been filled with a mixture of acetylene and oxygen of stoichiometric composition at the pressure P=4.1 atm gauge (gauge atmosphere).

The acceleration of a layer in this instrument occurs as follows. After blasting GEM the diaphragm is failed, a piston is
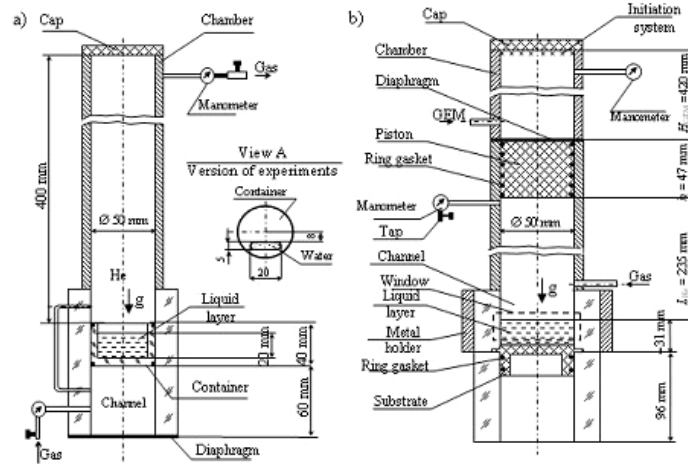
Fig. 2.1. Schemes of experimental instruments a) on creation of quasi-constant acceleration of liquid layer, b) on creation of pulse acceleration

accelerated and compresses gas under the piston. When we have a gas pressure higher than a critical pressure ($P \approx 100$ atm), a shoulder/pad of a substrate is cut off, and a layer together with a substrate is accelerated vertically downwards. In these experiments a maximum pressure of compressed helium reaches the order of 500 atm.

To improve optical resolution of TM zone structure, in both experimental set-ups we have also performed the experiments with a narrow water layer (width is 5 mm) in a version of the view A in fig. 2.1. A narrow groove of a transparent container has been filled with a layer of water in these experiments.

3 THE RESULTS OF THE EXPERIMENTS

Figures 3.1÷3.3 present some separate shots of moving image frames of several performed experiments, fig. 3.4 – inherent $g(2S)$ diagrams, figures 3.5, 3.6 show the dependencies of gas front penetration into liquid h_{lh} and show the dependencies of growth of a total width of mixing zone H on layer displacement S as: $\sqrt{h_{lt}}\,(\sqrt{A \cdot 2S}\,)$, $\sqrt{H}\,(\sqrt{A \cdot 2S}\,)$, respectively, here A – Atwood number.

Fig. 3.1. Some shots of moving image frames of experiments with $g \approx 10^3 g_0$ (displacement of the layer $S \approx 24$ mm). Designations: He – compressed helium; C – container; R – container ring; TMZ – turbulent mixing zone; J - jet
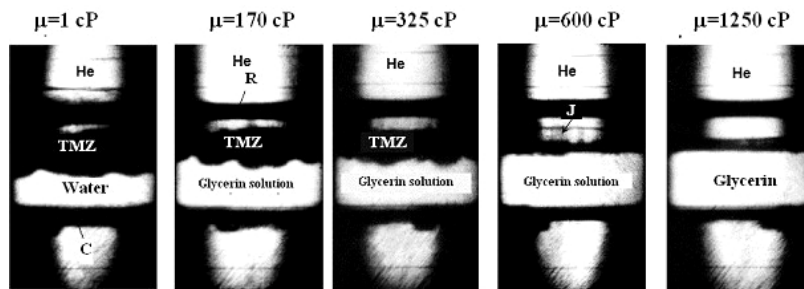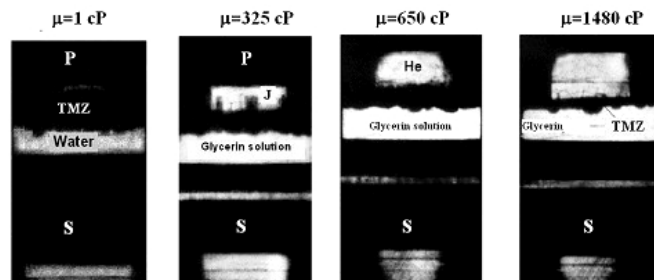

Fig. 3.2. Some shots of moving image frames of experiments with $g \approx 10^5 g_0$ (displacement of the layer $S \approx 17$ mm) Designations: He – compressed helium; S – substrate; P – piston; TMZ – turbulent mixing zone; J – jet
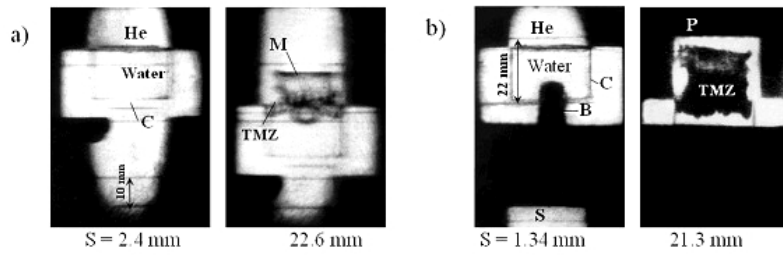
Fig. 3.3. Shots of moving image frames of experiments on mixing development in a narrow (width is 5 mm) layer of water (experimental set-up, figure 1, version view A): a) layer acceleration $g \approx 10^3 g_0$; b) layer acceleration $g \approx 10^5 g_0$ Designations: TMZ – turbulent mixing zone; P – piston; C – container; S – substrate; B – screw (out of flow); He-compressed helium; M – separation of water meniscus
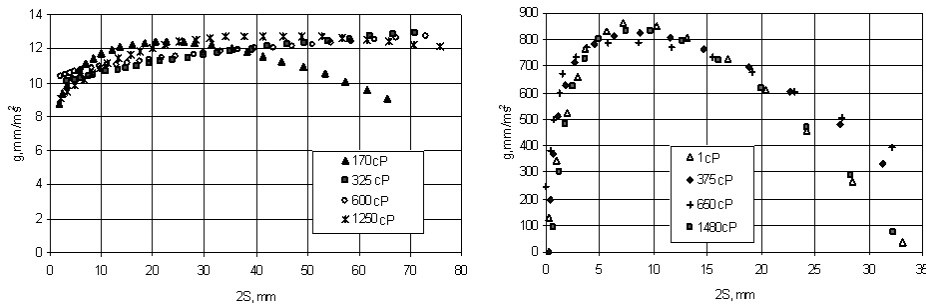
Fig. 3.4. Dependencies of liquid layer acceleration g on its displacement $2S$
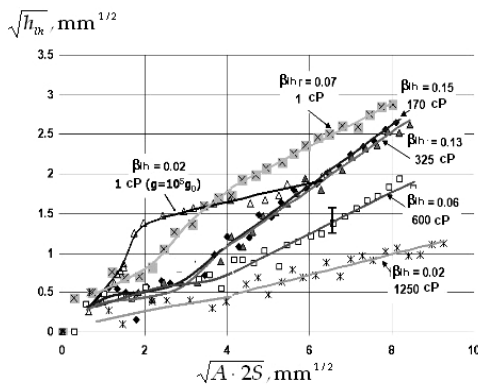
Fig. 3.5. Gas front penetration into liquid   **Fig. 3.6.** Growth of total width of mixing zone
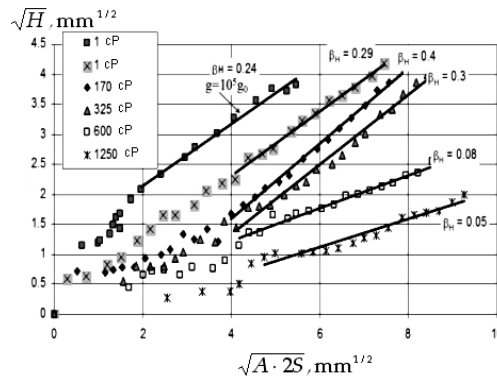
On the dependencies $\sqrt{h_{lh}}(\sqrt{A \cdot 2S})$, $\sqrt{H}(\sqrt{A \cdot 2S})$ we observe the areas close to linear areas. They can be regarded as a steady-state mode of R-T instability growth (of perturbations or TM). A square of a slope ratio of these areas towards the abscissa axis characterizes a rate constant (pace) of gas front penetration into liquid – β_{lh} or growth rate of total width of TM zone (perturbations) – β_H : under conditions $h_{lh} = \beta_{lh} \cdot A \cdot g t^2$, $H = \beta_H \cdot A \cdot g t^2$.

Experiments with $g \approx 10^3 g_0$. Referring to fig. 3.1 it will be observed that perturbations growth occurs principally at $\mu > 600$ cP in an observed range of layer displacements, and at $\mu < 600$ cP – TM development.

In glycerol and its aqueous solutions at displacement S≤8 mm h_{lh} (light into heavy) grows slowly, and then we observe a fast rise in this quantity. The opposite situation occurs with water: firstly h_{lh}(light into heavy) increases quickly, and then a growth velocity decreases. This connects with the known influence of fluid viscosity on perturbations growth: viscosity suppresses short-wave perturbations growth, available long-wave perturbations grow slowly in the initial stage. Big bubbles are formed at the stage of TM from long-wave perturbations. The big bubbles grow into liquid faster than small ones. In the experiment with a narrow layer of water big bubbles and thick jets of a mixing zone are easily observable (s. fig. 3.3a).

Under small initial perturbations the viscosity inhibits the instability growth in time (s. fig. 3.1).

With decreasing dynamic viscosity of liquid:

- The optically observable total width of the mixing zone increases (s. fig. 3.1), that can be connected both with the increase in a penetration rate of liquid into gas, and with a more faster penetration rate of a gas front into liquid in the initial stage of layer acceleration and with liquid drops (formed as a result of jets breakup), which move in gas slowly;
- Penetration rate of a gas front into liquid β_{lh}(light into heavy) increases from 0.02 to 0.15 at first, and then decreases up to 0.07 (s. fig. 3.5); a growth rate of a total width of a mixing zone β_H behaves qualitatively similar to β_{lh}(light into heavy) (s. fig. 3.6).

Experiments with c $g \approx 10^5 g_0$. According to the results of these experiments one can say that:

- A mixing zone in glycerol and its aqueous solutions develops faster than in the experiments with $g \approx 10^3 g_0$ (s. figs. 3.1,3.2);
- In contrast with water, in the experiments with glycerol and its aqueous solutions, as in the first experiments bigger bubbles and jets are formed (s. fig. 3.2): in the experiment with a narrow water layer the turbulent mixing zone is small-scale (s. fig. 3.3b);
- Value $\beta_{lh\text{(light into heavy) (water)}}$ is about 0.02, $\beta_H - 0.25$.

4 ASSESSMENT OF CHARACTERISTIC PERTURBATION SCALES

In the case of R-T instability of viscous liquids the increment of growth of perturbations amplitude with the wave number k is equal in linear approximation to $\gamma = \sqrt{Akg + \nu^2 k^4} - \nu k^2$.

It would appear reasonable that at the instant of transition to TM, a maximum size of heterogeneities on the order of magnitude is equal to a wave length of the most rapidly growing harmonic, which is determined by the condition $\partial\gamma/\partial k = 0$, whence it follows that $d_{max} = 2\pi\sqrt[3]{\nu^2/Ag}$.

Hence it follows that viscosity growth of liquid at fixed values of acceleration (in accordance with the data of fig. 3.1) brings about a growth of a characteristic size of heterogeneities in TM zone.

The transition time to the turbulent conditions of perturbation evolution on the order of magnitude is in inverse proportion to a maximum value of the increment of growth of perturbations amplitude $\tau = \sqrt[3]{\nu/(Ag)^2}$.

Therefore, the growth of liquid viscosity at fixed values of acceleration leads to the increase in the transition time towards TM (with increasing viscosity from 1 cP to 1.250 cP the transition time increases by a factor of 11, accordingly, the value of $2S = gt^2$ increases by a factor of 120). Seeing that in the time τ perturbation amplitude increases only a 3.7 times, over the course of the most part of the transition time perturbation amplitude does not change in the order of magnitude. The increase in acceleration brings about the reduction of the transition time (a hundredfold increase of layer acceleration results in the twenty-one-fold decrease in the transition time, but the quantity $2S = gt^2$ decreases only fourfold).

5 SUMMARY

1 With increasing liquid viscosity (with decreasing Reynolds number) the transition time towards the turbulent conditions of mixing grows and large-scale structures arise in TM zone.

2 In relatively viscous fluids a penetration rate of a gas front into liquid and a growth rate of a total width of a mixing zone may increase because of the formation of big bubbles and jets, whose growth velocity is higher than the growth velocity of small ones.

REFERENCES

[1]   Rayleigh, Lord. 1883, *Proc. London Math. Soc.*, **14**, p.170.
[2]   Taylor, G.I. 1950, The instability of liquid surfaces when accelerated in a direction perpendicular to their planes,/ *Proc. Roy. Soc.*, **A201**, p. 192.
[3]   Read, K.I. 1984, *Experimental* investigation of turbulent mixing by Rayleigh-Taylor instability, *Physica*, **D12**, p. 45.
[4]   Kucherenko, Yu.A., Tomashev, G.G., Shibarshov, L.I. 1988, Experimental study of gravity turbulent mixing in automodel conditions, *VANT*, **iss.1**, p.13.
[5]   Nevmerzhitsky, N.V. Sotskov, E.A. Drennov, A.O. 2003, Studies of turbulent mixing development at the gas/liquid interface at accelerations from $10^2 g_0$ to $10^5 g_0$, *Abstracts of papers for International Conference V Khariton's Topical Scientific Readings, Substances, materials and constructions at intensive dynamic effects* (Russia, Sarov, March 17-21), p.190.
[6]   Stadnik, A.L., Statsenko, V.P., Yanilkin, Yu.V. 2004, Consideration of molecular viscosity in the course of direct three-dimensional numerical modeling of gravity turbulent mixing, *Paper for the 9th International Seminar on Physics of Turbulent Mixing of Compressible Media* (England, Cambridge, July), in the press.

e-mail: `bonazza@engr.wisc.edu`

A Computational Parameter Study for Shock-Bubble Interactions in 3D, with and without Modeled Soap Film

John NIEDERHAUS[1], Jeffrey GREENOUGH[2], Jason OAKLEY[1], Devesh RANJAN[1], Mark ANDERSON[1] and Riccardo BONAZZA[1]

[1] *University of Wisconsin-Madison, Madison, WI 53706 USA*

[2] *Lawrence Livermore National Laboratory, Livermore, CA 94550 USA*

Abstract: Results from 3D simulations of shock-bubble interactions for varying Atwood (A) and Mach numbers (M) are presented here. Twelve scenarios are considered, including $-0.8 < A < 0.7$ and $1.1 < M \leq 5.0$. Each scenario is realized twice: once with the bubble as a bare spherical volume, and once with a thin soap-film-like cladding added to the bubble surface. In the filmless scenarios, integral quantities in the flowfield are tracked over time, including the mean bubble fluid density, the velocity circulation, and the mixedness. For fixed A, temporal trends in the mean density and mixedness at varying Mach numbers are found to collapse nearly to self-similar trends under scalings based on parameters derived from a 1D gasdynamics analysis. Transient phenomena observed in the trends indicate strong sensitivity to A, due to changes in shock refraction patterns with changing A. Further, circulation trends indicate that secondary vortical effects and azimuthal bending-mode instabilities become dramatically more significant with increasing A. Finally, comparison of simulations with and without modeled soap film indicates large deviations due to effects of the film only for $|A| < 0.2$.

1 INTRODUCTION

The shock-bubble interaction is the unsteady flow that results from the passage of a shock wave across a discrete, round inhomogeneity in an otherwise uniform medium of propagation. The development of the flowfield is driven by three nonlinearly coupled and simultaneous physical processes: (1) shock compression of the inhomogeneity; (2) complex reflection, refraction, and diffraction of the shock wave by the inhomogeneity ("nonlinear-acoustic effects"); and (3) baroclinic vorticity generation ($\nabla \rho \times \nabla p \neq 0$) and subsequent vorticity transport, leading to the formation of coherent vortex structures. For spherical bubbles, considered here, the latter results in the formation of a dominant vortex ring, as depicted schematically in Figure 1.1(b), along with secondary vortical features, whose properties depend on the incident shock Mach number, M, and the Atwood number $A = (\rho_2 - \rho_1)/(\rho_2 + \rho_1)$, where ρ_1 and ρ_2 are the unshocked ambient and bubble densities, respectively.
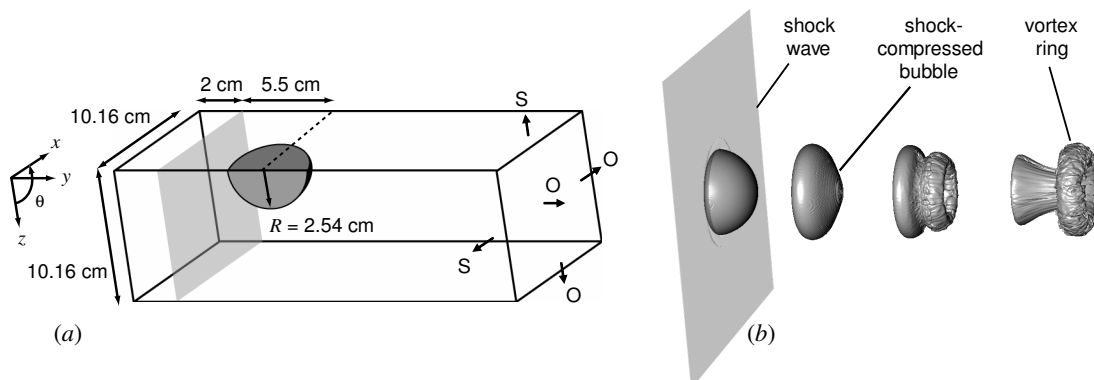
Fig. 1.1. (a) Schematic diagram of initial condition used in 3D, 1/4-symmetry calculations for shock-bubble interactions. "S" indicates symmetry boundaries; "O" indicates outflow boundaries. (b) 3D-rendered sequence showing compression of a helium bubble by a rightward-moving M=1.68 shock wave, and subsequent vortex ring formation.

This flow can be viewed as a simplification of systems in which shocks propagate in inhomogeneous media, where these same processes operate in a more complex setting. Such systems are found in natural and engineered

Scenario number	Gas pair	M	A	W_i [m/s]	u'_1 [m/s]	Scenario number	Gas pair	M	A	W_i [m/s]	u'_1 [m/s]
1	Air-He	1.20	-0.757	411.6	104.8	7	Air-Kr	1.20	0.486	411.6	104.8
2		1.50		514.5	238.3	8		1.50		514.5	238.3
3		1.68		576.2	310.2	9		1.68		576.2	310.2
4	N_2-Ar	1.33	0.176	463.9	168.1	10	Air-R12	1.14	0.613	391.0	75.15
5		2.88		1005	736.5	11		2.50		857.5	600.5
6		3.38		1179	896.8	12		5.00		1715	1373

Table 2.1. Parameter study overview, including, for each scenario, the incident shock Mach number M, the Atwood number A at the unshocked interface, and lab-frame speeds W_i and u'_1 of the incident shock and the shocked ambient gas, respectively, computed from 1D gasdynamics.

environments including the shocked interstellar medium, supersonic combustion engines, shock wave lithotripsy treatments, and inertial confinement fusion devices. In the present work, a computational parameter study is carried out using 3D numerical simulations configured as shown in Figure 1.1(a). Twelve scenarios are considered, including $-0.8 < A < 0.7$ and $1.1 < M \leq 5.0$, listed in Table 2.1. The parameter space includes nearly all of the experimental and 2D numerical work performed previously on this problem, for gaseous flow regimes that are accessible to mechanical shock tubes. The 2D numerical database existing for this problem is extended, here, to 3D in order to characterize complex turbulence-like features that are known to grow in the flowfield [1]. In the current work, integral quantities including compression, circulation, and mixedness are measured, and the effects of a film-like cladding on the bubble are investigated.

2 NUMERICAL METHOD AND SETUP

Simulations are performed in 3D using an adaptive hydrodynamics code called *Raptor*, which integrates the compressible Euler equations forward in time using an operator-split, second-order Godunov method (see Colella, 1985 [2] and Bell *et al.*, 1989 [3]). Multifluid capturing capability is added to the scheme by adopting a volume-of-fluid technique similar to that described by Miller and Puckett (1996) [4], which allows multiple fluids with distinct adiabatic exponents to be included in the calculation. The integration kernel is embedded within the block-structured adaptive mesh refinement (AMR) framework of Berger and Oliger (1984) [5], to maximize spatial resolution and accuracy for regions of interest that move across the Eulerian mesh.

The calculations using *Raptor* are set up on a Cartesian mesh subtending a quadrant of a typical shock tube flow field, including a quarter-spherical bubble of radius $R = 2.54$ cm. Refinement of the grid in the bubble region yields an effective spatial resolution of Δ=198 μm, implying that 128 refined grid cells are subtended in a distance R. In the initial condition, shown schematically in Figure 1.1(a), a planar shock wave approaches a quarter-spherical bubble of helium, argon, krypton, or R12, embedded in an otherwise uniform air or nitrogen environment at standard temperature and pressure. The shock wave moves in the $+y$-direction, and the bubble is centered on the y-axis. A smooth interface is created in the initialization using a subgrid volume-of-fluid model to suppress "stairstep" features associated with realizing a curved interface in a Cartesian mesh. This produces an interface with a maximum thickness of two grid cells, or $R/64$. Boundary conditions indicated in Figure 1.1(a) are applied to enforce symmetry and to exclude shock reflections at the boundaries.

Twelve scenarios are considered in the present study, including four gas pairings, with three shock strengths each. These scenarios, outlined in Table 2.1, are chosen to coincide with previous experimental or 2D numerical work. Although direct comparison of experimental and numerical results is beyond the scope of the present study, the results may be compared to experimental results independently or in future publications.

3 FLOWFIELD VISUALIZATIONS

Representative flowfield visualizations at high and low $|A|$, from two of the twelve scenarios, are shown in Figures 3.2 and 3.3, using slices on a plane oriented at $\theta = \pi/6$ to the $x = 0$ boundary, where θ is the azimuthal coordinate. The vorticity magnitude $\omega = \vec{\omega} \cdot \hat{\theta}$ and the density ρ are plotted on this slice, where $\hat{\theta}$ is the azimuthal unit vector, and $\vec{\omega} = \nabla \times \vec{V}$. A single contour of the bubble fluid volume fraction f is overlaid on each density plot to indicate the interface location. Plots are labeled by the dimensionless time $\tau = tW_i/R$,

where W_i is the speed of the incident shock wave and t is the time relative to initial shock impact on the upstream bubble surface.
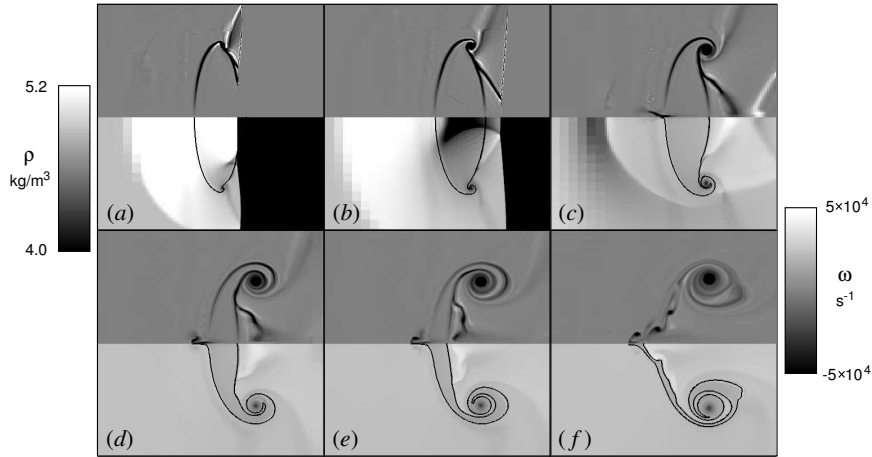

Fig. 3.2. Vorticity magnitude $\omega = \vec{\omega} \cdot \hat{\theta}$ (top) and density (bottom) on the $\theta = \pi/6$ plane, for the M=3.38, N$_2$-Ar scenario (A=0.176); superimposed on each density plot is the f=0.5 contour, in black: (a) τ=1.6, (b) τ=2.6, (c) τ=5.0, (d) τ=10.0, (e) τ=15.0, (f) τ=25.0. Shock propagation is left-to-right.

In Figure 3.2, ρ and ω fields from the N$_2$-Ar, M=3.38 (A=0.176) scenario are plotted. These are representative of the flowfields observed at low magnitudes of the Atwood number ($|A| < 0.2$), where nonlinear-acoustic effects are weak. The shock front seen in Figure 3.2(a-b) exhibits only subtle changes in shape, and vortical development is mostly limited to the formation of the primary vortex ring, visible as the dominant feature in Figure 3.2(d-f). The post-shock density contrast is also seen to be extremely small in this scenario. In Figure 3.3, however, ρ and ω fields from the air-R12, M=2.5 (A=0.613) scenario are plotted. Despite the decreased Mach number, the complexity of the flowfield is dramatically amplified, due to the strong nonlinear-acoustic mechanisms operating at this high A. These include, in particular, shock diffraction and shock focusing processes (see Figure 3.3a-b), which generate strong secondary shocks that traverse the bubble region at later times. A strongly disordered state also arises in the vorticity field, visible in Figure 3.3(d-f), due to enhanced density gradients at the interface, which intensify baroclinic vorticity generation associated with the incident shock, secondary shocks, and vortex-centripetal accelerations (see Peng, *et al.*, 2003 [6]). Qualitatively, these results indicate that shock-bubble interactions exhibit patterns of development at low $|A|$ that are fundamentally distinct from those seen at high $|A|$. Because the processes of shock refraction and vorticity generation are nonlinearly coupled via gradients in the density field, and density gradients persist to late times due to secondary shocks, differences in the initial value of A lead to vastly different end states in these flows.

4   INTEGRAL DIAGNOSTICS

In order to characterize these patterns of development over time, integral quantities in the flow are tracked over as many as 110 coarse-grid timesteps in each of the twelve scenarios, and plotted on dimensionless timescales. These include trends in the mean density of the bubble fluid, the velocity circulation, and the mixedness.

The mean density of the bubble fluid is computed as $\langle\rho(t)\rangle = \rho_2\pi R^3/(\int f(x,y,z,t)d\mathcal{V})$, where $\pi R^3/3$ is the initial volume of the quarter-sphere, $f(x,y,z,t)$ is local bubble fluid volume fraction, and $d\mathcal{V}$ is a differential element of volume. Values of $\langle\rho(t)\rangle$ are normalized to the density ρ' predicted from a 1D gasdynamics analysis of planar-shock transmissions and reflections in the corresponding gas slab-inhomogeneity, following Giordano and Burtschell (2006) [7]. A measure of the bubble fluid density relative to the 1D prediction is obtained by

$$\rho^* = \frac{\langle\rho(t)\rangle - \rho_2}{\rho' - \rho_2}. \tag{4.1}$$

Plots of the normalized mean density ρ^* shown in Figure 4.4 indicate that the mean density goes through an initial transient phase before equilibrating near the 1D gasdynamics prediction (ρ^*=1). It can also be observed
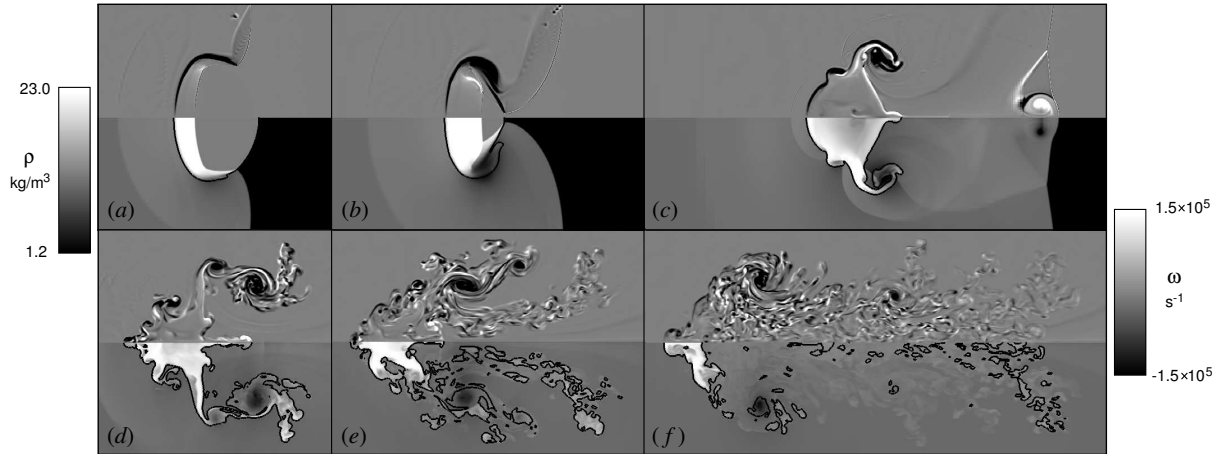
Fig. 3.3. Vorticity magnitude $\omega = \vec{\omega} \cdot \hat{\theta}$ (top) and density (bottom) on the $\theta = \pi/6$ plane, for the M=2.5, air-R12 scenario (A=0.613); superimposed on each density plot is the f=0.1 contour, in black: (a) τ=1.5, (b) τ=2.5, (c) τ=5.1, (d) τ=9.9, (e) τ=15.1, (f) τ=25.1. Shock propagation is left-to-right.

that $\rho^*(\tau)$ is nearly invariant under changes in M, for fixed $A > 0$. Oscillations in ρ^* during the transient phase for $A > 0$ can be shown to be driven by the $\nabla \cdot \vec{V}$ field. Since internally-reflected rarefactions ($\nabla \cdot \vec{V} < 0$) arise in $A > 0$ scenarios, the bubble fluid is subjected to decompressions after the initial shock transit in these cases, resulting in the oscillations observed in Figure 4.4(b-c). The intensity of these oscillations increases with increasing A. However, no internal rarefactions arise at these Mach numbers for the $A < 0$ cases, and the trend in ρ^* for $A < 0$ seen in Figure 4.4(a) is nearly monotonic. Further, ρ^* equilibrates to values greater than unity. Thus, trends in the mean density indicate the strong effect of shock refraction geometry, signified by the sign of A, on the development of the flow during the early transient phase.
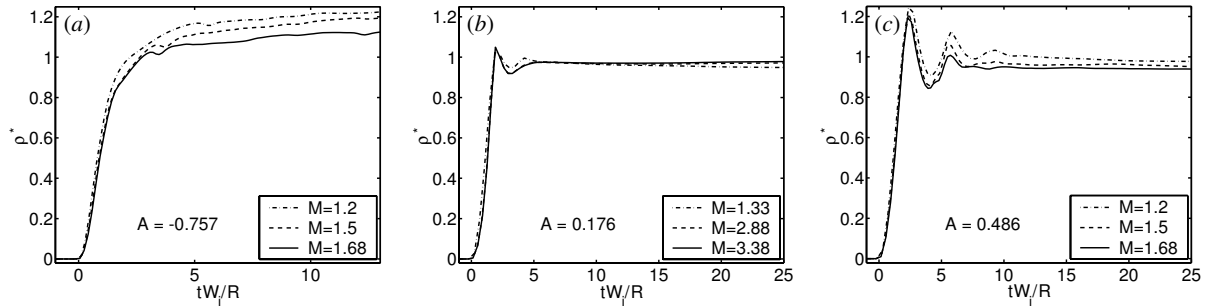
Fig. 4.4. Plots over dimensionless time of the mean bubble fluid density, normalized with respect to the prediction from 1D gasdynamics using Equation 4.1: (a) air-He, (b) N_2-Ar, (c) air-Kr.

A similar transient phase, followed by a stable phase at later times, is observed in the trends of the net velocity circulation, Γ. The circulation is measured in the 3D datasets by extracting data on 48 evenly-spaced slice planes perpendicular to $\hat{\theta}$, and evaluating the area integral

$$\Gamma_S(t) = \int_S \vec{\omega}(x,y,z,t) \cdot \hat{\theta}_S dA, \tag{4.2}$$

on each slice plane S. Data in the region with $f = 0$ are excluded, and the positive (Γ_+) and negative (Γ_-) components of circulation are obtained by including data only in regions with $\omega > 0$ and $\omega < 0$, respectively. Azimuthally averaged values of the circulation Γ and its components are then computed as the arithmetic mean over the 48 planes, and RMS fluctuations $\tilde{\Gamma}$ as the standard deviation.

Figure 4.5 shows that for $|A| > 0.2$, the generation of secondary vorticity is vastly enhanced, even at a lower Mach number. Secondary vorticity appears only in the components of the circulation, however, and eddies

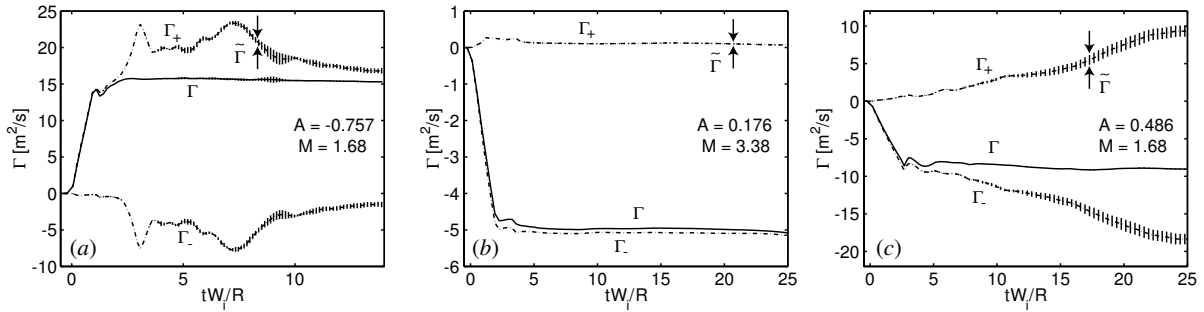**Fig. 4.5.** Plots over dimensionless time of the decomposed circulation, $\Gamma_{\pm}$, and RMS fluctuations $\tilde{\Gamma}$ plotted as vertical error bars: (*a*) M=1.68, air-He, (*b*) M=3.38, N_2-Ar, (*c*) M=1.68, air-Kr.

of opposite senses of rotation grow in strength at nearly equal rates after the first shock transit, so that the net circulation remains largely constant. Fluctuations from the azimuthal mean, associated with Widnall-type bending-mode instabilities [8], are also much more significant for $|A| > 0.2$. Hence, circulation trends indicate strong differences in phenomenologies associated with the magnitude of A, rather than its sign.
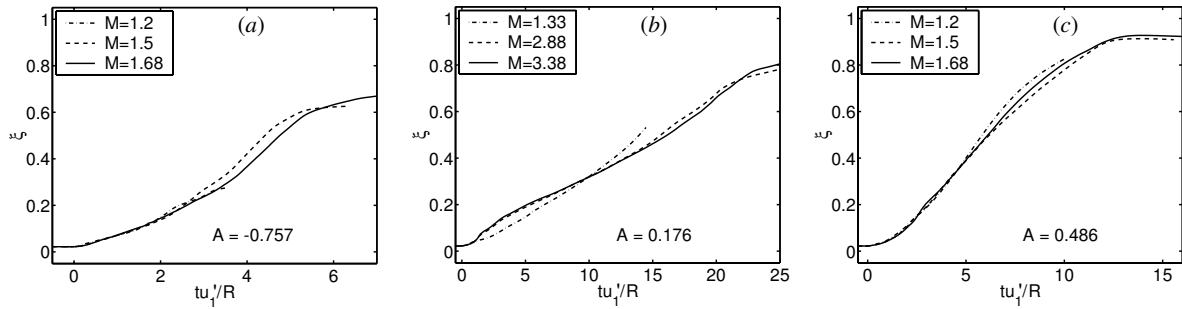

Fig. 4.6. Dimensionless-time plots of the mixedness ξ, defined in Equation 4.3: (*a*) air-He, (*b*) N_2-Ar, (*c*) air-Kr.

A third feature of concern in shock-bubble interactions is mixing of the bubble fluid into the ambient fluid. The mixedness $\xi(t)$ is defined here as the ratio of mixed to total bubble fluid volumes:

$$\xi(t) = \frac{\int \delta(f) f(x,y,z,t) d\mathcal{V}}{\int f(x,y,z,t) d\mathcal{V}}, \quad \delta(f) = \begin{cases} 1, & 0.1 < f < 0.9 \\ 0, & \text{else} \end{cases}. \tag{4.3}$$

Plots of ξ in Figure 4.6 for N_2-Ar and air-Kr scenarios indicate that mixing trends are nearly self-similar on a timescale based on the post-shock ambient flow speed u_1' (rather than W_i), for fixed A. Mixing proceeds at a relatively slow rate on this dimensionless time scale for $|A| < 0.2$, and this rate increases with $|A|$, due to enhanced Kelvin-Helmholtz growth and the increased complexity and total interfacial surface area at high $|A|$.

5 FILM EFFECTS

Effects associated with soap film used in experiments [9–11] to confine the bubble gas are characterized by repeating each scenario with modeled film material included. A third material is added in a concentric shell around the bubble of thickness $\delta R_f \approx 2\Delta$, with density corresponding to the true total mass of film material.

Circulation trends are computed from the resulting datasets as an indicator of the increased strength of vorticity generation due to the added film mass. Representative data from several scenarios are plotted on the dimensionless timescale tW_i/R in Figure 5.7. The late-time values of the total circulation Γ are nearly unchanged from the filmless results, and, for $|A| > 0.2$, trends in the components $\Gamma_{\pm}$ exhibit only subtle changes relative to the filmless data shown in Figure 4.5. In the A=0.176 scenario (Figure 5.7*b*), however, the peak transient-phase magnitudes of Γ_+ and Γ_- are increased dramatically relative to the filmless result. We conclude
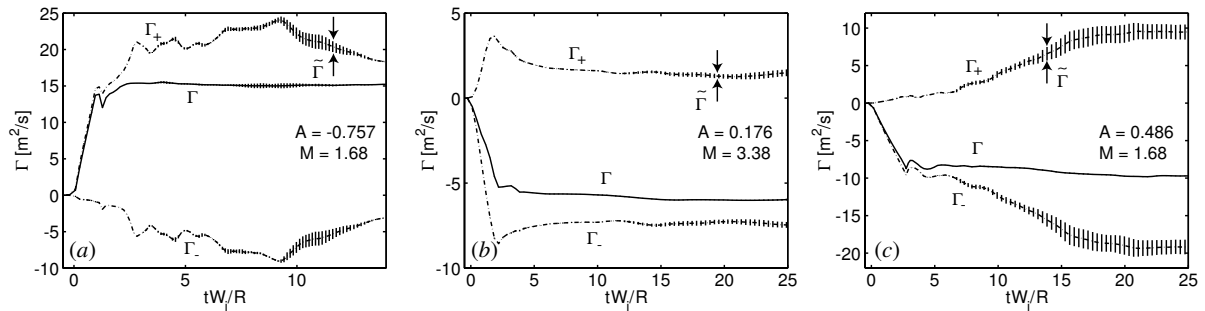
Fig. 5.7. Plots over dimensionless time of the decomposed circulation and RMS fluctuations, for scenarios with modeled film material included in the simulation: (*a*) M=1.68, air-He, (*b*) M=3.38, N_2-Ar, (*c*) M=1.68, air-Kr.

that film effects are significant for $|A| < 0.2$, where vorticity generation during the shock-bubble interaction is weak enough to become comparable in intensity to the effects of the added mass.

6 SUMMARY

Overall, the present results indicate that though scaling laws may be possible for various integral quantities in shock-bubble interactions at fixed A, such self-similar behavior cannot be expected across parameter spaces with variable A. This is due to the complexity of nonlinear-acoustic effects, which exhibit distinct phenomenologies that are highly sensitive to the initial contrast in densities and sound speeds. Further, we see that various timescaling parameters can be useful for analyses of trends in different features of the flow. Timescales based on W_i are successful for trends in the mean density, but u'_1 proves more useful for scaling in mixing trends. The results also indicate that the effect on circulation trends due to the additional mass associated with soap film is minimal in all scenarios, except in those with particularly low initial Atwood number magnitude. In future publications, the analysis of trends in integral features of the flow presented here will be extended further, to include the properties of the 3D, azimuthally-asymmetric features observed in these datasets.

REFERENCES

[1] Haas, J.-F., Sturtevant, B., 1987. Interaction of weak shock waves with cylindrical and spherical inhomogeneities, *J. Fluid Mech.* **181**, pp. 41-76.

[2] Colella, P., 1985. A direct Eulerian MUSCL scheme for gas dynamics, *SIAM J. Sci. Stat. Comput.* **6**(1), pp. 104-117.

[3] Bell, J.B., Colella, P., Trangenstein, J.A., 1989. Higher order Godunov methods for general systems of hyperbolic conservation laws, *J. Comput. Phys.* **82**, pp. 362-397.

[4] Miller, G.H., Puckett, E.G., 1996. A higher-order Godunov method for multiple condensed phases, *J. Comput. Phys.* **128**, pp. 134-164.

[5] Berger, M., Oliger, J., 1984. Adaptive mesh refinement for hyperbolic partial differential equations, *J. Comput. Phys.* **53**, pp. 484-512.

[6] Peng, G., Zabusky, N.J., Zhang, S., 2003. Vortex-accelerated secondary baroclinic vorticity deposition and late-intermediate time dynamics of a two-dimensional Richtmyer-Meshkov interface, *Phys. Fluids* **15**, pp. 3730-3744.

[7] Giordano, J., Burtschell, Y., 2006. Richtmyer-Meshkov instability induced by shock-bubble interaction: Numerical and analytical studies with experimental validation, *Phys. Fluids* **18**, 036102.

[8] Widnall, S.E., Bliss, D.B., Tsai, C.Y., 1974. The instability of short waves on a vortex ring, *J. Fluid Mech.* **66**, pp. 35-47.

[9] Layes, G., Jourdan, G., Houas, L., 2005. Experimental investigation of the shock wave interaction with a spherical gas inhomogeneity, *Phys. Fluids* **17**, 028103.

[10] Ranjan, D., Anderson, M., Oakley, J., Bonazza, R., 2005. Experimental investigation of a strongly shocked gas bubble, *Phys. Rev. Lett.* **94**, 184507.

[11] Ranjan, D., Niederhaus, J., Motl, B., Anderson, M., Oakley, J., Bonazza, R., 2007. Experimental investigation of primary and secondary features in high-Mach-number shock-bubble interaction, *Phys. Rev. Lett.* **98**, 024502.

e-mail: ololeg@vniief.ru

On the Possibility of Cumulative Behavior of Initial Perturbation Evolution on a Surface of Condensed Material Subjected to a Shock Wave

Samuil M. BAKHRAKH, Inna Yu. BEZRUKOVA, Al'bina D. KOVALEVA, Snezhana S. KOSARIM, Gennadiy B. KRASOVSKY, Sergey E. KURATOV, Aleksey Ye. LEVUSHOV, Evgeniy E. MESHKOV, Oleg V. OLKHOV, Andrew A. POLOVNIKOV, Evgeniy A. POLOVNIKOV

Russian Federal Nuclear Center – VNIIEF, pr. Mira, Sarov, Nizhni Novgorod Region, Russia

Abstract: It is shown numerically, theoretically and experimentally that when a shock wave reaches a curved surface of a condensed material the surface becomes unstable and the topology of this instability can differ from the classical Richtmyer-Meshkov instability. The obtained results prove that cumulative jets can form on a free surface of a condensed material.

The main laws that determine the characteristics of the resulting cumulative instability have been analyzed.

The effects of various physical factors, such as pressure magnitude, initial perturbation amplitude, elastoplasticity, spall strength and physical viscosity, on the evolution of cumulation processes developing on a free surface has been studied.

The work was partly supported by the Russian Foundation of Fundamental Researches (Project 05-01-00083).

1 INTRODUCTION

Free surface behavior of condensed matter under the action of intense dynamic loads is a set of complex processes, detailed conception of which in many aspects has not been found yet. One of insufficiently known phenomena is the process of instability development of free surface under shock loading.

This kind of instability results in ejection of material particles from the surface, which defines practical importance of this phenomenon and basic directions of experimental studies hold earlier. Particle ejection from free surface was obtained for the first time in 50-ies in VNNIEF by Kormer S.B., Grigoriev F.V. and others. The part of obtained results was later published in [1]. In mentioned work the results of experimental studies of particle ejection form plane surfaces, are given. Photochronographic registration technique and impulse X-ray radiography method were used in experiments. Initial disturbance of free surface forming the processes of hydrodynamic instability, is surface roughness with representative amplitude value (height of roughness) $R_z \sim 1..100$ μm. Experimental data of independence of material amount ejecting from free surface from samples composition, counts in favor of cumulative behavior of the process. It was determined that small particles ejection from free surface does not depend on internal structure of materials (presence and size of impurities, grains, lacunae, etc.), it is determined by surface cleanliness or by roughness size.

Similar investigations on particles ejection from the free surface were carried out in Sandia Laboratories by Asay J.R.[2] and in Livermore by Dunning M.J. and Jacoby B. [3], they studied the amount of material ejection from the surface and its velocity distribution. The term "surface dusting" was used for material ejection from the free surface. Holographic diagnostics with high resolution estimating 1 μm, was used. In [4] Asay J.R. studied the effect of shock wave thickness on the process of free surface instability development.

All mentioned experimental investigations deal with late stage of hydrodynamic instability development when the free surface of shock driven sample covers the distance of 10…50 mm, but initial perturbation level defining the process development was about 10 μm. One of the first works on perturbation development on the initial stage of their development, was [5]. In this work perturbation shape was X-rayed with a plane stationary shock wave arrival at the curved free surface of aluminum sample with amplitude ≈ 35GPa. It was shown that perturbations (if they develop at all) are jets in their behavior. At small initial perturbations, free surface perturbations may not develop because of stabilizing effect of strength properties of metal.

This work interprets the instability processes development on the free curved surface of condensed matter with shock wave arrival, as the process of cumulative jet formation. The applied approach lets us obtain the dependence of perturbation growth rate on geometric factor (wave length and initial perturbations amplitude), as well as on load intensity and material properties. The results obtained at consideration of cumulative behavior of perturbation growth on the free surface were verified by experiments on specially made facility – two-piston shock tube, as well as by numerical simulation results carried out according to LEGAK [6] technique.

2 ORGANIZATION OF EXPERIMENTS

The following plot (**Fig. 2.1**) is at the basis of experiments conducted on a shock tube studying instability of the free surface of condensed matter. Projectile (1) accelerated up to the rate u_1 hits the sample of investigated matter (3)

through the pad (2). Such a two- piston scheme lets us obtain shock wave intensity up to ~50MPa, as well as modify load level and behavior in investigated samples within wide limits.

As an investigated condensed matter we used jelly of gelatin aqueous solution (with weight concentration C = 4%) or clay. We used clay of two consistencies: *"hard"* clay – clay used to model ceramic samples, and *"soft"* clay – *"hard"* clay watered to a butter consistency at room temperature.

The initial two-dimensional perturbation approximating sinusoidal, with wave length λ and amplitude Δ_0 (from the top of the hump to the center of the bottom), was set at external layer boundary.

The projectile acceleration, its pad shock and further perturbation development on the investigated surface were recorded with the help of streak camera SFR in the case of time magnifier in transmitted light.
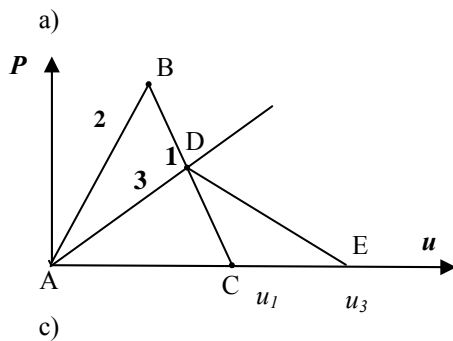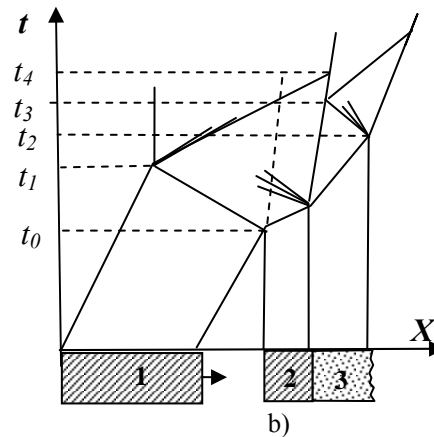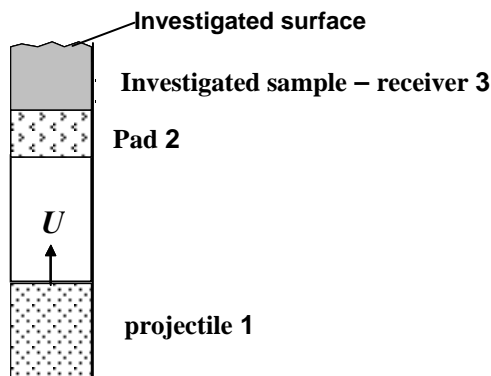

Fig. 2.1 The experiments organization scheme on a shock tube investigating free surface instability of condensed matter with shock wave arrival.
a) Experiments organization scheme
b) X-t diagram of a shock tube. 1 – projectile, 2 – pad, 3 – receiver (investigated sample).
c) P-u flow diagram. 1 – projectile, 2 – pad, 3 – receiver. u_1 – projectile running rate, u_3 – receiver free surface rate with shock wave arrival.

3 EXPERIMENTAL RESULTS AND THEIR DISCUSSION

A set of experiments was carried out with variation of the studied layer of material, wave length λ and initial perturbation of the investigated surface Δ_0. Experimental data are given in **Table 3.1**. The measured data of polyethylene projectile rate (density ρ = 920 kg/m³, sound speed C_0 = 2950 m/s) before acrylic-plastic gap shock are also given here, as well as the estimation of pressure in square piston. The estimation was carried out in acoustic approximation according to P-u diagram.

Experiment #	Studied layer material	Initial perturbation		Projectile rate, [m/s]	Pad rate, [m/s]	Shock wave pressure in the pad, [MPa]
		λ, [mm]	Δ, [mm]			
1	Jelly	~10	~3.7	32.4	23.8	49.1
2	Jelly	~20	~3	30.8	20.8	46.7
3	"Soft" clay	~10	~3.7	30.9	17.0	46.8
4	"Soft" clay	~20	~3	28.5	15.5	43.2

Table 3.1. Experiments organization

Fig. 3.1 gives experiments streak photographs and processing effect. **Fig. 3.2** gives time dependence of the surface perturbation amplitude in experiments 1 – 4. The time is always measured from the beginning of the process record (from the first picture of streak photograph).
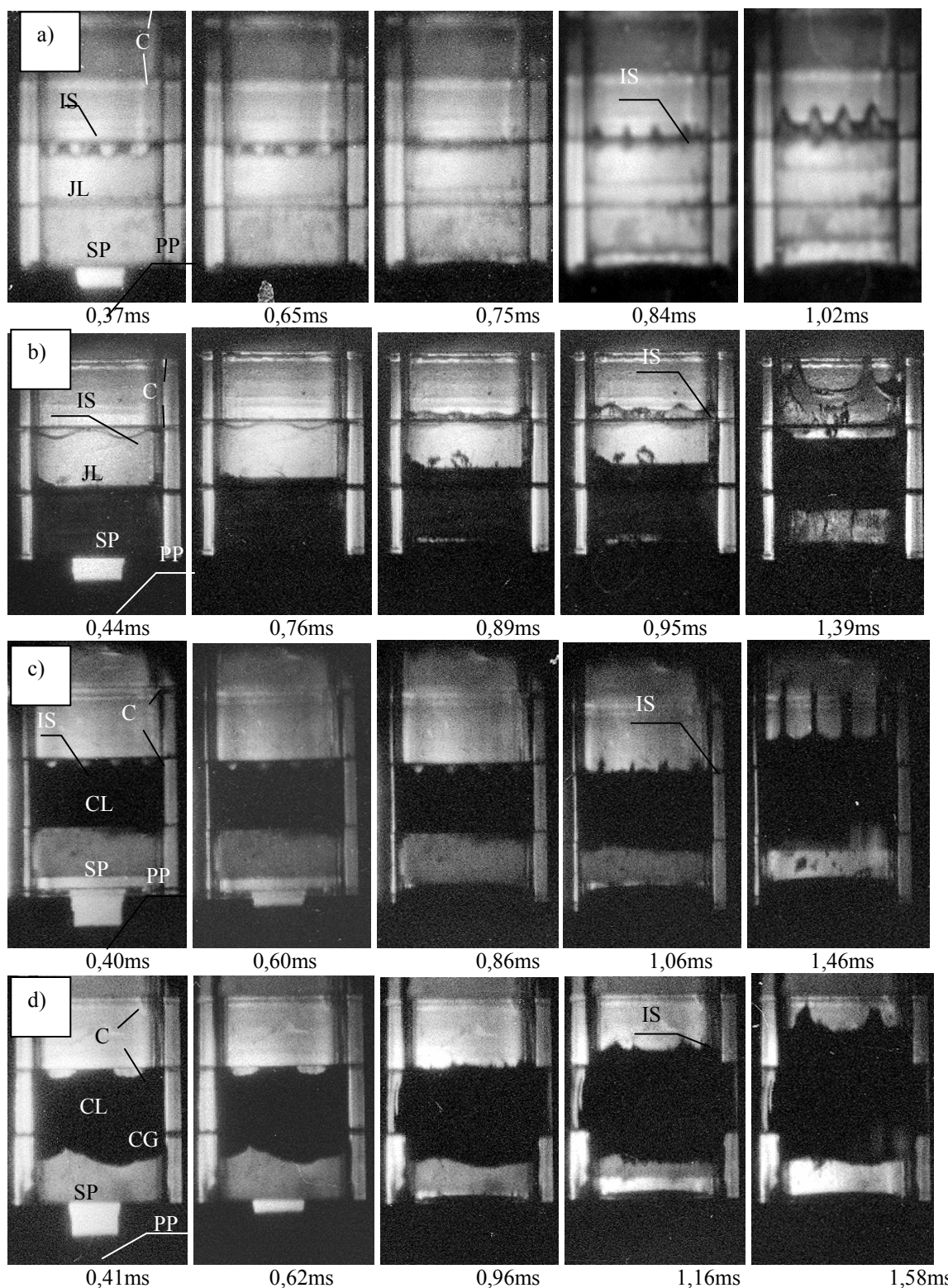
Fig. 3.1. a) Experiment 1 (jelly layer C = 4%, λ = 10mm, $\Delta_0 \approx 3,7$mm). b) Experiment 2 (jelly layer C = 4%, λ ≈ 20 mm, $\Delta_0 \approx 3$ mm). c) Experiment 3 ("soft" clay λ ≈ 20mm, $\Delta_0 \approx 3$ mm). d) Experiment 4 ("soft" clay λ ≈ 20 mm, $\Delta_0 \approx 3$ mm).

Notation: IS – investigated perturbation surface; PP – polyethylene projectile; SP– square piston; C – conjunction of square section channel; JL –jelly layer; CL – clay layer; CG – clay in the gap between the wall square piston.

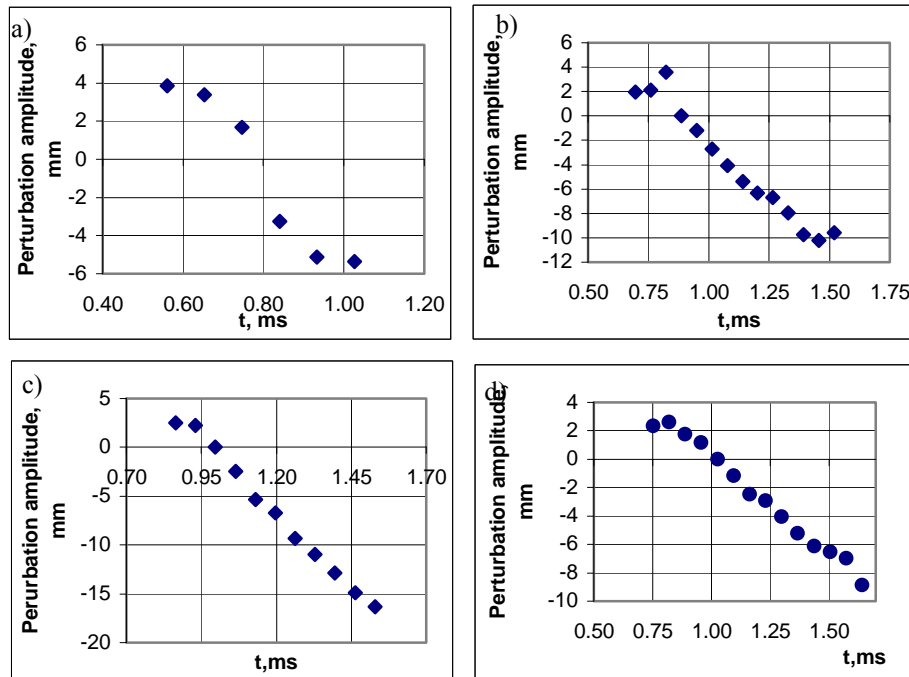**Fig. 3.2.** Time dependence of the investigated surface perturbation amplitude a) Experiment 1 (jelly layer, C = 4%, λ =10 mm, $\Delta_0 \approx 3,7$ mm), b) Experiment 2 (jelly layer C = 4%, λ ≈ 20 mm, $\Delta_0 \approx 3$ mm) c) Experiments 3 ("soft" clay, λ = 10 mm, $\Delta_0 \approx 3,7$), d) Experiment 4 ("soft" clay, λ = 20 mm, $\Delta_0 \approx 3$ mm)

4 THE MAIN DEPENDENCES OF FREE SURFACE JET-LIKE INSTABILITY DEVELOPMENT

A shock wave arrival at the curved free surface of condensed matter can be interpreted as a particular case of Richtmayer–Meshkov instability [9, 10] at great initial density ratio on either side of discontinuity, Atwood number approaching 1. However, behavior features of condensed matters can significantly change the process behavior versus classical version of Richtmayer – Meshkov instability with shock wave crossing the curved surface of two gases of different densities. The presence in solids of parameter $\rho_0 c_0^2$ with pressure dimension is a physical base of the mentioned difference. The wave configuration in condensed matter results in flows slightly different form those realized on the interface of gases of different density. **Fig.4.1** is given to illustrate the flow at the shock wave arrival at wedge-shaped pit.
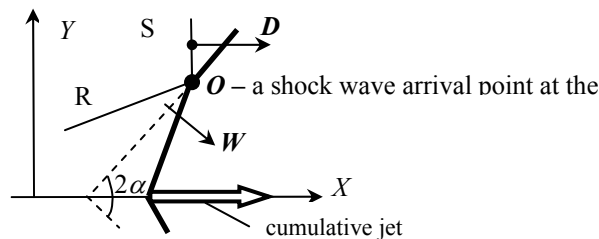
Fig4.1. Shock wave (S) arrival at wedge-shaped pit. R – rarefaction wave

At relatively low shock wave strength in condensed matter, the compression of the material at the front is insignificant, and material behavior over the front is defined by cold pressure component in the equation of state. After unloading in rarefaction wave, the matter recovers to its initial state with density ρ, which is insignificantly smaller than initial density ρ. Total specific volume change of the material slightly changes during the process, therefore, form of the surface describing the surface of condensed matter after a shock wave arrival, also slightly changes. Yet, the flow formed along the generatrix initial curved surface results in cumulative jets in the point of flows collision on the plane of pit symmetry. Topology and dynamics of the formed perturbations significantly differs from the perturbations in the case of classical Richtmayer – Meshkov instability.

To get the proportions describing instability development on the free surface in the framework of cumulative conception, let us consider the free surface of the material shown in Figure 7. For simplicity let us consider the surface form saw-shape. Let us neglect the flow configuration in the neighborhood of the free surface, considering only the incident

shock wave and the rarefaction wave outgoing from the cross point at the surface. The equation of state $P = A(\delta^n – 1)$, $\delta = \rho/\rho_0$ describes material behavior.

Under the assumption of incident shock wave weakness, we can neglect the width of rarefaction wave reflected from the free surface, substituting it for infinitely thin discontinuity. In the framework of the assumptions, the angle of a shock wave incidence on the free surface agrees exactly with the angle of refraction wave reflection. According to the conservation laws, it is easy to get (see for example [7]) that in the neighborhood of free surface of unloading region, the flow velocity is *W*, and it is directed to initial surface position (dot line in **Fig. 4.1**). The rate components in fixed coordinate system are given by:

$$W_x = U_{FS} \cdot \sin^2 \alpha, \; W_y = -2 U_{FS} \cdot \sin \alpha \; \cos \alpha \tag{3.1}$$

U_{FS} – free surface velocity in the case of undisturbed initial free surface.

The presence of *y*-component in the region of unloading material can result in cumulative jet stream directed to pit axis [8]. The jet rate can be estimated much as in classical theory of cumulative jets in approximation of incompressible fluid:

$$V_{jet} \approx U_{FS}\left(1 + \frac{\cos\alpha}{1 + 2(\delta - 1) \cdot \cos^2 \alpha}\right) \tag{3.2}$$

δ – material compression on the incident shock wave surface.

It is easy to see that within small initial perturbations *ak<<1*, the equation (3.2) reduces to classical Richtmayer expression [9]:

$$V_{jet} \approx U_{FS}(1 + (ak)) \tag{3.3}$$

Basing on equation (3.2), obtained in approximation of weak shock waves (neglecting heat pressure component in the equation of state, surface compression is $\delta = 1 + \varepsilon, \; \varepsilon << 1$), as well as using numerical simulation results, we have got the scaling which can be used for optional initial perturbations on the free surface and for optional pressure amplitudes on the shock wave surface [11]:

$$V_{jet} = U_{C\Pi}\left(1 + \frac{2.7 \; \cos\alpha}{1 + 2(\delta - 1) \; \cos^2 \alpha \; f(a/\lambda)}\right) \tag{3.4}$$

The angle α is connected with initial amplitude *a* and wave length λ by the formula $\mathrm{tg}\,\alpha = (\lambda/2)/(2a) = \frac{1}{4}\frac{\lambda}{a}$, the function $f(x)$ is evaluated in the following way:

$$f(x) = 8.61x^2 - 13.92x + 6.31.$$

The equation (3.4) can be applied to optional profile of initial ripple, including sinusoidal initial perturbation, as well as optional shock wave amplitude.

The strength has stabilizing influence on jet formation and their rate. In [11], the formula has been obtained for minimum permissible shock wave strength P_*, at which the jet stream is possible on the free surface with perturbations of wave length λ and amplitude *a*:

$$P_* \approx \frac{\sqrt{2\,\sigma_T\,\rho_0 c_0^2}}{\sin 2\alpha} = \sqrt{\frac{1}{2}\,\sigma_T\rho_0 c_0^2}\left(\frac{\lambda}{4a} + \frac{4a}{\lambda}\right) \tag{3.5}$$

σ_T - the parameter characterizing strength properties of materials, is close to the magnitude of dynamic yield stress [8]. LEGAK computations [6] verify the obtained dependence (3.5). Jet rate decrease (3.4) due to strength effects is determined by the equation [11]:

$$\frac{V_{jet}^{UP}}{V_{jet}} \approx 1 - \frac{\sigma_T}{\rho_0 U_{C\Pi}^2} \cdot \frac{1 + \left[1 - 2(\sigma - 1) \; \sin^2 \alpha\right] \cos\alpha}{\sin^2 \alpha \; \cos\alpha \; (1 + 2.7\cos\alpha)} \tag{3.6}$$

The experimental data (**Fig. 3.1**) agrees with the computational estimates. **Fig. 4.2** shows the comparison between experimental and theoretical results.
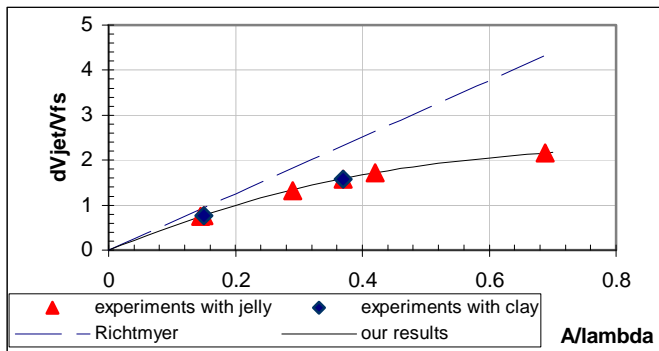
Fig. 4.2. Perturbation growth velocity relatively to free surface velocity - comparison experimental data with theoretical results. For jelly experiments we consider only initial study of perturbation growth when elastic properties don't influence on the rate of instability increase

The most pronounced jet-like behavior is observed in experiment 3 (**Fig. 3.1c**) with the material having the lowest strength ("soft" clay) and the highest amplitude of initial perturbation $\Delta_0/\lambda \approx 0.37$. Reducing the relative magnitude of initial perturbation (experiment 4, "soft" clay, $\Delta_0/\lambda \approx 0.15$, **Fig. 3.1d**) results in a lower perturbation growth rate, and using a higher-strength material ("hard" clay instead of "soft") leads to fast deceleration and cease of perturbation development at the very beginning. It is interesting to note the significant difference in perturbation development between "soft" clay and jelly. Jelly used in the experiments discussed above has low strength (~ 10 kPa) [12], but the perturbation behavior in the jelly layer of experiment 1 (**Fig. 3.1a**) is essentially different from that in the identical experiment with "soft" clay (experiment 3). In the latter case, the perturbation not only stops growing, but even starts decaying (**Fig. 3.2d**). This result, which seems surprising at first sight, can be explained if we recall that these materials strongly differ in their elasto-plastic properties. Whereas jelly has an anomalously extended region of elastic deformation and almost no plastic region [12], clay, on the contrary, has pronounced plastic properties and almost no elastic region. As a result, in experiment 1, the full-grown jelly jets, once they get free of tension effects, start shrinking very rapidly like a piece of rubber, first stretched and then released. At the same time, the jet of stretched clay in experiment 3 preserves this condition even after the load is removed.

CONCLUSION

It is shown that when the shock wave arrives at the free surface of condensed matter, the instability on the free surface behaves like a jet. Expressions were obtained to estimate the rate of perturbation amplitude growth depending on some initial and boundary conditions in the process of interest. At small initial perturbation amplitudes, the expression obtained reduces to the classical Richtmyer formula. A specially developed experimental setup – two-piston shock tube – was used to conduct experiments, which demonstrated qualitative agreement with theoretical predictions.

REFERENCES

[1]. Ogorodnikov V.A., Ivanov A.G., Mikhailov A.L. et al, 1998. On particles ejection from metal free surfaces upon shock arrival and diagnostic techniques. *FGV. V.* **34**, *No.6. pp.*103-107.

[2]. Asay J.R. 1976. Material ejection from shock-loaded free surfaces of aluminum and lead. *Sandia Laboratories Report, Sand 76-0542*.

[3]. Dunning M.J. Jacoby B. 1995. Ejecta production from shocked metal samples. *The Fourth Zababakhin Scientific Talks, Russian Federal Nuclear Center, October* 16-20, *Chelyabinsk region, Russia.*

[4]. Asay J.R. 1977. Effect of shock wave rise time on material ejection from aluminum surfaces. *Sandia Laboratories Report, Sand 77-0731*.

[5]. Lebedev A.I., Igonin V.V., Nizovtsev P.N., Raevsky V.A., Soloviev V.P. 2001. Studies of shock-driven instabilities on free surfaces of solids. *Transactions of RFNC-VNIIEF, Issue 1, Sarov*

[6]. Bakhrakh S.M., Spiridonov V.F., Shanin A.A. 1984. Method for hydrodynamic heterogeneous flow computations in Lagrange-Eulerian variables. *Papers of the Soviet Academy of Sciences*. V.**278**, No.4. pp. 829-833.

[7]. Zababakbin E.I. 1997. Some issues of detonation hydrodynamics. – Snezhinsk: RFNC-VNIITF, 208 p.

[8]. Kinelovsky S.A., Trishin Yu.A. 1980. Physical aspects of cumulation. *FGV*. No.5. pp.26-40.

[9]. Richtmyer R.D. 1960. Taylor instability in shock acceleration of compressible fluids. *Commun. Pure Appl. Math.* V.**13**, p.297

[10]. Meshkov E.E. 1969. Instability of the interface of two gases accelerated by a shock wave. *Izv. Acad. Nauk SSSR. Mekh. Zhidk Gaza.* **4**, p.151

[11]. Bakhrakh S.M., Bezrukova I.Yu., Kovaleva A.D., Kosarim S.S., Olkhov O.V. 2005. Cumulative instability behavior of shock-driven condensed matter. *Voprosy atomnoi nauki I tekhniki. Series: Mathematical modeling of physical processes. Issue* **3**. pp. 14-25.

[12]. Bliznetsov M.V., Meshkov E.E., Nevmerzhitsky N.V., Nizovtsev P.N., Sen'kovsky E.D., Sotskov E.A., Tochilina L.V. 1999. On the possibility of modeling some aspects of Rayleigh-Taylor instability in strong media. *VANT. Series: Theoretical and Applied Physics. Issue* **3**, pp. 54-57

e-mail: `pierre.pailhories@cea.fr`

A general formulation of buoyancy-drag equations for bubbles and spikes growth at an unstable interface

Pierre PAILHORIES[1] and Eric VAN RENTERGHEM[1]

[1]*CEA/DAM Ile de France BP 12 91680 Bruyères-le-Châtel France*

Abstract Buoyancy-drag equations have demonstrated good capacities in describing the non linear growth of Rayleigh-Taylor instability taking place at an interface between a light and a heavy fluid submitted to acceleration. At high density ratios, the mixing zone becomes asymmetric, which makes necessary the distinction between "spikes" of heavy fluid penetrating the light fluid, and "bubbles" of light fluid penetrating the heavy fluid.

Standard buoyancy-drag equations strictly apply to incompressible fluids separated by a plane interface. In the first part of this paper, we suggest a global formulation of this type of equations, suitable under these conditions. It recovers the classical balance between buoyancy and drag forces, and accounts in a simplified manner for added mass effects as well as interpenetration of the fluids. As proposed by G. Dimonte in his "spanwise homogeneous model", the coefficients of the equations depend on the ratio χ between the height of the spikes h_1 and of the bubbles h_2. The determination of these coefficients can be achieved using appropriate heuristic postulates and/or empirical results.

In the second part of the paper, we derive a particular pair of weakly coupled buoyancy-drag equations from the general formalism, using mainly the Linear Electric Motor (LEM) experimental findings to close the unknown terms. Constant and impulsive acceleration histories have been considered. Remaining uncertainties and behaviour of this model at high Atwood numbers (outside of the range explored in the LEM experiments) are discussed in the paper.

1 INTRODUCTION

We consider in this paper mixing occurring at a plane interface, submitted to variable acceleration $\gamma(t)$, between two incompressible fluids 1 and 2 of densities ρ_1 and ρ_2. The non linear phase of the instability growth is characterized by a loss of memory of initial conditions, self similar volume fraction profiles in the mixing zone, and the development of "spikes" of heavy fluid 2 penetrating the light fluid 1 and of "bubbles" of light fluid penetrating the heavy fluid.

The lengths of spikes and bubbles with respect to the position of an ideal non perturbed interface will be referred to as h_1 and h_2 respectively. Experiments on the Linear Electric Motor (LEM) [1] have evidenced power laws variation of the h_i in two particular cases. For a constant acceleration, the mixing lengths evolve as:

$$h_i = \alpha_i A_0 \gamma t^2 , \tag{1.1}$$

where A_0 is the Atwood number, related to the density ratio R_0 via :

$$A_0 = \frac{R_0 - 1}{R_0 + 1} = \frac{\rho_2 - \rho_1}{\rho_2 + \rho_1} . \tag{1.2}$$

For an impulsive acceleration (non null only during a short time interval), the mixing lengths vary asymptotically as:

$$h_i = B t^{\theta_i} . \tag{1.3}$$

The simplest way to model the evolution of the spikes and bubbles heights is through ordinary differential equations. The asymptotic growth laws (1.1) and (1.3) can be properly obtained using buoyancy-drag (BD) equations [2]. Ramshaw demonstrated in [3] the relevance of these equations at low Atwood numbers, and this justification is extended to arbitrary Atwood number in [4].

2 FORMULATION OF THE BUOYANCY DRAG EQUATIONS

Buoyancy-drag equations express an energy balance between inertia, buoyancy and drag. Since dissymmetry arises, two different equations, possibly coupled, must be used for "bubbles" and "spikes" growth.

The equations of incompressible fluid mechanics should be linear with respect to fluid densities, so a general form for the BD equations is:

$$(A_{11}\rho_1 + A_{12}\rho_2)\ddot{h}_1 = (B_{12}\rho_2 - B_{11}\rho_1)\gamma - (C_{11}\rho_1 + C_{12}\rho_2)\frac{\dot{h}_1^2}{h_1}, \tag{2.1}$$

$$(A_{21}\rho_1 + A_{22}\rho_2)\ddot{h}_2 = (B_{22}\rho_2 - B_{21}\rho_1)\gamma - (C_{21}\rho_1 + C_{22}\rho_2)\frac{\dot{h}_2^2}{h_2} \tag{2.2}$$

Each acting force is characterized by an effective density equal to a linear combination of the fluid densities, which expresses the interpenetration of the fluids. This formalism notably accounts for added mass effects (in the inertia term) and possible dissipation inside the penetrating structures (in the drag term).

We have introduced twelve unknown functions A_{ij}, B_{ij}, C_{ij}, independent on the acceleration history. Following G. Dimonte's idea [3] and in order to couple the two equations, we will suppose that these functions depend on the most straightforward adimensioned variable that can be built with the quantities h_i, that is the asymmetry rate defined as:

$$\chi = \frac{h_1}{h_2}. \tag{2.3}$$

3 GENERAL STATEMENTS ABOUT THE FUNCTIONS OF THE BD EQUATIONS

Since both equations can be multiplied by arbitrary constants, we can assume without loss of generality:

$$A_{11} + A_{12} = A_{21} + A_{22} = 1. \tag{3.1}$$

The symmetry of equations inverting the two fluids enforces for each function X=A, B, C:

$$X_{21}(\chi) = X_{12}\left(\frac{1}{\chi}\right) \text{ and } X_{22}(\chi) = X_{11}\left(\frac{1}{\chi}\right). \tag{3.2}$$

Finally, the buoyancy is proportional to the difference between fluid densities (see [4]), so:

$$B_{11} = B_{12} \text{ and } B_{22} = B_{21}. \tag{3.3}$$

These considerations and the available experimental results from the LEM are clearly insufficient to determine all the unknown functions: additional postulates have to be made. Sections 4 and 5 display two different sets of postulates.

4 MODEL A: "SPANWISE HOMOGENEOUS MODEL" OF G. DIMONTE

G. Dimonte proposed in [2] a model that compares favourably with other existing BD models and recovers the results of the LEM tests within the experimental uncertainties (see **Fig. 5.1**). This approach is based on the idea that bubbles and spikes can be seen as homogeneous media with linear volume fraction profiles, submitted to the buoyancy motor term and to drag from the pure fluids. This implies:

$$A_{12}(\chi) = \frac{1}{2(1+\chi)}, \tag{4.1}$$

$$\text{and } C_{12}(\chi) = 0. \tag{4.2}$$

Free fall of the spikes at Atwood number equal to 1 ($\rho_1=0$) is invoked to infer the value of the buoyancy function:

$$B_{11} = A_{12}.$$ (4.3)

The drag functions are assumed to be constant and equal to C_D in both equations. Parameter C_D was taken equal to 2.35 to draw **Fig. 5.1**, as a compromise to fit correctly both constant and impulsive experiments.

$$C_{11}(\chi) = C_{22}(\chi) = C_D = 2.35 \pm 0.65.$$ (4.4)

5 MODEL B BASED ON LEM EXPERIMENTAL RESULTS

We present in this section an alternative and complementary model, based on other postulates and aiming at recovering exactly (as shown on **Fig. 5.1**) the empirical fits of the LEM results [1] in the self similar regime:

$$\alpha_2 = 0.05 \text{ and } \alpha_1(\chi) = \alpha_2 \chi \text{ for constant acceleration experiments,}$$ (5.1)

$$\theta_2 = 0.25 \text{ and } \theta_1 = \theta_2 R_0^{n_\theta} \text{ with } n_\theta = 0.21 \text{ for impulsive acceleration experiments.}$$ (5.2)

The asymmetry rate is assumed to be quasi-constant in the LEM experiments, and related to the density ratio by:

$$\chi = R_0^{n_\chi} \text{ with } n_\chi = 0.34.$$ (5.3)

The impulsive acceleration experiments provide a direct measurement of the drag function:

$$\frac{C_{21}(\chi)}{A_{21}(\chi)} = \frac{C_{22}(\chi)}{A_{22}(\chi)} = \frac{1}{\theta_2} - 1 \text{ for bubbles,}$$ (5.4)

$$\frac{C_{12}(\chi)}{A_{12}(\chi)} = \frac{C_{22}(\chi)}{A_{11}(\chi)} = \frac{1}{\theta_2 \chi^{\frac{n_\theta}{n_\chi}}} - 1 \text{ for spikes.}$$ (5.5)

For the constant acceleration experiments, we adopt postulate (4.3) and deduce the value of functions A_{21} and A_{12}:

$$A_{21}(\chi) = \frac{1}{\dfrac{1 + \chi^{\frac{1}{n_\chi}}}{\alpha_2\left(\dfrac{4}{\theta_2} - 2\right)} + 1 - \chi^{\frac{1}{n_\chi}}} \text{ for bubbles,}$$ (5.6)

$$A_{12}(\chi) = \frac{1}{\dfrac{1 + \chi^{\frac{1}{n_\chi}}}{\alpha_2 \chi\left(\dfrac{4}{\theta_2 \chi^{\frac{n_\theta}{n_\chi}}} - 2\right)} + 1 - \chi^{\frac{1}{n_\chi}}} \text{ for spikes.}$$ (5.7)

The former expressions are valid only in the domain explored by the LEM experiments, that is for density ratios up to 49 or equivalently asymmetry rates up to 3.96. It is easy to see that relations (5.1), (5.2) and (5.3) for spikes are diverging when the Atwood number goes to 1. Hence, we introduce some physical limitations in order to adapt our model to high Atwood numbers:

$$\theta_1 = Min\left[\theta_2\chi^{\frac{n_\theta}{n_\chi}}, \frac{2}{3}\right] \tag{5.8}$$

$$\alpha_1 = Min\left[\alpha_2\chi, \frac{1+\chi^{\frac{1}{n_\chi}}}{\dfrac{4}{\theta_2\chi^{n_\theta}}-2\chi^{\frac{1}{n_\chi}}}\right] \tag{5.9}$$

The first condition arises from energy conservation principles [3,4]. The second one is required to ensure that function A_{12} remains lower than 1. This implies that $\alpha_1 \rightarrow 0.25$ as $A_0 \rightarrow 1$.
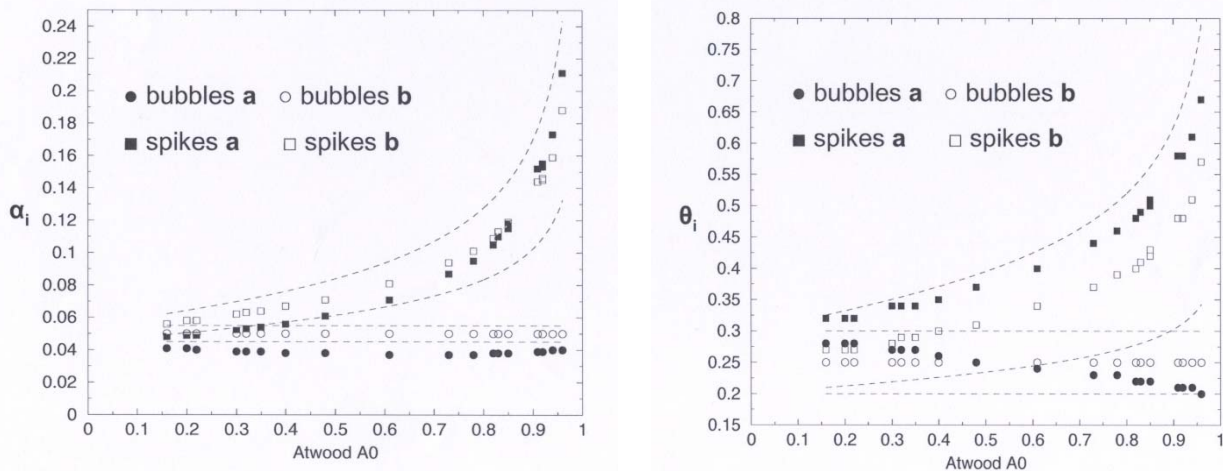

Fig. 5.1. Comparison between models a (with C_D=2.35) and b for constant acceleration (left) and impulsive acceleration (right) LEM experiments. Dotted lines figure the limits of experimental uncertainties.

8 CONCLUSIONS

This paper presents a general formalism for BD equations to describe bubbles and spikes growth at a plane interface between two incompressible fluids of arbitrary densities, submitted to a variable acceleration. The approach is valid only in self similar regime.

Two particular models a and b inheriting from this formalism and closed with heuristic postulates are described: model a is the "spanwise homogeneous" model of G. Dimonte and model b is built from experimental results on the LEM.

REFERENCES

[1]   Dimonte, G. & Schneider, M., 2000. Density ratio dependence of Rayleigh-Taylor mixing for sustained and impulsive acceleration histories; *Physics of Fluids* **12** (2), 304-32

[2]   Dimonte, G., 2000. Spanwise homogeneous model for Rayleigh-Taylor mixing and experimental evaluation; *Physics of Plasmas* **7** (6), 2255-2269.

[3]   Ramshaw, J.D. 1998 Simple model for linear and non linear mixing at unstable fluid surfaces with variable acceleration; *Physical Review E* **58** (5), 5834-5840

[4]   Pailhories, P. & Van Renterghem, E., 2005. A mixing model based on the principle of least action; Proceedings of *IWP*CTM10.

e-mail: `pierre.pailhories@cea.fr`

A mixing model based on the principle of least action

Pierre PAILHORIES[1] and Eric VAN RENTERGHEM[1]

[1]*CEA/DAM Ile de France BP 12 91680 Bruyères-le-Châtel France*

Abstract We propose in this paper a simple analytical model aiming at describing mixing between two fluids at an interface undergoing destabilizing variable acceleration. The model applies to interfaces of arbitrary shape, to fluids submitted to global compression or expansion (their densities are spatially uniform but can be time dependent). It covers both the linear and non linear phase of the instability growth.

The model is built following the approach of Ramshaw: considering small perturbations of the interface, we estimate the average kinetic energy K of the system formed by the two semi-infinite fluids. Under some simplifying assumptions, K can be calculated exactly during the linear phase. Its approximate expression in the non linear phase can be inferred using a generalized Wavelength Renormalization Hypothesis, as proposed by Ramshaw.

The equations of motion controlling the temporal evolution of the perturbation are then obtained using the principle of least action. This technique guarantees the construction of proper conservative equations, to which heuristic dissipative terms respecting the second law of thermodynamics are added.

This paper generalizes the work of Ramshaw: the model is valid at all Atwood numbers since "bubbles" and "spikes" are treated independently, compression effects are accounted for and the surface separating the fluids can be of arbitrary shape. In the case of a plane interface and of incompressible fluids, the models degenerates in classical buoyancy-drag equations, which are fully consistent with the formalism established in our poster [3].

1 INTRODUCTION

We are dealing in this paper with mixing at an unstable interface between two fluids undergoing destabilizing variable acceleration γ. This process can be divided into the linear regime, when the amplitudes of the perturbations remain small with respect to their wavelength, and the strongly non linear regime, characterized by the development of "bubbles" and "spikes", self similar volume fraction profiles in the mixing zone and possible transition to a turbulent state. Considering the case of a low Atwood number inducing a symmetric mixing, Ramshaw built in [1] a model based on the principle of least action covering these two regimes. This paper generalizes [1] to arbitrary Atwood numbers.

Section 2 sets the statistical approach used in self similar regime. In sections 3 to 5, we consider a plane interface between incompressible fluids, for sake of simplicity. In section 3, we build the Lagrangian of the system. Section 4 deals with energy conservation. In section 5, we derive the equations of motion and close the unknown terms. Finally, in Section 6, we show how to extend our model to interfaces of arbitrary shape and time dependent fluid densities.

2 STATISTICAL APPROACH

Let us consider a series of realizations of perturbations at an interface of area S between a light fluid of density ρ_1 and a heavy fluid of density ρ_2. These realizations differ by the initial interfacial perturbation. The realization index is p. A schematic view of different realizations is shown on **Fig. 2.1**.
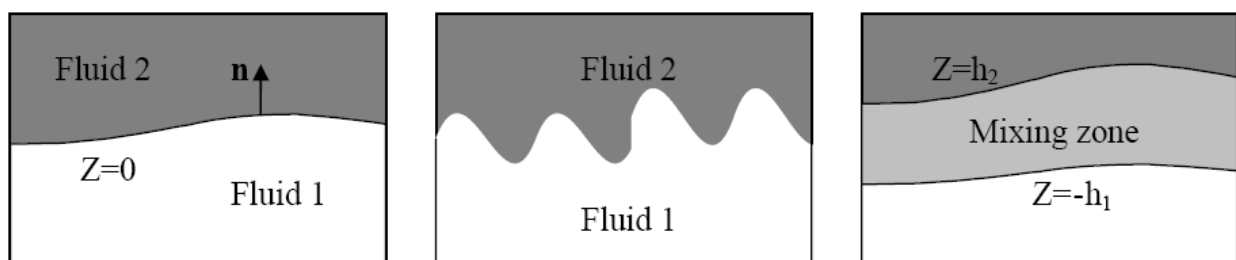

Fig. 2.1. Scheme of unperturbed realization p=0 (left), perturbed realization p≠0 (middle) and statistical average (right)

The case p=0 corresponds to an ideal unperturbed interface at which no small scale mixing occurs. Let $Z(\mathbf{x},t)$ be the distance to this interface, taken as negative in fluid 1 and positive in fluid 2, and $\mathbf{n}$ the unitary vector in the normal direction. The volume fractions of light fluid α_{10} and of heavy fluid α_{20} are simple Heaviside functions:

$$\alpha_{10}(\mathbf{x},t)=1 \text{ for } Z(\mathbf{x},t)\leq 0, \ \alpha_{10}(\mathbf{x},t)=0 \text{ for } Z(\mathbf{x},t)\geq 0 \text{ and } \alpha_{20}(\mathbf{x},t)=1-\alpha_{10}(\mathbf{x},t). \tag{2.1}$$

The local density is given by:

$$\rho_0 = \alpha_{10}\rho_1 + \alpha_{20}\rho_2. \tag{2.2}$$

Introducing the velocity field $\mathbf{U_0}=U_0\mathbf{n}$ of the unperturbed flow, we can calculate the Lagrangian L_0 of this realization, defined as the total kinetic of the unperturbed system:

$$L_0 = \iiint \frac{1}{2}\rho_0 \mathbf{U_0}^2 dV. \tag{2.3}$$

For a particular perturbed realization p≠0, we introduce similar conventions: α_{1p} and α_{2p} are the volume fractions of the fluids, ρ_P is the local density and $\mathbf{U_p}$ is the velocity field. The Lagrangian for realization p is:

$$L_p = \iiint \frac{1}{2}\rho_p \mathbf{U_p}^2 dV. \tag{2.4}$$

We define the statistical average of a given quantity X as:

$$\overline{X} = \frac{1}{N_p}\sum_{p=0}^{N_p-1} X_p, \text{ the number } N_p \text{ of realizations being large.} \tag{2.5}$$

We assume that for any function X, the average $\overline{X}$ depends only on the distance Z to the interface. **Fig. 2.1** illustrates this averaging process. The spikes extend spatially from $Z=-h_1$ to $Z=0$, and the bubbles from $Z=0$ to $Z=h_2$.

The approach followed by Ramshaw in [1] consists in calculating the Lagrangian L_p of the system for a particular monomode perturbation in linear phase, and to establish by analogy the expression to the average Lagrangian in the self similar phase. The equations of motion are inferred from these Lagrangians using the least action principle [2]. We will proceed in the same way.

3 CONSTRUCTION OF THE LAGRANGIAN

We calculate in this section the expression of the Lagrangian assuming small perturbations, up to second order in h_i and their time derivatives $\dot{h}_i$. From (2.3) and (2.4), the total Lagrangian can be decomposed as follows:

$$L_p = L_0 + K_p + C_p, \tag{3.1}$$

with $K_p = \iiint \frac{1}{2}\rho_p(\mathbf{U_p}-\mathbf{U_0})^2 dV$ intrinsic kinetic energy of the mixing zone, $\tag{3.2}$

and $C_p = \iiint \rho_p(\mathbf{U_p}-\mathbf{U_0}).\mathbf{U_0}dV + \iiint \frac{1}{2}(\rho_p-\rho_0)\mathbf{U_0}^2 dV$, buoyancy term. $\tag{3.3}$

We now assume that the interface is planar and that the fluids are incompressible. The velocity field $\mathbf{U_0}$ of the unperturbed flow is then uniform and the second term of expression (3.3) vanishes due to mass conservation:

$$C_p = \iiint \rho_p (\mathbf{U_p} - \mathbf{U_0}) . \mathbf{U_0} \, dV \tag{3.4}$$

It can be shown that the buoyancy term reduces to:

$$C_p = U_0 \frac{d}{dt}\left[\int (\rho_p - \rho_0) S z \, dz \right] = U_0 \frac{d\phi_p}{dt} \tag{3.5}$$

The buoyancy term hence depends mainly on the volume fraction profiles in the mixing zone.
In the linear regime, considering a symmetric sinusoidal perturbation ($h_1 = h_2 = h$), we have:

$$\alpha_{1lin} = 1 - \alpha_{2lin} = \frac{1}{\pi} ArcCos\left(1 - \frac{z}{h}\right), \text{ which implies } \phi_{lin}(h,t) = -(\rho_2 - \rho_1) S \frac{h^2}{4} \tag{3.6}$$

In the self similar regime, the mixing zone is no longer symmetric, and the average volume fraction profiles are usually considered as linear functions of the distance to the interface:

$$\overline{\alpha_1} = 1 - \overline{\alpha_2} = \begin{cases} \dfrac{h_1}{h_1 + h_2}\left(1 - \dfrac{h_2 z}{h_1^2}\right) for \; -h_1 \leq z \leq 0 \\[2ex] \dfrac{h_1}{h_1 + h_2}\left(1 - \dfrac{z}{h_2}\right) for \; 0 \leq z \leq h_2 \end{cases}, \text{ which implies } \overline{\phi}(h_i,t) = -(\rho_2 - \rho_1) S \frac{h_1 h_2}{6} \tag{3.7}$$

We now proceed to the calculation of the intrinsic kinetic energy. In the linear phase, for a monomode sinusoidal perturbation of wavelength λ_{lin}, the perturbed velocity field $\mathbf{U_p}$ is composed of decreasing exponentials, which leads to:

$$K_{lin} = \frac{\rho_1 + \rho_2}{8\pi} S\lambda_{lin} \dot{h}^2 \tag{3.8}$$

In self similar regime, the velocity field cannot be solved analytically and we postulate the following form for $\mathbf{U_p}$:

$$\mathbf{U_p} = \begin{cases} \mathbf{U_0} - \boldsymbol{\psi}_{11p}(\mathbf{x},t)\dot{h}_1 + \boldsymbol{\psi}_{12p}(\mathbf{x},t)\dot{h}_2 & in \; fluid \; 1 \\ \mathbf{U_0} - \boldsymbol{\psi}_{21p}(\mathbf{x},t)\dot{h}_1 + \boldsymbol{\psi}_{22p}(\mathbf{x},t)\dot{h}_2 & in \; fluid \; 2 \end{cases} \tag{3.9}$$
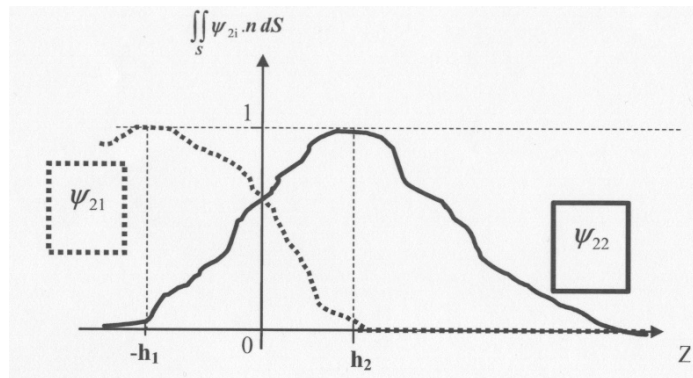
Fig. 3.1. Expected forms of the normal components of vectors $\boldsymbol{\psi}_{21p}$ and $\boldsymbol{\psi}_{22p}$.

Fig. 3.1 illustrates the expected form of the normal component of vectors ψ_{21p} and ψ_{22p}. This form is consistent with the values of the normal velocity $\mathbf{n}.\mathbf{U}_p(z = h_2) = U_0 + \dot{h}_2$ and $\mathbf{n}.\mathbf{U}_p(z = -h_1) = U_0 - \dot{h}_1$.

We inject (3.9) in (3.2) and neglect the crossed terms that correlate both sides of the mixing zone, to obtain:

$$\overline{K} = \left(\frac{\rho_1\lambda_{11} + \rho_2\lambda_{21}}{4}\right)S\dot{h}_1^{\,2} + \left(\frac{\rho_1\lambda_{12} + \rho_2\lambda_{22}}{4}\right)S\dot{h}_2^{\,2}. \tag{3.10}$$

We have introduced fours apparent wavelengths:

$$\lambda_{ij} = 2\int \overline{\alpha_{ip}\,\psi_{ijp}^{\,2}}\,dz. \tag{3.11}$$

Added mass effects appear naturally since the "inertial" densities are linear combinations of the pure fluid densities. In order to close the expression of the intrinsic kinetic energy in self similar regime, we appeal to a generalized form of the Wavelength Renormalisation Hypothesis (WRH) introduced by Ramshaw in [1]. Assuming complete loss of initial conditions memory and self similarity, the apparent wavelengths should grow proportionally to the lengths h_i:

$$\lambda_i = \sum_{j=1}^{2} \lambda_{ij} = \frac{h_i}{\beta_i}. \tag{3.12}$$

As mentioned by Ramshaw, the function β_i should remain of the order of 1 for finite density ratios. The final expression for the intrinsic kinetic energy in the self similar regime is then:

$$\overline{K} = \left(\frac{\rho_1\lambda_{11} + \rho_2\lambda_{21}}{\lambda_{11} + \lambda_{21}}\right)S\frac{h_1\dot{h}_1^{\,2}}{4\beta_1} + \left(\frac{\rho_1\lambda_{12} + \rho_2\lambda_{22}}{\lambda_{12} + \lambda_{22}}\right)S\frac{h_2\dot{h}_2^{\,2}}{4\beta_2}. \tag{3.13}$$

A simple interpolation function φ can be used to achieve a continuous transition between the Lagrangian functions in fully linear and strongly non linear regime:

$$L = \varphi L_{lin} + (1 - \varphi)\overline{L}. \tag{3.14}$$

This onset of non linearity occurs for a ratio m_i of h_i to λ_{lin} approximately equal to 0.1. A possible form for φ is then:

$$\varphi(h_i) = \left(\frac{\lambda_{lin}}{Max\left[\lambda_{lin}, \lambda_{lin} + \dfrac{h_i - m_i\lambda_{lin}}{\beta_i}\right]}\right)^{n_\varphi} \text{ with } m_i \approx 0.1 \text{ and } n_\varphi > 1. \tag{3.15}$$

4 ENERGY CONSERVATION

Two Lagrangians are equivalent if they differ by a total derivative to time of a function $F(h_i,t)$, because they give rise to identical solutions to the principle of least action [2]. This property can be used to bring to light the effective potential energy which is responsible for the mixing process:

for $F(h_i,t) = -U_0(t)\phi(h_i,t)$, $L^{'} = L + \dot{F} = L_0 + K - V$ where $V = \gamma\phi$ is the potential energy. (4.1)

V is perfectly analogous to potential energy in a gravity field. It is proportional to the center of mass displacement due to the mixing process. The principle of least action takes the following form, where the Q_i are dissipative forces:

$$\frac{d}{dt}\left[\left(\frac{\partial L^{'}}{\partial \dot{h}_i}\right)_{h_i,t}\right] = \left(\frac{\partial L^{'}}{\partial h_i}\right)_{\dot{h}_i,t} + Q_i \tag{4.2}$$

The total energy E associated to the modified Lagrangian is then:

$$E = \sum_i \left(\frac{\partial L^{'}}{\partial \dot{h}_i}\right)_{h_i,t} \dot{h}_i - L^{'} = E_0 + K + V \;\;, \text{ with } E_0 = -L_0. \tag{4.3}$$

The total energy evolves in time according to:

$$\dot{E} = \dot{E}_0 + \dot{D} + \left(\frac{\partial V}{\partial t} - \frac{\partial K}{\partial t}\right)_{h_i,\dot{h}_i}, \text{ with } \dot{D} = \sum_i Q_i \dot{h}_i \tag{4.4}$$

The term between parenthesis indicates that the system is not isolated (the acceleration of the interface has to be generated by exterior means). We adopt the phenomenological form of a Reynolds drag for the dissipation forces in non linear regime, whereas dissipation forces are neglected in the linear regime:

$$Q_{i\,lin} = 0 \;\; \text{and} \;\; Q_i = \frac{S}{2\beta_i}\left(\sum_j \rho_j q_{ij}\right)\dot{h}_i|\dot{h}_i|. \tag{4.5}$$

This implies no correlation between the velocities on both sides of the mixing zone, which is consistent with (3.10).

5 LAGRANGE'S EQUATIONS IN SELF SIMILAR REGIME

We can now derive explicitly the equations governing the evolution of the penetration lengths h_i in the self similar regime. We develop equation (4.2) using (3.14) and (4.1), to obtain the two Lagrange equations (for i=1,2):

$$\frac{d}{dt}\left[\sum_j \frac{\rho_j \lambda_{ij}}{\lambda_i}S\frac{h_i \dot{h}_i}{2\beta_i}\right] = \sum_j\left(\frac{\rho_j \lambda_{ij}}{\lambda_i}\right)S\frac{\dot{h}_i^2}{4\beta_i} - \gamma\frac{\partial\bar{\phi}}{\partial h_i} + Q_i. \tag{5.1}$$

We identify these equations with the general formalism for buoyancy-drag equations developed in [3]:

$$\left[\sum_j \rho_j A_{ij}(\chi)\right]\ddot{h}_i = A_{i(3-i)}(\chi)(\rho_2 - \rho_1)\gamma - \left[\sum_j \rho_j C_{ij}(\chi)\right]\frac{\dot{h}_i^2}{h_i}, \text{ where } \chi = \frac{h_1}{h_2} \tag{5.2}$$

By identifying the added mass functions and buoyancy terms of (5.1) and (5.2), we get using (3.7):

$$\frac{\lambda_{ij}}{\lambda_i} = A_{ij}(\chi), \tag{5.3}$$

$$\beta_1(\chi) = \beta_2\left(\frac{1}{\chi}\right) = 3\chi A_{12}(\chi), \tag{5.4}$$

It is interesting to see that some of the "drag" terms of (5.1) are included in the conservative part of the equations. Assuming a constant χ, which is valid e.g. for constant acceleration, we can calculate the dissipative forces :

$$q_{11}(\chi) = q_{22}\left(\frac{1}{\chi}\right) = C_{11}(\chi) - \frac{\chi}{2}\frac{A'_{12}(\chi)}{A_{12}(\chi)} - 1 + A_{12}(\chi)\left(1 + \frac{1}{2\chi}\right), \tag{5.5}$$

$$\text{and} \quad q_{12}(\chi) = q_{21}\left(\frac{1}{\chi}\right) = C_{12}(\chi) - A_{12}(\chi) + \frac{A_{12}(\chi)}{2\chi A_{21}(\chi)}\left(1 - A_{21}(\chi) - \frac{\chi A'_{21}(\chi)}{A_{21}(\chi)}\right). \tag{5.6}$$

This closes the model for given functions A_{ij} and C_{ij}: the reader can refer to [3] for possible values of these functions. Two checks should however be realized: the obtained β_i should be of the order of 1 for the self-consistency of the WRH, and the dissipation forces must satisfy the second law of thermodynamics $\dot{D} \leq 0$, which can be enforced by :

$$Q_i = \frac{S}{2\beta_i} Min\left(\sum_j \rho_j q_{ij}, 0\right)\dot{h}_i\left|\dot{h}_i\right|, \text{ so that } \dot{D} = \sum_i Q_i \dot{h}_i \leq 0. \tag{5.7}$$

6 GENERALIZATION TO ARBITRARY INTERFACE SHAPE AND TO TIME DEPENDENT DENSITIES

If the interface is spherical or cylindrical and the fluid densities depend on time, the Lagrangian of the system can still be calculated, but the unperturbed velocity $\mathbf{U_0}$ field is no longer uniform. We estimate the velocity gradient induced by compression and curvature effects near the interface, $\Re$ and $\Re'$ being the principal radii of curvature of the surface:

$$u'_i = \left(\frac{\partial U_0}{\partial z}\right)_{z=0^\pm} \approx -\frac{\dot{\rho}_i}{\rho_i} - U_0(z=0)\left(\frac{1}{\Re} + \frac{1}{\Re'}\right). \tag{6.1}$$

The velocity field assumed in (3.9) remains correct if we replace $\dot{h}_i$ by W_i defined as follows:

$$W_i = \dot{h}_i - u'_i h_i \tag{6.2}$$

This substitution agrees for the spherical case with Ramshaw results in [4]. It affects the intrinsic kinetic energy (3.13) and the dissipative forces (4.5). The expression of the buoyancy term (3.5) remains unchanged. The wavelength in the linear phase λ_{lin} has to be adapted to the considered geometry (planar, cylindrical, spherical …) and initial perturbation.

7 CONCLUSIONS

We propose in this paper a simple model based on coupled ordinary differential equations to evaluate the mixing zone growth under variable acceleration for arbitrary Atwood numbers. In the linear regime, a monomode perturbation is considered. In self similar regime, the model reduces to standard buoyancy-drag equations [3] when applied to a planar interface between incompressible fluids, which justifies the relevance of these equations. The use of the principle of least action in the construction of the model, as originally proposed by Ramshaw, guarantees energy conservation and gives access to useful information, such as the intrinsic kinetic energy and the dissipation rate in the mixing zone.

REFERENCES

[1] Ramshaw, J.D. 1998 Simple model for linear and non linear mixing at unstable fluid surfaces with variable acceleration; Physical Review E 58 (5), 5834-5840
[2] Landau, L. & Lifchitz, E. 1969 Course of theoretical Physics. Volume 1: Mechanics ; Mir publishers Moscow
[3] Pailhoriès, P. & Van Renterghem, E. 2006 A general formulation of buoyancy-drag equations for bubbles and spikes growth at an unstable interface; Proceedings of IWPCTM 10
[4] Ramshaw, J.D. 1999 Simple model for linear and non linear mixing at unstable fluid surfaces in spherical geometry; *Physical Review E* **60** (2), 1775-1780

Buoyant Mixing and Turbulent Structure in Plume Arrays and RT Fronts: Experiments on the role of initial conditions

Pilar L. Gonzalez-Nieto[1], Jose L. Cano[1] & Jose M. Redondo[2]

[1]Facultad Ciencias Fisicas. Universidad Complutense de Madrid, Avda. Ciudad Universitaria s/n. 28040 Madrid. Spain. azufre2@hotmail.com, jlcano@fis.ucm.es
[2]Departamento de Física Aplicada, Universidad Politécnica de Cataluña. Barcelona, Spain

Abstract. The turbulent mixing is a very important ussue at the study of geophysical phenomena. The reason is that the greatest part of the fluxes deriving from geophysic fluids are turbulent. In many of the physical phenomena ocurring in nature the diffusion of physical quantities is governed by the mixing generated by turbulence.

The study of the turbulent mixing due to gravitatory convection makes use of an experimental model with two fluids of unequal density under an unstable density distribution. The mixing process is generated by the evolution of a bidimensional array of forced turbulent plumes and a gravity current due to the presence of the glass container. The global conclusions of this first experimental model are related to the mixing efficiency and the volume of the final mixed layer as functions of the Atwood number, which ranges from 0.010 to 0.134. The mixing efficiency has an upper limit of 0.18 and this efficiency is about 20% of the maximum mixing efficiency (0.5) in comparable experiments. We propose a theoretical explanation to understand this difference. To verify our hypothesis, we performed new experiments with a line of plumes –from one to nine plumes- with an Atwood number of 0.03. Measurements of the height of the final mixed layer as functions of the number of plumes are made to verify that the less the number of plumes the lower the mixing efficiency.

1 INTRODUCTION

An experimental study of the global mixing, as of the topological structure of the fronts produced by a plume array and a single plume has been performed following Gonzalez-Nieto, [1]. Mixing produced in convective flows is investigated comparing new experiments: we release brine through an array of holes, through a line of holes and through a single plume generating orifice have been compared. New measurements of ADV 2D velocity measurements as the plumes and fronts evolved will be used at future to relate spectral, fractal and mixing efficiency measures.

The initial instabilities are generated by gravitational acceleration and as the flow becomes non-linear the role of local turbulence is examined in experiments of Rayleigh-Taylor driven front, [2,3,4,5,6]. The advance of a mixing front due to the gravitational acceleration is responsible for the mixing and it constitutes typical configutation of a Rayleigh-Taylor (RT) instability in a high Reynolds number. The flow quickly becomes turbulent so the front between the two layers, which is believed to become independent of the initial conditions as turbulence evolves, and the range of scales increases. The advance of this front is described by differents authors and different experiments have been classified as producing internal or external mixing, but the role of initial and boundary conditions has not been explained enough.

The main goal of our experiments is to determine the influence of initial conditions on mixing. It would be interesting to compare different experimental conditions and evaluate which affects molecular mixing. Using a viscoelastic gel and a plate with holes in experiments similar to those reported by [2], we make the initial instabilities to be randomized into a set of plumes in a way in which the initial conditions (viscosity of gel and number of plumes) are seen to modify the overall mixing efficiency. Our first experimental setup is complicated because a bidimensional plume array interacts with a gravity current. To analyze better the mixing behavior of buoyant plumes, we performed new experiments with a line of plumes and a single plume generating hole, [7].

The growth of cumulus clouds in a turbulent atmosphere has usually been modeled as a rising thermal, in both numerical and experimental setups. A thermal is a small buoyant volume of fluid which is suddenly released into either a homogeneous or stably stratified environment. The growth of a thermal is expected to depend both on the buoyant momentum and the degree of external turbulence. So, it is important to elucidate the individual importance of the buoyancy induced (or internal) turbulence and the environmentally induced (or external) turbulence. The buoyant momentum causes internal turbulence and is dependent on the density gradient between the plume/thermal and its surroundings.

2 MIXING PROCESSES GENERATED BY TURBULENT PLUMES

We investigate turbulent mixing processes generated experimentally under an unstable density distribution in a fluid system. In our case, the fluids that constitute the unstable density stratification are miscible and the turbulence will produce molecular mixing. Because all experiments are performed with brine using common salt the molecular Schmidt number is almost same in all experiments (about 800) depending weakly on temperature. The global mass flow may be evaluated if the two different miscible layers have different solute concentrations. In our experiments the density difference is caused by salt heat and the Schmidt number for brine is S_c=812 (at 22ºC). These mixing processes are generated by a discrete number of forced turbulent plumes whose behaviour and interaction result in the mixing. We use a new experimental method to obtain an unstable density distribution, [1].

The fluid system consists of three homogeneous fluids with different densities that are initially at rest. At the bottom of the container there is a fluid with lower density ρ_L making a layer designated as the *light layer* with a height h_L. On top of this layer, a CMC gel stratum is placed with density ρ_G and a height of h_G. Finally, the fluid of greater density ρ_D which constitutes the *dense layer* which reaches a height h'_D and is coloured with sodium fluorescein –a passive tracer-.

The experiment begins when the dense fluid flows as jets and come into the gel layer; it goes through the gel locally arriving in the shape of jets which break down the surface tension of the gel. The result is the generation of several forced plumes which are gravitationally unstable. As the turbulent plumes develop, the denser fluid comes into contact with the lighter fluid layer and the mixing process between them begins. The behaviour of this fluid system is governed by the turbulent energy source generated by the buoyancy. Specifically, it depends on three factors: one, the CMC gel used which has viscosity ν_G; second, the Atwood number A and the third factor that influences overall mixing is the direct geometrical effect that the initial conditions have over the volume where mixing can take place, [1].

The final result of the mixing process is a mixed layer located at the bottom of the experimental container which is separated from the unmixed lighter fluid by means of the stable density interface which is clearly shown at digitalizations, [8]. Since not all of the lighter fluid participates in the mixing, we qualify it as a partial mixing process. The mixed layer height h_M represents the final height of this stable density interface. This height h_M is directly proportional to the final volume of the mixed fluid and therefore h_M could represent the volume of the mixed fluid.

The partial mixing process is characterized by two global properties: the mixing efficiency η and the mixed layer height h_M which depend on the characteristics of the fluid system in the initial and final states. As the mixing process is influenced by the initial buoyancy, these two global properties are analyzed versus the Atwood number A.

The first interesting result of our studies is represented in figure 2.1. We plot the average mixing efficiency as a function of the Atwood number of the fluid system. The mixing efficiency η of this process is defined as the fraction of the available energy that is used to mix the fluids. In general, we observe that the efficiency increases as the Atwood number A grows. Physically, the increase in Atwood number implies that the buoyancy effect grows, as does the convective acceleration. Therefore it produces a greater mixing process with a higher efficiency associated with it, [1].
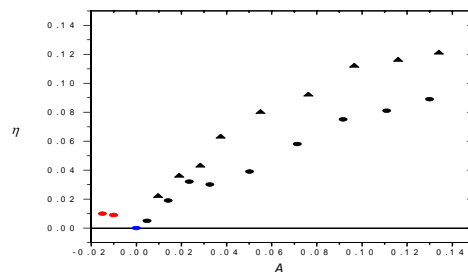

Figure 2.1. Mean mixing efficiency versus the Atwood number for experiments made with the more viscous CMC gel (Curve 1, •), and with the less viscous one (Curve 2, ▲). Aditionally, the results for initial stable (•) and neutral (•) situations are shown.

Curve 2 of figure 2.1 shows that the experiments done with the less viscous gel have a mixing efficiency greater than the one corresponding to the experiments with the more viscous gel shown in curve 1. Our hypothesis is that the greater number of turbulent plumes created when the gel viscosity is reduced, the greater mixing efficiency. The mixing efficiency values are small if we compare them with the efficiency of a RT instability –although the global variation is right-. There are two reasons for these different values. First, the presence of the CMC gel layer in the experimental setup which reduces efficiency about 40% if we compare it with experiments without gel.

The main reason is the turbulent plume array generated during the evolution of the experiments. This bidimensional plume array makes a conical volume without mixing process. This non-mixing volume produces a lower volume useful to mix because it is inside the light fluid layer. There is an interpenetration of the unstable plumes only through a fraction of the area at the top, precisely because once the dense fluid looses its potential energy it may not mix with lighter fluid above. Therefore, the denser fluid and the lighter one do not mix completely which implies that the mixing process is only partial. Therefore, the mixing efficiency must diminish.

All the turbulent plumes feed on the ambient light fluid. As a consequence there is a height h which represents the start of plume lateral interaction as figure 2.2 shows. This height h determines the non-mixing volume. The mixing process occurs from the height $h_L – h$ to the bottom of the experimental container, but not before. We suppose that all turbulent plumes start their lateral interaction at height h when they have a radius R and they are approximated by cones, [1].

We made a brief theoretical study of this plume effect using figure 2.2 and we deduced that adimensional mixing volume has the expressión:

$$V_{MIXING}^{*} = \left(1 - \frac{2h}{3h_L} \right) \quad , \tag{2.1}$$

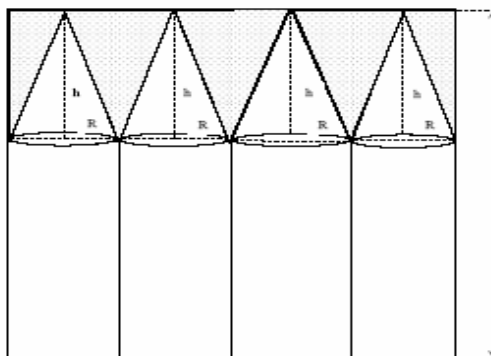which behaviour is represented in figure 2.3.

Figure 2.2. Initial growing scheme of a turbulent plume array. Every plume is represented, approximately, by a cone which radius is the plume radius, R.. The lateral interaction between plumes starts at a depth h. The height of the light fluid layer is h_L. The dotted region is the conical non-mixing volume.
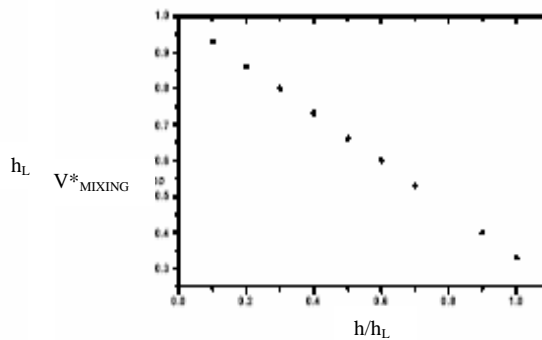
Figure 2.3. Graphic behaviour of adimensional mixing volume V^{*}_{MIXING} versus h/h_L.

We deduce that the adimensional mixing volume varies from 86% if the height ratios is $(h/h_L)=1/5$ to 66% if $(h/h_L)=1/2$. The figure 2.3 shows a decrease of the mixing volume V^{*}_{MIXING} if the height ratios h/h_L grows because then plumes reach a larger depth without interacting. The largest mixing volumes appear when plumes interact as soon as possible. The non-mixing volume $V^{*}_{NON-MIXING}$ has the inverse behaviour and its value influences the mixing efficiency.

We make new experiments with a line plume array to verify previous results and theoretical hypothesis. We want to investigate better the relation between the non-mixing volume $V^{*}_{NON-MIXING}$ and the mixing efficiency η and to evaluate the results showed in figure 2.1, i.e., the less the number of plumes the lower the mixing efficiency, [1]. The non-mixing height h_{NM} could represent this non-mixing volume $V^{*}_{NON-MIXING}$.

The new experiments are performed using different brine concentrations as the two mixing fluids, with Atwood number of 0.03. We don't use the viscoeleastic gel because we want to control the

number of plumes and their geometric configuration into a line array. This is the main difference of this new experimental setup. Figure 2.4 shows a frame of one of these new experiments with seven plumes in a line setup.

We measure the number of plumes, n_p, and the non-mixing height directly from the digitalizations of the experiments. The mixing efficiency η is related with the inverse of non-mixing height, h_{NM}, which represents the non-mixing volume $V*_{NON-MIXING}$ This is the reason why we measure the non-mixing height and we relate it with the number of plumes as it is deduced from figure 2.3 . The results are shown in figure 2.5.
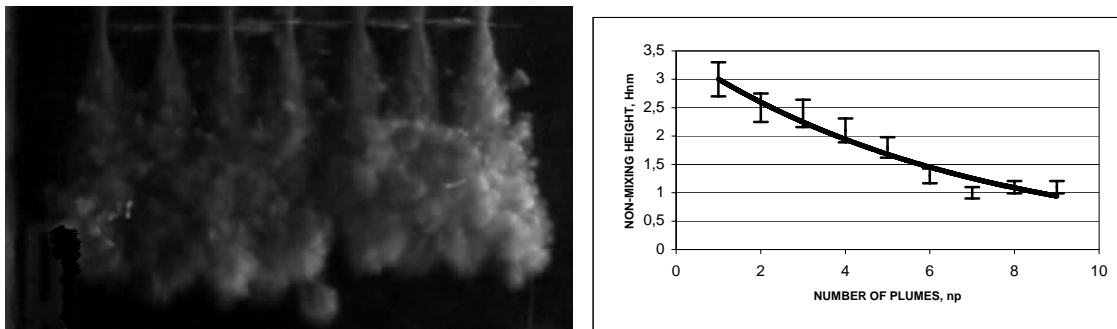

Figure 2.4. Experimental frame showing seven plumes in a line array.

Figure 2.5. Graphical behaviour of the non-mixing height, h_{NM}, versus the number of plumes, n_p.

The figure 2.5 shows us the larger the number of plumes, n_p, the lower the non-mixing height is, and then the larger the mixing efficiency. And this result agrees with results deduced from figure 1. Therefore, we have verified that the initial conditions modify the overall mixing efficiency, i. e., the number of plumes affects the mixing efficiency.

SUMMARY

This paper present some important conclusions related to the global mixing efficiency variation for different forcings. Our main purpose is to clarify the relation between the mixing efficiency and the number of plumes formed initially. We have deduced that the less the number of plumes the lower the mixing efficiency because the larger the number of plumes, n_p, the lower the non-mixing height is.

The structure of the plume array may be seen in the digitalizations of the experiments. The front growth in accordance with other authors [5] and analysed with DigIFlow [8] is seen to depend strongly on initial conditions, i.e. the number and structure of the plume array. The advance of the front may change between linear and quadratic with time as the role of the initial momentum and buoyancy.

REFERENCES

[1]   Gonzalez Nieto, P.L., 2004, PhD Thesis. Universidad Complutense, Madrid.
[2]   Linden P.F. & Redondo J.M. (1991) "Molecular mixing in Rayleigh-Taylor instability. Part 1. Global mixing". Phys. Fluids. 5 (A), 1267-1274.
[3]   Linden P.F., Redondo J.M. and Youngs D. (1994) "Molecular mixing in Rayleigh-Taylor Instability" Jour. Fluid Mech. 265, 97-124.
[4]   Redondo J.M. and Linden P.F.(1990) Mixing produced by Rayleigh-Taylor instabilities Proceedings of Waves and Turbulence in stably stratified flows, IMA conference. Leeds 18 Dec 1989. Ed. S.D. Mobbs.
[5]   Sharp, D. H. (1984). An overview of Rayleigh-Taylor Instability, Physica 12D, 3.
[6]   Redondo, J.M., *The structure of density interfaces,* PhD. Thesis: Cambridge University.
[7]   Redondo, J.M. & Yague, C. (1995) Plume entrainment in stratifed fows Recent Research Advances in the Fluid Mechanics of Turbulent Jets and Plumes , 209-222.
[8]   Dalziel S. (2005) DigiFlow DL Research Partners DigiFlow userguide Version 1.0, Cambridge.
[9]   Yague C., 1993, PhD Thesis. Universidad Complutense, Madrid.

e-mail: `olivier.poujade@cea.fr`

Some features of Rayleigh-Taylor turbulent spectrum with a simple model

Olivier POUJADE[1]

[1] *CEA/DAM Île-de-France BP 12 91680 Bruyères-le-Châtel FRANCE*

Abstract: An increasing number of numerical simulations and experiments [1, 12] describing the turbulent spectrum of Rayleigh-Taylor (RT) mixing layers came to light over the past few years. However, the results reported in these studies are far too diverse to draw any conclusions on the mechanisms that shape the spectrum, $E_{RT}(k)$, in a RT situation. Indeed, depending on initial conditions, molecular viscosity or numerical viscosity, Atwood×acceleration, experimental setup or numerical approach, the RT turbulent spectrum $E_{RT}(k)$ may behave in all or part of the spectrum like $\sim k^{-1}$, $k^{-5/3}$, k^{-3}, k^{-4} or k^{-5}. It contrasts with the "simple" homogeneous isotropic turbulent situation where the Kolmogorov spectral law $E(k) = C_K \epsilon^{2/3} k^{-5/3}$ is well established numerically, experimentally and theoretically. Although the answer to that question would allow to gain some insight into the physics of RT mixing layers, it is also essential in the industrial applications (ICF) when it comes to modelling the turbulence in such layers. Results reported in recent studies allow to rule out a turbulence *à la Kolmogorov* as a mechanism acting on a self similar RT turbulent mixing layer. A different mechanism is presented, which complies with both numerical and experimental results and relates RT flow to other buoyant flows.

1 INTRODUCTION

Turbulence in Rayleigh Taylor mixing layers has been thought to behave as in free shear flows. Actually, the mechanism is significantly different.

When a fluid is made turbulent by continuous stirring, the mechanical power injected creates big whirls which transfer their energy to smaller whirls until viscous effects overcome this process. The transfer of energy to the inertial range (from large scales to small scales) occurs at the constant rate of viscous dissipation at small scales.

Kolmogorov's vision is accurate for free shear flows but it does not explain turbulence in Rayleigh Taylor mixing layers. In this case, the injected power is due to buoyancy motion on a broad range of length scales. It tends to accumulate at large scales so that big whirls can get bigger as the mixing layer thickness increases. Only a small fraction of this power is transferred to small scales through a Kolmogorov cascade and dissipated. This balance between the accumulation of energy at large scales and the buoyancy production can also be applied to Rayleigh-Bénard instabilities. It explains the Bolgiano-Obukov scaling predicted and experimentally observed for these flows. The detail of this work can be found on [13].

2 SELF-SIMILARITY HAS CONSEQUENCES ON THE RT TURBULENT SPECTRUM

The RT developed turbulent regime, as complex as it may look, is thought to evolve self similarly [15]. The size of the largest significant turbulent structure, therefore, grows like the size of the turbulent mixing zone which evolves as $L(t) = \alpha \mathcal{A} g t^2$ [6] where α is the mixing-zone-width growth rate parameter whose value is around ~ 0.06 experimentally and between 0.03 and 0.07 numerically. It can be assumed that at low wave numbers in the self similar regime the velocity spectrum $E(k,t) = 0$ for $k < k_l(t)$, where $k_l(t)$ is the wave number corresponding to the maximum of the velocity spectrum (this point will be called λ due to the shape of the idealized spectrum at this location), and $E(k,t) \approx \Psi_l(t) k^{-n_l}$ for $k \geq k_l(t)$. Nothing else is assumed concerning the behavior of $E(k,t)$ at intermediate and high wave numbers $k \gg k_l(t)$. In the self similar regime, it is found that the point λ must evolve on the curve

$$E_\lambda \sim (\mathcal{A}g) \, k_\lambda^{-2} \, , \tag{2.1}$$

independently of the slope of the spectrum (n_l). This behaviour has been checked by A. Cook and W. Cabot and presented, among other things, at this meeting.

3 A KOLMOGOROV MECHANISM IS RULED OUT BY NUMERICAL SIMULATIONS

If it is assumed that RT turbulence follows Kolmogorov's mechanism [14,15], the turbulent spectrum has the well known form $E(k) = C_K \, \epsilon^{2/3} \, k^{-5/3}$. Then, it can be shown [14] that $\epsilon \sim t$ and $k_\eta(t) = \left(\epsilon/\nu^3\right)^{1/4} \sim t^{1/4}$ meaning that the velocity spectrum must grow. This conclusion is incompatible with recent DNS/LES simulations [2,8] showing the velocity spectrum evolution in time. Even though it is not stated in these references, it can clearly be noticed that the level of the velocity spectrum at low wave number does not grow as time goes by but remains still.

4 GENERALIZATION OF LIN'S EQUATION FOR BUOYANT FLOWS

The RT flow of two incompressible fluids in the low Atwood limit, $\mathcal{A} = (\rho_2 - \rho_1)/(\rho_2 + \rho_1) \ll 1$ (Boussinesq approximation), is governed by a concentration equation (4.1), the Navier Stokes equation supplemented with a buoyant source term (4.2) and the incompressibility constraint (4.3)

$$
\begin{aligned}
\partial_t \, c + (u\nabla) \, c &= \kappa \, \Delta c \, , & (4.1)\\
\partial_t \, u + (u\nabla) \, u &= -\nabla P + \mathcal{A}g \, c + \nu \, \Delta u \, , & (4.2)\\
\nabla u &= 0 \, , & (4.3)
\end{aligned}
$$

where g is a stationary and uniform gravitational acceleration vector field (i.e. planar symmetry is assumed). The coefficient κ is the molecular diffusion coefficient and ν is the kinematic viscosity of the mixture. By taking the fourier transform of Eq.(4.2) and after some algebraic manipulations it is possible to write the equation governing the evolution of $E(k,t)$ (a generalisation of Lin's equation [16]) to make the buoyancy production term appear :

$$
\partial_t E = T(k) - 2\nu k^2 E + \beta \mathcal{A}g E_c^{1/2} E^{1/2} \, , \tag{4.4}
$$

where $E_c(k,t)$ is the concentration spectrum. In the self similar regime, it is then possible to prove that the velocity spectrum is closely related to the concentration spectrum through its slope $-n_c$:

$$
E(k) \sim c_0 \, (\mathcal{A}g)^{\frac{3-n_{cl}}{2}} \, t^{1-n_{cl}} \, k^{-\frac{3+n_{cl}}{2}} \, . \tag{4.5}
$$

It is to be noticed that when $n_{cl} = 1$, the previous time evolution is changed to $\log(t)$. This is due to a balance between buoyancy production and spectral transfert. This mechanism also explains the Bolgiano scaling for Rayleigh-Bénard instabilities.

REFERENCES

[1] Y. N. Young, H. Tufo, A. Dubey & R. Rosner, J. Fluid Mech. **443**, 69 (2001).

[2] A. W. Cook & Y. Zhou, Phys. Rev. E **66**, 026312 (2002).

[3] W. Cabot, O. Schilling & Y. Zhou, Phys. Fluids **16**, 495 (2004).

[4] S. Dalziel, P. Linden & D. Youngs, J. Fluid Mech. **399**, 1 (1999).

[5] A. W. Cook & P. E. Dimotakis, J. Fluid Mech. **443**, 69 (2001).

[6] G. Dimonte *et al.*, Phys. Fluids **16**, 1668 (2004).

[7] P. Ramaprabhu, G. Dimonte & M. J. Andrews, J. Fluid Mech. **536**, 285 (2005).

[8] A. W. Cook, W. Cabot & P. L. Miller, J. Fluid Mech. **511**, 333 (2004).

[9] W. Cabot, Phys. Fluids **18**, 045101 (2006).

[10] P. Ramaprabhu & M. Andrews, J. Fluid Mech.**502**, 233 (2004).

[11] P. Wilson, M. Andrews & F. Harlow, Phys. Fluids **11**, 2425 (1999).

[12] P. Wilson & M. Andrews, Phys. Fluids **14**, 938 (2002).

[13] O. Poujade, Phys. Rev. Lett. **97**, 185002 (2006)

[14] M. Chertkov, Phys. Rev. Lett. **91**, 115001 (2003).

[15] J. R. Ristorcelli & T. T. Clark, J. Fluid Mech. **507**, 213 (2004).

[16] S .B. Pope, *Turbulent Flows*, Cambridge University Press (2000).

e-mail: praveen@lanl.gov

New insights in to the single-mode Rayleigh Taylor instability

P. RAMAPRABHU[1], Guy DIMONTE[1], Y.-N. YOUNG[2], A.C. CALDER[3] and B. FRYXELL[1]

[1]Los Alamos National Laboratory, Los Alamos, NM 87545 USA
[2]New Jersey Institute of Technology, Newark, NJ 07102, USA
[3]University of Chicago,Chicago, IL 60637, USA

Abstract: The dependence of the single-mode Rayleigh-Taylor (RT) instability on density difference effects is investigated using four different numerical codes. As the density difference driving the flow approaches infinity, bubbles reach a constant terminal velocity, in agreement with the classical result of Layzer [1]. At the same time, spikes are narrow and in free-fall, a result which can be understood through simple drag-buoyancy arguments. The extension of these ideas to finite density differences is characterized by terminal velocity for bubbles early in time in agreement with a corresponding potential flow theory (Goncharov [2]), and an accelerating flow at late-times. The late-time acceleration is a new result and appears to be driven by the formation of Kelvin-Helmholtz rollups, an effect that is not included in existing nonlinear models of RT.

1 INTRODUCTION

A sharp interface separating two fluids of different densities is Rayleigh-Taylor unstable if an acceleration is directed from the light fluid to the heavy. In this paper, we consider only monochromatic or single-mode interfacial perturbations of wavelength λ and amplitude h_0. It has been shown [3] that an understanding of this simple flow is necessary before considering the fully turbulent RT instability. The growth of such perturbations at the interface is at first exponential [4]

$$h = h_0 e^{\boldsymbol{g}} \,, \tag{1.1}$$

with a growth rate γ, and then linear in time, with a corresponding terminal velocity given by

$$v = Fr\sqrt{\frac{Ag\boldsymbol{l}}{1+A}} \,, \tag{1.2}$$

where *Fr* is a Froude number. The initial growth stage is often referred to as "linear" since only linear terms in the perturbation equations are important, while the latter stage is termed nonlinear. In the nonlinear stage, the light fluid rises as bubbles due to buoyancy, displacing the heavy fluid, which descends as spikes. While (1.1) is an exact result in the absence of viscosity or other stabilizing effects, the behavior of bubbles and spikes in the nonlinear stage as a function

of the Atwood number ($A = \dfrac{\boldsymbol{r}_2 - \boldsymbol{r}_1}{\boldsymbol{r}_2 + \boldsymbol{r}_1}$) is controversial due to disagreement among proposed models [2,5,6]. The differe-

rences stem from the choice of potential functions and boundary conditions. In this work, we evaluate competing nonlinear models using numerical simulations, and extend their description to late-times. The results are of interest in describing the turbulent growth rate $\boldsymbol{a}$ which can be related to the Froude number of the dominant bubbles in a bubblefront using

$$\boldsymbol{a} = \frac{Fr^2}{8} \frac{\boldsymbol{r}_1 + \boldsymbol{r}_2}{\boldsymbol{r}_2} \frac{D_b}{h_b} \,. \tag{1.3}$$

Image analysis from the Linear Electric Motor experiments show that $h_b/D_b > 1$ for leading RT bubbles in a turbulent flow. To evaluate bubble dynamics in a regime relevant to turbulent flow, we calculate RT single-mode flow in an elongated box, and at late-times.

2 RESULTS

We report on numerical simulations of the single-mode Rayleigh-Taylor problem up to intermediate and late-times. The calculations were performed using four different codes, and in an elongated box (1x1x81) to accommodate the late-time growth. 3D perturbations of the form

$$h(x, y) = h_0\{\cos(kx) + \cos(ky)\} \qquad (2.1)$$

were used, with the amplitude chosen such that $kh_0 << 1$. Three of the codes belong to the MILES category, while a fourth Direct Numerical Simulation (DNS) was also employed. Other details of the calculations, including descriptions of the algorithms used are provided in [7].

Figure 2.1 is a plot of the Froude numbers deduced from the intermediate-time saturation velocities of bubbles from the codes used in this study as a function of the Atwood number. All the codes give a constant $Fr = 0.56$ in agreement with [2], but not with [5] and [6] who predict a different functional form for the Froude numbers. This is because the form of potential functions used in [2] satisfies the condition of zero net mass-flux across the interface.
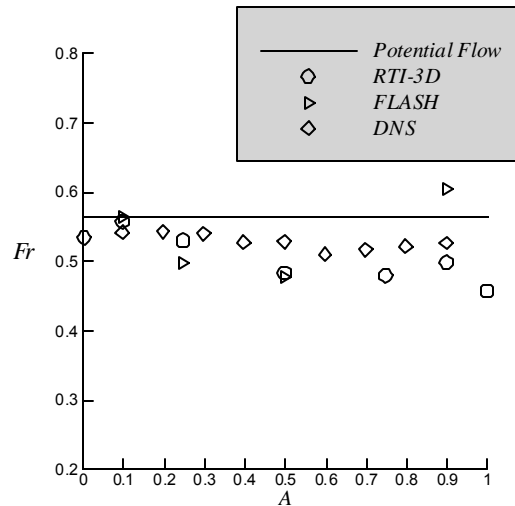

Figure 2.1 Froude numbers from 3D NS and potential flow theory of [2].

While bubbles reach a terminal velocity for intermediate times at all A, figure 2.2 (a) shows that spikes resemble bubble behavior at small A, but accelerate at larger density differences. As $A \rightarrow 1$, $v_s \sim \sqrt{\dfrac{2A}{1-A}\dfrac{g}{k}}$ from drag-buoyancy models [8] and potential flow theory of [2] becomes unbounded, and spikes are in free-fall. This can be understood from a simple balance of drag and buoyancy terms on the spike objects:

$$\ddot{h}_s = Ag - C\dot{h}_s^2 \frac{r_1}{r_1 + r_2}\frac{1}{h_s} \qquad (2.2)$$

For $A \rightarrow 1$ ($r_1 \rightarrow 0$), equation (2.2) and our NS (figure 2.2 (b)) give $h_s \sim \dfrac{1}{2}gt^2$. Finally, by applying mass conservation on any horizontal plane, it also follows that as $A \rightarrow 1$, bubble diameters increase while spike diameters become vanishingly small.
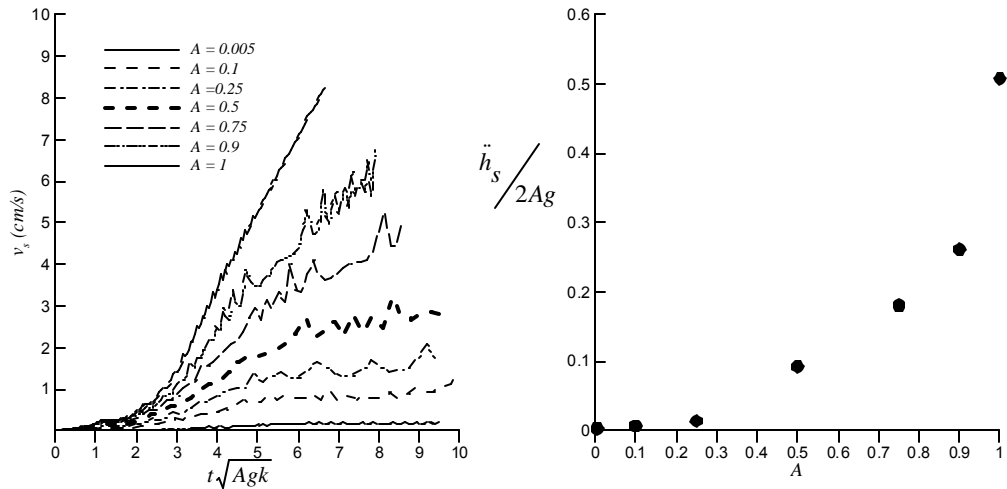
Figure 2.2 (a) Time evolution of spike velocities at different A. (b)Non-dimensional spike acceleration coefficient vs. A.

Figure 2.3 shows the evolution of bubble Froude numbers up to late times for different Atwood numbers. The Froude number is plotted against the bubble aspect ratio h_b/D_b. The small A calculations exhibit a curious acceleration away from the terminal velocity, followed by a saturation to a higher Fr late in time, while the large A cases ($A>0.5$) remain terminal. This behavior is observed in all of the codes used here, and occurs at $h_b/D_b \sim 1$. Such a deviation from the classical potential flow result has been observed earlier by [9] who attribute the effect to bubble-tip curvature effects. However, our image analysis indicates that this is not the case.
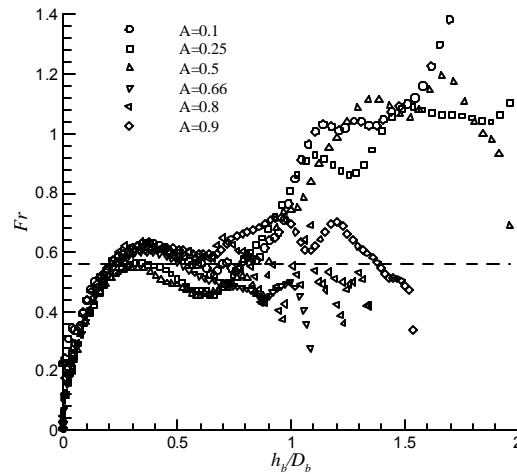

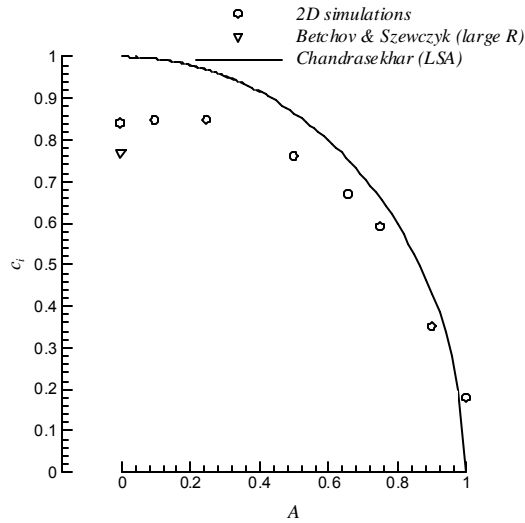Figure 2.3 Time history of bubble Froude numbers from NS at different A.

Figure 2.4 Kelvin-Helmholtz growth rates from 2D NS and linear stability theory.

We attribute the observed behavior to the formation of secondary Kelvin-Helmholtz (KH) vortices on the neck of the bubbles at small density differences. The induced flow from such secondary vortices creates a momentum jet that accelerates the bubbles to a higher Froude number. Such a mechanism has been identified in boosting the rise velocity of turbulent RT bubbles [10], and by certain species of fish to propel themselves [11]. However, note that the appearance of secondary KH instabilities in RT is confined to small density differences. This is consistent with linear stability analysis of KH flow [4] which suggests that at large density differences, the shear layer growth c_i is suppressed inertially according to

$$c_i = \pm \sqrt{-k_x^2 (\Delta U)^2 \frac{r_1 r_2}{(r_1 + r_2)^2}} \; , \tag{2.3}$$

where ΔU is the velocity difference driving the flow. Thus, from (2.3) $c_i \rightarrow 0$ for A $\rightarrow$ 1. This is also observed in our 2D simulations of KH flow, the growth rates from which are summarized in figure 2.4. The calculations used a square domain (λxλ) with the velocity contrast ΔU spread across 3 zones and g = 0, since buoyancy is not relevant here. Our calculations which correspond to a piecewise linear profile are in good agreement with the linear stability analysis of [4] who assumed a step-function for the velocity profile, and with [12] who considered a tangent hyperbolic function. Furthermore, the growth rates from theory and NS are only weakly sensitive to A for small density differences. This explains why the observed acceleration in RT appears at approximately the same point in time for cases with small A (at h_b/D_b ~1), since the growth rates of the underlying KH instability remains nearly uniform under such conditions.

These ideas can be further verified by quantifying the size of secondary vortex cores in RT for different A. We adopt the definition proposed by [13] that identifies connected regions with two negative eigen-values of the velocity gradient tensor as a vortex. This condition ensures that a local pressure minimum exists in a vortex core, while at the same time eliminating false positives due to unsteady straining and viscous effects. Figure 2.5 shows the evolution of the % volume occupied by vortex cores (identified using this technique) within the computational domain, as a function of h_b/D_b at $A = 0.005$ and 1.0. Clearly, there is a sudden development of secondary vortex structures near $h_b/D_b \sim 1$, for the low Atwood case. This event coincides with the onset of the observed acceleration. Conversely, the high Atwood case shows no such trend, consistent with the lack of observed acceleration.
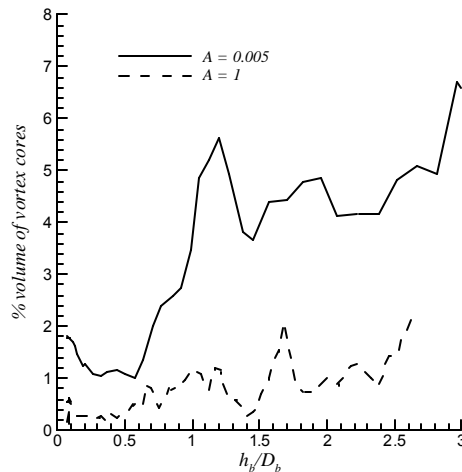
Figure 2.5 Evolution of % volume of computational box occupied by vortex cores at A = .005 and 1.0.

3 SUMMARY

We have investigated the single-mode Rayleigh -Taylor instability in a long box, and at late-times, so that the results bear direct relevance to the turbulent flow. We find that initially, the nonlinear flow is in agreement with the model of [2], because their choice of the velocity potential function satisfies the no flux condition across the interface. At late-times, the behavior depends on the Atwood number. At small A, secondary Kelvin-Helmholtz vortices form on the neck of the primary bubble, the induced flow from which accelerates the bubbles away from the expected terminal velocity. The formation of KH vortices at large A is suppressed, consistent with the linear stability theory of [4]. We conclude that potential flow models are accurate in the regime they are applicable (at high A). At low A, the development of secondary instabilities complicate the evolution due to the associated vertical momentum jet propelling the bubbles forward. We suggest further numerical simulations of this simple problem to verify our conclusions.

REFERENCES

[1]   D. Layzer, Astrophys. J 122, 1 (1955).
[2]   V.N. Goncharov, Phys. Rev. Lett. **88**, 134502 (2002).
[3]   Guy Dimonte, Phys. Rev. E **69**, 056305 (2004).
[4]   S. Chandrasekhar, *Hydrodynamic and Hydromagnetic Stability* (Oxford University Press, Oxford, 1961).
[5]   S-I. Sohn, Phys. Rev. E 67, 26301 (2003).
[6]   S. I. Abarzhi, K. Nishihara, and J. Glimm, Phys. Letters A 317, 470 (2003).
[7]   P. Ramaprabhu, Guy Dimonte, Y_N. Young, A.C. Calder, B. Fryxell, Phys. Rev. E 74, 066308 (2006).
[8]   D. Oron et al., Phys. Plasmas **8**, 2883 (2001).
[9]   J. Glimm *et al.*, Phys. Fluids **A 2**, 2046 (1990).
[10]   N.A. Inagamov *et al.*, J. Expt. Theo. Phys. **92(4)**, 715 (2001).
[11]   F.E. Fish & G.V. Lauder, Ann. Rev. Fluid Mech. **38**, 192 (2006)
[12]   R. Betchov and A. Szewczyk, Phys. Fluids **6**, 1391 (1963).
[13]   J. Jeong and F. Hussain, J. Fluid Mech. **285**, 69 (1995).

e-mail: `bonazza@engr.wisc.edu`

Experimental Study of the Interaction of a Planar Shock with a Free-Rising Bubble

Devesh RANJAN[1], John NIEDERHAUS[1], Mark ANDERSON[1], Bradley MOTL[1], Jason OAKLEY[1], Riccardo BONAZZA[1] and Jeffrey GREENOUGH[2]

[1] *University of Wisconsin-Madison, Madison, WI 53706 USA*
[2] *Lawrence Livermore National Laboratory, Livermore, CA 94550 USA*

Abstract: Results are presented from experiments studying the interaction of a planar shock wave of strength $1.4 < M < 3.0$ with a spherical soap bubble composed of helium using planar laser diagnostics. Experiments are performed in a 9.2m-long, vertical shock tube with a square internal cross-section, 0.254 m on the side, equipped with a pneumatically-driven retractable bubble injector. The absence of a bubble holder during shock wave passage allows for a cleaner initial condition while avoiding complications associated with holder/shock interaction. In parallel with laboratory experiments, a computational investigation is carried out using a 3-D compressible hydrodynamics code called *Raptor*. As the planar shock passes over the bubble, intense vortical and nonlinear acoustic phenomena are observed, including vortex ring formation, mixing, and growth of turbulence-like features. The origin and growth of distinctive counter-rotating secondary vortical features are observed in the case of a high-Mach number experiment.

1   INTRODUCTION

The evolving flow field generated by the interaction of a shock wave with a discrete density inhomogeneity is a problem of fundamental interest which can be used as a "building block" to develop an understanding of more complicated problems involving shock propagation through random media. The shock-bubble interaction (SBI) is a fundamental configuration for studying shock accelerated inhomogeneous flows (AIF), *i.e.*, an extension of the Richtmyer-Meshkov instability (RMI). The test gas is contained inside a large spherical soap bubble. Soap bubbles represent the simplest form of gas enclosure with their natural tendency towards spherical shape, ideal for a 3-D problem. The soap membrane is thin and tenuous which keeps the film effects to a minimum.
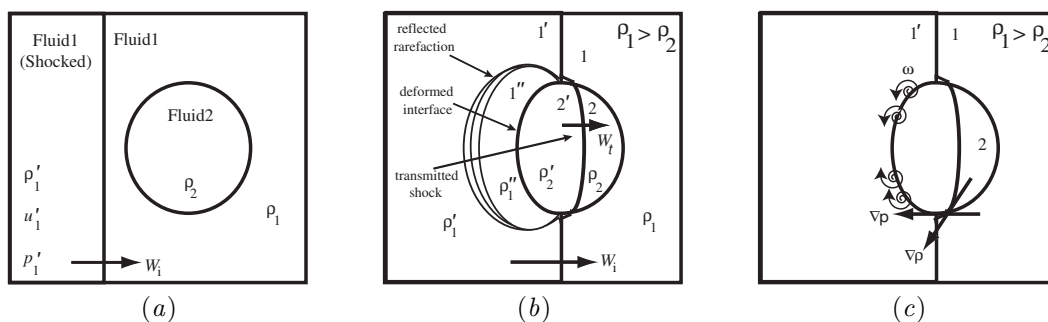

Fig. 1.1. Schematic diagram of shock reflection, transmission and vorticity distribution in the early phase of a shock-bubble interaction for a light bubble: (*a*) pre-shock; (*b*) post-shock wave pattern; (*c*) vorticity distribution.

Previous studies of the shock-bubble interaction include the seminal work of Haas and Sturtevant [1] and the recent works of Layes *et al.* [2,3]. These previous experiments were conducted in horizontal shock tubes with the bubble supported by a holder and subjected to a $M < 1.3$ shock wave in air. The presence of a vortex ring structure was suggested by the shadowgraphs; however, due to the integral visualization technique employed, the detailed structure of the vortex was not captured. These experiments were later modeled numerically in two dimensions [4,5] with the results being in reasonable agreement with the experiment. Recently, experiments have been reported studying the shock-bubble interactions at higher Mach numbers [6], in an attempt to

bridge the gap between the low-Mach number shock-tube experiments and very high-Mach number laser-driven experiments. These recent experiments show the presence of secondary vortex rings at late times which are absent in the case of low-Mach number experiments. We present here results from experiments and numerical simulations studying the interaction of a planar shock-wave of strength $1.4 < M < 3.0$ with a spherical soap bubble composed of helium.

Figure 1.1 shows the wave pattern and vorticity deposition during the early phase of a shock-bubble interaction for a light bubble. At low angles of incidence, regular refraction occurs where the transmitted wave and the incident wave intersect the interface at the same point. At higher angles, various aspects of irregular refractions are observed where usually the interaction of the transmitted wave with the interface runs ahead of the incident wave or of a Mach stem, as shown in Fig. 1.1(b).

2   EXPERIMENT DESCRIPTION

The experimental setup used here is a slightly modified version of the setup described by Ranjan *et al.* [6] where the interaction of a strong planar shock wave $M = 2.88$ with an isolated argon bubble in nitrogen was studied. In these experiments, the retractable injector has been inverted so that the bubble can rise freely once released from the injector, without hitting the injector itself. The release and free rise of the bubble sequence is illuminated with front white lighting and is recorded at 250 fps with a CCD camera (DALSA CA-D1-0256A). This allows the capture of the evolution of the bubble during its release from the injector and provides an initial condition image of the bubble prior to (within 10 ms) shock interaction, during which the vorticity is deposited and the RMI initiates. The evolution of the flow structures is captured using planar laser imaging. The flow is illuminated with a pulsed Nd:YAG laser (Continuum Surelite II) and a Lambda Physik excimer laser (LPX210). The laser beam is formed into a plane and transmitted through the center of the bottom of the shock tube. The Nd:Yag laser is capable of two pulses separated by a minimum of 100 ns, with a pulse width of 10 ns duration. Three 1024×1024 pixel array Andor (model 434) CCD cameras are used to capture the Mie scattered light resulting from the laser interaction with the soap film solution (the soap film is atomized into micron sized particles during interaction with the strong shock). Two images are recorded on a single CCD frame in dual exposure mode in the compression phase of the bubble. These two images are the Mie-scattered signal resulting from the interaction of the Nd:YAG laser pulses with the atomized soap film. A UV lens is used to focus the signal obtained from the interaction of the excimer laser and atomized soap film onto the CCD array. The shock strengths are chosen to investigate the distortion of the bubble in regimes where the post-shock velocity in the ambient gas is less than, approximately equal to, and greater than, the local sound speed. The experimental scenarios are presented in Table 2.1. Several experiments have been conducted and the bubble diameter after release in the initialization of the experiment is $D = 3.8$ cm, repeatable to within $\pm 5\%$.

Scenario #	Bubble gas	Ambient gas	M	A	u_1'/c_1'
1	Helium	Air	1.45	-0.757	**0.56**
2	Helium	Air	2.08	-0.757	**1.01**
3	Helium	Nitrogen	2.95	-0.750	**1.35**

Table 2.1. Experimental study overview. M is the Mach number of the initial incident shock wave; A is the pre-shock Atwood number at the bubble surface. u_1' and c_1' represent the flow speed and sound speed of the shocked ambient gas, respectively.

3   NUMERICAL SIMULATION

The experimental configuration described above is simulated numerically in 3-D using an adaptive Eulerian hydrodynamics code called *Raptor*. Numerical integration of the 3-D compressible Euler equations is accomplished using an operator-split, second-order Godunov method (see Colella, 1985 [7]). Multifluid capturing capability is added to the scheme by adopting a volume-of-fluid technique similar to that described by Miller and Puckett (1996) [8], which allows two fluids with distinct adiabatic exponents to be included in the calculation. The integration kernel is embedded within the block-structured adaptive mesh refinement (AMR)

framework of Berger and Oliger (1984) [9], to maximize spatial resolution and accuracy for regions of interest that move across the Eulerian mesh.

Calculations for the shock-bubble interaction using *Raptor* are set up on a Cartesian mesh subtending a quadrant of a typical shock tube flow field, including a quarter-spherical bubble of radius $R = 1.905$ cm. A coordinate system is defined whose y-axis is coincident with the shock tube long axis, with physical dimensions $12.7 \times 84.7 \times 12.7$ cm, and a base grid of $42 \times 280 \times 42$ cells. Two levels of AMR are applied in the region surrounding the bubble, with a refinement ratio of 4 each, yielding an effective spatial resolution of $\Delta = 190$ μm, implying 100 highest-level grid cells are subtended by a distance R. Symmetry conditions are applied on the transverse boundaries to enforce quarter-symmetry and allow wave reflections at the shock tube side walls. Inflow/outflow conditions are applied on the axial boundaries to maintain constant driving pressure and allow waves to exit the domain smoothly (no endwall is included).

In the initial condition, a planar shock wave ($1.4 < M < 3.0$) approaches a quarter-spherical bubble of helium ($\gamma = 1.667$, $\rho = 0.1614$ kg/m^3) in an otherwise uniform nitrogen environment ($\gamma = 1.399$, $\rho = 1.129$ kg/m^3). The shock moves in the $+y$-direction, and the bubble is centered on the y-axis. The interface at the surface of the bubble is created carefully in the initialization by using a subgrid volume-of-fluid model to suppress "stairstep" density features associated with realizing a curved interface in a Cartesian mesh. This produces a smoothed interface with a maximum thickness of $2\Delta = R/50$. The development of the flowfield is tracked at closely-spaced time intervals during and after the impact of the shock on the bubble. Planar visualizations and integral length scales obtained from the resulting datasets are shown below and compared in detail with experimental results.

4   RESULTS

Figure 4.2 shows the evolution of a shocked spherical helium bubble after contact with a $M = 1.45$ shock wave with a velocity of 505 m/s in air. The particle speed behind the shock in air is $u'_1 = 221$ m/s and the transmitted shock wave velocity in helium is $W_t = 1242$ m/s (computed from 1-D gas dynamics). Experimental and computational times, measured from the time of the initial shock-bubble interaction, are normalized by the quantity $t' = D/(2 \times W_t)$ where D is the initial bubble diameter and W_t the speed of the planar transmitted shock that would be achieved if the same shock accelerating the bubble struck a planar interface between the same two gases. Experimental images represent light scattered from atomized film material in the bubble midplane; computational images are 2-D plots (a slice plane) of the volume fraction of helium (left) and the vorticity field (right). Figure 4.2(a-d) illustrates the formation of the primary vortex ring (hereafter referred to as PVR), due to the vorticity deposited during the early interaction phase of the shock-bubble interaction (see Fig. 1.1c). The caving-in observed in Fig. 4.2(b) is analogous to the phase reversal observed in single-mode heavy/light RMI experiments. The observed caving-in is a consequence of vorticity generation due to $\nabla \rho \times \nabla p \neq 0$ which leads to the formation of the strong air jet moving towards the downstream interface. The atomized soap film traces the air jet from the upstream side of the bubble. The soap particles following the velocity field (strong air jet) can be seen piercing through the downstream end of the bubble which leads to the formation of the PVR. This was defined as the mechanism for the formation of the PVR by Haas and Sturtevant [1]. Finally in Fig. 4.2(d) one can clearly see the PVR at the downstream end of the bubble. The visualization technique utilized here highlights the fringes of the vortical cores but leaves the core itself as a distinct dark spot, as light-scattering soap film particles are centrifuged outwards. The PVR structure is thus much more clearly resolved and distinguishable in the present experiments. The other notable feature is the tear-drop shaped object formed behind the PVR. The tear-drop object consists mostly of the unmixed helium and therefore it is referred as "helium lobe". A small amount of vorticity is seen on the edges of the helium lobe. In both experiments and simulation, it can be observed that the PVR is the dominant vortical structure. Figure 4.2(a'-d') shows a good comparison of the numerical simulations with the experimental images. The helium volume fraction plot (left) in the simulation image shows that the dark core observed in the experimental images primarily consists of helium. The next phase of bubble evolution is driven by the vortex dynamics associated with the PVR. Figure 4.2(d-f) shows that the size of the PVR increases while that of the helium lobe decreases in time. This can be interpreted as a mass transfer (helium transfer) process operating between the helium lobe and the PVR . This interpretation views the behavior of the bubble as incompressible in this regime.

Figure 4.3 shows the late-time behavior of the low-Mach number ($M = 1.45$) and the high-Mach number ($M = 2.95$) shocked helium bubble which is further analyzed by Ranjan *et al.* [10]. Figure 4.3(a) shows a small
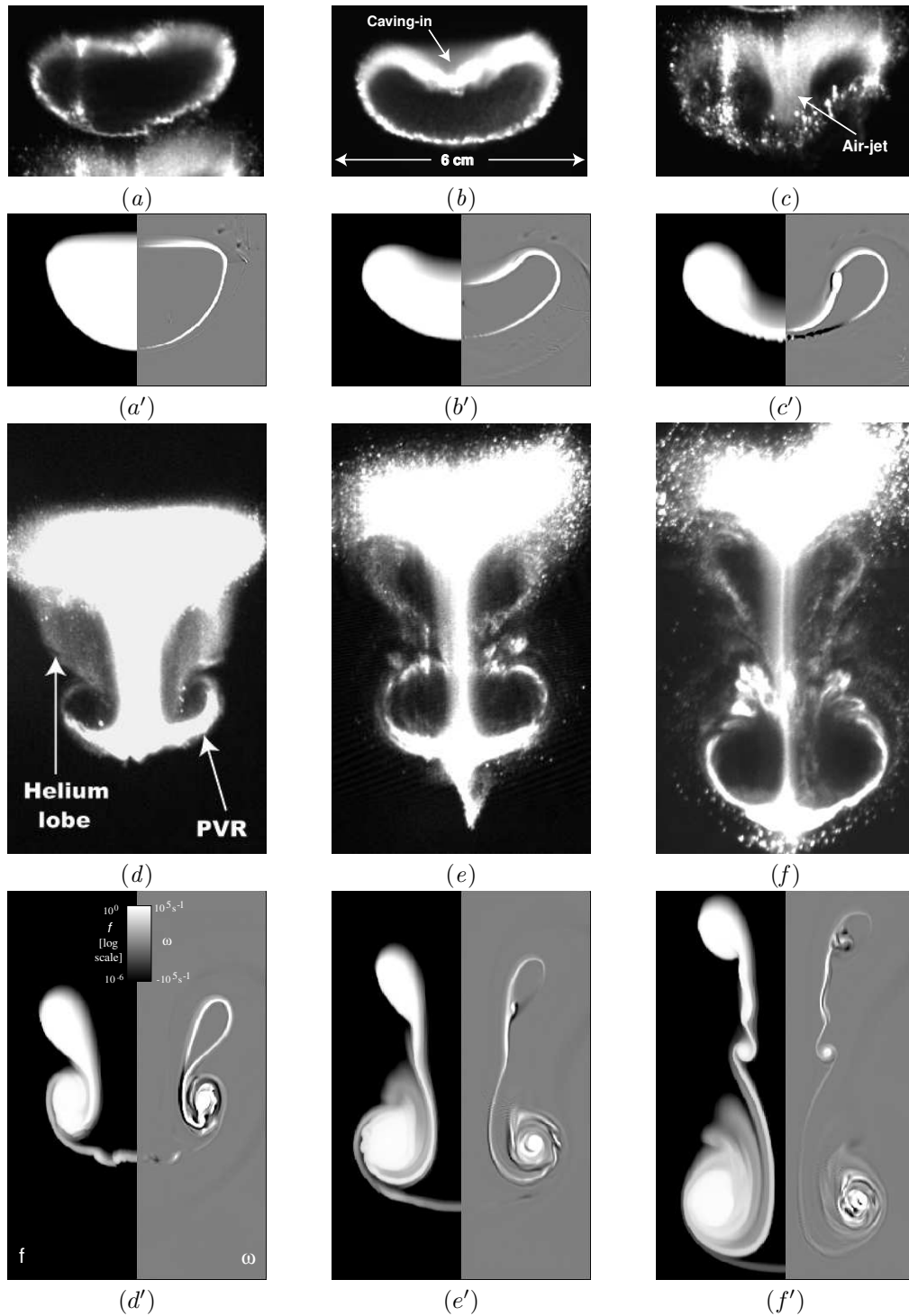
Fig. 4.2. Experimental and computational images of a shocked ($M = 1.45$) helium bubble in air: (a) $\tau = 2.4$, (b) $\tau = 4.8$, (c) $\tau = 7.7$ (d) $\tau = 20.5$, (e) $\tau = 38.9$, (f) $\tau = 56.9$. The time has been non-dimensionalized as $\tau = t/t'$, where t' is defined as $t' = D/(2 \times W_t)$. In numerical images, volume fraction of helium, f, is plotted on the left (logscale), and vorticity magnitude is plotted on the right. Shock motion is from top to bottom.

secondary vortical feature midway between the downstream PVR and the upstream helium lobe in the case of $M = 1.45$ accelerated helium bubble. The helium lobe's upper region is partially obscured by the edge of the imaging window. The late-time flow features are well reproduced by the numerical counterpart as shown

in Fig. 4.3(b). The vorticity plot (right) in Fig. 4.3(b) shows that the secondary vortex ring observed has the same sense of rotation as the PVR in the $M = 1.45$ case.

(a) (b) (c) (d)
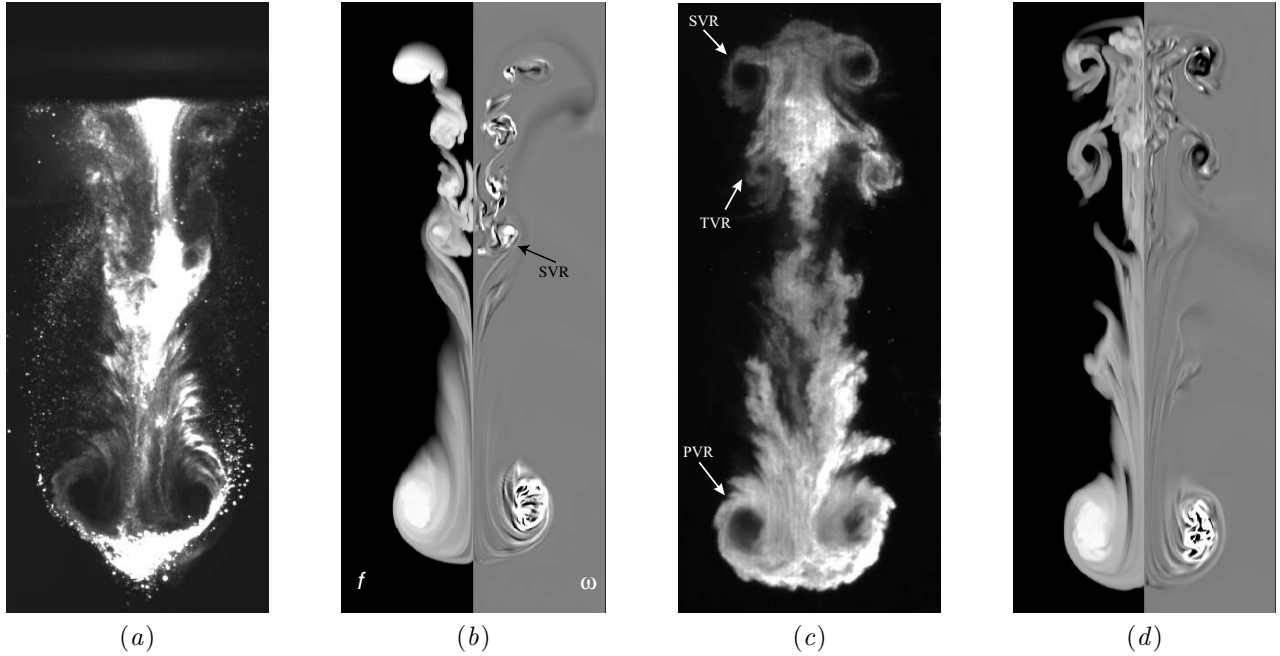
Fig. 4.3. Late-time images of low-Mach number and high-Mach number shock interaction with a helium bubble.(a) $M = 1.45, \tau = 105.8$, (b) $M = 1.45, \tau = 105.8$, (c) $M = 2.95, \tau = 69.5$ (d) $M = 2.95, \tau = 69.5$. The time has been non-dimensionalized as $\tau = t/t'$, where t' is defined as $t' = D/(2 \times W_t)$.

Figure 4.3(c) shows the late-time flow field in the case of the shocked helium bubble after contact with a $M = 2.95$ shock wave with a particle velocity of 1040 m/s in nitrogen. In Fig. 4.3(c) one can clearly identify three distinct vortex rings: the PVR at the bottom of the image, the secondary vortex ring (hereafter referred to as SVR) at the top of the image and a tertiary vortex ring just below the SVR. These features are well captured by the numerical simulation as shown in Fig. 4.3(d). The striking difference from the low-Mach number experiment ($M = 1.45$) is the sense of rotation of the SVR. In the case of high-Mach number experiment the SVR has opposite sense of rotation compared to the PVR, while in the low-Mach number case it has the same sense of rotation as the PVR. This difference can be attributed to the different formation mechanism for the SVR. The numerical simulations have shown that in the low-Mach number case, the SVR is formed due to the shear and the local density gradient imposed during the elongation of the bubble while in the high-Mach number case, it is generated by a secondary baroclinic source of vorticity associated with the slip line traced in the flow by the Mach stem and the triple point which develop at the early stages of the shock-bubble interaction, due to irregular shock refraction. The helium bubble accelerated by a $M = 2.08$ shock showed distortion patterns similar to that accelerated by a $M = 2.95$ shock wave.

In order to study the compression and unstable growth of the bubble, the axial dimension ("height," h) of the shocked bubble is measured over time and compared to the corresponding values extracted from the numerical results for $1.4 < M < 3.0$. The data are normalized by the initial bubble diameter as $L_h = h/D$, and plotted against the nondimensional timescale τ in Fig. 4.4. Computational and experimental results show very good agreement for the $M = 2.95$ case. In the $M = 1.45$ case, simulation overpredicts the experimental results after $\tau \approx 60$. The growth rate for $M = 2.95$ is significantly higher than the $M = 1.45$ case even on the nondimensional timescale τ. One can clearly see in Fig. 4.4 that the growth curve for the $M = 2.95$ case starts deviating from the $M = 1.45$ scenario at $\tau \approx 20$. This difference is due to the formation of the counter-rotating SVR in the $M = 2.95$ case. The experimental results for $M = 2.95$ reported by Ranjan *et.al* (2007) [10] show that the formation of SVR takes place around $\tau \approx 24$. The simulation results for $M = 2.08$ show a growth rate similar to the $M = 2.95$ case. The experimental results show a good agreement at the early phase of the interaction. There is only one data point at late time which shows good agreement with the high-Mach number experiment. In all the three cases, the growth of the bubble after compression is approximately linear in time.
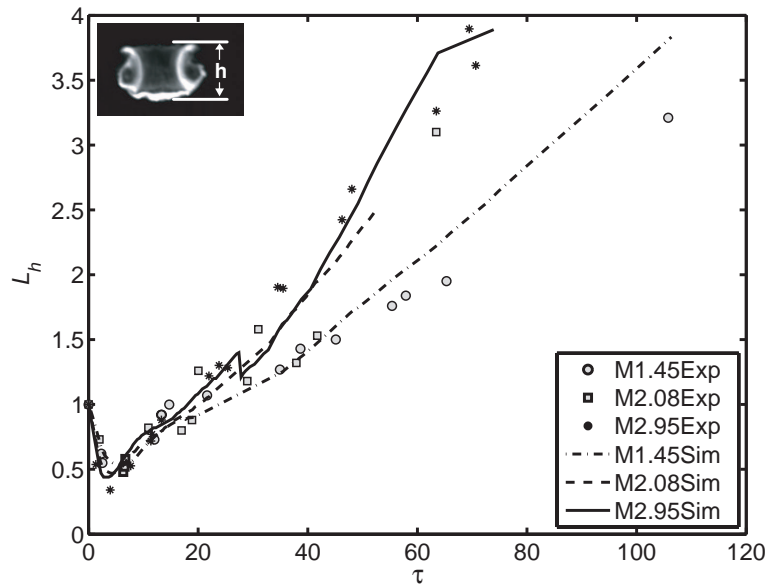
Fig. 4.4. Axial dimension (h) normalized by the initial bubble diameter D, plotted as a function of the dimensionless time τ for $1.4 < M < 3.0$ accelerated bubble.

5   SUMMARY

The present work represents a novel experimental approach which takes advantage of planar imaging, higher shock strengths than previous experiments, and a flow that is unobstructed by bubble holders or injectors. This approach facilitates the characterization of the large characteristic vortex ring that forms in the post-shock flow much more distinctly than in previous work. Comparison with computational results indicates good agreement in the axial distortion pattern of the bubble and in the secondary vortical features which are both observed in experiments and captured in calculations. Trends in the growth of the axial dimension ("height," h) of the shocked bubble exhibit the unsettling result that even on the nondimensionalized timescale τ, growth rates are significantly higher for $M > 2$ than for $M < 2$. It is speculated that this is due to compressibility effects where $u'_1 > c'_1$ in the post-shock flow.

REFERENCES

[1] Haas, J.-F., Sturtevant, B., 1987. Interaction of weak shock waves with cylindrical and spherical inhomogeneities, *J. Fluid Mech.* **181**, pp. 41-76.

[2] Layes, G., Jourdan, G., Houas, L., 2003. Distortion of a spherical gaseous interface accelerated by a plane shock wave, *Phys. Rev. Let.* **91**, 174502.

[3] Layes, G., Jourdan, G., Houas, L., 2005. Experimental investigation of the shock wave interaction with a spherical gas inhomogeneity, *Phys. Fluids* **17**, 028103.

[4] Picone, J.M., Boris, J.P., 1988. Vorticity generation by shock propagation through bubbles in a gas, *J. Fluid Mech.* **189**, pp. 23-51.

[5] Giordano, J., Burtschell, Y., 2006. Richtmyer-Meshkov instability induced by shock-bubble interaction: numerical and analytical studies with experimental validation, *Phys. Fluids* **18**, 036102

[6] Ranjan, D., Anderson, M., Oakley, J., Bonazza, R., 2005. Experimental investigation of a strongly shocked gas bubble, *Phys. Rev. Let.* **94**, 184507.

[7] Colella, P., 1985. A direct Eulerian MUSCL scheme for gas dynamics, *SIAM J. Sci. Stat. Comput.* **6**(1), pp. 104-117.

[8] Miller, G.H., Puckett, E.G., 1996. A higher-order Godunov method for multiple condensed phases, *J. Comput. Phys.* **128**, pp. 134-164.

[9] Berger, M., Oliger, J., 1984. Adaptive mesh refinement for hyperbolic partial differential equations, *J. Comput. Phys.* **53**, pp. 484-512.

[10] Ranjan, D., Niederhaus, J., Motl, B., Anderson, M., Oakley, J., Bonazza, R., 2007. Experimental investigation of primary and secondary features in a high Mach number shock-bubble interaction, *Phys. Rev. Let.* **98**, 024502.

EVOLUTION OF RICHTMYER-MESHKOV INSTABILITY AND TURBULENT MIXING IN A THREE-LAYERED PLANAR GAS SYSTEM

A.N.Razin

RFNC-VNIIEF, pr. Mira 37, Sarov, Nizhni Novgorod region, Russia,
E-mail: A.N.Razin@vniief.ru

Abstract: Numerical simulations have been performed of turbulent mixing arising in a three-layer planar gaseous system with Richtmyer-Meshkov instability. Two theoretical models are used to analyze interface instability development, turbulent mixing is computed using the V.V.Nikiforov model. The reliability of numerical results is validated using experimental data.

1 INTRODUCTION

Numerical simulations of turbulent mixing (TM) in stratified systems using semi-empirical models of turbulence have to handle the problem of turbulence initialization. In fact, semi-empirical turbulent models are designed for computations of developed turbulence. The instability development phase and transition to TM should be treated with some other models. In this situation, TM initialization parameters must be defined at each interface by the moment of turning on the semi-empirical turbulence model: the time of changing from instability development phase to TM, initial zone width and the values of turbulent quantities. In spite of numerous theoretical, experimental and numerical studies performed by various research laboratories in different countries [e.g., 1-25], our knowledge of instability development and subsequent transition to TM is yet to be improved.

The semi-empirical model suggested by V.V. Nikiforov [27] is used to compute TM in the VIKHR technique [26]. Two TM initialization approaches have been developed within the VIKHR technique in the latest years. The first approach is the TM initialization model suggested by V.I.Kozlov based on integrating the differential equation for the perturbation amplitude (the model has been implemented by I.V.Sapozhnikov). The second approach will be described below in this paper.

The approach suggested is described by the example of a calculation of TM arising in a three-layer planar gas system. The development of instability at interface with a sinusoidal perturbation is analyzed by models of Refs. [7], [15]. The moment of transition from instability development to turbulent mixing ($t = t_1$) is defined as the time at which perturbation evolution reaches weakly nonlinear phase (bubble growth rate starts to differ from spike growth rate). The light-to-heavy penetration depth (i.e. bubble amplitude) is determined at $t = t_1$ and heavy-to-light penetration depth (the amplitude of spikes). With this approach, the moment of switching on TM equations, the width and asymmetry of initial TM zone agree with the physics of this phenomenon (within the accuracy of theoretical models). A similar TM initialization algorithm was used in Ref. [28].

2 NUMERICAL SETUP AND THEORETICAL MODELS

Richtmyer-Meshkov (RM) instability and TM are considered at two interfaces (fig. 2.1). Shock tube experiments were performed by E.E.Meshkov et. al. and presented in Ref. [27]. The shock tube has $12 \times 4 \text{cm}^2$ rectangular cross-section. Air and He were used as working gases. Shock Wave was forming at the right edge of the tube and traveled from Air into He and then into Air. Shock Mach number in Air was ≈ 1.3.
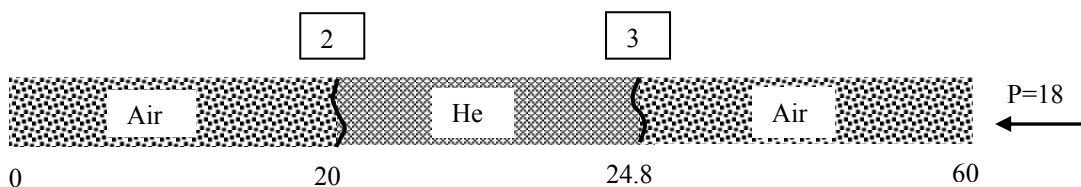

Fig. 2.1. The initial geometry of the problem

The results of numerical simulation of TM developing at the interfaces present in this problem have been published more than once, Refs. [27, 29], however, the method on TM initialization has not been discussed previously. This work is focused, mainly, on the method of TM initialization in interface vicinity, i.e. computation of the instability development phase and definition of the moment of transition to TM.

The numbering of interfaces in computation is shown in fig. 2.1. The initial parameters of the substances are given in table 2.1. The densities of the gases in table 2.1 correspond to initial pressure P_0=1bar, and specific internal energy corresponds to an initial temperature of 20^0C. Perfect gas equation of state was used in the calculations. The dimensions are: mg, cm, 10^{-4}sec.

	ρ_0	γ	P_0	E_0
He	0.1663	1.63	10.13	96.688
Air	1.205	1.40	10.13	20.757

Table 2.1. Initial parameters of the system

A shock forms in Air at the specified pressure $P = 18$ at the right boundary, which corresponds to the experimental setup. The relationship between the shock Mach number and pressure behind the shock front is

$$M = \sqrt{\frac{P + P_0 h}{P_0 (1+h)}} \approx 1.29 , \qquad h = \frac{\gamma - 1}{\gamma + 1} .$$

Gas density and velocity behind the shock front at these conditions are found from Rankine-Hugoniot relationships

$$\rho = \rho_0 \frac{M^2}{(1-h) + h M^2} = 1.8 , \qquad u = (1-h) c_0 \frac{M^2 - 1}{M} = -1.47 ,$$

where $c_0 = 3.43$ is sonic speed in Air before shock front, shock velocity in Air is $D = M c_0 = 4.42$. Shock reaches the interface 3 at time $t_1 = 35.2/D \approx 7.96$ (the time of shock arrival at interface 2 will be found below).

Fig. 2.2 shows how the shock travels from right to left across the system till the moment when the shock reflected from the left edge of the tube has interacted with the turbulent zones. The data shown in Fig. 2.2 were computed using the VIKHR code. When the incident shock reaches interface 3, a discontinuity disintegration occurs at the interface and with a shock wave (SW) generated that starts traveling in He, and a rarefaction wave (RW) traveling in air (SW-RW configuration). Two shocks are generated at interface 2 as a result of discontinuity breakup (SW-SW configuration). It should be noted that perturbation development at interface 3 is influenced by a weak shock reflected from interface 2 that reaches interface 3 at time $t_3 \approx 8.7$.
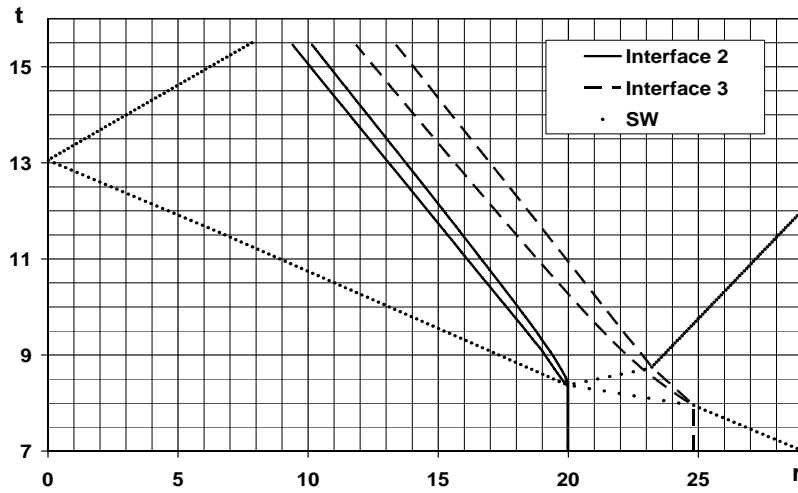

Fig. 2.2. Shock traveling in the system

Let's find the dimensionless parameter to characterize the density difference of the contacting gases, – the Atwood number: $A_{0-} = \frac{\rho_A - \rho_B}{\rho_A + \rho_B} = \frac{\delta - 1}{\delta + 1}$, where $\delta = \rho_A / \rho_B$ is the density ratio at interface. For interfaces 3 and 2, respectively, $A_{0-} \approx -0.76$, $A_{0-} \approx 0.76$.

No special perturbations were induced at planar interfaces in experiments of Ref. [27]. The most probable source of initial perturbation is the variable thickness of the film. Generation of perturbations in a film of variable thickness is accounted for by the film being torn by SW into fragments of different sizes, thus, generating a perturbation spectrum with variable wavelength and amplitude.

When considering qualitatively the interaction between incident shock and interfaces we will assume the interface perturbation to have an initially sinusoidal shape with wavelength $\lambda = 2\pi/k$ and amplitude a_{0-} (k is the wave number). Quantities before shock-interface interaction are assigned subscript 0-, while those after the interaction are assigned 0+. Assume that the initial perturbation amplitude at interfaces 2 and 3 (before shock-interface interaction) is $a(0-) = 6.0 \cdot 10^{-3} cm$, perturbation length is $\lambda = 0.25 cm$ $(k \approx 25.0)$.

The results of calculation of shock-interface interaction are needed for the analysis of perturbation evolution at both interfaces. The problem of interaction between shock and interface can be solved analytically in the planar case as a breakup of an arbitrary discontinuity (the Riemann problem). The solution provides all gas dynamical parameters that characterize the system state after a shock passage through the interface. The solution of discontinuity breakup at interfaces 2 and 3 are given below.

We will use the models of Alon et al Refs. [15, 21-23] and Zhang Refs. [7, 8]. Bubble amplitude growth rate (v_{bA}) and that of spikes (v_{sA}) are, according to the Alon model

$$v_{bA} = \frac{da_{bA}(t)}{dt} = \frac{U_0 \cdot (1+C)}{1+(1+A)\cdot C + D\cdot C^2}, \tag{1}$$

$$v_{sA} = \frac{da_{sA}(t)}{dt} = \frac{U_0 \cdot (1+C)}{1+(1-A)\cdot C + D\cdot \frac{1-A}{1+A}\cdot C^2}, \tag{2}$$

where $U_0 = A\cdot k\cdot U\cdot a_0$, $C = U_0\cdot k\cdot t$, $\quad D = \begin{cases} 1.0 & , \quad A \to 0 \\ 1.5 & , \quad A \geq 0 \end{cases}$.

According to Zhang Refs. [7, 8], the total perturbation growth rate (v), bubble growth rate (v_{bZ}) and spike growth rate (v_{sZ}) at linear and nonlinear phases of perturbation evolution are given by

$$v = \frac{v_{lin}}{1 + \lambda_1 v_{lin}\,\varepsilon\,a\,k^2\,t + \max\left[0, (a\,k\,\lambda_1)^2 - \lambda_2\right](k\,v_{lin}\,t)^2}, \tag{3}$$

$$v_{bZ} = \frac{da_{bZ}}{dt} = -v + Z, \qquad v_{sZ} = \frac{da_{sZ}}{dt} = v + Z, \tag{4}$$

where $Z = A\cdot k\cdot v_{lin}^2\cdot t\cdot\left\{1 + 2k^2\,\varepsilon\,a\,v_{lin}\,t + 4\left[(ka)^2 + \frac{1}{3}(1-A^2)\right](k\,v_{lin}t)^2\right\}^{-1}$,

$k = \sqrt{k_x^2 + k_y^2}$ is the common wave number of initial perturbations, λ is perturbation wavelength. Parameter ε in Eq. (3) is assumed 1 when there is no phase inversion, otherwise $\varepsilon = -1$. Dimensionless parameters λ_1, λ_2 depend on Atwood number, the problem dimensionality and the orientation of the wave vector (k_x, k_y). For a symmetric perturbed surface in 3D, $\lambda_1 \approx 0.0889\,A^2 + 0.456$, $\lambda_2 \approx 0.39\,A^2 - 0.228$. In a 2D case the parameters λ_1, λ_2 take the following values: $\lambda_1 = 1$, $\lambda_2 = A^2 - 0.5$.

Thus, the changing in time of bubble and spike amplitude in Alon and Zhang models is found by integrating (1)-(4). Let's comment on the selection of amplitude and Atwood number in Eqns.(1)-(4). It is shown by Richtmyer in [1] that the best fit to experimental data for a SW- SW configuration is achieved with the following Atwood number and amplitude: $A = A_{0+}$ (Atwood number found from densities on the left and on the right of the interface after shock passage); $a = a_{0+} = a_{0-}(1 - \Delta U / D)$ is perturbation amplitude after shock passage through interface, D is the velocity of incident shock on the interface, ΔU is interface velocity increment after the interaction with the incident shock (provided that the system was at rest at the initial moment, $\Delta U = U_1 = U_2$).

Meyer, Blewett [18] found using direct numerical simulations that the best results are achieved for a SW-RW configuration is Atwood number and amplitude are chosen in the following way $A = A_{0+}$, $a = 0.5(a_{0+} + a_{0-}) = a_{0-}\left[1 - \Delta U/(2D)\right]$. Thus, the selection of amplitude, wave number and Atwood number (a, k, A) in Eqns. (1)-(4) depends on the particular configuration taking place at a particular interface and will be discussed below.

3 TURBULENT MIXING INITIALIZATION

When a shock reaches interface 3 ($t_1 \approx 7.96$) an arbitrary discontinuity break-up occurs, as a result, there will be a shock traveling to the left (into He), a rarefaction wave will travel to the right, with a contact discontinuity (CD) between them. The flow pattern after interaction between the shock and the perturbed interface is schematically shown in Fig. 3.1 together with mean gasdynamic values.
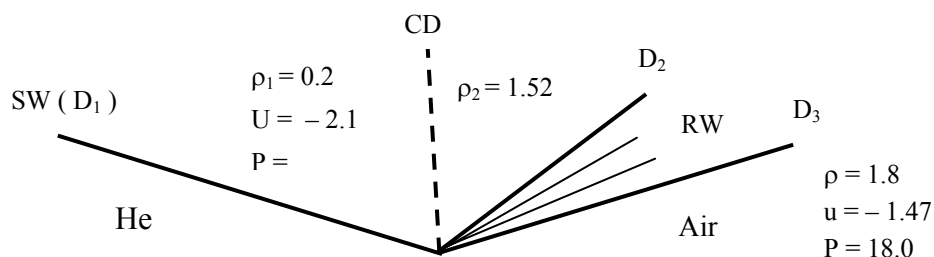

Fig. 3.1. Solution of the Riemann problem, Interface 3

The solution of the Riemann problem yields shock velocity in He ($D_1 = -11.44$) and the velocities of characteristics that limit the centered RW ($D_3 = 2.27$, $D_2 = 1.44$). The Atwood number determined from the densities to the right and to the left of the interface $\rho_1 = 0.2, \rho_2 = 1.52$ (after the interaction between shock and perturbed interface), $A_{0+} \approx -0.76$. The amplitude of perturbed interface after the interaction with the shock is found from Richtmyer correlation $a_{0+} = a_{0-}[1 - U/D] \approx 0.525 a_{0-} = 0.00316$.

Fig. 3.2 shows the amplitudes of bubbles and spikes as functions of time according to the Zhang model.
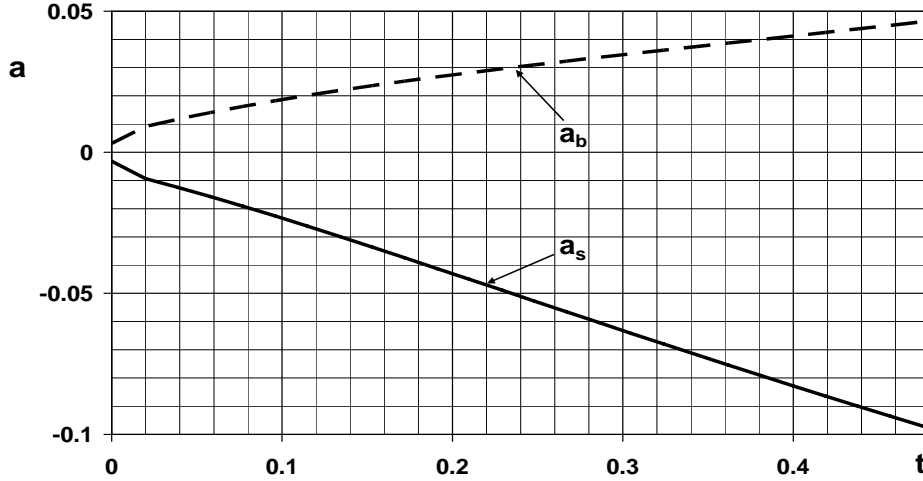
Fig. 3.2. Bubble and spike amplitude at interface 3

According to the data of Fig. 3.2, the time of switching on TM equations in calculation at interface 3 can be set to $t \approx t_1 + \Delta t_1$, where $t_1 \approx 7.96$ is the time of initiation at interface 3 (the time of shock arrival at the interface), and $\Delta t_1 \approx 0.35$ is the interval of time that corresponds to weakly nonlinear phase of perturbation evolution (bubble growth rate differs insignificantly from that of spikes). Bubble and spike penetration depth at the chosen moment of time ($t \approx 8.3$) are, respectively, $a_b \approx 0.04$, $a_s \approx 0.07$.

Let's find turbulent quantities to be set in the initial zone at $t \approx 8.3$. Assume that turbulence intensity is 5% of the velocity of interface 3, i.e. $I = \sqrt{\overline{u_1'^2}}/U = 0.05$, where $U = 2.1$ is the interface velocity. In this case we have the following correlation for turbulent kinetic energy

$$e_1 = \frac{\overline{u_1' u_1'}}{2} = \frac{(I \cdot U)^2}{2} \approx 0.0055 .$$

Assume $e_2 = e_1$ for transversal velocity fluctuations. Turbulent kinetic energy dissipation rate (Q) is determined by velocity fluctuation values (e_1), turbulence scale (ℓ) and an empirical constant α: $Q = \alpha e_1^{1.5}/\ell = \alpha_1 \cdot e_1^{1.5}$. At $\alpha = 0.15$, $\ell = 0.1$ ($\ell \le |a_s| + |a_b|$ (the initial value of turbulence scale cannot be larger than perturbation amplitude) find $Q \approx 0.00061$.

Relative intensity of square density fluctuations is found as $R = \frac{\overline{\rho' \rho'}}{\rho^2} = \frac{\rho_1 - \rho}{\rho} \frac{\rho_2 - \rho}{\rho}$, where ρ_1, ρ_2 are the densities of the gases, ρ is the average density of the mixture. Assume the following approximation for the mixture average density $\rho = 0.5 \cdot (\rho_1 + \rho_2)$, then we have $R = \frac{\overline{\rho' \rho'}}{\rho^2} = A^2$, (A is Atwood number).

Introduce an empirical coefficient into the latter equation which will yield, as a result, the correlation for relative intensity of square density fluctuations:

$$R = \beta \cdot A^2 . \tag{5}$$

The magnitude of the empirical coefficient ($\beta = 0.1$) will be determined from the condition that at moderate density ratio at interface the relative velocity should agree with V.V.Nikiforov's correlation

$$R = \frac{\overline{\rho' \rho'}}{\rho^2} = \alpha \frac{(\delta - 1)^2}{\delta}, \quad \delta = \frac{\rho_1}{\rho_2} \ge 1 .$$

For interface 3 $R = \beta \cdot A^2 \approx 0.0577$.

At a moment of time corresponding to nonlinear phase of perturbation development bubble and spike penetration depth has been found for interface 3 and values of turbulent quantities have been determined. A similar

analysis can be performed for interface 2. Shock velocity in He ($D_1 = -11.44$) that was found above permits to determine the time of shock arrival at interface 2 (instability development initiation) $t_2 = t_1 + 4.8/D_1 \approx 8.38$.

A schematic of flow after the shock interaction with perturbed interface and the flow parameters obtained by solving an arbitrary discontinuity break-up problem are shown in Fig. 3.3.
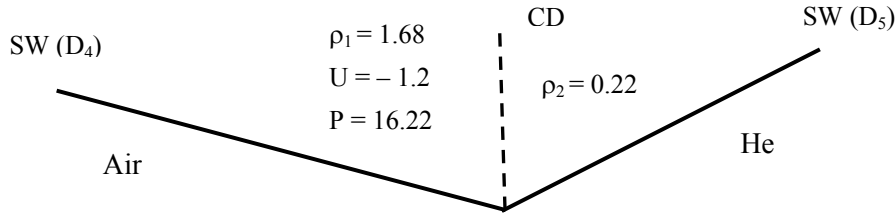
SW (D_4) $\rho_1 = 1.68$ CD   SW (D_5)

$U = -1.2$ $\rho_2 = 0.22$

$P = 16.22$

Air   He

Fig. 3.3. Flow schematic after discontinuity break-up at interface 2

Having solved an arbitrary discontinuity break-up problem, also obtain shock velocity in Air ($D_4 \approx -4.23$), shock velocity in He ($D_5 \approx 9.14$), Atwood number ($A_{0+} \approx 0.76$), the amplitude of perturbed interface $a_{0+} = a_{0-}\left[1 - U/D_1\right] \approx 5.37 \cdot 10^{-3}$. Assume, similarly to interface 3, that turbulence intensity is 5% of the velocity of interface 2, we have $e_1 = e_2 \approx 0.0018$, $Q \approx 0.00012$, $R \approx 0.0577$.

4 TURBULENT MIXING CALCULATION RESULTS

All information required for numerical setup has been derived above. A fine mesh is used in calculations with uniformly spaced nodes in regions (the regions are numbers from left to right). The number of nodes in region 1 is M_1=2000, M_2=480 in region 2, M_3=3520 in region 3.

Interface No.	t	R	e_1	e_2	Q	L_0
2	8.7	0.0577	0.0018	0.0018	0.00012	4+6
3	8.3	0.0577	0.0055	0.0055	0.00065	7+4

Table 4.1. Initial data for interfaces 2 and 3

The following notation is used in the table 4.1: t is the time when TM equations are switched on, R is relative square density fluctuation, e_1 is longitudinal turbulent kinetic energy, e_2 is transversal turbulent kinetic energy, Q is dissipation rate, L_0 is the initial width of the zone. The expression 4+6 for interface 2 corresponds to setting turbulent quantities shown in the table 4.1 in 4 points to the left and 6 points to the right of the interface (similarly to interface 3).

Fig. 4.1 presents R-t diagrams of TM zone calculated using VIKHR and measured. Fig. 4.1 suggests that calculated TM zone boundaries and calculated shock R-t diagram are shifted relative to the experimental points.
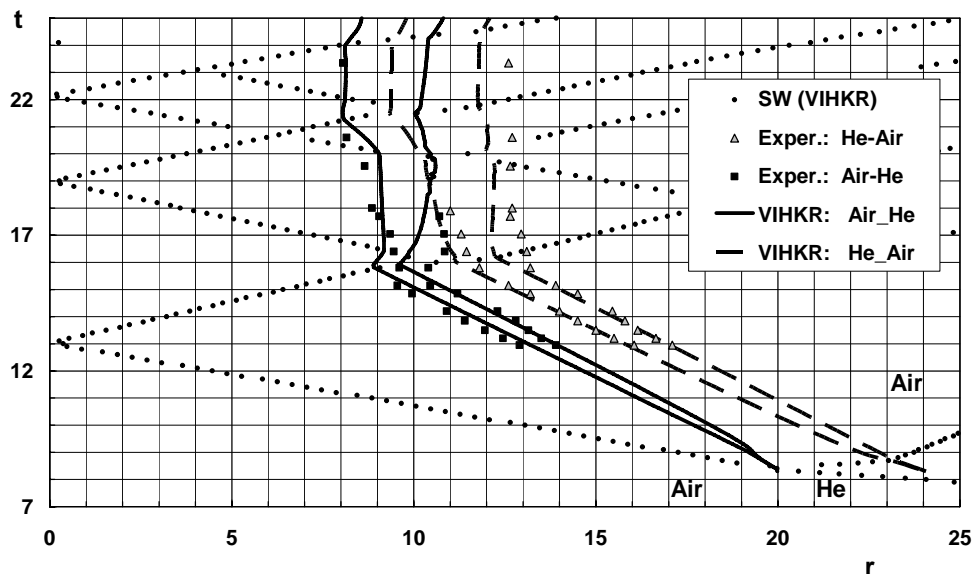
Fig. 4.1. R-t diagram of TM zone boundaries and shock

The interaction between shock reflected from the left edge and Air-He TM zone starts earlier in the experiment than in calculation, the time is t ≈ 0.5. This discrepancy can be accounted for by systematic error in measurements of time and TM zone boundaries. Calculated data plotted as functions of (r + 0.5; t - 0.5) are in good agreement with measurements.

5 SUMMARY

Numerical simulations of TM arising in a three-layer planar gaseous system with RM instability have been carried out using the VIKHR code.

The time transition from instability development phase to TM was set to $t \approx t_k + \Delta t_k$, where t_k is the onset of perturbation development at interface k (the time of shock arrival at the interface), Δt_k is the interval of time in which perturbation development reaches the weakly nonlinear phase (bubble growth rate starts to differ from spike growth rate). The width of the perturbed zone at interface is computed at time $t \approx t_k + \Delta t_k$ using the Zhang, Sohn model [7]. The light-to-heavy (bubbles) and heavy-to-light (spikes) penetration depths have been found in instability calculations. Thus, the moment of switching on TM equations, the width and asymmetry of the initial TM zone agree with the physics of this phenomenon (within the accuracy of the models).

The algorithm of setting longitudinal and transversal turbulent kinetic energy, dissipation rate and relative square velocity fluctuations in the initial zone is discussed.

The comparison between numerical data of simulation with two TM zones merging into each other and experimental data have demonstrated that the model works. Further verification will be performed and TM initialization model will be refined if necessary based on other problems.

REFERENCES

[1] **Robert D.Richtmyer** Commun. Pure Appl. Math., 13, pp.297-319, 1960
[2] **E.E.Meshkov** Izv. Akad. Sci. USSR, Fluid Dyn., n.5, p.151-158, 1969
[3] **A.N.Aleshin, E.V.Lazareva, S.G.Zaitsev et al.** Doc. Akad. Sci. USSR, n.5, v.310, p.1105, 1990
[4] **G.Dimonte, C.Eric Frerking, M.Schneider, B.Remington** Phys. Plasmas, 3(2), p.614, 1996
[5] **R.Benjamin, D. Besnard, J.Haas** LANL, LA-UR 92-1185, 1993
[6] **Y.Yang, Q.Zhang, D.H.Sharp** Phys. Fluids, 6(5), p.1856, 1994
[7] **Q.Zhang, S.I.Sohn** Phys. Lett. A212, pp.149-155, 1996
[8] **Q.Zhang, S.I.Sohn** Phys. Fluids, 9(4), pp.1106-1124, 1997
[9] **Q.Zhang, S.I.Sohn** Phys. Fluids, 13(11), p.3493, 2001
[10] **X.L.Li, Q.Zhang** Phys. Fluids, 9(10), p.3069, 1997
[11] **Q.Zhang** Phys. Rev. Lett., 81(16), p.3391, 1998
[12] **S.I.Sohn** Phys. Rev. E67, 026301-1, 2003
[13] **A.L.Velikovich** Phys. Fluids, 8(6), p.1666, 1996
[14] **K.O.Mikaelian** Phys. Fluids, 6(1), p.356, 1994
[15] **D.Sadot, L.Erez, U.Alon et al** Phys. Rev. Lett., 80(8), p.1654, 1998
[16] **D.Oron, L.Arazi, D.Kartoon et al** Phys. Plasmas, 8(6), p.2883, 2001
[17] **R.Holmes, G.Dimonte, B.Fryxell, M.Gittings et al** J. Fluid Mech., v.389, p.55, 1999
[18] **K.A.Meyer, P.J.Blewett** Phys. Fluids, 15(5), pp.753-759, 1972
[19] **T.Pham, D.I.Meiron** Phys. Fluids A, 5(2), pp.344-368, 1993
[20] **J.W.Grove, R.Holmes, D.H.Sharp, Yumin Yang, Q.Zhang** Phys. Rev. Lett., v.71, № 21, pp.3473-3476, 1993
[21] **U.Alon, J.Hecht, D.Ofer, D.Shvarts** Phys. Rev. Lett., v.74, № 4, p.534, 1995
[22] **J.Hecht, U.Alon, D.Shvarts** Phys. Fluids, 6(12), p.4019, 1994
[23] **U.Alon, J.Hecht, D.Mukamel, D.Shvarts** Phys. Rev. Lett., v.72, № 18, p.2867, 1994
[24] **J,G.Wouchuk** Phys. Plasmas, 8(6), p.2890, 2001
[25] **M. Vandenboomgaerde, S.Gauthier, C.Mugler** Phys. Fluids, 14(3), p.1111, 2002
[26] **V.A.Andronov, V.I.Kozlov, V.V.Nikiforov, A.N.Razin, Yu.A.Yudin** VANT, Ser. Metodiki I progr. chisl. resheniya zadach mat. fiziki, n.2, p.59, 1994
[27] **V.A.Andronov, S.M.Bakhrakh, E.E.Meshkov, V.V.Nikiforov, A.V.Pevnitskii, A.I.Tolshmyakov** Doc. Akad. Sci. USSR, n.1, v.264, p.76, 1982
[28] **V.I.Kozlov, A.N.Razin** VANT: Ser. TPF, n.3, p.3, 2001
[29] **A.N.Razin** VANT: Ser. TPF, n.1/2, p.3, 2003

e-mail: `ribeyre@celia.u-bordeaux1.fr`

Non-stationary Rayleigh-Taylor instability in spherical shell expansion

X. Ribeyre[1], L. Hallo[1], V.T. Tikhonchuk[1], S. Bouquet[2] and J. Sanz[3]

[1] *Centre Lasers Intenses et Applications, UMR 5107 CNRS-Université Bordeaux 1 - CEA, Université Bordeaux 1, 351, Cours de la Libération, 33405 Talence Cedex, France*

[2] *Commissariat à l'Energie Atomique, DIF/Département de Physique-Théorique et Appliquée, 91680, Bruyères le Châtel, France*

[3] *E.T.S.I., Aeronáuticos, Universidad Politécnica de Madrid, Madrid 28040, Spain*

Abstract: The Rayleigh-Taylor instability (RTI) plays an important role in the dynamics of several astronomical objects, in particular, in the supernovae (SN) evolution. In the present paper we examine the dynamics of a shell (representing a type II SN remnant) blown-up by a wind emitted by a central pulsar. The shell is accelerated by the pulsar wind and its inner surface experiences the RTI. We develop an analytical approach by using a specific transformation into the coordinate frame co-moving with the SN ejecta. We first derive a non-stationary spherically symmetric solution describing an expansion of a gas shell under the pressure of a central source (pulsar). Then, we analyze its 3D stability with respect to a small perturbation on the inner shell surface. The dispersion relation is derived in the co-moving reference frame. The growth rate of the perturbation is found and its temporal evolution is discussed. Finally, amplitude on time computed from the analytical growth rate is compared to that obtained from perturbation code PANSY.

1 INTRODUCTION

The Rayleigh-Taylor (R-T) instability plays an important role in several astronomical objects: pulsar nebulae [11], supernovae [8], supernova remnants [7, 9]. For a massive star, once the core has collapsed, the pulsar wind blows up the outer parts of the star, and the inner surface of the expanding shell becomes R-T unstable. This instability seems to lead to the filamentary structure observed in the Crab Nebula [13]. In type II supernovae explosions, this instability might be responsible for the mixing of the metallic layers Ni, Co with the He, H layers (SN 1987A for instance), and that provides a better interpretation of the light curve [1]. This process differs from the one, which arises later in the supernova remnant (SNR) expansion, when the ejecta of the supernova (SN) swept the interstellar medium. In this deceleration phase, the ejecta might become R-T unstable and lead to a non-spherical structure [19] for type Ia SN (Tycho), and bow-shock features in type II SN (Cassiopeia A) [10, 12].

In this paper, we are interested in the R-T instability that develops at the early stage of pulsar nebula evolution. In this phase the pulsar wind accelerates the ejecta shell: the pulsar radiation is absorbed at the inner surface of the ejecta dense shell and this configuration is R-T unstable (see Fig.2.1). We develop an analytical model which takes into account the non-stationary shell evolution. Moreover, we analyze the linear evolution of the perturbations for wavelengths comparable to the shell thickness. Since they are dangerous for the shell integrity, we estimate its fragility. Finally, we compare the analytical solution with the code PANSY.

2 PULSAR WIND NEBULA AND SUPERNOVA REMNANT MODEL

The figure 2.1 shows schematically the interaction between the pulsar wind nebula (PWN) and the SNR ejecta (shell). The pulsar wind blows the supernova ejecta and accelerates their expansion. The expanding shell is called "plerion", which constitutes a class of SNR similar to the Crab nebula [14]. The "plerion" evolution is a non-stationary problem because the pulsar wind pressure decreases with time, due to slowing down rotation [3, 16] of the pulsar. The shell evolution can be studied with the Euler's hydrodynamic equations, if we neglect all dissipative processes and the gravitational field:

$$\frac{\partial \rho}{\partial t} + \frac{1}{r^2}\frac{\partial (r^2 \rho v)}{\partial r} = 0, \quad \frac{\partial v}{\partial t} + v\frac{\partial v}{\partial r} = -\frac{1}{\rho}\frac{\partial p}{\partial r}, \quad p = K\rho^\gamma. \tag{2.1}$$

In first approximation we assume a spherical symmetry and $\rho(r,t)$, $p(r,t)$, $v(r,t)$ are respectively the density, the pressure and the velocity of the flow. The quantities K and γ are respectively a constant and the polytropic coefficient of the gas. This system of equations is difficult to solve because of the non-stationary character of the evolution. In order to
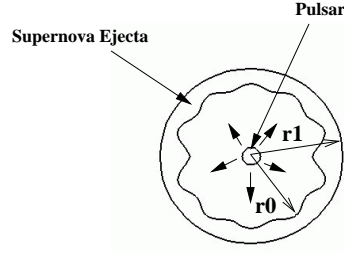
Fig. 2.1. Schematic representation of the classical type II supernova remnant (SNR) model. The figure shows the central pulsar blowing the expanding SNR, where r_0 (resp. r_1) is the inner (resp. outer) shell radius.

make possible an analytical study of the shell stability, a solution for the radial shell expansion has been expressed. This is achieved by using a special coordinate transformation into the non-stationary co-moving frame [4] where the flow becomes stationary. Once the solution is found in the co-moving frame, one can use the inverse transformation to return in the initial space. The transformation between the two frames is defined by the rescaling functions $A(t)$, $B(t)$, $C(t)$ and $D(t)$ according to:

$$r = C(t)\,\hat{r}, \quad dt = A(t)^2\,d\hat{t}, \quad \hat{v} = \frac{d\hat{r}}{d\hat{t}}, \tag{2.2}$$

$$p(r,t) = B(t)\,\hat{p}(\hat{r},\hat{t}), \quad \rho(r,t) = D(t)\,\hat{\rho}(\hat{r},\hat{t}). \tag{2.3}$$

Any physical quantity $q(= r,t,v,\rho,p)$ from the initial space (r,t) will be labeled with a hat '∧', i.e., $\hat{q}(= \hat{r},\hat{t},\hat{v},\hat{\rho},\hat{p})$ in the new space $(\hat{r},\hat{t})$. The two spaces coincide at $t=0$ and consequently, $A(0) = B(0) = C(0) = D(0) = 1$. The Euler's equations in the new frame read:

$$\frac{\partial \hat{\rho}}{\partial \hat{t}} + \frac{1}{\hat{r}^2}\frac{\partial (\hat{r}^2\hat{\rho}\hat{v})}{\partial \hat{r}} = -\frac{A^2}{D}\left(\frac{3\dot{C}}{C} + \frac{\dot{D}}{D}\right)\hat{\rho}, \tag{2.4}$$

$$\frac{\partial \hat{v}}{\partial \hat{t}} + \hat{v}\frac{\partial \hat{v}}{\partial \hat{r}} = -\left(\frac{BA^4}{C^2D}\right)\frac{1}{\hat{\rho}}\frac{\partial \hat{p}}{\partial \hat{r}} - 2A^2\left(\frac{\dot{C}}{C} - \frac{\dot{A}}{A}\right)\hat{v} - \frac{\ddot{C}A^4}{C}\hat{r}, \tag{2.5}$$

$$\hat{p} = K\left(\frac{D^\gamma}{B}\right)\hat{\rho}^\gamma, \tag{2.6}$$

where the dot stands for d/dt. The rescaling functions can be found from invariance considerations and conservation laws. In order to have a mass conservation in the $(\hat{r},\hat{t})$ space and to keep the continuity equation (2.4) identical to Eq.(2.1), the R.H.S of (2.4) should vanish: $3\dot{C}/C + \dot{D}/D = 0$, i.e. $D = C^{-3}$. Moreover, in momentum equation (2.5), two new forces appear, one is a friction proportional to $\hat{v}$ and another is a radial force proportional to $\hat{r}$ (see below). First, we remove the time-dependent coefficients in the pressure gradient term in (2.5) and in the polytropic equation (2.6). This provides $BA^4/(C^2D) = D^\gamma/B = 1$ and since $D = C^{-3}$, we obtain $B = C^{-3\gamma}$ and $A = C^{(3\gamma-1)/4}$. At this stage, we have derived the scaling functions $A(t)$, $B(t)$ and $D(t)$ in terms of $C(t)$, which is the function governing the relation between the spatial coordinates r and $\hat{r}$.

Having all these conditions fulfilled, one can look for a static solution, $\hat{v}(\hat{r},\hat{t}) = 0$, in the rescaled space $(\hat{r},\hat{t})$. Eq.(2.4) is identically satisfied since $\partial/\partial\hat{t} \equiv 0$ and the equation of motion reduces to the static equation $(1/\hat{\rho})(d\hat{p}/d\hat{r}) = -\hat{r}/\tau^2$. Finally, whatever γ we can read in the initial space (r,t):

$$\rho(r,t) = \frac{\rho_0}{C^3}\left(1 - R_0^2\right)^{-1/(\gamma-1)}\left(1 - \frac{r^2}{C^2 r_1^2}\right)^{1/(\gamma-1)}, \tag{2.7}$$

$$p(r,t) = K\frac{\rho_0^\gamma}{C^{3\gamma}}\left(1 - R_0^2\right)^{-\gamma/(\gamma-1)}\left(1 - \frac{r^2}{C^2 r_1^2}\right)^{\gamma/(\gamma-1)}, \tag{2.8}$$

$$v_r(r,t) = \frac{r}{C^2\tau}\left[\beta + (\beta^2 + 1)\frac{t}{\tau}\right], \tag{2.9}$$

where $\rho(r,t)$, $p(r,t)$, $v_r(r,t)$ are respectively the density, the pressure and the radial velocity, r_0 and r_1 are the inner and outer initial shell radii respectively. The parameter β defines the magnitude of the velocity profile at $t=0$ and τ

is the characteristic time for the dynamics of the shell. Moreover, $R_0 \equiv r_0/r_1$ and $\rho_0 \equiv \rho(r_0, 0)$ is the initial density at the inner border of the shell. A relation exist between the inner density, the constant K and r_1 $\rho_0 = [r_1^2(\gamma-1)(1-R_0^2)/2K\gamma\tau^2]^{1/(\gamma-1)}$. The scale function $C(t)$ is given by the solution of the following differential equation $\tau^{-2} = \ddot{C}C^{3\gamma-2}$, where the upper dot stands for the time derivative of C. For the polytropic constant $\gamma = 5/3$, i.e., for an ideal gas, an analytical expression for $C(t)$ reads as:

$$C(t) = \sqrt{\left(1 + \frac{\beta t}{\tau}\right)^2 + \frac{t^2}{\tau^2}}. \tag{2.10}$$

As explained earlier, it is clear that the parameter τ is the characteristic time of shell expansion and the constant $\beta \equiv \tau\dot{C}(0)$ characterizes its initial velocity, $v_0(r) = \beta r/\tau$. Moreover, the temporal evolution of the internal face is given by $r_0(t) = C(t)r_0$ and for the outer interface $r_1(t) = C(t)r_1$. The scale function $C(t)$ is a linear function of t for $t \gg \tau$, i.e., when the shell is in ballistic motion (see Fig.2.2a with $\beta = 0$). The function C(t) characterizes also the acceleration of the shell. Indeed, the temporal derivative of $v(t)$, is:

$$\dot{v} = \frac{r}{\tau^2 C^{3\gamma-1}}. \tag{2.11}$$

For $\gamma = 5/3$ and $\beta = 0$ the density and pressure are deduced according from Eqs. (2.7)–(2.9). The density profile $\rho(r, t = 0)$ is given in Fig.2.2b. The SNR shell is obtained from the hollow sphere where matter is removed ($\hat{\rho} = 0$) in the range $0 \leq \hat{r} \leq \hat{r}_0$ (see the density jump on Fig.2.2b). In the (r, t)-space, the shell thickness is $\Delta(t) = \Delta_0 C(t)$ where $\Delta_0 = \hat{r}_1 - \hat{r}_0$ is the thickness at $t = 0$. The unperturbed density profile in the shell is given by $\rho(r, t)$ where r moves in the range $r_0(t) \equiv \hat{r}_0 C(t) \leq r \leq r_1(t)$.

The pressure acting (pulsar wind) on the shell inner surface ($r = r_0$) is obtained from $p = K\rho^{5/3}$. Since the ratio $r_0(t)/r_1(t) = \hat{r}_0/\hat{r}_1$ is constant, we conclude that the pulsar pressure decreases according to C^{-5} (see Fig.2.2a). The corresponding non-perturbed time-dependent velocity is $v(r, t) = r\dot{C}(t)/C(t) = (rt/\tau^2)\{1/[1 + (t/\tau)^2]\}$ with $\beta = 0$.
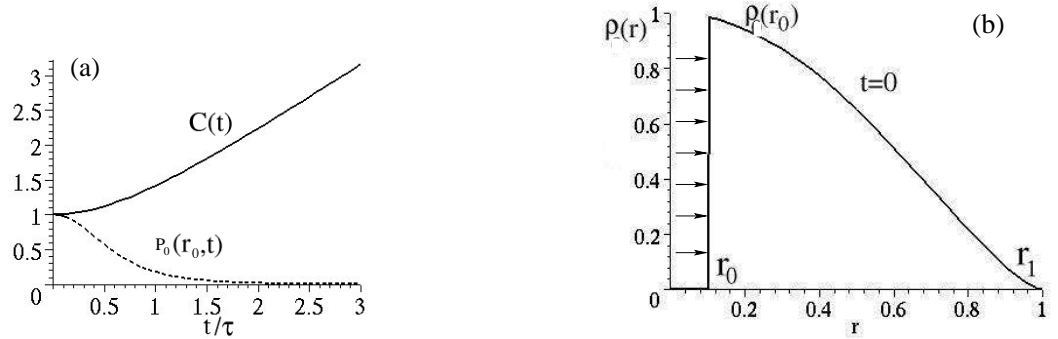

Fig. 2.2. For $\gamma = 5/3$ and $\beta = 0$, a. Scaling function $C(t)$ (solid line), $p(r = C(t)r_0, t)$, pressure evolution at the inner surface of the SNR shell (doted line), b. Normalized density profile of the SNR shell $\rho(r, t = 0)$ at $t = 0$.

3 RAYLEIGH-TAYLOR INSTABILITY

Bernstein and Book [2] obtained an exact expression for the incompressible perturbation evolution for a given radial flow. They consider a radially symmetric shell flow described by Eqs. (2.7)–(2.9) and a 3D perturbation with an angular dependence corresponding to the spherical harmonic: $Y_{lm}(\theta, \phi)$. Applying their expression to the case of an ideal gas, $\gamma = 5/3$, the time evolution of the perturbation δ, is given by :

$$\delta \propto C(t) \cosh\left[\sqrt{l+1} \arctan(t/\tau)\right]. \tag{3.1}$$

for $\beta = 0$, i.e., without initial shell velocity. A similar expression can be obtained by solving the perturbed Euler equations in the expanding co-moving frame [4, 17]. More precisely, for $\gamma = 5/3$, one can express the angular perturbed displacement evolution as:

$$\delta \sim e^{\omega\hat{t}/\tau} Y_{lm}(\theta, \phi), \tag{3.2}$$

where the relation between the co-moving time $\hat{t}$ and the time in the physical space t is given by:

$$\hat{t} \equiv \tau g(t) = \tau\{\arctan[\beta + (\beta^2 + 1)t/\tau] - \arctan\beta\}. \tag{3.3}$$

Moreover, although [2] did not exhibit a dispersion relation, the one we obtain is very simple. The parameter ω is given by the roots of the following equation :

$$\omega^4 - \omega^2 - l(l+1) = 0. \tag{3.4}$$

Therefore, there are four linearly independent eigenmodes:

$$\omega_{1,2} = \pm\sqrt{l+1}, \quad \omega_{3,4} = \pm i\sqrt{l}. \tag{3.5}$$

One mode ω_1 is unstable and three others are stable. One obtains the same expression (3.1) that [2] by considering a linear superposition of the modes ω_1 and ω_2 for $\beta = 0$. However this particular solution does not describe a general perturbation of the inner shell surface. By taking account of all four modes, one can describe various initial conditions for the shell perturbations and study their stability as well as the interaction between the inner and outer shell interfaces. The four linearly independent eigemodes can be found with another approach (for example Breil et al. [5] following Book approach [2]). It is supposed that an incompressible perturbation is derived from a potential and that the perturbation is divergence free which gives eigenmodes (3.5).

4   QUALITATIVE RTI ANALYSIS

The dispersion relation defined by the equation (3.4) and the solutions (3.5) are surprisingly simple and they correspond to the incompressible perturbations.

In particular, if one considers only the unstable mode $\omega_1 = \sqrt{l+1}$, then, the perturbation evolves as $\exp[\omega_1\hat{t}/\tau]$ [see equations (3.2) and (3.3)]. This behavior can be compared with a simple model, by supposing that at every moment the growth rate of the RTI is given by the formula $\omega = \tau\sqrt{w_0 k_0}$, describing the instability of a plane surface in acceleration w_0. In our case the acceleration of the inner interface is defined by equation (2.11). Consequently, the temporal evolution of the perturbation $\delta(t)$ in this model is given by:

$$\delta(t) \propto \exp\left[\int_0^t \sqrt{k_0(t')w_0(t')}dt'\right], \tag{4.1}$$

where $k_0(t)$ is the wave number of the perturbation. In spherical geometry, the wavelength of the perturbation λ evolves in time as, $2\pi/\lambda(t) = (l+1)/[r_0 C(t)]$ (where l is the mode number of the perturbation). Then using the expression (2.11) in equation (4.1) one obtains:

$$\delta(t) \propto \exp\left[\frac{\sqrt{l+1}}{\tau}\int_0^t \frac{dt'}{C^{\frac{3\gamma-1}{2}}}\right]. \tag{4.2}$$

In particular for $\gamma = 5/3$, one finds the exact solution (3.1) if $\beta = 0$ or a more general solution if $\beta \neq 0$.

One can go further and calculate the growth rate for an arbitrary γ. Then, the perturbation growth (4.2) can be presented in the following way:

$$\delta(t) \sim \exp\left[\sqrt{l+1}\int_1^{C(t)} \frac{C^{(1-3\gamma)/2}dC}{\sqrt{\beta^2 + \frac{2}{3(\gamma-1)}\left(1 - \frac{1}{C^{3\gamma-3}}\right)}}\right]. \tag{4.3}$$

Starting from this expression, one can find the asymptotic growth rate [$C(t) \rightarrow t$ for $t \rightarrow +\infty$] with $\beta = 0$ which could be compared with the expression of the asymptotic growth rate provided by [2] for an arbitrary γ [see their expression (51)].

In this case, for $l = 100$ and for three values of γ given by Bernstein and Book, $\gamma = 5/3$, $4/3$ and 2, the variations between the two growth rates do not exceed 8% (see Tableau 4.1).

Therefore, the instantaneous expression, $\omega = \tau\sqrt{w_0 k_0}$ gives a good approximation of the growth rate of RTI, even for $\gamma \neq 5/3$. On the other hand, there is a significant uncertainty, up to a factor five, on the value of the amplification of the perturbation, since one takes the exponential variation.

This simple analytical model can be successfully to compute the early evolution of the Crab nebula [18]. Starting with Jun's [11] input data, the main properties of the Crab nebula are recovered (mass of the filament, size of PWN and time corresponding to the early fragmentation of the shell ~ 400 years). In addition, it is found the most probable mode, l_{disup}, leading to the disruption of the shell is $l_{disrup} = 60$. This result in agreement with others studies [2, 6].

γ	Our approximate model	Bernstein and Book [2] solution
4/3	$21.63 - 2.48 \times 10^9$	$20.06 - 5.20 \times 10^8$
5/3	$15.09 - 3.60 \times 10^6$	$15.09 - 3.60 \times 10^6$
2	$12.19 - 1.98 \times 10^5$	$12.84 - 3.78 \times 10^5$

Table 4.1. *Comparison of the growth rate and the amplification of the perturbation for $t \rightarrow \infty$, given by Eq. (4.3) with $\beta = 0$ and the solution of [2] [see the equation (51) in [2]], for $\gamma = 4/3$, 5/3, 2 and for $l = 100$. One gives for each value of γ respectively, the growth rate and also the amplification which corresponds to exponential of the product growth rate time.*

5   SIMULATIONS OF THE PERTURBATION

The analytical solution presented above has been compared with the perturbation code PANSY (McCrory et al. [15]). It computes the time development of three-dimensional linear modes of coupled hydrodynamic, thermodynamic, and transport phenomena, including heat flow, viscosity, fully linearized about zeroth order spherically symmetric compressible flows. The zeroth order solutions are calculated on a typical one-dimensional Lagrangian grid and have the form $f^j(t)$, where the f's are all necessary hydrodynamic variables, and other variables including zone radius, and where j is the radial zone index. First order quantities, of the form $f_{l,m}^j(t)Y_{l,m}(\theta)\exp(im\phi)$ for spherical geometry, are calculated with difference equations which are linearly perturbed forms of the former discretized zeroth order equations, rather than discretizations of the linearly perturbed continuous zeroth order equations. This set resulting ordinary differential equations are solved with second order difference scheme in space and time. This relatively conservative/Hamiltonian approach produces considerably improved treatment of phenomena requiring high resolution, especially artificial viscosity for shocks in contrast with earlier form of PANSY which required higher resolution for the same accuracy (Henderson et al. [15]. In the discretized set of equations , angular variation only comes from angular divergences. For this reason, time dependent evolution equations are used for radial velocity and the angular part of the displacement and velocity divergences, rather than more complicated equations for transverse displacement and velocity. There are two reasons. First, this is a general and very convenient form since it can be used both in planar, cylindrical and spherical geometries. As an example, in planar geometry, the transverse part of divergence displacement writes $\nabla_{perp} \sim \vec{k} \cdot \vec{\xi}_{\perp}$. Second, algebraic relation exists between perturbed density and perturbed displacement divergence. This relation writes simply $\frac{\rho^1}{\rho} - \nabla \cdot \xi = \text{cste}$. The consequences is that an initially divergence free perturbed flow has no perturbation on density, i.e. is incompressible, as it is the case in the type of cumulative flows presented in this work.

The analytical solutions for the inner and outer shell displacement of the unstable mode has been compared with the simulations performed with the perturbation code PANSY. The agreement between the analytical solution and the simulations is very good. The difference is less than one percent. It is shown in Fig. 5.3 that the inner interface growth is more rapid because this surface is RT unstable, while the outer interface is in contact with vacuum and does not show a substantial growth. The deviation between the theory and simulations at the outer surface is larger than at the inner interface because it is more difficult for the code to handle the contact with vacuum. The advantage of the PANSY
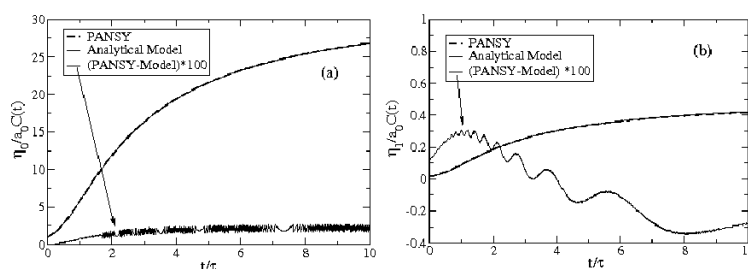

Fig. 5.3. Comparison between the time evolution of the inner (a) and outer (b) displacements of the shell for the unstable mode for $\gamma = 5/3$ in the case $l = 4$ ($\theta = \phi = 0$) with the inner radius $R_0 = 0.5$ and $\beta = 0$. The displacement is divided by the scale function $C(t)$ to exhibit clearly the perturbation growth due to the RTI. The plot shows a good agreement between the analytical solution (solid line) and the simulation (dashed curve) with the perturbation code PANSY. The difference between the two results is less than one percent.

perturbation code is that it allows a parametric study of parameters around a given solution. The effects of a variation of

initial conditions in the cumulative flow can be carried out. Fig. 5.4 shows the evolution on perturbed displacement of the external expansing interface on time for the l=12 eigenmode. The time evolution from PANSY simulations is similar with a initial divergence free perturbation is very similar to that predicted by the analytical model. If only the spatial perturbed displacement is used for PANSY initialization, we obtain a lower amplification than the one for divergence free initialization (curve 3), which shows the influence of compressibility effect.
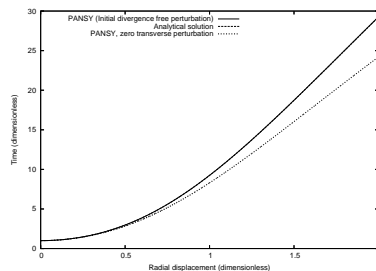
Fig. 5.4. Comparison between the time evolution of the outer displacements of the shell for the unstable mode $l = 4$ ($\theta = \phi = 0$) with the inner radius $R_0 = 0.9$ and $\beta = 0$. Again, the plot shows a good agreement between the analytical solution and the PANSY simulation with a divergence free initialization of perturbation. If a radial initial perturbation is used with PANSY, a lower amplification is obtained which shows the influence of the compressibility effect.

6   CONCLUSION

We examined the dynamics of a shell (representing a type II SN remnant) blown by the strong wind emitted by a central pulsar. Assuming that the shell mass is constant and evolves in vacuum, we developed a simplified model describing a non-stationary shell evolution. Moreover, we derive a simple dispersion relation for the RTI growth rate for an ideal polytropic gas ($\gamma = 5/3$). We compare our approach with the work achieved by [2] and show that the RTI growth and the growth rate of perturbation can be described with a sufficient accuracy by a simple formula for the instantaneous RTI growth rate at a plane surface even for a small l-modes. Moreover we find a good agreement between the analytical solution and the code PANSY. Finally, this model can be applied to the Crab nebula and results are in pretty agreement with others studies [6, 11] and with observations as well [13].

REFERENCES

[1]   Arnett, W.D. and Fryxell B., 1987, Instabilities and nonradial motion in SN 1987A *ApJ* **341**, L63

[2]   Bernstein, I. B., Book, D.L., 1978, Rayleigh-Taylor instability of the self-similar spherical expansion *ApJ* **225**, 633

[3]   Blondin, J. *et al.*, 2001, Pulsar wind nebulae in evolved supernova remnants , *ApJ* **563**, 806

[4]   Bouquet S. *et al.*,1985, Density bifurcation in homgeneous isotropic collapsing star, *ApJ* **293**, 494

[5]   Breil, J. *et al.*, 2005, Hydrodynamic instabilities in axisymmetric geometry self-similar models *Laser and Particle Beams* **23**, 155

[6]   Bucciantini, N.*et al.*, 2004, Magnetic Rayleigh-Taylor instability for pulsar wind nebulae in expanding supernova remnant, *A&A* **423**, 253

[7]   Chevalier, R.A. *et al.*, 1992, Hydrodynamic instabilities in supernovae remnants: self similar driven waves *Astrophysical Journal* **392**, 118

[8]   Fryxell, B. *et al.*,1991, Instabilities and clumping in SN 1987A. I. Early evolution In two dimensions, *ApJ* **367**, 619

[9]   Gull, S. F., 1975, optical and radio properties of young supernova remnants, *MNRAS* **171**, p. 263

[10]   Gotthelf, E. *et al.*, 2001, CHANDRA detection of the formward and reverse shocs in cassiopeia A, *ApJ* **552**, L39

[11]   Jun B-I., 1998, Interaction of a pulsar Wind with the expanding supernova remnant, *ApJ* **499**, 282

[12]   Jun B-I. and Norman, M. L., 1995, A numerical study of Rayleigh-Taylor instability in magnetic fluids, *ApJ* **453**, 332

[13]   Hester J. J. *et al.*, 1996 , WFPC2 Studies of the Crab nebula, III. Magnetic RT instabilities and the origin of the filaments, *ApJ* **456**, 225

[14]   Lequeux J., 2002, Le millieu interstellaire, CNRS edtions

[15]   McCrory, R. L., Morse, R. L. & Taggart, K. 1977, Nuclear Sci. and Eng., **64**, 163

[16]   Reynolds S. P. and Chevalier R., 1984, Evolution of pulsar driven supernova remnants, *ApJ* **278**, 630

[17]   Ribeyre, X., Tikhonchuk, V. T., Bouquet, S.,2005 *Ap&SS* **298**, 75

[18]   Ribeyre, X., Hallo L., Tikhonchuk, V. T., Bouquet, S. and Sanz, J.: publication to be submitted to Astron.& Astrophysics (2007)

[19]   Velásquez, P. *et al.*, 1998, Study of Rayleigh-Taylor instability in Tycho's supernova remnants, *A&A* **334**, 1060

e-mail: `mkrivera@lanl.gov`

The Rayleigh-Taylor instability in small-aspect-ratio chambers

Michael K. RIVERA[1] and Robert E. ECKE[2]

[1] *Materials Process & Applications Division, Los Alamos National Laboratory, Los Alamos, NM 87545*

[2] *Center for Nonlinear Studies, Los Alamos National Laboratory, Los Alamos, NM 87545*

Abstract: We present experimental measurements of density and velocity obtained from the mixing zone of buoyancy-driven turbulence initiated by the Rayleigh-Taylor instability in a small-aspect-ratio chamber (a chamber in which the vertical height is significantly larger than its lateral dimension). The mixing front propagates at a slightly slower rate than the expected t^2 behavior obtained from earlier experiments and numerics. Once the front has propagated significantly far away, we observe that the mixing zone develops to a statistically stationary state. In this stationary state, the spectral distributions of energy and density deviate from the familiar $k^{-5/3}$ ubiquitous to homogeneous, isotropic turbulence in three dimensions.

1   INTRODUCTION

Only a handful of experimental studies have examined the properties of the buoyancy driven turbulence within the mixing zone of Rayleigh-Taylor turbulence [1, 3, 9]. All of these experiments were done in systems where the height, *i.e.*, the dimension parallel to the acceleration of gravity, was comparable with the lateral extent of the system. In these works, it was found that the resultant mixing layer was not affected by the lateral system boundaries. Indeed, in the work of Dalziel et al. [3] the finite height of the system was determined to be an important feature controlling the deviation of spectral, $E(k)$, slopes from the standard turbulence expectation of $k^{-5/3}$ due to global stratification suppressing large scale modes, preventing the lateral boundaries from becoming an important factor.

In systems of significantly larger height the properties of the mixing zone may be significantly affected by the lateral boundaries. The Rayleigh-Taylor mixing front continuously develops large modes which sweep energy from the accelerating front into the turbulent bulk. In numerical simulations (commonly done in periodic lateral boundaries) this has led to continuously increasing kinetic energy within the mixing zone [2]. Introducing lateral boundaries could truncate the development of large global modes. Lateral boundaries, then, should allow the turbulence in the mixing zone to reach an energetically steady state where the fluctuations are driven only by remnant kinetic energy deposited initially by the passing of the front and by *local*, rather than global, fluctuations in buoyancy. Lateral boundaries should also influence the spectral distribution of velocity and density fluctuations, dissipating modes that approach the lateral system size.

In this work, we look at some early results obtained from the development of Rayleigh-Taylor turbulence in a smaller-aspect-ratio chamber than in previous work. The system has lateral dimensions less than one tenth its height. The ultimate intent of this study is to understand the behavior of turbulent mixing sustained by local buoyancy fluctuations, a simplified version of the Rayleigh-Taylor mixing zone. Here, we look at the impact of the lateral boundaries on the bulk energy properties and associated spectral distributions.

2   SYSTEM

To initiate the Rayleigh-Taylor instability, we utilize a stretched latex membrane to separate an upper chamber of dense fluid (salt water) from a lower chamber of less dense fluid (alcohol and water). Both chambers have cross section 8×8 cm^2 and height 45 cm, so the total system height is 90 cm. A schematic of the system is shown in Fig. 2.1. The two fluids were chosen so that their indices of refraction match, which is important because measurements are made using visualization techniques. Using this choice of fluids, Atwood numbers, $A \equiv (\rho_H - \rho_L)(\rho_H + \rho_L)^{-1}$, as high as 0.1 can be obtained while maintaining index matching. Here, ρ_H is the density in the upper chamber and ρ_L is the density of the lower chamber. Results reported here were done at $A \approx 0.003$. The instability begins when the latex membrane is ruptured with a needle. For timing purposes, a photo-diode is used to detect the membrane rupture and trigger the data acquisition (sometimes with a delay). Initially there is a large amount of shearing in the fluids due to the rupture, but, after an initial
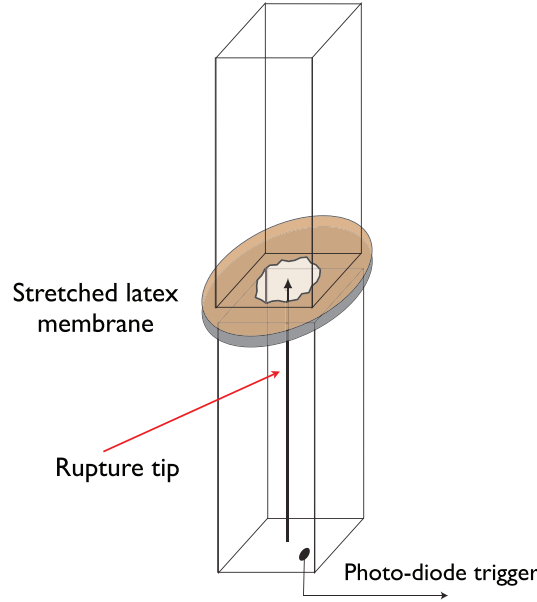
Fig. 2.1. Schematic illustration of the Rayleigh-Taylor system. The upper (dense) and lower (light) fluid are initially separated by a latex membrane. The membrane is ruptured to begin the instability. A photo-diode trigger is utilized to synchronize data acquisition with membrane rupture. Note the small aspect ratio.

transient phase, the instability proceeds normally when the membrane breaks symmetrically. On occasion the membrane will not rupture symmetrically, and this incites a large-scale roll in the fluids. Data from such asymmetrical ruptures are discarded and not included in the ensembles.

This system is significantly less complex than other Rayleigh-Taylor experiments [1, 3, 7, 9]. The lateral boundaries help a great deal in this regard. They should suppress the influence of the front on the mixing zone behavior once the front has moved away from the mixing region a distance large compared to the lateral system size . So long as the initial interface is "flat enough" we assume that the mixing zone behavior will be insensitive to perturbations of that interface.

Measurements of the turbulence generated by the fronts and the buoyant plumes is done by simultaneous particle tracking velocimetry (PTV) [5, 6] and planar laser induced fluorescence (PLIF) [8]. Our particular realization of these well-documented techniques uses high speed digital imaging cameras with a Nd:Ylf laser for illumination. Images are taken in a plane with one component parallel to gravity and 1 cm removed from the centerline of the chamber. Rhodamine dye is mixed in the upper (more dense fluid) chamber for use in the PLIF. This setup allows for simultaneous acquisition of velocity and density fields with fast time resolution. Due to the design of the apparatus only the upper chamber is imaged during the experiment.

A run consists of approximately 1000 sequential images taken at a given data rate. At this Atwood number we use 60 Hz, starting from some delay time that is dependent on the time of interest and the distance that the acquisition area is removed from the initial interface. For time averages reported here the data are averaged over three to five separate runs.

3   RESULTS

Utilizing several acquisition windows placed at different heights allows us to track the motion of the mixing front. The front position in the vertical direction, d, is defined by the point where the lateral average of the density drops by a specified amount. Defining the average density $\rho_0 \equiv (\rho_H + \rho_L)/2$ and the density fluctuation $\delta\rho \equiv \rho(\mathbf{x}, t) - \rho_0$, the front position is defined as the point where:

$$|\langle \delta\rho \rangle_{lat}/(\rho_0 A)| < \text{threshold} \tag{3.1}$$
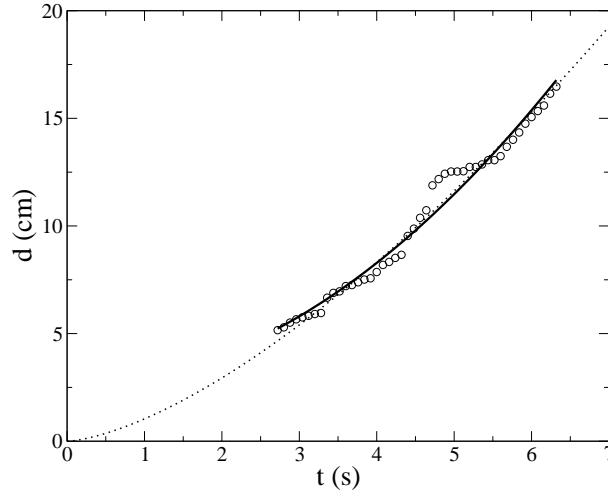
Fig. 3.2. Growth of the mixing front as a function of time. The dotted line represents a global fit of approximately $t^{1.5}$. Allowing a offset of 2.6cm at $t = 0$ yields an equally good global t^2 fit, as shown by the solid line.

By using the Atwood number in this definition the left hand side assumes the value of 1 if the lateral average (denoted here by $\langle\rangle_{lat}$) is equal to the density of the upper chamber, ρ_1, and -1 if it assumes the value of the lower chamber ρ_0. The threshold we chose was 0.9, and the absolute value may be dropped since we are considering the upper chamber.

The front position as a function of time using this definition is displayed in Fig. 3.2. The expected behavior is a quadratic growth in the mixing width layer. We get a somewhat less steep growth rate when a exponent is extracted from the entire data set, namely a rate of $t^{1.5}$. Allowing for an offset at the origin of 2.6cm (*i.e.*, $d(t = 0) = 2.6$cm rather than 0 cm) and mandating a t^2 growth rate yields an equally good fit with quadratic coefficient 0.355. The offset could be due to disturbances caused by the initial sheet rupture or possibly a transient exponential growth period that is known to precede the asymptotic t^2 growth. Using the coefficient for this offset quadratic fit and the inviscid approximation, $d = cAgt^2$, where d is the front height, we get a growth coefficient $c \approx 0.12$, which is somewhat larger than results obtained by Dalziel et al. but still within the range reported by Linden at this Atwood number.

There does seem to be a slight inflection in the data around $t = 5$s; it is possible that this time scale corresponds to the time it takes for the mixing-zone fluctuations to grow to scales comparable with the lateral system size. Once this growth is achieved, the front might feel the effect of the walls and, thus, decrease its acceleration. Quadratic fits before this time scale do not notably alter the front growth rate.

Using the front-growth plot, and extrapolating the $t^{1.5}$ scaling to the height of the chamber, we find that it takes about 12s for the mixing front to travel the full extent of the chamber and reach the chamber top. At this point the system starts to globally stratify, as noted in the work of Dalziel et al. Bracketing this time (that is focusing on the times from 10 to 14 s) and focusing our measurement volume near the initial position of the interface ensures that the mixing front is as far as possible from the measurement volume and that the vertical limits of the system are playing a minimal role in the statistics.

Several average quantities within this measurement area over the bracket time scales of 10 s to 14 s, are shown in Fig. 3.3. Averages are taken over the measurement area as well as over ensembles of system runs. At this point in the time evolution of the system, the mean density within the measurement volume has converged to the average density in the system. The rms density fluctuations are roughly ten percent of A, indicating a significant amount of potential energy left in the system. The vertical velocity component is not identically 0 cm/s on average as would be expected, but the deviation is within experimental error due to the small number of runs in the ensemble. The rms velocity fluctuations are also, to within error, approximately constant. To within our measurement error the potential and kinetic energies in the system are relatively steady, though more runs should be performed to absolutely conclude that this is the case. Clearly, though, the measurement area is well mixed, given that the average density is close to the global average of the system and has no net vertical momentum.

We note one curiosity about the rms velocity fluctuations. Prior to 12.5s the fluctuations seem to be steadily

decaying. At 12.5 s the fluctuations experience rapidly increase. Recall that around 12s is the time it takes for the front to reach the top of the chamber. This could indicate that the system is setting up a global stratification, but we are skeptical that the behavior of the front so far away from the measurement volume could directly affect the mixing zone behavior almost instantaneously. The correspondence in time is curious. More ensembles would aid in drawing stronger conclusions here and will be the subject of future work.

Accepting that the system has reached a statistically steady state in the bracketed range (10 to 14 s), we consider the spectra of density and velocity fluctuations. These are shown in Fig. 3.4. The kinetic-energy spectrum scales as $k^{-1.1}$ over wavenumbers from around 4 to 20 cm^{-1}, corresponding to spatial scales 0.3 to 1.6 cm. We note that the lower bound on this range is likely much smaller than 0.3 cm; this is just the limit of the PTV accuracy. Over a similar wavenumber range, 6 to 30 cm^{-1}, the density (or equivalently the potential energy) spectrum scales as $k^{-1.3}$.

Prior experimental data indicates that in larger aspect ratio containers the spectra both scale as $k^{-5/3}$ [3,9]. Deviations from this scaling noted by Dalziel et al. were associated with times larger than the time it takes for the interface to reach the vertical system size and the system began to globally stratify. The spectra we present are averaged from runs taken prior to the interface reaching the system height (recall this was 12.5 s), so the global stratification effect should be playing no role in our results. The observed deviation from $k^{-5/3}$ is possibly due to the lateral boundaries truncating large-scale modes. This effect would explain the less-steep slope, since there is less energy in large modes compared to small.

If this explanation is correct one would expect the spectra to smoothly roll over from the expected scaling. The density spectrum, however, seems to have a slight build up of energy in larger scale modes. At this time we do not understand the origins of this build up. It may be a residual artifact of the initial membrane rupture (which causes a global strain mode in the system), but, were this the case one would expect similar modes to be present in the velocity. These modes do not seem to be present in the energy spectrum.

Another difference between our spectra and earlier results [3,9] is that the energy and density spectra have a measurably different scaling. If the density fluctuations were initially smooth, then the velocity-scaling statistics should be echoed by the density at this small Atwood number [4]. We get a slight difference, perhaps again due to density fluctuations caused by the initial rupture depositing excess energy in a variety of modes.

A considerable amount of work needs to be done to better understand some of the more subtle issues, but it is clear that the turbulence generated by the Rayleigh-Taylor instability in this smaller-aspect-ratio system are significantly different than its larger-aspect-ratio predecessors. In particular, the front growth happens at a significantly slower rate of $t^{1.5}$ versus t^2. This can be accounted for if one introduces a considerable shift (2.6 cm) in the initial front position. In this case the quadratic range yields a consistent acceleration coefficient with respect to prior experiments. The system reaches a steady state, in contrast with earlier numerical work which has continuously increasing kinetic energies. This, again, is a result of the boundaries truncating the large scale modes. Finally, the spectra are less steep than the Kolmogorov $k^{-5/3}$ scaling found in prior experiments, likely again due to the suppression of large modes by the boundary. There might be small deviations due to
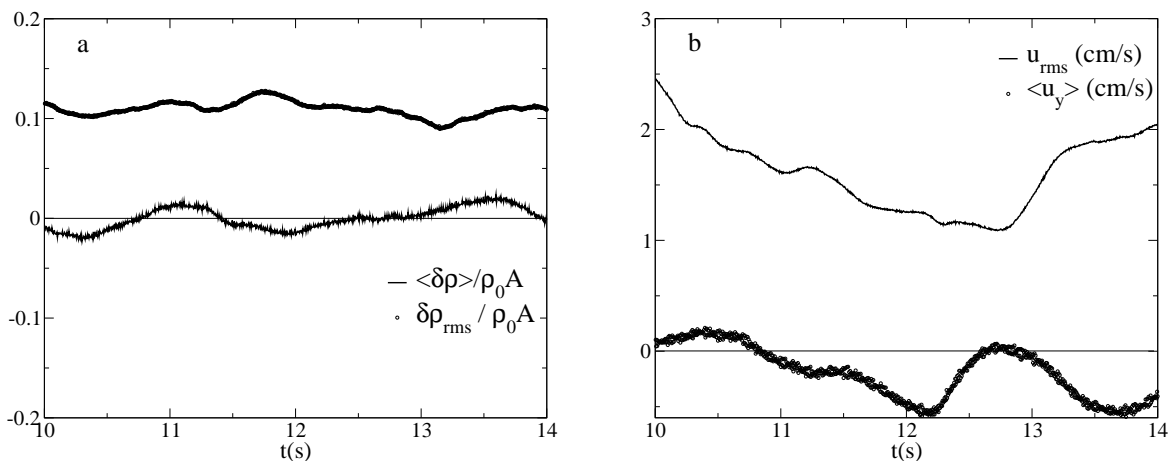

Fig. 3.3. (a) Area averaged density and density fluctuation. (b) Area averaged vertical velocity and total velocity fluctuation over a four second time interval.
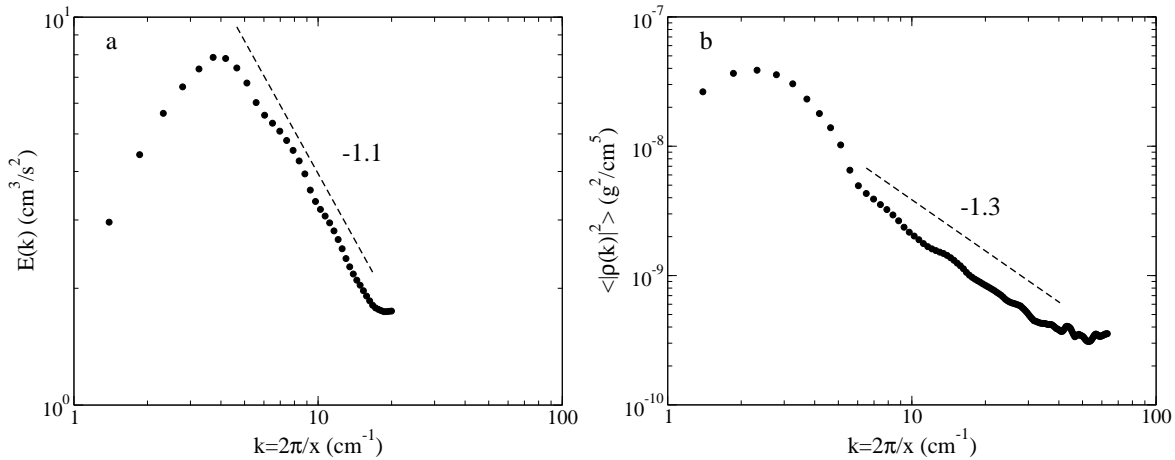
Fig. 3.4. The (a) kinetic energy and (b) density (equivalently potential energy) spectrum averaged over a four second time interval.

the initial rupture of the film, such as the deviation in the spectral scaling between density and energy but these are small. Future work will investigate into the transport properties of the buoyancy-driven turbulence in the bulk.

REFERENCES

[1] A. Banerjee and M. Andrews. Statistically steady measurements of rayleigh-taylor mixing in a gas channel. *Physics of Fluids*, 18(3):035107, 2006.

[2] A. Cook and P. Dimotakis. Transition stages of rayleigh-taylor instability between miscible fluids. *J. Fluid Mech.*, 443:69–99, 2001.

[3] S. Dalziel, P. Linden, and D. Youngs. Self-similarity and internal structure induced by rayleigh-taylor instability. *J. Fluid Mech.*, 399:1–48, 1999.

[4] U. Frisch. *Turbulence: The Legacy of A. N. Kolmogorov.* Cambridge University Press, 1995.

[5] M. Ishikawa, Y. Murai, and F. Yamamoto. Numerical validation of velocity gradient tensor particle tracking velocimetry for highly deformed flow fields. *Measurement Science Technology*, 11:677–684, 2000.

[6] K. Ohmi and H. Li. Particle-tracking velocimetry with new algorithms. *Exp. in Fluids*, 11:603–616, 2000.

[7] P. Ramaprabhu and M. Andrews. Simultaneous measurements of velocity and density in buoyancy-driven mixing. *Exp. in Fluids*, 34:98–106, December 2003.

[8] J. Sakakibara and R. Adrian. Whole field measurement of temperature in water using two-color laser induced fluorescence. *Exp. in Fluids*, 27(1):U1, 1999.

[9] P. Wilson and M. Andrews. Spectral measurements of rayleigh-taylor mixing at small atwood number. *Physics of Fluids*, 14(3):938–945, March 2002.

e-mail: `rozanov@sci.lebedev.ru`

The Evolution Model of Mixing Zone Growth in the Case of a Spherical Shell Compression

Igor Doskoch[1], Nadezhda Proncheva[2] , Vladislav Rozanov[1], Roman Stepanov[1], Rafael Yakhin[1] & Nikolay Zmitrenko[2]

[1] *P.N.Lebedev Physical Institute of the Russian Academy of Sciences, Moscow, RUSSIA*
[2] *Institute of Mathematical Modeling of the Russian Academy of Sciences, Moscow, RUSSIA*

Abstract

A series of calculations of the Rayleigh-Taylor and Richtmyer-Meshkov instabilities was performed within the framework of the problem of a laser thermonuclear target compression under different initial conditions including the structure of initial perturbation modes, different amplitudes, mixing gases, different statistic realizations of similar calculations, and different geometries. A part of the calculations corresponds to the shock tube instability regime, and another part to the laser compression conditions.

The analytical expressions describing a development of mixing zones allowing for the initial conditions of perturbations were proposed on the basis of this data base and with account for the instability evolution model.

Introduction

Quite a number of experimental and theoretical studies are devoted to determination of the mixing zone width growth caused by a development of Rayleigh-Taylor (RT) and Richtmyer-Meshkov (RM) instabilities. Very interesting and important is the problem of a steady-state compression of a laser thermonuclear target treated within the framework of thermonuclear fusion investigations, particularly, a development of a target layer mixing due to the target compression.

Initial perturbations of a laser thermonuclear target are determined by symmetry and homogeneity of an energy source (laser and ion beams, pulsed systems), homogeneity, and quality of a target cell preparation, and so on. Only by taking into account the initial conditions one can devise a proper model of mixing, which could describe the effects of mixing at compression.

The aim of the work is to build an analytical model describing the RTI processes on the basis of the numerical calculation results.

Within the framework of our work we consider plane and spherical problems at the given initial conditions. In a plane case, we consider two pairs of gases, Xe-Ar and Xe-He. A shape of a contact boundary was set in the form of a sum of harmonics with randomly chosen phases. The calculations were performed for 6, 8, and 10 harmonics (the calculations corresponded to the instabilities in shock tubes, i.e. at pressures around atmosphere, densities 10^{-3}-10^{-4} g/cm^3, and acceleration 10^5 m/s^2). In a spherical problem, we used a small number of harmonics (the calculations parameters corresponded to the laser compression regime, i.e. pressure around 10^{12} Pa (10^7 atm), density 1-100 g/cm^3, acceleration 10^{16}-10^{18} m/s^2).

The calculations parameters determined for gases in shock tubes and targets at laser compression are essentially different. But this is not an obstacle for building a unified model because in these gas-dynamic problems the fundamental properties of a gas-dynamic similarity are fulfilled.

Basing on the obtained calculation data [1] and the previously proposed theoretical models we have built a model for the mixing zone development that takes into account the information about the initial perturbation conditions.

1 Results of the numerical calculations (the plane case).

To perform a systematic study of the influence of different initial conditions on the development of turbulence due to RTI and RMI, one has performed a series of the plane calculations using a numerical code NUT [2].

The results of this part of the calculations can be formulated as follows:

- basing on the plane numerical calculations one has elaborated an extensive data base for a development of instability and mixing of two gases at a constant acceleration for the regimes having different types of instabilities (RTI and RMI), Attwood number (0.941 and 0.532), different number of the modes that are taken into account, and respectively, the maximym number of the shortest mode (n=13 and n=37), different initial amplitudes, and the dependence of amplitude on the mode number (a=const/k and a=const);
- the mixing zone width depends essentially on the amplitude of initial perturbations and changes with time by the law close to linear;
- The mixing zone width depends weakly on the contribution of higher modes (it decreases with switching of higher modes).

2 Model for description of the mixing zone width.

Basing on the performed claculations one has elaborated a theoretical model to describe width and velocity of the mixing zone growth, in which the initial conditions are taken into account.

By assuming a regular asymptotics arising at the earlier and later stages one can make the following conclusions. A mixing zone increases with time quadratically at higher modes in the beginning of the process, which follows from the evolutionary model of instability development [3]. At a later stage, the zone growth velocity tends to a constant limiting value which is determined by the velocity of a bubble (ball) floating of a light liquid. The size of the bubble is determined by a lower harmonic developed by the given moment (according to the Layzer's model [4]). The number « i » harmonic makes the mixing zone higher by the following value :

$$L_i(t)= a_{0i}+ \frac{\lambda_i}{2\,\alpha_{eff}} \left(\sqrt{1 + \frac{(\alpha_{eff}\,\gamma_i\,t)^2}{2\,\pi}} - 1 \right), \qquad (2.1)$$

Here $\gamma^2 = \frac{2\pi}{\lambda_i} gA$, A= $\frac{\rho_2 - \rho_1}{\rho_2 + \rho_1}$, $\alpha_{eff} = \frac{\alpha_0 \cdot \alpha^*}{\alpha_0 + \alpha^*}$, $k_i = \frac{2\pi}{\lambda_i}$, $\alpha_0 = k_i a_{oi}$

According to [3], value α^* determines the amplitude, at which the exponential growth of the instability becomes slower due to the formation of a mushroom-shaped structure. Normally, for the 2D problem we have $\alpha^*_{2D} = 3 \div 5$, and for the 3D problem, $\alpha^*_{3D} = 10 \div 20$.

It is evident that at initial stage of mixing the zone width is determined by the amplitude of a linearly developing indestructable harmonic. At small t and small $a_o(\alpha_o < \alpha^*)$ we have $\frac{dL_i}{dt} = a_o k_i gAt = a_o \gamma_i^2 t$, $L_i \sim t^2$, $\ddot{a} = \gamma^2 a$ in accordance with a linear stage of instability at the zero initial velocity of the instability development. At larger t we have $\frac{dL_i}{dt} = \upsilon \sqrt{g\lambda_i}$. In the Layzer's model, this velocity determines full speed of a floatable bubble $V_{lim} = \upsilon \sqrt{g\lambda_i}$, where $\upsilon(A)$ is the coefficient depending on the problem geometry and the Attwood number A, for example, $\upsilon_{3D}(1)$ =0.23. In the formula for $\frac{dL_i}{dt} = \upsilon \sqrt{g\lambda_i}$ the coefficient υ takes into account both the floatable bubble velocity and a higher velocity of a heavy jet dropping. For the 2D problems that coefficient is normally 0.75÷1, and for 3D problems it is $\upsilon \cong$ 1-1.3. The zone width is determined by a contribution of all harmonics, but their contribution is different and changes with time. In the case of one harmonic, $L(t)=2a(t)$. At the given moment, the longwave perturbations may yield a contribution of $\approx 2a$, while the shortwave perturbations are not so important.

The full width will be represented in the following form:

$$L(t) = \sum_i L_i(t) w_i(t), \qquad (2.2)$$

where $w_i(t)$ is the weight coefficient that determines a contribution of the given harmonic. Initially, $w_i(0)$ is determined by a random phase of the given perturbation:

$$w_i(0) = \cos(k_i x_{max} + \varphi_i) - \cos(k_i x_{min} + \varphi_i) \qquad (2.3)$$

and may achieve $w_i(0) \cong 2$. From the latter relation it is seen that the zone width is determined by a maximally « high » position of light liquid and minimally «low» position of heavy liquid. Further on, $w_i(t)$ decreases, which corresponds to destruction of the given instability mode due to a development of the Kelvin-Helmholtz instability [3]. The behavior of $w_i(t)$ can be approximately represented by a dependence:

$$w_i(t) = w_i(0)e^{-t(\gamma_{KH})_i} \sim e^{-\frac{1}{2}k_i a_i \sqrt{1-A^2}} \sim e^{-\frac{1}{4}k_i a_i^0 (\gamma_{RT} t)^2 \sqrt{1-A^2}}$$

Here:

$$(\gamma_{KH})_i = k_i v_i \frac{\sqrt{\rho_1 \rho_2}}{\rho_1 + \rho_2}, \quad v_i t = \frac{a_i^0}{2}\left[e^{(\gamma_{RT})_i} + e^{-(\gamma_{RT})_i}\right] = a_i^0 \left[1 + \frac{(\gamma_{RT} t)^2}{2}\right]$$

where v_i is the rate of the heavy liquid jet growth in the RTI instability of the "i" harmonic.

Values γ_{KH} and γ_{RT} depend on the wave vector $k_i = \dfrac{2\pi}{\lambda_i} = \dfrac{2\pi}{L} n_i$ and thereby depend on the number of the « i »

harmonic. It is seen that the contribution into the zone width of the harmonic with the number n_i decreases the faster the greater the number n_i. If the spectrum of initial perturbations is $k_i a_i^o$=const, then $w_i(t) \sim e^{-c_1 n_i}$. If the initial

perturbations correspond to the law $a_i^0 = \text{const}$, then $w_i(t) \sim e^{-c_2 n_i^2}$. At the later stages, the contribution of higher harmonics is nonzero, and is to be taken into account. One may assume that a contribution of a harmonic after its damage into a zone width is of the order of a wavelength. Basing on the calculation results, and using a trial-and-error method we can suggest a formula for the i-th harmonic weight :

$$w_i(t) = w_i(0)[\ \frac{2}{i} + 2(1 - \frac{2}{i})\ \frac{1}{1 + \exp(\frac{\lambda^2_{i_{max}}}{\lambda^2_i} \cdot w^2_i(0) \cdot \gamma^2 t^2)}\ ] \tag{2.4}$$

At a mixing stage, the high-frequency modes make a contribution into the mixing zone width. For the 2D geometry it is $a_{mix} \cong (3 \div 5)\lambda/2\pi$, and for 3D, $a_{mix} \cong (10 \div 20)\lambda/2\pi$ [3]. A more important conclusion is that the main contribution into the mixing zone width is made by the long-wave perturbations developed by now. Because value $(\gamma_{RT})_i t$ achieves lesser values for these perturbations, it is easier to estimate their evolution by means of real numerical calculations or using the analytical models like, for example, [3]. In the end of this section, Fig.2.1 illustrates time dependence of the mixing zone width (the above theory is compared with the calculation results). The proposed expressions (2.1-2.4) describe satisfactorily the mixing zone width in the planar RTI problems.
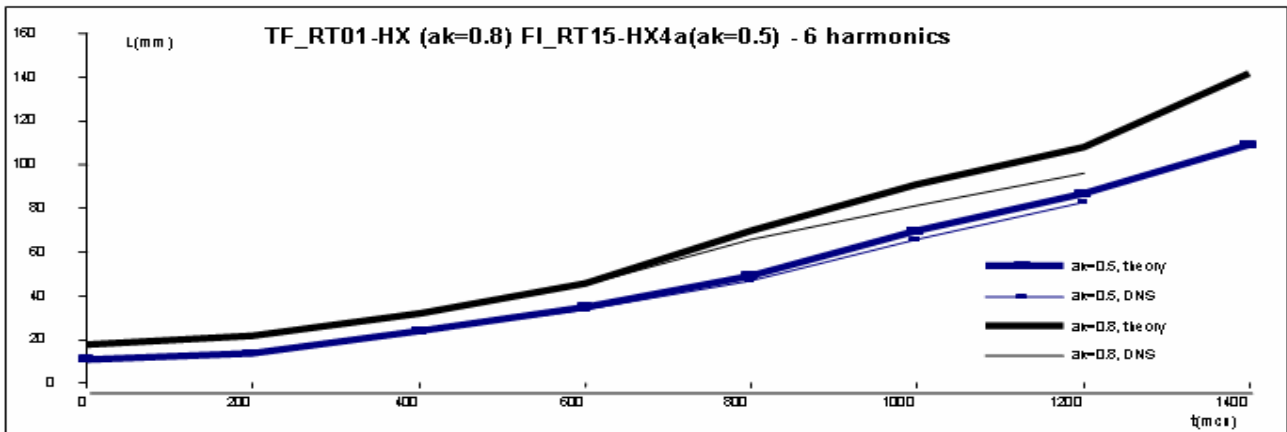
Fig.2.1. Time dependence of the mixing zone width.

3 Numerical simulations (spherical case).

The next stage in studying of the mixing processes in inertial thermonuclear fusion is the performance of numerical simulations of spherical shell compression maximally close to the the real laser ones, and an attempt to describe the targets by the above proposed theoretical model.

A spherical shell suggests the extistence of a number of new aspects, which essentially complicate the modeling of the mixing zone development: the finite time of compression, a complex initial spectrum of perturbation that contains the low and higher harmonics and is not always known exactly, the complexity of the shell, and an essential nonlinearity of the development dynamics at the late stage (the stage of a collapse), etc.

A series of numerical simulations with similar initial conditions has been performed using the NUT code [2]. Figure 3.1.a demonstrates the target with several concentric spherical shells meant for different functions: the external layers (a foam absorber, a heavy CH ablator (not shown in the figure) and a layer of DT fuel), and the inner gas layer (the target was discussed in the report at the IFSA 2005[1] conference [5]).

In our task we considered the process of shell compression during the last three nanoseconds (the shell at a stage of collapse). The density and radii of different layers were as follows: ablator (CH of the density of 12 g/cm^3 and the radius r_{CH} = 926 μm), DT fuel layer (the density, 0,5 g/cm^3 and the radius r_{DT} = 916 μm) ; the inner gas layer (the density, $3.5*10^{-3}$ g/cm^3 and the radius r_{in} = 768 μm). The inhomogeneities were given at the boundary DT-inner gas (Fig. 3.1.b). At the moment t (in our task 0 ns) the CH and DT layers started to move to the center along the radius with the velocity of V_0=300 km/s, and thus compressed the shell.

3.1.a   3.1.b
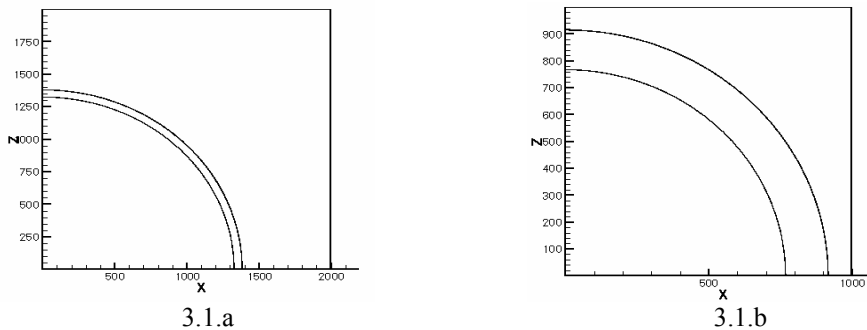
Fig. 3.1. Spherical target at the initial moment (3.1.a) and at the beginning of simulation (3.1.b) (the density field).

Figure 3.2 illustrates the simulations performed for the perturbations containing the 6-th and 15-th harmonics with the initial amplitudes of 4.5 and 18 μm, and the 48-th harmonic with an amplitude of 3 μm (the figure shows the concentration fields at time moments of 1, 1.5, 2, 2.5 ns).

The shape of a contact boundary was given by the law:

$$R = r_{in} + \sum_i a_{0i} \cos(n_i \theta) , \tag{3.1}$$

where θ was the angle responsible for the location of the interface point; n_i, the number of the "i"-th harmonic; a_{0i}, the initial amplotude of the "i"-th harmonic. The target compression time was 3 ns.

Next we present the diagrams for a number of target compression parameters calculated for the perturbations containing the 6-th and 15-th harmonic with an 18 μm amplitude (Fig. 3.3.).

We have also paid attention to the aspects associated with the sphericity of the task. We mean the compressibility and convergence. Having analyzed the simulation results, one can make a conclusion that the influence of the noted effects on the instability growth is small, and, moreover, they partially compensate each other.

Figure 3.4. presents a comparison between the obtained mixing zone width and that given by the formulas (2.1-2.4).

The formulas (2.1-2.4), which define the width of the mixing zone, can be introduced into the 1D numerical codes destined for the calculation of shell compression and thermonuclear burn.

The available simulations contain detailed information on the state of the interacting gases, the dimension of the mixing zone, etc. So, at the next stage of work we are planning to learn to define more accurately how the mixing effect influences the efficiency of a thermonuclear reaction.

---

[1] Fourth International Conference on Inertial Fusion Sciences and Applications

6-th and 15-th harmonic
with the amplitude of 4.5 μm

6-th and 15-th harmonic
with the amplitude of 18 μm

48-th harmonic
with the amplitude of 3 μm

t=1нс

t=1.5

t=2нс

t=2.5нс
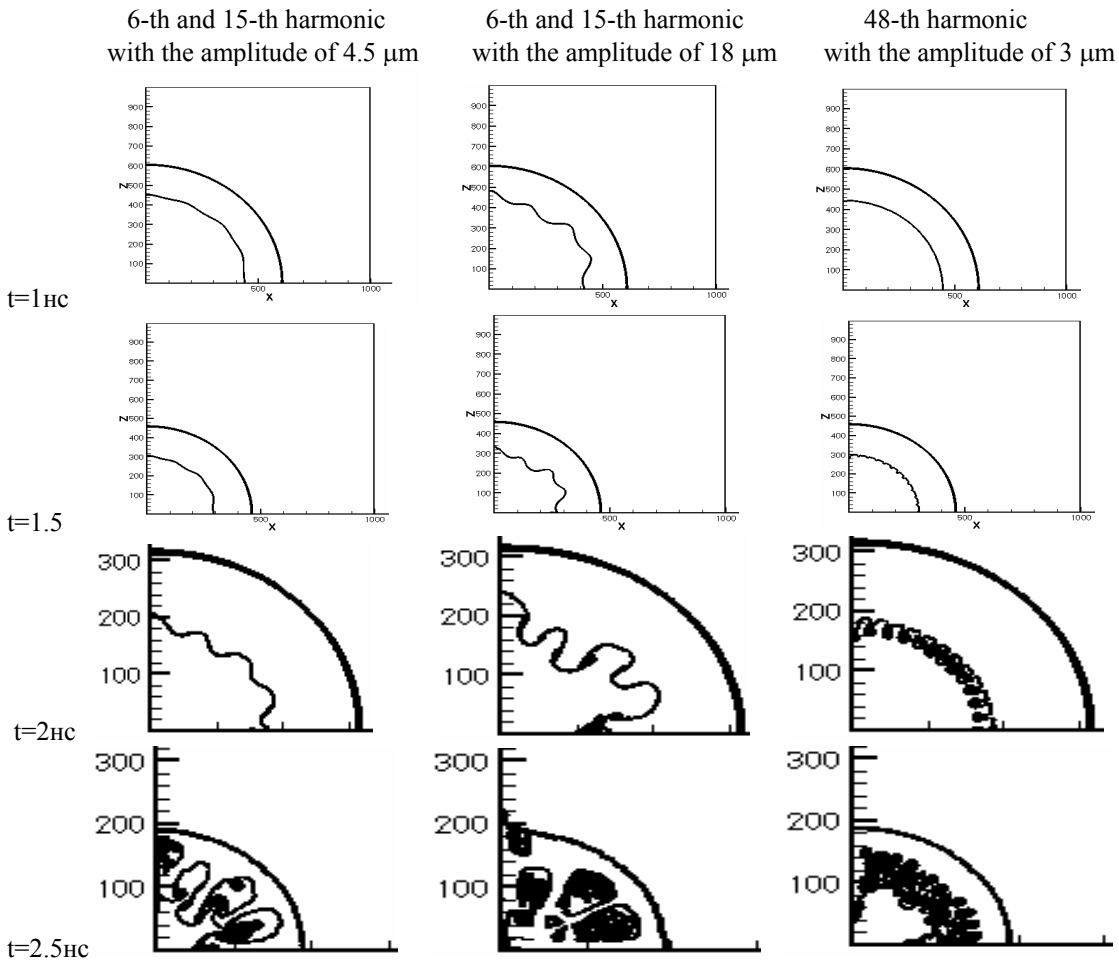
Fig. 3.2. Results from numerical simulations (1-st column - the 6-th and 15-th harmonics with a 4.5 μm initial amplitude; 2-nd column - 6-th and 15-th harmonics with a 18 μm initial amplitude; 3-rd column - 48-th harmonic with 3 μm initial amplitude). The scale of the pictures corresponding to the time moments of 2 and 2.5 ns is enlarged by approximately 3 times as compared to the others.
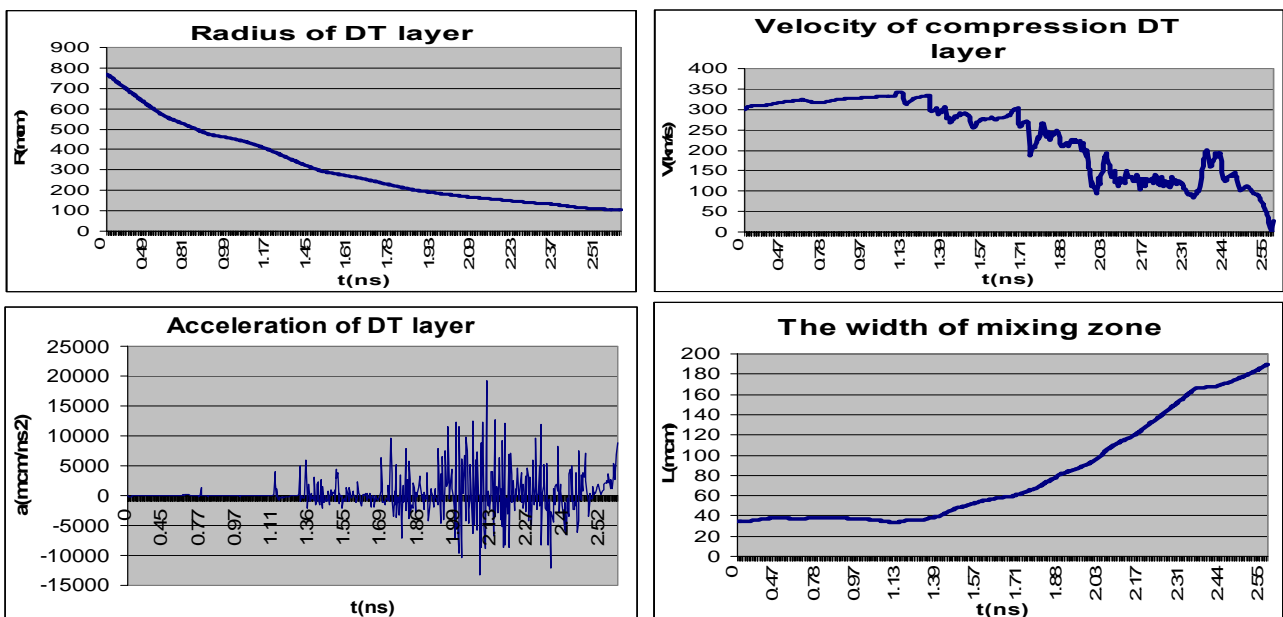
Fig. 3.3. Temporal characteristics of compression (n= 6 and 15, a=18 μm).
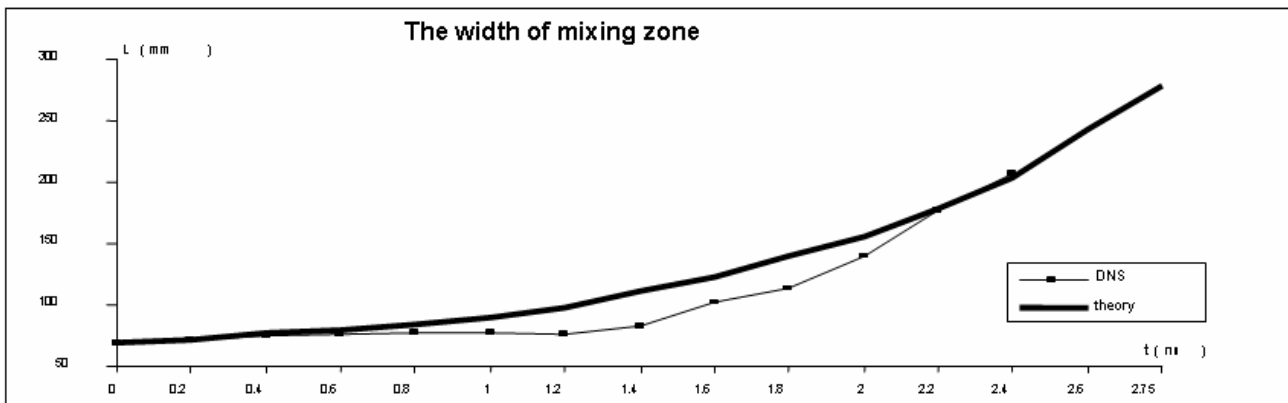
Fig. 3.4. Mixing zone width for the 6-th and 15-th harmonic with the amplitude of 18 μm (comparison of the calculated data and theoretical model).

Summary.

A series of simulations was performed on the development of RT and RM instabilities and turbulent mixing under different initial conditions: the initial perturbation mode composition; the amplitudes; the gases engaged in mixing; different statistical realizations of similar simulations; geometry; part of our simulations corresponded to the development of instability in shock tubes, and the other part – to the laser compression.

The results of numerical simulations, their processing, and the obtained relations allowed one to answer an important question for the LTF: the dependence of the mixing parameters on the initial conditions at thermonuclear shell compression. Note a weak dependence of the mixing zone width on the higher mode input revealed in our simulations (a large input from the higher modes slightly diminished the mixing zone width).

Basing on the investigation of instability development in plane and spherical simulations, and taking into account the evolution model of instability development, we proposed the analytical expressions (2.1-2.4), which describe the mixing zone development with account for the initial conditions, namely, the spectrum, the perturbation amplitudes, etc.

A comparison of the performed simulations and the proposed theory predictions brings one to a conclusion that the analytical expressions (2.1-2.4) agree quite satisfactorily with the simulations.

A very important advantage of the obtained expressions lies in a possibility of their further application to the description of mixing processes within a rather wide range of physical parameters (verification of the theory based on modeling of fundamentally different regimes).

Later on it is planned to carry out a set of simulations with account for the mixing process influence on the LTF shell compression and a possibility of counting the thermonuclear reactions.

References

[1] V. Rozanov, R. Stepanov, A. Nuzhny, R. Yakhin, M. Anuchin, N. Proncheva, N. Zmitrenko, Yu. Yanilkin, V. Tishkin "Скорость роста зоны перемешивания в прямом численном моделировании и вейвлет-анализ развития многомодо-вой Релей-Тейлоровской неустойчивости". Препринт ФИАН № 28, 2004.

[2] V.F. Tishkin, V.V. Nikishin, I.V. Popov, A.P. Favorsky. "Разностные схемы трехмерной газовой динамики для решения задачи о неустойчивости Рихтмайера-Мешкова". Математическое моделирование 7(5), 15, 1995.

[3] N.V. Zmitrenko, N.G. Proncheva, V.B. Rozanov. "An evolutionary model of a turbulent mixing layer". Preprint FIAN № 65, 1997.

[4] D. Layzer "Astrophysical Journal On the stability of superpose fluids in a gravitational field ", v. 122, №1, p.1-12, 1995.

[5] V. Rozanov, I. Doskoch, S. Guskov, R. Stepanov, N. Zmitrenko "Green House Target Advanced Design". IFSA 2005, Biarritz, France, 4-9 September. Proceedings, Journal de Physique IV, Volume 113, p. 213-217.

e-mail: `sorens@bgu.ac.il`

Experimental Observation on the Nonlinear Rayleigh-Taylor Instability Under Ablative Conditions

Oren SADOT,[1,2,3] Vladimir A. SMALYUK,[1] Jacques A. DELETTREZ,[1]
David D. MEYERHOFER,[1,4] Thomas C. SANGSTER,[1] Riccardo BETTI,[1,4]
Valeri N. GONCHAROV,[1] AND Dov SHVARTS[2,3]

[1] *Laboratory for Laser Energetics, University of Rochester250 East River Road, Rochester, NY 14623, USA*
[2] *NRCN Beer- Sheva 84190, Israel*
[3] *Ben Gurion University of the Negev, Beer Sheva 84015, Israel*
[4] *Departments of Mechanical Engineering and Physics and Astronomy, University of Rochester USA*

Abstract: The Rayleigh–Taylor instability growth of laser-seeded, 3-D broadband perturbations was experimentally measured in the laser-accelerated, planar plastic foils. The first experimental observation showing the self-similar behavior of the bubble size and amplitude distributions under ablative conditions is presented. In the nonlinear regime, the modulation σ_{rms} grows as $\alpha_\sigma g t^2$, where g is the foil acceleration, t is the time, and α_σ is a constant. The number of bubbles evolves as: $N(t) \sim (\omega \cdot t \cdot \sqrt{g} + C)^{-4}$ and the average size evolves as $\langle \lambda \rangle (t) \sim \omega^2 g \cdot t^2$ where C is a constant and $\varpi = 0.83 \pm 0.1$ is the measured scaled bubble-merging rate. It was found that the under the assumption that $\alpha_b \sim \sqrt{2} \sigma_{rms}$, that the growth factor $\alpha_b = 0.04$ and the self-similar constant is b=0.9 as predicted by the classical Rayleigh–Taylor theory.

1 INTRODUCTION

The Rayleigh–Taylor (RT)[1,2] instability is a subject of intensive experimental and theoretical research because of its critical importance in inertial confinement fusion (ICF)[3] and astrophysics [4]. In ICF, an imploding outer spherical shell is pushed by an intense radiation field toward the center. The nuclear fuel inside the shell compresses and heats until reaching ignition conditions. The RT instability developed on the fuel–shell surface can lead to target disruption and the degradation of implosion performance [3].

In the linear regime of the instability, small initial modulations grow exponentially in time with growth rates of $\gamma = \sqrt{(A \cdot k \cdot g)}$ for classical RT instability [5–7] and $\gamma = a \sqrt{(k \cdot g)} - \beta \cdot k \cdot V_a$ for ablative RT instability [8,9], where k is the modulation wave number, g is the target acceleration, A is the Atwood number, Va is the ablation velocity, and a and β are constants. Most ICF-related cases involve ablative drive, in which the growth rate is stabilized by the ablation term $\beta \cdot k \cdot V_a$. The growth rates of the linear RT instability have been calculated and measured in both classical [10] and ablative regimes [10–14]. The first indication of nonlinear RT effects is that the modulations develop into asymmetric shapes of bubbles (penetration of the lighter fluid into the heavier) and spikes (penetration of the heavier fluid into the lighter). There are two modeling approaches for nonlinear RT instability. Modal models predict modulation growth in Fourier space [15,16] while bubble competition models predict modulation growth in the real space [17–24]. The bubble competition approach is suit better for the very late nonlinear stage when which it is impossible to present the interface as a single value function, while the Fourier space presentation hold in the early nonlinear stage. Both types of models predict that the average modulation size shifts to longer wavelengths as the modulations grow. In Fourier space, the amplitudes of the shorter-wavelength modulation saturate at lower levels, while longer-wavelength modulations continue to grow and achieve higher velocities before they saturate. As a result, the spectral peak of the modes in Fourier space develops and shifts to longer wavelengths [25], as predicted by Haan's model [15] and confirmed experimentally by Smalyuk et al. [32].

The bubble competition models predict that smaller bubbles (with smaller nonlinear velocities) are overcome by larger bubbles (with higher nonlinear velocities) through bubble competition – large bubble push the smaller bubble back from the interface front, and bubble merger processes where two bubbles become one big bubble [5,20–24]. These models are based on the bubble merger concept and predict that the bubble size reaches self-similar behavior by looking at the growth of the mixing zone. These models also predict that the average size of modulations shifts to longer wavelengths as the modulations grow. Experiments in the turbulent regime of classical RT instability [7], supported by

computer simulations [5, 21–24] show that average bubble amplitudes grow as αgt^2 in the highly nonlinear regime, where the constant α may depend on the initial conditions [24].

2 EXPERIMENTAL APPROACHE

Followed Smalyuk et al.[25], in the experiment, CH targets (with thicknesses ranging from 20 to 90 μm) were driven by 12-ns square laser pulses at an intensity of $\sim 5 \times 10^{13}$ W/cm^2 on the OMEGA Laser System [27]. In order to create the 12 ns pulse width, four 3 ns laser pulses where cascaded. Initial 3-D, broadband modulations were created by the nonuniformities of the individual laser drive beams [25, 26]. Backlighter x-rays were used to measure the growing target modulations. The transmitted x-rays propagated through the target and were then imaged by a pinhole array onto a framing camera, allowing time-resolved (with ~80 ps temporal resolution) images of the target modulations to be recorded with a spatial resolution of ~10 μm. Details of the experimental setup are presented in Refs. 25 and 26. Figure 2.1 (a) shows the target and the backlighter orientation together with the intensity timing. In order to capture the instability at different time, the backlighter timing was varied. Figure 1 (b) shows the plate central portions of the recorded images of the target modulations. The window size is 333 μm × 333 μm. Images in Figs. 2.1 (b) I, ii, and, iii were recorded at different times with target distances traveled of 1, 18, and 67 μm. The light areas (higher x-ray transmission) represent bubbles, while the dark areas (lower x-ray transmission) represent spikes. As the modulations grow, the average bubble size shifts to longer wavelengths, big bubbles become bigger, and small bubbles disappear, as evident from the images in Fig.2.1 (b).
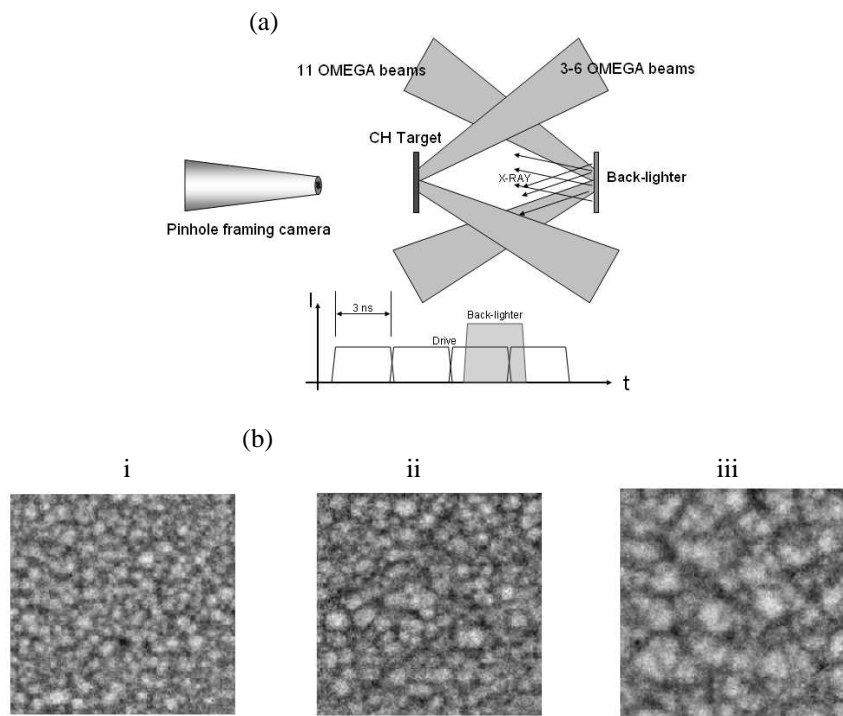
Fig 2.1 (a) the experimental configuration, planar target derived by a 12 ns laser pulse that initiates the RT instability. The soft x-ray created by illuminating a backlighter plate the instability was monitored. (b) Three different images capture by the pinhole camera at different dustiness travelled i) 1μm, ii) 18 μm and iii) 67 μm.

3 RESULTS AND ANALISYS

To measure bubbles characteristics such as size and amplitude, the images were processed with the watershed algorithm [28] to determine the bubble edges. Examples of a result of this procedure are shown in Figs. 3.1 (i), (ii), and (iii), where the bubble borders are superimposed on the Weiner-filtered images [26]. The bubbles near the edges of analysis regions were excluded from the analysis because the sizes and amplitudes of these bubbles could not be accurately determined. The bubbles sizes where determined by taking the squawroot of the area of each bubble and divided it by π. The evolution of the distributions of bubble sizes λ and their rms amplitudes σ [corresponding to images in Figs. 2.1(b), i, ii, and iii] are shown in Figs. 3.1 (i), (ii) and (iii), respectively.
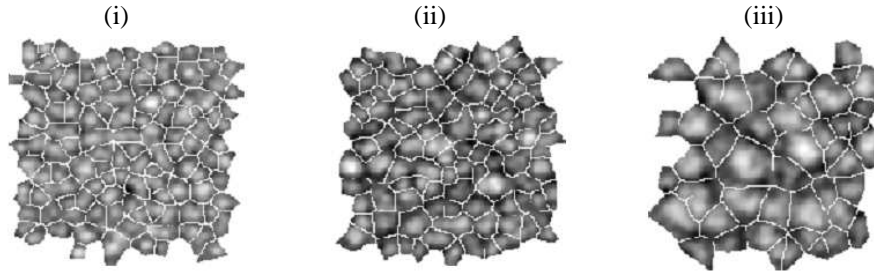
Fig 3.1: The processed images were the bubbles borders found using watershed algorithm.

As modulations grow, the number of bubbles decreases while their average size and average rms amplitude increase. The measured distributions of bubble sizes and amplitudes were fitted with the normal distribution from which average size $\langle\lambda\rangle$ and average rms amplitude $\langle\sigma\rangle$ were determined. Figures 2(c) and 2(d) show the normalized distributions as functions of normalized bubble size $\lambda/\langle\lambda\rangle$ and normalized amplitude $\sigma/\langle\sigma\rangle$ The dashed lines in Figs. 2(c) and 2(d) represent fits to the experimental data using normal distributions:

$$f_\sigma\left(a/\langle\sigma\rangle\right) = \exp\left[-\left(a/\langle\sigma\rangle - 1\right)^2 \big/ 2C_a^2\right]\big/\sqrt{2\pi}\cdot C_a$$

(1)

for bubble amplitude and

$$f_\sigma\left(\lambda/\langle\lambda\rangle\right) = \exp\left[-\left(\lambda/\langle\lambda\rangle - 1\right)^2 \big/ 2C_\lambda^2\right]\big/\sqrt{2\pi}\cdot C_\lambda$$

(2)

for the bubble size distributions, where $C_\lambda = 0.24\pm0.01$ and $C_a = 0.23\pm0.01$ are constants determined from these fits. Both bubble size and amplitude distributions are in the self-similar regime because the normalized distributions do not change in time. The self-similarity of RT growth is explicitly measured in our experiments by the evolution of bubble size and amplitude distributions, while in earlier simulations and experiments, the self-similarity was inferred from the growth of the size of the mixing zone. The dotted and dot-dashed lines in Fig. 3.2(c) are the distributions predicted from the 2-D and 3-D models, respectively (presented in Refs. 5, 29, and 30). As expected, the 3-D model prediction is a better representation of the experimental results.
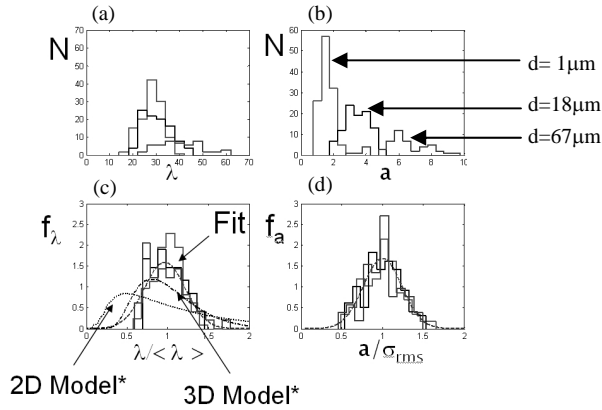
Fig 3.2: (a) The measured bubble size distribution at three different times. (b) The measured bubble amplitude distribution at three different times. (a) The normalized bubble size distribution and, (b) The normalized bubble amplitude distribution at the same three different times.

The evolutions of the average size $\langle\lambda\rangle$ and the average rms amplitude $\langle\sigma\rangle$ also compare very well with self-similar growth where these quantities are expected to grow proportionally to gt^2 (g is the target acceleration and t is time). Figure 3.3 shows the measured evolution of the total number of bubbles N [Fig. 3.3 (a)] and the average bubble size $\langle\lambda\rangle$ [Fig. 3.3(b)] as a function of the distance traveled by the driven target $d = 0.5gt^2$. The distance traveled represents the amount of the growth because the growth factors are related to the distance traveled. Following Refs. 5, 29, and 30, we assume that the total number of bubbles N decreases with the scaled average merging rate ϖ according to:

$$\frac{dN}{dt} = -\sqrt{\frac{g}{\langle\lambda\rangle(t)}}\varpi\cdot N(t)$$

(3)

The conservation of the total area of all bubbles leads to the following equation for the evolution of the average bubble size $\langle\lambda\rangle$:

$$\frac{d\langle\lambda\rangle}{dt} = \sqrt{\frac{g}{\langle\lambda\rangle}} \cdot \frac{\varpi}{2} \cdot \langle\lambda\rangle.$$

(4)

The solutions to these equations are:

$$N(t) = D\left(\varpi \cdot t \cdot \sqrt{g} + 2C\right)^{-4}$$

(5)

and

$$\langle\lambda\rangle(t) = \varpi^2 \cdot gt^2 \big/ 16 + \sqrt{g} \cdot t\varpi \cdot C/4 + C^2 \big/ 4,$$

(6)

respectively. In Figs. 3.3(a) and 3.3 (b) these solutions are plotted as fits to the experimental data (solid lines). The constants D and C are related to the initial average bubble size $\langle\lambda\rangle_0$ and the initial number of bubbles N_0, respectively, as D $= N_0(2C)^4$ and C=2$\sqrt{}$<λ>$_0$ From the fit to the data, it was found that $N_0 = 230\pm10$ and $\langle\lambda\rangle_0 = 27\pm1$ μm. The same scaled average merging rate $\varpi = 0.83\pm0.1$ was found (using the two fits independently) when two generations of bubble change, corresponding to the reduction in the number of bubbles by factor of ~4.

Figure 3.3 (c) shows the evolution of the modulation σ_{rms} as a function of the distance traveled. It was calculated by dividing the measured σ_{rms} of areal-density (target density multiplied by its thickness) modulations by the calculated (using 1-D hydrocode LILAC [31]) target density. The solid line is the linear fit to the data without the two filled points, showing that the modulation σ_{rms} growing as $\alpha_\sigma gt^2$, where $\alpha_\sigma=0.027\pm0.003$ is the constant determined from the fit. By adapting the relation between the bubble height and the rms amplitude measured from Ofer [16] to be $h_b = \sqrt{2}\,\sigma_{rms}$, one can fined the growth scale α_b to be 0.04 ± 0.004, the self-similar constant b = <h_b>/<λ> was found to be 0.86 ± 0.16 both as predicted from classical theory without ablation.
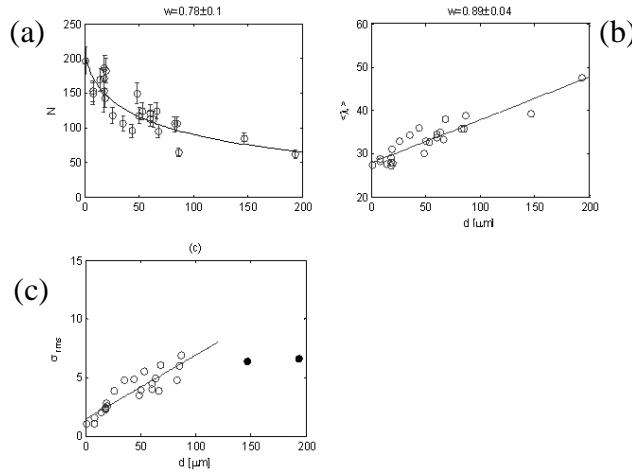
Fig 3.3 (a). The numbers of bubbles vs. time. (b) The size of bubbles vs. time.
(c) The rms amplitude of bubbles vs. time.

The overall behaviour of the instability in the self-similar stage can be described in the σ-λ plan as follow: At early stages modulations created and grow and saturate according to Haan's model, in the self-similar stage bubbles are expand and grow as a result of the competition and merger processes. Some bubbles grow larger, while others shrink and disappear. The number of bubbles n(t,a,λ) in the intervals of a to a + da and λ to λ + dλ at time t can be expressed as

$$n(t;a,\lambda) = \frac{da \cdot d\lambda}{2\pi\langle\lambda\rangle\langle a\rangle C_\lambda C_a} \cdot N(t) \cdot e^{-\frac{\left(\frac{\lambda}{\langle\lambda\rangle}-1\right)^2}{2C_\lambda^2}} \cdot e^{-\frac{\left(\frac{a}{\langle a\rangle}-1\right)^2}{2C_a^2}},$$

(7)

where $\langle\lambda\rangle$ and N(t) evolve according to the solution to Eqs. (1) and (2), and the modulation rms amplitudes evolve as $\langle a\rangle = \langle a\rangle_0 + \alpha_b gt^2$. Graphical description of that behaviour presented in figure 3.4.
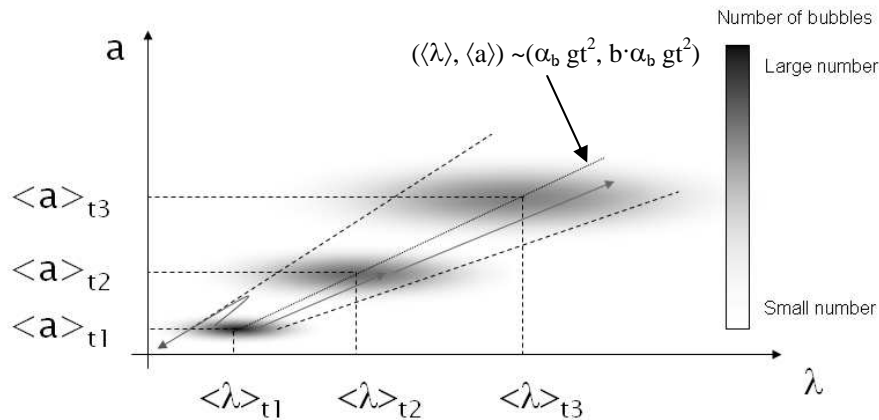
Fig. 3.4. The evolution of the instability on the a-λ plane.

4 SUMMARY

In summary, the nonlinear Rayleigh–Taylor evolution under ablation conditions was measured. The evolution of 3-D broadband modulations was investigated in the nonlinear stage. The instability created by driving the target by high intensity relatively long laser pulse. The modulations were monitored using x-ray face-on radiography. By measuring the individual size and amplitude of each bubble, the distributions of bubble sizes and amplitudes were constructed. These distributions evolve self-similarly as the target modulations grow. During this growth, the modulations shift to longer wavelengths as bubbles compete and merge. The number of bubbles N evolves as $N(t) \sim t^{-4}$ and both the average bubble size and average rms amplitude grow proportionally to gt^2, as predicted by the self-similar growth and scaling theory. From the results it was found that α_b to be 0.04 ± 0.004 and the self-similar constant to be $b=0.86\pm0.16$ as predicted in the classical (without ablation) RT case. These results suggest that at late times there is little effect of the ablation. A simple phenomenological model was built to describe the complex physics of nonlinear RT evolution in the weakly nonlinear regime.

REFERENCES

[1] L. Rayleigh, Proc. London Math Soc. **XIV**, 170 (1883).

[2] G. Taylor, Proc. R. Soc. London Ser. A **201**, 192 (1950).

[3] J. D. Lindl, " Development of the indirect-drive approach to inertial confinement fusion and the target physics basis for ignition and gain" Phys. Plasmas 2, 3933 (1995).

[4] B. A. Remington, D. Arnett, R. P. , Drake, H. Takabe", Modeling Astrophysical Phenomena in the Laboratory with Intense Lasers " Phys. Plasmas 4, 1994 (1997).

[5] U. Alon, J. Hecht, D. Ofer, and D. Shvarts, "Power Laws and Similarity of Rayleigh-Taylor and Richtmyer-Meshkov Mixing Fronts at All Density Ratios" Phys. Rev. Lett. 72, 2867 (1994).

[6] G. Dimonte and M. Schneider, "Density ratio dependence of Rayleigh–Taylor mixing for sustained and impulsive acceleration histories", Phys. Fluids 12, 304 (2000).

[7] K. I. Read, "Experimental investigation of turbulent mixing by Rayleigh-Taylor instability", Physica 12D, 45 (1984).

[8] H. Takabe K. Mima L. Montierth and R. L. Morse," Self-consistent growth rate of the Rayleigh–Taylor instability in an ablatively accelerating plasma" Phys. Fluids 28, 3676 (1985).

[9] R. Betti, V. N. Goncharov, R. L. McCrory, and P. Sorotokin C. P. Verdon, "Self-consistent stability analysis of ablation fronts in inertial confinement fusion" Phys. Plasmas 3, 2122 (1996).

[10] K. S. Budil, B. A. Remington, T. A. Peyser, K. O. Mikaelian, P. L. Miller, N. C. Woolsey, W. M. Wood-Vasey, and A. M. Rubenchik, "Experimental Comparison of Classical versus Ablative Rayleigh-Taylor Instability " Phys. Rev. Lett. 76, 4536 (1996).

[11] S. G. Glendinning, S. N. Dixit, B. A. Hammel, D. H. Kalantar, M. H. Key, J. D. Kilkenny, J. P. Knauer, D. M. Pennington, B. A. Remington, R. J. Wallace, and S. V. Weber, "Measurement of a Dispersion Curve for Linear-Regime Rayleigh-Taylor Growth Rates in Laser-Driven Planar Targets" Phys. Rev. Lett. 78, 3318 (1997).

[12] C. J. Pawley et al., Phys. Plasmas 6, 565 (1999).

[13] J. P. Knauer, R. Betti, D. K. Bradley, T. R. Boehly, T. J. B. Collins, V. N. Goncharov, P. W. McKenty, D. D. Meyerhofer, and V. A. Smalyuk, C. P. Verdon, S. G. Glendinning, and D. H. Kalantar, R. G. Watt, " Single-mode, Rayleigh-Taylor growth-rate measurements on the OMEGA laser system" Phys. Plasmas 7, 338 (2000).

[14] T. Sakaiya, H. Azechi, M. Matsuoka, N. Izumi, M. Nakai, K. Shigemori, H. Shiraga, A. Sunahara, H. Takabe, and T. Yamanaka, " Ablative Rayleigh-Taylor Instability at Short Wavelengths Observed with Moiré Interferometry", Phys. Rev. Lett. 88, 145003 (2002).

[15] S. W. Haan, "Onset of nonlinear saturation for Rayleigh-Taylor growth in the presence of a full spectrum of modes", Phys. Rev. A, Gen. Phys. 39, 5812 (1989).

[16] D. Ofer U. Alon, D. Shvarts, R. L. McCrory and C. P. Verdon , " Modal model for the nonlinear multimode Rayleigh–Taylor instability" Phys. Plasmas 3, 3073 (1996).

[17] D. H. Sharp, Physica 12D, 3 (1984).

[18] C. L. Gardner J. Glimm, O. McBryan, R. Menikoff D. H. Sharp and Q. Zhang"The dynamics of bubble growth for Rayleigh–Taylor unstable interfaces" Phys. Fluids 31, 447 (1988).

[19] Q. Zhang, Phys. Lett. A 151, 18 (1990).

[20] J. Glimm and X. L. Li, Phys. Fluids 31, 2077 (1988).

[21] U. Alon J. Hecht, D. Ofer, and D. Shvarts, " Power Laws and Similarity of Rayleigh-Taylor and Richtmyer-Meshkov Mixing Fronts at All Density Ratios", Phys. Rev. Lett. 74, 534 (1995).

[22] D. L. Youngs, Phys. Fluids A 3, 1312 (1991).

[23] G. Dimonte et al., Phys. Fluids 16, 1668 (2004).

[24] G. Dimonte, " Dependence of turbulent Rayleigh-Taylor instability on initial perturbations", Phys. Rev. E 69, 056305 (2004).

[25] V. A. Smalyuk, T. R. Boehly, D. K. Bradley, V. N. Goncharov, J. A. Delettrez, J. P. Knauer, D. D. Meyerhofer, D. Oron, and D. Shvarts, "Saturation of the Rayleigh-Taylor Growth of Broad-Bandwidth Laser-Imposed Nonuniformities in Planar Targets", Phys. Rev. Lett. 81, 5342 (1998).

[26] V. A. Smalyuk T. R. Boehly, D. K. Bradley, V. N. Goncharov, J. A. Delettrez, J. P. Knauer, D. D. Meyerhofer, D. Oron D. Shvarts, Y. Srebro, R. P. J. Town "Nonlinear evolution of broad-bandwidth, laser-imprinted nonuniformities in planar targets accelerated by 351-nm laser light", Phys. Plasmas 6, 4022 (1999).

[27] T. R. Boehly et al., Opt. Commun. 133, 495 (1997).

[28] L. Vincent and P. Soille, IEEE Trans. Pattern Anal. Mach. Intell. 13, 583 (1991).

[29] D. Oron, L. Arazi D. Kartoon A. Rikanati U. Alon D. Shvarts " Dimensionality dependence of the Rayleigh–Taylor and Richtmyer–Meshkov instability late-time scaling laws", Phys. Plasmas 8, 2883 (2001).

[30] D. Oron, U. Alon, and D. Shvarts, " Scaling laws of the Rayleigh–Taylor ablation front mixing zone evolution in inertial confinement fusion", Phys. Plasmas 5, 1467 (1998).

[31] J. Delettrez, R. Epstein, and M. C. Richardson, P. A. Jaanimagi and B. L. Henke, "Effect of laser illumination nonuniformity on the analysis of time-resolved x-ray measurements in uv spherical transport experiments" Phys. Rev. A, Gen. Phys. 36, 3926 (1987).

[32] V. A. Smalyuk, O. Sadot, J. A. Delettrez, D. D. Meyerhofer, S. P. Regan, and T. C. Sangster, "Fourier-Space Nonlinear Rayleigh-Taylor Growth Measurements of 3D Laser-Imprinted Modulations in Planar Targets", Phys. Rev. Lett. 95, 215001 (2005)

e-mail: `schilling1@llnl.gov`

Richtmyer–Meshkov instability-induced mixing: initial conditions modeling, three-dimensional simulations and comparisons to experiment

Marco LATINI[1], Oleg SCHILLING[2] and Wai Sun DON[3]

[1] *California Institute of Technology, Pasadena, California 91125, USA*

[2] *University of California, Lawrence Livermore National Laboratory, Livermore, California 94551, USA*

[3] *Brown University, Providence, Rhode Island 02912, USA*

Abstract: The reshocked multi-mode Richtmyer–Meshkov instability is investigated using a three-dimensional ninth-order weighted essentially non-oscillatory shock-capturing simulation. A two-mode initial perturbation with superposed random noise is used to model the Mach 1.5 air/SF$_6$ Vetter–Sturtevant shock tube experiment [8]. The mass fraction isosurfaces and density cross-sections show the detailed structure before, during, and after reshock. The amplification effects of reshock are quantified using the baroclinic enstrophy production, buoyancy production, and shear production terms in the enstrophy and turbulent kinetic transport equations. The mixing layer growth is shown to agree well with the experimentally measured growth rate before and after reshock. The post-reshock growth rate is also in good agreement with the prediction of the Mikaelian model [5].

1 INTRODUCTION

The purpose of this research is to investigate turbulent transport in reshocked multi-mode Richtmyer–Meshkov instability using three-dimensional ninth-order weighted essentially non-oscillatory (WENO) simulations for the development and validation of turbulent transport and mixing models [7]. Here the high-resolution, finite-difference, Eulerian, shock-capturing WENO method is applied to a model of the Vetter–Sturtevant Richtmyer–Meshkov instability shock tube experiment. The numerical model of the experiment is validated by comparing to experimental amplitude data, and the simulations are extended to longer times than in the experiment.

2 EQUATIONS SOLVED AND THE NUMERICAL METHOD

A simulation was performed using the characteristics-based finite-difference WENO method. The Euler equations were augmented by the mass fraction to track the mixing dynamics:

$$\frac{\partial}{\partial t}\begin{bmatrix} \rho \\ \rho\,u \\ \rho\,v \\ \rho\,w \\ \rho\,e \\ \rho\,m \end{bmatrix} + \frac{\partial}{\partial x}\begin{bmatrix} \rho\,u \\ \rho\,u^2+p \\ \rho\,u\,v \\ \rho\,u\,w \\ (\rho\,e+p)\,u \\ \rho\,m\,u \end{bmatrix} + \frac{\partial}{\partial y}\begin{bmatrix} \rho\,v \\ \rho\,u\,v \\ \rho\,v^2+p \\ \rho\,v\,w \\ (\rho\,e+p)\,v \\ \rho\,m\,v \end{bmatrix} + \frac{\partial}{\partial z}\begin{bmatrix} \rho\,w \\ \rho\,u\,w \\ \rho\,v\,w \\ \rho\,w^2+p \\ (\rho\,e+p)\,w \\ \rho\,m\,w \end{bmatrix} = 0\,. \qquad (2.1)$$

Here, ρ is the density, $\mathbf{u} = (u, v, w)$ is the velocity, p is the pressure, $e = \left(u^2 + v^2 + w^2\right)/2 + p/(\gamma - 1)$ is the total energy per unit mass, m is the mass fraction (here of the denser sulfur hexafluoride gas, SF$_6$) and $p = \rho R T$ is the ideal gas pressure (R is the gas constant). Lax–Friedrichs flux-splitting was used. A convex nonlinearly-weighted combination of all polynomial flux reconstructions is used to achieve the *essentially non-oscillatory* property and formally high-order accuracy in smooth flow regions. The boundary conditions were symmetry in the directions transverse to the shock propagation and reflecting at the shock tube end wall. The implicit numerical dissipation is a surrogate for physical dissipation. Ninth-order reconstruction was used for its desirable properties of reducing the numerical dissipation and preserving small-scale structures [3].

3 THE MODEL OF THE INITIAL CONDITIONS

A two-mode initial perturbation with random noise was used to model the $Ma = 1.5$ air/SF$_6$ Vetter–Sturtevant [8] shock tube experiment, in which a membrane pushing on a wire mesh initially separated the gases. The
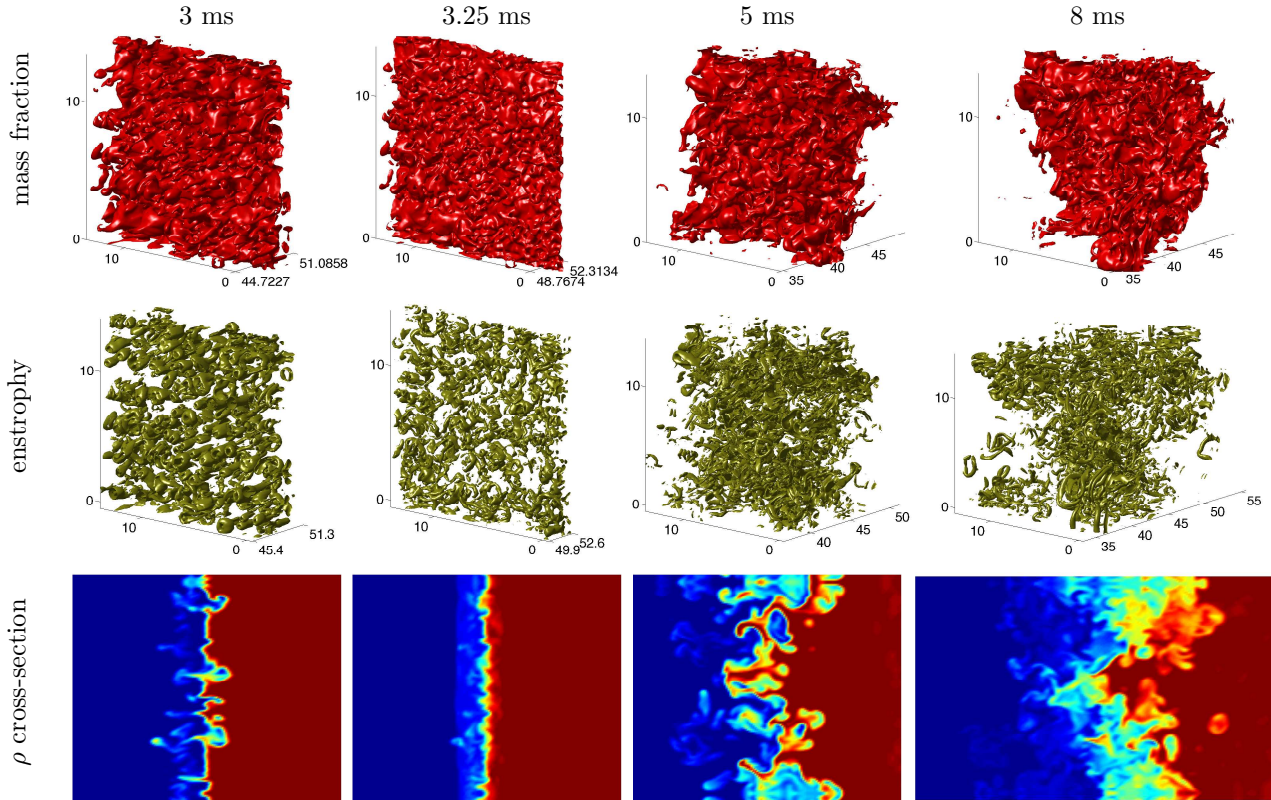
Fig. 4.1. Visualization of the mass fraction isosurface (top row), enstrophy isosurface (middle row), and density (x, y)-cross-section, where blue is air and red is SF_6 (bottom row) at 3, 3.25, 5, and 8 ms.

initial conditions adopt the two-mode model of Cohen et al. [1], but with random noise similar to that of Hill et al. [2],

$$\eta(y, z) = a \left| \sin\left(\frac{10\pi y}{27}\right) \right| \left| \sin\left(\frac{10\pi z}{27}\right) \right| - b \cos\left(\frac{2\pi y}{27}\right) \cos\left(\frac{2\pi z}{27}\right) + \psi(y, z) \,. \tag{3.1}$$

The first term models the membrane pushed through the wire mesh, the second term models the mesh distortion, and $\psi(y, z)$ models the membrane fragmentation. The noise is superimposed on the two-mode perturbation to break symmetry and accelerate the development of nonlinearity. Simulations were performed on a domain $[0, L_x] \times [0, L_y] \times [0, L_z]$, where $L_x = 61$ and $L_x = L_y = 27$ cm (matching the dimensions of the test section of the experiment), on a $513 \times 257 \times 257$ grid using a pre-shock Atwood number $A^- = 0.641$ and initial parameters $a = 0.0675$ and $b = 0.00675$ cm (0.25% and 0.025% of L_z, respectively).

4   INSTABILITY DYNAMICS AND THE EFFECTS OF RESHOCK

The instability dynamics and vorticity are visualized using the mass fraction and enstrophy isosurfaces on the air (spike) side in Fig. 4.1. Reshock occurs at 3.25 ms and the reflected rarefaction wave arrives at 5 ms. Following reshock, the instability develops complex structure while the enstrophy transforms from elongated tubular structures into short disordered tubular structures with random orientations. The density cross-sections illustrate the development of a well-mixed complex layer at late time.

The effects of reshock are investigated by considering key production terms in the enstrophy ($\Omega = \omega^2/2$)
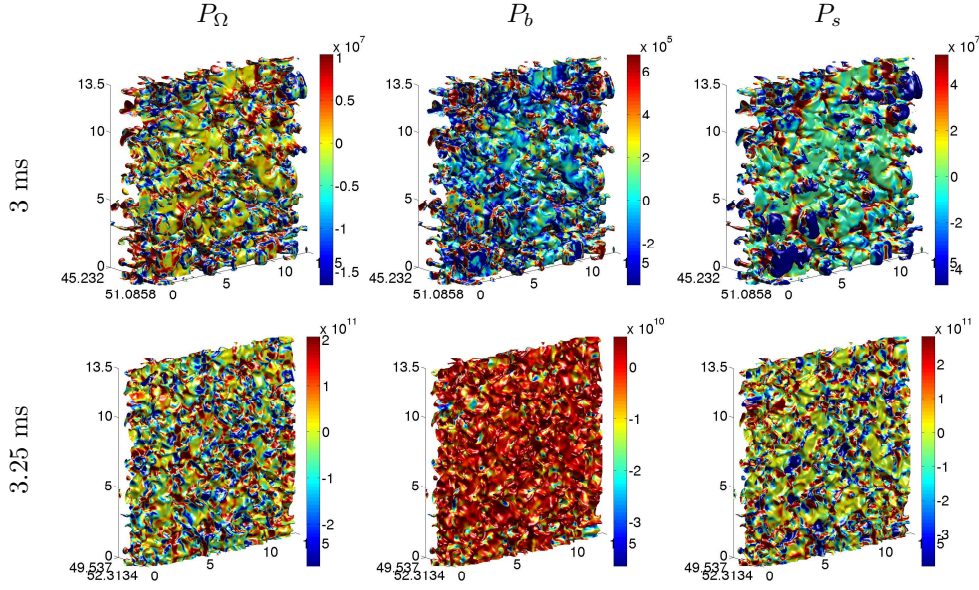
Fig. 4.2. The baroclinic enstrophy production P_Ω, buoyancy production P_b, and shear production P_s visualized on the mass fraction isosurface $m = 1/2$ before (3 ms) and after reshock (3.25 ms).

and turbulent kinetic energy transport equations

$$\rho \frac{d\Omega}{dt} = P_\Omega + S_\Omega + C_\Omega \,, \quad P_\Omega \equiv \frac{\boldsymbol{\omega}}{\rho} \cdot (\boldsymbol{\nabla}\rho \times \boldsymbol{\nabla}p) \,, \quad S_\Omega \equiv \rho\,\boldsymbol{\omega} \cdot (\boldsymbol{\omega} \cdot \boldsymbol{\nabla}\boldsymbol{u}) \,, \quad C_\Omega \equiv -2\,\rho\,\Omega\,\boldsymbol{\nabla} \cdot \boldsymbol{u} \,, \quad (4.1)$$

$$\overline{\rho} \frac{d\widetilde{E''}}{dt} = P_b + P_s + T + \Pi \,, \quad P_b \equiv -\overline{u_j''} \frac{\partial \overline{p}}{\partial x_j} \quad P_s \equiv -\overline{\rho\,u_i''u_j''} \frac{\partial \widetilde{u}_i}{\partial x_j} \quad T \equiv -\frac{\partial}{\partial x_j} \left(\overline{\rho E'' u_j''} + \overline{p' u_j''} \right) \,, \quad (4.2)$$

$$\Pi \equiv \overline{p' \frac{\partial u_i''}{\partial x_i}} \,,$$

where $d/dt \equiv \partial/\partial t + \boldsymbol{u} \cdot \boldsymbol{\nabla}$, $\overline{\phi}(z,t) = \frac{1}{L_x L_y} \int_0^{L_y} \int_0^{L_x} \phi(\mathbf{x},t) dx dy$ and $\phi(\mathbf{x},t)' = \phi(\mathbf{x},t) - \overline{\phi}(z,t)$, are the Reynolds averaged and fluctuating fields, respectively, and $\widetilde{\phi}(z,t) = \overline{\rho\phi}/\overline{\rho}$ and $\phi(\mathbf{x},t)'' = \phi(\mathbf{x},t) - \widetilde{\phi}(z,t)$ are the Favre averaged and fluctuating fields, respectively.

Figure 4.2 shows the baroclinic enstrophy production P_Ω, buoyancy production P_b, and shear production P_s on the mass fraction isosurface at 3 and 3.25 ms, indicating the strong amplification of these fields by reshock. Reshock is necessary to achieve a sufficiently complex mixing layer so that applying turbulent averages is meaningful [4, 6, 7].

5 COMPARISON OF THE MIXING LAYER WIDTH WITH EXPERIMENTAL DATA AND WITH THE MIKAELIAN RESHOCK MODEL

The bubble and spike position $\ell_s(t)$ and $\ell_b(t)$ are defined from the mass fraction fields as the locations where $m < 0.01$ and $m > 0.99$, respectively. The mixing layer width from the simulation, $h(t) = \ell_b(t) - \ell_s(t)$, is shown in Fig. 5.3. The growth rates dh/dt agree well with the Vetter–Sturtevant experimental measurements of 0.4 cm/ms (before reshock) and 3.26 cm/ms (after reshock) [8]. The mixing layer width also quantitatively agrees with the experimental data after reshock, but overpredicts the data before reshock. Smaller values of a (requiring increased spatial resolution) may provide better quantitative agreement with the pre-reshock amplitude data.

The post-reshock mixing layer width was also compared to the prediction of the Mikaelian [5] model

$$h(t) = 0.28\,A_1^+\,\Delta u_1\,t \qquad\qquad (5.1)$$
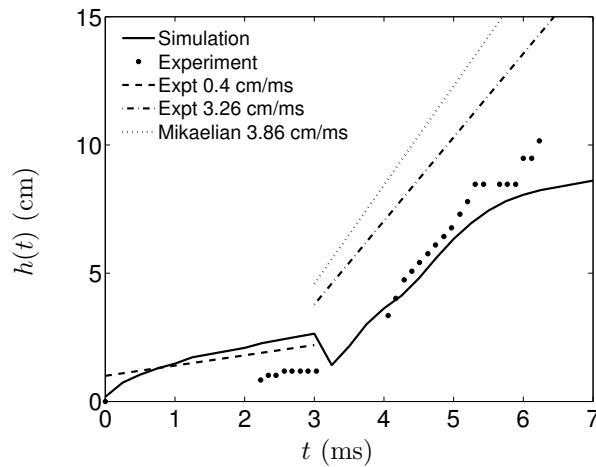
Fig. 5.3. Comparison of the mixing layer width from the simulation with the Vetter–Sturtevant experimental growth rates and data points, and with the prediction of the Mikaelian reshock model.

in Fig. 5.3, where A_1^+ is the post-reshock Atwood number, and Δu_1 is the change in velocity of the interface after reshock. For a short time following reshock (and before the arrival of the reflected rarefaction), the Mikaelian model predicts a growth rate in good agreement with the simulation.

6   CONCLUSIONS

A two-mode initial perturbation with random noise was constructed to model the mixing layer in the reshocked Mach 1.5 air/SF$_6$ Vetter–Sturtevant experiment. Random noise is needed to break symmetry and to accelerate the development of nonlinearity. A visualization of the instability evolution through the mass fraction and enstrophy isosurfaces, and density cross-sections was presented. The effects of reshock were quantified by showing the amplification of the baroclinic enstrophy production, buoyancy production, and shear production terms on the mass fraction isosurface. The enstrophy isosurface showed a qualitative change after reshock from long, elongated tubes aligned along the direction of shock propagation to small, short tubular structures with random orientations. The growth rate of the mixing layer before and after reshock agreed with the experimentally measured growth rates and with the prediction of the Mikaelian reshock model [5]. The WENO amplitude overpredicted the experimental amplitudes before reshock, but was in good agreement after reshock.

REFERENCES

[1] Cohen, R. H., Dannevik, W. P., Dimits, A. M., Eliason, D. E., Mirin, A. A., Zhou, Y., Porter, D. H. and Woodward, P. R., 2002. Three-dimensional simulation of a Richtmyer–Meshkov instability with a two-scale initial perturbation. *Phys. Fluids* **14**, pp. 3692–3709.

[2] Hill, D. J., Pantano, C. and Pullin, D. I., 2006. Large-eddy simulation and multiscale modelling of a Richtmyer–Meshkov instability with reshock. *J. Fluid Mech.* **557**, pp. 29–61.

[3] Latini, M., Schilling, O. and Don, W. S., 2007. Effects of WENO flux reconstruction order and spatial resolution on reshocked two-dimensional Richtmyer–Meshkov instability. *J. Comput. Phys.*, in press.

[4] Latini, M., Schilling, O. and Don, W. S., 2007. High-resolution simulations and modeling of reshocked single-mode Richtmyer–Meshkov instability: comparison to experimental data and to amplitude growth model predictions. *Phys. Fluids*, in press.

[5] Mikaelian, K. O., 1989. Turbulent mixing generated by Rayleigh–Taylor and Richtmyer–Meshkov instabilities. *Physica D* **36**, pp. 343–357.

[6] Schilling, O., Latini, M. and Don, W. S., 2007. Physics of reshock and mixing in single-mode Richtmyer–Meshkov instability. *Phys. Rev. E*, submitted.

[7] Schilling, O., Mueschke, N. J. and Latini, M., 2007. Assessment of gradient-diffusion closures for modeling Rayleigh–Taylor and Richtmyer–Meshkov instability-induced mixing, in *Proceedings of the Tenth International Workshop on the Physics of Compressible Turbulent Mixing*, 17–21 July 2006, Paris, France, edited by M. Legrand and M. Vandenboomgaerde.

[8] Vetter, M. and Sturtevant, B., 1995. Experiments on the Richtmyer–Meshkov instability of an air/SF$_6$ interface. *Shock Waves* **4**, pp. 247–252.

e-mail: `schilling1@llnl.gov`

Assessment of gradient-diffusion closures for modeling Rayleigh–Taylor and Richtmyer–Meshkov instability-induced mixing

Oleg SCHILLING[1], Nicholas MUESCHKE[2] and Marco LATINI[3]

[1] *University of California, Lawrence Livermore National Laboratory, Livermore, California 94551, USA*

[2] *Texas A&M University, College Station, Texas 77843, USA*

[3] *California Institute of Technology, Pasadena, California 91125, USA*

Abstract: The validity of gradient-diffusion closures for modeling turbulent transport in multi-mode Rayleigh–Taylor and reshocked Richtmyer–Meshkov instability-induced mixing is investigated using data from three-dimensional spectral/tenth-order compact difference and ninth-order weighted essentially non-oscillatory simulations, respectively. Details on the numerical methods, initial and boundary conditions, and validation of the simulations are discussed elsewhere [2,3]. First, mean and fluctuating fields are constructed using spatial averaging in the two periodic flow directions. Then, quantities entering eddy viscosity-type gradient-diffusion closures, such as the turbulent kinetic energy and its dissipation rate (or turbulent frequency), and the turbulent viscosity are constructed. The magnitudes of the terms in the turbulent kinetic energy transport equation are examined across the mixing layers to identify the dominant processes. It is shown that the buoyancy (or shock) production term is the dominant term in the transport equation, and that the shear production term is relatively small for both the Rayleigh–Taylor and Richtmyer–Meshkov cases. Finally, *a priori* tests of gradient-diffusion closures of the unclosed terms in the turbulent kinetic energy transport equation are performed by comparing the terms constructed directly using the data to the modeled term. A simple method for estimating the turbulent Schmidt numbers appearing in the closures is proposed. Using these turbulent Schmidt numbers, it is shown that both the shape and magnitude of the profiles of the dominant terms in the turbulent kinetic energy transport equation across the mixing layer are generally well captured.

1 INTRODUCTION

The purpose of this work is to investigate the mechanisms and modeling of turbulent transport in multi-mode Rayleigh–Taylor and reshocked Richtmyer–Meshkov instability-induced mixing using three-dimensional high-resolution numerical simulation data. The equations solved and the numerical methods used are summarized elsewhere [2,3]. Using the numerical simulation data validated by comparing to available experimental data, Favre-averaged quantities used in turbulence models closed using the gradient-diffusion approximation are computed from the simulation data. The budget of the terms in the turbulent kinetic energy transport equation is investigated to determine which physical processes are most important to model. Finally, the unclosed terms in the turbulent kinetic energy transport equation are modeled using standard gradient-diffusion (eddy viscosity) closure models and are compared to the same terms computed directly from the simulation data.

2 DEFINITIONS OF AVERAGES AND THE EXACT TURBULENT KINETIC ENERGY TRANSPORT EQUATION

As only one realization each of the Rayleigh–Taylor and Richtmyer–Meshkov unstable flows is considered, ensemble averaging is approximated here by spatial averaging over the two periodic (homogeneous) directions in the simulations: the directions perpendicular to gravity and the directions perpendicular to the shock propagation. The Reynolds and Favre average of a field $\phi(\mathbf{x}, t)$ are taken as

$$\overline{\phi}(z, t) = \frac{1}{L_x L_y} \int_0^{L_y} \int_0^{L_x} \phi(\mathbf{x}, t)\, \mathrm{d}x\, \mathrm{d}y \quad , \quad \widetilde{\phi}(z, t) = \frac{\overline{\rho\,\phi}}{\overline{\rho}} \tag{2.1}$$

with corresponding fluctuations

$$\phi(\mathbf{x}, t)' = \phi(\mathbf{x}, t) - \overline{\phi}(z, t) \quad , \quad \phi(\mathbf{x}, t)'' = \phi(\mathbf{x}, t) - \widetilde{\phi}(z, t) \,. \tag{2.2}$$
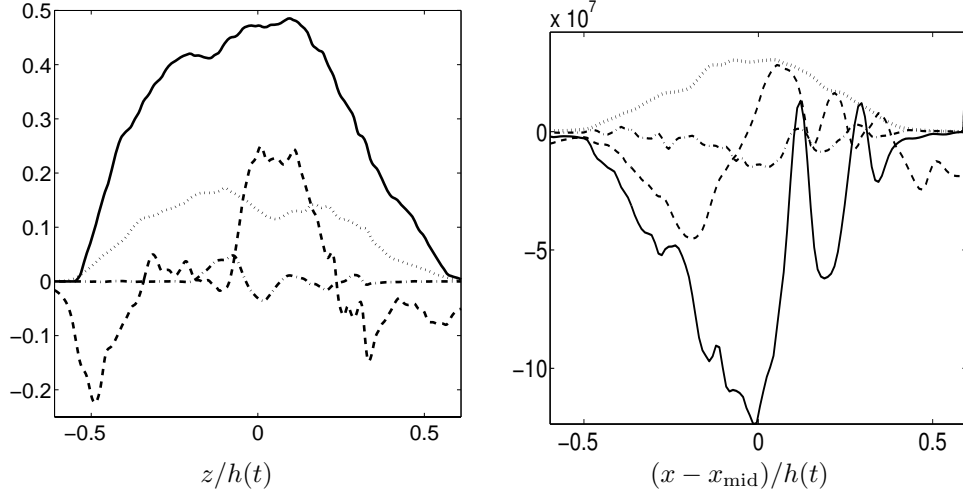
Fig. 3.1. The budget of the terms in the turbulent kinetic energy equation at $\tau = 1$ for the Rayleigh–Taylor flow (left) and at 5 ms for the reshocked Richtmyer–Meshkov flow (right). The buoyancy (shock) production term P_b, the shear production term P_s, the turbulent diffusion term T, and the turbulent kinetic energy dissipation term D are shown using a solid, dash-dot, dashed, and dotted line, respectively.

Here, L_x and L_y are the lengths of the domain in the periodic directions.

The exact, unclosed turbulent kinetic energy ($\widetilde{E''} = \widetilde{u''^2}/2$) transport equation is

$$\overline{\rho}\frac{\mathrm{d}\widetilde{E''}}{\mathrm{d}t} = P_b + P_s + T + D + \Pi \,, \tag{2.3}$$

where $\mathrm{d}/\mathrm{d}t = \partial/\partial t + \widetilde{u}_j \partial/\partial x_j$ and the buoyancy (or shock) production, shear production, turbulent diffusion, turbulent dissipation, and pressure-dilatation terms are

$$P_b \equiv -\overline{u''_j}\left(\frac{\partial \overline{p}}{\partial x_j} - \frac{\partial \overline{\sigma}_{ij}}{\partial x_i}\right) \,, \quad P_s \equiv -\overline{\rho\, u''_i\, u''_j}\frac{\partial \widetilde{u}_i}{\partial x_j} \,, \quad T \equiv -\frac{\partial}{\partial x_j}\left(\overline{\rho\, E''\, u''_j} + \overline{p'\, u''_j} - \overline{u''_i\, \sigma''_{ij}}\right) \,, \tag{2.4}$$

$$D \equiv -\overline{\sigma''_{ij}\frac{\partial u''_i}{\partial x_j}} \,, \quad \Pi \equiv \overline{p'\frac{\partial u''_j}{\partial x_j}} \,,$$

respectively. In the shock-capturing simulation of the Richtmyer–Meshkov instability, viscous terms are not explicitly included, so that $\widetilde{\sigma}_{ij} = \sigma''_{ij} = 0$ formally in P_b and T. The terms involving $\widetilde{\sigma}_{ij}$ and σ''_{ij} are also very small in the Rayleigh–Taylor simulation (except in D), and are not considered further. The turbulent dissipation D is computed explicitly in the Rayleigh–Taylor case, but can only be modeled in the Richtmyer–Meshkov case.

3   BUDGET OF TERMS IN THE EXACT TURBULENT KINETIC ENERGY TRANSPORT EQUATION

The budget of terms in the exact turbulent kinetic energy transport equation is considered here for both the Rayleigh–Taylor and Richtmyer–Meshkov flow cases to determine which terms are dominant in these instabilities. For each term, the profile across the mixing layer is shown, *i.e.*, the term in (2.3) integrated over the periodic directions using the Favre and Reynolds average definitions. The coordinate in the direction of gravity or the shock is scaled by the mixing layer width $h(t)$. In addition, in the Richtmyer–Meshkov flow case, the coordinate is recentered by the midpoint, x_{mid}, between the bubble and spike fronts.

3.1   Rayleigh–Taylor Unstable Flow

The budget of terms in the turbulent kinetic energy transport equation (2.3) across the mixing layer is shown in Fig. 3.1 at time $\tau = 1$, where $\tau = t/\sqrt{gAH}$ (see [3] for further details of the simulation). It is evident that the

buoyancy production term is dominant, with additional significant contributions from the turbulent diffusion and dissipation terms. The shear production term is nearly zero, as expected in a flow with either a nearly constant mean velocity or zero mean velocity. The turbulent diffusion is both positive and negative over the layer, with zero integral, indicating that this term redistributes turbulent kinetic energy conservatively within the layer. The buoyancy production and dissipation terms are positive everywhere, and are peaked near the centerplane of the layer, $z = 0$. The relative importance of these terms and the trends are also true for earlier times (not shown here).

3.2 Richtmyer–Meshkov Unstable Flow

The budget of terms in the turbulent kinetic energy transport equation (2.3) across the mixing layer is shown in Fig. 3.1 at 5 ms (see [2] for further details of the simulation). In the absence of explicit molecular dissipation, the dissipation term is modeled as in the $\widetilde{E''}$-$\widetilde{\omega''}$ model [4]

$$D = -\overline{\rho}\,\widetilde{E''}\,\widetilde{\omega''}\,, \tag{3.1}$$

where $\widetilde{\omega''} = \sqrt{2\widetilde{\Omega''}}$ is the turbulent frequency. The shock production term dominates the other terms, and has largest (negative) value near the centerplane of the mixing layer. As in the Rayleigh–Taylor case, the turbulent diffusion and dissipation terms also contribute significantly. The shear production is oscillatory and averages to nearly zero, as expected in a flow with a nearly constant mean velocity. The turbulent diffusion is both positive and negative over the layer, with zero integral, indicating that this term redistributes turbulent kinetic energy conservatively within the layer. The dissipation term is positive everywhere, and is peaked near the centerplane of the layer.

4 A PRIORI ANALYSIS OF THE GRADIENT-DIFFUSION APPROXIMATION

In the *a priori* analysis of the gradient-diffusion (eddy viscosity) approximation for closing the terms in the exact turbulent kinetic energy transport equation, the profiles of the closed terms across the mixing layer are computed using the models summarized below. Modeled terms were constructed from the appropriately averaged simulation data. The model predictions and the directly computed (unclosed) terms are compared to evaluate the predictive capability of the gradient-diffusion closures of the key terms in the turbulent kinetic energy equation.

4.1 The Modeled Turbulent Kinetic Energy Transport Equation

Using the gradient-diffusion hypothesis, the modeled terms (2.4) are given by the algebraic closures [1]

$$P_b = -\frac{\nu_t}{\sigma_\rho\,\overline{\rho}}\,\frac{\partial\overline{\rho}}{\partial x_j}\,\frac{\partial\overline{p}}{\partial x_j}\,, \tag{4.1}$$

$$P_s = -\left[\frac{2}{3}\,\overline{\rho}\,\widetilde{E''}\,\delta_{ij} - 2\,\mu_t\left(\widetilde{S}_{ij} - \frac{\delta_{ij}}{3}\,\frac{\partial\widetilde{u}_k}{\partial x_k}\right)\right]\frac{\partial\widetilde{u}_i}{\partial x_j}\,, \tag{4.2}$$

$$T = \frac{\partial}{\partial x_j}\left(\frac{\mu_t}{\sigma_k}\,\frac{\partial\widetilde{E''}}{\partial x_j}\right)\,, \tag{4.3}$$

$$D = -\overline{\rho}\,\widetilde{\epsilon''}\,, \tag{4.4}$$

where $\widetilde{S}_{ij} = (1/2)(\partial\widetilde{u}_i/\partial x_j + \partial\widetilde{u}_j/\partial x_i)$ is the mean strain-rate tensor, $\widetilde{\epsilon''}$ is the turbulent kinetic energy dissipation rate per unit mass, the pressure-dilatation term Π and the pressure-flux $\overline{p'u_j''}$ contribution to T are not considered in the current study, and σ_ρ and σ_k are dimensionless turbulent Schmidt numbers. With the definitions of the Favre and Reynolds averages, these terms are profiles across the mixing layer depending only on the coordinate in the inhomogeneous direction and on time. In the above expressions,

$$\nu_t = \begin{cases} 0.09(\widetilde{E''})^2/\widetilde{\epsilon''} & \text{for Rayleigh–Taylor flow} \\ \widetilde{E''}/\widetilde{\omega''} & \text{for Richtmyer–Meshkov flow} \end{cases} \tag{4.5}$$
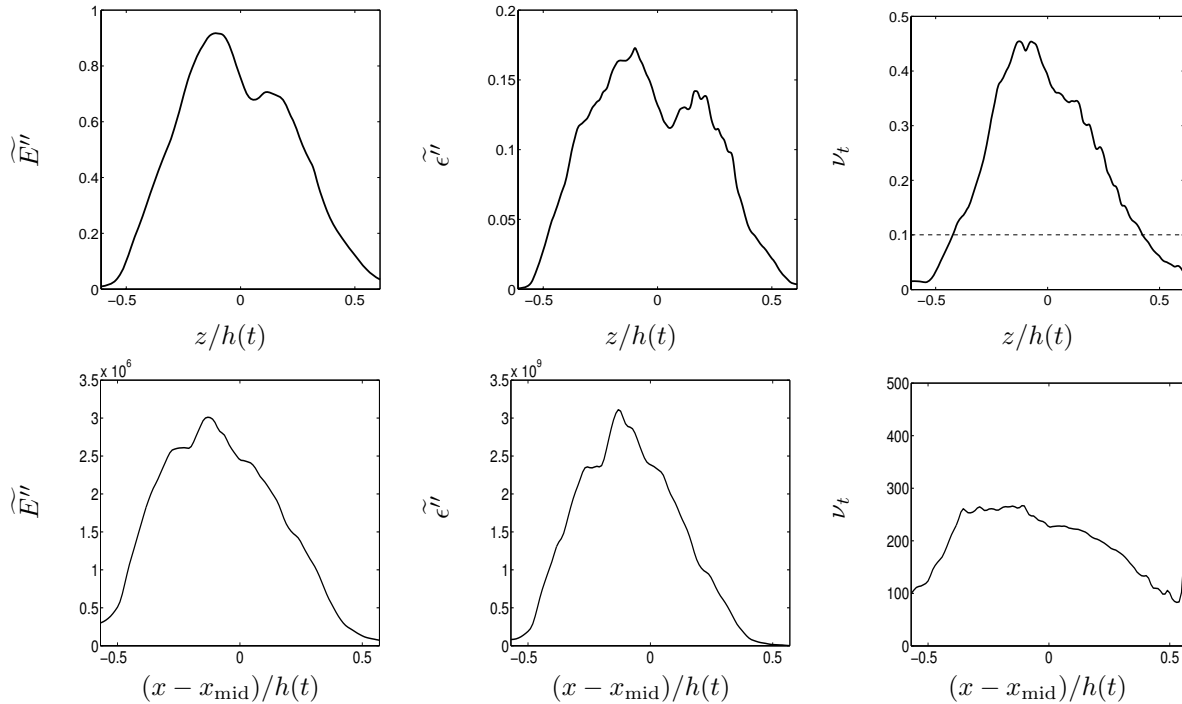
Fig. 4.2. The turbulent kinetic energy $\widetilde{E''}$, turbulent kinetic energy dissipation rate $\widetilde{\epsilon''}$, and turbulent viscosity ν_t at $\tau = 1$ for the Rayleigh–Taylor flow (top) and at 5 ms for the Richtmyer–Meshkov flow (bottom).

is the turbulent viscosity ($\mu_t = \overline{\rho}\nu_t$).

The turbulent kinetic energy, turbulent kinetic energy dissipation rate, and turbulent viscosity profiles across the mixing layer are shown for the Rayleigh–Taylor and Richtmyer–Meshkov flows in Fig. 4.2. For the Rayleigh–Taylor case, all three quantities are peaked near the center of the mixing layer. Note that the turbulent viscosity is considerably larger than the molecular viscosity $\nu \approx 0.1$ cm^2/s. In order to obtain better correlation between the modeled and directly computed term, the time-dependent turbulent Schmidt numbers were first calculated by algebraically solving for them in Eqs. (4.1) and (4.3) and integrating over the layer for both the Rayleigh–Taylor and Richtmyer–Meshkov flows. The resulting time-dependent values of σ_ρ and σ_k were then used in the closures. Note that this rescaling of the terms does not change their shape, but only adjusts their magnitude.

4.2 Rayleigh–Taylor unstable flow

In the Rayleigh–Taylor flow, it was found that σ_ρ approaches a value of ~ 0.1, while σ_k approaches unity at the latest time in the simulation. The profiles are shown as a function of $z/h(t)$, where z is the coordinate direction parallel to gravity and $h(t)$ is the mixing layer width. Thus, the mixing layer is contained within $z/h(t) \in [-0.5, 0.5]$. As seen in Fig. 4.3, the overall agreement between the model and DNS data for $\overline{w''}$ is good. In particular, the shape and magnitude are generally well captured. However, the figure shows that the gradient-diffusion approximation does not completely capture the kinetic energy transfer across the layer. The large-amplitude excursions in the model are a consequence of the poor statistical convergence of the mean density and turbulent kinetic energy gradients due to the limited spatial resolution of the data.

4.3 Richtmyer–Meshkov unstable flow

In the Richtmyer–Meshkov flow, it was found that σ_ρ and σ_k both approach a value of ~ 0.1 in the simulation. The profiles are shown as a function of $(x - x_{\mathrm{mid}})/h(t)$, where x is the coordinate direction parallel to the shock propagation, x_{mid} is the midpoint of the layer, and $h(t)$ is the mixing layer width. Thus, the mixing layer is contained within $(x - x_{\mathrm{mid}})/h(t) \in [-0.5, 0.5]$. As shown in Fig. 4.3, the Reynolds-averaged Favre fluctuating velocity $\overline{u''}$ is in good agreement with the model up to the interaction of the layer with the reflected rarefaction
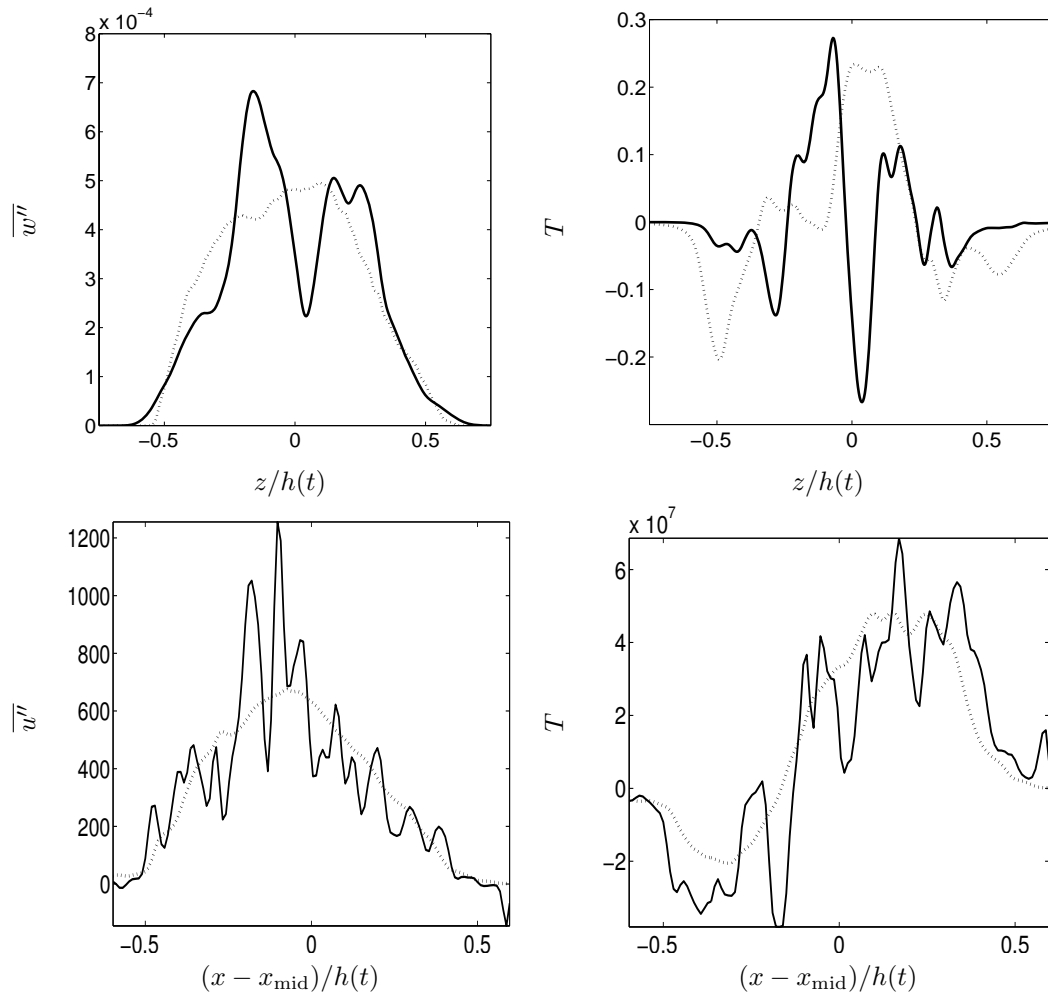
Fig. 4.3. Comparison of the computed and modeled averaged Favre fluctuating velocity and turbulent diffusion, T, at $\tau = 1$ for the Rayleigh–Taylor flow (top) and at 5 ms for the Richtmyer–Meshkov flow (bottom). The model and simulation results are shown using a solid and dotted line, respectively.

at ~ 5 ms. The turbulent kinetic energy diffusion shown in Fig. 4.3 is also in good agreement with the model up to the interaction with the reflected rarefaction. Both quantities exhibit large-amplitude excursions in the model due to the poor statistical convergence of the mean density and turbulent kinetic energy gradients.

5 CONCLUSIONS

Using spatially-averaged data from numerical simulation models of the Texas A&M University water channel Rayleigh–Taylor experiment [3] and the reshocked Mach 1.5 air/SF$_6$ Vetter–Sturtevant Richtmyer–Meshkov instability experiment [2], it was shown that: (1) the buoyancy (shock) production, turbulent dissipation, and turbulent diffusion terms are dominant, while the shear production term is nearly zero in Rayleigh–Taylor flow and less important than the other terms in the Richtmyer–Meshkov flow; (2) using spatial averaging to define Favre and Reynolds averaged and fluctuating fields, it is possible to compute quantities (such as the turbulent viscosity) entering gradient-diffusion turbulence closures, and; (3) using adjusted values of the turbulent Schmidt numbers (smaller than typically used in compressible and stratified Reynolds-averaged turbulent flow modeling), the gradient-diffusion models for the key terms in the turbulent kinetic energy transport equation are in reasonable qualitative and quantitative agreement with the data in *a priori* comparisons. While the gradient-diffusion approximation cannot correctly capture the anisotropy of the Reynolds stress tensor components in these flows, this approximation is evidently quite reasonable for most of the important terms in the

turbulent kinetic energy balance. The only term in the turbulent kinetic energy equation that requires the Reynolds stress tensor is the shear production (4.2): this term is generally of little importance in the overall energy balance in both Rayleigh–Taylor and Richtmyer–Meshkov instability-induced turbulence.

This investigation demonstrates that high-resolution simulations can be used to provide essential data concerning turbulent transport and mixing processes in three-dimensional Rayleigh–Taylor and reshocked Richtmyer–Meshkov instability. In particular, simulations provide quantities not presently possible (or difficult) to measure experimentally, such as the turbulent Schmidt numbers.

REFERENCES

[1] Chassaing, P., Antonia, R. A., Anselmet, F., Joly, L. and Sarkar, S., 2002. *Variable Density Fluid Turbulence*, Fluid Mechanics and its Applications Vol. 69, Kluwer Academic.

[2] Latini, M., Schilling, O. and Don, W. S., 2006. Richtmyer–Meshkov Instability-Induced Mixing: Initial Conditions Modeling, Three-Dimensional Simulations and Comparisons with Experiment, in *Proceedings of the Tenth International Workshop on the Physics of Compressible Turbulent Mixing*, 17–21 July 2006, Paris, France, edited by M. Legrand and M. Vandenboomgaerde.

[3] Mueschke, N., Schilling, O. and Andrews, M. J., 2006. Rayleigh–Taylor Instability-Induced Mixing: Initial Conditions Modeling, Three-Dimensional Simulations and Comparisons with Experiment, in *Proceedings of the Tenth International Workshop on the Physics of Compressible Turbulent Mixing*, 17–21 July 2006, Paris, France, edited by M. Legrand and M. Vandenboomgaerde.

[4] Wilcox, D. C., 2006. *Turbulence Modeling for CFD*, third edition, DCW Industries.

e-mail: `schilling1@llnl.gov`

Rayleigh–Taylor instability-induced mixing: initial conditions modeling, three-dimensional simulations and comparisons with experiment

Nicholas MUESCHKE[1], Oleg SCHILLING[2] and Malcolm ANDREWS[3]

[1] *Texas A&M University, College Station, Texas 77843, USA*

[2] *University of California, Lawrence Livermore National Laboratory, Livermore, California 94551, USA*

[3] *Los Alamos National Laboratory, Los Alamos, New Mexico 87545, USA*

Abstract: A spectral/compact finite-difference method with a third-order Adams–Bashforth–Moulton time-evolution scheme is used to perform a direct numerical simulation (DNS) of Rayleigh–Taylor flow. The initial conditions are modeled by parameterizing the multi-mode velocity and density perturbations measured just off of the splitter plate in water channel experiments. Parameters in the DNS are chosen to match the experiment as closely as possible. The early-time transition from a weakly-nonlinear to a strongly-nonlinear state, as well as the onset of turbulence, is examined by comparing the DNS and experimental results. The mixing layer width, molecular mixing parameter, vertical velocity variance, and density variance spectrum obtained from the DNS are shown to be in good agreement with the corresponding experimental values.

1 INTRODUCTION

The purpose of this research is to elucidate the physics of turbulent transport, and transitional dynamics in Rayleigh–Taylor instability-driven mixing layers using coupled experiments and high-resolution three-dimensional direct numerical simulations (DNS). To accomplish this, experimental measurements characterizing the initial conditions and the evolution of various large-scale and turbulence statistics were performed within a small Atwood number, incompressible, miscible Rayleigh–Taylor mixing layer [1,2]. A DNS model of the experiment was formulated using parameters that closely correspond to the experiment and experimentally-measured initial density and velocity perturbations. Data from this DNS was also used to investigate the relative importance of terms in the turbulent kinetic energy transport equation and the validity of the gradient-diffusion approximation in modeling these terms [3].

2 EXPERIMENTAL FOUNDATION

Measurements were taken in an open-loop water channel facility at Texas A&M University. A schematic of the water channel and the associated diagnostics can be found elsewhere [1,2]. An adverse density stratification was created by heating the bottom water stream. The temperature difference ($\Delta T \approx 5°C$) created a density difference through thermal expansion of the bottom stream, resulting in an Atwood number $A = (\rho_1 - \rho_2)/(\rho_1 + \rho_2) \approx 7.5 \times 10^{-4}$. Downstream distance, x, is converted to time using Taylor's hypothesis and normalized such that $\tau = (x/U_m) \sqrt{gA/H}$, where $U_m = 4.5$ cm/s is the mean velocity of the water streams, $g = 981$ cm/s^2, and $H = 32$ cm is the height of the channel.

3 EQUATIONS SOLVED AND THE NUMERICAL METHOD

The DNS uses a hybrid spectral and tenth-order compact differencing spatial discretization scheme to solve the conservation of mass, momentum, and mass fraction evolution equations [4]:

$$\frac{\partial \rho}{\partial t} + \frac{\partial}{\partial x_j}(\rho\,u_j) = 0\,, \tag{3.1}$$

$$\frac{\partial}{\partial t}(\rho\,u_i) + \frac{\partial}{\partial x_j}(\rho\,u_i\,u_j) = \rho\,g_i - \frac{\partial p}{\partial x_i} + \frac{\partial \sigma_{ij}}{\partial x_j}\,, \tag{3.2}$$

$$\frac{\partial}{\partial t}(\rho\,m_r) + \frac{\partial}{\partial x_j}(\rho\,m_r\,u_j) = \frac{\partial}{\partial x_j}\left(\rho\,D\,\frac{\partial m_r}{\partial x_j}\right)\,, \tag{3.3}$$
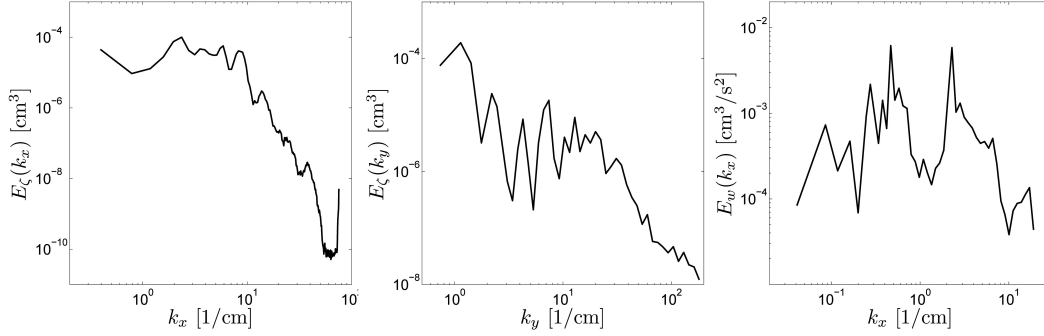
Fig. 4.1. The initial one-dimensional spectra for the DNS. Left: interfacial perturbations in the x-direction. Middle: interfacial perturbations in the y-direction. Right: vertical velocity fluctuations at the centerplane of mixing layer in the x-direction.

where ρ is the density, u_i is the velocity, g_i is gravity, p is the pressure, $\sigma_{ij} = \mu \left(\partial u_i / \partial x_j + \partial u_j / \partial x_i \right) - (2/3)\mu\delta_{ij}\partial u_k/\partial x_k$ is the viscous stress tensor [with $\mu = \rho\nu$ the dynamic viscosity and $\nu = (\mu_1 + \mu_2)/(\rho_1 + \rho_2)$ the constant kinematic viscosity], m_r is the mass fraction of fluid $r = 1, 2$, and D is the constant mass diffusivity. Time integration is performed using a third-order Adams–Bashforth–Moulton predictor-corrector scheme. The physical and numerical parameters are given in Table 3.1. Periodicity is assumed in the x and y directions.

Parameter	Value
ρ_1	0.9986 g/cm^3
ρ_2	0.9970 g/cm^3
A	7.5×10^{-4}
g_z	-981 cm/s^2
μ_1	0.009 g/(cm s)
μ_2	0.011 g/(cm s)
Pr (ν/D in DNS)	7
$L_x \times L_y \times L_z$	16 cm $\times 10$ cm $\times 16$ cm
$N_x \times N_y \times N_z$	$384 \times 240 \times 512$

Table 3.1. Parameters used in the DNS of the water channel experiment.

4 THE MODEL OF THE INITIAL CONDITIONS

The initial fluid interface was parameterized by orthogonal perturbations in the x- and y-directions:

$$\zeta(x,y) = \sum_{k_x} \hat{\zeta}_x(k_x)\, e^{ik_x x} + \sum_{k_y} \hat{\zeta}_y(k_y)\, e^{ik_y y} , \qquad (4.1)$$

where k_x and k_y are the perturbation wavenumbers. The initial velocity was constructed from a potential formulation, where the potential field is perturbed to give the measured initial vertical velocity fluctuations,

$$\phi_r(x,z) = \sum_{k_x} \frac{\hat{w}(k_x)}{k_x} \sin\left[k_x\, x + \varphi(k_x)\right] e^{-k_x|z|} , \qquad (4.2)$$

where $\varphi(k_x)$ are the phases. The initial velocity field is the gradient of the potential field. In Eqs. (4.1) and (4.2), the perturbation amplitudes $\hat{\zeta}_x(k_x)$, $\hat{\zeta}_y(k_y)$, and $\hat{w}(k_x)$ are taken directly from the corresponding experimentally-measured one-dimensional spectra [2]. The measured initial interfacial and velocity spectra from the water channel [1,2] are shown in Fig. 4.1 to illustrate the high degree of anisotropy at the onset of the instability.
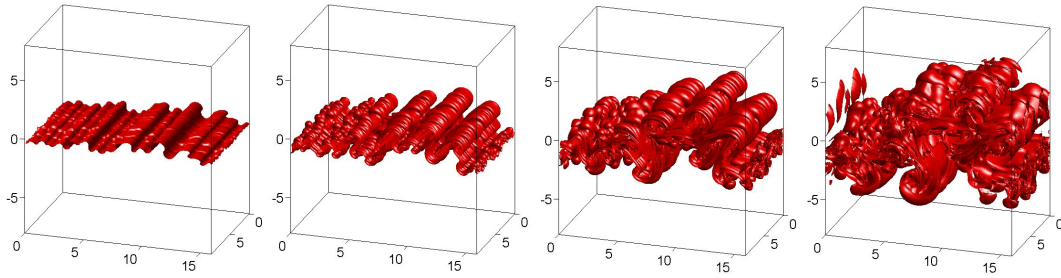
Fig. 5.2. The volume fraction $f_1 = 0.5$ isosurface at $\tau = 0.25, 0.50, 0.75, 1.00$.
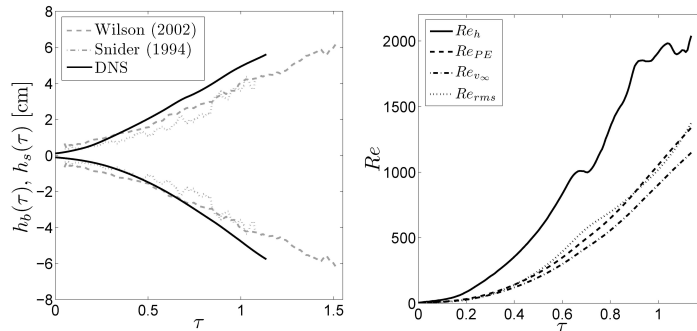
Fig. 5.3. The evolution of the bubble and spike fronts, h_b and h_s, and integral-scale Reynolds numbers, Re.

5 COMPARISON OF DNS RESULTS WITH EXPERIMENTAL DATA

5.1 Mixing Layer Growth

The evolution of the $f_1 = 0.5$ volume fraction isosurface is shown in Fig. 5.2. Qualitatively, the mixing layer growth is dominated by the initial velocity perturbations in the x-direction. The early ($\tau < 0.5$) structure of the mixing layer is predominantly two-dimensional, as observed in the experiments. For $\tau > 0.5$, perturbations to the initial density interface become important as the mixing layer dynamics become highly-nonlinear and more three-dimensional structure develops.

The mixing layer width is measured by the 5–95% thresholds of the volume fraction profiles. The evolution of the bubble and spike front penetrations is shown in Fig. 5.3. The DNS agrees fairly well with the mixing layer growth measurements of Snider [5] and Wilson [6]; however, the DNS grows slightly faster than the experiment, which may be due to the lack of statistical convergence in longer wavelengths. As the mixing layer develops, the dominant structures determining its growth become larger, and thus fewer structures exist within the finite computational domain.

Figure 5.3 also shows the evolution of the integral-scale Reynolds numbers of the DNS, where $Re = UL/\nu$ and U and L are characteristic velocity and lengthscales, respectively. The mixing layer width $h(t) = h_b(t) + h_s(t)$ is chosen as the lengthscale for all of the Reynolds numbers shown. Various velocity scales have been used, including the total penetration rate of the mixing layer dh/dt, the terminal velocity of the dominant bubble diameter v_∞, the rms centerplane vertical velocity fluctuations $\overline{w'^2}$, and a velocity scale based upon the conversion of potential energy into kinetic energy. Depending upon the velocity scale used, the final Reynolds number achieved in the DNS ranges from 1200–2000.

5.2 Turbulence and Mixing Statistics

In addition to comparisons of integral-scale quantities, turbulence and mixing statistics are also compared between the DNS and experiment. First, the degree of molecular mixing between the two fluids at the centerplane of the mixing layer, $\theta(z,t) = 1 - \overline{f_1'^2}/(\overline{f_1\,f_2})$, is compared, where f_r is the volume fraction of fluid r (all averages are taken at the centerplane). A value $\theta = 1$ indicates that the fluids are completely mixed, and $\theta = 0$ indicates complete segregation. Values from the DNS and experiment are shown in Fig. 5.4. The DNS
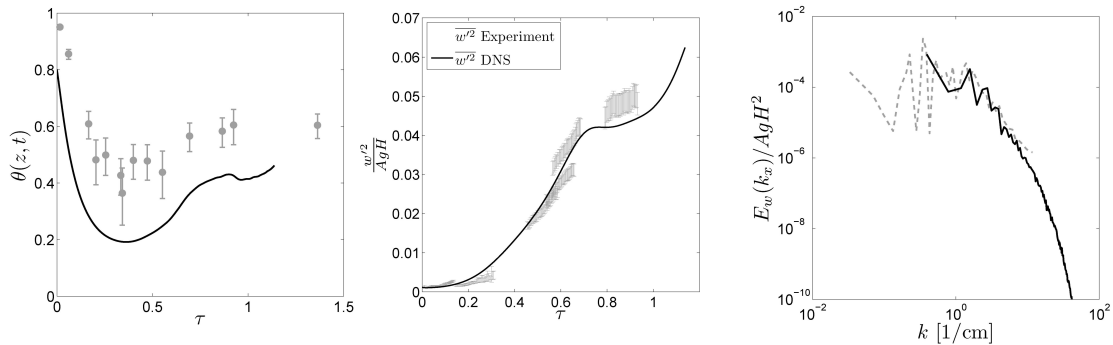
Fig. 5.4. Comparison of DNS results (solid lines) with the experimental measurements of θ, the normalized vertical velocity variance, and the normalized density variance spectrum. Error bars are shown on the measurements of θ and the normalized vertical velocity variance.

follows the experimentally measured trends closely, but underpredicts the total amount of mixed fluid. This may be associated with the method of implementing the initial velocity conditions and how energy from the initial spectrum is distributed among the discrete modes that can be supported on the computational grid.

The vertical velocity fluctuations at the centerplane of the mixing layer $\overline{w'^2}/(AgH)$, and the one-dimensional energy spectrum of the centerplane vertical velocity fluctuations $E_w(k_x)/(AgH^2)$ is shown at $\tau = 0.92$ from the DNS and experiment in Fig. 5.4. Both quantities compare very well. In particular, the DNS and experimental spectra agree quite well over the entire range of scales that overlap.

6 CONCLUSIONS

A DNS of a small Atwood number, multi-mode Rayleigh–Taylor mixing layer was initialized using interfacial and velocity perturbations parameterized from experimental measurements. Results from the DNS and experiment showed favorable agreement. Differences are attributed to details in the method of parameterizing the initial conditions, and the lack of statistical convergence at late time due to a limited computational domain size. Both of these are strongly related to the inclusion of longer wavelengths, which affect the integral-scale and turbulence statistics compared. A transition to highly-nonlinear dynamics was observed at $\tau \approx 0.4$, which was seen in the rapid increase of vertical velocity fluctuations and the increase in the degree of molecular mixing. This transition point and the magnitudes of $\overline{w'^2}$ and θ at this point were observed to be a function of the exact implementation of the initial conditions. Accordingly, higher resolution DNS investigating the effects of longer wavelengths on the quantities considered here are in progress.

REFERENCES

[1] Mueschke, N. J., 2004. An Investigation of the Influence of Initial Conditions on Rayleigh–Taylor Mixing. M.S. thesis, Texas A&M University.

[2] Mueschke, N. J., Andrews, M. J. and Schilling O., 2006. Experimental characterization of initial conditions and spatio-temporal evolution of a small Atwood Rayleigh–Taylor mixing layer. *J. Fluid Mech.* **567**, pp. 27–63.

[3] Schilling, O., Mueschke, N. J. and Latini, M., 2007. Assessment of gradient-diffusion closures for modeling Rayleigh–Taylor and Richtmyer–Meshkov instability-induced mixing, in *Proceedings of the Tenth International Workshop on the Physics of Compressible Turbulent Mixing*, 17–21 July 2006, Paris, France, edited by M. Legrand and M. Vandenboomgaerde.

[4] Cook, A. W. and Dimotakis, P. E., 2001. Transition stages of Rayleigh–Taylor instability between miscible fluids. *J. Fluid Mech.* **443**, pp. 69–99. Corrigendum. *J. Fluid Mech.* **457**, pp. 410–411 (2002).

[5] Snider, D. M. and Andrews, M. J., 1994. Rayleigh–Taylor and shear driven mixing with an unstable thermal stratification. *Phys. Fluids A* **6**, pp. 3324–3334.

[6] Wilson, P. N., 2002. An Investigation into the Spectral Evolution of Turbulent Mixing by Rayleigh–Taylor Instability. Ph.D thesis, Texas A&M University.

e-mail: `olivier.soulard@cea.fr`

Second-order turbulence model for predicting RMI/RTI driven turbulence: derivation of scalar correlation equations from a PDF approach

Olivier SOULARD[1] and Denis SOUFFLAND[1]

[1] *CEA/DAM Île-de-France BP 12 91680 Bruyères-le-Châtel FRANCE*

Abstract: The second order turbulence model proposed in [4] is extended by deriving equations for the concentration fluxes, variances, and for the concentration-density correlations. For this purpose, a probability density function (PDF) approach is used, in order to preserve the self-coherency of the model, and reduce the number of additional coefficients.

The properties of the extended model are assessed on the gas accelerator configuration studied in [6]. Besides, a potential shock tube experiment is proposed. Both applications aim to emphasize the effects of counter-gradient tranport.

1 INTRODUCTION

Turbulence in variable density flows has gained an increasing interest because of its importance in various industrial and environmental applications [2, 8]. Within this framework, shock tube and gas accelerator experiments are challenging flows for turbulence model designers because they emphasize the effects of density variations due to mixing as well as compressibility.

Shock tube and gas accelerator experiments are most often used to study instabilities at fluid interfaces, such as Richtmyer-Meshkov instabilities (RMI), or Rayleigh-Taylor instabilities (RTI). However, instabilities are not the only hydrodynamic processes which can be encountered in these experiments. For instance, in shock tubes, the impact of a rarefaction wave on a turbulent mixing zone can lead to a stable stratification, in which the acceleration and the density gradient are directed in the same direction. Similarly, in gas accelerator devices, acceleration can be chosen so as to create a stably stratified environment. Stably stratified turbulent flows have been extensively analyzed in other fields [5], and have been shown to lead to counter-gradient transport. As a result, the simulation of shock tube and gas accelerator experiments requires a turbulent model capable of accounting for two regimes: a regime dominated by RMI/RTI, but also a regime corresponding to stably stratified turbulence with potential counter-gradient transport.

Grégoire, Souffland and Gauthier [4] have developed a reliable and robust second order turbulent model with the aim of modeling RMI/RTI generated turbulence. This model is hereafter named GSG model, and will serve as a reference model throughout this paper. This model addresses the issue of compressibility and density fluctuations by introducing transport equations for the turbulent mass flux and the density variance. However, the GSG model deals with the crucial question of modeling the concentration fluxes with a simple gradient diffusion hypothesis. Consequently, it cannot account for counter-gradient situations for the concentrations.

Thus, the objective of this work is to extend the GSG model by adding to it modeled transport equations for the concentration fluxes, but also for the concentration variances and for the density-concentration correlation.

The derivation of additional equations is constrained by two requirements: the new models have to be coherent with those already defined, and they should introduce a number of additional constants as small as possible. In order to ensure those constraints, we base ourselves on a probability density function (PDF) approach. Following the methodology first proposed by Pope [11], we establish stochastic models for the density and the velocity, coherent with the GSG model. Then, we add a stochastic model for the concentrations. As a result, we obtain a PDF model, which, by construction, is compatible with the GSG model. Finally, we derive, from this PDF model, the desired equations for the concentration correlations. By following this path, we ensure coherency between all the closures. Indeed, they all originate from the same PDF model. Besides, the number of constants is fixed once the PDF model has been set. Only the PDF model constants appear in the additional equations for the concentration correlations.

The new model is then confronted against the gas accelerator experiment proposed in [6], in which both a stable and an unstable regime are encountered. Finally, a shock tube configuration is proposed with the aim of emphasizing the effects of stable stratification and counter-gradient transport. Such a configuration might be studied experimentally.

2   OVERVIEW OF THE GSG MODEL

The GSG model [4] has been designed to solve compressible gaseous mixtures in which density fluctuations are significant, even if the turbulence remains weakly compressible. A crucial issue for this class of flows is the additional production of turbulent kinetic energy due to density gradients. To address this point, authors in [4] chose to emphasize the correlations involved in the turbulent energy production. Thus, the GSG model solves equations for the turbulent mass flux $\overline{u_i''}$ and for the density variance $\overline{\rho'^2}$, in addition to the usual equations for the mean density $\overline{\rho}$, velocity $\widetilde{U}$, energy $\widetilde{e}$, mass fraction $\widetilde{c}_\alpha$, Reynolds stress tensor $\widetilde{R}_{ij}$, and dissipation rate $\widetilde{\varepsilon}$. Note that, throughout this paper, $\overline{Q}$ and Q' will respectively denote the Reynolds average and fluctuation of a quantity Q, and $\widetilde{Q}$ and Q'' its Favre average and fluctuation.

The Reynolds stress equation is based on the LRR proposal [7], as modified in [1] to account for a redistribution of the enthalpy production. The dissipation rate equation is also modified to include this supplementary effect. The other equations are closed with standard procedures devised for passive scalar transport equations. The complete model can be found in [4]. Here, we only detail the equations for the second order correlations $\overline{u_i''}$, $\overline{\rho'^2}$, and $\widetilde{R}_{ij}$:

$$\frac{D\widetilde{R}_{ij}}{Dt} = \mathcal{D}_{ij}^R + \mathcal{P}_{S_{ij}}^R + \mathcal{P}_{H_{ij}}^R + \Phi_{ij}^R - \mathcal{E}_{ij}^R \tag{2.1}$$

$$\frac{D\overline{u_i''}}{Dt} = \mathcal{D}_i^u + \mathcal{P}_{S_i}^u + \mathcal{P}_{H_i}^u + \Phi_i^u - \mathcal{E}_i^u \tag{2.2}$$

$$\frac{D\overline{\rho'^2}}{Dt} = \mathcal{D}^\rho + \mathcal{P}_S^\rho + \mathcal{P}_H^\rho + \Phi^\rho - \mathcal{E}^\rho \tag{2.3}$$

In equations (2.1)-(2.3), the $\mathcal{D}^\#$ terms correspond to turbulent diffusion, and are modeled with a tensorial gradient diffusion hypothesis. $\mathcal{P}_S^\#$ and $\mathcal{P}_H^\#$ are the shear and enthalpic production terms. Their expressions are not detailed here, but can be found in [4]. The terms denoted by $\Phi^\# - \mathcal{E}^\#$ correspond to redistribution and dissipation. They are the terms of interest in this article, and are modeled as:

$$\Phi_{ij}^R - \mathcal{E}_{ij}^R = -\gamma_S^R(\mathcal{P}_{S_{ij}}^R - \frac{1}{3}\mathcal{P}_{S_{kk}}^R\delta_{ij}) - \gamma_H^R(\mathcal{P}_{H_{ij}}^R - \frac{1}{3}\mathcal{P}_{H_{kk}}^R\delta_{ij}) - \gamma_\omega^R\omega(\widetilde{R}_{ij} - \frac{1}{3}\widetilde{R}_{kk}\delta_{ij}) - \frac{2}{3}\widetilde{\varepsilon}\delta_{ij} \tag{2.4}$$

$$\Phi_i^u - \mathcal{E}_i^u = -\gamma_S^u\mathcal{P}_{S_i}^u - \gamma_{H_1}^u\widetilde{R}_{ik}\frac{1}{\overline{\rho}}\frac{\partial\overline{\rho}}{\partial x_k} + \gamma_{H_2}^u\frac{\overline{\rho'^2}}{\overline{\rho}^2}\frac{1}{\overline{\rho}}\frac{\partial\overline{P}}{\partial x_i} - \gamma_\omega^u\omega\overline{u_i''} \tag{2.5}$$

$$\Phi^\rho - \mathcal{E}^\rho = -\gamma_S^\rho\mathcal{P}_S^\rho - \gamma_H^\rho\mathcal{P}_H^\rho - \gamma_\omega^\rho\omega\overline{\rho'^2} \tag{2.6}$$

$$\Phi^\varepsilon - \mathcal{E}^\varepsilon = -\gamma_\omega^\varepsilon\omega\widetilde{\varepsilon} \tag{2.7}$$

$\omega = \widetilde{\varepsilon}/\widetilde{k}$ is the mean turbulent frequency, and $\widetilde{k} = \frac{1}{2}\widetilde{R}_{kk}$ is the turbulent kinetic energy. $\gamma_\omega^\#$, $\gamma_S^\#$ and $\gamma_H^\#$ are constants, which values are given in table 2.1.

	γ_S^R	γ_H^R	γ_ω^R	γ_S^u	$\gamma_{H_1}^u$	$\gamma_{H_2}^u$	γ_ω^u	γ_S^ρ	γ_H^ρ	γ_ω^ρ
Coeff. used in [4]	0.6	0.3	1.8	0.3	0.3	0.3	3	0	0	3
Coeff. used in this article	0.6	0.3	1.8	0.6	0.15	0.3	2.4	0	0.15	3

Table 2.1. Model coefficients for the density-velocity correlations

3   PDF MODEL COHERENT WITH THE GSG MODEL

In this section, we derive a PDF model which yields redistribution and dissipation terms coherent with those proposed in the GSG model for the Reynolds stresses, for the turbulent mass flux, and for the density variance.

The models that we will examine for the velocity, concentration and density fields will only involve the energy through its mean value. Consequently, they do not require the explicit specification of the model for the energy and can be detailed without it. The model for the energy, though essential, is beyond the scope of this study and will be described in a further work.

The PDF model is hereafter expressed as a set of stochastic partial differential equations (SPDEs) (see [12] for more details on SPDEs). These SPDEs govern the evolution of stochastic velocity, density and concentration fields, respectively noted U_i^*, ρ^* and c_α^*.

For the stochastic velocity field, the effects of the fluctuating pressure and of the molecular transport are closed with a Generalized Langevin model (GLM) [10], modified in order to account for variable density effects. A linear redistribution of the density fluctuations is indeed added to the classical expression of the GLM. For the stochastic density field, the fluctuating velocity divergence is closed by using a simple linear relaxation model based on density and velocity. Finally, for the stochastic concentration field, the effects of molecular mixing are closed with the Interaction by Exchange with the Mean (IEM) model modified in order to account for velocity fluctuations. The resulting model resembles the one proposed in [9], but with the addition of a bounding function, in order to preserve physical values of the concentration. As a result, the following SPDEs are obtained for U_i^*, ρ^* and c_α^*:

$$\frac{DU_i^*}{Dt} = -\frac{1}{\rho}\frac{\partial \overline{P}}{\partial x_i} + G_{ik}\left(U_k^* - \widetilde{U}_k\right) - C_H \frac{1}{\overline{\rho}}\frac{\partial \overline{P}}{\partial x_i}\frac{\rho^* - \overline{\rho}}{\rho^*} + \sqrt{C_0 \widetilde{\varepsilon}}\dot{W}_i \tag{3.1}$$

$$\frac{D\rho^*}{Dt} = -\rho^* div\,\overline{U} - \rho^*\left[C_1^\rho \omega \frac{(\rho^* - \overline{\rho})}{\overline{\rho}} - C_2^\rho \frac{1}{\overline{\rho}}\frac{\partial \overline{\rho}}{\partial x_i}\frac{\rho^*\left(U_i^* - \widetilde{U}_i\right)}{\overline{\rho}}\right] \tag{3.2}$$

$$\frac{Dc_\alpha^*}{Dt} = -C_1^c \omega\left(c_\alpha^* - \widetilde{c_\alpha}\right) + C_2^c \frac{\partial \widetilde{c_\alpha}}{\partial x_j}\left[b(c_\alpha^*)\left(U_j^* - \widetilde{U}_j\right) - \widetilde{bu_j''}\right] \tag{3.3}$$

W_i are independent standard Brownian processes and $\dot{W}_i$ are their time derivatives. $b(c)$ is a bounding founction defined by: $b(c) = c\,(1 - c)/(\widetilde{c}\,(1 - \widetilde{c}))$. G_{ik}, C_H, C_0, C_1^ρ, C_2^ρ, C_1^c and C_2^c are model parameters, and are set in order to make the PDF and GSG models coherent.

From SPDEs (3.1)-(3.2), we can derive closed equations for the Reynolds stresses, the mass flux and the density variance. Strict equivalence cannot be achieved between these equations and the GSG model. Still, we can ensure some coherency between the two. Thus, we require that the Reynolds stress closures must be identical in both approaches. Besides, we impose that the dissipation term in the density variance equation must be the same. Finally, we note that, in the GSG model, the redistribution term linked to mean density gradients is null in the density variance equation and is piloted by $\gamma_{H_1}^u$ in the mass flux equation. In the PDF model, we decide to take an intermediate averaged value. With these conditions, we obtain:

$$G_{ij} = -\frac{1}{2}\gamma_\omega^R \omega \delta_{ij} + \gamma_S^R \frac{\partial \widetilde{U}_i}{\partial x_j} + \frac{3}{2}\left(1 - \gamma_S^R\right)\frac{\widetilde{R}_{ik}}{\widetilde{R}_{ll}}\left(\frac{\partial \widetilde{U}_k}{\partial x_j} - \frac{\partial \widetilde{U}_j}{\partial x_k}\right) \quad,$$

$$C_0 = \frac{2}{3}\left[-1 + \gamma_\omega^R - \gamma_S^R \frac{\partial \widetilde{U}_j}{\partial x_k}\frac{\widetilde{u_k''u_j''}}{\widetilde{\varepsilon}} - \gamma_H^R \frac{1}{\overline{\rho}\widetilde{\varepsilon}}\frac{\partial \overline{P}}{\partial x_k}\overline{u_k''}\right] \quad,$$

$$C_H = \gamma_H^R \quad, \quad C_1^\rho = \frac{1}{2}\gamma_\omega^\rho \quad \text{and} \quad C_2^\rho = \frac{1}{2}\left(\gamma_H^\rho + \gamma_{H_1}^u\right) \tag{3.4}$$

The coefficients for the density-velocity correlation closures deduced from the PDF model are given in the second line of table 2.1. They are the ones used in this article. Note that the model is realizable when $C_0 > 0$. This condition can be fulfilled using, for instance, the same procedure as in [3].

As for the micro-mixing model, we choose a standard value for C_1^c [10], and set C_2^c so that the diffusion coefficient $C_d = \frac{1 - C_2^c}{C_1^c + \frac{1}{2}\gamma_\omega^R}$, meaningfull in the limit $\omega \to \infty$, is equal to 0.18:

$$C_1^c = 1.5 \quad \text{and} \quad C_2^c = 0.55 \tag{3.5}$$

4   EQUATIONS FOR THE CONCENTRATION CORRELATIONS

From SPDEs (3.1)-(3.3), we derive the following evolutions for the concentration correlations:

$$\frac{D\widetilde{u_i''c_\alpha''}}{Dt} = \mathcal{D}_i^\alpha + \mathcal{P}_{S_i}^\alpha + \mathcal{P}_{H_i}^\alpha + \mathcal{P}_{G_i}^\alpha + \Phi_i^\alpha - \mathcal{E}_i^\alpha \tag{4.1}$$

$$\frac{D\overline{c_\alpha''}}{Dt} = \mathcal{D}^{\rho\alpha} + \mathcal{P}_S^{\rho\alpha} + \mathcal{P}_H^{\rho\alpha} + \mathcal{P}_G^{\rho\alpha} + \Phi^{\rho\alpha} - \mathcal{E}^{\rho\alpha} \tag{4.2}$$

$$\frac{D\widetilde{c''_\alpha c''_\beta}}{Dt} = \mathcal{D}^{\alpha\beta} + \mathcal{P}_S^{\alpha\beta} + \mathcal{P}_H^{\alpha\beta} + \mathcal{P}_G^{\alpha\beta} + \Phi^{\alpha\beta} - \mathcal{E}^{\alpha\beta} \tag{4.3}$$

where the $\mathcal{D}^\#$ terms correspond to turbulent diffusion, and are modeled with a tensorial gradient diffusion hypothesis. $\mathcal{P}^\#$, $\mathcal{P}_H^\#$, $\mathcal{P}_G^\#$ are the shear, enthalpic and gradient production terms, and are treated exactly. Their expressions are not detailed here, but can be found for instance in [1]. The terms denoted by $\Phi^\# - \mathcal{E}^\#$ correspond to redistribution and dissipation. Their expressions are directly obtained from the PDF model:

$$\Phi_i^\alpha - \mathcal{E}_i^\alpha = -\gamma_S^c \mathcal{P}_{S_i}^\alpha - \gamma_H^c \mathcal{P}_{H_i}^\alpha - \gamma_G^c \mathcal{P}_{G_i}^\alpha - \gamma_\omega^c \omega \widetilde{u''_i c''_\alpha} + \frac{3}{2}\left(1 - \gamma_S^R\right)\frac{\widetilde{u''_i u''_k}}{2\widetilde{k}}\left(\frac{\partial \widetilde{U}_k}{\partial x_j} - \frac{\partial \widetilde{U}_j}{\partial x_k}\right)\widetilde{u''_j c''_\alpha} \tag{4.4}$$

$$\Phi^{\rho\alpha} - \mathcal{E}^{\rho\alpha} = -\gamma_H^{cp}\mathcal{P}_H^{\rho\alpha} - \gamma_G^{cp}\mathcal{P}_G^{\rho\alpha} - \gamma_\omega^{cp}\omega\overline{c''_\alpha} \tag{4.5}$$

$$\Phi^{\alpha\beta} - \mathcal{E}^{\alpha\beta} = -\gamma_G^v\mathcal{P}_G^{\alpha\beta} - \gamma_\omega^v\omega\widetilde{c''_\alpha c''_\beta} \tag{4.6}$$

The coefficients are also deduced from the PDF model:

$$\gamma_S^c = \gamma_S^R \;\;,\;\; \gamma_H^c = \gamma_H^R \;\;,\;\; \gamma_G^c = C_2^c \;\;,\;\; \gamma_\omega^c = C_1^c + \frac{1}{2}\gamma_\omega^R \tag{4.7}$$

$$\gamma_H^{cp} = C_2^\rho \;\;,\;\; \gamma_G^{cp} = C_2^c \;\;,\;\; \gamma_\omega^{cp} = C_1^c + \frac{1}{2}\gamma_\omega^\rho \tag{4.8}$$

$$\gamma_G^v = C_2^c \;\;,\;\; \gamma_\omega^v = 2C_1^c \tag{4.9}$$

The coefficients values are recapitulated in table 4.2. By construction, equations (4.1)-(4.3) are compatible with the remaining of the GSG model, when using the modified set of model parameters deduced from the PDF analysis (2nd line of table 2.1). Indeed, all the closures can then be derived from the same PDF model. Besides, the number of constants is fixed once the PDF model has been set. Only the PDF model constants appear in the equations for the concentration correlations. Thus, only 2 additional constants have been introduced in the extended GSG model ($C_\#^c$), whereas 9 constants should have been fixed otherwise.

γ_S^c	γ_H^c	γ_G^c	γ_ω^c	γ_H^{cp}	γ_G^{cp}	γ_ω^{cp}	γ_G^v	γ_ω^v
0.6	0.3	0.55	2.4	0.15	0.55	3.	0.55	3

Table 4.2. Model coefficients for the concentration correlations

5   EXPERIMENT BY KUCHERENKO *ET AL.*

The model derived in the previous section is now applied to the experiment proposed by Kucherenko *et al.* [6]. The experimental set-up consists in a gas accelerator device, in which a vial containing two fluids with densities $\rho_1 = 2.04 \; g/cm^3$ and $\rho_2 = 0.69 \; g/cm^3$ is placed. The vial undergoes a variable acceleration $a(t)$ with two main stages. During the first stage, from $t = 0$ to $t = t^* = 8.2 \; ms$, the acceleration is such that the stratification is unstable and Rayleigh-Taylor instabilities develop. During the second stage, the acceleration is reversed, so that the stratification becomes stable and a separation process occur.

Figure 5.1 shows the evolution of the length of the mixing zone in the light fluid L_l obtained from the experiment, and from calculations performed with two variants of the GSG model. The *standard GSG* model refers to the GSG model with a gradient diffusion hypothesis for closing the concentration flux. The *extended GSG* model corresponds to the GSG model with the additional equations derived in this article.

We observe that during the unstable phase, both models yield a similar increase of L_l. Besides, the length obtained at the end of the unstable phase is close to the experimental value. Differences become significant in the stable phase. In the experiment, L_l first stagnates and eventually decreases. On the contrary, the standard GSG model predicts a continuous increase of L_l. This is the only behaviour that can be expected from a diffusion model. As for the extended GSG model, it yields a stagnation of the mixing length followed by a slight decrease. This behaviour is qualitatively coherent with experimental observations, but, from a quantitative point of view, differences remain. They could be explained by the fact the fluids are treated in the calculations as perfect gases, whereas they are liquids in the experiment.

Figure 5.2 shows a profile of the scalar flux at time $t = 0.0165s$ during the second phase. It can be seen that the extended GSG model predicts significant counter-gradient transport, while the standard GSG model cannot, by definition, predict it. Counter-gradient is at the origin of the mixing length stagnation and decrease.
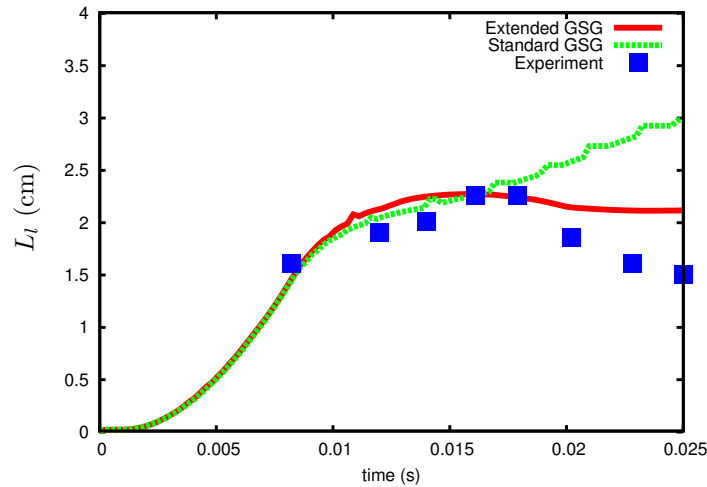
Fig. 5.1. Evolution of the length of the mixing zone in the light fluid
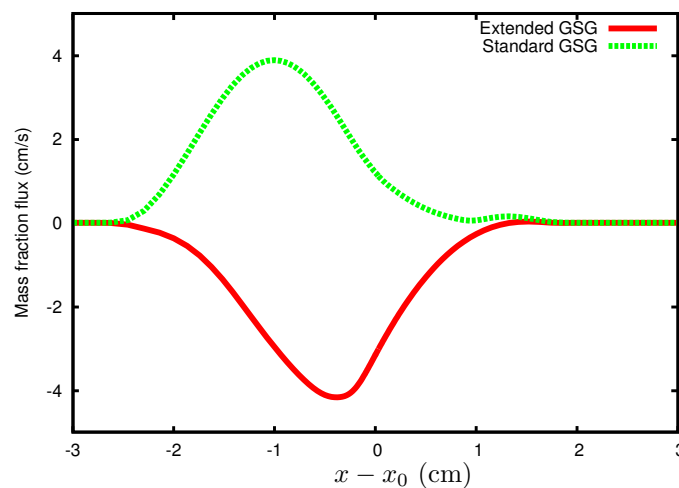
Fig. 5.2. Profile of the normalized scalar flux at time $t = 0.0165s$ (x_0 is the center of the mixing zone)

6 POTENTIAL SHOCK TUBE EXPERIMENT

In this section, we suggest a configuration that could be studied experimentally in a shock tube. This configuration aims at emphasizing the effects of counter-gradient transport. It could constitute a good validation benchmark for models used to predict RMI/RTI driven turbulence as well as stably stratified turbulence.

The principle of the experiment is the following. In a shock tube, a shock is generated by a high-pressure chamber and travels from a light fluid to a heavy fluid. Meanwhile, a rarefaction wave is generated in the high pressure chamber, and is reflected at the rear of the shock tube. The reflected wave follows the shock at a distance which can be controlled by the high pressure chamber length. When the shock impacts the interface between the two fluids, a mixing zone is generated and becomes turbulent. This mixing zone is in turn impacted by the reflected rarefaction wave. This second interaction corresponds to a situation of stably stratified turbulence, and may lead to counter-gradient transport.

Such a configuration has been studied numerically with the characteristics summarized on figure 6.3. Counter-gradient is indeed predicted by the extended GSG model, leading to strong differences with the standard GSG model. The evolution of the mixing length is shown on figure 6.3. Note that the rarefaction wave impacts the mixing zone at $t = 5.8\,ms$. Thus, this potential experiment should have the ability to discriminate models in the case of stably stratified turbulence.
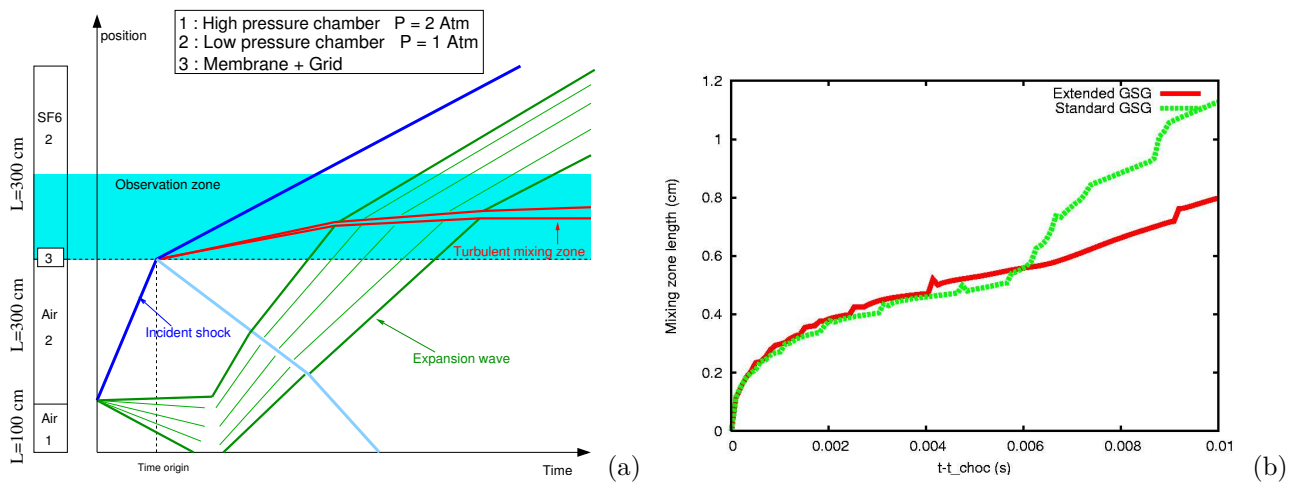
Fig. 6.3. Potential shock tube experiment: set up (a) and mixing length evolution (b)

7 CONCLUSIONS

In this work, we extend the GSG second order turbulence model [4] by formulating equations for the concentration correlations. A PDF model stochastically equivalent to the existing GSG model is derived, and completed with a stochastic concentration equation. Then, concentration correlation equations are deduced. The interest of this method is to preserve the self-coherency of the second order model. In particular, the new closures in the concentration flux equations are found to be dependent on the ones used in the Reynolds stress equation.

The extended GSG model is then applied to the experimental configuration studied by Kucherenko *et al* [6]. It is shown that the model has the ability to predict the transition from gradient to counter-gradient transport observed in this experiment. Finally, an experimental shock-tube configuration is proposed in order to validate further the model.

As a side consequence of this work, we also derived a PDF model (eq. (3.1)-(3.3)) suitable for computing turbulent flows with strong density and pressure variations, as well as stably stratified turbulent flows with counter-gradient situations. This model contains an equation for a stochastic density, and a Langevin model with an explicit dependence on density.

REFERENCES

[1] P. Bailly, M. Champion, and D. Garréton. Counter-gradient diffusion in a confined turbulent premixed flame. *Phys. Fluids*, 9(3):766–775, 1997.

[2] P. Chassaing, R. A. Antonia, F. Anselmet, Joly L., and S. Sarkar. *Variable density fluid turbulence*. Kluwer Academic Press, 2002.

[3] S. K. Das and P. A. Durbin. A Lagrangian stochastic model for dispersion in stratified turbulence. *Phys. Fluids*, 17:025109, 2005.

[4] O. Grégoire, D. Souffland, and S. Gauthier. A second-order turbulence model for gaseous mixtures induced by Richtmyer-Meshkov instabilities. *J. of Turbulence*, 6(29), 2005.

[5] H. Hanazaki and J. C. R. Hunt. Linear processes in unsteady stably stratified turbulence. *J. Fluid Mech.*, 318:303–337, 1996.

[6] V. E. Kucherenko, Yu. A.and Neuvazhaev and A. P. Pylaev. Behavior of a region of gravity-induced turbulent mixing under conditions leading to separation. *Physics Doklady*, 39(2):114–117, 1994.

[7] B.E. Launder, B.J. Reece, and W. Rodi. Progress in the development of a Reynolds-stress turbulence closure. *J. Fluid. Mech.*, 68(3):537–511, 1975.

[8] J.D. Lindl. *Inertial Confinement Fusion Flow*. Springer-Verlag, 1998.

[9] M. R. Overholt and S. B. Pope. Direct numerical simulation of a passive scalar with imposed mean gradient in isotropic turbulence. *Phys. Fluids*, 8(11):3128–3148, 1996.

[10] S. B. Pope. *Turbulent flows*. Cambridge Univ. Press, 2000.

[11] S.B. Pope. On the relationship between stochastic Lagrangian models of turbulence and second-moment closures. *Phys. Fluids*, 6:973–985, 1994.

[12] V. A. Sabel'nikov and O. Soulard. Rapidly decorrelating velocity field model as a tool for solving Fokker-Planck PDF equations of turbulent reactive scalars. *Phys. Rev. E*, 72:016301, 2005.

Minkowski Functionals for Quantitative Assessments of Shock-Induced Mixing Flows

Richard A. Strelitz[1] and James R. Kamm[2]

[1]*Computer & Computational Sciences, CCS-3, Los Alamos National Laboratory, Los Alamos, NM 87545*
[2] *Applied Physics, X-1-MV, Los Alamos National Laboratory, Los Alamos, NM 87545*

Abstract :
We describe the morphological descriptors known as Minkowski Functionals (MFs) on a shock-induced mixing problem. MFs allow accurate and compact characterization of complex images[1].. MFs characterize connectivity, size, and shape of disordered structures [2,9]. They possess several desirable properties, such as additivity, smoothness, and a direct relationship to certain physical properties. The scalar MFs that we describe can be extended to a moment-based tensor form that allows more thorough image descriptions. We apply MFs to experimental data for shock-induced mixing experiments conducted at the LANL shock tube facility. Those experiments, using low Mach number shock waves in air to induce the Richtmyer-Meshkov instability on air-SF_6 interfaces, provide high-resolution, quantitative planar laser-induced fluorescence (PLIF) images. We describe MFs and use them to quantify experimental PLIF images of shock-induced mixing. This method can be used as a tool for validation, i.e., the quantitative comparison of simulation results against experimental data.

1 INTRODUCTION

Turbulent mixing plays a critical role in many important physical situations, from combustion to multi-phase flow. Questions about how a shock front evolves from a simple form to the more intricate ones seen in later stages are difficult to answer; even more vexing are those questions that deal with the break up of a coherent front into disconnected regions of turbulent mixing. Our experimental data set consists of 11 PLIF (pulse laser induced fluorescence) images of a SF_6 shock front that mixes with the ambient air. Treating those images as a series of approximately concentric level sets, we reduce the images to a series of silhouettes. We apply metrics derived from consideration of integral geometry called the Minkowski Functionals (MFs) to characterize these shapes and thereby reduce the evolution of the shape into a time series for each of the 3 MF's.

2 EXPERIMENT and DATA

The shock-tube facility at LANL, depicted in Fig.2.1, provides high-resolution experimental data that captures the evolution of Richtmyer-Meshkov instability and the transition to turbulence in a low Mach number (≈ 1.2) shock-driven air/SF_6 interface. See the works of Prestridge et al. [11,16], and references contained therein for a description of the experimental facilities, diagnostics, and data. We focus on the shock-accelerated evolution of a cylinder of SF_6 [12}. The shock-induced instability evolves from an ordered, vorticity-driven structure to a significantly disordered, transitionally turbulent structure in first 1200 µs subsequent to the shock-cylinder interaction. During this evolution, both baroclinic (e.g., Richtmyer-Meshkov) and shear-driven (e.g., Kelvin-Helmholtz) instabilities act on different parts of the structure at different times.
um, high) concentrations levels. It is these contours that will be subjected to the MF analysis.
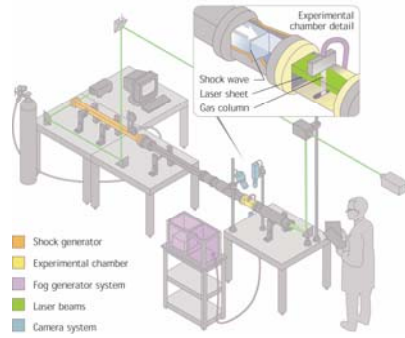
Fig. 2.1. Schematic of the LANL shock-tube experimental facility.
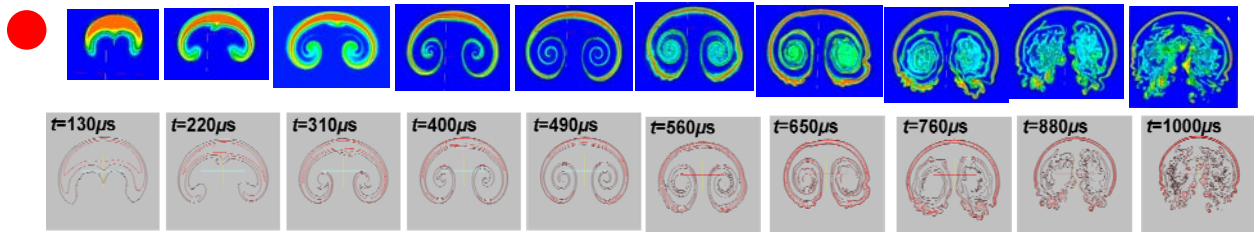
Fig. 2.2. contains PLIF images of the experimental concentration of the SF_6 for a series of experiments. In these images, the shock travels from top-to-bottom. The initial condition schematic (far left, top row) depicts an idealized horizontal "slice" through the vertical gas cylinder before shock passage. As time progresses (top row, from left to right), the early-time primary instability gives way to later-time secondary instability in the pseudo-color, quantitative PLIF images. The bottom row contains images, at each of the post-shock times, of contours associated with three (low, medium and high) levels.

3 MINKOWSKI FUNCTIONALS

The Minkowski functionals are defined in terms of parallel bodies, that is, the set of all points within a fixed distance of the body in question (hence the term *parallel*). Despite the somewhat daunting notation and language used to define the MFs, the MFs in 2 and 3 space are very simple, as seen in Table. What is really important about the MFs are their very useful properties. First, they are very small in number; to describe an object in d-dimensions, there are only (d+1) MFs needed. Furthermore, according to the very elegant Hadwiger's Theorem[1,2,3,13], any additive measure of shape can be described as a linear combination of the MFs, in any d-dimensional space. Third, the MFs are additive, in the sense that the MFs of a composite body are the sum of the components, minus the MFs of the shared regions, particularly important for treating aggregate material[9,10]. This not only means that the MFs can be used to describe how a body can split and join, it also means that there is no loss of functionality in going from continuous data to gridded (for example, using pixels or voxels[4]). It also means that the computation of the MFs is both easy and readily adaptable to distributed and parallel processing[7]. The MFs have the nice property of being independent of position and orientation, although knowledge of these parameters can be retrieved by computing the standard spatial moments of the MFs.[2].

For bodies in $\mathbb{R}^d$, the intrinsic volume $V_d(K)$ is increased when the original body is extended to a parallel body by an amount ε according to Steiner's Formula :

$$V_d(K \oplus B_\varepsilon(0)) = \sum_{j=0}^{d} \varepsilon^{d-j} \kappa_{d-j} V_j(K) \tag{1.1}$$

where κ_i is the volume of the unit ball B_r^d in d-space and the $V_i(K)$ are the (d+1) Minkowski functionals for objects in d-space.

This formula establishes the finite (d+1) number of functionals for an object in *d*-dimensions, although it does not make clear how to compute them or their significance. The complete mathematical derivation of both the functionals and an algorithm to compute them from this expansion is given by Klenk, et al. [7], but the problem can be simplified much further by writing the functionals themselves as integrals.

$$\tag{1.2}$$

$$V_i(K) = \frac{1}{i+2} \left| \begin{matrix} n \\ i+2 \end{matrix} \right|^{-1} \int_{\partial K} \Theta_i(R_1^{-1}...,R_{n-1}^{-1}) dK, \quad 1=0..n$$

where the R_i are the radii of curvature and the Θ_i are the coefficients in the polynomial expansion

$$\prod_{i=1}^{n-1}(x+R_i^{-1}) = \sum_{i=1} x^{n-i}\Theta(R_1^{-1},...R_n^{-1}) \text{ so that} \tag{1.3}$$

$$\Theta_1 = 1, \Theta_2 = R_1^{-1}+...+R_n^{-1}, \Theta_n = R_1^{-1}\bullet R_2^{-1}\bullet...R_n^{-1}$$

As integrals in this form, the MFs clearly have both a physical significance and physical units, in addition to the obvious geometric interpretation. Furthermore, written as integrals over the surface or across the volume, the MFs have an obvious relationship to the volume integrals and surface integrals that are so common in computing forces, moments, and energies, as well as energy exchanges and fluxes through the surface integrals, thereby becoming meaningful in the sense of the underlying physics. Readers interested in the details of the mathematics and derivation are directed to the excellent summaries provided elsewhere [1,9,10,13].

Minkowski Functional Order	2-D, Plane Object	3D, Volume Object
0	No. of Distinct Objects	Euler Number
1	Area (A)	Volume (V)
2	Perimeter (L)	Surface Area (S)
3	N/A	Mean Curvature (H)

Table 1Minkowski Functionals for 2 and 3-Dimensions

The simple geometric interpretation of the 2-D (planar) MFs almost obviates the computational issue; but as in any conversion from an abstract integral to a numerical value, the devil is in the details. The computation is much simplified by converting the volume integrals into surface or line integrals using Stokes' Theorem, as described best in [6,15,16].

4 RESULTS

The results of this analysis are depicted in Fig. 4.1. In each of these plots, the functional is plots along the ordinate with time along the abscissa. The left plot shows the evolution of connectivity; the middle plot shows the area, and the right plot shows the perimeter. For the connectivity (left plot), the early times have a single structure (cf. Fig. 2.2), so $M_0 = 1$; at late times, however, the low concentration (red) consists of many "islands", while the medium (blue) and high (black) concentrations have fewer "islands." For the area (middle plot), the low concentration (red) grows with time, while the medium concentration (blue) is erratic for $t > 650\,\mu$s and the high conc. (black) decreases for $t > 650\,\mu$s. The perimeter (right plot) for the low concentration (red) grows with time, while the medium (blue) and high (black) concentrations decrease for $t > 650\mu$s (Kumar et al. [8] discuss a perimeter analysis of the two-cylinder case).
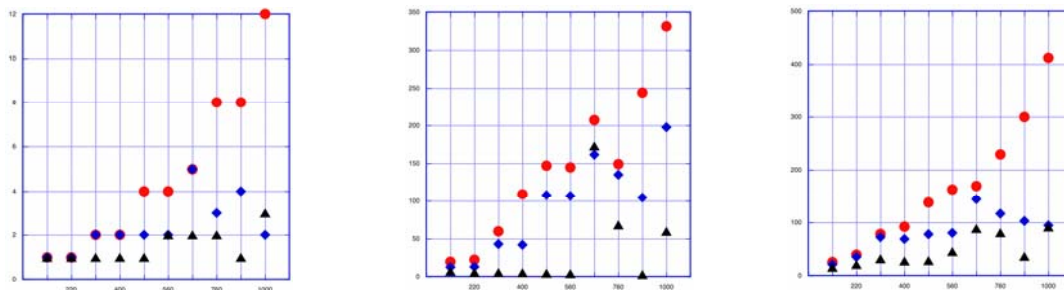
Fig. 4.1. MF for the shock-tube data of Fig. 3.2: M_0 connectivity (left), M_1 area (middle), M_2 perimeter (right).

5 DISCUSSION

The results of applying the MF methodology to the data are shown in Fig. 4.1. Note that we applied a completely general metric to the data, yet even so, the measures confirm one's intuition, and, most important, they efficiently and effectively convert one's qualitative sense of the gross features of the mixing into numbers and trends. In fact, by looking

not just at one contour value of concentration but three, further details about the interaction of mixing and dissipation become more apparent and open to analysis.

6 Future Work

The MFs possess properties that can quantify complex mixing flows, and given their signature properties of additivity, motion-invariance, and continuity, they can be used to compute features of both the coherent stage of mixing as well as the more dispersed and diffuse later stages. The transition to 3-dimensional data is clear; even the apparently more complicated definition of curvature for a flat faced polyhedra has been adequately dealt with by the practitioners of animation and surface simplification [5], and thus presents no problem.

The MFs can be extended to reveal information about location and orientation of bodies using simple spatial moments [moments] and can be computed without even adding new loops by applying Stokes' Theorem again and integrating inductively by parts [15,16] .

Finally, the ease of computation of the MFs will facilitate the statistical analysis of the MFs that is so necessary before they can actually be used to make comparisons or defensible inferences.

We believe that the MFs offer a powerful mathematical and physics tool that will accelerate the analysis of numerical simulations for these cylinder experiments (for quantitative validation), as well as for new turbulent mixing experiments and simulations

REFERENCES

[1]   Arms, C., Knackstedt, M. and Mecke, K. 2004, Characterisation of irregular spatial structures by parallel sets and integral geometric measures, Colloids and Surfaces A : Physiohem. Eng. Aspects, **241**,pp. 351-372.
[2]   Beisbart, C. R. Dahlke, K. Mecke, and H. Wagner, 2002. Vector- and Tensor-Valued Descriptors for Spatial Patterns, *Lecture Notes in Physics* **600**, pp. 238–260 (2002).
[3]   Beisbart, C., Buchert, T. and Wagner, H. 2001. Morphometry of spatial pattens. Physica A, **293**, 592-604.
[4]   Blasquex, I. and Poiraudeau, J.-F. 2003. Efficient processing of Minkowski functionals on a 3D binary image using binary decision diagrams, Journal of WSCG, **11**,
[5]   Bobenko, A. and Schroder, P. 2005. Discrete Willmore flow. Eurographics Symposium on Geometry Processing, > Desbruns and H. Pottmann (eds), 101-110.
[6]   Eberly, D. 2003. Polyhedral mass properties (revisited), http://www.geometrictools.com
[7]   Klenk, S, Schmidt, V. and Spodarov, E. 2006. A new algorithmic approach to the computation of Minkowski functionals of polyconvex sets, Comp. Geom. **34**, 127-148.
[8]   Kumar, S., Orlicz, G., Tomkins, C., Goodenough, C., Prestridge, K., Vorobieff, P., and Benjamin, R. 2005 S tretching of material lines in shock-accelerated gaseous flows, *Phys. Fluids* **17**, pp.1-11.
[9]   Mecke, K., 2002 Additivity, convexity, and beyond: applications of Minkowski Functionals in statistical physics *Lecture Notes in Physics* **600**, pp. 111-184
[10]   Michielsen,K. H. De Raedt 2001. Integral-Geometry Morphological Image Analysis, *Physics Reports* **347**, pp. 461–538.
[11]   Prestridge, K., Rightley, P., Vorobieff, P., Benjamin, R., and Kurnit, N. 2000, Simultaneous density-field visualization and PIV of a shock-accelerated gas curtain, *Exp. Fluids* **29**, pp. 339–346. Pre2000a
[12]   Prestridge, K., Zoldi, C., Vorobieff, P., Rightley, P., and Benjamin, R. 2000, Experiments and simulations of instabilities in a shock-accelerated gas cylinder, Los Alamos National Laboratory Report LA-UR-00-3973. Pre2000b
[13]   Schmalzing, J. and Buchert, T. 1997. Beyond genus statistics : A unifying approach to the morphology of cosmic structure. The Astrophysical Journal, **482**, L1-L4.
[14]   Steger, Carsten, 1996. On the calculation of moments of polygons, Technical Report FGBV-96-04, Technische Universitat Munchen.
[15]   Steger, Carsten, 1996. On the calculation of arbitrary moments of polygons, Technical Report FGBV-96-05, Technische Universitat Munchen.
[16]   Tomkins, C., Prestridge, K., Rightley, P. Marr-Lyon, M., Vorobieff, P., Benjamin, R., Kurnit, N. 2003, A quantitative study of the interaction of two Richtmyer-Meshkov-unstable gas cylinders, *Phys. Fluids* **15**, pp. 986–1004.

e-mail: terrones@lanl.gov

Onset of Plastic Flow in Accelerated Plates of Finite Thickness

Guillermo Terrones

Los Alamos National Laboratory, Applied Physics Division, Los Alamos, New Mexico 87545, USA

Abstract: For accelerated, incompressible, ideal elastoplastic plates of finite thickness with a preformed sinusoidal perturbation at the interface, we investigate the spatiotemporal evolution of the stress tensor to construct the boundaries that demarcate the transition between elastically stable modes and the onset of stable dynamic plastic flow.

1 INTRODUCTION

In accelerated solids, one has to distinguish between two kinds of phenomena both of which lead to dynamic plastic deformation and are oftentimes perceived as one and the same under the name of 'instability growth.' First, there is the exponential growth of modes whose cutoff and most-unstable wavelengths are determined by the elastic behavior of the medium (elastically unstable modes) [1]. Second, there is the plastic deformation of small initial material perturbations in elastically stable oscillatory configurations whose onset depends on the yield stress of the medium. The first falls into the category of dynamic elastic stability problems known as Rayleigh-Taylor instability (RTI) in solids. However, the second is a stable dynamic plastic flow problem for which there is no counterpart in fluids and is often confused with a stability problem. Instability of a system is the transition from a basic state into a different one that arises because the system is unable to dampen down small perturbations in the field variables, which is not the case when the elastic limit is reached in a solid undergoing stable oscillations. In the literature on accelerated solids, the usage of the term 'instability' to describe the onset of dynamic plastic flow and sustained flow in the plastic regime that originated from an elastically stable state is ubiquitous [2-11]. This has also led some investigators to think about the process of stable oscillatory plastic deformation of interfacial disturbances as if it were the result of a 'growth rate' process akin to the RTI.

2 MOST UNSTABLE ELASTIC DISTURBANCES

The dispersion relation for an elastic plate of finite thickness [12] in dimensionless variables is

$$\Phi(\alpha;\kappa,\theta)=\kappa^2\left[16\kappa^4(\alpha^2+\kappa^2)-\alpha^4\right]+$$
$$+(\alpha^2+2\kappa^2)^2\left[(\alpha^2+2\kappa^2)^2-8\kappa^3\beta\left(\coth\theta\kappa\,\coth\beta\theta-\operatorname{csch}\theta\kappa\,\operatorname{csch}\beta\theta\right)\right]=0 \tag{2.1}$$

where the dimensionless growth rate and wave number are $\alpha=\sigma/a(G/\rho)^{1/2}$ and $\kappa=Gk/(\rho a)$, respectively, the dimensionless thickness is $\theta=\rho a h/G$, and $\beta=(\alpha^2+\kappa^2)^{1/2}$. Since the most-unstable modes are those with a maximum value of α in the $\alpha-\kappa$ plane, they must satisfy Eq. 2.1, $\partial\alpha/\partial\kappa=0$, and $\partial^2\alpha/\partial\kappa^2<0$ at $\kappa=\kappa_m$. Thus, for a given θ, there is a unique wave number κ_m that corresponds to a maximum value of the growth rate α_m. Disturbances that neither grow nor decay are neutral ($\alpha=0$) and demarcate the elastic stability boundary corresponding to the cutoff perturbations of dimensionless wave number κ_c. A relationship between κ_c and θ can be derived from Eq. 2.1

$$(1-4\kappa_c^2)\sinh^2\theta\kappa_c+(2\theta\kappa_c^2)^2=0. \tag{2.2}$$

Figure 2.1a shows the most-unstable and the cutoff wavelengths as a function of the plate thickness, both scaled with the cutoff wavelength for an infinitely thick plate $\lambda_{c\infty}$ ($=4\pi G/\rho a$) [6,13,14]. In this figure, the abscissa $h/\lambda_{c\infty}$ and the ordinate $\lambda/\lambda_{c\infty}$ are related to θ and κ by $\theta/4\pi$ and $1/2\kappa$, respectively. For $h/\lambda_{c\infty}>2.55$, λ_m is practically constant and larger than twice λ_c ($\lambda_m/\lambda_c=2.2159$). It is interesting to note that the largest perturbation

wavelength ($\lambda_m/\lambda_{c\infty} = 2.2654$) that can maximize the growth rate corresponds to a finite thickness plate ($h/\lambda_{c\infty} = 0.8380$, at which the maximum occurs). This is surprising, since the largest λ_c corresponds to an infinitely thick plate (dotted line in Fig. 2.1a). Figure 2.1b shows that α_m is bound between two asymptotes ($\alpha_m = 1/2$ as $h/\lambda_{c\infty} \to 0$, and $\alpha_m = 0.3119$ as $h/\lambda_{c\infty} \to \infty$) and decreases as $h/\lambda_{c\infty}$ increases (the abscissa in Fig. 2.1b has been extended to show the bounding asymptotes). In practice, disturbances on a solid plate may arise from different sources, such as the system or device that imparts the acceleration or they could be preformed on the solid intentionally or as part of the manufacturing process. However, whether or not a particular disturbance wavelength is destabilizing will also depend on the lateral dimensions of the solid.
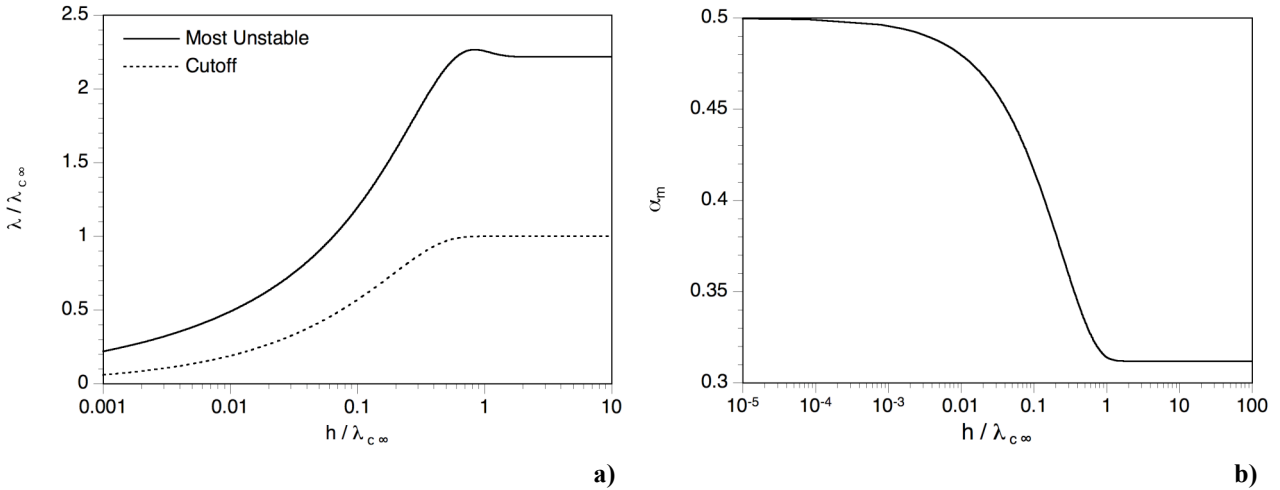
Fig. 2.1 Dimensionless most-unstable wavelengths and growth rates. a) $\lambda_m/\lambda_{c\infty}$ and $\lambda_c/\lambda_{c\infty}$ as a function of the dimensionless plate thickness $h/\lambda_{c\infty}$, b) α_m as a function of $h/\lambda_{c\infty}$.

3 STABLE OSCILLATORY MODES

We consider the dynamics of plates of thickness h, with a preformed sinusoidal perturbation at the interface of small amplitude Δh ($<< h$) and wave number k, density ρ, shear modulus G, yield strength in uniaxial tension Y, which are accelerated to a constant value a. Plohr and Sharp [12] derived the governing equations that describe the motion of this system, obtained the Laplace transform of the stream function $\widehat{\Psi}(x,y,\sigma;k,h,\Delta h,\rho,G,a)$, and the form of the solutions for the displacement at the interface and the vorticity distribution. However, they did not present any numerical results and did not investigate the onset of plastic flow. In order to shed some light into the spatiotemporal behavior of stable oscillatory modes and to understand how the onset of plastic flow unfolds, we derive the deviatoric stress tensor $\mathbf{S}$ explicitly and compute the effective stress as a function of the controlling parameters. We introduce the dimensionless variables $z = \rho\, a\, x/G$, $\xi = \rho\, a\, y/G$, $\tau = a(\rho/G)^{1/2}\, t$, $\widehat{\psi} = \rho\, a/(G\Delta h)\,\widehat{\Psi}$, and $\mathbf{s} = \mathbf{S}/(\rho\, a\, \Delta h)$. In terms of $\widehat{\psi}$, the four components of $\mathbf{s}(z,\xi,\tau;\kappa,\theta)$ are

$$\mathbf{s}(z,\xi,\tau;\kappa,\theta) = 2\int_0^\tau \left\{ \frac{1}{2\pi i}\int_{c-i\infty}^{c+i\infty} e^{\alpha\tau}\begin{bmatrix} -\partial^2\widehat{\psi}/\partial z\partial\xi & (\partial^2\widehat{\psi}/\partial z^2 - \partial^2\widehat{\psi}/\partial\xi^2)/2 \\ (\partial^2\widehat{\psi}/\partial z^2 - \partial^2\widehat{\psi}/\partial\xi^2)/2 & \partial^2\widehat{\psi}/\partial z\partial\xi \end{bmatrix} d\alpha \right\} d\tau \qquad (3.1)$$

To facilitate the graphical visualization of the effective stress, the time variable can be eliminated by integration over time to obtain the root-mean-square (RMS) of the effective stress $\langle s_{eff}\rangle_{rms}$

$$\langle s_{eff}\rangle_{rms}^2 = \lim_{\tau\to\infty} 1/\tau \int_0^\tau 3(s_{zz}^2 + s_{z\xi}^2)\, d\tau \text{'} \qquad (3.2)$$

Since the components of the stress tensor are not time-periodic and neither is the effective stress, the time integral in Eq. 3.2 must be carried out to infinity. Figure 3.1a shows the distribution of $\langle s_{eff}\rangle_{rms}$ along the plate thickness ξ at different

horizontal locations z for $\theta = 0.01$ and $\lambda/\lambda_{c\infty} = 0.005$. At $\kappa z = \pi/2$, $\langle s_{eff} \rangle_{rms}$ is entirely due to the normal stress component and the maxima occur at $\xi = 0$ and $\xi = \theta$. The distribution of $\langle s_{eff} \rangle_{rms}$ along ξ is not linear and the minimum, which is not zero, does not occur at the midplane as one would expect for a thin plate in static equilibrium. For the same θ but decreasing $\lambda/\lambda_{c\infty}$ to 0.00167, Fig. 3.1b shows dramatic changes when compared to the distribution in Fig. 3.1a.

a)   b)
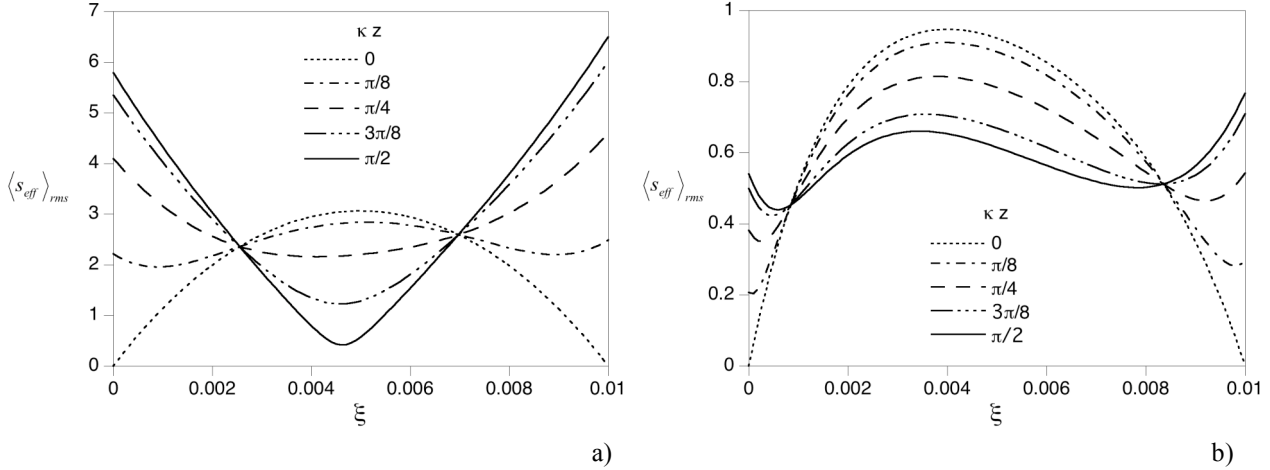
Fig. 3.1. Spatial variation of the root-mean-square of the effective stress $\langle s_{eff} \rangle_{rms}$ as a function of the vertical coordinate ξ for different values of z, a) $\theta = 0.01$, $\lambda/\lambda_{c\infty} = 0.005$, b) $\theta = 0.01$, $\lambda/\lambda_{c\infty} = 0.00167$.

4 ONSET OF PLASTIC FLOW

We define the onset of plastic flow boundaries $\Gamma_{cr}(\kappa,\theta)$ as the locus of states for which the absolute maximum of the effective stress reaches the yield stress of the solid along the lower plate boundary during the initial transient, which in terms of dimensionless variables can be represented as

$$\Gamma_{cr}(\kappa,\theta) = [2 \max s_{eff}(z,0,\tau;\kappa,\theta)]^{-1} \tag{4.1}$$

To construct a boundary $\Gamma_{cr}(\kappa,\theta)$ for constant θ, it is necessary to compute the time evolution of s_{zz} at $\xi = 0$ for each κ in the interval $0 \le \lambda/\lambda_{c\infty} \le \lambda_c(\theta)/\lambda_{c\infty}$ in order to find the maximum s_{eff}, which could be in tension or compression. We compare the boundaries $\Gamma_{cr}(\kappa,\theta)$ (see Eq. 4.1) based on the exact stress tensor from Eq. 3.1, with the equation developed by Nizovtsev and Raevskii [5], which in our dimensionless variables is

$$\Gamma_{NR} = (1 - 0.856 \, e^{-\kappa\theta/\sqrt{3}})[(1 - e^{-\kappa\theta/\sqrt{3}})^2 - 1/4\kappa^2] \tag{4.2}$$

Figure 4.1a shows that for $\theta = 10$ the discrepancy between Eq. 4.2 and the exact result 4.1 is not only substantial but also misses the cutoff, which occurs at $\lambda_c/\lambda_{c\infty} = 0.998$, and a region that is not monotonic and varies rapidly (in this instance, four main regions of different behavior comprise Γ_{cr}). Equation 4.2 predicts that the largest amplitude disturbance is always at $\lambda = 0$ regardless of thickness and that the susceptibility to the onset of plastic flow decreases uniformly as the wavelength decreases from λ_c to 0. This assertion holds only for thin plates. For instance, for $\theta = 10$, the largest Δh before the onset of plastic flow corresponds to $\lambda/\lambda_{c\infty} = 0.512$. As λ decreases from this point, a smaller Δh will be needed to reach the elastic limit reaching a minimum at $\lambda/\lambda_{c\infty} = 0.208$, and further decrease in λ towards zero allows larger values of Δh. Figure 4.1b shows the onset of plastic flow boundaries for constant θ spanning two orders of magnitude from 0.1 to 10. In all cases, the value of Γ_{cr} at $\lambda = 0$ is the same, i.e., $\lim_{\lambda \to 0} \Gamma_{cr}(\lambda,\theta) = 0.693$.

Large plastic deformations lie in a different regime from the values predicted by either Γ_{NR} or Γ_{cr}. Yet, Eq. 4.2 has been used to compare with experiments and simulations where plastic deformations have more than doubled

their initial amplitude [5,6,9-12,14], and it has also been argued that experiments are in reasonable agreement with Γ_{NR}. The metric used to ascertain 'instability' hinged on large deformations, which are incompatible with the postulates of Eq. 4.2. To make such comparisons consistent a criterion based on a prescribed large plastic deformation must be formulated.

a)   b)
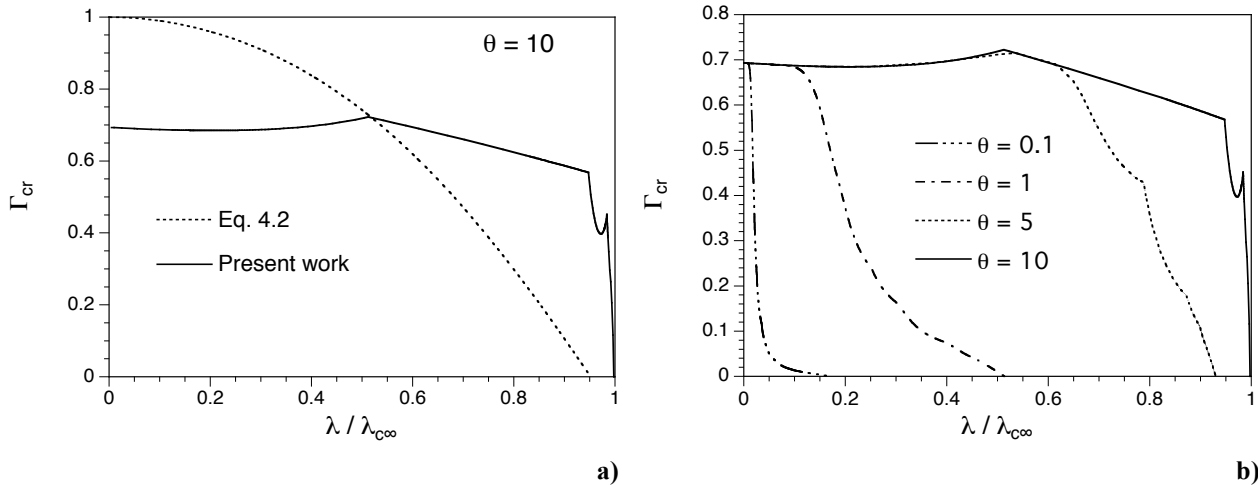
Fig. 4.1. Onset of plastic flow boundary curves represented in terms of the critical dimensionless amplitude Γ_{cr} as a function of the dimensionless wavelength $\lambda/\lambda_{c\infty}$ for various dimensionless thicknesses θ. a) Comparison between Γ_{cr} and Γ_{NR} for $\theta=10$. b) Exact boundaries Γ_{cr} for $\theta=0.1, 1, 5,$ and 10.

5 SUMMARY

For elastically unstable accelerated plates, we calculated the most-unstable modes and determined that the largest perturbation wavelength that can maximize the growth rate corresponds to a finite thickness plate. By examining the exact solution of accelerated elastic plates of arbitrary thickness, we computed the temporal evolution of the stress tensor, which led to the construction of the boundaries Γ_{cr} that demarcate the transition from elastically stable oscillatory modes to the onset of stable plastic flow. Earlier estimates of these boundaries using the thin-plate approximation and its variants differ substantially from the present results. In the zero wavelength limit, we found that when the onset is reached the amplitude disturbance satisfies $\rho\,a\,\Delta h_{cr}/2Y = 0.693$, regardless of plate thickness.

REFERENCES

[1]   G. Terrones, Phys. Rev. E **71**, 036306 (2005).
[2]   J. F. Barnes, P. J. Blewett, R. G. McQueen, K. A. Meyer, and D. Venable, J. Appl. Phys. **45**, 727 (1974).
[3]   J. F. Barnes, D. H. Janney, R. K. London, K. A. Meyer, and D. H. Sharp, J. Appl. Phys. **51**, 4678 (1980).
[4]   J. W. Swegle and A. C. Robinson, J. Appl. Phys. **66**, 2838 (1989).
[5]   P. N. Nizovtsev and V. A. Raevskii, VANT Ser. Teor. Prikl. Fizika **3**, 11 (1991).
[6]   S. M. Bakhrakh, O. B. Drennov, N. P. Kovalev, A. I. Lebedev, E. E. Meshkov, A. L. Mikhailov, N. V. Nevmerzhitsky, P. N. Nizovtsev, V. A. Rayevsky, G. P. Simonov, V. P. Solovyev, and I. G. Zhidov, Lawrence Livermore National Laboratory Report No. UCRL-CR-126710, 1997.
[7]   G. Dimonte, R. Gore, and M. Schneider, Phys. Rev. Lett. **80**, 1212 (1998).
[8]   J. D. Colvin, M. Legrand, B.A. Remington, G. Schurtz, and S.V. Weber, J. Appl. Phys., **93**, 5287 (2003).
[9]   B. A. Remington, G. Bazan, J. Belak, E. Bringa, M. Caturla, J.D. Colvin, M.J. Edwards, S.G. Glendinning, D.S. Ivanov, B. Kad, D.H. Kalantar, M. Kumar, B.F. Lasinski, K.T. Lorenz, J.M. Mcnaney, D.D. Meyerhofer, M.A. Meyers, S.M. Pollaine, D. Rowley, M. Schneider, J.S. Stölken, J.S. Wark, S.V. Weber, W.G. Wolfer, B. Yaakobi, and L.V. Zhigilei, Metall. Mat. Trans. A, **35A**, 2587 (2004).
[10]   K. T. Lorenz, M.J. Edwards, S.G. Glendinning, A.F. Jankowski, J. McNaney, S.M. Pollaine, and B.A. Remington, Phys. Plasmas **12**, 056309 (2005).
[11]   J. J. López, A.R. Piriz, M. Temporal, N.A. Tahir, and M.C. Serna Moreno, Eur. Phys. J. Appl. Phys. **29**, 247–252 (2005).
[12]   B. Plohr and D. H. Sharp, Z. Angew. Math. Phys. **49**, 786 (1998).
[13]   S. M. Bakhrakh and N. P. Kovalev, Proc. 5th All-Union Conference on Numerical Methods for the Solution of Elasticity and Plasticity Theory Problems, Novosibirsk, 1978, p.15-23.
[14]   S. M. Bakhrakh and N. P. Kovalev, Numerical Methods for Solid State Mechanics, Novosibirsk, 1980, **2**, p.5-21.

e-mail: `b.j.r.thornber@cranfield.ac.uk,d.drikakis@cranfield.ac.uk,David.Youngs@awe.co.uk`

High Resolution Methods for Planar Richtmyer-Meshkov Instabilities

Ben THORNBER[1], Dimitris DRIKAKIS[1] and David YOUNGS[2]

[1] *Fluid Mechanics & Computational Science Group,Cranfield University*
http://www.cranfield.ac.uk/soe/fluid/
[2] *AWE, Aldermaston, UK*

Abstract: This paper investigates ability of a Lagrange-remap method (Turmoil) and a Godunov method (CNS3D) to capture the growth of unstable modes and complex turbulent mixing. They are compared through simulations of a single mode Richtmyer-Meshkov instability, and the half-height experiment of Holder *et al.* (IWPCTM9,2004). It is shown that both codes agree well with experiment and theory in terms of growth of the mixing layer and ability to capture principal flow features. CNS3D captures shock waves with no oscillations, however Turmoil allows the grows of smaller perturbations as the dissipation is not Mach number dependent

1 INTRODUCTION

The Richtmyer Meshkov instability (RMI) develops as a shock wave passes through a perturbed interface between two different materials or gases [8]. This instability is of fundamental importance in the understanding of inertial confinement fusion [13] and supernovae [1]. Numerical codes for the simulation of such complex flows are typically calibrated against theoretical, experimental, or previous numerical studies. The solution gained when simulating flow instabilities depends greatly on the numerical schemes used, thus it is important to establish the independence of certain reference results from the choice of numerical scheme.

This paper investigates the influence of numerical method and grid resolution on the growth of a three dimensional single mode planar RMI. The test case adopted is that of Li and Zhang [7]. Using these initial conditions the solution in the linear and non-linear regime is compared to theoretical solutions developed in Zhang and Sohn [14] and Richtmyer [8]. The same numerical methods are then employed to simulate the half-height experiment [6], a turbulent mixing experiment involving Richtmyer-Meshkov and Kelvin-Helmholtz instabilities. In the final section conclusions are drawn about the relative performance of each scheme.

2 NUMERICAL METHODS

Two significantly different numerical methods are employed. CNS3D is a finite volume Godunov method using a characteristics based Riemann solver [4], where second order accuracy is achieved through van Leer's MUSCL limiting technique [10] and the Total Enthalpy Conservation of the Mixture model is employed to model the gas mixture [11]. Time advancement is achieved using a 3rd order Runge Kutta method [9]. Turmoil uses a Lagrange-remap method [12]. A finite difference technique with quadratic artificial viscosity is used in the Lagrange phase and a third order van Leer monotonic advection method is used in the remap phase. For turbulent mixing problems a mass fraction advection equation is used for gas mixtures [13]. For shock tube applications the x-direction mesh (the direction of shock propagation) moves with the mean x-velocity i.e a semi-Lagrangian calculation is performed. Although the experiment is turbulent, the simulations do not have an explicit subgrid model and are thus classed as Implicit Large-Eddy Simulation (ILES) [3]. This is a class of structural subgrid models, where the dissipation inherent within the solution of the Riemann problem or the remap phase is employed to remove the turbulent kinetic energy from the resolved scales in a manner similar to that of a turbulence model.

3 SINGLE MODE RM

3.1 Initialisation

The initialisation for the single mode problem is identical to that used in Li and Zhang [7]. The size of the computational domain is $6 \times 1 \times 1$ and the boundary conditions are periodic in the y and z directions with

an extended one dimensional domain in the x direction to reduce the effects of reflected waves. The incident shock Mach number is 1.5 and travels in the positive x direction. The initial interface perturbation is defined as $a = a_0(cos(ky) + cos(kz))$ where $k = 2\pi$ and $ka_0 = 0.238$. The fluids have a density ratio $\rho_1/\rho_2 = 1/5$, and $\gamma_1 = \gamma_2 = 1.4$. Several grid resolutions have been employed, $30 \times 5 \times 5$, $60 \times 10 \times 10$, $120 \times 20 \times 20$, $240 \times 40 \times 40$ and $480 \times 80 \times 80$. In presenting the results, all lengths are non-dimensionalised by the wavelength of the initial perturbation, and times by the wavelength and post-shock interface velocity. All theoretical results are computed using the post-shock Atwood number $A^+ = 0.65$, and the post-shock amplitude $a_0^+ = 0.43$. Figure 3.1 shows the time development of the instability at the maximum grid resolution using CNS3D, through the linear and non-linear growth of the instability. It can be seen that the growth of the instability is dominated by the ring vortex structure as also seen in experimental studies [2].

(a) $t = 0$ (b) $t = 3.0$ (c) $t = 6.3$ (d) $t = 12.9$
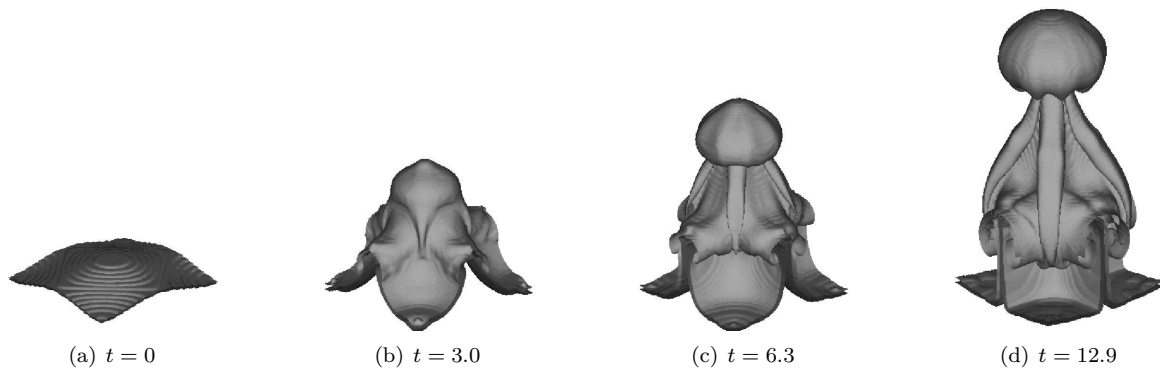
Fig. 3.1. Isosurfaces of constant volume fraction = 0.5 illustrating the development of the single mode RMI using CNS3D at the highest grid resolution

3.2 Results and Discussion

(a) Mixing layer width   (b) Bubble and Spike height
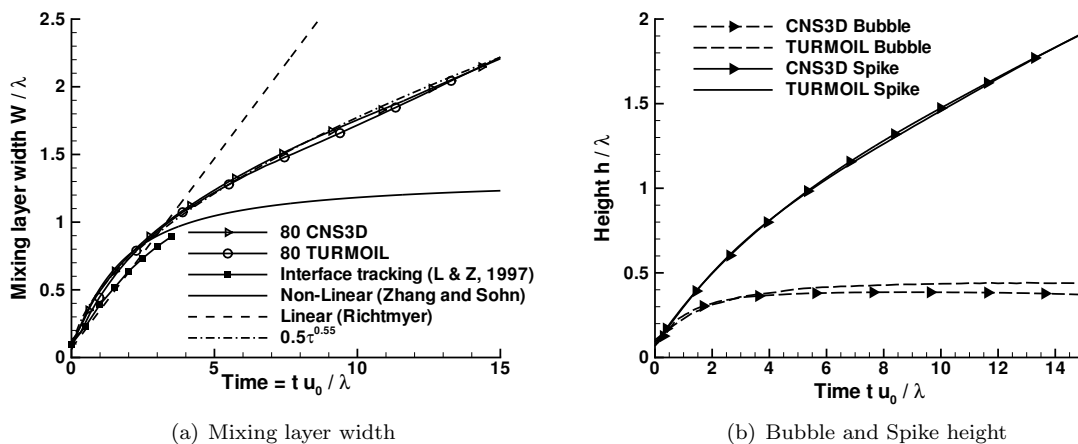
Fig. 3.2. Grid converged mixing layer widths

Figure 3.2 a) and b) show the grid converged mixing layer width compared to nonlinear theory [14] by Zhang and Sohn and linear by Richtmyer [8], and bubble and spike size as a function of time. It is clear that there is excellent agreement between the two numerical methods at both early and late times. The results of Li and Zhang [7] appear to grow more slowly, however, comparing their images it appears that the numerical scheme is more dissipative, and hence the simulation is under-resolved. The mixing layer width grows more rapidly than predicted by linear theory, however it is an excellent match for the non-linear theory of Zhang and Sohn [14] up to a non-dimensional time of about 2.5. After this time the growth is dominated by the

strong vortex ring which self-convects at a constant velocity. The dominance of this coherent structure causes the departure from non-linear theory, which depends on $1/t^2$ at late time. The behaviour over the time-scales considered within this study match a power law of $\tau^{0.55}$, where τ is the non-dimensional time.

(a) High Resolution
(b) Low Resolution
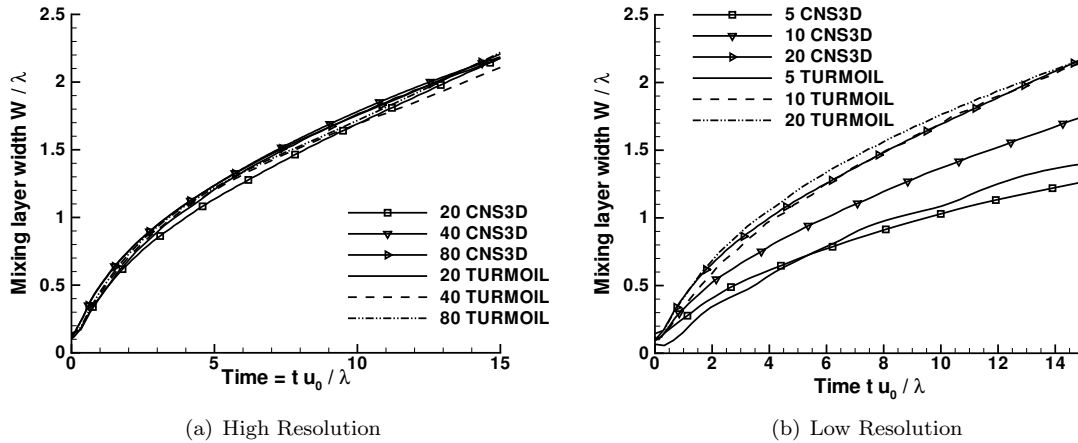
Fig. 3.3. Development of the mixing layer widths as a function of grid resolution and numerical method

The bubble and spike widths are also in excellent agreement. Given these initial conditions the spike exhibits continued growth due to the vortex ring, however bubble growth stagnates very rapidly. At very late time the bubble begins to grow again due to interaction with the developing turbulent mixing layer. In addition to the plots shown, identical runs using CNS3D with several different limiting methods (van Albada, Minmod, a third order limiter) have resulted in the same growth rates, as have simulations using a Roe scheme.

Figures 3.3a) and b) show the development of the mixing width as a function of mesh resolution for both numerical methods. The total width of the mixing layer reaches an approximately converged solution for 10 cells for Turmoil and 20 cells for CNS3D. The growth of the bubble and spike at the lower resolutions is shown in Figure 3.4 a) and b) for both numerical methods. The bubble growth is captured more accurately at low resolution using the Godunov method than the Lagrange-remap method. However, as resolution increases the Lagrange-remap method performs better. Examining the spike growth it can be seen that this is consistently underestimated at low resolutions as the numerical scheme damps the strength of the ring vortex. If the grid resolution is too low then the total circulation is too low and thus the vortex ring does not advect itself at the correct velocity. The Godunov scheme removes kinetic energy more rapidly than the Lagrang-remap scheme, leading to a weaker vortex at a given grid size (when under-resolved).
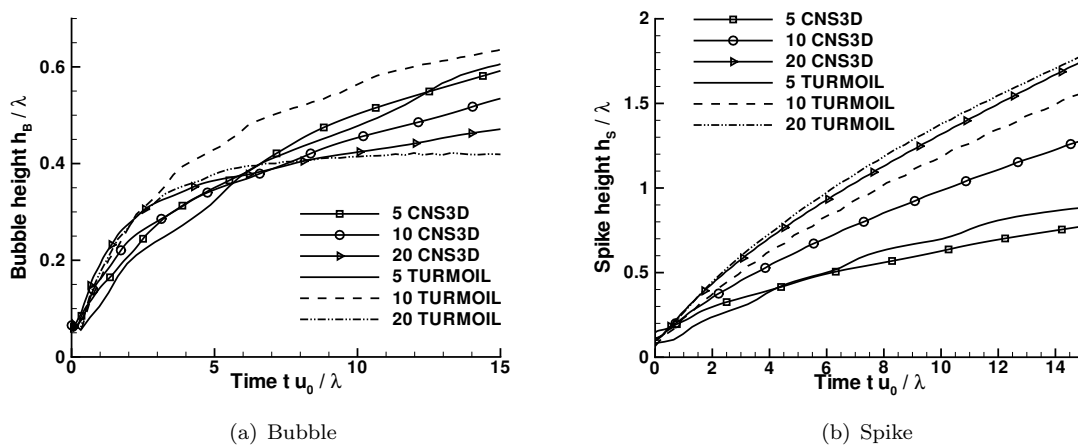
(a) Bubble
(b) Spike

Fig. 3.4. Development of the bubble and spike as a function of grid resolution and numerical method

Turmoil captures the growth rates in fewer cells as the dissipation inherent within the numerical scheme does not have a Mach number dependence. It is well known that at low Mach numbers Godunov schemes can be excessively dissipative [5]. Once the shock wave has passed, the maximum Mach number is 0.1, and decreases significantly with time. The Godunov schemes dissipate more heavily thus impeding the development of the vortex ring at low resolutions. This also changes the shape of the spike, in the Lagrange-remap schemes the spike is flatter at late times, whereas the Godunov method predicts a more spherical shape.

4 HALF-HEIGHT EXPERIMENT

4.1 Initialisation

The half-height experiment consists of a Mach 1.26 shock wave in air passing through a block of SF_6 filling half the shock tube. A schematic of the initial condition can be seen in Figure 4.5 (see [6] for more details). As the shock wave travels passes through the SF_6 it travels more rapidly through the air than the block, creating a strong Kelvin-Helmholtz shear and a complex series of reflected and transmitted shock waves. The main shock front reflects off the back wall of the shock tube and passes back through the mixing zone bringing it to a rest, and further increasing the mixing rate.
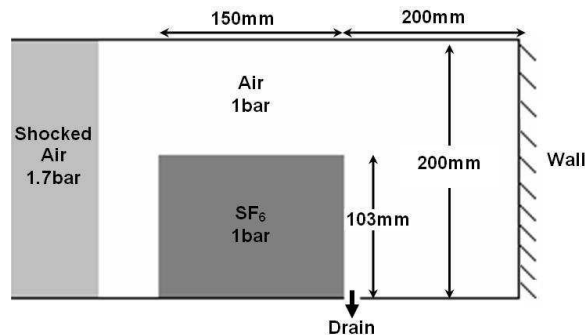
Fig. 4.5. Schematic of the half-height experiment, note that the shock tube is 100mm deep

The total domain size (initially in the case of the semi-Lagrangian code) extends from -0.45m to 0.35m in x, where $x = 0$ at the left SF_6 interface, and takes the shock tube dimensions in the other two directions. The mesh sizes chosen were $600 \times 160 \times 320$ for CNS3D and $640 \times 160 \times 320$ for Turmoil. The effects of grid size were investigated using a coarse resolution grid of $300 \times 80 \times 160$ with CNS3D, and a fine resolution grid of $1280 \times 320 \times 640$ with Turmoil. The boundary conditions are free slip walls in the z direction, with supersonic inlet and free slip wall in the left and right x direction. The y direction boundary conditions are periodic. Turmoil employs a one dimensional domain in the x direction instead of the inlet condition to allow waves to exit the domain without reflection. The drain hole was not modelled in TUMOIL3D as it was considered not to have a large effect on the turbulent mixing of the primary vortex. The initial perturbation imparted on the vertical gas interface by the membrane was modelled as a summation of random modes with RMS amplitude of 0.1mm at wavelengths between 5mm to 50mm satisfying a power spectra proportional to the wavenumber of the mode. The density of SF_6 and air were 6.34kg/m^3 and 1.153kg/m^3, and the Ratios of specific heats 1.076 and 1.4 respectively.

4.2 Results and Discussion

A comparison of the results from both codes and experiment at several different time instants are shown in Figure 4.6. At the first two time instants the shock wave is passing through the SF_6 block and the beginnings of the Kelvin-Helmholtz roll up is seen. Both simulations and the experimental images agree extremely well. The first differences can be seen at 1ms, where the higher resolution of Turmoil permits the growth of an unstable mode on the primary vortex generated by the Kelvin-Helmholtz instability, whereas CNS3D has damped this motion. In this frame the refracted shock wave converges at the lower right hand side of the block creating a high pressure, velocity and density region which leads to the visible 'bump' in numerical and experimental images.

At 2ms the reflected shock has passed through the 'bump' creating an almost single mode quasi-two-dimensional Richtmyer-Meshkov mushroom shaped spike. Also visible in experiment and simulations is the growth of an instability in the outer arm of the primary vortex. This is in almost the same position in experiment and simulation. At 3ms the simulations show that the mushroom shaped feature is pointed upwards, however in the experiment it is more horizontal. This is caused by the drain hole which acts as a supersonic jet exiting to atmospheric pressure, entraining the mushroom shaped perturbation. The primary vortex reaches the top of the shock tube at 3ms in both experiment and simulations, indicating that the growth of the length scales present in the experiment are captured well.

In comparing the two codes it is observed that the Godunov method captures the shock wave more accurately (without oscillations), however the Lagrange-remap method is generally less dissipative and allows the formation of many small scale features. The Turmoil simulation has approximately double the resolved turbulent kinetic energy at a given time instant. However, both codes predict the location of maximum plane averaged turbulent kinetic energy at 3ms to be at $x = 0.24 \pm 0.005m$. Convergence of the results has been examined via a simulation run at resolution $1280 \times 320 \times 640$ using Turmoil. It was found that profiles of plane averaged mixing ($< f_1 >< f_2 >$) and molecular mixing ($< f_1 f_2 >$) agree to within 15% for all simulations.

5   CONCLUSIONS

The converged growth rates of the single mode Richtmyer-Meshkov instability have been shown to be in good agreement with the theory of Zhang and Sohn [14] until the growth is dominated by the coherent ring vortex. Bubble growth stagnates very rapidly after the early non-linear stage, whereas the spike continues to grow due to self advection of the vortex ring. Comparing the two codes employed, the Godunov scheme requires more cells to resolve a single mode due to the Mach number dependence of numerical dissipation. The dissipation within the Lagrange-remap code is Mach uniform and hence the low Mach features of the mixing layer are better resolved. This is also reflected in simulations of the half-height mixing experiment, where both codes agree very well with experimental images, but Turmoil permits the evolution of relatively low Mach number modes.

REFERENCES

[1] W.D. Arnett, J.N. Bahcall, R.P. Kirshner, and S.E. Woosley. Supernova 1987a. *Annu. Rev. Astron. Astrophys.*, 27:629–700, 1989.

[2] P.R. Chapman and J.W. Jacobs. Experiments on the three-dimensional incompressible richtmyer-meshkov instability. *Phys. Fluids*, 18:074101, 2006.

[3] D. Drikakis and W. Rider. *High-Resolution Methods for Incompressible and Low-Speed Flows*. Springer Verlag, 2004.

[4] A. Eberle. Characteristic flux averaging approach to the solution of euler's equations. Technical report, VKI Lecture Series, 1987.

[5] H. Guillard and C. Viozat. On the behaviour of upwind schemes in the low mach number limit. *Comput. Fluids*, 28:63–86, 1999.

[6] D.A. Holder and C.J. Barton. Shock tube richtmyer-meshkov experiments: inverse chevron and half height. In *Proceedings of the 9th IWPCTM*, 2004.

[7] X.L. Li and Q. Zhang. A comparative numerical study of the richtmyer-meshkov instability with nonlinear analysis in two and three dimensions. *Phys. Fluids*, 9(10):3069–3077, 1997.

[8] R.D. Richtmyer. Taylor instability in shock acceleration of compressible fluids. *Comm. Pure Appl. Math.*, 13:297–319, 1960.

[9] R.J. Spiteri and S.J. Ruuth. A class of optimal high-order strong-stability preserving time discretization methods. *SIAM J. Sci. Comput.*, 4(2):469–491, 2002.

[10] B. van Leer. Towards the ultimate conservative difference scheme.iv. a new approach to numerical convection. *J. Comput. Phys.*, 23:276–299, 1977.

[11] S.P. Wang, M.H. Anderson, J.G. Oakley, and R. Corradini, M.L.and Bonazza. A thermodynamically consistent and fully conservative treatment of contact discontinuities for compressible multi-component flows. *J. Comput. Phys.*, 195:528–559, 2004.

[12] D.L. Youngs. Time-dependent multimaterial flow with large fluid distortion. In *Numerical Methods for Fluid Dynamics*, pages 273–285. Academic Press, 1982.

[13] D.L. Youngs. Three-dimensional numerical simulation of turbulent mixing by rayleigh-taylor instability. *Phys. Fluids A*, 3(5):1312–1320, 1991.

[14] Q. Zhang and S-I. Sohn. Nonlinear theory of unstable fluid mixing driven by shock wave. *Phys. Fluids*, 9(4):1106–1124, 1997.
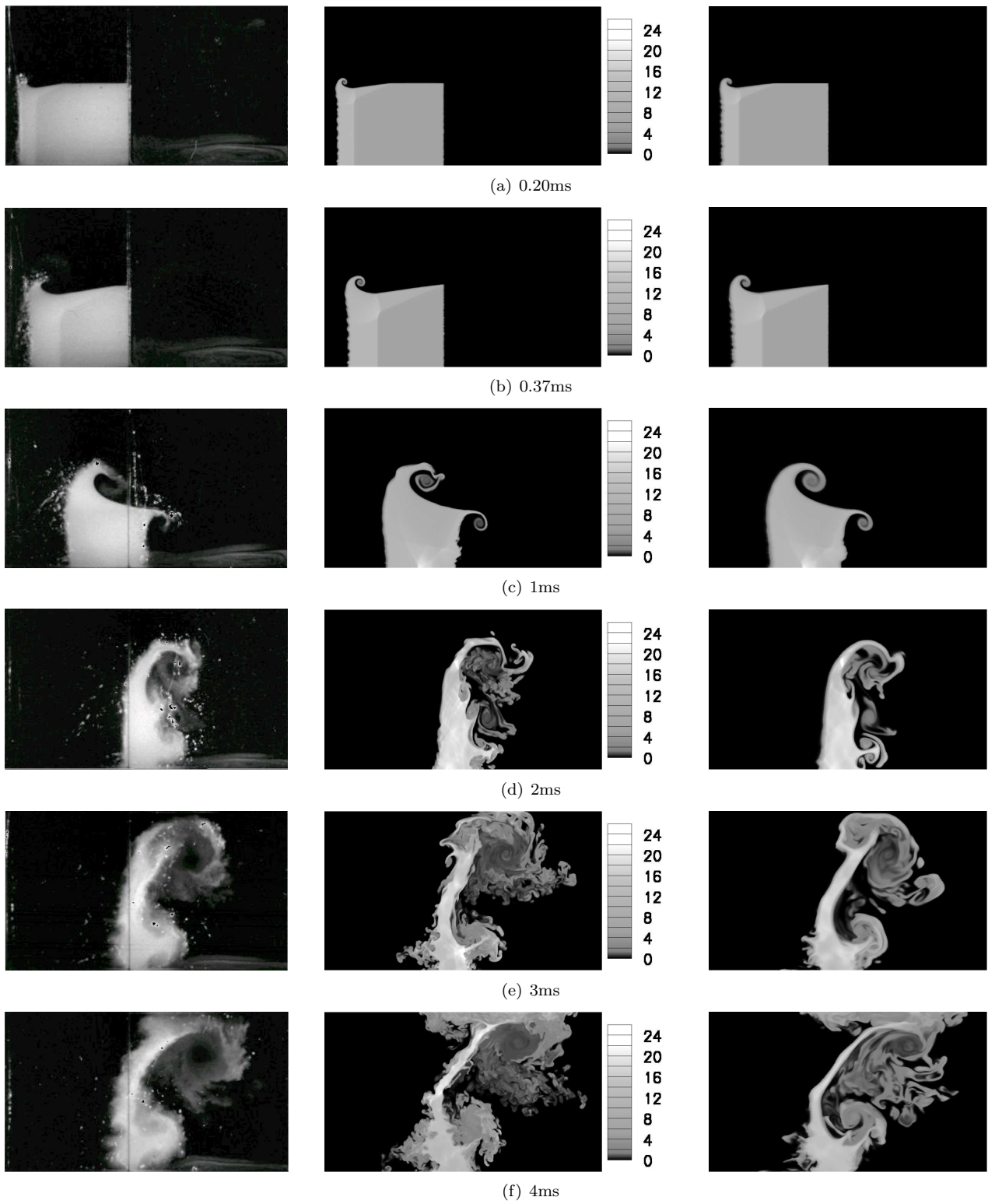
Fig. 4.6. Comparison of experimental images (left,©British Crown Copyright 2006/MOD) and SF_6 density (kg/m^3) for Turmoil at $640 \times 160 \times 320$ (centre) and CNS3D (right) at $600 \times 160 \times 320$

e-mail: marc.vandenboomgaerde@cea.fr

Nonlinear Richtmyer-Meshkov instability: Validation of theoretical models by comparisons with new experimental results and numerical simulations

M. Vandenboomgaerde[1], C. Boudesocque-Dubois[1], J. Griffond[1] & M. Boulet[1]

[1]*CEA/DAM Ile de France, BP 12, 91680 Bruyères-le-Châtel, France*

Abstract : We have derived two models in order to predict the nonlinear growth of the Richtmyer-Meshkov instability (IRM). Comparisons with experimental, numerical and other theoretical results are presented.

1 INTRODUCTION

The IRM occurs at the interface between two materials at the passage of a shock wave. Any perturbation of this interface first grows linearly, then nonlinearly; at late time, complex structures appear at the interface which then reaches a pre-turbulent regime. The nonlinear regime of the IRM, in the planar geometry, has been studied by numerous authors who derived algebraic solutions [1-3]. These ones have a limited range of validity due to a secular behaviour which leads to a divergence of the series in time. As a result, only the weakly nonlinear stage of the IRM can be studied by these methods. Others authors use boundary integral methods [4] which derivation is complex, or generalized Layzer-type solutions [5-8] which focus on the bubble and the spike.

In this paper, we present attempts to derive two tractable models to predict nonlinear IRM. The first one still uses algebraic solutions but some hypotheses allow to remove the secularity and therefore to study the nonlinear regime. It describes a single mode interface but deals with two fluid interface. The second one rewrites former work [9] using conformal mapping and Fourier transforms. It deals with a multimode interface but, at this time, only one fluid is considered.

The paper is organized as follows. In Sec. 2, we summarize the derivations of theses two nonlinear theories. In Sec. 3, some comparisons between our models and direct numerical simulation [10], experiments [11] and other models [6-8] are presented.

2 THEORETICAL DERIVATIONS

We consider a single-mode sinusoidal perturbation, described by $z = \eta(x,t)$ between two gases (see **Fig.2.1**). The fluids are considered inviscid and incompressible. The flow is supposed irrotational and the velocity in each fluid derives from a potential. The Atwood number is defined as $At = (\rho' - \rho)/(\rho' + \rho)$. The equations that have to be solved are the Laplacian equation for the potentials Φ, the motion equation of the interface in each fluid, and the Bernoulli's equation at the interface. In order to simplify these equations, we use the following change of variable:

Fig. 2.1: Sketch of the configuration

$$X = x, Z = z - \eta(x,t), T = t , \qquad (2.1)$$

which leads to a new set of equations. In a previous model [3], which used perturbation methods, the interface and the velocity potentials were written as:

$$\eta(x,t) = \sum_{n=1}^{\infty} \eta^{(n)}(x,t), \ \Phi(x,z,t) = \sum_{n=1}^{\infty} \Phi^{(n)}(x,z,t), \text{ where } \eta^{(n)} \text{ and } \Phi^{(n)} \text{ are propor-}$$

tional to the non-dimensional time, $\tau = a_0 k\sigma t$, to the power *n* and *n-1*, respectively. The parameters a_0, k, $a_0 \sigma$, are the post-shocked amplitude of the perturbation, its wave number, and the initial growth rate of the instability, respectively. Perturbation methods lead to divergent results for $\tau \approx 1$. In order to build a new approach, we use the following

expression for the interface: $\eta(X,T) = \sum_{i=1}^{\infty} A_i(T)\cos kX$, where the $A_i(T)$ are supposed to be continuous monotonic

functions of time. For the classical perturbation method, the main hypothesis was: $A_1 \gg A_2 \gg A_3 \gg \dots$ With the new model, this hypothesis evolves with τ: as τ grows, the $A_i(T)$ become of the same order. Let us remark that the perturbation method is exact for $\tau < 1$; so, classical and new approaches must match asymptotically for $\tau = 1$.

In order to solve the set of equations, several hypotheses are made:
- the potential velocities are written as in Eqs. 2.2

$$\Phi(X, Z, T) = \sum_{i=0}^{+\infty} \phi_i(Z, T) \; cos(ikX) \quad \text{with}$$

$$
\begin{cases}
\phi_0(Z,T) = B_{0,0}(T) + B_{0,1}(T)e^{-\frac{kZ}{\sqrt{(1)}}} + B_{0,2}(T)e^{-\frac{2kZ}{\sqrt{(2)}}} + B_{0,3}(T)e^{-\frac{3kZ}{\sqrt{(3)}}} + \dots \\[2mm]
\phi_1(Z,T) = \qquad\quad B_{1,1}(T)e^{-\frac{kZ}{\sqrt{(1)}}} + B_{1,2}(T)e^{-\frac{2kZ}{\sqrt{(2)}}} + B_{1,3}(T)e^{-\frac{3kZ}{\sqrt{(3)}}} + \dots \\[2mm]
\phi_2(Z,T) = \qquad\qquad\qquad\qquad B_{2,2}(T)e^{-\frac{2kZ}{\sqrt{(2)}}} + B_{2,3}(T)e^{-\frac{3kZ}{\sqrt{(3)}}} + \dots \\[2mm]
\phi_3(Z,T) = \qquad\qquad\qquad\qquad\qquad\qquad\qquad B_{3,3}(T)e^{-\frac{3kZ}{\sqrt{(3)}}} + \dots \\[2mm]
\dots
\end{cases}
\tag{2.2}
$$

$$\dot{A}_i = \frac{ikB_{i,i}}{\sqrt{(i)}} \quad \text{and} \quad B_{i,i} = -B'_{i,i} \tag{2.3}$$

- the dynamics of the interface is controlled by the $B_{i,i}$ (see Eqs.2.2). These hypotheses lead to Eqs.2.3 for the motion equation, and Eqs.2.4 from the Bernoulli's equations (parameters *(i)* are expressed in the first 3 expressions of Eqs.2.4).
- the $B_{i,j}$ are computed in order to cancel the terms leading to divergent solutions

As divergent terms, or terms leading to unphysical behaviour of the solutions are cancelled out by the $B_{i,j}$, the set of equations is expanded and simplified. The following system is obtained when three harmonics are considered:

$$
\begin{cases}
\dot{A}_1 = \dfrac{kB_{1,1}}{\sqrt{1 + \frac{1}{4}k^2A_1^2 + 2k^2A_2^2 + \frac{9}{2}k^2A_3^2}} \\[4mm]
\dot{A}_2 = \dfrac{2kB_{2,2}}{\sqrt{1 + \frac{1}{2}k^2A_1^2 + A_2^2 + \frac{9}{2}k^2A_3^2}} \\[4mm]
\dot{A}_3 = \dfrac{3kB_{3,3}}{\sqrt{1 + \frac{1}{2}k^2A_1^2 + 2A_2^2 + \frac{9}{4}k^2A_3^2}} \\[4mm]
\dot{B}_{1,1} = At\left(-k^2 B_{1,1}B_{2,2}(1 - \dfrac{1 + k^2A_2^2 + \frac{3}{2}k^2A_1A_3 + \frac{9}{2}k^2A_3^2}{\sqrt{1 + \frac{1}{4}k^2A_1^2 + 2k^2A_2^2 + \frac{9}{2}k^2A_3^2}\sqrt{1 + \frac{1}{2}k^2A_1^2 + A_2^2 + \frac{9}{2}k^2A_3^2}})\right. \\[4mm]
\quad -3k^2 B_{2,2}B_{3,3} + kA_2 \dfrac{k^2 B_{2,2}^2}{1 + \frac{1}{2}k^2A_1^2 + A_2^2 + \frac{9}{2}k^2A_3^2}(kA_1 + 3kA_3) \\[4mm]
\quad \left. -\frac{1}{2}k^2 A_1A_2 \dfrac{3k^2 B_{1,1}B_{3,3}}{\sqrt{1 + \frac{1}{4}k^2A_1^2 + 2k^2A_2^2 + \frac{3}{2}A_1A_3 + \frac{9}{2}k^2A_3^2}\sqrt{1 + \frac{1}{2}k^2A_1^2 + 2A_2^2 + \frac{9}{4}k^2A_3^2}}\right) \\[8mm]
\dot{B}_{2,2} = At\left(\frac{1}{4}\dfrac{k^2 B_{1,1}^2}{1 + \frac{1}{4}k^2A_1^2 + 2k^2A_2^2 + \frac{9}{2}k^2A_3^2}(1 + k^2A_2^2 + \frac{3}{2}k^2A_1A_3 + \frac{9}{2}k^2A_3^2)\right. \\[4mm]
\quad + k^2 A_1A_2 \dfrac{k^2 B_{1,1}B_{2,2}}{\sqrt{1 + \frac{1}{2}k^2A_1^2 + A_2^2 + \frac{9}{2}k^2A_3^2}\sqrt{1 + \frac{1}{2}k^2A_1^2 + 2A_2^2 + \frac{9}{2}k^2A_3^2}} \\[4mm]
\quad \left. -\frac{3}{4}k^2 A_1^2 \dfrac{k^2 B_{2,2}^2}{1 + \frac{1}{2}k^2A_1^2 + A_2^2 + \frac{9}{2}k^2A_3^2} - 3k^2 A_1A_2 \dfrac{k^2 B_{2,2}B_{3,3}}{\sqrt{1 + \frac{1}{2}k^2A_1^2 + A_2^2 + \frac{9}{2}k^2A_3^2}\sqrt{1 + \frac{1}{2}k^2A_1^2 + 2A_2^2 + \frac{9}{4}k^2A_3^2}}\right) \\[8mm]
\dot{B}_{3,3} = At\left(-\frac{1}{4}k^2 A_1A_2(\dfrac{k^2 B_{1,1}^2}{1 + \frac{1}{4}k^2A_1^2 + 2k^2A_2^2 + \frac{9}{2}k^2A_3^2} + \dfrac{4k^2 B_{2,2}^2}{1 + \frac{1}{2}k^2A_1^2 + A_2^2 + \frac{9}{2}k^2A_3^2} + \dfrac{27k^2 B_{3,3}^2}{1 + \frac{1}{2}k^2A_1^2 + 2A_2^2 + \frac{9}{4}k^2A_3^2}, \right. \\[4mm]
\quad + \dfrac{k^2 B_{1,1}B_{2,2}}{\sqrt{1 + \frac{1}{4}k^2A_1^2 + 2k^2A_2^2 + \frac{9}{2}k^2A_3^2}\sqrt{1 + \frac{1}{2}k^2A_1^2 + A_2^2 + \frac{9}{2}k^2A_3^2}}(1 + \frac{1}{4}k^2A_1^2 + k^2A_2^2 + \frac{9}{4}k^2A_3^2) \\[4mm]
\quad \left. - \dfrac{6k^2 B_{2,2}B_{3,3}}{\sqrt{1 + \frac{1}{2}k^2A_1^2 + A_2^2 + \frac{9}{2}k^2A_3^2}\sqrt{1 + \frac{1}{2}k^2A_1^2 + 2A_2^2 + \frac{9}{4}k^2A_3^2}}(\frac{1}{4}k^2A_1^2 + \frac{1}{2}k^2A_2^2 - \frac{3}{4}k^2A_1A_3)\right)
\end{cases}
\tag{2.4}
$$
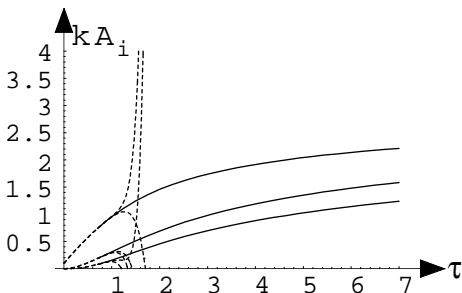
Fig. 2.2: Growth of harmonics from Eq. 2.4. Asymptotic matching with perturbation theory (dotted lines) is done for $\tau \approx 1$. At=1.
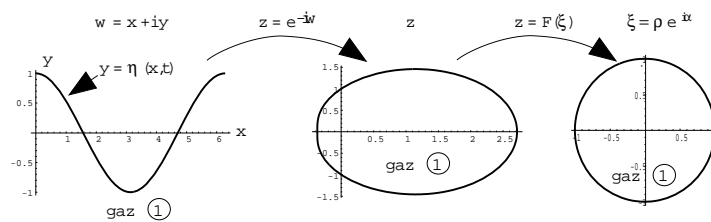
Fig. 2.3: Principle of the conformal mapping solution. At=1.

As we suppose that the dynamics of the instability is "led" by the $B_{i,i}$, we will hereafter refer to this model as the leading term model.

The solutions of Eqs.2.4 are obtained numerically with symbolic computation software and lead to saturated growths of each harmonics, as shown for *At=1* in **Fig.2.2**. However, such results are not exact solutions of the initial problem: once put back in the initial system of Laplacian, motion and Bernoulli equations, some residues remain. It has been checked that these residues tend toward zero with time. So we are confident that the Eqs. 2.4 give a solution which tends to and approximates the exact solution.

The other model which has been derived studies nonlinear IRM via conformal mapping [9]. Only one incompressible fluid is considered. The initial set of equations is solved on a circle by conformal transforms of the physical interface (see **Fig. 2.3**) and potentials. Unfortunately, as this mapping is estimated through Fourier transforms, aliasing errors occur and the estimated solution diverges. Application of anti-aliasing filters is under progress.

3 VALIDATION OF THE MODELS AND QUANTITATIVE RESULTS

Simulations of a shock tube experiment [11] have been carried out by the CEA hydro-code TRICLADE [10]. The post-shocked Atwood number is 0.635. Gases are a mix of air and acetone, and SF$_6$. The Mach number of the incident shock wave is 1.3. The initial perturbation is a single-mode sinusoidal. In **Fig.3.1**, we present a comparison between results from TRICLADE and two theoretical models: perturbation method and leading term model. It can be noticed that the perturbation method [3] over-estimates numerical data before the secularity; this could indicate that the range of validity of this theory is shorter than anticipated with the rule $\tau \approx 1$. On the other hand, the leading term nonlinear model, once initiated with numerical data, predicts a growth which only slightly over-estimates the simulation, even far beyond the weakly nonlinear regime. Let us remark that both numerical and leading term results are in good agreement with the experimental data presented in [12].
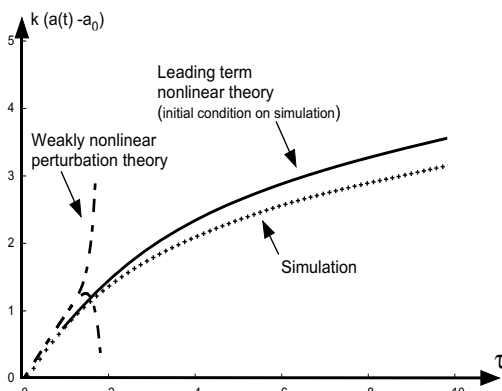
Fig. 3.1: Half peak-to-valley amplitude for simulation (symbols), perturbation theory (dashed-dotted line) and leading term model (full line). At=0.635.
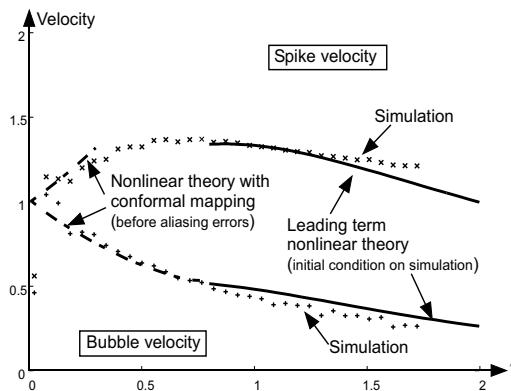
Fig. 3.2: Bubble and spike velocities for simulation (symbols), and nonlinear models with conformal mapping (dashed-dotted line) and leading terms (full lines). At=1.

Bubble and spike velocities are now studied by comparisons between numerical simulation [10] (*At=0.99*) and our models for *At=1*. The results are presented in **Fig. 3.2**. For the bubble velocity, both models show good agreement with the numerical simulation in their respective range of validity, *i.e.,* before aliasing for conformal mapping model and for *ka(t) > 1* for leading term model. For the spike velocity, the range of validity is very small for the conformal mapping model; this is not the case for the other model which under-estimates slightly the nu-

merical results. Some models [6-8] give the evolution of the bubble velocity as a function of time. We present in **Fig. 3.3**, comparisons between the results of Sohn's model [7] and our nonlinear models for *At=1*. Once again, the agreement between the different theories is very good in their range of validity. It has been checked that this good agreement is also true for the other cited models [6,8].
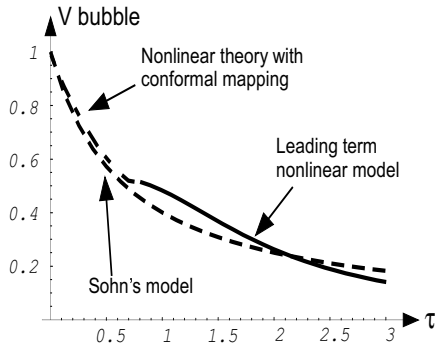
Fig. 3.3: Bubble velocity. Dashed curves are from Sohn [7], dashed-dotted and full lines are obtained from conformal mapping and leading term models, respectively. At=1.
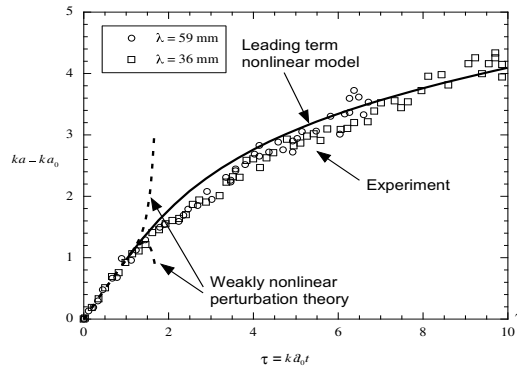
Fig. 3.4: Half peak-to-valley amplitude for M=1.3, air-acetone/SF$_6$ shock tube experiment [11] and leading term nonlinear model. At=0.635.

Finally, in order to validate the nonlinear model derived from the leading term hypotheses, we present in **Fig. 3.4** a comparison between experimental results [11] and theory. Here, in order to fit with the experimental data, the initial conditions of the model are obtained by asymptotic matching with the weakly nonlinear perturbation model [3]. It can be verified that the agreement between the model and the experiment is excellent, even for time as long as $\tau=10$. At this time, the experiment shows that the interface presents mushroom structures and is multivalued. Our model cannot describe such interface; nevertheless, the amplitude is correctly predicted. This could mean that the form of potentials, Eqs.2.2, is correct for the bubble and the spike, even in far nonlinear regime.

4 CONCLUDING REMARKS AND DISCUSSION

New nonlinear models have been derived; the first one uses some hypotheses in order to get rid off the secular behaviour of perturbation method: the main one is that the dynamics of each harmonics is led by the first term in the expansion of its potential (see Eqs. 2.2). This model gives the growth of a single-mode perturbation for the IRM. This result is obtained by solving a set of coupled ordinary differential equations. The pseudo-solution which is obtained seems to be a good approximation of the exact solution. Indeed, several comparisons with experimental, theoretical and numerical results show good agreements for a wide range of Atwood numbers. This remains true from linear to nonlinear regime. The second model uses conformal mapping in order to solve the equations of the dynamics of the interface on a circle with Fourier transforms. First results show a good agreement with numerical and theoretical results before aliasing errors make the solution to diverge.

New experiments [13] are in progress in order to further validate the leading term model. These experiments use a new grid which is built by stereo-lithography; this gives a good knowledge of the initial shape of the interface which will allow precise comparisons between experimental and theoretical data.

REFERENCES

[1] Q. Zhang and S-I. Sohn, Phys. Fluids **9**, 1106 (1996).
[2] A.L. Velikovich and G. Dimonte, Phys. Rev. **76**, 3112 (1996).
[3] M. Vandenboomgaerde, S. Gauthier and C. Mügler, Phys. Fluids **14**, 1111 (2002).
[4] C. Matsuoka and K. Nishihara, Phys. Rev. E **73**, 026304 (2006).
[5] D. Layzer, Astropys. J. **122**, 1 (1995).
[6] K.O. Mikaelian, Phys. Rev. E **67**, 026319 (2003).
[7] S-I. Sohn, Phys. Rev. E **67**, 026301 (2003).
[8] V.N. Goncharov, Phys. Rev. Lett. **88**, 134502 (2002).
[9] D.I. Meiron and S.A. Orszag, J. Comp. Phys. **40**, 345 (1981).
[10] M. Boulet and J. Griffond, "3D numerical simulation of experiments on the RM induced mixing with reshock", Proceedings of the 10th IWPCTM.
[11] J.W. Jacobs and V.V. Krivets, Phys. Fluids **17**, 034105 (2005).
[12] B. Motl, J. Oakley, M. Anderson and R. Bonazza, "Shock accelerated two-dimensional interface", Proceedings of the 10th IWPCTM.
[13] C. Mariani, G. Jourdan and L. Houas, "Experimental investigation of the interaction of a plane shock wave with sinusoidal and spherical gaseous interfaces" , Proceedings of the 10th IWPCTM.

e-mail: `bonazza@engr.wisc.edu`

The Rayleigh-Taylor Instability at a Water/Magnetorheological Fluid Interface

Jeremy WHITE, Jason OAKELY, Mark ANDERSON, and Riccardo BONAZZA

University of Wisconsin-Madison, Madison WI 53706, USA

Abstract: We report on experiments that make use of a magnetorheological (MR) fluid to form a membraneless interface with water. An MR fluid can be "frozen" into well-defined shapes by applying a magnetic field of sufficient magnitude. When the magnetic field is released, the MR fluid behaves as a nearly Newtonian fluid. This magnetic property is used to study 2-D single mode interfaces in a test chamber of rectangular cross section. The MR fluid is a suspension of Fe particles [~30% by volume] in hexane. The MR fluid is optically opaque and the interface is imaged with diffuse back lighting. The growth rates are compared with previous MR experiments and with potential theory-based asymptotic solutions.

1 INTRODUCTION

An interface between two different fluids that is accelerated such that the light fluid pushes the heavy fluid is considered unstable. Such a configuration is considered Rayleigh-Taylor unstable if that acceleration is sustained, whereas the Richtmyer-Meshkov instability involves an impulsive acceleration [1,2]. These types of hydrodynamic instabilities have been found to occur in many settings, such as astrophysics and inertial confinement fusion. Their presence in the fusion process is the main motivation for their study, as these instabilities cause unwanted mixing, thereby reducing the yield of the fusion reaction. Studying these instabilities has presented a particularly interesting challenge: how to set-up the initial conditions. One of the biggest hurdles to setting up a Rayleigh-Taylor experiment is generating the initial conditions. The interface needs to have no initial velocity and, ideally, the spectral content of the perturbations should be well characterized. Accomplishing this experimentally is an interesting challenge, and has resulted in many different approaches. These techniques include: two parallel channels of flowing water at different temperatures initially separated by a wall [3], an initially stable configuration of immiscible fluids subjected to an arbitrary acceleration [4] and an unstable configuration where the two fluids are initially separated by a removable barrier [5]. Another technique uses the unique properties of a magnetorheological fluid to generate the interface [6]. This technique has been expanded upon here by using an MR fluid with a lower viscosity and surface tension to enhance the interfacial mixing.

2 EXPERIMENTAL SETUP

A magnetorheological (MR) fluid is a suspension of carbonyl iron powder in a carrier fluid. The previous experiments utilized mineral oil for the carrier fluid, while the experiments described here use hexane. The carrier fluid was changed to significantly lower the viscosity and surface tension of the MR fluid. Oleic acid is also added in small amounts to prevent agglomeration of the iron particles after the magnetic field is released. A useful advantage of using a suspension like this, as can be seen in Table 1.1, is that the Atwood number can be adjusted by varying the volume fraction of the iron particles. The major properties of the MR fluids studied so far are summarized below in Table 1.1, which gives the volume fractions of the carbonyl iron powder (ϕ), density (ρ), viscosity (μ), interfacial tension (T), time constant (τ) and Atwood number (A).

Carrier Fluid	ϕ	$\rho\ [kg/m^3]$	$\mu\ [Pa\text{-}s]$	A	$\tau\ [s]$	$T\ [N/m]$
Hexane	0.317	2735	Est. ~ 0.002	0.465	0.1179	~ 0.05
Mineral Oil	0.15	1782	0.1	0.282	0.1515	~ 0.51
Mineral Oil	0.2	2050	0.15	0.345	0.1369	~ 0.51
Mineral Oil	0.3	2772	0.77	0.471	0.1173	~ 0.51

Table 1. 1. Magnetorheological Fluid Properties

The MR fluid is shaped inside a test section of rectangular cross section (6.35 x 1.27 cm^2). A single mode, 2-D sinusoidal perturbation with a wavelength of 2.12 cm and an initial amplitude of 0.32 cm is created by freezing water over a

machined plunger. The MR fluid is then poured over this ice and then frozen using two banks of magnets (Figure 1). Then, once the ice is melted and replaced with water, the magnets are removed and the growth of the interfacial perturbations is imaged using diffuse backlighting and a high-speed digital camera. Figures 1 and 2 below show the test section placed between the banks of magnets and the shaped plunger in the test section.
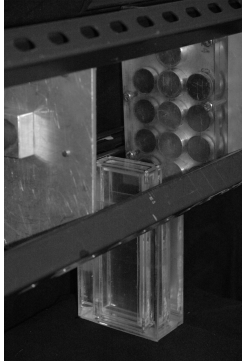
Fig. 2.1. Test Section and Magnets
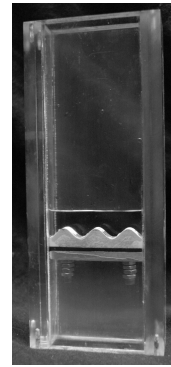
Fig. 2.2. Test Section Before Freezing

3 RESULTS
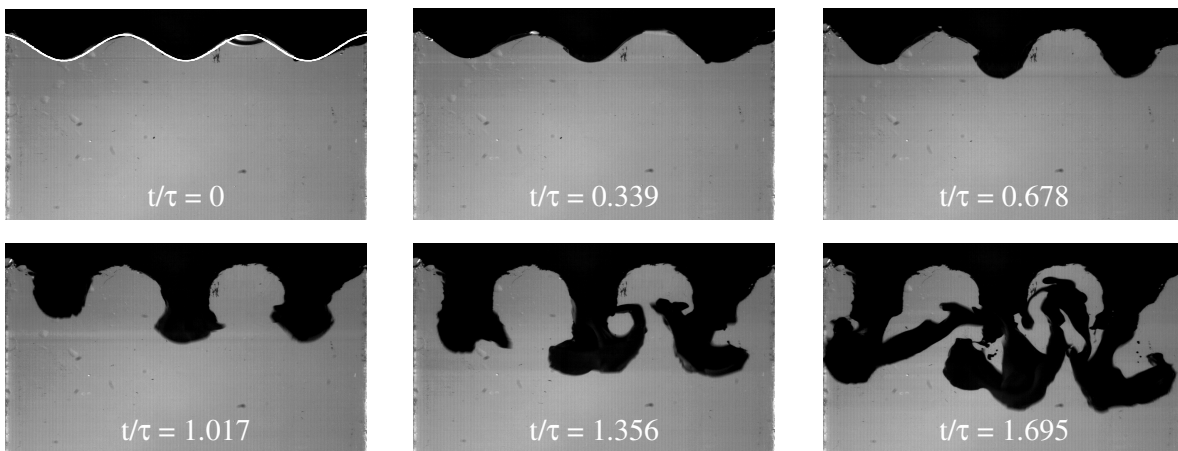
Fig. 3.1. Montage from a single mode initial condition experiment

The set of images in Fig. 3.1 is a sequence from a single experiment using a hexane based MR fluid (opaque) superposed over water. The desired initial conditions are superposed on the first image, showing that the interface shaping process works very well. The interface that is produced is very well defined, with the only discrepancy being the presence of a small air bubble that is due to various challenges in preparing the interface. The opaque nature of the MR fluid precludes the observation of the water rising and so we are limited to observing the MR fluid falling into the water.

Some asymmetry can be seen in the development of the interfacial mixing in Fig. 3.1. The MR fluid on the right side of the test section seems to fall slightly earlier than that on the left side. This can be attributed to the presence of the air bubble near the interface as this will have greater buoyancy than the water and hence will initially push up the MR fluid faster than if there were only water present. The side-walls of the test section do not appear to have any significant effect on the growth of the perturbations until late times, when the MR fluid veers towards the wall on the left side. This is consistent with previous experiments done with mineral oil based MR fluids, where the effect was found to increase in strength with perturbations located closer to the walls [6]. Further comparisons with the previous experiments reveal that the width of the perturbations grow much more quickly with the lower viscosity MR fluid, yielding more well defined Kelvin-Helmholtz rollups and faster mixing.

The following figures give a brief comparison of the growth using the two different kinds of MR fluids. Figure 3.2 shows the data for the hexane MR fluid compared with data from a mineral oil MR fluid. These are presented in non-dimensional form where L is the width of the test section and $\tau = (L/Ag)^{0.5}$ is the time constant taken from Table 1.1. This non-dimensionalization works quite well as the two data sets nearly collapse to a single line, with the error bars overlapping, even though the Atwood numbers are very different. Figure 3.3 compares the asymptotic velocities with predictions based on a potential theory solution [7], which is given for an RT spike by Equation 3.1:

$$V_{s,\infty}^{2D} = \sqrt{\frac{2A}{1-A}\frac{g}{3k}} \quad , \qquad\qquad (3.1)$$

The asymptotic velocity is thus just a function of three parameters: the Atwood number A, the acceleration constant g, and the wave number of the perturbation k. The measured velocities grow with increasing Atwood number, just as the theory predicts, but the values are under predicted by the theory. This theory was derived using inviscid, incompressible assumptions, which may account for the differences, as the fluids used here can hardly be considered inviscid. Comparing MR fluids of similar iron concentrations (similar Atwood number), we can see that the terminal velocity of the lower viscosity fluid is closer to the inviscid theory predictions. It is interesting to note that the viscosity of the mineral oil-based fluids increases with increasing Atwood number, though the experimental results still seem to have the same relationship to the Atwood number as the inviscid theory.
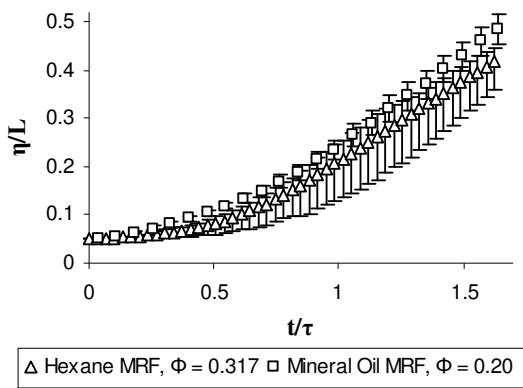
Fig. 3.2. Normalized Amplitudes
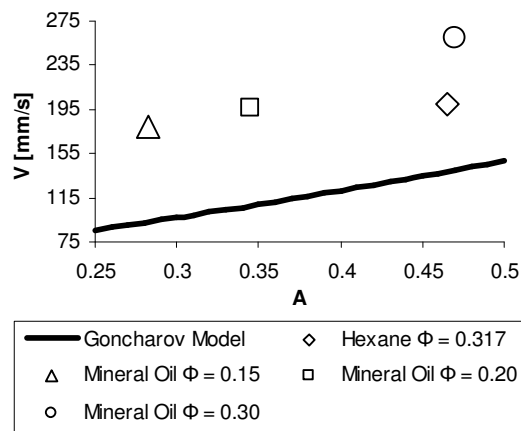
Fig. 3.3. Asymptotic Velocities

4 SUMMARY

An extension of the magnetorheolgical fluid experiments [6] using lower viscosity fluids has been carried out with few additional complications. This reduced viscosity has been found to lower the asymptotic velocity of the Rayleigh-Taylor spikes, as well as promote more intense mixing as witnessed by the increased size and faster development of the Kelvin-Helmholtz vortices at late times. Reasonably good comparisons were found with an inviscid theory even though the viscosity of the MR fluids is too large to be neglected. Further comparisons will be done with other available theories and with numerical results. The experimental apparatus has already been modified slightly for future work to remove the air bubbles for even better initial conditions. With the updated equipment, this new fluid will be used to study what effects, if any, different perturbations have on each other. Growth from interfaces with single and multiple perturbations will be compared, and multimode perturbations will also be looked at to study modal competition effects. The ability to change the carrier fluid of the MR fluid will also allow for examination of the effects of different viscosities as well as help to expand the Atwood number space of the data.

REFERENCES

[1]   Lord Rayleigh. "Investigation of the Character of Equilibrium of an Incompressible Heavy Fluid of Variable Density." *Proceedings of the London Mathematical Society*, Vol. XIV, 1883.

[2]   Taylor, Sir G. "The Instability of Liquid Surfaces when Accelerated in a Direction Perpendicular to their Planes. I" *Proceeding of the Royal Society*, A. Vol. 201, 1950.

[3]   Andrews, M.J; Ramaprabhu, P. "Experimental investigation of Rayleigh-Taylor mixing at small Atwood numbers." *Journal of Fluid Mechanics*, Vol. 502, 2004.

[4]   Dimonte, G; Schneider, M. "Density ratio dependence of Rayleigh-Taylor mixing for sustained and impulsive accleration histories." *Physics of Fluids*, Vol. 12-2, 2000.

[5]   Dalziel, S. B; Linden, P. F; Youngs, D. L. "Self-similarity and internal structure of turbulence induced by Rayleigh-Taylor instability." *Journal of Fluid Mechanics*, Vol. 399, 1999.

[6]   White, J; Selig, C; Oakley, J; Anderson, M; Bonazza, R. "The Rayleigh-Taylor Instability at a Water/Magnetorheological Fluid Interface." *Proceedings of the 9th International Workshop on the Physics of Compressible Turbulent Mixing*, July 2004.

[7]   Goncharov, V. N. "Analytical Model of Nonlinear, Single-Mode, Classical Rayleigh-Taylor Instability at Arbitrary Atwood Numbers." *Physical Review Letters*, Vol 88, Iss. 12, 2002.

e-mail: `robin.williams@awe.co.uk`

Richtmyer-Meshkov mixing at stably accelerated interfaces

R. J. R. WILLIAMS[1] and D. L. YOUNGS[1]

[1] *AWE Aldermaston, Reading, RG7 4PR, UNITED KINGDOM*

Abstract: The dispersion relation for surface modes on interfaces stable to Rayleigh-Taylor instability suggests that linear modes should propagate across them with constant amplitude. For nonlinear perturbations, it would be expected that significant losses in amplitude may occur. To investigate this, we study the late-stage development of Richtmyer-Meshkov instability on surface which is Rayleigh-Taylor stable after shock passage using high resolution three dimensional simulations with TURMOIL 3D. In particular, we investigate the variation in turbulent energy and mixing parameters with time. We compare the results to a 1D mix model, to quantify the effectiveness of demixing in this regime.

1   INTRODUCTION

When a shock passes across a density jump, deposition of vorticity due to the presence of surface perturbations leads to the growth of a mixing layer, a process described as Richtmyer-Meshkov instability. In most analyses, the flow is treated assuming that after the shock passage the flow is at constant velocity. However, in many practical situations, the subsequent flow may be accelerated or decelerated.

Depending on the direction of this post-shock acceleration, the interface will either be unstable or stable to the subsequent growth of Rayleigh-Taylor instability. Where it is unstable, the RM growth will create the initial conditions for subsequent RT growth, but at late time the effects of the RT growth will dominate the RM driving.

Where the subsequent acceleration is in the stable direction, one would expect that the RM mixing would be suppressed, but not completely so. Indeed, for small amplitudes the surface modes have constant amplitude. However, damping by viscosity or nonlinear mode-coupling should eventually lead to mixing.

In this paper, we explore this process using three dimensional MILES modelling with TURMOIL 3D. We compare the results of these simulations with one-dimensional mix model results, as a means of validating the form of additional terms required to treat mixing processes in this situation.

2   SIMULATION CONDITIONS

Stable post-shock acceleration can occur in a variety of circumstances in physical systems. Where the shock propagates from a fast medium to a slow medium, this will occur if the shock is followed by a rarefaction, as is typical for a blast wave. In the present paper, we look at the case where the shock propagates from a slow to a fast medium, where the stable post-shock acceleration can be driven, for example, if the shock had formed within an initially resolved compression wave or by the effects of geometrical convergence on the post shock flow.

The initial conditions for the Richtmyer-Meshkov growth may be set either by explicit shock modelling, or using analytic results for the vorticity deposited at the surface by the shock passage.

Explicit modelling can be physically accurate, including the details of the large scale flow in which the interface is embedded and interface-scale effects such as shock proximity (Glendinning et al 2003). However, such simulations either require a large domain to be calculated, or tend to suffer from unphysical reflections from boundaries. When the principal interest is in the small scale dynamics of the mixing region, it makes sense instead to concentrate on idealized small-scale regions.

To apply the vorticity deposition conditions, the fluid is perturbed using linear modes with amplitudes which depend on the initial surface profile. The relationship between profile and vorticity deposition may approximated by one of two means. Weak shocks may be approximated as impulsive acceleration and deceleration
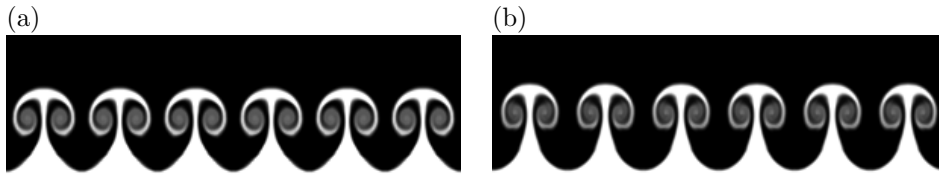
Fig. 3.1. Comparison of 2D simulation results with (a) explicit initial surface amplitude and shock; (b) vorticity deposition model. Colours give the mass fraction of each phase.

of the front, so the standard Rayleigh-Taylor formula for mode growth can be used to determine the change in flow velocity (Richtmyer 1960; Mikaelian 1985). Alternatively, the circulation deposited may be determined for the oblique shock-plane surface interaction at the local surface inclination (e.g. Samtaney et al 1998). In both cases, the linear growth of Fourier modes is given by $a = a_0 + ut$, so the initial velocity pertubation soon dominates the surface profile.

In the simulations presented here, we model a region $0.5 \times 0.5 \times 2$ units in size, with the initial interface half way across the long dimension. We use a numerical resolution of 300 cells per unit length in each dimension. The initial density and pressure are set using a Riemann problem where a Mach 1.844 shock interacts with an interface between gas of density 3 and and of density 1, where the initial pressure is 1. The materials modelled are perfect gases with $\gamma = 5/3$, and the more diffuse phase has a specific heat capacity 3 times that of the less diffuse one. We vary the conditions away from the interface using an adiabatic lapse law to ensure that each phase is marginally stable to buoyant perturbations, although for the grid sizes and accelerations we use, this does not change the phase properties by a significant amount.

The vorticity perturbation is calculated from an initial surface form where the perturbations are in a narrow wave band $\lambda = 16\Delta x - 32\Delta x$ in all cases, apart from single-mode calculations used to validate the vorticity deposition model.

3 VALIDATING THE INITIAL CONDITIONS

In Figure 3.1, we compare the results of two-dimensional simulations both using a single-mode sinusoidal perturbation calculated by using an explicit surface profile and modelling the shock transit, and also by including modes determined from vorticity depostion by impulsive Rayleigh-Taylor growth, reduced by shock compression factor, as inferred by Richtmyer (1960). We see that the vorticity deposition model does a good job of reproducing the explicit results, without the need for an extended grid or elaborate boundary conditions to avoid shock reflections. We therefore use vorticity deposition for the initial conditions for the further simulations presented here.

4 THREE-DIMENSIONAL SIMULATIONS

With no applied acceleration, Figure 4.2, the interface grows as usual for self-similar Richtmyer-Meshkov instability. There is strong mixing at the interface, with discrete vortex rings escaping the mixing region at early time.

With a gravitational acceleration $g = -2 \times 10^{-3}$ suppressing the instability, Figure 4.3, while the initial growth seems similar to the non-accelerated case, at later times the flow relaxes towards stable stratification. Escaping vortices are decelerated by buoyancy and break up (in two dimensional simulations, they follow looping paths, eventually coming back to the mixing layer). Significant mixing occurs, nonetheless, and the front continues to oscillate at late times. Motions in the plane of the stratification remain, but do not contribute significantly to mixing as a result of the density stratification.

We attempted to characterise the mixing efficiency by comparing the potential energy gain with the initial flow kinetic energy for a range of gravitational suppressions. For $g = 2 \times 10^{-3}$, approximately 2.5% of the initial KE is converted into potential energy, while for $g = 10^{-2}$ this increases to 7.5%. These numbers are only approximate, however, since about one third as much energy remains in long-wavelength gravity waves within the structure, leading to large fluctuations in the potential energy at late time.
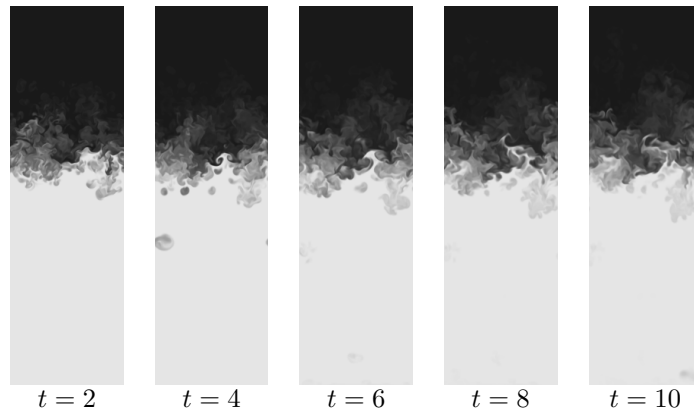
Fig. 4.2. Results for a pure Richtmyer-Meshkov simulation.
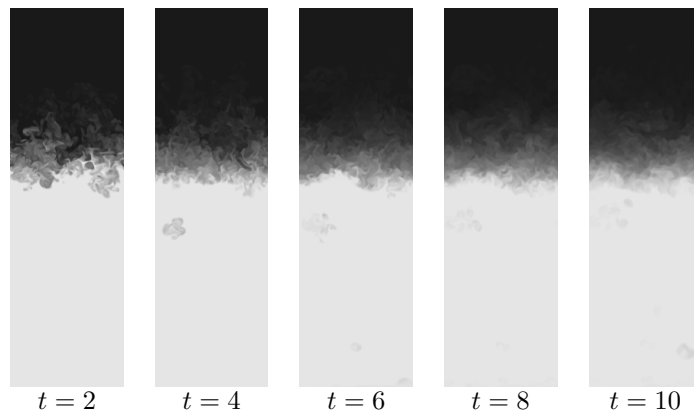
Fig. 4.3. Results for a Richtmyer-Meshkov simulation with an imposed acceleration $g = -2 \times 10^{-3}$ acting to suppress the instability.

4.1 Comparing LES with a 1D mix model

In Figure 4.4, we compare 3D MILES results (black, widths at 1% and 99%) with Youngs' buoyancy-drag model (red, widths scaled ×2.5) with an initial lengthscale equal to that of the shortest wavelength perturbation. In the buoyancy-drag model, ordinary differential equations are solved for the height and velocity of the bubbles and spikes which dominate the mixing layer. The stabilizing gravity force acts to decelerate both bubbles as spikes, but we assume that the velocity never becomes negative, i.e. that no demixing can occur at or below the dominant scale at any time.

The results at early time agree well, although the drag to zero velocity for $g < 0$ somewhat too fast and the long timescale oscillations at late time are not captured. It remains to compare the results with a dynamic mix model.

5 CONCLUSIONS

RM mixing still occurs in gravitationally stable interfaces. At late times, the density stratification becomes closely planar, but significant long wavelength motion remains. Simple buoyancy-drag models treat the growth of these instabilities with good accuracy. However, the departure of the flow from a state of self-similar growth means that the simple buoyancy-drag model may not apply if the front acceleration changes significantly at late time, if the relationship between perturbation lengthscale and bubble or spike height changes.

$g = 0$ $\qquad\qquad\qquad\qquad g = -2 \times 10^{-3}$
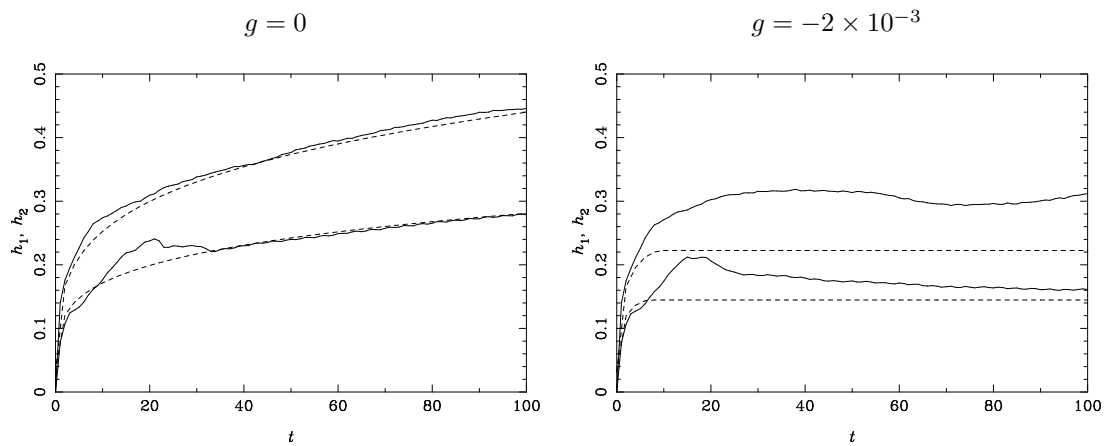
Fig. 4.4. Comparison of MILES results (solid) with Youngs' buoyancy-drag model (dashed).

REFERENCES

[1] Glendinning S.G., et al, 2003. Phys. Plasmas, 10, 1931

[2] Mikaelian K.O., 1985. Phys. Rev. A, 31, 410

[3] Richtmyer R.D., 1960. Commun. Pure Appl. Math., 13, 297

[4] Samtaney R., Ray J., Zabusky N.J., 1998. Phys. Fluids, 10, 1217

e-mail: `robin.williams@awe.co.uk`

Modelling of laser-driven jet experiments

R. J. R. WILLIAMS[1] and P. A. ROSEN[1]

[1] *AWE Aldermaston, Reading, RG7 4PR, UNITED KINGDOM*

Abstract: In experiments using the OMEGA laser, a rapidly moving jet of material is driven from a metal target into a foam envelope. Recent diagnostic developments have allowed data of exceptional detail to be obtained. We present high resolution three-dimensional simulations of these results using Turmoil, focusing on the mechanisms of vorticity deposition in the foam and the consequent break up of the dense jet.

We discuss the modelling of symmetrically-driven jets using a 2D turbulent mix model.

1   INTRODUCTION

Jets are a common feature of astrophysical systems, on scales ranging from young stellar objects to active galactic nuclei. They are frequently associated with accretion flows forced by angular momentum conservation to form discs. The highly collimated outflows flow for distances many times greater than the size of their sources. The interaction with the surrounding interstellar or intergalactic medium provides important observational information on the structure and dynamics both of the jet and the medium.

In some cases, particularly the class of young stellar objects known as Herbig-Haro objects, large scale jets are resolved into numerous discrete clumps on the fine scale. This clumpy flow structure has been most clearly demonstrated for HH110 by multiple-epoch observations using the Hubble Space Telescope, where the kinematics and structural development of numerous individual clumps is clearly demonstrated (Hartigan et al. 2005). Each clump drives a separate bow shock into the surrounding medium. Additional evidence for such structures comes from the distribution of emission in lines characteristic of different shock strengths, and the Doppler broadened profiles of these lines (Tedds et al. 1999).

An international team has used experiments on the OMEGA to study the dynamics of these jet interactions in the lab (Foster et al. 2005). In this paper, we briefly describe these experiments. The jets have been modelled using a variety of time-dependent hydrodynamic codes: we discuss results obtained using turbulent mix models, and high-resolution 3D LES simulations which show the formation and development of clump-driven composite bowshocks similar to those seen both in the experiments and in astrophysics. Simple analytic results suggest that the clumps formed in the experiment may have a characteristic size determined by a balance between initial flow structure and surface tension, and give criteria for the presence of a bow shock leading the clump distribution.

2   EXPERIMENTAL SETUP

The experiments were performed on the Omega laser at LLE, Rochester, in collaboration with a large team (see Foster et al. 2005 for detail, and also Blue in these proceedings).

Experiments used targets driven directly by laser beams (as illustrated) or by a gold hohlraum which converts the laser energy into X-ray irradation of the rear of the target. Using hohlraum drive lessens the dependence of the experiments on details of the laser pointing and beam quality.

The results were obtained by point-projection backlighting at right angles to the axis of the experiment. This technique provides high resolution results, but unfortunately only one image per shot, so the time-development of the jet has to be inferred from multiple experiments.

3   EXPERIMENTAL RESULTS

In Figure 3.2 we show a selection of experimental results. With no foam present, the flow from the Ti washer has two components. An initial hot, diffuse plume of material results from the thin layer of material heated by the
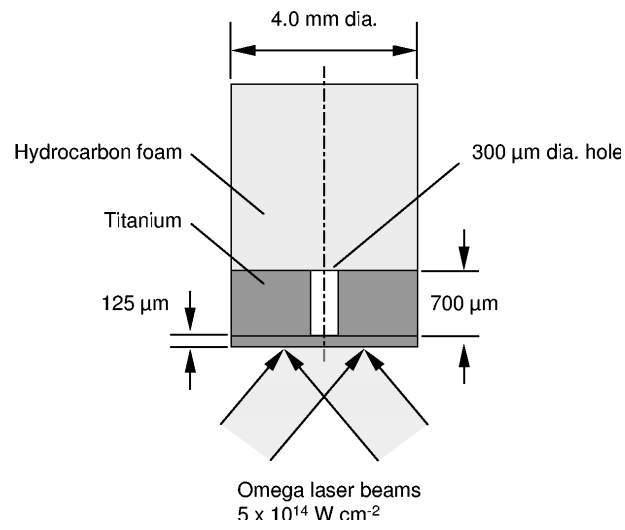
Fig. 2.1. Schematic of direct-drive experiment

(a)

(b)   (c)
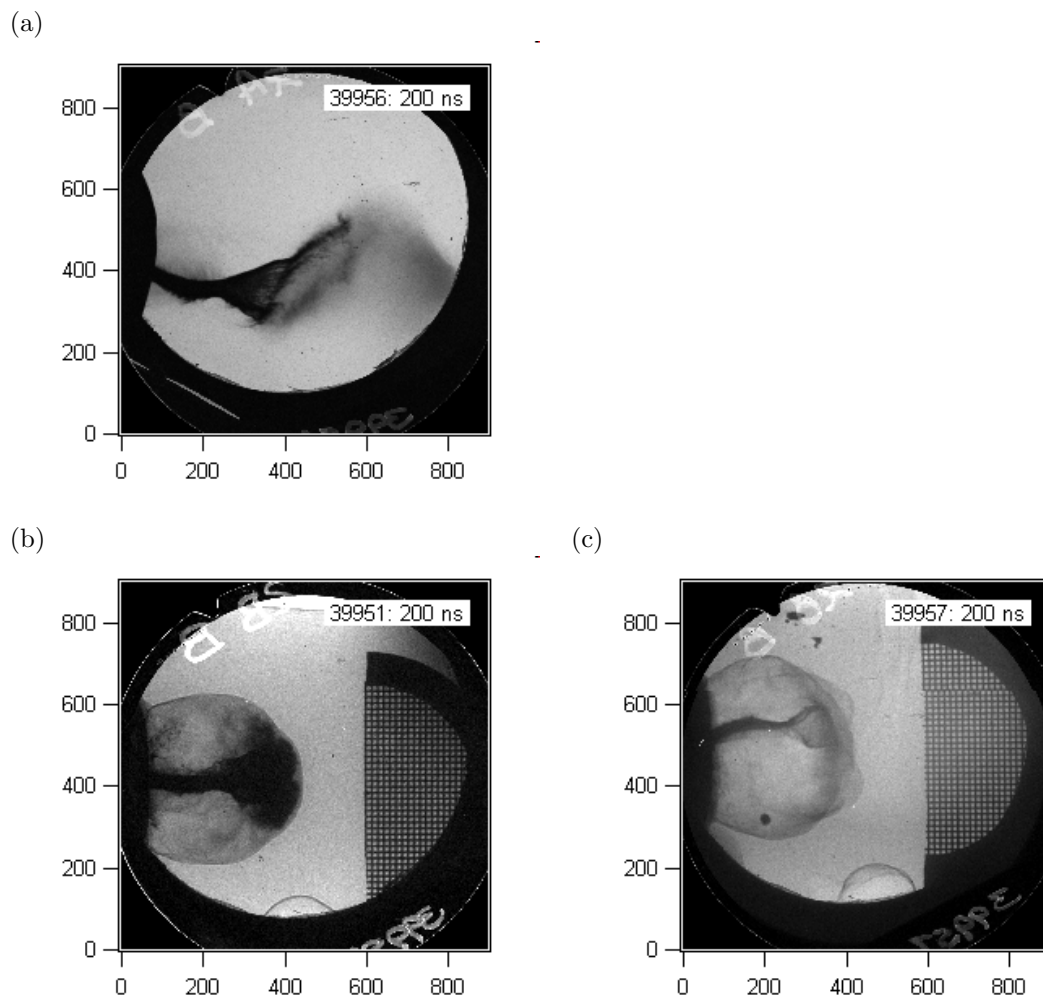
Fig. 3.2. Experimental images at 200 ns. (a) No foam, (b) standard V backlighter, (c) penetrating Fe backlighter.
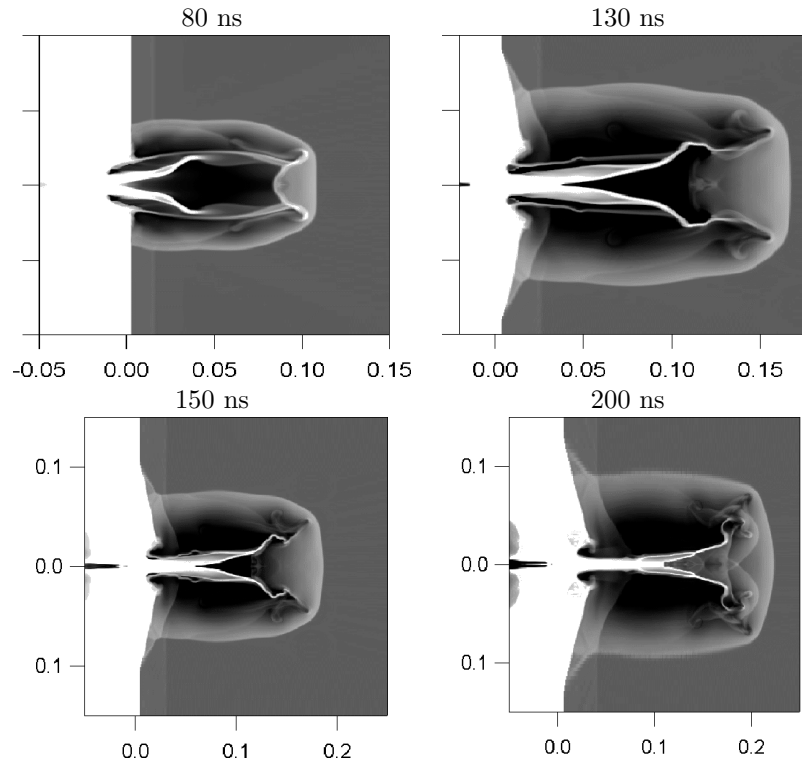
Fig. 4.3. Two-dimensional NYM/PETRA results with detailed physics.

laser illumination expanding along the centre of the washer. Subseqently, the shock driven by the illumination collapses the bore of the washer, driving a denser high-velocity flow by a shaped-charge mechanism.

With foam present, the diffuse plume of Ti drives an initial flow into the foam, but the structures which are seen most clearly in the radiographs shown here are the dense second jet and the leading shocks into the foam. With the standard backlighter, the dense plume is saturated, while with a more penetrating backlighter the inner core of the jet is visible. At the base of the jet cocoon, a Mach stem structure is formed where it interacts initially with the surface of the washer and later with the main shock moving into the foam. Fine scale Ti ejecta are also driven from the washer surface.

4 NUMERICAL MODELLING

4.1 Two-dimensional modelling with detailed physics

The collapse of the trumpet of dense ejected Ti gives tree-like structure. In the trunk, the pressure from the shocked cocoon of foam material recollimate the ejecta to form a dense core. In the branches, however, the cone of dense material is kept open by a reverse shock driven into its low-pressure core by the swept up foam material.

These two-dimensional calculations with detailed physics were used to determine appropriate values of the material specific heat to allow calculations to be performed using the three-dimensional LES code Turmoil. Turmoil can treat two material species, using a separate perfect gas equation of state for each species. Comparison calculations in two-dimensional axisymmetric coordinates confirm that these values provide a good match to the detailed physics results.

4.2 3D LES results

In Figures 4.4 and 4.5, we show results from a typical three-dimensional MILES simulation using Turmoil. The surfaces of the Ti in the initial conditions were roughened to seed instabilities. We see that the flow breaks up during the recollimation stage, with braiding and density filamentation of the jet core and fragmentation
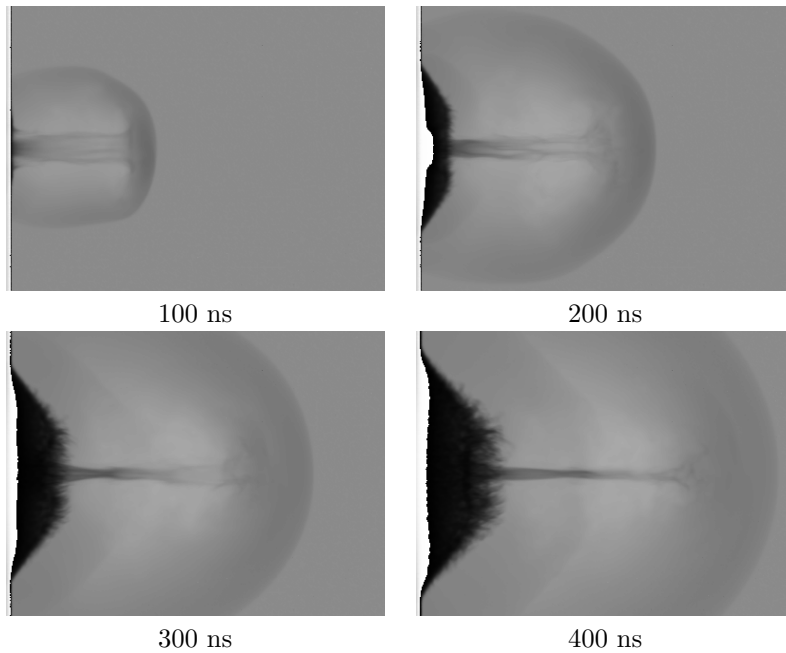
Fig. 4.4. Results from three-dimensional simulations with roughened surfaces.
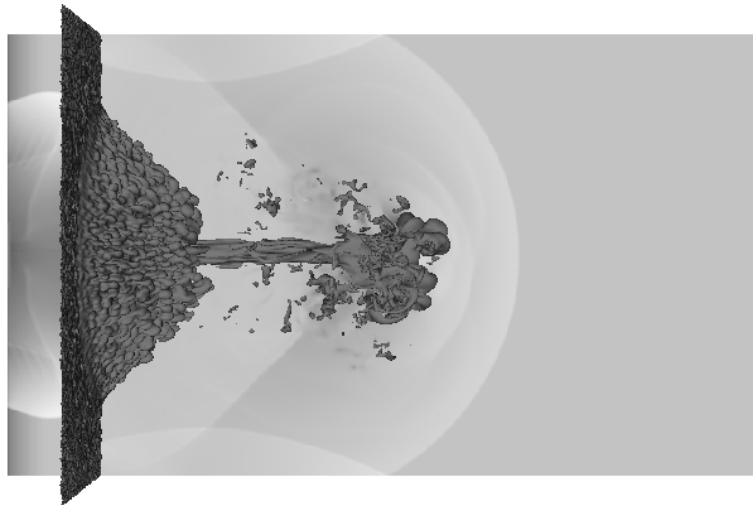
Fig. 4.5. Results from a 3D numerical simulation with roughening applied to the surfaces of the Ti. This plot shows the 50% mass-fraction isosurface at 400 ns, with the flow pressure shown on the midplane.

of the dense Ti material within the cocoon. The Ti reaches close to the shock surface at the head of the jet at early time, but the shock eventually escapes forward.

4.3 Mix model comparison

In Figure 4.6, we compare experimental results with those from 3D LES using Turmoil, and with axisymmetric simulations using the PETRA and BHR mix models. The Turmoil calculation captures the overall features of the flow, but is only a specific realization. In particular, the core of the jet seems rather smooth compared to the experimental result.

The mix model results illustrate the range of results which are possible using these techniques. The PETRA results appear very diffusive, while those with BHR includes detailed features absent in the experimental data.

(a) (b)

(c) (d)
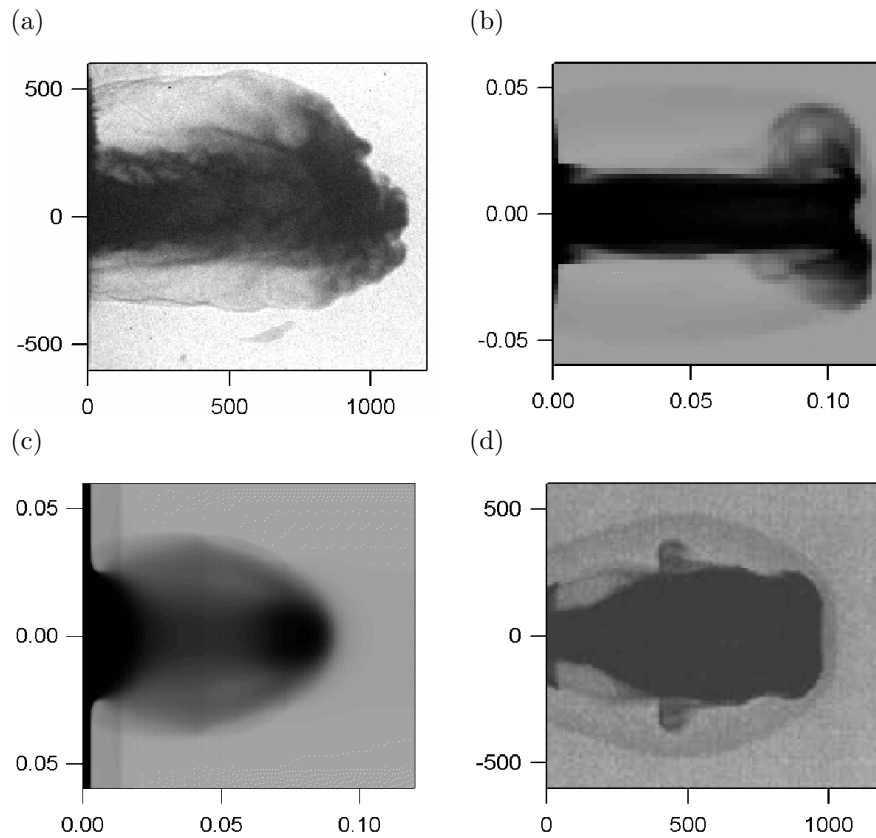
Fig. 4.6. (a) Experiment, (b) Turmoil 3D LES; 2D modelling with mix models: (c) PETRA, (d) BHR (from B. H. Wilde, LANL).

A significant choice must be made when applying a mix model: an ensemble average of possible results will always appear diffusive compared to a specific realization, and may include material in states which only occur with unrealistically high levels of atomic mixing.

5   PARTICULATE EJECTA PRODUCTION

Two-dimensional simulations produce a narrow trunk and thin sheets for branches. In both cases, non-axisymmetric flow in three dimensional simulations leads to frgamentation. For the trunk, the recollimation of the dense Ti shell by the cocoon pressure is analogous to the implosion of an irregular cylindrical shell. Where the surface density of the shell is somewhat higher than usual, the flow accelerates more slowly while where the surface density is lower it moves more rapidly. As a result, the fluctuations amplify, with a signficant fraction of the imploding shell mass forming streamers lagging the main shell surface. When these streamers do eventually reach the axis of the simulation, their collisions squirt material into outgoing jets.

While the branches are prevented from collapsing to the axis by the reverse shock driven from the foam, they remain unstable to thin-shell fragmentation. The axial striations seen in the trumpet in the experimental results without a target foam are evidence for the initiation of this fragmentation process in the velocity structure set up in the jet driving region.

The overall structure of the dense high velocity material will be kinematically dominated, and so described by a three-dimensional Burgers equation. The effect of initial velocity perturbations may be treated by a Zel'dovich approximation, with smooth flows forming sheets at caustics, these sheets breaking up to form threads, and from these droplets. At the finest scales, drag may result in further fragmentation, but surface tension or viscosity can suppress it. These processes are being modelled in detail by Batha (see these proceedings).

6 CAN EJECTA DRIVE A LEADING SHOCK?

In both the experimental results and our three-dimensional numerical simulations, we find that the Ti in the dense clumpy ejecta jet penetrates close to leading shock at early time, while roughened surface leads to 'grass' at base. The vorticity deposition from curved shocks will drive turbulence which can destroy the dense clumps. If a leading shock is driven ahead of the clumpy flow, it will have lower curvature than bowshocks around individual clumps, so the clumps may survive for longer. This may be significant for flows such as the jets in HH-47 (Hartigan et al. 2005) or the Orion BN-KL knots (Tedds et al. 1999).

To investigate this, we consider a simplified model in which the clumps have constant size, mass and velocity, and all the energy lost as a result of drag heats the diffuse flow. In the frame of the clumps, the steady hydrodynamic equations are

$$\rho v = \Phi = const \tag{6.1}$$

$$\frac{d}{dx}\left(p + \rho v^2\right) = -f_{\rm p} C_{\rm D} \rho v^2 \tag{6.2}$$

$$\frac{\gamma}{\gamma - 1}\frac{p}{\rho} + \frac{1}{2}v^2 = \mathcal{E} = const. \tag{6.3}$$

Assuming the velocity at leading edge of the particle cloud, v_1, is positive, these give

$$(\gamma + 1)\log(v/v_0) + (\gamma - 1)\mathcal{E}\left(\frac{1}{v^2} - \frac{1}{v_0^2}\right) = -2\gamma C_{\rm D}\int_{-\infty}^{x} f_{\rm p}(x)dx. \tag{6.4}$$

We assume that the particles are confined to a region $x_1 < x < x_2$.

In cases of interest, the form of the solution depends on the incident flow parameters, ρ_1, v_1 and p_1, the downstream pressure, p_2 and the system drag coefficient $S_{\rm D} = C_{\rm D}\int f_{\rm p}dx$. Equations (6.1) and (6.3) give

$$v_i = \left(\left[\frac{\gamma}{\gamma - 1}\frac{p_i}{\Phi}\right]^2 + 2\mathcal{E}\right)^{1/2} - \frac{\gamma}{\gamma - 1}\frac{p_i}{\Phi}. \tag{6.5}$$

for positions i of x_1 and x_2.

At x_1, there are two solutions to this equation: v_1 based on the properties at x_1, v_2 based on those at x_2. The physical solution is whichever has highest ram pressure $\Pi = p + \rho v^2$.

For supersonic inflow, the solution can either be supersonic throughout (where $\Pi_1 > \Pi_2$ through at all x), have an internal shock (where $\Pi_1 > \Pi_2$ for small x, $\Pi_1 < \Pi_2$ for large x) or have a leading shock (when $\Pi_1 < \Pi_2$ throughout). In the latter case, there is no valid *steady* solution to the one-dimensional problem. Instead, a shock will continue moving towards $-\infty$ for a strictly 1D flow. For a finite region of particles in 3D, the standoff will be limited by geometrical divergence effects.

7 SUMMARY

Laser driven jet experiments have proved excellent test-beds to study the structure and dynamics of dense jets, the interaction of clouds of particles with high speed turbulence in a jet cocoon. Two and three-dimensional numerical tools have been tested by modelling these flows.

REFERENCES

[1] Foster J.M., Wilde B.H., Rosen P.A., Williams R.J.R., Blue B.E., Coker R.F., Drake R.P., Frank A., Keiter P.A., Khokhlov A.M., Knauer J.P., Perry T.S., 2005. *Astrophysical Journal Letters*, **634**, L77

[2] Hartigan P., Heathcote S., Morse J.A., Reipurth B., Bally J., *Astronomical Journal*, **130**, 2197

[3] Tedds J.A., Brand P.W.J.L., Burton M.G., 1999. *Monthly Notices of the Royal Astronomical Society*, **307**, 337

[4] Youngs D.L., 1994. *Laser and Particle Beams*, **12**, 725

e-mail: `n_yanilkina@vniief.ru`

The Degree of Mixing Homogeneity During Direct 3D Numerical Simulation of Gravitational Turbulent Mixing

Vyacheslav STATSENKO, Yuri YANILKIN , Olga SIN'KOVA, and Anna STADNIK

Russian Federal Nuclear Center – VNIIEF Russia

Abstract: The paper analyses the results of incompressible turbulent mixing simulations by TREK code [1]. The dependence between the method of computations and statistical treatment of results and the degree of mixing homogeneity is determined. The molecular viscosity effect is clarified. Computation results are compared to the data of experiments [2,3].

1 INTRODUCTION

Knowledge of the degree of mixing homogeneity in turbulent flows is of great importance for finding the rate of reactions, both chemical and nuclear.

The paper determines the degree of mixing homogeneity of turbulent flows with characteristics found by direct numerical simulation (DNS) and LES, by which we imply finding solutions to Navier-Stokes and Euler equations using no sub-grid models of turbulence.

Similar to the earlier computations [4], one computation has been carried out with two materials (with the interface tracking) and another computation has been carried out with one material (without interface tracking). Note that such computations have bee also carried out and described in some other papers. Table 1 below gives some available calculated and experimental data (for miscible materials) on the degree of homogeneity of the flow of interest.

	Measurements	No tracking	Interface tracking
Linden & Redondo [3], $A_t \approx 0.04 \div 0.05$	0.6-0.7		
Kucherenko et al. [2], $A_t = 0.083$	0.7		
Ramaprebhu & Andrews [17], $A_t \approx 0.04 \div 0.05$		0.8	
Wilson & Andrews [16], $A_t \approx 0.04 \div 0.05$		0.7	
Dimonte et al. [7], $A_t = 0.5$		0.8	0.3
Weber, Dimonte, Marinak [5], $A_t = 0.5$		0.7-0.75	0.25
Cook, Cabot, Miller [11], $A_t = 0.5$		0.75-0.8	
Youngs [6,13], $A_t = 0.5$		0.75-0.8	
Mellado, Sarkar [14], $A_t = 0.5$		0.75-0.8	
Yanilkin et al. [10], $A_t = 0.5$		0.75-0.8	0.25-0.3
Stadnik et al. [4], $A_t = 0.5$		0.75-0.8	0.25-0.3

Table 1.1. The calculated and experimental data on the mixing homogeneity degree

One can see from Table 1 that, first, the calculated data is significantly scattered in the homogeneity degree θ and, second, there is a rather large difference between the calculations with interface tracking and experimental data [2,3]. The paper describes an attempt to understand the nature of such differences for computations by TREK code [1] using grids 100x100x200 and 200x200x400.

For this purpose, the dependence between the value of θ and the computational method (either with interface tracking, or without it), as well as the result processing method, has been found. The similar dependence has been found for the PDF of concentration of one of the materials. The calculated results are compared to the data of experiments from [3] and [2], as well as results of computations using the phenomenological model of non-isotropic turbulence [8].

2 ANALYTICAL CORRELATIONS FOR THE MIXING HOMOGENEITY DEGREE

Let us have two incompressible fluids with undisturbed densities ρ_1, ρ_2. The volume concentrations of materials are β_1 and $\beta_2 = 1 - \beta_1$. Assume that averaging ($< f > = \left(\sum f \cdot \Delta x \cdot \Delta y \right) / S$) is performed in a horizontal plane of area $S = \sum \Delta x \cdot \Delta y$, similar to the problem of gravitational mixing of a plane mixed layer (see [4]). Therefore, according to [9], the mean value of the mixing homogeneity degree is defined as $\theta = \left(< \beta_1 > - < \beta_1^2 > \right) / \left(< \beta_1 > \cdot \left(1 - < \beta_1 > \right) \right)$.

For **immiscible** materials we have: $\beta_1 = \left(\rho - \rho_2 \right) / \left(\rho_1 - \rho_2 \right)$.

For **miscible** materials, it follows from the ideal gas pressure constancy and internal energy conservation in approximation to incompressibility that: $\beta_1 = \left(\rho - \rho_2 \right) / \left[\rho \cdot \left(1 - \rho_2 / \rho_1 \right) \right]$.

Introduce also the value of mixing homogeneity degree integral over the TMZ width, which is defined similar to [7]

$$\Theta = \int \left(< \beta_2 > - < \beta_2^2 > \right) \cdot dz / \int \left(< \beta_2 > \cdot \left(1 - < \beta_2 > \right) \right) \cdot dz . \tag{2.1}$$

3 THE MIXING HOMOGENEITY DEGREE IN COMPUTATIONS WITH AND WITHOUT VISCOSITY

Consider the data on $< \rho'^2 >$ and $< \rho >$ from [4] for computations with a interface tracking that has been obtained for gravitational turbulent mixing with Atwood number =0.5. This data can give us the values of $< \beta_1 >, < \beta_1^2 >$, and θ according to expressions of section 2.

The resultant profiles of θ are shown in **Fig. 3.1** for computation with small molecular viscosity. Here **N** is proportional to the Z-coordinate of the cell. It follows from **Fig. 3.1** that the value of θ does not change, actually, over the TMZ width. The time-dependence of θ at the point of maximum of RMS density fluctuations is shown in **Fig. 3.2** for computations with various molecular viscosity.

In each version of computations, according to expectations, $\theta = 1$ at the very beginning because of the undeveloped turbulence. Then the value of θ decreases and achieves an approximately constant value $\theta \approx \theta_c$. One can see that in each computation, except the highest molecular viscosity, these values are close to each other and equal to $\theta_c \approx 0.25 \div 0.3$.

Consider now the results of computation of the integral value of homogeneity degree, **Θ** (see expression (2.1)) without interface tracking. $\Theta = 1$ during at the initial phase (**Fig. 3.3**) and then lowers, however, upon achievement of its minimum value $\Theta_{min} \approx 0.2$, it starts growing and achieves the value $\Theta_a \approx 0.8$, which is typical for the self-similar phase of computations without interface tracking (see **Table 1.1**).

It has been found that the value of $\Theta_{min} = 0.43$ [7], 0.62 [11], 0.43 [14], 0.32 [5].
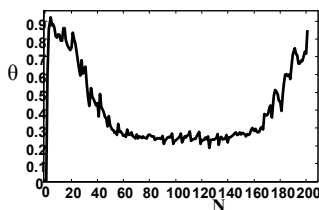
Fig. 3.1. Profiles of θ(N) at the end of self-similar phase: $\nu = 5 \cdot 10^{-6}$
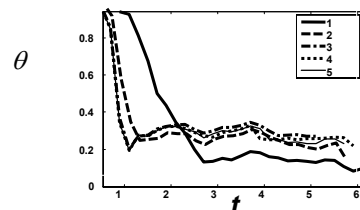
Fig. 3.2. The mixing homogenity degree θ at the TMZ center versus time: 1 - $\nu = 5 \cdot 10^{-3}$, 2 - $\nu = 5 \cdot 10^{-4}$, 3 - $\nu = 5 \cdot 10^{-5}$, 4 - $\nu = 5 \cdot 10^{-6}$, 5 - $\nu = 0$
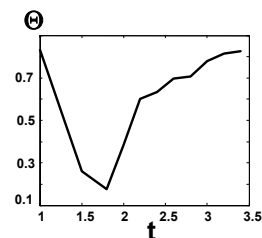
Fig. 3.3. The TMZ-integral mixing homogeneity degree versus time

In experiments [2], $\Theta_c \approx 0.32$ has been obtained in the early phase of TMZ growth (we speak here about the initial experimental data from [2], prior to their further correction). The authors of this paper made an attempt to correct data of measurements to obtain the linear law of θ growth. Note that such a law can take place in the early phase (at small Re numbers), it does not agree with the self-similar turbulent behavior in TMZ. Really, if it were the self-similar turbulent behavior in TMZ, the fluid would have been absolutely homogeneously mixed. However, turbulence grows under such conditions and availability of turbulence and non-mixed fluid outside TMZ must lead to concentration fluctuations in it, which make absolute homogeneity impossible. We think that in the experiments described in [2] the authors observed the behavior of Θ(t) analogous to that which takes place in computations without the interface tracking (**Fig. 3.3**).

The effect of molecular viscosity. Increasing molecular viscosity leads to lowering the homogeneous mixing degree, up to $\theta_c \approx 0.15$ in self-similar phase. The explanation is that a rather large value of molecular viscosity leads to suppression of turbulence on small scales, of the order of a cell size. As it will be shown below, it is the small-scale turbulence

that determines the homogeneity degree and, apparently, suppression of turbulence leads to lowering its value. However, molecular viscosity should have the same effect in experiments. Really, it has been shown in [2] that increase of acceleration, i.e. increase of Re with the same flyways leads to increase of the degree of mixing homogeneity.

4. PDF OF THE VOLUME CONCENTRATION IN COMPUTATIONS

Consider the PDF of the volume concentration of a heavy material, $F(\beta_2, z, t)$, which is calculated using the original $\tilde{\beta}_2(x, y, z, t)$ arrays (see [10]).

If one uses the original array of values of concentration β_2 during computation with a interface tracking, the maximum values of $F(\beta_2)$ inside TMZ are achieved, as one can see from **Fig. 4.1**, mainly near the limits of the range of concentration values, i.e. either at $\beta_2 \approx 0$, or at $\beta_2 \approx 1$. In so doing, the values of $F(\beta_2)$ inside the range of values $0 < \beta_2 < 1$ are small and, hence, the values at the limits of this range make up the integral value. Near the TMZ boundary adjusting the heavy material $F(\beta_2)$ has the form of δ-function concentrated at $\beta_2 \approx 1$ and near the TMZ boundary adjusting the light material $F(\beta_2)$ has the form of δ-function concentrated at $\beta_2 \approx 0$. In other words, in this case $F(\beta_2)$ corresponds to a higher degree of mixing heterogeneity.

Contrariwise, if the original array of values of concentration $\tilde{\beta}_2$ is used in computation without interface tracking, function $F(\beta_2)$ is concentrated near $\beta_2 \approx \langle \beta_2 \rangle \equiv \int_0^1 \beta_2 \cdot F(\beta_2) d\beta_2$ that corresponds to a higher mixing homogeneity degree.

Average now the original arrays of $\tilde{\beta}_2$ values in squares of side r $\overline{\tilde{\beta}}_2(r, x, y, z) = \langle \tilde{\beta}_2 \rangle|_{r, x, y, z}$, where $r = l_s \cdot h$, h is a computational cell size (but $l_s \ll \min(N_x, N_y)$). The arrays of $\overline{\tilde{\beta}}_2$ values obtained in such a way allowed us to calculate the corresponding PDF of the heavy material concentration, $F(\beta_2)$, for various values of l_s they are also shown in **Fig. 4.1** for various points of TMZ.

These figures illustrate also the reduced values of coordinates at these points in the coordinate system related to fluid $\zeta \equiv (z - z_c)/L$, where z_c is the initial coordinate of the material interface, L is the TMZ width determined by the values of concentration $\beta_1 = \varepsilon \ll 1$. As one can see from these figures, $F(\beta_2)$ insignificantly differs from that obtained in computation without interface tracking (without original array processing), even with $l_s = 2$.
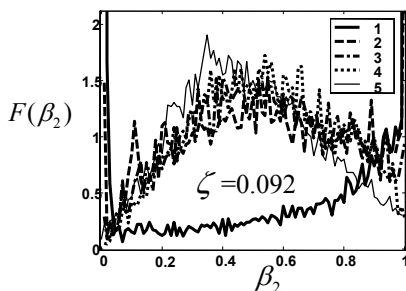
Fig. 4.1. PDF of the heavy material concentration:

Fig. 4.2. The homogeneous mixing degree:

1 – computations with interface tracking; 2-4 – computation with interface tracking ($\overline{\tilde{\beta}}_2$), with $l_s = 2, 3, 4$, respectively; 5 – computation without interface tracking ($\tilde{\beta}_2$).
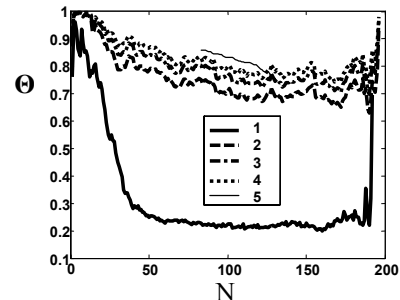
Close results are obtained at $l_s = 3$ and $l_s = 4$, i.e. one can observe a faster approach to some stable value of $F(\beta_2)$ independent of l_s and further increase of the value of l_s does not change the statistical distribution until the requirement of $l_s \ll \min(N_x, N_y)$ is met. Note that PDFs of concentration obtained in computations without interface tracking [11, 12] have the same behavior. The values of PDF $F(\beta_2)$ obtained in such a way were used to find the values of

$$< \beta_2 >= \int_0^1 \beta_2 F(\beta_2) d\beta_2 \quad \text{and} \quad < \beta_2^2 >= \int_0^1 \beta_2^2 F(\beta_2) d\beta_2.$$

Expression (2.2) allowed us to calculate the corresponding profiles of the homogeneous mixing degree θ for various values of l_s, which are shown in **Fig. 4.2** below. As one can see from **Fig. 4.2** hat even with $l_s = 2$ the profile significantly differs from that calculated without interface tracking (without processing of the original array).

5 COMPARISON BETWEEN THE RESULTS OF COMPUTATIONS AND THE PHENOMENOLOGICAL MODEL

The paper uses the model of non-isotropic turbulence from [8]. It is applicable to describe the problem of gravitational turbulent mixing we are dealing with. We use equilibrium approximation for the following turbulent quantities: Reynolds tensor components $R_{zz} \equiv <(u_z')^2>$ and $R_{xx} \equiv <(u_x')^2> = R_{yy} \equiv <(u_y')^2>$, turbulent mass flow $R_z \equiv <\rho' u_z'>$ and the reduced quadratic density fluctuation of density $R \equiv <\rho'^2>/<\rho>^2$. Spatial turbulent scale Λ is used for the value closing the system of equations, i.e. we take $\Lambda = \alpha L_t$. Here $L_t \equiv z_2 - z_1$, $\beta_2(z_1)=\varepsilon$, $\beta_2(z_2)=1-\varepsilon$. We assume below that $\varepsilon=0.05$.

Thus, the problem is reduced to solving the differential equation

$$\frac{\partial \rho}{\partial t} = -\frac{\partial}{\partial z} R_z , \qquad (5.1)$$

where $R_z \equiv \langle \rho' u_z' \rangle = \frac{-3bc\Lambda}{a} \frac{\partial \rho}{\partial z} q$, $q^2 \equiv <u_i'^2> = -\frac{2c\Lambda^2}{a} \frac{g}{\rho} \frac{\partial \rho}{\partial z}$. Here, $\zeta = \frac{b}{1-3b}$, $c \equiv 1 + \frac{1}{\zeta} + \frac{1}{\kappa}$.

For self-similar mode, equation (5.1) is written in the form

$$2\eta + \lambda\left(3y' - y^3\right) = 0 , \quad \text{or} \quad 2x + 3Y' - Y^3 = 0 \qquad (5.2)$$

with the following introduced self-similar variables $\eta \equiv (z - z_c)/gt^2/$; $\psi(\eta) \equiv \rho/\rho_1$, $y \equiv \sqrt{-\psi'/\psi}$; $\psi' \equiv d\psi/d\eta$, and coefficient $\lambda \equiv c_\lambda \eta_L^2$; $c_\lambda = \sqrt{2c/a} \cdot 3\alpha^2 bc/a$.

To solve equation (5.2) numerically, we specify $x_1 < 0$, $Y(x_1) = 0$, $Y'(x_1) = -2x_1/3$. Equation (5.2) is integrated up to the point $x_2 > 0$, at which $Y(x_2) = 0$, with the density ratio n, $\ln(n) = \int_{x_1}^{x_2} Y^2 dx = \int_{\eta_1}^{\eta_2} y^2 d\eta$ being determined by the value of x_1; it equals $x_1 = -1.69$ for n=3.

It is clearly seen that $\eta_L \equiv \eta_2 - \eta_1 = c_\lambda^2 x_{L\varepsilon}^5$, where $x_L \equiv x_2 - x_1$. The solution found to equation (5.2) gives us $\xi \equiv x_{L\varepsilon}/x_L$; $x_{L\varepsilon} \equiv x_{2\varepsilon} - x_{1\varepsilon}$, where the values of $\beta_2 = (\rho-1)/2 = \varepsilon$ correspond to the values of quantities $x_{2\varepsilon}, x_{1\varepsilon}$. The meaning $\xi = 0.615$ corresponds to n=3, ε=0.05. Note that $\alpha_Y \equiv \eta_L/A_t$ coincides with the known quantity (introduced in the paper [9]) that characterizes the rate of TMZ growth in self-similar phase $L_t = \alpha_Y A_t gt^2$).

Turbulent energy $\tilde{k} \equiv k(L_t g) = c\alpha^2 Y^2 x_{L\varepsilon}/a$ is a one more reduced quantity, with anisotropy of diagonal components of Reynolds tensor being described as $k_{xz} \equiv R_{xx}/R_{zz} = (1/3-b)/(1/3+b)$; $R_{yy}/R_{xx} = 1$. The relative RMS fluctuation is $R \equiv <\rho'^2>/\rho^2 = 6bc\alpha^2 Y^4 x_{L\varepsilon}^2/(a\kappa)$.

This quantity along with ψ allows us to find the values of θ using expressions of section 2.

The semi-empirical coefficients of the model were specified, as 3D computations were carried out with more and more fine computational grids. The paper uses the following values of coefficients: $a = 0.5; b = 0.13; \kappa = 0.45; \alpha = 0.055$. The profiles of $\psi(\chi), k_{xz}(\chi), \tilde{k}(\chi), R(\chi), \theta(\chi)$, as functions of a variable $\chi \equiv (z - z_c)/(A_t gt^2) = c_\lambda^2 x_{L\varepsilon}^4 x/A_t$ are shown in **Fig. 5.1-5.5** for these values of coefficients.

The figures also illustrate the data of 3D computations of the problem, both with and without interface tracking. For $\psi(\chi), k_{xz}(\chi), \tilde{k}(\chi)$ this results are in good agreement with each other and with the results calculated using the phenomenological model. However, for a relative quadratic density fluctuation the result of 3D computation with interface tracking significantly exceeds the result of 3D computation without interface tracking, which is close to the data calculated using the phenomenological model. Note that this expression is valid both for miscible fluids (it follows from expression for "dissipation" [8] in the equation of $<\rho'^2>$ transport) and immiscible fluids, for which, however, the original arrays have been averaged in l_s scale exceeding r_{st} scale of surface tension forces. In fact, the phenomenological model describes large-scale fluctuations, where values of turbulent quantities in 3D computations for

miscible and immiscible fluids (i.e. with and without interface tracking), as we have seen above, are close to each other. That's why all values of turbulent quantities obtained using the phenomenological model must coincide also.

Note that in 3D computations regular values of θ can be obtained at the TMZ center only. The behavior of quantity θ is irregular at TMZ edges, where density deviations from the unperturbed density are small. Note that the results of 3D computations from [7] are similar to those shown in **Fig. 5.2**. The results from [9] obtained in computations without interface tracking are close in the θ profile shape to the corresponding results of our computations.

The paper [15] also offers the phenomenological model to describe the degree of homogeneous mixing. Profiles of θ significantly differ from that in **Fig. 5.5**, though the obtained maximum values in this paper are close to θ≈0.8.
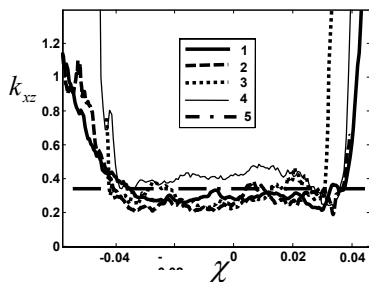
Fig. 5.1. Reynolds tensor anisotropy   **Fig. 5.2.** Density profile   **Fig. 5.3.** The profiles of the squared density pulsation
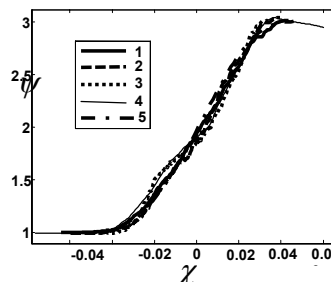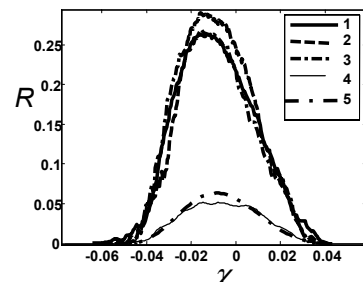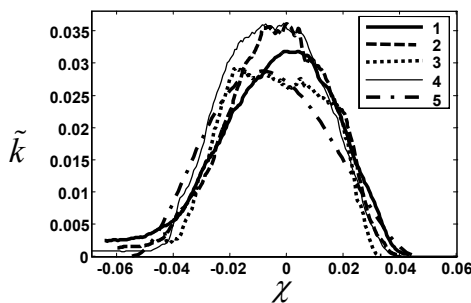
Fig. 5.4. The scaled turbulent energy profiles   **Fig. 5.5.** The homogeneous mixing degree profiles
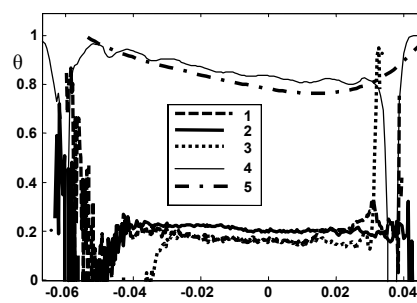
1, 2 – t=4, t=5.5, respectively, in computation with interface tracking [10] using grid 200x200x400; 3 – computation with interface tracking, grid 100x100x200; 4 – computation without interface tracking, grid 100x100x200; 5 – phenomenological model for miscible fluids

6 DISCUSSION OF COMPUTATION RESULTS AND EXPERIMENTAL MEASUREMENTS

Averaging of the original density arrays in computations with singled out interface on a small scale of r values ($r = l_s \cdot h$, $l_s = 2, 3, 4$ computational cells), which is smaller than the outer scale of turbulence L_t, is equivalent to averaging on the scale large than interatomic scale for homogeneously mixed miscible fluids (the homogeneity degree appears to be close to zero without such averaging). Hence, the h scale plays the role of interatomic distance, or in other words it plays the role of r_{st} scale, which is determined by surface tension in a real flow.

As we have seen above, averaging on $L<<r<<h$ scale in computations with singled out interface leads us to function $F(β_2)$ of the form close to its form in computation without singled out interface. The values of mixing homogeneity degree θ also appear to be close to each other.

Similarly, averaging in the experiments with immiscible fluids should be performed on the scale exceeding the scale of r_{st} determined by surface tension. As a result, both the homogeneity degree θ and the volume concentration PDF $β_2$ of one of the materials should be close to that for miscible fluids, if r_{st} scale is small enough, as compared to the outer turbulence scale L_t.

Decrease of the homogeneity degree θ in TMZ up to the minimum, relatively small values θ≈0.2÷0.3 corresponds to the initial (non-self-similar) phase of gravitational turbulent mixing of miscible fluids; then the value of θ starts rising and achieves a relatively large value, θ≈0.7÷0.9, in self-similar mode. Note that, when studying the *self-similar mode* of

gravitational turbulent mixing of miscible fluids, the self-similar form of the homogeneity degree $\theta = \theta\,(\zeta)$, with $\theta_m = \max(\theta) < 1$ being dependent of the Atwood number alone) should be also achieved. $\theta_m = 1$ is possible only in the limit of damping turbulence. So, the law of linear increase of θ (along the flyway distance) in the paper [2] implies that there is no self-similar mode. We would like to mention also the paper [13], where the TMZ-averaged value of θ achieves $\theta = 0.75 \div 0.8$ with acceleration constant in time and approaches to θ≈1 only with alternating-sign acceleration in the phase of damping turbulence.

REFERENCES

[1] Stadnik A.L., Shanin A.A., Yanilkin Yu.V. Eulerian Technique TREK for computation of 3D gas dynamic multi-material flows //VANT. Ser.: Math. Model. Phys. Process. Is.4, 1994.

[2] Yu.A.Kuchrenko, A.P.Pylayev, V.D.Murzakov, et al. Experimentally finding the degree of molecular mixing in the phase of Rayleigh-Taylor instability growth using the chemical indicator technique. Presentation at Zababakhin's Scientific Readings, 2005.

[3] Linden P.F., Redondo J.M., Molecular mixing in Rayleigh-Taylor instability //J. Fluid Mech, A 3 (5), pp.1269-1277., 1991.

[4] Stadnik A.L., Statsenko V.P., Yanilkin Yu.V. Direct 3D numerical simulation of gravitational turbulent mixing with regard to molecular viscosity // IX-th International Workshop on the Physics of Compressible Turbulent Mixing (Cambridge, England), 2004.

[5] S.V. Weber, G. Dimonte, and M.M. Marinak. ALE simulations of turbulent Rayleigh-Taylor instability in 2-D and 3-D// VIII-th International Workshop on the Physics of Compressible Turbulent Mixing (Pasadena, USA), 2001.

[6] Youngs D.L. Numerical simulation of mixing by Rayleigh-Taylor and Richtmyer-Meshkov instabilities //Laser and Particle Beams, vol.12, No.4, pp-725-750, 1994.

[7] Guy Dimonte, D.L.Youngs, A.Dimits, S.Weber, M.Marinak, S.Wunsch, C.Garasi, A.Robinson, M.J.Andrews, P.Ramaprabhu, A.C.Calder, B.Fryzell, J.Biello, L.Dursi, P.MacNeice, K.Olson, P.Ricker, R.Rosner, F.Timmes, H.Tufo, Y.-N.Young, M.Zingale. A comparative study of the turbulent Rayleigh-Teylor instability using high-resolution three-dimensonal numerical simulations: The Alpha-Group collaboration //Phys. Fluids, v.16, No.5, pp.1668-1693, 2004.

[8] Statsenko V.P. Testing of the turbulence model with Reynolds tensor anisotropy //VANT. Ser.: Theor. And Appl.Phys., 1996, Is.3, pp. 43-51.

[9] Linden P.F., Redondo J.M., Youngs D.L. Molecular mixing in Rayleigh-Taylor instability //J. Fluid Mech, Vol.265, pp.97-124, 1994.

[10] Yu.V.Yanilkin, V.P.Statsenko, S.V.Rebrov, N.I.Selchenkova, O.G.Sinkova, A.L.Stadnik, A.Ya.Uchayev. Studying the gravitational turbulent mixing with large density ratios by direct three-dimensional numerical simulation // Presentation at the VIII-th International Workshop on the Physics of Compressible Turbulent Mixing, Pasadena, USA, December 2001.

[11] Cook A.W., Cabot W. and Miller P.L. The mixing transition in Rayleigh-Taylor instability // J. Fluid Mech., 2004, Vol. 511, pp.333-362.

[12] Youngs D.L. 3D Variable acceleration Rayleigh-Taylor mixing// International Workshop on the Physics of Compressible Turbulent Mixing (Marseille, France), 1997, pp.534-538.

[13] Youngs D.L. 3D numerical simulation of turbulent mixing by Rayleigh-Taylor instability //Phys. Fluids, Vol.A3(5), pp.1312-1319, 1991.

[14] Mellado J.P. and Sarkar S. Large-eddy simulation of Rayleigh-Taylor turbulence with compressible miscible fluids //Phys.Fluids, v.17, 076101, pp.1-20, 2005.

[15] A.S. Kozlovskih and D.V. Neuvazhayev. Coefficient of heterogeneity in turbulent mixing zone, Lazer and Particle beams, 18, pp.207-212, 2000.

[16] M.Wilson and M.J.Andrews. Spectral measurements of Rayleigh-Taylor mixing at small Atwood number. Phys. Fluids, 14, p.938, 2002.

[17] P.Ramaprebhu and M.J.Andrews. Experimental investigation of Rayleigh-Taylor mixing at small Atwood number. J. Fluid Mech. 502, p.233, 2004.

e-mail: `n_yanilkina@vniief.ru`

Direct 3D Numerical Simulation of Turbulent Mixing in Buoyant Jet

V.P. Statsenko, O.G.Sin'kova and Yu.V.Yanilkin,

RFNC-VNIIEF, Sarov, Russia

Abstract: Computational investigation of evolution of a turbulent buoyant jet in gravity field under statistically time-independent flow of a more light fluid from local source into a homogeneous incompressible environment is described. Computations were carried out by direct numerical simulation of turbulence using 3D hydrodynamic code TREK. Results of computations are compared to the available data of experiments.

1 INTRODUCTION

The paper [2] describes experimental investigations of the axially symmetric, on average, buoyant jet generated by heated air vertically flowing out of a reservoir to the atmosphere. The paper [3] describes numerical simulation of this experiment with 2D hydrodynamic code EGAK using the semi-empirical k-ε model of turbulent mixing. Though some results of these simulations were close enough to the experimentally measured values, there were discrepancies especially noticeable for turbulent energy profiles.

The given paper describes direct 3D numerical simulation of the problem of interest using TREK code and compares the calculated results with the experimental data [2] and computation results from [3].

2 COMPUTATION SETUP

A computational domain has the following dimensions: $l_0 \geq x \geq -l_0$, $l_0 \geq y \geq -l_0$, $L_0 \geq z \geq 0$. A buoyancy source is described by the specified longitudinal velocity component u_z at the central part of the lower face (z=0) of the computational volume (see **Fig. 2.1**). There is a square aperture with side l =5.63cm, $l_0 = 35$ cm in this domain: $l/2 \geq y \geq -l/2$, $l/2 \geq x \geq -l/2$. Its area equals the area of a circular aperture of diameter D=6.35 cm. The velocity of flowing into the given computational volume, u_{z0} is specified in this aperture. The average velocity is u_{zo}=67 cm/s. At each time point, random perturbations of the amplitude equal to 10 % of the value of u_{zo} generated by random number
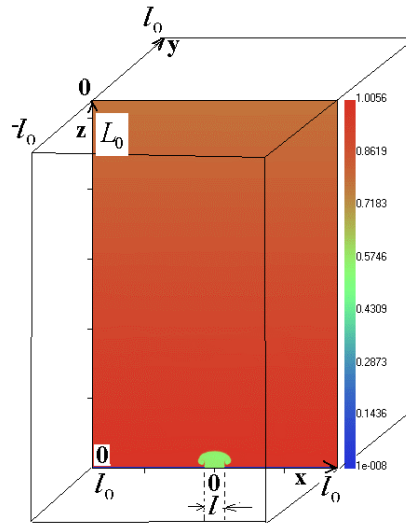
generator are superimposed on this value.
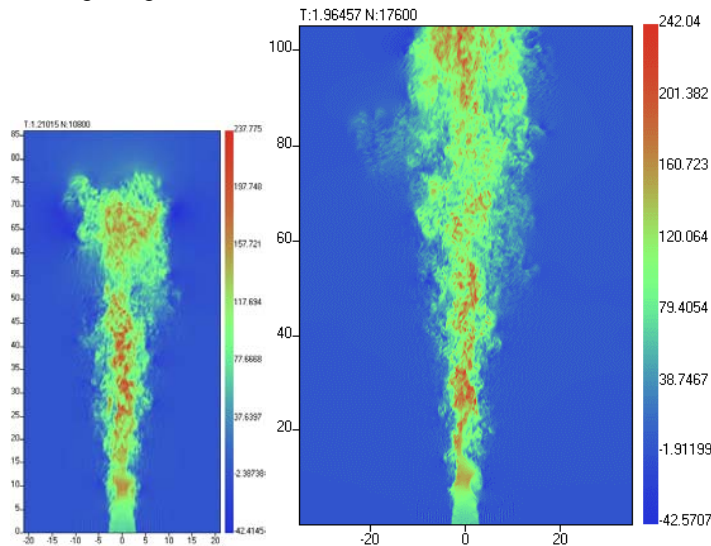
Fig. 2.1.Original geometry   **Fig. 3.1.** Raster patterns of u_z in variant 2: a) t=1.21, b) t=1.96

The lower boundary outside this aperture and the lateral boundaries are "rigid walls", on the upper boundary the condition of free flow is set. At initial time, fluid is at rest at any point inside the computational domain. The inflowing gas density is $\rho_1=0.5585$ and the unperturbed air density is $\rho_o=1$. We randomly selected the unit mass, because only the relative density value is important for the given incompressible flow. For the same reasons, we arbitrarily specify the

maximum value of pressure p_0 in the initial pressure profile: $\rho = \left(\rho_0^{\gamma-1} - \dfrac{\gamma-1}{\gamma\sigma_0} \cdot gz \right)^{\frac{1}{\gamma-1}}$; $\qquad p = \sigma_0 \cdot \rho^{\gamma}$,

$\qquad\qquad$ (2.1)

where $\quad \sigma_0 \equiv \dfrac{p_0}{\rho_0^{\gamma}}, \quad \rho_0 \equiv \rho(z=0) = 1$. The value $\quad p_0 \equiv p(z=0) = 3\cdot10^5$ has been chosen so as to provide

incompressibility of the flow: $c^2 = \gamma p / \rho \gtrsim 4.2\cdot10^5 >> u_{z0}^2 \approx 4.5\cdot10^3$.

EOS of an ideal gas with γ=1.4 has been taken, $c_V = 2.34\cdot10^3$. Gravitational acceleration is $g_z= -980$.

In various variants the computational domain has dimensions given in **Table 2.1**. The table also gives the number of computational cells along each coordinate axis ($N_x=N_y$), as well as the number of computational cells, N_l, falling to the input aperture side.

Variant No.	Number of cells	Computational domain size along Z-axis.	Number of cells N_l

| 1 | 83x83x256 | 120 | 12 |
| 2 | 165x165x421 | 105 | 24 |

Table 2.1. Computation setup

3 COMPUTATION RESULTS

The buoyant jet evolution can be seen from the raster patterns of velocity component u_z in **Fig. 3.1** (computations on a fine grid). Numerical results of the experiment are given in the paper [2] in the form of properly scaled values of buoyancy, vertical velocity and fluctuation momenta for three cross-sections of the jet - $z = 8D, 12D, 16D$ - depending on the self-similar variable η≡r/z (r,z are cylindrical coordinates):

$$F_1 = \left(\frac{z^5}{F_o^2}\right)^{\frac{1}{3}} g \frac{\Delta\rho}{\rho_\infty}, \qquad F_2 = <u_z> \left(\frac{z}{F_o}\right)^{\frac{1}{3}}, \qquad F_3 = \frac{(<T'^2>)^{\frac{1}{2}}}{\Delta T} = \frac{(<\rho'^2>)^{\frac{1}{2}}}{\Delta\rho},$$

$$F_4 = \frac{(<u_z'^2>)^{\frac{1}{2}}}{<u_z>}, \qquad F_5 = \frac{<u_z'T'>}{(<u_z'^2><T'^2>)^{\frac{1}{2}}} = \frac{<u_z'\rho'>}{(<u_z'^2><\rho'^2>)^{\frac{1}{2}}},$$

where $\Delta\rho = \rho_\infty - <\rho>$; $\Delta T = <T> - T_\infty$; $F_0 \equiv 2\pi \int_o^\infty u_{z0} \, g \frac{(\Delta\rho)_0}{\rho_\infty} r dr = 10^6 \, \mathrm{cm^4/s^3}$.

Thus, the following quantities are represented in the experiment: F_1 is the average buoyancy profile; F_2 is profile of the average vertical velocity $<u_z>$; F_3 is profile of relative mean-square temperature fluctuations; F_4 is profile of mean-square velocity fluctuations; F_5 is correlation coefficient.

Similar to the paper [2], averaging in the given paper was performed in time at points of the above-mentioned cross-sections ($z = 8D, 12D, 16D$) beginning from the time, when the jet had achieved the given cross-section, i.e. the values

of $<f> = \int_{t_0}^t f(t')dt' / (t - t_0)$, $f = \rho, u_z$ were found.

Fig. 3.2-3.6 gives profiles of quantities F_i obtained in computations for various cross-sections along with the experimental data.
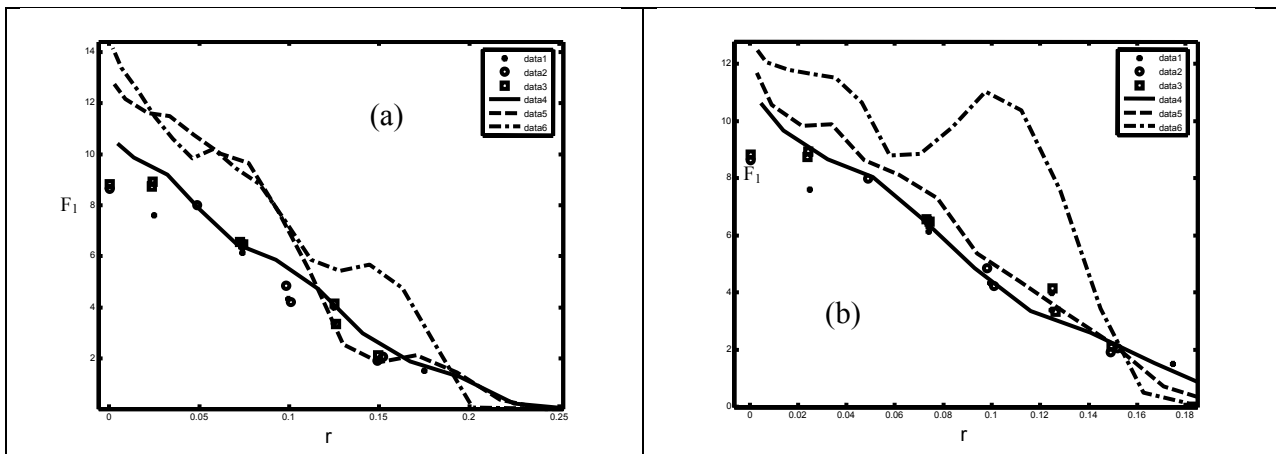
Fig. 3.2. Radial distribution of F_1 values in cross-sections: 1, 4 - $z = 8D$; 2,5 - $z = 12D$; 3, 6 - $z = 16D$. 1-3 – experiment, 4-6 – calculations; a) - b) variants 1 – 2.
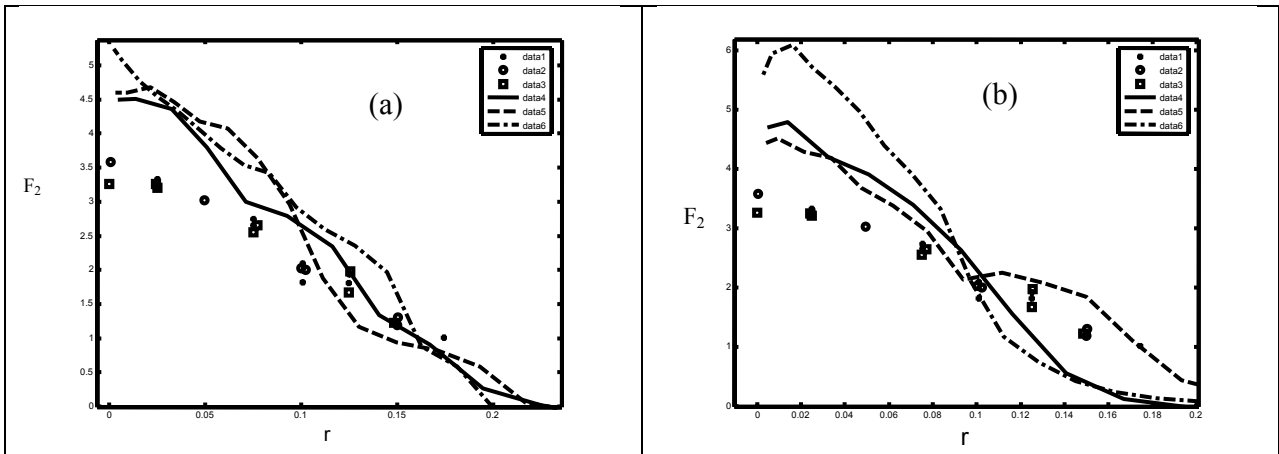
Fig. 3.3. Radial distribution of F_2 values in cross-sections; notations are the same as in Fig. 3.2
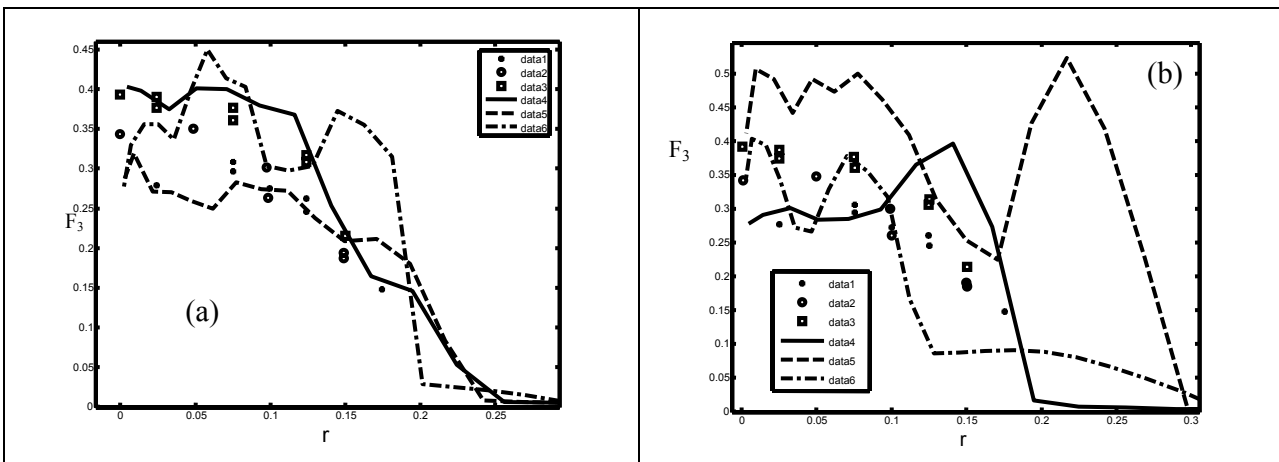
Fig. 3.4. Radial distribution of F_3 values in cross-sections; notations are the same as in Fig. 3.2
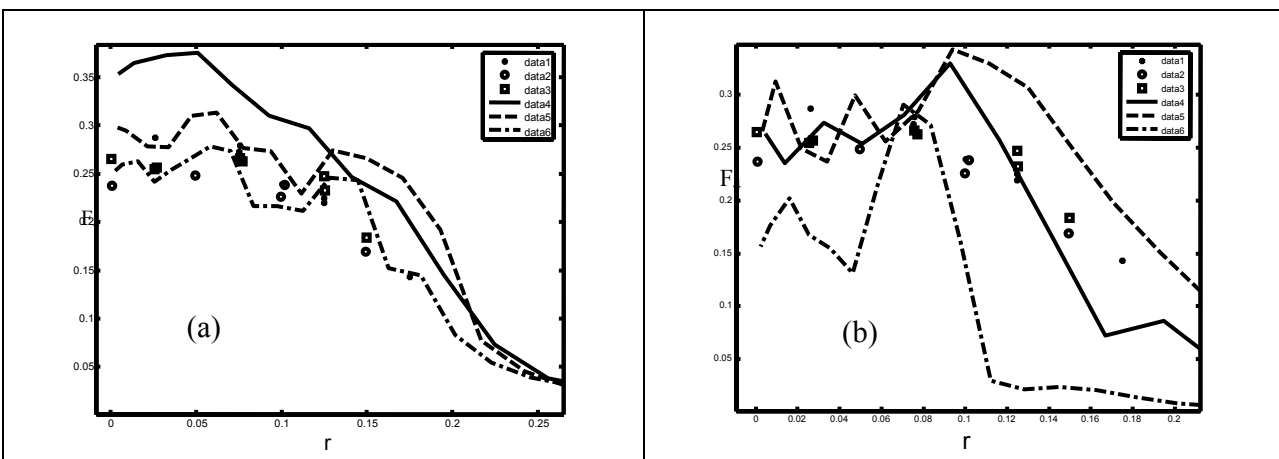
Fig. 3.5. Radial distribution of F_4 values in cross-sections; notations are the same as in Fig. 3.2.
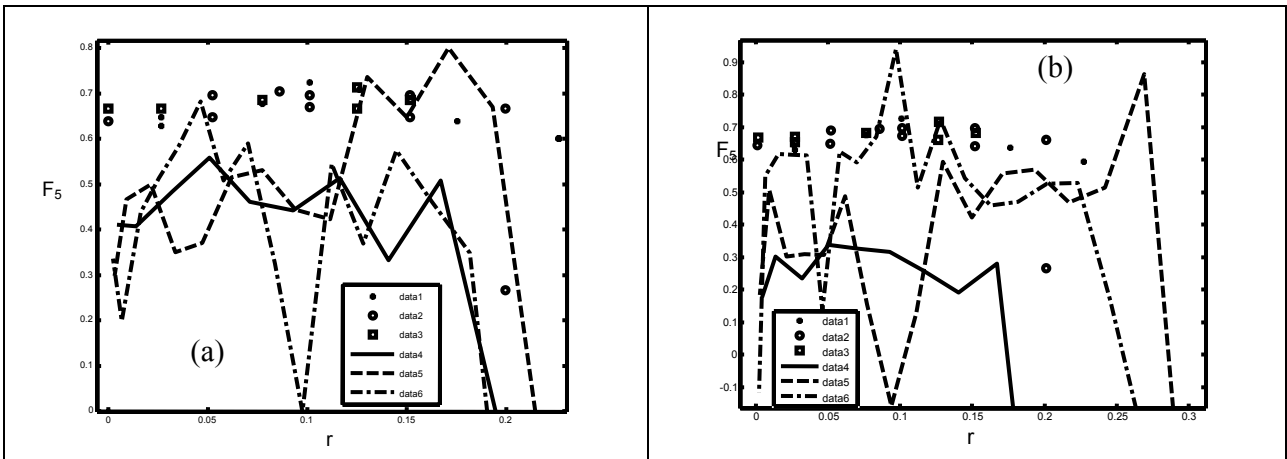
Fig. 3.6. Radial distribution of F_5 values in cross-sections; notations are the same as in Fig. 3.2

4 CONCLUSIONS

1. Profiles of average values of quantities and fluctuation momenta are, generally, in good agreement with the corresponding results of measurements, however, in the last cross-section ($z = 16D$)the upper boundary influence can be observed.
2. The computational grid varying has no significant influence on the results obtained for cross-sections 1 and 2, however, the upper boundary influence becomes noticeable with a smaller length of the computational domain (for a finer grid).

REFERENCES

[1] Stadnik A.L., Shanin A.A., Yanilkin Yu.V. Eulerian technique TREK for 3D gas dynamic multiple-component flow computations // VANT. Ser.: Math. Model. Phys. Process. 1994. Issue 4.
[2] William K.George.Jr., Ronald L.Alpert and Francesko Tamanini. Turbulence measurements in an axisymmetric bouyant plume, Int.J. Heat Mass Transfer, vol.20, pp.1145-1154, 1977.
[3] Statsenko V.P., Yanilkin Yu.V., Zharova G.V., F.Jeffry Martin, Kin Lam. Generation of a buoyant jet // VANT, Ser.: Theor. And Appl.Phys, Issues.3/1, 1994/1995.

e-mail: `yan@md08.vniief.ru`

Numerical Simulation of Perturbations and Turbulent Mixing Evolution at an Air-SF$_6$ Interface at High-Mach Shock Propagation

Olga SIN'KOVA, Vyacheslav STATSENKO and Yuri YANILKIN

Russian Federal Nuclear Center – VNIIEF Russia

Abstract: Data of our EGAK and TREK simulations of turbulent mixing at an air-SF$_6$ interface driven by a high-Mach shock wave ($Ma_{sw} > 5$) propagating though a shock tube are analyzed. The calculations were performed using both the $k - \varepsilon$ model and direct (without any turbulence models) 2D and 3D numerical simulations. Statistical processing of simulation data to determine correlation moments and fluctuation spectra was carried out. The simulation data are compared with known data of Nevmerzhitsky et al. experiments [1].

1 INTRODUCTION

Ref. [1] gives the results of experimental studies on the development of turbulent mixing at an interface between gases with different densities for shock Mach numbers from 2 to 9.

The shock wave was produced in a shock tube by detonating a combustible acetylene-oxygen gas mixture and passed from the "light" gas into the "heavy" gas. The initial pressure of the combustible mixture varied between 3 atm and 9.5 atm that allowed producing shock waves in the gases with Mach numbers from ≈2 to 9. Oxygen was used as the "light" gas, and SF$_6$, as the "heavy" gas. The experiments demonstrated that as the Mach number of the incident shock wave in the relatively strongly compressed "heavy" gas grows, the gas interface and the shock wave draw together, and this may cause the shock wave and turbulent mixing to influence each other.

In order to theoretically validate such a turbulence behavior, the problem of interest was calculated using direct 2D and 3D simulations without any phenomenological turbulence models.

Statistical processing of simulation data to determine correlation moments and fluctuation spectra was carried out.

The results of simulations using R-t curves for the shock wave and the turbulent mixing zone (TMZ) are compared with experimental data [1]. The paper also gives a comparison with 1D *k*-ε turbulence simulation data.

2 PROBLEM SETUP

The computational domain of the 3D problem is shown in **Fig.1.1**. Its upper region is occupied by a combustible gas mixture (GEM, stoichiometric acetylene-oxygen mixture). The mixture's pressure is varied to give different Mach numbers of the shock wave in SF$_6$ and different values of total energy release with its specific value being constant, $Q = 72,700$ (here and below, *m* - *g, t* - *ms, l* - *cm*). Beneath the mixture is air and SF$_6$ at atmospheric pressure. The temperature, t=0, is constant throughout the domain, and each region's EOS of ideal gas has its own value of γ given in **Fig.1.1**. Density perturbations, $\rho = \rho_0 \pm \delta\rho$ (the sign at transition between cells was given using a random number generator), were introduced in a small region of the problem domain.

The 2D simulations were performed with the same problem geometry and setup, with the difference that there was one horizontal coordinate *x*.
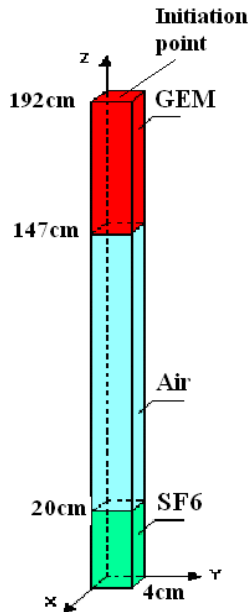
GEM: P_0 = 6.8atm (variant 1),
P_0 = 16 atm, (variant 2),
$\rho_0 = 1.2375 \cdot 10^{-3} \cdot P_0$.

Air: P_{a0} = 1atm,
$\rho_{a0} = 1.23 \cdot 10^{-3}$.

SF₆: P_1 = 1atm,
$\rho_1 = 6.5 \cdot 10^{-3}$.

3D grid: N_x=100, N_y=100, N_z=1200,
Nx=200, Ny=200, Nz=2400,
2D grid: Nx=100, Nz=800

h=(192-147) –GEM layer thickness

Fig.2.1. Problem setup

3 2D SIMULATION RESULTS

Shock propagation through the SF$_6$ region results in the emergence and growth of TMZ. In our simulations, for the shock Mach numbers of interest, the shock wave in the SF$_6$ region merges with the front boundary of TMZ at Mach numbers $Ma_{sw} \gtrsim 6.5$, which also was observed in the experiment [1]. **Fig.3.1** gives the calculated and experimental R-t diagrams of the TMZ rear boundary and the shock wave for Ma=7.8. The function of TMZ width (L) versus time is shown in **Fig. 3.2**. The same figure gives the distance between the shock front and the TMZ front boundary. The curve $L(t)$ for the simulations with a smaller pressure is situated lower.
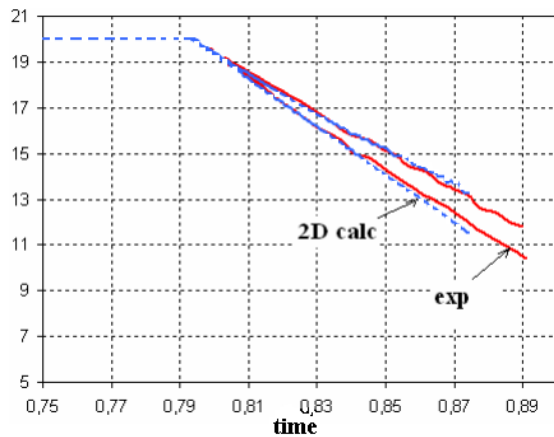
Fig.3.1. R-t diagrams of TMZ rear boundary and shock wave (Ma=7.8)
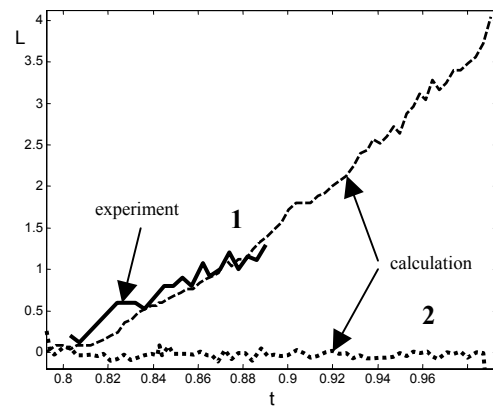
Fig.3.2. TMZ width (1) and distance between shock front and TMZ front boundary (2)

Let us examine the correlation of these data with the initial-stage Sedov's flat blast model. For the shock front radius, we may obtain: $R_F = \left[1.5a(t - t_0) + \left(h + \hat{R} \right)^{3/2} \right]^{2/3} - \hat{R}$. Here, $\hat{R} = h(\rho_0 - \rho_{a0}) / \rho_{a0}$, $a = \sqrt{(h \cdot \rho_0 \cdot Q / \rho_{a0}) \cdot (\gamma - 1) \cdot (\gamma + 1)^2 / (3\gamma - 1)}$. Let us assume that when the shock arrives at the air-SF$_6$ interface, the rate of TMZ width growth caused by the Richtmeyer-Meshkov instability is proportional to the mass

velocity u_a at the shock front. At this instant of time, the shock wave is strong: $p_a \gg p_{a0}$. Shock pressure: $p_a \sim 1/E$. Shock velocity in the air (formula (4.22) in [2]): $D_a = (p_a - p_{a0})/(\rho_{a0}u_a) \approx p_a/(\rho_{a0}u_a)$. Then: $M \equiv L_2/L_1 = (E_2 D_1)/(E_1 D_2)$, where D_1, D_2 $(D \equiv dR_F/dt)$ are the shock velocities in variants 1 and 2 at the time of shock arrival at the air-SF$_6$ interface.

Fig. 3.3 also shows a curve produced by multiplying L_1 in version 1 by M; it is almost identical to the curve L_2 in version 2 (time is counted from the moment of shock arrival at the air-SF$_6$ interface).

The distance between the shock front and the TMZ boundary, as evidenced by **Fig.3.2**, is zero, which agrees with the experimental results [1].

1 – variant 1
2 – variant 2
3 – conversion of (3) to (1) in accordance with approximate analytic theory
4 – distance between SW front and TMZ
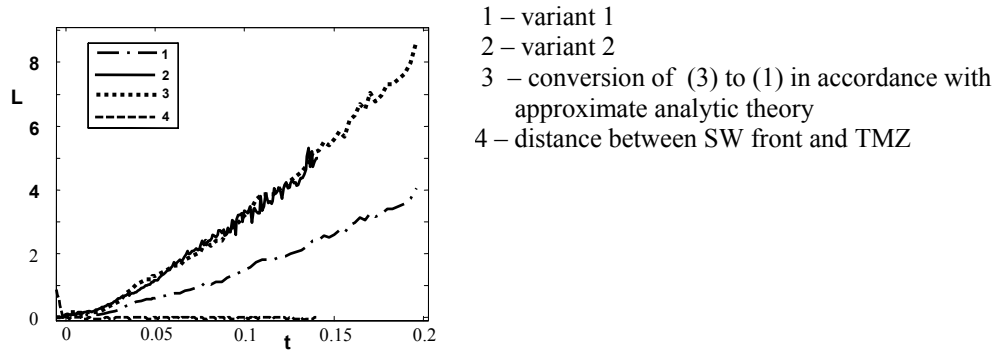
Fig.3.3. TMZ width (2D calculations)

Fig. 3.4a shows the spectra of longitudinal, u_y, and transverse, u_x, velocity components in the simulation with Ma=7.8 at $t \approx 0.7$ before the shock front arrives at the air-SF$_6$ interface. The spectra were obtained using Fourier transformation for the section $y = 30.6$. One can see that the spectra of both components are close to the Kolmogorov spectrum, but the intensity of their longitudinal component is an order higher than that of the transverse component.
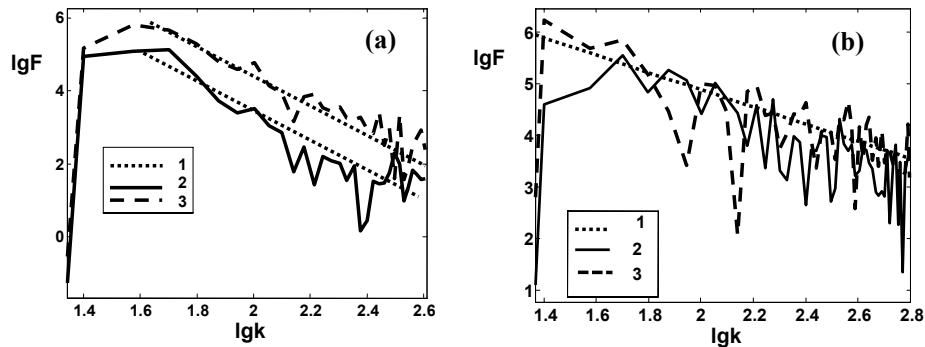
Fig.3.4. Fourier spectrum in variant 1 (a), t=0.7, y=30.6 and in variant 4 (b) z=12, x=2, t=0.74:
1 – Kolmogorov spectrum, 2 - u_z, , 3 - u_x.

4 3D SIMULATION RESULTS

Fig. 4.1 illustrates the simulation for Ma=7.8 on a 200 x 200 x 2400 grid in the form of isosurfaces of SF$_6$ volume fraction β=0.98. The same data for the simulation with Ma=10.6 are presented in **Fig. 4.2**.
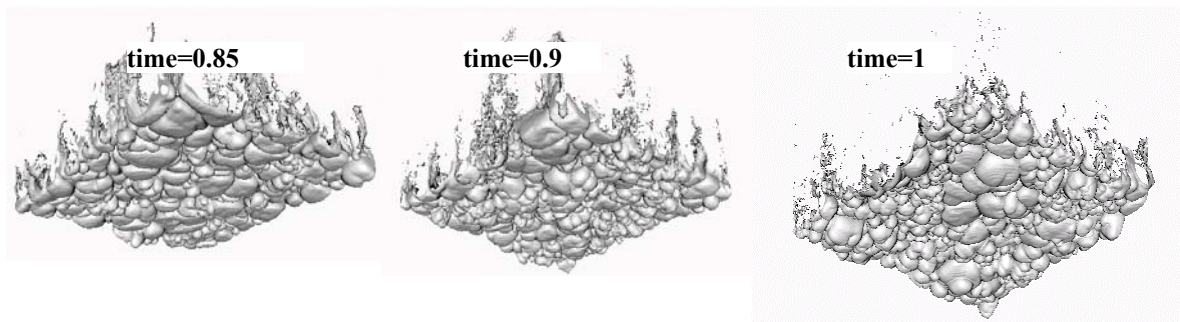
Fig.4.1. Isosurfaces of SF6 volume fraction β=0.98 (Ma=7.8)
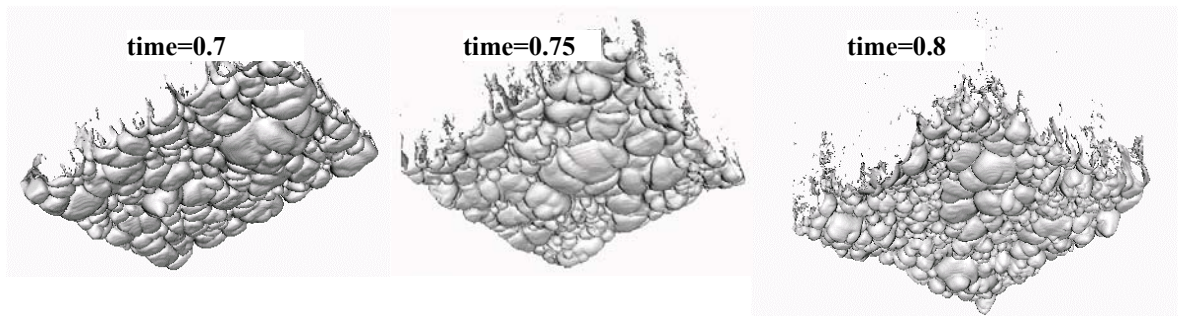
Fig.4.2. Isosurfaces of SF_6 volume fraction β=0.98 (Ma=10.6)
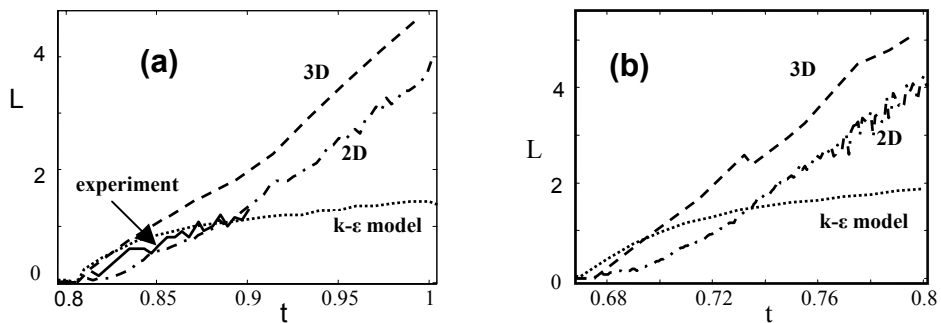
Fig.4.3. TMZ width; a) Ma=7.8, b) Ma=10.6

Fig. 4.3 shows TMZ widths for all the simulations with Ma=7.8 and Ma=10.6. One can clearly see close agreement between 2D and 3D simulations. Let us note the fairly developed TMZ in the 3D simulation with Ma=10.6 at t=0.74. The fluctuation spectrum of different velocity components in the section closest to the shock wave at this instant of time is shown in **Fig. 3.4b**. On the whole, it is close to the Kolmogorov spectrum. At small scales (large k), fluctuations of the longitudinal component prevail.

References

[1]   M.V.Bliznetsov, N.V.Nevmerzhitsky, A.N.Razin et al. Studies of Turbulent Mixing Development at a Gas-Gas Interface at Mach Numbers from 2 to 9. *Proceedings of 9th International Workshop on the Physics of Compressible Turbulent Mixing*, Cambridge, England, July 2003.

[2]   Baum F.A., Orlenko F.A., Stanyukovich K.P. et al. "Detonation Physics", "Nauka", M., 1975.

e-mail: `ye_wenhua@iapcm.ac.cn`

Preheating Effects on Nonlinear Ablative Rayleigh-Taylor Instability

Wen-Hua Ye and X. T. He

Institute of Applied Physics and Computational Mathematics, P. O. Box 8009, Beijing 100088, China

Abstract: Jet-like spikes of ablative Rayleigh-Taylor instability (ARTI) often occur in laser ficility experiments, also in the Eagle Nebula. They can quench ignition of ICF. For ARTI, our simulations by the LARED-S code show that preheating significantly reduces the linear growth rate, but also weaks nonlinear interaction. Preheating leads to formation of the long jet-like spike and large scale ARTI mixing. Appearance of the harmonic spikes results in rupture of the fundamental spike and small scale ARTI mixing. There exists the critical L_c for spike rupture and long jet-like spike formation. Main reason for formation of the jet-like spike is that preheating reduces vorticity generation, baroclinic term, thus weakens KHI growth.

1 INTRODUCTION

The ablative Rayleigh-Taylor instability is the critical issue for inertial confinement fusion (ICF)[1], and for astrophysics, such as the Eagle Nebula[2,3]. It can break up the implosion shell of ICF during the acceleration stage and destroy the central ignition hot-spot during the deceleration stage. Simulations show that the spike ruptures in the weak preheating case, such as for the Spitzer-Harm electron conduction, but we see long spike formation in our recent Shengguang-II experiment and in many other side-on experiments on the ICF laser facility[4,5,6]. Thus understanding the long spike formation is significant for ICF and astrophysics.

2 PHYSICAL MODEL

Direct-drive experiments on the GEKKO XII[7] and the NOVA[8] showed the large reduction of linear growth rate of the ARTI, and preheating by the Fokker-Planck simulation of non-local electron conduction gives good explanation for the reduced growth rate.
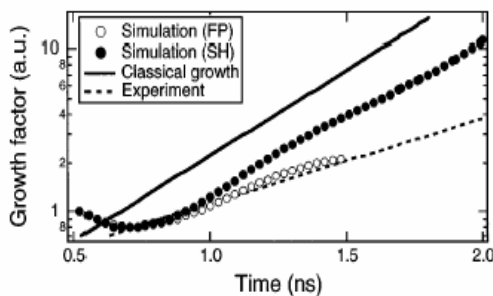
Fig. 1 GEKKO XII experiment and Fokker-Planck simulation
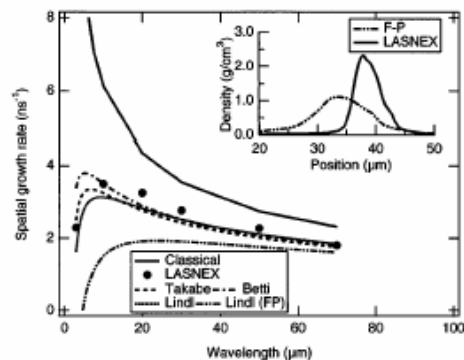
Fig. 2 NOVA experiment and LASNEX simulation

The Fokker-Planck results can be reproduced by the preheating model $\kappa = \kappa_{SH}[1 + f(T)]$. Fitted parameter a_i in the preheating function $f(T) = \sum_{i=1}^{5} a_i T^{-(i-1)/2}$ can be obtained by the comparison with the Fokker-Planck result[9]. *f(T)* interprets the preheating tongue effect in the cold plasma ahead of the ablative front and return to SH electron conductivity outside the ablative front for the blow-off high temperature plasmas. Because of high cost for solving the 2D Fokker-Planck equation of electron and alpha particle or the transport equation of radiation, this method can is used to study the ARTI in preheating for electrons, alpha particle, or X-ray.

The LARED-S code[10] is used in numerical study of the nonlinear ARTI, which consider fluid dynamics, electron conductivity, multi-group radiation diffusion, 1D laser absorption, etc. For simplification in simulation, ideal EOS is used and radiation effect is ignorant. FCT or PPM method is used to solve fluid dynamic equations, and slide fine mes-

hes is used to track the ablative front. Our simulation results show that the spike ruptures in the weak preheating case and long jet-like spike forms in the preheating case, seeing in fig. 3. In the different preheating cases, the acceleration g and the ablative velocity V_a only have a little change, but density gradient scale length, $L \propto \kappa_0 T^{5/2} f(T)/\rho_a V_a$, changes largely, which significantly affects evolution of the nonlinear ARTI.

3 SIMULATION RESULTS AND ANALYSIS

First, the 100μm CH foil is simulated with the initial density 1.0g/cm^3. Laser wavelength is 0.264μm, and laser intensity linearly grows 4ns to peak, 3×10^{14}W/cm^2, then remains invariable. We chose $f(T)=a/T+b/T^{3/2}$, T in the unit of 10^6 °K. Results of linear growth rate are given for four different preheating cases: (A) a=1.0, b=0.5; (B) a=1.5,b=0.75; (C) a=2.0,b=1.0; (D) a=4.0,b=2.0. Acceleration changes very little, V_a only increases from 0.5 to 0.68μm/ns, but L has big change, from 0.45 to 1.0 μm, 2.2 times large. Linear growth rates are shown in fig. 4 (left).
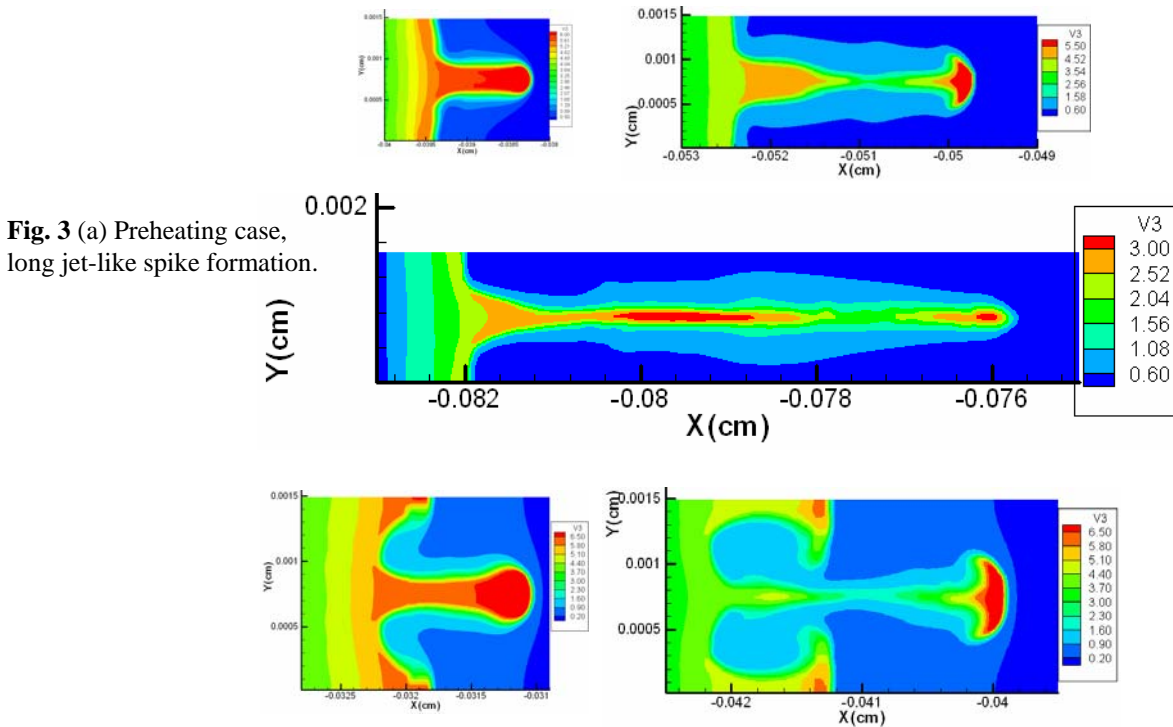
Fig. 3 (a) Preheating case, long jet-like spike formation.

Fig. 3 (b) Less preheating case, master spike ruptures.

Interestingly, between the spike rupture and the formation of the long jet-like spike, there exists the critical L_c between (B) and (C), about 0.65μm.

Second, we simulate the 200μm CH foil with the initial density 1.0g/cm^3. Laser wavelength is 0.35μm, and laser intensity linearly grows 0.5ns to peak, 10^{15}W/cm^2, then remains invariable.
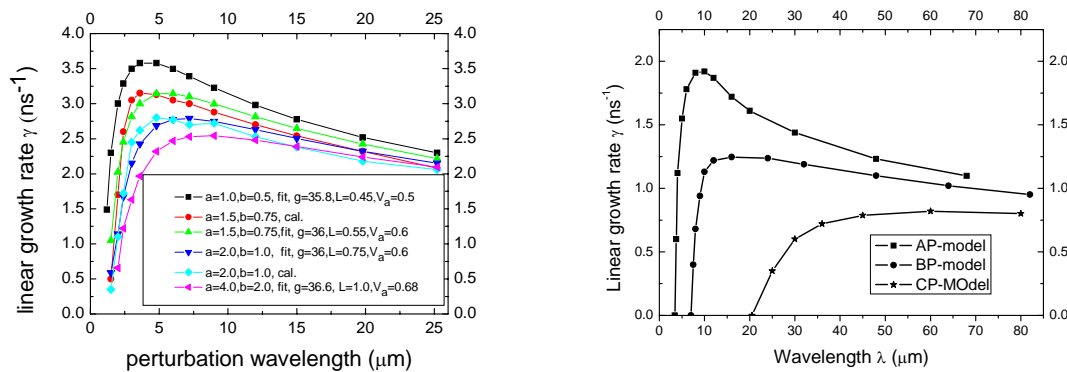
Fig. 4 Left: Comparison of linear growth rate of the ARTI between the Takabe formula $\gamma = 0.9\sqrt{kg/(1+kL)} - 2kV_a$ and LARED-S simulation for the 100μm CH foil. Acceleration g, ablation V_a and the density gradient scale length L are in units of μm/ns^2, μm/ns and μm, respectively. $f(T)=a/T+b/T^{3/2}$, T in unit of 10^6 °K. AP: a=1.0,b=0.3; BP: a=10, b=2.0; CP: a=100, b=10. The cut-off wavelengths are 3.5, 6.7 and 20μm, and L are 0.55, 1.46 and 4.88μm for AP, BP and CP, respectively.

Right: curves of linear growth rate of the ARTI for the 200μm CH foil in three different preheating cases.

Second and third harmonic generation coefficients $C(k_2)$ and $D(k_3)$ are defined according to the formulas below from comparison of the weak nonlinear theory[11] between the classical RTI and the ARTI

$$\eta_2^{(2)} = \frac{1}{2}C(k_2)k_1(\eta_1^L)^2, \quad \eta_3^{(3)} = \frac{3}{8}D(k_3)k_1^2(\eta_1^L)^3$$

$C(k_2)$ and $D(k_3)$ can be easily obtained by fitting simulation results to above formulas.
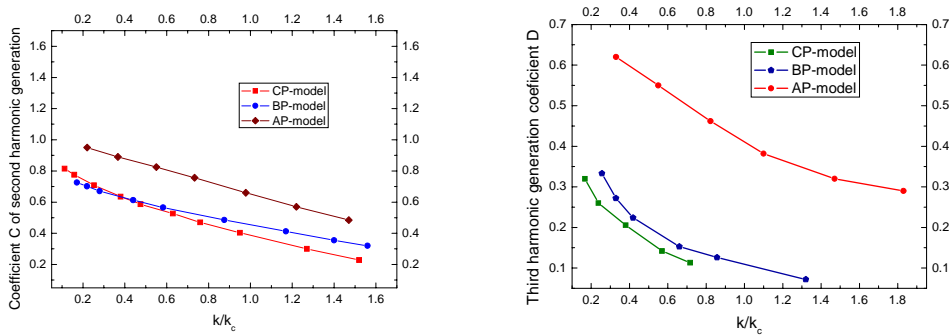
Fig. 5 Second and third harmonic generation coefficients $C(k_2)$ and $D(k_3)$. As shown in figure, $C(k)$ reduces 40 to 80% , and $D(k)$ reduces 10 to 30%, compared with the classical RTI.

Appearance of the second harmonic spike is the cause for rupture of the spike. Material in the root of the fundamental spike flows to the second harmonic spike region and the head of the fundamental spike, which leads do rupture of the fundamental spike.
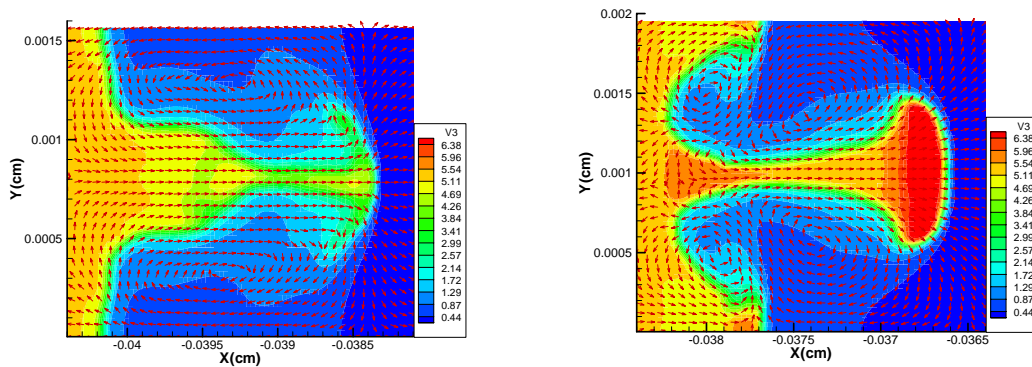
Fig. 6 Left: spike do not rupture in the preheating case. Right: harmonic spikes occur and spike ruptures in the weak preheating case.
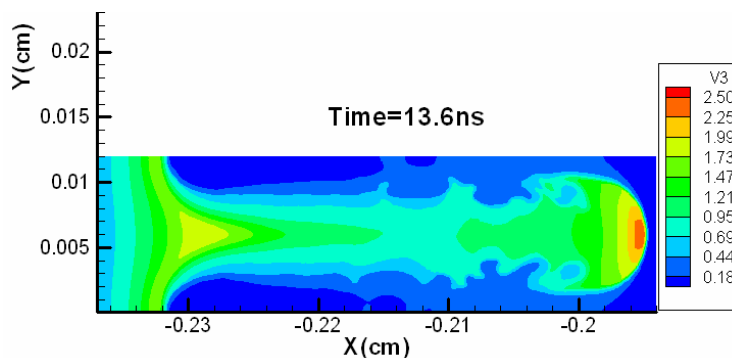
Fig. 7 Very long jet-like spike forms at late time for the 400µm CH foil in the preheating case.
We have simulated spike growth for the 400µm CH foil with the 120µm single mode perturbation in the preheating case (a=100,b=10). Laser intensity linear grows 0.5ns to peak, 10^{15}W/cm^2. The simulation shows that a 360µm long spike forms at 13.6ns and mixing zone width (MZW) h is proportional to t, not h $\propto$ t^2.
Preheating reduces the temperature and density gradients, enhances the density (or temperature) gradient scale length L, smoothes effectively out the KHI curl, therefore leads to RTI mixing in the acceleration direction.

4 SUMMARY

Preheating significantly enlarges the density gradient scale length, weakens nonlinear ARTI mode coupling, smoothes the KHI curl, and leads to formation of the long jet-like spike and large scale RTI mixing. Appearance of the harmonic spikes results in rupture of the fundamental spike and small scale RTI mixing. There exists the critical L_c for spike rupture and long jet-like spike formation. The study can help understand the physics of long spike formation in the nonlinear ARTI experiments on the ICF laser facility as well as in astrophysics.

Necessary condition of formation of the jet-like spike: enhanced density gradient stabilization due to preheating that weakens nonlinear ARTI interaction, and the fundamental mode dominates nonlinear RTI growth. Main reason of formation of the jet-like spike: preheating reduces vorticity generation, baroclinic term, thus weakens KHI growth.

REFERENCES

1. J. D. Lindl, P. Amendt, R. L. Berger, et al., Phys. Plasmas **11**, 339(2004).
2. B. Remington, D. Arnett, P. Drake, and H. Takabe, Science **284**,1488(1999).
3. B. Remington, D. Arnett, P. Drake and H. Takabe (ed), Astrophys. J. suppl. 127(2000), part 1, No.2.
4. S. Atzeni and J. Meyer-ter-Vehn, *Inertial Fusion*, Clarendon Press, Oxford, 2003.
5. B. A. Remington, et al., Phys. Fluids B **5**(7), 2589(1993).
6. R. J. Mason, et al., Phys. Plasmas **8**(5), 2338(2001).
7. K. Shigemori, et al., Phys. Rev. Lett.**78**(2), 250(1997).
8. S. G. Glendinning et al., Phys. Rev. Lett.**78**(17), 3318(1997).
9. Ye Wenhua, Zhang Weiyan and He Xiantu, Phys. Rev. E 65, 057401, 21(2002).
10. Ye Wenhua, Zhang Weiyan, Chinese Phy. Lett., Proc. APFA&APPTC, 178(1999).
11. J. Sanz, J. Ramis, R. Bett and R. P. Town, Phys. Rev. Lett. **89**, 195002(2002).

e-mail: `ajoseph@bgu.ac.il`

Richtmyer-Meshkov Instability: Asymptotic Velocities of Three Dimensional Bubbles and Spikes

Arnon YOSEF-HAI[1,2], Daniela KARTOON[1,2], Oren SADOT[1,2], Yonatan ELBAZ[2], Gabi BEN-DOR[1], Dov SHVARTS[1,2]

[1]*Ben-Gurion Universtiy of the Negev, Beer-Sheva 84105, ISRAEL*
[2]*Nuclear Research Center, Negev, Beer-Sheva 84190, ISRAEL*

Abstract: The time evolution of the Richtmyer-Meshkov instability was experimentally and numerically studied for two-dimensional (2D) and three-dimensional (3D) single-mode initial perturbations. The results for the dimensionality dependence of the bubbles were found to be in good agreement with the theoretical prediction of late time 1/t decay, with the correct proportionality factors. On the other hand the spikes displayed no obvious dependence on their dimensionality. Furthermore the 1/t decay expected also for the spikes was not observed in the experiments or in the numerical simulations.

1 INTRODUCTION

During the late time evolution of a single-mode interface under Richtmyer-Meshkov Instability (RMI), the drag and buoyancy forces govern the motion of the tip of the bubble and this results in a 1/t decrease of the bubble velocity with time. A simple analysis [1,2,3] taking into account these forces results in the following expression for the asymptotic velocity of the bubble:

$$u_B^{asy} = \frac{1}{C_d}\left(\frac{1-A}{1+A} + C_a\right)\frac{\lambda}{t}, \tag{1.1}$$

where A is the Atwood number, λ is the wavelength of the bubble, t is the time that passed since the passage of the shock wave and C_a and C_d are geometric coefficients that are dictated by the dimensionality. In the two-dimensional (2D) case C_a=2 and C_d=6 and in the three-dimensional (3D) case C_a=1 and C_d=2. Equations (1.2) give the 2D and 3D asymptotic velocities for the limiting case of high Atwood number A→1:

$$u_{2D\,B}^{asy} = \frac{1}{3\pi}\cdot\frac{\lambda}{t}, \qquad\qquad u_{3D\,B}^{asy} = \frac{1}{2\pi}\cdot\frac{\lambda}{t}, \tag{1.2}$$

Analysis based on the assumption that similar drag-buoyancy forces considerations can be applied to the tip of a RMI single-mode spike, using the same C_a and C_d coefficients as used for the bubbles yields 1/t late time velocity dependence also for the spikes, with different proportionality factors [3,4].

The model used in the current work to describe the complete time-dependent evolution of a single-mode RMI interface is similar to a previously reported model [5] which reproduces early evolution accurately to the second order and an asymptotic stage of the form 1/t with the correct proportionality factors. The original model was generalized for arbitrary Atwood number and was adapted also for the 3D case.

2 EXPERIMENTAL SETUP

The experiments were carried out in a 8cm x 8cm square cross section shock tube. In order to generate the shock wave the 2.5m-long driver section is slowly filled with air until a mylar sheet separating the driver section from the driven section is ruptured. The air-filled driven section is 2.5m long, which ensures that when the shock wave reaches the 0.6m-long test section the shock is fully stabilized. Both driven section and test section are initially at ambient pressure. In this configuration an incident shock wave of Mach number 1.2 is produced with less than a 5% variation. The actual shock-wave velocity for each specific experiment is measured from the schlieren images of that experiment.

The test section is initially separated into two parts by a very thin membrane. Each part is filled with one of the two investigated gases. The side upstream of the membrane is filled with air, while the side downstream of the membrane is filled with SF_6. Both sides are initially at ambient pressure. Upon the passage of the shock wave through the membrane, the membrane is ruptured and the mixing process begins. The Atwood number after the shock passes the interface between the two gases is about 0.7.

To create a well-defined initial perturbation thin copper wires are stretched across the frame holding the membrane at different heights and the membrane is placed on them. More details can be found in the next section.

A piezoelectric pressure transducer is flush mounted on the shock-tube wall near the end of the driven section. The signal that is generated when the shock wave passes the transducer is used to trigger the diagnostics timing sequence.

Windows are built into the sides of the test section. Their height spans the entire 8cm height of the test section, allowing optical diagnostics of the complete cross section. The length of the windows is 20cm, beginning at the frame holding the membrane.

The schlieren technique is used to visualize the flow field in the test section. The light source for the schlieren system in these experiments is a pulsed copper-vapor laser. The laser produces 30ns-long pulses with a repetition rate of about 10kHz. A shutterless rotating-prism camera records the schlieren photographs. An external shutter is used to create a laser pulse train at the right time, starting just before the shock passes the interface, and ending before double exposure of the film occurs.

The resulting negative images on the film are converted into digital images using a film scanner. Using a specially written computer application the images are calibrated and the same application is used to measure any required length on the images (such as the shock-wave position, bubble-front position etc.).

3 THE MEMBRANE CARRYING FRAME

Two types of membrane are used to create the initial conditions imposed on the interface between the two gases in the test section: In order to create a 2D perturbation the membrane is sandwiched between two parts of the frame - one carrying copper wires to create the crests and the other for the troughs, as shown in Fig 3.1.a . In order to create a 3D perturbation a formation of pyramids which will form the crests is created using copper wires, next, the thin membrane is laid over these pyramids and finally two additional copper wires are stretched over the membrane in order to force it into the troughs. Fig.3.1.b. shows this construction without the membrane for the sake of clarity.
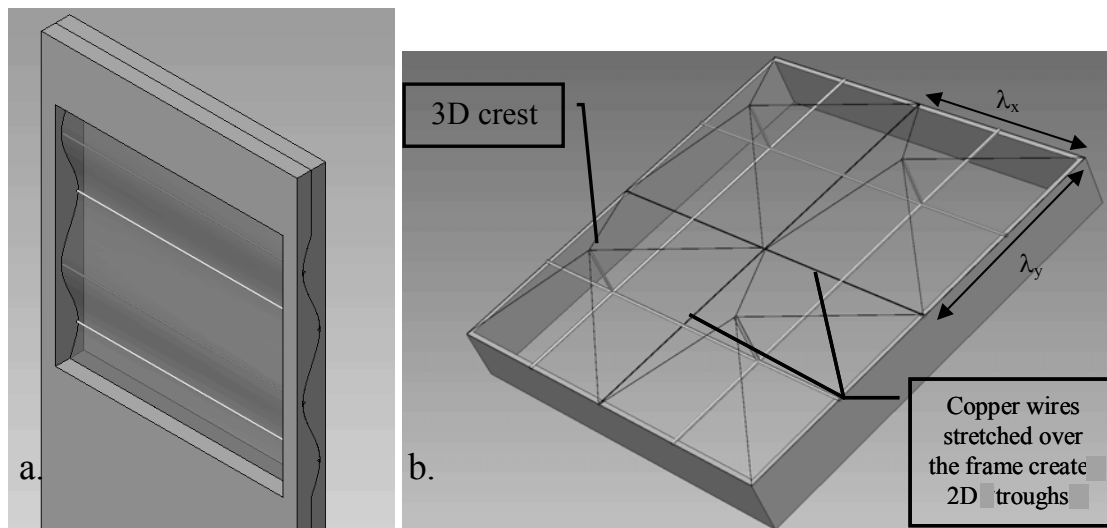
Fig. 3.1. The wire frames used to hold the membrane: a. 2D configuration b. 3D configuration

As can be seen clearly, the crests created using this kind of frame are of 3D nature while the troughs are 2D. The frame can be used to create 3D bubbles with 2D spikes between them by positioning the frame with the 3D crests facing the heavy gas or 2D bubbles with 3D spikes between them by positioning it with the 3D crests facing the light gas. Experiments with the frame in the first position are termed here "3D bubble experiments" and experiments with the frame in the latter position are termed "3D inverse experiments". In the case of the 3D constructions, the effective wavelength that can be attributed to the bubbles or spikes is given by equation (3.1):

$$\lambda_{\text{eff}} = \frac{1}{\sqrt{\lambda_x^{-2} + \lambda_y^{-2}}} \, , \tag{6.1}$$

where λ_x and λ_y are the wavelengths in the x and y directions respectively.

4 EXPERIMENTAL RESULTS

The time evolution of the bubble and spike heights is plotted in Fig. 4.1a for the 3D bubbles experiment with an effective wavelength 28mm and in Fig4.1b for the inverse 3D experiment of the same effective wavelength. In both graphs the results are compared to the same 2D experiment with bubbles of wavelength 27mm, and to the 2D and 3D models. Since these three experiments have the same initial amplitude (6mm peak to peak) and almost the same wavelength, they can all be plotted on the same un-normalized axes. The results for the bubbles are plotted with positive values of the y-axis, while the results for the spikes are plotted using negative values of the y-axis. This convention is maintained throughout this work.
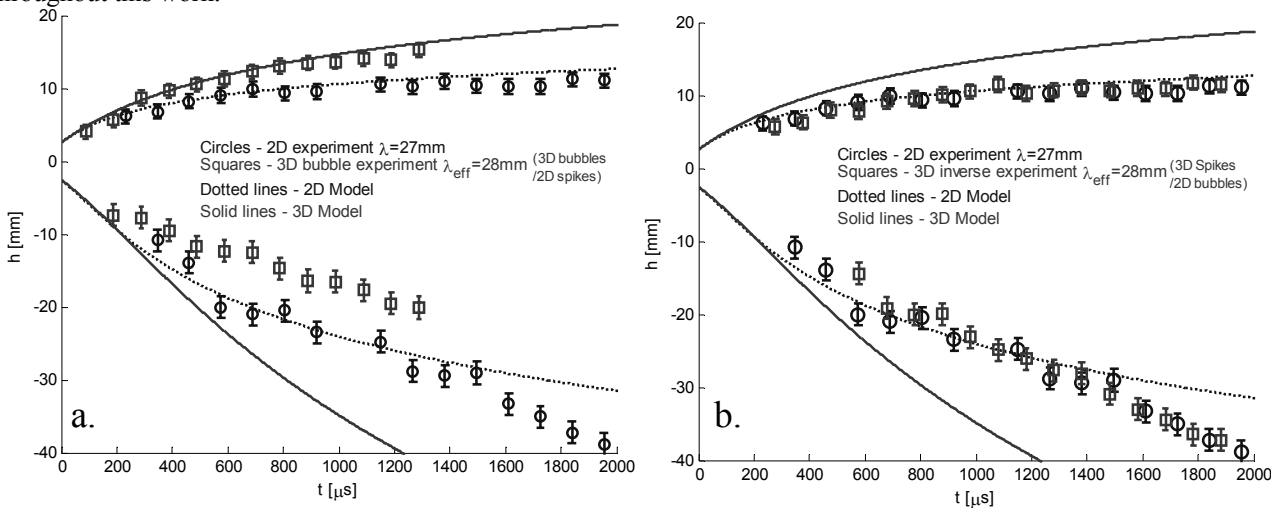
Fig. 4.1. a. Results of 2D and 3D experiments b. Results of 2D and inverse 3D experiments

These graphs clearly show that 3D bubbles grow faster than 2D bubbles (both in 2D and in inverse 3D experiments). The theoretical models predict well the dimensional dependent time evolution of the bubbles. The spikes on the other hand display no clear dimensionality dependence – as can be seen in Fig. 4.1b, both 2D and 3D spikes exhibit the same growth rate. Furthermore, their late time evolution does not agree with neither the 2D nor the 3D models, and their velocity does not seem to decay at the expected asymptotic rate of 1/t.

Experiments with several other wavelengths were performed, and their results are summarized in Fig. 4.2 using normalized coordinates. It can be seen that the bubbles fall into clear categories according to their dimensionality, while there is no similar distinction for the spikes.
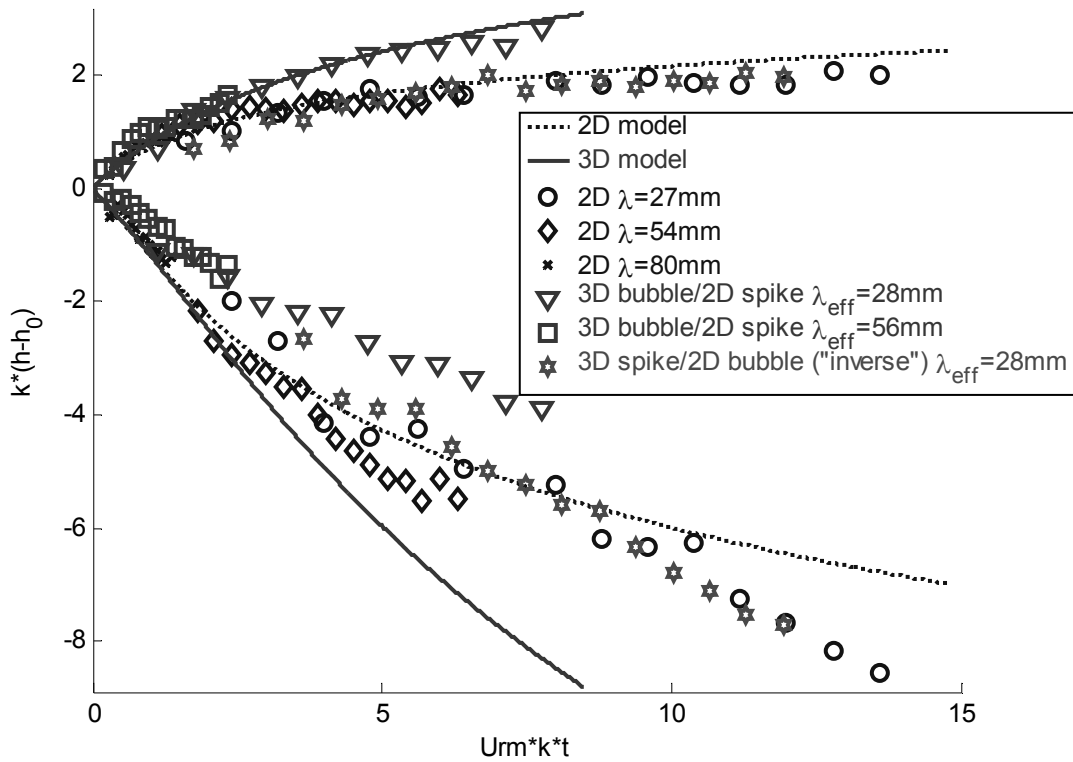
Fig. 4.2. Summary of 2D and 3D experiments in normalized coordinates

Full 2D and 3D numerical simulations (NS) of the experimental setups were performed using the ALE hydrodynamic code LEEOR3D. The heights of the bubbles and spikes from these simulations are plotted in Fig 4.3a and compared to the models. The bubble and spike tips velocities were also extracted from the NS and compared to the asymptotic velocities predicted by the models (Fig. 4.3b).
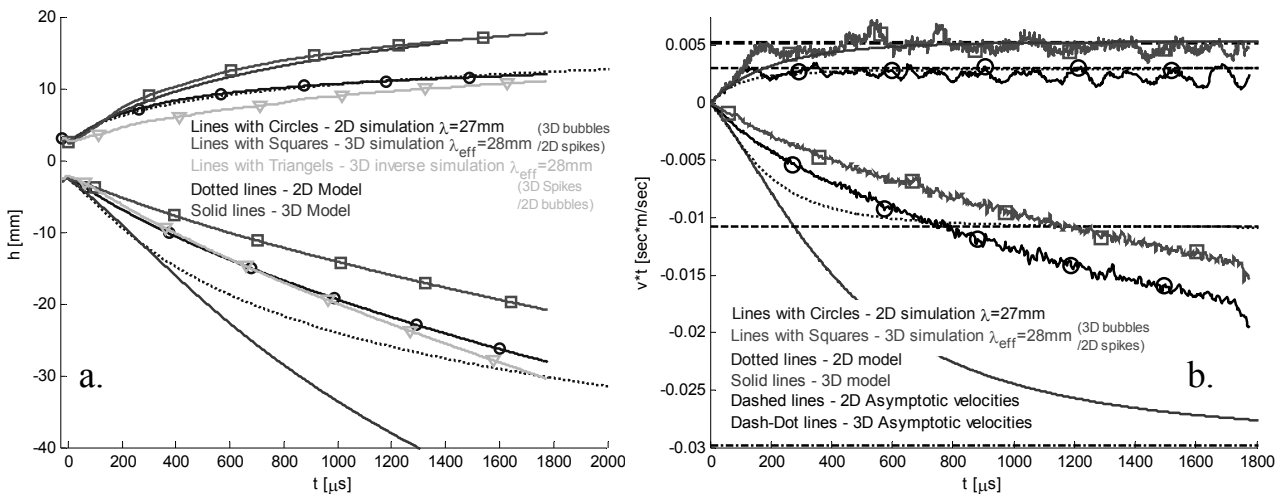
Fig. 4.3. a. Results of simulation for the 2D, 3D, and "inverse" 3D setups b. Velocities from simulation for the 2D and 3D experiments

The NS results further establish the main conclusions obtained from the experiments - Bubbles' rise depends on their dimensionality: 3D bubbles rise faster than 2D bubbles throughout their evolution. This phenomenon is well predicted by the analytical model. Spikes exhibit the same growth rate in both 2D setups and experiment in which the bubbles were 2D and the spikes were 3D ("3D inverse experiment"). At late times these spikes grow faster than predicted by the 2D model. In experiments with 3D bubbles and 2D spikes ("3D bubble experiments"), the spikes grow slower than in any other setup. In contrast to the drag-buoyancy model prediction that 3D spikes should have higher terminal velocity

than 2D spikes, no clear dimensionality dependence was manifested in the experiments. In all cases examined no 1/t saturation of the spike velocities was observed.

5 EXTENDING THE STUDY USING NUMERICAL SIMULATIONS

An extensive use of NS was made in order to further examine the interface behavior under conditions inaccessible through experiments. These NS were made so as to best satisfy the assumptions of the model regarding the initial conditions of the RMI, in contrast to the NS shown above which were made to simulate the experimental setup. Two main features of the initial condition were studied: the geometry of the perturbed interface and the impulsivity of the shock. As was explained above in detail, the membrane shaping method used in the experiments does not allow creating fully 3D perturbations. Using NS allowed us to study ideal 3D interfaces, with both 3D bubbles and 3D spikes, and having sinusoidal shapes in accordance with the potential model assumptions rather than the saw-tooth shapes of the experimental initial perturbation. The NS also helped to assure us that the experimental initial amplitudes were not too big, using initial amplitudes much smaller than experimentally realizable. The influence of the shock wave was examined using an initial velocity field consistent with the flow potential which was used in the analytical model instead of a physical shock wave, thus eliminating the inconsistencies with the model resulting from the finite time it takes the shock wave to pass through the initial interface. As an example Fig. 5.1 shows the comparison between NS with sinusoidal and saw-tooth initial perturbations both in 2D and 3D configurations. It is apparent that the bubbles show no sensitivity to the exact shape of the initial perturbation, but only to its dimensionality. At late times the spikes do show some sensitivity to the initial conditions which can not be attributed to their dimensionality, but in all cases examined there was no 1/t decay of their velocity.
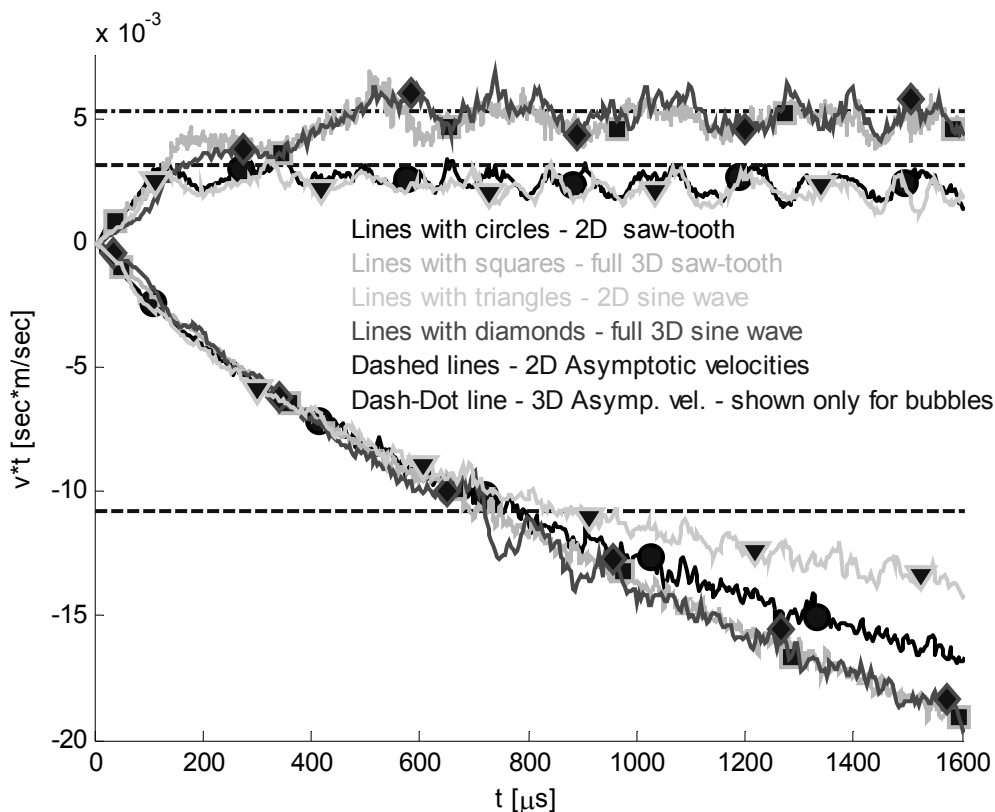
Fig. 5.1. Bubbles and spikes velocities from NS with different shapes of initial perturbation

6 SUMMARY

This work examined experimentally the evolution of 3D single-mode perturbations upon the passage of a shock wave between two gases with different density ratios. The experiments were performed in a low-Mach shock tube (M~1.2), with diagnostics consisting of fast schlieren photography of the contact surface, enabling the tracing of the evolution with time of the bubbles and spikes. The experiments were performed for several wavelengths, and their results were

compared with 2D experiments done in the same shock tube. The experimental results were also compared to an analytical model, adapted to the 3D case, and to the results of full-scale 3D numerical simulations.

The comparison of the results for the bubbles from the 3D and the 2D experiments shows that the 3D bubbles grow faster, as could be expected due to their smaller area-to-volume ratio. Good agreement with the analytical model and the numerical simulations was obtained, thus confirming the theoretical prediction of the asymptotic velocity of 3D bubbles and its dependence on the wavelength and the density ratio of the two gases. This asymptotic velocity is one of the key elements of a statistical model describing the evolution of a multimode TMZ [3].

The experiments gave somewhat more surprising, less clear results for the 3D spikes. Comparison to the 2D experiments shows no obvious dimensional dependence for the spikes. Furthermore, comparisons to the theoretical model and the numerical simulations show that the spikes (both 2D and 3D) do not reach an asymptotic velocity proportional to 1/t as suggested by the model, but instead decay more slowly. In order to deepen the understanding of the spikes' behavior, extensive use was made of numerical simulations in order to examine a variety of parameters and configurations which are not accessible through experiments. Both the experimental and the numerical results undermine the fundamental assumptions used to adapt the drag-buoyancy model to the spikes, and emphasize the differences between the evolution of bubbles and spikes in the nonlinear regime.

Similar results have already been reported for the Rayleigh-Taylor instability [6] and were attributed to the formation of vortices in the proximity of the spike tip. When the Atwood number is high enough the vortices move with the spike. This change to the velocity field which accelerates the spike into the light fluid is not taken into account by the naïve drag-buoyancy model.

REFERENCES

[1]   Layzer, D. 1955, Astrophys. J. **122**, 1.

[2]   Hecht, J., Alon, U. and Shvarts, D. 1994, Potential flow models of Rayleigh-Taylor and Richtmyer-Meshkov bubble fronts. Phys. Fluids, **6**, p. 4019.

[3]   Oron, D., Arazi, L., Kartoon, D., Rikanati, A., Alon, U. and Shvarts, D. 2001, Dimensionality dependence of the Rayleigh–Taylor and Richtmyer–Meshkov instability late-time scaling laws. Phys. Plasmas **8**, p. 2883.

[4]   Arazi, L. 2001. A drag-buoyancy based study of the late-time RT and RM scaling laws. MSc Thesis. Tel-Aviv University, Israel.

[5]   Sadot O., Erez L., Alon U., Oron D., Levin L.A., Erez G., Ben-Dor G. & Shvarts D. 1998, Study of nonlinear evolution of single-mode and two-bubble interaction under Richtmyer-Meshkov instability, Phys. Rev. Lett., **80**, p. 1654.

[6]   Goncharov V. N. 2002, Analytical Model of Nonlinear, Single-Mode, Classical Rayleigh-Taylor Instability at Arbitrary Atwood Numbers. Phys. Rev. Lett. **88**, 134502

e-mail: `david.youngs@awe.co.uk`

3D Numerical Simulation of Turbulent Mixing in Spherical Implosions

David L YOUNGS

AWE, Reading, Berkshire, United Kingdom, RG7 4PR

Abstract : A spherical polar mesh option has been added to the hydrocode TURMOIL and this has been used to calculate turbulent mixing in spherical implosions. TURMOIL is essentially an Eulerian hydrocode. However, for calculating implosions near-Lagrangian mesh motion is used in the radial direction and this gives a significant increase in accuracy. Results are shown for a simplified implosion: hydrodynamics only, with perfect gas equations of state. Realistic initial perturbations are used, based on typical power spectrum measurements for ICF-related targets. The effect of mesh size is investigated. Three-dimensional simulation of turbulent mixing for real applications is considered impractical at present. However, simplified simulations of the type shown here are extremely useful for validation of the engineering models which can be used for real problems. To illustrate this approach, results from the 3D simulations are compared with a simple buoyancy-drag model implemented in a 1D Lagrangian hydrocode .

1 INTRODUCTION

The MILES code TURMOIL has previously been used to calculate turbulent mixing due to Rayleigh-Taylor (RT) and Richtmyer-Meshkov (RM) instabilities in planar geometry [1,2]. Application to mixing in a simple spherical implosion, a much simplified version of an Inertial Confinement Fusion implosion is considered in this paper. Fluid viscosities are assumed to be very small so that high Reynolds number turbulent mixing occurs.

2 A SIMPLE SPHERICAL IMPLOSION

The initial geometry for the unperturbed spherical implosion , in dimensionless units, is

$0 < r < 10$: density=0.05, pressure = 0.1
$10 < r < 12$: density=1.0 , pressure = 0.1

Perfect gas equations of state are used with $\gamma = 5/3$. The ratio of the specific heats for the two fluids is 20:1, thus giving equal initial temperatures in the two regions. The implosion is driven by applying a prescribed pressure, p, versus time at the outer boundary, initially at r=12. This is obtained by linear interpolation in time between the values:-

t=0.0 p=10.0, t= 0.5   p=10.0, t= 3.0 p= 0.0
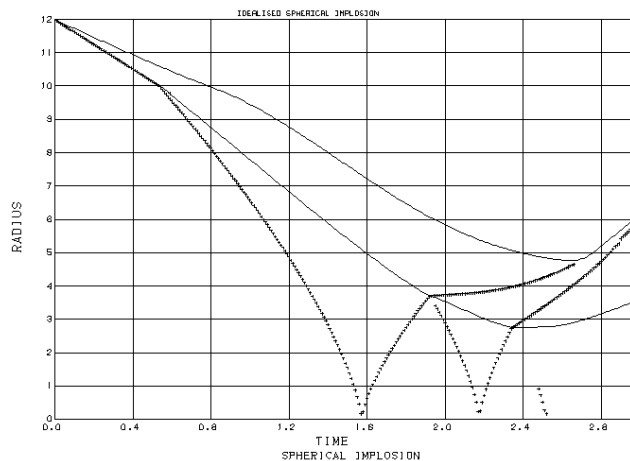
Fig. 2.1. Radius-time plot for the spherical implosion. Solid lines: interfaces. Dotted lines: shock positions.

The resulting radius-time plot obtained from a 1D Lagrangian calculation is shown **Fig.2.1** . RM instability occurs when the incident shock wave passes through the dense fluid/light fluid interface at t~0.5. This amplifies the initial perturbation. Turbulent mixing occurs towards the end of the implosion, when the interface decelerates, due to a combination of RT and RM instabilities.

3 THREE DIMENSIONAL SIMULATIONS

Three dimensional simulation is carried out for a sector of the sphere centered at the equator :

$$\frac{\pi}{2} - \frac{\pi}{8} < \theta, \phi < \frac{\pi}{2} + \frac{\pi}{8}$$

This reduces the computational resources needed and avoids the mesh singularity at θ=0. Lagrangian zoning is used in the radial direction. Moreover, regions of 1D Lagrangian zoning are used near the origin, $0 < r_0 < 2.5$, and near the outer boundary, $11.3 < r_0 < 12$, where r_0 denotes the initial radius. This overcomes the problem associated with the mesh singularity at the origin and also limits the 3D calculation to the region near the interface where mixing occurs. The number of meshes used in the r, θ and ϕ directions is as follows:

    Coarse mesh: 220 x 120 x 120
    Standard mesh: 440 x 240 x 240
    Fine mesh: 880 x 480 x 480

Random amplitude perturbations are initially applied to the light fluid/dense fluid interface. The power spectrum used is

$$P(k) = \begin{cases} C\,k^{-2} & \text{if} \quad k_{min} < k < k_{max} \\ 0 & \text{otherwise} \end{cases} \qquad \text{where } k_{min} = 2\pi/(2.0) \quad \text{and} \quad k_{max} = 2\pi/(4\Delta s)$$

Δs is the radial mesh width and the constant C is chosen so that the s.d of the perturbation is $\sigma = 0.0005$,

where $\sigma^2 = \int_{k_{min}}^{\infty} P(k)dk$
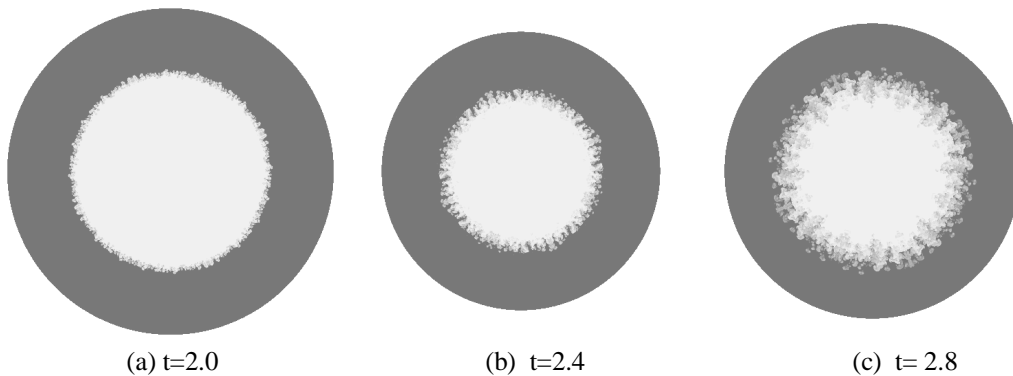
(a) t=2.0   (b) t=2.4   (c) t= 2.8
Fig. 3.1. 2D sections before, near and after maximum compression

Fig. 3.1 shows sections from the standard mesh simulation. The grey scale represents the volume fraction of the denser fluid. The sector used in the computation has been repeated eight times to produce a full circle. **Fig.3.2** shows plots of the turbulent mixing zone limits versus time for the three simulations. These limits are defined as the values of r where the dense fluid volume fraction averaged over θ and ϕ, $\bar{f}_1$, is equal to 0.01 and 0.99. The width of the mixing zone reduces slightly as the mesh is refined. However, the effect of mesh size is not very large and this suggests that the fine mesh calculation should give a good indication of the amount of mixing. A measure of the amount of mixing which is less susceptible to statistical fluctuations is given by the integral mix width, $W = \int \bar{f}_1 \bar{f}_2 \, dr$. This is plotted in **fig3.2** for the three simulations. Again, a slight reduction in mixing is indicated as the mesh is refined.
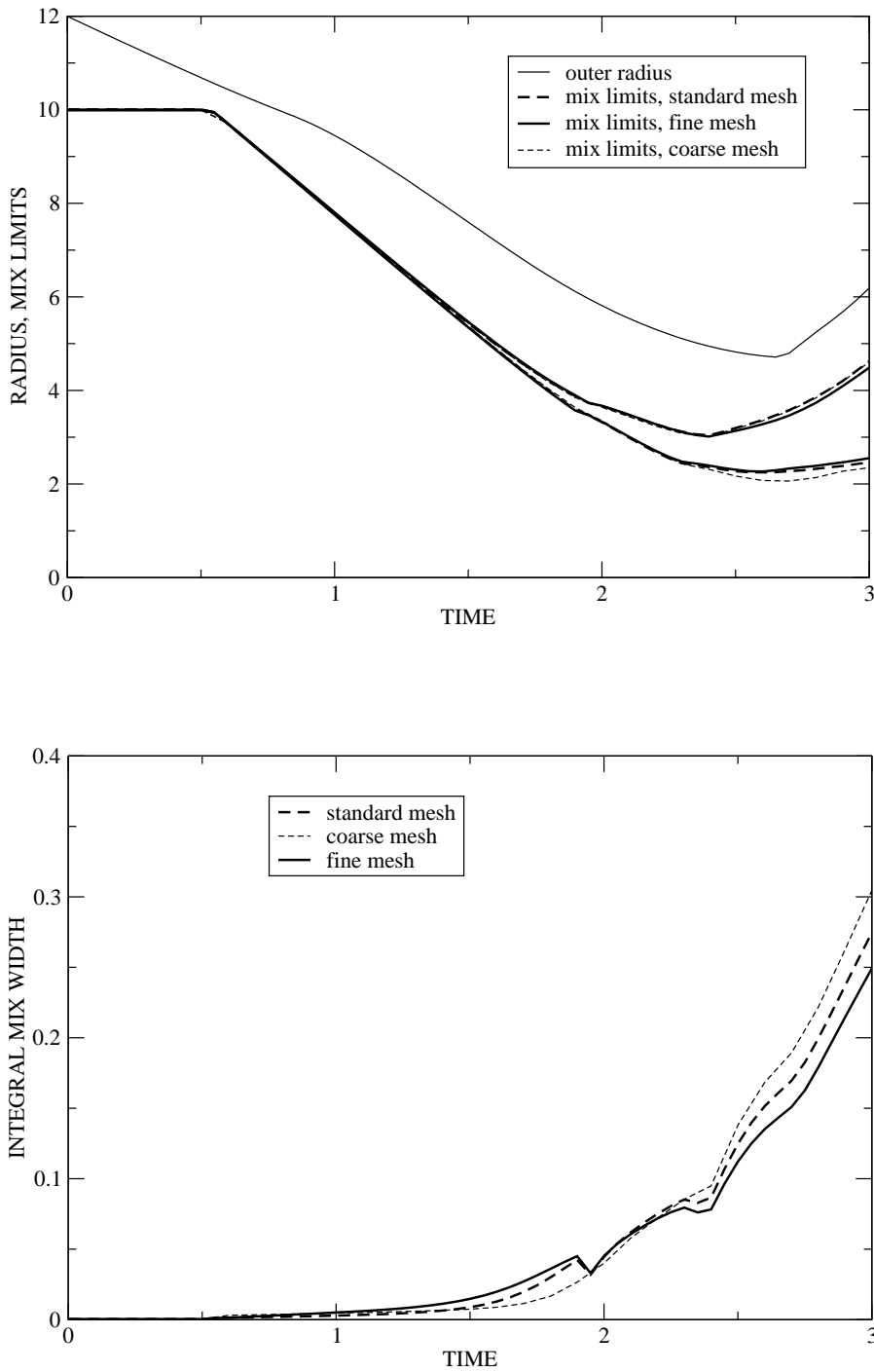
Fig. 3.2. Variation with time of mixing zone limits (top) and integral mix width (bottom).

Figs. 3.3 shows plots of the volume fraction and resolved turbulence kinetic energy , k, distributions at the end of the simulations. The latter is defined as

$$k = \tfrac{1}{2} \overline{\rho\{(u - \tilde{u})^2 + v^2 + w^2\}} / \overline{\rho}$$ where the overbar denotes the angular average

and $\tilde{u}$ is the mass-weighted mean radial velocity.

The effect of mesh size is relatively small. It is interesting to note that the resolved turbulence kinetic energy is similar for the standard and fine mesh.
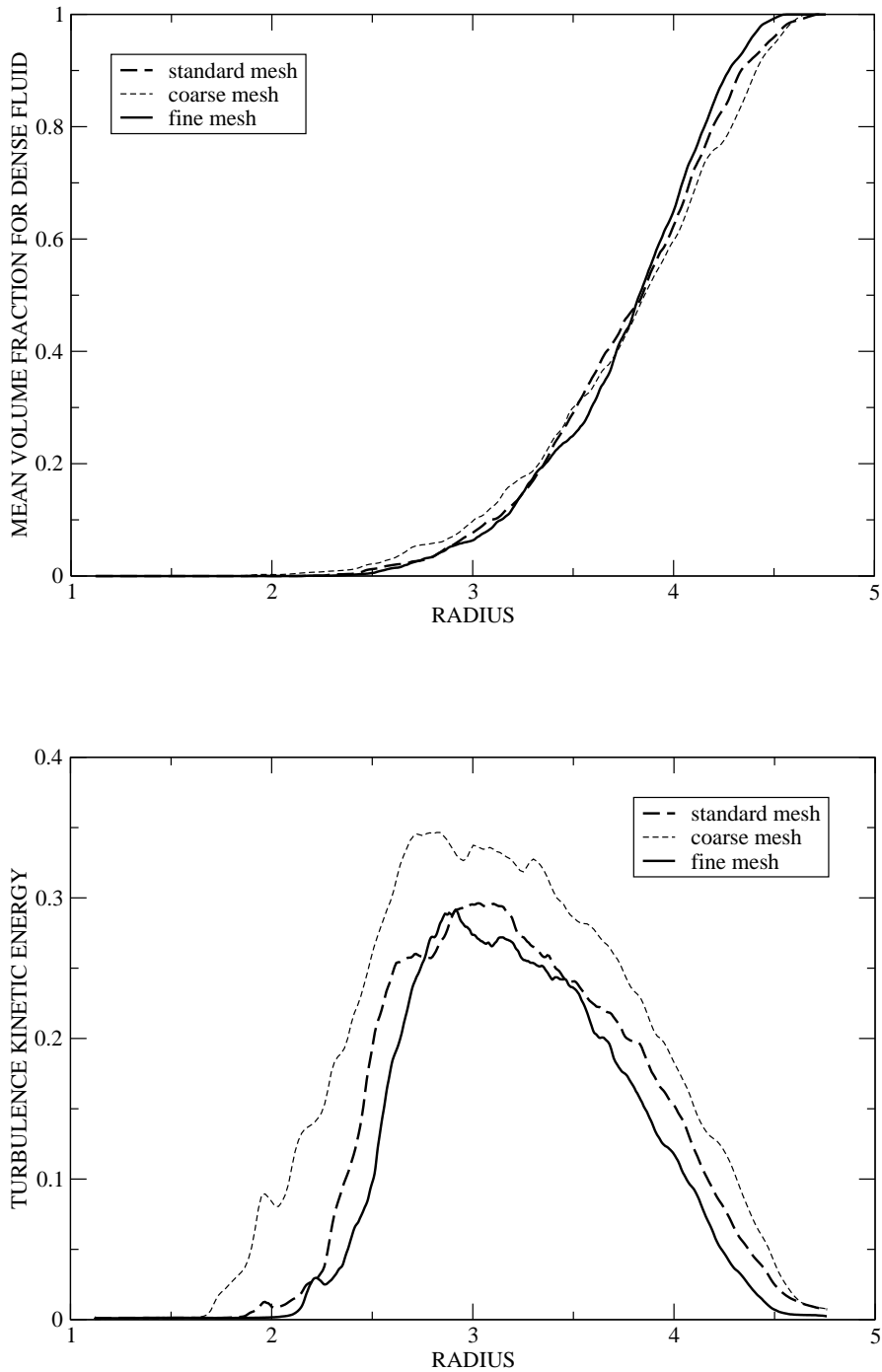
Fig. 3.3. Radial distributions at t=3: volume fraction, $\bar{f}_1$ (top), resolved turbulence kinetic energy, k (bottom).

4 COMPARISON WITH A BUOYANCY-DRAG MODEL

Results from the 3D simulations are used to calibrate or validate the engineering models which can be applied to real problems. To illustrate this approach, results are compared with a simple buoyancy-drag model of the type described in [3,4]. For incompressible fluids with densities $\rho_1 > \rho_2$, and for acceleration, g, the bubble (h_1) and spike (h_2) penetrations are given by:

$$(\rho_1 + \rho_2)\frac{dV_1}{dt} = B(\rho_1 - \rho_2)g - C_d \frac{\hat{\rho}_1 |V_1| V_1}{L} \; , \qquad (\rho_1 + \rho_2)\frac{dV_2}{dt} = B(\rho_1 - \rho_2)g - C_d \frac{\hat{\rho}_2 |V_2| V_2}{L} \; ,$$

$$\frac{dh_1}{dt} = V_1 \; , \qquad \frac{dh_2}{dt} = V_2 \; , \qquad L = h_1 \; , \quad \hat{\rho}_1 = \rho_1 + \rho_2 \; , \qquad \hat{\rho}_2 = \hat{\rho}_1 \left(\frac{\rho_2}{\rho_1}\right)^s \qquad (4.1)$$

There are three model coefficients, B, C_d and s. C_d is determined by matching post-shock RM mixing for which experiments indicate $h_1 \sim t^\theta$. This gives

$$\frac{dV_1}{dt} = -C_d \frac{V_1^2}{h_1} \quad \Rightarrow \quad C_d = \frac{1-\theta}{\theta}$$

B is then found by matching the RT growth rate for constant acceleration:-

$$h_1 = \alpha \frac{\rho_1 - \rho_2}{\rho_1 + \rho_2} g t^2 \quad \Rightarrow \quad B = 2\alpha(1 + 2C_d)$$

Finally, the coefficient s is chosen to give the required mixing zone asymmetry h_2/h_1 and is chosen here to give $h_2/h_1 = 2$ at $\rho_1/\rho_2 = 20$.

For compressible flow in a 1D Lagrangian Hydrocode, a few simple modifications are made [3]. The bubble and spike velocities V_1, V_2 are interpreted as velocities *relative* to the Lagrangian mesh. The bubble and spike positions X_1 , X_2 are given by:-

$$\frac{dX_1}{dt} = u_1 + V_1 \; , \qquad \frac{dX_2}{dt} = u_2 + V_2 \qquad \text{where } u_1 \text{ and } u_2 \text{ are the fluid velocities and the bubble and spike tips.}$$

The accelerations, g_1 and g_2 , used in the bubble and spike equations (4.1), are set to the fluid accelerations at the bubble and spike tips as obtained from the 1D calculation. Finally the initial values of h_1 and h_2 need to be set to an appropriate initial amplidute a_0.
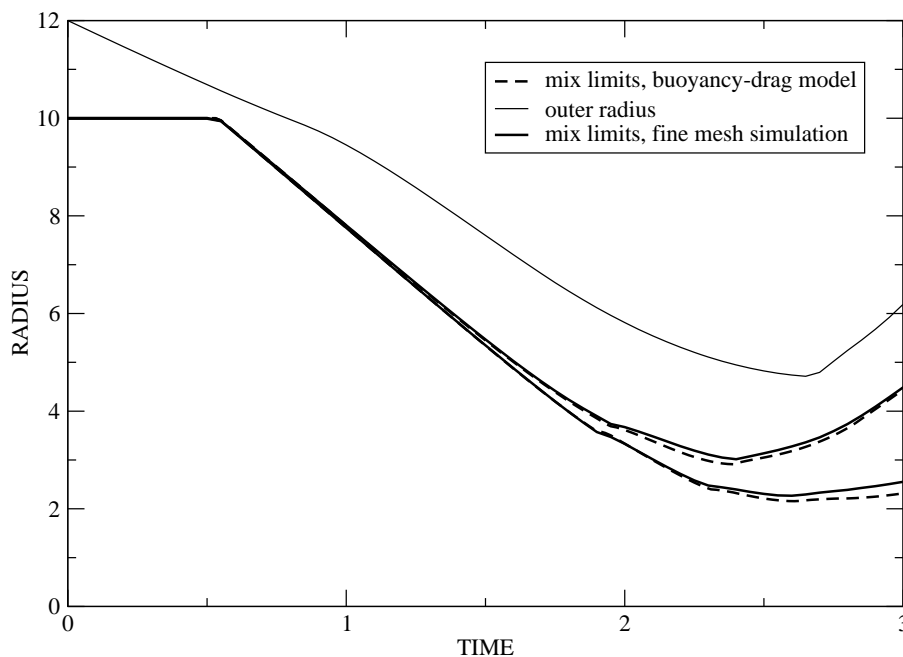
Fig. 4.1. Comparison of mixing zone limits: buoyancy-drag model versus 3D simulation.

For comparison with the 3D simulation, θ=0.3 is assumed [4] and α=0.07 is used, the high-end of the observed range. The model constants are then C_d=7/3, B=0.7933 and s=0.543. The initial amplitude a_0 is taken to be 0.001, twice the s.d of the initial perturbation. **Fig.4.1** then shows that there is a reasonable good match between the model and the fine mesh simulation.

The RT growth rate parameter, α, has a weak dependence on initial conditions [5] and θ, the RM power law coefficient should depend on the shape of the initial perturbation spectrum [6]. Moreover, the effect of spherical convergence is treated in a very simply way in the buoyancy-drag model. Hence there are concerns about the accuracy of the model. It is argued here that the only way to be confident that the simple buoyancy-drag model – or any more advanced engineering model – gives adequate results , is to compare with 3D simulation for simplified problems as shown here.

5 CONCLUSIONS

Accurate 3D numerical simulations can be performed for turbulent mixing in very simple spherical implosions. Higher resolution simulations are planned in the near future using the AWE Cray XT3 (8000 processing elements) to confirm mesh convergence.

3D simulation is impractical for many real problems. However, it is argued here that the results obtained from simplified 3D simulations, of the type shown here, are essential for calibrating and validating the engineering models which can be used for real applications.

© British Crown Copyright 2006/MOD

REFERENCES

[1]   Youngs, D.L. 1991. Three-dimensional numerical simulation of turbulent mixing by Rayleigh-Taylor instability. *Phys. Fluids*, **A3**, pp1312-1320.

[2]   Youngs, D.L. 1994, Numerical simulation of mixing by Rayleigh-Taylor and Richtmyer-Meshkov instabilities. *Laser and Particle Beams* **12**, pp725-750.

[3]   Hansom, J. C. V. et al. 1990. Radiation driven planar foil instability and mix experiments at the AWE HELEN laser. *Laser and Particle Beams*, **8**, pp51-71.

[4]   Dimonte, G. & Schnieder, M. 2000. Density ratio dependence of Rayleigh-Taylor mixing for sustained and impulsive accelerations. *Phys. Fluids*, **12**, pp304-321.

[5]   Dimonte, G. 2004. Dependence of turbulent Rayleigh-Taylor instability on initial perturbations. Phys. Rev. E69, 056305 (14 pages).

[6]   Inogamov, N.A. 1999.The role of Rayleigh-Taylor and Richtmyer-Meshkov instabilities in astrophysics : an introduction. *Astrophys. Space Phys*. **10**, pp1-335.

Index of authors

Paris, July 17-21 2006
FRANCE